

Quantum Science and Technology

Abolfazl Bayat
Sougato Bose
Henrik Johannesson *Editors*

Entanglement in Spin Chains

From Theory to Quantum Technology
Applications

 Springer

Quantum Science and Technology

Series Editors

Raymond Laflamme, University of Waterloo, Waterloo, ON, Canada

Daniel Lidar, University of Southern California, Los Angeles, CA, USA

Arno Rauschenbeutel, Vienna University of Technology, Vienna, Austria

Renato Renner, Institut für Theoretische Physik, ETH Zürich, Zürich, Switzerland

Jingbo Wang, Department of Physics, University of Western Australia, Crawley, WA, Australia

Yaakov S. Weinstein, Quantum Information Science Group, The MITRE Corporation, Princeton, NJ, USA

H. M. Wiseman, Griffith University, Brisbane, QLD, Australia

Section Editor

Maximilian Schlosshauer, Department of Physics, University of Portland, Portland, OR, USA

The book series Quantum Science and Technology is dedicated to one of today's most active and rapidly expanding fields of research and development. In particular, the series will be a showcase for the growing number of experimental implementations and practical applications of quantum systems. These will include, but are not restricted to: quantum information processing, quantum computing, and quantum simulation; quantum communication and quantum cryptography; entanglement and other quantum resources; quantum interfaces and hybrid quantum systems; quantum memories and quantum repeaters; measurement-based quantum control and quantum feedback; quantum nanomechanics, quantum optomechanics and quantum transducers; quantum sensing and quantum metrology; as well as quantum effects in biology. Last but not least, the series will include books on the theoretical and mathematical questions relevant to designing and understanding these systems and devices, as well as foundational issues concerning the quantum phenomena themselves. Written and edited by leading experts, the treatments will be designed for graduate students and other researchers already working in, or intending to enter the field of quantum science and technology.

Abolfazl Bayat • Sougato Bose •
Henrik Johannesson
Editors

Entanglement in Spin Chains

From Theory to Quantum Technology
Applications

 Springer

Editors

Abolfazl Bayat
Institute of Fundamental and Frontier
Sciences
University of Electronic Science and
Technology of China
Chengdu, China

Sougato Bose
Department of Physics and Astronomy
University College London
London, UK

Henrik Johannesson
Department of Physics
University of Gothenburg
Göteborg, Sweden

ISSN 2364-9054 ISSN 2364-9062 (electronic)
Quantum Science and Technology
ISBN 978-3-031-03997-3 ISBN 978-3-031-03998-0 (eBook)
<https://doi.org/10.1007/978-3-031-03998-0>

© The Editor(s) (if applicable) and The Author(s), under exclusive license to Springer Nature Switzerland AG 2022

This work is subject to copyright. All rights are solely and exclusively licensed by the Publisher, whether the whole or part of the material is concerned, specifically the rights of translation, reprinting, reuse of illustrations, recitation, broadcasting, reproduction on microfilms or in any other physical way, and transmission or information storage and retrieval, electronic adaptation, computer software, or by similar or dissimilar methodology now known or hereafter developed.

The use of general descriptive names, registered names, trademarks, service marks, etc. in this publication does not imply, even in the absence of a specific statement, that such names are exempt from the relevant protective laws and regulations and therefore free for general use.

The publisher, the authors, and the editors are safe to assume that the advice and information in this book are believed to be true and accurate at the date of publication. Neither the publisher nor the authors or the editors give a warranty, expressed or implied, with respect to the material contained herein or for any errors or omissions that may have been made. The publisher remains neutral with regard to jurisdictional claims in published maps and institutional affiliations.

This Springer imprint is published by the registered company Springer Nature Switzerland AG
The registered company address is: Gewerbestrasse 11, 6330 Cham, Switzerland

Preface

The study of spin chains has played a pivotal role in furthering our understanding of quantum many-body systems. Maybe most important, spin chain models have served as a theoretical laboratory for developing novel concepts and methods in this endeavor. A well-known example is the early attempt by Hans Bethe to diagonalize the Hamiltonian of the Heisenberg chain, bringing forth the *Bethe Ansatz* [1] and, as an offshoot, the notion of quantum integrability. Another example is the use of the transverse-field Ising chain as a paradigm for systems exhibiting quantum phase transitions [2]. More recently, work on the integer-spin Heisenberg chains [3] and their generalizations [4] has become a pillar of our conception of symmetry-protected topological quantum matter, as acknowledged by the 2016 Nobel Prize in Physics awarded Duncan Haldane.

Even more recently, the notions of quench dynamics and relaxation in integrable models, ergodicity, thermalization, as well as the breaking of ergodicity in certain circumstances have also been captured by spin chain models [5–8]. In short, by allowing for multiple strongly anharmonic quantum systems (spins) with local physical interactions, albeit within a reduced spatial dimensionality, spin chains can be a toy universe: much of the emergent principles of the physical world around us can be seen in a fully quantum setting through spin chains.

Entanglement is perhaps the most striking feature of general states of multiple interacting quantum particles. Thus, spin chains offer a most natural arena to study entanglement, as it provides states that should be physically accessible in nature, in equilibrium or through dynamics. Motivated by that, almost as soon as one of the earliest measures of quantum entanglement between two qubits in mixed states, namely the concurrence, was formulated by Wootters [9], he, and others [10, 11], applied it to ground and thermal states of spin chains. Using this measure, the behavior of entanglement at quantum phase transitions was first characterized [12, 13]. A practical application of spin chains as a quantum communication channel was also quantified using concurrence [14]. It was understood that to characterize the more global aspects of entanglement, one would need to calculate the von Neumann entropy [15] between the complementary parts of a many-body system [16, 17], and field theoretical methods to compute the same were formulated [18]. Entanglement

between non-complementary parts of a spin chain, as quantified by the negativity [19–21], were also studied [22–24].

Another reason for the renewed interest in spin chains in the last two decades has been their realization using experimental quantum simulators, based on, e.g., ultracold atoms [25], trapped ions [26, 27], superconducting circuits [28], electrons in solid state spin arrays [29, 30], and NMR systems [31]. This interest has been further fueled by a remarkable cross-fertilization between condensed matter physics and quantum information theory, some of which has been noted in the preceding paragraph. Work has flowed in two directions, mostly centered around the very concept of quantum entanglement: “How to better understand quantum many-body systems by exploiting various entanglement measures (with spin chains being arguably the simplest such systems)?” and, conversely, “How to use spin chains for practical purposes; analyzing, drafting, and eventually building working quantum information devices drawing on entanglement resources?” These are the two circles of problems addressed by the contributors to this volume.

We envision two categories of readers. First, the volume will be useful for graduate students at the start of their PhDs as an up to date and comprehensive review on the rich and highly diverse area that the field of entanglement in spin chains has now become. Secondly, active researchers knowledgeable in some aspects of the field can acquire a quick insight into other topics of interest to which they can potentially contribute. In this way, our volume is intended to serve as a bridge between condensed matter theorists, quantum information and quantum computation theorists, and experimentalists working on spin chain systems in various platforms.

The first four chapters are on the simplest scenario—that of static (equilibrium) phases of spin chains and the various measures of quantum entanglement one can use to understand their strongly correlated character. We begin with Chap. 1 by Thomale, which, after a pedagogic introduction to entanglement in spin chains, introduces one of the most fundamental quantities that characterize the many-body quantum correlated aspects of a spin chain, namely its entanglement spectrum. It is described how the entanglement spectrum, when computed for various cuts of a spin chain, in both position and momentum space, reveals aspects of a spin chain such as its topological features, as well as the nature of its low energy excitations. Next, in Chap. 2, we present a contribution by Li, Yu, and Lin, which again, starts pedagogically by introducing the concept of quantum phase transitions in spin chains, and the simplest quantities such as concurrence, entanglement entropy, quantum discord, and measures of quantum coherence, which can be used to characterize them and their quantumness. In Chap. 3, we include a contribution by Roy and Saleur which brings about the area of computation of entanglement entropies in conformal field theories (CFTs) through which spin chains are generically described near the critical point. In particular, spin chains may have boundaries and defects; the authors discuss the contribution of these to the entanglement entropy. Next, in Chap. 4, Laflorencie provides a contribution on entanglement measures for phases of disordered spin chains, starting with free fermion models and then advancing to interacting fermions and models of many-body localization.

We next proceed to include research on spin chains at the interface of quantum information processing and quantum computation. We start by Chap. 5, which contains a contribution by Wei, Raussendorf, and Affleck. This chapter first introduces the background on the AKLT models of gapped integer spin chains and important topics such as tensor networks and matrix product states in this context. Subsequently, their applications in the study of topological order and in measurement-based quantum computation are discussed among other topics. In Chap. 6, Banchi discusses the application of machine learning in measuring the entanglement negativity in spin chains. In this chapter, first an efficient method for estimating the moments of partially transposed density matrices is introduced, then, by feeding these moments into a neural network, the entanglement negativity is measured. Next, in Chap. 7, Amico, Korepin, Hamma, Giampaolo, and Franchini discuss the local convertibility in spin systems just by means of local operations and classical communication with respect to a given bipartition of the system. They show that the absence of differential local convertibility is an indicator of a higher computational power of the system's quantum phase, which is also usually connected with the existence of long-range entanglement, topological order, or edge states. In Chap. 8, Rattacaso, Passarelli, Lucignano, and Fazio address the inverse problem of finding a parent Hamiltonian for a given quantum state. In particular, the scaling of complexity for reconstructing the parent Hamiltonian with respect to the system size is investigated.

The emergence of quantum simulators in various physical platforms have put spin chains at the forefront of quantum simulation. Two chapters of the book are devoted to this important subject. In Chap. 9, Potter and Vasseur review the dynamics of quantum information in ensembles of random quantum circuits from a statistical mechanics perspective. The chapter first explores universal features for entanglement growth, operator spreading, thermalization, and chaos in unitary random quantum circuits. The text then goes through the dynamics of monitored random circuits and exhibits new types of measurement-induced phases and criticality. Proceeding to Chap. 10, Lunt, Richter, and Pal investigate the quantum simulation in noisy quantum circuits. Two classes of dynamics and their phase transitions are studied using random-circuit models. First, hybrid circuits consisting of unitary gates interspersed with nonunitary projective measurements are investigated. Second, random-circuit sampling experiments are considered and the usefulness of random quantum states for simulating quantum many-body dynamics are discussed.

The dynamics of spin chains have been the subject of many studies, and thus four chapters of this book have been dedicated to this topic. In Chap. 11, Bentsen, Daley, and Schachenmayer investigate the dynamics of entanglement in spin chains with long-range interaction. Several types of long-range interacting systems, such as sparse coupling graphs and spin chains with algebraically decaying interactions, are discussed. In Chap. 12, Lorenzo, Plastina, Consiglio, and Apollaro provide a formalism for describing quantum state transfer and multi-qubit entanglement distribution and generation in spin networks. Next, in Chap. 13, Papic presents a pedagogical introduction to weak ergodicity breaking phenomena, including Hilbert space fragmentation and quantum many-body scars, through the lens of quantum

entanglement. In such systems, while most initial states quickly equilibrate, certain initial conditions may lead to slow relaxation. In Chap. 14, Murciano, Alba, and Calabrese provide a conformal field theory perspective to the quench dynamics of the moments of the partially transposed density matrices and their corresponding Renyi negativities. While these results are generic to interacting integrable systems, numerical simulations are provided for free-fermionic and bosonic lattices.

Thanks to the advancement of quantum technologies, spin chains can now be tested in several experimental platforms. The first such system discussed in the book is cold atoms. In Chap. 15, Sengupta provides a review on accessible phases and the dynamics of ultracold bosons in tilted optical lattices. Quenches, ramps, and periodic drives for inducing Floquet dynamics are investigated in this chapter. Next, in Chap. 16, Cappellaro, Peng, and Ramanathan focus on NMR systems for realization of spin chains. In particular, Hamiltonian engineering tools and metrics of correlation and entanglement are discussed through several paradigmatic examples of integrable and non-integrable dynamics in large nuclear spin systems. Finally, in Chap. 17, Nichol provides a review on the fundamental aspects of semiconductor quantum dots and the Heisenberg exchange coupling that occurs between neighboring quantum dots. Such couplings allow for quantum information processing, quantum state transfer, and the simulation of spin-chain dynamics.

Chengdu, China
London, UK
Göteborg, Sweden

Abolfazl Bayat
Sougato Bose
Henrik Johannesson

References

1. H. Bethe, *Z. Physik* **71**, 205 (1931)
2. P. Pfeuty, *Ann. Phys.* **57**, 79 (1970)
3. F.D.M. Haldane, *Phys. Lett.* **93A**, 464 (1983); *Phys. Rev. Lett.* **50**, 1153 (1983)
4. I. Affleck, T. Kennedy, E. Lieb, H. Tasaki, *Phys. Rev. Lett.* **59**, 799 (1987); *Commun. Math. Phys.* **115** (1988)
5. K. Sengupta, S. Powell, S. Sachdev, *Phys. Rev. A* **69**, 053616 (2004)
6. P. Calabrese, F.H.L. Essler, M. Fagotti, *Phys. Rev. Lett.* **106**, 227203 (2011)
7. M. Žnidarič, T. Prosen, P. Prelovšek, *Phys. Rev. B* **77**, 064426 (2008)
8. A. Pal, D.A. Huse, *Phys. Rev. B* **82**, 174411 (2010)
9. W.K. Wootters, *Phys. Rev. Lett.* **80**, 2245 (1998)
10. K.M. O'Connor, W.K. Wootters, *Phys. Rev. A* **63**, 052302 (2001)
11. M.C. Arnesen, S. Bose, V. Vedral, *Phys. Rev. Lett.* **87**, 017901 (2001)
12. A. Osterloh, L. Amico, G. Falci, R. Fazio, *Nature* **416**, 608 (2002)
13. T.J. Osborne, M.A. Nielsen, *Phys. Rev. A* **66**, 032110 (2002)
14. S. Bose, *Phys. Rev. Lett.* **91**, 207901 (2003)
15. S. Popescu, D. Rohrlich, *Phys. Rev. A* **56**, R3319(R) (1997)
16. G. Vidal, J.I. Latorre, E. Rico, A. Kitaev, *Phys. Rev. Lett.* **90**, 227902 (2003)

17. B.-Q. Jin, V.E. Korepin, *J. Stat. Phys.* **116**, 79 (2004)
18. P. Calabrese, J. Cardy, *J. Stat. Mech.* P06002 (2004)
19. K. Zyczkowski, P. Horodecki, A. Sanpera, M. Lewenstein, *Phys. Rev. A* **58**, 883 (1998)
20. J. Lee, M. Kim, Y. Park, S. Lee, *J. Mod. Opt.* **47**, 2151 (2000)
21. G. Vidal, R.F. Werner, *Phys. Rev. A* **65**, 032314 (2002)
22. H. Wichterich, J. Molina-Vilaplana, S. Bose, *Phys. Rev. A* **80**, 010304(R) (2009)
23. A. Bayat, P. Sodano, S. Bose, *Phys. Rev. B* **81**, 064429 (2010)
24. P. Calabrese, J. Cardy, E. Tonni, *Phys. Rev. Lett.* **109**, 130502 (2012)
25. T. Fukuhara, P. Schauß, M. Endres, S. Hild, M. Cheneau, I. Bloch, C. Gross, *Nature* **502**, 76 (2013)
26. P. Richerme, Z.-X. Gong, A. Lee, C. Senko, J. Smith, M. Foss-Feig, S. Michalakis, A.V. Gorshkov, C. Monroe, *Nature* **511**, 198 (2014)
27. P. Jurcevic, B.P. Lanyon, P. Hauke, C. Hempel, P. Zoller, R. Blatt, C.F. Roos, *Nature* **511**, 202 (2014)
28. R. Barends, et. al., *Nature* **534**, 222 (2016)
29. H. Qiao, Y.P. Kandel, K. Deng, S. Fallahi, G.C. Gardner, M.J. Manfra, E. Barnes, J.M. Nichol, *Phys. Rev. X* **10**, 031006 (2020)
30. C.J. van Diepen, T.-K. Hsiao, U. Mukhopadhyay, C. Reichl, W. Wegscheider, L.M.K. Vandersypen, *Phys. Rev. X* **11**, 041025 (2021)
31. M. Steffen, W. van Dam, T. Hogg, G. Breyta, I. Chuang, *Phys. Rev. Lett.* **90**, 067903 (2003)

Contents

Entanglement Spectra of Spin Chains	1
Ronny Thomale	
Detecting Quantum Phase Transitions in Spin Chains	13
Yan-Chao Li, Wing Chi Yu, and Hai-Qing Lin	
Entanglement Entropy in Critical Quantum Spin Chains with Boundaries and Defects	41
Ananda Roy and Hubert Saleur	
Entanglement Entropy and Localization in Disordered Quantum Chains	61
Nicolas Laflorencie	
Some Aspects of Affleck–Kennedy–Lieb–Tasaki Models: Tensor Network, Physical Properties, Spectral Gap, Deformation, and Quantum Computation	89
Tzu-Chieh Wei, Robert Raussendorf, and Ian Affleck	
Machine Learning-Assisted Entanglement Measurement in Quantum Many-Body Systems	127
Leonardo Banchi	
Local Convertibility in Quantum Spin Systems	151
Luigi Amico, Vladimir Korepin, Alioscia Hama, Salvatore Marco Giampaolo, and Fabio Franchini	
Optimal Parent Hamiltonians for Many-Body States	189
Davide Rattacaso, Gianluca Passarelli, Procolo Lucignano, and Rosario Fazio	
Entanglement Dynamics in Hybrid Quantum Circuits	211
Andrew C. Potter and Romain Vasseur	

Quantum Simulation Using Noisy Unitary Circuits and Measurements ..	251
Oliver Lunt, Jonas Richter, and Arijeet Pal	
Entanglement Dynamics in Spin Chains with Structured Long-Range Interactions	285
Gregory S. Bentsen, Andrew J. Daley, and Johannes Schachenmayer	
Quantum Map Approach to Entanglement Transfer and Generation in Spin Chains	321
Salvatore Lorenzo, Francesco Plastina, Mirko Consiglio, and Tony J. G. Apollaro	
Weak Ergodicity Breaking Through the Lens of Quantum Entanglement	341
Zlatko Papić	
Quench Dynamics of Rényi Negativities and the Quasiparticle Picture ...	397
Sara Murciano, Vincenzo Alba, and Pasquale Calabrese	
Phases and Dynamics of Ultracold Bosons in a Tilted Optical Lattice	425
Krishnendu Sengupta	
NMR Experimental Study of Out-of-Equilibrium Spin Models	459
Paola Cappellaro, Pai Peng, and Chandrasekhar Ramanathan	
Quantum-Dot Spin Chains	505
John M. Nichol	
Index	539

Editors and Contributors

About the Editors

Abolfazl Bayat is Professor of Physics at the University of Electronic Science and Technology of China. He completed his PhD in 2008 from Sharif University of Technology in Iran and then held postdoctoral positions at the University of Ulm in Germany and University College London in the UK. His research interest lies at the intersection of quantum technologies and condensed matter physics. Currently, his research activities focus on quantum simulation of strongly correlated systems and many-body quantum sensors.

Sougato Bose is Professor of Physics at University College London. He obtained his master's degree from the Indian Institute of Technology, Kharagpur, India in 1996, and his PhD from Imperial College, London, in 2000. He held postdoctoral positions in Oxford and Caltech. A primary area of his research has been in the characterization and exploitation of entanglement in many-body spin systems, for which he was awarded the Maxwell Medal and Prize of the Institute of Physics, UK, in 2008. Additional interests involve quantum simulators, quantum optics, and foundational work on the quantum nature of large masses and gravity.

Henrik Johannesson is Professor of Theoretical Physics at the University of Gothenburg. He gained his undergraduate degree from Stockholm University in 1980 and received a PhD from Rutgers University in 1985. He has held postdoctoral positions at the University of California at San Diego and Chalmers University of Technology. Johannesson's research focus is on correlation effects in low-dimensional quantum matter, topological phases, and quantum systems out of equilibrium.

Contributors

Ian Affleck Department of Physics and Astronomy, University of British Columbia, Vancouver, BC, Canada

Stewart Blusson Quantum Matter Institute, University of British Columbia, Vancouver, BC, Canada

Vincenzo Alba Institute for Theoretical Physics, Universiteit van Amsterdam, Amsterdam, The Netherlands

Dipartimento di Ingegneria Industriale, Università degli Studi di Salerno, Fisciano, Salerno, Italy

Dipartimento di Fisica, Università di Pisa, INFN Sezione di Pisa Largo Bruno, Pisa, Italy

Luigi Amico Quantum Research Centre, Technology Innovation Institute, Abu Dhabi, UAE

Centre for Quantum Technologies, National University of Singapore, Singapore, Singapore

On leave from Dipartimento di Fisica e Astronomia, Catania, Italy

LANEF 'Chaire d'excellence', Université Grenoble-Alpes and CNRS, Grenoble, France

Tony J. G. Apollaro Department of Physics, University of Malta, Msida, Malta

Leonardo Banchi Department of Physics and Astronomy, University of Florence, and INFN Sezione di Firenze, Florence, Italy

Gregory S. Bentsen Martin A. Fisher School of Physics, Brandeis University, Waltham, MA, USA

Pasquale Calabrese SISSA and INFN Sezione di Trieste, Trieste, Italy

International Centre for Theoretical Physics (ICTP), Trieste, Italy

Paola Cappellaro Massachusetts Institute of Technology, Cambridge, MA, USA

Mirko Consiglio Department of Physics, University of Malta, Msida, Malta

Andrew J. Daley Department of Physics and SUPA, University of Strathclyde, Glasgow, UK

Fabio Franchini Ruđer Bošković Institute, Bijenička cesta 54, Zagreb, Croatia

Rosario Fazio Dipartimento di Fisica "E. Pancini", Università di Napoli "Federico II", Napoli, Italy

Salvatore Marco Giampaolo Ruđer Bošković Institute, Bijenička cesta 54, Zagreb, Croatia

Alioscia Hamma Physics Department, University of Massachusetts Boston, Boston, MA, USA

Vladimir Korepin C. N. Yang Institute for Theoretical Physics, Stony Brook University, Stony Brook, NY, USA

Nicolas Laflorencie Laboratoire de Physique Théorique, Université de Toulouse, CNRS, UPS, Toulouse, France

Donostia International Physics Center, San Sebastián, Spain

Yan-Chao Li Center of Materials Science and Optoelectronics Engineering, College of Materials Science and Opto-Electronic Technology, University of Chinese Academy of Sciences, Beijing, China

Beijing Computational Science Research Center, Beijing, China

Hai-Qing Lin Beijing Computational Science Research Center, Beijing, China

Department of Physics, Beijing Normal University, Beijing, China

Salvatore Lorenzo Dipartimento di Fisica e Chimica, Università di Palermo, Palermo, Italy

Procolo Lucignano Dipartimento di Fisica “E. Pancini”, Università di Napoli “Federico II”, Napoli, Italy

Oliver Lunt School of Physics and Astronomy, University of Birmingham, Birmingham, UK

Sara Murciano SISSA and INFN Sezione di Trieste, Trieste, Italy

John M. Nichol Department of Physics and Astronomy, University of Rochester, Rochester, NY, USA

Arijeet Pal Department of Physics and Astronomy, University College London, London, UK

Zlatko Papić School of Physics and Astronomy, University of Leeds, Leeds, UK

Gianluca Passarelli CNR-SPIN, Napoli, Italy

Francesco Plastina Dipartimento Fisica, Università della Calabria, Rende, Malta

Pai Peng Massachusetts Institute of Technology, Cambridge, MA, USA

Andrew C. Potter Department of Physics and Astronomy, and Quantum Matter Institute, University of British Columbia, Vancouver, BC, Canada

Chandrasekhar Ramanathan Dartmouth College, Hanover, NH, USA

Davide Rattacaso Dipartimento di Fisica “E. Pancini”, Università di Napoli “Federico II”, Napoli, Italy

Robert Raussendorf Department of Physics and Astronomy, University of British Columbia, Vancouver, BC, Canada

Jonas Richter Department of Physics and Astronomy, University College London, London, UK

Ananda Roy Department of Physics and Astronomy, Rutgers University, Piscataway, NJ, USA

Hubert Saleur Institut de Physique Théorique, Paris Saclay University, CEA, CNRS, Gif-sur-Yvette, France

Department of Physics and Astronomy, University of Southern California, Los Angeles, CA, USA

Johannes Schachenmayer CNRS, ISIS (UMR 7006), and Université de Strasbourg, Strasbourg, France

Krishnendu Sengupta School of Physical Sciences, Indian Association for the Cultivation of Science, Jadavpur, India

Ronny Thomale Institute for Theoretical Physics and Astronomy, University of Würzburg, Würzburg, Germany

Romain Vasseur Department of Physics, University of Massachusetts, Amherst, MA, USA

Tzu-Chieh Wei C. N. Yang Institute for Theoretical Physics and Department of Physics and Astronomy, State University of New York at Stony Brook, Stony Brook, NY, USA

Wing Chi Yu Department of Physics, City University of Hong Kong, Kowloon, Hong Kong

City University of Hong Kong Shenzhen Research Institute, Shenzhen, China

Entanglement Spectra of Spin Chains



Ronny Thomale

Abstract We discuss the use of entanglement spectra in analysing spin chains. First discovered in the context of many-body ground states in fractional quantum Hall effect, entanglement spectra facilitate the resolution of the phenomenology of a spin chain. In particular, this includes its nature of low-energy excitations and topological classification.

1 Entanglement Spectra of Many-Body Ground States

Quantum entanglement encodes the essence of quantum mechanical phenomenology. It allows to describe aspects of interconnectivity of quantum systems which go beyond the notion of correlations and sets the basis for potential future technological applications of quantum systems for communication, information processing and computation. Entanglement also helps a great deal to analyse and classify quantum systems. This particularly applies to the entanglement entropy, which has appeared as a useful tool in a broad and diverse range of theoretical physics [4, 17]. By comparison, the computation of entanglement spectra is a rather new approach added to the theorist's toolkit to analyse quantum many-body systems, which was initiated in the context of fractional quantum Hall effect [14]. There, an important observation was made for the entanglement analysis of a fractional quantum Hall ground state with an excitation gap on a spherical geometry [8]. The entanglement spectrum resulting from a decomposition of the Hilbert space into an upper and lower hemisphere allowed to read off the state counting and quantum numbers of elementary edge excitations the same quantum Hall state would exhibit on a disc geometry, which thus gives way to resolving the topological order of a given ground state wave function. The analysis of entanglement spectra has ever since become an indispensable approach to analyse wave functions in different many-body contexts,

R. Thomale (✉)

Institute for Theoretical Physics and Astronomy, University of Würzburg, Würzburg, Germany
e-mail: rthomale@physik.uni-wuerzburg.de

© The Author(s), under exclusive license to Springer Nature Switzerland AG 2022

A. Bayat et al. (eds.), *Entanglement in Spin Chains*, Quantum Science and Technology, https://doi.org/10.1007/978-3-031-03998-0_1

including spin chains. Among other pioneering findings resulting from there, it is the perspective of entanglement spectra which has allowed for a fairly complete understanding of interacting topological phases in one spatial dimension [21].

The purpose of this chapter is to introduce the reader to the principal topic, through discussing a selection of key ideas that have proven pivotal to our today's understanding of entanglement spectra in spin chains. This synopsis does neither intend to be complete nor self-contained but hopes to encourage the reader to deepen their understanding by following up on it via the additional literature within and beyond the chapter. The chapter is organised as follows. In Sect. 2, we provide a principal definition of entanglement spectra for the context in which we intend to discuss it. This means that we highlight those Hilbert space decompositions, and their descendant entanglement spectra, which so far have been considered in the context of spin chains. In order to present the material in a concise way, it proves useful to classify spin chains by the existence or absence of an excitation gap. Section 3 focusses on entanglement spectra for gapped spin chains, which is explicated by a discussion of the Haldane phase from multiple perspectives. Section 4 discusses entanglement spectra for gapless spin chains at the example of the spin-1/2 Heisenberg chain. In Sect. 5, we conclude that entanglement spectra will continue to establish a vital tool for future research on spin chains.

It is assumed that the reader will be triggered by many interesting connections to other chapters in this book. In order to avoid overlap, we intend to sharply constrain ourselves to the topic of entanglement spectra, with only occasional highlighting of connections drawn to other subfields of quantum spin chains.

2 Decomposition of Spin Chain Hilbert Spaces

In the following, we assume a zero-temperature density operator ρ , which is determined by a spin chain ground state $|\Psi_0\rangle$, i.e., $\rho = |\Psi_0\rangle\langle\Psi_0|$. Assuming a tensor product decomposition of the spin chain Hilbert space into a region A and B according to $\mathcal{H} = \mathcal{H}_A \times \mathcal{H}_B$, we define the reduced density matrix

$$\rho_A := \text{Tr}_B \rho. \quad (1)$$

Since Tr_B represents a partial trace, ρ_A is not invariant under a unitary transformation of $|\Psi_0\rangle$ in \mathcal{H} . Stated differently, ρ_A is basis-dependent and hence crucially depends on how \mathcal{H} is decomposed. Assuming a Schmidt decomposition according to

$$|\Psi_0\rangle = \sum_{\alpha} \lambda_{\alpha} |\alpha A\rangle |\alpha B\rangle, \quad (2)$$

the eigenvalues of ρ_A are λ_α^2 . Following a form-invariant Boltzmann-type definition according to ρ , we define an entanglement Hamiltonian

$$\rho_A =: \exp(-H_E), \quad (3)$$

where the temperature scale is set to unity. The entanglement spectrum $\{\xi_\alpha\}$ is defined as the spectrum of H_E , which relates to the spectrum of ρ_A , and hence the Schmidt decomposition (2), via $\xi_\alpha = -2\log\lambda_\alpha$.

Since the early days of quantum entanglement, these quantities have been known and appear in any definition of quantum information measures such as the entanglement entropy $S_A = -\text{Tr}\rho_A \log\rho_A$, which will likely be extensively covered in other chapters of this book. Furthermore, properties of the entanglement spectrum for non-interacting problems have likewise been studied previously [18]. The key insight put forward in [14] in the context of quantum many-body physics is to analyse the block diagonal structure or, equivalently, the symmetries of ρ_A . Obviously, this depends on the chosen cut as much as on $|\Psi_0\rangle$. If a real space cut is chosen and $|\Psi_0\rangle$ is a spin singlet, we find $[S_A^\gamma, \rho_A] = 0$, where $S_A^\gamma = \sum_{i \in A} S_i^\gamma$, $\gamma = x, y, z$, which yields an $SU(2)$ multiplet structure $[S_A^2, \rho_A] = 0$, characterised by the eigenvalues $s_A(s_A + 1)$. For a finite-size spin chain and periodic boundary conditions (Fig. 1a up), the decomposition of a compact state always yields two bonds subject to the subdivision into regions A and B. (Note that this will constrain s_A to $SO(3)$ multiplets.) For a non-compact semi-infinite real space cut (Fig. 1a down), the decomposition reduces to a single bond. In general, all those symmetries of $|\Psi_0\rangle$ are projectively inherited by ρ_A that allow for a symmetry operator decomposition which is commensurate with the chosen cut. For the rung cut of a spin ladder (Fig. 1b), for instance, all symmetries are accordingly retained that concern one individual chain of the ladder. In particular, if we assume a spin ladder ground state

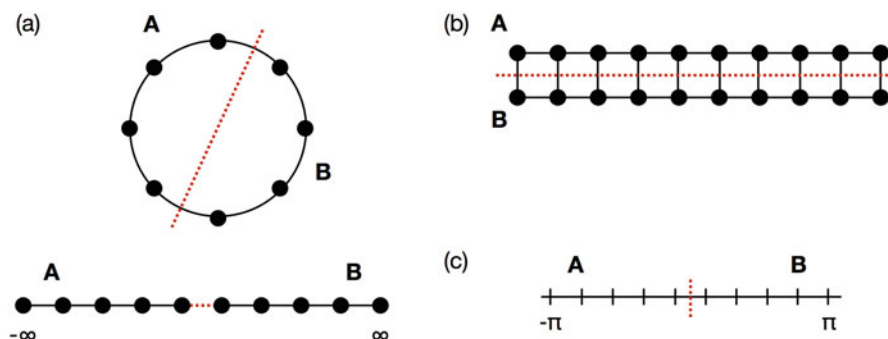


Fig. 1 Typical entanglement cuts for spin chains. (a) Real space cut. For finite-size and periodic boundary conditions, the partition into subregions yields two cuts (marked dashed red). In a quasi-infinite real space representation such as for matrix product states, a single cut is performed. (b) Rung cut. A spin ladder ribbon is divided into subregions of individual chains. (c) Momentum cut. All momentum modes are split into two different subregions of momenta

for periodic boundary conditions, this includes translation symmetry along the spin chain. For any momentum cut (Fig. 1c) of a spin chain, the details of which will be described later, a representation of $|\Psi_0\rangle$ is required in terms of momentum modes, which are then grouped into different regions A and B .

There are in principle several other entanglement cuts which have been used in the context of many-body ground states and which might acquire scientific relevance for spin chains in the future. Among others, this includes the particle cut [26], where a reduced density matrix is reached by integrating out particle modes while leaving the single particle Hilbert space unspoiled. Such a particle cut would promise a particular use in combination with the momentum cut.

3 Gapped Spin Chains

For a spin chain spectrum with an energy gap, $\rho = |\Psi_0\rangle\langle\Psi_0|$ is rigorously defined in the thermodynamic limit. Furthermore, due to locality and the exponential decay of correlation functions due to the gap, a real space cut suggests itself as a natural choice.

In order to elucidate the power of an entanglement spectrum analysis of gapped spin chains, we choose the Haldane phase as a textbook example to illustrate the concepts. The Haldane phase [7, 9] found its first realisation in $SU(2)$ symmetric spin-1 chains and is a symmetry protected topological phase in one spatial dimension [24]. Before a rigorous entanglement spectral analysis had been formulated, the necessary and sufficient symmetry conditions for the Haldane phase had not been completely resolved. The issue had been that while certain topological classifications such as through a non-local string order parameter [13] proved to be the correct indicator in the presence of certain other supporting symmetries, the parametric realisation range of the Haldane phase exceeded the one of the string order. Similarly, the Haldane phase seemed to transcend the regime in which a ground state realisation of the Haldane phase for open boundary conditions would show degenerate edge states in line with the bulk-boundary correspondence of topological phases.

We start by employing a Haldane phase ground state realisation from the bilinear-biquadratic (bb) $SU(2)$ spin-1 Hamiltonian class $H_{\text{bb}} = \sum_i \cos\theta \mathbf{S}_i \mathbf{S}_{i+1} + \sin\theta (\mathbf{S}_i \mathbf{S}_{i+1})^2$, where the Haldane phase is found for $-\pi/4 \leq \theta \leq \pi/4$. As shown in Fig. 2a and explained above, the entanglement spectrum reveals an $SO(3)$ multiplet structure according to s_A [30]. The dominant entanglement weight is carried by a singlet and a triplet state, while the rest of the entanglement levels appear to be separated by a gap. Note that for the AKLT point [1], the triplet and singlet level would be the only non-zero weights λ , i.e., the only finite entanglement spectral eigenvalues.

If we were to diagonalise H_{bb} on an open chain, we would obtain a similar low-energy spectrum. By analogy to the lessons from entanglement spectra for fractional quantum Hall effect, this observation provokes the hypothesis that the entanglement

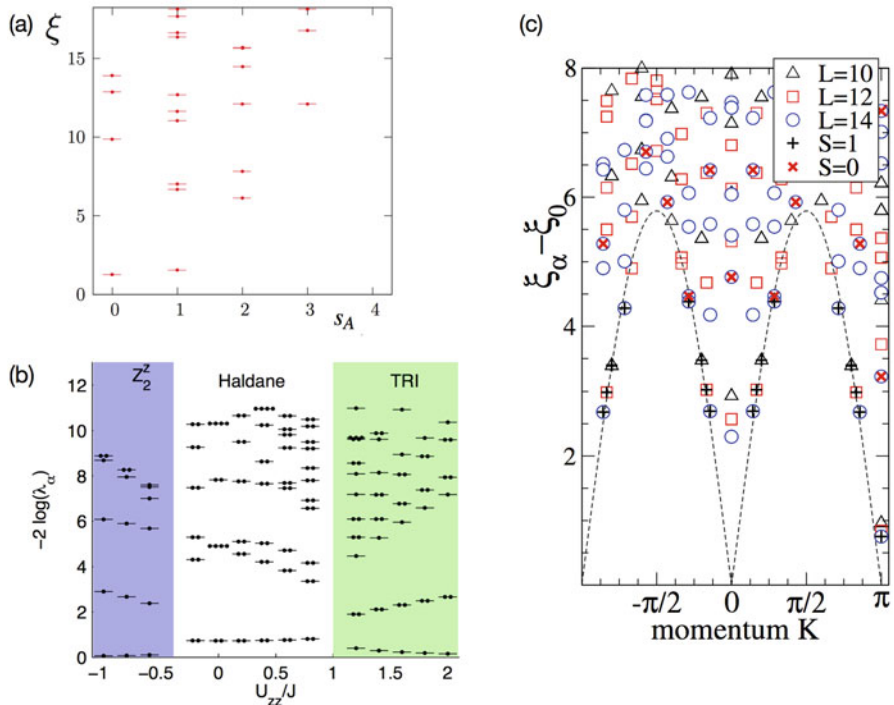


Fig. 2 Entanglement cuts in the Haldane phase. (a) Finite-size real space cut for an $N = 12$ site ground state of H_{bb} against the multiplet index s_A [30]. (b) Semi-infinite real space cut of H_{ju} as a function of U_{zz}/J [21]. (c) Rung cut for a ground state of H_{sl} plotted against the chain momentum and offset by the lowest entanglement level ξ_0 [20]

spectrum of a spin-1 chain ground state for periodic boundary conditions relates to the low-energy spectrum of the same Hamiltonian for open boundaries [23]. More careful finite-size scaling shows that this is indeed true. For a topological phase with dimensionally reduced edge mode excitations, it is suggestive that such a real space entanglement cut induces entanglement eigenstates of dominant weight λ (and hence the lowest value ξ) which feature related properties to energy edge modes of the open chain.

Further information beyond the compact real space cut can be retrieved from a semi-infinite real space cut [21]. This is conveniently obtained through a matrix product state (MPS) representation of $|\Psi_0\rangle$:

$$|\Psi_0\rangle = \lim_{N \rightarrow \infty} \sum_{\{m\}} \text{Tr} \Gamma_{m_1} \Lambda \Gamma_{m_2} \Lambda \dots \Gamma_{m_N} \Lambda |m_1 m_2 \dots m_N\rangle, \quad (4)$$

where m_i denotes the $S_i^z = -1, 0, 1$ eigenvalue for a spin-1 chain. A gapped spin chain allows for a finite matrix representation of Γ_{m_i} and Λ , where the eigenvalues

of Λ are the λ_α 's in (2). Furthermore, in anticipation of resolving the Haldane phase according to its core topological structure free from overlaying superfluous symmetries, we investigate the MPS ground state representation of the Hamiltonian $H_{\text{ju}} = \sum_i JS_i \mathbf{S}_{i+1} + U_{zz} (S_i^z)^2$. Here, starting from the spin-1 Heisenberg chain, the U_{zz} term breaks the $SU(2)$ symmetry. (A complete symmetry analysis with additional terms is discussed in [21, 22]). By monitoring the eigenvalues of Γ , the semi-infinite real space cut (Fig. 1a down) is realised. The core insight of [21] is that the entanglement spectrum provides us with a necessary and sufficient criterion for the Haldane phase: as visible in Fig. 2b, the Haldane phase is characterised by an even multiplicity of Schmidt eigenvalues for the entire entanglement spectrum. This roots in the fact that the irreducible projective symmetry representations in the Haldane phase must be higher dimensional, which accordingly brings about the spectral degeneracy. As a side remark, one readily observes that departing from $U_{zz}/J = 0$, the breaking of $SU(2)$ symmetry shows no spectral relevance for the Haldane phase. It is already suggestive from here that the successful entanglement spectrum classification of the Haldane phase generalises to other gapped topological phases in one dimension [31].

Spin chain spectra can also emerge as the entanglement Hamiltonian of spin ladders [20]. We investigate a spin-1/2 ladder ribbon given by the Hamiltonian $H_{\text{sl}} = \sum_i J_{\parallel} (\mathbf{S}_i^I \mathbf{S}_{i+1}^I + \mathbf{S}_i^{II} \mathbf{S}_{i+1}^{II}) + J_{\perp} \mathbf{S}_i^I \mathbf{S}_i^{II}$, where J_{\parallel} (J_{\perp}) denotes the coupling along the chains (between the chains I and II). For $J_{\parallel} > 0$ and $J_{\perp} < 0$, this yields another realisation of the Haldane phase. Performing a rung cut according to Fig. 1c, along with spin rotation symmetry, the reduced density matrix keeps translation symmetry along the chain, which allows the resolution of the entanglement spectrum with respect to chain momentum (Fig. 2c). Both in terms of spectral and eigenstate structure, the entanglement Hamiltonian resulting from the rung cut of the ground state of H_{sl} is similar to the energy spectrum of a spin-1/2 Heisenberg spin chain.

4 Gapless Spin Chains

Our assumed hitherto definition of ρ as a projector onto a spin chain ground state appears particularly reasonable for the case of a gapped spin chain in the zero-temperature limit. It is less transparent how to go about a gapless spin chain, where ρ should be susceptible to arbitrarily weak perturbations. The hallmark results from entanglement entropy for real space cuts, however, suggest a different perspective [2]. The entanglement entropy exhibits a scaling law $S_A \propto (c/3) \log l$, where l is the length of the real space interval A and c is the central charge of the associated conformal field theory. Due to this result, the entanglement entropy has become one of the paradigmatic parameters to retrieve from the finite-size realisation of a given spin chain Hamiltonian, which is particularly amenable to numerical observability [5, 19]. While no strong spectral resemblance is expected between the energy spectrum and the associated entanglement spectrum as we

encountered for gapped spin chains, a lesson from real space cuts of gapless spin chains is that fundamental features of the physical systems can still be extracted from the entanglement spectrum and its derivative quantities.

An extended momentum cut (Fig. 1c) performed on the ground state of a gapless spin chain Hamiltonian helps to resolve a universal fingerprint of its critical theory [16, 27]. To illustrate this hypothesis, we consider spin-1/2 spin chains on even-membered rings with periodic boundary conditions. The N sites are placed on a circle of radius unity and are thus described by the N th roots of unity: $z_j = \exp(2\pi i j/N)$; $j \in \{1, \dots, N\}$. Any singlet ground state of an $SU(2)$ -invariant Hamiltonian in hardcore boson notation takes the form

$$|\Psi_0\rangle = \sum_{j_1, \dots, j_K} \psi(z_{j_1}, \dots, z_{j_K}) S_{j_1}^- \dots S_{j_K}^- |F\rangle, \quad (5)$$

where $|F\rangle = |\uparrow \dots \uparrow\rangle$ is a polarised reference state. The sum extends over all ways to distribute $K = \frac{1}{2}N$ down-spins on the ring, and the weights $\psi(z_{j_1}, \dots, z_{j_K})$ depend only on the position of the spin \downarrow sites. We Fourier transform the spin operators on each site according to $\tilde{S}_m^- = \frac{1}{N} \sum_j z_j^m S_j^-$ so that

$$|\Psi_0\rangle = \sum_{m_1, \dots, m_K} \tilde{\psi}(m_1, \dots, m_K) \tilde{S}_{m_1}^- \dots \tilde{S}_{m_K}^- |F\rangle, \quad (6)$$

where

$$\tilde{\psi}(m_1, \dots, m_K) = N^{-K} \sum_{j_1, \dots, j_K} z_{j_1}^{m_1} \dots z_{j_K}^{m_K} \psi(z_{j_1}, \dots, z_{j_K}). \quad (7)$$

This extended momentum monomial basis is non-orthogonal and represented by bosonic occupation numbers n_m for crystal momentum m , yielding a total state momentum $M = \sum_m m n_m$. The total particle number is given by $K = \sum_m n_m$ and the physical crystal momentum by $Q = M \bmod N$. The regions A and B for the extended momentum cut are decomposed with respect to the number of particles and total momentum according to $N_A + N_B = N$ and $M_A + M_B = M$. The extended momentum hence bears close resemblance to the entanglement cut on a quantum Hall sphere, where the momentum M_A is replaced by the angular momentum on the hemisphere L_A [14]. The entanglement spectrum for a spin-1/2 Heisenberg chain is plotted in Fig. 3.

To better understand the relation between the extended momentum cut entanglement spectra and the critical theory of a gapless spin chain, it is best to start from the viewpoint of the Haldane–Shastry (HS) model [10, 25], a spin-1/2 chain which, due to its Yangian quantum group structure [11], resolves the Wess–Zumino–Witten (WZW) $SU(2)_1$ field theory at finite size without logarithmic corrections. Furthermore, the HS ground state wave function, aside from a gauge factor to ensure

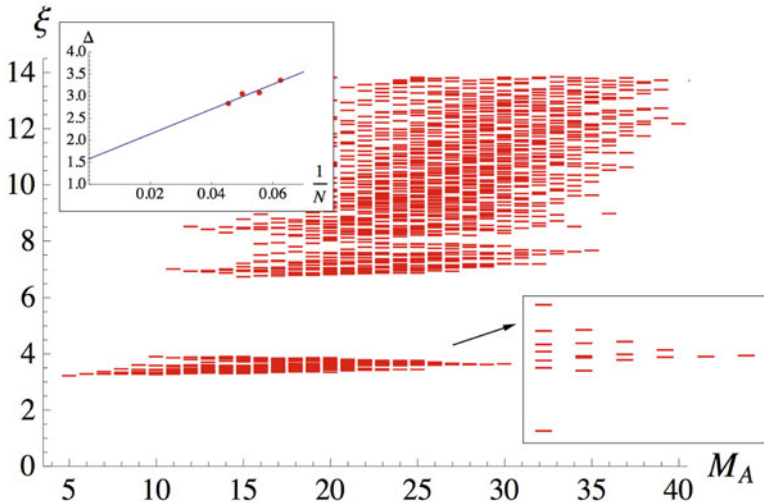


Fig. 3 Extended momentum entanglement cut for the spin-1/2 Heisenberg spin chain [27]. A low entanglement energy manifold is separated from higher level contributions through an entanglement gap Δ which persists in the thermodynamic limit (left inset). The state counting of the low-lying levels matches that of a bosonic $U(1)$ state counting (right inset)

its singlet property, matches the form of the bosonic Laughlin fractional quantum Hall state at magnetic filling $\nu = 1/2$:

$$\psi_{\text{HS}} = \prod_{i < j}^K (z_i - z_j)^2 \prod_{i=1}^K z_i. \quad (8)$$

One finds that the entanglement spectrum of the HS ground state is composed of only few eigenstates of ρ_A with finite entanglement weight and a large remainder part with zero entanglement weight, i.e., $\xi \rightarrow \infty$. Furthermore, the state count per sector M_A reads $1, 1, 2, 3, 5, 7, \dots$ and thus agrees with the $U(1)$ bosonic state counting which matches the low-energy excitations of this universality class of gapless spin chains. (Note that such state countings are subtle and necessitate a significant system size for unambiguous resolution. This is because, for instance, a counting $1, 1, 2, 3, 5, 8, \dots$ would have hinted at a Fibonacci state counting.) The upshot of the extended momentum cut is that for the entire spin-1/2 fluid phase including the Heisenberg spin chain, which is described by $SU(2)_1$ WZW field theory, these levels serve as the low entanglement Hamiltonian spectral fingerprint. Figure 3 depicts the extended momentum cut entanglement spectrum for the spin-1/2 Heisenberg chain. The low-energy part is the universal component, which in terms of state counting and eigenstates is identical to the HS point. All other entanglement levels are higher up in entanglement energy and separated by an entanglement gap Δ which appears to persist in the thermodynamic limit. While

the $U(1)$ state counting can only conveniently be resolved through the extended momentum cut with respect to M , the entanglement gap would still be visible for a crystal momentum cut with respect to Q . This entanglement gap frames a notion of topological adiabaticity, where two spin chain models are defined to be topologically connected if the entanglement gap from their ground state momentum cut persists along the interpolation [28]. To which extent this hypothesis is applicable to arbitrary gapless models in one spatial dimension, or in fact the predictive power of entanglement spectra in general still is a subject of debate [3, 15].

The extended momentum cut appears suitable to resolve deconfined spinon excitations of gapless spin chains. The HS model, which can be thought of as the free spinon gas related to $SU(2)_1$ WZW field theory where the spinons only interact through their fractional statistics, plays a similar role for the extended momentum cut entanglement spectra as the AKLT point does for the real space cut entanglement spectra of the Haldane phase. Subsequent studies of gapless spin chains with other critical theories such as the $SU(2)_2$ and $SU(3)_1$ WZW field theory [16] suggest that the extended momentum cut indeed serves as a way to resolve the low-energy critical theory of spin chains from the entanglement analysis of finite-size ground state wave functions. Here, the analogue to the HS Point for $SU(2)_k$ WZW field theories is formed by the Greiter $S = k/2$ spin chain Hamiltonians [6, 29].

5 Conclusion

The strong dependence of entanglement spectra on the chosen cut inhibits advantages and drawbacks at the same time. We could witness the former in this chapter, where the right cut adjusted to the spin chain at hand would allow one to learn in tremendous detail about the spin chain properties solely from the ground state wave function. Regarding the latter, it is still a matter of ongoing research to determine under which conditions there is reliable universality extractable from entanglement spectra [3, 15]. Furthermore, due to its manifest basis-dependent, i.e., gauge-dependent character, it is a subtle question whether any of these entanglement spectra immediately relate to observable quantities. As one promising sign in this direction, the measurement of entanglement entropy has at least been successfully performed in a highly tunable and accessible environment of ultra-cold gases deposited into an optical lattice [12], while the knowledge of all Renyi entropies would in principle allow to reconstruct the entanglement spectrum.

Despite these open questions, it is evident that entanglement spectra have become an indispensable diagnosis tool for quantum many-body systems in general and spin chains in particular. It should be considered likely that further fundamental insights will be gained from future entanglement spectral analyses of spin chains.

References

1. I. Affleck, T. Kennedy, E.H. Lieb, H. Tasaki, Rigorous results on valence-bond ground states in antiferromagnets. *Phys. Rev. Lett.* **59**, 799–802 (1987)
2. P. Calabrese, J. Cardy, Entanglement entropy and quantum field theory. *J. Stat. Mech: Theory Exp.* **2004**(06), P06002 (2004)
3. A. Chandran, V. Khemani, S.L. Sondhi, How universal is the entanglement spectrum? *Phys. Rev. Lett.* **113**, 060501 (2014)
4. J. Eisert, M. Cramer, M.B. Plenio, Colloquium: Area laws for the entanglement entropy. *Rev. Mod. Phys.* **82**, 277–306 (2010)
5. M. Fühlinger, S. Rachel, R. Thomale, M. Greiter, P. Schmitteckert, DMRG studies of critical SU(N) spin chains. *Ann. Phys.* **17**(12), 922–936 (2008)
6. M. Greiter, *Mapping of Parent Hamiltonians: From Abelian and Non-Abelian Quantum Hall States to Exact Models of Critical Spin Chains*. Springer Tract of Modern Physics, vol. 244 (Springer, Berlin, 2011)
7. F.D.M. Haldane, Continuum dynamics of the 1-d Heisenberg antiferromagnet: identification with the O(3) nonlinear sigma model. *Phys. Lett. A* **93**(9), 464–468 (1983)
8. F.D.M. Haldane, Fractional quantization of the Hall effect: a hierarchy of incompressible quantum fluid states. *Phys. Rev. Lett.* **51**, 605–608 (1983)
9. F.D.M. Haldane, Nonlinear field theory of large-spin Heisenberg antiferromagnets: semiclassically quantized solitons of the one-dimensional easy-axis néel state. *Phys. Rev. Lett.* **50**, 1153–1156 (1983)
10. F.D.M. Haldane, Exact Jastrow-Gutzwiller resonating-valence-bond ground state of the spin- $\frac{1}{2}$ antiferromagnetic Heisenberg chain with $1/r^2$ exchange. *Phys. Rev. Lett.* **60**, 635–638 (1988)
11. V.I. Inozemtsev, On the connection between the one-dimensionals= $1/2$ Heisenberg chain and Haldane-Shastry model. *J. Stat. Phys.* **59**(5), 1143–1155 (1990)
12. R. Islam, R. Ma, P.M. Preiss, M. Eric Tai, A. Lukin, M. Rispoli, M. Greiner, Measuring entanglement entropy in a quantum many-body system. *Nature* **528**(7580), 77–83 (2015)
13. T. Kennedy, H. Tasaki, Hidden $Z_2 \times Z_2$ symmetry breaking in Haldane-gap antiferromagnets. *Phys. Rev. B* **45**, 304–307 (1992)
14. H. Li, F.D.M. Haldane, Entanglement spectrum as a generalization of entanglement entropy: identification of topological order in non-abelian fractional quantum Hall effect states. *Phys. Rev. Lett.* **101**, 010504 (2008)
15. R. Lundgren, J. Blair, M. Greiter, A. Läuchli, G.A. Fiete, R. Thomale, Momentum-space entanglement spectrum of bosons and fermions with interactions. *Phys. Rev. Lett.* **113**, 256404 (2014)
16. R. Lundgren, J. Blair, P. Laurell, N. Regnault, G.A. Fiete, M. Greiter, R. Thomale, Universal entanglement spectra in critical spin chains. *Phys. Rev. B* **94**, 081112 (2016)
17. T. Nishioka, Entanglement entropy: Holography and renormalization group. *Rev. Mod. Phys.* **90**, 035007 (2018)
18. I. Peschel, On the reduced density matrix for a chain of free electrons. *J. Stat. Mech: Theory Exp.* **2004**(06), P06004 (2004)
19. R.N.C. Pfeifer, G. Evenbly, G. Vidal, Entanglement renormalization, scale invariance, and quantum criticality. *Phys. Rev. A* **79**, 040301 (2009)
20. D. Poilblanc, Entanglement spectra of quantum Heisenberg ladders. *Phys. Rev. Lett.* **105**, 077202 (2010)
21. F. Pollmann, A.M. Turner, E. Berg, M. Oshikawa, Entanglement spectrum of a topological phase in one dimension. *Phys. Rev. B* **81**, 064439 (2010)
22. F. Pollmann, E. Berg, A.M. Turner, M. Oshikawa, Symmetry protection of topological phases in one-dimensional quantum spin systems. *Phys. Rev. B* **85**, 075125 (2012)
23. X.-L. Qi, H. Katsura, A.W.W. Ludwig, General relationship between the entanglement spectrum and the edge state spectrum of topological quantum states. *Phys. Rev. Lett.* **108**, 196402 (2012)

24. T. Senthil, Symmetry-protected topological phases of quantum matter. *Ann. Rev. Condens. Matt. Phys.* **6**(1), 299–324 (2015)
25. B.S. Shastri, Exact solution of an $s=1/2$ Heisenberg antiferromagnetic chain with long-ranged interactions. *Phys. Rev. Lett.* **60**, 639–642 (1988)
26. A. Sterdyniak, N. Regnault, B.A. Bernevig, Extracting excitations from model state entanglement. *Phys. Rev. Lett.* **106**, 100405 (2011)
27. R. Thomale, D.P. Arovas, B.A. Bernevig, Nonlocal order in gapless systems: Entanglement spectrum in spin chains. *Phys. Rev. Lett.* **105**, 116805 (2010)
28. R. Thomale, A. Sterdyniak, N. Regnault, B.A. Bernevig, Entanglement gap and a new principle of adiabatic continuity. *Phys. Rev. Lett.* **104**, 180502 (2010)
29. R. Thomale, S. Rachel, P. Schmitteckert, M. Greiter, Family of spin- s chain representations of $SU(2)_k$ Wess-Zumino-Witten models. *Phys. Rev. B* **85**, 195149 (2012)
30. R. Thomale, S. Rachel, B.A. Bernevig, D.P. Arovas, Entanglement analysis of isotropic spin-1 chains. *J. Stat. Mech. Theory Exp.* **2015**(7), P07017 (2015)
31. A.M. Turner, F. Pollmann, E. Berg, Topological phases of one-dimensional fermions: An entanglement point of view. *Phys. Rev. B* **83**, 075102 (2011)

Detecting Quantum Phase Transitions in Spin Chains



Yan-Chao Li, Wing Chi Yu, and Hai-Qing Lin

Abstract Quantum entanglement is a unique physical property that distinguishes quantum systems from classical systems. Entanglement in spin chain models has potential application in quantum information processing. Studying quantum phase transitions of such models from the quantum information point of view is the foundation of quantum physics and an effective means in understanding and applying quantumness. This method achieves extensive research and rapid development because no a priori knowledge of symmetry of the system is needed. However, some key issues have not been effectively addressed, such as the determination of order parameters and the effectiveness and universality of each detector. Therefore, we focus on the performance of entanglement and its related quantum correlations in the characterization of quantum phase transitions under different conditions. The natural connection between quantum correlation and quantum phase transitions is mainly discussed, and a general context and the possible direction of its development are sorted out to provide help for the deep understanding of quantumness and the improvement of research methods of quantum phase transition.

Y.-C. Li

Center of Materials Science and Optoelectronics Engineering, College of Materials Science and Opto-Electronic Technology, University of Chinese Academy of Sciences, Beijing, China

Beijing Computational Science Research Center, Beijing, China

e-mail: ycli@ucas.ac.cn

W. C. Yu

Department of Physics, City University of Hong Kong, Kowloon, Hong Kong

City University of Hong Kong Shenzhen Research Institute, Shenzhen, China

e-mail: wingcyu@cityu.edu.hk

H.-Q. Lin (✉)

Beijing Computational Science Research Center, Beijing, China

Department of Physics, Beijing Normal University, Beijing, China

e-mail: haiqing0@csrc.ac.cn

© The Author(s), under exclusive license to Springer Nature Switzerland AG 2022

A. Bayat et al. (eds.), *Entanglement in Spin Chains*, Quantum Science and Technology, https://doi.org/10.1007/978-3-031-03998-0_2

1 Introduction to Quantum Entanglement

1.1 *Quantum Entanglement and Quantum Phase Transitions*

An essential feature that discriminates quantum mechanics from classical mechanics is quantum entanglement. Entanglement is a pure quantum phenomenon that has no classical counterpart. It describes a state of a system with multiple particles or multiple degrees of freedom that may not be written as a product of the states of its component systems [1]. In such an entangled state, the change of one particle is immediately reflected on other entangled particles, no matter how far away they are. Understanding this nonlocality that seems not limited by the speed of light has puzzled the scientific community [2–4]. However, the majority of experiments that have been done thus far are in favor of the nonlocality of quantum entanglement [5]. On the contrary, the fundamentally related property described by entanglement is considered an important resource in quantum information processing [6, 7]. Well-entangled states are the carriers of information; thus, the preparation of these states has always been an important issue in quantum computation and communication [8, 9]. Entanglement is the key to understanding quantum systems and future technological breakthroughs.

However, the essence of quantum entanglement still lacks a thorough understanding. Researchers are looking for the hidden variable behind entanglement and quantum theory [10–13]. Moreover, as the core of an information carrier, the stability of an entanglement state is crucial. However, decoherence in such a state remains a key to the unsolved problem in quantum information processing. The understanding of a quantum state and the control of its stability are related to quantum phase transitions' research. Therefore, we study quantum phase transition from the perspective of quantum informatics instead of the traditional order parameter method by starting from quantum entanglement that is a representative physical quantity of quantum information theory. Quantum phase transition is also a pure quantum effect. The divergence of the correlation length is controlled by quantum correlation, which cannot be described by classical statistical mechanics. On the one hand, we can fully explore the quantum phases and phase transitions of different systems from the quantum correlation itself by studying the relationship between entanglement and quantum phase transition. On the other hand, we can deeply understand quantum entanglement and explore the origin of quantumness.

In the field of quantum information, spin chain system has always been considered the best candidate in solid state systems that carry quantum entanglement information because of its integrability and scalability in quantum communication. Any logic gate of quantum computing can be realized in such models as long as it is properly encoded [14, 15]. Many physical systems, such as nuclear spin, electron spin, molecular spin, quantum dot, and quantum optical lattice, can be modulated by spin chain models [16, 17]. Spin chain system is a natural quantum system in quantum information processing and exhibits potential application value in quantum information science. A spin chain can also be mapped to a fermion chain through

Jordan-Wigner transformation [18]. Therefore, without loss of generality, we take the quasi one-dimensional system based on spin chain as the platform and quantum entanglement as the tool and object in the research of quantum phase transition and quantum cognition.

Phase transitions are widely used in our daily lives. Examples include the preparation of glass and ceramic materials and the production of austenitic and martensitic stainless steel with different flexibility and strength requirements. At present, many technological developments use phase transitions, for instance, the application of phase change materials in solar energy storage, waste heat recovery, engineering insulation, and corrosion-resistant metallic glass and the preparation of artificial superhard materials [19].

Quantum phase transitions belong to one kind of phase transition. In contrary to a thermal phase transition [20], which is driven by thermal fluctuations, a quantum phase transition occurs at absolute zero temperature. At such a temperature, thermal fluctuations are absent, and quantum effect dominates. According to Heisenberg uncertainty principle arising from the wave-particle duality in quantum mechanics, the momentum and the position of quantum particles cannot be determined precisely at the same time. These particles still possess zero-point energy even at absolute zero temperature, thereby leading to quantum fluctuations in the ground state of the system. Let us take a simple spin-1/2 system as an example. The principle of superposition indicates that any state of the system can be written as a linear combination of the spin up $|\uparrow\rangle$ and the spin down $|\downarrow\rangle$, i.e.,

$$|\psi\rangle = \alpha |\uparrow\rangle + \beta |\downarrow\rangle, \quad (1)$$

where α and β are complex numbers, and they satisfy the normalization condition $|\alpha|^2 + |\beta|^2 = 1$. The above equation shows that the arbitrary quantum state $|\psi\rangle$ can be regarded as a fluctuation between $|\uparrow\rangle$ and $|\downarrow\rangle$. A quantum phase transition is caused by such kind quantum fluctuations and a purely quantum mechanical process. In a general system, the energy spectrum of the system suffers an abrupt change when a slight change of a parameter λ near a so-called quantum critical point is added to the Hamiltonian. This scenario leads to a macroscopic change in the system's properties, resulting in a quantum phase transition. In this work, λ is usually called the driving term. It can be a coupling constant or an external parameter, such as external magnetic or pressure.

The study of quantum phase transitions plays an important role in understanding quantum many-body systems. It not only reveals the relationship of microscopic energy spectrum and electronic structure with the macroscopic properties of materials from the viewpoint of condensed matter physics [21] but also helps us to understand quantumness deeply from the viewpoint of quantum information. A typical example of quantum phase transition is the superfluid-Mott insulator transition. It is observed experimentally in the trapped cold atoms in optical lattices by tracking the velocity distribution of runaway molecules [22]. When the potential barrier of the optical lattice is small, the cold atoms can shuttle freely in each potential well, and the system is in superfluid phase. The cold atoms are confined

in the wells and cannot hop between different lattice sites when the barrier is raised above a certain threshold. The system becomes an insulator in this case [23]. In addition to the superfluid-Mott insulator transition, other examples of quantum phase transitions include the magnetic phase transitions in spin systems [24–26], charge density wave–superconducting phase transition in fermion systems [27, 28], and superconducting–insulator phase transition [29].

In recent decades, quantum computing and quantum communication based on quantumness have become an important research field in the frontier of science and technology with the improvement of the stability of quantum bit control and the continuous development of quantum algorithm. The discoveries of new phases of matter promoted by quantum phase transitions, such as unconventional superconductivity in a heavy-fermion system [30], and the close relationship between criticality and decoherence in the quantum computation and quantum communication [31] have greatly aroused scientists’ enthusiasm of studying quantum phase transitions.

As an analogy to thermal phase transitions, quantum phase transitions can also be understood as a result of the reconstruction in Hamiltonian’s energy spectrum [32]. In particular, the ground state or the low-lying energy spectra determines the quantum state of the system. From this point of view, the structure of the low-energy spectra changes when the driving parameter crosses the critical point, leading to a different quantum phase with quite different macroscopic properties. According to the reconstruction mechanisms, quantum phase transitions can be divided into different types and are incarnated in the nonanalytic behavior of the derivative of the ground-state properties at the transition point. The first type is the first-order phase transition corresponding to a level crossing in the ground state, in which the first derivative of the ground-state energy with respect to the driving parameter is usually discontinuous. The second one is the continuous phase transition, including the second-order and higher-order types, in which the energy levels of the ground state and the first excited state become infinitely close to one another with the increase of the system size. However, the occurrence of interlacing is always avoided. This type of phase transition usually corresponds to a low-lying excited state reconstruction and possesses discontinuity in an order higher than one in the derivative of the ground-state energy [33]. Figure 1 shows the illustration of the two cases [21].

1.2 Methodologies from the Viewpoint of Quantum Information Theory

The traditional method for studying quantum phase transitions belongs to the category of Landau–Ginzburg–Wilson spontaneous symmetry-breaking theory. Researchers use local order parameters to characterize different quantum phases. However, quantum phase transitions, such as the topological phase transitions [34, 35] and Berezinskii-Kosterlitz-Thouless phase transitions [36], occur between phases that are not characterized by any local order parameter or symmetry-

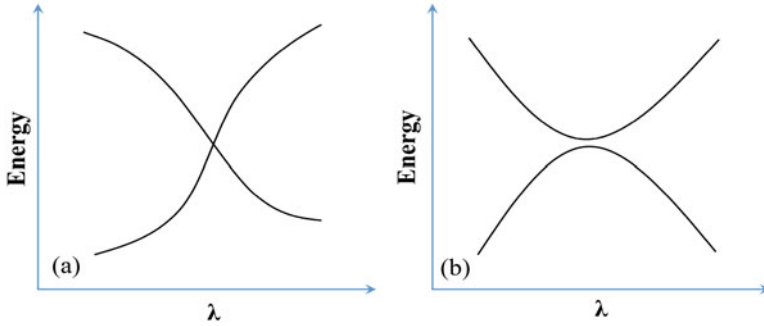


Fig. 1 (a) When the energy levels of the ground state and the excited state intersect at a certain point in the parameter space, the properties of the ground state of the system change; (b) the situation in which the energy levels of the ground state and the excited state avoid the intersection

breaking description. Moreover, conducting a complete phase diagram analysis for a multistate system is usually difficult because each quantum state needs a specific characteristic order. Obtaining all possible orders of the system is a challenge, particularly for systems with unknown symmetry. Therefore, the traditional research on the quantum phase of multibody system has made slow progress for a long time.

The new method to study quantum phase transitions from the perspectives of quantum information begins from Ref. [31], where the entanglement concept from quantum information theory is originally borrowed to study quantum phase transitions in condensed matter physics. The authors determined the close relationship between quantum phase transition and entanglement through the scale analysis of entanglement near the critical point of the system. In this approach, no a priori knowledge of the symmetry of a system is needed, and the phase diagram of the system is obtained by studying this single quantity. The simplicity and effectiveness of this method have attracted a wide range of research enthusiasm. Along this direction, the research of quantum phase transition has made rapid and long-term development. Subsequently, many new concepts borrowed from quantum information theory have been successfully used to characterize quantum phase transition.

These concepts mainly include quantum entanglement [31], quantum fidelity (QF) [37], quantum discord (QD) [38], and quantum coherence (QC) based on Wigner and Yanase skewed information [39]. Quantum entanglement approach including the use of various measures, such as concurrence, von Neumann entropy, and negativity [40, 41], has been successfully applied to various systems, including interacting spin models [42], fermion models [38], and Bose Hubbard model [43]. This approach has been recently used to calibrate the superconducting phase and metal phase of one-dimensional fermion wire [44]. The connection between geometric Berry phase and quantum phase transitions for the case of a spin-XY model has also been studied [45]. Quan et al. showed a remarkable relationship between Loschmidt echo and quantum phase transitions [37, 46]. Based on this

finding, a simple quantity QF and its related fidelity susceptibility [26, 47] have been successfully applied to different types of quantum phase transitions, such as topological type [48, 49], and verified experimentally by a nuclear magnetic resonance quantum simulator [50]. Time correlations, Leggett-Garg inequalities, and Loschmidt echo have also been recently introduced into the study of static quantum phase transition and time domain dynamic quantum phase transition in multibody quantum systems [51, 52].

1.3 Open Questions

Although each of the above-mentioned quantum phase transition detectors has its successful examples, it also has limitations. The effectiveness and universality of these examples are not fully analyzed. Although fidelity reflects the quantum phase transition of Bose Hubbard model more clearly than quantum entanglement [43], it is ineffective in detecting Berezinskii-Kosterlitz-Thouless (BKT) quantum phase transition, such as the XXZ model [25], and QD can effectively describe this phase transition [38]. Our recent research determined that QC cannot only effectively detect such a BKT type quantum phase transition but also avoid the singularity of QD in nonquantum-critical points [53]. Determining whether QC is a more generic indicator for quantum phase transition than QD needs further exploration.

Moreover, absolute zero cannot be achieved in reality. Thus, the study of quantum phase transition at finite temperature has a high experimental value. However, research in this field is still insufficient. We showed that quantum entanglement and its temperature scaling behavior can be used to detect the quantum critical point of a spin system [42]. Similar works have also been done in Refs. [54, 55]. However, temperature has a great influence on the entanglement detection of quantum phase transition, and the influence degree can vary different for different detectors. For example, QD is more robust to thermal fluctuations than quantum entanglement [38]. Recent finding has indicated that QC spectrum is more robust to thermal fluctuations than QD and QC, and it is expected to be a powerful tool to detect quantum phase transitions [53]. The response to thermal fluctuations or the expression intensity of the quantum properties of the detected quantum states directly affects the ability of each detector to characterize the phase transition at finite temperature. The research in this area is still immature and lacks comprehensive and systematic analysis.

Although quantum information measures can clearly demarcate the quantum phase boundary, they cannot directly reveal the information of the order parameter for each of the quantum phases of the system. This scenario hinders us from understanding further the specific properties of quantum states. Therefore, developing a method to derive the order parameters from the same perspective of quantum information is urgently needed. The order parameters for some simple spin and fermion systems were constructed starting from the mutual information involved in entanglement and correlation through the spectral analysis of the

reduced density matrix [56–58]. Magnifico et al. have further applied recently the order parameter we obtained to characterize the quantum phase transition in the topological Schwinger model [59]. This method is still in its infancy. Further investigations on its applicability to characterize different types of quantum phase transitions, such as those that involve low-lying excited energy levels or different topological phases, are required.

Quantum phase transitions and quantum entanglement have a close connection. Although open questions exist, quantum entanglement is an effective and promising method to reveal quantum phase transitions from the perspective of quantum correlations. Therefore, we try to establish a possible connection among various correlation detectors and quantum phase transition. We hope that this work will help to find an effective and universal quantum phase transition detector and improve and perfect the research method of quantum phase transition. Furthermore, we also hope that it will enlighten the understanding of the nature of quantumness and contribute in bridging condensed matter physics and quantum information science.

2 Concurrence and Quantum Phase Transitions in Spin Chains

Entanglement, which is absent in classical systems, is regarded as a purely quantum correlation. It serves as the resource to enable quantum computation and quantum communication and thus plays a core role in quantum informatics [8]. It can also be a good detector for quantum phase transitions in multibody system. The main idea is that the quantum phase transition changes the quantum correlation of the system, and the degree of entanglement inside the system is also changed, resulting in the extreme value of the quantum entanglement or its derivative near the phase transition point.

In 2002, Osterloh et al. studied the entanglement behavior near the critical point of XY spin chain by using concurrence measure. The Hamiltonian of the XY model reads

$$H = - \sum_{j=1}^N \left(\frac{1+\gamma}{2} \sigma_j^x \sigma_{j+1}^x + \frac{1-\gamma}{2} \sigma_j^y \sigma_{j+1}^y + \lambda \sigma_j^z \right), \quad (2)$$

where the parameter N is the number of spins in the chain, γ describes the anisotropy of the system arising from the spin–spin interaction, λ is external magnetic field, σ^α ($\alpha = x, y, z$) are the Pauli matrices. When $\gamma = 1$, the Hamiltonian corresponds to the transverse-field Ising model.

For a given local reduced density matrix $\rho_{ab} = Tr_{ab} |\psi\rangle \langle\psi|$, where Tr_{ab} stands for tracing the overall sites except the two arbitrary sites a and b in the chain, the quantum concurrence is defined as $C_{\rho_{ab}} = \max\{0, \lambda_1 - \lambda_2 - \lambda_3 - \lambda_4\}$, where $\lambda_1, \lambda_2, \lambda_3$, and λ_4 are the square roots of the eigenvalues of $\rho_{ab} \tilde{\rho}_{ab}$ in descending order.

Here, $\tilde{\rho}_{ab} = (\sigma_a^y \otimes \sigma_b^y) \rho_{ab}^* (\sigma_a^y \otimes \sigma_b^y)$ is the time-reversed matrix of ρ_{ab} . ρ_{ab}^* is the complex conjugation of ρ_{ab} .

The authors found by analyzing the behaviors of the concurrence in the vicinity of the transition that the first derivative of concurrence with respect to λ shows a minimum at λ_m near the critical point. The minimum becomes increasingly considerable, and its position gradually approaches the true critical value $\lambda_c = 1$ as N increases. Although the concurrence itself does not show a singular behavior at the critical point, its first-order derivative is divergent in the thermodynamic limit. Similar phenomena were also observed for other critical points in the system. These results supplied direct evidences for the validity of concurrence in quantum phase transition detection.

The relationship between concurrence and quantum phase transitions is further studied in Refs. [60, 61]. At the quantum phase transition point $\Delta = 1$ of the spin XXZ chain model, the ground-state concurrence shows a maximum behavior instead of the singularity behavior for the XY model in Ref. [31]. This conclusion is also suitable for the dimensionality $d \geq 2$ cases [61]. Different behaviors of quantum phase transition for different systems seem to indicate a certain nontrivial relationship between quantum concurrence behavior and phase transition types. Further study evidently is needed.

The types of the quantum phase transitions in several well-known spin systems were clarified by comparing the analyses of low-lying excited state spectra and quantum entanglement behaviors [33]. The different behaviors of the corresponding quantum concurrence were explained, and the relationship between quantum entanglement and phase transition types was tried to be established. According to the continuity and extremum of quantum concurrence, quantum phase transitions can be divided into three categories: The first one is the first-order quantum phase transition, which is caused by the level crossing of the ground state. The concurrence as a measure of ground-state entanglement information shows discontinuous behavior because of the change of ground state at the phase transition point. The second type is the case in which both sides of the corresponding phase transition point are in order or disorder usually because of the level crossing in low excited states, leading to a maximum behavior of the concurrence. The third kind of quantum phase transition corresponds to the transition from order to disorder with an energy gap opening, where the concurrence is continuous, but its high-order derivative shows extremum at the phase transition point. This work reveals that quantum entanglement and quantum phase transition are not only related to the ground state of the system but also affected by the excited states. Their relationship can be reflected by the behaviors of concurrence.

Concurrence can reflect the quantum phase transition of a system by measuring the entanglement between the two spins embedded in the system. However, some quantum information related to multiparticles is not reflected completely by concurrence because of the limitation of the definition itself. In particular, the quantum information in the two local spins may be too limited to reflect the quantum information of the whole system. For example, compared with physical

quantities, such as the von Neumann entropy and QD, the concurrence as a measure of entanglement eventually loses the ability to detect quantum phase transition with temperature disturbance [38, 62].

3 von Neumann Entropy and Quantum Phase Transitions

3.1 Single-Site Entanglement

Gu et al. introduced a different entanglement measure, namely von Neumann entropy, to study the quantum phase transition of the one-dimensional extended Hubbard model [40]. The corresponding Hamiltonian of the model reads

$$H = \sum_{i,\sigma} \left(c_{i,\sigma}^\dagger c_{i+1,\sigma} + c_{i+1,\sigma}^\dagger c_{i,\sigma} \right) + U \sum_i n_{i\uparrow} n_{i\downarrow} + V \sum_i n_i n_{i+1}, \quad (3)$$

where $i = 1, \dots, N$; $\sigma = \uparrow, \downarrow$; $c_{i,\sigma}^\dagger$ and n_i are the creation and number operators at site i , respectively; U and V define the on-site and the nearest-neighbor Coulomb interactions. The von Neumann entropy for a single site is then defined by the ground-state $|\psi\rangle$ of the system as

$$E_v(\rho_j) = -Tr \rho_j \ln \rho_j, \quad (4)$$

where ρ_j is the reduced density matrix of the ground state for the j th site. The authors calculated the one-site entropy E_v as functions of U and V . They determined that the extreme point of the von Neumann entropy corresponds to the phase transition point of the system, and the ground-state phase diagram of the system can be easily captured by the single quantity.

3.2 Multisite Entanglement

The success of the entanglement method has attracted researchers' attention. Legeza et al. found that the one-site von Neumann entropy is not suitable for some quantum phase transitions, such as the phase transitions between the dimerized state, Haldane state, quantum spin-nematic state in spin-1 spin chain, the Ising-like phase transition, and BKT phase transition in the ionic Hubbard model. Therefore, they proposed to use two-site entropy, namely the reduced density matrix in Eq. (4) is taken for two neighboring sites instead of for one single site, to study the quantum phase transition. They found that compared with the single-site entanglement, the two-site entanglement entropy better reflects many phase transitions that cannot be recognized by the single-site entanglement entropy [41]. The phase information

of the one-dimensional isotropic spin-1 chain presented by the two-site entropy is better than that presented by one-site entropy.

The block–block entanglement measured by the von Neumann entropy was also studied based on the above findings; its structure is richer than that of the local site entanglement for the one-dimensional extended Hubbard model because the nonlocal correlation is included [63]. Multisite entropy was also used to analyze quantum phase transitions in the frustrated spin ladder with next-nearest-neighbor (NNN) interactions [64]. The system is sketched in Fig. 2. Its Hamiltonian reads

$$H = \sum_{\alpha=1,2,i}^N [(J_1 \mathbf{S}_{\alpha,i} \cdot \mathbf{S}_{\alpha,i+1} + J_2 \mathbf{S}_{\alpha,i} \cdot \mathbf{S}_{\alpha,i+2}) + J_{\perp} \mathbf{S}_{1,i} \cdot \mathbf{S}_{2,i} + J_{\times} (\mathbf{S}_{1,i} \cdot \mathbf{S}_{2,i+1} + \mathbf{S}_{1,i+1} \cdot \mathbf{S}_{2,i})], \quad (5)$$

where $\mathbf{S}_{\alpha,i}$ denotes spin-1/2 operators at site i of the α^{th} leg of the ladder, and N is the number of rungs; the other parameters J_1 , J_2 , J_{\perp} , and J_{\times} correspond to the interactions between different spins, as indicated in Fig. 2.

Given the spin alignment frustration, materials with the spin-ladder structure exhibit rich quantum states, and many of them are still not fully understood. A good example is the highly controversial intermediated columnar dimer (CD) state in the frustrated antiferromagnetic state. The introduction of the in-chain NNN interaction further increases frustration among spins and may induce new quantum phases of great interest. Such in-chain NNN interaction does exist in real materials, e.g., BiCu_2PO_6 [65]. Therefore, studying the quantum phase diagram of the spin ladder with the in-chain NNN interaction is necessary and insightful. In such a system, the four-site entropy E_{4-L} (the subscript represents the four spins in the middle of the chain, as circled by the wine square marked L in Fig. 2) contains richer quantum information than the two-site entropy E_{13} does because of the symmetry of the system. As shown in Fig. 3, E_{4-L} presents a clearer indication than E_{13} does at the phase boundary of II and III. The controversial CD phase was confirmed by analyzing the four-site entropy combined with the correlation function, and an exotic

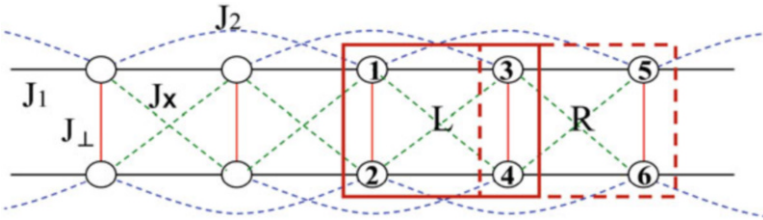


Fig. 2 (Color online) Schematic diagram of the two-leg spin-1/2 ladder with diagonal and in-chain NNN interactions. Circles denote spin-1/2 sites coupled by exchange constants J_1 (black solid lines), J_2 (blue dashed lines), J_{\perp} (red solid lines), and J_{\times} (green dashed lines). The wine-pane L represents the four spins at the middle of the chain, and the dashed-pane R circles the four spins at its right side, where $\alpha = 1, \dots, 6$ denotes the number of spins on L and R

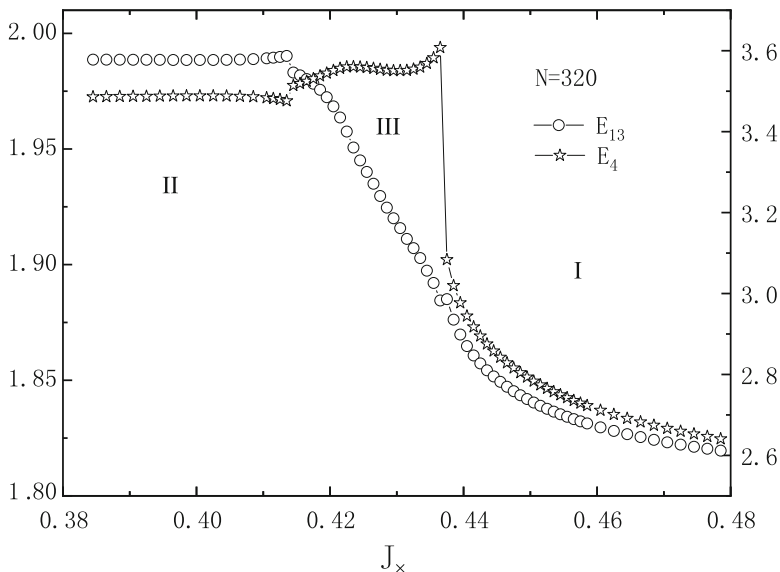


Fig. 3 E_{4-L} and E_{13} as a function of J_x at $J_2 = 0.4$, $J_1 = -1.0$, and $J_{\perp} = -0.5$ for rung number $N=320$. Dramatic changes in E_{4-L} show a clearer indicator than those in E_{13} do in delimiting the three phases I, II, and III

tetramer phase was found. Finally, the quantum phase diagram of the system was obtained [64].

In addition, two difficult issues related to quantum phase transition were solved using quantum entanglement: (I) the BKT type critical point at $J_2/J_1 \approx 0.241$ in the $J_1 - J_2$ model, which corresponds to a transition from spin fluid to dimerized phase and is difficult to be detected because of the problem of logarithmic correction [24, 66]; (II) the controversy—whether the bond-order-wave (BOW) state at a narrow strip along the $U \simeq 2V$ line exists in the half-filled one-dimensional extended Hubbard model [67]. The BKT phase transition in the $J_1 - J_2$ model [68] and the intermediated BOW and superconducting states in the half-filled one-dimensional extended Hubbard model were successfully detected with the help of the two-site and block-site entanglement measured by von Neumann entropy and density matrix renormalization group (DMRG) numerical technique [63, 69].

Given that the local entanglement can be conveniently obtained by the exact diagonalization or density matrix renormalization group algorithms, the method can be applied to much complex systems that cannot be exactly solved. Many related studies on entanglement and phase transition of different quantum systems under different conditions can be performed [9].

Furthermore, the entanglement spectrum can also be used to study quantum phase transitions. Compared with the entanglement entropy, which is just a single number, entanglement spectrum can reveal much more information on quantum

phase transition [70]. Some related works on different types of quantum phases can be found in Refs. [71–73].

The concurrence and the von Neumann entropy are the two main entanglement measures used in detecting quantum phase transitions. Although both of them can measure the degree of entanglement, they possess different physical natures. The concurrence describes the entanglement between the two sites constructing the reduced density matrix, whereas von Neumann entropy measures the entanglement of states on the selected sites with that on the remaining sites in the chain. The concurrence and the von Neumann entropy actually reflect different entanglement information in the system. Different abilities can detect quantum phase transitions for different detectors [62]. The main reason might be that the detectors actually contain different degrees of correlation. Further discussion about this topic is provided in Sects. 3.4 and 4.

3.3 Entanglement and Quantum Phase Transitions at Finite Temperatures

When the temperature is not too high to destroy the quantum order, the system is still dominated by quantumness, and quantum phase transitions still exist. The study on quantum phase transition at finite temperature has a high experimental value because absolute zero cannot be achieved in an actual experiment. However, related research in this field is sparse. The transfer matrix renormalization group (TMRG) technique [74], which is based on the Trotter-Suzuki decomposition of the partition function of a system and can directly handle infinite chains, is used in calculating the two-site thermal entanglement of the $S = 1/2$ distorted diamond chain model to avoid the finite-size effect [42]. The model is sketched in Fig. 4. Its Hamiltonian is written as follows:

$$H = \sum_{i=1}^N (J_1 (\mathbf{S}_{2i-1} \cdot \mathbf{S}_{2i,a} + \mathbf{S}_{2i,b} \cdot \mathbf{S}_{2i+1}) + J_2 (\mathbf{S}_{2i-1} \cdot \mathbf{S}_{2i,b} + \mathbf{S}_{2i,a} \cdot \mathbf{S}_{2i+1}) + J_3 \mathbf{S}_{2i,a} \cdot \mathbf{S}_{2i,b}), \quad (6)$$

where \mathbf{S}_i are spin-1/2 operators at site i , and J_i with $i = 1, 2, 3$ denote exchange integrals along different directions.

The definition of the thermal entanglement E_t is the same as that in Eq. (4), but the reduced density matrix is obtained from the thermodynamical average values of some correlation functions (see Ref. [42]). The results are shown in Fig. 5 for $J_2 = J_1$ antiferromagnetic spin frustrated case. As temperature T decreases, two dramatic changes appear near the two critical points $J_3 = 1.0$ and $J_3 = 2.0$ for $T = 0.67$, as shown in Fig. 5a. The derivative of E_t peaks near the two critical points, and the peak is pronounced as T decreases, as shown in Fig. 5b. The scaling

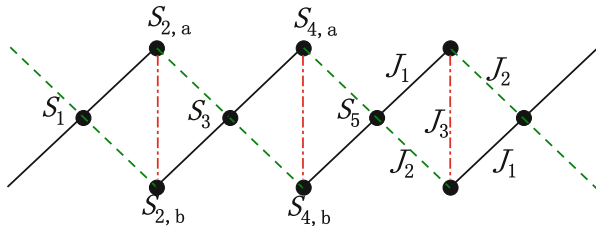


Fig. 4 (Color online) Schematic diagram of the spin-half distorted diamond chain model, where the black circle represents the spin. J_1 (black solid lines), J_2 (green dashed lines), and J_3 (red dashed lines) indicate the exchange constants between spins

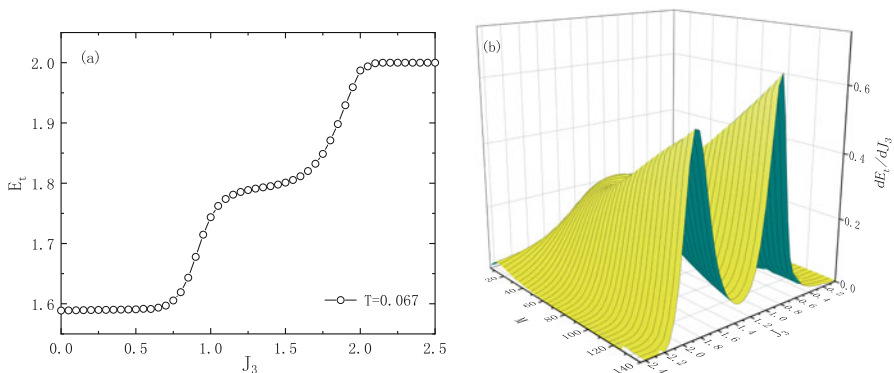


Fig. 5 (Color online) (a) The thermal entanglement E_t for the antiferromagnetic case as a function of J_3 at $J_1 = J_2 = 1.0$ and $T = 0.067$. (b) The derivative of E_t with respect to J_3 under different values of M , where M is the Trotter number in the TMRG calculation, and $T = 1/(M\varepsilon)$ with $\varepsilon = 0.1$

behavior for the peak illustrates that it diverges at zero temperature [42]. The peak behavior of E_t reflects the quantum phase transition of the system at finite temperature. Therefore, we conclude that detecting quantum phase transitions at finite temperature by entanglement is possible and provides theoretical guidance for the experimental study of quantum phase transition.

3.4 Entanglement and Quantum Correlations

The essence of entanglement is a kind of quantum correlation, which plays a role in detecting quantum phase transition. However, it does not include all types of quantum correlations, and some quantum states have quantum correlations without quantum entanglement. For example, the authors pointed out that quantum correlations still exist in separable mixed states where the entanglement is absent [75]. Entanglement may fail to detect the quantum phase transitions in

such a system [25, 38]. Correlation among different parts of a system is the main information to obtain in many-body physics and is believed to play a key role in quantum phase transitions detection. From this point of view, a quantity that can measure a larger amount of quantum correlation of a state may present an excellent performance.

An alternative measure of quantum correlations is the QD. The existing results showed that QD can detect the quantum correlations present in certain separable mixed states [76, 77] and may be responsible for the speeding up of a mix-state-based quantum computation [78, 79]. The related researches confirmed its advantage in detecting quantum phase transitions: QD can be more robust against temperature and shows more detailed information than entanglement does [38, 80]. The main reason could be that QD reflects the changes of quantum correlation in which entanglement is absent in such quantum phase transitions. In Refs. [83], the authors established the hierarchical relationship of different manifestations of quantum correlations on the basis of quantum relative entropy. Three kinds of quantum correlations measured by quantum entanglement, QD, and QC are mainly considered. The authors confirmed the above viewpoint and further determined that the amount of information contained in QC, QD, and entanglement decreases in turn. Given that QC contains the most correlation information, it can seem to be the best in detecting quantum phase transitions. Therefore, compared with the potential advantages of quantum entanglement, the potential advantages of QD and QC on quantum phase transition detections are focused in the later parts.

4 Quantum Discord, Quantum Coherence, and Quantum Phase Transitions

4.1 Quantum Discord

Introduced by Ollivier and Zurek [76], QD presents an alternative measure of quantum correlations. Given its application prospect in mixed state quantum computing, much attention has been focused on the properties of QD [81]. The relation between QD and quantum phase transition is an important aspect. One important finding is that QD is more robust against thermal fluctuations than entanglement is, and it can detect quantum phase transitions at finite temperatures [38].

The quantum discord is related to mutual information. Two equivalent mutual information expressions, $I(\rho_{ab})$ and $\mathcal{C}(\rho_{ab})$, exist in classical information theory to describe the correlation between two arbitrary parts, a and b . However, they become unequal when the quantum nature dominates, and the minimum of their difference is called QD [76]:

$$D(\rho_{ab}) = I(\rho_{ab}) - \mathcal{C}(\rho_{ab}) \quad (7)$$

with

$$I(\rho_{ab}) = S(\rho_a) + S(\rho_b) - S(\rho_{ab}), \quad (8)$$

$$\mathcal{C}(\rho_{ab}) = S(\rho_a) - \min_{\{b_k\}} \tilde{S}(\rho_{ab}|\{b_k\}), \quad (9)$$

where $S(\rho)$ is von Neumann entropy and $\tilde{S}(\rho_{ab}|\{b_k\})$ is the conditional entropy and can be written as

$$\tilde{S}(\rho_{ab}|\{b_k\}) = \sum_k p_k S(\rho_{ab}^k), \quad (10)$$

with $\rho_{ab}^k = \frac{1}{p_k} (I \otimes b_k) \rho_{ab} (I \otimes b_k)$ and $p_k = \text{Tr} [(I \otimes b_k) \rho_{ab} (I \otimes b_k)]$. The minimum in Eq. (9) is achieved from a complete set of projective measures $\{b_k\}$ on site b . With the spin system as an example, the projectors in Eq. (10) can be written as

$$b_k = V |k\rangle \langle k| V^\dagger, \quad (11)$$

where $\{|k\rangle\}$ is the standard basis $\{|\uparrow\rangle, |\downarrow\rangle\}$ of any two selected spins, and the transform matrix V is parameterized as [81]

$$V = \begin{pmatrix} \cos \theta & \sin \theta e^{-i\varphi} \\ \sin \theta e^{i\varphi} & -\cos \theta \end{pmatrix}. \quad (12)$$

Then, the minimum of condition entropy $\tilde{S}(\rho_r)$ only depends on θ and φ (traversing from 0 to π). We can determine from the definition that $I(\rho_{ab})$ should be the total correlation, and $\mathcal{C}(\rho_{ab})$ corresponds to the classical correlation. The QD reflects the quantum part included in the mutual information [38, 81].

The entanglement of formation (EOF) is a monotonically increasing function of the concurrence $C_{\rho_{ab}}$ defined in Sect. 2. It can be written as follows [38]:

$$EOF(\rho_{ab}) = -f(C_{\rho_{ab}}) \log_2 f(C_{\rho_{ab}}) - [1 - f(C_{\rho_{ab}})] \log_2 [1 - f(C_{\rho_{ab}})], \quad (13)$$

where $f(C_{\rho_{ab}}) = (1 + \sqrt{1 - C_{\rho_{ab}}^2})/2$. It satisfies the criteria for entanglement monotone. Thus, we use it as a measure of entanglement instead of the concurrence itself.

In Ref. [38], one-dimensional spin XXZ model is used as an example model to demonstrate well the advantages of QD in quantum phase transition detection. The Hamiltonian of the model reads as

$$H_{XXZ} = \sum_j^N \sigma_j^x \sigma_{j+1}^x + \sigma_j^y \sigma_{j+1}^y + \Delta \sigma_j^z \sigma_{j+1}^z, \quad (14)$$

where N is the number of spins in the chain, Δ describes the anisotropy of the system arising from the spin-spin interactions, and σ_j^x , σ_j^y , and σ_j^z are the usual Pauli matrices of the j -th spin. This model has two critical points at zero temperature: an infinite-order phase transition at $\Delta = 1$ and a first-order transition caused by the level crossing of ground state at $\Delta = -1$ [82]. The continuous critical point at $\Delta = 1$ is hardly detected by most detectors, such as the fidelity and the entanglement entropy [25, 53]. However, QD presents a clear signature for this critical point.

The advantages of QD in detecting quantum critical phenomena, particularly at finite temperatures, were further explored in the XY spin chain model in a transverse field with three-spin interaction (XYT) [80]. The Hamiltonian is given by

$$H = - \sum_{j=1}^N \left(\frac{1+\gamma}{2} \sigma_j^x \sigma_{j+1}^x + \frac{1-\gamma}{2} \sigma_j^y \sigma_{j+1}^y + \lambda \sigma_j^z \right) - \sum_{j=1}^N \alpha \left(\sigma_{j-1}^x \sigma_j^z \sigma_{j+1}^x + \sigma_{j-1}^y \sigma_j^z \sigma_{j+1}^y \right), \quad (15)$$

where N is the number of spins in the chain, γ describes the anisotropy of the system arising from the spin-spin interaction, λ is the external magnetic field, and α denotes the three-spin interaction.

This system can be diagonalized in momentum space by introducing Jordan-Wigner transformation. Thus, it is a good experimental model. The capabilities of QD and entanglement in detecting quantum phase transitions at both zero and finite temperatures were analyzed. The pairwise QD of two neighboring spins is more reliable than entanglement in identifying quantum phase transitions. We obtained the quantum phase diagram of the system by the derivative of QD and further confirmed the robustness of QD against thermal fluctuations compared with entanglement (see Fig. 6). At $T = 0$, the vanishing EOF clearly detects the critical points at $\alpha = \pm 0.5$. However, the EOF deviates from the critical points as T increases and tends to zero in the whole parameter region when T is larger than 1.0, as shown in Fig. 6a. Entanglement cannot detect the quantum phase transition

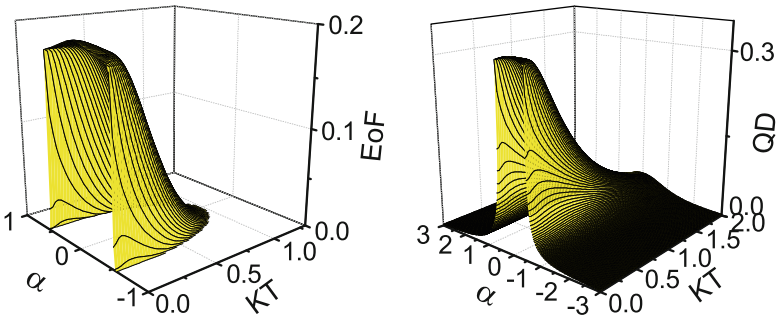


Fig. 6 (Color online) (Left) EOF and (Right) QD as functions of λ and T for $\gamma = 0.5$ and $\lambda = 0.0$ at $N = 2001$

when thermal fluctuation is added. On the contrary, even when T is as high as 2.0, QD is not zero (see Fig. 6b), and the peak structure of its derivative still points to the position of the phase transition point. Therefore, QD is more robust than quantum entanglement in resisting thermal disturbance and can be used to detect quantum phase transition at finite temperature. The advantage of QD in quantum phase transition detection fits the conclusion in Refs. [83] that QD contains more quantum correlation than entanglement.

4.2 Quantum Coherence and Quantum Coherence Spectrum

Based on Wigner and Yanase skew information (WYSI), the simplified alternative version of K -coherence of a quantum state can be written as [84, 85]

$$I^L(\rho, K) = -\frac{1}{4} \text{Tr} \left[[\rho, K]^2 \right], \quad (16)$$

where ρ is the density matrix of a quantum state, K is an observable, and $[\dots]$ denotes the commutator. This definition satisfies all the criteria for coherence monotonies and can be used as an efficient measure to quantify QC [84]. For a subsystem with two sites, A and B , if we choose A as the observable, then K is written as $K_A \otimes I_B$. Thus, $I^L(\rho, K)$ is written as $I_{AB}^L(\rho_{AB}, K_A \otimes I_B)$, which quantifies the QC between A and B . The effectiveness of the WYSI-based QC and its derivatives in detecting different types of quantum phase transitions is carefully analyzed based on the one-dimensional Hubbard model, XY spin model, and Su-Schrieffer-Heeger (SSH) model. QC is more robust than quantum entanglement in resisting thermal fluctuation. It can effectively characterize quantum phase transitions of the system at a relatively high temperature, where entanglement is not competent anymore. The main results are as follows. First, QC clearly shows the existence of the BOW state of the one-dimensional extended Hubbard model (see Eq. (3) for the Hamiltonian), which is not detected easily by entanglement [40] and fidelity [62]. QC results as a function of V at $U = 2.0$ under different system sizes N , plotted in Fig. 7. For a given N , an obvious difference exists between the two neighboring two-site QDs, namely $I_{i,i+1}^L$ for $i = N/2$ and $i = N/2 + 1$. The difference becomes clear as N increases and does not disappear in the thermodynamic limit. This scenario corresponds to the BOW state that possesses the dimerized property (details see Ref. [62]). Second, QC shows the same effectiveness as QD in detecting quantum phase transition at finite temperatures, where the entanglement becomes incapable (see Fig. 8). The thermal fluctuation weakens the EOF when the temperature is added. For example, when $T = 0.5$, the turning point from zero to nonzero shifts away from the critical point at $\alpha = 0.5$. EOF becomes zero in the whole parameter range when the temperature T increases to 1.0. EOF cannot reflect the continuous quantum phase transition at $\alpha = 0.5$ of the XY spin model in a transverse field with three-spin interaction (see Eq. 14 for its Hamiltonian). However, QC shows

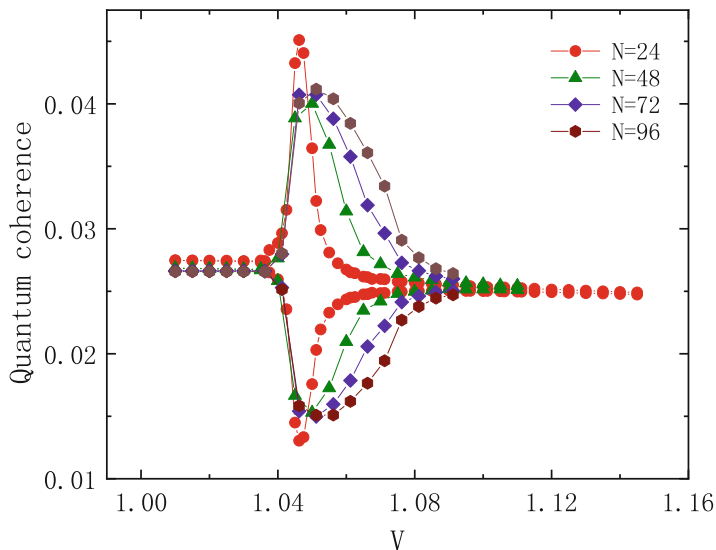


Fig. 7 (Color online) QC for neighboring two sites $i = N/2$ and $i = N/2 + 1$ of the extended Hubbard model at $U = 2.0$ under different system sizes N

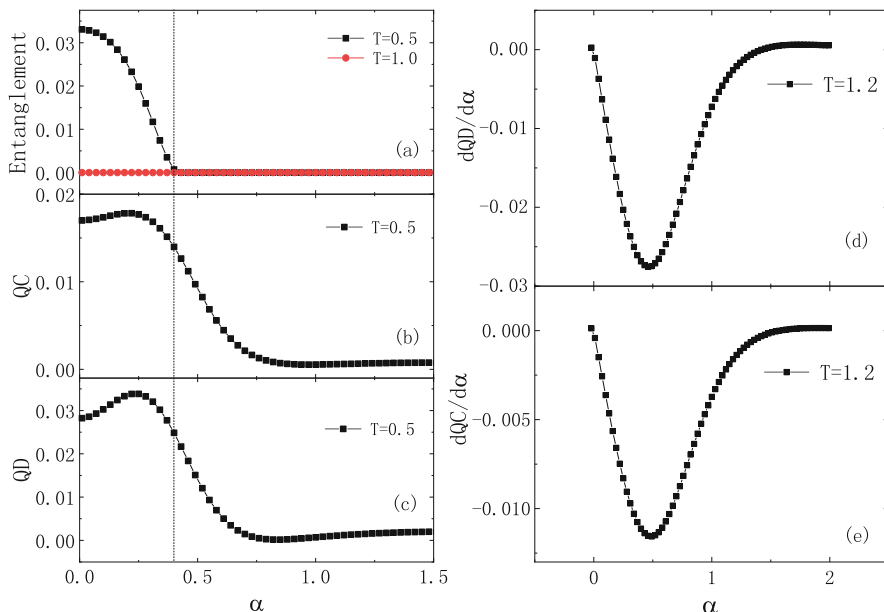


Fig. 8 (Color online) (a) The EOF, (b) QD, and (c) QC as a function of α under specific temperatures at $\lambda = 0.0$ and $\gamma = 0.5$ with $N = 1001$ for the XYT model. (d) and (e) show the derivative of QD and QC , respectively, with respect to α at $T = 1.2$. The dashed line on the left panel indicates the turning point at $\alpha = 0.4$ for EOF under $T = 0.5$

similar effectiveness as QD under such condition: the increment with α for them shows a turning point at the critical point $\alpha = 0.5$ (see Fig. 8b,c for $T = 0.5$), and their derivative can still reflect the quantum phase transition even at a relative high temperature $T = 1.2$, as shown in Fig. 8d,e.

QC is indeed more prominent than entanglement in detecting quantum phase transitions. However, its performance is not better than QD. Moreover, it cannot detect the BKT type critical point of the XXZ model. Given the correlation information theory proposed in Ref. [83] and as mentioned in Sect. 3.4 that QC contains the most amount of correlation information compared to quantum discord and entanglement, we attempt to reveal further its internal relationship with quantum phase transitions. We showed its advantages in characterizing quantum phase transitions by analyzing the spectrum of QC [53].

The definition of QC in Eq. (16) is a single number. Some information may be covered up by neutralization in the process of summation. Therefore, we turned to the basic source of information, that is, its construction spectrum. We defined two quantities to determine the change of information in each coherence energy level and reflect the distribution property of the spectrum. The two quantities, namely coherence entropy S_{QC} and logarithm of the spectrum L_{QC} , are as follows:

$$S_{QC} = - \sum_{n=1}^4 \alpha_n \ln \alpha_n, \quad (17)$$

$$L_{QC} = - \sum_{n=1}^4 \ln \alpha_n, \quad (18)$$

where α_n with $n = 1, 2, 3,$ and 4 is the four eigenvalues of I in Eq. (16), which consists of the four components in its spectrum.

Using the TMRG technique, we calculated the QD for the infinite XXZ spin chain, and the analytical method was used to deal with the XY and Ising models. The results for the XXZ model are shown in Fig. 9. The BKT type critical point at $\Delta = 1$ is clearly detected by the sharp peaks of L_{QC} at different temperatures, whereas QD (considered the only effective detector for this critical point at present) tends to zero at a relatively high temperature. The two critical points are also characterized by the minimum point in S_{QC} (see Ref. [53]). Compared with QC, which is a single number, coherent spectrum contains complete coherent information. L_{QC} here acquires the disappearance of coherence information in some specific coherence energy levels by analyzing the spectrum. S_{QC} possesses the form of information entropy. It reflects the distribution property of the coherence spectrum and presents more considerable correlation information than QC itself. The conclusion is also suitable for the quantum phase transitions in the XY and the topological-type quantum phase transition in the spin Kitaev models [53].

However, S_{QC} for the one-dimensional spin Kitaev model does not seem to be as robust against temperature as that for the other quantum phase transitions. The Hamiltonian of this model is as follows:

$$H = \sum_j^N \left(J_1 \sigma_{2j-1}^x \sigma_{2j}^x + J_2 \sigma_{2j}^y \sigma_{2j+1}^y \right), \quad (19)$$

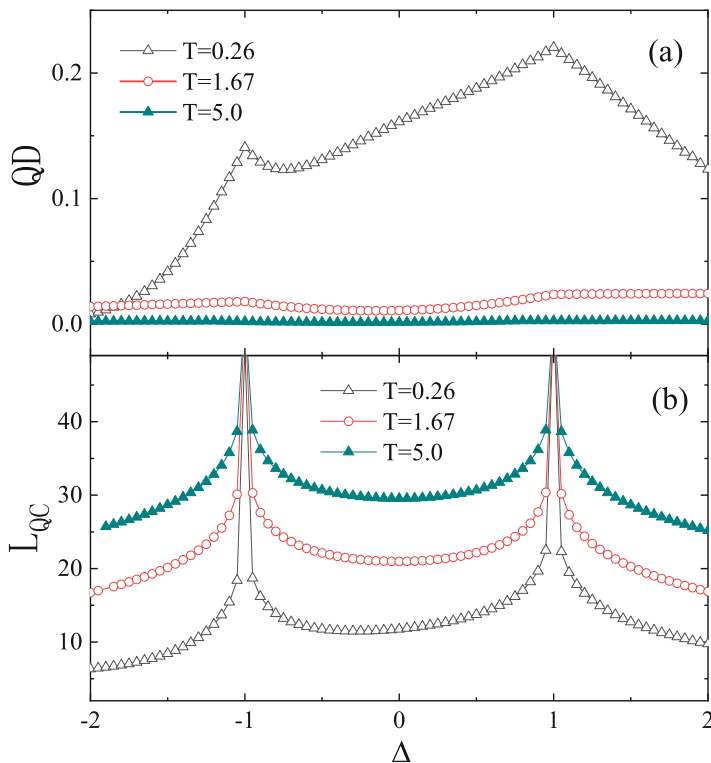


Fig. 9 (Color online) (a) QD and (b) L_{QC} as functions of Δ under different temperature T . QD tends to zero, and its cusp signature of CP disappears at a relative high T . (Reproduced from Ref. [53])

where J_1 and J_2 describe the spin–spin interactions alternatively along the chain. A topological critical point occurs at $J_2/J_1 = 1.0$ in this model [86]. The peak moves away from the critical point at a low temperature $T = 0.25$. The weak robustness may come from the detector or the detected quantum state itself. The phase transition at $J_2 = 1.0$ here belongs to the topological type. No symmetry-breaking behaviors occur for such phase transition; thus, it cannot be characterized by a local order parameter [21, 34, 86]. Therefore, we considered that the weak robustness probably comes from the weak ability against thermal fluctuations of the state itself. This conclusion was verified by the specific heat result. The thermal excitation peak in the specific heat for Kitaev model is considerably lower than that in XXZ model, representing an easily destroyed quantum order by thermal fluctuation in Kitaev model. Therefore, the relatively weak robustness against the temperature behavior of S_{QC} for the Kitaev model should not be attributed to S_{QC} . Moreover, S_{QC} is more accurate in detecting the critical point than other detectors in this case (details see Ref. [53]).

In summary, for a detector, the more information about the quantum correlation it contains, the more effective it is in resisting thermal fluctuations. Qc is considered the most important physical quantity in quantifying the quantum correlation contained in the system thus far. Therefore, it possesses natural advantages in signaling the quantum phase transitions. The above-mentioned results further proved this claim.

5 Deducing Order Parameters from Entanglement Based Method

The quantum information methods introduced in the previous sections have succeeded in detecting the quantum phase transition points. However, a challenge still remains: they can only detect the phase boundaries and give us little information about the corresponding phase property, which is a core issue in understanding the phase diagram of a system. Therefore, deducing the potential order parameters for various phases, particularly the topological phases, from the quantum information point of view can help us to learn about the phases' properties in unknown systems.

Several independent proposals to derive the order parameter exist. Furukawa et al. proposed a method by investigating a set of low-energy “quasi-degenerate” states that lead to the symmetry breaking in the thermodynamic limit [87]. Cheong and Henley [88] suggested to study the singular-value decomposition of the correlation density matrix to obtain the order parameter. Gu et al. [56] proposed a nonvariational and relatively more intuitive approach than the above-mentioned methods. Moreover, this approach may help establish the connection between the quantum phase transition detectors and the order parameters.

The main idea of Gu et al.'s approach is as follows. The order parameter is usually described by an operator. If an operator has a nonzero long-range expectation value, then a symmetry-breaking phase exists in the system. This operator can be used as an order parameter to describe the characteristic order of the quantum phase. The order parameter is usually expressed by the correlation function. For example, one can analyze the magnetic order of the system through the spin correlation to study the magnetic characteristics of a system. For one-dimensional case, the zero mode represents ferromagnetism, whereas the π mode predicts the antiferromagnetic order. The reduced density matrix, which is the core in the definition of each quantum phase transition detector, can be expressed by correlation function. Therefore, one can analyze the structure of the reduced density matrix to deduce the order parameter for a given unknown state. Along this direction, Gu et al. [56] proposed that if and only if the mutual information is nonvanishing at a long distance, then a long-range order exists in the system. One only needs to find the minimum block with the nonzero mutual information. Then, obtaining diagonal and off-diagonal long-range orders is possible depending on the reduced density matrix of the block (see Ref. [56] for detail). The method

was applied analytically on several imaginary simple examples in Ref. [56]. We applied the method using DMRG and exactly diagonalization numerical techniques to a practical and relative complex model, namely the SSH model with interactions, to verify and develop the method further.

This model is given by the Hamiltonian

$$\begin{aligned}
 H = & -t \sum_j \left[(1 + \eta) c_{j,B}^\dagger c_{j,A} + (1 + \eta) c_{j,A}^\dagger c_{j,B} \right. \\
 & \left. + (1 - \eta) c_{j+1,A}^\dagger c_{j,B} + (1 - \eta) c_{j,B}^\dagger c_{j+1,A} \right] \\
 & + U \sum_j n_{j,A} n_{j,B} + V \sum_j n_{j,B} n_{j+1,A}. \tag{20}
 \end{aligned}$$

The operator $c_{j,\alpha}$ destroys a spinless fermion at the unit cell j of type $\alpha = A, B$. The amplitude t is the hopping strength, η describes the dimerization, and U and V are local Hubbard-like term coupling fermions from the same unit cell and from the adjacent unit cells, respectively. This model initially describes a dimerized chain of spinless fermions hopping in a tight-binding band. Given the dimerization, the unit cell indexed by j contains two atoms of types A and B . We add the interaction terms. For the noninteracting case, a phase transition exists between the topological and topological-trivial phases at $\eta = 0$.

The mutual information or correlation entropy defined in Eq.(8) should be calculated to implement the method. The subsystem is taken as a single unit cell consisting of two atoms of type A and B . The mutual information and the reduced density matrix spectrum are calculated. The results showed that, for $\eta < 0$, nonzero long-range mutual information exists, indicating that we can use Gu et al.'s method to deduce the order parameter. On the basis of $|n_{j,A}, n_{j,B}\rangle = \{|00\rangle, |01\rangle, |10\rangle, |11\rangle\}$, the eigenstates denoted by $|A\rangle, |B\rangle, |C\rangle$, and $|D\rangle$ are equally weighted. According to the scheme, the order parameter can be defined as

$$O_- = w_A |A\rangle\langle A| + w_B |B\rangle\langle B| + w_C |C\rangle\langle C| + w_D |D\rangle\langle D|. \tag{21}$$

However, all four unknown coefficients must be fixed. This scenario is too much to deal with, because only the traceless and cut-off conditions exist. Therefore, we transformed the basis to the diagonal expression with the Majorana fermion operators to decrease the number of dominated states. In the transformed basis, the Hamiltonian is diagonalized, and the ground state is given by the vacuum state of the number operators n_f and n_d . The reduced density matrix is solely contributed by the state $|n_f = 0, n_d = 0\rangle$. Thus, the order parameter can be defined by $O_- = |00\rangle\langle 00|$ in the diagonal basis. Then, we transformed the diagonal operators back to the original spinless fermion operators and obtained a quasi-local order parameter that characterizes the topological phase in the model [57].

For the topological-trivial phase for $\eta > 0$, we took the block consisting of a B atom at site j and an atom A at site $j + 1$ instead of the single-site block with

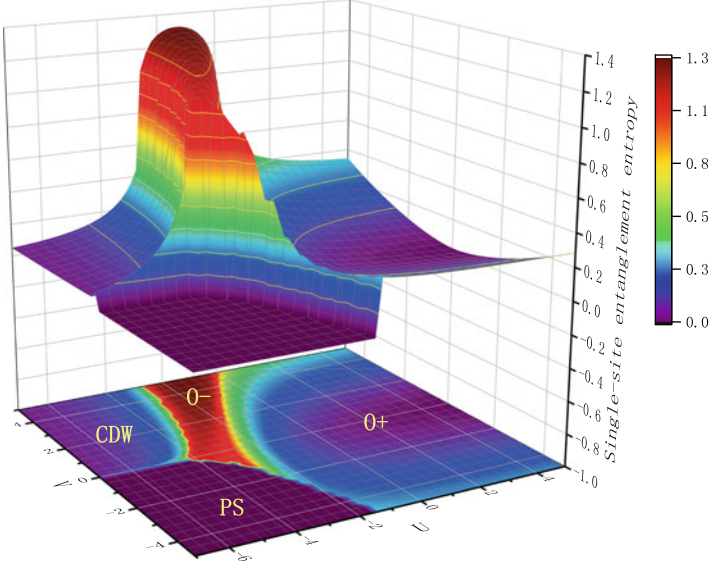


Fig. 10 (Color online) Single-site entanglement entropy and its contour map for $\eta = 0.6$ as a function of U and V . In each region, the dominant order parameters are shown (Reproduced from Ref. [57])

atoms A and B at the same site. The mutual information is also nonzero in this case, and only one dominating eigenstate of the reduced density matrix exists. The order parameter O_+ for the topological-trivial phase can be deduced directly without a basis transformation [57].

The order parameters were deduced for all the phases when U and V in Eq. (20) were added. Together with the entanglement entropy results and electronic configuration analysis, the order parameters results were verified, and the ground-state phase diagram of the system was obtained. Figure 10 shows the entanglement results where the confirmed phases are marked on its contour map. The deduced order parameter O_- that characterizes the topological state in the interacting SSH model was further used to study the quantum phases in the Schwinger model (the model introduces gauge bosons to regulate the interaction between fermions) and successfully characterize the topological quantum phases in that model [59].

The SSH model described in Eq. (20) (without U and V terms) becomes the SSH-Kitaev model by adding triplet TS pairing. A new Kitaev order topological phase is present in this system. The Hamiltonian is written as follows:

$$\begin{aligned}
 H = & -t \sum_j \left[(1 + \eta) c_{j,B}^\dagger c_{j,A} + (1 + \eta) c_{j,A}^\dagger c_{j,B} + (1 - \eta) c_{j+1,A}^\dagger c_{j,B} + (1 - \eta) c_{j,B}^\dagger c_{j+1,A} \right] \\
 & + \Delta \sum_j \left[(1 + \eta) c_{j,B}^\dagger c_{j,A}^\dagger + (1 + \eta) c_{j,A} c_{j,B} + (1 - \eta) c_{j+1,A}^\dagger c_{j,B}^\dagger + (1 - \eta) c_{j,B} c_{j+1,A} \right].
 \end{aligned}
 \tag{22}$$

The phase diagram needs four order parameters to be described. We further deduced the order parameters O_+^K and O_-^K of the Kitaev-type topological states by using the operator basis transformation similar to the Majorana fermion operators, as mentioned above (see Ref. [89]). Under the transformed basis, the Hamiltonian of the system is diagonalized at the parameter value that is taken deep inside each phase, and its ground state is the vacuum state of the corresponding operator. Thus, the order parameter can be simply written as the expectation value of the projection operator on a subset of the system's ground state. For example, at $\eta = 0$, the order parameters can be written as follows:

$$\begin{aligned} O_{j,+}^K &= |0\rangle\langle 0| = 1 - n_d \\ &= \frac{1}{2} - \frac{1}{2}H_j(t = \Delta = 1) \end{aligned} \quad (23)$$

and

$$O_{j,-}^K = \frac{1}{2} - \frac{1}{2}H_j(t = -\Delta = 1), \quad (24)$$

where H_j is the contribution from site j to the Hamiltonian. This observation indicates that the local Hamiltonian H_j itself may be used as the order parameter. The Hamiltonian of the system is expressed as $H = \sum_j H_j$. Thus, H_j from deep inside each of the four phases can serve as the corresponding quantum state order parameters of the system. We verified the conclusion by comparing the results of local H_j for different phases with the deduced order parameters from the reduced density matrix approach. This method is simple and expected to be useful in deducing the order parameters for complex quantum states.

6 Summary and Outlook

Entanglement and its related quantum correlations are the cornerstones of quantum mechanics. The quantum effects encoded in entanglement are the essence of high-performance quantum computing and high-efficiency quantum communication in the future. Studying quantum phase transition in spin chain systems from the perspective of quantum correlation not only paves a way to detect the entire critical regions of a system without empirical knowledge but also contributes to the understanding of quantum property and its application in spin chain-based quantum processing.

In this chapter, we present a brief but comprehensive introduction about the gradual development of the related research methods. We focus on the success of each relevant work, while the possible problems are also collected. From the correlation point of view, the more quantum correlation that the detector can capture, the more useful it is in detecting the quantum phase transition. Therefore, among

the three concepts, QC seems to be the best potential detector for quantum phase transitions because of its capability in detecting multiple types of phase transitions and its resistance to thermal fluctuations. Nevertheless, the research on QC are still far from complete. Its universality still needs further studies.

Another issue focuses on the systematic construction of the potential order parameters. We briefly introduce an approach to derive the order parameters starting from the reduced density matrix closely related to entanglement and quantum correlation. On this basis, we extend the approach to deal with the system with the relatively complex reduced density matrix spectrum by transforming the basis to the diagonalized basis of the Hamiltonian at specific values of the driving parameter. The connection between the order parameter and the reduced density matrix spectrum is established preliminarily, but the direct connection between the order parameter and the quantum phase transition detectors needs further analysis. A comprehensive method for the derivation of order parameters is constructive not only for the understanding of the properties of quantum states and quantum phase diagram construction but also for understanding of the performance of quantumness in quantum information science.

In addition, quantum simulators can successfully study the real-time dynamics of quantum many-body systems with the development of quantum level control technology. In recent years, the studies on dynamical quantum phase transitions have increased. Dynamical quantum phase transition studies have been developed to try to understand the dynamical behavior of quantum many-body systems by introducing the concept of phase transition in the time domain. At present, the research has two approaches: one is the order parameter method [90, 91], and the other is the nonresolution of the physical quantity, which mainly includes the Loschmidt echo and its correlation [52, 92] and the out-time-ordered correlation [93]. Dynamical quantum phase transitions in the case of quantum quench have been experimentally realized recently [92, 94]. For a detailed introduction, one can see the review article in Ref. [95]. In addition, the quantum phase transition of an equilibrium system is also studied from the dynamical correlation point of view [51]. The study of dynamic quantum phase transition is just at its beginning. The related work, such as definition understanding, phase transition classification, detection methods, and dynamical behaviors, must be further developed. In addition, the previous study of order parameter derivation has just been applied to equilibrium systems, whether it can be extended to such non-equilibrium systems is also an important issue.

Finally, finding efficient and universal quantum phase transition detectors and developing the methods for constructing the potential order parameters exhibit a lot of hope and challenge from the perspective of quantum information. Moreover, the essential relationship between entanglement and quantum phase transition still needs to be further explored. Further research on this topic is not only constructive to the improvement of the method itself but also expected to promote the development and utilization of quantumness in this process. We take this introductory text to sort out the relevant research and provide insights for future research. We hope that this work can stimulate advance ideas in building a real bridge between condensed matter physics and quantum informatics.

Acknowledgments We acknowledge financial support from the National Natural Science Foundation of China (Grants No. 12074376, No. 12088101, and 12005179) and the NSAF U1930402.

References

1. R. Horodecki, P. Horodecki, M. Horodecki, K. Horodecki, Quantum entanglement. *Rev. Mod. Phys.* **81**, 865 (2009)
2. Hardy, Lucien, *Phys. Rev. Lett.* **71**(11), 1665 (1993)
3. D. Loss, E.V. Sukhorukov, *Phys. Rev. Lett.* **84**, 1035 (2000)
4. J. Bell, *Speakable and Unsayable in Quantum Mechanics* (Cambridge University Press, Cambridge, 1987)
5. A. Peres, *Quantum Theory: Concepts and Methods* (Kluwer, Dordrecht, 1993)
6. P.W. Shor, J. Preskill, *Phys. Rev. Lett.* **85**, 441 (2000)
7. H.K. Lo, *New J. Phys.* **5**, 36 (2003)
8. M. Nielsen, I. Chuang, *Quantum Computation and Quantum Communication* (Cambridge University Press, Cambridge, 2000)
9. L. Amico, R. Fazio, A. Osterloh, V. Vedral, *Rev. Mod. Phys.* **80**, 517 (2008)
10. D. Bohm, *Phys. Rev.* **85**, 2 (1952)
11. D. Kershaw, *Phys. Rev.* **136**, B1850 (1964)
12. S. Aaronson, *Phys. Rev. A* **71**, 032325 (2005)
13. A. Budiyono, D. Rohrllich, *Nat. Commun.* **8**, 1306 (2017)
14. M.P. Kostyleva, A.A. Serga, T. Schneider, B. Leven, B. Hillebrands. *App. Phys. Lett.* **87**, 153501 (2005)
15. T. Nguyen, C.D. Hill, L.C.L. Hollenberg, M.R. James, *Sci. Rep.* **7**, 13386 (2017)
16. M. Hase, H. Kuroe, K. Ozawa, O. Suzuki, H. Kitazawa, G. Kido, T. Sekine, *Phys. Rev. B* **70**, 104426 (2004)
17. M. Enderle, B. Fäk, H.J. Mikeska, R.K. Kremer, A. Prokofiev, W. Assmus, *Phys. Rev. Lett.* **104**, 237207 (2010)
18. E. Lieb, T. Schultz, D. Mattis, *Phys. Rev.* **127**, 1508 (1962)
19. C. Chen, D. Yin, T. Kato, T. Taniguchi, Y. Ikuhara, *Proc. Natl. Acad. Sci.* **116**, 11181 (2019)
20. S.K. Ma, *Modern Theory of Critical Phenomena* (Addison-Wesley, Reading, 1976)
21. S. Sachdev, *Quantum Phase Transitions* (Cambridge University Press, Cambridge, 1999)
22. M. Greiner, O. Mandel, T. Esslinger, T.W. Hänsch, I. Bloch, *Nature* **415**, 39 (2002)
23. D. Jaksch, C. Bruder, J.I. Cirac, C.W. Gardiner, P. Zoller, *Phys. Rev. Lett.* **81**, 3108 (1998)
24. S. Chen, L. Wang, S.J. Gu, Y. Wang, *Phys. Rev. E* **76**, 061108 (2007)
25. S. Chen, L. Wang, Y.J. Hao, Y.P. Wang, *Phys. Rev. A* **77**, 032111 (2008)
26. P. Zanardi, N. Paunkovic, *Phys. Rev. E* **74**, 031123 (2006); P. Zanardi, H.T. Quan, X.G. Wang, C.P. Sun, *Phys. Rev. A* **75**, 032109 (2007)
27. H.Q. Lin, D.K. Campbell, R.T. Clay, *Chin. J. Phys.* **38**, 1 (2000)
28. H.Q. Lin, D.K. Gagliano, E.H. Campbell, J.E. Fradkin, Gubernatis, in *The Hubbard Model: Its Physics and Mathematical Physics*, ed. by D. Baeriswyl et al. (Plenum, New York, 1995), p. 315
29. X.L. Qi, S.C. Zhang, *Rev. Mod. Phys.* **83**, 1057 (2011)
30. N.D. Mathur, F.M. Grosche, S.R. Julian, I.R. Walker, D.M. Freye, R.K.W. Haselwimmer, G.G. Lonzarich, *Nature* **394**, 39 (1998)
31. A. Osterloh, L. Amico, G. Falci, R. Fazio, *Nature* **416**, 608 (2002)
32. G.S. Tian, H.Q. Lin, *Phys. Rev. B* **67**, 245105 (2003)
33. S.J. Gu, G.S. Tian, H.Q. Lin, *Chin. Phys. Lett.* **24**, 2737 (2007)
34. X.G. Wen, *Quantum Field Theory of Many-body Systems* (Oxford University, New York, 2004)
35. Q. Faure, S. Takayoshi, S. Petit, V. Simonet, S. Raymond, L. Regnault, M. Boehm, J. S. White, M. Månsson, C. Regg, P. Lejay, B. Canals, T. Lorenz, S.C. Furuya, T. Giamarchi, B. Grenier, *Nat. Phys.* **14**, 716 (2018)

36. V.L. Berezinskii, JETP **32**, 493 (1971)
37. H.T. Quan, Z. Song, X.F. Liu, P. Zanardi, C.P. Sun, Phys. Rev. Lett. **96**, 140604 (2006)
38. T. Werlang, C. Trippé, G.A.P. Ribeiro, G. Rigolin, Phys. Rev. Lett. **105**, 095702 (2010)
39. G. Karpat, B. Cakmak, F.F. Fanchini, Phys. Rev. B **90**, 104431 (2014)
40. S.J. Gu, S.S. Deng, Y.Q. Li, H.Q. Lin, Phys. Rev. Lett. **93**, 086402 (2004)
41. Ö. Legeza, J. Sólyom, Phys. Rev. Lett. **96**, 116401 (2006)
42. Y.C. Li, S.S. Li, Phys. Rev. B **78**, 184412 (2008)
43. P. Buonsante, A. Vezzani, Phys. Rev. Lett. **98**, 110601 (2007)
44. R. Berkovits, Phys. Rev. Lett. **115**, 206401 (2015)
45. S.L. Zhu, Phys. Rev. Lett. **96**, 077206 (2006)
46. Y.C. Li, S.S. Li, Phys. Rev. A **76**, 032117 (2007)
47. W.L. You, Y.W. Li, S.J. Gu, Phys. Rev. E **76**, 022101 (2007)
48. A. Hamma, W. Zhang, S. Haas, D.A. Lidar, Phys. Rev. B **77**, 155111 (2008)
49. D.F. Abasto, A. Hamma, P. Zanardi, Phys. Rev. A **78**, 010301(R) (2008)
50. J. Zhang, X. Peng, N. Rajendran, D. Suter, Phys. Rev. Lett. **100**, 100501 (2008)
51. F.J. Gómez-Ruiz, J.J. Mendoza-Arenas, F.J. Rodríguez, C. Tejedor, L. Quiroga, Phys. Rev. B **93**, 035441 (2016)
52. M. Heyl, A. Polkovnikov, S. Kehrein, Phys. Rev. Lett. **110**, 135704 (2013)
53. Y.C. Li, J. Zhang, Q.L. Hai, Phys. Rev. B **101**, 115142 (2020)
54. J. Sirker, Phys. Rev. Lett. **105**, 117203 (2010)
55. Y.W. Dai, Q.Q. Shi, S.Y. Cho, M.T. Batchelor, H.Q. Zhou, Phys. Rev. B **95**, 214409 (2017)
56. S.J. Gu, W.C. Yu, H.Q. Lin, Ann. Phys. **336**, 118 (2013)
57. W.C. Yu, Y.C. Li, P.D. Sacramento, H.Q. Lin, Phys. Rev. B **94**, 245123 (2016)
58. W.C. Yu, S.J. Gu, H.Q. Lin, Eur. Phys. J. B **89**, 212 (2016)
59. G. Magnifico, D. Vodola, E. Ercolessi, S. P. Kumar, M. Müller, A. Bermudez, Phys. Rev. D **99**, 014503 (2019)
60. S.J. Gu, H.Q. Lin, Y.Q. Li, Phys. Rev. A **68**, 042330 (2003)
61. S.J. Gu, G.S. Tian, H.Q. Lin, Phys. Rev. A **71**, 052322 (2005)
62. Y.C. Li, H.Q. Lin, Sci. Rep. **6**, 26365 (2016)
63. S.S. Deng, S.J. Gu, H.Q. Lin, Phys. Rev. B **74**, 045103 (2006)
64. Y.C. Li, H.Q. Lin, New. J. Phys. **14**, 063069 (2012)
65. A.A. Tsirlin, I. Rousochatzakis, D. Kasinathan, O. Janson, R. Nath, F. Weickert, C. Geibel, A.M. Läuchli, H. Rosner, Phys. Rev. B **82**, 144426 (2010)
66. I. Affleck, D. Gepner, H.J. Schulz, T. Ziman, J. Phys. A **22**, 511 (1989)
67. G.P. Zhang, Phys. Rev. B **68**, 153101 (2003)
68. Y.C. Li, Y.H. Zhu, Z.G. Yuan, Phys. Lett. A **380**, 1066 (2016)
69. Y.C. Li, Z.G. Yuan, Phys. Lett. A **380**, 272 (2016)
70. P. Fries, I.A. Reyes, Phys. Rev. Lett. **123**, 211603 (2019)
71. B.T. Ye, L.Z. Mu, H. Fan, Phys. Rev. B **94**, 165167 (2016)
72. E. Prodan, T.L. Hughes, B.A. Bernevig, Phys. Rev. Lett. **105**, 115501 (2010)
73. D. Poilblanc, Phys. Rev. Lett. **105**, 077202 (2010)
74. S.R. White et al., *Density-Matrix Renormalization: A New Numerical Method in Physics* (Springer, Berlin, 1999)
75. R.F. Werner, Phys. Rev. A **40**, 4277 (1989)
76. H. Ollivier, W.H. Zurek, Phys. Rev. Lett. **88**, 017901 (2001)
77. C.H. Bennett, D.P. DiVincenzo, J.A. Smolin, W.K. Wootters, Phys. Rev. A **54**, 3824 (1996)
78. E. Knill, R. Laflamme, Phys. Rev. Lett. **81**, 5672 (1998)
79. A. Datta, A. Shaji, C.M. Caves, Phys. Rev. Lett. **100**, 050502 (2008)
80. Y.C. Li, H.Q. Lin, Phys. Rev. A **83**, 052323 (2011)
81. M.S. Sarandy, Phys. Rev. A **80**, 022108 (2009)
82. M. Takahashi, *Thermodynamics of One-dimensional Solvable Models* (Cambridge University Press, Cambridge, 1999)
83. Y. Yao, X. Xiao, L. Ge, C.P. Sun, Phys. Rev. A **92**, 022112 (2015)
84. T. Baumgratz, M. Cramer, M.B. Plenio, Phys. Rev. Lett. **113**, 140401 (2014)

85. D. Girolami, Phys. Rev. Lett. **113**, 170401 (2014)
86. X.Y. Feng, G.M. Zhang, T. Xiang, Phys. Rev. Lett. **98**, 087204 (2007)
87. S. Furukawa, G. Misguich, M. Oshikawa, Phys. Rev. Letts. **96**, 047211 (2006)
88. S.A. Cheong, C.L. Henley, Phys. Rev. B **79**, 212402 (2009)
89. W.C. Yu, P.D. Sacramento, Y.C. Li, D.G. Angelakis, H.Q. Lin, Phys. Rev. B **99**, 115113 (2019)
90. J. Lang, B. Frank, J.C. Halimeh, Phys. Rev. Lett. **121**, 130603 (2018)
91. B. Zunkovic, M. Heyl, M. Knap, A. Silva, Phys. Rev. Lett. **120**, 130601 (2018)
92. P. Jurcevic, H. Shen, P. Hauke, C. Maier, T. Brydges, C. Hempel, B.P. Lanyon, M. Heyl, R. Blatt, C.F. Roos, Phys. Rev. Lett. **119**, 080501 (2017)
93. M. Heyl, F. Pollmann, B. Dora, Phys. Rev. Lett. **121**, 016801 (2018)
94. N. Fläschner, D. Vogel, M. Tarnowski, B.S. Rem, D.-S. Lühmann¹, M. Heyl, J.C. Budich, L. Mathey, K. Sengstock, C. Weitenberg, Nat. Phys. **14**, 265 (2017)
95. M. Heyl, Rep. Prog. Phys. **81**, 054001 (2018)

Entanglement Entropy in Critical Quantum Spin Chains with Boundaries and Defects



Ananda Roy and Hubert Saleur

Abstract Entanglement entropy (EE) in critical quantum spin chains described by 1+1D conformal field theories contains signatures of the universal characteristics of the field theory. Boundaries and defects in the spin chain give rise to universal contributions in the EE. In this work, we analyze these universal contributions for the critical Ising and XXZ spin chains for different conformal boundary conditions and defects. For the spin chains with boundaries, we use the boundary states for the corresponding continuum theories to compute the subleading contribution to the EE analytically and provide supporting numerical computation for the spin chains. Subsequently, we analyze the behavior of EE in the presence of conformal defects for the two spin chains and describe the change in both the leading logarithmic and subleading terms in the EE.

1 Introduction

Entanglement, one of the quintessential properties of quantum mechanics, plays a central role in the development of long-range correlations in quantum-critical phenomena. Thus, quantification of the entanglement in a quantum-critical system provides a way to characterize the universal properties of the critical point. The von Neumann entropy of a subsystem serves as a natural candidate to perform this task. For zero-temperature ground states of 1+1D quantum-critical systems described by conformal field theories (CFTs), the von Neumann entropy [equivalently in this case, entanglement entropy (EE)] for a subsystem exhibits universal logarithmic

A. Roy (✉)

Department of Physics and Astronomy, Rutgers University, Piscataway, NJ, USA

e-mail: ananda.roy@physics.rutgers.edu

H. Saleur

Institut de Physique Théorique, Paris Saclay University, CEA, CNRS, Gif-sur-Yvette, France

Department of Physics and Astronomy, University of Southern California, Los Angeles, CA, USA

e-mail: saleur@usc.edu

scaling with the subsystem size [1, 2]. The coefficient of this scaling determines a fundamental property of the bulk CFT: the central charge, which quantifies, crudely speaking, the number of long-wavelength degrees of freedom. The aforementioned scaling, together with strong subadditivity property of entropy [3] and Lorentz invariance, leads to an alternate proof [4] of the celebrated c -theorem [5] in $1 + 1$ dimensions. At the same time, the scaling of EE in these gapless systems [6] and their gapped counterparts [7] lies at the heart of the success of numerical techniques like density matrix renormalization group (DMRG) [8, 9] in simulating $1 + 1$ D quantum systems.

Given the widespread success of EE in characterizing bulk properties of quantum-critical points, it is natural to ask if EE also captures signatures of boundaries and defects in gapless conformal-invariant systems. Consider CFTs on finite systems with conformal boundary conditions. For these systems, the EE receives a universal, subleading, boundary-dependent contribution, the so-called boundary entropy [10, 11]. The latter, related to the “ground-state degeneracy” of the system, plays a central role in a wide range of problems both in condensed matter physics [12, 13] and in string theory [14]. The boundary contribution in the EE is a valuable diagnostic for identifying the different boundary fixed points of a given CFT [15–17].

Conformal defects or interfaces comprise the more general setting. In the simplest case, a CFT, instead of being terminated with vacuum, is glued to another CFT [18]. In general, the two CFTs do not have to be the same and have not even the same central charges [19]. Unlike the case of boundaries, conformal defects can affect not just the subleading terms in the EE but also the leading logarithmic scaling [20–22]. Of particular interest are the (perfectly transmissive) topological defects which can glue together CFTs of identical central charges [18, 23–26]. These defects commute with the generators of conformal transformations and, thus, can be deformed without affecting the values of the correlation functions as long as they are not taken across field insertions (hence the moniker topological). They reflect the internal symmetries of the CFT and relate the order-disorder dualities of the CFT to the high-low temperature dualities of the corresponding off-critical model [24, 27, 28]. They also play an important role in the study of anyonic chains and in the correspondence between CFTs and three-dimensional topological field theories [29]. For these topological defects, the EE receives nontrivial contributions due to zero-energy modes of the defect Hamiltonian [30, 31], which in turn can be used to identify the different defects [31]. Note that although the EE of a subsystem in the presence of a defect contains information about the latter [20, 32, 33], the exact behavior of the EE depends on the geometric arrangement of the subsystem with respect to the defect.

The goal of this work is to describe the behavior of the EE for the Ising and the free, compactified boson CFTs in the presence of boundaries and defects. First, we compute the boundary entropy for these two models for free (Neumann) and fixed (Dirichlet) boundary conditions for the continuum theory using analytical techniques. This is done by computing the corresponding boundary states [34, 35]. We compare these analytical predictions with numerical computations of the EE for

suitable lattice regularizations. Subsequently, we investigate EEs in the two CFTs in the presence of defects when the defect is located precisely at the interface between the subsystem and the rest. For the Ising model, we consider the energy and duality defects. The computation of EE is performed by mapping the defect Hamiltonian to a free-fermion Hamiltonian and computing the ground-state correlation function. Finally, we analyze the EE across a conformal interface of two free, compactified boson CFTs. The numerical computation is done using DMRG for two coupled XXZ chains with different anisotropies.

2 Entanglement Entropy in CFTs with Boundaries

Consider the ground state, $|\Psi\rangle$, of a many-body system described by a CFT at zero temperature. Then, the EE of a spatial region, A, is the von Neumann entropy:

$$S_A = -\text{Tr}_A(\rho_A \ln \rho_A) = -\lim_{n \rightarrow 1} \frac{\partial}{\partial n} \text{Tr} \rho_A^n. \quad (1)$$

Here n is the replica index and $\rho_A = \text{Tr}_B(|\Psi\rangle\langle\Psi|)$. Furthermore, B denotes the rest of the system. The density matrix ρ_A can be computed using the path-integral formalism in Euclidean space-time cut open at the intersection of the region A (for a detailed derivation, see Ref. [11]). In particular, the EE can be obtained from a computation of the partition function Z_1 on the surface and Z_n on its n -sheeted cover $\text{Tr}_A \rho_A^n = Z_n/Z_1^n$. For the geometries and models under consideration, this amounts to computation of the partition functions on annuli after suitable conformal transformations [16]. We directly state the results for the EE for three different geometries (see Fig. 1) and refer to the reader to Ref. [16] for the derivations. In

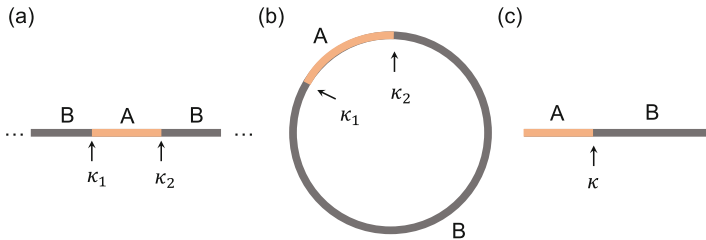


Fig. 1 Schematic of the three different geometries considered: (a) a finite region (A) of length r in an infinite system, (b) a finite region of length r in a periodic ring of length L , and (c) a finite region of length r in a finite system of length L . In the last case, one end of the subsystem coincides with the end of the system. The cuts separating A from B are denoted by $\kappa_{1,2}$. Note that in panel (c), one of the entanglement cuts coincides with the physical termination of the total system, resulting in the geometry having only one entanglement cut. This leads to a different leading order dependence of the EE [see Eqs. (3,4)]

particular, for a finite region of length r within an infinite system (Fig. 1a), the EE is given by

$$S_A = \frac{c}{3} \ln \frac{r}{a} + s_1 + s_2 + \dots, \quad (2)$$

where c is the central charge of the CFT and a is the non-universal constant related to the UV cutoff. Furthermore, $s_{1,2} = \ln g_{1,2}$ are $\mathcal{O}(1)$ contributions to the EE that arise due to the ‘entanglement cuts’, $\kappa_{1,2}$, at the junction of the subsystem (A) and the rest (B). The $g_{1,2}$ are the corresponding g -functions [10, 12]. For identical regularization procedures for the two cuts κ_1 and κ_2 , $s_1 = s_2$. The dots correspond to subleading corrections [16, 17]. Analogous results hold for a region within a periodic ring of length (L) (Fig. 1b), where the EE for subsystem A is given by:

$$S_A = \frac{c}{3} \ln \left[\frac{L}{\pi a} \sin \left(\frac{\pi r}{L} \right) \right] + s_1 + s_2 + \dots, \quad (3)$$

where the various variables are interpreted as before. Finally, we consider the case of a finite system of length L with identical boundary conditions¹ at the two ends, with one end of the subsystem coinciding with physical boundary of the total system (Fig. 1c). In this case, the EE is given by

$$S_A = \frac{c}{6} \ln \left[\frac{2L}{\pi a} \sin \left(\frac{\pi r}{L} \right) \right] + s_1 + s_2 + \dots \quad (4)$$

Note that the coefficient of the leading logarithmic term is $c/6$ as opposed to $c/3$ of the previous cases. This accounts for the difference in the number of entanglement cuts in this case compared to the previous two. In particular, while the $\mathcal{O}(1)$ -term s_2 arises from the entanglement cut κ , s_1 arises due to the physical boundary condition of the system. For generic systems, the boundary condition arising out of the entanglement cut is free boundary condition [17, 36, 37].

Below, we describe the two cases of the Ising and the free, compactified boson CFTs with different boundary conditions for the geometry in Fig. 1c.

2.1 Ising Model

The Ising model is the unitary, minimal model $\mathcal{M}(4, 3)$ with central charge $c = 1/2$ (see, for example, Chapters 7 and 8 of Ref. [38]). It contains three primary fields, I, σ, ϵ , with conformal dimensions: $h_I = 0, h_\sigma = 1/16$, and $h_\epsilon = 1/2$. We will consider two cases: (i) free/Neumann (N) boundary conditions at both ends and (ii)

¹ See Ref. [16] for discussion on different boundary conditions at the two ends.

fixed/Dirichlet (D) boundary conditions at both ends. The boundary states for the different boundary conditions are given by Cardy [35]

$$\begin{aligned} |\tilde{0}\rangle &= \frac{1}{\sqrt{2}}|0\rangle + \frac{1}{\sqrt{2}}|\epsilon\rangle + \frac{1}{2^{1/4}}|\sigma\rangle, \\ \left|\frac{\tilde{1}}{2}\right\rangle &= \frac{1}{\sqrt{2}}|0\rangle + \frac{1}{\sqrt{2}}|\epsilon\rangle - \frac{1}{2^{1/4}}|\sigma\rangle, \\ \left|\frac{\tilde{1}}{16}\right\rangle &= |0\rangle - |\epsilon\rangle, \end{aligned} \quad (5)$$

where the first two correspond to Dirichlet boundary conditions and the last corresponds to Neumann boundary condition (see Chap. 11 of Ref. [38] for further details). The corresponding g -functions are

$$g_N = \left\langle 0 \left| \frac{\tilde{1}}{16} \right\rangle \right\rangle = 1, \quad g_D = \langle 0 | \tilde{0} \rangle = \left\langle 0 \left| \frac{\tilde{1}}{2} \right\rangle \right\rangle = \frac{1}{\sqrt{2}}. \quad (6)$$

This straightforwardly reveals the change in boundary entropy as the boundary condition is changed from Neumann to Dirichlet:

$$\Delta S = s_N - s_D = \ln \frac{g_N}{g_D} = \frac{1}{2} \ln 2. \quad (7)$$

Next, we compute using DMRG, the EE in a critical transverse field Ising chain and compare with the analytical CFT predictions derived above. The Neumann condition is implemented by a spin chain with open boundaries. The lattice Hamiltonian is given by

$$H_{\text{TFI}}^N = -\frac{1}{2} \sum_{i=1}^{L-1} \sigma_i^x \sigma_{i+1}^x - \frac{1}{2} \sum_{i=1}^L \sigma_i^z. \quad (8)$$

The Dirichlet boundary condition is implemented by adding a small longitudinal boundary field at the two ends of the chain:

$$H_{\text{TFI}}^D = H_{\text{TFI}}^N - h_b(\sigma_1^x + \sigma_L^x). \quad (9)$$

The boundary field sets a correlation length-scale. By looking at the change in the EE for a subsystem size much larger than this correlation length, we can extract the boundary entropy contribution in the scaling limit. In our simulations, we chose the system size to be $L = 1600$ and a bond-dimension of 600 to keep truncation errors below 10^{-12} . We verify the central charge (c) to be $\simeq 1/2$. This is done by evaluating the entanglement entropy S for a finite block (of length r) within the system (of length L) and fitting to Eq. (4) for Neumann and Dirichlet boundary conditions at

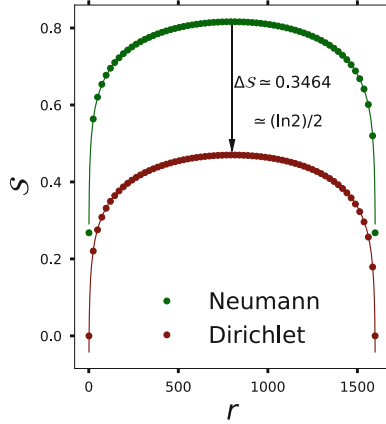


Fig. 2 DMRG results for the critical transverse field Ising chain. The system size $L = 1600$. Entanglement entropy S as a function of the subsystem size r for Neumann (green) and Dirichlet (maroon) boundary conditions. The central charge was verified to be $\simeq 1/2$ by fitting the data for Neumann boundary conditions to Eq. (4). As the boundary condition changes from Neumann to Dirichlet, the entanglement entropy changes by 0.3464 which is close to the expected change in the boundary entropy given by $(\ln 2)/2$

both ends of the chain. By changing the boundary conditions, we obtain a change in entropy that is very close to the expected value of $(\ln 2)/2$ (see Fig. 2).

2.2 The Free, Compactified Boson Model

Consider the free, compactified boson CFT with a compactification radius R over an interval $[0, L]$ with either Neumann or Dirichlet boundary conditions. The Euclidean action is given by

$$\mathcal{A}_0 = \frac{1}{2} \int_0^\beta dt \int_0^L dx \left[(\partial_t \phi)^2 + (\partial_x \phi)^2 \right], \quad (10)$$

where β is the inverse temperature. At the boundary, Neumann boundary condition corresponds to $\partial_x \phi = 0$, while Dirichlet corresponds to $\phi = \phi_0$, where ϕ_0 is a constant. The boundary states for this model are well-known [39, 40]. They are

$$|N(\tilde{\phi}_0)\rangle = \sqrt{R\sqrt{\pi}} \sum_m e^{-\frac{im\tilde{\phi}_0 R}{2\sqrt{\pi}}} \exp\left[+ \sum_{k>0} \tilde{a}_{-k}^\dagger \tilde{a}_k^\dagger \right] |0, m\rangle, \quad (11)$$

$$|D(\phi_0)\rangle = \frac{1}{\sqrt{2R\sqrt{\pi}}} \sum_n e^{-\frac{in\phi_0}{R\sqrt{\pi}}} \exp\left[- \sum_{k>0} \tilde{a}_{-k}^\dagger \tilde{a}_k^\dagger \right] |n, 0\rangle. \quad (12)$$

Note the duality between Neumann and Dirichlet boundary conditions: $R \leftrightarrow 2/R$ and $\tilde{\phi}_0$ is the field dual to ϕ_0 . Recall that the integers m, n determine the winding number and the quantization of the zero-mode momenta, respectively. The normalizations for the boundary states directly yield the corresponding g -functions leading to the following change in the boundary entropies:

$$g_N = \sqrt{R\sqrt{\pi}}, g_D = \frac{1}{\sqrt{2R\sqrt{\pi}}} \Rightarrow \Delta S = \ln \frac{g_N}{g_D} = \frac{1}{2} \ln(2R^2\pi). \quad (13)$$

Next, we provide numerical verification of the above result. To that end, we consider a finite XXZ spin chain. The open spin chain realizes the Neumann boundary condition:

$$H_{\text{XXZ}}^N = -\frac{1}{2} \sum_{i=1}^{L-1} \left[\sigma_i^x \sigma_{i+1}^x + \sigma_i^y \sigma_{i+1}^y + \Delta \sigma_i^z \sigma_{i+1}^z \right], \quad (14)$$

where Δ is the anisotropy parameter. As is well-known, the long-wavelength properties of this spin chain, in the paramagnetic regime, $-1 \leq \Delta \leq 1$, are well-described by the free, compactified boson CFT [see Eq. (10)] [41, 42]. The compactification radius is related to the Luttinger parameter (K) in the following way:

$$R = \frac{1}{\sqrt{\pi K}}, K = \frac{2}{\pi} \cos^{-1} \Delta. \quad (15)$$

The Dirichlet boundary condition is realized by adding a small-transverse field along the σ_x direction at the boundaries:

$$H_{\text{XXZ}}^D = H_{\text{XXZ}}^N - h_b(\sigma_1^x + \sigma_L^x), \quad (16)$$

where h_b is the boundary field strength. Bosonizing the Hamiltonian with boundary fields leads to the boundary sine-Gordon Hamiltonian [43, 44] with massless bulk [45] in the scaling limit (we follow the bosonization rules of Ref. [46]):

$$\mathcal{A}_{\text{bSG}} = \mathcal{A}_0 + M_b \int dt \left[\cos \frac{\beta\phi(x=0)}{2} + \cos \frac{\beta\phi(x=L)}{2} \right], \quad (17)$$

where $\beta = \sqrt{4\pi K}$ and M_b is the boundary potential strength which depends on the lattice parameter h_b . A nonzero M_b (equivalently, a nonzero h_b) induces the boundary RG flow from Neumann to Dirichlet boundary conditions. In terms of the Luttinger parameter, the corresponding change in the boundary entropy is given by

$$\Delta S = \frac{1}{2} \ln \frac{2}{K}. \quad (18)$$

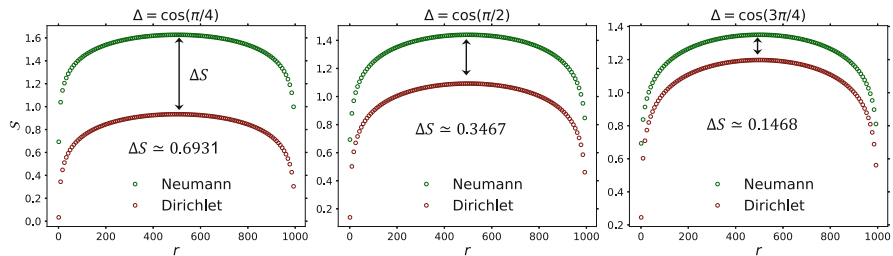


Fig. 3 DMRG results for the XXZ chain. The anisotropy parameters are $\Delta = \cos(\pi/4)$ (left), $\cos(\pi/2)$ (center) and $\cos(3\pi/4)$ (right). The corresponding Luttinger parameters are $K = 0.5, 1.0$ and $K = 1.5$. The system size $L = 1000$. Entanglement entropy, S , as a function of the subsystem size r for Neumann (green) and Dirichlet (maroon) boundary conditions. The central charge was verified to be $\simeq 1$ by fitting to Eq. (4). As the boundary condition changes from Neumann to Dirichlet, the EE changes by 0.6931, 0.3467, and 0.1468, respectively. The obtained results are close to the expected changes in the boundary entropy: $\ln 2$, $(\ln 2)/2$, and $[\ln(4/3)]/2$, respectively

Figure 3 shows the results of the computation of the EE for the various bipartitions of the system for $\Delta = \cos(\pi/4)$, $\cos(\pi/2)$, and $\cos(3\pi/4)$. The corresponding Luttinger parameters are given by $K = 1/2, 1$, and $3/2$. The change in the boundary entropy is computed by taking the difference of the EE values near the center of the chain. The obtained [expected] values of ΔS are $\simeq 0.6931$ [$\ln 2$], 0.3467 [$(\ln 2)/2$], and 0.1468 [$[\ln(4/3)]/2$] for the chosen values of the Δ .

3 Entanglement Entropy in CFTs with Defects

In this section, we consider the more general setting of two CFTs glued together by a defect and investigate the behavior of the interface EE, i.e., the EE across the defect. The latter measures the amount of entanglement between the two CFTs glued together at the defect as long as the state of the total system remains pure. Intuitively, the presence of the defect leads to back-scattering of the information-carrying modes of the system. This leads to a diminishing of entanglement between the left and right halves of the system connected at the defect compared to the case when there is no defect. In particular, we concentrate on those defects which are marginal perturbations around fixed point without any defects. For these models, the interface EE exhibits still the logarithmic scaling characteristic of the CFT without defects. However, unlike the case without defects, the coefficient of the logarithmic scaling yields a continuously varying “effective central charge”—a manifestation of the well-known effect that marginal perturbations lead to continuously varying scaling exponents [47, 48]. In fact, the central charge depends continuously on the transmission coefficient, t , of the scattering matrix in the scattering picture.

Next, we describe the behavior of the interface EE for the Ising and the free, compactified boson models in the presence of such defects. We will always consider

the case where the defect lies at the center of a chain with open boundary conditions and compute the interface EE for a subsystem extending from the left end of the system up to the defect. Then, the interface EE ($S_{\mathcal{I}}$) for a total system size L scales as:

$$S_{\mathcal{I}}[t(b)] = \frac{c_{\text{eff}}[t(b)]}{6} \ln \frac{L}{a} + s_1 + s_2[t(b)] + \dots, \quad (19)$$

where $c_{\text{eff}}[t(b)]$ is a continuously varying “effective central charge” and b is the defect strength. It occurs with a factor $1/6$ since there is effectively only one entanglement cut for a system with open boundary conditions (see discussion in Sect. 2). The subleading term has two contributions: s_1 arises from the boundary condition on the left and $s_2[t(b)]$ from the defect. Finally, the dots indicate terms that are smaller than $\mathcal{O}(1)$. The explicit dependence of the c_{eff} on the defect strength is nontrivial and has been analytically obtained for the free, real fermion [21, 32] and the free, compactified boson [20, 22]. They are provided below.

3.1 The Ising Model

In this section, we describe the two defect classes: energy and duality of the Ising model.

3.1.1 Energy Defect

The energy defect for the Ising model arises due to a ferromagnetic coupling with an altered strength b_ϵ [40, 49]. The Hamiltonian is given by

$$H_{\text{TFI}}^\epsilon = -\frac{1}{2} \sum_{j=1}^{L-1} \sigma_j^x \sigma_{j+1}^x - \frac{1}{2} \sum_{j=1}^L \sigma_j^z + \frac{1-b_\epsilon}{2} \sigma_{i_0}^x \sigma_{i_0+1}^x, \quad (20)$$

where $i_0 = L/2$ (for definiteness, we take L even). For our purposes, it is sufficient to consider $b_\epsilon \in [-1, 1]$. In particular, $b_\epsilon = 1$ corresponds to the case when there is no defect, while $b_\epsilon = 0$ splits the chain in two halves.² Finally, $b_\epsilon = -1$ corresponds to an antiferromagnetic bond in the middle of the chain. Note that for an open chain, unlike for a periodic chain, any defect Hamiltonian with defect strength $-b_\epsilon$ can be transformed to one with defect strength b_ϵ under a nonlocal unitary transformation. The latter involves flipping all the spins on one half of the chain. In this way, a $b_\epsilon = -1$ defect can be transformed away to the case without a defect.

² Note that the open chain can be obtained from the periodic Ising chain by introducing an energy defect between the sites L and 1 with strength $b_\epsilon = 0$.

As is evident from Eq. (20), the defect part of the Hamiltonian is indeed a marginal perturbation by the primary operator ϵ at a point in space (recall that the conformal dimensions of ϵ are $h_\epsilon = \bar{h}_\epsilon = 1/2$). This model can be mapped, using standard folding maneuvers [13, 40], to a boundary problem of the \mathbb{Z}_2 orbifold of the free-boson. This allows computation of relevant spin-spin correlation functions across the defects [40]. Since our interest is in the interface EE, we use a different, exact, solution of the problem by mapping it to a fermionic model. The Hamiltonian of the latter model is bilinear in fermionic creation and annihilation operators and can be diagonalized semi-analytically [50, 51]. This leads to very efficient computation of EE from the ground-state correlation matrix using techniques of Refs. [52–54].

This is done using the Jordan-Wigner (JW) transformation:

$$\gamma_{2k-1} = \sigma_k^x \prod_{j=1}^{k-1} \sigma_j, \quad \gamma_{2k} = \sigma_k^y \prod_{j=1}^{k-1} \sigma_j, \quad (21)$$

where γ_j -s are real, fermion operators obeying $\{\gamma_j, \gamma_k\} = 2\delta_{j,k}$. Note that $-i\gamma_{2k-1}\gamma_{2k} = \sigma_k^z$. The resulting fermionic Hamiltonian is given by

$$H_{\text{TFI}}^{\epsilon,f} = \frac{i}{2} \sum_{j=1}^{L-1} \gamma_{2j}\gamma_{2j+1} + \frac{i}{2} \sum_{j=1}^L \gamma_{2j-1}\gamma_{2j} - \frac{i(1-b_\epsilon)}{2} \gamma_{2i_0}\gamma_{2i_0+1}. \quad (22)$$

Now, we diagonalize this Hamiltonian numerically and compute the EE for different bipartitionings of the system by computing the ground-state correlation matrix (similar results have been obtained in Ref. [55]). Figure 4(left) shows the EE for varying b_ϵ from 0 to 1.0 in steps of 0.2. The interface EE is obtained by choosing $r = L/2$. The scaling of the interface EE with L for $b_\epsilon = 0.2$ is shown on the top right panel. Fitting to Eq. (19) leads to a $c_{\text{eff}} = 0.112$. The analytical prediction for the effective central charge is [21, 32]

$$c_{\text{eff}}(t) = \frac{|t|}{2} - \frac{1}{2} - \frac{3}{\pi^2} \left[(|t|+1) \ln(|t|+1) \ln(|t|) + (|t|-1) \text{Li}_2(1-|t|) + (|t|+1) \text{Li}_2(-|t|) \right], \quad (23)$$

where $t = \sin[2(\cot^{-1} b_\epsilon)]$ and Li_2 is the dilogarithm function [56]. The results obtained by the free-fermion technique are compatible with that predicted by Eq. (23) up to the third decimal place. Figure 4 shows a comparison of the effective central charges (top right panel) and the corresponding offsets (bottom right panel). We compute the offsets normalized with respect to the case of no defect and plot $s_2[t(b_\epsilon)] - s_2[t(b_\epsilon = 1)]$ for different values of b_ϵ . We do not know of an analytical expression for the normalized offsets.

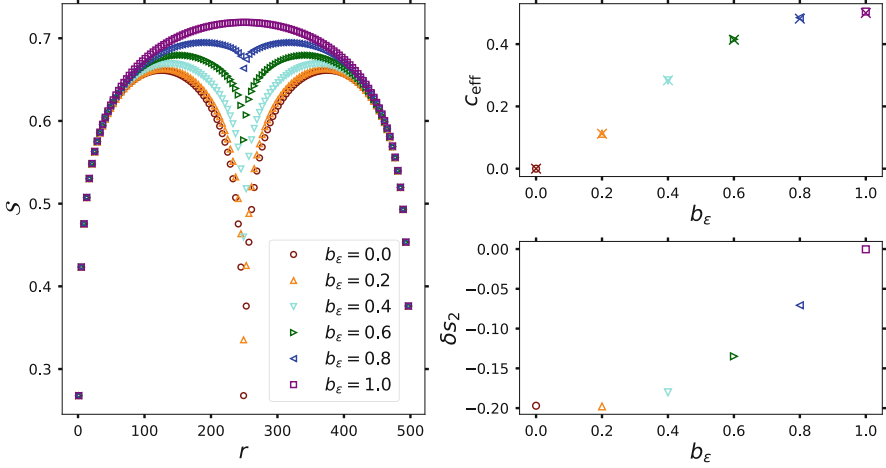


Fig. 4 Results for EE (S) for an open Ising chain with an energy defect. The defect strength is varied from 0 to 1 in steps of 0.2. (Left) The EE for different bipartitions of the in a system, with a total system size, $L = 500$. The dip around the center of the chain for the EE is due to the defect. (Top right) Effective central charge from the scaling of the interface EE (S_I) for varying system sizes from $L = 100$ to $L = 500$. Fitting to Eq. (19) yields the corresponding c_{eff} -s, which are plotted in the top right panel. For comparison, the analytical predictions from Eq. (23) are shown with crosses of the corresponding color. The corresponding offsets, normalized with respect to the case of no defect: $\delta s_2 = s_2[t(b_\epsilon)] - s_2[t(b_\epsilon = 1)]$, are obtained from the linear fit and are plotted in the bottom right panel. We do not know of an analytical expression for the δs_2 -s

3.1.2 Duality Defect

The duality defect [26, 57] of the Ising model between the sites at i_0 and $i_0 + 1$ arises due to an interaction of the form $\sigma_{i_0}^x \sigma_{i_0+1}^y$ instead of the usual ferromagnetic coupling. Equally important, there is no transverse field at the site $i_0 + 1$. The resulting defect Hamiltonian is given by

$$H_{\text{TFI}}^\sigma = -\frac{1}{2} \sum_{\substack{j=1, \\ j \neq i_0}}^{L-1} \sigma_j^x \sigma_{j+1}^x - \frac{1}{2} \sum_{\substack{j=1, \\ j \neq i_0+1}}^L \sigma_j^z - \frac{b_\sigma}{2} \sigma_{i_0}^x \sigma_{i_0+1}^y. \quad (24)$$

The duality defect for $b_\sigma = 1$ (equivalently $b_\sigma = -1$, which is related by a local unitary rotation) is the topological defect for the Ising CFT. Note that this duality defect Hamiltonian is related by a local unitary rotation on the $(i_0 + 1)^{\text{th}}$ spin to the one considered in Refs. [40], which has $\sigma_i^x \sigma_{i+1}^z$ interaction. We do not use this alternate form since it no longer leads to a bilinear Hamiltonian under JW transformation and cannot be solved by the free-fermion technique.

The fundamental difference between the duality and the energy defect Hamiltonians is best captured by the JW transformation. In the fermionic language, the defect Hamiltonian is given by

$$H_{\text{TFI}}^{\sigma,f} = \frac{i}{2} \sum_{\substack{j=1, \\ j \neq i_0}}^{L-1} \gamma_{2j} \gamma_{2j+1} + \frac{i}{2} \sum_{\substack{j=1, \\ j \neq i_0+1}}^{L-1} \gamma_{2j-1} \gamma_{2j} + \frac{i b_\sigma}{2} \gamma_{2i_0} \gamma_{2i_0+2}. \quad (25)$$

Note that the operator γ_{2i_0+1} does not occur in $H_{\text{TFI}}^{\sigma,f}$. It commutes with the Hamiltonian: $[\gamma_{2i_0+1}, H_{\text{TFI}}^{\sigma,f}] = 0$ and anticommutes with the conserved \mathbb{Z}_2 charge: $\{\gamma_{2i_0+1}, Q\} = 0$, where $Q = \prod_{j=1}^L \sigma_j^z = 1$. Thus, it is a zero mode of the model which is perfectly localized in space. It has a partner zero mode which is completely delocalized:

$$\Lambda(b_\sigma) = b_\sigma \sum_{k=1}^{i_0} \gamma_{2k-1} + \sum_{k=i_0+1}^L \gamma_{2k}. \quad (26)$$

Note that the zero modes exist for all values of b_σ and are not special features of the topological point. The fermionic Hamiltonian also reaffirms a CFT result [57, 58]: $H_{\text{TFI}}^{\sigma,f}$ describes a chain of $2L - 1$ Majorana fermions or equivalently, $L - 1/2$ spins. This is important for quantifying finite-size effects.

Now, we compute the EE for different bipartitionings of the system from the ground-state correlation matrix. However, unlike the energy defect for an open chain, as was just described, there are zero-energy states of the defect Hamiltonian. The existence of these states raises the question: are the zero-energy states empty or occupied in the ground state? Yet another possibility is to consider an incoherent superposition of filled and empty states. The latter possibility leads to the total system being in a mixed state but is appropriate when taking the zero-temperature limit of a thermal ensemble [59]. The question is crucial to the computation since zero-energy modes nontrivially affect the EE. In fact, for a periodic chain of free, real fermions, when the total system is in a mixed state, the zero modes give rise to nontrivial corrections to the EE of a subsystem of size r within a total system of size L [30, 59]. The correction is given by

$$\Delta S\left(\frac{r}{L}\right) = \frac{\pi r}{L} \int_0^\infty \tanh\left(\frac{\pi r h}{L}\right) [\coth(\pi h) - 1]. \quad (27)$$

For $r \ll L$, the EE is oblivious to the existence of the two nonlocal zero modes spread throughout the system: $\Delta S \simeq \pi^2 r^2 / 12 L^2 \rightarrow 0$. The situation changes as the subsystem occupies appreciable fraction of the total system ($r \sim L$) culminating in $\Delta S(r = L) = \ln 2$, the latter being the entropy of the two-fold degenerate ground state of a periodic chain of free, real fermions. Similar corrections occur for the Ising chain with the duality defect for different choices of the total system being pure or

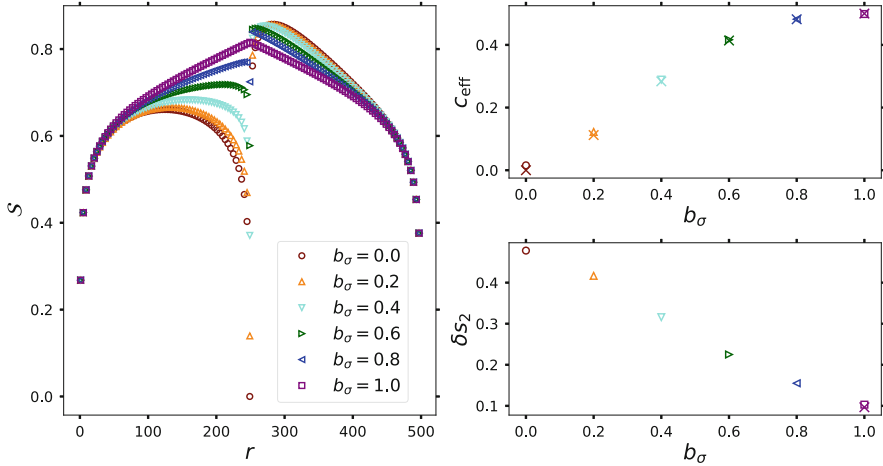


Fig. 5 Results for EE (S) for an open Ising chain with a duality defect. The defect strength is varied from 0 to 1 in steps of 0.2. (Left) The EE for different bipartitionings of the in a system, with a total system size, $L = 500$. The dip around the center of the chain for the EE is due to the defect. (Top right) Effective central charge from the scaling of the interface EE ($S_{\mathcal{I}}$) for varying system sizes from $L = 100$ to $L = 500$. Fitting to Eq. (19) yields c_{eff} , which are plotted in the top right panel. For comparison, the analytical predictions from Eq. (23) are shown with crosses of the corresponding color. The difference in offsets [$\delta s_2 = s_2(b_\sigma) - s_2(b_\epsilon = 1)$] from the linear fit are plotted in the bottom right panel. Only for $b_\sigma = 1$, the δs_2 is known exactly and is given by $\Delta S(1/2)/2 = -1/4 + (\ln 2)/2$ [31]

mixed [31]. Below, we describe the results for the case when the total system is in a pure state and refer the reader to Ref. [31] for the mixed state results.

Figure 5 (left) shows the results for the EE for various bipartitionings of the system of size 500. The strength of the defect (b_σ) is varied from 0.0 to 1.0 in steps of 0.2. The scaling of the interface EE with different system sizes L yields, as for the energy defect, the effective central charge [see Eq. (19)]. The obtained values of c_{eff} are shown in the top right panel, with the expected values from Eq. (23). The offsets from this fit, normalized with respect to the case $b_\epsilon = 1$, are shown in the bottom right panel. Analytical result for the offset is known only for $b_\sigma = 1$, when $\delta s_2 = \Delta S(1/2)/2 = -1/4 + (\ln 2)/2$ [31].

3.2 The Free, Compactified Boson Model

In this section, we describe conformal interfaces of two free, compactified boson CFTs with different compactification radii R_A and R_B [18, 60]. Unlike the Ising case, the “defect” is extended throughout one half of the system (see below for a lattice realization). For $R_A \neq R_B$, the EE across the interface is lower compared to the case $R_A = R_B$. This can be again understood due to the reflections of the

incident wave at the interface for $R_A \neq R_B$. The relevant quantity is the scattering matrix which can be derived by a variety of methods [18]. Below, we present an intuitive explanation based on elementary notions of electrical engineering.

The free, compact boson model with compactification radius R_α can be viewed as describing a quantum transmission line [17, 37, 61, 62], where the impedance (Z_α) of the α^{th} line is related to the compactification radius as: $Z_\alpha \sim 1/R_\alpha^2$. At the interface of two transmission lines with impedances Z_A, Z_B , the reflection coefficient for incoming waves is given by Pozar [63], Clerk et al. [64]

$$r = \frac{Z_B - Z_A}{Z_B + Z_A} = \frac{R_A^2 - R_B^2}{R_A^2 + R_B^2} = \cos(2\theta), \quad \theta = \tan^{-1} \frac{R_B}{R_A}. \quad (28)$$

The corresponding transmission coefficient is given by $t = \sin(2\theta)$ with $|r|^2 + |t|^2 = 1$. As for the Ising model, the interface EE is determined by the transmission coefficient t [see Eq. (19)]. However, the explicit form of the central charge is different from the Ising case and is given by Sakai and Satoh [20], Peschel and Eisler [22]:

$$c_{\text{eff}}(|t|) = \frac{1}{2} + |t| + \frac{3}{\pi^2} \left[(|t| + 1) \ln(|t| + 1) \ln |t| + (|t| - 1) \text{Li}_2(1 - |t|) + (|t| + 1) \text{Li}_2(-|t|) \right]. \quad (29)$$

This conformal interface is realized on the lattice by two XXZ chains with anisotropies Δ_A and Δ_B on the two sides of the interface. Thus, the defect Hamiltonian is given by

$$H_{\text{XXZ}}^{\mathcal{I}} = -\frac{1}{2} \sum_{i=1}^{L-1} \left[\sigma_i^x \sigma_{i+1}^x + \sigma_i^y \sigma_{i+1}^y + \Delta_i \sigma_i^z \sigma_{i+1}^z \right], \quad \Delta_i = \Delta_A \theta(i_0 - i) + \Delta_B \theta(i - i_0), \quad (30)$$

where θ is the Heaviside theta function. The role of the impedance is played the Luttinger parameter times the impedance quantum ($6.5k\Omega$). Thus,

$$r = \frac{K_B - K_A}{K_B + K_A}, \quad \theta = \tan^{-1} \sqrt{\frac{K_A}{K_B}}. \quad (31)$$

As expected, for $K_A = K_B$, which corresponds to $\Delta_A = \Delta_B$, the interface disappears with $r = 0, t = 1$ and $c_{\text{eff}}(1) = 1$. On the other hand, for $\Delta_A \neq \Delta_B$, either $\Delta_A = 1$ or $\Delta_B = 1$ corresponds to $r = 1, t = 0$ and $c_{\text{eff}}(0) = 0$.

Figure 6 shows the EE for different bipartitionings of the system for a total system size $L = 2000$. The Luttinger parameter for the left half of the chain is fixed to $K_1 = 0.6$, while that for the right half is varied from 0.1 to 0.6 in steps of 0.1. For $K_1 = K_2$, we recover the standard expression for EE [see Eq. (4)] which leads to a central charge of $\simeq 0.992$. Note that we use much larger system sizes

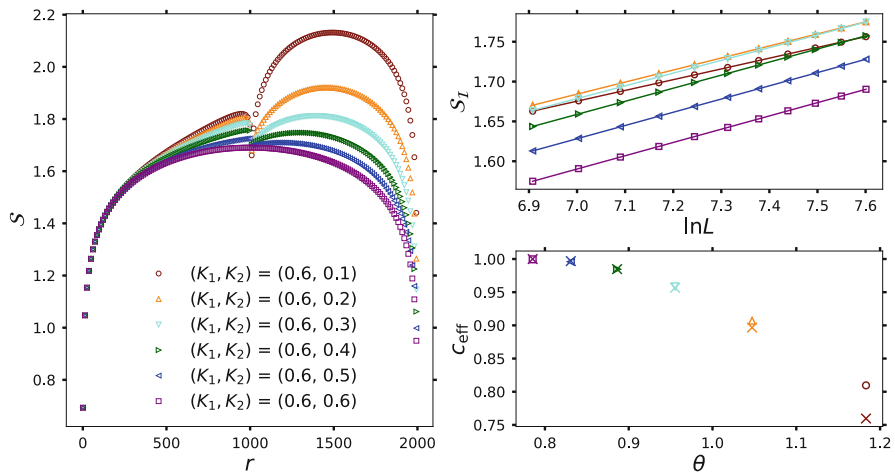


Fig. 6 Results for interface EE (S) for an open XXZ chain with an interface defect. The left half of the chain has a Luttinger parameter $K_1 = 0.6$, while the same for the right half (K_2) is varied from 0.1 to 0.6 [see Eq. (15) for relation to the anisotropy parameters]. (Left) The EE for different bipartitionings of the in a system, with a total system size, $L = 2000$. The dip around the center of the chain for the EE is due to the defect. (Top right) Scaling of the interface EE (S_I) with the system size for varying system sizes from $L = 1000$ to $L = 2000$. (Bottom right panel) Effective central charge, c_{eff} , obtained by fitting to Eq. (19). For comparison, the analytical predictions from Eq. (23) are shown with crosses of the corresponding color. *Note the deviation from the predicted central charge value for $K_2 < 0.3$. This manifests itself in both the top and bottom right panels. This is due to finite-size effects as the isotropic point ($K_2 = 0$) is approached for the right half of the chain*

compared to the Ising chain due to larger finite-size effects in the current model. As K_2 is lowered, the interface is clearly apparent in the EE (see left panel). The scaling of the interface EE for different system sizes [see Eq. (19)] is shown in the top right panel. The effective central charge obtained from the scaling is plotted in the bottom right panel. Note that as K_2 approaches the value 0 (the isotropic point for the right half of the XXZ chain), we start seeing deviations from the predicted central charge value due to the finite size of the system. This is manifested in both the top right and the bottom right panels. It will be interesting to provide an analytical prediction for this finite-size effect.

4 Conclusion

In this work, we have described the behavior of EE in the CFTs with boundaries and defects. First, we considered the Ising and the free, compactified boson models with Neumann and Dirichlet boundary conditions and computed the change in universal, boundary-dependent contribution to the EE. Next, we computed the behavior of

the EE in these models in the presence of conformal defects. In particular, we considered the energy and the duality defects of the Ising model and the interface defect of the free, boson theory. We showed that defects and interfaces, unlike boundaries, manifest themselves in both the leading logarithmic scaling and the $\mathcal{O}(1)$ term in the EE.

Here, we concentrated on the von Neumann entropy as the measure of entanglement. However, entanglement measures like mutual information [65] and entanglement spectrum [66, 67] have seen much use in the characterization of CFTs with boundaries [17, 68–70] and defects [71] for certain geometric arrangements of the subsystem with respect to the boundary or the defect. A particularly simple situation arises for the entanglement Hamiltonian (\mathcal{H}_A) of a subsystem (A) after bipartitioning a CFT with identical boundary conditions on the two ends [16]. Then, \mathcal{H}_A is related to the CFT Hamiltonian with appropriate boundary conditions α, β :

$$\mathcal{H}_A = -\frac{1}{2\pi} \ln \frac{e^{-2\pi H_{\alpha\beta}}}{\text{Tr} e^{-2\pi H_{\alpha\beta}}}, \quad (32)$$

where the denominator inside the logarithm originates from the fact that the reduced density matrix ρ_A should be normalized. The above align is to be understood as an equality of the eigenvalues of the two sides the align up to overall shifts and rescalings, which can be absorbed by rescaling the velocity of sound in the corresponding boundary CFT. The first boundary condition α is inherited from the original system, while the second β originates from the entanglement cut and is the free/Neumann boundary condition. Then, the partition function of the CFT on a cylinder with appropriate boundary conditions leads directly to the entanglement Hamiltonian spectrum [17].

Consider the case when $\alpha = \text{Neumann}$ for the Ising CFT. Then, the corresponding partition function can be written as a sum over characters of the Ising CFT [see Eq. (5)]:

$$Z_{\text{NN}}(q) = \text{Tr} e^{-2\pi H_{\text{NN}}} = \sum_{j=0,\sigma,\epsilon} \left| \left\langle \frac{\tilde{1}}{16} \middle| j \right\rangle \right|^2 \chi_j(\tilde{q}) = \chi_0(\tilde{q}) + \chi_\epsilon(\tilde{q}) = \chi_0(q) + \chi_\epsilon(q). \quad (33)$$

Here the parameter q is defined as:

$$q = e^{-2\pi^2/\tilde{L}}, \quad \tilde{q} = e^{-2\tilde{L}}, \quad \tilde{L} = \ln \left(\frac{2L}{\pi a} \sin \frac{\pi r}{L} \right), \quad (34)$$

r is the subsystem size and we have used the explicit form of the modular S-matrix of the Ising CFT [35]. Thus, we find that the partition function gets contribution

from two primary fields: I, ϵ . We use the explicit formulas for the characters (see Chapter 8 of Ref. [38]):

$$\chi_0(q) = \frac{1}{\eta(q)} \sum_{n \in \mathbb{Z}} \left[q^{(24n+1)^2/48} - q^{(24n+7)^2/48} \right], \quad (35)$$

$$\chi_\epsilon(q) = \frac{1}{\eta(q)} \sum_{n \in \mathbb{Z}} \left[q^{(24n+5)^2/48} - q^{(24n+11)^2/48} \right], \quad (36)$$

where $\eta(q)$ is the Dedekind function defined as

$$\eta(q) = q^{1/24} \varphi(q) = q^{1/24} \prod_{n>0} (1 - q^n). \quad (37)$$

Expanding in q , we get

$$\chi_j(q) = q^{-1/48+h_j} \sum_{n \geq 0} p_j(n) q^n, \quad j = 0, \epsilon, \quad (38)$$

where $p_{0,\epsilon}(i)$ are obtained to be

$$p_0(n) = 1, 0, 1, 1, 2, 2, 3, \dots, \quad (39)$$

$$p_\epsilon(n) = 1, 1, 1, 1, 2, 2, 3, \dots \quad (40)$$

Thus, the entanglement energies, labeled by two indices: (j, n) , are given by

$$\begin{aligned} \varepsilon_N(j, n) &= -\frac{1}{2\pi} \ln \frac{q^{-1/48+h_j+n}}{\tilde{q}^{-1/48} \sum_{k=0, \epsilon} \sum_{m \geq 0} p_k(m) \tilde{q}^{h_k+m}} \\ &= \frac{\bar{L}}{48\pi} + \frac{\pi}{\bar{L}} \left(-\frac{1}{48} + h_j + n \right) \\ &\quad + \frac{1}{2\pi} \ln \sum_{k=0, \epsilon} \sum_{m \geq 0} p_k(m) e^{-2\bar{L}(h_k+m)} \end{aligned} \quad (41)$$

with degeneracy at the level (j, n) being given by $p_j(n)$. The lowest entanglement energy level is given by

$$\varepsilon_N(0, 0) = \frac{\bar{L}}{48\pi} - \frac{\pi}{48\bar{L}} + \frac{1}{2\pi} \ln \sum_{k=0, \epsilon} \sum_{m \geq 0} p_k(m) e^{-2\bar{L}(h_k+m)}. \quad (42)$$

With respect to this lowest level, the entanglement energies are given by

$$\Delta\varepsilon_N(j, n) \equiv \varepsilon_N(j, n) - \varepsilon_N(0, 0) = \frac{\pi}{\bar{L}}(h_j + n), \quad (43)$$

and, thus, occur at integer (half-integer) values in units of π/\bar{L} for $j = 0(\epsilon)$. Similar computations can be done for $\alpha = \text{Dirichlet}$ [17]. It will be interesting to generalize this computation to the case of CFTs with defects.

Acknowledgments We are particularly grateful to David Rogerson and Frank Pollmann for numerous discussions and collaboration on a related project. AR is supported by a grant from the Simons Foundation (825876, TDN). HS is supported by the ERC Advanced Grant NuQFT.

References

1. C. Holzhey, F. Larsen, F. Wilczek, Geometric and renormalized entropy in conformal field theory. *Nucl. Phys. B* **424**, 443 (1994)
2. P. Calabrese, J. Cardy, Entanglement entropy and quantum field theory. *J. Stat. Mech: Theory Exp.* **2004**, P06002 (2004)
3. H. Casini, Geometric entropy, area and strong subadditivity. *Classical Quantum Gravity* **21**, 2351 (2004)
4. H. Casini, M. Huerta, A c-theorem for the entanglement entropy. *J. Phys. A* **40**, 7031 (2007)
5. A.B. Zamolodchikov, Irreversibility of the flux of the renormalization group in a 2d field theory. *JETP Lett.* **43**, 565 (1986)
6. F. Pollmann, S. Mukerjee, A.M. Turner, J.E. Moore, Theory of finite-entanglement scaling at one-dimensional quantum critical points. *Phys. Rev. Lett.* **102**, 255701 (2009)
7. M.B. Hastings, An area law for one-dimensional quantum systems. *J. Stat. Mech: Theory Exp.* **2007**, P08024 (2007)
8. S.R. White, Density matrix formulation for quantum renormalization groups. *Phys. Rev. Lett.* **69**, 2863 (1992)
9. U. Schollwöck, The density-matrix renormalization group in the age of matrix product states. *Ann. Phys.* **326**, 96 (2011). January 2011 Special Issue
10. I. Affeck, A.W.W. Ludwig, Universal noninteger “ground-state degeneracy” in critical quantum systems. *Phys. Rev. Lett.* **67**, 161 (1991)
11. P. Calabrese, J. Cardy, Entanglement entropy and conformal field theory. *J. Phys. A* **42**, 504005 (2009)
12. I. Affeck, Conformal field theory approach to the Kondo effect. *Acta Phys. Polon. B* **26**, 1869 (1995)
13. H. Saleur, Lectures on nonperturbative field theory and quantum impurity problems (1998)
14. M.R. Gaberdiel, Lectures on non-BPS Dirichlet branes. *Class. Quant. Grav.* **17**, 3483 (2000)
15. I. Affeck, N. Laflorencie, E.S. Sørensen, Entanglement entropy in quantum impurity systems and systems with boundaries. *J. Phys. A Math. Theor.* **42**, 504009 (2009)
16. J. Cardy, E. Tonni, Entanglement Hamiltonians in two-dimensional conformal field theory. *J. Stat. Mech: Theory Exp.* **2016**, 123103 (2016)
17. A. Roy, F. Pollmann, H. Saleur, Entanglement Hamiltonian of the 1+1-dimensional free, compactified boson conformal field theory. *J. Stat. Mech.* **2008**, 083104 (2020)
18. C. Bachas, J. de Boer, R. Dijkgraaf, H. Ooguri, Permeable conformal walls and holography. *JHEP* **06**, 027 (2002)

19. T. Quella, V. Schomerus, Symmetry breaking boundary states and defect lines. *JHEP* **06**, 028 (2002)
20. K. Sakai, Y. Satoh, Entanglement through conformal interfaces. *JHEP* **12**, 001 (2008)
21. V. Eisler, I. Peschel, Entanglement in fermionic chains with interface defects. *Ann. Phys.* **522**, 679 (2010)
22. I. Peschel, V. Eisler, Exact results for the entanglement across defects in critical chains. *J. Phys. A Math. Theor.* **45**, 155301 (2012)
23. V.B. Petkova, J.B. Zuber, Generalized twisted partition functions. *Phys. Lett. B* **504**, 157 (2001)
24. J. Fröhlich, J. Fuchs, I. Runkel, C. Schweigert, Kramers-Wannier duality from conformal defects. *Phys. Rev. Lett.* **93**, 070601 (2004)
25. J. Fröhlich, J. Fuchs, I. Runkel, C. Schweigert, Duality and defects in rational conformal field theory. *Nucl. Phys. B* **763**, 354 (2007)
26. D. Aasen, R.S.K. Mong, P. Fendley, Topological defects on the lattice I: the Ising model. *J. Phys. A* **49**, 354001 (2016)
27. H.A. Kramers, G.H. Wannier, Statistics of the two-dimensional ferromagnet. Part I. *Phys. Rev.* **60**, 252 (1941)
28. R. Savit, Duality in field theory and statistical systems. *Rev. Mod. Phys.* **52**, 453 (1980)
29. M. Buican, A. Gromov, Anyonic chains, topological defects, and conformal field theory. *Commun. Math. Phys.* **356**, 1017 (2017)
30. I. Klich, D. Vaman, G. Wong, Entanglement Hamiltonians for chiral fermions with zero modes. *Phys. Rev. Lett.* **119**, 120401 (2017)
31. A. Roy, H. Saleur, Entanglement entropy in the Ising model with topological defects (2021)
32. E.M. Brehm, I. Brunner, Entanglement entropy through conformal interfaces in the 2D Ising model. *JHEP* **09**, 080 (2015)
33. M. Gutperle, J.D. Miller, A note on entanglement entropy for topological interfaces in RCFTs. *JHEP* **04**, 176 (2016)
34. N. Ishibashi, The boundary and crosscap states in conformal field theories. *Mod. Phys. Lett. A* **4**, 251 (1989)
35. J.L. Cardy, Boundary conditions, fusion rules and the Verlinde formula. *Nucl. Phys. B* **324**, 581 (1989)
36. G.Y. Cho, A.W.W. Ludwig, S. Ryu, Universal entanglement spectra of gapped one-dimensional field theories. *Phys. Rev. B* **95**, 115122 (2017)
37. A. Roy, D. Schuricht, J. Hauschild, F. Pollmann, H. Saleur, The quantum sine-Gordon model with quantum circuits. *Nucl. Phys. B* **968**, 115445 (2021)
38. P. Di Francesco, P. Mathieu, D. Sénéchal, *Conformal Field Theory*. Graduate Texts in Contemporary Physics (Springer, Berlin, 1997)
39. C.G. Callan Jr., C. Lovelace, C.R. Nappi, S.A. Yost, Adding holes and crosscaps to the superstring. *Nucl. Phys. B* **293**, 83 (1987)
40. M. Oshikawa, I. Affeck, Boundary conformal field theory approach to the critical two-dimensional Ising model with a defect line. *Nucl. Phys. B* **495**, 533 (1997)
41. S.L. Lukyanov, Low energy effective Hamiltonian for the XXZ spin chain. *Nucl. Phys. B* **522**, 533 (1998)
42. S. Lukyanov, Correlation amplitude for the XXZ spin chain in the disordered regime. *Phys. Rev. B* **59**, 11163 (1999)
43. S. Ghoshal, A. Zamolodchikov, Boundary S-matrix and boundary state in two-dimensional integrable quantum field theory. *Int. J. Mod. Phys. A* **09**, 3841 (1994)
44. P. Fendley, H. Saleur, N. Warner, Exact solution of a massless scalar field with a relevant boundary interaction. *Nucl. Phys. B* **430**, 577 (1994)
45. J.S. Caux, H. Saleur, F. Siano, The two-boundary sine-Gordon model. *Nucl. Phys. B* **672**, 411 (2003)
46. S. Lukyanov, V. Terras, Long-distance asymptotics of spin-spin correlation functions for the XXZ spin chain. *Nucl. Phys. B* **654**, 323 (2003)
47. J.L. Cardy, Continuously varying exponents and the value of the central charge. *J. Phys. A Math. Gen.* **20**, L891 (1987)

48. F. Iglói, I. Peschel, L. Turban, Inhomogeneous systems with unusual critical behaviour. *Adv. Phys.* **42**, 683 (1993)
49. L.P. Kadanoff, H. Ceva, Determination of an operator algebra for the two-dimensional Ising model. *Phys. Rev. B* **3**, 3918 (1971)
50. M. Henkel, A. Patkós, M. Schlottmann, The Ising quantum chain with defects (i). The exact solution. *Nucl. Phys.* **314**, 609 (1989)
51. M. Baake, P. Chason, M. Schlottmann, The Ising quantum chain with defects (ii). The $SO(2n)$ Kac-Moody spectra. *Nucl. Phys. B* **314**, 625 (1989)
52. G. Vidal, J.I. Latorre, E. Rico, A. Kitaev, Entanglement in quantum critical phenomena. *Phys. Rev. Lett.* **90**, 227902 (2003)
53. I. Peschel, Calculation of reduced density matrices from correlation functions. *J. Phys. A Math. Gen.* **36**, L205 (2003)
54. J.I. Latorre, E. Rico, G. Vidal, Ground state entanglement in quantum spin chains. *Quantum Inf. Comput.* **4**, 48 (2004)
55. F. Iglói, Z. Szatmári, Y.-C. Lin, Entanglement entropy with localized and extended interface defects. *Phys. Rev. B* **80**, 024405 (2009)
56. L. Lewin, *Polylogarithms and Associated Functions* (North Holland, Amsterdam, 1981)
57. U. Grimm, Spectrum of a duality twisted Ising quantum chain. *J. Phys. A* **35**, L25 (2002)
58. U. Grimm, G.M. Schutz, The spin-1/2 XXZ Heisenberg chain, the quantum algebra $U(q)[sl(2)]$, and duality transformations for minimal models. *J. Stat. Phys.* **71**, 921 (1993)
59. C.P. Herzog, T. Nishioka, Entanglement entropy of a massive fermion on a torus. *JHEP* **03**, 077 (2013)
60. I. Affeck, M. Oshikawa, H. Saleur, Quantum Brownian motion on a triangular lattice and $c=2$ boundary conformal field theory. *Nucl. Phys. B* **594**, 535 (2001)
61. M. Goldstein, M.H. Devoret, M. Houzet, L.I. Glazman, Inelastic microwave photon scattering off a quantum impurity in a Josephson-junction array. *Phys. Rev. Lett.* **110**, 017002 (2013)
62. A. Roy, H. Saleur, Quantum electronic circuit simulation of generalized Sine-Gordon models. *Phys. Rev. B* **100**, 155425 (2019)
63. D. Pozar, *Microwave Engineering*. Addison-Wesley Series in Electrical and Computer Engineering (Addison-Wesley, Boston, 1990)
64. A.A. Clerk, M.H. Devoret, S.M. Girvin, F. Marquardt, R.J. Schoelkopf, Introduction to quantum noise, measurement, and amplification. *Rev. Mod. Phys.* **82**, 1155 (2010)
65. L. Amico, R. Fazio, A. Osterloh, V. Vedral, Entanglement in many-body systems. *Rev. Mod. Phys.* **80**, 517 (2008)
66. H. Li, F.D.M. Haldane, Entanglement spectrum as a generalization of entanglement entropy: identification of topological order in non-Abelian fractional quantum Hall effect states. *Phys. Rev. Lett.* **101**, 010504 (2008)
67. R. Haag, *Local Quantum Physics: Fields, Particles, Algebras*. Theoretical and Mathematical Physics (Springer, Berlin, 2012)
68. H. Casini, M. Huerta, R.C. Myers, A. Yale, Mutual information and the F-theorem. *JHEP* **10**, 003 (2015)
69. H. Casini, I. Salazar Landea, G. Torroba, The g-theorem and quantum information theory. *JHEP* **10**, 140 (2016)
70. M. Mintchev, E. Tonni, Modular Hamiltonians for the massless Dirac field in the presence of a boundary. *JHEP* **03**, 204 (2021)
71. M. Mintchev, E. Tonni, Modular Hamiltonians for the massless Dirac field in the presence of a defect. *JHEP* **03**, 205 (2021)

Entanglement Entropy and Localization in Disordered Quantum Chains



Nicolas Laflorencie

Abstract This chapter addresses the question of quantum entanglement in disordered chains, focusing on the von-Neumann and Rényi entropies for three important classes of random systems: Anderson localized, infinite randomness criticality, and many-body localization (MBL). We review previous works and also present new results for the entanglement entropy of random spin chains at low and high energy.

1 Introduction

1.1 Generalities

Random impurities, disorder, and quantum fluctuations have the common tendency to conspire, destroy classical order, and drive physical systems toward new states of matter. Whether intrinsically present, chemically controlled via doping materials, or explicitly introduced via a random potential (as in ultra-cold atomic setups) or for instance by varying 2D film thickness, randomness can lead to dramatic changes in many properties of condensed matter systems, as exemplified by Anderson localization phenomena [1, 2], the Kondo effect [3, 4], or spin-glass physics [5]. In such a context, the introduction of quantum entanglement witnesses provides new tools to improve our understanding of quantum disordered systems. Among the numerous entanglement estimates, one of the simplest is the so-called von-Neumann entropy, which will be described in this chapter for various one-dimensional disordered localized states of matter.

N. Laflorencie (✉)

Laboratoire de Physique Théorique, Université de Toulouse, CNRS, UPS, Toulouse, France
Donostia International Physics Center, San Sebastián, Spain
e-mail: laflo@irsamc.ups-tlse.fr

1.2 Random Spin Chain Models

1.2.1 Disordered XXZ Hamiltonians

(i) *Models* Several spin systems will be discussed along this chapter. The first (prototypical) example is the U(1) symmetric disordered spin-1/2 XXZ model

$$\mathcal{H}_s = \sum_{i,j} J_{ij} \left(S_i^x S_j^x + S_i^y S_j^y + \Delta S_i^z S_j^z \right) + \sum_i h_i S_i^z, \quad (1)$$

where the total magnetization is conserved $[\mathcal{H}, \sum_i S_i^z] = 0$. This Hamiltonian is quite generic as it can also describe bosonic or fermionic systems. Indeed, using the Matsubara–Matsuda mapping [6] $b_i^\dagger = S_i^+ b_i = S_i^-$, and $n_i = S_i^z + 1/2$, the above spin problem, Eq. (1), equally describes hard-core bosons

$$\mathcal{H}_b = \sum_{i,j} \frac{J_{ij}}{2} \left(b_i^\dagger b_j + b_j^\dagger b_i + 2\Delta n_i n_j \right) + \sum_i h_i n_i + \text{constant}. \quad (2)$$

A fermionic version can also be obtained from the Jordan–Wigner transformation [7], which maps hard-core bosons onto spinless fermions through:

$$c_\ell = \exp \left[i\pi \sum_{j=1}^{\ell-1} b_j^\dagger b_j \right] b_\ell \quad \text{and} \quad c_\ell^\dagger = b_\ell^\dagger \exp \left[-i\pi \sum_{j=1}^{\ell-1} b_j^\dagger b_j \right]. \quad (3)$$

The Jordan–Wigner string, although making the transformation nonlocal, ensures that c_ℓ and c_ℓ^\dagger satisfy anticommutation relations and are indeed fermionic operators. In one dimension, if hopping terms are restricted to nearest neighbor, the original XXZ spin model, Eq. (1), takes the simple spinless fermion form

$$\mathcal{H}_f = \sum_i \frac{J_i}{2} \left(c_i^\dagger c_{i+1} + c_{i+1}^\dagger c_i + 2\Delta n_i n_{i+1} \right) + h_i n_i. \quad (4)$$

(ii) *Ground-State Phase Diagram in the Presence of Disorder* Building on field theory and renormalization group (RG) results [8–10], as well as numerical investigations [11–14], the global zero-temperature phase diagram of the above disordered XXZ chain is depicted in Fig. 1a with 3 parameters. Δ is the (non-random) interaction strength, repulsive ($\Delta > 0$), or attractive ($\Delta < 0$), $\Delta = 0$ being the free-fermion point; W_J controls the randomness in the antiferromagnetic exchanges $J_i > 0$, which can be drawn from a power-law $P(J) \sim J^{-1+1/W_J}$ (while the precise form of the distribution is irrelevant); W_h is the disorder strength of the random fields h_i , often chosen to be a uniform box $P(h) = \text{Box}[-W_h, W_h]$, but again its precise form is not relevant. In Fig. 1a, one sees three main regimes:

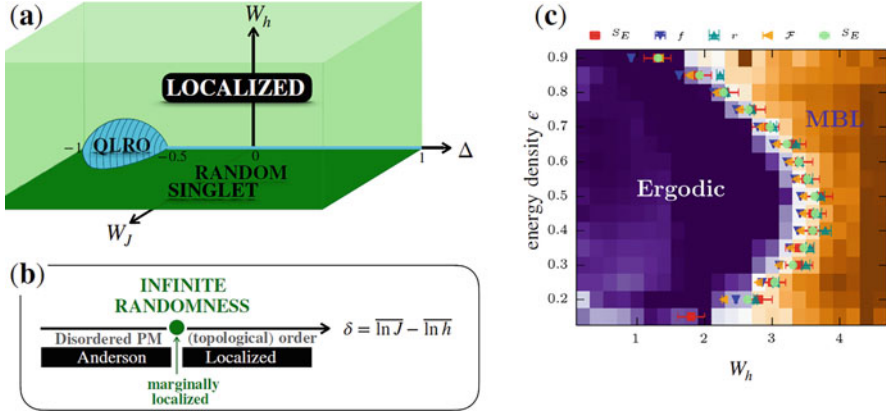


Fig. 1 Schematic phase diagrams for the three different systems considered. **(a)** Ground-state phase diagram of the disordered XXZ chain model Eq.(1). $\Delta \in [-1, 1]$ is the interaction parameter, and W_J, W_h are the disorder strengths for couplings and fields (see text). Three phases are expected. In the attractive regime $\Delta \in [-1, -1/2]$, a small pocket is robust against weak disorder, showing quasi-long-range order (QLRO). In the absence of random field ($W_h = 0$) random bonds induce a random singlet phase. In the largest part of the diagram, a localized phase is expected. **(b)** The random one-dimensional TFIM Eq.(5) displays two localized phases (disordered PM and topological ordered) surrounding an infinite randomness fixed point (IRFP) at $\delta = \overline{\ln J} - \overline{\ln h} = 0$. **(c)** Energy-resolved MBL diagram for the random-field Heisenberg chain, the standard model for 1D MBL (this panel is adapted from Luitz et al. [15])

- (1) In the absence of randomness, and inside a small pocket (blue region), the quasi-long-range order (QLRO) is stable, with Luttinger-liquid-like critical properties [16], such as power-law decaying pairwise correlations at long distance.
- (2) At zero random field ($W_h = 0$), random antiferromagnetic couplings can drive the ground-state to the random singlet phase (RSP) [10]: a critical glass phase controlled by an infinite randomness fixed point (IRFP) [17], having power-law (stretched exponential) average (typical) correlations.
- (3) IRFP and RSP are destabilized by nonzero (random) fields, driving the systems to a localized ground-state, also known as the Bose glass state [18]. This localized regime is directly connected to the non-interacting limit.

1.2.2 Random Transverse Field Ising Chains

Another class of disordered spin chain models is given by the famous transverse-field Ising model (TFIM)

$$\mathcal{H}_{\text{TFIM}} = \sum_i J_i \sigma_i^x \sigma_{i+1}^x + h_i \sigma_i^z, \quad (5)$$

which can also be recasted into a free-fermion model

$$\mathcal{H}_{\text{TFIM}} = \sum_{i=1}^L \left[J_i \left(c_i^\dagger c_{i+1}^\dagger + c_i^\dagger c_{i+1} - c_i c_{i+1}^\dagger - c_i c_{i+1} \right) + h_i \left(1 - 2c_i^\dagger c_i \right) \right]. \quad (6)$$

This system is equivalent to the celebrated Kitaev chain [19], but here with equal pairing and hopping terms, and in the presence of disorder. Despite the great tour de force achieved by Kitaev who showed the non-trivial topological properties of the TFIM Eq. (5) (with edge Majorana zero modes, also discussed by Fendley [20]), many of the properties of Eq. (6) were studied several decades before (in the disorder-free case) by Lieb, Schultz, Mattis [21], and Pfeuty [22].

The random case, also discussed for a long time [17, 23–25], has been deeply understood by D. S. Fisher [17, 25] who solved the strong disorder renormalization group (SDRG) method for the critical point of the random TFIM at $\delta = \overline{\ln J} - \overline{\ln h} = 0$, which also exhibits an IRFP. This (non-interacting) quantum glass displays marginal localization for single-particle fermionic orbitals [26], while a genuine Anderson localization is observed for $\delta \neq 0$, with the following physical phases: a disordered paramagnet (PM) when $\delta < 0$ and a topological ordered magnet if $\delta > 0$. Physical properties of the 1D random TFIM have been studied numerically using free-fermion diagonalization techniques [27–29], but most of these studies have focused on zero-temperature properties. Below we will address entanglement for low- and (very) high-energy states.

1.2.3 Many-Body Localization

Here, we briefly discuss the main properties of many-body localization (MBL) physics, while referring the interested reader to recent reviews on this broadly discussed topic [30–33]. The excitation spectrum of disordered quantum interacting systems has been a fascinating subject for more than two decades now [34–40]. While the very first analytical studies focused on the effect of weak interactions [35, 36], the majority of the subsequent numerical studies then addressed strongly interacting 1D systems, such as the random-field spin-1/2 Heisenberg chain model [15, 38]

$$\mathcal{H} = \sum_{i=1}^L \left(\vec{S}_i \cdot \vec{S}_{i+1} - h_i S_i^z \right), \quad (7)$$

for which there is now a general consensus in the community for an infinite-temperature MBL transition [15, 41–45]. The very existence of MBL has also been mathematically proven (under minimal assumptions) [40] for random interacting Ising chains, and there is a growing number of experimental evidences in 1D [46–49]. MBL physics is reasonably well-characterized, mostly thanks to exact diagonalization (ED) techniques [15, 50] probing Poisson spectral statistics,

low (area-law) entanglement of eigenstates and its out-of-equilibrium logarithmic spreading, eigenstates multifractality. In Fig. 1c, we show the energy-resolved MBL phase diagram, as obtained in Luitz et al. [15], for the “standard model” Eq. (7), where h_i are independently drawn from a uniform distribution $[-W_h, W_h]$, and $\epsilon = (E - E_{\min})/(E_{\max} - E_{\min})$ is the energy density above the ground-state.

1.3 Chapter Organization

The rest of the chapter will be organized as follows. We start in Sect. 2 with perhaps the simplest case of Anderson localized chains, through the study of the XX spin-1/2 chain model in a random-field. We first briefly discuss its localization properties in real space and then present numerical (free-fermion) results for the entanglement entropy of many-body (at half-filling) eigenstates, for both the ground-state and at high energy. Upon varying the intensity of the random-field, we observe interesting scaling behaviors with the localization length, as well as remarkable features in the distribution of von-Neumann entropies. We then move to infinite randomness physics in Sect. 3 with the celebrated logarithmic growth of entanglement entropy for random-bond XX chains where we unveil an interesting crossover effect and also for the quantum Ising chain that is studied at all energies. We then provide a short review of the existing results beyond free-fermions, e.g., random singlet phases with higher spins, and also discuss the cases of engineered disordered systems with locally correlated randomness or the so-called rainbow chain model. We then continue in Sect. 4 with the entanglement properties for the many-body localization problem. Eigenstates entanglement entropies at high energy will be discussed for the standard random-field Heisenberg chain model, paying a particular attention to the shape of the distributions in both regimes and at the transition. Finally, concluding remarks will close this chapter in Sect. 5.

2 Entanglement in Non-interacting Anderson Localized Chains

2.1 Disordered XX Chains and Single-Particle Localization Lengths

Before discussing the entanglement properties, we first focus on the Anderson localization in real space which occurs in disordered XX chains. In the easy-plane limit ($\Delta = 0$) of Eq. (1), the XX chains are equivalent to free fermions

$$\mathcal{H} = \sum_{i=1}^{L-1} \left[\frac{J_i}{2} (c_i^\dagger c_{i+1} + c_{i+1}^\dagger c_i) - \sum_{i=1}^L h_i n_i \right] + \mathcal{H}_B, \quad (8)$$

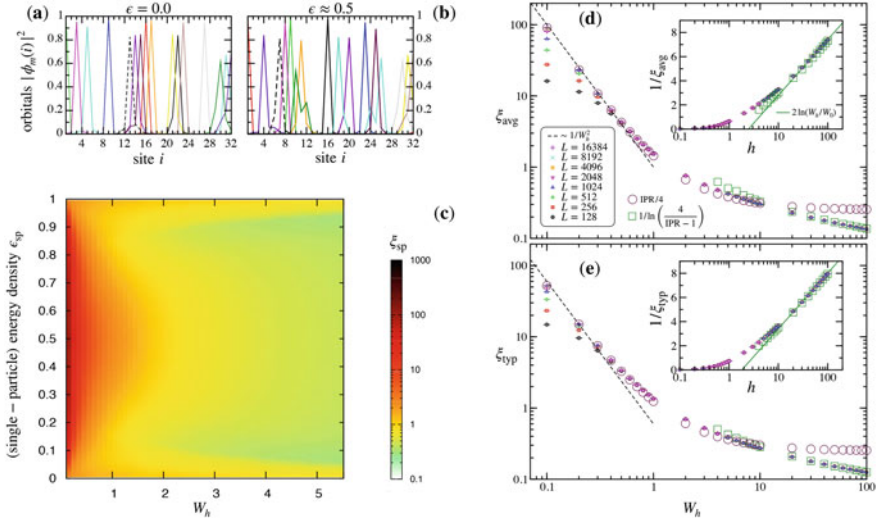


Fig. 2 Exact diagonalization results for Anderson localization in one dimension Eq. (8). Panels (a, b): exponentially localized orbitals for a single $L = 32$ sample (with $W_h = 5$). Two examples of $L/2 = 16$ occupied orbitals for (a) the many-body ground-state ($\epsilon = 0$) and (b) a random high-energy many-body state ($\epsilon \approx 0.5$). Panel (c): color map of the single-particle localization length, computed for $L = 512$ from the PR Eq. (10) and averaged over thousands of disordered samples and small single-particle energy windows. Single-particle energies are normalized, such that for each sample $\epsilon_{\text{sp}} = (\mathcal{E} - \mathcal{E}_{\text{min}})/(\mathcal{E}_{\text{max}} - \mathcal{E}_{\text{min}})$, where \mathcal{E} are the single-particle energies. Panels (d), (e) show typical and average single-particle localization lengths, computed for various chain lengths L from the PR Eq. (10) and averaged over all single-particle states and thousands of random independent samples. Limiting cases of large and weak localization lengths are shown with open symbols. Black dashed lines show $1/W_h^2$ divergences. Insets: logarithmic divergence of the inverse localization length at strong disorder, Eq. (11) (green lines) with $W_0 \approx 2.46$ for the average (d) and $W_0 \approx 1.82$ for the typical (e). Overall, typical and average localization lengths display similar behaviors in the Anderson localized regime

$\mathcal{H}_{\mathcal{B}}$ being a boundary term.¹ This quadratic Hamiltonian takes the diagonal form $\mathcal{H} = \sum_{m=1}^L \mathcal{E}_m b_m^\dagger b_m$, using new operators $b_m = \sum_{i=1}^L \phi_m(i) c_i$. For nonzero random field, all single-particle orbitals $\phi_m(i)$ are exponentially localized in real space, as exemplified in Fig. 2a,b for a small chain of $L = 32$ sites.

2.1.1 Localization Length from the Participation Ratio (PR)

Assuming exponentially localized orbitals ϕ_m of the simple (normalized) form

$$|\phi_m(i)|^2 = \tanh\left(\frac{1}{2\xi_m}\right) \exp\left(-\frac{|i - i_0^m|}{\xi_m}\right), \quad (9)$$

¹ $\mathcal{H}_{\mathcal{B}} = -\frac{J}{2} e^{-i\pi N_f} (c_L^\dagger c_1 + c_1^\dagger c_L)$ is the boundary term for PBC ($\mathcal{H}_{\mathcal{B}} = 0$ for OBC), with N_f the number of fermions ($N_f = S_{\text{tot}}^z + L/2$).

the participation ratio (PR) [51, 52] is given by

$$\text{PR}_m = \frac{1}{\sum_i |\phi_m(i)|^4} = \frac{\tanh\left(\frac{1}{\xi_m}\right)}{\tanh^2\left(\frac{1}{2\xi_m}\right)}. \quad (10)$$

In the limit $\xi_m \gg 1$, one recovers the fact that the PR is a good estimate of the actual localization length: here $\text{PR}_m \approx 4\xi_m$. The opposite limit ($\xi \ll 1$) is more tricky. For large disorder W_h , a perturbative expansion of the wave function in the vicinity of its localization center i_0^m yields amplitudes vanishing $\sim W_h^{-2r}$, where r is the distance from i_0^m . Therefore, for strong randomness, the localization length slowly vanishes, following

$$1/\xi \propto 2 \ln W_h \quad (W_h \gg 1), \quad (11)$$

and thus ξ can become formally smaller (and even much smaller) than the lattice spacing (which has been set to unity). However, in the case of a perfectly localized orbital with $\xi \rightarrow 0$, the PR will saturate to one, since by definition $\text{PR} \geq 1$. Therefore, in order to quantify very small localization lengths, one has to slightly modify the way we estimate ξ_m . Coming back to the above definition of the PR, Eq. (10), ξ will be solution of a cubic equation $X^3 + X = 2\text{PR}^{-1}$, where $X = \tanh\left(\frac{1}{2\xi}\right)$, thus yielding (using Cardano's formula) $X = \left(\text{PR}^{-1} + \sqrt{\frac{1}{27} + \text{PR}^{-2}}\right)^{1/3} + \left(\text{PR}^{-1} - \sqrt{\frac{1}{27} + \text{PR}^{-2}}\right)^{1/3}$. At strong disorder (when $\text{PR} \rightarrow 1$), we get $\xi \approx 1/\ln\left(\frac{4}{\text{PR}-1}\right)$, while in the other limit ($\text{PR}_m \gg 1$) we recover $\xi \approx \text{PR}/4$.

2.1.2 Numerical Results for the Localization Lengths

Building on Eq. (10) and the above cubic equation, we have numerically evaluated the average and typical localization lengths for disordered XX chains with constant couplings $J_i = 1$ and random fields uniformly distributed in $[-W_h, W_h]$. In Fig. 2d,e, we report the disorder dependence of $\xi_{\text{avg/typ}}$, where average is done over all single-particle states and 10^4 independent samples. At weak disorder, we observe the expected divergence $\xi \sim 1/W_h^2$ [53], while at strong disorder the perturbative result Eq. (11) is nicely recovered. In Fig. 2c, the energy-resolved single-particle localization length ξ_{sp} (here averaged over disorder and small energy windows) is shown against W_h as a color map (collected for $L = 512$ sites) where we clearly observe an interesting (albeit weak) delocalization effect at the spectrum edges upon increasing the disorder, a tendency already discussed by Johri and Bhatt [54].

As we will see below, this localization length is an important quantity for the entanglement properties, as ξ will show up in the entanglement entropy.

2.2 Entanglement Entropy for Many-Body (Anderson Localized) Eigenstates

In the non-interacting case, many-body eigenstates are straightforwardly built by filling up a certain number νL of single-particle states $|m\rangle = b_m^\dagger|\text{vac.}\rangle$ (in the following, we will work at half-filling $\nu = 1/2$). Two types of eigenstates will be considered: the ground-state, occupying the $L/2$ lowest energy states $|\text{GS}\rangle = \prod_{m=1}^{L/2} b_m^\dagger|\text{vac.}\rangle$, and high-energy randomly excited states $|\text{ES}\rangle = \prod_{m=1}^L \theta_m b_m^\dagger|\text{vac.}\rangle$, where $\theta_m = 0$ or 1 , with probability $1/2$ but with the global constraint $\sum \theta_m = L/2$.

2.2.1 Free-Fermion Entanglement Entropy

The free-fermion entanglement entropy of a subsystem \mathcal{A} ($i = 1, \dots, \ell \in \mathcal{A}$) is easy to compute [55] using the $\ell \times \ell$ correlation matrix $\mathcal{C}_{\mathcal{A}}$, defined by

$$\mathcal{C}_{\mathcal{A}} = \begin{pmatrix} \langle c_1^\dagger c_1 \rangle & \langle c_1^\dagger c_2 \rangle & \cdots & \langle c_1^\dagger c_\ell \rangle \\ \langle c_2^\dagger c_1 \rangle & \langle c_2^\dagger c_2 \rangle & \ddots & \vdots \\ \vdots & & \ddots & \\ & & & \langle c_\ell^\dagger c_\ell \rangle \end{pmatrix}, \quad (12)$$

with matrix elements $\langle c_i^\dagger c_j \rangle$ evaluated in a given many-body (ground or excited) eigenstate. The von-Neumann entanglement entropy is then given by

$$S_{\text{vN}} = - \sum_n \left[\lambda_n \ln \lambda_n + (1 - \lambda_n) \ln(1 - \lambda_n) \right], \quad (13)$$

where the λ_n are the eigenvalues of $\mathcal{C}_{\mathcal{A}}$.

2.2.2 Low and High Energy

(i) *Zero Temperature* In the absence of disorder, the $T = 0$ entanglement entropy of a periodic XX chain follows the famous log scaling [56–58]

$$S_{\text{vN}}^{W_i=0}(\ell) = \frac{c}{3} \ln \ell + \text{constant}, \quad (14)$$

with the central charge $c = 1$. For Anderson localized chains, the log growth is cutoff by the finite localization length, as clearly visible in Fig. 3a for periodic

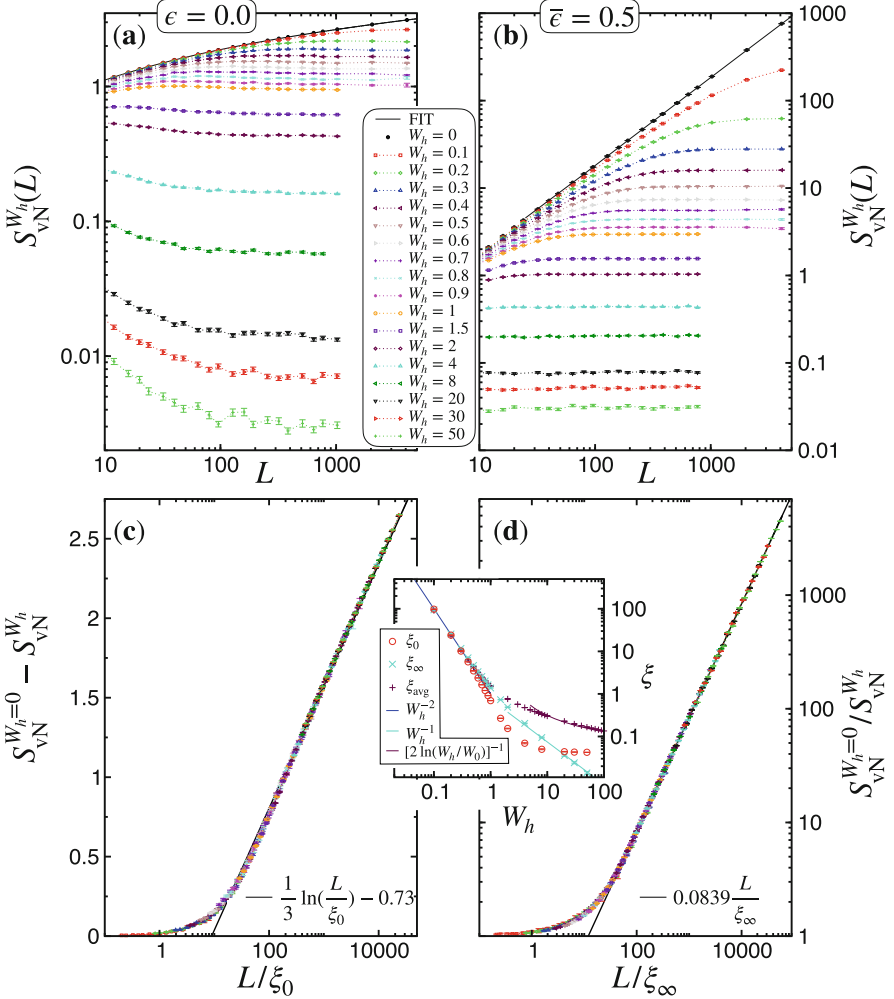


Fig. 3 Von-Neumann entanglement entropies (with half-chain entanglement cuts) for Anderson localized chains [periodic XX chains in a random field, Eq. (8)]: ED results for ground-state ($\epsilon = 0$, left panels) and randomly excited states ($\bar{\epsilon} = 0.5$, right panels), averaged over thousands of independent disordered samples. **(a, b)** Entanglement scaling $S_{vN}^{W_h}(L)$ shown for various disorder strengths W_h . The black lines are fits to the clean case forms: Eq. (14) with $c = 1$ and constant = 0.344 for the ground-state **(a)**, and Eq. (17) with $s_0 \approx 0.1845$, and constant ≈ -0.476 for high energy **(b)**. Panels **(c)** and **(d)** show data collapses using the scaling forms, Eqs. (15) and (18). Lines are the asymptotic forms, indicated on the plots. Inset: log-log plot of the disorder dependence of the different length scales: ξ_0 and ξ_∞ are shown together with the average single-particle localization length ξ_{avg} (see also Fig. 2). They all display the same W_h^{-2} divergence at weak disorder, while the strong disorder behavior is nonuniversal (see text)

systems with a half-chain entanglement cut ($\ell = L/2$). Perhaps more interestingly, the following scaling behavior emerges:

$$S_{\text{vN}}^{W_h=0} - S_{\text{vN}}^{W_h} \propto \frac{1}{3} \ln \left(\frac{L}{\xi_0} \right) \quad \text{if } L \gg \xi_0 \quad (15)$$

$$\rightarrow 0 \quad \text{if } L \ll \xi_0, \quad (16)$$

as visible in panel (c) of Fig. 3. The extracted length scale ξ_0 is plotted against W_h in the inset of Fig. 3 together with the average single-particle localization length ξ_{avg} (also previously shown in Fig. 2). The W_h^{-2} divergence at weak disorder is clearly observed, while at stronger disorder the behavior is nonuniversal (see below for a discussion).

(ii) *Infinite Temperature* The high-energy case is also very interesting, see Fig. 3b,d. In the absence of disorder, the following volume-law entanglement entropy is observed:

$$S_{\text{vN}}^{W_h=0}(\ell) = s_0 L + \text{constant}, \quad (17)$$

with a volume-law coefficient $s_0 \approx 0.1845$, which clearly departs from Page's law [59] (as clearly understood in Ref. [60]), and an additive constant ≈ -0.476 . As for the zero-temperature situation, as soon as $W_h \neq 0$ Anderson localization leads to the saturation of the von-Neumann entropy, even at infinite temperature. In addition, we also observe in Fig. 3d a scaling behavior for

$$S_{\text{vN}}^{W_h=0} / S_{\text{vN}}^{W_h} \sim L / \xi_\infty \quad \text{if } L \gg \xi_\infty \quad (18)$$

$$\rightarrow 1 \quad \text{if } L \ll \xi_\infty. \quad (19)$$

The extracted length scale ξ_∞ , visible in Fig. 3 (inset), also diverges $\sim W_h^{-2}$ at weak disorder and equally coincides with ξ_0 and ξ_{avg} .

2.2.3 Strong Disorder Limit

It is worth briefly discussing the strong disorder situation, which may also be relevant for the MBL problem (see Sect. 4). Despite their similar weak disorder properties, the three length scales ξ_{avg} , ξ_0 , and ξ_∞ (inset of Fig. 3) display distinct behaviors at strong W_h , and neither ξ_0 nor ξ_∞ shows the logarithmic divergence Eq. (11) of ξ_{avg} . This is in fact easy to understand from the strong disorder limit of S_{vN} .

(i) *Ground-State* At $T = 0$, the average is dominated by rare singlet pairs yielding $S_{\text{vN}} = \ln 2$, appearing only if two neighbors have weak disorder, which occurs with a very low probability $\sim 1/W_h^2$. We therefore expect for the strong disorder-

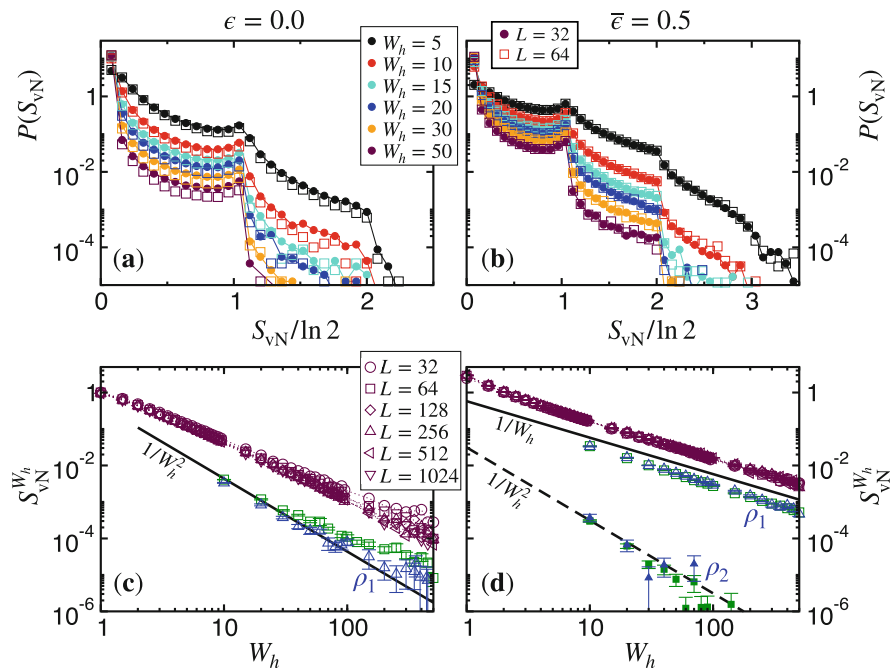


Fig. 4 Strong disorder behavior of the half-chain entanglement entropies for Anderson localized chains. ED results for ground-state ($\epsilon = 0$, left panels) and randomly excited states ($\bar{\epsilon} = 0.5$, right panels). Top panels (a), (b) show histograms of $S_{vN}/\ln 2$ collected for $L = 32, 64$ over several hundred thousands of independent random samples for varying disorder strengths, as indicated on the plot. One clearly sees significant peaks at integer values, thus signaling anomalously weak disordered sites at the entanglement cut (see text). Bottom panels (c), (d) show the strong disorder behavior of the average entropy, consistent with power-law decay (see text) with distinct exponents between ground and excited states. Note also the strong finite-size effects at $\epsilon = 0$ are almost absent at high energy. The strong disorder scaling of S_{vN} is dominated by the probability $\rho_1 = P(|S_{vN}/\ln 2 - 1| \leq 0.05)$

average entropy $S_{vN} \sim W_h^{-2}$, and hence a non-vanishing localization length $\xi \sim \exp(AW_h^{-2})$, even at very strong disorder. This simple argument can be numerically confirmed. In Fig. 4a, the histograms $P(S_{vN})$ clearly show a peaked structure with a dominant peak at 0 and a secondary one at $\ln 2$. This is further checked in Fig. 4c where the disorder-average entanglement entropy, together with the probability to observe $\ln 2$, $\rho_1 = P(|S_{vN}/\ln 2 - 1| \leq 0.05)$ both show a clear W_h^{-2} decay at large disorder, thus validating the above scenario. Note that non-negligible finite-size effects are present for the ground-state, while randomly excited states (discussed below) shown in panels (b, d) are much less spoiled by finite chain effects.

(ii) *Excited-States* In the same spirit, one can also make some predictions for the high-energy behavior. Indeed, at high temperature thermalization, is expected for each individual site having locally a weak disorder, which occurs with a higher probability $\sim 1/W_h$. We therefore expect $S_{vN} \sim W_h^{-1}$ at strong disorder, thus implying that $\xi_\infty \sim W_h^{-1}$, a behavior nicely observed in Fig. 3 (inset). Again, such a simple strong disorder argument is numerically confirmed in Fig. 4b where the histograms $P(S_{vN})$ also have a peaked structure with a dominant peak at 0 and a richer secondary peak arrangement, with one at $\ln 2$ and another visible at $2 \ln 2$. This is further checked in panel (d) where the disorder-average von-Neumann entropy, together with the probability ρ_1 , both display a nice W_h^{-1} decay at large disorder, almost size-independent contrasting with the ground-state. The third peak at $2 \ln 2$ can also be tracked with $\rho_2 = P(|S_{vN}/2 \ln 2 - 1| \leq 0.05)$, which agrees with a $\sim W_h^{-2}$ decay, while it reaches the limit of numerics.

3 Entanglement and Infinite Randomness Criticalities

In the context of random quantum magnets, the strong disorder renormalization group (SDRG) method [25, 61, 62] has proven to be very useful, in particular for the celebrated infinite randomness fixed point (IRFP) physics, which has been deeply described by D. S. Fisher in a series of seminal papers for $d = 1$ [10, 17, 25], then later extended to $d > 1$ [63–65], and applied to a broad range of systems [62, 66].

3.1 Entanglement in Disordered XXZ and Quantum Ising Chains

3.1.1 Random Singlet State for Disordered $S = 1/2$ Chains

Building on the SDRG framework for random-exchange antiferromagnetic XXZ chains [10] (Eq. (1) with $h_i = 0$), or for the random $d = 1$ TFIM [25] at criticality (Eq. (5) with $\delta = \overline{\ln J} - \overline{\ln h} = 0$), Refael and Moore [67, 68] have shown that infinite randomness criticality is accompanied by a logarithmic scaling for the disorder-average entanglement entropy, of the form

$$S(\ell) = \frac{c_{\text{eff}}}{3} \ln \ell + \text{constant}, \quad (20)$$

thus contrasting with the previously discussed Anderson localization case where S is bounded by the finite localization length. In the above form, the coefficient $c_{\text{eff}} = c \ln 2$ has been reduced by a factor $\ln 2$ as compared to the disorder-free (conformally invariant) case in Eq. (14). This result is a direct consequence of the random singlet structure of the ground-state of the random XXZ chain [10] where the probability to

form a singlet between two sites at distance ℓ is $\propto \ell^{-2}$ [10, 69] (see also the recent work by Juhász [70] for an SDRG analysis of subleading corrections).

(i) *Large-Scale Numerics for Random XX Chains* The SDRG analytical prediction Eq. (20) with $c_{\text{eff}} = c \ln 2$ has been numerically confirmed using free-fermion exact diagonalization calculations at the XX point for large chains [69, 71–74]. Here, in this work, we will discuss new numerical results (see Fig. 5) for random XX chains, governed by

$$\mathcal{H}_{\text{random XX}} = \sum_{i=1}^L J_i \left(S_i^x S_j^x + S_i^y S_j^y \right) \quad (21)$$

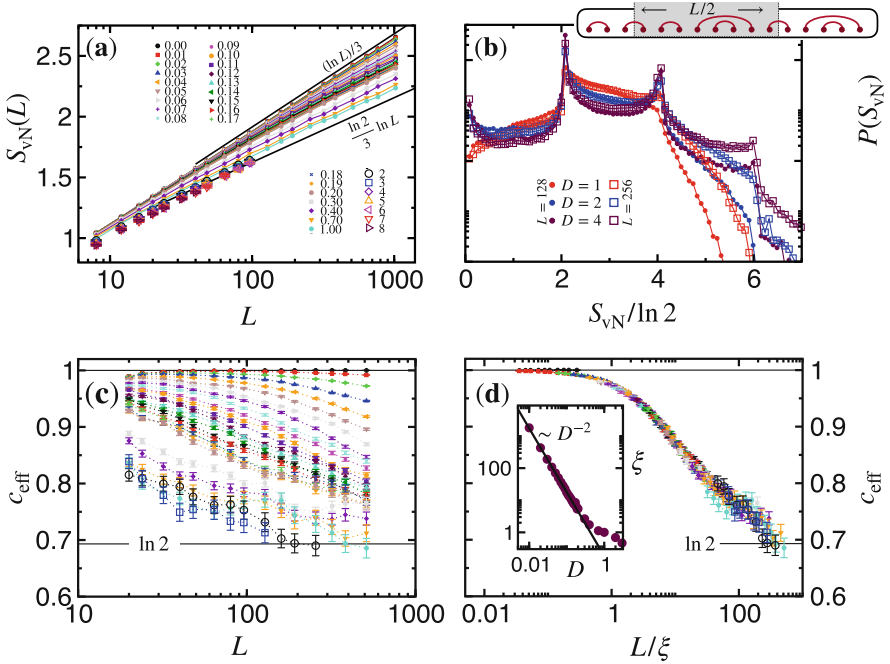


Fig. 5 Exact diagonalization results for the (half-chain) ground-state von-Neuman entropy of $S = 1/2$ XX chains with random bonds, Eq. (21), with power-law distributed couplings $P(J) \propto J^{-1+1/D}$, averaged over several thousands of disordered samples. (a) Logarithmic scaling Eq. (20) shown for many disorder strength $D = 0, \dots, 8$ (indicated on the plot), thus emphasizing the crossover between clean and RSP behaviors. The prefactor c_{eff} of the logarithmic growth, extracted from fits to the form Eq. (20) over sliding 7-point windows, is shown for $D \in [0.01, 3]$ in panel (c) and by rescaling the system size $L \rightarrow L/\xi$ in panel (d) where a reasonable data collapse is obtained. Inset (d): the extracted crossover length scale diverges $\sim D^{-2}$ (we have fixed $\xi = 1$ for $D = 1$). Panel (b) shows histograms of $S_{vN}/\ln 2$ collected for $L = 128, 256$ over several hundred thousands of independent random samples for varying disorder strengths, as indicated on the plot. The random singlet structure (see also the schematic picture on top right) clearly develops upon increasing disorder and/or system size, with peaks at even integer values

with power-law distributed AF couplings $P(J) \propto J^{-1+1/D}$. Note that such a distribution allows to describe a broad range of disorder strengths: from clean physics $D \rightarrow 0$ to the infinite randomness fixed point distribution where $D \rightarrow \infty$.

Figure 5a shows the finite-size behavior of the disorder-average von-Neumann entropy $S_{\text{vN}}(L)$ (here again we focus on half-chain cuts), for a broad range of initial disorder strengths $D = 0.01, \dots, 8$. We clearly observe the logarithmic scaling Eq. (20), with a smooth finite-size crossover from clean physics $c_{\text{eff}} = 1$ to the SDRG asymptotic result [67] $c_{\text{eff}} = \ln 2$ observed at large enough D or L .

(ii) *Crossover Phenomenon* This crossover is controlled by a disorder-dependent length scale ξ , as studied in panels (c, d). There, the prefactor of the logarithmic growth has been extracted from simple fit to the form Eq. (20) over sliding windows containing 7 points. The disorder and size-dependent crossover for the “effective central charge” $c_{\text{eff}}(L, D)$ (between 1 and $\ln 2$) exhibits a “universal” scaling form $c_{\text{eff}}(L/\xi)$, as extracted in Fig. 5d. Moreover, ξ plotted in panel (d) inset is found to diverge $\propto D^{-2}$ at weak disorder. This remarkable behavior is in perfect agreement with a crossover already identified for the average correlation functions [75–77]. As a matter of fact, ξ gives a simple quantitative scale beyond which asymptotic results from SDRG can be expected. For instance, on finite chains, the random singlet structure (depicted in Fig. 5b inset) becomes effectively visible, either when the initial disorder D is strong enough or for increasing system size, as clearly visible in Fig. 5b.

(iii) *Random Singlets: Significant Others* The situation is also very interesting for higher Rényi indices, as discussed by Fagotti et al. [73]. Depending on how the averaging over disorder is performed, one should expect the different scalings

$$S_q = \frac{\overline{\ln \text{Tr} \rho_A^q}}{1-q} = \frac{\ln 2}{3} \ln L + \text{const}_q, \quad (22)$$

$$\tilde{S}_q = \frac{\overline{\ln \text{Tr} \rho_A^q}}{1-q} = f_q \frac{\ln 2}{3} \ln L + \text{const}'_q, \quad (23)$$

with the non-trivial prefactor $f_q = \frac{3(\sqrt{5+2^{3-q}}-3)}{2 \ln 2(1-q)} \leq 1$, vanishing at large q and $f_q \rightarrow 1$ in the von-Neumann (or Shannon) limit $q \rightarrow 1$. This peculiar dependence on the disorder averaging is one of the hallmarks of infinite randomness physics, as deeply discussed by D. S. Fisher for correlations functions [10, 25].

It is also worth mentioning how the works on entanglement in the RSP (given by a rather simple counting of singlet bonds crossing the entanglement cut) led to the emergence of the idea of a valence bond entanglement entropy [78–83]. This alternative entanglement witness turns out to be much easier to access within quantum Monte Carlo frameworks, as compared to the von-Neumann or Rényi entanglement entropies [84–90], despite some recent impressive progresses [91, 92].

Random singlet physics has also recently triggered new studies, such as the investigation of the entanglement negativity in Refs. [93, 94] or the extension of the concept of symmetry-resolved entanglement equipartition [95–98] to the RSP by Turkeshi et al. in Ref. [99].

3.1.2 Infinite Randomness Criticality at High Energy

As expected from high-energy SDRG approaches [100–103], the zero-temperature quantum criticality of the disordered quantum Ising chain, Eq. (5), must remain unchanged at *all* energies, so far only confirmed by a single numerical study [104]. Here, we present and discuss our numerical results obtained for the 1D random TFIM in Fig. 6. First, at criticality when $\delta = \overline{\ln J} - \overline{\ln h} = 0$, we check in the inset of Fig. 6 the logarithmic scaling for the disorder-average entropy with open boundary conditions with a cut at half-chain (see schematic picture in Fig. 6, top right)

$$S_{\text{VN}}(L/2, \epsilon, \delta = 0) = \frac{\ln 2}{12} \ln L + \text{const}(\epsilon), \quad (24)$$

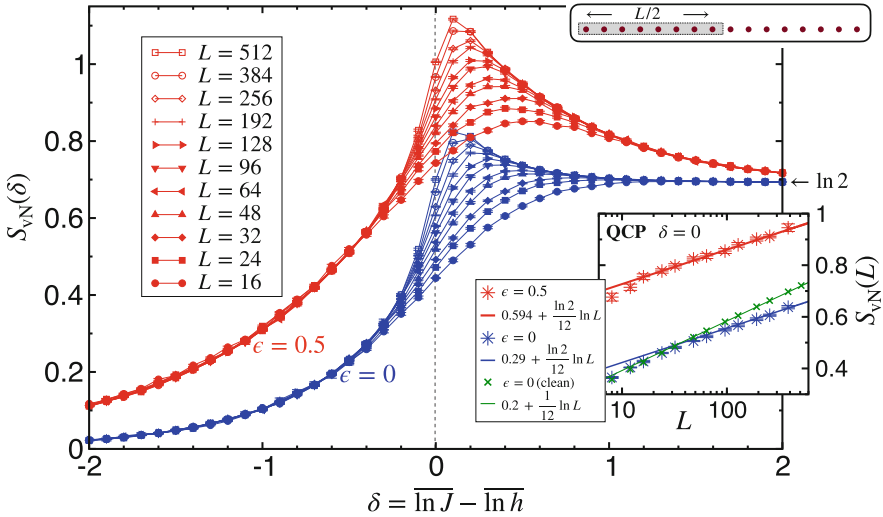


Fig. 6 Exact diagonalization results for the random TFIM Eq. (5) with open boundary conditions. Results are averaged over several thousands of samples for various system lengths L , as indicated on the plot. The half-chain von-Neumann entropy (see schematic picture, top right) is plotted against the control parameter δ for (zero-temperature) ground-state ($\epsilon = 0$, blue symbols) and infinite-temperature ($\epsilon = 0.5$, red symbols), in both cases showing qualitatively similar behaviors (see text). Inset: the critical scaling at $\delta = 0$ takes the expected logarithmic form, Eq. (24). Note also the crossover between the clean case ($\epsilon = 0$, green symbols) and the asymptotic behavior

where the only dependence on the energy density ϵ comes in the nonuniversal additive constant. We remind that ground-state is at $\epsilon = 0$, while $\epsilon = 0.5$ corresponds to infinite-temperature states. Interestingly, we also remark that $\text{const}(0.5) \approx 2 \times \text{const}(0)$. In a way similar to the previously discussed crossover from clean to IRFP for the random-bod XX chain, we also observe the same effect here. However, we will not vary the disorder strength, but instead vary the control parameter $\delta = \ln \bar{J} - \ln \bar{h} = 2 \ln W$, keeping couplings and fields drawn from box distributions: $P_{J/h} = \text{Box}[0, W_{J/h}]$ uniform between 0 and $W_{J/h}$, with $W_J = W_h^{-1} = W$.

In the main panel of Fig. 6, upon varying δ , the von-Neumann entropy displays qualitatively similar behaviors for zero and infinite temperature: (i) area-law entanglement, even at high temperature, (ii) $S_{\text{vN}} \rightarrow \ln 2$ for positive δ , signaling localization protected quantum order [105] with a “cat-state” structure for the eigenstates, and (iii) IRFP log scaling Eq. (24) at criticality (see inset).

3.2 Other Systems Showing Infinite Randomness Criticality

3.2.1 Higher Spins, Golden Chain, and RG Flows

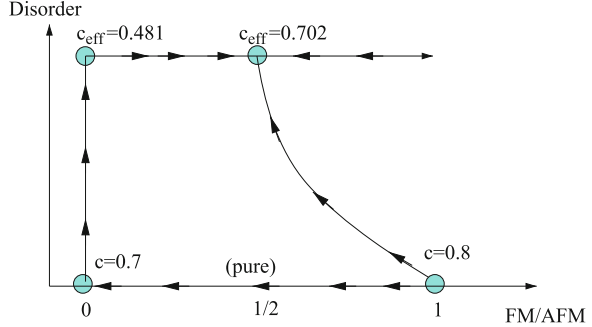
Back to zero temperature, infinite randomness physics also occurs for higher spin systems with $S > 1/2$ chains [106–109], for which it was shown [110, 111] that

$$S_{\text{vN}} = \frac{\ln(2S + 1)}{3} \ln L + \text{constant}. \quad (25)$$

Non-abelian RSP is also expected for disordered chains of Majorana or Fibonacci anyons [112–114], with a logarithmic von-Neumann entropy whose “effective central charge” prefactor is given by $\ln \mathcal{D}$, where \mathcal{D} is the quantum dimension, e.g., $\mathcal{D} = \sqrt{2}$ for a Majorana chain (quantum Ising chain at criticality), and $\mathcal{D} = (1 + \sqrt{5})/2$ for Fibonacci anyons.

There is an important issue concerning the entanglement gradient along RG flows. In the absence of disorder, the famous Zomolodchikov’s c -theorem [115] implies a decay of entanglement along RG flows. The observation of decreasing entropies along infinite randomness RG flows [67, 71, 110] then raised a similar question for random systems. However, two clear counter examples have ruled out such a scenario, due to Santachiara [116] for generalized quantum Ising chains including the N -states random Potts chain and later by Fidkowski et al. [113] for disordered chains of Fibonacci anyons. The RG flow phase diagram of disordered golden chains from Ref. [113] is given in Fig. 7, see also Ref. [68].

Fig. 7 RG flow diagram of pure and random golden chains. In the clean case, Zamolodchikov's c -theorem is verified, while this is not necessarily true in the disordered case. Figure taken from Fidkowski et al. [113]



3.2.2 $d > 1$ Infinite Randomness

Infinite randomness physics is not restricted to $d = 1$, but also occurs for $d \geq 2$ random quantum Ising models [63, 65, 117, 118], while $d > 1$ random-exchange antiferromagnets do not host random singlet physics since the $T = 0$ Néel order is very robust against disorder [64, 119].

There has been some controversy regarding the precise scaling of the von-Neumann entropy for higher dimensional IRFP in the random TFIM, in particular for the $d = 2$ square lattice [120, 121]. Building on an improved SDRG algorithm,² Kovács and Iglói [65, 117] unambiguously found a pure area-law scaling with additive (negative) logarithmic corrections [121, 122], coming from the subsystem corners:

$$S_{\text{vN}} = \alpha L + 4\ell_1(\pi/2) \ln L + \text{const.} \quad (26)$$

with $\ell_1(\pi/2) \approx -0.03$. These logarithmic corrections, induced by sharp subsystem boundaries, only occur at the infinite randomness criticality [122]. Interestingly, they are of the same order of magnitude as the corner terms which show up in (disorder-free) $2 + 1$ CFT [123–125].

3.3 Engineered Disorders

In this part, we discuss a class of disordered spin chains where some local correlations have been included, thus making the systems not entirely random. Two main examples will be addressed: (i) a simple TFIM with purely local correlations

² In Refs. [65, 117], the $\mathcal{O}(N^3)$ CPU time scaling of the simplest SDRG approaches was scaled down to $\mathcal{O}(N \ln N)$ for arbitrary dimension, allowing to study the entanglement of $d = 2, 3, 4$ disordered quantum Ising models up to $N \sim 10^6$ spins, see also Ref. [122].

between random couplings and fields [126, 127] and (ii) the so-called “rainbow model” introduced in Ref. [128] and its subsequent extensions.

(i) *Random Quantum Ising Chains with Locally Correlated Disorder* Binosi et al. [126] first proposed the following quantum Ising chain model with a very simple purely local correlation in the disorder parameters:

$$\mathcal{H} = - \sum_i J_i (\sigma_i^x \sigma_{i+1}^x + \sigma_i^z), \quad (27)$$

as an example that exhibits growing entanglement upon increasing disorder. In the above Hamiltonian, it is remarkable to see that the very same (random) number J_i acts on a site i as a field as well as a coupling on its adjacent bond, such that a perfect correlation (while purely local, with a minimal correlation length) is achieved. Building on field theory, SDRG, and free-fermion numerics, this model was studied by Hoyos et al. in Ref. [127]. First, it was found that any tiny breaking of the perfect coupling–field correlation drives the system to IRFP physics. However, when the perfect correlation in the Hamiltonian Eq. (27) is maintained, weak disorder is *irrelevant* for the clean critical point, and quite large disorder is required to drive the system toward a non-trivial line of critical points, where unusual properties emerge, such as an increase of the entanglement entropy with the disorder strength. These numerical results from Ref. [127] are reproduced in Fig. 8a.

Model Eq. (27) is an interesting example whereby construction of the disordered system is always strictly critical at the local level, satisfying the condition $J_i = h_i$ in Eq. (5), and thus naturally yielding $\delta = 0$. This apparent suppression of local randomness protects the clean physics against small disorder D , but at strong

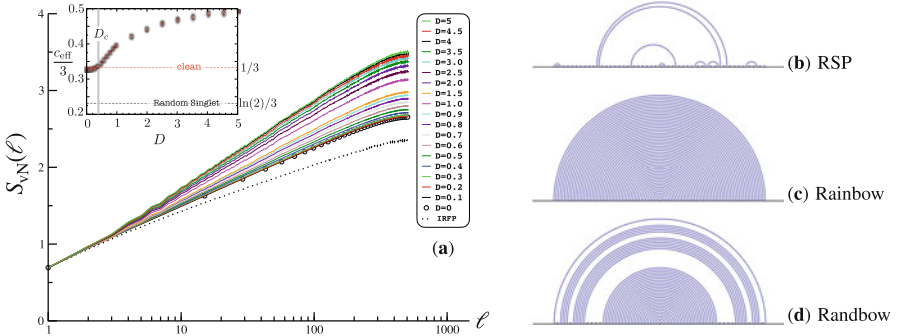


Fig. 8 Left (a): random TFIM with local correlations, Eq. (27). Disorder-averaged entanglement (von-Neumann) entropy plotted against subsystem lengths ℓ for the ground-state of Eq. (27) with various disorder strengths D , couplings being power-law distributed $P(J) \propto J^{-1+1/D}$, for $L = 1024$ sites and 5000 disorder realizations. Inset: the disorder dependence of the effective central charge exhibits a transition for $D_c \approx 0.3$. Figure taken from Ref. [127]. Right: sketch of the three regimes of the Rainbow chain model Eq. (28) with randomness in the couplings J_i . (b) RSP when $h \ll 1$. (c) Rainbow phase $h \rightarrow \infty$. (d) Rainbow regime $h \sim 1$. Figure taken from Ref. [130]

enough D a new physics appears where entanglement increases with D . The effective central charge, extracted from the logarithmic growth in the main panel of Fig. 8a, is shown in the inset. Note that an extension to an interacting XXZ version was studied in Ref. [129], reaching similar conclusions as compared to the above non-interacting situation.

(ii) *Rainbow and Randbow States* There is another family of engineered disordered models which has motivated an important number of works: the so-called rainbow model [130, 131] and its extensions, in particular the “Randbow” XX chain [128]

$$\mathcal{H}_{\text{Randbow XX}} = \sum_{i=-L}^{L+1} J_i e^{-h|i|} (S_i^x S_{i+1}^x + S_i^y S_{i+1}^y). \quad (28)$$

For the disorder-free ($J_i = \text{constant}$) case, the spatial structure of its inhomogeneity, exponentially decaying from the center of the chain, allows to apply the SDRG rule and construct the ground-state: the concentric singlet phase depicted in Fig. 8c. Analyzing its entanglement properties [131–133], a volume-law scaling emerges with the entropy proportional to the number of sites inside the subsystem. This remains true for any nonzero value of the exponentially decaying parameter h , with the particularly interesting volume-law asymptotic scaling [133], in the limit $h \ll 1$ and $h\ell \gg 1$

$$S_{\text{vN}}(h, \ell) \approx \frac{1}{6} \ln \left(\frac{e^{\ell h} - 1}{h} \right) \sim \frac{h}{6} \ell. \quad (29)$$

The introduction of a true randomness in the couplings J_i (on top of this exponentially decaying pattern) has led Alba et al. [130] to the so-called Randbow case, with the following results for the asymptotic forms, at large ℓ :

$$S_{\text{vN}}(\ell) \propto \begin{cases} \frac{\ln 2}{6} \ln \ell & \text{if } h = 0 \text{ (RSP)} \\ \ell \ln 2 & \text{if } h \rightarrow \infty \text{ (Rainbow)} \\ \sqrt{\ell} & \text{otherwise (Randbow).} \end{cases} \quad (30)$$

It is remarkable to observe that the RSP scaling only survives in the limit $h = 0$ of no decaying couplings. In the opposite limit, the rainbow concentric singlet phase can only overcome the effect of disorder in J_i for a “vertically decaying” inhomogeneity $h \rightarrow \infty$. Finally, the entire regime $0 < h < \infty$ falls in the intermediate situation, the so-called “Randbow” phase, see Fig. 8d, with an unusual $\sqrt{\ell}$ area-law violation. This exotic scaling is a direct consequence of the ground-state structure: exponentially rare “rainbow” regions having long-distance singlets, coexist with “bubble” regions (made of short-range singlets) having a power-law decaying probability [130].

Let us finally comment on the effect of interactions in the XXZ version of the Randbow chain. While irrelevant for the RSP physics, here there very structure of

the SDRG iterations lead to the fact that the above area-law violation appears to be specific to the free-fermion point. From SDRG calculation, attraction is found to restore the volume-law scaling, while repulsive interactions induce a strict area-law scaling [130].

4 Many-Body Localization Probed by Quantum Entanglement

4.1 Area vs. Volume-Law Entanglement for High-Energy Eigenstates

Entanglement is a key concept to gain some insight on many-body localization (MBL) physics, briefly described in Sect. 1.2.3, see also Refs. [30–33] for recent reviews. In isolated quantum systems, thermalization implies that the system acts as its own heat bath. This is the case for the so-called ergodic regime, adjacent of the MBL phase, see Fig. 1c where the eigenstate thermalization hypothesis (ETH) [134, 135] is expected to hold. In this delocalized phase, the reduced density matrix of a high-energy eigenstate can be interpreted as an equilibrium (high-temperature) thermal density matrix. Therefore, the entanglement entropy of such a highly excited eigenstate must be very close to the thermodynamic entropy of the subsystem at high temperature, thus exhibiting a volume-law scaling. Such delocalized infinite-temperature eigenstates are usually well described by random states having a maximal entanglement entropy [59].

Volume-law entanglement at high temperature has been clearly observed for clean quantum spin chains [60, 136–139], as well as in the ergodic side of weakly disordered chains [15, 140–142]. In contrast, the MBL regime violates ETH and eigenstates display a much weaker area-law entanglement, quantitatively closer to the entanglement entropy of a ground-state [143, 144]. Such qualitatively distinct properties have been observed numerically in various studies [15, 141, 145, 146]. In order to illustrate this, Fig. 9 shows exact diagonalization results for the half-chain von-Neumann entanglement entropy, obtained together with D. Luitz and F. Alet in Ref. [15] for the random-field Heisenberg chain model Eq. (7). When S_{vN} is normalized by the system size, the transition from volume- to area-law is clearly visible around $h_c \sim 2.5$ (random fields are drawn from a box $[-h, h]$) at this energy density $\epsilon = 0.8$, see also the scaling plot in panel (b). Our numerical data are compatible with a volume-law entanglement at criticality [147], and with a strict area-law scaling in the MBL regime, shown as a dashed line in Fig. 9b. Note that in the MBL phase, Bauer and Nayak [140] reported a weak logarithmic violation of the area law for the maximum entropy, obtained from the (sample-dependent) optimal cut, see also [144, 148].

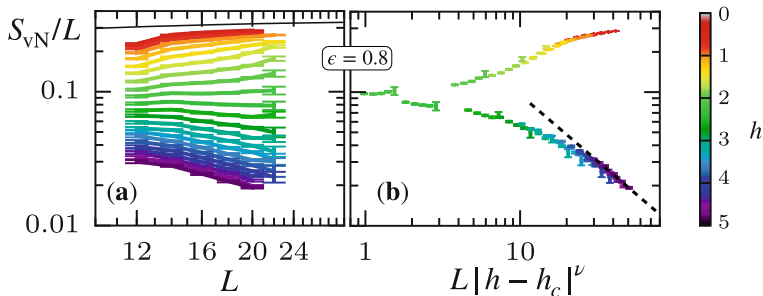


Fig. 9 Entanglement entropy density S_{vN}/L for the MBL problem at high energy. Shift-invert exact diagonalization results for half-chain cuts performed over periodic Heisenberg chains with a random field Eq. (7), obtained for high-energy ($\epsilon = (E - E_{\min})/(E_{\max} - E_{\min}) = 0.8$) eigenstates with various chain lengths $L = 12, \dots, 22$. In panel (a), a clear qualitative change is visible upon increasing disorder h , from volume-law (black line shows Page’s law [59]) to area-law, with a critical point observed for $h_c \sim 2.5$. Panel (b) shows a scaling plot obtained with $h_c = 2.27$ and $\nu = 1$. The dashed line $\sim 1/L$ represents the strict area-law situation. Figure adapted from Luitz et al. [15]

4.2 Distributions of Entanglement Entropies

4.2.1 Distribution Across the ETH-MBL Transition

In order to go beyond the disorder and eigenstate average entropies, a systematic study of their distributions turns out to be extremely instructive, as first discussed in Refs. [15, 140, 141, 149]. An enhancement of the variance with increasing system sizes L was reported when approaching the critical region, thus providing a quantitative tool, see, for instance, Fig. 10 (left). Another very thorough and exhaustive study was provided by Yu et al. [150] for the standard model Eq. (7), see Fig. 10 (right) where the four panels show a remarkable qualitative change in the distributions of entanglement slopes upon increasing the disorder. In addition, a bimodal structure was found at criticality, a feature surprisingly observed also for a *single* disorder realization (see inset, where the distribution is computed from eigenstates in the *same* disorder sample). As argued by Khemani et al. [146, 151], a key for understanding the MBL transition may come from the differences between fluctuations of entanglement coming from different eigenstates in the *same* disordered sample, as compared to fluctuations coming from different samples, see Fig. 10 (right) taken from Ref. [146].

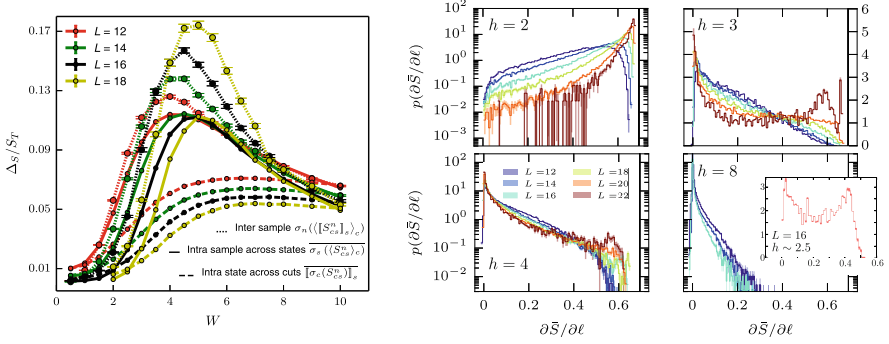


Fig. 10 Entanglement entropy distributions across the ETH-MBL transition. Left: from Khemani et al. [146], (normalized) standard deviation of the von-Neumann entropy Δ_S/S_T plotted against disorder strength W for the standard model Eq. (7) with additional second neighbor exchange (yielding a critical disorder strength $W_c \sim 7$). In the critical region, Δ_S is dominated by sample-to-sample fluctuations. Figure taken from Ref. [146]. Right: distribution of entanglement slopes, from Yu et al. [150], for model Eq. (7). Upon increasing the disorder strength h , there is a clear qualitative change in the distributions. When the transition is approached, a bimodal shape is identified, a structure also observed at the level of a single disordered sample (inset) for 6000 eigenstates. Figure taken from Ref. [150]

4.2.2 Strong Disorder Distributions

At strong disorder, deep in the MBL regime the entanglement entropy is obviously very small. However, following our previous discussion for the non-interacting case (Sect. 2.2.3 and Fig. 4), it is also instructive to take a look at the histograms in the interacting case at large disorder. Figure 11 displays several panels for $P(S_{\text{vN}})$ at various disorder strengths $h = 5, 10, 15, 20, 30, 50$, computed for $L = 12, 14, 16, 18, 20$ at infinite temperature $\epsilon = 0.5$. One can observe the following remarkable effects:

- (i) Finite-size effects are almost absent, confirming the fact that the localization length is very small deep in the MBL phase [152, 153].
- (ii) Upon increasing h , the influence of interactions becomes gradually less visible, clearly noticeable when comparing the MBL data (symbols) with the non-interacting case (full lines, data from panel (b) of Fig. 4). A qualitative difference is only apparent below $h \approx 10$, when more pronounced at $h = 5$ when the MBL-ETH transition is approached.
- (iii) The peaked structure is also clearly present, signaling anomalously weakly disordered sites. We have also checked that the probability $\rho_1 = P(|S_{\text{vN}}/\ln 2 - 1| \leq 0.05)$ decays $\sim h^{-1}$, like in the non-interacting case. One can therefore anticipate that the entanglement entropy will be dominated by such “rare” events.

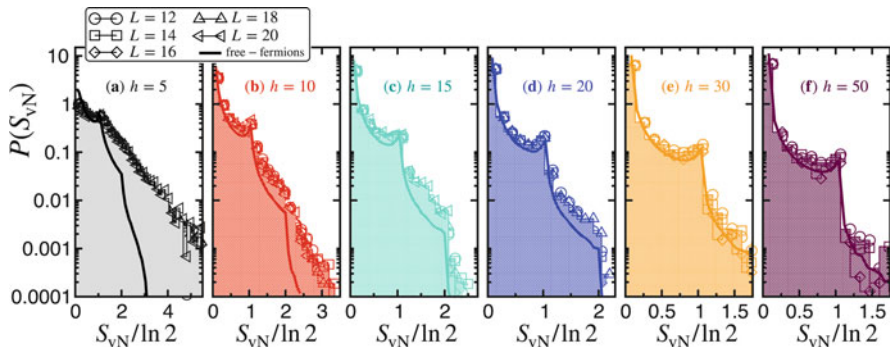


Fig. 11 Strong disorder behavior of the half-chain entanglement entropy distributions for the random-field Heisenberg chain model Eq. (7), deep in the MBL regime. Shift-invert ED results for highly excited states at $\epsilon = 0.5$. Different panels (a)–(f) show histograms of $S_{vN}/\ln 2$ collected for $L = 12, 14, 16, 18, 20$ (different symbols) over several thousands of independent random samples for varying disorder strengths $h = 5, 10, 15, 20, 30, 50$, as indicated on the plot. The non-interacting (free-fermions) case for $L = 32$ is also shown (lines) for comparison. One sees the peaked structure gradually developing when h increases. Note the quasi-absence of finite-size effects

5 Concluding Remarks

In this chapter, the entanglement properties of various disordered quantum chains have been discussed, with a global focus on the von-Neumann entanglement entropy S_{vN} for three different classes of random spin chains. Extensive numerical results have been presented and reviewed together with an important literature on this topic.

For Anderson localized XX chains in a random magnetic field, S_{vN} exhibits universal scaling with different forms which depends on the energy. Nevertheless, it was shown that there is a unique length scale which controls the real space localization of single-particle states and the scaling functions of the many-body entanglement entropy. For very strong randomness, the behavior of the distributions is also remarkable, showing some peculiar features that clearly capture some salient low- and high-energy properties.

A second set of systems that we discussed concerns infinite randomness physics. For random-bond XX chains at zero temperature, we unveiled a nice finite-size crossover for the effective central charge, controlling the logarithmic scaling of the von-Neumann entropy, from the clean behavior to the random singlet asymptotic form. As another example of infinite randomness, the quantum Ising chain was studied at and away from criticality, for both zero and infinite temperatures. The logarithmic critical scaling is similar (and therefore universal) at all energies, with only a nonuniversal constant which depends on the energy.

We have also reviewed on the existing results beyond free fermions, e.g., random singlet phases with higher spins, and also discuss the cases of engineered disordered

systems with locally correlated randomness or the so-called rainbow/randbow chain models.

Finally, the strongly debated problem of many-body localization has also been discussed through the properties displayed by eigenstates entanglement entropies at high energy. Going beyond the volume-law to area-law paradigm for the ETH-MBL transition, the shape of the distributions has been investigated and discussed for all regimes, including strong disorder where Anderson and MBL insulator displays almost similar entanglement structure, despite their clearly different dynamical response [37, 39, 154–156].

Acknowledgments It is a great pleasure to thank all my collaborators on this topic of entanglement properties in quantum disordered systems: Fabien Alet, Maxime Dupont, José Hoyos, Gabriel Lemarié, David Luitz, Nicolas Macé, Eduardo Miranda, André Vieira, and Thomas Vojta. This work was supported by the Agence Nationale de la Recherche under programs GLADYS ANR-19-CE30-0013, and ANR-11-IDEX-0002-02, reference ANR-10-LABX-0037-NEXT.

References

1. P.W. Anderson, Phys. Rev. **109**, 1492 (1958)
2. F. Evers, A.D. Mirlin, Rev. Mod. Phys. **80**, 1355 (2008)
3. J. Kondo, Prog. Theor. Phys. **32**, 37 (1964)
4. A.C. Hewson, *The Kondo Problem to Heavy Fermions* (Cambridge, UK, 1993)
5. K. Binder, A.P. Young, Rev. Mod. Phys. **58**, 801 (1986)
6. T. Matsubara, H. Matsuda, Prog. Theor. Phys. **16**, 569 (1956)
7. P. Jordan, E. Wigner, Zeitschrift für Physik **47**, 631 (1928)
8. T. Giamarchi, H.J. Schulz, Phys. Rev. B **37**, 325 (1988)
9. C.A. Doty, D.S. Fisher, Phys. Rev. B **45**, 2167 (1992)
10. D.S. Fisher, Phys. Rev. B **50**, 3799 (1994)
11. G. Bouzerar, D. Poilblanc, J. Phys. I France **4**, 1699 (1994)
12. P. Schmitteckert, T. Schulze, C. Schuster, P. Schwab, U. Eckern, Phys. Rev. Lett. **80**, 560 (1998)
13. E.V.H. Doggen, G. Lemarié, S. Capponi, N. Laflorencie, Phys. Rev. B **96**, 180202 (2017)
14. S.-H. Lin, B. Sbierski, F. Dorfner, C. Karrasch, F. Heidrich-Meisner, SciPost Physics **4**, 002 (2018)
15. D.J. Luitz, N. Laflorencie, F. Alet, Phys. Rev. B **91**, 081103 (2015)
16. T. Giamarchi, *Quantum Physics in One Dimension* (2003)
17. D.S. Fisher, Phys. Rev. Lett. **69**, 534 (1992)
18. M.P.A. Fisher, P.B. Weichman, G. Grinstein, D.S. Fisher, Phys. Rev. B **40**, 546 (1989)
19. A.Y. Kitaev, Phys.-Usp. **44**, 131 (2001)
20. P. Fendley, J. Stat. Mech. P11020 (2012)
21. E. Lieb, T. Schultz, D. Mattis, Ann. Phys. **16**, 407 (1961)
22. P. Pfeuty, Ann. Phys. **57**, 79 (1970)
23. B.M. McCoy, T.T. Wu, Phys. Rev. **176**, 631 (1968)
24. B.M. McCoy, Phys. Rev. **188**, 1014 (1969)
25. D.S. Fisher, Phys. Rev. B **51**, 6411 (1995)
26. R. Nandkishore, A.C. Potter, Phys. Rev. B **90**, 195115 (2014)
27. A.P. Young, H. Rieger, Phys. Rev. B **53**, 8486 (1996)
28. F. Iglói, H. Rieger, Phys. Rev. B **57**, 11404 (1998)
29. D.S. Fisher, A.P. Young, Phys. Rev. B **58**, 9131 (1998)

30. R. Nandkishore, D.A. Huse, *Annu. Rev. Condens. Matter Phys.* **6**, 15 (2015)
31. D.A. Abanin, Z. Papic, *Ann. Phys.* **529**, 1700169 (2017)
32. F. Alet, N. Laflorencie, *Comptes Rendus Physique Quantum Simulation/Simulation quantique*, **19**, 498 (2018)
33. D.A. Abanin, E. Altman, I. Bloch, M. Serbyn, *Rev. Mod. Phys.* **91**, 021001 (2019)
34. P. Jacquod, D.L. Shepelyansky, *Phys. Rev. Lett.* **79**, 1837 (1997)
35. I.V. Gornyi, A.D. Mirlin, D.G. Polyakov, *Phys. Rev. Lett.* **95**, 206603 (2005)
36. D.M. Basko, I.L. Aleiner, B.L. Altshuler, *Ann. Phys.* **321**, 1126 (2006)
37. M. Žnidarič, T. Prosen, P. Prelovšek, *Phys. Rev. B* **77**, 064426 (2008)
38. A. Pal, D. A. Huse, *Phys. Rev. B* **82**, 174411 (2010)
39. J.H. Bardarson, F. Pollmann, J.E. Moore, *Phys. Rev. Lett.* **109**, 017202 (2012)
40. J.Z. Imbrie, *J Stat Phys* **163**, 998 (2016)
41. A. De Luca, A. Scardicchio, *EPL* **101**, 37003 (2013)
42. E.V.H. Doggen, F. Schindler, K.S. Tikhonov, A.D. Mirlin, T. Neupert, D.G. Polyakov, I.V. Gornyi, *Phys. Rev. B* **98**, 174202 (2018)
43. T. Chanda, P. Sierant, J. Zakrzewski, *Phys. Rev. B* **101**, 035148 (2020)
44. P. Sierant, D. Delande, J. Zakrzewski, *Phys. Rev. Lett.* **124**, 186601 (2020)
45. D.A. Abanin, J.H. Bardarson, G. De Tomasi, S. Gopalakrishnan, V. Khemani, S.A. Parameswaran, F. Pollmann, A.C. Potter, M. Serbyn, R. Vasseur, *Ann. Phys.* **427**, 168415 (2021)
46. M. Schreiber, S.S. Hodgman, P. Bordia, H.P. Lüchen, M.H. Fischer, R. Vosk, E. Altman, U. Schneider, I. Bloch, *Science* **349**, 842 (2015)
47. J. Smith, A. Lee, P. Richerme, B. Neyenhuis, P.W. Hess, P. Hauke, M. Heyl, D.A. Huse, C. Monroe, *Nat. Phys.* **12**, 907 (2016)
48. J.-y. Choi, S. Hild, J. Zeiher, P. Schauß, A. Rubio-Abadal, T. Yefsah, V. Khemani, D.A. Huse, I. Bloch, C. Gross, *Science* **352**, 1547 (2016)
49. P. Roushan, C. Neill, J. Tangpanitanon, V.M. Bastidas, A. Megrant, R. Barends, Y. Chen, Z. Chen, B. Chiaro, A. Dunsworth, A. Fowler, B. Foxen, M. Giustina, E. Jeffrey, J. Kelly, E. Lucero, J. Mutus, M. Neeley, C. Quintana, D. Sank, A. Vainsencher, J. Wenner, T. White, H. Neven, D.G. Angelakis, J. Martinis, *Science* **358**, 1175 (2017)
50. F. Pietracaprina, N. Macé, D.J. Luitz, F. Alet, *SciPost Physics* **5**, 045 (2018)
51. R.J. Bell, P. Dean, *Discuss. Faraday Soc.* **50**, 55 (1970)
52. J.T. Edwards, D.J. Thouless, *J. Phys. C: Solid State Phys.* **5**, 807 (1972)
53. D.J. Thouless, *J. Phys. C: Solid State Phys.* **5**, 77 (1972)
54. S. Johri, R.N. Bhatt, *Phys. Rev. Lett.* **109**, 076402 (2012)
55. I. Peschel, *J. Stat. Mech.* **2004**, P06004 (2004)
56. G. Vidal, J.I. Latorre, E. Rico, A. Kitaev, *Phys. Rev. Lett.* **90**, 227902 (2003)
57. P. Calabrese, J. Cardy, *J. Stat. Mech.* **2004**, P06002 (2004)
58. V.E. Korepin, *Phys. Rev. Lett.* **92**, 096402 (2004)
59. D.N. Page, *Phys. Rev. Lett.* **71**, 1291 (1993)
60. L. Vidmar, L. Hackl, E. Bianchi, M. Rigol, *Phys. Rev. Lett.* **119**, 020601 (2017)
61. S.-k. Ma, C. Dasgupta, C.-k. Hu, *Phys. Rev. Lett.* **43**, 1434 (1979)
62. F. Iglói, C. Monthus, *Phys. Rep.* **412**, 277 (2005)
63. O. Motrunich, S.-C. Mau, D.A. Huse, D.S. Fisher, *Phys. Rev. B* **61**, 1160 (2000)
64. Y.-C. Lin, R. Mélin, H. Rieger, F. Iglói, *Phys. Rev. B* **68**, 024424 (2003)
65. I.A. Kovács, F. Iglói, *Phys. Rev. B* **83**, 174207 (2011)
66. F. Iglói, C. Monthus, *Eur. Phys. J. B* **91**, 290 (2018)
67. G. Refael, J.E. Moore, *Phys. Rev. Lett.* **93**, 260602 (2004)
68. G. Refael, J.E. Moore, *J. Phys. A* **42**, 504010 (2009)
69. J.A. Hoyos, A.P. Vieira, N. Laflorencie, E. Miranda, *Phys. Rev. B* **76**, 174425 (2007)
70. R. Juhász, *Phys. Rev. B* **104**, 054209 (2021)
71. N. Laflorencie, *Phys. Rev. B* **72**, 140408 (2005)
72. F. Iglói, Y.-C. Lin, *J. Stat. Mech.* **2008**, P06004 (2008)
73. M. Fagotti, P. Calabrese, J.E. Moore, *Phys. Rev. B* **83**, 045110 (2011)

74. M. Pouranvari, K. Yang, *Phys. Rev. B* **88**, 075123 (2013)
75. N. Laflorencie, H. Rieger, *Phys. Rev. Lett.* **91**, 229701 (2003).
76. N. Laflorencie, H. Rieger, A.W. Sandvik, P. Henelius, *Phys. Rev. B* **70**, 054430 (2004)
77. N. Laflorencie, H. Rieger, *EPL* **40**, 201 (2004)
78. F. Alet, S. Capponi, N. Laflorencie, M. Mambrini, *Phys. Rev. Lett.* **99**, 117204 (2007)
79. R.W. Chhajlany, P. Tomczak, A. Wójcik, *Phys. Rev. Lett.* **99**, 167204 (2007)
80. M. Mambrini, *Phys. Rev. B* **77**, 134430 (2008)
81. J.L. Jacobsen, H. Saleur, *Phys. Rev. Lett.* **100**, 087205 (2008)
82. F. Alet, I.P. McCulloch, S. Capponi, M. Mambrini, *Phys. Rev. B* **82**, 094452 (2010)
83. H. Tran, N.E. Bonesteel, *Phys. Rev. B* **84**, 144420 (2011)
84. M. Hastings, I. González, A. Kallin, R. Melko, *Phys. Rev. Lett.* **104**, 157201 (2010)
85. A.B. Kallin, M.B. Hastings, R.G. Melko, R.R.P. Singh, *Phys. Rev. B* **84**, 165134 (2011)
86. S. Humeniuk, T. Roscilde, *Phys. Rev. B* **86**, 235116 (2012)
87. J. Helmes, S. Wessel, *Phys. Rev. B* **89**, 245120 (2014)
88. D.J. Luitz, X. Plat, N. Laflorencie, F. Alet, *Phys. Rev. B* **90**, 125105 (2014)
89. B. Kulchitskyy, C.M. Herdman, S. Inglis, R.G. Melko, *Phys. Rev. B* **92**, 115146 (2015)
90. F.P. Toldin, F.F. Assaad, *J. Phys. Conf. Ser.* **1163**, 012056 (2019)
91. J. D'Emidio, *Phys. Rev. Lett.* **124**, 110602 (2020)
92. O. Francesconi, M. Panero, D. Preti, *J. High Energ. Phys.* **2020**, 233 (2020)
93. P. Ruggiero, V. Alba, P. Calabrese, *Phys. Rev. B* **94**, 035152 (2016)
94. X. Turkeshi, P. Ruggiero, P. Calabrese, *Phys. Rev. B* **101**, 064207 (2020)
95. N. Laflorencie, S. Rachel, *J. Stat. Mech.* **2014**, P11013 (2014)
96. M. Goldstein, E. Sela, *Phys. Rev. Lett.* **120**, 200602 (2018)
97. J.C. Xavier, F.C. Alcaraz, G. Sierra, *Phys. Rev. B* **98**, 041106 (2018)
98. S. Murciano, G. Di Giulio, P. Calabrese, *SciPost Physics* **8**, 046 (2020)
99. X. Turkeshi, P. Ruggiero, V. Alba, P. Calabrese, *Phys. Rev. B* **102**, 014455 (2020)
100. D. Pekker, G. Refael, E. Altman, E. Demler, V. Oganesyan, *Phys. Rev. X* **4**, 011052 (2014)
101. R. Vasseur, A.C. Potter, S.A. Parameswaran, *Phys. Rev. Lett.* **114**, 217201 (2015)
102. Y.-Z. You, X.-L. Qi, C. Xu, *Phys. Rev. B* **93**, 104205 (2016)
103. C. Monthus, *J. Phys. A: Math. Theor.* **51**, 115304 (2018)
104. Y. Huang, J.E. Moore, *Phys. Rev. B* **90**, 220202 (2014)
105. D.A. Huse, R. Nandkishore, V. Oganesyan, A. Pal, S.L. Sondhi, *Phys. Rev. B* **88**, 014206 (2013)
106. R.A. Hyman, K. Yang, *Phys. Rev. Lett.* **78**, 1783 (1997)
107. C. Monthus, O. Golinelli, T. Jolicoeur, *Phys. Rev. B* **58**, 805 (1998)
108. G. Refael, S. Kehrein, D.S. Fisher, *Phys. Rev. B* **66**, 060402 (2002)
109. K. Damle, D.A. Huse, *Phys. Rev. Lett.* **89**, 277203 (2002)
110. G. Refael, J.E. Moore, *Phys. Rev. B* **76**, 024419 (2007)
111. A. Saguia, M.S. Sarandy, B. Boechat, M.A. Continentino, *Phys. Rev. A* **75**, 052329 (2007)
112. N.E. Bonesteel, K. Yang, *Phys. Rev. Lett.* **99**, 140405 (2007)
113. L. Fidkowski, G. Refael, N.E. Bonesteel, J.E. Moore, *Phys. Rev. B* **78**, 224204 (2008)
114. L. Fidkowski, H.-H. Lin, P. Titum, G. Refael, *Phys. Rev. B* **79**, 155120 (2009)
115. A.B. Zamolodchikov, *JETP Letters* **43**, 730 (1986)
116. R. Santachiara, *J. Stat. Mech.* **2006**, L06002 (2006)
117. I.A. Kovács, F. Iglói, *Phys. Rev. B* **82**, 054437 (2010)
118. C. Monthus, T. Garel, *J. Stat. Mech.* **2012**, P01008 (2012)
119. N. Laflorencie, S. Wessel, A. Läuchli, H. Rieger, *Phys. Rev. B* **73**, 060403 (2006)
120. Y.-C. Lin, F. Iglói, H. Rieger, *Phys. Rev. Lett.* **99**, 147202 (2007)
121. R. Yu, H. Saleur, S. Haas, *Phys. Rev. B* **77**, 140402 (2008)
122. I.A. Kovács, F. Iglói, *EPL* **97**, 67009 (2012)
123. P. Bueno, R.C. Myers, W. Witczak-Krempa, *Phys. Rev. Lett.* **115**, 021602 (2015)
124. P. Bueno, R.C. Myers, W. Witczak-Krempa, *J. High Energ. Phys.* **2015**, 1 (2015)
125. P. Bueno, R.C. Myers, *J. High Energ. Phys.* **2015**, 1 (2015)
126. D. Binosi, G. De Chiara, S. Montangero, A. Recati, *Phys. Rev. B* **76**, 140405 (2007)

127. J.A. Hoyos, N. Laflorencie, A.P. Vieira, T. Vojta, *EPL* **93**, 30004 (2011)
128. G. Vitagliano, A. Riera, J.I. Latorre, *New J. Phys.* **12**, 113049 (2010)
129. J.C. Getelina, F.C. Alcaraz, J.A. Hoyos, *Phys. Rev. B* **93**, 045136 (2016)
130. V. Alba, S.N. Santalla, P. Ruggiero, J. Rodríguez-Laguna, P. Calabrese, G. Sierra, *J. Stat. Mech.* **2019**, 023105 (2019)
131. G. Ramírez, J. Rodríguez-Laguna, G. Sierra, *J. Stat. Mech.* **2014**, P10004 (2014)
132. G. Ramírez, J. Rodríguez-Laguna, G. Sierra, *J. Stat. Mech.* **2015**, P06002 (2015)
133. J. Rodríguez-Laguna, J. Dubail, G. Ramírez, P. Calabrese, G. Sierra, *J. Phys. A: Math. Theor.* **50**, 164001 (2017)
134. J.M. Deutsch, *Phys. Rev. A* **43**, 2046 (1991)
135. M. Srednicki, *Phys. Rev. E* **50**, 888 (1994)
136. E.S. Sørensen, M.-S. Chang, N. Laflorencie, I. Affleck, *J. Stat. Mech.* **2007**, P08003 (2007)
137. J. Sato, B. Aufgebauer, H. Boos, F. Göhmann, A. Klümper, M. Takahashi, C. Trippé, *Phys. Rev. Lett.* **106**, 257201 (2011)
138. V. Alba, *Phys. Rev. B* **91**, 155123 (2015)
139. J.P. Keating, N. Linden, H.J. Wells, *Commun. Math. Phys.* **338**, 81 (2015)
140. B. Bauer, C. Nayak, *J. Stat. Mech.* **2013**, P09005 (2013)
141. J.A. Kjäll, J.H. Bardarson, F. Pollmann, *Phys. Rev. Lett.* **113**, 107204 (2014)
142. D.J. Luitz, Y.B. Lev, *Ann. Phys. (Berlin)* **529**, 1600350 (2017)
143. J. Eisert, M. Cramer, M.B. Plenio, *Rev. Mod. Phys.* **82**, 277 (2010)
144. M. Dupont, N. Laflorencie, *Phys. Rev. B* **99**, 020202 (2019)
145. S.P. Lim, D.N. Sheng, *Phys. Rev. B* **94**, 045111 (2016)
146. V. Khemani, S. Lim, D. Sheng, D.A. Huse, *Phys. Rev. X* **7**, 021013 (2017)
147. T. Grover, arXiv:1405.1471 [cond-mat, physics:quant-ph] (2014)
148. D.M. Kennes, C. Karrasch, arXiv:1511.02205 [cond-mat] (2015)
149. S.P. Lim, D.N. Sheng, *Phys. Rev. B* **94** (2016)
150. X. Yu, D.J. Luitz, B.K. Clark, *Phys. Rev. B* **94**, 184202 (2016)
151. V. Khemani, D.N. Sheng, D.A. Huse, *Phys. Rev. Lett.* **119**, 075702 (2017)
152. N. Macé, F. Alet, N. Laflorencie, *Phys. Rev. Lett.* **123**, 180601 (2019)
153. N. Laflorencie, G. Lemarié, N. Macé, *Phys. Rev. Research* **2**, 042033 (2020)
154. M. Serbyn, Z. Papic, D.A. Abanin, *Phys. Rev. Lett.* **110**, 260601 (2013)
155. R. Vosk, E. Altman, *Phys. Rev. Lett.* **110**, 067204 (2013)
156. F. Andraschko, T. Enss, J. Sirker, *Phys. Rev. Lett.* **113**, 217201 (2014)

Some Aspects of Affleck–Kennedy–Lieb–Tasaki Models: Tensor Network, Physical Properties, Spectral Gap, Deformation, and Quantum Computation



Tzu-Chieh Wei, Robert Raussendorf, and Ian Affleck

Abstract Affleck, Kennedy, Lieb, and Tasaki constructed a spin-1 model that is isotropic in spins and possesses a provable finite gap above the ground state more than three decades ago. They also constructed models in two dimensions. Their construction has impacted subsequent research that is still active. In this review article, we review some selected progresses, such as magnetic ordering of the AKLT models, emerging phases under deforming the AKLT Hamiltonians, symmetry-protected topological order in several AKLT models, their spectral gap, and applications for quantum computation.

1 Introduction

The Affleck–Kennedy–Lieb–Tasaki (AKLT) model [1] gave important confirmation of the Haldane conjecture [2, 3] via an exactly solvable model which can be shown to have an excitation gap and exponentially decaying correlation functions. The simplest example is for a spin-1 chain. The Hamiltonian is

$$H_{\text{AKLT}}^{S=1} = \sum_j P^{S=2}(\vec{S}_j + \vec{S}_{j+1}) = \frac{1}{24} \sum_j (\vec{S}_j + \vec{S}_{j+1})^2 \cdot [(\vec{S}_j + \vec{S}_{j+1})^2 - 2I], \quad (1)$$

T.-C. Wei

C. N. Yang Institute for Theoretical Physics and Department of Physics and Astronomy, State University of New York at Stony Brook, Stony Brook, NY, USA

e-mail: tzu-chieh.wei@stonybrook.edu

R. Raussendorf · I. Affleck (✉)

Department of Physics and Astronomy, University of British Columbia, Vancouver, BC, Canada

Stewart Blusson Quantum Matter Institute, University of British Columbia, Vancouver, BC, Canada

e-mail: raussen@phas.ubc.ca; iaffleck@phas.ubc.ca

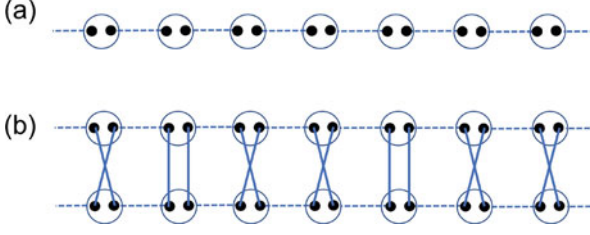


Fig. 1 (a) Sketch of the $S = 1$ AKLT chain. (b) One example term that contributes to the norm square of the AKLT state: $\langle \Psi_{\text{AKLT}} | \Psi_{\text{AKLT}} \rangle$. The two parallel vertical lines and the two cross lines connecting the upper and lower sites come from, respectively, the first and second terms in the expression: $\langle \{\alpha, \beta\} | \{\gamma, \delta\} \rangle = \delta_{\alpha\gamma} \delta_{\beta\delta} + \delta_{\alpha\delta} \delta_{\beta\gamma}$. Each dashed line represents an antisymmetric tensor arising from the singlet shared between neighboring virtual qubits. The overlap is a sum of all possible terms

where $P^{S=2}$ denotes projection onto spin-2, and we shall for convenience denote $P_{j,j+1}^{S=2} \equiv P^{S=2}(\vec{S}_j + \vec{S}_{j+1})$. Using $\vec{S}_j \cdot \vec{S}_j = 2$ for spin-1, this can be rewritten as

$$H_{\text{AKLT}}^{S=1} = \sum_j P_{j,j+1}^{S=2} = \frac{1}{2} \sum_j [\vec{S}_j \cdot \vec{S}_{j+1} + (1/3)(\vec{S}_j \cdot \vec{S}_{j+1})^2 + 2/3]. \quad (2)$$

The ground state must not have a spin-2 state for any pair of neighboring spins. The simplest way of visualizing the ground state $|\Psi_{\text{AKLT}}\rangle$ is to decompose the spin-1 into 2 spin-1/2's which are combined into the spin-1 state. A pair of spin-1/2's (or qubits) is then combined into a singlet state on every link as in Fig. 1. (We call these valence bonds.) This implies that on two neighboring sites the net spin can only be 0 or 1, and hence such a wave function is annihilated any term $P_{j,j+1}^{S=2}$ in the above Hamiltonian: $P_{j,j+1}^{S=2} |\Psi_{\text{AKLT}}\rangle = 0$. That the ground satisfies the lowest possible energy of each term in the Hamiltonian is called being frustration-free. For N sites with open boundary conditions, the ground state $|\Psi_{\text{AKLT}}\rangle$ can be written explicitly as

$$|\Psi_{\text{AKLT}}\rangle = \epsilon^{\alpha_2 \alpha_3} \epsilon^{\alpha_4, \alpha_5} \dots \epsilon^{\alpha_{2n}, \alpha_{2n+1}} \dots \epsilon^{\alpha_{2N-2} \alpha_{2N-1}} \quad (3)$$

$$\{|\alpha_1, \alpha_2\rangle; \{\alpha_3, \alpha_4\}; \dots; \{\alpha_{2n-1} \alpha_{2n}\}; \dots; \{\alpha_{2N-1} \alpha_{2N}\}\},$$

where $\alpha_i = 0, 1$ is used to denote the two levels of a spin-1/2 entity, repeated indices are summed over, and $\{|\alpha_{2k-1}, \alpha_{2k}\rangle\} \equiv (|\alpha_{2k-1}\rangle \otimes |\alpha_{2k}\rangle + |\alpha_{2k}\rangle \otimes |\alpha_{2k-1}\rangle) / \sqrt{2}$ denotes an un-normalized triplet state formed by two virtual qubits on the same physical site k . Note that α_1 and α_{2N} are uncontracted. This implies effective $S = 1/2$ degrees of freedom at the two ends of the chain. These can be combined into a singlet or triplet state which are degenerate for the AKLT model. It turns out that the basic Heisenberg model also has $S = 1/2$ edge states although they have a coupling which drops off exponentially with the system size. If a spin-1 chain contains some

random spin=0 defects, then pairs of $S = 1/2$ states occur on each side of the defect [4]. If they are weakly coupled together (but much more strongly coupled than between the 2 edges of each chain), then we get random $S = 0$ and $S = 1$ states at each defect. These have been observed [5]. Experimental confirmation of the Haldane gap in spin-1 chains was provided by Buyers et al. [6] and Renard et al. [7] in two different quasi-one-dimensional materials.

This model has various generalizations. For a spin chain with spin S (an integer), we may form n valence bonds on every link where $n = S$. This is the ground state of the Hamiltonian:

$$H = \sum_j \sum_{S'=1}^S \alpha_{S'} P^{S'}(\vec{S}_j + \vec{S}_{j+1}), \quad (4)$$

where $\alpha_{S'} > 0$. In the rest of the article, we will mostly be concerned with the AKLT model defined in the original paper, i.e., the magnitude of the spin S at a site is determined by the number z of its neighbors: $S = z/2$.

The exact ground state correlation function was calculated for the $S = 1$ case in [1] and is

$$\langle 0 | S_j^\alpha S_k^\beta | 0 \rangle = \frac{4}{3} (-1)^{k-j} 3^{-|k-j|} \delta_{\alpha\beta}. \quad (5)$$

We shall see below the alternative approach using matrix-product states (MPSs) [8, 9] other than that in the original work. Such an exponential decay in the correlation function suggests the existence of a gap. A rigorous proof of the gap between the ground state and first excited state for periodic boundary conditions was also given in [1]. (We shall also see other approaches for one and two dimensions below.) Therefore, this spin-1 model has $SO(3)$ rotational symmetry and possesses a unique magnetically disordered ground state (in the thermodynamic limit) and a nonzero energy gap. This model is recognized as an example of symmetry-protected topological order (SPTO) [10–12]. It is manifested in the fractionalization (from spin-1 to spin-1/2) of gapless excitations at the boundary. Their response to the symmetry action is $SU(2)$, a projective representation of the original $SO(3)$. We refer the readers to the review article [13] on the relation of the Haldane gap to the vanishing of a topological theta term with $\theta = 2\pi s$, i.e., equivalent to zero for integer s spins, and the Lieb–Schultz–Mattis theorem for half-odd integer s to the existence of the θ term in the nonlinear sigma model, whose Lagrangian is

$$\mathcal{L} = \frac{1}{2g} \partial_\mu \vec{n} \cdot \partial^\mu \vec{n} + \frac{\theta}{8\pi} \epsilon^{\mu\nu} \vec{n} \cdot \partial_\mu \vec{n} \times \partial_\nu \vec{n}, \quad (6)$$

where $\vec{n}(x, t)$ is the vector order parameter with unit length.

The AKLT states can be extended to two and three dimensions. The simplest extension, relevant to the quantum computing applications discussed below, is the honeycomb lattice with spin-3/2. Each site has 3 nearest neighbors. We decompose

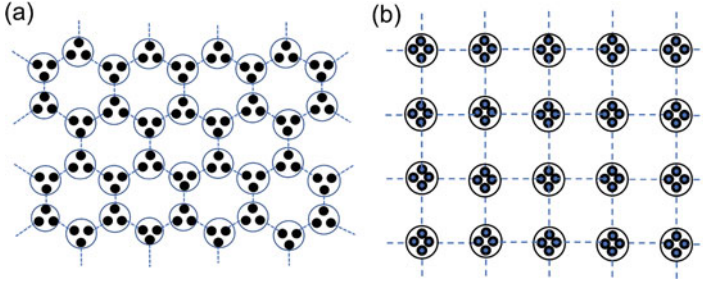


Fig. 2 Sketch of valence-bond construction for (a) the $S = 3/2$ AKLT state on the honeycomb lattice and (b) the $S = 2$ AKLT state on the square lattice

the spin-3/2 into 3 spin-1/2's and form a valence bond on every link, as illustrated in Fig. 2. The above 1D spin-1 wave function provides one of the earliest examples of matrix-product states, and the 2D spin-3/2 AKLT wave function is an example of projected entangled pair states (PEPSs) [14]. These tensor-network representations turn out to give a useful tool. For example, the wave function (3) can be normalized in a diagrammatic way, using the property of the triplet $\langle\{\alpha, \beta\}|\{\gamma, \delta\}\rangle = \delta_{\alpha\gamma}\delta_{\beta\delta} + \delta_{\alpha\delta}\delta_{\beta\gamma}$, and observables and correlation functions can also be evaluated by summing various diagrams; see, e.g., Fig. 1. By employing MPS, these can be evaluated using elementary transverse matrix calculation.

An alternative way of studying the AKLT states was developed in [15]. We may introduce 2 bosons on every site, a and b with

$$S^z = (1/2)(a^\dagger a - b^\dagger b), \quad S^+ = a^\dagger b, \quad S^- = b^\dagger a. \quad (7)$$

The AKLT state, for a general lattice, then becomes

$$|\psi\rangle = \prod_{ij} (a_i^\dagger b_j^\dagger - b_i^\dagger a_j^\dagger)^M |0\rangle, \quad (8)$$

where M is the number of valence bonds on each link. The wave function by using the coherent state representation gives rise to a classical partition function of antiferromagnets. The magnetic ordering of the corresponding AKLT state can be studied via the classical partition function.

The remaining structure of this book chapter is as follows. In Sect. 2, we describe AKLT states using tensor-network representations, including matrix-product states MPS and PEPS. In Sect. 3, we describe the magnetic ordering of AKLT models. In Sect. 4, we describe some understanding of symmetry-protected topological order in several AKLT states. In Sect. 5, we describe certain hidden orders in AKLT states; one of this is related to symmetry-protected topological order, and the other is related to cluster states and is useful for quantum computation. In Sect. 6, we give an explanation of how AKLT states can be used for quantum computation,

in particular, via the scheme of measurement-based quantum computation. AKLT states are among a few spin systems being explored for such a measurement-based approach [16]. In Sect. 7, we explain techniques that lead to rigorous establishment of some two-dimensional AKLT models, such as the one on the hexagonal lattice. In Sect. 8, we discuss the scenario beyond the AKLT models by deforming them locally. We conclude this chapter in Sect. 9.

2 Tensor-Network Picture: MPS and PEPS

A modern perspective of AKLT states is that they can be represented by tensor-network states, such as the matrix-product states (MPSs) in one dimension and the projected entangled pair states (PEPSs) in one and higher dimensions. To describe these states, one places certain number of virtual qudits on each lattice sites according to the lattice coordination number, and the two qudits associated with an edge form a maximally entangled states. Then, one maps the Hilbert space of the qudits on a site to that of a physical spin.

2.1 1D AKLT Chain

Each virtual qubit is entangled with a virtual qubit on its neighboring site in the form of a spin-singlet (un-normalized and conveniently expressed in a product of a row vector of kets with a column vector of kets):

$$|01\rangle - |10\rangle = (|0\rangle |1\rangle) \begin{pmatrix} |1\rangle \\ -|0\rangle \end{pmatrix}, \quad (9)$$

where the virtual qubit on the right side of a site is represented by the row vector and the one on the left side of the next site is represented by a column vector. Combining the two virtual qubits on each site, we have

$$\begin{pmatrix} |1\rangle \\ -|0\rangle \end{pmatrix} (|0\rangle |1\rangle) = \begin{pmatrix} |10\rangle & |11\rangle \\ -|00\rangle & -|01\rangle \end{pmatrix}, \quad (10)$$

which is the local matrix whose product represents pairs of singlets, with the boundary condition unspecified.

The local mapping from two virtual qubits to a single spin 1 (with basis states $|S = 1, S_z = +1\rangle$, $|S = 1, S_z = 0\rangle$, $|S = 1, S_z = -1\rangle$) is given by (omitting the S and S_z labels)

$$P_v = | + 1 \rangle \langle 00 | + | 0 \rangle \langle (| 01 \rangle + | 10 \rangle) / \sqrt{2} + | - 1 \rangle \langle 11 |, \quad (11)$$

where $|0\rangle$ on the second term is $|S = 1, S_z = 0\rangle$. The action of P_v on the two virtual qubits yields

$$P_v \begin{pmatrix} |10\rangle & |11\rangle \\ -|00\rangle & -|01\rangle \end{pmatrix} = \begin{pmatrix} |0\rangle/\sqrt{2} & |-1\rangle \\ -|+1\rangle & -|0\rangle/\sqrt{2} \end{pmatrix} = |0\rangle \frac{1}{\sqrt{2}} \sigma_z + |+1\rangle (-\sigma^-) + |-1\rangle \sigma^+. \quad (12)$$

Thus, we derive the three matrices corresponding to the three physical degrees $|0\rangle$, $|+1\rangle$, and $|-1\rangle$, i.e.,

$$A_0 = \sigma_z/\sqrt{2}, \quad A_{+1} = -\sigma^-, \quad A_{-1} = \sigma^+. \quad (13)$$

These matrices describe the system in the bulk, and one can specify the boundary condition. For example, for the open boundary condition, we can specify the left and right vectors $\vec{v}_{L/R}$ applied to the product of matrices:

$$|\psi_{\text{open}}\rangle = \sum_{s=0,\pm 1} v_L^T A_{s_1} A_{s_2} \cdots A_{s_N} v_R |s_1, s_2, \dots, s_N\rangle, \quad (14)$$

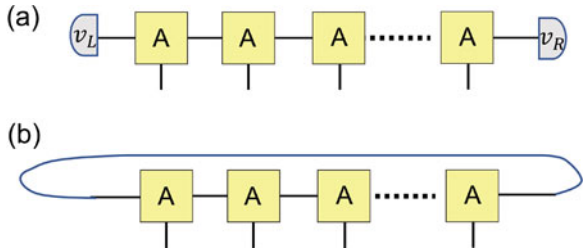
which represents the ground state of the spin-1 AKLT chain with open boundary (i.e., the first spin is not coupled to the last spin $H = \sum_{j=1}^{N-1} P_{j,j+1}^{S=2}$); see Fig. 3a. The boundary spin-1/2 degrees of freedom are seen from the two-component vectors v_L and v_R being arbitrary.

To describe the ground state of the periodic AKLT chain, we simply take the trace of the matrix product,

$$|\psi_{\text{periodic}}\rangle = \sum_{s=0,\pm 1} \text{Tr}(A_{s_1} A_{s_2} \cdots A_{s_N}) |s_1, s_2, \dots, s_N\rangle. \quad (15)$$

This is illustrated in Fig. 3b. The Hamiltonian such that $|\psi_{\text{periodic}}\rangle$ is the ground state is $H = \sum_{i=1}^N P_{i,i+1}^{[S=2]}$, with site $N + 1$ identified with site 1. We will discuss the degeneracy of the ground states, calculations of observables and correlations, and the proof of gap below.

Fig. 3 Schematic of matrix-product states: (a) open boundary condition and (b) periodic boundary condition



2.2 Two Dimensions

Here, we review the AKLT states on the hexagonal and square lattices and their Hamiltonians.

2.2.1 Honeycomb/Hexagonal Lattice

Each site contains three virtual qubits, each forming a singlet with its neighboring virtual qubit; see Fig. 2a. The local projection is from that of three virtual qubits to their symmetric subspace, which is identified as the Hilbert space of a physical spin-3/2 site. The projection is given as

$$P_v = |S_z = +3/2\rangle\langle 000| + |S_z = -3/2\rangle\langle 111| + |S_z = +1/2\rangle\langle W| + |S_z = -1/2\rangle\langle \bar{W}|, \quad (16)$$

where we have defined for convenience

$$|W\rangle \equiv \frac{1}{\sqrt{3}}(|001\rangle + |010\rangle + |100\rangle), \quad (17)$$

$$|\bar{W}\rangle \equiv \frac{1}{\sqrt{3}}(|110\rangle + |101\rangle + |011\rangle). \quad (18)$$

One can generalize the representation of the matrix-product states to 2D and in this case is the tensor product. Here, we can choose two different types of sites, labelled A and B, respectively, to write the nonzero components of a tensor corresponding to a physical index s for tensor A_s or s' for tensor $B_{s'}$. There are three virtual indices for each A_s and $B_{s'}$, whose structure is illustrated in Fig. 4. The nonzero elements in tensor A can be read off from P_v in Eq. (16). For example, $A[3/2]_{000} = 1$, $A[-3/2]_{111} = 1$, etc. Those in tensor B can be obtained from

$$P_v(i\sigma_y) \otimes (i\sigma_y) \otimes (i\sigma_y) \quad (19)$$

$$= |S_z = +3/2\rangle\langle 111| - |S_z = -3/2\rangle\langle 000| - |S_z = +1/2\rangle\langle W| + |S_z = -1/2\rangle\langle \bar{W}|.$$

The parent Hamiltonian can also be straightforwardly obtained from the projector onto the join spin-3 subspace of two neighboring sites i and j : $H = \sum_{(i,j)} P_{i,j}^{(S=3)}$ as there are 6 virtual qubits with two forming a singlet, indicating that the total spin magnitude cannot exceed $S = 2$. Thus, the constructed AKLT state is the ground state of this Hamiltonian composed of a sum of projectors. Translating it to the spin-3/2 operators, we have

$$H_{\text{AKLT}}^{S=3/2} = \sum_{\text{edge}(i,j)} \hat{P}_{i,j}^{(S=3)} = \frac{27}{160} \sum_{\text{edge}(i,j)} \left[\vec{S}_i \cdot \vec{S}_j + \frac{116}{243} (\vec{S}_i \cdot \vec{S}_j)^2 + \frac{16}{243} (\vec{S}_i \cdot \vec{S}_j)^3 + \frac{55}{108} \right]. \quad (20)$$

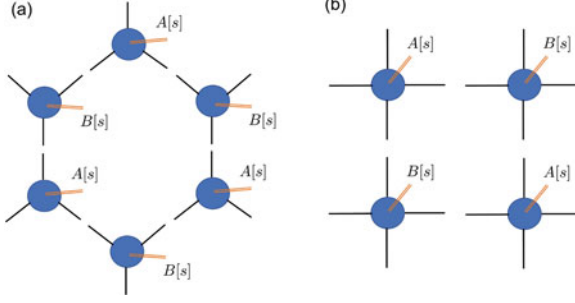


Fig. 4 Schematic of tensors for AKLT ground states on (a) the hexagonal lattice and (b) the square lattice. The double lines represent physical degrees of freedom, whereas the thin lines represent the virtual indices. For a fixed set of physical indices, the amplitude for the component is proportional to the value given by the tensor contraction of all virtual indices

The original paper [1] uses a different representation (i.e., a polymer representation) via links and shows that the correlation function $C(r)$ is bounded above by an exponential decaying function.

2.2.2 Square Lattice

We refer to see Fig. 2b for the schematic of the construction. For $S = 2$ case, the local mapping from 4 virtual qubits to $S = 2$ Hilbert space is as follows:

$$P_v^{[S=2]} = | +2 \rangle \langle 0000 | + | -2 \rangle \langle 1111 | + | +1 \rangle \langle S(4, 1) | + | -1 \rangle \langle S(4, 3) | + | 0 \rangle \langle S(4, 2) |, \quad (21)$$

where $|S(n, k)\rangle$ is the Dicke state with superposition of k 1's and $(n - k)$ 0's. Due to the singlets along edges, we can choose to have two types of tensors on A and B sublattices, with tensor A being readily read off from $P_v^{[S=2]}$. The tensor on the other sublattice (B) is related to that of A via $P_v^{[S=2]} \sigma_y \otimes \sigma_y \otimes \sigma_y \otimes \sigma_y$. We note that it is also possible to choose the tensors uniformly for each site, e.g., $P_v^{[S=2]} \sigma_y \otimes \sigma_y \otimes I \otimes I$.

The parent Hamiltonian for $S = 2$ AKLT model is obtained from the two-site projector onto the joint $S = 4$ subspace,

$$H_{\text{AKLT}}^{S=2} = \sum_{\text{edge } (i,j)} \hat{P}_{i,j}^{(S=4)} = \frac{1}{28} \sum_{(i,j)} \left[\vec{S}_i \cdot \vec{S}_j + \frac{7}{10} (\vec{S}_i \cdot \vec{S}_j)^2 + \frac{7}{45} (\vec{S}_i \cdot \vec{S}_j)^3 + \frac{1}{90} (\vec{S}_i \cdot \vec{S}_j)^4 \right]. \quad (22)$$

The tensors in the PEPS representation can be read off from $P_v^{[S=2]}$, and the schematic picture is given in Fig. 4b. Similar to previous arguments, the AKLT state above is a ground state of the Hamiltonian (22). The correlation function in its ground state was shown in Ref. [17] to be bounded by an exponentially decay function.

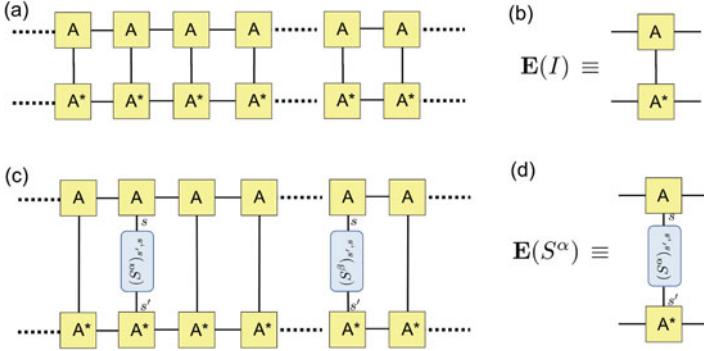


Fig. 5 Illustration of how to compute expectation values (such as the correlation functions) using the MPS formalism. **(a)** The diagram represents the normal square of the wavefunction $\langle \psi | \psi \rangle$. **(b)** The local transfer matrix $\mathbf{E}(I) \equiv \sum_s A[s] \otimes A^*[s]$. **(c)** The correlation function $\langle \psi | S_i^\alpha S_{i+r}^\beta | \psi \rangle$, which should be normalized by the expression in **(a)**. **(d)** The local transfer matrix associated with a spin operator S^α : $\mathbf{E}(S^\alpha) \equiv \sum_{s,s'} (S^\alpha)_{s',s} A[s] \otimes A^*[s]$

2.3 Boundary Conditions and Degeneracy of AKLT Models

Kennedy, Lieb, and Tasaki used the polynomial representation (in terms of “spinors” u_j and v_j , see Sect. 3) of Arova, Auerbach, and Haldane and showed that the AKLT model on any lattice has its ground state wave function written as [17]

$$\Psi = \Phi \prod_{i,j|(i,j)\text{edge}} (u_i v_j - u_j v_i), \tag{23}$$

where Φ is a unique polynomial of those u ’s and v ’s on the boundary. This means that if there is degeneracy, it can only come from the boundary via Φ . In particular, in the periodic boundary condition, $\Phi = 1$, and hence, the finite-volume ground state is unique. One may naively think that in the infinite-volume limit, AKLT models have a unique ground state. This would be correct if one can show that there is no Néel order or alternatively that the correlation functions are exponentially decaying, as done by KLT [17].

Pomata and Wei showed the degeneracy of open boundary condition is related to the number of open legs at the boundary; see Supplemental Materials of Ref. [18]. In particular, any boundary site that has k dangling virtual qubits (not forming singlets with other sites) contributes to a degeneracy of $k + 1$. In terms of the tensor-network description, by symmetrizing these dangling tensors, the resultant tensor that maps from these uncontracted bonds to the degenerate ground state is a bijective tensor. Their proof uses induction by beginning with a disjointed subgraph (which is bijective) and then showing that bijectivity is preserved when edges are added.

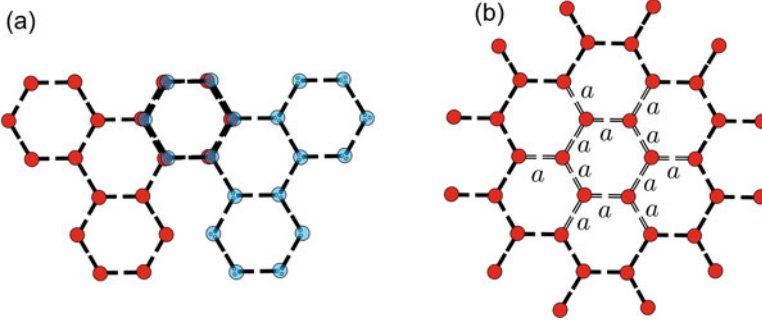


Fig. 6 Examples of $n = 1$ decorated lattices on the original: (a) Bethe lattice with $z = 3$, (b) honeycomb lattice, and (c) square lattice. Smaller dots represented the inserted $S = 1$ sites on every edge of the original lattice

3 Magnetic Ordering

The valence-bond construction of AKLT states seems to imply that there is no magnetic ordering. It turns out that this issue is slightly complicated as one needs to consider the thermodynamic limit. For the one-dimensional AKLT state, it was shown in Ref. [1] that there is no magnetic ordering, i.e., $\sum_i (-1)^i \langle S_i^\alpha \rangle / N = 0$ or $\langle S_i^\alpha S_{i+r}^\alpha \rangle = (-1)^r 4/3^{r+1} \rightarrow 0$ as $r \rightarrow \infty$. This can be calculated using the MPS formalism, illustrated in Fig. 5. We note that in the infinite system limit, one only needs to use the eigenvector of the transfer matrix corresponding to the largest eigenvalue in magnitude when evaluating the expectation value from both the left and right boundaries. We leave the details for readers to work out on their own. Although there is no Néel order, we do see the weak antiferromagnetic correlation from the factor $(-1)^r$.

However, antiferromagnetic ordering does occur on the Bethe lattice (or the Cayley tree) with coordination number $z = 5$ or larger as shown in the original work of AKLT [1]. It seems that $z_c = 4$ is the critical coordination number. We note that recently Pomata considered decorating each edge in the Bethe lattice by adding n spin-1 sites (i.e., a spin-1 chain with n sites; see, e.g., Fig. 6a) and showed that the critical coordination number $z_c(n) = 3^{n+1} + 1$ [19]. This is consistent with the picture that smaller spin- S has larger quantum fluctuations than large spin- S ; for the coordination number z , the spin magnitude is $S = z/2$ and decoration of n $S = 1$ sites on each edge pushes the ordering to occur at a larger coordination $z_c(n)$.

One useful approach to tackle the issue of ordering is to use the Schwinger-boson representation by Arovas, Auerbach, and Haldane and consider the wavefunction in the coherent state basis $|\hat{n}\rangle = \frac{1}{\sqrt{(2S)!}} (u\hat{a}^\dagger + v\hat{b}^\dagger)^{2S} |\text{vacuum}\rangle$. The AKLT wavefunction becomes $\Psi(\{u, v\}) = \langle \{\hat{n}\} | \psi_{\text{AKLT}} \rangle = \prod_{(i,j)} (u_i v_j - u_j v_i)^M$, where M is the number of singlets on an edge (which is 1 for the original AKLT states). One maps the norm square of the wavefunction to a classical O(3) antiferromagnetic model, i.e.,

$$\Psi^* \Psi = e^{-H_{\text{cl}}(\{\hat{n}\})/T}, \quad (24)$$

where $T = 1/M$ and

$$H_{\text{cl}} = - \sum_{\langle i,j \rangle} \ln \frac{1 - \hat{n}_i \cdot \hat{n}_j}{2}. \quad (25)$$

This is essentially an antiferromagnetic interaction, as one can see from expanding the logarithm: $H_{\text{cl}} \sim \sum_{\langle i,j \rangle} \hat{n}_i \cdot \hat{n}_j - (\hat{n}_i \cdot \hat{n}_j)^3/3 + \dots$. On a bipartite lattice, this is equivalent to a ferromagnetic model by setting $\hat{n}'_j = (-1)^j \hat{n}_j$.

Using the Mermin–Wagner theorem, one readily sees that there is no magnetic ordering for AKLT models on 1D and 2D regular lattices [20]. However, it was shown by Monte Carlo simulations that there is an antiferromagnetic ordering for the AKLT model on the 3D cubic lattice, but not on the 3D diamond lattice. The ordering implies spontaneous symmetry breaking and shows that the AKLT model has ground state degeneracy greater than one on the cubic lattice in the thermodynamic limit [20].

4 Symmetry-Protected Topological Order

In this section, we examine several AKLT models from the perspective of symmetry-protected topological order.

4.1 SPT Order of 1D AKLT State

AKLT is a symmetry-protected topological (SPT) state, e.g., by $Z_2 \times Z_2$ symmetry (generated by rotation around x or z by 180°), a discrete subgroup of $SO(3)$. We can examine the action of these group elements on the local matrices of MPS. The symmetry group is generated by the two rotations on the physical spin basis ($|x\rangle$, $|y\rangle$, and $|z\rangle$),

$$U_x(\pi) = \begin{pmatrix} 0 & 0 & -1 \\ 0 & -1 & 0 \\ -1 & 0 & 0 \end{pmatrix}, \quad U_y(\pi) = \begin{pmatrix} 0 & 0 & 1 \\ 0 & -1 & 0 \\ 1 & 0 & 0 \end{pmatrix}, \quad U_z(\pi) = \begin{pmatrix} -1 & 0 & 0 \\ 0 & 1 & 0 \\ 0 & 0 & -1 \end{pmatrix}. \quad (26)$$

By directly applying their actions on the local matrices in Eq. (13), we have, for examples,

$$\sum_{\beta} [U_x(\pi)]_{\alpha,\beta} A_{\beta} = \sigma_x \cdot A_{\beta} \cdot \sigma_x, \quad \sum_{\beta} [U_z(\pi)]_{\alpha,\beta} A_{\beta} = \sigma_z \cdot A_{\beta} \cdot \sigma_z. \quad (27)$$

We see that σ_x , σ_y , and σ_z form a projective representation of U_x , U_y , and U_z , respectively. They generate the single-qubit Pauli group and represent the symmetry action on the boundary degree of a semi-infinite chain, which exhibits fractionalization. Thus, the 1D AKLT state exhibits a nontrivial SPT order [10–12]. Such an SPT order can also be detected by the string order parameter [21, 22]; see Eq. (31) below.

Another approach to understand the SPTO in this 1D AKLT chain is the topological theta term in Eq. (6) with $\theta = 2\pi$, and the ground state wave function of the SPT phase described the nonlinear sigma model can be expressed as superposition of these spin vectors decorated by a local phase given by a Wess–Zumino–Witten term [23],

$$|\Psi\rangle \sim \int_{S^d} d^d x e^{-\frac{1}{g}(\nabla\vec{n})^2 - \text{WZW}_d[\vec{n}]} |\vec{n}(x)\rangle, \quad (28)$$

where the 1D WZW term is related to the theta term in 6,

$$\text{WZW}_1[\vec{n}] = \int_0^1 du \frac{i2\pi}{8\pi} \epsilon^{\mu\nu} \vec{n} \cdot \partial_\mu \vec{n} \times \partial_\nu \vec{n}, \quad \text{with } \mu, \nu = x, u, \quad (29)$$

where u extends the space to an additional dimension. Based on this picture, You et al. propose a strange correlator [24],

$$C(\vec{r}, \vec{r}') = \frac{\langle \Omega | \phi(\vec{r}) \phi(\vec{r}') | \Psi \rangle}{\langle \Omega | \Psi \rangle} \quad (30)$$

for some local operator $\phi(\vec{r})$, to detect the presence of SPTO in the state of concern $|\Psi\rangle$, where $|\Omega\rangle$ is a product trivial state. According to You et al., this strange correlator for SPT states is either constant or polynomially decaying. Using the MPS formalism illustrated in Fig. 5, one can easily calculate this and obtain that $C(r, r') = 2$ for $|\Psi\rangle$ being the 1D spin-1 AKLT wave function and $|\Omega\rangle = |00\dots 0\rangle$.

4.2 Two Dimensions: Honeycomb and Square Lattices

Here, we will also examine the symmetry action in terms of virtual degrees of freedom using the PEPS formalism, we will find that it forms only a projective representation, and this seems to imply weak SPT order for both the 2D AKLT models on both the honeycomb lattice and square lattices. However, the study of the strange correlator shows the difference between the two models, indicating the AKLT state on the square lattice exhibits nontrivial SPTO.

First, the U_x , U_y , and U_z of rotations around the three respective axes by an angle of π in the spin-3/2 representation are

$$U_x(\pi) = \begin{pmatrix} 0 & 0 & 0 & i \\ 0 & 0 & i & 0 \\ 0 & i & 0 & 0 \\ i & 0 & 0 & 0 \end{pmatrix}, \quad U_y(\pi) = \begin{pmatrix} 0 & 0 & 0 & -1 \\ 0 & 0 & 1 & 0 \\ 0 & -1 & 0 & 0 \\ 1 & 0 & 0 & 0 \end{pmatrix}, \quad U_z(\pi) = \begin{pmatrix} i & 0 & 0 & 0 \\ 0 & -i & 0 & 0 \\ 0 & 0 & i & 0 \\ 0 & 0 & 0 & -i \end{pmatrix},$$

which does not give a faithful representation of $Z_2 \times Z_2$, as, e.g., $U_x(\pi)U_z(\pi) = -U_z(\pi)U_x(\pi)$ and $U_x(\pi)^2 = -I$. It is actually a representation of the quaternion group. One can check that, similar to the 1D case, the symmetry action on the physical index can be replaced by action on the virtual indices with Pauli matrices, up to a global phase. This shows that the action on the boundary is at best a projective representation of $Z_2 \otimes Z_2$, but for the strong SPTO, the symmetry actions on the boundary need to be a manifestation of third group cohomology group [25, 26]. Hence we conclude that the 2D AKLT state on the honeycomb lattice is only a weak SPT order. This is confirmed by the strange correlator calculations by Wierschem and Beach [27], which display exponential decay.

One can perform a similar analysis for the square-lattice case and find that the symmetry action of $U_\alpha(\pi)$ on the physical index is equivalent to applying Pauli σ_α on all four virtual indices, which is a projective representation of $Z_2 \otimes Z_2$. This suggests that the AKLT state on the square lattice is also weak SPT ordered in terms of cohomology. However, the issue of the SPT order for the square-lattice AKLT model is tricky. You et al. calculated the strange correlator for the AKLT state on the square-lattice AKLT state and found that it is power-law decaying, as opposed to the exponential decay in the former. This shows that there is strong SPT order in the 2D AKLT state on the square lattice [24].

We also mention that a work by Haldane in 1988 [28] on an $O(3)$ nonlinear sigma model study for 2D quantum Heisenberg antiferromagnets shows that certain tunneling processes between states of different topology have amplitudes sensitive to whether the microscopic spin is a half integer, odd integer, or even integer. The AKLT model on the square lattice is such an example of even integer S , which has a unique disordered ground state, likely with a gap.

5 Hidden Order in AKLT States

5.1 String Order Parameter

The 1D AKLT state such as in Eq. (14) written in the MPS form allows us to see the hidden antiferromagnetic ordering in the state. The components in the wavefunction cannot have two equal $S_z = 1$ (or $S_z = -1$) spaced by any number of $S_z = 0$. The allowed ones are $\dots (+1)0\dots 0(-1)\dots$ or $\dots (-1)0\dots 0(+1)\dots$. The spin configuration after stripping off the 0's should be antiferromagnetic. This result can be understood by the MPS picture, as $\sigma^\pm(\sigma_z)^n\sigma^\mp = 0$.

This hidden ordering can also be probed by a string order parameter [21, 22]

$$\Pi_{i,i+r}^\alpha = S_i^\alpha e^{i\pi \sum_{j=i+1}^{i+r-1} S_j^\alpha} S_{i+r}^\alpha, \quad \alpha = x, y, z. \quad (31)$$

Den Nijs and Rommelse argued that this order parameter is nonzero in the Haldane phase and can be used to distinguish from other gapped phases [21]. Kennedy and Tasaki found a nonlocal unitary transformation U that takes $-\Pi^\alpha$ to $S_i^\alpha S_{i+r}^\alpha$, and thus the latter detects ferromagnetic ordering in the transformed Hamiltonian $\tilde{H} = U H U^{-1}$. The essential symmetry of concern is the $Z_2 \times Z_2$ of \tilde{H} , and the Haldane phase corresponds to complete breaking of $Z_2 \times Z_2$ in \tilde{H} . Note that Oshikawa found that the nonlocal unitary can be written as [29]

$$U = \prod_{j < k} e^{i\pi S_j^z S_k^x}. \quad (32)$$

This string order parameter is now understood as one of the order parameters to detect nontrivial SPT order in one dimension [30], and it can be computed using the MPS representation and examining how local tensors are transformed, along the line discussed in Sect. 4.1.

5.2 Hidden Cluster Order

There is another kind of hidden order in AKLT states. Consider local projectors of rank 2: $F_\alpha = |S_\alpha = S\rangle\langle S_\alpha = S| + |S_\alpha = -S\rangle\langle S_\alpha = -S|$. It was shown that AKLT state can be converted to the so-called cluster state [31] by the action of appropriate local projector [32],

$$|\psi_{\text{cluster}}\rangle = c \prod_{v \in A} \prod_{u \in B} F_x^{[v]} F_z^{[u]} |\psi_{\text{AKLT}}\rangle, \quad (33)$$

where c is a normalization constant and the effective qubit is defined by the two levels $|S_x = +S\rangle$ and $|S_x = -S\rangle$ on the A sublattice and $|S_z = +S\rangle$ and $|S_z = -S\rangle$ on the B sublattice. In fact, one can place F 's arbitrarily and randomly on a bipartite lattice that hosts the AKLT model, this will convert the AKLT state to some random graph state, and this was used in the measurement-based quantum computation with AKLT states [32]; see also below in Sect. 6.

5.3 *Hidden Frustration on Frustrated Lattices*

If the lattice is not bipartite, there is some frustration that is only revealed by considering these F 's. It turns out that on any loop with odd number of sites, one cannot place F_α with the same label α along such a loop. Product of such operators will annihilate the AKLT state [33]. This is due to the singlet construction of the AKLT wave function and the frustration of antiferromagnetism on such a loop. The simplest example is a periodic three-site spin-1 chain (i.e., a triangle). Another nontrivial example is the triangles on the star lattice, which hosts a spin-3/2 AKLT state.

6 Applications in Quantum Computation

AKLT states play a role in a scheme of universal quantum computation, the so-called measurement-based quantum computation (MBQC) [34]. Therein, the process of quantum computation is driven by local measurements; no unitary evolution ever takes place. The computation begins in an appropriately entangled state such as a cluster state. What the cluster state is to MBQC is what a blank sheet of paper is to the artist: a great number of possibilities. Every quantum circuit can be imprinted on it by the local measurements. Because of this property, cluster states are *universal* resources for measurement-based quantum computation.

One may now ask: are cluster states the only universal resource states? If not, how rare are universal resource states in Hilbert space?—Both questions have in fact been answered. Universal resource states are very rare [35], but the cluster states are not the only ones. In fact, AKLT states on various lattices in 2D are universal [16, 32, 33, 36–38]. The purpose of this section is to explain why this is so. To prepare for the main argument, we review the simpler but nonuniversal case of one dimension first.

6.1 *One Dimension*

From the perspective quantum computation, our main interest is in the two-dimensional scenario—quantum computationally universal. However, the basic techniques that MBQC employs with AKLT states are easier to understand in 1D than in 2D. We therefore start out with the one-dimensional case.

6.1.1 Logical Identity and One-Qubit Gates

We explain the computational power of the AKLT chain in terms of its matrix-product representation. This method is intuitive and has the added benefit of preparing for the stronger result that the MBQC power found at the AKLT point is uniform across the entire surrounding symmetry-protected phase with $\mathbb{Z}_2 \times \mathbb{Z}_2$ -symmetry [39].

We have derived earlier the matrix-product form for the 1D spin-1 AKLT state as shown in Eq. (16), where we have used the basis defined by $+1$, 0 , and -1 . If we define a different orthonormal basis for the spin-1 states via

$$|0\rangle \equiv |z\rangle, \quad | + 1\rangle \equiv -(|x\rangle + i|y\rangle)/\sqrt{2}, \quad | - 1\rangle \equiv (|x\rangle - i|y\rangle)/\sqrt{2}.$$

Then, we obtain the matrix-product representation in this new basis:

$$P_v \begin{pmatrix} |10\rangle & |11\rangle \\ -|00\rangle & -|01\rangle \end{pmatrix} = \frac{1}{\sqrt{2}}(|x\rangle\sigma_x + |y\rangle\sigma_y + |z\rangle\sigma_z).$$

Thus, measuring the physical degrees of freedom in the orthonormal basis $\mathcal{B}_0 = \{|x\rangle, |y\rangle, |z\rangle\}$ has the effect of applying sequences of Pauli matrices on the virtual space. The “virtual” quantum register, initialized in the state described by the right boundary condition v_R , is thus propagated across the chain [40],

$$v_R \rightarrow \sigma_{\alpha_N} v_R \rightarrow \sigma_{\alpha_{N-1}} \sigma_{\alpha_N} v_R \cdots \rightarrow \prod_{i=1}^N \sigma_{\alpha_i} v_R. \quad (34)$$

This is the simplest conceivable quantum protocol—a quantum wire. The Pauli matrices applied to the virtual quantum register are random but known, as in quantum teleportation.

To progress from wire to logical quantum gates, one simply changes the measurement basis. For example, a measurement in the basis

$$\mathcal{B}(\phi) = \{|x_\phi\rangle = \cos \phi|x\rangle + \sin \phi|y\rangle, |y_\phi\rangle = -\sin \phi|x\rangle + \cos \phi|y\rangle, |z\rangle\}$$

produces a logical gate

$$U(\phi) = \begin{cases} \sigma_x e^{i\phi\sigma_z}, & \text{if outcome } x_\phi, \\ \sigma_y e^{i\phi\sigma_z}, & \text{if outcome } y_\phi, \\ \sigma_z, & \text{if outcome } z. \end{cases}$$

This is a probabilistic heralded rotation about the z -axis. When the outcome z is obtained, the gate fails; but it can be reattempted as often as needed. By similar deviations from the basis $\mathcal{B}(0)$, logical rotations about the x - or y -axis can be realized, together forming a one-qubit universal set of quantum gates.

It has been observed by Else et al. [41] that the capability for teleportation is not only a property of the AKLT state but also of the entire Haldane phase. It is a manifestation of symmetry-protected topological order. Namely, the generic state in the Haldane phase can be written in the MPS form with

$$A_\alpha = \sigma_\alpha \otimes B_\alpha, \quad (35)$$

where B_α 's are not fixed by symmetry. One may now divide the correlation space into a logical system on which the Pauli operators act and a “junk subsystem” on which the unknown matrices B_α act. The former supports wire as before, and the latter is simply not used.

As it turns out, the capability to enact logical gates also extends beyond the AKLT state to the entire surrounding SPT phase with $\mathbb{Z}_2 \times \mathbb{Z}_2$ symmetry. See [39, 42] for the techniques by which this is accomplished; here, we merely point out what the additional difficulty is. Namely, to do more than wire, the spins in the chain need to be measured in bases other than $\mathcal{B}(0)$. But then the factorization property Eq. (35) no longer holds. As a consequence, the logical and the junk subsystem become entangled, which leads to decoherence on the logical subsystem. This decoherence must be very carefully managed.

6.1.2 Reduction to the 1D Cluster State

We now provide a second proof of the usefulness of 1D AKLT states as computational resources in measurement-based quantum computation, by mapping them to 1D cluster states under local operations. It is this argument that will generalize to lattice dimension two and also to higher spins.

To simplify the discussion, we consider both the 1D AKLT state and the 1D cluster state on rings rather than chains. This does not affect quantum computational power.

The one-dimensional AKLT state can be understood within the valence-bond picture, as illustrated in Fig. 1a. Therein, the spin-1 particle at each site v on a ring is viewed as a pair of virtual spin-1/2 particles, or qubits, to which a projection P_v onto the spin-1 subspace is applied. The projector takes the explicit form

$$P = |S_z = 1\rangle\langle 00| + |S_z = -1\rangle\langle 11| + |S_z = 0\rangle\langle \psi^+|,$$

where $|\psi^+\rangle = (|01\rangle + |10\rangle)/\sqrt{2}$, and $|S_z\rangle$ denote the eigenstates of the z -component \hat{S}_z of the spin operator. The virtual spin-1/2 particles form spin singlets (Bell states) $|\psi^-\rangle = (|01\rangle - |10\rangle)/\sqrt{2}$ between neighboring sites. Denoting the edges between neighboring sites by e , the 1D AKLT state thus takes the form

$$|\text{AKLT}_{1D}\rangle = \bigotimes_v P_v \bigotimes_e |\psi^-\rangle_e. \quad (36)$$

Our task is to convert this AKLT state to the 1D cluster state by local operations. The latter is already known to be a computational resource [34].

The 1D cluster state is a multi-qubit state, one qubit on each site $i = 1, \dots, N$ of a ring. Up to a global phase, the cluster state is uniquely specified by the stabilizer relations

$$|\mathcal{C}_{1D}\rangle = Z_{i-1}X_iZ_{i+1}|\mathcal{C}_{1D}\rangle, \quad (37)$$

where here and below $X \equiv \sigma_x$, $Y \equiv \sigma_y$, and $Z \equiv \sigma_z$.

The local reduction from the AKLT state to the cluster state proceeds by a generalized measurement, or POVM, with the three elements

$$\begin{aligned} F_z &= (|S_z = 1\rangle\langle S_z = 1| + |S_z = -1\rangle\langle S_z = -1|) / \sqrt{2}, \\ F_x &= (|S_x = 1\rangle\langle S_x = 1| + |S_x = -1\rangle\langle S_x = -1|) / \sqrt{2}, \\ F_y &= (|S_y = 1\rangle\langle S_y = 1| + |S_y = -1\rangle\langle S_y = -1|) / \sqrt{2}. \end{aligned} \quad (38)$$

These POVM elements satisfy the required completeness relation

$$\sum_{\alpha \in \{x, y, z\}} F_\alpha^\dagger F_\alpha = \mathbb{I}_{S=1}. \quad (39)$$

Denoting by $s_v \in \{x, y, z\}$ the POVM outcome at v , for all sites v , the post-POVM states are

$$|\Psi(\{s_v\})\rangle := \bigotimes_v F_{v, s_v} |\text{AKLT}_{1D}\rangle. \quad (40)$$

In the following, we identify the spin-1 Hilbert space with the symmetric subspace of the pairs of the virtual spin-1/2 particles, e.g., $|S_z = 1\rangle = |00\rangle$, $|S_z = -1\rangle = |11\rangle$. Up to this identification, we have $F_\alpha P = \tilde{F}_\alpha$, $\alpha = x, y, z$, with

$$\begin{aligned} \tilde{F}_z &= (|00\rangle\langle 00| + |11\rangle\langle 11|) / \sqrt{2}, \\ \tilde{F}_x &= (|++\rangle\langle ++| + |--\rangle\langle --|) / \sqrt{2}, \\ \tilde{F}_y &= (|i, i\rangle\langle i, i| + |-i, -i\rangle\langle -i, -i|) / \sqrt{2}. \end{aligned} \quad (41)$$

Therein, $|\pm\rangle = (|0\rangle \pm |1\rangle) / \sqrt{2}$ and $|\pm i\rangle = (|0\rangle + i|1\rangle) / \sqrt{2}$. Thus, Eq. (40) simplifies to

$$|\Psi(\{s_v\})\rangle = \bigotimes_v \tilde{F}_{v, s_v} \bigotimes_e |\psi^-\rangle_e. \quad (42)$$

We observe that the POVM elements \tilde{F}_α all have rank 2. Therefore, after the POVM Eq. (38), we remain with one qubit worth of Hilbert space per site.

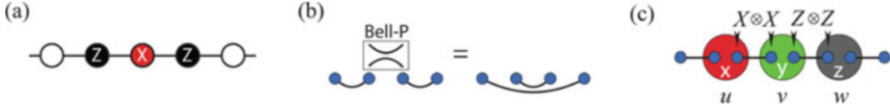


Fig. 7 Conversion of the AKLT state to the cluster state in 1D. (a) 1D cluster state with stabilizer generator. (b) Bell measurement on the virtual qubits of a given site leads to entanglement swapping. (c) Element of the stabilizer of the state $|\tilde{\Psi}(\{s_v\})\rangle$. For explanation, see the text

We now show that, irrespective of the set of POVM outcomes $\{s_v, v = 1..N\}$, the post-POVM states $|\Psi(\{s_v\})\rangle$ are indeed 1D cluster states, up to local unitary equivalence and an encoding. Related to the encoding—the precise form of which depends on the POVM outcomes $\{s_v\}$ —we first need to discuss “domains” and how to shrink them to individual qubits. As a remark, there is actually an alternative measurement scheme that converts the 1D AKLT state into a 1D cluster state [43].

Domains Ring segments of nearest-neighboring sites on which the same POVM outcome was obtained are called “domains.” We extract one cluster qubit per domain, undoing the encoding mentioned above. This proceeds by measuring all but one site in each domain in the basis

$$\begin{aligned} \mathcal{B}_z &= \left\{ |z, \pm\rangle := (|00\rangle \pm |11\rangle)/\sqrt{2} \right\} & \text{if } s = z, \\ \mathcal{B}_x &= \left\{ |x, \pm\rangle := (|++\rangle \pm |--\rangle)/\sqrt{2} \right\} & \text{if } s = x, \\ \mathcal{B}_y &= \left\{ |y, \pm\rangle := (|ii\rangle \pm |-i, -i\rangle)/\sqrt{2} \right\} & \text{if } s = y. \end{aligned}$$

It is easily checked that all $\langle \alpha, \pm | \tilde{F}_\alpha$ are Bell states (bras). Therefore, after the local POVM with the outcome $s = \alpha$, the measurement in the basis \mathcal{B}_α amounts to the projection onto a Bell state, regardless of its outcome. We thus implement entanglement swapping, disentangling the measured site, and otherwise leaving the entanglement structure intact. See Fig. 7b for a graphical illustration. In this way, we can eliminate all redundant sites in a domain. The result is a state very similar to that of Eq. (40), but with three differences: (a) there are fewer qubits than initially, (b) now all pairs of neighboring sites the POVM outcomes differ, and (c) the Bell states in the PEPS representation are not necessarily spin singlets $|\psi^-\rangle$ anymore but can be either Bell state due to the measurement outcomes invoked in the entanglement swapping. Properties (a) and (b) are important for the subsequent argument, and (c) poses no obstacle. To summarize, the state after shrinking the domains is

$$|\tilde{\Psi}(\{s_v\})\rangle = \bigotimes_v \tilde{F}_{v,s_v} \bigotimes_e |\text{Bell}(e)\rangle_e. \tag{43}$$

Cluster States We now show that the state resulting from shrinking the domains is an encoded cluster state, with the encoding depicted in Table 1. We observe that

Table 1 Encoding of graph state qubits, resulting from the POVM Eq. (38) on a 1D AKLT state. The site label “ $v : 1$ ” means left virtual qubit in site v , etc.

POVM outcome	z	x	y
Stabilizer generator	$Z_{v:1}Z_{v:2}$	$X_{v:1}X_{v:2}$	$Y_{v:1}Y_{v:2}$
\bar{X}	$X_{v:1}X_{v:2}$	$Z_{v:1}Z_{v:2}$	$Z_{v:1}Z_{v:2}$
\bar{Z}	$Z_{v:1}$	$-X_{v:1}$	$Y_{v:1}$
\bar{Y}	$Y_{v:1}X_{v:2}$	$Y_{v:1}Z_{v:2}$	$-X_{v:1}Z_{v:2}$

$(\sigma_\alpha)_{v:1}(\sigma_\alpha)_{v:2}\tilde{F}_{v,\alpha} = \tilde{F}_{v,\alpha}$, for all $\alpha = x, y, z$, and with Eq. (43), the operators in the first line of Table 1 do indeed stabilize the state $|\tilde{\Psi}(\{s_v\})\rangle$.

Now, the various combinations of distinct POVM outcomes on three adjacent sites need to be considered on three consecutive sites u, v , and w . For illustration, here we consider the POVM outcomes ($s_u = x, s_v = y, s_w = z$). The state $\bigotimes_e |\text{Bell}(e)\rangle$ is an eigenstate of the Pauli observable $(X_{u:2}X_{v:1})(Z_{v:2}Z_{w:1})$, irrespective of the precise Bell state we find on the edges $e = (u, v)$ and $e' = (v, w)$. The latter affects only the eigenvalue ± 1 . Since $X_{v:1}Z_{v:2}$ commutes with $\tilde{F}_{v,y}$, the state $|\tilde{\Psi}(\{s_v\})\rangle$ of Eq. (43) is also an eigenstate state of $(X_{u:2}X_{v:1})(Z_{v:2}Z_{w:1})$. Consulting Table 1, we find

$$(X_{u:2}X_{v:1})(Z_{v:2}Z_{w:1}) \cong X_{u:1}(X_{v:1}Z_{v:2})Z_{w:1} = \bar{Z}_u\bar{Y}_v\bar{Z}_w.$$

Therein, “ \cong ” means equivalent up to stabilizer. See Fig. 7c for a graphical illustration.

All that remains to be considered is the other five orderings of x, y, z . The argument and result for them are analogous. In all cases, we find stabilizers of the form $\pm\bar{Z}_u\bar{Y}_v\bar{Z}_w$ or $\pm\bar{Z}_u\bar{X}_v\bar{Z}_w$. Thus, the state $|\tilde{\Psi}(\{s_v\})\rangle$ is, up to local z -rotations, a 1D cluster state as defined in Eq. (37).

6.2 Two Dimensions: Universal Computation

Spin-3/2 AKLT states on a two-dimensional honeycomb lattice are universal resources for MBQC. This result has been established independently by Miyake [36] and Wei et al. [32].

Here, we explain the method employed in [32]. The overall strategy of quantum computation is the same as in the 1D case discussed in Sect. 6.1.2, namely, to reduce the AKLT state to a cluster 2D state by suitable local measurements. The construction is probabilistic, with a success probability approaching unity in the thermodynamic limit. At the center of the proof is a percolation argument that involves random planar graph states.

We thus begin by explaining graph states [44], which are a generalization of the cluster states we already discussed. Both cluster and graph states belong to the class of stabilizer states [45], which are eigenstates of maximal sets of commuting Pauli

operators. Specifically, a graph state $|G\rangle$ corresponding to the graph G with vertex set $V(G)$ and edge set $E(G)$ is the unique stabilizer state defined by the constraints $K_v |G\rangle = |G\rangle, \forall v \in V(G)$, with

$$K_v := X_v \bigotimes_{w \in V(G) | (v,w) \in E(G)} Z_w.$$

A graph state becomes a cluster state when the underlying graph G is that of a lattice in some spatial dimension. Cluster states in dimension 2 are universal for MBQC.

The universality proof [32] consists of three steps: (i) the reduction of the honeycomb AKLT state to a random planar graph state by local POVM measurement, with the resulting graph state depending on the measurement outcomes,¹ (ii) showing that the computational power only hinges on simple connectivity properties of the resulting graph states and is thus a percolation problem, and (iii) demonstrating by Monte Carlo simulation that the typical graph states resulting from initial POVM satisfy these connectivity properties. Here, we only give an outline of the proof, drawing on the analogy with the 1D case described in Sect. 6.1.2, and pointing to differences where they arise. The complete technical argument can be found in [32, 46].

Step 1: Mapping to Graph States by a POVM The first operation in MBQC on spin-3/2 AKLT states defined through Eq. (16) is a generalized measurement (a POVM). One such measurement is applied on each site v of the honeycomb lattice \mathcal{L} , and it consists of 3 rank 2 elements $F_{v,\alpha}$. We denote $|\pm 3/2, \alpha\rangle$ as the state of the highest (+) or lowest (−) magnetic quantum number, in the direction $\alpha = \{x, y, z\}$. In close analogy to the one-dimensional case of Eq. (41), the POVM elements then are

$$\begin{aligned} \tilde{F}_{v,z} &= \sqrt{\frac{2}{3}} (|000\rangle\langle 000| + |111\rangle\langle 111|), \\ \tilde{F}_{v,x} &= \sqrt{\frac{2}{3}} (|+++ \rangle\langle +++| + |--- \rangle\langle ---|), \\ \tilde{F}_{v,y} &= \sqrt{\frac{2}{3}} (|i, i, i\rangle\langle i, i, i| + |-i, -i, -i\rangle\langle -i, -i, -i|), \end{aligned} \quad (44)$$

where $|0/1\rangle, |\pm\rangle = (|0\rangle \pm |1\rangle)/\sqrt{2}$, and $|\pm i\rangle = (|0\rangle \pm i|1\rangle)/\sqrt{2}$ are eigenstates of the Pauli operators X, Y , and Z respectively.

The linear operators $\tilde{F}_{v,z}, \tilde{F}_{v,x}$, and $\tilde{F}_{v,y}$ do indeed form a POVM on the symmetric subspace projected onto by P_v (cf. Eq. (16), $\sum_{\alpha=x,y,z} \tilde{F}_{v,\alpha}^\dagger \tilde{F}_{v,\alpha} = P_v$). Every POVM element is proportional to a projector onto a two-dimensional subspace, and the resulting state

¹ This operation is in fact the starting point of both proofs [36] and [32].

$$|\Psi(\mathcal{A})\rangle = \bigotimes_{v \in V(\mathcal{L})} \tilde{F}_{v, \alpha_v} |\Phi_{\text{AKLT}}\rangle,$$

with $\mathcal{A} = \{\alpha_v, v \in V(\mathcal{L})\}$ the measurement record, is therefore a state of qubits—one for every vertex v .

Up to local unitaries, the resulting state $|\Psi(\mathcal{A})\rangle$ is an encoded graph state $|\overline{G(\mathcal{A})}\rangle$, where the graph $G(\mathcal{A})$ is a function of the measurement record \mathcal{A} . The effect of the randomness of the measurement outcomes is more severe now than it was in 1D. Like in dimension one, we find domains, i.e., connected regions of lattice sites on which the same POVM outcome was obtained. As before, each domain gives rise to one encoded cluster qubit, and the encoding is undone in a similar way as before. The new feature in dimension two is that the cluster qubits resulting from the domains are connected in a random planar fashion. The graph $G(\mathcal{A})$, depending on the random measurement record \mathcal{A} and describing the resulting graph state $|\overline{G(\mathcal{A})}\rangle$, is obtained from the honeycomb lattice \mathcal{L} and the measurement record \mathcal{A} via the following two rules:

- (R1) [Edge contraction]: Contract all edges $e \in E(\mathcal{L})$ that connect sites with the same POVM outcome.
- (R2) [Edge deletion]: In the resulting multigraph, delete all edges of even multiplicity, and convert edges of odd multiplicity in standard edges of multiplicity 1.

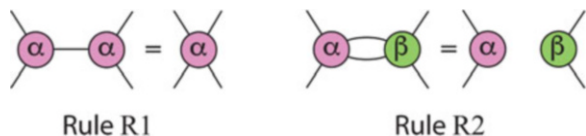
For the general proof of correctness of the rules (R1) and (R2), see [32]. See Fig. 8 for graphical illustration.

Step 2: The Percolation Problem The next step is to show that the random graph state $|\overline{G(\mathcal{A})}\rangle$ can be converted to a standard 2D cluster state by further local measurement, if the following two conditions hold for typical graphs resulting from Step 1: (C1) The domain size is microscopic, i.e., the size of the largest domain scales at most logarithmically with $|V(\mathcal{L})|$. (C2) A left–right traversing path through $G(\mathcal{A})$ exists.

Condition (C1) ensures that the graph $G(\mathcal{A})$ is macroscopic if \mathcal{L} is, which is required for the resulting graph state to have computational power. Condition (C2) ensures that the resulting graph states are sufficiently long-range connected. It also illustrates that we are dealing with a percolation problem. We will comment on this observation further below.

(C1) and (C2) are natural conditions to invoke; however, we still need to show that they are sufficient for universality. The basic argument is as follows. In the supercritical phase, where a macroscopic spanning cluster exists with high

Fig. 8 Graphical illustration of rules (R1) and (R2)



probability, this spanning cluster contains a subgraph that is topologically equivalent to a coarse-grained 2D lattice structure. Essentially, if one left–right traversing path exists, then very many such paths exist, and by symmetry of the honeycomb lattice, also very many top–bottom traversing paths exist. The coarse-grained 2D subgraph can be carved out, cleaned from imperfections, and finally contracted to a standard 2D grid by further local Pauli measurements on $|G(\mathcal{A})\rangle$. For details, see [46].

We remarked above that the reduction of the AKLT state to a random planar graph state is a percolation problem, but what kind of percolation problem is it?—It resembles site percolation in as far as the random variables (POVM outcomes) live on the sites. However, it is not site percolation because no site is ever deleted. Furthermore, the present problem resembles bond percolation in as far as edges are switched on and off (rule R2). But it is not exactly bond percolation because whether or not an edge persists is decided not simply by a probability associated with that edge. Rather, it is decided by random processes associated with the nearby sites. Thus, we conclude that our percolation problem defies simple characterization, and we defer its classification to further study.

Step 3: Testing the Conditions (C1) and (C2) To complete the argument for quantum computational universality, it needs to be checked whether the typical graph state resulting from the POVM Eq. (44) satisfies the conditions (C1) and (C2). This is done numerically.

By rotational symmetry, for any site, all three possible POVM outcomes are equally likely. However, these outcomes are correlated with outcomes on neighboring sites, and this represents a complication. For a reliable simulation, these correlations need to be taken into account. Fortunately, the joint probability for any given configuration \mathcal{A} of POVM outcomes on all sites can be efficiently calculated exactly [32]. Monte Carlo simulation is thus viable, and the results are shown in Fig. 9. Conditions (C1) and (C2) are satisfied. This concludes the argument for computational universality of spin-3/2 AKLT states.

We conclude this section with a brief description of related work on ground states of lattice Hamiltonians as MBQC resources and the role of symmetry. First, the argument above has been generalized to AKLT states on lattices other than honeycomb, including spin-2 [33, 37, 38]. For most lattices, but not all, computational universality persists.

Furthermore, for a one-dimensional manifold of deformed AKLT Hamiltonians with reduced symmetry, the known transition from disorder to Néel order [47] was reinvestigated. It was found numerically that the location of the physical phase transition coincides with the transition in computational power [48]. This gave early support to the notion of “computational phase of quantum matter,” which refers to the property of certain quantum phases—for example, symmetry-protected phases—to have *uniform* computational power. Any ground state in such a phase is equally as good a resource for MBQC as any other ground states.

The phenomenon of computational phases of matter was conceived in [49], where for a hybrid of measurement-based and adiabatic quantum computation, it

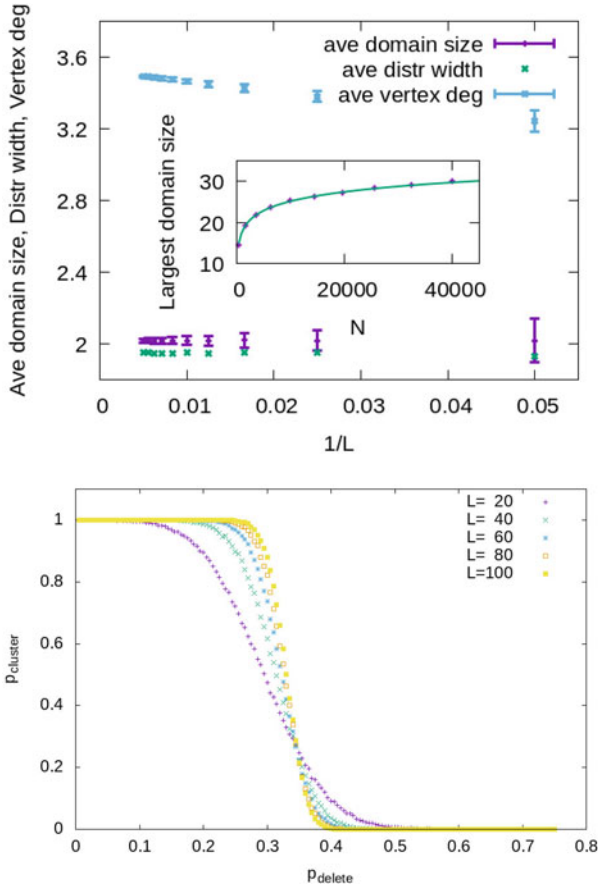


Fig. 9 (a) [Top panel] Statistics of the average domain size, average width of domain size distribution, average degree of a vertex, and the largest domain size (inset) in the typical graphs as a function of the linear size L . (b) [Bottom panel] Site percolation study by deleting randomly any vertex on typical random graphs and measuring the probability of a spanning cluster. The crossing represents the location of the percolation phase transition in the thermodynamic limit. Figures were reproduced from the data of the work [32]

was shown that proper operation only relies on the presence of symmetry. Detailed knowledge of the Hamiltonian or its ground state is not required. The connection with symmetry-protected topological order was already recognized and emphasized in this work. Subsequently, uniformity of MBQC power in symmetry-protected phases was established for one-dimensional [39, 41, 42, 50] and two-dimensional systems. In particular, 2D computationally universal phases have been identified [51–54].

7 Spectral Gap for AKLT Models

The 1D spin-1 AKLT model was proven to be gapped in the original AKLT paper [1]. The significance of the result was the first proved gapped integer-value spin chain that is both isotropic in spin symmetry and gapped in the spectrum. This model differs from the spin-1 Heisenberg spin chain by the biquadratic spin–spin interaction $(\vec{S}_i \cdot \vec{S}_{i+1})^2$. Till now, the spectral gap of the spin-1 Heisenberg model has not been rigorously established, despite accurate numerics from DMRG. The proof in the original work of AKLT analyzes in detail the ground spaces in successively increasing regions, including those being ground states in a smaller region but orthogonal to the ground space in a larger region. In the end, they were able to upper bound the projector P_L to the complement of the ground space in a whole chain of size L by some additive constant and a term proportional to the total Hamiltonian [1], which we quote here,

$$P_L \leq 16(l+1)\epsilon(l) + \left(\frac{2(l+1)}{e_{l+1}} + \frac{1}{e_l} \right) H_{1,L}, \quad (45)$$

where e_l is the gap of the chain with size l and $\epsilon(l)$ is an exponentially small quantity, i.e., $\epsilon(l) \leq c \cdot 3^{-l}$. The finite gap exists as $16(l+1)\epsilon(l)$ can be made smaller than 1 as long as l is sufficiently large. The infinite chain result was generalized from the finite chain by considering a chain with sites from $-L$ to L and taking $L \rightarrow \infty$.

The technique of proving the gap in 1D had also been generalized by Knabe [55] and Fannes, Natchtergaele, and Werner [8]. There were also more recent works [56–58], not necessarily limited to 1D. Instead of directly bounding the Hamiltonian H , many of the latter developments consider bounding H^2 , and we will discuss two variations below, which also apply to two dimensions.

Beyond one dimension, the correlation functions with respect to the ground state wave function from the hexagonal and square lattices were shown to decay exponentially [1, 17], suggesting that the models are gapped. There were some prior numerics with tensor network [59, 60] that estimate the gap values in the thermodynamic limit. Several 2D AKLT models were recently shown to be gapped rigorously [18, 61–63] and one breakthrough came from the work of Abdul-Rahman et al. on decorated hexagonal lattices [61], where a certain number n of spin 1 sites are added to each edge of the hexagonal lattice; see, e.g., Fig. 6b. For $n \geq 4$, they showed analytically that the decorated hexagonal lattices host AKLT models that possess a finite gap. This analytic result was generalized to other decorated lattices [62], including decorated square lattices and beyond two dimensions; see, e.g., Fig. 6c.

AKLT Hamiltonians belong to the so-called frustration-free models, for which the ground state satisfies the lowest energy of each local term. One can simply shift the ground state energy to be zero for convenience (which is already the case for AKLT models by the construction of projectors),

$$H_{\text{AKLT}}|\Psi_{\text{AKLT}}\rangle = \tilde{H}|\Psi_{\text{AKLT}}\rangle = 0.$$

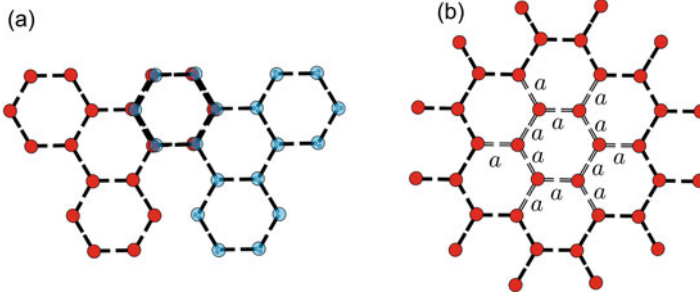


Fig. 10 (a) Two overlapping regions used to demonstrate the gap of the hexagonal AKLT model in Ref. [18]. One elementary cell consists of four hexagons, e.g., indicated by the red dots (or separately the blue dots). It overlaps with $z = 6$ neighboring cells. (b) The finite-size problem of weighted AKLT model used to demonstrate the nonzero gap of the hexagonal AKLT model in Ref. [63]. The symbols a 's are used to indicate the weights of the Hamiltonian terms that are not unity

For the purpose of proving the spectral gap, one can also replace each local term by a projector. We can thus consider the following Hamiltonian, $\tilde{H} = \sum_i \tilde{H}_i$, where $\tilde{H}_i^2 = \tilde{H}_i$ and $\tilde{H}_i|GS\rangle = 0$. If one can show that $\tilde{H}^2 > \epsilon \tilde{H}$ for $\epsilon > 0$, then \tilde{H} has a nonzero gap (at least ϵ) above the ground state(s). Thus, one squares the Hamiltonian:

$$(\tilde{H})^2 = \sum_i \tilde{H}_i + \sum_{i \neq j} \tilde{H}_i \tilde{H}_j = \tilde{H} + \underbrace{\sum_{i \& j \text{ overlap}} \tilde{H}_i \tilde{H}_j}_{Q \text{ type}} + \underbrace{\sum_{i, j \text{ no overlap}} \tilde{H}_i \tilde{H}_j}_{R \text{ type}}. \quad (46)$$

There are at least two main different approaches that one can proceed from here.

Approach (i) First, the product of two non-overlapping projectors is still positive semi-definite, $\tilde{H}_i \tilde{H}_j \geq 0$ (if the two supports do not overlap), one can drop them to obtain a lower bound:

$$(\tilde{H})^2 \geq \tilde{H} + \sum_{\langle i, j \rangle} \{\tilde{H}_i, \tilde{H}_j\}. \quad (47)$$

For the two projectors that overlap, their anticommutator $\{\tilde{H}_i, \tilde{H}_j\}$ can have negative eigenvalues. However, one can also find a positive $\eta > 0$ such that $\{\tilde{H}_i, \tilde{H}_j\} \geq -\eta(\tilde{H}_i + \tilde{H}_j)$, and if this η is small enough (i.e., $\eta < 1/z$, where z is the coordination number), then we have

$$(\tilde{H})^2 \geq \tilde{H} + \sum_{\langle i, j \rangle} (\tilde{H}_i + \tilde{H}_j) = (1 - z\eta)\tilde{H}. \quad (48)$$

We note that it is necessary to choose \tilde{H}_i to be supported nontrivially on a region larger than just nearest two neighboring sites, e.g., consecutive n sites in one dimension and, e.g., a few sites in small patches, which union cover all lattice sites. This method was recently used to demonstrate the existence of the gap for AKLT models on various degree-3 lattices, in particular the hexagonal lattice, and other decorated lattices, see, e.g., Fig. 6, such as the singly decorated hexagonal, square, and diamond lattices, as well as two other planar degree-4 lattices [18, 64]. One key ingredient is to choose an appropriate tiling with a unit cell that contains a sufficiently large (but not too large) number of sites. Figure 10a shows a particular choice of two unit cells and their overlap for the hexagonal lattice. There are 30 spin-3/2 sites involved, with the Hilbert space dimension being 2^{60} . By employing tensor-network methods, this is substantially (numerically exact) reduced to 2^{26} , for which the computation of η can be made with high precision. That the obtained $\eta = 0.1445124916$ is less than $1/z = 1/6$ demonstrates the existence of a nonzero gap for the AKLT model in the thermodynamic limit.

Approach (ii) A second method is to consider additionally a subset of terms in \tilde{H} and the relation of its square to that of \tilde{H} . Let us first illustrate it with one-dimensional model: $\tilde{H} = \sum_i \tilde{H}_{i,i+1}$ and define

$$h_{n,i} = \sum_{j=i}^{n+i-1} \tilde{H}_{j,j+1}, \quad (49)$$

where $\tilde{H}_{j+N,j+1+N} = \tilde{H}_{j,j+1}$. Let us assume the gap of this finite system of size n is ϵ_n , i.e., $h_{n,i}^2 \geq \epsilon_n h_{n,i}$. Equation (46) in this one-dimensional case becomes

$$(\tilde{H})^2 = \tilde{H} + \sum_{|i-j|=1} \tilde{H}_{i,i+1} \tilde{H}_{j,j+1} + \sum_{|i-j|>1} \tilde{H}_{i,i+1} \tilde{H}_{j,j+1}. \quad (50)$$

We will seek to lower bound it in the form

$$(\tilde{H})^2 \geq \alpha \sum_{i=1}^N (h_{n,i})^2 - \beta \tilde{H}. \quad (51)$$

By inspection, we find that the choice with $\alpha = 1/(n-1)$ and $\beta = 1/(n-1)$ works. This leads to

$$(\tilde{H})^2 \geq \left(\frac{n\epsilon_n}{n-1} - \frac{1}{n-1} \right) \tilde{H} \geq \frac{n}{n-1} \left(\epsilon_n - \frac{1}{n} \right) \tilde{H}. \quad (52)$$

If the finite-size gap ϵ_n is greater than $1/n$, the system with periodic boundary condition is gapped for any size greater than n . Knabe calculated that $\epsilon_4 = 0.3333 >$

$1/4$, and thus by checking just a simple four-site problem, the existence of a nonzero gap in the 1D spin-1 AKLT chain is established. This method by Knabe [55] can be generalized to two dimensions, and one can even allow projectors in the n -size unit cell \mathcal{F} to have different weights, e.g., $h_{\mathcal{F}} = \sum_{j \in \mathcal{F}} w_j \tilde{H}_j$ with a gap $\gamma_{\mathcal{F}}(\{w\})$.

One then considers $A = \sum_{\mathcal{F}} h_{\mathcal{F}}^2$ and can derive two relations [63],

$$A \geq f(\{w\})\gamma_{\mathcal{F}}(\{w\})\tilde{H}, \quad (53)$$

$$A \leq f(\{w^2\})\tilde{H} + g(\{w\})(Q + R). \quad (54)$$

From these, one obtains that

$$(\tilde{H})^2 \geq \frac{f(\{w\})}{g(\{w\})} \left(\gamma_{\mathcal{F}}(\{w\}) - \frac{f(\{w^2\}) - g(\{w\})}{f(\{w\})} \right) \tilde{H}. \quad (55)$$

One has the freedom to adjust the positive weights w_j 's, and if the finite-size gap $\gamma_{\mathcal{F}}(\{w\})$ for such a choice of weights is larger than the threshold

$$\Delta_{\text{TH}}(\{w\}) \equiv \frac{f(\{w^2\}) - g(\{w\})}{f(\{w\})}, \quad (56)$$

then the Hamiltonian \tilde{H} is gapped. By using this latter approach and DMRG numerical method for computing the finite-size gap, such as that shown in Fig. 10b, Lemm, Sandvik, and Wang showed the existence of a gap for the honeycomb lattice AKLT model [63]. The Numerical DMRG method was used to compute the finite-size gap for the problem involving 36 spin-3/2 sites, and they found that the numerically obtained gap at $a = 1.4$ is $\gamma_{\mathcal{F}}(a = 1.4) \approx 0.14599$, within sufficient accuracy, being greater than the threshold $\Delta_{\text{TH}}(a = 1.4) = 0.138$. This demonstrates that the AKLT model on the hexagonal lattice is gapped in the thermodynamic limit.

Let us mention some numerical estimates of the gap value for a few AKLT models: $\Delta_{\text{1D}} \approx 0.350$, $\Delta_{\text{Hex}} \approx 0.10$, $\Delta_{\text{Sq}} \approx 0.015$ [59, 60]. Both kinds of approaches described above have been successfully applied to showing the existence of the gap in the particular AKLT model on the honeycomb lattice. However, rigorous establishment of the gap on the square-lattice AKLT model is still missing.

8 Deformed AKLT Models and Phase Transitions

In this section, we describe examples beyond the original AKLT models by certain form of deformation. We will first discuss a one-dimensional example and then describe a few two-dimensional deformed models.

8.1 1D Deformed AKLT Chain

In a work by Verstraete, Martín-Delgado, and Cirac [65], they consider deforming the 1D AKLT Hamiltonian,

$$H_{\text{VMC}}(\phi) = \sum_k h_{k,k+1}(\phi) = \sum_k (\Pi_\phi)^{-1} \otimes \Pi_\phi P_{k,k+1}^{S=2} (\Pi_\phi)^{-1} \otimes \Pi_\phi, \quad (57)$$

where

$$\Pi_\phi = \begin{pmatrix} e^\phi & 0 & 0 \\ 0 & 1 & 0 \\ 0 & 0 & e^{-\phi} \end{pmatrix}. \quad (58)$$

The ground state can also be represented by a translation-invariant MPS, via $A_s(\phi) = A_s^{\text{AKLT}} V_\phi$, where A_s^{AKLT} 's are matrices shown in Eq. (13) and

$$V_\phi \equiv \begin{pmatrix} e^\phi & 0 \\ 0 & e^{-\phi} \end{pmatrix}. \quad (59)$$

The point $\phi = 0$ is the original 1D AKLT chain. The action Π_θ on a local spin can be translated to that on the virtual degrees of freedom,

$$\sum_{s'} (\Pi_\theta)_{ss'} A_{s'}(\phi) = V_{-\theta/2} A_s(\phi) V_{\theta/2}, \quad (60)$$

which represents a symmetry in the MPS. We can easily see that $h_{k,k+1}(\phi)$ annihilates $\sum_{s,s'} A_s A_{s'} |s, s'\rangle_{k,k+1}$, and thus the claim of the MPS represents the ground state of $H_{\text{VMC}}(\phi)$ is verified; see Fig. 11. As $\phi \rightarrow \pm\infty$, the ground state of $H_{\text{VMC}}(\phi)$ is a product state $|..000..$, having zero correlation length and zero entanglement length. As ϕ decreases its magnitude toward 0 (which represents the AKLT state), the correlation increases and reaches the maximum at the AKLT point ($\phi = 0$). However, the so-called entanglement length [66], i.e., the largest distance between any two sites that entanglement can be concentrated via measurement on all other sites, increases and approaches infinity at $\phi = 0$. The deformed model does not possess any conventional phase transition but has a transition in the localizable entanglement [65].

8.2 2D Deformed AKLT Models and Their Phase Transitions

Niggemann, A. Klümper, and J. Zittartz consider deformation from the original AKLT states on hexagonal and square lattices [47, 68], and they find that using an approximate mapping to classical vertex models, there is a transition to a Néel

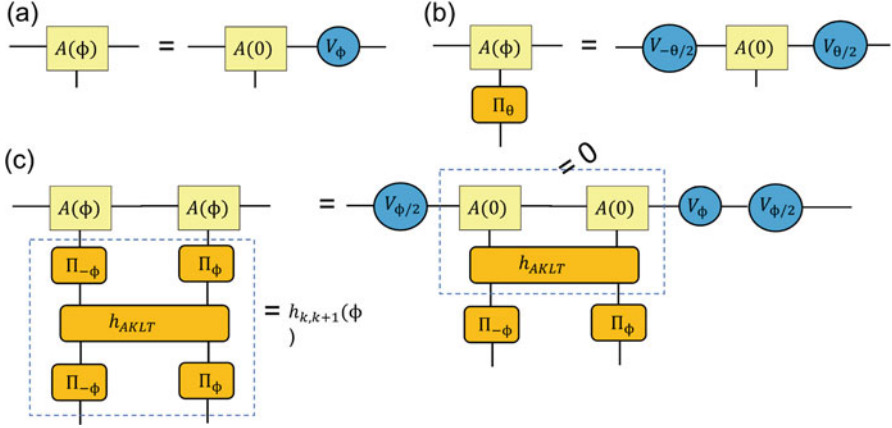


Fig. 11 1D deformed AKLT state: **(a)** relation of the local matrix to that of the undeformed AKLT state, **(b)** symmetry of the matrix under the action of Π_ϕ , and **(c)** the illustration of how the individual term in the Hamiltonian annihilates the local two-site MPS. We use h_{AKLT} to denote a Hamiltonian term $P_{k,k+1}^{S=2}$ in the spin-1 AKLT chain

ordered state. Numerics using tensor-network methods also confirm this [67, 69, 70]. In the case of the square lattice, the deformation such that the weights of $|S = 2, S_z = \pm 2\rangle$ and $|S = 2, S_z = \pm 1\rangle$ are small relative to that of $|S = 2, S_z = 0\rangle$ gives rise to an XY phase [67], which was unexpected.

Hexagonal and Other Trivalent Lattices The deformation Niggemann, A. Klümper, and J. Zittartz found of the AKLT state on trivalent lattices, including the hexagonal lattice, can be achieved by the following operator:

$$\Pi^{S=3/2}(a) = \frac{a}{\sqrt{3}}(|+3/2\rangle\langle+3/2| + |-3/2\rangle\langle-3/2|) + (|+1/2\rangle\langle+1/2| + |-1/2\rangle\langle-1/2|), \quad (61)$$

and applying this operator on all sites to the AKLT state gives rise to the following deformed wave function:

$$|\psi_{\text{deformed}}(a)\rangle \sim \Pi^{S=3/2}(a)^{\otimes N} |\psi_{\text{AKLT}}\rangle. \quad (62)$$

The coefficients $(a/\sqrt{3}, a/\sqrt{3}, 1, 1)$ correspond to local rescaling of the wave-function on $S_z = \pm 3/2$ and $S_z = \pm 1/2$, respectively. They also constructed a (5-parameter) family of parent Hamiltonians such that $|\psi_{\text{deformed}}(a)\rangle$ is the ground state. We refer the readers to their paper for the details of the Hamiltonians [47]. As far as the ground states are concerned, we can define the parent Hamiltonian as (when $a \neq 0$)

$$H_{\text{deformed}}^{[S=3/2]}(a) = \sum_{\langle i,j \rangle} \Pi^{S=3/2}(a)_i^{-1} \otimes \Pi^{S=3/2}(a)_j^{-1} h_{ij}^{\text{AKLT}} \Pi^{S=3/2}(a)_i^{-1} \otimes \Pi^{S=3/2}(a)_j^{-1}, \quad (63)$$

in a way similar to the deformed Hamiltonian in one dimension.

By approximating the norm square $\langle \psi_{\text{deformed}}(a) | \psi_{\text{deformed}}(a) \rangle$ to a classical 8-vertex model, Niggemann, A. Klümper, and J. Zittartz were able to show that the weights of the vertex model satisfy the free-fermion condition, and thus there is an Ising-type transition at $a_c = \sqrt{3 + \sqrt{12}} \approx 2.54$ from the valence-bond solid phase to a Néel phase as a increases. The existence of the Néel order at large a 's can be understood easily, as in this limit local S_z components are dominated by $S_z = \pm 3/2$, and due to the singlet construction in the AKLT wavefunction, the neighboring sites cannot share the same S_z value, and hence there is the Néel order. The transition was later confirmed by Huang, Wagner, and Wei [70] using a tensor-network method without the approximation used by Niggemann, A. Klümper, and J. Zittartz to a vertex model.

Similar consideration was applied to the square-octagon lattice (still a spin-3/2 model) and Niggemann and Zittartz [71] used an 8-vertex model analysis and found the VBS–Néel transition at $a_c \approx 2.65158$. The tensor-network methods by Huang, Wagner, and Wei yield some improvement at $a_c \approx 2.6547$, and they also found a different vertex model that gives a value close to 2.6547. They additionally discussed other trivalent lattices, such as the cross or star lattices, and calculated spontaneous magnetization.

We note that construction of AKLT states via spin triplet valence bonds can also be used and their deformation can be considered. On bipartite lattices, models with other valence bonds are equivalent under local transformations, but those that are not bipartite can have different phase diagrams under deformation. For example, using the two types of triplet $|\phi^\pm\rangle = (|00\rangle \pm |11\rangle)/\sqrt{2}$ on the star lattice, as the deformation parameter a varies, there is a ferromagnetic phase for $a \leq a_{c1} \approx 0.5850$, a VBS phase for $a_{c1} \leq a \leq a_{c2} \approx 3.0243$, and another ferromagnetic phase for $a \geq a_{c2}$ for the deformed AKLT model on the star lattice [70]. The two ferromagnetic phases differ in the axis of magnetization, e.g., x vs. y axis for different triplet bonds $|\phi^\pm\rangle$.

Square Lattice Different from the trivalent lattices, the AKLT model on the square lattice is spin-2. Niggemann, Klümper, and Zittartz consider the following deformation on the original AKLT wave function [68]:

$$D(a_1, a_2) = \frac{a_2}{\sqrt{6}} (|+2\rangle\langle+2| + |-2\rangle\langle-2|) + \frac{a_1}{\sqrt{3/2}} (|+\rangle\langle+1| + |-\rangle\langle-1| + |0\rangle\langle 0|). \quad (64)$$

They also constructed a family of parent Hamiltonians such that

$$|\psi^{[S=2]}(a_1, a_2)\rangle \sim D(a_1, a_2)^{\otimes N} |\psi_{\text{AKLT}}\rangle \quad (65)$$

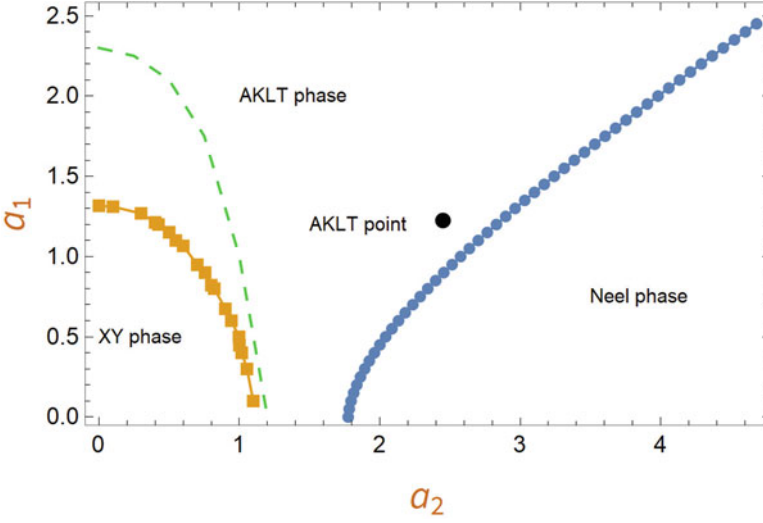


Fig. 12 Phase diagram of deformed AKLT model on the square lattice, reproduced from the data of the work [67]. In the region between green dashed line and the XY phase, there is a large correlation length. But there is no phase transition across the green dashed line

is the ground state. The parent Hamiltonian, as far as the ground states are concerned, can be defined as (for $a_1 \neq 0$ and $a_2 \neq 0$)

$$H(a_1, a_2)^{[S=2]} = \sum_{\langle i,j \rangle} D(a_1, a_2)_i^{-1} \otimes D(a_1, a_2)_j^{-1} h_{ij}^{S=2 \text{ AKLT}} D(a_1, a_2)_i^{-1} \otimes D(a_1, a_2)_j^{-1}. \quad (66)$$

Using a classical vertex model and solving it via a Monte Carlo method, Niggemann, Klümper, and Zittartz found transitions from VBS to Néel phase across a transition line defined approximated by $a_2^2 \approx 3.0a_1^2 + 3.7$. With tensor-network methods, the precise boundary between the VBS phase (which was referred to as the AKLT phase in Ref. [67]) and the Néel phase was obtained. Furthermore, an XY phase was found, which is gapless and has infinite correlation. Close to the XY boundary but inside the AKLT-VBS phase, there is a region of finite but large correlation length; see Fig. 12. Such a pseudo quasi-long-range region also occurs in the deformed AKLT model on the honeycomb lattice, but there does not exist an XY phase [67].

Quantum Computation with Deformed AKLT States For these states, it is also interesting to ask whether they are also useful for quantum computation away from the exact AKLT point. This was first studied by Darmawan, Brennen, and Bartlett on the honeycomb case [48]. We have seen in Sect. 6 that POVMs $\{F_x^\dagger F_x, F_y^\dagger F_y, F_z^\dagger F_z\}$ applied to all sites convert the AKLT state to a random graph that depends on the measurement outcomes. What Darmawan, Brennen, and Bartlett found is essentially a modified set of POVMs that undoes the operation $\Pi^{S=3/2}(a)$ and at the same time

applies the above POVM, which is possible for $a \geq 1$. However, for a large enough, there is a transition to the Néel phase, and they found that the ability for universal quantum computation disappears at this transition. This makes sense, as we do not expect a quantum Néel state has the entanglement necessary for MBQC. This result was generalized to other trivalent lattices with spin-3/2 AKLT states and the square lattice with a spin-2 AKLT state [38, 70].

9 Conclusion

The AKLT model was invented [1] as a concrete example of Haldane’s conjecture on the spectral gap of isotropic spin chains [2, 3]. The construction of the wave functions in both one and two dimensions was a precursor of modern matrix-product states [8, 9] and projected entangled pair states [14]. Their short-ranged entanglement in the presence of symmetry is also a manifestation of symmetry-protected topological order [10–12]. In low dimensions such as one and two, AKLT states are disordered, possessing no local magnetization [1, 20]. However, in the cubic lattice [20] and in the Bethe lattice with a large enough coordination number [1], AKLT states display Néel order. In deformed AKLT models, the valence-bond solid phase can turn into a Néel phase as model parameters vary that locally favor maximal magnitude of S_z components [47, 68, 70, 71]. Surprisingly, a gapless XY-like phase can emerge in such a deformed model [68] on the square lattice at a region where the $S_z = 0$ component is locally favored [67].

The 2D hexagonal AKLT model was conjectured to be gapped in the original work more than three decades ago [1]. AKLT models on other lattices have also been proved, such as other degree-3 2D lattices and their decorated version lattices [18, 61, 62, 64]. But the existence of the gap for the models on the square and kagomé lattices remains unproved. Interestingly, the proof was recently established with two different methods [18, 63], both utilizing techniques of tensor network, combining analytic reduction and high-precision numerics. Perhaps the most surprising aspect of AKLT states is that many of them can be used as a resource to realize universal quantum computation [32, 33, 36–38].

In terms of experiments, we mentioned earlier that the $S = 1/2$ edge degrees of a Heisenberg ferromagnet was observed [5], and confirmation of the Haldane gap was made previously [6, 7]. A short AKLT chain was created in the photonic [72] and trapped-ion systems [73]. Very recently, fractional excitations were observed in nanographene spin chains, which were modeled as an $S = 1$ bilinear-biquadratic spin chain [74], to which the AKLT chain is a special case. There are other theoretical proposals for the 1D AKLT spin, such as using measurement-induced steering on quantum spin systems [75] and driven-dissipative control of cold atoms in tilted optical lattices [76]. Realization of two-dimensional AKLT states is more challenging. We mention that there is a theoretical work by Sela et al. on AKLT on solid state material [77]. Using 2D AKLT states for universal quantum computation

may still be years ahead. But knowing that they are in principle a useful resource is intriguing, as it is a somewhat unexpected development from AKLT models.

Acknowledgments T.-C.W. acknowledges support from National Science Foundation under Grants No. PHY 1314748, No. PHY 1620252, and No. PHY 1915165 on subjects related to AKLT models. R.R. is supported by the Canada First Research Excellence Fund, Quantum Materials, and Future Technologies Program.

References

1. I. Affleck, T. Kennedy, E. Lieb, H. Tasaki, Rigorous results on valence-bond ground states in antiferromagnets, *Phys. Rev. Lett.* **59**, 799–802 (1987); Valence bond ground states in isotropic quantum antiferromagnets. *Comm. Math. Phys.* **115**, 477–528 (1988)
2. F.D.M. Haldane, Continuum dynamics of the 1-d Heisenberg antiferromagnet: identification with the $O(3)$ nonlinear sigma model. *Phys. Lett.* **93**, 464 (1983)
3. F.D.M. Haldane, Nonlinear field theory of large-spin Heisenberg antiferromagnets: semiclassically quantized solutions of the one-dimensional easy-axis Neel state. *Phys. Rev. Lett.* **50**, 1153 (1983)
4. T. Kennedy, Exact diagonalisations of open spin-1 chains. *J. Phys. Cond. Mat.* **2**, 5737 (1990)
5. I. Hagiwara, K. Katsumata, I. Affleck, B.J. Halperin, J.P. Renard, Observation of $S = 1/2$ degrees of freedom in an $S = 1$ linear-chain Heisenberg antiferromagnet. *Phys. Rev. Lett.* **65**, 3181–3184 (1990)
6. W.J. Buyers, R.M. Morra, R.L. Armstrong, M.J. Hogan, P. Gerlach, A.K. Hirakawa, Experimental evidence for the Haldane gap in a spin-1 nearly isotropic antiferromagnetic chain. *Phys. Rev. Lett.* **56**, 371 (1986)
7. J.P. Renard, L.P. Regnault, M. Verdaguier, Experimental evidence for an Haldane gap in quasi-one dimensional antiferromagnets. *J. Phys. Colloques* **49**, C8 (1988)
8. M. Fannes, B. Nachtergaele, R.F. Werner, Finitely correlated states on quantum spin chains. *Commun. Math. Phys.* **144**, 443 (1992)
9. D. Perez-Garcia, F. Verstraete, M.M. Wolf, J.I. Cirac, Matrix product state representations. *Quantum Inf. Comput.* **7**, 401 (2007)
10. Z.-C. Gu, X.-G. Wen, Tensor-entanglement-filtering renormalization approach and symmetry protected topological order. *Phys. Rev. B* **80** 155131 (2009)
11. F. Pollmann, E. Berg, A.M. Turner, M. Oshikawa, Symmetry protection of topological order in one-dimensional quantum spin systems. *Phys. Rev. B* **85**, 075125 (2012)
12. X. Chen, Z.-C. Gu, Z.-X. Liu, X.-G. Wen, Symmetry-protected topological orders in interacting bosonic systems. *Science* **338**, 1604 (2012)
13. I. Affleck, Quantum spin chains and the Haldane gap. *J. Phys. Condens. Matt.* **1**, 3047 (1989)
14. F. Verstraete, J.I. Cirac, Renormalization algorithms for Quantum-Many Body Systems in two and higher dimensions (2004). arXiv:cond-mat/0407066v1
15. D.P. Arovas, A. Auerbach, F.D.M. Haldane, Extended Heisenberg models of antiferromagnetism: analogies to the fractional quantum Hall effect. *Phys. Rev. Lett.* **60**, 531 (1988)
16. T.-C. Wei, Quantum spin models for measurement-based quantum computation. *Adv. Phys. X* **3**, 1 (2018)
17. T. Kennedy, E.H. Lieb, H. Tasaki, A two-dimensional isotropic quantum antiferromagnet with unique disordered ground state. *J. Stat. Phys.* **53**, 383 (1988)
18. N. Pomata, T.-C. Wei, Demonstrating the Affleck-Kennedy-Lieb-Tasaki spectral gap on 2D degree-3 lattices. *Phys. Rev. Lett.* **124**, 177203 (2020)
19. N. Pomata, Order, disorder, and transitions in decorated AKLT states on bethe lattices. e-print. arXiv:2103.11819

20. S.A. Parameswaran, S.L. Sondhi, D.P. Arovas, Order and disorder in AKLT antiferromagnets in three dimensions. *Phys. Rev. B* **79**, 024408 (2009)
21. M. den Nijs, K. Rommelse, Preroughening transitions in crystal surfaces and valence-bond phases in quantum spin chains. *Phys. Rev. B* **40**, 4709 (1989)
22. T. Kennedy, H. Tasaki, Hidden symmetry breaking and the Haldane phase in $S = 1$ quantum spin chains. *Commun. Math. Phys.* **147**, 431–484 (1992)
23. C. Xu, T. Senthil, Wave functions of bosonic symmetry protected topological phases. *Phys. Rev. B* **87**, 174412 (2013)
24. Y.-Z. You, Z. Bi, A. Rasmussen, K. Slagle, C. Xu, Wave function and strange correlator of short-range entangled states. *Phys. Rev. Lett.* **112**, 247202 (2014)
25. X. Chen, Z.-C. Gu, Z.-X. Liu, X.-G. Wen, Symmetry protected topological orders and the group cohomology of their symmetry group. *Phys. Rev. B* **87**, 155114 (2013)
26. D.V. Else, C. Nayak, Classifying symmetry-protected topological phases through the anomalous action of the symmetry on the edge. *Phys. Rev. B* **90**, 235137 (2014)
27. K. Wierschem, K.S.D. Beach, Detection of symmetry-protected topological order in AKLT states by exact evaluation of the strange correlator. *Phys. Rev. B* **93**, 245141 (2016)
28. F.D.M. Haldane, $O(3)$ Nonlinear σ Model and the topological distinction between integer- and half-integer-spin antiferromagnets in two dimensions. *Phys. Rev. Lett.* **61**, 1029 (1988)
29. M. Oshikawa, Hidden $Z_2 \times Z_2$ symmetry in quantum spin chains with arbitrary integer spin. *J. Phys. Condens. Matter* **4**, 7469 (1992)
30. F. Pollmann, A.M. Turner, Detection of symmetry-protected topological phases in one dimension. *Phys. Rev. B* **86**, 125441 (2012)
31. H.J. Briegel, R. Raussendorf, Persistent entanglement in arrays of interacting qubits. *Phys. Rev. Lett.* **86**, 910 (2001)
32. T.-C. Wei, I. Affleck, R. Raussendorf, Affleck-Kennedy-Lieb-Tasaki state on a honeycomb lattice is a universal quantum computational resource. *Phys. Rev. Lett.* **106**, 070501 (2011)
33. T.-C. Wei, Quantum computational universality of spin-3/2 Affleck-Kennedy-Lieb-Tasaki states beyond the honeycomb lattice. *Phys. Rev. A* **88**, 062307 (2013)
34. R. Raussendorf, H.J. Briegel, A one-way quantum computer. *Phys. Rev. Lett.* **86**, 5188 (2001)
35. D. Gross, S. Flammia, J. Eisert, Most quantum states are too entangled to be useful as computational resources. *Phys. Rev. Lett.* **102**, 190501 (2009)
36. A. Miyake, Quantum computational capability of a 2D valence bond solid phase. *Ann. Phys.* **326**, 1656 (2011)
37. T.-C. Wei, P. Haghnegahdar, R. Raussendorf, Hybrid valence-bond states for universal quantum computation. *Phys. Rev. A* **90**, 042333 (2014)
38. T.-C. Wei, R. Raussendorf, Universal measurement-based quantum computation with spin-2 Affleck-Kennedy-Lieb-Tasaki states. *Phys. Rev. A* **92**, 012310 (2015)
39. R. Raussendorf, D. Wang, A. Prakash, T.-C. Wei, D. Stephen, *Phys. Rev. A* **96**, 012302 (2017)
40. D. Gross, J. Eisert, Novel schemes for measurement-based quantum computation. *Phys. Rev. Lett.* **98**, 220503 (2007)
41. D.V. Else, I. Schwarz, S.D. Bartlett, A.C. Doherty, *Phys. Rev. Lett.* **108**, 240505 (2012)
42. D.T. Stephen, D.-S. Wang, A. Prakash, T.-Ch. Wei, R. Raussendorf, Computational power of symmetry-protected topological phases. *Phys. Rev. Lett.* **119**, 010504 (2017)
43. X. Chen, R. Duan, Z. Ji, B. Zeng, Quantum state reduction for universal measurement based computation. *Phys. Rev. Lett.* **105**, 020502 (2010)
44. M. Hein, J. Eisert, H.J. Briegel, Multi-party entanglement in graph states. *Phys. Rev. A* **69**, 062311 (2004)
45. D. Gottesman, *Proceedings of the XXII International Colloquium on Group Theoretical Methods in Physics* (International Press, Cambridge, 1999), pp. 32–43
46. T.-C. Wei, I. Affleck, R. Raussendorf, The 2D AKLT state on the honeycomb lattice is a universal resource for quantum computation. *Phys. Rev. A* **86**, 032328 (2012)
47. H. Niggemann, A. Klümper, J. Zittartz, Quantum phase transition in spin-3/2 systems on the hexagonal lattice—optimum ground state approach. *Z. Phys. B* **104**, 103 (1997)

48. A.S. Darmawan, G.K. Brennen, S.D. Bartlett, Measurement-based quantum computation in a two-dimensional phase of matter. *New J. Phys.* **14**, 013023 (2012)
49. A. Miyake, Quantum computation on the edge of a symmetry-protected topological order. *Phys. Rev. Lett.* **105**, 040501 (2010)
50. J. Miller, A. Miyake, Resource quality of a symmetry-protected topologically ordered phase for quantum computation. *Phys. Rev. Lett.* **114**, 120506 (2015)
51. R. Raussendorf, C. Okay, D.S. Wang, D.T. Stephen, H.P. Nautrup, A computationally universal quantum phase of matter. *Phys. Rev. Lett.* **122**, 090501 (2019)
52. D.T. Stephen, H.P. Nautrup, J. Bermejo-Vega, J. Eisert, R. Raussendorf, Subsystem symmetries, quantum cellular automata, and computational phases of quantum matter. *Quantum* **3**, 162 (2019)
53. T. Devakul, D.J. Williamson, Universal quantum computation using fractal symmetry-protected cluster phases. *Phys. Rev. A* **98**, 022332 (2018)
54. A.K. Daniel, R.N. Alexander, A. Miyake, Computational universality of symmetry-protected topologically ordered cluster phases on 2D Archimedean lattices. *Quantum* **4**, 228 (2020)
55. S. Knabe, Energy gaps and elementary excitations for certain VBS-quantum antiferromagnets. *J. Stat. Phys.* **52**, 627 (1988)
56. D. Gosset, E. Mozgunov, Local gap threshold for frustration-free spin systems. *J. Math. Phys.* **57**, 091901 (2016)
57. M. Lemm, E. Mozgunov, Spectral gaps of frustration-free spin systems with boundary. *J. Math. Phys.* **60**, 051901 (2019)
58. M. Lemm, Finite-size criteria for spectral gaps in D -dimensional quantum spin systems. *Contemp. Math.* **741**, 121–132 (2020)
59. A. Garcia-Saez, V. Murg, T.-C. Wei, Spectral gaps of Affleck-Kennedy-Lieb-Tasaki Hamiltonians using tensor network methods. *Phys. Rev. B* **88**, 245118 (2013)
60. L. Vanderstraeten, M. Mariën, F. Verstraete, J. Haegeman, Excitations and the tangent space of projected entangled-pair states. *Phys. Rev. B* **92**, 201111(R) (2015)
61. H. Abdul-Rahman, M. Lemm, A. Lucia, B. Nachtergaele, A. Young, A class of two-dimensional AKLT models with a gap, in *Analytic Trends in Mathematical Physics*, ed. by H. Abdul-Rahman, R. Sims, A. Young, Contemporary Mathematics, vol. 741 (American Mathematical Society, Providence, 2020), pp. 1–21
62. N. Pomata, T.-C. Wei, AKLT models on decorated square lattices are gapped. *Phys. Rev. B* **100**, 094429 (2019)
63. M. Lemm, A.W. Sandvik, L. Wang, Existence of a spectral gap in the Affleck-Kennedy-Lieb-Tasaki model on the hexagonal lattice. *Phys. Rev. Lett.* **124**, 177204 (2020)
64. W. Guo, N. Pomata, T.-C. Wei, Nonzero spectral gap in several uniformly spin-2 and hybrid spin-1 and spin-2 AKLT models. *Phys. Rev. Res.* **3**, 013255 (2021)
65. F. Verstraete, M.A. Martín-Delgado, J.I. Cirac, Diverging entanglement length in gapped quantum spin systems. *Phys. Rev. Lett.* **92**, 087201 (2004)
66. F. Verstraete, M. Popp, J.I. Cirac, Entanglement versus correlations in spin systems. *Phys. Rev. Lett.* **92**, 027901 (2004)
67. N. Pomata, C.-Y. Huang, T.-C. Wei, Phase transitions of a two-dimensional deformed Affleck-Kennedy-Lieb-Tasaki model. *Phys. Rev. B* **98**, 014432 (2018)
68. H. Niggemann, A. Klümper, J. Zittartz, Ground state phase diagram of a spin-2 antiferromagnet on the square lattice. *Eur. Phys. J. B* **13**, 15 (2000)
69. Y. Hieida, K. Okunishi, Y. Akutsu, Numerical renormalization approach to two-dimensional quantum antiferromagnets with valence-bond-solid type ground state. *New J. Phys.* **1**, 7 (1999)
70. C.-Y. Huang, M.A. Wagner, T.-C. Wei, Emergence of the XY-like phase in the deformed spin-3/2 AKLT systems. *Phys. Rev. B* **94**, 165130 (2016)
71. H. Niggemann, J. Zittartz, Ground state properties of a spin-3/2 model on a decorated square lattice. *Eur. Phys. J. B* **13**, 377–379 (2000)
72. R. Kaltenbaek, J. Lavoie, B. Zeng, S.D. Bartlett, K.J. Resch, Optical one-way quantum computing with a simulated valence-bond solid. *Nat. Phys.* **6**, 85 (2010)

73. C. Senko, P. Richerme, J. Smith, A. Lee, I. Cohen, A. Retzker, C. Monroe, Realization of a quantum integer-spin chain with controllable interactions. *Phys. Rev. X* **5**, 021026 (2015)
74. S. Mishra, G. Catarina, F. Wu, R. Ortiz, D. Jacob, K. Eimre, J. Ma, C.A. Pignedoli, X. Feng, P. Ruffieux, J. Fernández-Rossier, R. Fasel, Observation of fractional edge excitations in nanographene spin chains. *Nature* **598**, 287–292 (2021)
75. S. Roy, J.T.Chalker, I.V. Gornyi, Y. Gefen, Measurement-induced steering of quantum systems. *Phys. Rev. Res.* **2**, 033347 (2020)
76. V. Sharma, E.J. Mueller, Driven-dissipative control of cold atoms in tilted optical lattices. *Phys. Rev. A* **103**, 043322 (2021)
77. M. Koch-Janusz, D.I. Khomskii, E. Sela, Two-dimensional Valence Bond Solid (AKLT) states from t_{2g} electrons. *Phys. Rev. Lett.* **114**, 247204 (2015)

Machine Learning-Assisted Entanglement Measurement in Quantum Many-Body Systems



Leonardo Banchi

Abstract Measuring entanglement in quantum many-body systems is a challenging task, especially for mixed states. All known computable entanglement measures depend non-linearly on the state, so the standard approach to quantify entanglement would require a complete state tomography, a highly demanding and not scalable experimental procedure, followed by complex manipulations of matrices whose dimension increases exponentially in the number of qubits. Here, we review a different method, first proposed in Gray et al. (Phys Rev Lett 121(15):150503, 2018) and then expanded in Elben et al. (Phys Rev Lett 125(20):200501, 2020); Zhou et al. (Phys Rev Lett 125(20):200502, 2020), based on the reconstruction of the partially transposed moments of a quantum many-body mixed state. The experimental procedure for such reconstructions scales linearly in the number of qubits and has already been demonstrated in different physical setups, such as quantum dot arrays and cold atoms in optical lattice. The method first proposed in Gray et al. (Phys Rev Lett 121(15):150503, 2018) is based on the observation that the mapping between partially transposed moments to the logarithmic negativity is basically smooth, so that it can be learnt by machine learning interpolation methods, e.g. based on neural networks. More precisely, a neural network model trained using just measurement outcomes from random quantum states, with no knowledge of the underlying physical systems, is able to accurately estimate the logarithmic negativity for different states, e.g. ground states of physical Hamiltonians or states appearing in the quench dynamics of quantum many-body systems.

L. Banchi (✉)

Department of Physics and Astronomy, University of Florence, and INFN Sezione di Firenze, Florence, Italy

e-mail: leonardo.banchi@unifi.it

1 Introduction

Quantum entanglement is one of the most striking properties of microscopic systems, which is of paramount importance for both technological applications [1–8] and understanding quantum many-particle systems [9–17]. Unlike for pure quantum states, where bipartite entanglement can be uniquely quantified via the entropy of either subsystems, for mixed quantum states, different entanglement measures have been proposed [18–20]. In experiments, it is almost impossible to deal with pure states, so it is very important to be able to detect and quantify entanglement of mixed states [21, 22]. Very few measures of entanglement can be actually efficiently computed, and some of these are restricted to two qubit states [23] or bosonic Gaussian states [24, 25]. The only measure of bipartite entanglement that can be, in principle, explicitly computed for arbitrary bipartite quantum states is the (logarithmic) negativity [26–30]. From the practical point of view, the (logarithmic) negativity can be used to bound the distillable entanglement and the teleportation capacity [28], and it has important applications in quantum information theory [18, 19, 31] and for understanding strongly interacting systems in condensed matter [32].

The (logarithmic) negativity is a non-linear function of the quantum state, whose computation and experimental estimation become very challenging for many-particle systems. Indeed, on the one hand, there is no direct observable to measure it, thus requiring full-state tomography, a highly demanding experimental procedure whose complexity increases exponentially in the system size. On the other hand, being a non-linear function of the quantum state, it requires the explicit manipulation of operators acting on exponentially large Hilbert spaces. Moreover, both the logarithmic negativity and many other entanglement measures are not continuous [20], so even if the tomographically reconstructed state approximates the true state closely, the two may have significantly different logarithmic negativities.

In this chapter, we review a different method, first proposed in Ref. [33], for estimating the logarithmic negativity in realistic experimental settings. This is based on two central ideas: the first one is that the mapping from the moments of the partially transposed density matrix to the (logarithmic) negativity is generally smooth, so it can be learnt using machine learning techniques, e.g. based on neural networks. The second one is that such moments can be estimated efficiently with a number of measurements that scale linearly in the number of qubits. The neural network-based entanglement estimator represents a new front in the application of classical machine learning to quantum problems [10, 34–38], and it is remarkably accurate for highly entangled states, which are exactly those states where approximate tomographic reconstruction methods generally fail.

This chapter is structured as follows: in Sect. 2, we review the PPT criterion and introduce the logarithmic negativity and then study the relationship between moments and negativity in a few analytical cases. In Sect. 3, we introduce an efficient scheme to measure the moments, and in Sect. 4, we show how to learn

the mapping from moments to negativity using neural networks. Numerical results are shown in Sect. 5, and conclusions are drawn in Sect. 6.

2 PPT Criterion and Entanglement Measurement

Consider a generic mixed state ρ_{AB} that describes the collective state of two subsystems A and B . The PPT criterion [39, 40], which stands for positive partial transpose, states that the subsystems A and B are separable in ρ_{AB} if $\rho_{AB}^{T_A}$ and $\rho_{AB}^{T_B}$ are positive operators, where the operation T_X is a partial transposition with respect to subsystem X only. In other terms, if $\rho_{AB}^{T_{A/B}}$ has negative eigenvalues, then the subsystems A and B must be entangled. However, there exist some entangled states (called bound entangled) with positive partial transpose. It is possible to turn the PPT criterion into an entanglement measure called negativity. Here, we will focus on the logarithmic negativity [26–29], which is defined as

$$\mathcal{E} = \log_2 \left| \rho_{AB}^{T_A} \right| = \log_2 \left| \rho_{AB}^{T_B} \right| = \log_2 \sum_k |\lambda_k|, \quad (1)$$

where $|\cdot|$ is the trace norm, and $\{\lambda_k\}$ are the eigenvalues of $\rho_{AB}^{T_X}$, which are equal for both $X = A$ or $X = B$. Since the logarithmic negativity is a non-linear functional of ρ_{AB} , there is no state-dependent observable that can measure it: one has to first reconstruct ρ_{AB} with full-state tomography, a highly demanding and generally inefficient experimental procedure, and then numerically compute the negativity through Eq. (1). A different method was proposed in Ref. [33], based on the observation that the full information about $\{\lambda_k\}$ is contained in the moments of the partially transposed density matrix (hereafter called PT moments), which are defined as

$$\mu_m = \text{Tr} \left[\left(\rho_{AB}^{T_B} \right)^m \right] = \sum_k \lambda_k^m. \quad (2)$$

Different methods for extracting the moments were proposed in [33, 41–45], which will be discussed in the next section. The first PT moment is trivial since $\mu_1 = \text{Tr}[\rho_{AB}] = 1$, while μ_0 is the dimension of the Hilbert space. Additionally, it can be easily shown that the second PT moment is equal to the purity of the state $\mu_2 = \text{Tr}[\rho_{AB}^2]$, which is not enough to study the entanglement in mixed states. As such, at least the third PT moment is required for such purpose [33]. From the moments, it is possible to readily check whether the PPT criterion is satisfied or not by the following test [44]:

$$\mu_3 < \mu_2^2 \implies \rho_{AB} \text{ is entangled,} \quad (3)$$

which is independent on the state, unlike entanglement witnesses [46, 47]. While, in general, this criterion can only be used in one direction, it provides a necessary sufficient condition for detecting entanglement for certain classes of quantum states, such as the so-called Werner states [44]. However, violation of (3) cannot be used to rigorously certify *how much* entanglement is present in a system. To do that, in Ref. [33], before the discovery of condition (3), we proposed the use of a heuristic method based on machine learning and on the estimation of the first M moments $\{\mu_m : m \leq M\}$. Remarkably, it was found that neural networks were able to accurately predict the logarithmic negativity from the first three moments, namely with $M = 3$, and that more accurate predictions were possibly with slightly larger values of M .

In this way, one completely sidesteps the estimation of the $\{\lambda_k\}$ that are necessary for the exact computation via Eq. (1). The latter is problematic for two reasons: on the one hand, the problem of extracting $\{\lambda_k\}$ from the moments is notoriously ill-conditioned, since this is closely related to general Hausdorff moment problem in statistics [48], which is known to be unstable from a numerical perspective [49]. On the other hand, an exponential number of moments respective to the size of AB are needed to exactly solve the equations. The central idea in [33] is that a precise knowledge of all λ_k is not required to estimate the logarithmic negativity. Indeed, since $-\frac{1}{2} \leq \lambda_k \leq 1$ for all k [50] and $\sum_k \lambda_k = 1$, in general, $|\mu_m|$ quickly decreases with m , so the first few moments carry the most information.

2.1 Werner States

In order to motivate the above predictions, let us consider an important class of states for which analytic arguments can be obtained. We focus on the $d^2 \times d^2$ Werner states [51] defined as

$$\rho_{AB}^W = \frac{p}{d(d+1)}(\mathbb{I} + S) + \frac{1-p}{d(d-1)}(\mathbb{I} - S), \quad (4)$$

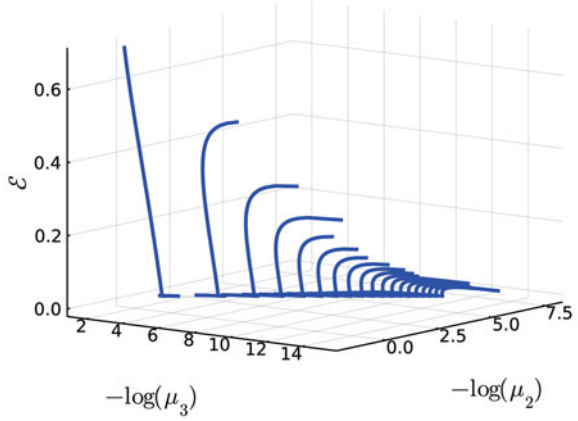
where the dimension of both Hilbert spaces A and B is equal to d , S is the SWAP operator, exchanging A and B , and $0 \leq p \leq 1$. Werner states are invariant under local transformations $U \otimes U$ for any unitary U . Moreover, for these states, the partial transpose can be easily computed since

$$S^{TB} = S^{TA} = \sum_{ij} |ii\rangle\langle jj|, \quad (5)$$

and we find the simple expression for the logarithmic negativity

$$\mathcal{E}^W = \log \left[1 + \frac{2(1-2p)}{d} \right] \quad \text{if } p < \frac{1}{2}, \quad (6)$$

Fig. 1 Functional relationship between logarithmic negativity \mathcal{E} and the moments, μ_2 and μ_3 , for different Werner states (4) with $p \in [0, 1]$ and $d \in [2, 20]$. Each continuous line corresponds to a single value of d and multiple p . Higher values of d have generally lower entanglement. Only values with $\mu_3 > 0$ have been plotted



while $\mathcal{E}^W = 0$ for $p > 1/2$. Similar expressions for μ_j are not shown, since they are more complex, though we get

$$\mu_3 - \mu_2^2 = (2p - 1) \frac{(d - 2p + 1)(1 - 2dp + d)^2}{d^2 (d^2 - 1)^2}. \quad (7)$$

From the above equation, we see that, according to the condition (3), for $p < 1/2$, the Werner state must be entangled irrespective of d . The amount of entanglement can be obtained from Eq. (6), where we see that, with the same p , higher dimensional states have lower entanglement.

For this particular class of states, one can reconstruct p and d from the measurement of μ_2 and μ_3 and hence reconstruct the amount of entanglement. Moreover, as shown in Fig. 1, the dependence of \mathcal{E} on the moments can be embedded in a smooth surface, even though not all possible pairs μ_2, μ_3 are physically possible. In Ref. [33], this idea was fully exploited with more general states, showing that a neural network can be trained in order to reliably map the non-trivial moments (μ_0, μ_2, μ_3) to an accurate prediction of \mathcal{E} . More precisely, since μ_0 is a discrete quantity, if we are interested in states with fixed dimension, we can train a surface function $f(\mu_2, \mu_3)$ in order to reproduce the logarithmic negativity. When different dimensions are considered, we may also put μ_0 as an extra input for the neural network.

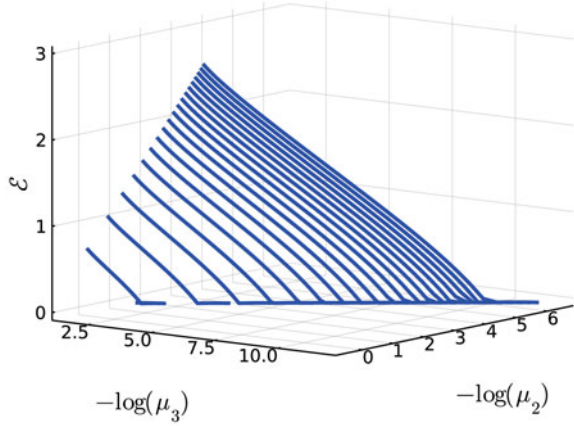
We also focus on the following $U \otimes U^*$ invariant states:

$$\rho_{AB}^{W*} = p |\Phi\rangle\langle\Phi| + \frac{1-p}{d^2} \mathbb{I}, \quad (8)$$

where $|\Phi\rangle = d^{-1/2} \sum_j |jj\rangle$. For this state, we may write

$$\rho_{AB}^{W*T_B} = \lambda_+ P_+ + \lambda_- P_-, \quad \lambda_{\pm} = \frac{p \pm d(1-p)}{d^2}, \quad (9)$$

Fig. 2 Functional relationship between logarithmic negativity \mathcal{E} and the moments, μ_2 and μ_3 , for different invariant states (8) with $p \in [0, 1]$ and $d \in [2, 20]$. Each continuous line corresponds to a single value of d and multiple p . Only values with $\mu_3 > 0$ have been plotted



where $P_{\pm} = (\mathbb{I} \pm S)/2$ are the projectors onto the symmetric or antisymmetric subspaces, whose dimension is, respectively, $d_{\pm} = d(d \pm 1)/2$. From the above equations, we see that entanglement is present for $p < \frac{d}{d+1}$, with logarithmic negativity given by

$$\mathcal{E}^{W*} = \log\left(d + \frac{p}{d} - dp\right) \quad \text{if } p < \frac{d}{d+1}. \quad (10)$$

The functional relationship between the logarithmic negativity and the moments, μ_2 and μ_3 , is then shown in Fig. 2.

3 Measuring the PT Moments

There are three different protocols for measuring the PT moments. The first proposal for measuring μ_m uses m copies of the state and controlled swap operations [41], while a simpler protocol, for 4 moments only, was provided in [43]. However, controlled swap operations require 3-body interactions and thus must be compiled into simpler 2-body gates. A different procedure, still involving m copies, was proposed in [33], generalizing another procedure for estimating Renyi entropies [17]. A third procedure, based on randomized gates, has been proposed in Refs. [44, 45].

Here, we review the procedure proposed in [33], providing extra details. This procedure starts with the simple observation that each moment can be written as an expectation value of permutation operators acting on m copies of ρ_{AB}^{TB} , similar to Ref. [52, 53], by mapping the partial transposition onto the observable one gets

$$\mu_m = \text{Tr} \left[\left(\bigotimes_{c=1}^m \rho_{A_c B_c}^{TB} \right) \mathbb{P}^m \right] = \text{Tr} \left[\left(\bigotimes_{c=1}^m \rho_{A_c B_c} \right) (\mathbb{P}^m)^{TB} \right], \quad (11)$$

where \mathbb{P}^m is any linear combination of cyclic permutation operators of order m , and in the second equality, we use of the identity $\text{Tr}(\rho_{AB}^{T_B} O) = \text{Tr}(\rho_{AB} O^{T_B})$, valid for any operator O . Extra care must be used in choosing \mathbb{P}^m in such a way that $(\mathbb{P}^m)^{T_B}$ is Hermitian and hence observable without other ancillary qubits. In the next sections, we consider two operational measures that provide different choices of \mathbb{P} , which can be neatly implemented in spin or bosonic systems, e.g. optical lattices. For both platforms, our procedure requires $\mathcal{O}(N_A + N_B)$ measurements for each m , where N_X is the number of particles in X . This is in stark contrast with full tomographic methods that require a number of measurements that grow exponentially with N_A and N_B .

Remarkably, even though partially transposed density matrices are generically unphysical, the measurement of their moments is possible. Our procedure was inspired by recent operational methods for measuring Renyi entropies in spin and bosonic lattices [17, 54, 55] but differs in many ways. The most important difference is that Renyi entropies do not provide a measure of entanglement for mixed states. Moreover, while for entropies, the operations are only performed on a single subsystem, for the PT moments, one must perform both ‘forward’ and ‘backward’ operations on two subsystems at once, as we explain in the next more technical sections.

3.1 Measurement in Spin Systems

In spin systems, the measurement of the PT moment μ_m involves the following steps:

1. Prepare m copies of the state ρ_{AB} .
2. Sequentially measure a ‘forward’ sequence of adjacent swaps, $S_A^{c,c+1}$ between neighbouring copies $(c, c+1)$ of system A from $c = 1$ to $m - 1$.
3. Sequentially measure a ‘backward’ sequence of adjacent swaps, $S_B^{c,c-1}$ between neighbouring copies of system B from $c = m$ to 2 .
4. Repeat these steps in order to yield an expectation value.

Step 2 of the above procedure is depicted in Fig. 3 for $m = 3$, where each swap measurement can be effectively implemented via singlet–triplet measurements [17].

We now give a proof of the above procedure, by first showing how to measure $\text{Tr}[\rho^m]$ and then the PT moments. Let $S_X^{c,d}$ be the operator that swaps copies c and d on subsystem X , which can be written as $S_X^{c,d} = \prod_{j \in X} \Xi_j^{c,d}$, where $\Xi_j^{c,d} = (\mathbb{I} + \sigma^{j,c} \cdot \sigma^{j,d})/2$, and $\sigma^{j,d}$ is a vector of Pauli matrices acting on spin j in copy d . The projective measurement of $\Xi_j^{c,d}$ corresponds to a singlet–triplet measurement

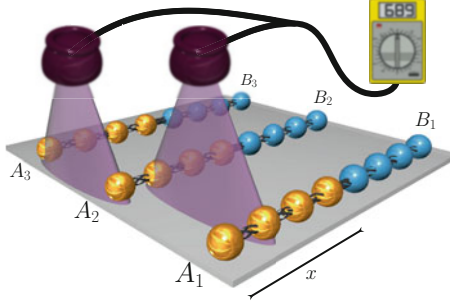


Fig. 3 One step for the measurement of the PT moment μ_m with $m = 3$, using m copies of the same many-particle mixed state ρ_{AB} . The particles in each copy are arranged into a spin chain, where each spin in the chain is either part of A (yellow spins) or B (blue spins). The measurement involves sequential swap measurements between pair of spins in neighbouring chains. Reprinted from [17]

(ST measurement) between spins sitting at the same site j , but different copies c and d . Indeed, $\Xi_j^{c,d}$ has an outcome -1 for the singlet state and 1 for the triplet states. In view of this, we write $S_X^{c,d} = \Pi_+^{c,d} - \Pi_-^{c,d}$, where $\Pi_{\pm}^{c,d}$ correspond to the eigen-projections with corresponding eigenvalues ± 1 . We first focus on $m=3$ and then generalize the procedure to arbitrary m . For $m = 3$, we perform a sequential set of ST measurements on copies (1, 2), with outcome β_1 , and then do the same measurement on copies (2, 3), with outcome β_2 . In the following, we write $S_X^{2,3} \circ S_X^{1,2}$ to describe this process. After the first measurement, the (non-normalized) state of the system will be $\Pi_{\beta_1}^{1,2} \rho^{\otimes 3} \Pi_{\beta_1}^{1,2}$, while after the two sets of measurements, it is $\Pi_{\beta_2}^{2,3} \Pi_{\beta_1}^{1,2} \rho^{\otimes 3} \Pi_{\beta_1}^{1,2} \Pi_{\beta_2}^{2,3}$. Therefore,

$$\begin{aligned}
 \langle S_X^{2,3} \circ S_X^{1,2} \rangle &= \sum_{\beta_2} \sum_{\beta_1} \beta_1 \beta_2 \operatorname{Tr} \left[\Pi_{\beta_2}^{2,3} \Pi_{\beta_1}^{1,2} \rho^{\otimes 3} \Pi_{\beta_1}^{1,2} \Pi_{\beta_2}^{2,3} \right] \\
 &= \sum_{\beta_1} \beta_1 \operatorname{Tr} \left[\Pi_{\beta_1}^{1,2} S_X^{2,3} \Pi_{\beta_1}^{1,2} \rho^{\otimes 3} \right] \\
 &= \frac{1}{2} \left(\operatorname{Tr} \left[S_X^{1,2} S_X^{2,3} \rho^{\otimes 3} \right] + \operatorname{Tr} \left[S_X^{2,3} S_X^{1,2} \rho^{\otimes 3} \right] \right) = \operatorname{Tr}(\rho^3), \quad (12)
 \end{aligned}$$

where we used the identity $\Pi_{\pm}^{c,d} = (\mathbb{I} \pm S_X^{c,d})/2$. The above equality shows how to effectively measure $\operatorname{Tr}[\rho^3]$ with a series of SWAP measurements.

We now generalize the above argument for higher values of m . We apply sequential ST measurements on neighbouring copies, using the notation $S_X^{m,m-1} \circ \dots \circ S_X^{2,3} \circ S_X^{1,2}$, meaning that we first perform $S_X^{1,2}$, and so forth. Taking the averages,

one then finds that

$$\left\langle S_X^{m-1,m} \circ \dots \circ S_X^{1,2} \right\rangle = \text{Tr} \left[\mathcal{P}^{m-1,m} [\dots \mathcal{P}^{23} [\mathcal{P}^{12} [\rho^{\otimes m}]]] \dots \right],$$

where $\mathcal{P}^{j,j+1}[\rho] = \sum_{\beta_j} \beta_j \Pi_{\beta_j}^{j,j+1} \rho \Pi_{\beta_j}^{j,j+1}$. We define the operators $S_X^{a,b,c,\dots}$ recursively as $\mathcal{P}^{j+1,j} [S_X^{j,a,b,\dots}] = [S_X^{j+1,j,a,\dots} + S_X^{j,j+1,a,\dots}] / 2$. Then, using the cyclic property of the trace, one finds that $\left\langle S_X^{m-1,m} \circ \dots \circ S_X^{1,2} \right\rangle = 2^{2-m} \sum_{\kappa} \langle S_X^{\kappa} \rangle$, where the κ is 2^{m-2} different cyclic permutation of the elements $1, \dots, m$. For instance, for $m=3$, one has $\kappa = \{123, 132\}$.

In summary, when X is equal to both A and B , one can use a set of sequential ST measurements to implement the operator $\mathbb{P}_X^m = 2^{2-m} \sum_{\kappa} S_X^{\kappa}$ such that $\text{Tr}[\rho_X^{\otimes m} \mathbb{P}_X^m] = \text{Tr}[\rho_X^m]$. Indeed, for each cyclic permutation, $\text{Tr}[\rho_X^{\otimes m} S_X^{\kappa}] = \text{Tr}[\rho_X^m]$. In view of the above derivation, such Hermitian operator can also be written via the following recursion relations (see also Ref. [17]): $\mathbb{P}^m = \left(S_A^{m,m-1} S_B^{m,m-1} \mathbb{P}^{m-1} + \text{h.c.} \right) / 2$. Moreover, the effect of the partial transpose on the recursion relation is as follows:

$$(\mathbb{P}^m)^{T_B} = \left(S_A^{m,m-1} (\mathbb{P}^{m-1})^{T_B} S_B^{m,m-1} + \text{h.c.} \right) / 2. \quad (13)$$

We take $m = 3$ as an example to get $(\mathbb{P}^3)^{T_B} = \left(S_A^{3,2} S_A^{2,1} \otimes S_B^{2,1} S_B^{3,2} + \text{h.c.} \right) / 2$. The above equation shows that, as described in the operational steps at the beginning of the section, for measuring the PT moments, the order of measurements on A and B is reversed. Indeed, for A , the ST measurement is performed between copies 1 and 2 and then 2 and 3, whereas for B , the ST measurement is performed for copies 2 and 3 and then 1 and 2. Because of the non-commutative nature of these measurements, this ordering is crucial to estimate μ_3 .

From the above derivation, we find that $\mu_m = \text{Tr}[\rho_{AB}^{\otimes m} \mathbb{P}_m]$. The variance of the above measurement can be found by noting the SWAP measurements satisfy $S^2 = \mathbb{I}$. More formally,

$$\begin{aligned} (\Delta \mu_m)^2 &= \left(\sum_{\beta_m} \dots \sum_{\beta_1} \beta_1^2 \dots \beta_m^2 \text{Tr} \left[\Pi_{\beta_{m-1}}^{m-1,m} \dots \Pi_{\beta_1}^{1,2} \rho^{\otimes m} \Pi_{\beta_1}^{1,2} \dots \Pi_{\beta_{m-1}}^{m-1,m} \right] \right) - \mu_m^2 \\ &= \left(\sum_{\beta_m} \dots \sum_{\beta_1} \text{Tr} \left[\Pi_{\beta_{m-1}}^{m-1,m} \dots \Pi_{\beta_1}^{1,2} \rho^{\otimes m} \Pi_{\beta_1}^{1,2} \dots \Pi_{\beta_{m-1}}^{m-1,m} \right] \right) - \mu_m^2 \\ &= 1 - \mu_m^2, \end{aligned}$$

where we used the fact that $\beta_i^2 = 1$ and $\sum_{\beta_i} (\Pi_{\beta_i}^{i,i+1})^2 = \sum_{\beta_i} \Pi_{\beta_i}^{i,i+1} = \mathbb{I}$. Repeating the experiment R times, we find the standard deviation

$$\Delta^R \mu_m = \sqrt{\frac{1 - \mu_m^2}{R}}. \quad (14)$$

3.2 Measurement in Bosonic Systems

In bosonic systems, the procedure for measuring the PT moment μ_m involves the following steps:

1. Prepare m copies of the state ρ_{AB} .
2. Perform ‘forward’ Fourier transforms between modes in different copies for each site in A , e.g. using a series of beam splitters [56].
3. Perform ‘backwards’ (reverse) Fourier transform between modes in different copies for each site in B , via reverse beam splitter transformations.
4. Measure the boson occupation numbers $n_{j,c}$ on all sites $j \in \{A, B\}$ and all copies c to compute $\phi = e^{i \sum_{j \in \{A, B\}, c} 2\pi c n_{j,c} / m}$.
5. Repeat these steps to obtain the expectation value μ_m as an average of ϕ

$$\mu_m = \langle e^{i \sum_{j \in \{A, B\}, c} 2\pi c n_{j,c} / m} \rangle. \quad (15)$$

The proof of Eq. (15) goes as follows: unlike in spin systems, we directly choose the operator \mathbb{P}_m as a product of a specific non-Hermitian permutations π , such that

$$\mathbb{P}_m^{TB} = \bigotimes_{j \in A} V_{j,\pi} \bigotimes_{j \in B} V_{j,\pi}^T, \quad (16)$$

where $V_{j,\pi} = \sum_{\{n_{j,c}\}} |n_{j,1}, \dots, n_{j,m}\rangle \langle \pi(n_{j,1}), \dots, \pi(n_{j,m})|$, and $n_{j,c} = 0, \dots, \infty$ labels the number of bosons in copy c and physical site j . We can write this operator in second quantized form as

$$V_{j,\pi} = :e^{\sum_c a_{j,c}^\dagger a_{j,\pi(c)} - a_{j,c}^\dagger a_{j,c}}:, \quad (17)$$

where $:O:$ denotes the normal ordering of the operator O , and $a_{j,c}$ denotes the annihilation operator acting on site j and copy c . We choose π as the shift permutation such that $\pi(c) = c + 1$ and note that $V_{j,\pi}^T = V_{j,\pi^{-1}}$. In order to

diagonalize $V_{j,\pi}$, we introduce independent Fourier transforms for each site j as

$$\begin{aligned}\tilde{a}_{j,c} &= \frac{1}{\sqrt{m}} \sum_{c'=0}^{m-1} e^{+\frac{i2\pi}{m}cc'} a_{j,c'}, & \text{for } j \in A, \\ \tilde{a}_{j,c} &= \frac{1}{\sqrt{m}} \sum_{c'=0}^{m-1} e^{-\frac{i2\pi}{m}cc'} a_{j,c'}, & \text{for } j \in B.\end{aligned}\quad (18)$$

After such a transformation, both the operators $V_{j,\pi}$ for $j \in A$ and $V_{j,\pi^{-1}}$ for $j \in B$ take the form $:e^{\sum_c (e^{\frac{i2\pi}{m}c} - 1) \tilde{a}_{j,c}^\dagger \tilde{a}_{j,c}}:$. The normal ordering can be removed by using the identity [57] $:e^{\lambda a - 1} a^\dagger a: = e^{\lambda a^\dagger a}$ bringing Eq. (16) to the form:

$$\mathbb{P}_m^{TB} = \prod_{j \in \{A, B\}, c} e^{\frac{i2\pi c}{m} \tilde{a}_{j,c}^\dagger \tilde{a}_{j,c}}. \quad (19)$$

This shows that the expectation value can be measured according to the procedure introduced at the beginning of this section and summarized by Eq. (15): firstly, we need to perform the Fourier (inverse Fourier) transform between copies at the sites belonging to A (B), as written in Eq. (18). Secondly, we need to measure the bosonic occupation number with outcome $n_{j,c}$ at every site and compute the outcome of the permutation operator as $\phi = e^{\sum_{j \in \{A, B\}, c} \frac{i2\pi c}{m} n_{j,c}}$. The final step involves the computation of the expectation value as an average over many repetitions of the above steps.

The standard deviation can be obtained from the fact that $\phi^* = \phi$. As such $(\Delta \mu_m)^2 = \langle \phi \phi^* \rangle - \langle \phi \rangle^2 = 1 - \mu_m^2$ and after R repetitions, we find the same result of Eq. (14).

4 Neural Network Entanglement Estimator

We have seen that for some particular classes of states, the mapping from the first few moments μ_m to the logarithmic negativity $\mathcal{E} \approx f(\mu_0, \dots, \mu_M)$ is mostly smooth. One may hence employ different interpolation methods to approximate f from a few known examples. A different approach based on numerical extrapolation, first proposed in the quantum field theory literature [32, 58], uses the odd moments up to high orders and, as such, necessitates many copies.

The simplest interpolation method is based on a polynomial functional approximation. Gray et al. [33] proposed the polynomial approximation of the absolute value function in order to estimate the moments. More precisely, considering that $\mathcal{E} = \log_2 \text{Tr} g(\rho_{AB}^{TB})$ with $g(x) = |x|$, if we can find a polynomial expansion $g(x) \approx \sum_{m=0}^M \alpha_m x^m$, then by linearity of the trace, $\mathcal{E} = \log_2 \sum_{m=0}^M \alpha_m \mu_m$,

with μ_m as given in Eq. (2). Since the absolute value function is non-analytic, the Taylor expansion cannot be used. Gray et al. [33] used an interpolation method based on Chebyshev polynomials, for which the coefficients α_m can be analytically computed, together with some analytical estimations of the approximation error. The Chebyshev expansion becomes exact in the limit $M \rightarrow \infty$. However, it was numerically observed that machine learning methods based on neural networks were significantly more accurate with a smaller number of moments. The reason is that the Chebyshev expansion is based on a linear mapping between the moments and the negativity, despite this relationship being inherently non-linear. Due to the universal approximation theorem, neural networks with suitable number of neurons can approximate any non-linear mapping and thus should be more optimal for smaller M , namely fewer copies. In what follows, we therefore review the machine learning approach first proposed by Gray et al. [33].

Following the supervised learning paradigm, we consider a parametric approximation $f_\theta(\mu_0, \dots, \mu_M)$, e.g. using a neural network, of the mapping from the moments to the logarithmic negativity and train the parameters θ in order to minimize some distance $\|\mathcal{E} - f_\theta(\mu_0, \dots, \mu_M)\|$ for some chosen norm. Since the above distance cannot be computed for all possible values of inputs and outputs, one uses a training set made of different tuples of data $\mathcal{T} = \{(\mathcal{E}, \mu_0, \dots, \mu_M)\}$, where each tuple contains both the moments, as inputs, and the true corresponding logarithmic negativity, as output. Training is then performed by finding the parameters θ that minimize the empirical distance

$$\sum_{(\mathcal{E}, \mu_0, \dots, \mu_M) \in \mathcal{T}} \|\mathcal{E} - f_\theta(\mu_0, \dots, \mu_M)\|. \quad (20)$$

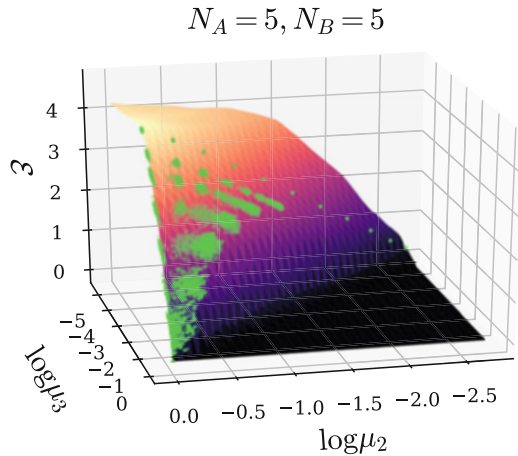
The model f_θ generalizes if it is able to predict the true logarithmic negativity for moments that do not belong to the training set. See Ref. [59] for a description of generalization using the language of quantum information theory. Some of the most accurate machine learning algorithms for non-linear interpolation are based on support vector machines [60], random decision forests [61], and deep neural networks [62, 63]. We studied all of these algorithms and found that, using the same training set, neural networks are superior when it comes to predicting logarithmic negativity for a wide range of states beyond the training set. Indeed, for this particular problem, it was found that neural networks show higher generalization capabilities with as few as $M = 3$ copies.

In a deep neural network, the function f_θ is represented as a directed graph organized in layers, where the first layer is the input data and the last one is the output. As already mentioned, the first moment μ_0 depends only on the dimension of the Hilbert space. In reality, we assume to know both the dimensions of each of the subsystems A and B , which for simplicity here are considered as qubit systems with N_A and N_B qubits. We use N_X in place of μ_0 , and, since $\mu_1 = 1$ does not

provide any information, we consider the numbers $(N_A, N_B, \mu_2, \dots, \mu_M)$ as inputs for our neural network. We call $s_k^{(\ell)}$ the value of the k th node in layer ℓ , which is updated in a feed-forward way via the equation $s_k^{(\ell)} = A^\ell \left[\sum_j w_{kj}^{(\ell-1)} s_j^{(\ell-1)} \right]$, where A^ℓ is the so-called activation function and $w_{kj}^{(\ell-1)}$ is the weight between node k in layer ℓ and node j in $\ell-1$. Therefore, the parameters θ are made of all possible weights, which are optimized during training in order to minimize Eq. (20). In the numerical experiments performed in Ref. [33], the network structure, e.g. number and connectivity of hidden layers, was not fixed a priori, but rather optimized via the Hyperopt [64] and Keras [65] packages. It was found that, for example, when $M = 3$, the resulting optimal network consists of two hidden layers, both with rectified linear unit (ReLU) activation functions, with 100 and 56 neurons, respectively. For a larger number of moments, $M = 10$, the resulting optimal network was found with three hidden layers, with, respectively, exponential linear unit (ELU), ReLU and linear activation functions, with 61, 87 and 47 neurons respectively.

After training with given M , the resulting model $\mathcal{E}_M^{\text{ML}}$ can be used to predict \mathcal{E} from a set of experimentally measured moments. The machine learning predictions, using a trained neural network with moments up to $M = 3$, are shown in Fig. 4 as a smooth surface (aside from the non-analyticity due to enforced constraint $\mathcal{E} \geq 0$), while real data are represented as discrete points. As shown in the Figure, the predictions from the neural network are very accurate and interpolate very well the real mapping. In that figure, we consider fixed Hilbert space dimensions, with $N_A = N_B$ qubits in A and B , so the first moment μ_0 is the same for all data, unlike what has been shown in Figs. 1 and 2.

Fig. 4 Logarithmic negativity as a function of μ_2 and μ_3 for a random set of density matrices with $N_A = N_B = 5$. The green points represent the real logarithmic negativities, while the surface shows the neural network's predictions for the whole space. Reprinted from [33].



4.1 Choice of the Training Set

Training is performed by taking a large set of states for which μ_m and \mathcal{E} can be computed on a classical computer. The experimental system of interest motivates the choice of the states to generate the training data. For instance, one may use states that share similar entanglement features to the ones that can be obtained in experiments.

We can always think of the mixed state ρ_{AB} as being the reduced density matrix of a tripartite pure state $|\Psi_{ABC}\rangle$. Without loss of generality, we assume that each subsystem is made of N_A , N_B and N_C qubits, respectively. From an entanglement perspective, relevant states in condensed matter physics can be classified as either area-law or volume-law. In area-law states, the entanglement of a subsystem A with the rest is proportional to the number of qubits along their boundary, while in volume-law states, this entanglement is proportional to N_A . Area-law states arise as low-energy eigenstates of local gapped Hamiltonians, with logarithmic corrections in critical systems. Volume-law states, however, are associated with the eigenstates found in the mid-spectrum and as such arise in non-equilibrium dynamics, such as quantum quenches [66, 67].

In the numerical experiments performed in Ref. [33], the training set consisted of very general classes of random states, constructed in such a way to contain both area- and volume-law states. More precisely, such random mixed states were generated by first obtaining a random pure state $|\Psi_{ABC}\rangle$ according to the different protocols described below, for different values of N_A , N_B , and N_C , and then performing a partial trace over C . The random pure states were generated either as

RGPS *Random Generic Pure States*, obtained by generating random vectors with complex elements distributed according to the normal distribution. RGPSs obtained by sampling from the Haar measure have also been considered, though they are numerically more demanding, and provided the same results. Both of these states typically have volume-law entanglement [68, 69].

RMPS *Random Matrix Product States* with fixed bond dimension D , which satisfy an area-law by construction [10]. These can be obtained by writing

$$|\psi\rangle = \sum_{\{i_j\}} \text{Tr} \left[A^{(1),i_1} A^{(2),i_2} \dots A^{(N),i_N} \right] |i_1, i_2, \dots, i_N\rangle \quad (21)$$

for random tensor components $A_{kl}^{(j),i}$ drawn from a normal distribution, where the indices run as $j = 1, \dots, N$, $i = 0, 1$, and $k, l = 1, \dots, D$.

Generation of the Training Set

In order to generate a training set with a wide range of entanglement features, subsystem sizes, and mixedness, the following procedure can be performed:

1. For a fixed number of qubits N , take either an RGPS or RMPS with bond dimension D .
2. Take different tri-partitions such that $N = N_A + N_B + N_C$, and for each calculate μ_m and \mathcal{E} for ρ_{AB} .
3. Repeat for different random instances, while separately varying N and D .

4.2 Sensitivity and Error Analysis

In an experimental setting predicting the expected logarithmic negativity is not enough, as it is also important to estimate eventual error bars. Although error estimates in neural networks are a theoretical open problem, one can infer the errors from training statistics, as discussed in Ref. [33], for example, by calculating the standard deviation in the error of the neural network predictions for unseen test data. Another important aspect is what happens when the input moments $\{\mu_m\}$ given to the trained neural network are inaccurate, for instance, due to imperfect measurements of finite sample statistics. For the latter point, small errors will only produce small changes to the estimate, since neural networks produce a smooth interpolating function. More precisely, the error in the entanglement estimation is given by the gradient of the neural network estimator with respect to the set of input moments $\{\mu_m\}$, multiplied by the measurement error, namely,

$$\Delta\mathcal{E} \approx \sum_m \Delta\mu_m \partial\mathcal{E}/\partial\mu_m, \quad (22)$$

where the partial derivative denotes the neural network sensitivity. With the procedure described in the previous sections, measuring the moments requires a number of operations that scale linearly with the system size. Moreover, in Ref. [33], it has been shown that the standard error (14) scales efficiently and that the number of repetitions R to have a good estimate of the moments scales sub-exponentially in the system size.

4.3 Comparison with Approximate State Reconstruction Methods

We now briefly compare our procedure with approximate state reconstruction scheme with a polynomial number of measurements. For instance, those based on tensor networks [31, 70] or neural network states [71, 72] are normally focused on finding an approximate representation of a state that accurately reproduces experimental observables. To state this in a mathematically precise way, let ρ_r be the experimentally reconstructed state from a polynomial number of measurements and suppose that the expectation values predicted by this state are ‘close enough’ to those predicted by the true state ρ , namely that $\text{Tr}[\rho_r A] \approx \text{Tr}[\rho A]$. Because of Helstrom’s theorem [20], if the states ρ and ρ_r are close with respect to the trace distance, $\|\rho - \rho_r\|_1 \sim \mathcal{O}(\epsilon)$, any expectation value obtained from the reconstructed state is ϵ -close to the true value. We may therefore assume that for a ‘good reconstruction’, such distance is small. Although this is true for any expectation value, entanglement measures are non-analytic functions of expectation values and, as such, may display a higher sensitivity to small errors in the reconstruction. Indeed, many entanglement measures are not continuous and, in particular, the entanglement negativity does not even satisfy the requirement of asymptotic continuity¹ (see Table 15.2 in [20]). As a consequence of the lack of this property, the entanglement of two ‘close’ many-body states can diverge $\mathcal{O}(N)$ for large N ; namely, the negativity computed from an approximate reconstruction of the state may be significantly different from the true one. Moreover, even if ρ_r is approximated with a polynomial number of measurements, since its Hilbert space grows exponentially with N and the negativity is a non-linear function of ρ_r , it is unclear whether the negativity can be obtained efficiently. In contrast, our method sidesteps all these problems by not trying to reconstruct the state, but rather accessing a single quantity, the logarithmic negativity from carefully designed measurements.

5 Numerical Results

The difference between the true logarithmic negativity \mathcal{E} and the machine learning prediction $\mathcal{E}_M^{\text{ML}}$ was extensively studied in Ref. [33], both for random states and for states generated in physical evolutions. For instance, for random states, the distribution of $\mathcal{E}_M^{\text{ML}} - \mathcal{E}$ was found to have a sharp peak in zero, with standard deviations ~ 0.09 for $M = 3$ and ~ 0.07 for $M = 10$. Although a higher number of copies were particularly good in diminishing outliers, they did not increase too

¹ Consider two N qubit states ρ and σ such that $\|\rho - \sigma\| \rightarrow 0$ for large N (many particles). A measure is asymptotically continuous if $\|\rho - \sigma\|_1 \rightarrow 0$ implies $|\mathcal{E}(\rho) - \mathcal{E}(\sigma)|/\log(d_N) \rightarrow 0$, where $d_N = 2^N$ is the Hilbert space dimension.

much the accuracy of the *average* prediction, which was remarkably good already with a maximum of $M = 3$ copies. Moreover, the following central observation was found:

The machine learning entanglement estimator works particularly well for highly entangled states with large logarithmic negativity. This is particularly important since approximate state reconstruction methods normally fail in this regime.

In the following sections, we demonstrate the ability of our machine learning estimator, which we remind is trained only with random states and no underlying knowledge of any physical evolution, to predict the amount of entanglement in different classes of physical states. Some of the considered states have particular symmetries and structure that is completely unknown to the machine learning model and not present in the training set made with random states. It is therefore possible that these predictions can be significantly enhanced by using a training set where the states possess all the symmetries of the physical model of interest.

5.1 Ground States Through a Quantum Phase Transition

We consider a paradigmatic model of many-particle spin systems whose ground state has interesting entanglement content, namely the one-dimensional isotropic XY spin chain with transverse field

$$H_{XX} = \sum_{i=1}^{L-1} \left(\sigma_i^X \sigma_{i+1}^X + \sigma_i^Y \sigma_{i+1}^Y \right) + B_Z \sum_{i=1}^L \sigma_i^Z, \quad (23)$$

where B_Z is the strength of the transverse field, L is the length of the chain and σ_j^α are the Pauli matrices acting on site j . The above model displays a quantum phase transition at $B_Z = 1$, above which the system enters a phase with a separable ground state.

The true and predicted logarithmic negativities are shown in Fig. 5 as a function of B_Z for a variety of configurations and different number of moments $M = 3, 6$. The different configurations are obtained by dividing the chain of length $L = N_A + N_B + N_C$ into three adjacent blocks of sizes N_A , N_B and N_C , respectively. For each value of B_Z , one first calculates the ground state of H_{XX} and then generates ρ_{AB} by tracing out system C . For entangled ground states, in general, ρ_{AB} is mixed as long as $N_C > 0$. As clearly shown in Fig. 5, the machine learning model, trained solely with random states, is able to accurately reproduce the amount of entanglement and to clearly spot both the phase transition point and the different entanglement

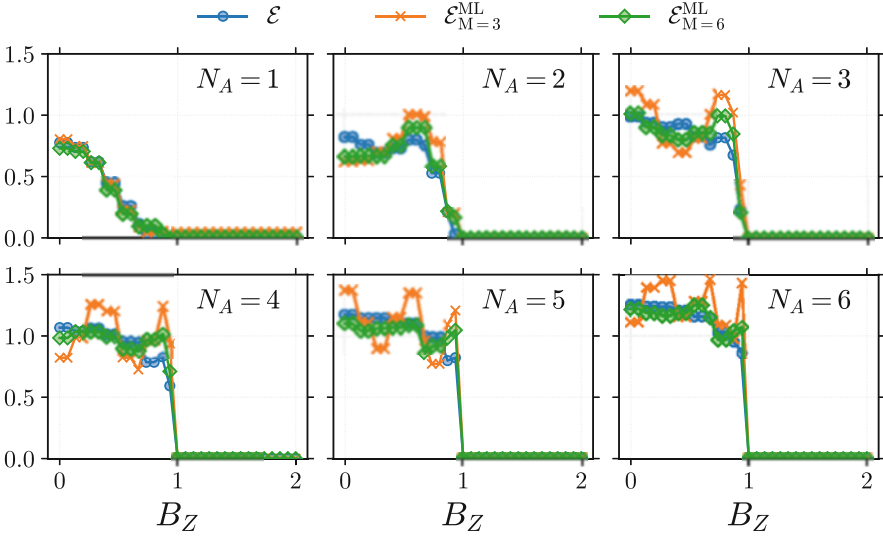


Fig. 5 Entanglement estimation in the ground state of the XX model phase across the phase transition driven by transverse field, B_Z . The ground state of total length $L = 20$ is tri-partitioned, with two adjacent subsystems of size $N_A = N_B$ and environment size $N_C = L - N_A + N_B$. The entanglement between A and B is then computed and estimated from ρ_{AB} . The blue, orange and green lines show the true logarithmic negativity, the neural network estimated quantity with 3 copies, and the neural network estimated quantity with 6 copies, respectively. Reprinted from [33]

content in the two phases. The model with $M = 3$ displays some small fluctuations for $N_A \geq 4$ that are significantly suppressed by the model trained with $M = 6$. It is remarkable that the neural network can capture the entanglement properties of these highly symmetric ground states despite having only been trained with random states.

5.2 Quench Across a Phase Transition

In this section, we study the states generated by a quantum quench in a many-body system. In strongly interacting many-body systems, the eigenstates of the Hamiltonian typically change if the model parameters are changed. A quantum quench exploits this mathematical fact to generate interesting quantum dynamics, often with a high amount of entanglement. More precisely, in a quantum quench, the evolution starts at $t = 0$ in the ground state of the model Hamiltonian with certain parameters, and then for $t > 0$, the state is let to evolve according to the same Hamiltonian but with different parameters. Here, we consider the transverse

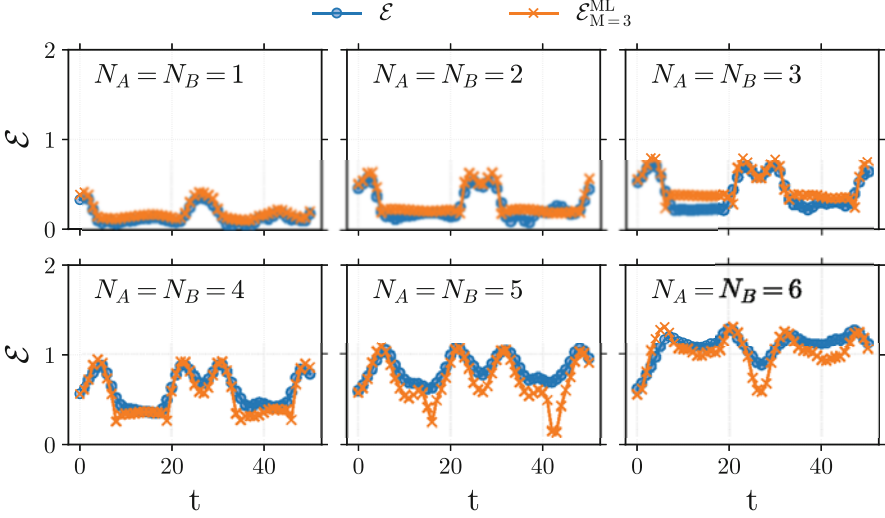


Fig. 6 Estimated entanglement when quenching across the Ising phase transition at $B_X = 1$. The initial state is the ground state at $B_X = 1 + \Delta$, and dynamics are generated by quenching with the Hamiltonian at $1 - \Delta$, taking $\Delta = 0.2$. The total size is $L = 20$ and the tri-partition is chosen so that subsystems A and B are adjacent and of equal size. The blue and orange lines show the true logarithmic negativity and the neural network estimated quantity with 3 copies, respectively. Reprinted from [33]

field Ising chain, whose Hamiltonian is

$$H_{\text{Ising}}(B_X) = \sum_{i=1}^{L-1} \sigma_i^Z \sigma_{i+1}^Z + B_X \sum_{i=1}^L \sigma_i^X, \quad (24)$$

where B_X is the strength of the magnetic field and L is the chain length. This model displays a second-order phase at the critical point $B_X = 1$. As in the previous section, we divide the chain into three adjacent blocks and study the entanglement between blocks A and B , here generated during the quench dynamics. We initially set the system in the ground state of $H_{\text{Ising}}(1 + \Delta)$ and then consider its evolution under the Hamiltonian $H_{\text{Ising}}(1 - \Delta)$ for different times t . The true and predicted logarithmic negativities as a function of t are shown in Fig. 6 for different block lengths. Only results with $M = 3$ are shown since they already have good accuracy. This numerical test shows that our method is particularly accurate in predicting the logarithmic negativity of highly entangled states, such as those typically occurring in quantum quenches.

5.3 *W-State*

In this section, we try to stress our machine learning model, by using states with very different properties than those used in the training set, which is made of random states with no symmetries and typically large amounts of entanglement. Here, on the other hand, we focus on the so-called *W-states*, a class of lowly entangled and highly symmetric states defined as

$$|W_L\rangle = \frac{1}{\sqrt{L}} (|100\cdots 0\rangle + |010\cdots 0\rangle + \cdots + |000\cdots 1\rangle), \quad (25)$$

for L qubits. This state can be exactly represented as a matrix product state with bond dimension 2, making it a non-trivial many-body state with basically lowest entanglement. Moreover, it is fully symmetric upon qubit permutations and is therefore very different from the random states in the training set. Similarly to the previous sections, the L qubits are partitioned into three adjacent blocks, where block C is traced out and the entanglement between A and B is studied. The resulting state ρ_{AB} is mixed for $N_C > 0$. Since the state is fully symmetric, the choice of the partition is irrelevant.

The true and predicted logarithmic negativities are shown in Fig. 7 for some representative combinations of sizes and for two different neural network models built with either $M = 3$ or $M = 6$. In Fig. 7, we see that good accuracy is provided by the 6-copy scheme, while the 3-copy scheme is only able to capture the overall trend. As previously mentioned, these states were expected to be among the most difficult, given our choice of the training set. It is likely that better results can be obtained by training the machine learning model with data generated by highly symmetric and lowly entangled states. Nonetheless, we remark that, as also more extensively discussed in Ref. [33], the machine learning prediction based on moments works better for highly entangled states, while for lowly entangled states, it would be feasible to use MPS-tomography [31], which is efficient for low levels of entanglement.

6 Conclusions

The measurement of entanglement in quantum many-body systems is a challenging task, especially for mixed states. All known computable entanglement measures depend non-linearly on the state, so the standard approach to quantify entanglement would require a complete state tomography, a highly demanding and not scalable experimental procedure, followed by complex manipulations of matrices whose dimension increases exponentially in the number of qubits. Here, we have reviewed a different method, first proposed in Ref. [33], based on the reconstruction of the ‘PT moments’, namely the moments of the partially transposed density matrix

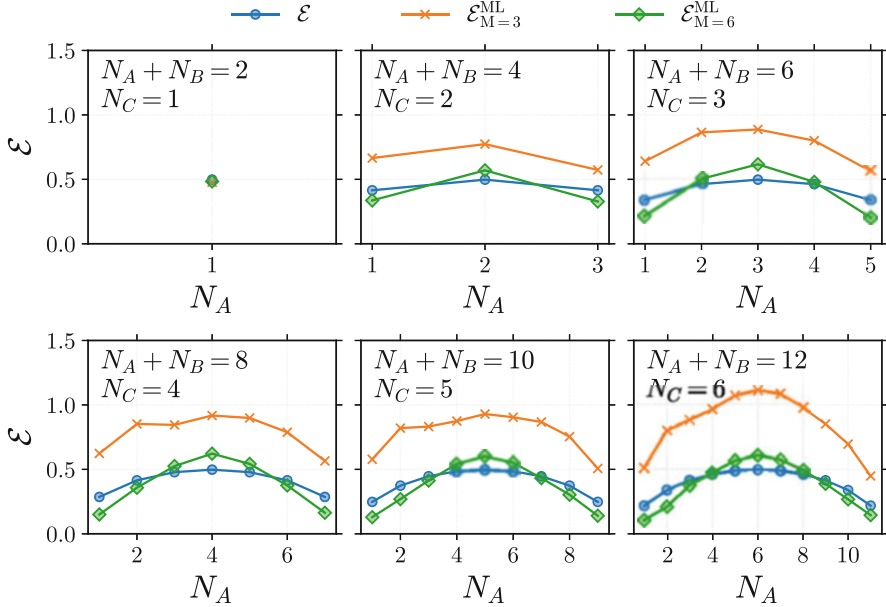


Fig. 7 Entanglement estimation in the W-state. We show here a representative sample of the entanglement estimation in the W-state for various lengths ($L = N_{A+B} + N_C$) and partitions, as a function of subsystem A size, N_A . The blue, orange and green lines show the true logarithmic negativity, the neural network estimated quantity with 3 copies, and the neural network estimated quantity with 6 copies, respectively. Reprinted from [33]

of a quantum many-body mixed state, using efficient experimental procedures. Related experimental techniques have already been demonstrated with different physical platforms such as quantum dot arrays [73, 74] and cold atoms in optical lattices [21, 75]. Our method is based on the observation that the relation between PT moments and logarithmic negativity is basically smooth, so that it can be learnt by machine learning interpolation methods. By extensive numerical simulations, it was found that neural networks, trained with outcomes coming from random quantum states, generally provide the most accurate and generalizable results. Here, the neural network-based approach has been reviewed and applied to different states that appear either in the ground state or in the dynamics of quantum many-body systems. We find quite remarkable that a model trained using random quantum states, with no knowledge of the underlying physical system, is able to accurately estimate the logarithmic negativity for all checked bipartitions and with as few as three copies of the physical system. We finally note that although different schemes are needed to measure the moments in fermionic and bosonic systems, once these are obtained, there should be no difference in extracting the logarithmic negativity, since the random data used for training the neural network could either represent spins or hard-core bosons.

Acknowledgments The author acknowledges support by the programme “Rita Levi Montalcini” for young researchers.

References

1. C.R. Rao, Bull. Calcutta Math. Soc **37**(3), 81 (1945)
2. P.W. Shor, SIAM Rev. **41**(2), 303 (1999)
3. A.W. Harrow, A. Hassidim, S. Lloyd, Phys. Rev. Lett. **103**(15), 150502 (2009)
4. C.H. Bennett, G. Brassard, C. Crépeau, R. Jozsa, A. Peres, W.K. Wootters, Phys. Rev. Lett. **70**(13), 1895 (1993)
5. A.K. Ekert, Phys. Rev. Lett. **67**(6), 661 (1991)
6. S. Pirandola, R. Laurenza, C. Ottaviani, L. Banchi, Nat. Commun. **8**(1), 1 (2017)
7. S. Pirandola, U.L. Andersen, L. Banchi, M. Berta, D. Bunandar, R. Colbeck, D. Englund, T. Gehring, C. Lupo, C. Ottaviani, et al., Adv. Opt. Photon. **12**(4), 1012 (2020)
8. L. Banchi, Q. Zhuang, S. Pirandola, Phys. Rev. Appl. **14**(6), 064026 (2020)
9. L. Amico, R. Fazio, A. Osterloh, V. Vedral, Rev. Mod. Phys. **80**(2), 517 (2008)
10. U. Schollwöck, Ann. Phys. **326**(1), 96 (2011)
11. B. Reznik, Found. Phys. **33**(1), 167 (2003)
12. A. Bayat, P. Sodano, S. Bose, Phys. Rev. B **81**(6), 064429 (2010)
13. B. Alkurtass, A. Bayat, I. Affleck, S. Bose, H. Johannesson, P. Sodano, E.S. Sørensen, K. Le Hur, Phys. Rev. B **93**(8), 081106 (2016)
14. J. Gray, S. Bose, A. Bayat, Phys. Rev. B **97**(20), 201105 (2018)
15. L. Banchi, F. Colomo, P. Verrucchi, Phys. Rev. A **80**(2), 022341 (2009)
16. T. Roscilde, P. Verrucchi, A. Fubini, S. Haas, V. Tognetti, Phys. Rev. Lett. **93**(16), 167203 (2004)
17. L. Banchi, A. Bayat, S. Bose, Phys. Rev. B **94**(24), 241117 (2016)
18. R. Horodecki, P. Horodecki, M. Horodecki, K. Horodecki, Rev. Mod. Phys. **81**(2), 865 (2009)
19. M.B. Plenio, S. Virmani, Quantum Inf. Comput. **7**(1), 1 (2007)
20. I. Bengtsson, K. Życzkowski, *Geometry of Quantum States: An Introduction to Quantum Entanglement* (Cambridge University, Cambridge, 2006)
21. R. Islam, R. Ma, P.M. Preiss, M.E. Tai, A. Lukin, M. Rispoli, M. Greiner, Nature **528**(7580), 77 (2015)
22. I. Pitsios, L. Banchi, A.S. Rab, M. Bentivegna, D. Caprara, A. Crespi, N. Spagnolo, S. Bose, P. Mataloni, R. Osellame, et al., Nat. Commun. **8**(1), 1 (2017)
23. W.K. Wootters, Phys. Rev. Lett. **80**(10), 2245 (1998)
24. C. Weedbrook, S. Pirandola, R. García-Patrón, N.J. Cerf, T.C. Ralph, J.H. Shapiro, S. Lloyd, Rev. Mod. Phys. **84**(2), 621 (2012)
25. M.M. Wolf, G. Giedke, O. Krüger, R. Werner, J.I. Cirac, Phys. Rev. A **69**(5), 052320 (2004)
26. K. Życzkowski, P. Horodecki, A. Sanpera, M. Lewenstein, Phys. Rev. A **58**(2), 883 (1998)
27. J. Lee, M. Kim, Y. Park, S. Lee, J. Mod. Opt. **47**(12), 2151 (2000)
28. G. Vidal, R.F. Werner, Phys. Rev. A **65**(3), 032314 (2002)
29. M.B. Plenio, Phys. Rev. Lett. **95**(9), 090503 (2005)
30. Y. Huang, New J. Phys. **16**(3), 033027 (2014)
31. B. Lanyon, C. Maier, M. Holzäpfel, T. Baumgratz, C. Hempel, P. Jurčević, I. Dhand, A. Buyskikh, A. Daley, M. Cramer, et al., Nat. Phys. **13**(12), 1158 (2017)
32. P. Calabrese, J. Cardy, E. Tonni, Phys. Rev. Lett. **109**(13), 130502 (2012)
33. J. Gray, L. Banchi, A. Bayat, S. Bose, Phys. Rev. Lett. **121**(15), 150503 (2018)
34. J. Carrasquilla, R.G. Melko, Nat. Phys. **13**(5), 431 (2017)
35. G. Carleo, M. Troyer, Science **355**(6325), 602 (2017)
36. A. Hentschel, B.C. Sanders, Phys. Rev. Lett. **104**(6), 063603 (2010)
37. L. Banchi, N. Pancotti, S. Bose, npj Quantum Inf. **2**, 16019 (2016)

38. L. Banchi, E. Grant, A. Rocchetto, S. Severini, *New J. Phys.* **20**(12), 123030 (2018)
39. A. Peres, *Phys. Rev. Lett.* **77**(8), 1413 (1996)
40. M. Horodecki, P. Horodecki, R. Horodecki, *Phys. Lett. A* **283**(1–2), 1 (2001)
41. H.A. Carteret, *Phys. Rev. Lett.* **94**(4), 040502 (2005)
42. J. Cai, W. Song, *Phys. Rev. Lett.* **101**(19), 190503 (2008)
43. K. Bartkiewicz, P. Horodecki, K. Lemr, A. Miranowicz, K. Życzkowski, *Phys. Rev. A* **91**, 032315 (2015)
44. A. Elben, R. Kueng, H.Y.R. Huang, R. van Bijnen, C. Kokail, M. Dalmonte, P. Calabrese, B. Kraus, J. Preskill, P. Zoller, et al., *Phys. Rev. Lett.* **125**(20), 200501 (2020)
45. Y. Zhou, P. Zeng, Z. Liu, *Phys. Rev. Lett.* **125**(20), 200502 (2020)
46. M. Horodecki, P. Horodecki, R. Horodecki, *Phys. Lett. A* **223**(1), 1 (1996)
47. M. Lewenstein, B. Kraus, J. Cirac, P. Horodecki, *Phys. Rev. A* **62**(5), 052310 (2000)
48. L.R. Mead, N. Papanicolaou, *J. Math. Phys.* **25**(8), 2404 (1984)
49. G. Viano, *J. Math. Anal. Appl.* **156**(2), 410 (1991)
50. S. Rana, *Phys. Rev. A* **87**(5), 054301 (2013)
51. R.F. Werner, *Phys. Rev. Lett.* **40**(8), 4277 (1989)
52. A.K. Ekert, C.M. Alves, D.K. Oi, M. Horodecki, P. Horodecki, L.C. Kwak, *Phys. Rev. Lett.* **88**(21), 217901 (2002)
53. P. Horodecki, A. Ekert, *Phys. Rev. Lett.* **89**(12), 127902 (2002)
54. A. Daley, H. Pichler, J. Schachenmayer, P. Zoller, *Phys. Rev. Lett.* **109**(2), 020505 (2012)
55. D.A. Abanin, E. Demler, *Phys. Rev. Lett.* **109**(2), 020504 (2012)
56. M. Reck, A. Zeilinger, H.J. Bernstein, P. Bertani, *Phys. Rev. Lett.* **73**(1), 58 (1994)
57. J.P. Blaizot, G. Ripka, *Quantum Theory of Finite Systems*, vol. 3 (MIT Press, Cambridge, 1986)
58. C. De Nobili, A. Coser, E. Tonni, *J. Stat. Mech: Theory Exp.* **2015**(6), P06021 (2015)
59. L. Banchi, J. Pereira, S. Pirandola, *PRX Quantum* **2**, 040321 (2021)
60. N. Cristianini, J. Shawe-Taylor, *An Introduction to Support Vector Machines and Other Kernel-Based Learning Methods* (Cambridge University, Cambridge, 2000)
61. T.K. Ho, *IEEE Trans. Pattern Anal. Mach. Intell.* **20**(8), 832 (1998)
62. R. Rojas, *Neural Networks: A Systematic Introduction* (Springer, Berlin, 2013)
63. J. Schmidhuber, *Neural Netw.* **61**, 85 (2015)
64. J. Bergstra, D. Yamins, D. Cox, in *International Conference on Machine Learning* (2013), pp. 115–123
65. F. Chollet, et al. Keras (2015)
66. P. Barmettler, M. Punk, V. Gritsev, E. Demler, E. Altman, *Phys. Rev. Lett.* **102**(13), 130603 (2009)
67. A. Nandori, H. Kim, D.A. Huse, *Phys. Rev. B* **90**(6), 064201 (2014)
68. S. Popescu, A.J. Short, A. Winter, *Nat. Phys.* **2**(11), 754 (2006)
69. A. Hama, S. Santra, P. Zanardi, *Phys. Rev. Lett.* **109**(4), 040502 (2012)
70. M. Cramer, M.B. Plenio, S.T. Flammia, R. Somma, D. Gross, S.D. Bartlett, O. Landon-Cardinal, D. Poulin, Y.K. Liu, *Nat. Commun.* **1**, 149 (2010)
71. G. Torlai, G. Mazzola, J. Carrasquilla, M. Troyer, R. Melko, G. Carleo, *Nat. Phys.* **14**(5), 447 (2018)
72. G. Torlai, R.G. Melko, *Phys. Rev. Lett.* **120**(24), 240503 (2018)
73. J.R. Petta, A.C. Johnson, J.M. Taylor, E.A. Laird, A. Yacoby, M.D. Lukin, C.M. Marcus, M.P. Hanson, A.C. Gossard, *Science* **309**(5744), 2180 (2005)
74. M. Schuld, I. Sinayskiy, F. Petruccione, *Contemp. Phys.* **56**(2), 172 (2015)
75. S. Trotzky, P. Cheinet, S. Fölling, M. Feld, U. Schnorrberger, A.M. Rey, A. Polkovnikov, E. Demler, M. Lukin, I. Bloch, *Science* **319**(5861), 295 (2008)

Local Convertibility in Quantum Spin Systems



Luigi Amico, Vladimir Korepin, Alioscia Hamma, Salvatore Marco Giampaolo, and Fabio Franchini

Abstract Local Convertibility refers to the possibility of transforming a given state into a target one, just by means of LOCC with respect to a given bipartition of the system, and it is possible if and only if all the Rényi entropies of the initial state are smaller than those of the target state. We apply this concept to adiabatic evolutions and ask whether they can be rendered through LOCC in the sense above. We argue that a lack of differential local convertibility (dLC) signals a higher computational power of the system's quantum phase, which is also usually connected with the existence of long-range entanglement, topological order, or edge states. Remarkably, dLC can detect these global properties already by considering small subsystems. Moreover, we connect dLC to spontaneous symmetry breaking by arguing that states with finite order parameters must be the most classical ones and thus be locally convertible.

Entanglement is one of the primary resources for quantum technology [1–7], as it encodes the possibility of storing a large amount of information on a registry on

L. Amico

Quantum Research Centre, Technology Innovation Institute, Abu Dhabi, UAE

Centre for Quantum Technologies, National University of Singapore, Singapore, Singapore
On leave from Dipartimento di Fisica e Astronomia, Catania, Italy

LANEF 'Chaire d'excellence', Université Grenoble-Alpes and CNRS, Grenoble, France
e-mail: luigi.amico@tii.ae

V. Korepin

C. N. Yang Institute for Theoretical Physics, Stony Brook University, Stony Brook, NY, USA
e-mail: vladimir.korepin@stonybrook.edu

A. Hamma

Physics Department, University of Massachusetts Boston, Boston, MA, USA
e-mail: alioscia.hamma@umb.edu

S. M. Giampaolo · F. Franchini (✉)

Ruder Bošković Institute, Bijenička cesta 54, Zagreb, Croatia
e-mail: sgiampa@irb.hr; fabio@irb.hr; Fabio.Franchini@irb.hr

one side and to change a state even in parts that are not directly manipulated [8, 9]. However, it is also clear that it is not the mere amount of entanglement, which is important, but rather how it is distributed and how effectively it can be used [citealgorithm, gottesman, vidal2003a, vandernest2007, Briegel08, winter, eisert, Briegel09, vandernest2013, Raussendorf13].

The quantum adiabatic algorithm provides a good paradigm to test the properties of a given phase of matter, as it has been proven to provide a universal platform for quantum computation [20]. It is based on the idea that starting from a simple system with a known ground state, through a suitable adiabatic evolution, the final ground state can encode the result of a computation or the state of a quantum system one aims at simulating. Since the closing of the gap forces a dramatic slowdown in the rate at which the Hamiltonian can be changed and the system expected to remain in its instantaneous ground state, crossing a phase transition through the evolution typically impairs the efficacy of an adiabatic algorithm. Hence, for this algorithm to provide a nontrivial advantage, the choice of the initial quantum phase is crucial.

A criterion for this choice is provided by the concept of *differential Local Convertibility* (dLC), which addresses the question of whether it is possible to reproduce the adiabatic evolution of a bipartite quantum system through Local Operations and Classical Communications (LOCCs) [21, 22]. Namely, upon partitioning a many-body system into two blocks A and B , one questions whether the response of the ground state $|0\rangle$ to an external perturbation can be rendered through LOCC *restricted to A and B individually*? If affirmative, the ground state can be moved around within a given quantum phase by LOCC. If negative, the adiabatic evolution induced by the perturbation cannot be captured classically (due to the long-range coherence present in the system). Quantitatively, it accounts for the response of the Rényi entropy

$$S_\alpha \doteq \frac{1}{1-\alpha} \log \text{Tr} \rho_A^\alpha \quad (1)$$

to the changing of a control parameter g in the Hamiltonian. Here, $\rho_A \doteq \text{Tr}_B |0\rangle\langle 0|$ is the reduced density matrix of the block A and α is a free parameter which tunes different entanglement measures [23]. For instance, while low α 's weight more evenly all eigenvalues of ρ_A , higher values of α enhance the role of the larger eigenvalues. If all the Rényi entropies decrease along a given path, this evolution can also be rendered through LOCC (at least concerning the chosen partition of A and B) [24, 25], and thus the adiabatic algorithm cannot provide a significant improvement. This observation was at the heart of [26, 27].

Naïvely, one expects entanglement to always grow toward a phase transition. In particular, $S_0 = \log R$, where R is the Schmidt rank of the state, i.e., the number of nonzero eigenvalues of ρ_A (while S_1 is the von Neumann entropy measuring the entanglement entropy for the subsystem A). Generically, R and thus S_0 increase with ξ because more degrees of freedom get entangled by increasing the range of correlations. Nonetheless, the study of Local Convertibility shows that the picture is more complex when higher α entropies are considered. Certain systems

can support other forms of entanglement not captured by local correlation, which are referred to as long-range entanglement (LRE) [28]. If the latter would decrease approaching a phase transition, the competition between the different forms of entanglement could be detected as a lack of dLC in all directions.

A simple form of LRE is connected to the existence of edge states at distant boundaries of a system [29, 30]. Furthermore, these edge states are usually the reflection of the existence of some sort of topological order. Interestingly, upon partitioning a system into two, new pairs of edge states are created also at the boundaries of the partitions. While for thermodynamic systems, the LRE connecting the edge states is maximal, when the size of one of the partitions becomes comparable with the correlation length, the edge state can undergo a process of recombination which reduces their LRE. Through this mechanism, higher R enyi entropies can decrease as the correlation length increases, thus destroying dLC in any directions of the adiabatic evolution. The behavior of dLC in relation to quantum phase transitions and at criticality has been analyzed, respectively, in [31] and [32].

In addition to shedding new light on the role of edge states in providing a key advantage in a universal quantum computational platform, dLC also proves useful in identifying phases characterized by LRE. LRE is defined as that entanglement that cannot be destroyed by reducing the state to a trivial (factorized) one through a finite depth quantum circuit [28]. As such, it is usually revealed through nonlocal string order parameters whose lengths exceed the order of usual correlations. Remarkably, dLC can detect LRE using partitions of the order of the correlation length, thus providing a somewhat local probe of an elusive long-range property [33–37]. We will analyze a few examples of models displaying topological order in light of their local convertibility. Topological phases have attracted a lot of attention for their ability to defy the Ginzburg–Landau paradigm by not having any finite local order parameter, but rather a topological one [38, 39].

However, dLC has also been connected to the usual spontaneous symmetry breaking mechanism responsible for the ensuing of local order [40]. In particular, on the whole, the complete understanding of the physical mechanism that selects the symmetry-breaking ground states in the thermodynamic limit remains an open problem [41, 42]. In complete analogy with the case of classical phase transitions driven by temperature, the common explanation of this phenomenon invokes the unavoidable presence of some local, however small, perturbing external field that selects one of the maximally symmetry-breaking ground states (MSBGSs) among all the elements of the quantum ground space [43]. Crucially, in this type of reasoning, it is assumed that the MSBGSs are the most classical ones and thus the ones that are selected in real-world situations, under the effect of decoherence that quickly destroys macroscopic coherent superpositions.

At first glance, this notion appears to be obvious. For instance, in the paradigmatic case of the quantum Ising model, the ground space of the ferromagnetic phase at zero transverse fields h is spanned by two orthogonal product states $|0\rangle^{\otimes N}$ and $|1\rangle^{\otimes N}$ which are in the same class of pointer states of the typical decoherence argument, while the symmetric states $\Psi_{\pm} = 1/\sqrt{2}(|0\rangle^{\otimes N} \pm |1\rangle^{\otimes N})$ realize macroscopic coherent superpositions (Schrodinger cats) that are not stable

under decoherence [44, 45]. Therefore, at zero transverse fields h , the situation is very clear: the only stable states are those that maximally break the symmetry of the Hamiltonian and at the same time those that feature vanishing macroscopic total correlations, including entanglement, between spatially separated regions.

On the other hand, as we turn on the external field h , we have a whole range of values, below the critical field $h = h_c$, where it remains a finite magnetic order associated with spontaneous symmetry breaking [46], which implies an application of the decoherence argument within the entire, globally ordered phase. This means that, again, the only stable states are those that maximally break the Hamiltonian symmetry. However, now the symmetry-breaking states are entangled, and their mixed-state reductions on arbitrary subsystems possess in general nonvanishing pairwise entanglement [1, 48, 49], as well as pairwise quantum [50–52] and classical correlations [46]. It is thus now unclear if and in what sense the MSBGSs are the most classical among all quantum ground states.

Below we will provide a general conjecture on the nature of ordered quantum phases and the origin of spontaneous symmetry breaking, by comparing various quantifiers of local and global quantum correlations in symmetry-breaking and symmetry-preserving quantum ground states. We will first compare measures of local, pairwise quantum correlations and show that in symmetry-preserving ground states the two-body entanglement captures only a modest portion of the local, two-body quantum correlations, while in maximally symmetry-breaking ground states it accounts for the largest contribution. Next, we will introduce proper criteria and quantifiers of the degree of classicality of quantum states for their global contents of macroscopic entanglement and quantum correlations. Finally, we will show that, within the quantum ground space corresponding to macroscopically ordered phases with nonvanishing local order parameters, the MSBGSs are the most classical ground states in the sense that they are the only quantum ground states that satisfy the following two criteria for each set of Hamiltonian parameters consistent with an ordered quantum phase in the thermodynamic limit:

- *Local convertibility*—All global ground states are convertible into MSBGSs applying only local operations and classical communication (LOCC transformations), while the reverse transformation is impossible.
- *Entanglement distribution*—The MSBGSs are the only global ground states that minimize the residual tangle between a dynamical variable and the remainder of a macroscopic quantum system. Stated otherwise, the MSBGSs are the only ground states that satisfy the monogamy inequality—a strong constraint, with no classical counterpart, on the shared bipartite entanglement between all components of a macroscopic quantum system—at its minimum among all other possible ground states and thus minimize the macroscopic multipartite entanglement as measured by the residual tangle.

Verification of these two features amounts to proving that the mechanism of spontaneous symmetry breaking selects the most classical ground states associated with globally ordered phases of quantum matter with nonvanishing local order parameters.

This chapter is organized as follows: in Sects. 1, 2, and 3, we will analyze the dLC of the Cluster-Ising chain, of the $\lambda - D$ model and of the two-dimensional toric code with different perturbative terms, to show how all these models, characterized by different types of topological order, are not locally convertible. In Sect. 4, we will use the paradigmatic example of the Quantum Ising Chain to elucidate the role of edge states in dLC and thus to provide a picture of how LRE prevents convertibility and why small partitions can detect it. In Sect. 5, we detail the conjecture on the characterization of MSBGS as the most classical ones. Finally, we draw some conclusions in Sect. 6.

1 The Cluster-Ising Model

The first Hamiltonian we consider is

$$H(g) = - \sum_{j=1}^N \sigma_{j-1}^x \sigma_j^z \sigma_{j+1}^x + g \sum_{j=1}^N \sigma_j^y \sigma_{j+1}^y, \quad (2)$$

where σ_i^α and $\alpha = x, y, z$, are the Pauli matrices, and, except otherwise stated, we take open boundary conditions $\sigma_{N+1}^\alpha = \sigma_0^\alpha = 0$. The phase diagram of (2) has been investigated in [53, 54]. For large g , the system is an Ising antiferromagnet with a finite local order parameter. For $g = 0$, the ground state is a cluster state. It results that the correlation pattern characterizing the cluster state is robust up to a critical value of the control parameter, meaningfully defining a “cluster phase” with vanishing order parameter and string order [53, 54]. Without symmetry, the cluster phase is a (non-topological) quantum spin liquid since there is a gap and no symmetry is spontaneously broken. Protected by a $Z_2 \times Z_2$ symmetry, the cluster phase is characterized by a topological fourfold ground state degeneracy, reflecting the existence of edge states and fanning out from $g = 0$ where 4 Majorana fermions are left free at the ends of the chain [53, 55]. In the DMRG, we resolve the ground state degeneracy, by adding a small perturbation $\sigma_1^x \sigma_2^z \pm \sigma_{N-1}^z \sigma_N^x$ to the Hamiltonian. The Cluster and Ising phases are separated by a continuous quantum phase transition with central charge $c = 3/2$. Let us also note that the Hamiltonian (2) can be mapped to three decoupled Ising chains [53, 54].

Through a Jordan–Wigner transformation $\sigma_k^+ = c_k^\dagger \prod_{j < k} \sigma_j^z$, $\sigma_k^- = c_k \prod_{j < k} \sigma_j^z$, $\sigma_k^z = 2c_k^\dagger c_k - 1$, the Hamiltonian of the Cluster-Ising model can be written as

$$H(g) = -i \sum_k \left[f_k^{(2)} f_{k+2}^{(1)} - g f_k^{(1)} f_{k+1}^{(2)} \right], \quad (3)$$

where $f_k^{(1)} = c_k + c_k^\dagger$ and $f_k^{(2)} = -i(c_k - c_k^\dagger)$ are two types of Majorana fermion operators. Although no local order parameters exist to characterize the topological phase, the topological order in the Cluster-Ising model can be detected, see Fig. 1, by the edge states (a1) and string order parameters (a3).

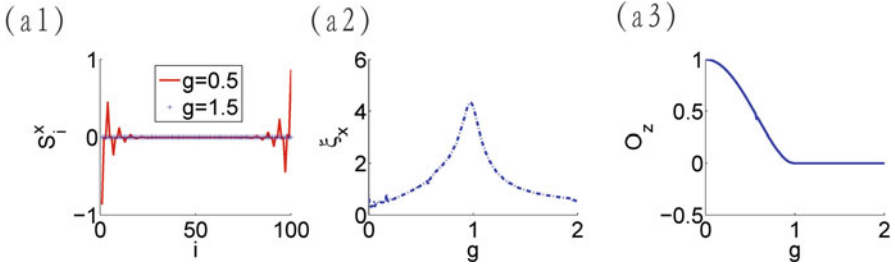


Fig. 1 The edge state, correlation length, and the string order parameter of the Cluster-Ising model. (a1) shows that there is edge state in the cluster phase, whereas there is no edge state in Ising antiferromagnetic phase. (a2) shows the correlation length of $\langle \sigma_n \sigma_{n+3} \rangle - \langle \sigma_n \rangle \langle \sigma_{n+3} \rangle$ displaying a critical behavior. (a3) is the string order parameter $O_z = (-)^{N-2} \langle \sigma_1^y \prod_{j=1}^{N-1} \sigma_j^z \sigma_N^y \rangle$

We find that the symmetric partition $A|A$ displays local convertibility, Fig. 2: (a1), (a2). This is indeed a fine-tuned phenomenon since the cluster phase results nonlocally convertible, for a generic block of spins, both of the type $A|B$ and the $B|A|B$, Fig. 2. We remark that such a property holds even for size region A smaller than the correlation length. Indeed, the entanglement spectrum is doubly degenerate in all the cluster phases, as far as the size of the blocks A and B is larger than the correlation length, see Fig. 3. In contrast, the antiferromagnet is locally convertible, with nondegenerate entanglement spectrum.

2 The $\lambda - D$ Model

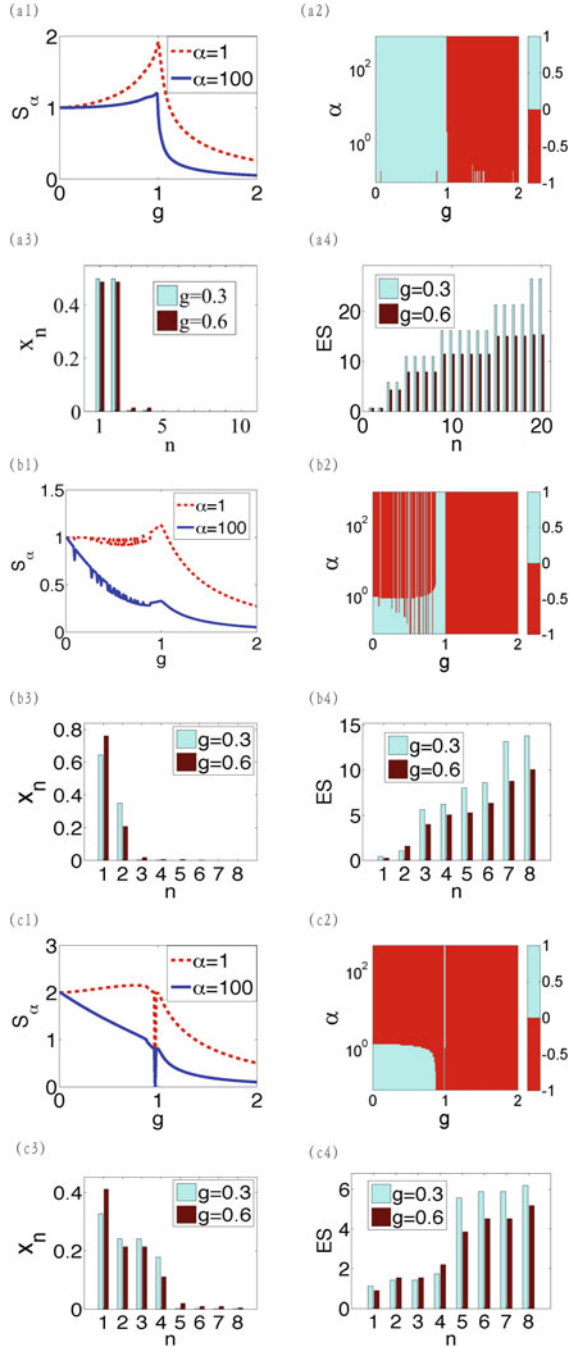
In this section, we study the local convertibility of the $\lambda - D$ model Hamiltonian describing an interacting spin-1 chain with a single-ion anisotropy

$$H = \sum_i \left[(S_i^x S_{i+1}^x + S_i^y S_{i+1}^y) + \lambda S_i^z S_{i+1}^z + D (S_i^z)^2 \right], \quad (4)$$

where S^u and $u = \{x, y, z\}$ are spin-1 operators: $S^z |\pm\rangle = \pm |\pm\rangle$ and $S^z |0\rangle = 0$. The phase diagram has been investigated by many authors [56–58]. The Hamiltonian above enjoys several symmetries, including time reversal $S^{x,y,z} \rightarrow -S^{x,y,z}$, parity $S^{x,y} \rightarrow -S^{x,y}$, $S^z \rightarrow S^z$ generating $Z_2 \times Z_2$, and the link inversion symmetry $S_j^u \rightarrow S_{-j+1}^u$.

We only consider $\lambda > 0$. For small/large D and fixed λ , the system is in a polarized state along $|+\rangle \pm |-\rangle$ or $|0\rangle$, respectively. For large λ and fixed D , the state displays antiferromagnetic order. At intermediate D and λ , the state is a “diluted antiferromagnet” with strong quantum fluctuations, defining the Haldane phase, which cannot be characterized through any local order parameter. With symmetry protection, the topological order in the Haldane phase can be detected by the edge

Fig. 2 The local convertibility and the entanglement spectrum of the Cluster-Ising model Eq. (2). We characterize the differential local convertibility in terms of the slopes of the Rényi entropies. Panel (a) is for bipartition $A|A$, $A = 50$. There is differential local convertibility throughout the two different phases because, for fixed g , $\partial_g S_\alpha$ does not change sign with α . Panel (b) is for bipartition $A|B$, $A = 3$, $B = 97$. Panel (c) is for $A|B|C$, being one block $A \cup C$ with $A = 48$, $C = 49$, and $B = 3$. Panels (a3, b3, c3) and (a4, b4, c4) display respectively the reduced density matrix eigenvalues x_n and the entanglement spectrum. The larger and the smaller eigenvalues of reduced density matrix x_n , respectively; $ES \doteq \{-\log x_n\}$. In convertible phases, we observe that the change in the largest eigenvalues is “faster” than the rate at which the smallest eigenvalues are populated. In contrast, the non-differential local convertibility arises because the sharpening of the first part of the spectrum is over-compensated by the increasing of the smallest x_n



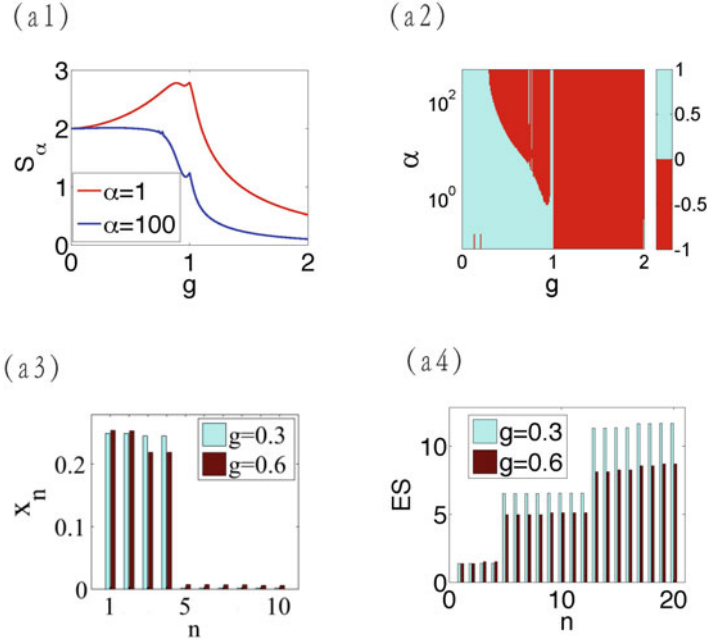


Fig. 3 The local convertibility and the entanglement spectrum of the Cluster-Ising model with bipartition 45|10|45. We characterize the differential local convertibility in terms of the slopes of the Rényi entropies. $\partial_g S_\alpha$ changes sign in the cluster phase. (a3) and (a4) display the largest and the smaller eigenvalues of reduced density matrix x_n , respectively; $ES \doteq \{-\log x_n\}$. In convertible phases, we observe that the change in the largest eigenvalues is “faster” than the rate at which the smallest eigenvalues are populated. In contrast, the non-differential local convertibility arises because the sharpening of the first part of the spectrum is over-compensated by the increasing of the smallest x_n

states and string order parameters defined in Fig. 4 (see [59]). Without symmetry, the ground state is gapped and no symmetry is spontaneously broken, making the Haldane phase a quantum spin liquid. In fact, for open boundary conditions (which we apply in the present analysis), the Haldane ground state displays a fourfold degeneracy, which cannot be lifted without breaking the abovementioned symmetry of the Hamiltonian. This is the core mechanism defining the Haldane phase as a symmetry-protected topological ordered phase [60, 61].

In Fig. 5, we display the schematic phase diagram of the $\lambda - D$ model. We sweep through the phase diagram in the following two ways: (1) fix $\lambda = 1$ and change D ; the Haldane phase is approximately located in the range $-0.4 \lesssim D \lesssim 0.8$. (2) Fix $D = 0$, varying on λ ; the Haldane phase is located in the range $0 \lesssim \lambda \lesssim 1.1$ (see Fig. 5). We analyzed the four states separately adding the perturbation to the Hamiltonian $\sim (S_1^z \pm S_N^z)$ with a small coupling constant to resolve the ground state degeneracy.

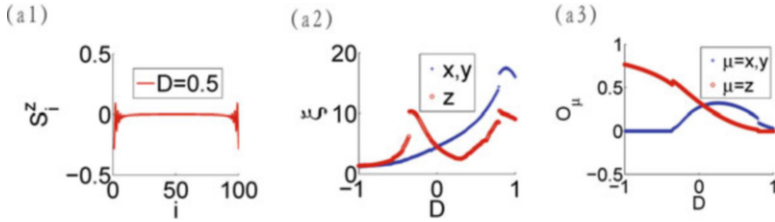


Fig. 4 The edge states, correlation lengths, and string order parameters of the $\lambda - D$ model. The sweep (1) through the $\lambda - D$ phase diagram is considered (see text). In (a1), $\lambda - D$ phase diagram is considered (see text). In (a1), we show the Haldane phase edge states; we do not find edge states in the other phases. In (a2), the string order parameters $\mathcal{O}_u = (-)^{N-2} \langle S_1^u \prod_{j=1}^{N-1} e^{i\pi S_j^u} S_N^u \rangle$. In (a3), the correlation length of $\langle S_j^u S_{j+n}^u \rangle - \langle S_j^u \rangle \langle S_{j+n}^u \rangle$

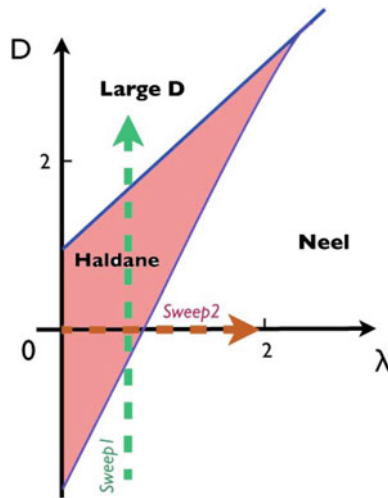


Fig. 5 We sweep through the phase diagram in the following two ways: (1) fix $\lambda = 1$ and change D ; the Haldane phase is approximately located in the range $-0.4 \lesssim D \lesssim 0.8$. (2) Fix $D = 0$, varying on λ ; the Haldane phase is located in the range $0 \lesssim \lambda \lesssim 1.1$

We find that the Néel, ferromagnetic, and the large D phases are locally convertible (see Fig. 6: (a1), (a2)). Consistently with [62], all of the Haldane ground states are characterized by doubly degenerate entanglement spectrum for the symmetric $A|B$ partitions with $A = B$, for both sweep ways (Fig. 6: (a3) and (a4)) (see [63] for an understanding of doubly degenerate entanglement spectrum). Such a property is not recovered in the cases of asymmetric $A|B$ and $A|B|A$ partitions: in these cases, the entanglement spectrum is not found doubly degenerate, because we broke the link inversion symmetry [62] (Fig. 6: (b3), (b4)). See also [64] for an analysis of the entanglement spectrum close to the quantum phase transitions.

We find that the Haldane phase is not locally convertible (see Figs. 6: (b1), (b2), 7, and 8). We remark that for both ways to partition the system the nonlocal-convertibility phenomenon is found even in the case of sizes of B smaller than the

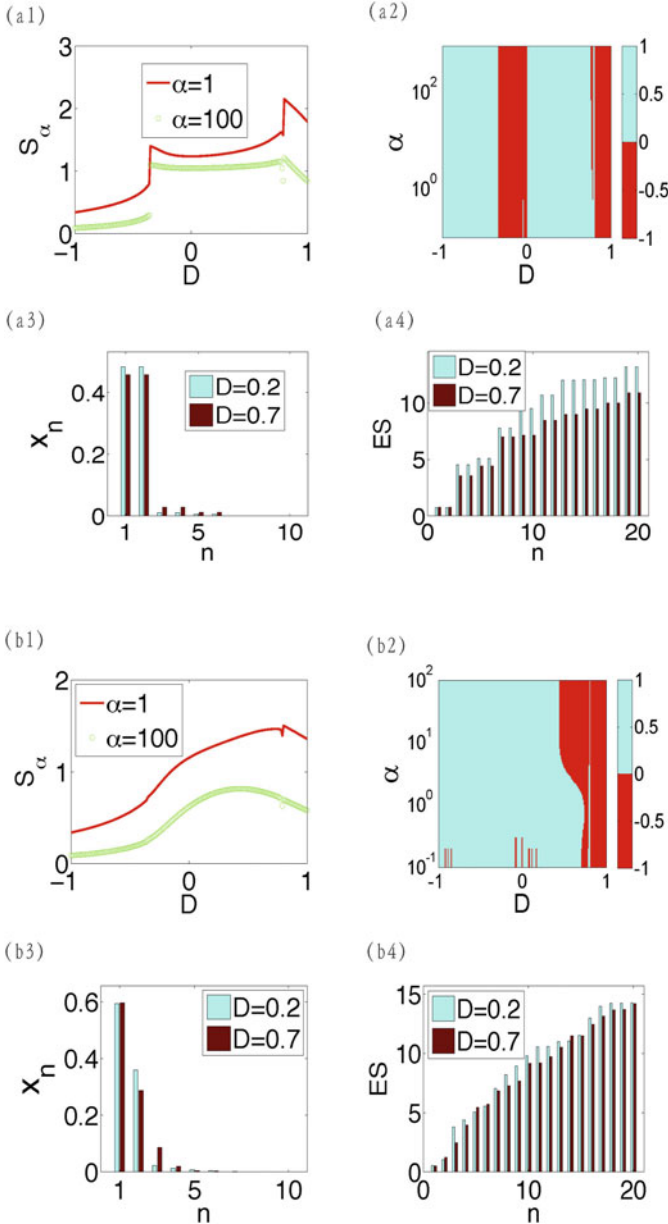


Fig. 6 The local convertibility for the partition $A|B$. The sweep (1) through the $\lambda - D$ phase diagram is considered (see also Fig. 5 for the schematic phase diagram). The upper panels display the results for the symmetric case $A|A$. The bottom panels refer to the antisymmetric case $A = 96, B = 4$. The Rényi entropies are presented in (a1), (b1). The sign distributions of the entropies' derivatives are shown in (a2), (b2). The eigenvalues of reduced density matrix x_n and the entanglement spectrum are shown in (a3), (a4), (b3), (b4) as in Fig. 2. The features of differential local convertibility are characterized by the slopes of the Rényi entropies and correspond to specific features of the entanglement spectrum as explained in Fig. 2

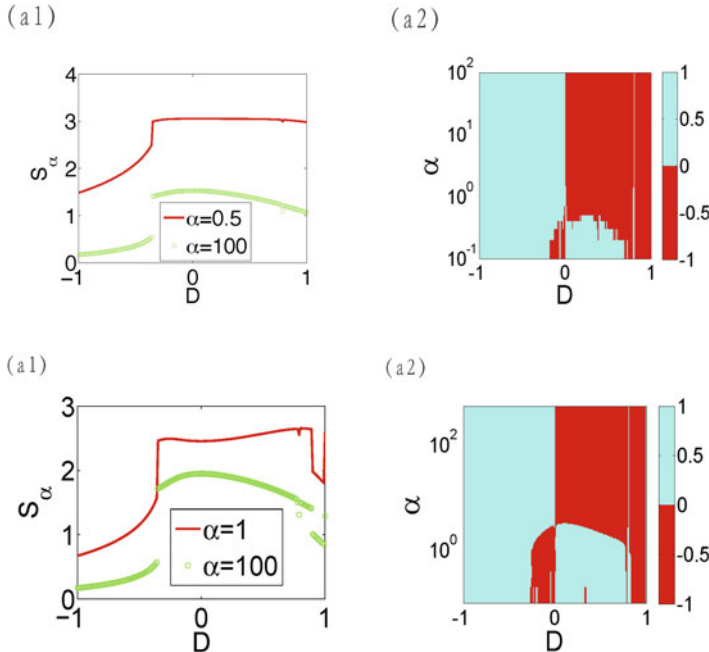


Fig. 7 Sweep (1) through the $\lambda - D$ model: $\lambda = 1$, $D \in \{-1, 1\}$. The sign distribution of the derivative of the Rényi entropies $\partial_D S_\alpha$ for partitions $A|B|A$, $A = 48$ and $B = 4$ (upper panels) and $A = 45$ and $B = 10$ (lower panels); both with $N = 100$ are presented in (a2). The features of differential local convertibility are characterized by the slopes of the Rényi entropies and correspond to specific features of the entanglement spectrum as explained in Fig. 2. The S_α 's are presented in (a1) for $\alpha = 0.5, 100$ decreasing from top to low. All such quantities are calculated for the ground state in $S_z^{tot} = 1$ sector

correlation length ξ . As for the model Eq. (2), we find that the symmetric bipartition $A = B$ displays local convertibility as a fine-tuned effect, which is broken for generic partitions, see Figs. 7 and 8.

3 The Perturbed Toric Code

We now study a set of spin-1/2 localized at the edges of a $2D$ square lattice with periodic boundary conditions in presence of a perturbation V :

$$\mathcal{H} = - \sum_s \prod_{i \in s} \sigma_i^x - \sum_p \prod_{i \in p} \sigma_i^z + V(\lambda), \tag{5}$$

where s and p label the vertices and plaquettes of the lattice, respectively, while σ_i^x and σ_i^z are Pauli operators of the spin living at the edge i . For $V(\lambda) = 0$ the Hamiltonian above is the celebrated toric code, a paradigmatic model for topological

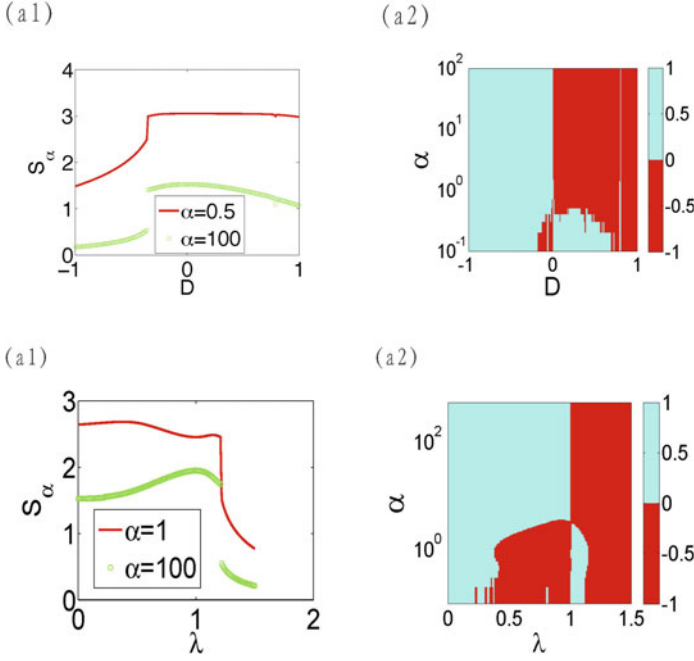


Fig. 8 Sweep (2) through the $\lambda - D$ model: $D = 0$, $\lambda \in \{0, 1.5\}$ (see Fig. 5 for a schematic phase diagram). The sign distribution of the derivative of the Rényi entropies $\partial_\lambda S_\alpha$ for partitions $A|B|A$, $A = 48$ and $B = 4$ (upper panels) and $A = 45$ and $B = 10$ (lower panels); both with $N = 100$ are presented in (a2). The features of differential local convertibility are characterized by the slopes of the Rényi entropies and correspond to specific features of the entanglement spectrum as explained in Fig. 2. The S_α 's are presented in (a1) for $\alpha = 100, 0.2$ increasing from low to top. All such quantities are calculated for the ground state in $S_z^{tot} = 1$ sector

order [65]. For the analysis below, we remark that in this case, the ground state of this model features $\xi = 0$. We consider different $V(\lambda)$ (see Table 1), where λ stands for $\{\lambda_1, \dots, \lambda_N\}$ which are the parameters controlling the perturbation. The perturbation in (5) is such that the correlation length is increasing with λ_i until it diverges at a critical point λ_c . For a discussion of this criticality, see [66].

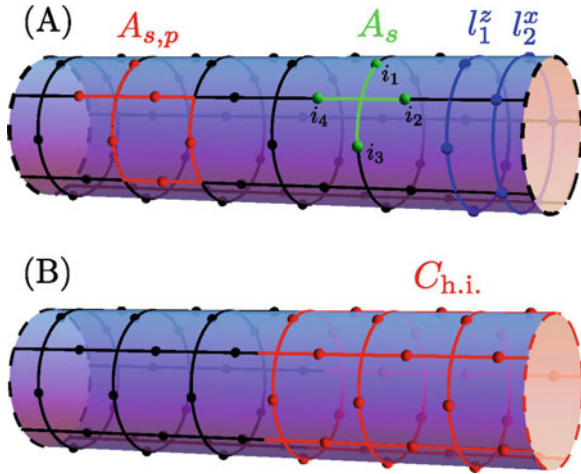
For $\lambda < \lambda_c$, these systems are topologically ordered, while for $\lambda > \lambda_c$, they are trivial paramagnets. In both phases, there is no local order parameter. This model belongs to a class of so-called quantum double models that correspond to those phases whose low-energy theory is a lattice gauge theory [65]. We demonstrate that one can distinguish the topological from the paramagnetic phases of (5) using dLC, even when small subsystems A are considered.

For each $V(\lambda)$, we compute the ground state wavefunction $|\psi(\lambda)\rangle$ and its reduced density matrix $\rho_A(\lambda)$. For some $V(\lambda)$, we can apply exact analytical approach; for the generic perturbation $V_{xz}(\lambda) = \sum_i (\lambda_z \sigma_i^z + \lambda_x \sigma_i^x)$, we resort to numerical analysis.

Table 1 List of the various perturbation used in the topological toric code and some of their properties. dLC, i.e., no splitting of the Rényi entropies, only occurs if the perturbation is fine tuned in order to keep the system with $\xi = 0$. The left column shows the type of perturbation studied. The first column details whether the considered model is gauge invariant. The second column indicates whether dLC occurs. For certain perturbations, the ground state of the system is accessible exactly (third column). The last column provides the information on ξ

Perturbation $V(\lambda)$	G.I.	DLC	Exact	ξ
$\sum_s e^{-\lambda_s \sum_{i \in s} \sigma_i^z}$	✓	✓	✓	0
$\lambda_h \sum_{i \in H} \sigma_i^z$	✓	✗	✓	$\neq 0$
$\lambda_z \sum_i \sigma_i^z$	✓	✗	✗	$\neq 0$
$\lambda_z \sum_i \sigma_i^z + \lambda_x \sum_j \sigma_j^x$	✗	✗	✗	$\neq 0$

Fig. 9 Cylinder of infinite length and width $L_y = 5$ used in 2D DMRG calculation. **(a)** Subsystems on which Rényi entropies are calculated: A_s —one star and $A_{s,p}$ —composition of star and plaquette. Loops l_1^z and l_2^x used to distinguished between topological sectors are also depicted. **(b)** Subsystem $C_{h.i.}$ that contains half of the infinite cylinder



The numerical method employed here is an infinite DMRG algorithm [67] in two dimensions. The method provides Matrix Product State (MPS) representation of a complete set of ground states on a cylinder of infinite length and finite width L_y (Fig. 9) for a given Hamiltonian that realizes topological order. As argued in [68], each ground state has a well-defined flux threading through the cylinder. The flux is measured by (in general) dressed Wilson loop operators that enclose the cylinder in the vertical direction.

In the case of fixed-point toric code (Eq. (5) with $V = 0$), these loops are given by l_1^z and l_2^x (Fig. 9a). Four topological sectors are then distinguished by $\langle l_1^z \rangle, \langle l_2^x \rangle = \pm 1$. Once the perturbation is present, Wilson loops may change, but as long as the perturbation is small, $\langle l_1^z \rangle$ and $\langle l_2^x \rangle$ can still be used to identify topological sectors because $\langle l_1^z \rangle, \langle l_2^x \rangle \simeq \pm 1$.

Simulations are carried out with cylinders of width up to $L_y = 5$ for $\sqrt{\lambda_x^2 + \lambda_z^2} \leq 0.05$ and $0 \leq \lambda < 0.7$ as shown in Figs. 10 and 11 respectively. In the topological phase, the outcome of each simulation is four quasi-degenerate ground states, from which the one with $\langle l_1^z \rangle, \langle l_2^x \rangle \simeq +1$ is chosen for further investigation. This is done

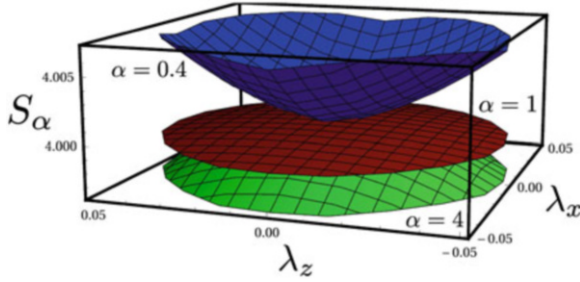


Fig. 10 The splitting phenomenon. The figure displays the splitting with opposite slopes between the small and large α Rényi entropies. We see the splitting occurring around $\alpha \simeq 0.6$. The Rényi entropies are calculated for the partition $A_{s,p}$ of Fig. 9a for the ground state of $\mathcal{H} = \mathcal{H}_{TC} + V_{xz}$

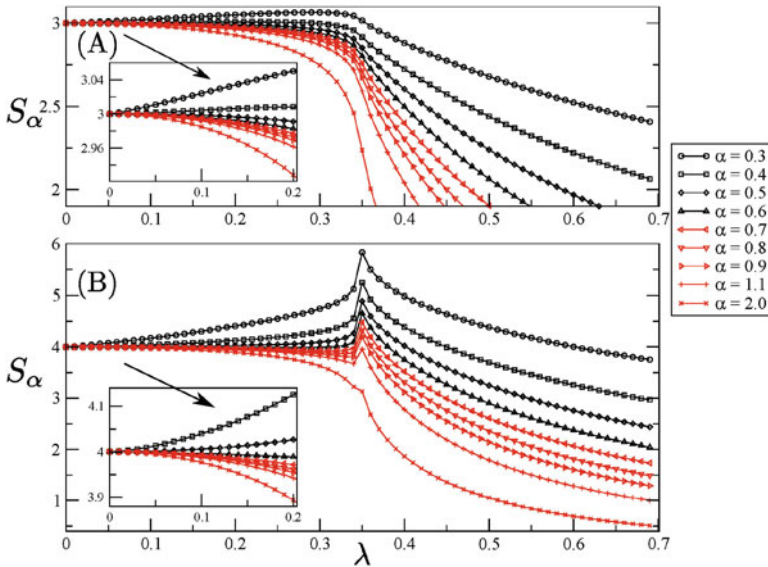


Fig. 11 Rényi entropies as a function of λ for the ground state of $\mathcal{H} = \mathcal{H}_{TC} + V_{xz}$ with $\lambda_x = \lambda$ and $\lambda_z = \lambda/2$. Here, $L_y = 5$. The reduced system A consists of A_s and $C_{h.i.}$ in panels A and B, respectively. As λ increases, the correlation length increases. The Schmidt rank R and the low $\alpha < \alpha_0$ -Rényi entropies increase as well. The value of α_0 is 0.4 and 0.6 in panels A and B, respectively. Nevertheless, the total entanglement S_1 and all the higher Rényi entropies are decreasing with ξ . Notice the spike in panel B marking the quantum phase transition to the paramagnetic phase at $\lambda_c \sim 0.35$

to ensure that finite size effects have the least possible impact on results. In the limit $L_y \rightarrow \infty$ all four ground states become locally indistinguishable. The results are converged in bond dimension of MPS which acts as a refinement parameter. A reduced density matrix of a half-infinite cylinder $C_{h.i.}$ (Fig. 9b) is calculated

throughout the simulation. The bond dimension is increased until convergence of its spectrum is reached.

In Fig. 10, we can see the behavior of the S_α Rényi entropies as we span the parameter space λ_x, λ_z for the perturbation V_{xz} . We see clearly that in the topologically ordered phase a splitting of S_α 's occurs: $\partial_\lambda S_\alpha \leq 0$ at a given value of $\alpha = \alpha_0$; we found $\alpha_0 \simeq 0.6$ (see the caption of Fig. 10). We will henceforth refer to this phenomenon as α splitting. In the paramagnetic phase, all the Rényi entropies are monotones with λ . This behavior is generically independent of the size and shape of the subsystem A , as long as A contains some bulk [35]. Below, we explain the phenomenon. The topologically ordered phase we consider is characterized by the presence of a state (at $\lambda = 0$) with $\xi = 0$ and a flat entanglement spectrum (and an area law) [69]. The flat entanglement spectrum implies that small perturbations result in decreasing S_α for $\alpha > \alpha_0$ being $\alpha_0 < 1$, because the distribution becomes less flat in the most represented eigenvalues in the entanglement spectrum. In contrast, S_0 must increase with ξ as an effect of the perturbation (new degrees of freedom are involved in the entanglement spectrum). So the α splitting results from the insertion of a finite ξ in the state evolving from a state with a flat spectrum and zero ξ . We also observe that such property is shared with the so-called G -states that include all the topologically ordered quantum double models and states like the cluster states [70], and therefore our findings apply to this class of models as well [69] (see [71] for a discussion of the cluster phase diagram). Here, we remark that the splitting effectively distinguishes a class of quantum spin liquids (states with finite correlation length and no local order parameter), which are notoriously very difficult to detect, since one cannot measure correlation functions of all the possible local observables. To further distinguish non-topologically ordered quantum spin liquids like the cluster states from topologically ordered states, we need to measure the degeneracy of the ground state, since the former have a unique ground state, while topological states possess a degeneracy protected by topology.

Moreover, notice that the splitting occurs no matter how we perturb in the plane λ_x, λ_z , and it is, therefore, a robust property of the phase. Note again that in the paramagnetic phase, all the $\partial_\lambda S_\alpha$ have the same sign and no splitting ever occurs, which is easily understood from the presence (at very large λ) of a completely factorized state, see Fig. 11.

We remark that the splitting phenomenon effectively distinguishes the topologically ordered state from a topologically trivial ordered state (like a ferromagnet). As discussed above, the latter states have typically S_α increasing with ξ and no splitting occurs. Summarizing, we can distinguish between the topological phase and the paramagnet of (5); furthermore, we can distinguish between the topological phase and a symmetry-breaking phase.

To corroborate our findings, we resort to exact analysis for suitable perturbations $V(\lambda)$'s. We consider two cases: (i) $V_h = \lambda_z \sum_{i \in h} \sigma_i^z$, corresponding to placing the external field $\propto \sigma^z$ only along the horizontal links of the lattice; and (ii) $V(\lambda) = \sum_s e^{-\lambda \sum_{i \in s} \sigma_i^z}$ leading to the Castelnovo–Chamon model [72]. Since these perturbations commute with the plaquette operators of Eq. (5), the ground state of these models can be written as the superposition of loop states $|g\rangle$ with amplitudes

$\alpha(g)$. A loop state $|g\rangle$ is obtained from the completely polarized state in the z direction, by flipping down all the spins intersected by a loop drawn on the lattice. The corresponding loop operators g form a group G called the gauge group of these theories.

In case (i), the star operators $\prod_{i \in s} \sigma_i^x$ interact only along the rows of the lattice. The model maps onto the product of arrays of Ising chains by the duality $A_s \rightarrow \tau_\mu^z$, $\sigma_i^z \rightarrow \tau_\mu^x \tau_{\mu+1}^x$: $\mathcal{H}_{TC} + V_h \mapsto \mathcal{H}_{ff} = \bigoplus_{i=1}^L (-\lambda \sum_\mu \tau_\mu^x \tau_{\mu+1}^x - \sum_\mu \tau_\mu^z)$ [73, 74]. The relevant correlators in the variables σ can be obtained through the correlators in the dual variables τ that can be accessed exactly [46]. In the following, we sketch a proof that the splitting phenomenon does occur in this model (see [35] for additional details). We consider the star $A_s = \{i_1, i_2, i_3, i_4\}$ as subsystem A (see Fig. 9); ρ_{A_s} is block diagonal with 2×2 blocks labeled by $|i_1 i_2 i_3 i_4\rangle$ and $A_s |i_1 i_2 i_3 i_4\rangle$. It results that ρ_A has maximum rank unless $\alpha(g) = \alpha(g_1)\alpha(g_2)$, implying there is a zero eigenvalue in each block. In the dual picture, this is equivalent to require $\langle \tau_i \tau_j \rangle = \langle \tau_i \rangle \langle \tau_j \rangle$. Such condition holds at $\lambda = 0$ only, and therefore R increases at $\lambda \neq 0$. The factorization of the amplitudes also proves that both $\alpha = 1, 2$ -Rényi entropies decrease at small λ [35].

The case (ii) is important to test the argument of the interplay between splitting and increasing of the correlation length. This argument implies that a perturbation for which $\xi(\lambda) = \text{const}$ does not lead to a splitting in the Rényi entropies. The model of Castelnovo–Chamon features exactly this since spin–spin correlation functions $\langle \sigma_i^x \sigma_j^x \rangle$ are vanishing for every value of λ . The exact ground state is made of loops with amplitudes $\alpha(g) = e^{-\lambda/2 \sum_{i \in s} \sigma_i^z(g)}$, where $\sigma_i^z(g) = \langle g | \sigma_i^z | g \rangle$. The topological phase is ($\lambda < \lambda_c \approx 0.44$). A lengthy calculation leads to $S_\alpha(\rho_A) = (1 - \alpha)^{-1} \log Z^{-\alpha}(\lambda) \sum_{g \in G} e^{-\lambda L_g} w^{\alpha-1}(\lambda, g)$, where $Z = \sum_g e^{-\lambda L_g}$ and $w(\lambda, g) := \sum_{h \in G_A, k \in G_B} e^{-\lambda L_{hgk}}$, and L_m is the length of the loop m of the gauge group G ; here, G_A and G_B are the gauge groups of the subsystems A and B , respectively. The analysis of small and large λ expansions reveals that $\partial_\lambda S_\alpha(\lambda) \leq 0$ [35]. As a particular case, S_0 is constant for every value of λ . Accordingly, for this fine-tuned perturbation, all Rényi entropies decrease, and therefore no splitting is observed. This is consistent with the fact that also in this model, the amplitudes $\alpha(g)$ factorize as discussed in (i).

4 The Quantum Ising Chain

To better extract the effect of edge states on local convertibility, it is desirable to have a model with three properties: (i) it should support edge states, (ii) quasi-particle excitations should be identifiable, and (iii) there should be a mechanism for destroying the edge states and observing the different behavior. The one-dimensional transverse field Ising model fulfills these requirements [46, 75]. It is

defined by the Hamiltonian

$$H_1 = - \sum_{j=1}^N \left(t \sigma_j^x \sigma_{j+1}^x + h \sigma_j^z \right), \quad (6)$$

where t is a hopping amplitude (which we can set to $t = 1$) and h is the control parameter for the external magnetic field. A quantum phase transition for $h = t = 1$ happens in the thermodynamic limit of $N \rightarrow \infty$. This QPT's signatures have been recently observed experimentally [76].

The Hilbert space of (6) can be described in terms of eigenstates of the string operator $\mu_N^x = \prod_{j=1}^N \sigma_j^z$, which generates the \mathbb{Z}_2 symmetry of (6). For $h > 1$, the system is paramagnetic with $\langle \sigma^x \rangle = 0$. For $h < 1$, the spectrum of the Ising model becomes doubly degenerate. A ground state that is also an eigenstate of μ_N^x has a vanishing order parameter $\langle \sigma_x \rangle = 0$. This ground state is known as the ‘‘thermal ground state.’’ This is the state employed in the 2-Sat problem and adiabatic quantum computation protocols for finite N [20]. In the thermodynamic limit ($N \rightarrow \infty$), σ^x can acquire a nonzero expectation value. The symmetry will be broken spontaneously and the ground state will be given by the (anti)symmetric combination of the two eigenstates of μ_N^x . For $h < 1$, we consider both the ferromagnetic ground state (MSBGS) with nonvanishing order parameter $\langle \sigma^x \rangle$ and the thermal one enjoying the same \mathbb{Z}_2 symmetry as the Hamiltonian.

The quantum Ising model (6) can be mapped exactly, although nonlocally, to a system of free spinless fermions $\{c_j, c_j^\dagger\}$, see [75]. We remark that this mapping preserves the entanglement between A and B [77, 78] and generates the *Kitaev chain*. As emphasized in [79], this formulation highlights the presence of Majorana edge states as emergent degrees of freedom. Majorana fermions are the elusive particles (coinciding with their own anti-particles), proposed by E. Majorana. Many research groups are trying to find and manipulate them [29, 30]. Each Dirac fermion of the chain can be used to define two Majorana fermions:

$$f_j^{(1)} \equiv \left[\prod_{l < j} \sigma_l^z \right] \sigma_j^x = c_j^\dagger + c_j, \quad f_j^{(2)} \equiv \left[\prod_{l < j} \sigma_l^z \right] \sigma_j^y = i(c_j^\dagger - c_j) \quad (7)$$

We represent this mapping pictorially in Fig. 12. In the paramagnetic phase ($h > 1$), the Hamiltonian pairs predominantly Majoranas on the same site j (this correlation is drawn as a double line in the picture). In the ferromagnetic phase ($h < 1$), the dashed line connecting different sites is dominant. In Kitaev’s approach, the double degeneracy of this phase emerges as the first and last Majoranas are left unpaired and can be combined into a complex fermion (the occupancy/vacancy of this fermion costs no energy). We will see that the same picture applies when the system is divided into two partitions: in the ferromagnetic phase, this operation cuts the dominant link and leaves unpaired Majorana edge states on each side of the cut.

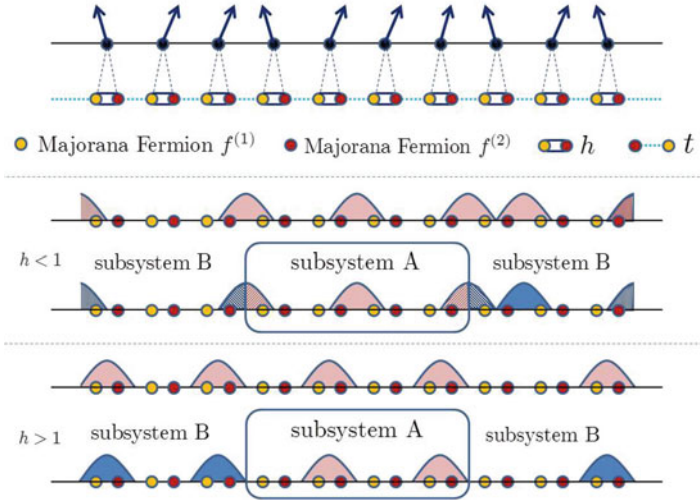


Fig. 12 Top: the Ising chain is mapped into a system of Majorana fermions by doubling the lattice sites. Middle and bottom: a schematic cartoon of the quasi-particle excitations in the two phases of the model and the effect of bipartitioning the system; for small h , edge states form at the opposite boundaries of the subsystem A. The property of local convertibility depends on the correlations between such edge states

This is a key many-body feature that renders phases supporting boundary states more “quantum” than other systems and hence more powerful when employed as simulators. Since any subsystem develops its edge states, in these phases, q-bits of information are stored nonlocally between the sites, and we will see that this is mirrored by the nontrivial entanglement behavior, yielding nonlocal convertibility. Such phenomenology, which can hardly be implemented in a classical setting, must be a fundamental ingredient of a machine aimed at simulating a generic quantum system, and this is the reason for which nonlocal convertibility is a strong indicator of a higher computational power.

4.1 The Rényi Entropies

An advantage of working with a quadratic theory such as the Ising chain is that many-body states can be constructed exactly out of individual quasi-particle excitations. The latter can be found as the linear combination of the fermionic operators $\{c_j, c_j^\dagger\}$, which diagonalizes the Hamiltonian. Doing so, we define a new set of operators $\{\tilde{c}_j, \tilde{c}_j^\dagger\}$ so that the ground state $|0\rangle$ is annihilated by all \tilde{c}_j . On top of it, one can excite quasi-particles by progressively applying all possible combinations of \tilde{c}_j^\dagger , giving a total of 2^N states in the Hilbert space.

To calculate the entanglement between the subregions A and B , we use the Schmidt decomposition of the ground state

$$|0\rangle = \sum_l \sqrt{\lambda_l} |\psi_l^{(A)}\rangle |\psi_l^{(B)}\rangle, \quad (8)$$

where $|\psi_l^{(A,B)}\rangle$ span the Hilbert space of block A and B , respectively [23]. We are after the eigenvalues λ_l , which can be found, for instance, as

$$\lambda_l = \langle 0 | \psi_l^{(A)} \rangle \langle \psi_l^{(A)} | 0 \rangle, \quad (9)$$

where a tracing over the B degrees of freedom is implicitly assumed. Similarly to what is done for the whole system, the states $|\psi_l^{(A)}\rangle$ can be constructed in terms of individual excitations. However, these are different from those of the whole chain, as they are completely contained inside the block. If A consists of L consecutive sites, these block excitations $\{d_j, d_j^\dagger\}$ are the linear combinations of the c -operators within the block, which diagonalize the correlation matrix constructed out of all their two-point correlation functions, as shown below. Each state $|\psi_l^{(A)}\rangle$ of this 2^L -dimensional Hilbert space can thus be characterized by the occupation number 0 or 1 of each block excitation. Moreover, the eigenvalues v_j of the aforementioned correlation matrix provide us with the expectation values

$$\langle 0 | d_j d_j^\dagger | 0 \rangle = \frac{1 + v_j}{2}, \quad \langle 0 | d_j^\dagger d_j | 0 \rangle = \frac{1 - v_j}{2}, \quad (10)$$

all other correlations being zero. Note that $v_j \simeq 1$ indicates that d_j annihilates the vacuum $|0\rangle$. It follows that certain quasi-particle excitations of the Hamiltonian are completely contained within the block, since $d_j |0\rangle = 0$ implies that d_j is just a superposition of \tilde{c}_j 's. Since d_j is defined just within the block, it follows that these \tilde{c}_j 's are also contained in the block. Conversely, smaller values of v_j are related to excitations lying only partially within a subregion. In turn, $d_j d_j^\dagger$ acts on the ground state as a projection operator which selects the component with 0 occupation number for the l th block excitation, while $d_j^\dagger d_j$ projects it on an occupied l th excitation. Hence, (9) can be written as the expectation value of a string of operators of this type. Using (10) as the building blocks of these correlators, we have

$$\{\lambda_l\} = \prod_{j=1}^L \left(\frac{1 \pm v_j}{2} \right), \quad (11)$$

with all the possible combinations of plus/minus signs, corresponding to the occupation/unoccupation of the different block excitations.

Finally, the Rényi entropies read [77, 78]

$$S_\alpha(\rho_A) = \frac{1}{1-\alpha} \sum_{j=1}^L \log \left[\left(\frac{1+v_j}{2} \right)^\alpha + \left(\frac{1-v_j}{2} \right)^\alpha \right]. \quad (12)$$

4.2 The Correlation Matrix

As we just discussed, the Rényi entropies are accessed through the “eigenvalues” of the reduced density matrix of a block of L consecutive spins for the thermal ground state [77, 78]. Such “eigenvalues” can be obtained from the diagonalization of the $2L \times 2L$ correlation matrix: $\langle f_k^{(a)} f_j^{(b)} \rangle = \delta_{j,k} \delta_{a,b} + i (\mathcal{B}_L)_{(j,k)}^{(a,b)}$, with

$$\mathcal{B}_L \equiv \begin{pmatrix} \Pi_0 & \Pi_1 & \dots & \Pi_{L-1} \\ \Pi_{-1} & \Pi_0 & & \vdots \\ \vdots & & \ddots & \vdots \\ \Pi_{1-L} & \dots & \dots & \Pi_0 \end{pmatrix}, \quad (13)$$

where j, k specifies the entry $\Pi_{j-k} \equiv \begin{pmatrix} 0 & g_{j-k} \\ -g_{k-j} & 0 \end{pmatrix}$, which is itself a 2×2 matrix whose a, b entries are defined as

$$g_j \equiv \frac{1}{2\pi} \int_0^{2\pi} \frac{\cos \theta - h + i \sin \theta}{\sqrt{(\cos \theta - h)^2 + \sin^2 \theta}} e^{ij\theta} d\theta. \quad (14)$$

The antisymmetric matrix \mathcal{B} can be brought into a block-diagonal form by a $SO(2L)$ rotation, with each block of the form

$$\tilde{\Pi}_j = v_j \begin{pmatrix} 0 & 1 \\ -1 & 0 \end{pmatrix}$$

This rotation defines a new set of Majorana fermions $\tilde{f}_j^{(a)}$ with only pair-wise correlations. This rotated operator basis can be used to introduce the new set of complex operators: $d_j = (\tilde{f}_j^{(1)} + i\tilde{f}_j^{(2)})/2$ (and their Hermitian conjugated). The matrix (13) contains all the information to completely solve the model. By taking $L = N$, i.e., extending the correlation matrix to the whole system, the d -modes coincide with the \tilde{c} -operators, one would obtain from the diagonalization of the Hamiltonian.

For $L = 2$, the two eigenvalues of the correlation matrix are easily found to be

$$v_{\pm} = \sqrt{\left(\frac{g_1 - g_{-1}}{2}\right)^2 + g_0^2} \pm \frac{g_1 + g_{-1}}{2}, \quad (15)$$

which allows for a complete analytical study of the entanglement entropy and its derivative (see Fig. 14).

4.3 The \mathbb{Z}_2 Symmetric Ground State

Thus, in the Ising chain, the 2^L states within a block of L consecutive sites can be constructed in terms of individual quasi-particle excitations, which can be either occupied or empty. These excitations are in general delocalized, with a typical size set by the correlation length. However, a \mathbb{Z}_2 symmetric state possesses one special excitation, with support lying at the opposite edges of the block and formed by two Majorana edge states [79]. When the block is extended to the whole system ($L = N$), the block excitations coincide with the system's excitations, including the boundary states.

The entanglement between two subsystems A and B can be extracted from the $2L$ eigenvalues $\pm iv_j$ of the correlation matrix Eq. (13) incorporating the correlations of the excitations within the spin block. Here, L is the number of lattice sites in A . The eigenvalues of the reduced density matrix can then be constructed out of the v_j 's, using (11) in the *method section*. The v 's can be interpreted as sort of *occupation numbers*, since they capture the overlaps between each block quasi-particle excitation and the ground state, according to (10): $v_j = 0$ means that this block excitation is half-filled and half-empty in the ground state, while $v_j = 1$ indicates that the excitation is either completely occupied or not present at all.

In Fig. 13, we plot these eigenvalues v_j as a function of the magnetic field for $L = 2$ and $L = 10$. Notice that in both cases only one block excitation has a

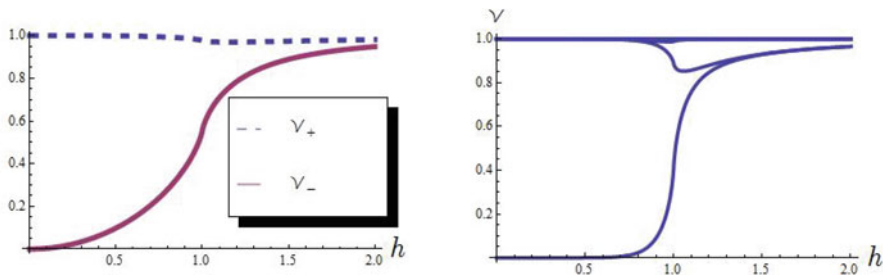


Fig. 13 Plot of the occupation number v_j obtained from the correlation matrix (13) as a function of h for $L = 2$ (left) and $L = 10$ (right). For $L = 2$, the explicit form of the eigenvalues v_{\pm} is given in (15). Notice that only one of the v 's shows a nontrivial behavior: it corresponds to the boundary state, which is only partially contained in the subregion

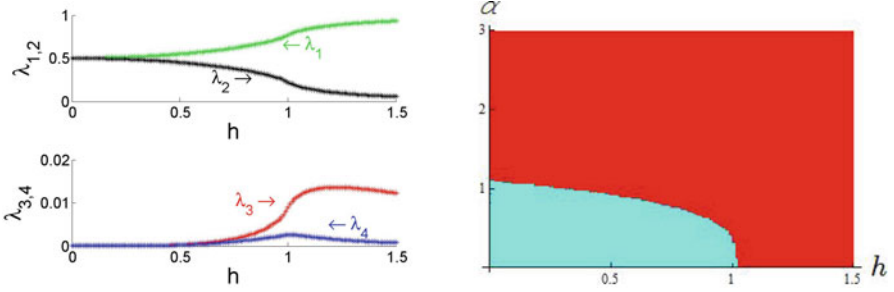


Fig. 14 Left: plot of the four eigenvalues of ρ_A for $L = 2$, as a function of h . The solid lines are the analytical results, while the crosses show the numerical ones with $N=200$ (notice the different scales in the vertical axis between the top and bottom panels). Right: contour plot of the sign of the derivative by h of the Rényi entropy for different values of h and α

nontrivial behavior, while the other eigenvalues stay approximately constant around unity in all phases. Significant deviations happen only close to the QPT (as the correlation length diverges). As discussed, the modes with $\nu_j \simeq 1$ define *bulk states*. In contrast, the nontrivial eigenvalue is close to zero for $h \simeq 0$ and rises rapidly toward 1 crossing the QPT at $h = 1$: in the ferromagnetic phase, it corresponds to a block excitation which is neither occupied nor empty. By cutting the chain into two subregions, we severed the dominant inter-site correlation and hence generated two unpaired Majorana edge states (see Fig. 12). We noticed, however, that as h increases, the occupation number of this edge excitation increases, indicating edge state recombination.

Having discussed the behavior of the eigenvalues ν_j 's and the role of the boundary states, it is straightforward to analyze the Rényi entropy and address the issue of differential local convertibility. It is interesting to concentrate on the two extreme limits: $L = 2$ and $L \rightarrow \infty$.

The two occupation numbers ν_{\pm} for $L = 2$ are shown in the left panel of Fig. 13, and the resulting four eigenvalues of the reduced density matrix, according to (11), are plotted in the left panel of Fig. 14. While in locally convertible phases, the largest eigenvalue(s) decrease approaching the QPT, indicating an increase of the entanglement; here, we see that the edge state recombination results in a growing larger eigenvalue. The right panel of Fig. 14 presents the sign of the entanglement entropy derivative, to be considered with dLC. We see that in the paramagnetic phase, the Rényi entropy always decreases. Instead, in the doubly degenerate phase, the entropy derivative vanishes at some value of α and changes sign, indicating that local (differential) convertibility is lost in this phase (as already observed numerically for small N and larger L in [26]). It is important to notice here that these results imply that classical local gates operating on two sites project out the half-occupied state and hence lose the edge state entanglement.

For the $L \rightarrow \infty$ limit, we can take advantage of the results of [80–82], where the full spectrum (eigenvalues and multiplicities) of the reduced density matrix and the Rényi entropies were calculated analytically. Figure 15 shows a plot of the first

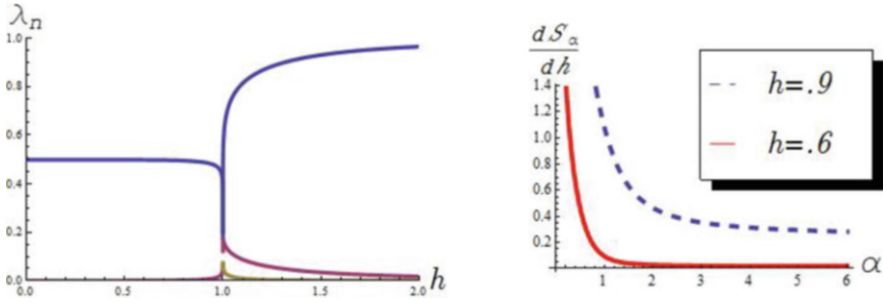


Fig. 15 Left: plot of the first few eigenvalues of ρ_A , for an infinite size block, as a function of h . The eigenvalues’ multiplicities are not shown (for instance, the highest eigenvalue is doubly degenerate for $h < 1$ and unique for $h > 1$, see [82]). Right: plot of the derivative of the Rényi entropy with respect to the magnetic field h , as a function of α , for two different values of h in the ferromagnetic region

few eigenvalues of ρ_A and a plot of the entropy derivative as a function of α for $h = 0.6$ and $h = 0.9$. We see that the largest eigenvalue (doubly degenerate in the ferromagnetic phase) decreases monotonously toward the QPT, while smaller eigenvalues are allowed to grow, yielding a monotonous increase of all the Rényi entropies. It is thus clear that local convertibility is restored in the infinite L limit.

We checked these results numerically for systems up to $N = 200$ and with different partitions. We considered different block sizes and move the blocks within the chain. The qualitative picture does not change significantly as one varies $(A|B)$, but the location of the curve where the entropy derivative vanishes moves in the (h, α) space. It tends toward the phase transition line $h = 1$ as the block sizes grow bigger, confirming our expectation on the role of the boundary excitations. Namely, we see that as long as the edge states from different boundaries do not overlap, their occupation number eigenvalue stays constant and vanishes. It starts increasing only once the correlation length grows comparable to one of the block sizes, *indicating the recombination of the edge states and a decrease in the entanglement contribution from the edge states.*

4.4 Symmetry Broken Ground State

To further confirm our interpretation on the role of boundary modes, in the ordered phase $h < 1$, we also considered the ferromagnetic ground state for which $\langle \sigma^x \rangle \neq 0$. Since this state does not support well-defined Majorana edge states, we expect a restoration of local convertibility. We calculate the Rényi entropy of this symmetry broken ground state numerically. Namely, we add a very small perturbation $\epsilon(\sigma_1^x + \sigma_N^x)$ to Hamiltonian (6) and apply the variational MPS routine to obtain the ground state [47]. In this work, the converge tolerance is 10^{-6} . Figure 16 shows the plots

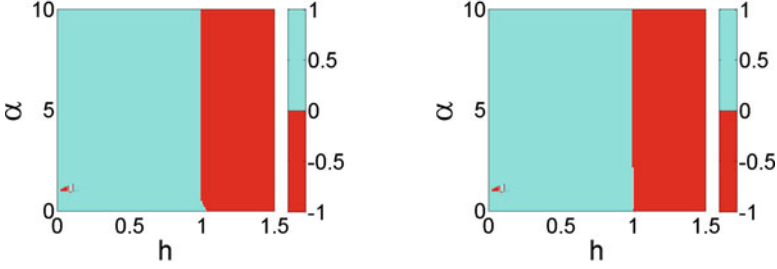


Fig. 16 Numeric results of differential local convertibility for the ferromagnetic (symmetry broken). On the left, a partition $200 = 2|198$ and on the right $200 = 50|100|50$

of the sign of the entropy derivative for two possible partitions (small and large A block) and validates our expectation that both phases are locally convertible. We considered several partitioning choices and the results are not distinguishable from those in Fig. 16.

In conclusion, we see that for $h > 1$, the disordered ground state is always locally convertible. In the ordered phase, the ferromagnetic ground state, i.e., with broken symmetry, is also locally convertible for any chosen partition. For the thermal ground state, however, the convertibility depends on the interplay between the size of the partitions ($A|B$) and the correlation length of the system. This phenomenon is a manifestation of edge state recombination. These entangled pairs lie on opposite boundaries of the partition (see Fig. 12), but with finite support intruding in the bulk about the order of the correlation length. For sufficiently large block sizes, the entanglement between boundary states does not depend on the correlation length and remains constant throughout the phase. However, as this length increases approaching a QPT, the edge states effectively grow closer to one another. If either of the subregions A and B is sufficiently small, the tails of these states can overlap, and we see their occupation number increasing and *their entanglement decreasing*, yielding nonlocal convertibility.

5 Classical nature of ordered quantum phases and origin of spontaneous symmetry breaking

To discuss the differences among different ground states of a model with a degenerate lowest energy manifold, we take as an example the ferromagnetic one-dimensional spin-1/2 XY in the presence of a transverse field and periodic boundary conditions. The Hamiltonian of such model reads [46, 75, 83, 84]

$$H = - \sum_{i=1}^N \left[\left(\frac{1+\gamma}{2} \right) \sigma_i^x \sigma_{i+1}^x + \left(\frac{1-\gamma}{2} \right) \sigma_i^y \sigma_{i+1}^y + h \sigma_i^z \right], \quad (16)$$

where γ is the anisotropy parameter in the xy plane, h is the transverse local field, and the periodic boundary conditions $\sigma_{N+1}^\mu \equiv \sigma_1^\mu$ ensure a perfect invariance under spatial translations.

For this class of models, the phase diagram can be determined exactly in great detail [75, 84, 85]. In the thermodynamic limit, for any $\gamma \in (0, 1]$, a quantum phase transition occurs at the critical value $h_c = 1$ of the transverse field. For $h < h_c$, the system is characterized by a bidimensional ground state manifold in which two elements are living in both parity sectors. As a consequence, in such a manifold, it is possible to define elements showing a ferromagnetic order along the x axis which highlights the fact that they violate the \mathbb{Z}_2 parity symmetry. Indeed, given the two symmetric ground states, the so-called even $|e\rangle$ and odd $|o\rangle$ states belonging to the two orthogonal subspaces associated with the two possible distinct eigenvalues of the parity operator, any symmetry-breaking linear superposition of the form

$$|g(u, v)\rangle = u|e\rangle + v|o\rangle \quad (17)$$

is also an admissible ground state, with the complex superposition amplitudes u and v constrained by the normalization condition $|u|^2 + |v|^2 = 1$. Taking into account that the even and odd ground states are orthogonal, the expectation values of operators that commute with the parity operator are independent of the superposition amplitudes u and v . On the other hand, spin operators that do not commute with the parity may have nonvanishing expectation values on such linear combinations and hence break the symmetry of the Hamiltonian (16).

Consider observables O_S that are arbitrary products of spin operators and anti-commute with the parity. Their expectation values in the superposition ground states (17) are of the form

$$\langle g(u, v) | O_S | g(u, v) \rangle = uv^* \langle o | O_S | e \rangle + vu^* \langle e | O_S | o \rangle . \quad (18)$$

Both $\langle o | O_S | e \rangle$ and $\langle e | O_S | o \rangle$ are real and independent of u and v , and hence the expectation (18) is maximum for $u = \pm v = 1/\sqrt{2}$ [84]. These are the values of the superposition amplitudes that realize the maximum breaking of the symmetry and identify the order parameter as well as the MSBGs.

Besides the quantum critical point, there exists another relevant value of the external magnetic field, that is, $h_f = \sqrt{1 - \gamma^2}$, the *factorizing field*. Indeed, at this value of h , the system admits a twofold degenerate, completely factorized ground state [86–90].

To discuss the entanglement and discord-type correlations of quantum ground states, we consider arbitrary bipartitions $(A|B)$ such that subsystem $A = \{i_1, \dots, i_L\}$ is any subset made of L spins, and subsystem B is the remainder. Given any global ground state of the total system, the reduced density matrix ρ_A (ρ_B) of subsystem A (B) can be expressed in general in terms of the n -point correlation functions [48]:

$$\rho_A(u, v) = \frac{1}{2^L} \sum_{\mu_1, \dots, \mu_L} \langle g(u, v) | \sigma_{i_1}^{\mu_1} \cdots \sigma_{i_L}^{\mu_L} | g(u, v) \rangle \sigma_{i_1}^{\mu_1} \cdots \sigma_{i_L}^{\mu_L} \quad (19)$$

and analogously for ρ_B . All expectations in Eq.(19) are associated with spin operators that either commute or anti-commute with the parity along the spin-z direction. Therefore, the reduced density matrix ρ_A can be expressed as the sum of a symmetric part $\rho_A^{(s)}$, i.e., the reduced density matrix obtained from $|e\rangle$ or $|o\rangle$, and a traceless matrix $\rho_A^{(a)}$ that includes all the terms that are nonvanishing only in the presence of a breaking of the symmetry:

$$\rho_A(u, v) = \rho_A^{(s)} + (uv^* + vu^*)\rho_A^{(a)}. \quad (20)$$

Both $\rho_A^{(s)}$ and $\rho_A^{(a)}$ are independent of the superposition amplitudes u and v , while the reduced density matrix depends on the choice of the ground state. This implies that the elements of the ground space are not locally equivalent. Explicit evaluation of expectations and correlations in symmetry-breaking ground states in the thermodynamic limit is challenging even when the exact solution for the symmetric elements of the ground space is available.

We will now sketch a method that allows overcoming this difficulty and whose general validity is not in principle restricted to the particular model considered. To obtain $\rho_A^{(s)}$, it is sufficient to transform the spin operators into fermionic ones and then apply Wick's theorem. Such algorithm cannot be applied to spin operators O_A , acting on subsystem A , that anti-commute with the parity. To treat this case, we first introduce the symmetric operator $O_A O_{A+r}$, for which, by applying the previous procedure, we can evaluate $\langle e | O_A O_{A+r} | e \rangle$. Then, the desired expectation $\langle e | O_A | o \rangle$ can be computed by exploiting the property of asymptotic factorization of products of local operators at infinite separation [41, 43, 84] that yields $\langle e | O_A | o \rangle = \sqrt{\lim_{r \rightarrow \infty} \langle e | O_A O_{A+r} | e \rangle}$, where the root's sign is fixed by imposing positivity of the density matrix $\rho_A(u, v)$. Having obtained the exact reduced density matrix $\rho_A(u, v)$ for all possible subsystems A and superposition amplitudes u and v , we are equipped to investigate the nature of quantum ground states for their properties of classicality and quantumness.

5.1 Two-Body Quantum Correlations

Among all the different possibilities, in the present section, we focus on the analysis of the behavior of one-way discord-type correlations and entanglement between any two spins for different ground states. One-way discord-type correlations are properties of quantum states more general than entanglement. Operationally, they are defined in terms of state distinguishability for the so-called *classical-quantum* states. The latter are quantum states that, besides being separable, i.e., not entangled,

remain invariant under the action of at least one nontrivial local unitary operation. In geometric terms, a valid measure of quantum correlations must quantify how much a quantum state *discords* from classical-quantum states and must be invariant under the action of all local unitary operations. A computable and operationally well-defined geometric measure of quantum correlations is then the *discord of response* [91, 92]. The pairwise discord of response D_R for a two-spin reduced density matrix is defined as

$$D_R(\rho_{ij}^{(r)}(u, v)) \equiv \frac{1}{2} \min_{U_i} d_x \left(\rho_{ij}^{(r)}(u, v), \tilde{\rho}_{ij}^{(r)}(u, v) \right)^2, \quad (21)$$

where $\rho_{ij}^{(r)}(u, v)$ is the state of two spins i and j at a distance r , obtained by taking the partial trace of the ground state $|g(u, v)\rangle$ with respect to all other spins in the system, $\tilde{\rho}_{ij}^{(r)}(u, v) \equiv U_i \rho_{ij}^{(r)}(u, v) U_i^\dagger$ is the two-spin state transformed under the action of a local unitary operation U_i acting on spin i , and d_x is any well-behaved, contractive distance (e.g., Bures, trace, Hellinger) of $\rho_{ij}^{(r)}$ from the set of locally unitarily perturbed states, realized by the least-perturbing operation in the set. The trivial case of the identity is excluded by considering only unitary operations with *harmonic* spectrum, i.e., the fully nondegenerate spectrum on the unit circle with equispaced eigenvalues.

For pure states, the discord of response reduces to an entanglement monotone, whose convex-roof extension to mixed states is the so-called *entanglement of response* [93–95]. Therefore, the entanglement and the discord of response quantify different aspects of bipartite quantum correlations via two different uses of local unitary operations. The discord of response arises by applying local unitaries directly to the generally mixed state, while the entanglement of response stems from the application of local unitaries to pure states. Under their common origin, it is thus possible to perform a direct comparison between these two quantities.

In terms of the trace distance, which will be relevant in the following, the two-qubit entanglement of response is simply given by the squared concurrence [91, 96], whereas the two-qubit discord of response relates nicely to the trace distance-based geometric discord [97], whose closed formula is known only for a particular class of two-qubit states [98], although it can be computed for a more general class of two-qubit states through a very efficient numerical optimization.

Symmetry-Preserving Ground States

We first compare the two-body entanglement of response and the two-body discord of response in symmetry-preserving ground states. For two neighboring spins, these two quantities are plotted in Fig. 17 as functions of the external field h and for different values of the anisotropy γ . For any intermediate value of γ , the nearest-neighbor entanglement of response E_1 exhibits the following behavior. If $h < h_f$, E_1 decreases until it vanishes at the factorizing field $h = h_f$. Otherwise, if $h > h_f$, E_1 first increases until it reaches a maximum at some value of h higher than the critical point $h_c = 1$, and then it decreases again until it vanishes asymptotically for very large values of h in the paramagnetic phase (saturation). Overall, E_1 features

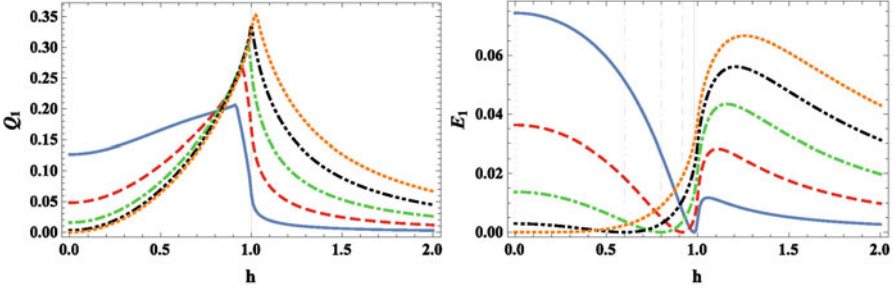


Fig. 17 Nearest-neighbor trace distance-based discord of response (left panel) and nearest-neighbor trace distance-based entanglement of response (right panel) for symmetry-preserving ground states, in the thermodynamic limit, as functions of the external field h , and for different values of the anisotropy γ . Solid blue curve: $\gamma = 0.2$; dashed red curve: $\gamma = 0.4$; dot-dashed green curve: $\gamma = 0.6$; double-dot-dashed black curve: $\gamma = 0.8$; and dotted orange curve: $\gamma = 1$. In the lower panel, to each of these curves, there corresponds a vertical line denoting the associated factorizing field h_f . In the upper panel, the solid vertical line denotes the critical field $h_c = 1$

two maxima at $h = 0$ and $h > h_c$ and two minima at $h = h_f$ (factorization) and $h \rightarrow \infty$ (saturation). For the Ising model ($\gamma = 1$), the point $h = 0$ corresponds instead to a minimum, since it coincides with the factorizing field $h_f = \sqrt{1 - \gamma^2}$.

On the other hand, regardless of the value of γ , the nearest-neighbor discord of response Q_1 always features a single maximum. Depending on the value of γ , such maximum can be either in the ordered phase $h < h_c$ or in the disordered (paramagnetic) phase $h > h_c$, moving toward higher values of h with increasing γ . Remarkably, Q_1 never vanishes at the factorizing field, except in the extreme case of $\gamma = 1$. Indeed, at the factorizing field $h = h_f$, and for any $\gamma \neq 0, 1$, the symmetry-preserving ground state is not completely factorized but rather is a coherent superposition with equal amplitudes of the two completely factorized MSBGSs. Consequently, while the two-body entanglement of response must vanish by the convex roof extension, the two-body discord of response remains always finite.

When increasing the inter-spin distance r , the pairwise entanglement of response E_r and discord of response Q_r behave even more differently (see Fig. 18). Due to the monogamy of the squared concurrence [99, 100], E_r dramatically drops to zero as r increases, except in a small region around the factorizing field $h = h_f$ that gets smaller and smaller as r increases, in agreement with the findings of Ref. [101]. On the other hand, while in the disordered and critical phases, Q_r vanishes as r increases, in the ordered phase Q_r survives even in the limit of infinite r . Indeed, in both the disordered and critical phases, and when r goes to infinity, the only nonvanishing one-body and two-body correlation functions in the symmetry-preserving ground states are $\langle \sigma_i^z \rangle$ and $\langle \sigma_i^z \sigma_{i+r}^z \rangle$, so that the two-body reduced state can be written as a classical mixture of eigenvectors of $\sigma_i^z \sigma_{i+r}^z$. On the other hand, in the ordered phase, also the two-body correlation function $\langle \sigma_i^x \sigma_{i+r}^x \rangle$ appears, while

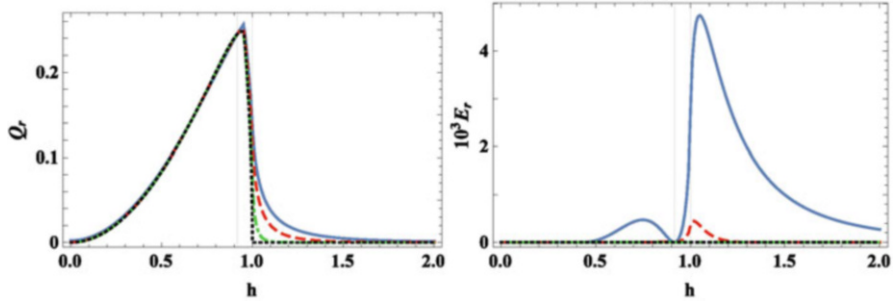


Fig. 18 Two-body trace distance-based discord of response (left panel) and two-body trace distance-based entanglement of response (right panel) for symmetry-preserving ground states, in the thermodynamic limit, as functions of the external field h , in the case of $\gamma = 0.4$, for different inter-spin distances r . Solid blue curve: $r = 2$; dashed red curve: $r = 3$; dot-dashed green curve: $r = 8$; and dotted black curve: $r = \infty$. In both panels, the two solid vertical lines correspond, respectively, to the factorizing field (left) and to the critical field (right)

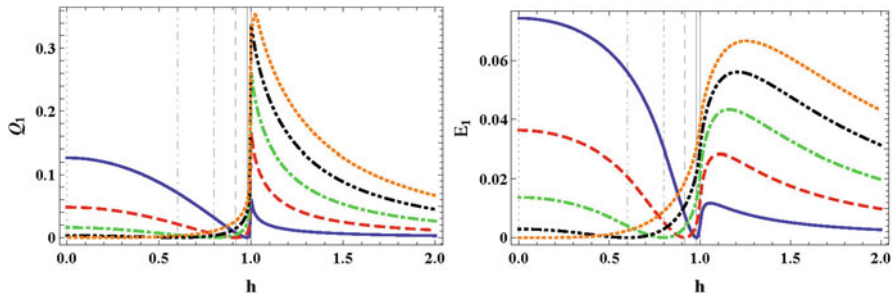


Fig. 19 Nearest-neighbor trace distance-based discord of response (left panel) and nearest-neighbor trace distance-based entanglement of response (right panel) in MSBGSs as functions of the external field h , for different values of the anisotropy γ . Solid blue curve: $\gamma = 0.2$; dashed red curve: $\gamma = 0.4$; dot-dashed green curve: $\gamma = 0.6$; double-dot-dashed black curve: $\gamma = 0.8$; and dotted orange curve: $\gamma = 1$. In both panels, to each of these curves, there corresponds a vertical line denoting the associated factorizing field h_f . The rightmost vertical line denotes the critical point

$\langle \sigma_i^x \rangle$ vanishes due to symmetry preservation, thus preventing the two-body marginal of the symmetry-preserving ground state from being a mixture of classical states.

Maximally Symmetry-Breaking Ground States

In this section, we move the focus of the comparison between two-body entanglement of response and discord of response from symmetry-preserving to MSBGSs. Spontaneous symmetry breaking manifests itself in the thermodynamic limit, in the ordered phase $h < h_c = 1$ and for any nonzero anisotropy γ , so that hereafter we will restrict the region of the phase space under investigation accordingly.

Figure 19 shows that, as soon as symmetry breaking is taken into account, only the discord of response is affected by symmetry breaking at the critical point

$h_c = 1$. In fact, according to Ref. [102], the concurrence and, consequently, the two-body entanglement of response attain the same value for any $h \geq h_f$ both in the symmetry-preserving and in MSBGSs. Otherwise, if $h < h_f$, there is a slight enhancement in the pairwise entanglement of response in the MSBGSs compared to the corresponding symmetry-preserving ones. Conversely, in general, the pairwise discord of response undergoes a dramatic suppression in the entire ordered phase $h < h_c$ when moving from symmetry-preserving to MSBGSs.

Considering the dependence on the inter-spin distance, we observe that the pairwise discord of response loses its long-range nature when moving from symmetry-preserving to MSBGSs (see Fig. 20). More precisely, both the pairwise entanglement of response and the pairwise discord of response vanish asymptotically with increasing inter-spin distance. In the case of the pairwise entanglement of response, this result is again due to the monogamy of the squared concurrence [99, 100]. In the case of the pairwise discord of response, it is instead due to the fact that not only the correlation function $\langle \sigma_i^x \sigma_{i+r}^x \rangle$ but also $\langle \sigma_i^x \rangle$ and $\langle \sigma_i^x \sigma_{i+r}^z \rangle$ are nonvanishing in the limit of infinite inter-spin distance r . This feature allows writing any two-spin reduced density matrix obtained from the MSBGSs as a classical mixture of eigenvectors of $O_i O_{i+r}$, where O_i is an Hermitian operator defined on the i th site as $O_i = \cos \beta \sigma_i^z + \sin \beta \sigma_i^x$ with $\tan \beta = \frac{\langle \sigma_i^x \rangle}{\langle \sigma_i^z \rangle}$.

Overall, the quantum correlations between any two spins decrease significantly in the entire ordered phase when symmetry breaking is taken into account and are almost entirely made up by contributions due to entanglement. In particular, at the factorizing field h_f , both the entanglement of response and the discord of response vanish. Indeed, we recall that the factorizing field h_f owes its name to the two MSBGSs that are completely separable (product) at such value of the external magnetic field.

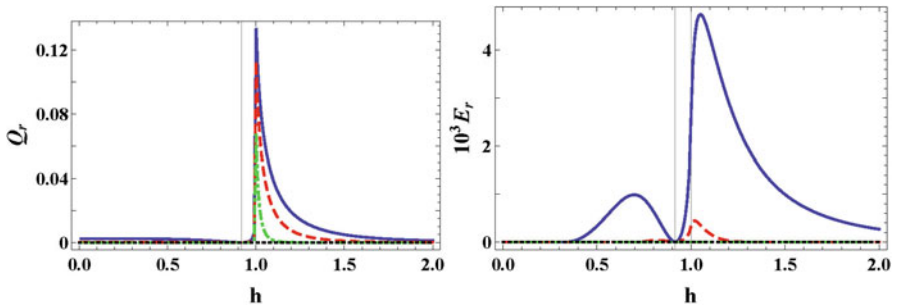


Fig. 20 Two-body trace distance-based discord of response (left panel) and two-body trace distance-based entanglement of response (right panel) in MSBGSs as functions of the external field h , at $\gamma = 0.4$, for different inter-spin distances r . Solid blue curve: $r = 2$; dashed red curve: $r = 3$; dot-dashed green curve: $r = 8$; and dotted black curve: $r = \infty$. In both panels, the two solid vertical lines correspond, respectively, to the factorizing field (left) and to the critical field (right)

5.2 Global Properties: Local Convertibility and Many-Body Entanglement Sharing

We now investigate the nature of quantum ground states in the ordered phase concerning the properties of local convertibility of the global ground states and the many-body entanglement distribution.

Local Convertibility of Many-Body Quantum Ground States

We begin by studying the property of the local convertibility of quantum ground states in an ordered phase. It was previously shown that symmetric ground states are always locally convertible among themselves for $h_f < h < h_c$ and never for $h < h_f < h_c$ [103]. Here, thanks to the general methods developed before, we can investigate the local convertibility property of *all* quantum ground states in the ordered phase. In Fig. 21, we report the behavior of the Rényi entropies S_α as functions of the different ground states for a bipartition of the system in which subsystem A is made of ℓ contiguous spins, while in Fig. 22 we report it for subsystem A made of two spins with various inter-spin distances.

We observe that the MSBGSs are the ground states characterized by the smallest value of all Rényi entropies, independently of the size ℓ of the subsystem and the inter-spin distance r . Therefore, all elements in the ground space are always locally convertible to a MSBGS, while the opposite is impossible. This first quantitative criterion for classicality is thus satisfied only by MSBGSs.

5.3 Many-Body Entanglement Distribution

We now compare symmetry-breaking and symmetry-preserving ground states with respect to entanglement distribution. The monogamy inequality quantifies in a simple and direct way the limits that are imposed on how bipartite entanglement may be shared among many parties [99, 100]. For a given many-body system of N $1/2$ -spins, it reads

$$\tau(i|N-1) \geq \sum_{j \neq i} \tau(i|j) \quad , \quad \forall i . \quad (22)$$

In the above expression, $\tau = C^2$ is known as the tangle, where C is the concurrence [96, 104], and the sum in the r.h.s. runs over all $N-1$ spins excluding spin i . The l.h.s. quantifies the bipartite entanglement between one particular, arbitrarily chosen, spin in the collection (reference spin i) and all the remaining $N-1$ spins. The r.h.s. is the sum of all the pairwise entanglements between the reference spin and each of the remaining $N-1$ spins. The inequality implies that entanglement cannot be freely distributed among multiple quantum parties $N \geq 3$, a constraint of quantum origin with no classical counterpart.

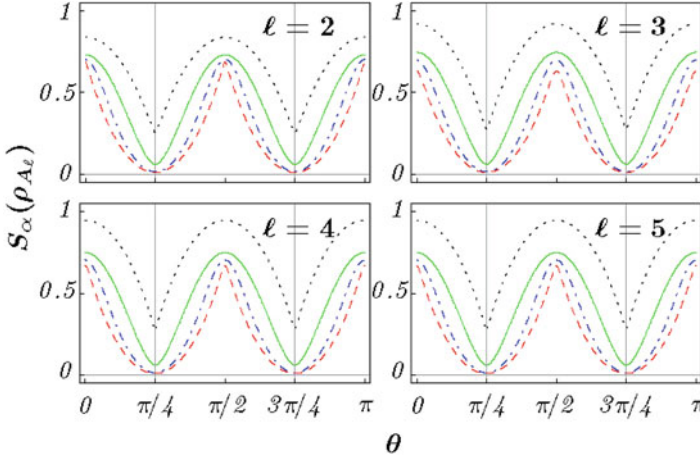


Fig. 21 Behavior of the Rényi entropies $S_\alpha(\rho_{A_\ell})$ as functions of the different ground states in the ordered phase, $h < h_c$, in the case of a subsystem A_ℓ made of ℓ contiguous spins. Each line stands for a different value of α . Black dotted line: $\alpha = 0.5$. Green solid line: $\alpha \rightarrow 1^+$ (von Neumann entropy). Blue dot-dashed line: $\alpha = 3$. Red dashed line: $\alpha \rightarrow \infty$. The different ground states are parameterized by the superposition amplitudes $u = \cos(\theta)$ and $v = \sin(\theta)$. The two vertical lines correspond to the two MSBGs, respectively, obtained for $\theta = \pi/4$ and $\theta = 3\pi/4$. The Hamiltonian parameters are set at the intermediate values $\gamma = 0.5$ and $h = 0.5$. Analogous behaviors are observed for different values of the anisotropy and external field

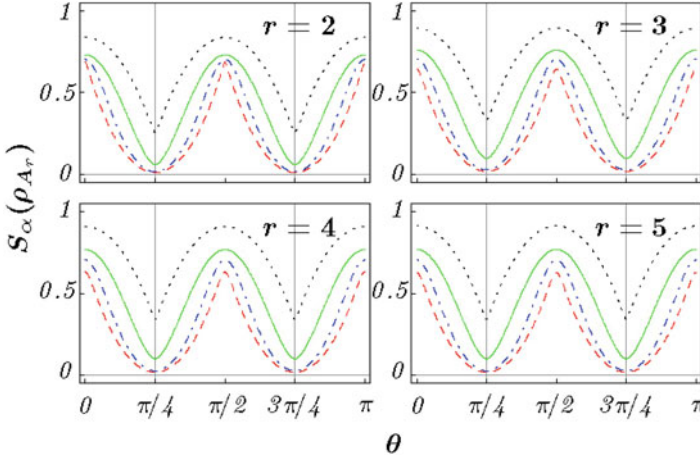


Fig. 22 Behavior of the Rényi entropies $S_\alpha(\rho_{A_r})$ as functions of the different ground states in the ordered phase, $h < h_c$, in the case of a subsystem A_r made by two spins, for different inter-spin distances r . Each line stands for a different value of α . Black dotted line: $\alpha = 0.5$. Green solid line: $\alpha \rightarrow 1^+$ (von Neumann entropy). Blue dot-dashed line: $\alpha = 3$. Red dashed line: $\alpha \rightarrow \infty$. The different ground states are parameterized by the superposition amplitudes $u = \cos(\theta)$ and $v = \sin(\theta)$. The two vertical lines correspond to the two MSBGs, respectively, obtained for $\theta = \pi/4$ and $\theta = 3\pi/4$. The Hamiltonian parameters are set at the intermediate values $\gamma = 0.5$ and $h = 0.5$. Analogous behaviors are observed for different values of the anisotropy and external field

The residual tangle $\tilde{\tau}$ is the positive semi-definite difference between the l.h.s. and the r.h.s. in Eq. (22). It measures the amount of entanglement not quantifiable as elementary bipartite spin–spin entanglement. Its minimum value compatible with monogamy provides yet another quantitative criterion for classicality.

Specializing, for simplicity but without loss of generality, to translationally invariant XY spin systems in magnetically ordered phases, since the expectation value of σ_i^y vanishes on every element of the ground space, the expressions of the tangle τ and the residual tangle $\tilde{\tau}$ for any arbitrarily chosen spin in the chain read, respectively,

$$\tau = 1 - m_z^2 - (u^*v + v^*u)^2 m_x^2, \quad (23)$$

$$\tilde{\tau} = \tau - 2 \sum_{r=1}^{\infty} C_r^2(u, v) \geq 0, \quad (24)$$

where $m_z = \langle e | \sigma_i^z | e \rangle = \langle o | \sigma_i^z | o \rangle$ is the on-site magnetization along z , the order parameter $m_x = \langle e | \sigma_i^x | o \rangle = \sqrt{\lim_{r \rightarrow \infty} \langle e | \sigma_i^x \sigma_{i+r}^x | e \rangle}$, and $C_r(u, v)$ stands for the concurrence between two spins at a distance r when the system is in any one of the possible ground states $|g(u, v)\rangle$, Eq. (17).

As already mentioned, by comparing the symmetric ground states with the MSBGSs, the spin–spin concurrence is larger in the MSBGSs [102] if $h < h_f < h_c$, where $h_f = \sqrt{1 - \gamma^2}$ is the factorizing field, while for $h_f < h < h_c$ they are equal. We have verified that these two results are much more general. We have compared all ground states (symmetric, partially symmetry breaking, and MSBGSs), and we have found that for $h < h_f < h_c$ the spin–spin concurrences are maximum in the MSBGSs for all values of the inter-spin distance r , while for $h_f < h < h_c$ and for all values of r they are independent of the superposition amplitudes u and v and thus acquire the same value irrespective of the chosen ground state.

Finally, it is immediate to see that the third term in the r.h.s. of Eq. (23) is maximized by the two MSBGSs. Collecting all these results, it follows that the many-body, macroscopic multipartite entanglement, as quantified by the residual tangle, is minimized by the two MSBGSs and therefore also this second quantitative criterion for classicality is satisfied only by the MSBGSs among all possible quantum ground states.

6 Conclusions

We have shown that phases characterized by topological order or systems prepared in a ground state supporting edge states lack differential global convertibility, due to the long-range entanglement that these conditions entail. Moreover, the breaking of dLC is detectable even more clearly when small partitions are considered. This means that dLC constitutes a semi-local probe to detect LRE, which is instead an

inherently nonlocal property, usually accessible through string operators stretching for distances much larger than the correlation length ξ .

We also argue that the competition between ξ and LRE is the reason for the lack of dLC, because when the size of a partition becomes comparable with ξ , local correlations reduce the LRE between the farthest point of the partition. Thus, as ξ increases, bulk entanglement increases, but LRE decreases, thus creating a non-monotonous behavior in the Rènyi entropies as α is varied.

Since LRE is an intrinsic property of a quantum phase that cannot be created or destroyed, except by passing through a phase transition, our analysis highlighted once more the higher computational power phase with LRE is endowed. The lack of dLC renders them *more quantum* than phases that are locally convertible.

This intuition was then used to investigate the classical nature of globally ordered phases associated with nonvanishing local order parameters and spontaneous symmetry breaking. We have put on quantitative grounds the long-standing conjecture that the maximally symmetry-breaking ground states (MSBGSs) are macroscopically the most classical ones among all possible ground states. We have proved the conjecture by introducing and verifying two independent quantitative criteria of macroscopic classicality. The first criterion states that all global ground states in the thermodynamic limit are locally convertible to MSBGSs, while the opposite is impossible. The second criterion states that the MSBGSs are the ones that satisfy at its minimum the monogamy inequality for globally shared bipartite entanglement and thus minimize the macroscopic multipartite entanglement as quantified by the residual tangle. We have thus verified that, according to these two criteria, the MSBGSs are indeed the most classical ones among all possible quantum ground states.

Acknowledgments We thank our collaborators with whom the results presented in this chapter have been originally published, in particular Jian Cui, Heng Fan, Mile Gu, Alioscia Hamma, Vlatko Vedral, Lukasz Cincio, Siddhartha Santra, Paolo Zanardi, Marco Cianciaruso, Leonardo Ferro, Giuseppe Zonzo, Wojciech Roga, Massimo Blasone, and Fabrizio Illuminati. VK is supported by the U.S. Department of Energy, Office of Science, National Quantum Information Science Research Centers, Co-design Center for Quantum Advantage (C2QA) under contract number DE-SC0012704. SMG and FF acknowledge support from the QuantiXLie Center of Excellence, a project co-financed by the Croatian Government and European Union through the European Regional Development Fund—the Competitiveness and Cohesion (Grant KK.01.1.1.01.0004) and from the Croatian Science Foundation (HrZZ) Projects No. IP-2019-4-3321.

Bibliography

1. L. Amico, R. Fazio, A. Osterloh, V. Vedral, Entanglement in many-body systems. *Rev. Mod. Phys.* **80**, 517 (2008)
2. J. Eisert, M. Cramer, M.B. Plenio, Area laws for the entanglement entropy. *Rev. Mod. Phys.* **82**, 277 (2010)
3. J.I. Cirac, P. Zoller, Goals and opportunities in quantum simulation. *Nat. Phys.* **8**, 264 (2012)

4. I. Bloch, J. Dalibard, S. Nascimbene, Quantum simulations with ultracold quantum gases. *Nat. Phys.* **8**, 267 (2012)
5. A. Aspuru-Guzik, P. Walther, Photonic quantum simulators. *Nat. Phys.* **8**, 285 (2012)
6. A.A. Houck, H.E. Tureci, J. Koch, On-chip quantum simulation with superconducting circuits. *Nat. Phys.* **8**, 292 (2012)
7. L.M.K. Vandersypen, I.L. Chuang, NMR techniques for quantum control and computation. *Rev. Mod. Phys.* **76**, 1037 (2005)
8. R.P. Feynman, Simulating Physics with Computers. *Int. J. Th. Phys.* **21**, 467 (1982)
9. S. Lloyd, Universal Quantum Simulators. *Science* **273**, 1073 (1996)
10. E. Knill, R. Laflamme, R. Martínez, C.-H. Tseng, An algorithmic benchmark for quantum information processing. *Nature* **404**, 368 (2000)
11. D. Gottesman, *Stabilizer Codes and Quantum Error Correction* (California Institute of Technology, Pasadena, 1997). quant-ph/9705052
12. G. Vidal, Efficient classical simulation of slightly entangled quantum computations. *Phys. Rev. Lett.* **91**, 147902 (2003)
13. M. Van den Nest, W. Dür, G. Vidal, H.J. Briegel, Classical simulation versus universality in measurement-based quantum computation. *Phys. Rev. A* **75**, 012337 (2007)
14. M. Van den Nest, W. Dür, H.J. Briegel, Completeness of the classical 2D Ising model and universal quantum computation. *Phys. Rev. Lett.* **100**, 110501 (2008)
15. M.J. Bremner, C. Mora, A. Winter, Are random pure states useful for quantum computation? *Phys. Rev. Lett.* **102**, 190502 (2009)
16. D. Gross, S.T. Flammia, J. Eisert, Most quantum states are too entangled to be useful as computational resources. *Phys. Rev. Lett.* **102**, 190501 (2009)
17. G. De las Cuevas, W. Dür, M. Van den Nest, H.J. Briegel, Completeness of classical spin models and universal quantum computation. *J. Stat. Mech.* **2009**, P07001 (2009)
18. M. Van den Nest, Universal quantum computation with little entanglement. *Phys. Rev. Lett.* **110**, 060504 (2013)
19. R. Raussendorf, Contextuality in measurement-based quantum computation. *Phys. Rev. A* **88**, 022322 (2013)
20. E. Farhi, J. Goldstone, S. Gutmann, J. Lapan, A. Lundgren, D. Preda, A quantum adiabatic evolution algorithm applied to random instances of an NP-complete problem. *Science* **292**, 472 (2001)
21. M.A. Nielsen, Conditions for a class of entanglement transformations. *Phys. Rev. Lett.* **83**, 436 (1999)
22. D. Jonathan, M.B. Plenio, Entanglement-assisted local manipulation of pure quantum states. *Phys. Rev. Lett.* **83**, 3566 (1999)
23. M.A. Nielsen, I.L. Chuang, *Quantum Computation and Quantum Information*. (Cambridge University, Cambridge, 2004)
24. S. Turgut, Catalytic transformations for bipartite pure states. *J. Phys. A: Math. Theor.* **40**, 12185 (2007)
25. M. Klimesh, Inequalities that collectively completely characterize the catalytic majorization relation. Preprint at *arXiv:0709.3680* (2007)
26. J. Cui, M. Gu, L.C. Kwek, M.F. Santos, H. Fan, V. Vedral, Quantum phases with differing computational power. *Nature Commun.* **3**, 812 (2012)
27. F. Franchini, J. Cui, L. Amico, H. Fan, M. Gu, V.E. Korepin, L.C. Kwek, V. Vedral, Local convertibility and the quantum simulation of edge states in many-body systems, *Phys. Rev. X* **4**, 041028 (2014)
28. Z.C. Gu, X.G. Wen, Tensor-entanglement-filtering renormalization approach and symmetry-protected topological order. *Phys. Rev. B* **80**, 155131 (2009)
29. M.Z. Hasan, C.L. Kane, Topological Insulators. *Rev. Mod. Phys.* **82**, 3045 (2010)
30. V. Mourik, K. Zuo, S.M. Frolov, S.R. Plissard, E.P. Bakkers, L.P. Kouwenhoven, Signatures of Majorana fermions in hybrid superconductor-semiconductor nanowire devices. *Science* **336**, 1003 (2012)

31. H. Braganca, E. Mascarenhas, G.I. Luiz, C. Duarte, R.G. Pereira, M.F. Santos, M.C.O. Aguiar, Non universality of entanglement convertibility. *Phys. Rev.* **B 89**, 235132 (2014)
32. L.-P. Huai, Y.-R. Zhang, S.-Y. Liu, W.-L. Yang, S.-X. Qu, H. Fan, Majorization relation in quantum critical systems. *Chin. Phys. Lett.* **31**, 076401 (2014)
33. J. Cui, L. Amico, H. Fan, M. Gu, A. Hamma, V. Vedral, Local characterization of 1d topologically ordered states. *Phys. Rev.* **B 88**, 125117 (2013)
34. A. Hamma, L. Cincio, S. Santra, P. Zanardi, L. Amico, Local response of topological order to an external perturbation. *Phys. Rev. Lett.* **110**, 210602 (2013).
35. S. Santra, A. Hamma, L. Cincio, Y. Subasi, P. Zanardi, L. Amico, Local convertibility of the ground state of the perturbed Toric code. *Phys. Rev.* **B 90**, 245128 (2014)
36. L. Dai, M.-C. Chung, Breakdown of local convertibility through Majorana modes in a quantum quench. *Phys. Rev.* **A 91**, 062319 (2015)
37. Y.-C. Tzeng, L. Dai, M.-C. Chung, L. Amico, L.-C. Kwak, Entanglement convertibility by sweeping through the quantum phases of the alternating bonds XXZ chain. *Sci. Rep.* **6**, 26453 (2016)
38. X.-G. Wen, *Quantum Field Theory of Many-body Systems* (Oxford University, Oxford, 2004)
39. X. Chen, Z.-C. Gu, X.-G. Wen, *Phys. Rev.* **B 82**, 155138 (2010); *ibid* *Phys. Rev. B* **83**, 035107 (2011); *ibid* *Phys. Rev. B* **84**, 235128 (2011)
40. M. Cianciaruso, L. Ferro, S.M. Giampaolo, G. Zonzo, F. Illuminati, Classical nature of ordered phases: origin of spontaneous symmetry breaking, arXiv:1408.1412 (2014). M. Cianciaruso, S.M. Giampaolo, L. Ferro, W. Roga, G. Zonzo, M. Blasone, F. Illuminati, Classical nature of ordered quantum phases and origin of spontaneous symmetry breaking, arXiv:1604.06403 (2016)
41. O. Bratteli, D.W. Robinson, *Operator Algebras and Quantum Statistical Mechanics: Volume I: C*-and W*-Algebras. Symmetry Groups. Decomposition of States* (Springer Science & Business Media, Berlin, 2012)
42. H. Arodz, J. Dziarmaga, W.H. Zurek, eds., *Patterns of Symmetry Breaking*, vol. 127 (Springer, Berlin, 2012)
43. S. Sachdev, *Quantum Phase Transitions* (Cambridge University, Cambridge, 2000)
44. W. H. Zurek, *Rev. Mod. Phys.* **75**, 715 (2003)
45. J. van Wezel, *Phys. Rev.* **B 78**, 054301 (2008)
46. E. Barouch, B.M. McCoy, Statistical mechanics of XY-model. II. Spin-correlation functions. *Phys. Rev. A* **3**, 786 (1971).
47. F. Verstraete, J.I. Cirac, V. Murg *Adv. Phys.* **57**, 143 (2008).
48. T.J. Osborne, M.A. Nielsen, *Phys. Rev. A* **66**, 032110 (2002)
49. A. Osterloh, L. Amico, G. Falci, R. Fazio, *Nature* **416**, 608 (2002)
50. L. Amico, D. Rossini, A. Hamma, V.E. Korepin, *Phys. Rev. Lett.* **108**, 240503 (2012)
51. B. Tomasello, D. Rossini, A. Hamma, L. Amico, *Int. J. Mod. Phys. B* **26**, 1243002 (2012)
52. S. Campbell, J. Richens, N. Lo Gullo, T. Busch, *Phys. Rev. A* **88**, 062305 (2013)
53. W. Son, L. Amico, R. Fazio, A. Hamma, S. Pascazio, V. Vedral, *Europhys. Lett.*, **95**, 50001 (2011)
54. P. Smacchia, L. Amico, P. Facchi, R. Fazio, G. Florio, S. Pascazio, V. Vedral, *Phys. Rev. A* **84**, 022304 (2011)
55. W. Son, L. Amico, V. Vedral, *Quant. Inf. Proc.* **11**, 1961 (2012)
56. W. Chen, K. Hida, B.C. Sanctuary, *Phys. Rev. B.* **67**, 104401 (2003)
57. C. Degli Esposti Boschi, E. Ercolessi, G. Morandi, in *Symmetries in Science XI* (Kluwer, 2004), pp. 145–173; arXiv:cond-mat/0309658
58. S. Hu, B. Normand, X. Wang, L. Yu, *Phys. Rev. B* **84**, 220402(R) (2011)
59. E. Polizzi, F. Mila, E.S. Sørensen, *Phys. Rev. B* **58**, 2407 (1998)
60. F. Pollmann, E. Berg, A.M. Turner, M. Oshikawa, *Phys. Rev. B* **85**, 075125 (2012)
61. S.-P. Kou, X.-G. Wen, *Phys. Rev. B* **80**, 224406 (2009)
62. F. Pollmann, E. Berg, A.M. Turner, M. Oshikawa, *Phys. Rev. B* **81**, 064439 (2010)
63. W. Li, A. Weichselbaum, J. von Delft, Identifying symmetry-protected topological order by entanglement entropy. *Phys. Rev.* **B 88**, 245121 (2013)

64. L. Lepori, G. De Chiara, A. Sanpera, arXiv:1302.5285; G. De Chiara, L. Lepori, M. Lewenstein, A. Sanpera, Entanglement spectrum, critical exponents and order parameters in quantum spin chains. *Phys. Rev. Lett.* **109**, 237208 (2012)
65. A.Y. Kitaev, *Ann. Phys. (N. Y.)* **303**, 2 (2003)
66. J. Vidal, S. Dusuel, K.P. Schmidt, *Phys. Rev. B* **79**, 033109 (2009); F. Wu, Y. Deng, N. Prokof'ev, *Phys. Rev. B* **85**, 195104 (2012)
67. S.R. White, *Phys. Rev. Lett.* **69**, 2863 (1992); I.P. McCulloch, arXiv:0804.2509; G.M. Crosswhite, *Phys. Rev. B* **78**, 035116 (2008)
68. L. Cincio, G. Vidal, Characterizing topological order by studying the ground states of an infinite cylinder. *Phys. Rev. Lett.* **110**, 067208 (2013)
69. S.T. Flammia, A. Hamma, T.L. Hughes, X.-G. Wen, *Phys. Rev. Lett.* **103**, 261601 (2009)
70. A. Hamma, R. Ionicioiu, P. Zanardi, *Phys. Rev. A* **72**, 012324 (2005)
71. H. Kalis, D. Klagges, R. Orus, K.P. Schmidt, *Phys. Rev. A* **86**, 022317 (2012)
72. C. Castelnovo, C. Chamon, *Phys. Rev. B* **77**, 054433 (2008)
73. J. Yu, S.-P. Kou, X.-G. Wen, *Europhys. Lett.* **84**, 17004 (2008)
74. G.B. Halász, A. Hamma, Probing topological order with Rényi entropy. *Phys. Rev. A* **86**, 062330 (2012)
75. E. Lieb, T. Schultz, D. Mattis, Two soluble models of an antiferromagnetic chain. *Ann. Phys.* **16**, 407 (1961)
76. R. Coldea, D. A. Tennant, E.M. Wheeler, E. Wawrzynska, D. Prabhakaran, M. Telling, K. Habicht, P. Smeibidl, K. Kiefer, Quantum criticality in an Ising chain: experimental evidence for emergent E_8 symmetry. *Science* **327**, 177 (2010)
77. G. Vidal, J.I. Latorre, E. Rico, A. Kitaev, Entanglement in quantum critical phenomena. *Phys. Rev. Lett.* **90**, 227902 (2003)
78. J.I. Latorre, E. Rico, G. Vidal, Ground state entanglement in quantum spin chains. *Quant. Inf. Comput.* **4**, 48 (2004)
79. A. Kitaev, Unpaired Majorana fermions in quantum wires. *Phys.-Usp.* **44**, 131 (2001)
80. A.R. Its, B.-Q. Jin, V.E. Korepin, *J. Phys. A* **38**, 2975 (2005)
81. F. Franchini, A.R. Its, V.E. Korepin, Renyi entropy of the XY spin chain. *J. Phys. A: Math. Theor.* **41**, 25302 (2008)
82. F. Franchini, A.R. Its, V.E. Korepin, L.A. Takhtajan, Entanglement spectrum for the XY model in one dimension. *Quantum Inf. Proc.* **10**, 325 (2011)
83. P. Pfeuty, The one-dimensional Ising model with a transverse field. *Ann. Phys.* **57**, 79–90 (1970)
84. E. Barouch, B.M. McCoy, M. Dresden, *Phys. Rev. A* **2**, 1075 (1970)
85. F. Franchini, An introduction to integrable techniques for one-dimensional quantum systems. *Lect. Notes Phys.* **940**, Springer (2017)
86. J. Kurmann, H. Thomas, G. Müller, *Physica A* **112**, 235 (1982)
87. T. Roscilde, P. Verrucchi, A. Fubini, S. Haas, V. Tognetti, *Phys. Rev. Lett.* **94**, 147208 (2005)
88. S.M. Giampaolo, G. Adesso, F. Illuminati, *Phys. Rev. Lett.* **100**, 197201 (2008)
89. S.M. Giampaolo, G. Adesso, F. Illuminati, *Phys. Rev. B* **79**, 224434 (2009)
90. S.M. Giampaolo, G. Adesso, F. Illuminati, *Phys. Rev. Lett.* **104**, 207202 (2010)
91. W. Roga, S.M. Giampaolo, F. Illuminati, Discord of response. *J. Phys. A: Math. Theor.* **47**, 365301 (2014)
92. S.M. Giampaolo, A. Streltsov, W. Roga, D. Bruss, F. Illuminati, *Phys. Rev. A* **87**, 012313 (2013)
93. S.M. Giampaolo, F. Illuminati, *Phys. Rev. A* **76**, 042301 (2007)
94. A. Monras, G. Adesso, S.M. Giampaolo, G. Gualdi, G.B. Davies, F. Illuminati, *Phys. Rev. A* **84**, 012301 (2011)
95. S. Gharibian, *Phys. Rev. A* **86**, 042106 (2012)
96. W.K. Wootters, *Phys. Rev. Lett.* **80**, 2245 (1998)
97. T. Nakano, M. Piani, G. Adesso, *Phys. Rev. A* **88**, 012117 (2013)
98. F. Ciccarello, T. Tufarelli, V. Giovannetti, *New J. Phys.* **16**, 013038 (2014)
99. V. Coffman, J. Kundu, W.K. Wootters, *Phys. Rev. A* **61**, 052306 (2000)

100. T.J. Osborne, F. Verstraete, Phys. Rev. Lett. **96**, 220503 (2006)
101. L. Amico, F. Baroni, A. Fubini, D. Patanè, V. Tognetti, P. Verrucchi, Phys. Rev. A **74**, 022322 (2006)
102. A. Osterloh, G. Palacios, S. Montangero, Phys. Rev. Lett. **97**, 257201 (2006)
103. S.M. Giampaolo, S. Montangero, F. Dell'Anno, S. De Siena, F. Illuminati, Phys. Rev. B **88**, 125142 (2013)
104. S. Hill, W.K. Wootters, Phys. Rev. Lett. **78**, 5022 (1997)

Optimal Parent Hamiltonians for Many-Body States



Davide Rattacaso, Gianluca Passarelli, Procolo Lucignano, and Rosario Fazio

Abstract After presenting the main features and challenges of the quantum inverse problem, we illustrate numerous results of recent literature, with a particular focus on the different Parent Hamiltonian reconstruction methods and on the scaling of their complexity with the system size.

1 Introduction

Many-body quantum systems possess a large spectrum of features that can be exploited to efficiently solve classically exponentially complex problems [1–3]. Topic of the present chapter is to give a brief review of a problem that has recently attracted attention, the so-called quantum inverse problem. Given a quantum state how can we determine a physically meaningful Hamiltonian—called *Parent Hamiltonian* (PH)—that captures the physics of the system, i.e., a Hamiltonian having such state as an eigenstate (or ground state) [4–13]. In the case of time-dependent states, the problem can be recast in the form of finding a Hamiltonian that can generate the observed time evolution [14–16].

A physically meaningful (realistic) Hamiltonian is an arbitrary Hamiltonian that is compatible with some fundamental constraints. For example, we can consider as physical any Hamiltonian that is the span of interactions involving only particles

D. Rattacaso · P. Lucignano
Dipartimento di Fisica “E. Pancini”, Università di Napoli “Federico II”, Napoli, Italy
e-mail: davide.rattacaso@unina.it; procolo.lucignano@unina.it

G. Passarelli
CNR-SPIN, Napoli, Italy
e-mail: gianluca.passarelli@spin.cnr.it

R. Fazio (✉)
Abdus Salam ICTP, Trieste, Italy

Dipartimento di Fisica “E. Pancini”, Università di Napoli “Federico II”, Napoli, Italy
e-mail: fazio@ictp.it

within a certain distance, e. g., nearest-neighboring spins, or among a limited number of particles, e. g., only two-body interactions. Anyway, we can also consider a stronger constraint on the space of the realistic Hamiltonians, for example, we can consider only Hamiltonians that are the span of elementary interactions that can be engineered on a given synthetic quantum system. While the search for a parent Hamiltonian that is just a Hermitian operator always has a solution, the constraint of locality drastically increases the difficulty of the inverse problem. Moreover, while a solution to this problem always exists in the space of all the Hermitian operators, a local solution may not exist. In this case, one defines a so-called *Optimal Parent Hamiltonian* (OPH), that is a realistic Hamiltonian that optimizes a figure of merit designed to estimate how close the OPH is to being the real PH.

The inverse problem is relevant in several different contexts, touching both fundamental aspect of quantum theory as well as quantum technological applications. Some of the questions that can be answered by solving this problem are: (1) How many possible models are compatible with our observation on a quantum system? (2) How many and which observables do we need to measure in order to identify the physical laws that govern a quantum system? (3) Can we deduce the high energy behavior of a quantum system from its low-energy behavior or from its stationary behavior [17]? (4) Which state evolutions are possible and which ones are not in a world governed by local interactions [18]? (5) All these questions can be recast in terms of the inverse problem: how many solutions does the problem have for a given quantum state? (6) How many observables do we need to measure in order to have enough information to reconstruct the PH? In which cases is the PH associated with a ground state unique? (7) In which cases is there no exact PH? We will address several of these questions in the following sections.

The technological impact of the inverse problem is a consequence of our increasing capability of engineer and dynamically control many-body Hamiltonians. Indeed, *quantum state preparation* and *quantum state control* [19–28] are based on our ability to prepare and control Hamiltonians. The resolution of the inverse problem gives us a recipe to implement and manipulate states, for example, by cooling down a system in which the PH has been engineered [29–32] or by performing a quantum annealing [33–36]. Moreover, we can use an optimal Hamiltonian to follow the ground state of a parametric family of Hamiltonians [16], defining new shortcuts to adiabaticity [37–44]. Finally, the search for PHs is also useful for quantum verification, in which one has to verify that the synthetic quantum system prepared in the laboratory is effectively governed by some target Hamiltonian [3, 45–49]. In particular, learning the Hamiltonian that governs our system under some constraint on the tunable interactions [50–53] is the most direct way to verify what is really happening in a quantum device.

Motivated by all these reasons, in the last years several papers have proposed different methods to attack the inverse problem. Among these proposals we can identify three different, but related, classes:

1. In the first class, one tries to reconstruct a local PH starting from one of its eigenstates [4–9]. We call this kind of PH *symmetry of the state*. Section 2 of this work is devoted to discussing this topic.

2. In the second class, one tries to reconstruct a local PH from one of its ground states [10–13]. We refer to this class of PHs as *proper PHs* (PPH). We discuss them in Sect. 3. PPHs for a given state are, of course, a subset of the symmetries of the state.
3. In the latter class, one tries to reconstruct a PH for a time-dependent state. Since the state is not stationary, it cannot be an eigenstate of the PH, which must be thought as the generator of its evolution. This generator could be in principle time-independent or time-dependent; therefore, one can search for a *time-independent PH* [14, 15], or for a *time-dependent PH* [16]. The methods to reconstruct this kind of PHs and the resources needed, in terms of measurements on the state, are analyzed in Sect. 4.

Even if in this paper we focus our attention only on the inverse problem for unitary evolutions, that is the search for a PH, clearly one can extend this investigation to open quantum systems and search for a *parent Lindbladian*. Many proposals in this direction are a direct extension of a corresponding reconstruction method for closed system [54, 55]. Even if this chapter has some focus on our contribution to this problem, the aim is to give an overview of the different directions explored in the existing literature together with its main achievements.

2 The Space of Symmetries

An important problem in this area is the search for the space of symmetries: given the state $|\psi\rangle$ we look for the realistic parent Hamiltonians for which $|\psi\rangle$ is an eigenstate. This approach is relevant in quantum Hamiltonian learning, whose goal is reconstructing the interactions governing a quantum system performing local measurements on a stationary pure state, instead of employing an exponential amount of resources to perform process tomography. There are two main different approaches to this problem. One of them [4–7] exploits the knowledge of the local correlation functions of the state $|\psi\rangle$, while the other [8, 9] only requires the knowledge of local expectation values.

Both of these approaches are based on the assumption that the space of realistic Hamiltonians is a vector space, spanned by a set $\mathcal{L} = \{L_i\}$ of local interactions. For qubit systems, interactions in \mathcal{L} are tensor products of the Pauli operators $\{\sigma_i^\mu\}$ acting on the i -th spin of a lattice, where $\sigma^\mu \in \{\mathbb{1}, \sigma^x, \sigma^y, \sigma^z\}$. As a consequence of the algebraic properties of the Pauli operators, elements in \mathcal{L} are orthogonal with respect to the inner product $(A, B) \equiv \text{Tr}(AB)$, and, therefore, they form an orthogonal basis for the space of realistic Hamiltonians:

$$H = \sum_i h_i L_i. \quad (1)$$

Since if $|\psi\rangle$ is an eigenstate for H_1 and H_2 it is also an eigenstate for $\alpha H_1 + \beta H_2$, the symmetries for a state form a vector subspace of the space of linear operators; therefore, the most general solution to the problem consists in finding a basis $\{S_k\}$ for the space of symmetries.

As shown in [4–7], the space of symmetries of a state $|\psi\rangle$ can be reconstructed starting from the knowledge of correlation functions of local operators $\langle\psi|L_i L_j|\psi\rangle$. In general, these are not easily accessible; however, they can be efficiently estimated in some significant contexts, such as the Hamiltonian learning, when the state is already implemented on a quantum device and correlations can be measured, or for some classes of states, like MPS [56] or ground states of the Ising model in transverse field where an exact solution can be expressed in terms of fermions [57].

Early results in this direction have been obtained in Refs. [4, 5]. In these works, the authors start by observing that a realistic Hamiltonian $H = \sum_i h_i L_i$ is a symmetry for the state $|\psi\rangle$ if and only if the variance of H on $|\psi\rangle$ is zero:

$$\langle H^2 \rangle - \langle H \rangle^2 = 0, \quad (2)$$

where, from now on, $\langle O \rangle = \langle\psi|O|\psi\rangle$. Replacing $H = \sum_i h_i L_i$ in the latter equation, we obtain

$$\sum_{ij} h_i h_j (\langle L_i L_j \rangle - \langle L_i \rangle \langle L_j \rangle) = 0, \quad (3)$$

that is equivalent to

$$\sum_{ij} h_i h_j C_{ij} = 0, \quad (4)$$

where

$$C_{ij} := \langle\{L_i, L_j\}\rangle - 2\langle L_i \rangle \langle L_j \rangle \quad (5)$$

is a semi-definite positive matrix called Quantum Covariance Matrix (QCM). We will show in Sect. 4 that this matrix also has a central role in the search for time-dependent parent Hamiltonians. Clearly, if the coefficients h_i of a Hamiltonian are in the kernel of the QCM, the variance is zero and the Hamiltonian is a symmetry. Therefore, given a basis $n_i^{(k)}$ for the kernel of the QCM, the local operators $S_k := \sum_i n_i^{(k)} L_i$ are a basis for the space of symmetries, which can be written as

$$S = \sum_k s_k S_k. \quad (6)$$

Moreover, if the vectors $n_i^{(k)}$ are orthogonal with respect to the standard scalar product, $\{S_k\}$ is an orthogonal basis, indeed

$$\text{Tr}(S_k S_l) = \sum_{ij} n_i^{(k)} n_j^{(l)} \text{Tr}(L_i L_j) \propto \sum_{ij} n_i^{(k)} n_j^{(l)} \delta_{ij} \propto \delta_{kl}. \quad (7)$$

One of the most successful aspects of this approach is that the size of the QCM and the number of local operators in \mathcal{L} are polynomial in the system size. This makes the search for symmetries very efficient once the local correlations are known. Another important advantage of looking for symmetries through the kernel of the QCM is that, in absence of null eigenvalues, we can also consider as *optimal symmetries* the local Hamiltonians associated with the minimum eigenvalue of the QCM. In the stationary case these optimal symmetries can correspond to exact solutions when, for example, correlation functions contain a measurement error.

Studying the kernel of the QCM is not the only way to proceed. For example, in Ref. [6], it has been shown how parent Hamiltonians can be recovered from a different QCM containing non-connected correlations. Another possible approach has been proposed in Ref. [7], in which one starts from the Ehrenfest equation for the evolution of the local expectation values $\langle L_i \rangle$ generated by the Hamiltonian $H = \sum_i h_i L_i$:

$$\partial_t \langle L_i \rangle = i \sum_j h_j \langle [L_j, L_i] \rangle. \quad (8)$$

This equation can be written as

$$\partial_t \langle L_i \rangle = \sum_j h_j K_{ij} \quad (9)$$

if we define the correlation matrix $K_{ij} = -i \langle [L_j, L_i] \rangle$. When a state is stationary for the Hamiltonian H the expectation values of local operators do not evolve and the LHS of the last equation becomes zero. Therefore, the coefficients of each symmetry correspond to zero-eigenvalue eigenvectors of the matrix K . More generally, optimal solutions can be obtained by looking at the minimum-eigenvalue eigenvectors of the correlation matrix $\mathcal{M} \equiv K^T K$. In this method, there is a caveat: Hamiltonians that only affect the mean values of non-local operators are in the kernel of \mathcal{M} even though they are not symmetries. Anyway, the authors of Ref. [7] have shown for some relevant examples that, when the set of measured observables is sufficiently enlarged, this approach is able to effectively distinguish real symmetries without requiring the measurement of non-local observables. It is remarkable that, when all the possible expectation values are taken into account, the matrix \mathcal{M} becomes the previously introduced QCM.

We have shown how the local correlations can be efficiently exploited to determine the symmetries of a quantum state. However, as shown by Bairey et

al. [7], local expectation values may contain sufficient information to reconstruct a symmetry. As stressed in Ref. [8], the possibility of using local expectation values instead of correlation to reconstruct symmetries is strictly related to the quantum marginal problem [10, 58, 59], that is, the reconstruction of a quantum state starting from a set of local expectation values. In this context, it is known that some quantum states are fully determined by local expectation values. As a consequence, one might expect that for some states it is possible, though possibly computationally hard, to solve the inverse problem by only knowing the expectation values of the operators in \mathcal{L} . This was proposed and analyzed in Refs. [8, 9].

In Ref. [8], the authors start from noticing that, if $|\psi\rangle$ is the unique ground state of some local Hamiltonian H , then one can define a thermal density matrix that, for a sufficiently large inverse temperature β :

$$|\psi\rangle\langle\psi| = \frac{e^{-\beta H}}{\text{Tr}(e^{-\beta H})}. \quad (10)$$

As a consequence, the state is directly related to the Hamiltonian and, since the free parameters of the Hamiltonian are only the coefficients h_i associated with local operators, the expectation values of local operators on $|\psi\rangle$ can be sufficient to determine H . This approach can be easily extended to the symmetry search problem, where one starts from an arbitrary eigenstate instead of the ground state. In this case, if $H = \sum_i h_i L_i$ is a symmetry for $|\psi\rangle$, $|\psi\rangle$ is the ground state of the non-local Hamiltonian \tilde{H}^2 , with

$$\tilde{H}(\mathbf{h}) = \sum_i h_i L_i - \langle H \rangle \mathbb{1} = \sum_i h_i (L_i - \langle L_i \rangle \mathbb{1}). \quad (11)$$

Therefore, one can reconstruct H looking for the vector \mathbf{h} of local couplings such that $|\psi\rangle$ is the Gibbs state of \tilde{H}^2 for a sufficient large inverse temperature:

$$|\psi\rangle\langle\psi| = \frac{e^{-\beta \tilde{H}^2(\mathbf{h})}}{\text{Tr}(e^{-\beta \tilde{H}^2(\mathbf{h})})}. \quad (12)$$

Since the free parameters that determine \tilde{H} are local couplings, the convergence of the Gibbs state to $|\psi\rangle\langle\psi|$ is verified through the convergence of local expectation values:

$$\lim_{\beta \rightarrow \infty} \frac{\text{Tr}(L_i e^{-\beta \tilde{H}^2(\mathbf{h})})}{\text{Tr}(e^{-\beta \tilde{H}^2(\mathbf{h})})} = \langle L_i \rangle. \quad (13)$$

This condition can be formulated as an optimization problem: we can indeed define the optimal symmetries as the minimum of the cost function

$$f_\beta(\mathbf{h}) \equiv \sum_i \left(\langle L_i \rangle - \frac{\text{Tr}(L_i e^{-\beta \tilde{H}^2(\mathbf{h})})}{\text{Tr}(e^{-\beta \tilde{H}^2(\mathbf{h})})} \right)^2 + \text{Tr} \left(\frac{\tilde{H}^2(\mathbf{h}) e^{-\beta \tilde{H}^2(\mathbf{h})}}{\text{Tr}(e^{-\beta \tilde{H}^2(\mathbf{h})})} \right) \quad (14)$$

for large values of β . The first term of f_β encodes the condition in Eq. (13). While the second term ensures that the Gibbs state is the ground state of \tilde{H}^2 .

The limit of f_β for $\beta \rightarrow \infty$ can be impractical in numerical simulations hence the trick proposed in Ref. [8] is to fix $\beta = 1$ and amplify the spectral gaps.

Supervised learning with a neural network have been also adopted in Ref. [9], where the authors have shown that the more excited is the initial state $|\psi\rangle$ for its symmetry H , the more difficult it is for a neural network to reconstruct H from local expectation values. The neural network can be trained with the coefficients h_i of randomly chosen Hamiltonians of the form

$$H = \sum_i h_i L_i, \quad (15)$$

and with the corresponding expectation values a_i on the k -th level eigenstate $|\psi_k\rangle$ of H :

$$a_i = \langle \psi_k | L_i | \psi_k \rangle. \quad (16)$$

Finally, in Ref. [8], the authors show that supervised learning can be used to select appropriate initial points of the minimization technique of Ref. [9].

To summarize, the space of symmetries can be efficiently reconstructed starting from the knowledge of the correlation functions [4–7] but also using only local expectation values. The price to pay, in the second case, is a greater computational cost because we need to either minimize an extremely complicated cost function [9] or train a neural network with the results obtained from the diagonalization of exponentially large Hamiltonian matrices [8].

These results help us answer two of the theoretical questions posed in the introduction.

- The possible models—local Hamiltonians—that are compatible with a stationary state are in general a vector space. The dimension of this space is larger than one for several physically significant states [5].
- The PH of a stationary state can be determined only by the local expectation values. The complexity of this approach is unlikely to present an affordable scaling in the system size compared with methods assuming the knowledge of correlations functions. This is consistent with the quantum marginal problem: correlation functions, for some state, are determined by local expectation values, but these correlations can be hard to achieve. [10, 58, 59]

3 From Ground States to Parent Hamiltonians

In the previous section, we have described how to search local symmetries of a given quantum state. However, in some cases it is more desirable to find a parent Hamiltonian such that the state $|\psi\rangle$ is its ground state. Such a Hamiltonian, when it exists, can be a precious tool in quantum state preparation, for example, if we want to implement $|\psi\rangle$ by cooling down a device in which the PPH has been implemented, or by adiabatically driving states by implementing the corresponding PHs. Analogously, the capability of reconstructing the PPH can be exploited to learn the Hamiltonian of a low-temperature system through measurements on its state.

This version of the inverse problem, of course, is harder than the search for symmetries. In principle, a solution can be obtained by exploiting the thermodynamic approach in Sect. 2, replacing \tilde{H} with H in the cost function of Eq. (13) in order to select only Hamiltonians having $|\psi\rangle$ as their ground state. The locality of H simplifies the evaluation of the cost function f_β , however, the exponential complexity of the problem is generally maintained. In this section, we present the relevant features of the inverse problem in exam and we show an efficient method to attack the problem in some particular cases [12, 13].

The search for PHs does not generally have a unique solution. For an interacting spin system, a trivial example is given by the product state $|\uparrow \dots \uparrow\rangle$, whose PH can either be the single-particle Hamiltonian $H_1 = -\sum_i \sigma_i^z$ or the ferromagnetic Ising-like Hamiltonian $H_2 = -\sum_i \sigma_i^z \sigma_{i+1}^z$. As symmetries form a vector space, we can linearly combine many solutions of the inverse problem in order to obtain a new solution. The question, here, is whether that can be done for PHs.

First of all, PPHs are a subset of symmetries, thus the search for PHs can be simplified by first reconstructing the space of symmetries.

In Ref. [5], the authors have identified PPH among symmetries via exact diagonalization, an approach that requires a huge computational cost for large systems.

The main problem is that the set of PPHs is not a vector space. As a simple example we may notice that if H is a PPH for $|\psi\rangle$, the same does not hold for $-H$. As a consequence, we cannot identify a vector basis for this set. In particular, it can be shown that the set in exam is a *convex cone*, that is if H_1 and H_2 are PPHs, also

$$H(\alpha, \beta) = \alpha[\beta H_1 + (1 - \beta)H_2] \quad (17)$$

is a PPH for each $\alpha > 0$ and $\beta \in [0, 1]$. The fact that the set of PPHs is a convex cone gives an important insight about the difficulty of its reconstruction: while the identification of the space of symmetries is obtained by finding a finite number of vectors—a basis—a convex cone is identified by its extremal points that can be infinite even if the cone lies in a finite-dimensional space.

Let us consider a local Hamiltonian H . To check if this Hamiltonian is a parent Hamiltonian for $|\psi\rangle$, it is sufficient to measure the expectation value $\langle\psi|H|\psi\rangle$ and compare it with the minimum eigenvalue of H . Since $\langle\psi|H|\psi\rangle = \sum_i h_i \langle\psi|L_i|\psi\rangle$,

it is sufficient to measure local expectation values to verify that H is a PPH for $|\psi\rangle$. Moreover if $|\psi\rangle$ is the unique ground state for some local Hamiltonian H , it has to be the unique pure state for which the expectation values of the L_i 's are $\langle\psi|L_i|\psi\rangle$. We can conclude that:

- Local expectation values of a state fully determine its PPHs.
- States that cannot be distinguished by local measurements are degenerate ground states of the same PPHs. GHZ states $|\text{GHZ}\rangle_{\pm} = |\uparrow \dots \uparrow\rangle \pm |\downarrow \dots \downarrow\rangle$ are an example in this direction: one can easily check that all the 1 and 2-spins operator have the same expectation values for these states, as a consequence there is no PPH spanned by these operators such that $|\text{GHZ}\rangle_+$ is the unique ground state.

In Ref. [10], the authors have shown a Hamiltonian reconstruction method for PPHs. They have shown how to find, if they exist, frustration free (FF) PPHs for a given state. A FF PPH is a local Hamiltonian

$$H = \sum_X H_X, \quad (18)$$

where H_X is a local Hamiltonian acting non-trivially only on a fixed-size connected subset X of the lattice—for example, only on pairs of neighboring spins—such that $|\psi\rangle$ is a ground state for each H_X . FF parent Hamiltonians can be identified as the convex cone spanned by all the H_X . The Hamiltonians H_X for the state $|\psi\rangle$ are the projectors on the null space of the reduced density matrices of $|\psi\rangle$ on X . This condition is equivalent to system of three equations for H_X . First of all one needs that H_X acts non-trivially only on X , in equations:

$$H_X = \text{Tr}_{\bar{X}}(H_X) \otimes \mathbb{1}_{\bar{X}}, \quad (19)$$

where $\text{Tr}_{\bar{X}}$ is the partial trace with respect the complement of X . Moreover H_X has to be a projector, hence

$$H_X^2 = H_X. \quad (20)$$

In this way we can be sure that the eigenvalues of H_X are 0 or 1. At this point $|\psi\rangle$ is a ground state for H_X only if

$$\langle\psi|H_X|\psi\rangle = \text{Tr}(\text{Tr}_{\bar{X}}(H_X)\text{Tr}_{\bar{X}}(|\psi\rangle\langle\psi|)) = 0. \quad (21)$$

The conditions above, and then the FF proper PH, can be checked easily also for a large quantum system once one knows the local expectation values, that is equivalent to know the reduced density matrices. On the other hand, this approach has two important limitations. The first one is that when a state is sufficiently entangled its reduced density matrices have all nonzero eigenvalues, so the null space of these matrices is empty and there are no FF proper PHs. This makes this approach suitable only for states with small entanglement such as MPSs, for which an analogous

method has been proposed [11]. The second limit is that many physically significant local Hamiltonians, for example, the Ising Hamiltonian in transverse field, are not FF proper PHs for their ground states.

A promising approach to find PPHs has been recently proposed in Refs. [12, 13], where the idea is to approximate the reduced density matrix of the ground state of a trial Hamiltonian using the Bisognano-Wichmann theorem and minimize a distance between this matrix and the reduced density matrix of the input state $|\psi\rangle$. When this distance goes to zero the trial Hamiltonian is a PPH for $|\psi\rangle$.

The authors start from the Bisognano-Wichmann (BW) theorem, which holds in the context of relativistic quantum field theories, and use this theorem to propose an ansatz for the reduced density of the ground state of the trial Hamiltonian. As a consequence, it is particularly interesting for trial Hamiltonians whose low-energy physics is well described by a relativistic theory. Remarkably, some of these Hamiltonians generate physically relevant phenomena such as quantum criticality, topological matter, and quantum ferromagnets [12].

In order to exploit the ansatz for spin models, local operators $\{L_i\}$ are written as $\{O_{r,\alpha}\}$, where r points to the lattice site and α labels the local spin operator - e.g., $\sigma_r^x \sigma_{r+1}^x$ or $\sigma_r^y \sigma_{r+1}^y$ -. The trial Hamiltonian is written as

$$H = \sum_{r,\alpha} h_{r,\alpha} O_{r,\alpha}. \quad (22)$$

In short, the BW ansatz states that the reduced density matrix of the Hamiltonian H on a half space—for example, the sites with $r > 0$ in a linear lattice—is

$$\sigma_{\text{BW}}(H) = \frac{e^{-H_{\text{BW}}}}{\text{Tr}(e^{-H_{\text{BW}}})}, \quad (23)$$

with

$$H_{\text{BW}} = \beta \sum_{r>0,\alpha} r h_{r,\alpha} O_{r,\alpha}, \quad (24)$$

for some value of β called inverse *entanglement temperature*. This ansatz is very similar to Gibbs representation of the state given in Eq. (10), where here β is an inverse entanglement temperature. However, the state σ_{BW} is a reduced density matrix and it is related to the Hamiltonian acting only on a given region of the lattice, as expressed in Eq. (24).

The inverse method consists in exploring the space of local Hamiltonians, defined by their couplings $h_{r,\alpha}$, in order to minimize the relative entropy

$$f(\mathbf{h}) = \text{Tr}(\rho \log(\rho)) - \text{Tr}(\rho \log(\sigma_{\text{BW}}(H))) \quad (25)$$

between the BW state $\sigma_{\text{BW}}(H)$ and the reduced density matrix of the input state $|\psi\rangle$ on the half space. When this entropy vanishes, the reduced density matrix ρ

of $|\psi\rangle$ is equal to $\sigma_{\text{BW}}(H)$ and, if the BW ansatz holds, $|\psi\rangle$ is a ground state for H . The minimization of $f(\mathbf{h})$ can be performed via gradient descent, so one has to evaluate the derivatives $\frac{\partial f}{\partial h_{r,\alpha}}$, which only depend on the expectation values of the local operators for ρ and $\sigma_{\text{BW}}(H)$.

One of the most promising aspects of this method is that in some cases [13] the BW ansatz can be used to evaluate the density matrix of a sub-lattice whose extension does not depend on the size of the entire system, instead of the density matrix of the half space. For these cases, the difficulty of performing the gradient descent on $f(\mathbf{h})$ does not increase with the system size.

In this section, we have seen that given a state, the corresponding local parent Hamiltonian, if it exists, is generally not unique. As a consequence, the full spectral properties of the Hamiltonian are encoded in its low-energy behavior. More specifically, the set of PPHs is a convex cone and is a subset of the vector space of symmetries. We have also shown that all the information that one needs about a quantum state in order to determine a PPH is contained in local expectation values. If two states cannot be distinguished through local expectation values, they are degenerate ground states for a possible PPH.

Promising reconstruction methods are capable of determining only FF PPHs [10, 11] or can be applied under the restriction that the state mimics the low-energy behavior of some relativistic theory [12, 13]. It is remarkable that the efficient techniques developed in the context of symmetries reconstruction and based on quantum correlations [4–7] have not been extended until now to this inverse problem.

4 The Time-Dependent Inverse Problem

There are several physical situations in which one may want to know the Hamiltonian that is responsible for the dynamics of the system. For example, when one wants to learn the time-independent parent Hamiltonian of a synthetic quantum system by looking at the evolution of expectation values [14, 15], or when one wants to find an engineerable time-dependent parent Hamiltonian that can drive a quantum state along a target evolution [16].

The capability of reconstructing a parent Hamiltonian from the evolution of local expectation values is an important resource for quantum analog device verification [15]. A possible problem consists in verifying if the Hamiltonian that is effectively evolving the system corresponds to the Hamiltonian that we are trying to implement in a quantum device. For this purpose, a time-independent PH identification method has been presented in a recent paper [15] for a superconducting quantum processor system and successfully exploited to benchmark the implementation precision of the Google Sycamore processor. There is a crucial difference between this inverse method and the ones illustrated in the previous sections. The inverse problem in the form we are considering in this paper consists

in finding all the possible PHs for a single state. Yet, when the goal is to perform Hamiltonian learning for an engineered system, we need to find a way to select a single parent Hamiltonian within that set. In most cases, this goal is achieved by considering different input states and looking for simultaneous parent Hamiltonians through the methods that we have illustrated until now [7]. In this way these methods, originally intended as solutions to the inverse problem for a single state, are extended to multiple states. In Ref. [15], the PH reconstruction exploits the algebraic properties of the bosonic operators to design a condition for the parent Hamiltonian that takes simultaneously into account the evolution of a set of input states.

In this section we examine recent papers proposing solutions to this inverse problem, stressing on the relationship between these inverse methods, the search for symmetries, and other related topics in the literature such as adiabatic and counterdiabatic driving [33, 60, 61].

In Sect. 2, we have shown how measurement of correlation can be exploited to find the symmetries of a stationary state. Here, we extend this approach exploiting correlation functions and derivatives of time-dependent expectation values to infer the instantaneous PH that generates the evolution of the state $|\psi(t)\rangle$.

Our starting point is the Schrödinger equation for the density operator $\rho(t) = |\psi(t)\rangle\langle\psi(t)|$:

$$\partial_t \rho(t) = -i[H(t), \rho(t)]. \quad (26)$$

Given the time-dependent state $\rho(t)$, our goal is to find the couplings of the local Hamiltonian $H(t)$ —if it exists—for which the Schrödinger equation holds.

To reach this goal, we exploit a vector representation of the state and of the Hamiltonian. Since the Hamiltonian is local, given the basis $\mathcal{L} = \{L_i\}$. For the local Hermitian operators, we have

$$H(t) = \sum_i h_i(t) L_i. \quad (27)$$

On the other hand, a generic state is not a local operator, so we need a basis $\mathcal{B} = \{B_\gamma\}$ for the space of all the Hermitian operators. We choose both \mathcal{L} and \mathcal{B} to be orthonormal bases with respect to the operator scalar product. For spin systems, a convenient choice for construct these basis is formed by products of Pauli operators (appropriately normalized). For example, one can choose \mathcal{L} as an orthonormal basis of Pauli operators representing one-spin and two-neighboring-spins interactions

$$\mathcal{L} = \{\sigma_i^\mu\} \cup \{\sigma_i^\mu \sigma_{i+1}^\nu\}, \quad (28)$$

and \mathcal{B} as an orthonormal basis of generic strings of Pauli operators

$$\mathcal{B} = \{\sigma_1^{\mu_1} \sigma_2^{\mu_2} \cdots \sigma_N^{\mu_N}\}. \quad (29)$$

At this point, using the resolution of the identity, the state can be written as

$$\rho(t) = \sum_{\gamma} o_{\gamma} B_{\gamma}, \quad (30)$$

where the o_{γ} 's are the time-dependent expectation values $\text{Tr}(B_{\gamma}\rho(t))$ of the operators in \mathcal{B} . Replacing Eqs. (30) and (27) in Eq. (26), after some algebra [16], we obtain the following system of equations:

$$\partial_t o_{\gamma} = \sum_i h_i(t) K_{i\gamma}(t), \quad (31)$$

where $K_{i\gamma}(t) \equiv -i\langle\psi(t)|[B_{\gamma}, L_i]|\psi(t)\rangle$. Once the correlations in $K_{i\gamma}$ at time t have been measured, and the derivatives of the expectation values o_{γ} have been reconstructed from their evolution, Eq. (31) can be solved to find the couplings $h_i(t)$ of the parent Hamiltonian at time t .

Equation (31) forms an inhomogeneous linear system, hence all the PHs correspond to a single solution of the equations plus an arbitrary element of the kernel of the matrix $K_{i\gamma}(t)$. This kernel coincides with the kernel of the QCM for the state $|\psi(t)\rangle$ at time t [7, 16], and, therefore, with the space of instantaneous local symmetries for the state. We can conclude that, at fixed time, the space of possible PHs for a time-dependent state inherits its degeneracy from the space of symmetries. From this point of view, each PH $H(t)$ can be considered as the sum of an adiabatic potential $H_A(t)$, for which $|\psi(t)\rangle$ is an eigenstate, and a counterdiabatic potential [37–43, 60–67] that counteracts the Landau–Zener transitions in order to constraint the state $|\psi(t)\rangle$ to remain an eigenstate of $H_A(t)$ [16].

A significant application of Eq. (31) has been shown in Ref. [7], where the authors reconstruct the time-independent Hamiltonian of a synthetic quantum system. Since the parent Hamiltonian is considered to be time-independent, one only needs to measure correlations at the time t_0 at which the state is implemented, and expectation values at times t_0 and $t_0 + dt$ in order to extract the time derivatives $\partial_t o_{\gamma}$ and calculate the time-independent couplings h_i of the parent Hamiltonian.

Equation (31) has two important limitations: it has multiple solutions and it requires the measurement of non-local observables. The first difficulty can be overcome by simultaneously solving the system for different initial states $|\psi_n\rangle$, while the second one by measuring only local operators L_i and correlations $-i[L_i L_j]$. In this way, the matrix $K_{i,\gamma}$ reduces to the local correlation matrix $K_{i,j}$ defined in Sect. 2. Through this approach the authors prove two points that are significant for the dynamical inverse problem in general:

- If the initial states are separable, local expectation values and local correlations are sufficient to solve the inverse problem.
- The number of initial separable states necessary to identify the Hamiltonian of the system through this approach is independent of the system size.

These features could be ultimately related to the fact that local correlations spread out at finite velocity when the Hamiltonian is local and initial connected local correlations of separable states are null [68].

In the previous section, we have introduced a system of equations that relates the instantaneous evolution of state, that is the state and its derivative at time t , with the local PH $H(t)$ that generates this evolution. When a time-dependent state has been effectively implemented in a quantum system, as in the cases examined in Refs. [14, 15], this PH always exists. This is not true for a generic quantum states $|\psi(t)\rangle$, whose evolution could be impossible to generate through a local Hamiltonian. When this is the case, we need to look for an optimal time-dependent PH, that is a local Hamiltonian that generates an evolution as close as possible to the target $|\psi(t)\rangle$. Following Ref. [16], in this section we present an inverse method to find this optimal Hamiltonian.

We represent the target state through its density matrix $\rho(t) = |\psi(t)\rangle\langle\psi(t)|$ and consider as a cost function the difference between the instantaneous evolution of the target state, expressed through its derivative $\partial_t\rho$, and the instantaneous evolution $-i[H(t), \rho(t)]$ generated by a trial Hamiltonian $H(t)$. For a time-dependent state in a time interval $[0, T]$, a cost functional that estimates this difference is

$$\mathcal{F}[H(t)] \equiv \int_0^T dt \|\partial_t\rho(t) + i[H(t), \rho(t)]\|, \quad (32)$$

where $\|A\| \equiv \sqrt{\text{Tr}(A^2)}$ is the Frobenius norm. Since this cost functional does not depend on the derivative of the Hamiltonian, the optimal PH at time t is

$$\text{Min}_{H(t)} f(H(t)), \quad (33)$$

where $f(H(t)) = \|\partial_t\rho(t) + i[H(t), \rho(t)]\|^2$ is an instantaneous cost function. To find this minimum we introduce the operators $l_i(t) = -i[L_i, \rho(t)]$. Since $-i[H(t), \rho(t)] = \sum_i h_i(t)l_i(t)$, these operators are a basis for all the infinitesimal evolutions that can be generated by a local Hamiltonian, that we call *local tangent space* for $\rho(t)$. The vector of the local tangent space that optimally approximates the infinitesimal evolution $\partial_t\rho(t)$ can be obtained through a projection of $\rho(t)$ on this space. In this way, we obtain a linear system of equations for the couplings h_i of the optimal time-dependent PH [16]:

$$\text{Tr}(l_a(t)\partial_t\rho(t)) = \sum_b \text{Tr}(l_a(t)l_b(t))h_b(t), \quad (34)$$

where the matrix $\text{Tr}(l_a(t)l_b(t))$ can be shown to correspond to the QCM introduced in Sect. 2, so that this last equation is the time-dependent generalization of Eq. (4).

In analogy with Eq. (31), the homogeneous and inhomogeneous solutions of Eq. (34) can be, respectively, considered as a local adiabatic Hamiltonian and the corresponding optimal counterdiabatic potential. From this point of view, one could

ask if this optimal counterdiabatic potential is equivalent to the one introduced by Sels and Polkovnikov [61] in the context of shortcuts to adiabaticity, in which the target state $|\psi(t)\rangle$ that has to be generated is an eigenstate of a local Hamiltonian. In this regard, it has been shown [16] that the difference between the inhomogeneous solution of Eq. (34) and the counterdiabatic potential in Ref. [61] consists in the fact that, while the former is suited to exploit all the available local resources to drive the target state $|\psi(t)\rangle$ alone, the latter tries to simultaneously drive all the eigenstates of the adiabatic Hamiltonian.

In Ref. [16], Eq. (34) has been exploited in order to find time-dependent optimal parent Hamiltonians for three classes of time-dependent states: ground states of an Ising chain in a tunable transverse field [57], ground states of a p -spin Hamiltonian in a tunable transverse field [69], and linear superpositions of two states in different phases of the p -spin Hamiltonian. As a paradigmatic example, let us briefly summarize the results obtained for the Ising model in a time-dependent transverse field $\lambda(t)$, where the optimal PH is analytically calculated thanks to the Jordan–Wigner transformations [57]. In this case, the target state $|\psi(\lambda(t))\rangle$ is the instantaneous ground state of the Hamiltonian

$$H_I(\lambda(t)) = - \sum_{i=1}^L \sigma_i^x \sigma_{i+1}^x - \lambda(t) \sum_{i=1}^L \sigma_i^z, \quad (35)$$

with periodic boundary conditions $\sigma_{L+1}^\mu = \hat{\sigma}_1^\mu$. An exact parent Hamiltonian for $|\psi(\lambda(t))\rangle$ is [16, 70]:

$$H_{\text{parent}}(t) = \frac{\lambda}{2L} \sum_{j'>j} \left(\sum_{k \in \mathcal{K}^+} \frac{\sin(k) \sin[k(j' - j)]}{1 + \lambda^2 - 2\lambda \cos(k)} \right) \mathcal{S}_{jj'}, \quad (36)$$

where

$$\mathcal{S}_{jj'} = \sigma_j^x \sigma_{j+1}^z \dots \sigma_{j'-1}^z \sigma_{j'}^y + \sigma_j^y \sigma_{j+1}^z \dots \sigma_{j'-1}^z \sigma_{j'}^x$$

is a string of Pauli operators acting on the spins from i to j , in which the dots represent a string of σ_z operators, and $\mathcal{K}^+ = \{\frac{(2i-1)\pi}{L}, \text{ with } i = 1, \dots, L/2\}$ is the momentum spectrum for the Ising model. This exact PH, as well as any other one for $|\psi(\lambda(t))\rangle$, is the span of non-local operators. We want to find an optimal PH that only involves one-spin and two-adjacent-spins interactions in

$$\mathcal{L} = \{\sigma_i^\mu, \sigma_i^\mu \otimes \sigma_{i+1}^\nu\}. \quad (37)$$

This goal is reached by solving Eq. (34). Taking advantage of the Ising Hamiltonian symmetries and of the Jordan–Wigner transformations, we can show [16] that a

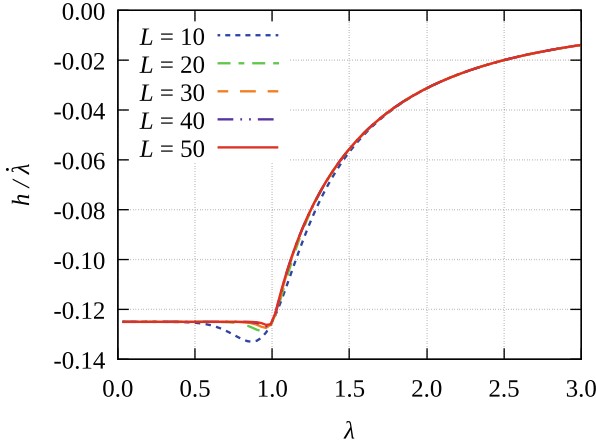


Fig. 1 Evolution of the (rescaled) optimal coupling h/λ for different system sizes. $\lambda \in [0, 3]$ is an arbitrary smooth function of time. Adapted from [16]

solution for this equation is the optimal PH

$$H_{\text{opt}} = h(\lambda(t)) \sum_i (\sigma_i^x \sigma_{i+1}^y + \sigma_i^y \sigma_{i+1}^x), \quad (38)$$

with

$$h(\lambda(t)) = -\lambda \frac{\sum_{k \in \mathcal{K}^+} \frac{\sin^2(k)}{1 + \lambda^2 - 2\lambda \cos(k)}}{8 \sum_{k \in \mathcal{K}^+} \sin(k)^2}. \quad (39)$$

The optimal coupling $h(\lambda(t))$ is shown in Fig. 1 for different system sizes. We can see that the magnitude of this coupling does not depend on the size of the system, and its behavior is different for states in the ordered and disordered quantum phases. In Fig. 2, we show the instantaneous cost $f(H_{\text{opt}}(\lambda(t)))$ of the optimal PH, that is the distance between the derivative of the state and the infinitesimal evolution generated by $H_{\text{opt}}(\lambda(t))$. We can see that this cost scales with the square root of the system size and diverges at the critical point, where it is impossible to generate the state evolution with a local Hamiltonian. The behavior of the instantaneous cost of the optimal solution is reflected in the behavior of the instantaneous fidelity between the target state and the state $|\psi'(\lambda(t))\rangle \equiv \mathcal{T}e^{-i \int_0^t H_{\text{opt}}(\lambda(t')) dt'} |\psi(0)\rangle$ generated by the optimal evolution. This fidelity indeed is close to one before the critical point $\lambda = 1$, where the peak of the instantaneous cost is reflected in a drastic drop of fidelity (see Fig. 3).

More generally, results in [16] for both the Ising and p -spin models ground states show that the possibility of finding a low-cost optimal time-dependent PH, and, therefore, the possibility of exploiting that Hamiltonian to prepare $|\psi(t)\rangle$ with

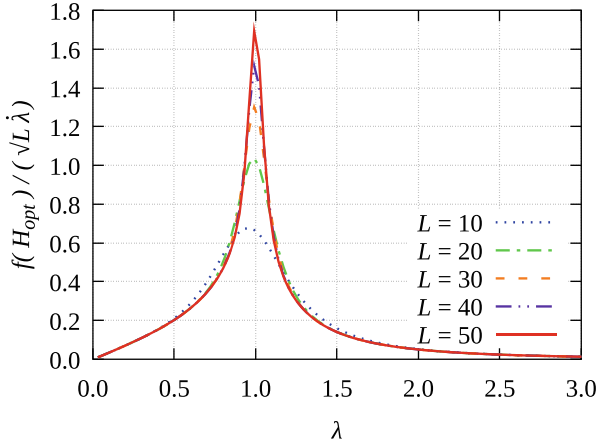


Fig. 2 Evolution of the (rescaled) optimal cost $f(H_{\text{opt}})/(\sqrt{L}\lambda)$ for different system sizes. $\lambda \in [0, 3]$ is an arbitrary smooth function of time. Adapted from [16]

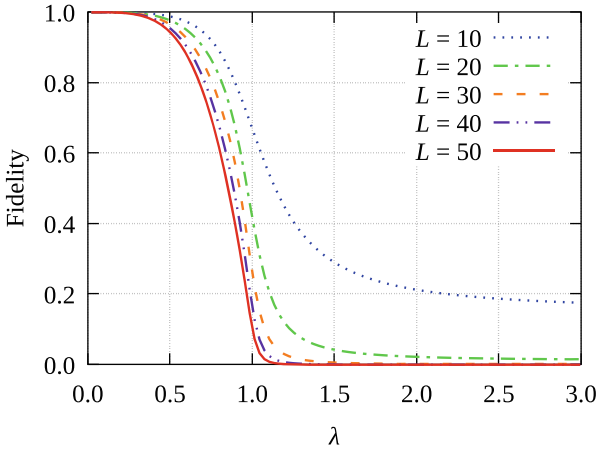


Fig. 3 Evolution of the fidelity between the target state and the state evolved through the optimal parent Hamiltonian for different system sizes. $\lambda \in [0, 3]$ is an arbitrary smooth function of time. Adapted from [16]

high fidelity is related to the behavior of correlation functions: we obtain low cost and large fidelity in correspondence with states that do not become critical in the thermodynamic limit, while for critical states the cost of the optimal solution has a peak and the fidelity drops irreversibly.

We have shown different solutions to the time-dependent inverse problem, which can be exploited both to learn the Hamiltonian governing the evolution of a synthetic quantum system [14, 15] or to find possible Hamiltonians to drive a target time-dependent state [16]. We have seen that the solution to a dynamical inverse problem

is generally non-unique, and its degeneracy is directly inherited from the degeneracy of the space of symmetries.

The analyzed results demonstrate that the behavior of correlation functions of the target state plays an important role in the dynamical inverse problem: on the one hand, PHs can be reconstructed from the observation of local expectation values and correlations for separable states [14], on the other hand, the capability of driving the evolution of a state through local operators is negatively influenced by the emergence of long-range correlations [16]: long-range correlated states of the Hilbert space seem harder to be reached through a realistic evolution.

5 Conclusions

In this paper, we have analyzed different kinds of parent Hamiltonians: symmetries [4–9], PPHs [10–13], and dynamical PHs [14–16]. Reconstruction methods proposed until now have been presented with their computational cost and with the measurements that one has to perform on the state in order to identify the solutions to the inverse problem. These methods have been related to important technological goals such as the verification of analog quantum devices and quantum state preparation and control.

The solution to the inverse problem, when it exists, is generally not unique [4–7, 16]. For this reason, one cannot reconstruct the entire physical behavior of a system from measurements on a single state. We have also seen that the knowledge of local correlations is sufficient to efficiently solve the inverse problem [4–7]. In most cases, the PH is uniquely determined by local expectation values and can be extrapolated by these values with computational resources that scale exponentially with the system size [8, 9]. Finally, the relationship between the capability of driving a quantum state through local operators and the behavior of its correlation can shed a new light on the accessibility of the Hilbert space under the constraint of realistic interactions [16].

Inverse methods have been extended to reconstruct a realistic Lindbladian for open quantum systems [55]. This version of the inverse problem has some significant applications as it could be used to identify the sources of decoherence or to verify a target dissipative dynamics for an engineered environment, or can be exploited to design a recipe to control a time-dependent mixed quantum state.

Regarding closed quantum systems, some important challenges remain open, in particular, the definition of efficient algorithms to reconstruct PPHs. The design of such an algorithm would also give a significant boost to the related field of quantum marginal problems: once one can design a PH for a state from its local expectation values, such a Hamiltonian could then be used to efficiently prepare the state and measure correlation functions. Finally, until now the possibility of solving the inverse problem through quantum mechanics, for example, via a quantum circuit algorithm or a quantum annealer, remains unexplored.

References

1. P. Zoller, Th. Beth, D. Binosi, R. Blatt, H. Briegel, D. Bruss, T. Calarco, J.I. Cirac, D. Deutsch, J. Eisert, A. Ekert, C. Fabre, N. Gisin, P. Grangiere, M. Grassl, S. Haroche, A. Imamoglu, A. Karlson, J. Kempe, L. Kouwenhoven, S. Kröll, G. Leuchs, M. Lewenstein, D. Loss, N. Lütkenhaus, S. Massar, J.E. Mooij, M.B. Plenio, E. Polzik, S. Popescu, G. Rempe, A. Sergienko, D. Suter, J. Twamley, G. Wendin, R. Werner, A. Winter, J. Wrachtrup, A. Zeilinger, *Eur. Phys. J. D* **36**(2), 203 (2005). <https://doi.org/10.1140/epjd/e2005-00251-1>
2. J. Preskill, *Quantum* **2**, 79 (2018). <https://doi.org/10.22331/q-2018-08-06-79>
3. I.H. Deutsch, *PRX Quantum* **1**, 020101 (2020). <https://doi.org/10.1103/PRXQuantum.1.020101>
4. X.L. Qi, D. Ranard, *Quantum* **3**, 159 (2019). <https://doi.org/10.22331/q-2019-07-08-159>
5. E. Chertkov, B.K. Clark, *Phys. Rev. X* **8**, 031029 (2018). <https://doi.org/10.1103/PhysRevX.8.031029>
6. M. Greiter, V. Schnells, R. Thomale, *Phys. Rev. B* **98**, 081113 (2018). <https://doi.org/10.1103/PhysRevB.98.081113>
7. E. Bairey, I. Arad, N.H. Lindner, *Phys. Rev. Lett.* **122**(2) (2019). <https://doi.org/10.1103/physrevlett.122.020504>
8. S.Y. Hou, N. Cao, S. Lu, Y. Shen, Y.T. Poon, B. Zeng, *New J. Phys.* **22**(8), 083088 (2020). <https://doi.org/10.1088/1367-2630/abaacf>
9. C. Cao, S.Y. Hou, N. Cao, B. Zeng, *J. Phys.: Condens. Matter* **33**(6), 064002 (2020). <https://doi.org/10.1088/1361-648x/abc4cf>
10. J. Chen, Z. Ji, B. Zeng, D.L. Zhou, *Phys. Rev. A* **86**, 022339 (2012). <https://doi.org/10.1103/PhysRevA.86.022339>
11. C. Fernández-González, N. Schuch, M.M. Wolf, J.I. Cirac, D. Pérez-García, *Commun. Math. Phys.* **333**(1), 299–333 (2014). <https://doi.org/10.1007/s00220-014-2173-z>
12. X. Turkeshi, T. Mendes-Santos, G. Giudici, M. Dalmonte, *Phys. Rev. Lett.* **122**, 150606 (2019). <https://doi.org/10.1103/PhysRevLett.122.150606>
13. X. Turkeshi, M. Dalmonte, *SciPost Phys.* **8**, 42 (2020). <https://doi.org/10.21468/SciPostPhys.8.3.042>
14. A. Zubida, E. Yitzhaki, N.H. Lindner, E. Bairey, arXiv:2108.08824 [quant-ph] (2021). <https://doi.org/10.48550/arXiv.2108.08824>
15. D. Hangleiter, I. Roth, J. Eisert, P. Roushan, arXiv:2108.08319 [quant-ph] (2021). <https://doi.org/10.48550/arXiv.2108.08319>
16. D. Rattacaso, G. Passarelli, A. Mezzacapo, P. Lucignano, R. Fazio, *Phys. Rev. A* **104**(2) (2021). <https://doi.org/10.1103/physreva.104.022611>
17. J.R. Garrison, T. Grover, *Phys. Rev. X* **8**, 021026 (2018). <https://doi.org/10.1103/PhysRevX.8.021026>
18. D. Poulin, A. Qarry, R. Somma, F. Verstraete, *Phys. Rev. Lett.* **106**(17) (2011). <https://doi.org/10.1103/physrevlett.106.170501>
19. I.H. Deutsch, P.S. Jessen, *Phys. Rev. A* **57**, 1972 (1998). <https://doi.org/10.1103/PhysRevA.57.1972>
20. R. van Handel, J.K. Stockton, H. Mabuchi, *J. Opt. B: Quantum Semiclassical Opt.* **7**(10), S179 (2005). <https://doi.org/10.1088/1464-4266/7/10/001>
21. F. Verstraete, M.M. Wolf, J. Ignacio Cirac, *Nat. Phys.* **5**(9), 633 (2009). <https://doi.org/10.1038/nphys1342>
22. M. Plesch, C. Brukner, *Phys. Rev. A* **83**, 032302 (2011). <https://doi.org/10.1103/PhysRevA.83.032302>
23. J. Werschnick, E.K.U. Gross, *J. Phys. B: At. Mol. Opt. Phys.* **40**(18), R175 (2007). <https://doi.org/10.1088/0953-4075/40/18/r01>
24. C. Brif, R. Chakrabarti, H. Rabitz, *New J. Phys.* **12**(7), 075008 (2010). <https://doi.org/10.1088/1367-2630/12/7/075008>

25. D. Dong, I. Petersen, *IET Control Theory Appl.* **4**(12), 2651–2671 (2010). <https://doi.org/10.1049/iet-cta.2009.0508>
26. S.J. Glaser, U. Boscain, T. Calarco, C.P. Koch, W. Köckenberger, R. Kosloff, I. Kuprov, B. Luy, S. Schirmer, T. Schulte-Herbrüggen, et al., *Eur. Phys. J. D* **69**(12) (2015). <https://doi.org/10.1140/epjd/e2015-60464-1>
27. C.P. Koch, *J. Phys. Condens. Matter* **28**(21), 213001 (2016). <https://doi.org/10.1088/0953-8984/28/21/213001>
28. S. Deffner, S. Campbell, *J. Phys. A: Math. Theor.* **50**(45), 453001 (2017). <https://doi.org/10.1088/1751-8121/aa86c6>
29. H. Wang, *Sci. Rep.* **7**(1), 16342 (2017). <https://doi.org/10.1038/s41598-017-16396-0>
30. D. Lee, J. Bonitati, G. Given, C. Hicks, N. Li, B.N. Lu, A. Rai, A. Sarkar, J. Watkins, *Phys. Lett. B* **807**, 135536 (2020). <https://doi.org/10.1016/j.physletb.2020.135536>
31. L. Lin, Y. Tong, *Quantum* **4**, 372 (2020). <https://doi.org/10.22331/q-2020-12-14-372>
32. M. Raghunandan, F. Wolf, C. Ospelkaus, P.O. Schmidt, H. Weimer, *Sci. Adv.* **6**(10), eaaw9268 (2020). <https://doi.org/10.1126/sciadv.aaw9268>
33. T. Albash, D.A. Lidar, *Rev. Mod. Phys.* **90**, 015002 (2018). <https://doi.org/10.1103/RevModPhys.90.015002>
34. E. Farhi, J. Goldstone, S. Gutmann, M. Sipser, arXiv preprint quant-ph/0001106 (2000)
35. J. Brooke, D. Bitko, T.F. Rosenbaum, G. Aeppli, *Science* **284**(5415), 779 (1999). <https://doi.org/10.1126/science.284.5415.779>
36. J. Brooke, T.F. Rosenbaum, G. Aeppli, *Nature* **413**(6856), 610 (2001). <https://doi.org/10.1038/35098037>
37. M. Demirplak, S.A. Rice, *J. Phys. Chem. A* **107**(46), 9937 (2003)
38. M. Demirplak, S.A. Rice, *J. Phys. Chem. B* **109**(14), 6838 (2005). <https://doi.org/10.1021/jp040647w>
39. A. del Campo, *Phys. Rev. Lett.* **111**, 100502 (2013). <https://doi.org/10.1103/PhysRevLett.111.100502>
40. S. Deffner, C. Jarzynski, A. del Campo, *Phys. Rev. X* **4**, 021013 (2014). <https://doi.org/10.1103/PhysRevX.4.021013>
41. S. An, D. Lv, A. del Campo, K. Kim, *Nat. Commun.* **7**(1), 12999 (2016). <https://doi.org/10.1038/ncomms12999>
42. K. Funo, J.N. Zhang, C. Chatou, K. Kim, M. Ueda, A. del Campo, *Phys. Rev. Lett.* **118**, 100602 (2017). <https://doi.org/10.1103/PhysRevLett.118.100602>
43. C.W. Duncan, A. del Campo, *New J. Phys.* **20**(8), 085003 (2018). <https://doi.org/10.1088/1367-2630/aad437>
44. D. Guéry-Odelin, A. Ruschhaupt, A. Kiely, E. Torrontegui, S. Martínez-Garaot, J.G. Muga, *Rev. Mod. Phys.* **91**, 045001 (2019). <https://doi.org/10.1103/RevModPhys.91.045001>
45. A. Gheorghiu, T. Kapourniotis, E. Kashefi, *Theory Comput. Syst.* **63**(4), 715–808 (2018). <https://doi.org/10.1007/s00224-018-9872-3>
46. J. Eisert, D. Hangleiter, N. Walk, I. Roth, D. Markham, R. Parekh, U. Chabaud, E. Kashefi, *Nat. Rev. Phys.* **2**(7), 382–390 (2020). <https://doi.org/10.1038/s42254-020-0186-4>
47. I. Šupić, J. Bowles, *Quantum* **4**, 337 (2020). <https://doi.org/10.22331/q-2020-09-30-337>
48. J. Carrasco, A. Elben, C. Kokail, B. Kraus, P. Zoller, *PRX Quantum* **2**, 010102 (2021). <https://doi.org/10.1103/PRXQuantum.2.010102>
49. M. Kliesch, I. Roth, *PRX Quantum* **2**, 010201 (2021). <https://doi.org/10.1103/PRXQuantum.2.010201>
50. N. Wiebe, C. Granade, C. Ferrie, D. Cory, *Phys. Rev. Lett.* **112**(19) (2014). <https://doi.org/10.1103/physrevlett.112.190501>
51. J. Wang, S. Paesani, R. Santagati, S. Knauer, A.A. Gentile, N. Wiebe, M. Petruzzella, J.L. O’Brien, J.G. Rarity, A. Laing, et al., *Nat. Phys.* **13**(6), 551–555 (2017). <https://doi.org/10.1038/nphys4074>
52. T. Bertalan, F. Dietrich, I. Mezić, I.G. Kevrekidis, *Chaos: Interdiscip. J. Nonlinear Sci.* **29**(12), 121107 (2019). <https://doi.org/10.1063/1.5128231>

53. P. Bienias, A. Seif, M. Hafezi, arxiv:2104.04453 [quant-ph] (2021). <https://arxiv.org/abs/2104.04453>
54. E.F. Dumitrescu, P. Lougovski, Phys. Rev. Res. **2**, 033251 (2020). <https://doi.org/10.1103/PhysRevResearch.2.033251>
55. E. Bairey, C. Guo, D. Poletti, N.H. Lindner, I. Arad, New J. Phys. **22**(3), 032001 (2020). <https://doi.org/10.1088/1367-2630/ab73cd>
56. R. Orús, Ann. Phys. **349**, 117 (2014). <https://doi.org/10.1016/j.aop.2014.06.013>
57. G.B. Mbeng, A. Russomanno, G.E. Santoro, arxiv:2009.09208 [quant-ph] (2021). <https://arxiv.org/abs/2009.09208>
58. N. Linden, W.K. Wootters, Phys. Rev. Lett. **89**, 277906 (2002). <https://doi.org/10.1103/PhysRevLett.89.277906>
59. D.L. Zhou, Phys. Rev. Lett. **101**(18) (2008). <https://doi.org/10.1103/physrevlett.101.180505>
60. M.V. Berry, J. Phys. A: Math. Gener. **42**(36), 365303 (2009). <https://doi.org/10.1088/1751-8113/42/36/365303>
61. D. Sels, A. Polkovnikov, Proc. Nat. Acad. Sci. **114**(20), E3909 (2017). <https://doi.org/10.1073/pnas.1619826114>
62. S. An, D. Lv, A. del Campo, K. Kim, Nat. Commun. **7**(1), 1 (2016). <https://doi.org/10.1038/ncomms12999>
63. T. Hatomura, J. Phys. Soc. Jpn. **86**(9), 094002 (2017). <https://doi.org/10.7566/JPSJ.86.094002>
64. P.W. Claeys, M. Pandey, D. Sels, A. Polkovnikov, Phys. Rev. Lett. **123**, 090602 (2019). <https://doi.org/10.1103/PhysRevLett.123.090602>
65. G. Passarelli, V. Cataudella, R. Fazio, P. Lucignano, Phys. Rev. Res. **2**, 013283 (2020). <https://doi.org/10.1103/PhysRevResearch.2.013283>
66. G. Passarelli, R. Fazio, P. Lucignano, in preparation.
67. P.R. Hegde, G. Passarelli, A. Scocco, P. Lucignano, Phys. Rev. A **105**, 012612 (2022). <https://doi.org/10.1103/PhysRevA.105.012612>
68. S. Bravyi, M.B. Hastings, F. Verstraete, Phys. Rev. Lett. **97**, 050401 (2006). <https://doi.org/10.1103/PhysRevLett.97.050401>
69. D. Gross, M. Mezard, Nucl. Phys. B **240**(4), 431 (1984). [https://doi.org/10.1016/0550-3213\(84\)90237-2](https://doi.org/10.1016/0550-3213(84)90237-2)
70. A. del Campo, M.M. Rams, W.H. Zurek, Phys. Rev. Lett. **109**, 115703 (2012). <https://doi.org/10.1103/PhysRevLett.109.115703>

Entanglement Dynamics in Hybrid Quantum Circuits



Andrew C. Potter and Romain Vasseur

Abstract The central philosophy of statistical mechanics (stat-mech) and random-matrix theory of complex systems are that while individual instances are essentially intractable to simulate, the statistical properties of random ensembles obey simple universal “laws.” This same philosophy promises powerful methods for studying the dynamics of quantum information in ideal and noisy quantum circuits—for which classical description of individual circuits is expected to be generically intractable. Here, we review recent progress in understanding the dynamics of quantum information in ensembles of random quantum circuits, through a stat-mech lens. We begin by reviewing discoveries of universal features of entanglement growth, operator spreading, thermalization, and chaos in unitary random quantum circuits, and their relation to stat-mech problems of random surface growth and noisy hydrodynamics. We then explore the dynamics of monitored random circuits, which can loosely be thought of as noisy dynamics arising from an environment monitoring the system, and exhibit new types of measurement-induced phases and criticality. Throughout, we attempt to give a pedagogical introduction to various technical methods and to highlight emerging connections between concepts in stat-mech, quantum information, and quantum communication theory.

1 Introduction

While many-body physics has traditionally focused on the properties of cold matter in equilibrium, emerging atomic, molecular, optical, and qubit platforms allow access to far from equilibrium dynamics with local space and time control over

A. C. Potter

Department of Physics and Astronomy, and Quantum Matter Institute, University of British Columbia, Vancouver, BC, Canada

e-mail: andrew.potter@ubc.ca

R. Vasseur (✉)

Department of Physics, University of Massachusetts, Amherst, MA, USA

e-mail: rvasseur@umass.edu

interactions. A key challenge is to identify universal features of non-equilibrium quantum dynamics and approach to thermalization. The dynamics of the scrambling of local quantum information into non-local degrees of freedom by many-body unitary dynamics plays a central role in addressing those questions. The growth of entanglement is not only important to diagnose thermalization (or lack thereof), but also characterizes the complexity of tensor network descriptions of quantum dynamics. Of particular interest are *universal* properties that do not depend on particular microscopic details and hold for generic quantum systems.

Insights into generic non-equilibrium dynamics can be gained by considering minimally structured models, such as *random unitary circuits* [1–8], which capture the salient ingredients of generic quantum systems, namely *unitarity* of the dynamics and *locality* of the interactions. Using random quantum circuits, the growth of entanglement in one-dimensional system was elegantly mapped to the celebrated Kardar–Parisi–Zhang universality class [9] of random surface growth [7]. This mapping also uncovered deep connections to the Ryu–Takayanagi formula in holographic AdS/CFT correspondences [10, 11], by establishing a relation between entanglement dynamics and a geometric minimal-cut picture. Random unitary circuits were also used to characterize exactly the local spreading of operators in the Heisenberg picture [8, 12], providing a complementary picture on chaotic dynamics and scrambling from the perspective of operator growth. Other probes of many-body quantum chaos, e.g., related to level statistics, have also been computed exactly in Floquet (time-periodic) circuits [13–18]. In turn, those exact results led to a coarse-grained, “hydrodynamic” description of operator spreading that was conjectured to universally apply to non-integrable quantum systems in one dimension. Since then, random quantum circuits have become part of the standard toolbox to study chaotic quantum dynamics and provided crucial insights into, e.g., the emergence of irreversible hydrodynamics from unitary evolution in the presence of a conserved charge [19, 20].

Motivated by the advent of noisy intermediate-scale quantum simulators [21], random quantum circuits have also been used to study the dynamics of entanglement in open quantum systems, which are continuously “monitored” by their environments. Non-unitary random circuits provide a natural tool to study the competition between unitary dynamics, which leads to chaotic evolution and rapid entanglement growth, and non-unitary operations resulting from measurements and noisy couplings to the environment, which tend to irreversibly destroy quantum information by revealing it [22, 23]. More generally, non-unitary circuits and random tensor networks [24–29] can exhibit a variety of “phases” and phase transitions with different entanglement scalings. The most studied representative example of such an entanglement transition that results from the competition between unitary dynamics and non-unitary processes is the so-called measurement-induced phase transition [22, 23]. This transition occurs in monitored random quantum circuits (MRCs) made up of random unitary gates, combined with local projective measurements occurring at a fixed rate, separating two phases with very different entanglement properties. Importantly, such measurement-induced phase transitions (MIPTs) are only visible in an individual quantum trajectory (i.e., the pure state

of the system conditional on a set of measurement outcomes) and in trajectory averages of quantities that are non-linear functions of the density matrix. When measurements are frequent enough, they are able to efficiently extract quantum information from any initial state, and Zeno collapse it into a weakly entangled state with area-law entanglement. In contrast, for a small enough measurement rate, the unitary dynamics scrambles quantum information into non-local degrees of freedom that can partly evade local measurements. In this entangling phase (volume law), initial product states become highly entangled over time, while initial mixed states remain mixed for extremely long times [30]. There are different perspectives on this measurement-induced transition, either as a purification transition [30] or from the language of quantum communication and error correction. In the volume-law phase, the unitary dynamics is effectively able to hide non-local degrees of freedom that span a decoherence-free subspace in which the dynamics is effectively unitary [30–33]: this subspace can be regarded as the code space of a quantum error-correcting code.

Measurement-induced transitions have been investigated numerically and theoretically in various contexts, dimensionality, geometries, with different families of gates [22, 23, 26, 27, 30–72], establishing that it is a generic property of quantum trajectories of open quantum systems. A particularly fruitful approach to understand the phenomenology and universality class of measurement-induced transitions is to use exact mappings onto effective statistical mechanics models that emerge from using a replica trick to deal with the intrinsic non-linearities of the problem, and after averaging over the random gates. This systematic statistical mechanics approach based on replica permutation “spins” was first developed in the context of random tensor networks [24, 25] and then extended to deal with random unitary [73] and monitored [39, 40] circuit dynamics. Such stat-mech mappings provide an appealing picture of the entanglement transition in terms of a (replica) symmetry-breaking transition, where the volume-law coefficient of entanglement has a simple interpretation as a domain wall surface tension. In turn, these recent theoretical developments raise the intriguing prospect of using well-developed statistical mechanics tools to study quantum communication channel capacity and error-correction thresholds [30–33, 64, 74], and computational complexity [75, 76]. Finite-size evidence for such an entanglement MIPT was even recently observed experimentally in trapped-ion chains [77]. The phase structure and dynamics of non-unitary circuits are being actively explored at the time of writing of this chapter.

The outline of this chapter is as follows: in Sect. 2, we introduce random quantum circuit dynamics and derive exact results on entanglement growth and operator spreading in such circuits. We also comment on the role of symmetries in the dynamics. In Sect. 3, we introduce measurements and describe the phenomenology of measurement-induced entanglement transitions from different perspectives. Section 4 derives exact statistical mechanics mappings for random unitary circuits with and without measurements, using a replica trick. Various consequences for entanglement dynamics and criticality are discussed. Finally, in Sect. 5, we discuss progress in understanding measurement-induced symmetry-

breaking and topological orders and related criticality, which would be forbidden in equilibrium and are stabilized by dissipation.

2 Random Unitary Quantum Circuits

We begin by studying entanglement growth in ensembles of unitary random quantum circuit (RC) dynamics. The growth of entanglement is an important metric to diagnose dynamical thermalization and distinguish this behavior from other dynamical universality classes such as many-body localization. Entanglement growth also reflects the complexity of matrix-product state (MPS) and tensor network state (TNS) descriptions of quantum dynamics. Just as in the statistical mechanics of many interacting particles, or random-matrix theory of complex Hamiltonians, the statistical properties of random ensembles of circuits can often be captured with a far-simpler theoretical description than the (generically exponentially difficult) task of computing the detailed output of a given circuit instance. In this section, we review two equivalently complementary perspectives of entanglement growth and thermalization in RCs; first we work in the “Schrödinger” picture and examine the growth of bipartite entanglement in the evolution of quantum states, and second, we adopt a “Heisenberg” picture and examine the evolution and spreading of operators under RC dynamics. These two descriptions are elegantly united [7] in a mapping of the entanglement growth problem onto Kardar–Parisi–Zhang (KPZ) dynamics of random surface growth [9]. We recount the connection of surface growth to an equivalent picture in terms of directed random polymers, which has a geometrical interpretation closely analogous to the Ryu–Takayanagi relation between geometry and entanglement in holographic AdS/CFT correspondences [10, 11].

2.1 Entanglement Growth

For this discussion, we adopt the model of [7], which consists of a length L chain of d -level qudits, in which, at every time step a randomly selected pair of neighboring qubits is subjected to a random two-qudit entangling gate drawn uniformly from the Haar distribution on $U(d^2)$. To study entanglement growth, consider the bipartite von Neumann entropy: $S(x, t) = -\text{tr} \rho_{[x+1, \infty)} \log_d \rho_{[x+1, \infty)}$, for bipartitioning the system across the bond $(x, x + 1)$, where $\rho_{[x, x']}$ is the reduced density matrices for sites in the interval $[x, x']$.

2.1.1 Mapping to KPZ Dynamics of Random Surface Growth

Due to the subadditivity property of entanglement, the entanglement entropy for neighboring cuts is bounded by

$$|S(x, t) - S(x + 1, t)| \leq 1, \quad (1)$$

i.e., if S behaves like a “surface” with bounded slope. The stochastic dynamics of this “surface” can be understood by a simple heuristic rule. When a gate acts on bond $(x, x + 1)$, the corresponding entanglement grows as

$$S(x, t + 1) = \min\{S(x - 1, t), S(x + 1, t)\} + 1, \quad (2)$$

which turns out to be exact (almost surely) in the limit of large onsite dimension $d \rightarrow \infty$, but which is believed to capture the universal aspects of RC dynamics for any finite- d . This rule can be understood as follows: if $S(x, t) = S(x - 1, t)$ or $S(x - 1, t) - 1$, i.e., implying that site $x + 1$ is unentangled with $(-\infty, x]$ at time t , then the gate increases the entanglement by an amount that is generically proportional to 1 and becomes precisely 1 (almost surely) in the large- d limit. If on the other hand, $S(x, t) = S(x - 1, t) + 1$, this implies that site $x + 1$ is already maximally entangled with $(-\infty, x]$ and the gate is very unlikely to disentangle it, so $S(x, t)$ remains unchanged. We can see that since $S(x, 0) = 0 \forall x$, and since $S(x, t)$ changes by quantized amounts (at $d \rightarrow \infty$), then $S(x, t)$ is always an integer, and these cases exhaust the possibilities. Concrete examples of updates are shown in Fig. 1a,b. Notice that locally flat parts of the surface tend to grow (top left of Fig. 1b), while bonds with negative local curvature get converted to having local positive curvature (bottom left of Fig. 1b), and regions with positive slope of s do not grow (bottom right of Fig. 1b).

To study the long-time dynamics, it is useful to “zoom-out” and coarse-grain the spatial lattice and integral step of the circuit by introducing an average entropy $s(x, t)$ over blocks of sites of size $\ell \gg 1$ (similar to moving from a lattice description of magnetic moments, to a continuum description of coarse-grained average magnetization), and coarse-grain our time step by L so that a finite density of gates is applied in a coarse-grained time step. The continuum limit of the “update rule” Eq. (2) can then be written in the form of a KPZ equation:

$$\frac{\partial s}{\partial t} = \nu \partial_x^2 s - \frac{\lambda}{2} (\partial_x s)^2 + \eta(x, t) + c, \quad (3)$$

where c reflects the average rate of growth of entanglement, $\eta(x, t)$ is a random noise (capturing the stochastic placement of gates in space and time in the RC model), the ν term suppresses local curvature reflecting suppression of negative curvature from processes like the one shown in the bottom left of Fig. 1b, and finally the λ term reflects that the entanglement growth is slower in regions with non-zero slope of s as described above. Other terms with more derivatives or higher

non-linearities are irrelevant in the renormalization group sense, so that this KPZ equation captures the universal aspects of the coarse-grained entanglement growth.

The overall trend of Eq.(3) is that entanglement grows linearly in time $\langle s(x, t) \rangle \sim v_E t + \dots$ with constant “entanglement-velocity” v_E , and (...) reflects subleading contributions that grow more slowly than $\sim t$. Universal scaling of fluctuations about this average trend is governed by the exactly solved KPZ universality class. Measurable quantities at distance x and time t scale as universal functions of the ratio $x/\xi(t)$ with correlation length $\xi(t) \sim t^{1/z}$ where the dynamical exponent $z = \frac{3}{2}$. For example, the difference in entanglement for cuts separated by distance r at equal times t scales like $\langle (S(x+r, t) - S(x, t))^2 \rangle \sim r^\alpha g(r/\xi(t))$, where g is a universal function and $\alpha = \frac{1}{2}$. Another important critical exponent, β , characterizes the RMS fluctuations in entanglement: $\sqrt{\langle (s(x, t))^2 \rangle - \langle s(x, t) \rangle^2} \sim t^\beta$ with $\beta = \frac{1}{3}$ and similarly controls the dominant subleading correction to the entanglement growth: $\langle s(x, t) \rangle \sim v_E t + Bt^\beta$.

2.1.2 Directed Polymer and Minimal-Cut Interpretation

KPZ dynamics arises in a wide variety of problems besides random surface growth. A prominent example is the dynamics of a directed polymer in a random environment, i.e., a sequence of monomer segments arranged along one direction: (“time”), which can be inclined but not turn back on itself. This directed polymer perspective on KPZ dynamics has a natural geometric interpretation in the RC dynamics. To estimate $S(x, t)$, consider the following geometric construction: draw a curve through the random circuit starting from bond $(x, x+1)$ at time t and moving back through the circuit to time $t=0$ without crossing any gates. The length of this upper-bounds the Schmidt rank of the bipartition across bond $(x, x+1)$ (see Fig. 1) and hence also upper-bounds the entropy $S(x, t)$. The best upper-bound estimate for $S(x, t)$ from this procedure is therefore given by the length of the minimal such cut through the circuit. Reference [7] showed that this upper-bound is in fact saturated in the large- d limit. Identifying the cut line with the shape of a directed polymer, and the constraints imposed by the constraint that the line does not cross the (randomly placed) gates as a random environment, then the problem of finding minimum length cut is equivalent to minimizing the free energy of this directed polymer in said random environment. This picture led to a more general and universal “entanglement membrane” formalism to compute entanglement in chaotic quantum systems [7, 78, 79].

This geometric interpretation of entanglement of a quantum state output by a RC via the geometry of a minimal surface through the circuit is strikingly reminiscent of the Ryu–Takayanagi formula relating the entanglement of a spatial region of a conformal field theory ground-state to the surface area of a spanning geodesic the dual bulk gravity description [10, 11], and to similar relation in high-bond dimension tensor networks which can in a sense be viewed as lattice discretizations of the gravity/CFT correspondence [24].

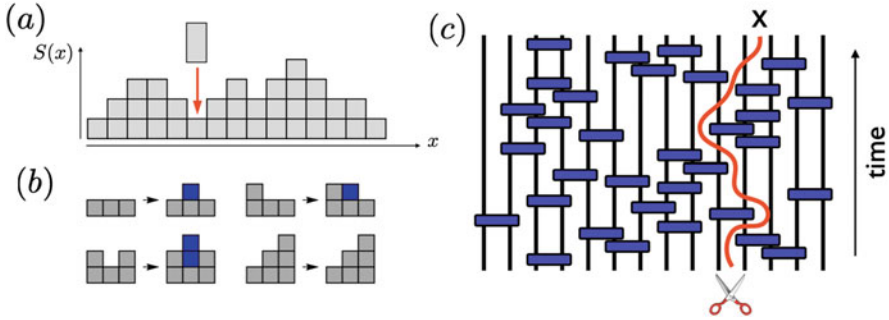


Fig. 1 KPZ dynamics of entanglement growth in random circuits. In a random circuit model consisting of randomly placed nearest-neighbor two-site gates (c), the entanglement dynamics as a random surface growth where each gate on a bond tends to increase the height at that bond by one block (a). (b) shows the surface growth steps for a gate acting on a bond with different pre-existing entanglement configurations. (c) Shows an alternative, but equivalent picture of entanglement growth in terms of a minimal cut: entanglement is upper-bounded by the minimal number of bonds cut by a line that bipartitions the circuit without cutting through any gates. This minimal cut can be viewed as the minimal free-energy configuration of a directed polymer in a random medium, which is well-known to be equivalent to the random surface growth model. Reproduced from Ref. [7]

2.2 Operator Spreading

Examining the evolution of operators under RC dynamics provides a complementary perspective on thermalization and chaos. The spreading of operators in the Heisenberg picture can be computed exactly for random quantum circuits [8, 12]. Let us focus on the case of $d = 2$ (qubits) for simplicity, although the concepts will extend straightforwardly to arbitrary d , and consider the dynamics of an initially local operator \mathcal{O} , which we take to be a Pauli matrix. Under unitary time evolution, this operator is going to become more complicated, and we expand it onto the basis of *Pauli strings* \mathcal{S}

$$\mathcal{O}(t) = U^\dagger(t)\mathcal{O}(0)U(t) = \sum_{\mathcal{S}} a_{\mathcal{S}}(t)\mathcal{S}, \quad (4)$$

where \mathcal{S} are any product of Pauli matrices on distinct sites. Unitarity as well as the normalization of the initial operator implies the conservation law: $\sum_{\mathcal{S}} |a_{\mathcal{S}}(t)|^2 = \sum_{\mathcal{S}} |a_{\mathcal{S}}(0)|^2 \equiv 1$. The average evolution of the weights $|a_{\mathcal{S}}|^2$ under random Haar evolution is particularly easy to work out. Let us consider a single gate, acting on two sites for simplicity. There are two cases: if the string \mathcal{S} happens to be the identity I at time t , then it is unchanged by the unitary gate and remains identity at time $t + 1$. On the other hand, if the string \mathcal{S} is any other operator in the operator Hilbert space, the random Haar evolution evolves it to any other non-identity string with equal

probability. This means that the string weights obey the Markov process:

$$|a_{\mathcal{S}}(t+1)|^2 = \sum_{\mathcal{S}'} \mathcal{W}_{\mathcal{S},\mathcal{S}'} |a_{\mathcal{S}'}(t)|^2, \quad (5)$$

with the Markov operator

$$\mathcal{W}_{\mathcal{S},\mathcal{S}'} = \delta_{\mathcal{S},\mathcal{I}}\delta_{\mathcal{S}',\mathcal{I}} + \frac{(1-\delta_{\mathcal{S},\mathcal{I}})(1-\delta_{\mathcal{S}',\mathcal{I}})}{d^4-1}. \quad (6)$$

Instead of keeping track of the d^L coefficients $a_{\mathcal{S}}$, it is convenient to focus on simpler quantities. Here we follow Refs. [8, 12] and focus on the *right weight* $\rho(x, t)$, defined as the fraction of strings ending at position x

$$\rho(x, t) = \sum_{\mathcal{S} \text{ ending at } x} |a_{\mathcal{S}}(t)|^2. \quad (7)$$

Intuitively, the right weight keeps track of the ‘‘operator front’’ and can also be related to out-of-time ordered correlators [8, 12] that are used in diagnostics of quantum chaos. Because the right weight is locally conserved, $\sum_x \rho(x, t) = 1$, we expect it to obey a coarse-grained (hydrodynamic) continuity equation

$$\partial_t \rho + \partial_x j = 0. \quad (8)$$

The dynamics of the right weight can be readily understood from the Markov process (5). Consider the action of a random unitary gate acting on sites x and $x+1$, on a string at ending at position x at time t . There are only d^2-1 operators out of d^4-1 non-identity operators that the random evolution can generate with an identity operator at position x . We conclude that with probability $p = (d^2-1)/(d^4-1)$, the operator front does not move and remains at position x (on average), whereas it moves right with probability $1-p$. This immediately implies that the right weight follows a *biased random walk*: the operator front moves ballistically to the right since $p < 1/2$ and will broaden diffusively with time as $\sim \sqrt{t}$. Using standard results, this implies that the current in the hydrodynamic equation (8) can be expressed within a gradient expansion as

$$j = v_B \rho - D \partial_x \rho + \dots, \quad (9)$$

with $v_B = 1 - 2p = \frac{d^2-1}{d^2+1}$, and $D = 2p(1-p) = \frac{2d^2}{(1+d^2)^2}$. This right weight thus behaves as $\rho(x, t) \sim \frac{1}{\sqrt{t}} e^{-(x-v_B t)^2/(4Dt)}$ at long times, and as $d \rightarrow \infty$, the front becomes sharp since $D \rightarrow 0$, and $v_B \rightarrow 1$. This diffusive broadening of the operator front is believed to be a generic feature of chaotic (non-integrable) quantum systems in one dimension. (The operator front also broadens diffusively in interacting integrable systems through a very different physical mechanism [80]). Note that

one-dimensional hydrodynamics is known to be unstable in one dimension [81]: sound waves that would naively broaden diffusively acquire some anomalous KPZ scaling in fluctuating hydrodynamics due to non-linearities. This does not happen in the context of operator spreading as the butterfly velocity v_B does not depend linearly on the right weight, and the operator front is believed to generically broaden diffusively rather than with KPZ dynamics.

2.3 $U(1)$ Symmetric Circuits

Random quantum circuits can be enriched by including global symmetries [19, 20], for example, adding a conserved $Q = \sum_x q(x)$, and demanding that random gates decompose into Haar random operations within each block of the total charge in order to ensure charge conservation. There are several ways to enforce charge conservation: following [19], we can consider a one-dimensional chain in which each site hosts a two-level system (“qubit”) whose computational basis states $\{|0\rangle, |1\rangle\}$ have charge $q = 0, 1$, respectively, and an auxiliary d -level system (“qudit”) of charge-neutral degrees of freedom, i.e., with onsite Hilbert space $\mathbb{C}^2 \otimes \mathbb{C}^d$. The dynamics will consist of local unitary gates and measurements, which are chosen to conserve the $U(1)$ charge associated with the z component of the qubits. As before, the symmetry-preserving two-site unitary gates are arranged in a brickwork geometry but now take the form:

$$U_{i,i+1} = \begin{pmatrix} U_{d^2 \times d^2}^0 & 0 & 0 \\ 0 & U_{2d^2 \times 2d^2}^1 & 0 \\ 0 & 0 & U_{d^2 \times d^2}^2 \end{pmatrix}, \quad (10)$$

where i labels a site, $U_{D \times D}^q$ is a unitary matrix of size $D \times D$ acting on the charge $q_1 + q_2 = q \in \{0, 1, 2\}$ sector (a local charge is defined to take values 0 and 1), and D is the dimension of the Hilbert space of the charge sector. Each matrix is drawn independently from the Haar random ensemble of unitary matrices of the appropriate size.

Those random unitary gates spread the charge uniformly with equal probability, so the charge performs a random walk

$$q(x, t + 1) = q(x + 1, t + 1) = \frac{1}{2} (q(x, t) + q(x + 1, t)), \quad (11)$$

independently of the onsite Hilbert space dimension d . Upon coarse-graining, this naturally leads to a diffusion equation for the local charge

$$\partial_t q = D_q \partial_x^2 q, \quad (12)$$

with the diffusion constant $D_q = 1/2$ for all d . Charge diffusion has some interesting consequences on operator spreading that we will not discuss here; we refer the reader to the original references [19, 20].

Charge conservation has particularly dramatic consequences on the dynamics of entanglement [82–86]: the charge contributions to the Rényi entropies grow diffusively, $S_{n>1} \sim \sqrt{t}$, while the von Neumann entropy remains ballistic as in the absence of symmetry $S_{n=1} \sim t$. This phenomenon arises from rare fluctuations that leave a region empty (or maximally filled). Consider for concreteness $d = 1$ (no neutral degree of freedom), corresponding to the onsite charge states $q = 0$ and $q = 1$. We are interested in the entanglement across a cut at $L/2$ following the dynamics of an initial product state for the qubit such as $|\psi\rangle = \otimes_{i=1}^L |+\rangle_i$, where $|+\rangle = \frac{1}{\sqrt{2}}(|0\rangle + |1\rangle)$ (the generalization to other initial states will be readily apparent). We can divide the system into three regions: a central region of radius $\ell = \sqrt{Dt}$ centered at the entanglement cut, and regions to the left and right. We then define a configuration to have a “dead-region” of size ℓ if the spins in a region of size $\sim \ell$ are either all 0, or all 1, e.g., $|\psi_{\text{dead}}\rangle = |\cdots + + + 00 \dots 00 + + + \cdots\rangle$. The amplitude for this state in the initial configuration is generically exponentially small in ℓ (e.g., for the particular initial and dead-region states mentioned above, it is $\sim 2^{-\ell/2}$). So one might be tempted to ignore contributions from large dead regions with $\ell \gg 1$. However, a crucial point is that these rare dead regions make an outsized contribution to Rényi entropies with Rényi index $n > 1$. To see this, consider the evolution for time t of an amplitude in the initial state having a dead region of size $\ell \gtrsim t^2/D_q$. In this time, particles begin to diffuse into the dead region from the edge but do not have time to fluctuate across the entanglement cut. Hence, the time-evolved state is still separable into left- and right-Schmidt states. The Schmidt weight for such rare dead regions is given by their probability to occur in the initial state, which is $\approx 2^{-\ell} \approx 2^{-\sqrt{Dt}}$. By contrast, typical configurations without dead regions all evolve into highly entangled states with much smaller Schmidt weight $\approx 2^{-v_E t}$, where v_E is the entanglement velocity. All Rényi entropies with $n > 1$ are dominated by the log of the largest Schmidt coefficient and grow as \sqrt{t} . The von Neumann entropy S_1 is dominated instead by *typical* Schmidt coefficients: the number of these grows exponentially in t , but they are also exponentially small in t and are therefore subleading for $n > 1$. We note that, in systems with both charged and neutral degrees of freedom (such as the qubit \times qudit model mentioned above), this diffusive charge contributions to Rényi entropy add to a dominant ballistic ($\sim t$) growth from neutral degrees of freedom. However, in a purely charged models with bounded maximal or minimal charge on each site, Rényi entropies will always grow diffusively.

3 Measurement-Induced Phase Transitions

The random circuit dynamics discussed above represents the unitary evolution of an ideal closed quantum system. In practice, no system is truly isolated, and understanding the interplay of unitary operations with environmental noise and decoherence is a key challenge for quantum computing. Environmental decoherence can be modeled as the environment “monitoring” (i.e., effectively measuring) the system, which we will idealize as strong projective measurements that collapse the qubits in the measured basis removing their entanglement with the rest of the system that had been generated by the unitary gates (extensions of this to weak/partial measurements are also possible [38, 70]). While there has been a resurgence of investigation of this question, the idea of quantum to classical phase transitions driven by noise has a long history going back to an early work by Aharonov [87] from over 20 years ago. Specifically, we consider the model introduced by [22, 23] consisting of alternating circuit layers with random unitary gates and measurement layers in which each qubit is projectively measured with probability p , which reduces to random circuit dynamics for $p = 0$. In the other extreme limit, $p = 1$, the system’s state is repeatedly collapsed to an unentangled product state.

At first glance, one might expect that any non-vanishing measurement probability $0 < p \leq 1$ would eventually collapse the system into a short-range entangled after sufficient time evolution. For example, bipartite entanglement S_A between a region A and its complement A^c is generated only by local gates that straddle the boundary ∂A and is generated at rate $\sim |\partial A|$, whereas the rate of measurement-induced collapse is extensive $\sim p|A|$ [35]. However, this naive argument ignores a critical feature of the random circuit evolution: scrambling. Namely, random circuit evolution tends to obscure the information stored in a single qubit by encrypting it in a random highly entangled superposition of many qubits. Consequently, measuring any single qubit in A does not reveal one qubit’s worth of information about the state of A^c (as for measuring half of a simple EPR pair), but rather only reveals partial information that roughly scales with the mutual information between the measured qubit and A^c : $\mathcal{I}(x) = S_x + S_{A^c} - S_{x \cup A^c}$, where x denotes the distance of the measured qubit from the boundary ∂A . In the highly entangled states generated by random circuit evolution with local gates, this mutual information generically falls to zero at large distances.

Considering a $1d$ circuit with $A = (-\infty, 0]$ for concreteness, a back-of-the-envelope estimate suggests that if $\mathcal{I}(x)$ falls off faster than $1/x$, then the rate that measurements reduce S_A is $\sim p \int_{-\infty}^0 \mathcal{I}(x) dx$, which is a finite constant. Some approximate mean-field-like arguments suggest $\mathcal{I}(x) \sim x^{-3/2}$ in this context [32, 33], and numerically, one finds $\mathcal{I}(x) \sim x^{-1.25}$ compatible with the interpretation of this quantity in terms of the return probability of a directed polymer in a random environment [88]. Therefore, despite the extensive fraction $\sim p$ of qubits measured after each circuit layer, only measurements close to the boundary of A remove an appreciable amount of entanglement, and the rate of entanglement production by circuit dynamics and entanglement loss due to measurement collapse both scale

like $|\partial A|$, such that the outcome of their competition depends on p . These simple arguments predict the existence of a sharp measurement-induced phase transition (MIPT) at critical measurement probability $0 < p_c < 1$, with the scrambling dynamics producing highly-entangled states for $p < p_c$, and measurements collapsing the system into short-range entangled states for $p > p_c$. Indeed, clear numerical evidence for such a measurement-induced entanglement phase transition has been observed in this model for large-scale random Clifford circuits, and smaller-scale circuits with Haar random gates via exact diagonalization [34].

3.1 Entanglement Transition

The hallmark of the entanglement MIPT in this model is a singular change in the “average” entanglement entropy, $S(\ell)$, for a continuous region of size ℓ of the typical state produced by the monitored random circuit from volume law, $S(\ell) \sim \ell$ for infrequent measurements ($p < p_c$) to area law ($p > p_c$). Specifically, referring to the output, $|\psi_{\mathbf{m}}(t)\rangle$, of a particular instance of the random circuit with measurement outcomes \mathbf{m} as a *trajectory*, we define the trajectory-averaged (Renyi) entanglement entropies for region A as

$$\overline{S_A^{(n)}} = \mathbb{E}_{U, \mathbf{m}} \left[\frac{1}{1-n} \log \text{tr}_A (\rho_{A, \mathbf{m}}^n(t)) \right], \quad (13)$$

where n is the Renyi index (von Neumann entropy is defined through the limit $n \rightarrow 1$), $\mathbb{E}_{\mathbf{m}}$ denotes averaging over measurement outcomes (weighted by the Born probability of obtaining that outcome) and measurement locations, and $\rho_{A, \mathbf{m}}(t) = \text{tr}_{A^c} |\psi_{\mathbf{m}}(t)\rangle \langle \psi_{\mathbf{m}}(t)|$ is the reduced density matrix for the trajectory.

To be specific, consider the trajectories produced by evolving initially unentangled product states by monitored random circuit evolution with $1 + 1d$ connectivity, and choose entanglement interval A to be a single contiguous interval of length ℓ . Numerical simulations [34] (Fig. 2b) show that for $p < p_c$ $\overline{S}(\ell, t)$ grows linearly ($\sim t$) until a time scale of $t \gtrsim \ell$ where it saturates to a volume-law behavior $\overline{S}(\ell) \sim s(p)\ell + \dots$, with volume-law coefficient $\log 2 \geq s(p) > 0$, and where (\dots) denotes further subleading-in- ℓ terms, including universal $\ell^{1/3}$ corrections [88]. By contrast, for $p > p_c$, the entanglement quickly saturates to an area-law behavior $\overline{S}_A \sim |\partial A|$ in $O(1)$ time. Precisely at the transition, $p = p_c$, the entanglement appears to grow logarithmically in time $\overline{S}_A(t) \sim \log t$, saturating to $\overline{S}_A(t \gg |A|) \sim \log \ell$.

The collapse of numerical data for bipartite entropy $\ell = L/2$ over a range of p and system size L is consistent with a universal scaling function:

$$\overline{S}(\ell) = G \left[(p - p_c)L^{1/\nu}, t/L^z \right] + \overline{S}_{\text{non-universal}}, \quad (14)$$

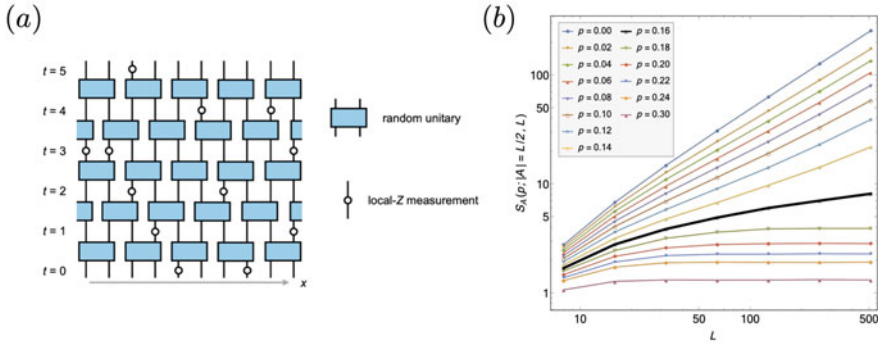


Fig. 2 Measurement-induced entanglement phase transition . (a) in a monitored random circuit (MRC). (b) Finite-size scaling of measurement-trajectory-averaged bipartite entanglement entropy, S_A for region of size $|A| = L/2$, for random Clifford circuits at long times, shows a continuous phase transition at critical measurement rate $p_c \approx 0.16$, with volume-law entanglement $S \sim L$ for $p < p_c$, and area-law entanglement $S \sim \text{const}$. for $p > p_c$. At criticality, long-time entanglement grows logarithmically in L (and also builds up logarithmically with time). Reproduced from Ref. [34]

with scaling exponents $z \approx 1$, and $\nu \approx 1.3$ for random Clifford circuits and universal scaling function $G(x, \tau)$ coexists with a non-universal area-law background $\bar{S}_{\text{non-universal}}$ that evolves smoothly across the transition. For $e^L \gg t \gg L$, the entanglement saturates to a steady-state value with scaling form:

$$G(x, \tau \gg 1) \sim \begin{cases} |x|^\nu & x \rightarrow -\infty \text{ (entangling-phase)} \\ \alpha \log(|x|) & x \ll 1 \text{ (critical-regime)} \\ 0 & x \rightarrow +\infty \text{ (collapsed-phase)} \end{cases} \quad (15)$$

Critical phenomena aficionados may notice that the critical exponents ν, z are suspiciously close to those of a $1 + 1d$ bond percolation transition $\nu_{\text{percolation}} = 4/3$, $z_{\text{percolation}} = 1$. Indeed, the entanglement for monitored random circuits can be mapped to percolation-like statistical mechanical models (see below); however, the transition is believed to be generically different from simple percolation except in the limit of infinite onsite Hilbert space dimension. For completeness, we note that a distinct but related entanglement transition between thermalizing and many-body localized (MBL) arises in the purely unitary dynamics (no measurements) generated by a constant or time-periodic Hamiltonians without temporal randomness [89–91]. In this context, percolation-type entanglement critical phenomena have also been observed in random Clifford models [92].

A subtle, but crucial point is that the entanglement transition is only visible if one first computes the entanglement of a trajectory and then averages over trajectories. By contrast, the trajectory-averaged state $\bar{\rho} = \mathbb{E}_{\mathbf{m}}(\rho_{\mathbf{m}})$ is generically volume law entangled for any p (including $p = 1!$). As a corollary, the entanglement transition

is not visible in averages of local operators: $\mathbb{E}_{\mathbf{m}}[\langle O \rangle] = \text{tr} \bar{\rho} O$, but only in their higher moments such as: $\mathbb{E}_{\mathbf{m}}[\langle O_1 \rangle \langle O_2 \rangle]$. This poses a significant challenge to experimentally observing measurement-induced phase transitions: since computing non-linear functions of a trajectory (entanglement, higher moments of observables, etc.) requires measuring many copies of the same trajectory $|\psi_{\mathbf{m}}\rangle$. Since we cannot simply copy this state (no-cloning theorem!), one must instead sample many times from the circuit to obtain multiple copies with the same measurement outcomes \mathbf{m} . For such non-linear functions of state, this post-selection on measurement outcomes generically adds sampling overhead that is exponential in the space-time volume of the circuit: $\sim \exp(pLt)$ for a circuit of depth t acting on L qubits.

We will discuss below a possible route to avoiding post-selection through measuring different types of observables involving an ancillary reference qubit initially entangled with the system, designing a classical decoder to avoid the need to prepare multiple copies of a trajectory to detect the area-law phase. Using this strategy, moderate-scale experiments have been successfully performed on trapped-ion experiment [77] by identifying a model in which the MIPT occurs at very low measurement density. We note that these methods are currently specific to Clifford circuits, and it is not clear what their overhead would be for MRCs with computationally universal gate sets. We also note that in recently investigated space-time duals of RC dynamics [54] (or equivalently in random tensor network states in which the tensors are generated by random circuits [93, 94]), a closely related entanglement transition arises, which can be observed by post-selection only on the *final* measurements of physical qubits in the Bell basis [54], incurring exponential overhead only in spatial volume ($\sim e^L$ cost) rather than space-time volume ($\sim e^{pLT}$ cost).

3.2 Alternative Perspectives on MIPTs

Above, we considered a setup where initially unentangled states were evolved under MRC dynamics resulting in either extensive entanglement production ($p < p_c$) or continuation of short-range entanglement due to measurement collapse ($p > p_c$). A fruitful alternative perspective if we instead consider feeding mixed states into MRCs (or equivalently states that initially share entanglement with other degrees of freedom), which will expose intriguing connections between the entanglement transition with themes from quantum information, communication, and error correction.

3.2.1 Purification Transition

First consider the trajectories arising from inputting a maximally mixed (“infinite temperature”) state $\rho_{\infty} = \frac{1}{2^L} \mathbb{1}$ with entanglement $S = -\text{tr} \rho \log \rho = L \log 2$ into an MRC. For $p = 1$, every qubit is measured, and the state immediately “purifies”

the maximally mixed into a pure quantum state with vanishing total entanglement entropy. By contrast, for $p = 0$, the purely unitary RC evolution does not affect S , and the state remains maximally mixed at all times. Given our experience with pure-state inputs, it is natural to expect that there is a critical measurement probability p_c , where MRC dynamics undergoes a phase transition between regimes where densely repeated measurements purify any mixed initial state ($p > p_c$) or fail to do so due to scrambling dynamics that obscure whether the measured qubit is in a mixed state due to environmental entanglement or entanglement of other qubits in the system ($p < p_c$). A priori it might not be obvious that the purification transition [30] for mixed state inputs should coincide precisely with entanglement transitions; however, numerically, they appear to do so [30], and we will see below in the context of statistical mechanical mappings that these transitions have a unified “dual” interpretation as the same bulk-ordering transition of a replica-spin model.

An important caveat to the purification interpretation is that at ultra-long time scales ($t \sim \exp L$), MRCs for any non-zero measurement fraction ($p > 0$) will eventually purify an arbitrary input state. Hence, the purification transition is only evident in the limit $e^L \gg t \gg L \gg 1$.

3.2.2 Ancilla Probe of Purification Transition

We can view the maximally mixed input state ρ_∞ as arising from having each qubit in the system being entangled with an ancilla qubit that does not participate in the circuit dynamics. The purification perspective then suggests a useful way to characterize the entanglement/purification transition via examining whether the mutual information between ancillas and the system (S) survives to long times or is killed by measurement collapse (Fig. 3).

In fact, to observe the transition, it suffices to examine just a single “reference” ancilla, R , and look at the trajectory average of the reference ancilla [41]:

$$\overline{S_R} = \mathbb{E}_{U,m} [S_R] \equiv \mathbb{E}_{U,m} [-\text{tr}_R \rho_R \log \rho_R]. \quad (16)$$

Measured at times $2^L \gg t \gg L$, and in the limit $L \rightarrow \infty$, $\overline{S_R}$ exhibits a discontinuous jump across the transition. This jump provides a convenient numerical signature that precisely locates the transition via a crossing in curves of $\overline{S_R}$ versus p for different L .¹ This single-ancilla feature has been referred to as a *scalable* probe of MIPT, in the sense that it avoids the exponential-in- L cost of measuring many-body entanglement of a trajectory.

¹ As an aside, we note that if the ancilla qubit, R , is initially entangled non-locally with the system, e.g., by applying a scrambling unitary before undergoing MRC dynamics, then in the $L \rightarrow \infty$ limit, $\overline{S_R}$ precisely jumps from $\log 2$ for $p < p_c$ to 0 for $p > p_c$. On the other hand, if the ancilla qubit is locally entangled with a single system qubit, $\overline{S_R}$ is not quantized (for example, with probability p that qubit could immediately get measured even for $p < p_c$) and its jump across the transition is non-universal.

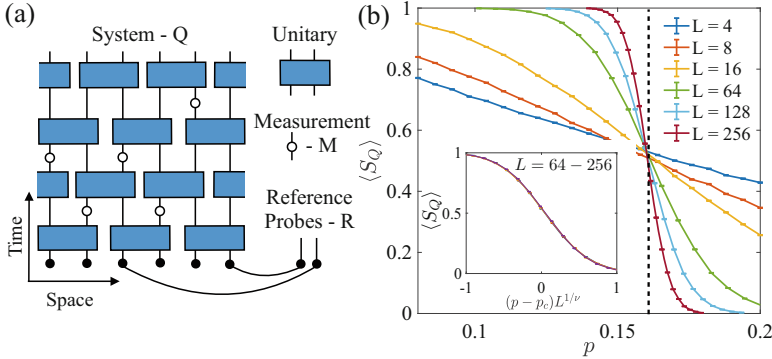


Fig. 3 Quantum information perspectives on the MIPT entanglement transition— adapted from [30]. (a) Entanglement transition as a purification transition for entangled reference ancilla qubits (R). The entanglement entropy of the reference, \overline{S}_R , serves as an order parameter for the transition. When a pre-scrambling unitary is included before the MRC dynamics, \overline{S}_R jumps from $\log(2)$ to 0 in the infinite size limit as evidenced by finite-size scaling shown in (b) for random Clifford circuits. (c) Shows an alternative quantum communications perspective of this setup, where the pre-scrambling circuit is viewed as a random encoding of the quantum information between R and the system (S), the MRC channel \mathcal{N} represents a communications channel, including monitoring by an environment E , and then one attempts to decode the information at the output (with a hypothetical optimal decoder). The entanglement transition represents a phase transition in the quantum channel capacity of this communications setup (c)

3.2.3 Experimental Observation of MIPT in Trapped Ions

Using a standard method of measuring the reference qubit entanglement entropy (e.g., using tomography to determine its density matrix) would still require many copies of a given trajectory that would incur a much larger post-selection overhead. However, Refs. [30, 77] highlight a method to potentially avoid post-selection. In the purifying phase, the measurements collapse the reference ancilla into a pure state disentangled from the system. This pure state may be in a random basis determined by various measurement outcomes, so that further measurements of the ancilla in a fixed (e.g., computational) basis would generally see a large-entropy mixture of 0 and 1 outcomes. However, if this basis can be determined using the knowledge extracted from the measurement outcomes in the circuit, then one could observe the purity of the entangled state without preparing multiple copies of the same trajectory. This idea can be carried out for Clifford circuits [77], whose classically efficient simulations permit one to design a feedforward circuit using quantum logic to transform the ancillas into the computational basis when they are purified. Using this technique, Ref. [77] was able to observe finite-size signatures of a MIPT in a trapped-ion chain without post-selection (Fig. 4). While this experiment was relatively small scale, involving 8 system qubits and one reference qubit and a variable small number (≤ 4) of measurements, clear signs of the limiting behavior in the large- and small-measurement regime were observed, and the methods

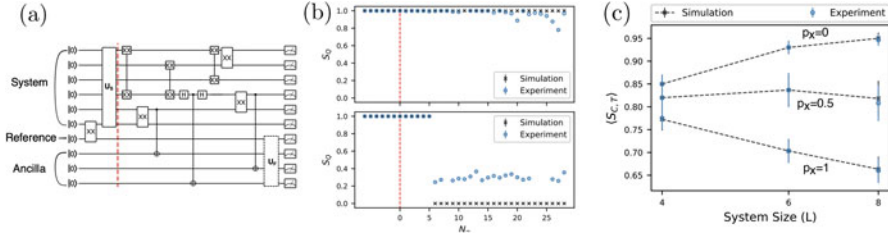


Fig. 4 Finite-size evidence of MIPT entanglement transition in trapped-ion chain—adapted from [77]. **(a)** Circuit schematic of experiment: a reference qubit R is entangled with the system S through an entangling XX gate (unitary $u_{XX} = e^{i\pi/4X \otimes X}$). The information is then scrambled with scrambling circuit U_C and subjected to random Clifford MRC dynamics. Four ancillas A hold the intermediate measurement outcomes, deferring measurement to the end of the circuit. Before measurement, a feedback decoding circuit U_F is then applied to the R and A to attempt to disentangle the reference and measurement ancilla and place the reference in the computational basis (which will be successful if the ancilla is purified). **(b)** Quantum entanglement S_Q of R determined through tomography and averaged over $\sim 10^3$ – 10^4 shots for two trajectories where R stays mixed (top) or is purified (bottom). **(c)** Classical entropy of R after a thresholding procedure, $\langle S_{C,T} \rangle$, for various system sizes and measurement rates show a qualitative change in system-size dependence across the MIPT (determined by simulation to occur at $p \approx 0.72$)

developed pave the way for larger-scale experiments (e.g., in architectures where mid-circuit measurements can be performed to avoid the need to sacrifice ancilla qubits as a classical register to hold measurement outcomes). Recent work [95] further shows that related ideas can allow detection of the scrambling phase without post-selection through entanglement distillation methods.

We emphasize that the efficient measurement-decoding implementations in these works are special to Clifford circuits and exploited their efficient classical simulability. While Clifford circuits are an interesting important class of quantum circuits that play an important role in many areas of quantum information such as stabilizer codes (among others), they are also in a sense fine-tuned and non-generic in that they are not capable of universal quantum computation and that small deviations from Cliffordness ultimately spoil their efficient simulation. It remains an important open question whether similar decoding strategies can be used to reduce the overhead associated with post-selection to observe MIPTs in MRCs with universal gate sets.

3.2.4 Connection to Quantum Channel Capacity and Quantum Error Correction

The purification perspective also suggests intriguing connections between MIPTs to quantum communication and error correction [30, 31]. Specifically, one can view the MRC as a communication channel transmitting input mixed state ρ_{in} initially entangled with reference system R through the MRC dynamics to an output. A key metric for the quality of a quantum communication channel is quantum

channel capacity (QCC), which is roughly speaking the number of qubits' worth of information that can be transmitted through a noisy channel, optimized over all possible encoding and decoding protocols. A famous result [96] of Lloyd, Shor, and Devetak [LSD] relates the QCC for a channel \mathcal{N} to the coherent information: $I_C[\mathcal{N}, \rho_{\text{in}}] = S_{A'} - S_{A'R}$, where S_X is the von Neumann entanglement entropy of subsystem X , ρ_{in} is the input state of system A , A' denotes the system qubits after transmission through the channel, and R is the reference ancilla system with which A is initially entangled, and which does not undergo any dynamics. This quantity can be understood as the amount of entanglement that survives from input to output by subtracting off "incoherent" entanglement with the environment responsible for information loss in the channel. To see this, note that we can purify the channel as a unitary interaction between the system and an environment E , and $S_{A'R} = S_E$, where E is the environment that from the output. Namely, LSD showed that the quantum channel capacity is equal to the stabilizing limit of the coherent information maximized over input state:

$$\text{QCC} = \lim_{n \rightarrow \infty} \frac{1}{n} \max_{\rho_{\text{in}}} I_C[\mathcal{N}^{\otimes n}, \rho_{\text{in}}]. \quad (17)$$

Intuitively, taking a large number of copies reflects that channel capacity characterizes the ability to transmit long sequences of communications rather than a single message. For a certain class of the so-called degradable quantum channels, which generalize dephasing and erasure error channels, and which were shown [31] to include MRCs, the coherent information is simply additive, $I_C(\mathcal{N}^{\otimes n}) = nI_C(\mathcal{N})$, and it suffices to consider just a single copy of the channel. Further, the average coherent information for MRCs was shown [31] to be precisely equal to \overline{S}_R .

This strongly suggests that the entanglement/purification transition in MIPTs can also be regarded as a phase transition in quantum channel capacity (QCC) between a high-capacity phase where the MRC channel transmitting an extensive number of qubits ($p < p_c$) and a low-capacity phase where with vanishing fraction of qubit information transmitted ($p > p_c$).

Strictly speaking, \overline{S}_R is not precisely the same as QCC, but rather reflects a sort of "average" QCC. Namely, the typical formal definition of QCC involves optimizing over input state ρ_{in} for each random circuit instance (the encoding of the input may exploit specific knowledge of the circuit gates and measurement locations, e.g., to avoid encoding information near positions that are heavily measured), and average QCC would be obtained by averaging each optimized result over circuit configuration. Instead, \overline{S}_R captures a different order of limits, where averaging over the MRC ensemble is performed before optimization over inputs (it can be shown that the optimal input to the average channel is the maximally mixed state ρ_{∞} [31]). We note however that optimal communication capacity is rarely if ever achieved in practice, and a more physically relevant question is whether there exists a threshold error rate below which one can communicate encoded information at a finite rate. The above results (see also further detailed arguments and numerical simulations in [30, 31]) show that MRCs indeed have such a threshold.

The measurement-induced entanglement transition can also be understood as a quantum error-correction (QEC) threshold [31, 74]. Indeed, the QCC problem, which involves encoding information into a quantum state, and subjecting it to a noisy and error-prone channel before attempting to recover it using a decoder, is a form of QEC.

3.2.5 Information Gained by the Observer

A closely related perspective of the MIPT can be formulated in terms of the ability of the observer to extract information about the state of the system. In the volume-law phase, information scrambling by the unitary evolution hides information into highly non-local degrees of freedom that are hidden from the local measurements. As a result, in that phase, the observer would require a time scaling exponentially with the system size in order to extract all the information about the system. In contrast, in the area-law phase, the observer can learn everything about the state of the system in a time of order one. The amount of information extracted by the measurements about the initial state of the system can be quantified by the Fisher information [39], which is non-analytic at the MIPT.

4 Replica Statistical Mechanics Models

Most of the phenomenology of measurement-induced phase transitions described above relied on numerical results, either on small ($L \sim 20$ qubits) Haar circuits or larger ($\sim 10^3$ qubits or qudits) Clifford circuits. To understand the scaling properties and phase structure of monitored quantum circuits on a firmer ground, we now turn to an analytic approach by deriving an exact mapping onto a statistical mechanics model. Using a replica trick, entanglement properties can be mapped onto the free energy cost of a boundary domain wall in a classical “spin” model [25, 39, 40, 73], with the entanglement transition corresponding to a simple (replica) symmetry-breaking transition. This replica approach to performing statistical mechanics mappings for entanglement transitions was first introduced in the context of random tensor network states [25], which turn out to be very closely related to MIPTs in MRCs.

4.1 Replica Trick

Our goal is to compute the Renyi entropies of such individual quantum trajectories, averaged over measurement outcomes and random unitary gates. Each trajectory is weighted by the Born probability $p_{\mathbf{m}} = \text{tr} \rho_{\mathbf{m}}$, where $\rho_{\mathbf{m}} = |\psi_{\mathbf{m}}\rangle\langle\psi_{\mathbf{m}}|$ is the (pure)

density matrix of the system:

$$S_A^{(n)} = \mathbb{E}_U \sum_{\mathbf{m}} p_{\mathbf{m}} \frac{1}{1-n} \log \left[\frac{\text{tr} \rho_{A,\mathbf{m}}^n}{(\text{tr} \rho_{\mathbf{m}})^n} \right], \tag{18}$$

where \mathbb{E}_U refers to the Haar average over random unitary gates, and $\sum_{\mathbf{m}}$ denotes averaging over quantum trajectories (i.e., over measurement outcomes). Here, it will turn out to be convenient to work without an explicitly normalized density matrix in computing time evolution, and so we include the factors of $\sim \text{tr} \rho$ in the denominator to explicitly enforce normalization of the density matrix when computing observables. We will denote $\overline{S_A^{(n)}}$ the Renyi entropy averaged over measurement locations.

On the face of it, computing the Renyi entropies (19) might seem like a daunting task: entanglement properties are usually hard to access analytically, and the non-equilibrium time evolution combined with the non-linearity of the measurements makes the problem even harder. However, following Refs. [25, 39, 40, 73], we can use the replica trick to compute (19). As in the field of classical random spin models and spin glasses, the basic idea is to rely on the simple identity:

$$\log x = \lim_{k \rightarrow 0} \frac{x^k - 1}{k}. \tag{19}$$

This equation is exact, but the “trick” is to compute the average of the logarithm $\log x$ (here over random unitaries and measurement outcomes), which is a hard task in general, using the average of the moment x^k , where k is an integer, which is usually a lot easier. This step involves analytic continuation in k , which can be subtle in some cases. Using this replica trick, we can write the Renyi entropies as

$$S_A^{(n)} = \lim_{k \rightarrow 0} \mathbb{E}_U \sum_{\mathbf{m}} \frac{p_{\mathbf{m}}}{(1-n)k} \left((\text{tr} \rho_{A,\mathbf{m}}^n)^k - (\text{tr} \rho_{\mathbf{m}}^{\otimes n})^k \right). \tag{20}$$

We will write $Q = nk + 1$ to denote the total number of replicas, where the additional replica comes from the Born probability $p_{\mathbf{m}} = \text{tr} \rho_{\mathbf{m}}$ weighting different quantum trajectories. Within this replicated state, we can write

$$S_A^{(n)} = \lim_{k \rightarrow 0} \frac{1}{(1-n)k} \mathbb{E}_U \sum_{\mathbf{m}} \left(\text{tr} \left[S_{A,n}^{\otimes k} \rho_{\mathbf{m}}^{\otimes Q} \right] - \text{tr} \left[\rho_{\mathbf{m}}^{\otimes Q} \right] \right), \tag{21}$$

where $S_{A,n}$ is a permutation “swap” operator implementing the partial trace in the region A , acting on each of the first k replicas (which are themselves n -fold replicated states) as

$$S_{A,n} = \prod_x \chi_{g_x}, \quad g_x = \begin{cases} (12 \cdots n), & x \in A, \\ \text{identity} = e, & x \in \bar{A}. \end{cases} \tag{22}$$

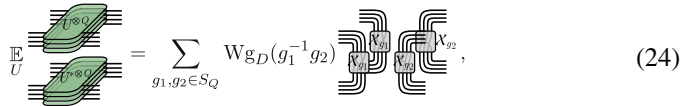
g_x labels the permutation on site x , and $\chi_{g_x} = \sum_{[i]} |i_{g_x(1)} i_{g_x(2)} \cdots i_{g_x(n)}\rangle \langle i_1 i_2 \cdots i_n|$ is its representation on the replicated onsite Hilbert space, i.e., on its n -fold tensor product. As indicated in the equation above, g_x is the cyclic (identity) permutation when x is in the region A (when x is in the region \bar{A}). Here, we use standard cycle notation to denote permutations, for example, $(123)4$ refers to the cyclic permutation $1234 \rightarrow 2314$.

4.2 Haar Calculus and Boltzmann Weights

The next step is to perform the average over the (replicated) random unitary gates, using the Haar measure (see [97] for a nice physicist-accessible review of some technical aspects of Haar averages over the unitary group). The average over each gate can be evaluated using the formula

$$\mathbb{E}_{U \in U(D)} (U^{*Q} \otimes U^Q) = \sum_{\sigma, \tau \in S_Q} \text{Wg}_D(g_1^{-1} g_2) \mathcal{X}_v(g_1) \otimes \mathcal{X}_v(g_2), \tag{23}$$

where g_1, g_2 are permutations of the replicas, Wg are called Weingarten functions, and $D = d^2$, $\mathcal{X}_v(g_1) = \mathcal{X}(g_1) \otimes \mathcal{X}(g_1)$ permutes the output legs of U by g_1 and contracts them with the corresponding legs of U^* , and similarly for $\mathcal{X}_v(g_2)$ acting on the input legs. The reason the average $\mathbb{E}_{U \in U(D)} (U^{*Q} \otimes U^Q)$ can be expanded onto permutations of the replicas is that such permutations commute with the action of the unitaries, which are the only terms surviving the Haar average. The commuting actions of the unitary and permutation groups on a tensor product Hilbert space is a mathematical statement known as *Schur–Weyl duality*. This step can be generalized to other subgroups of the unitary groups, see Ref. [98]. Using standard tensor network notations [99], we will write Eq. (23) as [40]



$$\mathbb{E}_U = \sum_{g_1, g_2 \in S_Q} \text{Wg}_D(g_1^{-1} g_2) \mathcal{X}_{g_1} \mathcal{X}_{g_2}, \tag{24}$$

Here $\text{Wg}_D(g)$ denotes the Weingarten function of the permutation g ,

$$\text{Wg}_D(g) = \frac{1}{Q!} \sum_{\lambda \vdash Q} \frac{\chi_\lambda(e) \chi_\lambda(g)}{\prod_{(i,j) \in Y(\lambda)} (D - i + j)}, \tag{25}$$

where the sum is taken over all integer partitions λ of Q [denoted in the above equation by the notation $\lambda \vdash Q$, such that $\lambda = (\lambda_1, \lambda_2, \dots)$ with $\lambda_1 \geq \lambda_2 \geq \dots$, $\lambda_i \in \mathbb{N}$ and $\sum_i \lambda_i = Q$], and the product is taken over all cells (i, j) in the Young diagram $Y(\lambda)$ of the shape λ . Here e denotes the identity group element, and $\chi_\lambda(g)$ is the irreducible character of the symmetric group S_Q indexed by the partition λ .

Those Weingarten coefficients $\text{Wg}_D(g)$ can also be computed by contracting the unitaries within each replica in the left-hand side of Eq. (23) to obtain a trivial result using $U^\dagger U = 1$. This yields

$$\mathcal{X}_v(e) = \sum_{g_1, g_2 \in S_Q} \text{Wg}_D(g_1^{-1}g_2) (\text{tr} \mathcal{X}_v(g_1)) \mathcal{X}_v(g_2), \quad (26)$$

where e is the identity permutation. The trace of $\mathcal{X}(g)$ simply counts the number of *cycles* in the permutation g ,

$$\text{tr} \mathcal{X}_v(g) = D^{C(g)}, \quad (27)$$

where $C(g)$ is the number of cycles in the permutation g . We thus find

$$\sum_{g_1 \in S_Q} \text{Wg}_D(g_1^{-1}g_2) D^{C(g_2)} = \delta_{g_2}, \quad (28)$$

where δ_g is equal to 1, that is $g = e$, and 0 otherwise. This equation can be used to define the Weingarten coefficients Wg_D , as the inverse of D^C . Equation (23) applied to the brick-wall pattern of unitary gates defines a statistical model on the honeycomb lattice, where permutations live on vertices. Contracting unitary gates can be done by assigning a weight to links connecting unitaries given by

$$W(g_1, g_2) = \text{tr}[\mathcal{X}^\dagger(g_1)\mathcal{X}(g_2)] = d^{C(g_1^{-1}g_2)}. \quad (29)$$

Note the factor of d here, instead of D , since we are focusing on a single leg of the unitary ($\mathcal{X}_v = \mathcal{X} \otimes \mathcal{X}$). This weight is associated to all links that were not measured. If a link was measured instead, all replicas are constrained to be in the same state, and the weight is instead d after averaging over possible measurement outcomes. Those equations fully determine the weights of the statistical model in monitored Haar random circuits. Upon averaging over measurement locations and outcomes, the weight assigned to a link is therefore given by [40]

$$W_p(g_1, g_2) = (1 - p)d^{C(g_1^{-1}g_2)} + pd. \quad (30)$$

Putting these results together and ignoring for the moment boundary conditions, we obtain an anisotropic statistical mechanics model defined on the honeycomb lattice,

$$Z = \sum_{\{g_i \in S_Q\}} \prod_{(ij) \in G_s} W_p(g_i^{-1}g_j) \prod_{(ij) \in G_d} \text{Wg}_D(g_i^{-1}g_j), \quad (31)$$

where G_s (G_d) denotes the set of solid (dashed) links on the lattice. In Fig. 5, the vertical (dashed) links on the honeycomb lattice represent the Weingarten functions that originated from averaging the two-site unitary gates, and the solid links keep track of the link weights originating from averaging over measurements.

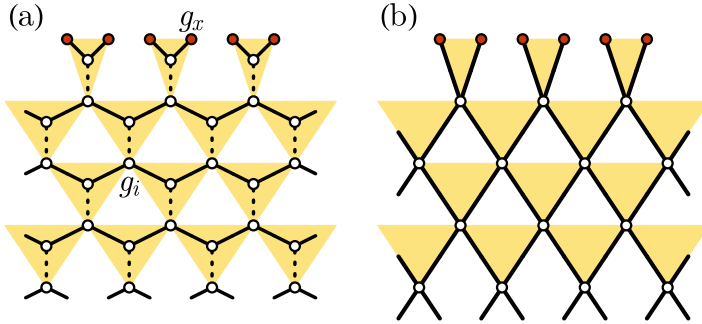


Fig. 5 Statistical mechanics model (a) Geometry of the statistical mechanics model of S_Q spins. The red sites correspond to the boundary spins to be pinned by the boundary condition. (b) In the $d = \infty$ limit, the model reduces to a Potts model on a square lattice. Reproduced from Ref. [40]

4.3 Boundary Conditions and Domain Wall Free Energy

By imposing different boundary conditions corresponding to fixing permutations at the boundary, the statistical mechanics model results in different partition functions

$$\begin{aligned} Z_A &= \mathbb{E}_{U, \text{mtr}} \left[\mathcal{S}_{A,n}^{\otimes k} \rho_{\mathbf{m}}^{\otimes Q} \right], \\ Z_0 &= \mathbb{E}_{U, \text{mtr}} \left[\rho_{\mathbf{m}}^{\otimes Q} \right], \end{aligned} \tag{32}$$

from which the averaged n th Rényi entropy $\overline{S_A^{(n)}}$ can be obtained in the replica limit via

$$\overline{S_A^{(n)}} = \frac{n}{1-n} \lim_{Q \rightarrow 1} \frac{Z_A - Z_0}{Q - 1}. \tag{33}$$

Using the fact that $Z_A = Z_0 = 1$ in the replica limit $k \rightarrow 0$ ($Q \rightarrow 1$), this can be rewritten in a more intuitive form as the free energy cost of the domain wall associated with changing the boundary condition in the entanglement region:

$$\overline{S_A^{(n)}} = \lim_{k \rightarrow 0} \frac{F_A - F_0}{k(n-1)}, \tag{34}$$

with $F_A = -\log Z_A$ and $F_0 = -\log Z_0$. The S_Q “spins” on the boundary, which are permutation group elements $g_x \in S_Q$ for boundary sites x , are pinned by the boundary condition that is uniform and set to $g_x = e$ for Z_0 , corresponding to a

trivial contraction. The partial trace in Z_A is implemented as follows:

$$g_x = \begin{cases} g_{\text{SWAP}} \equiv (12 \cdots n)^{\otimes k}, & x \in A, \\ \text{identity} = e, & x \in \bar{A}. \end{cases} \quad (35)$$

This equation follows immediately from k copies of (22).

Now that we have mapped the calculation of the entanglement entropies of the random circuit with projective measurements onto a (replica) statistical mechanics model, and many qualitative features of the entanglement transition can be understood naturally. At small p , the Boltzmann weights give a ferromagnetic interaction favoring group elements on neighboring sites to be equal, and we thus expect an ordered phase of the statistical mechanics model. In that phase, the free energy cost $F_A - F_0$ in (34) associated with changing the boundary conditions in the region A , and thus of creating a domain wall, scales with the size of the interval L_A of A at long times, corresponding to volume-law entanglement $\overline{S_A^{(n)}} \sim L_A$. As the measurement rate p gets closer to 1, the effective temperature of the statistical mechanics model is increased, leading to a disordered phase. The domain wall condensate present in this phase can freely absorb the domain wall at the boundaries of the entanglement interval, such that, for a distance exceeding the correlation length from the boundary, there is no additional free energy cost from the boundary domain. In this limit, the free-energy cost of the boundary domain will scale like the boundary of A , corresponding to area-law scaling of entanglement $\overline{S_A^{(n)}} \sim \text{const}$.

4.4 Symmetry and Conformal Invariance

A crucial property of the statistical mechanics model derived above (Eq. (31)) is that the Boltzmann weights are invariant under global right- and left-multiplication of all group elements

$$g_i \rightarrow h_L g_i h_R^{-1}, g_j \rightarrow h_L g_j h_R^{-1}, \text{ where } h_L, h_R \in S_Q. \quad (36)$$

This follows from the fact that both the cycle counting function and the Weingarten functions (which are inverse of each other) are *class functions*, that is, they depend only on the conjugacy class of the permutation group elements. Physically, the two factors of S_Q symmetry correspond to the separate invariance under permuting the replicas in the forward (U) and backward (U^*) time contours. This structure will be important in the next section and in the discussion of MRCs with symmetry below.

This general mapping indicates that the measurement-induced transition corresponds to a simple ordering, (replica) symmetry-breaking transition. In general, assuming that the transition is of second order, it should be described by a two-dimensional conformal field theory (CFT) with central charge $c = 0$ in the replica limit $Q \rightarrow 1$. (Recall that c measures the way the free energy changes when a finite

scale is introduced; since here the partition function $Z_0 = 1$ is trivial in the replica limit, we have $c = 0$.) Such CFTs at central charge $c = 0$ are non-unitary and are especially complicated even in two dimensions. However, there are a number of general properties that follow from general scaling considerations and conformal invariance.

Since the bulk properties of the transition only depend on Q , the statistical model approach naturally explains why all Rényi entropies with $n \geq 1$ have a transition at the same value of p_c , as observed in the numerics. Conformal invariance also allows us to derive the general scaling form of the entanglement entropy near criticality, by noting that the ratio of partition functions Z_A/Z_0 that appears in (34) corresponds in the CFT language to the two-point function of a boundary condition changing (BCC) operator ϕ_{BCC} [100, 101]

$$Z_A/Z_0 = \langle \phi_{\text{BCC}}(L_A)\phi_{\text{BCC}}(0) \rangle, \tag{37}$$

where the operators are inserted at the boundary of the entanglement interval A . Near criticality, this two-point function scales as $\sim 1/L_A^{2h(n,m)} f_{n,m}(L_A/\xi_Q)$ with $\xi_Q \sim |p - p_c(Q)|^{-\nu(Q)}$ the correlation length of the statistical mechanics model, and $f_{n,m}$ are universal scaling functions that depend on n and m independently. Plugging this expression into the replica formula (34), we find the general scaling of the entanglement entropy (up to non-universal additive terms)

$$\overline{S_A^{(n)}} = \alpha_n \log L_A + f_n \left(\frac{L_A}{\xi} \right), \tag{38}$$

with $\xi \sim |p - p_c|^{-\nu}$ the correlation length in the limit $Q \rightarrow 1$, and $\alpha_n = \frac{2}{n-1} \frac{\partial h}{\partial m} \Big|_{m=0}$ is a universal prefactor. Note that α_n is unrelated to the central charge of the theory and instead is a boundary critical exponent. In particular, conformal invariance predicts that $\overline{S_A^{(n)}} \sim \log L_A$ at criticality $p = p_c$, with a universal prefactor that depends on the Rényi index n .

4.5 Large Hilbert Space Dimension Limit

4.5.1 Mapping Onto Classical Percolation

In the limit of large onsite Hilbert space dimension, $d \rightarrow \infty$, the S_Q model above reduces to a Potts model with $Q!$ colors defined on the square lattice. To see this, we evaluate the partition function weight $J_p(g_i, g_j; g_k)$ associated with each down triangle in Fig. 5, integrating out the middle spin:

$$J_p(g_i, g_j; g_k) = \sum_{g_l \in \mathcal{S}_Q} W_p(g_i^{-1}g_l) W_p(g_j^{-1}g_l) W_{\mathbb{G}_D}(g_l^{-1}g_k). \tag{39}$$

The partition function can then be equivalently written in terms of the triangle weight J_p as

$$Z = \sum_{\{g_i \in S_Q\}} \prod_{\langle ij \rangle} J_p(g_i, g_j; g_k), \quad (40)$$

subject to the appropriate boundary conditions that distinguish Z_0 from Z_A . In the $d \rightarrow \infty$ limit, we have $d^{C(g)} \sim d^Q \delta_g$, where δ_g is the delta function that gives 1 if and only if $g = e$ is the identity element in the permutation group S_Q and gives 0 otherwise. This follows from the fact that the number of cycles $C(g)$ is maximized by the trivial permutation: $C(g) = Q$. Since the Weingarten weights are defined as the inverse of $D^{C(g)}$ with $D = d^2$, we immediately find that in the $d \rightarrow \infty$ limit, we have $\text{Wg}_D(g) = D^{-Q} \delta_g$. Substituting into the triangle weight, the triangle weight (39) and after some straightforward algebra, one finds [40]

$$J_p(g_i, g_j; g_k) = ((1-p)\delta_{g_i^{-1}g_k} + p)((1-p)\delta_{g_j^{-1}g_k} + p), \quad (41)$$

which further factorizes into partition function weights defined separately on the bonds $\langle ik \rangle$ and $\langle jk \rangle$. The partition function weight across the bond $\langle ik \rangle$ equals 1 if $g_i = g_k$ and p if $g_i \neq g_k$, and an analogous weight is assigned to the bond $\langle jk \rangle$. If we treat each onsite group element $g_i \in S_Q$ as a state (color) in a spin model, the partition function weight precisely matches that of a $Q!$ -state Potts model on a square lattice, whose links are between sites i and k , and between sites i and j in each unit cell.

In order to analytically continue $Q \rightarrow 1$, we rewrite the partition function of this Potts model in terms of the so-called Fortuin–Kasteleyn (FK) cluster expansion [102]. We expand the partition function as a product over links with weight $(1-p)\delta_{g_i^{-1}g_k} + p$, by assigning an ‘‘occupied’’ link to the term $(1-p)\delta_{g_i^{-1}g_k}$, while an empty link corresponds to picking the trivial term p in the product. The occupied links form clusters, where the permutation spins are forced to be the same due to the Kronecker delta functions. One can then perform the sum over permutations $\sum_{\{g_i \in S_Q\}}$ in the partition function (40) exactly, which allows us to rewrite it as a sum over FK clusters:

$$Z = \sum_{\text{clusters}} p^{\#\text{empty links}} (1-p)^{\#\text{occupied links}} (Q!)^{\#\text{clusters}}. \quad (42)$$

Using this exact rewriting of the partition function, we can now readily take the replica limit $Q \rightarrow 1$ since Q only appears in the Boltzmann weight of the clusters in that formulation. In the replica limit, all clusters carry a trivial weight, and the partition function (42) describes a classical bond percolation problem, where links are occupied with probability $1-p$ (no measurement) and are empty with probability p (corresponding intuitively to a local measurement cutting the circuit). This percolation picture of the transition is rather appealing and natural and predicts

critical exponents that are close to the ones measured even for finite d ($d = 2$ in most numerical simulations). For example, it predicts a diverging correlation length $\xi \sim |p - p_c|^{-4/3}$, with $p_c = 1/2$ in this percolation limit.

4.5.2 Entanglement and Minimal-Cut Picture

To compute the scaling of entanglement in this limit, it turns out to be more convenient to consider configurations with mixed measurement locations. Averaging over measurement outcomes and over Haar gates for a such given configuration of measurement locations, the statistical model mapping described above still goes through, with the link weight now being either $V_l(g_i^{-1}g_j) = d^{C(g_i^{-1}g_j)}$ if that link is not measured, or $V_l(g_i^{-1}g_j) = d$ if that link coincides with a measurement. Now in the limit $d \gg 1$, we have $V_l(g_i^{-1}g_j) \sim d^Q \delta_{g_i^{-1}g_j}$ as before so the statistical mechanics model for such fixed measurement locations is a fully ordered (zero temperature) ferromagnet on a lattice diluted by the measurements: each bond that is measured is effectively cut, while all other weights constrain the statistical model's spins to be the same in this limit. This is consistent with the percolation picture derived above.

As we show next, a frustrated link costs a large energy $\sim \log d$, leading to an effective minimal-cut picture in that limit [23]. To see this, recall that computing entanglement requires computing two different partition functions Z_A and Z_0 , which differs only by their boundary condition on the top boundary of the circuit. The boundary condition for the calculation of Z_A forces a different boundary condition in region A and thus introduces a domain wall (DW) near the top boundary. In the limit $d \rightarrow \infty$, the DW is forced to follow a minimal cut, defined as a path cutting a minimum number of unmeasured links (assumed to be unique for simplicity). Due to the uniform boundary condition in Z_0 , all vertex elements in Z_0 are equal, so Z_0 is trivial and given by a single configuration of spins. Z_A differs from Z_0 due to the fact the DW will lead to frustrated links that contribute different weights to Z_A . Each frustrated unmeasured link contributes a very large energy cost associated with this domain wall between $g = g_{\text{SWAP}}$ and $g = e$

$$\Delta E = (n - 1)m \log d, \quad (43)$$

using the energy weight on each link $E_l = -\log d C(g)$. Since this energy cost is very large as $d \gg 1$, the domain wall will follow a path through the circuit minimizing the number of unmeasured links it has to cut. This leads to the expression $Z_A = p^{(1-n)m\ell_{\text{DW}}} Z_0$, with ℓ_{DW} the number of unmeasured links that the DW crosses along the minimal cut [23, 63]. In the replica limit, this leads to a simple expression for the Renyi entropies

$$S_A^{(n)} = \ell_{\text{DW}} \log d, \quad (44)$$

where this equation is valid for any given configuration of measurement locations. We will use $\overline{\ell_{\text{DW}}}$ to denote the average of ℓ_{DW} over measurement locations, which are simply percolation configurations. This quantity has a simple scaling in percolation: it is extensive $\overline{\ell_{\text{DW}}} \sim L_A$ (volume law) for $p_0 < p_{0,c} = 1/2$, and constant $\overline{\ell_{\text{DW}}} \sim O(1)$ (area law) for $p_0 > p_{0,c} = 1/2$. At criticality, this implies a logarithmic scaling of the entanglement entropy [23, 103, 104]

$$\overline{S_A^{(n)}} \underset{d \gg 1}{\approx} \frac{\sqrt{3}}{\pi} \log d \log L_A. \quad (45)$$

Strictly speaking, this minimal-cut formula only applies for $d = \infty$, while for d large but finite, it is only valid up for distances smaller than a crossover length $L_A \ll \xi(d)$ that we briefly discuss in the next section.

4.6 Finite d Universality Class

The infinite onsite Hilbert space dimension limit discussed above has an accidentally enlarged symmetry. The Potts model has a symmetry group $S_Q!$ that is much larger than the $S_Q \times S_Q$ symmetry of the generic Boltzmann weights at finite d . (Note that $S_Q \times S_Q$ is a subgroup of $S_Q!$: the left and right actions of S_Q on itself have a permutation $g \in S_Q!$ representation—this is known as Cayley’s theorem.) The leading perturbation implementing this symmetry breaking in the Potts model was identified in Refs. [25, 40] and turns out to be relevant, with scaling dimension $\Delta = \frac{5}{4}$. For any large but finite onsite Hilbert space dimension d , we thus expect a crossover from percolation criticality for length scales $\ell \ll \xi(d) \sim d^{4/3}$ [23], to the finite d universality class (which does not depend on d) at long distances $\ell \gg \xi(d)$. The boundary and bulk conformal spectrum of this theory were recently studied numerically [36, 42, 62], and a Landau–Ginzburg action was proposed in Ref. [27]. In the case of Clifford circuits, the universality class of the transition depends in a more subtle way on the onsite Hilbert space dimension [29, 98].

5 Symmetry and Topology in Measurement-Induced Phases and Criticality

Looking beyond featureless Haar-random two-qubit gates and single-site measurements, there is a huge variety of possible variations on a theme, including considering circuits and measurements that obey symmetry constraints, including multi-site measurements that “collapse” into interesting, entangled states rather than featureless product states, and many others. Here, we briefly describe a small selection of these enrichments to give a flavor of the possibilities.

5.1 Symmetric Monitored Random Circuits

A simple extension of the MRC models described above is to include symmetry constraints in the random gates and measurement operations, i.e., demand that these preserve a symmetry group G . The appropriate symmetry depends on the microscopic realization of the qubits in question. For example, trapped-ion and Rydberg atom systems natural have interactions that respect a discrete Ising symmetries ($G = \mathbb{Z}_2$), superconducting qubit and cavity-QED systems typically have $U(1)$ -conserving interactions, and quantum dot spin-qubits often interact by $SU(2)$ -invariant spin-exchange (absent spin-orbit coupling). Of these, so only simpler Abelian symmetries such as $G = \mathbb{Z}_2$ [43, 45, 46, 59, 64] and $G = U(1)$ [63, 70] have been studied theoretically.

The inclusion of symmetry naturally begs two questions: (i) are the universal properties of the entanglement transition modified by the symmetry? and (ii) are there additional measurement-induced phases or critical phenomena that arise with symmetry [analogous to how symmetry distinguishes spontaneous-symmetry-broken and symmetry-protected topological (SPT) or symmetry-enriched topological (SET) phases in equilibrium]? So far, the answer to the question (i) appears to be negative [63]; at least in the limit of large onsite dimension d and small-scale numerics for $d = 2$, it appears that the entanglement transition occurs in a regime where the charge degrees of freedom are frozen by measurements and do not affect the entanglement transition bulk criticality. However, the answer to question (ii) is affirmative, and numerous examples of transitions in both the area-law and volume-law phases have been constructed in a wide range of universality classes.

To set the stage, let us consider the general symmetry structure of the statistical mechanics replica models. As detailed in [59] (see also [27]), in replicated statistical mechanics models, a symmetry group G of the circuit dynamics is incorporated into the Q -fold replicated theory as a separate G symmetry separately for each replica and, within each replica, separately for both each forward (U) and backward (U^*) “contours” of the time evolution. These symmetry factors are, respectively, permuted by the left (forward time contour) and right (backward time contour) replica-permutation symmetry of the permutation “spins” in the stat-mech description. Finally, hermiticity of the density matrix implies that exchanging the forward and backward contours and complex conjugating the coefficients are a symmetry. Since doing this Hermitian conjugation twice is trivial, this gives an extra \mathbb{Z}_2 factor to the symmetry group, but which acts non-trivially on the other replicated symmetry groups [27]. Combined, this gives the overall symmetry group:

$$\mathcal{G} = \left[\left(G_L^{\times Q} \rtimes S_{Q,L} \right) \times \left(G_R^{\times Q} \rtimes S_{Q,R} \right) \right] \rtimes \mathbb{Z}_2^{\text{H}}, \quad (46)$$

where \rtimes indicates that the replica permutation action of the symmetric group S_Q also permutes the associated G symmetries for each replica, and hence, these two factors do not generally commute, the left (L) and right (R) subscripts refer to the

forward and backward contours, respectively, and the \mathbb{H} superscript on the final \mathbb{Z}_2 factor reminds that this is associated with hermiticity. It is not yet clear whether or how the $\mathbb{Z}_2^{\mathbb{H}}$ factor plays a role in determining the structure of MIPTs, so we ignore it in the following, but simply mention it for completeness.

5.2 Area-Law Phases

As described above, the area-to-volume-law entangled transition is a transition between phases in which the replica permutation symmetry, respectively, remains intact or becomes spontaneously broken (Fig. 6).

Since the short-range entanglement structure of the area-law phase is identical to that found in ground states of local Hamiltonians, it is natural to guess that the area-law MRC phases with symmetry G coincide with equilibrium phases (i.e., paramagnetic, spontaneous-symmetry-broken, SPT, or SET) with the same symmetry.

Indeed, for discrete symmetries, it is straightforward to design models that achieve a large class of symmetry-breaking and topological orders in the measurement-dominated regime. To be specific, consider Ising-symmetric random Clifford circuits ($G = \mathbb{Z}_2$), with (space-time-random) measurements drawn from local generators of a stabilizer group \mathcal{S} (i.e., a group of mutually commuting Pauli strings). In the extreme limit of measurement-only dynamics, these stabilizer measurements project into a state specified by eigenvalues of $s = \pm 1$ for each $s \in \mathcal{S}$. Such stabilizer states can support a large class of interesting many-body orders

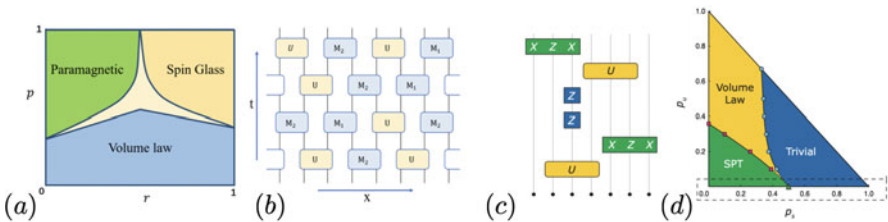


Fig. 6 Measurement-induced stabilizer orders. Phase diagram (a) and circuit model (b) of Ising-symmetric MRCs exhibiting area-law phases with- and without-order reproduced from Ref. [46]. The model in (a) consists of measurements with probability p or random two-qubit Clifford gates with probability $1-p$. Measurements are randomly chosen as $Z \otimes Z$ measurements with probability r or single-qubit $X \otimes \mathbb{1}$ or $\mathbb{1} \otimes Z$ measurements with probability $1-r$. The phase diagram in (b) includes a critical fan (center region) that would shrink to a phase boundary line for an infinite system. (c)-(d) are reproduced from Ref. [45] and show a model (c) that includes measurements of either $X \otimes Z \otimes X$ stabilizers for a cluster state (a $1d$ SPT protected by a pair of \mathbb{Z}_2 symmetries generated by $\prod_i Z_{2i}$ and $\prod_i Z_{2i+1}$, respectively), single-site Z operators, and random Clifford gates with probabilities p_t, p_s, p_u , respectively. In the measurement-dominated regime (dashed box), p_s tunes between area-law phases with trivial or SPT order. These give way to volume-law entangled phases at sufficiently large p_u

including discrete symmetry-breaking and symmetry-protected topological (SPT) orders, and non-chiral-topological or fracton orders (i.e., toric code like orders but not fractional quantum Hall effect with chiral edge modes).

5.2.1 Measurement-Induced Symmetry-Breaking Order in $1 + 1d$

For example, in a qubit chain with symmetry generated by $X = \prod_i X_i$, measuring $s \in \{Z_i Z_{i+1}\}$ on every bond projects into random spin-glass state(s) with frozen but random spin texture $s_{i,i+1} = Z_i Z_{i+1} = \pm 1 \forall i$. Here, a fixed set of measurement outcomes s_i actually correspond to two possible states. For example, for a 3-site chain states with $\{s_{12}, s_{23}\} = \{+1, -1\}$ form a two-dimensional subspace with basis states $\{| \uparrow \uparrow \downarrow \rangle, | \downarrow \downarrow \uparrow \rangle\}$ that each spontaneously break the \mathbb{Z}_2 symmetry (or equivalently, we can form cat-like superpositions of $| \uparrow \uparrow \downarrow \rangle \pm | \downarrow \downarrow \uparrow \rangle$ that have definite overall $X = \pm 1$, but have long-range mutual information between all spins). Thus, we see that the states stabilized by this measurement-only dynamics have the same form as the spontaneous-symmetry-breaking ground space of an ideal Ising magnet with couplings that are ferromagnetic or antiferromagnetic depending on $s_{i,i+1} = \pm 1$.

We note that different trajectories have different random frozen configurations, so that the trajectory average of long-range symmetry-breaking correlations such as $\lim_{|i-j| \rightarrow \infty} \mathbb{E}_{m,U} \langle Z_i Z_j \rangle = 0$ strictly vanishes (this could be anticipated on general grounds since such linear averages always behave like infinite-temperature averages), but where higher moments of symmetry-breaking correlations such as the Edwards–Anderson (EA)-type order parameter $\chi^{(2)} = \lim_{|i-j| \rightarrow \infty} \mathbb{E}_{m,U} |\langle Z_i Z_j \rangle|^2$ are non-vanishing.

So far, we have considered an idealized limit with only measurements. Numerical simulations [45, 46, 59] that perturb away from this fine-tuned point by including random unitary dynamics (e.g., by random Clifford circuits, which can be efficiently simulated) or by competing stabilizer measurements (e.g., of non-commuting observables such as $\{X_i\}$ that stabilize trivial symmetric product states) show clear evidence that these area-law orders survive over a finite range of couplings in thermodynamically large systems and extend to generic area-law phase with symmetry-breaking order in trajectories with area-law entanglement. We note that, generically, the spin-glass pattern found in the ordered trajectories is not frozen in time but undergoes (classical) stochastic fluctuations induced by competing measurements or unitary gates between each time step.

5.2.2 Measurement-Induced Topological Orders

The above recipe can be straightforwardly extended to produce models of area-law phases with more complicated measurement-induced orders including: SPT orders [45], intrinsic topological or SET order, and fracton orders—essentially any phase describable by stabilizer states. As for the measurement-induced spontaneous-

symmetry-breaking phase discussed above, these phases are characterized by glassy order in each trajectory, which can be diagnosed by various non-local analogs of the EA order parameter described above. Due to its relation to error correction, we briefly elaborate on a particular example: measurement-induced \mathbb{Z}_2 (a.k.a. “toric” or “surface” codes) topological order [105] in $2 + 1d$ MRCs.

Following [105], consider a standard model of the surface code consisting of a qubit array on a chess board (square lattice with two-site unit cell consisting of alternating “black” and “white” squares), whose dynamics are dominated by measurements of stabilizers consisting of product of X or Z operators, respectively, over the corners of the white and black squares or “plaquettes” (P), $s_P \in \{\prod_{i \in P_{\text{white}}} X_i, \prod_{i \in P_{\text{black}}} Z_i\}$. In the measurement-dominated regime, measurements then collapse the state into one adiabatically connected to a stabilizer state $s_P \in \{\pm 1\}$. If this model is defined on closed manifold, then specifying s_P for all plaquettes, P uniquely specifies a state. However, if the model is defined on a topologically non-trivial manifold, M , with genus g , e.g., a torus ($g = 2$), then the stabilizers only fix a ground space of dimension 4^g , which can be seen by noting that for each non-trivial cycle $c \in \pi_1(M)$, around a handle of M , one can define a pair of additional stabilizers, $X_c, Z_c = \prod_{i \in M} X_i, Z_i$, which are independent from, but commute with the measured stabilizers s . X_c and $Z_{c'}$ operator loops that intersect but wrap different cycles anticommute and hence cannot have simultaneous eigenstates. This topological ground space has been proposed as a promising quantum memory for fault-tolerant computation, since its states cannot be distinguished by local noise, but rather, only by measuring non-local string operators $(X, Z)_c$.

This gives rise to the topological degeneracy in the measurement-stabilized trajectories. In Ref. [105], it was shown that by tuning the fraction of surface-code stabilizer measurements with competing random circuit evolution or trivial product-state stabilizer measurements, one can obtain phase transitions between trajectories with and without \mathbb{Z}_2 topological order. Unlike for the symmetry-breaking example above, this distinction cannot be probed by any local measurement. Instead, one can diagnose topological order either by two alternative routes. Each trajectory would exhibit a quantized entanglement entropy $\gamma = \log 2$ [105–107] defined via the subleading constant part of the entanglement of a region A : $S_A = a|\partial A| - \gamma$, where a is a non-universal constant, and $|\partial A|$ is the length of the perimeter of region A .

Alternatively, one could consider the dynamics of a maximally mixed state: here, in the area-law phase, the measurements tend to purify the state. However, in the topologically ordered phase, measurements only purify the local degrees of freedom and leave an equal-weighted mixture over the 4^g states of the topological ground space resulting in entanglement $S \sim 2g \log 2$ in the steady state.

The model of Ref. [105] also exhibits an unconventional critical point with non-relativistic dynamics (dynamical exponent $z \neq 1$), and logarithmic violations of area-law scaling in $2d$, possibly related to emergent subsystem symmetries. This highlights the potential for novel types of critical phenomena arising in MRC dynamics, which do not naturally arise in more familiar equilibrium settings.

5.3 Volume-Law Phases

The prospect of measurement-induced orders in the area-law phase could be anticipated based on our knowledge of ground-state phases of equilibrium matter, which also exhibit area-law entanglement. Perhaps more surprising is the prospect of additional phases arising within the volume-law entangled regime, where the entanglement structure of trajectories is similar to that of finite-temperature equilibrium states, which do not support any quantum orders and rule out even classical orders in low dimensions.

5.3.1 Volume-Law Phases with Order—Stat-Mech Perspective

In the statistical mechanics language, the volume-law regime corresponds to spontaneously broken $S_{Q,L} \times S_{Q,R}$ replica permutation symmetry. However, the residual $G_{L,R}^{\times Q}$ symmetries remain and could conceivably be spontaneously broken, or protect or enrich topology. These various possibilities are discussed in detail in Ref. [59], which provided a particularly simple argument (supported by numerics) for volume-law phases with order: Consider stacking (and weakly coupling) two subsystems that, before coupling, respectively, form an ordered area-law phase, and a featureless volume-law phase of degrees of freedom with trivial symmetry properties. Since each of these systems corresponds to gapped phases in the stat-mech variables, weak coupling between the two will not destroy the symmetry-breaking or topological properties of the first subsystem, nor the volume-law entangled (replica-permutation-breaking order) of the second subsystem, and will therefore result in an ordered and volume-law entangled phase. While “obvious” in the stat-mech language, this predicts a highly non-trivial result in terms of the original degrees of freedom in the MRC. Namely, that it is possible to have stable phases with quantum-coherent orders in the highly entangled and scrambled trajectories of a quantum circuit! The coexistence of volume-law entanglement and symmetry-breaking spin-glass order (below the classical lower critical dimension) was also observed numerically in symmetric Clifford circuits in Refs. [46, 64].

5.3.2 Charge Sharpening Transitions in the Volume-Law Phase

Beyond the possibility of stabilizing ground-state orders in volume-law entangled trajectories, it turns out that there are additional phases and associated critical phenomena within the volume-law regime of symmetric MRCs that cannot be understood by any ground-state order parameter, but rather are distinguished by sharply distinct dynamics of symmetry quantum numbers (which we henceforth refer to as “charges”).

For concreteness, let us consider augmenting the $U(1)$ -symmetric RC model described above in Sect. 2.3, by adding random measurements of each site with

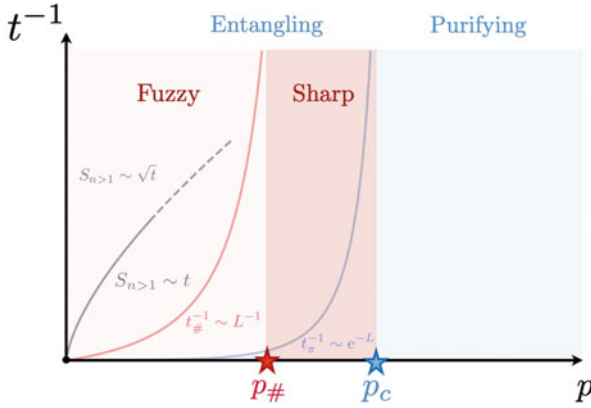


Fig. 7 Schematic phase diagram of $1 + 1d$ $U(1)$ Symmetry MRCs for the $U(1)$ symmetric MRC model described in the text (reproduced from Ref. [63]), includes both a volume-law entanglement (red) to area-law entanglement (blue) transition at critical measurement rate $p = p_c$, and a charge sharpening transition within the volume-law phase at $p = p_{\#}$. The diffusive growth of Renyi entropies, S_n , associated with diffusive dynamics and rare dead-region physics, for random unitary circuit evolution $p = 0$, immediately converts into ballistic growth for any non-zero measurement rate $p > 0$. $t_{\#}$ denotes the time scale for measurements to sharpen an initial state that is a superposition of different charge sectors into one with definite charge. The purification time for an initially mixed state to collapse into a pure state due to measurements is denoted by t_{π} . L denotes system size

probability p in the charge basis of the qubit and in any basis of the neutral large- d qudit [63]. This model can be analyzed by generalizing the statistical mechanics model to incorporate symmetry, which results in hardcore charge degrees of freedom that undergo a random walk on the replicated circuit network, and which are coupled to the replica-permutation spins by the measurements [63]. In the large- d limit, it is possible to take the replica limit exactly and analyze the charge dynamics as a classical stochastic evolution. In the large- d limit, standard Haar averaging formulas immediately imply that off-diagonal coherences between density matrix elements of different charges are strictly vanishing, i.e., this model does not support any spontaneous breaking of $U(1)$ symmetry. Nevertheless, two distinct phases are observed [63] within the volume-law entangled regime, separated by an apparently continuous phase transition at critical measurement probability $p_{\#} < p_c$, which precedes the entanglement transition at p_c ($p_c = 1/2$ in the large- d limit).

For $p < p_{\#}$, the measurements fail to collapse an initial superposition of different total charges into a given charge sector (Fig. 7), i.e., the global symmetry quantum number (“charge”) remains “fuzzy” up to a time scale $t \gtrsim L$ that diverges with system size L . By contrast, for $p > p_{\#}$, measurements collapse the system into a state with sharp total charge in finite time independent of system size (for $t \gg L$ measurements always sharpen the total charge). In $1 + 1d$ models, these charge “sharp” and charge “fuzzy” phases are distinguished by the behavior of charge

fluctuations [63, 108]:

$$C(r) = \mathbb{E}_{m,U} [\langle \sigma^z(r) \sigma^z(0) \rangle - \langle \sigma^z(r) \rangle \langle \sigma^z(0) \rangle] \sim \begin{cases} 1/r^2 & p \leq p_{\#} \\ e^{-r/\xi} & p > p_{\#} \end{cases}, \quad (47)$$

where the power-law decay for $p < p_{\#}$ is expected to become truly long-ranged $\lim_{r \rightarrow \infty} C(r) \sim \text{const.}$ in higher dimensions, or with discrete Abelian symmetries [108]. In addition, this work reveals that even a small amount of measurements singularly change the dynamics of entanglement growth and charge fluctuations from the diffusive (dynamical exponent $z = 2$) motion for $p = 0$, to ballistic ($z = 1$) for $0 < p \leq p_{\#}$, and eventually to exponentially fast relaxation ($z \rightarrow \infty$, massive dynamics) for $p > p_{\#}$.

We emphasize that unlike the measurement-induced symmetry-breaking and topological orders described above, which are smoothly connected to equilibrium ground-state orders,² this charge sharpening transition (like the entanglement transition) is a purely dynamical effect that is special to non-equilibrium MRC dynamics. While these examples give an idea of the possibilities for new types of non-equilibrium measurement-induced orders, at present, a rigorous/exhaustive classification of measurement-induced orders remains an open challenge.

6 Discussion

The examples reviewed above highlight the promise for using well-developed statistical mechanics tools to investigate universal aspects of emerging quantum dynamics and quantum information theory concepts and to uncover new regimes of measurement-induced non-equilibrium orders.

Despite rapid progress, several open challenges remain. The statistical mechanics model mapping of MRC dynamics onto a classical spin model establishes the existence of these transitions through convergence of strong- and weak- coupling expansions, establishes an equivalence between the entanglement- and purification-transition perspectives, and strongly suggests that the $1 + 1d$ entanglement transition is described by a (non-unitary) conformal field theory (CFT). However, a detailed analytic understanding of the precise universality class and CFT content remains unsolved (though these questions are being explored numerically [36, 42, 62]). To gain analytic insight into this question, and particularly to study measurement-induced criticality and orders in $2d$ and $3d$ circuits and incorporate more complex

² For example, by continuously turning off the coupling between the stabilizer-state qubits and volume-law entangled trivial degrees of freedom in the above construction, and then dialing the stabilizer measurement probability to unity, which, in the replicated statistical mechanics description corresponds to disentangling two gapped degrees of freedom and then smoothly changing couplings within a gapped phase, respectively, and does not produce a phase transition.

features such as multiple types of non-commuting measurements, it may be desirable to develop continuum quantum field theory methods for treating quantum circuits (see [70] for preliminary efforts along these lines for free-fermion circuits). The study of different classes of circuits, including e.g., Gaussian free-fermion circuits and tensor networks [37, 56, 65, 70, 109, 110], or self-dual unitary circuits [17, 18], might also help addressing some of those questions, as well as revealing new measurement-stabilized phases. Looking beyond these more detailed aspects, a natural question is whether there are other paradigms for obtaining universal phenomena in quantum circuit dynamics, for example, which do not require post-selection on measurement outcomes to observe and could be explored experimentally as well as theoretically.

Early studies have also suggested intriguing possibility of gaining universal insights into fundamental limits of quantum communication. However, there is significant room to put these suggested connections on more rigorous footing and to explore other connections between statistical mechanics of random circuits to random quantum error-correcting codes, or possibly even to fundamental quantum complexity theory. One could even imagine that studies of noise and error propagation in random circuits might yield practical design principles for optimizing aspects (e.g., dimensionality, connectivity, etc...) of qubit architectures in order to maximize their ability to generate complicated entangled states or minimize the impact of noise on quantum algorithms.

Acknowledgments We thank our collaborators Utkarsh Agrawal, Fergus Barratt, Matthew Fisher, Aaron Friedman, Sarang Gopalakrishnan, Michael Gullans, David Huse, Chao-Ming Jian, Yaodong Li, Andreas Ludwig, Adam Nahum, Javier Lopez-Piqueres, Jed Pixley, Hans Singh, Yi-Zhuang You, Brayden Ware, Justin Wilson, and Aidan Zabalo for many insightful discussions. We also thank Ehud Altman, Maissam Barkeshli, Xiao Chen, Michael Gullans, Tim Hsieh, Yaodong Li, Adam Nahum, and Jed Pixley for helpful comments on this manuscript. This research was supported in part from the US Department of Energy, Office of Science, Basic Energy Sciences, under Early Career Award No. DE-SC0019168 (RV), from the US National Science Foundation DMR-1653007 (ACP), and the Alfred P. Sloan Foundation through Sloan Research Fellowships (RV and ACP). This research was undertaken thanks, in part, to funding from the Max Planck-UBC-UTokyo Center for Quantum Materials and the Canada First Research Excellence Fund, Quantum Materials and Future Technologies Program (ACP).

References

1. P. Hayden, J. Preskill, *JHEP*, **2007**, 120 (2007)
2. Y. Sekino, L. Susskind, *JHEP*, **2008**, 065 (2008)
3. W. Brown, O. Fawzi, *Commun. Math. Phys.* **340**, 867 (2015)
4. P. Hosur, X.-L. Qi, D.A. Roberts, B. Yoshida, *JHEP*, **2016**, 4 (2016)
5. R. Oliveira, O.C.O. Dahlsten, M.B. Plenio, *Phys. Rev. Lett.* **98**, 130502 (2007)
6. F.G.S.L. Brandão, A.W. Harrow, M. Horodecki, *Commun. Math. Phys.* **346**, 397 (2016)
7. A. Nahum, J. Ruhman, S. Vijay, J. Haah, *Phys. Rev. X* **7**, 031016 (2017)
8. A. Nahum, S. Vijay, J. Haah, *Phys. Rev. X* **8** (2018)
9. M. Kardar, G. Parisi, Y.-C. Zhang, *Phys. Rev. Lett.* **56**, 889 (1986)

10. S. Ryu, T. Takayanagi, *Phys. Rev. Lett.* **96**, 181602 (2006)
11. S. Ryu, T. Takayanagi, **2006**, 045 (2006)
12. C.W. Von Keyserlingk, T. Rakovszky, F. Pollmann, S.L. Sondhi, *Phys. Rev. X* **8** (2018)
13. A. Chan, A. De Luca, J.T. Chalker, *Phys. Rev. X* **8**, 041019 (2018)
14. B. Bertini, P. Kos, T. Prosen, *Phys. Rev. Lett.* **121**, 264101 (2018)
15. A. Chan, A. De Luca, J.T. Chalker, *Phys. Rev. Lett.* **121**, 060601 (2018)
16. A.J. Friedman, A. Chan, A. De Luca, J.T. Chalker, *Phys. Rev. Lett.* **123**, 210603 (2019)
17. S. Gopalakrishnan, A. Lamacraft, *Phys. Rev. B* **100**, 064309 (2019)
18. B. Bertini, P. Kos, T. Prosen, *Phys. Rev. Lett.* **123**, 210601 (2019)
19. V. Khemani, A. Vishwanath, D.A. Huse, *Phys. Rev. X* **8**, 031057 (2018)
20. T. Rakovszky, F. Pollmann, C.W. von Keyserlingk, *Phys. Rev. X* **8**, 031058 (2018)
21. J. Preskill, *Quantum* **2**, 79 (2018)
22. Y. Li, X. Chen, M.P.A. Fisher, *Phys. Rev. B* **98**, 205136 (2018)
23. B. Skinner, J. Ruhman, A. Nahum, *Phys. Rev. X* **9** (2019)
24. P. Hayden, S. Nezami, X.-L. Qi, N. Thomas, M. Walter, Z. Yang, *J. High Energy Phys.* **2016**, 9 (2016)
25. R. Vasseur, A.C. Potter, Y.-Z. You, A.W.W. Ludwig, *Phys. Rev. B* **100**, 134203 (2019)
26. J. Lopez-Piqueres, B. Ware, R. Vasseur, *Phys. Rev. B* **102**, 064202 (2020)
27. A. Nahum, S. Roy, B. Skinner, J. Ruhman, *PRX Quantum* **2**, 010352 (2021)
28. R. Levy, B.K. Clark, arXiv:2108.02225 [cond-mat.stat-mech] (2021)
29. Z.-C. Yang, Y. Li, M.P.A. Fisher, X. Chen, arXiv:2107.12376 [cond-mat.stat-mech] (2021)
30. M.J. Gullans, D.A. Huse, *Phys. Rev. X* **10**, 041020 (2020)
31. S. Choi, Y. Bao, X.L. Qi, E. Altman, *Phys. Rev. Lett.* **125**, 030505 (2020)
32. Y. Li, M.P.A. Fisher (2020). arXiv:2007.03822
33. R. Fan, S. Vijay, A. Vishwanath, Y.-Z. You, arXiv:2002.12385 [cond-mat, physics:quant-ph] (2020).
34. Y. Li, X. Chen, M.P. Fisher, *Phys. Rev. B* **100**, 134306 (2019)
35. A. Chan, R.M. Nandkishore, M. Pretko, G. Smith, *Phys. Rev. B* **99**, 224307 (2019)
36. Y. Li, X. Chen, A.W.W. Ludwig, M.P.A. Fisher, arXiv:2003.12721 [cond-mat, physics:quant-ph] (2020)
37. X. Cao, A. Tilloy, A.D. Luca, *SciPost Phys.* **7**, 24 (2019)
38. M. Szyniszewski, A. Romito, H. Schomerus, *Phys. Rev. B* **100**, 064204 (2019)
39. Y. Bao, S. Choi, E. Altman, *Phys. Rev. B* **101** (2020)
40. C.M. Jian, Y.Z. You, R. Vasseur, A.W. Ludwig, *Phys. Rev. B* **101** (2020)
41. M.J. Gullans, D.A. Huse, *Phys. Rev. Lett.* **125** (2020)
42. A. Zabalo, M.J. Gullans, J.H. Wilson, S. Gopalakrishnan, D.A. Huse, J.H. Pixley, *Phys. Rev. B* **101** (2020)
43. A. Nahum, B. Skinner, *Phys. Rev. Research* **2**, 023288 (2020)
44. M. Ippoliti, M.J. Gullans, S. Gopalakrishnan, D.A. Huse, V. Khemani, *Quantum Physics* (2020). arXiv:2004.09560
45. A. Lavasani, Y. Alavirad, M. Barkeshli, *Nat. Phys.* **17**, 342–347 (2021)
46. S. Sang, T.H. Hsieh, *Phys. Rev. Research* **3**, 023200 (2021)
47. Q. Tang, W. Zhu, *Phys. Rev. Research* **2**, 013022 (2020)
48. X. Turkeshi, R. Fazio, M. Dalmonte, *Phys. Rev. B* **102** (2020)
49. Y. Fuji, Y. Ashida, arXiv:2004.11957 [cond-mat, physics:quant-ph] (2020)
50. O. Lunt, M. Szyniszewski, A. Pal, *Phys. Rev. B* **104**, 155111 (2021)
51. O. Lunt, A. Pal, *Phys. Rev. Research* **2**, 043072 (2020)
52. S. Vijay, arXiv:2005.03052 [quant-ph] (2020)
53. X. Turkeshi, A. Biella, R. Fazio, M. Dalmonte, M. Schiró, *Phys. Rev. B* **103**, 224210 (2021)
54. M. Ippoliti, V. Khemani, *Phys. Rev. Lett.* **126**, 060501 (2021)
55. T.-C. Lu, T. Grover, arXiv:2103.06356 [quant-ph] (2021)
56. C.-M. Jian, B. Bauer, A. Keselman, A.W.W. Ludwig, arXiv:2012.04666 [cond-mat.stat-mech] (2020)
57. S. Gopalakrishnan, M.J. Gullans, *Phys. Rev. Lett.* **126**, 170503 (2021)

58. X. Turkeshi, arXiv:2101.06245 [cond-mat.stat-mech] (2021)
59. Y. Bao, S. Choi, E. Altman, arXiv:2102.09164 [condmat.stat-mech] (2021)
60. M. Block, Y. Bao, S. Choi, E. Altman, N. Yao, arXiv:2104.13372 [quant-ph] (2021)
61. G. Bentsen, S. Sahu, B. Swingle, arXiv:2104.07688 [quant-ph] (2021)
62. A. Zabalo, M.J. Gullans, J.H. Wilson, R. Vasseur, A.W.W. Ludwig, S. Gopalakrishnan, D.A. Huse, J.H. Pixley, arXiv:2107.03393 [cond-mat.dis-nn] (2021)
63. U. Agrawal, A. Zabalo, K. Chen, J.H. Wilson, A.C. Potter, J.H. Pixley, S. Gopalakrishnan, R. Vasseur, arXiv:2107.10279 [cond-mat.dis-nn] (2021)
64. Y. Li, M.P.A. Fisher, arXiv:2108.04274 [quant-ph] (2021)
65. O. Alberton, M. Buchhold, S. Diehl, Phys. Rev. Lett. **126**, 170602 (2021)
66. S.-K. Jian, C. Liu, X. Chen, B. Swingle, P. Zhang, arXiv:2106.09635 [quant-ph] (2021)
67. E.V.H. Doggen, Y. Gefen, I.V. Gornyi, A.D. Mirlin, D.G. Polyakov, arXiv:2104.10451 [quant-ph] (2021)
68. P. Sierant, X. Turkeshi, arXiv:2109.06882 [cond-mat.statmech] (2021)
69. O. Lunt, M. Szyniszewski, A. Pal, arXiv arXiv:2012.03857 [quant-ph] (2020)
70. M. Buchhold, Y. Minoguchi, A. Altland, S. Diehl, arXiv:2102.08381 [cond-mat.stat-mech] (2021)
71. P. Sierant, G. Chiriaco, F.M. Surace, S. Sharma, X. Turkeshi, M. Dalmonte, R. Fazio, G. Pagano, Dissipative Floquet dynamics: from steady state to measurement induced criticality in trapped-ion chains (2021). arXiv:2107.05669 [quant-ph]
72. S. Sharma, X. Turkeshi, R. Fazio, M. Dalmonte, arXiv:2110.14403 [quant-ph] (2021)
73. T. Zhou, A. Nahum, Physical Review B **99** (2019)
74. M.J. Gullans, S. Krastanov, D.A. Huse, L. Jiang, S.T. Flammia, Phys. Rev. X **11**, 031066 (2021)
75. N. Hunter-Jones, arXiv:1905.12053 [quant-ph] (2019)
76. J. Napp, R.L. La Placa, A.M. Dalzell, F.G.S.L. Brandao, A.W. Harrow, (2019). arXiv:2001.00021 [quant-ph]
77. C. Noel, P. Niroula, D. Zhu, A. Risinger, L. Egan, D. Biswas, M. Cetina, A.V. Gorshkov, M.J. Gullans, D.A. Huse, C. Monroe, arXiv:2106.05881 [quant-ph] (2021)
78. C. Jonay, D.A. Huse, A. Nahum, arXiv:1803.00089 [cond-mat.stat-mech] (2018)
79. T. Zhou, A. Nahum, Phys. Rev. X **10**, 031066 (2020)
80. S. Gopalakrishnan, D.A. Huse, V. Khemani, R. Vasseur, Phys. Rev. B **98**, 220303 (2018)
81. D. Forster, D.R. Nelson, M.J. Stephen, Phys. Rev. A **16**, 732 (1977)
82. T. Rakovszky, F. Pollmann, C.W. Von Keyserlingk, Phys. Rev. Lett. **122**, 250602 (2019)
83. Y. Huang, arXiv:1902.00977 [cond-mat, physics.hep-th, physics.quant-ph] (2019)
84. T. Zhou, A.W.W. Ludwig, Phys. Rev. Research **2**, 033020 (2020)
85. T. Rakovszky, F. Pollmann, C.W. von Keyserlingk (2020). arXiv:2010.07969 [cond-mat.str-el]
86. M. Žnidarič, Commun. Phys. **3**, 100 (2020)
87. D. Aharonov, Phys. Rev. A **62**, 062311 (2000)
88. Y. Li, S. Vijay, M.P.A. Fisher, arXiv:2105.13352 [cond-mat.stat-mech] (2021)
89. S. Parameswaran, A.C. Potter, R. Vasseur, Annalen der Physik **529**, 1600302 (2017)
90. R. Nandkishore, D.A. Huse, Annu. Rev. Condens. Matter Phys. **6**, 15 (2015)
91. D.A. Abanin, E. Altman, I. Bloch, M. Serbyn, Rev. Mod. Phys. **91**, 021001 (2019)
92. A. Chandran, C. Laumann, Phys. Rev. B **92**, 024301 (2015)
93. M. Foss-Feig, D. Hayes, J.M. Dreiling, C. Figgatt, J.P. Gaebler, S.A. Moses, J.M. Pino, A.C. Potter, Phys. Rev. Research **3**, 033002 (2021)
94. E. Chertkov, J. Bohnet, D. Francois, J. Gaebler, D. Gresh, A. Hankin, K. Lee, R. Tobey, D. Hayes, B. Neyenhuis, R. Stutz, A.C. Potter, M. Foss-Feig, arXiv:2105.09324 [quant-ph] (2021)
95. B. Yoshida, arXiv:2109.08691 [quant-ph] (2021)
96. G. Smith, in *2010 IEEE Information Theory Workshop* (IEEE, New York, 2010) pp. 1–5
97. D.A. Roberts, B. Yoshida, JHEP, **2017**, 1 (2017)

98. Y. Li, R. Vasseur, M.P.A. Fisher, A.W.W. Ludwig, arXiv:2110.02988 [cond-mat.stat-mech] (2021)
99. R. Orús, *Ann. Phys.* **349**, 117 (2014)
100. J.L. Cardy, *Nucl. Phys. B* **240**, 514 (1984)
101. J. Cardy, *Encyclopedia of Mathematical Physics* (2006)
102. C. Fortuin, P. Kasteleyn, *Physica* **57**, 536 (1972)
103. J.T. Chayes, L. Chayes, R. Durrett, *J. Stat. Phys.* **45**, 933 (1986)
104. J. Jiang, C.-L. Yao, arXiv:1612.01803 [math.PR] (2016)
105. A. Lavasani, Y. Alavirad, M. Barkeshli, arXiv:2011.06595 [cond-mat.stat-mech] (2020)
106. A. Kitaev, J. Preskill, *Phys. Rev. Lett.* **96**, 110404 (2006)
107. M. Levin, X.-G. Wen, *Phys. Rev. Lett.* **96**, 110405 (2006)
108. F. Barratt, U. Agrawal, S. Gopalakrishnan, D.A. Huse, R. Vasseur, A.C. Potter, arXiv:2111.09336 [quant-ph] (2021)
109. X. Chen, Y. Li, M.P.A. Fisher, A. Lucas, *Phys. Rev. Research* **2**, 033017 (2020)
110. X. Turkeshi, M. Dalmonte, R. Fazio, M. Schirò, arXiv:2111.03500 [cond-mat.stat-mech] (2021)

Quantum Simulation Using Noisy Unitary Circuits and Measurements



Oliver Lunt, Jonas Richter, and Arijeet Pal

Abstract Many-body quantum systems are notoriously hard to study theoretically due to the exponential growth of their Hilbert space. It is also challenging to probe the quantum correlations in many-body states in experiments due to their sensitivity to external noise. Using synthetic quantum matter to simulate quantum systems has opened new ways of probing quantum many-body systems with unprecedented control, and of engineering phases of matter which are otherwise hard to find in nature. Noisy quantum circuits have become an important cornerstone of our understanding of quantum many-body dynamics. In particular, random circuits act as minimally structured toy models for chaotic nonintegrable quantum systems, faithfully reproducing some of their universal properties. Crucially, in contrast to the full microscopic model, random circuits can be analytically tractable under a reasonable set of assumptions, thereby providing invaluable insights into questions which might be out of reach even for state-of-the-art numerical techniques. Here, we give an overview of two classes of dynamics studied using random-circuit models, with a particular focus on the dynamics of quantum entanglement. We will especially pay attention to potential near-term applications of random-circuit models on noisy-intermediate scale quantum (NISQ) devices. In this context, we cover hybrid circuits consisting of unitary gates interspersed with nonunitary projective measurements, hosting an entanglement phase transition from a volume-law to an area-law phase of the steady state entanglement. Moreover, we consider random-circuit sampling experiments and discuss the usefulness of random quantum states for simulating quantum many-body dynamics on NISQ devices by leveraging the concept of quantum typicality. We highlight how emergent hydrodynamics can be studied by utilizing random quantum states generated by chaotic circuits.

O. Lunt

School of Physics and Astronomy, University of Birmingham, Birmingham, UK
e-mail: o.lunt@bham.ac.uk

J. Richter · A. Pal (✉)

Department of Physics and Astronomy, University College London, London, UK
e-mail: j.richter@ucl.ac.uk; a.pal@ucl.ac.uk

1 Introduction

Recent developments in quantum many-body physics have highlighted the importance of entanglement in understanding phases of matter in and out of equilibrium [1–3]. Even limited control of entanglement in quantum circuits has provided an opportunity for the fusion of ideas from quantum information science and condensed matter physics, and an exciting platform for testing our knowledge of quantum many-body physics [4, 5]. This has been particularly constructive for understanding phenomena far away from the ground state of quantum many-body systems such as quantum chaos [6–10] and many-body localization [11–16]. The quantum simulation of complex quantum phenomena exploring the exponentially large Hilbert space have been enriched by using entanglement as a probe. Entanglement provides a nontrivial parametrization of the many-body states which has ramifications for their simulability [17–19]. For non-equilibrium phenomena the dynamics of entanglement can exhibit universal features characterizing the phase of matter and its coarse-grained properties, which can be a useful tool for visualizing macroscopic quantum coherence.

Realizations of unitary quantum gates and fast measurements achieved in several physical systems, such as superconducting circuit QED systems [20–22] and trapped ions [23–25], have opened new avenues for quantum simulation. The low error rates in these unitary gates allow coherent evolution of many-body states over relatively long time scales enabling the study of quantum correlations in the form of entanglement. This experimental effort is in its early stages with 10s of qubits, but nonetheless is already in the realm of providing an advantage for simulating quantum systems compared to classical supercomputers. The quantum control of the microscopic degrees of freedom has also opened the avenue to realize exotic entangled states stabilized by non-equilibrium effects [26–29]. Digital quantum simulation using a gate-based architecture complements the earlier achievements in analogue quantum simulation using ultra-cold atoms [30–36] due to its connections to quantum error correction and complexity and provides a new lens for classifying quantum phases of matter [37–40].

The study of quantum circuits has enriched our understanding of quantum chaos, providing a toy model for describing entanglement dynamics in these systems [7, 41]. In contrast to the eigenstate thermalization hypothesis which is applicable to Hamiltonian and Floquet systems [1, 42, 43], where one is often limited to exact diagonalization to evaluate eigenstates, unitary circuits comprising of randomly chosen gates offer a simplified effective description for chaos. For a certain class of circuits, known as dual-unitary circuits [28, 44–46], constrained to be unitary along dual directions of space and time, the dynamics in the circuit are further simplified for certain observables while retaining their quantum chaotic properties. On introducing global conservation laws, the random unitary prescription naturally lends itself to describing the emergent hydrodynamics of the conserved quantities opening a new platform for studying quantum hydrodynamics.

These circuits are also fertile playground for studying dynamics induced by measurements on the qubits [47–49]. It opens a new regime for probing dynamics of entanglement of open quantum systems far from equilibrium. Despite measurements, the quantum trajectories of a many-body system for weak measurements can become highly entangled and far from a classical product state. In the strong measurement regime the trajectories become unentangled and lose their quantum correlations. Many questions related to the nature of the phase transitions between these two phases continue to be actively investigated [50–59]. The entanglement preserving phase can have error-correcting properties and is being considered for stabilizing novel many-body states with multipartite entanglement by monitoring local degrees of freedom [60–62].

In this chapter, we give an overview of random-circuit models, with a particular focus on the dynamics of quantum entanglement. We will especially pay attention to potential near-term applications of random-circuit models on noisy-intermediate scale quantum (NISQ) devices. To this end, consider a quantum many-body systems with physical degrees of freedom defined on discrete lattice sites. The degrees of freedom can, for instance, be quantum spins, in which case the local Hilbert-space dimension is $d = 2s + 1$ with s being the spin quantum number, but also fermionic or bosonic particles. In case of an isolated quantum system, its time evolution is unitary and governed by the time-dependent Schrödinger equation. Specifically, given some out-of-equilibrium initial state $|\psi(0)\rangle$, the time-evolved state at a later time t follows as, cf. Fig. 1a,

$$|\psi(t)\rangle = e^{-i\mathcal{H}t} |\psi(0)\rangle, \tag{1}$$

where \mathcal{H} denotes the Hamiltonian of the system. In practice, however, the evaluation of Eq. (1) is challenging due to the exponentially growing Hilbert space with increasing system size L ($D = d^L = 2^L$ for quantum spins with $s = 1/2$, i.e., qubits). Even though significant progress has been achieved in solving Eq. (1) also for large quantum systems due to the development of sophisticated numerical methods, especially matrix-product state techniques (see, e.g., [63]), such approaches are

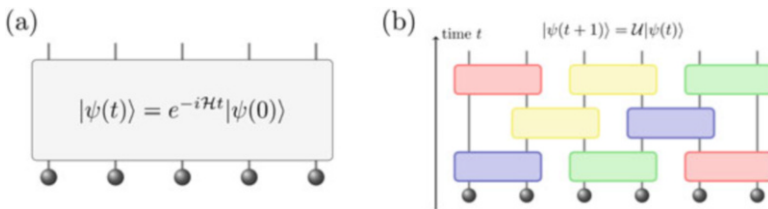


Fig. 1 (a) Given a (chaotic) quantum many-body system described by a Hamiltonian \mathcal{H} , the continuous time evolution of a quantum state $|\psi\rangle$ is generated by the unitary operator $\exp(-i\mathcal{H}t)$. (b) Random circuits act as minimal models to describe the properties of chaotic quantum many-body systems, with local gates acting on the degrees of freedom, with the time evolution now being discrete

typically limited by the growth of quantum entanglement during the time evolution,

$$S(t) = -\text{tr}[\rho_A \ln \rho_A], \quad \rho_A = \text{Tr}_B(|\psi(t)\rangle \langle \psi(t)|), \quad (2)$$

where ρ_A denotes the reduced density matrix for a bipartition of the system into subsystems A and B . In particular, $S(t)$ is typically expected to increase linearly in time, $S(t) \propto t$ [64], which causes the computational requirements to faithfully describe the state $|\psi(t)\rangle$ to grow exponentially. Note, however, that there are also cases where $S(t)$ builds up slower such as disordered models exhibiting many-body localization [3].

While the out-of-equilibrium dynamics of quantum many-body systems are hard to analyze, random circuits provide minimally structured models to describe their properties. The circuits consist of unitary gates acting locally on the degrees of freedom, for instance, in a brick wall pattern akin to well-known Trotter decompositions, see Fig. 1b. The gates are not chosen to reproduce the properties of a particular Hamiltonian but rather to capture the universal aspects of quantum chaotic dynamics. In particular, the gates are drawn at random, for instance, the two-site gates in Fig. 1b are $d^2 \times d^2$ matrices, which could be drawn from the unitarily invariant Haar measure or from the Clifford group [6]. Moreover, it is possible to consider the impact of symmetries, such as conservation of total magnetization or dipole moment, as well as kinetic constraints, by suitably choosing the gates (e.g., Haar-random matrices that are block-diagonal) [7, 8, 65]. In contrast to the intrinsically continuous time evolution of quantum systems [cf. Eq. (1)], the time evolution in circuit models is discrete,

$$|\psi(t+1)\rangle = \mathcal{U} |\psi(t)\rangle, \quad (3)$$

where \mathcal{U} is the full unitary operator of one layer of the circuit. Nevertheless, analogous to the Hamiltonian time evolution, the entanglement entropy $S(t)$ is found to grow very rapidly in random-circuit models [6, 7]. Crucially, random circuits not only capture the essential features of chaotic quantum many-body dynamics but in some cases also allow for analytical solutions of the dynamics. The latter makes these models very valuable to gain important insights that are out of reach for currently available numerical approaches.

In this chapter, we especially focus on two particular kinds of circuit models: In Sect. 2, we consider monitored circuits, where unitary gates are interspersed with local projective measurements. These circuits can be understood as toy models to describe the interaction of quantum systems with their environment, which constantly “measures” the system leading to decoherence. In particular, it has been found that the competition between unitary gates and projective measurements leads to a dynamical phase transition between a volume-law phase of $S(t)$ and an area-law phase of $S(t)$. Furthermore, in Sect. 3, we consider pseudo-random circuits consisting of one- and two-qubit gates drawn from a set of elementary gates available on today’s NISQ devices. These circuits have recently gained importance to demonstrate a quantum computational advantage, i.e., to perform a computational

task with a quantum computer that is out of reach for classical machines. We will discuss the main ideas of the random-circuit sampling task that was implemented and also describe how such circuits can be useful in the context of simulations of quantum many-body dynamics on NISQ devices.

2 Measurement-Induced Entanglement Transitions in Hybrid Quantum Circuits

In a many-body quantum system, the entanglement entropy typically follows a *scaling law*, where the entropy $S(A)$ of a contiguous subsystem A scales with some geometric property of A . There are several examples of scaling laws. A *volume-law* means the entropy $S(A) \propto |A| + \dots$ scales to leading order with the size of A , whereas an *area-law* means the entropy $S(A) \propto |\partial A| + \dots$ scales with the size of the boundary of A . The highly entangled volume-law states can be found, for example, as the steady states of chaotic quantum dynamics [1], while an area-law is often found in states with fast decay of correlations [66], such as the ground states of gapped Hamiltonians [67]. There are also scaling laws intermediate between volume and area laws; for example, the entropy of the ground state of a 1+1D conformal field theory scales *logarithmically* as $S(A) \propto \log |A| + \dots$ [68].

An *entanglement transition* is then a phase transition in which the scaling behavior of the entanglement entropy changes in some state of interest, such as an energy eigenstate or the steady state of some quantum dynamics. In this section we will mainly be interested in a particular class of entanglement transitions, known as *measurement-induced* transitions [17, 26, 27, 37–40, 47–56, 58–60, 69–106]. These occur in the steady state of *nonunitary* dynamics, where the nonunitarity is a result of quantum measurements being applied to the system at a constant rate. This setup can emerge quite naturally as a model for the interaction between a system and its environment. When the overall dynamics includes a mixture of measurements and also unitary dynamics, such as Hamiltonian time evolution representing a system’s internal dynamics, we will refer to this as “hybrid quantum dynamics.” Unitary dynamics often provides a natural route to generating entanglement, which is typically (though not always!) destroyed by measurements. However, it is known that entanglement transitions can also occur in *measurement-only* models [26, 54, 82, 85, 94], where the entanglement is generated as a result of frustration between the measurements.

2.1 Quantum Trajectories

When modeling the effect of an external environment on a quantum system, there are several complementary approaches. In the “mixed state approach,” we take

into account the fact that some information about the system will leak into the environment by modeling the state of the system with a density matrix. The mixed state $\rho(t)$ will then evolve in time according to some master equation. An alternative viewpoint is the “quantum trajectories approach,” where we model the system with a pure state and treat the effect of the environment through repeated measurements of the state. These approaches are equivalent in the sense that one can map between the two pictures: averaging over the possible quantum trajectories recovers the master equation for the density matrix ρ , and one can “unravel” the master equation to focus on individual quantum trajectories. Note that this unraveling is in general not unique; for example, consider the following trajectory equations, both describing Hamiltonian evolution of a fermionic chain undergoing continuous weak measurements [56]. The first class of trajectories, known as quantum state diffusion, is described by

$$d|\psi\rangle = \left[-iHdt + \sum_l \left(\frac{\gamma}{2} \hat{M}_{l,t}^2 dt + \xi_{l,t} \hat{M}_{l,t} \right) \right] |\psi\rangle, \quad (4)$$

where $\xi_{l,t}$ is a real-valued Gaussian variable with zero mean and covariance $\overline{\xi_{l,t} \xi_{m,t'}} = \gamma dt \delta_{l,m} \delta(t-t')$, and $\hat{M}_{l,t} = n_l - \langle n_l \rangle_t$ with n_l the local fermion occupation number. We could also consider the class of “quantum jump” trajectories, given by

$$d|\psi\rangle = \left[-iHdt + \sum_l \xi_{l,t} \left(\frac{n_l}{\sqrt{\langle n_l \rangle_t}} - 1 \right) \right] |\psi\rangle \quad (5)$$

for a state with conserved particle number, where now the noise is defined by $\xi_{l,t}^2 = \xi_{l,t}$ and $\overline{\xi_{l,t}} = \gamma dt \langle n_l \rangle_t$. Upon averaging the state $|\psi\rangle \langle \psi|$ over the noise $\{\xi_{l,t}\}$ to get the density matrix $\rho = \overline{|\psi\rangle \langle \psi|}$, both of these models give rise to the same master equation

$$\partial_t \rho = -i[H, \rho] + \gamma \sum_l \left(2n_l \rho n_l - \{n_l^2, \rho\} \right). \quad (6)$$

However, that is not to say that these two forms of trajectory are completely equivalent. In particular, some quantities do not commute with the average over states; in particular, if they are a *nonlinear* function of the state — in other words, we can have functions f of the state with

$$\mathbb{E}_i [f(|\psi_i\rangle \langle \psi_i|)] \neq f \left(\mathbb{E}_i [|\psi_i\rangle \langle \psi_i|] \right). \quad (7)$$

For our purposes the main example of such a quantity will be the entanglement entropy $S(A) = -\text{tr}[\rho_A \ln \rho_A]$, but the same is also true for connected correlation

functions of observables, $\langle O_A O_B \rangle_c \equiv \langle O_A O_B \rangle - \langle O_A \rangle \langle O_B \rangle$. One surprising aspect of measurement-induced transitions is that there can be phase transitions in quantities calculated along individual quantum trajectories that are completely invisible if one only looks at linear functions of the state. In particular, this means that for these phase transitions there can be no order parameter $\langle O \rangle = \text{tr}[O\rho]$ given by an expectation value taken with the average state. In the rest of this section, we will always average over trajectories only *after* first calculating the entanglement entropy or any other relevant quantities that can witness the phase transition.

2.2 Monitored Quantum Circuits

As a minimal model, consider the quantum circuit shown in Fig. 2a. This is a “hybrid” quantum circuit, consisting of rounds of nearest-neighbor unitary gates, followed by a round of measurements, where at each time step each spin has probability p of being measured. For each spin that is measured, the probability of each outcome is determined by the Born rule, and the state is subsequently updated via a projection on to the corresponding state.

The case with the least structure, retaining only locality and unitarity, is when the unitary gates are drawn uniformly (according to the Haar measure) from the unitary group $U(q^2)$, where q is the local Hilbert-space dimension. Haar-random unitaries are highly chaotic, generating entanglement ballistically [6, 7] and forming unitary designs in polynomial time [107]. For circuits with Haar-random gates on qubits, $q = 2$, there is a phase transition in the steady state entanglement from volume-law to area-law at measurement probability $p_c \approx 0.17$ [47, 53], where we can interpret p as the density of measurements in spacetime, cf. Fig. 2c. That this probability is nonzero may be surprising, given that naively local unitaries can only generate $\mathcal{O}(1)$ entanglement per time step, whereas local measurements can potentially destroy an extensive amount of entanglement. The resolution is that the local unitaries may “scramble” quantum information, such that the information about the state of a given subsystem is spread out over global degrees of freedom, with the effect that local measurements cannot learn much about the overall state of the system. This is very much in the spirit of quantum error correction, and indeed it has been argued that measurement-induced transitions can be viewed as phase transitions in the quantum channel capacity density Q/N , where the volume-law phase corresponds to $Q/N > 0$ [60].

2.3 Purification Transition

While the discussion in the previous section couched the measurement-induced transition in the language of an entanglement transition, it turns out that there is an alternative viewpoint in terms of a *purification transition* [60]. Imagine keeping

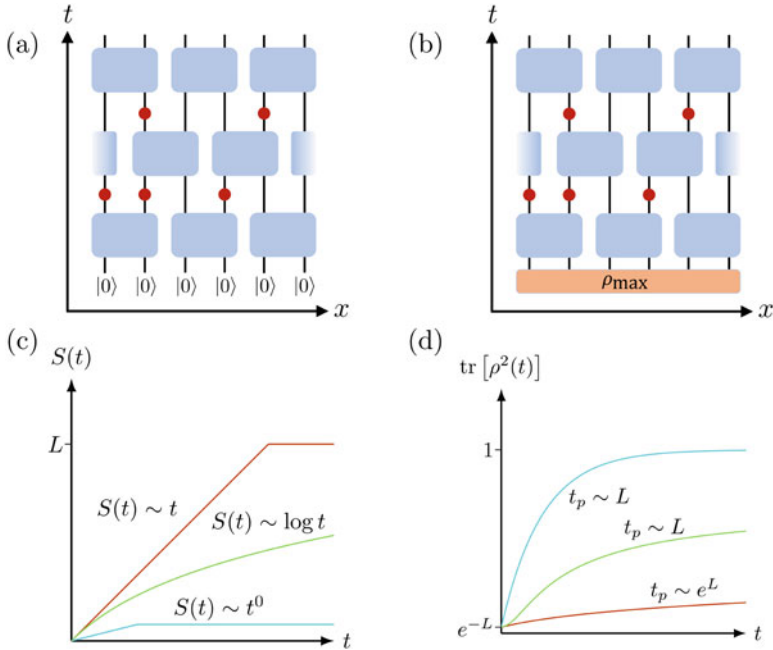


Fig. 2 A monitored quantum circuit starting from a product state, consisting of rounds of nearest-neighbor unitary gates (light blue rectangles), followed by rounds of projective measurements (red circles). Each spin independently has probability p of being measured at a given time step. **(b)** The purification picture uses the same hybrid circuit as in **(a)** but starts from the maximally mixed density matrix $\rho_{\max} = \mathbb{1}/\text{tr}[\mathbb{1}]$. **(c)** Entanglement dynamics in monitored quantum circuits. For $p < p_c$ the entropy $S(t)$ grows ballistically before saturating to a volume-law. At criticality $p = p_c$ this is replaced by logarithmic growth, while in the area-law phase $p > p_c$ the entropy saturates in $\mathcal{O}(1)$ time. **(d)** Purification dynamics in monitored quantum circuits. Starting from the maximally mixed state, the purity $\text{tr}[\rho^2]$ becomes $\mathcal{O}(1)$ in time $t_p \sim \mathcal{O}(L)$ in the purifying phase ($p > p_c$) and at criticality, whereas this takes time $t_p \sim \exp(\mathcal{O}(L))$ in the mixed phase $p < p_c$.

the same hybrid quantum circuit, but rather than using a product state as the initial state, using the maximally mixed state $\rho_{\max} = \mathbb{1}/\text{tr}[\mathbb{1}]$ instead, as shown in Fig. 2b. The action of the hybrid circuit will then be to purify the initial state, eventually reaching a pure state in the steady state. However, it turns out that there can be a phase transition in the *time* t_p taken for this purification—from exponential to polynomial in system size, as shown in Fig. 2d—and further that this transition seems to generically coincide with the entanglement transition for that class of hybrid quantum dynamics [55, 60]. Since in an experiment the effect of the environment is such that the state is generically mixed, unlike the pure-state setting of the entanglement transition, the purification transition may provide a more robust lens through which to observe measurement-induced transitions in experiments [60].

The purification picture also permits the introduction of an “order parameter” via coupling the system to an auxiliary system R [76]. In the simplest case, we can take R to be a single qubit. We maximally entangle R with a subset of the system at time t_0 , and then let the system evolve in time — the hybrid circuit acts only on the main system, so any dynamics in R are induced solely through its entanglement with the system. The purification dynamics of R then serve as a local probe of the measurement-induced phase structure [76]. By varying with which subsystem R is entangled, and the time t_0 at which it is entangled, we can probe different critical exponents, as will be discussed further in Sect. 2.6.

2.4 Transitions in the Rényi Entropies

There are many quantities that can characterize the entanglement of a quantum state. Focusing on pure states, the most common choice is the von Neumann entropy, $S(A) = -\text{tr}[\rho_A \log \rho_A]$, where ρ_A is the reduced density matrix for subsystem A . But the von Neumann entropy turns out to be very difficult to measure in a large-scale experiment since it requires something like full state tomography [108], whose resource cost scales exponentially with system size. Happily, there is a related family of entropies, the Rényi entropies, which are more amenable to experimental access. Given a non-negative number n , the n -Rényi entropy $S_n(A)$ is defined as

$$S_n(A) = \frac{1}{1-n} \log \text{tr}[\rho_A^n], \quad (8)$$

with the von Neumann entropy recovered in the limit $n \rightarrow 1$. For integer values of n — the easiest being $n = 2$ — the n -Rényi entropy can be measured in an “interferometry”-like experiment, where one prepares n identical copies of the quantum state in question, and then measures the Rényi entropy through the expectation value of a certain observable. While this remains a considerable challenge, it has already been demonstrated experimentally [109], and so provides a possible route to accessing entanglement transitions in an experimental setting.

Given the experimental relevance of the Rényi entropies, it is natural to ask whether each Rényi entropy undergoes an entanglement transition at the same critical point. It turns out that while in general not all the Rényi entropies will transition at the same critical point, it follows from some basic properties of the Rényi entropies that many of them will in fact undergo the same entanglement transition. By differentiating with respect to n the definition in Eq. (8) for the n -Rényi entropy, one can show that

$$\frac{dS_n(A)}{dn} = \frac{-1}{(1-n)^2} D(\sigma \parallel \lambda), \quad (9)$$

where $D(\sigma \parallel \lambda) = \sum_i \sigma_i \log(\sigma_i/\lambda_i)$ is the relative entropy, taken between the probability distributions $\lambda = \{\lambda_i\}$, given by the eigenvalues of ρ_A , and $\sigma \equiv \{\lambda_i^n / \sum_j \lambda_j^n\}$. As a consequence of the non-negativity of the relative entropy, this implies that

$$\frac{dS_n(A)}{dn} \leq 0. \quad (10)$$

In other words, the n -Rényi entropies are *non-increasing* as a function of n . In terms of the measurement-induced transition, this has the consequence that an area-law in the n -Rényi entropy implies an area-law in the ($m > n$)-Rényi entropies, and a volume-law in the n -Rényi entropy implies a volume-law in the ($m < n$)-Rényi entropies. Note, however, that we *do not* necessarily have the converse, which would imply that p_c is equal for all Rényi entropies.

However, we *do* have the converse for $m, n > 1$. This is a consequence of the following inequality, valid only for $n > 1$,

$$S_\infty \leq S_n \leq \frac{n}{n-1} S_\infty, \quad (11)$$

which implies that all the ($n > 1$)-Rényi entropies must have the same scaling behaviors. This inequality can be proven by using monotonicity of the Rényi entropies and the fact that $S_\infty(A)$ is the largest eigenvalue of ρ_A .

2.5 Analytically Tractable Limits

To determine the universality class of a phase transition, it is useful to have an analytic treatment. For measurement-induced transitions, such a treatment is currently available in a few select limits. A particularly simple treatment is available for the 0-Rényi entropy S_0 , also known as the Hartley entropy. $S_0(A)$ simply gives the logarithm of the number of nonzero eigenvalues of the reduced density matrix ρ_A . It can be accessed through an adaptation of the “minimal cut” prescription for calculating the entanglement entropy [48], which first appeared in the context of random unitary circuits [6], and provides a “coarse-grained” picture for entanglement growth. The upshot is that the measurement-induced transition in the Hartley entropy in d -dimensional hybrid quantum circuits with Haar-random gates is in the universality class of $(d + 1)$ -dimensional percolation, where the extra dimension comes from the time direction of the quantum circuit. Furthermore, the critical measurement probability is precisely the bond percolation threshold for percolation on a lattice determined by the geometry of the quantum gates.

Percolation also appears in a different limit, corresponding to the transition in the ($n \geq 1$)-Rényi entropies strictly in the limit of infinite local Hilbert-space dimension $q = \infty$. Here the connection to percolation is more subtle: it appears

only in a replica limit $Q \rightarrow 1$ of a $Q!$ -state Potts model obtained by averaging over unitary gates and measurements in a system where the gates are drawn from the Haar distribution over the unitary group [70]. This treatment indicates that all the ($n \geq 1$)-Rényi entropies undergo a phase transition at the same critical point, consistent with the discussion in Sect. 2.4. Interestingly, it turns out that the $q = \infty$ fixed point is unstable in the sense that finite q explicitly breaks an emergent symmetry, allowing for the presence of an RG-relevant perturbation that drives the system away from the percolation fixed point. At the time of writing, the ultimate fate of that new fixed point is unknown but remains a focus of current research.

2.6 Critical Properties of Measurement-Induced Transitions

In Sect. 2.5 we saw that in certain limits the measurement-induced transition was in the percolation universality class. However, both of these limits are somewhat unphysical: realistic quantum spin systems typically have finite local Hilbert-space dimension, and the 0-Rényi entropy can change discontinuously under arbitrarily small perturbations to the density matrix. Away from these limits, we turn to numerical probes to determine the relevant universality classes.

The critical exponents determining a universality class are typically obtained in numerics through finite-size scaling. In the rest of this section, we will mainly focus on numerics performed on *Clifford circuits*, where the unitary gates are drawn uniformly from the Clifford group. Clifford circuits are convenient to look at in the context of measurement-induced entanglement transitions because they can be efficiently simulated classically [110], while still being able to rapidly generate entanglement. Their classical simulability is important in enabling sufficiently large system sizes that finite-size scaling provides good estimates of critical exponents. Furthermore, Clifford operations often turn out to be relatively easy to implement on current quantum computing devices, so hybrid Clifford circuits may be some of the first to be simulated in experiments. Box 1 outlines a method to classically simulate Clifford circuits using a graph-state based algorithm which is particularly suitable in the context of entanglement phase transitions.

To extract the critical point numerically, a natural quantity to look at in 1+1D is the half-chain entanglement entropy $S(L/2)$ (all Rényi entropies are equal in Clifford circuits). However, this has the disadvantage that it appears to scale logarithmically with system size L , as in a 1+1D conformal field theory [68]. This means that at the critical point the entanglement entropy for different system sizes does not coincide, so one cannot simply “read off” the critical point by looking at the data. Furthermore, if one attempts to extract the critical point p_c and other critical exponents using standard finite-size scaling, these can have correlated errors depending on the extracted value of p_c . For a better estimator of the critical point, we turn to the *tripartite information* I_3 , defined as

$$I_3(A : B : C) \equiv I_2(A : B) + I_2(A : C) - I_2(A : BC), \quad (12)$$

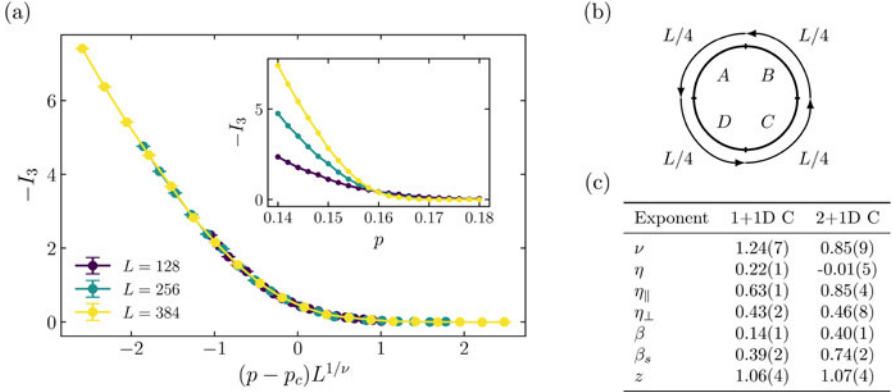


Fig. 3 (a) The steady state tripartite information I_3 as a function of $(p - p_c)L^{1/\nu}$, where $p_c \approx 0.158$ and $\nu \approx 1.33$. The inset shows the uncollapsed data. This dataset consists of 10^4 circuit realizations. (b) The partition used for the tripartite information I_3 on a chain of length L with periodic boundary conditions. (c) Critical exponents of the measurement-induced phase transition in 1+1D and 2+1D Clifford circuits, taken from Refs. [53, 55]

where $I_2(A : B) \equiv S(A) + S(B) - S(AB)$ is the mutual information. One can show that for pure states, given a partition into four subsystems, the tripartite information of three of the subsystems does not depend on the choice of subsystems, so we will simply write $I_3 \equiv I_3(A : B : C)$ from now on, with the partition in Fig. 3b in mind. One can then argue using the “minimal cut” prescription of Ref. [48] that for this choice of partition, I_3 cancels out the “boundary” contributions that give rise to the logarithmic scaling of the entanglement entropy at criticality [53], resulting in the scaling

$$I_3(p, L) \sim \begin{cases} \mathcal{O}(L), & p < p_c, \\ \mathcal{O}(1), & p = p_c, \\ 0, & p > p_c. \end{cases} \quad (13)$$

Notably, this means that at the critical point $I_3(p_c, L)$ should coincide for different system sizes L , providing a much more accurate estimator of the critical point. Figure 3a shows a data collapse of I_3 calculated in the steady state of 1+1D random Clifford circuits, which yields the estimate $p_c \approx 0.158$ for the critical point and $\nu \approx 1.33$ for the correlation length exponent. Notably, the latter is still very near the value of $\nu = 4/3$ for 2D percolation, despite the discussion in Sect. 2.5 that for finite local Hilbert-space dimension (here $q = 2$) we should expect the universality class to be distinct from percolation.

To measure other critical exponents, we turn to the “auxiliary system” method discussed in Sect. 2.3. For example, to extract the bulk exponent β , we initialize the system for a time $t_0 = 2L$ and then entangle a reference qubit R with the system qubit at position $x = L/2$, i.e., in the bulk. We then evolve the system for

a further time $t = 2L$ and measure the entanglement entropy of R . Close to the phase transition, the circuit-averaged entropy should scale as $\overline{S(R)} \sim (p_c - p)^\beta$, reaching zero in the area-law phase. This yields the values $\beta = 0.14(1)$ in 1D [53] and $\beta = 0.40(1)$ in 2D [55]. Again both of these values are reasonably close to the corresponding values for 2D and 3D percolation, $\beta_{2D} = 5/36 \approx 0.139$ and $\beta_{3D} \approx 0.43$. However, there is increasing evidence that, despite these similarities, the measurement-induced transition in Clifford circuits is indeed in a different universality class to percolation [53, 55, 71, 97].

We can also extend this method to measure correlation function exponents. We introduce two auxiliary systems, R_1 and R_2 , which are entangled with separate subsystems at a time t_0 , and then subject to dynamics again only through their entanglement with the main system. We can extract correlation function exponents by studying their mutual information $I_2(R_1 : R_2)$, which serves as an upper bound on all connected correlation functions of local observables [111]. For example, the exponent η governs the power-law decay of bulk correlation functions

$$|\langle A_r B_0 \rangle - \langle A_r \rangle \langle B_0 \rangle| \sim \frac{1}{r^{d-2+\eta}}, \quad (14)$$

for local observables A_r and B_0 supported at sites r and 0 , respectively. We can extract this exponent by initializing the system for time $t_0 = 2L$, entangling auxiliary qubits R_1 and R_2 with the bulk qubits at positions $x = L/4$ and $x = 3L/4$, and then letting the system evolve for a further time $t = 2L$. The mutual information should then decay as $I_2(R_1 : R_2) \sim 1/L^\eta$ in 1+1D, so we can extract η by optimizing for a data collapse of $L^\eta I_2(R_1 : R_2)$ for different system sizes L . We could also extract the corresponding surface correlation length exponents η_\perp and η_\parallel by choosing to entangle one or both of R_1 and R_2 to a surface qubit instead of a bulk qubit. In Fig. 3c we reproduce from Refs. [53, 55] the current numerical estimates of the critical exponents of the measurement-induced transition in 1+1D and 2+1D Clifford circuits, which were determined using the methods described here.

Box 1 | Simulating Clifford Circuits with Graph States

The Clifford group \mathcal{C}_n on n qubits is defined as the group that preserves the corresponding Pauli group \mathcal{P}_n under conjugation, modulo global phases. To be concrete, we focus on models with nearest-neighbor unitary gates drawn uniformly from the two-qubit Clifford group \mathcal{C}_2 , akin to the sketch in Fig. 2a, and with projective measurements in the σ^z basis. The two-qubit Clifford group can be generated by the gates $\{H, S, CZ\}$, where CZ is a two-qubit controlled- Z gate, and H and S are the single-qubit Hadamard and phase gates given in the computational basis by

$$H = \frac{1}{\sqrt{2}} \begin{pmatrix} 1 & 1 \\ 1 & -1 \end{pmatrix}, \quad S = \begin{pmatrix} 1 & 0 \\ 0 & i \end{pmatrix}. \quad (15)$$

(continued)

Box 1 (continued)

Ignoring overall phases, the resulting group has 11520 elements, which is sufficiently small that it can be hardcoded as a lookup table decomposing each group element into a product of the generators. This allows for simulations of random Clifford circuits using a graph-state based algorithm [112], which makes use of the fact that all stabilizer states resulting from a Clifford circuit can be written as a graph state, up to the action of some one-qubit Clifford gates [113]. Alternative simulation methods exist, most notably one based on storing a “stabilizer tableau” of the stabilizers fixing the quantum state, and then updating the tableau based on the action of Clifford gates [114]. However, the graph-state method is particularly well suited to the study of measurement-induced transitions, because its time complexity scales with the typical vertex degree of the graph storing the quantum state. This degree is generically reduced by the presence of measurements, such that it is possible to simulate very large system sizes in the area-law phase and near the critical point.

Graph States and Stabilizer States

The graph-state algorithm relies on a fortunate connection between graph states and stabilizer states, the latter being the states generated by Clifford circuits acting on the $|0\rangle^{\otimes N}$ initial state. Namely, all stabilizer states can be written as a graph state, up to the action of some one-qubit Clifford gates [113]. Given a graph $\mathcal{G} = (V, E)$, the graph state $|\mathcal{G}\rangle$ is defined by

$$|\mathcal{G}\rangle = \left(\prod_{(i,j) \in E} CZ_{ij} \right) |+\rangle^{\otimes N}, \quad (16)$$

where $|+\rangle = (|0\rangle + |1\rangle)/\sqrt{2}$, and N is the total number of qubits. That is, starting from the initial state $|+\rangle^{\otimes N}$, we perform a controlled- Z gate between all pairs of qubits (i, j) connected by an edge in the graph. Thus, to represent the graph state $|\mathcal{G}\rangle$ we just need to store the graph \mathcal{G} , which only takes $\mathcal{O}(N^2)$ memory. We can then write any stabilizer state as

$$|\mathcal{G}; \{C_i\}\rangle = \left(\bigotimes_{i=1}^N C_i \right) |\mathcal{G}\rangle, \quad (17)$$

where the C_i are drawn from the one-qubit Clifford group \mathcal{C}_1 . This group has only 24 elements up to phase, so this additional information is only an $\mathcal{O}(N)$ overhead.

The entanglement in a graph state is completely fixed by the graph \mathcal{G} . Suppose we wanted to calculate the entanglement entropy of a subsystem A .

(continued)

Box 1 (continued)

Partitioning the adjacency matrix Γ of \mathcal{G} into the block form

$$\Gamma = \begin{pmatrix} \Gamma_{AA} & \Gamma_{AB} \\ \Gamma_{AB}^T & \Gamma_{BB} \end{pmatrix}, \tag{18}$$

where B is the complement of A , the entanglement entropy S_A is given by

$$S_A = \text{rank}_{\mathbb{F}_2}(\Gamma_{AB}), \tag{19}$$

the rank over the binary field \mathbb{F}_2 of the subadjacency matrix Γ_{AB} characterizing connections between A and B [115].

Implementing Clifford Operations

Note that there is some “gauge freedom” in writing stabilizer states this way, so different combinations $(\mathcal{G}; \{C_i\})$ can correspond to the same quantum state. This freedom turns out to be useful in implementing two-qubit Clifford operations on the quantum state. Here we will summarize how one performs Clifford gates and Pauli measurements on stabilizer states represented in this way — for the full details we refer the reader to Ref. [112]. The relevant time complexities of the different operations are shown in Table 1.

One-qubit Clifford gates are trivial to perform since they leave the graph invariant — we merely have to update the one-qubit Clifford C_i corresponding to the site i of the gate, which takes $\Theta(1)$ time. This can be done with a lookup table of size $|\mathcal{C}_1|^2 = 24^2$. Two-qubit Clifford gates are more technical, since they involve both the graph and the one-qubit Cliffords. We only need to focus on implementing CZ gates, since this is the only two-qubit gate in the generating set of the two-qubit Clifford group. There are two cases in implementing CZ on a given pair of qubits (i, j) . The easy case is if the corresponding one-qubit Cliffords C_i and C_j commute with $CZ_{i,j}$. In this case, the CZ leaves the one-qubit Cliffords unchanged, and toggles the edge (i, j) in the graph. The harder case is if $CZ_{i,j}$ does not commute with the one-qubit Cliffords, and it is here that the “gauge freedom” becomes useful. The goal is to move to a gauge where the problem is reduced to the

Table 1 Time complexity of different Clifford operations. d is the maximum vertex degree of the qubits involved in the gate, whose scaling with system size depends on the entanglement phase

Clifford operation	Time complexity
One-qubit gate	$\Theta(1)$
Two-qubit gate	$\mathcal{O}(d^2)$
Pauli Z measurement	$\mathcal{O}(d)$

(continued)

Box 1 (continued)

easy case previously described. We do this using an operation called “local complementation,” which toggles all the edges in the subgraph induced by the neighborhood of a given vertex, say i , and then modifies the one-qubit Cliffords of site i and its neighbors. In this way, one can obtain C_i and C_j which commute with $CZ_{i,j}$. The local complementation is the dominant cost, taking time $\mathcal{O}(d^2)$, where d is the maximum vertex degree of qubits i and j . This scaling with d rather than system size N means the runtime of this algorithm depends strongly on the connectedness of the graph, and hence, roughly speaking, that less entangled states are quicker to simulate. This is especially pertinent in the context of entanglement phase transitions. In principle, d can be as large as $\mathcal{O}(N)$, and this scaling is relevant in the volume-law phase. However, in the area-law phase and near the critical point, the typical vertex degree can be $\mathcal{O}(1)$, so that even two-qubit gates are easy to implement.

Finally we describe how to perform single-site Pauli measurements. The basic idea is to reduce the measurement on the stabilizer state $|\mathcal{G}; \{C_i\}\rangle$ to a measurement on the underlying graph state $|\mathcal{G}\rangle$ without the one-qubit Cliffords. Suppose we measure Pauli P_a on site a , with outcome $\lambda \in \{\pm 1\}$. The stabilizer state will be updated to

$$\frac{\mathbb{1} + \lambda P_a}{2} |\mathcal{G}; \{C_i\}\rangle = \left(\prod_{b \in V \setminus \{a\}} C_b \right) \frac{\mathbb{1} + \lambda P_a}{2} C_a |\mathcal{G}\rangle \quad (20)$$

$$= \left(\prod_{b \in V \setminus \{a\}} C_b \right) C_a \frac{\mathbb{1} + \lambda C_a^\dagger P_a C_a}{2} |\mathcal{G}\rangle, \quad (21)$$

where we inserted a factor of $\mathbb{1} = C_a C_a^\dagger$ in the last step. Since C_a is a Clifford operator and preserves spectra, $P'_a \equiv C_a^\dagger P_a C_a \in \{\pm X_a, \pm Y_a, \pm Z_a\}$. Hence the effect of measuring Pauli P_a on the stabilizer state $|\mathcal{G}; \{C_i\}\rangle$ can be modelled by measuring Pauli P'_a on the graph state $|\mathcal{G}\rangle$. Relegating full details of graph-state measurements to Refs. [112, 113], we note that Pauli Z measurements are particularly simple: they simply remove all edges from the graph connected to the measured site, which takes $\mathcal{O}(d)$ time.

2.7 Entanglement Transitions in Experiments

2.7.1 Scalability Issues

As discussed in Sect. 2.4, it is very difficult to experimentally measure the von Neumann entropy, but this can possibly be ameliorated by instead measuring a Rényi entropy, such as the 2-Rényi entropy S_2 (related to the purity via $\text{tr}[\rho^2] = \exp[-S_2]$). However, before one can get to that point one has to reliably and repeatedly prepare a given steady state for which the entropy is to be calculated, and it is here that the probabilistic nature of the measurements can present an issue of scalability. Even if we fix the measurement locations for simplicity, their random outcomes mean that for T rounds of measurements with probability p , in a system of N spins with local Hilbert-space dimension q , the number of repetitions required to get $\mathcal{O}(1)$ samples of a given trajectory is of the order q^{pNT} , which is exponential in the system size. To make things worse, the equilibration time T is typically at least linear in the system size N , so the sampling overhead can be *doubly* exponential in N . In principle, this presents a severe barrier to scaling up these experiments to the large system sizes where phase transitions are most apparent.

There are several options to try to avoid this particular issue of postselection. One option is to relate entanglement entropy to a quantity which can be more easily measured. In particular, this is possible by relating a given hybrid quantum circuit to its *spacetime dual*. Given a unitary matrix U acting on a pair of spins, we denote its matrix elements by $[U]_{i_{\text{in}},j_{\text{in}}}^{i_{\text{out}},j_{\text{out}}}$. This matrix is unitary in the “time” direction, expressed by the condition $\sum_{kl} [U]_{i_{\text{in}},j_{\text{in}}}^{kl} [U^*]_{i_{\text{out}},j_{\text{out}}}^{kl} = \delta_{i_{\text{in}},j_{\text{in}},i_{\text{out}},j_{\text{out}}}$. However, we could decide to swap the space and time directions: viewing the unitary U as a tensor with four legs, two for input and two for output, we form an associated tensor \tilde{U} , where one of the original output legs of U becomes an input leg of \tilde{U} , and one of the original input legs of U becomes an output leg of \tilde{U} . The resulting \tilde{U} is generically nonunitary, and can be interpreted as a unitary gate followed by a weak measurement [17]. Thus by taking the spacetime dual we have a relation between a hybrid quantum circuit and an associated unitary circuit. It turns out that one can relate the 2-Rényi entropy in the hybrid circuit to a correlation function in the unitary circuit [93], which is typically much easier to measure in an experiment.

Another option is to consider a modification of the measurement protocol, where instead of having random measurements with outcomes distributed according to the Born rule, we consider a nonunitary but deterministic time evolution, such as that resulting from a non-Hermitian Hamiltonian [96]. In effect one can think of this as being similar to “forcing” certain measurement outcomes [77]. Non-Hermitian Hamiltonians can emerge quite naturally in certain open quantum systems undergoing continuous measurement. However, it is worth noting that the measurement-induced transition in these systems may be somewhat different in character to that in random quantum circuits with Born rule projective measurements—in replica treatments of the phase transition (see Sect. 2.5), the Born rule factor necessitates an additional replica compared to the case of forced

measurements [70], so the latter in fact appears to be more like closely related transitions in random tensor networks [116]. Additionally, the lack of quenched randomness with forced measurements may give rise to qualitatively different behavior of the entanglement domain walls that arise in statistical mechanical models describing these transitions.

2.7.2 Measurement-Induced Transition in a Trapped-Ion Experiment

Ref. [25] presented the first experimental observation of a measurement-induced transition. They studied a chain of 13 trapped $^{171}\text{Yb}^+$ ions, with relatively high gate fidelities of 99.96% for single-qubit gates and 98.5–99.3% for two-qubit gates. Instead of directly measuring the entanglement entropy, they focused on the measurement-induced transition in the purification picture, as discussed in Sect. 2.3, since this is typically more robust to experimental imperfections, and also made use of the following simplification. In this system certain operations are easier to perform than others: the “native” two-qubit gate they employ is an “Ising” XX gate of the form $U(\theta) = \exp(-i\theta\sigma_i^x\sigma_j^x)$, where the value of θ is controlled by the duration of a control pulse. The use of this gate implies that if measurements are performed in the σ^x basis then we will quickly approach a σ^x -basis product state, since the XX Ising gates cannot generate entanglement from σ^x basis states. Exploiting this fact, the authors consider a modification of the usual purification protocol, fixing the overall measurement probability p , but performing the measurements in two different bases, the σ^x and σ^z bases. There is an additional parameter p_x that controls the probability that a given measurement is performed in the σ^x basis. With p fixed to a small value to limit the overall number of measurements, there is a phase transition as a function of p_x between the slow- and fast-purifying phases.

3 Random Circuits on Noisy-Intermediate Scale Quantum Devices

As outlined so far, random circuits with different designs have proven extremely useful to understand the properties of quantum many-body systems and the dynamics of entanglement. Recently, random circuits have found a new application in quantum information science. In particular, they have been used to demonstrate “quantum supremacy” or, in other words, a quantum computational advantage, which refers to the fact that a quantum device can perform a task that is unfeasible for its classical counterpart [4]. Such a demonstration of a quantum advantage is especially nontrivial given the eponymous noise of today’s NISQ devices. This is not least the reason why, as a computational problem to achieve “quantum supremacy,” it was chosen to sample from the output probability distribution of a random circuit,

which is believed to be a hard task for classical supercomputers. In Sect. 3.1, we will provide an introduction to the main ideas of random-circuit sampling. Moreover, in Sect. 3.2, we will discuss that random circuits on NISQ devices are not just abstract tools to outperform classical computers, but are useful in a wider range of applications. To this end, we will leverage the concept of quantum typicality (see Box 2) and focus on the results reported in Ref. [117].

3.1 *Random-Circuit Sampling for Achieving a Quantum Computational Advantage*

Random circuits are natural candidates when striving to outperform classical computers. On the one hand, random circuits seem more appealing than some arithmetic calculation in view of the noise of today’s NISQ devices. On the other hand, these circuits are challenging for classical machinery due to the lack of structure and the quick generation of entanglement. The main idea of random-circuit sampling is as follows [118, 119]. Given a random circuit \mathcal{R} , apply \mathcal{R} to the L qubits of the system and measure all qubits afterwards, which yields a bitstring $|k\rangle = |010110\dots\rangle$ according to Born’s rule with probability $z = |\langle k|\mathcal{R}|0\rangle|^2$. Repeating this experiment many times then yields a set of bitstrings $|k_1\rangle, |k_2\rangle, |k_3\rangle, \dots$, which allows to draw conclusions on the underlying probability distribution. In particular, for random circuits that are sufficiently deep, it is expected that the resulting state is Haar-random [118, 120–124], i.e., it is a realization drawn from the uniform distribution on the $2D$ -dimensional unit sphere, where $D = 2^L$ is the dimension of the Hilbert space. In practice, this implies that the complex coefficients c_k of the wave function $\mathcal{R}|0\rangle = \sum_k c_k |k\rangle$ are drawn from a Gaussian distribution and that the probability distribution of $z = |c_k|^2$ follows as [118, 125],

$$p(z) = (D - 1)(1 - z)^{D-2} \approx e^{-Dz}, \quad (22)$$

where the approximation on the right hand side of Eq. (22) applies to large Hilbert-space dimensions D and is sometimes referred to as Porter-Thomas law [126].

In order to demonstrate a quantum computational advantage using random-circuit sampling, several key points have to be addressed [125]. First of all, it is important to execute the random circuit on a large system that surpasses the capacities of classical computers (currently the best supercomputers can evaluate circuits with $L \approx 45$ [127]). However, for such large systems, the corresponding Hilbert space is huge and reconstructing the probability distribution $p(z)$ would require an impracticably high number of bitstrings (experimental repetitions). Moreover, how can one verify that the quantum device indeed samples from the correct probability distribution if classical verification is impossible? An important step to overcome these difficulties has been achieved by the introduction of cross-entropy benchmarking (XEB) [118]. To understand XEB, consider an ideal

(quantum) computer that can execute \mathcal{R} and thus provides the probabilities $p(|k\rangle)$ of all 2^L bitstrings. Now, let a NISQ device execute \mathcal{R} and we collect N samples $\mathcal{S} = \{|k_1\rangle, \dots, |k_N\rangle\}$. If N is large enough, we could reconstruct the corresponding probability distribution $p_{\text{NISQ}}(|k\rangle)$ and compare it with the ideal distribution $p(|k\rangle)$ using standard statistical tools. However, even for a smaller number of samples, it was shown that conclusions on the quality of the NISQ device can be drawn based on an approximation of the cross entropy [118, 125],

$$S_{\text{XEB}} = - \sum_{k=1}^D p_{\text{NISQ}}(|k\rangle) \log p(|k\rangle) \approx - \frac{1}{N} \sum_{|k\rangle \in \mathcal{S}} \log p(|k\rangle), \quad (23)$$

where the second part results from replacing the sum over all D bitstrings by the sample average justified by the central limit theorem. In practice, the probabilities $p(|k\rangle)$ to perform XEB are obtained numerically by simulating the quantum circuit on a supercomputer. Obviously, this is not possible in the regime of system sizes and circuit depths where a quantum computational advantage occurs. Nevertheless, various sophisticated techniques have been developed (e.g., considering elided circuits with fewer entangling gates [119]) to estimate the cross entropy in Eq. (23) also in such cases. For more details on XEB, we refer to [118, 119, 125].

A quantum computational advantage based on random-circuit sampling has been announced for the first time using Google's NISQ device *Sycamore* [119]. In the experiment, the Josephson junction-based processor executed a random circuit consisting of layers of one-qubit and two-qubit gates. We will discuss such types of circuits in more detail in Sect. 3.2. Due to imperfections in the execution, it was found in [119] that the cross entropy decays exponentially with the number of qubits and the depth of the circuit. Nevertheless, a nonzero S_{XEB} was established even for the largest circuits with 53 qubits and 20 cycles of one-qubit and two-qubit gate layers, implying that the processor samples from a nontrivial probability distribution. In particular, according to Google's estimate at that time, a classical supercomputer would require 10,000 years for the same task (albeit significantly lower estimates have been suggested subsequently [128, 129]). In more recent experiments, a team from China used their superconducting quantum processor *Zuchongzhi* to perform random-circuit sampling for even larger qubit numbers and circuit depths, which impressively substantiate the fact that a quantum computational advantage has indeed been achieved [130, 131]. Eventually, it is important to note that a quantum computational advantage is of course a moving target since both quantum and classical hardware as well as algorithms are expected to further improve in the future [132].

3.2 Applications of Random Circuits in Quantum Many-Body Physics

While sampling the outcome of random circuits is arguably a rather abstract task, it is an intriguing question to what extent the current capabilities of NISQ devices can be leveraged to study a wider class of problems. In this context, we specifically refer to questions in quantum many-body dynamics, which are generally challenging for classical computers due to the exponentially large Hilbert space. Simulations on NISQ devices might provide an opportunity to tackle these challenges and, moreover, to open up novel directions of research. In particular, it is important to note that today’s NISQ devices, with of the order of 50 qubits, already operate in Hilbert spaces that are competitive to or even go beyond what is possible with the best supercomputers, as also demonstrated recently [133–135]

In this section, we discuss a recent proposal to simulate hydrodynamics in quantum many-body systems on NISQ devices using random circuits [117], which emphasizes that random circuits are not just useful to demonstrate “quantum supremacy,” but they in fact form tailor-made building blocks to study questions in quantum many-body physics. The two key points in this context are that (i) random circuits swiftly generate random highly entangled quantum states, and (ii) the properties of such random states can be exploited for efficient simulations by relying on the concept of quantum typicality [136–139] (see Box 2). More specifically, Ref. [117] presented a scheme to compute the infinite-temperature spatiotemporal correlation function $C_{\ell, \ell'}(t)$,

$$C_{\ell, \ell'}(t) = \frac{\text{tr}[S_{\ell}^z(t) S_{\ell'}^z]}{2^L}, \quad (24)$$

where S_{ℓ}^z is a spin-1/2 operator at lattice site ℓ , $S_{\ell}^z(t) = e^{i\mathcal{H}t} S_{\ell}^z e^{-i\mathcal{H}t}$ is the time-evolved operator with respect to a Hamiltonian \mathcal{H} (although, in principle, evolutions with respect to other unitaries $U(t)$ are conceivable as well), and L denotes the numbers of spins (qubits). The algorithm to simulate $C_{\ell, \ell'}(t)$ is sketched in Fig. 4a. First, all qubits are initialized in the $|0\rangle$ state. (We identify $|0\rangle \equiv |\uparrow\rangle$ and $|1\rangle \equiv |\downarrow\rangle$ in the following.) A random circuit \mathcal{R} then acts on $L - 1$ qubits (except for site ℓ'). The resulting state $|\psi_{\mathcal{R}, \ell'}\rangle = |0\rangle_{\ell'} \otimes \mathcal{R} |0\rangle^{\otimes L-1}$ is evolved in time, $|\psi_{\mathcal{R}, \ell'}(t)\rangle = e^{-i\mathcal{H}t} |\psi_{\mathcal{R}, \ell'}\rangle$, and the measurement at site ℓ yields the spatiotemporal correlation function according to (see [117] for a derivation),

$$C_{\ell, \ell'}(t) = \frac{1}{2} \langle \psi_{\mathcal{R}, \ell'}(t) | S_{\ell}^z | \psi_{\mathcal{R}, \ell'}(t) \rangle + \mathcal{O}(2^{-L/2}), \quad (25)$$

where the statistical error of the quantum-typicality approximation vanishes exponentially with increasing system size [125]. In this context, quantum typicality can be interpreted as a form of “quantum parallelism” [140, 141], as the time evolution of a single random state $|\psi_{\mathcal{R}, \ell'}\rangle$ already captures the full ensemble average. This

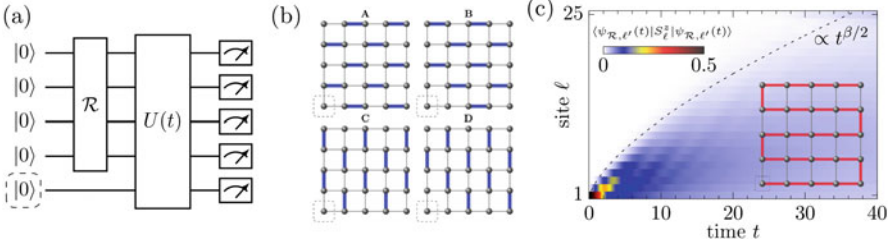


Fig. 4 (a) Algorithm to simulate dynamical spin-spin correlation function. A random circuit \mathcal{R} acts on $L - 1$ qubits (except site ℓ'), followed by a time evolution $U(t)$ on all L sites. Measurement on site ℓ then yields $C_{\ell,\ell'}(t)$. (b) We here consider a two-dimensional geometry. Similar to [118, 119], \mathcal{R} consists of layers of one-qubit and two-qubit gates, cf. Fig. 5c. The patterns **A–D** indicate the position of the two-qubit gates in different cycles. (c) For reference site $\ell' = 1$, the expectation value $\langle \psi_{\mathcal{R},\ell'}(t) | S_{\ell}^z | \psi_{\mathcal{R},\ell'}(t) \rangle$ yields $2C_{\ell,\ell'}(t)$. Data is shown for the Heisenberg chain with $L = 25$, where the dynamics of the one-dimensional system can be simulated by considering a snake-like path through the two-dimensional grid. Figure adapted from Ref. [117]

typicality-based approach to simulate dynamical two-point correlation functions such as $C_{\ell,\ell'}(t)$ on a quantum computer is complementary to other established schemes [142–144] and operates without an overhead of bath or ancilla qubits. Crucially, it is a direct extension of the random-circuit experiments already realized on today’s NISQ devices [119, 130, 131].

We now discuss the individual components of the algorithm in more detail. As in [118, 119], we consider a two-dimensional grid of qubits. The random circuit \mathcal{R} then consists of individual cycles, each composed of a layer of one-qubit gates and a layer of two-qubit gates, where we denote the total number of cycles with d . The two-qubit gates generate entanglement between different parts of the system, and different choices are possible such as CZ or CNOT gates [117, 145], or other hardware-specific gates [119, 133]. As shown in Fig. 4b, they are aligned in one of the patterns **A–D**, and the sequence **ABCD**... is repeated in subsequent cycles throughout \mathcal{R} . After d cycles, $|\psi_{\mathcal{R},\ell'}\rangle = \sum_{k=1}^{2^L} c_k |k\rangle$ is a superposition of computational basis states. In particular, even for moderately shallow \mathcal{R} , $|\psi_{\mathcal{R},\ell'}\rangle$ will approximate the properties of a full Haar-random state (we will discuss this fact further below in the context of Fig. 5), i.e., the coefficients c_k are approximately distributed according to a Gaussian distribution with zero mean. As a consequence, these states can be used within the typicality approach to calculate $C_{\ell,\ell'}(t)$.

As a numerical example, we here consider the dynamics with respect to the paradigmatic spin-1/2 Heisenberg chain, $\mathcal{H} = \sum_{\ell} (S_{\ell}^x S_{\ell+1}^x + S_{\ell}^y S_{\ell+1}^y + S_{\ell}^z S_{\ell+1}^z)$, where the one-dimensional model can be readily studied using a snake-like path through the two-dimensional grid, see Fig. 4c. The time evolution with respect to \mathcal{H} is then evaluated by decomposing $U(t) = \exp(-i\mathcal{H}t)$ into discrete Trotter steps [146, 147],

$$U(t) = \left(e^{-i\mathcal{H}\delta t} \right)^N \approx \left(e^{-i\mathcal{H}_e\delta t} e^{-i\mathcal{H}_o\delta t} \right)^N + \mathcal{O}(\delta t^2), \quad (26)$$

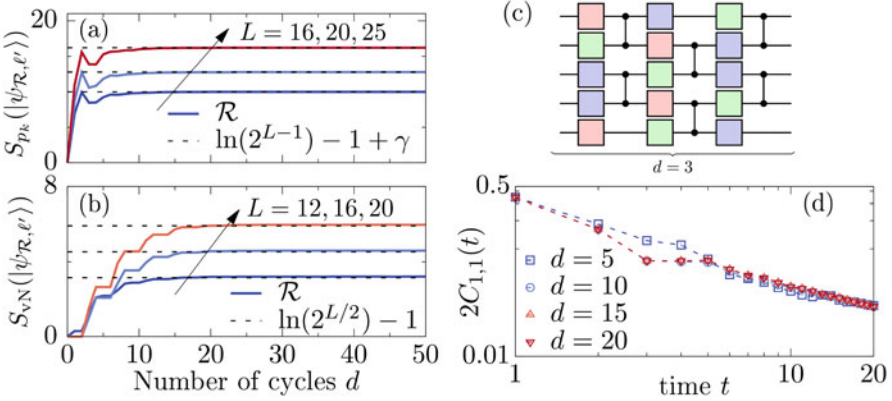


Fig. 5 (a, b) Buildup of randomness of $|\psi_{\mathcal{R}, \ell'}\rangle$ versus the depth d of \mathcal{R} (cf. panel (c)), measured by (a) S_{p_k} and (b) S_{v_N} . Both quantities reach their corresponding random-state values already at moderate d . The displayed values of L correspond to two-dimensional geometries 4×3 , 4×4 , 5×4 , and 5×5 . Data is averaged over 100 realizations of \mathcal{R} . (c) Sketch of the random circuit with depth $d = 3$, which consists of layers of one-qubit gates and two-qubit gates. CNOT gates are chosen as two-qubit entangling gates. (d) Expectation value $\langle \psi_{\mathcal{R}, 1}(t) | S_1^z | \psi_{\mathcal{R}, 1}(t) \rangle \approx 2C_{1,1}(t)$ for random circuits \mathcal{R} with different depths $d = 5, 10, 15, 20$. For sufficiently large d , data becomes independent of d and fluctuations around the exact dynamics of $C_{1,1}(t)$ vanish. Data is shown for the one-dimensional Heisenberg chain with system size $L = 25$ and Trotter time step $\delta t = 0.5$. Figure adapted from Ref. [117]

where \mathcal{H}_e (\mathcal{H}_o) denotes the even (odd) bonds of \mathcal{H} and $\delta t = t/N$ is a (short) time step.

The spatiotemporal correlation function $C_{\ell, \ell'}(t)$ can be interpreted as a spin excitation moving in front of an infinite-temperature background. As shown in Fig. 4c, using $\ell' = 1$, the excitation created at the edge spreads through the system under time evolution. In particular, as the total magnetization is conserved by \mathcal{H} , i.e., $[\mathcal{H}, \sum_{\ell} S_{\ell}^z] = 0$, $C_{\ell, \ell'}(t)$ is expected to show hydrodynamic behavior at long times [148, 149]. This hydrodynamic behavior can be conveniently analyzed either by inspecting the decay of the autocorrelation function $C_{1,1}(t)$ or by studying the spatial variance of the full density profile, $\Sigma^2(t) = \sum_{\ell} \ell^2 \tilde{C}_{\ell,1}(t) - [\sum_{\ell} \ell \tilde{C}_{\ell,1}(t)]^2$, where $\tilde{C}_{\ell,1}(t) = C_{\ell,1}(t) / \sum_{\ell=1}^L C_{\ell,1}(t)$ with $\sum_{\ell} \tilde{C}_{\ell,1}(t) = 1$. Specifically, their respective power-law exponents reflect the type of hydrodynamic transport, $\alpha(t) = -d \ln C_{1,1}(t) / d \ln t$, $\beta(t) = d \ln \Sigma^2(t) / d \ln t$, where for one-dimensional systems $\alpha = 0.5$ corresponds to normal diffusion, $\alpha = 1$ indicates ballistic transport, and $0 < \alpha < 0.5$ ($0.5 < \alpha < 1$) signal anomalous subdiffusion (superdiffusion) [148].

After having outlined the general principle of the algorithm, it is insightful to go back one step and study the buildup of randomness of $|\psi_{\mathcal{R}, \ell'}\rangle$ due to the action of \mathcal{R} . Such an analysis is presented in Fig. 5a and b in terms of the participation

entropy $S_{p_k}(|\psi_{\mathcal{R},\ell'}\rangle)$ and the von Neumann entanglement entropy $S_{\text{vN}}(|\psi_{\mathcal{R},\ell'}\rangle)$,

$$S_{p_k}(|\psi_{\mathcal{R},\ell'}\rangle) = -\sum_{k=1}^{2^L} p_k \ln p_k, \quad S_{\text{vN}}(|\psi_{\mathcal{R},\ell'}\rangle) = -\text{tr}[\rho_A \ln \rho_A], \quad (27)$$

with $p_k = |c_k|^2$, and $\rho_A = \text{Tr}_B |\psi_{\mathcal{R},\ell'}\rangle \langle \psi_{\mathcal{R},\ell'}|$ being the reduced density matrix for a half-system bipartition. As already mentioned above, \mathcal{R} consists of one-qubit and two-qubit gates, cf. Fig. 5c. For the simulations shown here, the one-qubit gates are drawn at random from the set $\{X^{1/2}, Y^{1/2}, T\}$, where $X^{1/2}$ ($Y^{1/2}$) are $\pi/2$ rotations around the x-axis (y-axis) of the Bloch sphere and T is the non-Clifford gate $T = \text{diag}(1, e^{i\pi/4})$. Similar to [118, 119], gates on a given site have to be different in subsequent cycles. As two-qubit gates, we here consider CNOT gates. As shown in Fig. 5a and b, both $S_{p_k}(|\psi_{\mathcal{R},\ell'}\rangle)$ and $S_{\text{vN}}(|\psi_{\mathcal{R},\ell'}\rangle)$ saturate towards their analytically known random-state values already for moderate depth d of \mathcal{R} . Specifically, $S_{p_k}(|\psi_{\mathcal{R},\ell'}\rangle)$ approaches $\ln(2^{L-1}) - 1 + \gamma$ with Euler constant $\gamma \approx 0.577$ [118] already at $d \lesssim 10$, with no major dependence on L . Likewise, $S_{\text{vN}}(|\psi_{\mathcal{R},\ell'}\rangle)$ approaches the ‘‘Page value’’ $\ln(2^{L/2}) - 1$ [150] appropriate for a random state on $L - 1$ sites, albeit the depth d to reach this value appears to grow slightly with L . It is important to stress that the design of \mathcal{R} chosen here is by no means optimized but already sufficient to create highly random and entangled states. In Fig. 5d, we analyze the dependence of the expectation value $\langle \psi_{\mathcal{R},1}(t) | S_1^z | \psi_{\mathcal{R},1}(t) \rangle$ on the depth d of \mathcal{R} . While this expectation value converges to the exact autocorrelation function $2C_{\ell,\ell'}(t)$ for sufficiently large d , we find in Fig. 5d that even for rather shallow circuits with $d = 10$, the resulting dynamics is almost indistinguishable from the dynamics for $d = 20$. Thus, even for states with entanglement below the Page value, cf. Fig. 5b, the resulting dynamics is still a good approximation to $C_{1,1}(t)$ and captures the correct hydrodynamic behavior.

Finally, let us comment on the accuracy of the typicality approach. In Fig. 6a, we compare the dynamics of two states that result from different realizations of the random circuit, \mathcal{R}_1 and \mathcal{R}_2 . Moreover, we also show data obtained from exact diagonalization. Even for the rather small system size $L = 16$ chosen here, we find that the dynamics obtained from $|\psi_{\mathcal{R}_1,\ell'}\rangle$ and $|\psi_{\mathcal{R}_2,\ell'}\rangle$ closely follow the exact result with only minor fluctuations. In particular, these residual fluctuations can be further suppressed by averaging over multiple random realizations of \mathcal{R} . As shown in Fig. 5a, the dynamics obtained by averaging over 10^2 realizations is indistinguishable from ED. Note that for larger system sizes (i.e., significantly larger Hilbert-space dimensions) quantum typicality becomes more and more accurate such that such an averaging is not necessary anymore and a single realization of \mathcal{R} is sufficient [125].

While we have so far focused on the full expectation value $\langle \psi_{\mathcal{R},\ell'}(t) | S_\ell^z | \psi_{\mathcal{R},\ell'}(t) \rangle$, this expectation value cannot be obtained on a quantum computer in a single run. In particular, $|\psi_{\mathcal{R},\ell'}(t)\rangle$ will generally be a superposition of computational basis states, $|\psi_{\mathcal{R},\ell'}(t)\rangle = \sum_{k=1}^{2^L} a_k |k\rangle$, and the coefficients a_k can

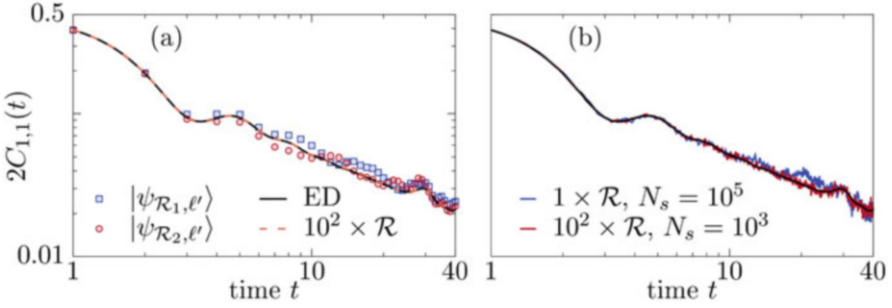


Fig. 6 Accuracy of the typicality approach in comparison with exact diagonalization for a one-dimensional Heisenberg chain with $L = 16$. **(a)** The full expectation value $\langle \psi_{\mathcal{R}, \ell'}(t) | S_\ell^z | \psi_{\mathcal{R}, \ell'}(t) \rangle$ for two different individual realizations of the random circuit ($\mathcal{R}_1, \mathcal{R}_2$) shows visible fluctuations, while averaging the expectation value over 100 random instances of \mathcal{R} yields results indistinguishable from ED. **(b)** Reconstructed expectation value from sampling the output of the circuit N_s times as required in an actual experiment, cf. Eq. (28). Note that N_s here denotes the number of samples for each individual realization of \mathcal{R} . In particular, averaging over \mathcal{R} and sampling over N_s can be combined with each other. Figure adapted from Ref. [117]

be reconstructed by repeating the experiment multiple times and averaging the final measurements of the qubits. More specifically, $C_{\ell, \ell'}(t)$ can be reconstructed as,

$$2C_{\ell, \ell'}(t) = \frac{1}{2} \left(\sum_{|k\rangle, \ell=\uparrow} |\tilde{a}_k|^2 - \sum_{|k\rangle, \ell=\downarrow} |\tilde{a}_k|^2 \right), \quad (28)$$

where $|\tilde{a}_k|^2$ is the experimentally obtained probability of the state $|k\rangle$, and the two sums in (28) run over all states for which the spin ℓ is up or down, respectively. The accuracy can be systematically improved by increasing the number of samples N_s such that $|\tilde{a}_k|^2 \rightarrow |a_k|^2$. Crucially, as we show in Fig. 6b, the sampling of the distribution of the $|a_k|^2$ can be combined with the averaging over random realizations of \mathcal{R} . Specifically, Fig. 6b compares the dynamics obtained from one realization of \mathcal{R} with $N_s = 10^5$ repetitions to the dynamics obtained from 10^2 realizations of \mathcal{R} with $N_s = 10^3$ repetitions each, i.e., the total number of runs is the same in both cases. While the noise level is found to be similar in both cases, we observe that the data averaged over multiple \mathcal{R} agrees better with ED. In this context, we note that varying \mathcal{R} on a NISQ device is straightforward experimentally.

Box 2 | Quantum Typicality

The notion of quantum typicality refers to the fact that the overwhelming majority (Haar measure) of quantum states within some energy shell yields expectation values of observables very close to the full microcanonical ensemble

(continued)

Box 2 (continued)

ble [136–139]. Speaking differently, given a single pure quantum state, drawn at random from a high-dimensional Hilbert space, the expectation values of observables with respect to this state will be effectively indistinguishable from their thermodynamic equilibrium values. As such, quantum typicality has been put forward as an important concept to explain the emergence of thermodynamic behavior in closed quantum systems [151, 152]. Here, we focus on the implications of typicality for efficient simulations (see [125, 153] for reviews).

Quantum Typicality as a Numerical Tool

The key idea in this context is that random quantum states are highly accurate *trace estimators* [154, 155]. To demonstrate this fact, let $|\psi\rangle$ be a random state, drawn from the unitarily invariant Haar measure,

$$|\psi\rangle = \sum_{k=1}^D (a_k + ib_k) |k\rangle, \quad (29)$$

where the coefficients a_k and b_k are Gaussian-distributed with zero mean and unit variance, and $|k\rangle$ denote a set of orthogonal basis states of the Hilbert space with dimension D . Given an observable \mathcal{O} , its trace can then be written as [125],

$$\text{tr}[\mathcal{O}] = \frac{D \overline{\langle \psi | \mathcal{O} | \psi \rangle}}{\langle \psi | \psi \rangle}, \quad \text{tr}[\mathcal{O}] \approx \frac{D \langle \psi | \mathcal{O} | \psi \rangle}{\langle \psi | \psi \rangle}, \quad (30)$$

where the overline means averaging over random realizations of $|\psi\rangle$. Importantly, the second equation in (30) emphasizes that for sufficiently large Hilbert-space dimensions, even a single realization of $|\psi\rangle$ provides an accurate approximation of $\text{tr}[\mathcal{O}]$. In particular, given some mild assumptions on the spectral properties of \mathcal{O} , the statistical error of the approximation vanishes for $D \rightarrow \infty$ (see, e.g., [125] for details on error bounds). It is straightforward to extend the scheme in Eq. (30) to equilibrium expectation values of \mathcal{O} at temperature $T = 1/\beta$ [156],

$$\langle \mathcal{O} \rangle_{\text{eq}} = \frac{\text{tr}[\mathcal{O} e^{-\beta \mathcal{H}}]}{\text{tr}[e^{-\beta \mathcal{H}}]} = \frac{\langle \psi_\beta | \mathcal{O} | \psi_\beta \rangle}{\langle \psi_\beta | \psi_\beta \rangle} + \epsilon, \quad |\psi_\beta\rangle = e^{-\beta \mathcal{H}/2} |\psi\rangle, \quad (31)$$

where $|\psi_\beta\rangle$ is sometimes referred to as thermal pure quantum state [156] and the standard deviation of the statistical error scales as $\sigma(\epsilon) \propto 1/\sqrt{d_{\text{eff}}}$, with $d_{\text{eff}} = \text{tr}[\exp(-\beta(\mathcal{H} - E_0))]$ being an effective dimension, and E_0 is the ground-state energy of \mathcal{H} [125, 156]. Furthermore, quantum typicality

(continued)

Box 2 (continued)

also carries over to time-dependent situations (see, e.g., [152, 157–160]), which has been particularly exploited in the context of dynamical two-point correlation functions, which can be approximated as [161–164],

$$\langle \mathcal{O}_1(t) \mathcal{O}_2 \rangle_{\text{eq}} = \frac{\text{tr}[\mathcal{O}_1(t) \mathcal{O}_2 e^{-\beta \mathcal{H}}]}{\text{tr}[e^{-\beta \mathcal{H}}]} \approx \frac{\langle \psi_\beta(t) | \mathcal{O}_1 | \varphi_\beta(t) \rangle}{\langle \psi_\beta(0) | \psi_\beta(0) \rangle}, \quad (32)$$

where $|\varphi_\beta(t)\rangle = e^{-i\mathcal{H}t} \mathcal{O}_2 e^{-\beta \mathcal{H}/2} |\psi\rangle$, $|\psi_\beta(t)\rangle = e^{-i\mathcal{H}t} e^{-\beta \mathcal{H}/2} |\psi\rangle$. The crucial ingredient why the pure-state approximations in Eqs. (31) and (32) are useful is given by the fact that the temperature- and time-dependence can be efficiently evaluated by using well-established sparse-matrix techniques [165] (e.g., Krylov-subspace methods [166], or Chebyshev-polynomial expansions [167–169]). These methods essentially rely on matrix-vector multiplications which can be carried out both time and memory efficient. In particular, no exact diagonalization of \mathcal{H} is required such that significantly larger Hilbert spaces can be handled.

Quantum Typicality Versus Eigenstate Thermalization Hypothesis (ETH)

The ETH asserts that the diagonal matrix elements of observables written in the eigenbasis of chaotic nonintegrable Hamiltonians are a smooth function of energy and agree with the corresponding microcanonical expectation value [1],

$$\mathcal{O}_{nn} = \langle n | \mathcal{O} | n \rangle \approx \mathcal{O}_{\text{mc}}(E), \quad \mathcal{O}_{\text{mc}}(E) = \frac{1}{N_E} \sum_{E_n \approx E} \langle n | \mathcal{O} | n \rangle. \quad (33)$$

While the ETH has been numerically confirmed for a variety of models and observables, it is known to break down, for instance, in strongly disordered models exhibiting many-body localization [3]. In this case, the diagonal matrix elements show pronounced eigenstate-to-eigenstate fluctuations, $\mathcal{O}_{nn} \neq \mathcal{O}_{(n+1)(n+1)} \neq \mathcal{O}_{\text{mc}}(E)$. In contrast, the concept of typicality remains valid irrespective of the ETH being fulfilled. Specifically, consider a state $|\psi_E\rangle$ that is constructed as a random superposition of eigenstates $|n\rangle$ in an energy shell with mean energy E . Then, the expectation value of \mathcal{O} with respect to $|\psi_E\rangle$ will again be very close to the microcanonical expectation value as long as the energy window contains sufficiently many eigenstates to

(continued)

Box 2 (continued)

reduce statistical errors,

$$\frac{\langle \psi_E | \mathcal{O} | \psi_E \rangle}{\langle \psi_E | \psi_E \rangle} \approx \mathcal{O}_{\text{mc}}(E),$$

$$|\psi_E\rangle = \sum_{E_n \approx E} c_n |n\rangle, \text{ where } c_n \text{ are Gaussian random numbers.} \quad (34)$$

As a consequence, quantum typicality can be exploited as a numerical tool to study the properties of integrable or many-body localized systems where the ETH breaks down [170–173], as well as to verify the validity of the ETH for system sizes beyond the range of exact diagonalization [174, 175].

4 Conclusion

The goal of this chapter was to give a brief overview of certain aspects of random quantum circuits. Such random circuits have recently gained increased attention as minimally structured models for quantum many-body systems, providing new insights into challenging questions, e.g., regarding the dynamics of entanglement or the emergence of hydrodynamics. In view of the vast literature, we here deliberately refrained from giving an in-depth review of all actively pursued directions but rather refer the interested reader to the pertinent references included in Sects. 1–3. Instead, we here focused in more detail on two particular topics, i.e., (i) entanglement transitions in monitored circuits, where random unitary gates are interspersed with measurements, and (ii) random quantum circuits recently implemented on noisy intermediate-scale quantum devices to achieve a quantum computational advantage.

In the context of monitored circuits, we have given an introduction to the notion of quantum trajectories and reviewed the equivalent pictures of a measurement-induced pure-state transition from volume-law to area-law scaling of the entanglement entropy and a purification transition from mixed to pure states with increasing measurement rate. We have particularly discussed the critical properties of the transition in one and two dimensions and explained how Clifford circuits, especially in combination with graph states, provide a powerful approach to explore this type of physics numerically. Moreover, we have touched on the challenges to realize and observe entanglement transitions in monitored circuits in actual experiments. While our understanding of measurement-induced criticality has increased substantially over the last couple of years, a variety of open questions still remain. For example, the exact nature of the critical point in realistic limits remains open, despite recent progress [77]. It has also been shown that it is possible to stabilize phases of matter using specific measurement protocols [26, 27, 94], which would otherwise

be unstable in thermal equilibrium. However, it is not yet clear what restrictions, if any, apply to the phases realizable in this way. Similar protection against equilibration can be afforded by many-body localization [176], but this is not possible in the presence of non-Abelian symmetries [177], for example, so it would be interesting if monitored quantum circuits could provide a route to avoiding these restrictions. Finally, it would be interesting to see if the quantum error-correcting properties of the volume-law phase, which have provided a useful lens on the phenomenology [37–39, 60, 178], could be put to practical use in quantum computers. While the hybrid dynamics encode quantum information, and a decoder is known to exist in the volume-law phase [60], it is not clear whether in general a “good” decoder exists which could efficiently detect and correct errors [61].

Regarding random circuits on NISQ devices, we have provided a brief introduction to the ideas of random-circuit sampling and cross-entropy benchmarking to achieve a quantum computational advantage. Furthermore, we have focused on a recently proposed random-circuit based algorithm to simulate hydrodynamics on NISQ devices [117], which emphasizes that random circuits are not just abstract tools to outperform classical computers for a specific computational problem, but are relevant also for a wider range of applications. In this context, we have demonstrated that random circuits can efficiently generate random and highly entangled quantum states. Importantly, we have explained that such random states are immediately useful for simulations, both on quantum and classical computers, by leveraging the concept of quantum typicality. Exploring in more detail the potential applications of random quantum states and quantum typicality on NISQ devices will be an interesting direction of future research. Such applications are particularly appealing from a complexity point of view as random states can be prepared on NISQ devices by random circuits of moderate depth. However, due to their high entanglement, they are usually not amenable to concepts such as matrix-product states, which makes classical representations very costly. Applications of random states thus fall naturally into a category that is classically hard, but might be accessible by NISQ devices. Let us note that quantum typicality has in fact been recently exploited in experiments on actual quantum hardware. In [133], a scheme very similar to that outlined in Sect. 3.2 was used to calculate dynamical spin-spin correlation functions in a driven Floquet spin chain in order to verify the occurrence of discrete time-crystalline eigenstate order. Moreover, in [179], quantum typicality was used to evaluate thermodynamic expectation values at finite temperature (cf. Box 2), which involved the approximation of the imaginary time evolution of random states on a NISQ device [180].

Acknowledgments We acknowledge discussions with Sougato Bose, Matthew Fisher, Andrew Green, Michael Gullans, David Huse, Lluís Masanes, Jed Pixley, Robin Steinigeweg, Marcin Szytniszewski, Curt von Keyserlingk, and Brayden Ware. This work was funded by the European Research Council (ERC) under the European Union’s Horizon 2020 research and innovation programme (Grant agreement No. 853368).

References

1. L. D'Alessio, Y. Kafri, A. Polkovnikov, M. Rigol, *Adv. Phys.* **65**, 239 (2016)
2. R. Nandkishore, D. A. Huse, *Annu. Rev. Condens. Matter Phys.* **6**, 15 (2015)
3. D.A. Abanin, E. Altman, I. Bloch, M. Serbyn, *Rev. Mod. Phys.* **91**, 021001 (2019)
4. J. Preskill, *Quantum* **2**, 79 (2018)
5. A.C. Potter and R. Vasseur, arXiv (2021), arXiv:2111.08018 [quant-ph]
6. A. Nahum, J. Ruhman, S. Vijay, J. Haah, *Phys. Rev. X* **7**, 031016 (2017)
7. C. W. von Keyserlingk, T. Rakovszky, F. Pollmann, S.L. Sondhi, *Phys. Rev. X* **8**, 021013 (2018)
8. V. Khemani, A. Vishwanath, D. A. Huse, *Phys. Rev. X* **8**, 031057 (2018)
9. B. Bertini, P. Kos, T. Prosen, *Phys. Rev. Lett.* **121**, 264101 (2018)
10. A. Chan, A. De Luca, J.T. Chalker, *Phys. Rev. X* **8**, 041019 (2018)
11. I.V. Gornyi, A.D. Mirlin, D.G. Polyakov, *Phys. Rev. Lett.* **95**, 206603 (2005)
12. D.M. Basko, I.L. Aleiner, B.L. Altshuler, *Ann. Phys. (N. Y.)* **321**, 1126 (2006)
13. A. Pal, D.A. Huse, *Phys. Rev. B* **82**, 174411 (2010)
14. F. Pollmann, V. Khemani, J.I. Cirac, S.L. Sondhi, *Phys. Rev. B* **94**, 041116 (2016)
15. T.B. Wahl, A. Pal, S.H. Simon, *Phys. Rev. X* **7**, 021018 (2017)
16. T.B. Wahl, A. Pal, S.H. Simon, *Nat. Phys.* **15**, 164 (2019)
17. J. Napp, R.L. La Placa, A.M. Dalzell, F.G.S.L. Brandao, A.W. Harrow, arXiv (2019), arXiv:2001.00021
18. K. Noh, L. Jiang, B. Fefferman, *Quantum* **4**, 318 (2020)
19. F. Azad, A. Hallam, J. Morley, A. Green, arXiv (2021), arXiv:2111.06408 [quant-ph]
20. K. Murch, S. Weber, C. Macklin, I. Siddiqi, *Nature* **502**, 211 (2013)
21. N. Roch, M.E. Schwartz, F. Motzoi, C. Macklin, R. Vijay, A.W. Eddins, A.N. Korotkov, K.B. Whaley, M. Sarovar, I. Siddiqi, *Phys. Rev. Lett.* **112**, 170501 (2014)
22. Z.K. Mineev, S.O. Mundhada, S. Shankar, P. Reinhold, R. Gutiérrez-Jáuregui, R.J. Schoelkopf, M. Mirrahimi, H.J. Carmichael, M.H. Devoret, *Nature* **570**, 200 (2019)
23. T. Sauter, W. Neuhauser, R. Blatt, P.E. Toschek, *Phys. Rev. Lett.* **57**, 1696 (1986)
24. J.C. Bergquist, R.G. Hulet, W.M. Itano, D.J. Wineland, *Phys. Rev. Lett.* **57**, 1699 (1986)
25. C. Noel, P. Niroula, A. Risinger, L. Egan, D. Biswas, M. Cetina, A.V. Gorshkov, M. Gullans, D.A. Huse, C. Monroe, arXiv (2021), arXiv:2106.05881 [quant-ph]
26. A. Lavasani, Y. Alavirad, M. Barkeshli, *Nat. Phys.* **17**, 342 (2021)
27. S. Sang, T.H. Hsieh, *Phys. Rev. Res.* **3**, 023200 (2021)
28. P.W. Claeys, A. Lamacraft, *Phys. Rev. Lett.* **126**, 100603 (2021)
29. M. Ippoliti, K. Kechedzhi, R. Moessner, S. Sondhi, V. Khemani, *PRX Quantum* **2**, 030346 (2021)
30. I. Bloch, J. Dalibard, S. Nascimbène, *Nat. Phys.* **8**, 267 (2012)
31. I. Bloch, J. Dalibard, W. Zwerger, *Rev. Mod. Phys.* **80**, 885 (2008)
32. M. Greiner, O. Mandel, T. Esslinger, T.W. Hänsch, I. Bloch, *Nature* **415**, 39 (2002)
33. M. Schreiber, S.S. Hodgman, P. Bordia, H.P. Lüschen, M.H. Fischer, R. Vosk, E. Altman, U. Schneider, I. Bloch, *Science* **349**, 842 (2015)
34. J. Simon, W. S. Bakr, R. Ma, M. E. Tai, P. M. Preiss, M. Greiner, *Nature* **472**, 307 (2011)
35. A.M. Kaufman, M.E. Tai, A. Lukin, M. Rispoli, R. Schittko, P.M. Preiss, M. Greiner, *Science* **353**, 794 (2016)
36. H. Bernien, S. Schwartz, A. Keesling, H. Levine, A. Omran, H. Pichler, S. Choi, A.S. Zibrov, M. Endres, M. Greiner, V. Vuletić, M.D. Lukin, *Nature* **551**, 579 (2017)
37. S. Choi, Y. Bao, X.-L. Qi, E. Altman, *Phys. Rev. Lett.* **125**, 030505 (2020)
38. Y. Li, M.P.A. Fisher, *Phys. Rev. B* **103**, 104306 (2021)
39. R. Fan, S. Vijay, A. Vishwanath, Y.-Z. You, *Phys. Rev. B* **103**, 174309 (2021)
40. M.J. Gullans, S. Krastanov, D.A. Huse, L. Jiang, S.T. Flammia, *Phys. Rev. X* **11**, 031066 (2020)
41. A. Nahum, S. Vijay, J. Haah, *Phys. Rev. X* **8**, 021014 (2018)

42. J.M. Deutsch, *Phys. Rev. A* **43**, 2046 (1991)
43. M. Srednicki, *Phys. Rev. E* **50**, 888 (1994)
44. B. Bertini, P. Kos, T. Prosen, *Phys. Rev. Lett.* **123**, 210601 (2019)
45. S. Gopalakrishnan, A. Lamacraft, *Phys. Rev. B* **100**, 064309 (2019)
46. L. Piroli, B. Bertini, J.I. Cirac, T. Prosen, *Phys. Rev. B* **101**, 094304 (2020)
47. Y. Li, X. Chen, M.P.A. Fisher, *Phys. Rev. B* **98**, 205136 (2018)
48. B. Skinner, J. Ruhman, A. Nahum, *Phys. Rev. X* **9**, 031009 (2019)
49. A. Chan, R.M. Nandkishore, M. Pretko, G. Smith, *Phys. Rev. B* **99**, 224307 (2019)
50. Y. Li, X. Chen, M.P.A. Fisher, *Phys. Rev. B* **100**, 134306 (2019)
51. M. Szyniszewski, A. Romito, H. Schomerus, *Phys. Rev. B* **100**, 064204 (2019)
52. X. Chen, Y. Li, M.P.A. Fisher, A. Lucas, *Phys. Rev. Res.* **2**, 033017 (2020)
53. A. Zabalo, M.J. Gullans, J.H. Wilson, S. Gopalakrishnan, D.A. Huse, J.H. Pixley, *Phys. Rev. B* **101**, 060301 (2020)
54. M. Ippoliti, M.J. Gullans, S. Gopalakrishnan, D.A. Huse, V. Khemani, *Phys. Rev. X* **11**, 011030 (2021)
55. O. Lunt, M. Szyniszewski, A. Pal, *Phys. Rev. B* **104**, 155111 (2021)
56. O. Albertson, M. Buchhold, S. Diehl, *Phys. Rev. Lett.* **126**, 170602 (2021)
57. A. Zabalo, M.J. Gullans, J.H. Wilson, R. Vasseur, A.W. Ludwig, S. Gopalakrishnan, D.A. Huse, J. Pixley, *arXiv* (2021), *arXiv:2107.03393* [cond-mat.dis-nn]
58. S. Sang, Y. Li, T. Zhou, X. Chen, T.H. Hsieh, M.P. Fisher, *PRX Quantum* **2**, 030313 (2021)
59. Q. Tang, X. Chen, W. Zhu, *Phys. Rev. B* **103**, 174303 (2021)
60. M.J. Gullans, D.A. Huse, *Phys. Rev. X* **10**, 041020 (2020)
61. M.B. Hastings, J. Haah, *Quantum* **5**, 564 (2021)
62. R. Verresen, N. Tantivasadakarn, A. Vishwanath, *arXiv preprint arXiv:2112.03061* (2021)
63. S. Paeckel, T. Köhler, A. Swoboda, S.R. Manmana, U. Schollwöck, C. Hubig, *Ann. Phys. (NY)* **411**, 167998 (2019)
64. H. Kim, D. A. Huse, *Phys. Rev. Lett.* **111**, 127205 (2013)
65. S. Pai, M. Pretko, R.M. Nandkishore, *Phys. Rev. X* **9**, 021003 (2019)
66. F.G.S.L. Brandão, M. Horodecki, *Nat. Phys.* **9**, 721 (2013)
67. M.B. Hastings, *J. Stat. Mech.: Theory Exp.* **2007** (08), P08024
68. P. Calabrese, J. Cardy, *J. Stat. Mech.: Theory Exp.* **2004** (06), P06002
69. Y. Bao, S. Choi, E. Altman, *Phys. Rev. B* **101**, 104301 (2020)
70. C.-M. Jian, Y.-Z. You, R. Vasseur, A.W.W. Ludwig, *Phys. Rev. B* **101**, 104302 (2020)
71. Y. Li, X. Chen, A.W.W. Ludwig, M.P.A. Fisher, *Phys. Rev. B* **104**, 104305 (2021)
72. O. Shtanko, Y.A. Kharkov, L.P. García-Pintos, A.V. Gorshkov, *arXiv* (2020), *arXiv:2004.06736* [cond-mat.dis-nn]
73. M. Szyniszewski, A. Romito, H. Schomerus, *Phys. Rev. Lett.* **125**, 210602 (2020)
74. L. Zhang, J.A. Reyes, S. Kourtis, C. Chamon, E.R. Mucciolo, A.E. Ruckenstein, *Phys. Rev. B* **101**, 235104 (2020)
75. X. Turkeshi, R. Fazio, M. Dalmonte, *Phys. Rev. B* **102**, 014315 (2020)
76. M.J. Gullans, D.A. Huse, *Phys. Rev. Lett.* **125**, 070606 (2020)
77. A. Nahum, S. Roy, B. Skinner, J. Ruhman, *PRX Quantum* **2**, 010352 (2021)
78. X. Cao, A. Tilloy, A. De Luca, *SciPost Phys.* **7**, 024 (2019)
79. Q. Tang, W. Zhu, *Phys. Rev. Res.* **2**, 013022 (2020)
80. S. Goto, I. Danshita, *Phys. Rev. A* **102**, 033316 (2020)
81. O. Lunt, A. Pal, *Phys. Rev. Res.* **2**, 043072 (2020)
82. N. Lang, H.P. Büchler, *Phys. Rev. B* **102**, 094204 (2020)
83. C. Liu, P. Zhang, X. Chen, *SciPost Phys.* **10**, 048 (2020)
84. Y. Fuji, Y. Ashida, *Phys. Rev. B* **102**, 054302 (2020)
85. M. Van Regemortel, Z.-P. Cian, A. Seif, H. Dehghani, M. Hafezi, *Phys. Rev. Lett.* **126**, 123604 (2021)
86. D. Aharonov, *Phys. Rev. A* **62**, 062311 (2000)
87. S. Vijay, *arXiv* (2020), *arXiv:2005.03052*
88. A. Nahum, B. Skinner, *Phys. Rev. Res.* **2**, 023288 (2020)

89. D. Rossini, E. Vicari, *Phys Rev B* **102**, 035119 (2020)
90. L. Fidkowski, J. Haah, M.B. Hastings, *Quantum* **5**, 382 (2021)
91. T. Maimbourg, D.M. Basko, M. Holzmann, A. Rosso, *Phys. Rev. Lett.* **126**, 120603 (2021)
92. J. Iaconis, A. Lucas, X. Chen, arXiv (2020). arXiv:2010.02196
93. M. Ippoliti, V. Khemani, *Phys. Rev. Lett.* **126**, 060501 (2021)
94. A. Lavasani, Y. Alavirad, M. Barkeshli, *Phys. Rev. Lett.* **127**, 235701 (2021)
95. B. Shi, X. Dai, Y.-M. Lu, arXiv (2020). arXiv:2012.00040
96. S. Gopalakrishnan, M.J. Gullans, *Phys. Rev. Lett.* **126**, 170503 (2021)
97. Y. Li, R. Vasseur, M.P.A. Fisher, A.W.W. Ludwig, arXiv (2021). arXiv:2110.02988 [cond-mat.stat-mech]
98. Y. Han, X. Chen, arXiv (2021). arXiv:2110.10726
99. X. Chen, arXiv (2021). arXiv:2110.12230
100. J. Iaconis, X. Chen, arXiv (2021). arXiv:2107.05565
101. S. Sharma, X. Turkeshi, R. Fazio, M. Dalmonte, (2021), arXiv:2110.14403
102. P. Sierant, G. Chiriaco, F.M. Surace, S. Sharma, X. Turkeshi, M. Dalmonte, R. Fazio, G. Pagano, (2021). arXiv:2107.05669
103. P. Sierant, X. Turkeshi, (2021). arXiv:2109.06882
104. X. Turkeshi, M. Dalmonte, R. Fazio, M. Schiró, (2021), arXiv:2111.03500
105. X. Turkeshi, (2021), arXiv:2101.06245.
106. X. Turkeshi, A. Biella, R. Fazio, M. Dalmonte, M. Schiró, *Phys. Rev. B* **103**, 224210 (2021)
107. F.G.S.L. Brandão, A.W. Harrow, M. Horodecki, *Commun. Math. Phys.* **346**, 397 (2016)
108. R. O'Donnell, J. Wright, in *Proceedings of the Forty-Seventh Annual ACM Symposium on Theory of Computing*, STOC '15 (Association for Computing Machinery, Portland, Oregon, USA, 2015), pp. 529–538
109. R. Islam, R. Ma, P.M. Preiss, M. Eric Tai, A. Lukin, M. Rispoli, M. Greiner, *Nature* **528**, 77 (2015)
110. D. Gottesman, arXiv (1998). arXiv:quant-ph/9807006
111. M.M. Wolf, F. Verstraete, M. B. Hastings, J.I. Cirac, *Phys. Rev. Lett.* **100**, 070502 (2008)
112. S. Anders, H.J. Briegel, *Phys. Rev. A* **73**, 022334 (2006)
113. M. Hein, J. Eisert, H.J. Briegel, *Phys. Rev. A* **69**, 062311 (2004)
114. S. Aaronson, D. Gottesman, *Phys. Rev. A* **70**, 052328 (2004)
115. M. Hein, W. Dür, J. Eisert, R. Raussendorf, M.V. den Nest, H.-J. Briegel, arXiv (2006). arXiv:quant-ph/0602096 [quant-ph]
116. R. Vasseur, A.C. Potter, Y.-Z. You, A.W.W. Ludwig, *Phys. Rev. B* **100**, 134203 (2019)
117. J. Richter, A. Pal, *Phys. Rev. Lett.* **126**, 230501 (2021)
118. S. Boixo, S.V. Isakov, V.N. Smelyanskiy, R. Babbush, N. Ding, Z. Jiang, M.J. Bremner, J.M. Martinis, H. Neven, *Nat. Phys.* **14**, 595 (2018)
119. F. Arute et al., *Nature* **574**, 505 (2019)
120. R. Oliveira, O.C.O. Dahlsten, M.B. Plenio, *Phys. Rev. Lett.* **98**, 130502 (2007)
121. Y.S. Weinstein, W.G. Brown, L. Viola, *Phys. Rev. A* **78**, 052332 (2008)
122. J. Emerson, Y.S. Weinstein, M. Saraceno, S. Lloyd, D.G. Cory, *Science* **302**, 2098 (2003)
123. A.W. Harrow, R.A. Low, *Commun. Math. Phys.* **291**, 257 (2009)
124. M. Žnidarič, *Phys. Rev. A* **76**, 012318 (2007)
125. F. Jin, D. Willsch, M. Willsch, H. Lagemann, K. Michielsen, H.D. Raedt, *J. Phys. Soc. Jpn.* **90**, 012001 (2021)
126. C.E. Porter, R.G. Thomas, *Phys. Rev.* **104**, 483 (1956)
127. H.D. Raedt, F. Jin, D. Willsch, M. Willsch, N. Yoshioka, N. Ito, S. Yuan, K. Michielsen, *Comput. Phys. Commun.* **237**, 47 (2019)
128. J. Gray, S. Kourtis, *Quantum* **5**, 410 (2021)
129. C. Huang, F. Zhang, M. Newman, J. Cai, X. Gao, Z. Tian, J. Wu, H. Xu, H. Yu, B. Yuan, M. Szegedy, Y. Shi, J. Chen, arXiv (2020). arXiv:2005.06787 [quant-ph]
130. Y. Wu et al., *Phys. Rev. Lett.* **127**, 180501 (2021)
131. Q. Zhu et al., *Sci. Bull.* (2021)
132. A. Zlokapa, S. Boixo, D. Lidar, arXiv (2020). arXiv:2005.02464 [quant-ph]

133. X. Mi et al., arXiv (2021), arXiv:2107.13571 [quant-ph]
134. X. Mi et al., *Science* **374**, 1479 (2021)
135. K. J. Satzinger et al., *Science* **374**, 1237 (2021)
136. S. Lloyd, *Pure State Quantum Statistical Mechanics and Black Holes*, Ph.D. Thesis, The Rockefeller University (1988), arXiv:1307.0378
137. S. Goldstein, J.L. Lebowitz, R. Tumulka, N. Zanghì, *Phys. Rev. Lett.* **96**, 050403 (2006)
138. S. Popescu, A.J. Short, A. Winter, *Nat. Phys.* **2**, 754 (2006)
139. P. Reimann, *Phys. Rev. Lett.* **99**, 160404 (2007)
140. J. Schliemann, A.V. Khaetskii, D. Loss, *Phys. Rev. B* **66**, 245303 (2002)
141. G.A. Álvarez, E.P. Danieli, P.R. Levstein, H.M. Pastawski, *Phys. Rev. Lett.* **101**, 120503 (2008)
142. B.M. Terhal, D.P. DiVincenzo, *Phys. Rev. A* **61**, 022301 (2000)
143. R. Somma, G. Ortiz, J.E. Gubernatis, E. Knill, R. Laflamme, *Phys. Rev. A* **65**, 042323 (2002)
144. J. Pedernales, R.D. Candia, I. Egusquiza, J. Casanova, E. Solano, *Phys. Rev. Lett.* **113**, 020505 (2014)
145. J. Bensa, M. Žnidarič, *Phys. Rev. X* **11**, 031019 (2021)
146. P. de Vries, H.D. Raedt, *Phys. Rev. B* **47**, 7929 (1993)
147. A. Smith, M.S. Kim, F. Pollmann, J. Knolle, *NPJ Quantum Inf.* **5**, 106 (2019)
148. B. Bertini, F. Heidrich-Meisner, C. Karrasch, T. Prosen, R. Steinigeweg, M. Žnidarič, *Rev. Mod. Phys.* **93**, 025003 (2021)
149. J. Richter, F. Jin, L. Knipschild, J. Herbrych, H. De Raedt, K. Michielsen, J. Gemmer, R. Steinigeweg, *Phys. Rev. B* **99**, 144422 (2019)
150. D.N. Page, *Phys. Rev. Lett.* **71**, 1291 (1993)
151. J. Gemmer, M. Michel, G. Mahler, *Quantum Thermodynamics* (Springer Berlin Heidelberg, 2010)
152. B.N. Balz, J. Richter, J. Gemmer, R. Steinigeweg, P. Reimann, Dynamical typicality for initial states with a preset measurement statistics of several commuting observables, in *Fundamental Theories of Physics* (Springer International Publishing, Berlin, 2018) pp. 413–433
153. T. Heitmann, J. Richter, D. Schubert, R. Steinigeweg, *Z. Naturforsch. A* **75**, 421 (2020)
154. A. Hams, H. De Raedt, *Phys. Rev. E* **62**, 4365 (2000)
155. J. Schnack, J. Richter, T. Heitmann, J. Richter, R. Steinigeweg, *Z. Naturforsch. A* **75**, 465 (2020)
156. S. Sugiura, A. Shimizu, *Phys. Rev. Lett.* **108**, 240401 (2012)
157. C. Bartsch, J. Gemmer, *Phys. Rev. Lett.* **102**, 110403 (2009)
158. T. Monnai, A. Sugita, *J. Phys. Soc. Jpn.* **83**, 094001 (2014)
159. J. Richter, M.H. Lamann, C. Bartsch, R. Steinigeweg, J. Gemmer, *Phys. Rev. E* **100**, 032124 (2019)
160. H. Endo, C. Hotta, A. Shimizu, *Phys. Rev. Lett.* **121**, 220601 (2018)
161. T.A. Elsayed, B.V. Fine, *Phys. Rev. Lett.* **110**, 070404 (2013)
162. T. Iitaka, T. Ebisuzaki, *Phys. Rev. E* **69**, 057701 (2004)
163. R. Steinigeweg, J. Gemmer, W. Brenig, *Phys. Rev. Lett.* **112**, 120601 (2014)
164. J. Richter, R. Steinigeweg, *Phys. Rev. B* **99**, 094419 (2019)
165. H. Fehske, J. Schleede, G. Schubert, G. Wellein, V.S. Filinov, A.R. Bishop, *Phys. Lett. A* **373**, 2182 (2009)
166. A. Nauts, R.E. Wyatt, *Phys. Rev. Lett.* **51**, 2238 (1983)
167. H. Tal-Ezer, R. Kosloff, *J. Chem. Phys.* **81**, 3967 (1984)
168. V.V. Dobrovitski, H.A.D. Raedt, *Phys. Rev. E* **67**, 056702 (2003)
169. J. Richter, T. Heitmann, R. Steinigeweg, *SciPost Phys.* **9**, 031 (2020)
170. J. Richter, D. Schubert, R. Steinigeweg, *Phys. Rev. Res.* **2**, 013130 (2020)
171. J. Richter, J. Herbrych, R. Steinigeweg, *Phys. Rev. B* **98**, 134302 (2018)
172. R. Steinigeweg, J. Herbrych, F. Pollmann, W. Brenig, *Phys. Rev. B* **94**, 180401 (2016)
173. D.J. Luitz, Y.B. Lev, *Ann. Phys. (Berlin)* **529**, 1600350 (2017)
174. R. Steinigeweg, A. Khodja, H. Niemeyer, C. Gogolin, J. Gemmer, *Phys. Rev. Lett.* **112**, 130403 (2014)

175. J. Wang, M.H. Lamann, J. Richter, R. Steinigeweg, A. Dymarsky, J. Gemmer, arXiv (2021). arXiv:2110.04085 [cond-mat.stat-mech]
176. D.A. Huse, R. Nandkishore, V. Oganesyan, A. Pal, S.L. Sondhi, Phys. Rev. B **88**, 014206 (2013)
177. A.C. Potter, R. Vasseur, Phys. Rev. B **94**, 224206 (2016)
178. Y. Li, M.P.A. Fisher, arXiv (2021). arXiv:2108.04274 [quant-ph]
179. C. Powers, L. Bassman, W.A. de Jong, arXiv (2021), arXiv:2109.01619 [quant-ph]
180. M. Motta, C. Sun, A.T.K. Tan, M.J. O'Rourke, E. Ye, A.J. Minnich, F.G.S. L. Brandão, G. K.-L. Chan, Nat. Phys. **16**, 205 (2019)

Entanglement Dynamics in Spin Chains with Structured Long-Range Interactions



Gregory S. Bentsen, Andrew J. Daley, and Johannes Schachenmayer

1 Introduction

The systems we encounter most often in condensed matter physics generally exhibit effective local interactions in regular 3D, 2D, or 1D structures. In these systems, correlations tend to spread and entanglement builds up in a way constrained by a so-called Lieb–Robinson bound—where the development of correlations in time is strong within a lightcone (often determined away from criticality by the maximum group velocity for quasiparticles in a system), and correlations tend to decay exponentially outside that lightcone. This constrains (or delays) the development of entanglement, especially between distant regions in such systems.

With quantum simulators in atomic, molecular, and optical physics, we now have opportunities to go beyond this paradigm. In non-relativistic settings, we can obtain effective long-range interactions, ranging from direct dipole–dipole interactions in polar molecules, to genuine long-range interactions for experimental setups such as chains of trapped ions (mediated by the collective motional modes of the trapped ions) or atoms in optical cavities (mediated by light in the cavity). Experiments with neutral atoms in tweezer arrays (where interactions are mediated by exciting atoms to a Rydberg level with high principal quantum number) typically give us short-ranged Van der Waals interactions, but we can generate effective long-range

G. S. Bentsen

Martin A. Fisher School of Physics, Brandeis University, Waltham, MA, USA
e-mail: gbentsen@brandeis.edu

A. J. Daley (✉)

Department of Physics and SUPA, University of Strathclyde, Glasgow, UK
e-mail: andrew.daley@strath.ac.uk

J. Schachenmayer

CNRS, ISIS (UMR 7006), and Université de Strasbourg, Strasbourg, France
e-mail: schachenmayer@unistra.fr

interaction graphs by moving atoms in the traps. This gives us the opportunity to ask how the build-up of entanglement changes in these unusual systems with long-range interactions.

In this chapter, we give an introduction to these concepts, beginning in Sect. 2 by describing techniques that can be used to analyze these systems (including Lieb–Robinson bounds, quasiparticle techniques, and numerical methods), before discussing examples of spin chains with interactions decaying with distance R as $R^{-\alpha}$ for some $\alpha \geq 0$ in Sect. 3, and then sparse coupling graphs in Sect. 4. Such sparse graphs could be used to realize fast scrambling of information, in which we build up entanglement on timescales growing as $t_* \propto \log(N)$ with the system size, N . In Sect. 5, we then briefly discuss the implementations of each of the classes of models that we treat in the chapter, across trapped ions, neutral atoms in optical cavities, and tweezer arrays for neutral atoms with Rydberg excitations.

2 Quantifying Entanglement and Information Spreading

2.1 Measures of Entanglement Entropy

Let us consider a quantum system Q defined on a Hilbert space \mathcal{H} , which we split into two sub-Hilbert spaces A and B , $\mathcal{H} = \mathcal{H}_A \otimes \mathcal{H}_B$ with dimensions $D_{A,B} = \dim(\mathcal{H}_{A,B})$. By definition, entanglement between A and B implies that a state $|\psi\rangle$ cannot be written in a product state form, i.e.,

$$|\psi\rangle \neq |\psi\rangle_A \otimes |\psi\rangle_B, \quad (1)$$

where the states $|\psi\rangle_{A,B}$ are defined on the sub-Hilbert spaces $\mathcal{H}_{A,B}$, respectively. The amount of entanglement can now be analyzed by constructing the reduced density matrix of either the sub-system A or B ; w.l.o.g., focusing on sub-system A , it is defined as

$$\rho_A = \text{tr}_B(|\psi\rangle\langle\psi|), \quad (2)$$

where the trace is taken over sub-system B . In case of a product state $|\psi_{\text{ps}}\rangle = |\psi_{\text{ps}}\rangle_A \otimes |\psi_{\text{ps}}\rangle_B$, the reduced density matrix trivially becomes $\rho_A^{\text{ps}} = |\psi_{\text{ps}}\rangle_A \langle\psi_{\text{ps}}|_A$ and is thus pure quantum states. This implies that all information about the state of sub-system A is contained in ρ_A and thus readily available through experimental probes of this sub-system. For a general entangled state that fulfills inequality (1), however, this is not true. The presence of entanglement implies that ρ_A will be a mixed density matrix. Now, information on the quantum state is encoded also in quantum correlations between A and B . Therefore, the entropy of ρ_A , i.e., the lack of information in ρ_A , provides a way to directly quantify the amount of such correlations.

Arguably, the most prominent definition for entropy is the von Neumann entropy,

$$S_A = S_{\text{VN}}(\rho_A) = -\text{tr}(\rho_A \log_2 \rho_A) = -\sum_{\alpha}^{D_A} \lambda_{\alpha} \log_2 \lambda_{\alpha}, \quad (3)$$

where in the last step we have introduced the positive eigenvalues of ρ_A , $\lambda_{\alpha} \geq 0$ that must fulfill $\sum_{\alpha} \lambda_{\alpha} = 1$. Note that the base of the logarithm in the definition varies throughout the literature, however for spin-1/2 models or qubits \log_2 is a convenient choice. For product states, it is easy to see that $S_{\text{VN}}(\rho_A^{\text{ps}}) = 0$ since the reduced density matrix only has one eigenvalue $\lambda_1 = 1$. The largest possible entropy occurs for maximally mixed states, for which all eigenvalues are $\lambda_{\alpha} = 1/D_A$, and thus for a bipartition of dimension D_A , the von Neumann entropy ranges between $0 \leq S_{\text{VN}}(\rho_A) \leq \log_2(D_A)$.

For example, considering a maximally entangled Bell state between two spin-1/2 particles, $|\phi^+\rangle = (|\uparrow\rangle \otimes |\uparrow\rangle + |\downarrow\rangle \otimes |\downarrow\rangle)/\sqrt{2}$, the reduced density matrix for the first spin becomes $\rho_1 = (|\uparrow\rangle\langle\uparrow| + |\downarrow\rangle\langle\downarrow|)/2$ corresponding to the largest possible von Neumann entropy of $S_{\text{VN}}(\rho_A) = -\log_2(1/2) = 1$.

Unfortunately, computing von Neumann entropies typically requires the knowledge of all eigenvalues of the reduced density matrix, i.e., knowledge of the full density matrix. Experimentally measuring full density matrices in experiments can be extremely cumbersome and becomes very difficult with increasing D_A . A quantity for measuring the ‘‘mixed-ness’’ of a reduced density matrix that can be experimentally more easily accessible is the purity $\text{tr}(\rho_A^2)$, or more generally, nonlinear functionals of the form $\text{tr}(\rho_A^n)$ with integer $n > 1$ [1, 2]. Those are directly connected to the Rényi entropy of order n , which is defined as

$$S_A^{(n)} = S_n(\rho_A) = \frac{1}{1-n} \log_2 \text{tr}(\rho_A^n). \quad (4)$$

Formally, taking n as an arbitrary real-valued number, the Rényi entropy becomes equivalent to the von Neumann entropy in the limit $S_{\text{VN}}(\rho_A) = \lim_{n \rightarrow 1} S_n(\rho_A)$. Furthermore, the second-order Rényi entropy provides a lower bound to the von Neumann entropy, $S_{\text{VN}}(\rho_A) \geq S_2(\rho_A)$, and combinations of different Rényi entropies can be constructed to yield stronger bounds such as $S_{\text{VN}}(\rho_A) \geq 2S_2(\rho_A) - S_3(\rho_A) \geq S_2(\rho_A)$, see Fig. 1.

In practical settings, entanglement entropies can be used to analyze the time-dependent growth of entanglement in spin chains after a quench both in experiments and theory. To avoid boundary effects and to accommodate as much entanglement as possible, it is common to split a chain of N spins into two halves of $N/2$ spins and to compute S_{VN} or S_n for the reduced density matrix of half of the chain. The time-dependent growth behavior of the entropy can then give important insight into the entanglement spreading and the correlation build-up in the chain. For example, a linear growth of S_{VN} or S_n can be a consequence of entangled quasiparticles with a linear dispersion relation (see below). Furthermore, linear entanglement growth

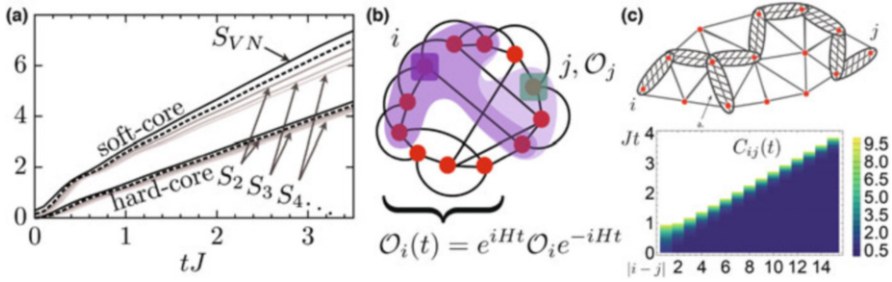


Fig. 1 Entanglement entropy, operator growth, and Lieb–Robinson Bounds. **(a)** The time-dependent growth of various entanglement entropies in a soft- and hard-core Bose–Hubbard model (hopping rate J). The hard-core model is equivalent to an XY spin chain. The Rényi entropies S_n can be experimentally more easily accessible than the von Neumann entropy S_{VN} . The Rényi entropies S_n for $n > 2$ constitute lower bounds to the von Neumann entropies S_{VN} and can be used in combination to construct tight bounds (dashed black line: $2S_2 - S_3$). Here, all entropies exhibit a growth behavior linear in time. Reprinted from [2]. **(b)** Growth of the operator $O_i(t)$ (purple) in the Heisenberg picture on a sparse nonlocal graph G . **(c)** Lieb–Robinson bounds for 2-local Hamiltonians. Top: The bound is obtained by summing over contributions from connected chains linking vertices i, j . Each new “link” in the chain need not be added at the end of the chain; it may be added anywhere along the chain as illustrated by the “dead end” link marked a. Bottom: Linear lightcone for a one-dimensional, nearest-neighbor spin chain (reproduced from [3])

can be connected to a computational complexity increasing exponentially in time (see Sect. 2.4) and is therefore of general interest for validating analog quantum simulation applications.

Note that in any realistic experiment, there will remain small but finite couplings to an environment. Then, the definition of entanglement as entropy in a bipartition becomes more delicate since a bipartition of the chain into two blocks is effectively a tripartition with the environment acting as third party. Then, entropy in sub-system A can originate from entanglement with the other chosen block B , or from entanglement with the environment. In such cases, statements about true entanglement in the chain can still be made in scenarios where the entropy of the full chain density matrix ρ remains sufficiently small, i.e., smaller than the sub-system entropies $S_{VN}(\rho) < S_{VN}(\rho_A)$ [or $S_n(\rho) < S_n(\rho_A)$].

Finally, what is the maximum amount of entanglement that a system of N degrees of freedom can support? Quantum states in which every particle is maximally entangled are referred to as *volume-law* or *scrambled* states and feature a von Neumann entropy $S_{VN} \propto |A|$ that grows like the number of degrees of freedom in region A for any bipartition $Q = A \cup B$ of the system (with $|A| < N/2$). Although such a high degree of entanglement is difficult to engineer in practice due to the destructive effects of decoherence, these volume-law states are actually quite generic, in the sense that a pure quantum state chosen uniformly at random from the

many-body Hilbert space will have, on average, volume-law entanglement entropy

$$S_{\text{VN}}(\rho_A) = -\frac{m-1}{2n} + \sum_{k=n+1}^{mn} \frac{1}{k} \approx \ln m - \frac{m}{2n} \quad (5)$$

so long as $1 \ll m \leq n$, where $|A| = \log_2 m$ and $|B| = \log_2 n$ [4].

2.2 Lieb–Robinson Bounds and OTOCs

In the previous section, we quantified entanglement growth by looking at the entropy of a local region A , quantified by the von Neumann entropy of the reduced density matrix ρ_A . Complementary to this state-centric notion of entanglement based on the Schrödinger picture, one can alternatively formulate an operator-centric notion of entanglement growth based on the Heisenberg picture. In many cases, this operator growth picture provides a more intuitive description for the growth of correlations in the system. It also naturally leads to discussion of fundamental Lieb–Robinson (LR) bounds and out-of-time-order correlators (OTOCs) that diagnose the spread of quantum information in the system.

Suppose we consider a system of N qubits, and we store information in a localized region A using an operator O_A . In particular, one can imagine starting from a particular reference state ρ and perturbing it by some local operator O_A that encodes some information in the perturbed state. The subsequent growth of correlations in the system can be completely captured by the evolution of the operator O_A in the Heisenberg picture:

$$O_A(t) = U_t O_A U_t^\dagger = \sum_{\mathbf{r}} a_{\mathbf{r}}(t) \sigma^{\mathbf{r}}. \quad (6)$$

In the last expression, we have expanded the operator in the orthonormal basis of many-body Pauli strings $\sigma^{\mathbf{r}} = \sigma_1^{r_1} \sigma_2^{r_2} \dots \sigma_N^{r_N}$, where $\sigma_i^{0,1,2,3}$ are the Pauli matrices on site i (with $\sigma_i^0 = \mathbb{I}_i$) and $\mathbf{r} = r_1 r_2 \dots r_N$ is a N -component string encoding which Pauli operators are present on each site. The time-dependent coefficients $a^{\mathbf{r}}(t)$ can be viewed as the “wavefunction” of the operator $O_A(t)$ when expanded in the Pauli string basis and can be obtained by taking an operator inner product

$$a_{\mathbf{r}}(t) = \text{Tr} [O_A(t) \sigma^{\mathbf{r}}]. \quad (7)$$

These coefficients are real and normalized $\sum a_{\mathbf{r}}(t)^2 = 1$ when O_A is Hermitian and normalized.

Under generic scrambling dynamics, the initially localized operator $O_A(0)$ rapidly grows into a complicated operator $O_A(t)$, where the operator wavefunction $a_{\mathbf{r}}(t)$ acquires significant weight on large many-body Pauli strings. We can

characterize this growth and simultaneously characterize the coefficients $a_r(t)$, by considering commutators $[O_A, \sigma_j^\alpha]$ between the growing operator O_A and localized Pauli operators σ_j^α , which we refer to as “probe” operators. A judicious choice of probe operators allows one to quantitatively map out the growth of the operator $O_A(t)$. In particular, at $t = 0$, probe operators σ_j^α localized on sites outside of the region A must necessarily commute with O_A : $[O_A(0), \sigma_j^\alpha] = 0$. As the operator $O_A(t)$ grows in time, however, it builds up nonzero weight on operators outside of A , causing the probe operators to fail to commute with $O_A(t)$: $C(t) = [O_A(t), \sigma_j^\alpha] > 0$. The size of this commutator, as measured by the operator norm $\|C(t)\| = \sqrt{\text{Tr}[C^\dagger C]}$, tells us “how much” of the operator O_A is present on site j (i.e., what fraction of O_A acts nontrivially on site j) (see Fig. 1b). These commutators provide direct evidence of entanglement growth in the system via a nonstandard correlation function called the out-of-time-order correlator (OTOC) [5–7].

Analysis of these commutators can be used to place fundamental bounds on the spread of information in the quantum system.

Historically, Lieb–Robinson bounds have been used to show the existence of an emergent “lightcone” in lattice systems that limits the speed of information propagation, similar to the speed of light in special relativity. Various forms of Lieb–Robinson bounds have been established for systems featuring both short-range [8, 9] and long-range [10–13] interactions. Here, we present generalized Lieb–Robinson bounds that apply to arbitrary 2-local Hamiltonians defined on any graph G , regardless of its connectivity or locality. In doing so, we demonstrate how the growth of operators $O_i(t)$ is intimately tied to the structure of the interaction graph. The beauty of this approach is that it expresses the spread of quantum information in terms of standard results from graph theory, a well-developed branch of mathematics for which many powerful techniques and results are readily available [14–16]. We therefore begin by introducing the requisite graph theory terminology.

For simplicity, we will consider here only 2-local Hamiltonians. Similar results for the more general k -local case are derived in Appendix B of Ref. [17]. To any 2-local Hamiltonian

$$H = \sum_{(i,j) \in E} H_{ij}, \quad (8)$$

we may associate a discrete, undirected graph $G = (V, E)$, where degrees of freedom live on the vertices $i \in V$ and interact pairwise via couplings H_{ij} if and only if the pair i, j is connected by an edge $e = (i, j) \in E$. The connectivity of the graph G is described by the *adjacency matrix*

$$\mathcal{A}_{ij} = \begin{cases} 1 & (i, j) \in E \\ 0 & (i, j) \notin E \end{cases} \quad (9)$$

and the *degree matrix* $\mathcal{D}_{ij} = k_i \delta_{ij}$, where the *degree* $k_i = \sum_j \mathcal{A}_{ij}$ of a given vertex i counts the number of vertices it is connected to. To be concrete, a familiar model of this form is the 2-dimensional Heisenberg spin model

$$H = J \sum_{\langle i,j \rangle} \mathbf{S}_i \cdot \mathbf{S}_j, \quad (10)$$

with interaction graph G given by a regular D -dimensional square lattice where the sum is over nearest neighbors $\langle i, j \rangle$. The spin-1/2 degrees of freedom \mathbf{S}_i reside on the vertices i of the lattice and interact via nearest-neighbor $SU(2)$ -symmetric 2-body terms $H_{ij} = J \mathbf{S}_i \cdot \mathbf{S}_j$ represented by the edges e of the graph, such that all vertices have degree $k_i = 4$ (assuming an infinite lattice).

We derive Lieb–Robinson bounds for 2-local models of the form (8) by expanding the commutator $C(t)$ in powers of t and bounding each term in the sum. For probe operators O_i, O_j on vertices $i \neq j$, we have

$$\|[O_j, O_i(t)]\| \leq \|[O_j, O_i]\| + t \|[O_j, [H, O_i]]\| + \frac{t^2}{2!} \|[O_j, [H, [H, O_i]]]\| + \dots, \quad (11)$$

where we have used the Baker–Campbell–Hausdorff formula to expand the exponentials in terms of nested commutators, and the triangle inequality to bound the commutator norm. The nested commutators on the right-hand side simplify considerably when we observe that commutators on disjoint sets vanish so that, for instance, $[O_j, [H, O_i]] = [O_j, [H_{ij}, O_i]]$. As a result, the only nested commutators that survive are those corresponding to connected chains of 2-body terms $(H_{jx}, H_{xy}, \dots, H_{zi})$ on the interaction graph G that begin on vertex j and end on vertex i , as illustrated in Fig. 1c. Note that the consecutive links of these chains need not connect end-to-end: new links are allowed to be connected *anywhere* along the existing chain. For simplicity, we have also ignored all onsite terms (which can always be absorbed into the two-site terms in (8)). The fact that the bound can be written in terms of connected chains on the graph clearly illustrates that the structure of the interaction graph G plays a central role in our bounds on OTOC growth. We further simplify the right-hand side by applying the inequality $\|[A, B]\| \leq 2 \|A\| \|B\|$ recursively to the nested commutators to obtain

$$\frac{\|[O_j, O_i(t)]\|}{2 \|O_j\| \|O_i\|} \leq 1 + 2t \|H_{ij}\| + \frac{(2t)^2}{2!} \sum_x \|H_{jx}\| \|H_{xi}\| + \dots \quad (12)$$

Finally, we choose a constant c that bounds all 2-body terms in the Hamiltonian

$$\frac{c}{K} \geq \|H_{ij}\|, \quad (13)$$

where $K = \frac{1}{N} \sum_i k_i$ is the mean degree of the graph G and c is a constant independent of N such that the Hamiltonian is extensive [10, 17]. Substituting the constant c/K into Eq. (12) and resumming the right-hand side, we obtain the normalized out-of-time-ordered correlator (OTOC):

$$C_{ij}(t) \equiv \frac{\| [O_j, O_i(t)] \|}{2 \| O_j \| \| O_i \|} \leq \exp \left[\frac{2c|t|}{K} (\mathcal{D} + \mathcal{A}) \right]_{ij}, \quad (14)$$

which depends only on the graph-theoretic quantities $\mathcal{A}_{ij}, \mathcal{D}_{ij}$ and time t in units of the constant c/K [17].

As a simple example, we can consider a one-dimensional chain with closed boundary conditions. In this case, the matrix $\mathcal{A} + \mathcal{D}$ is simply a circulant matrix:

$$\mathcal{A} + \mathcal{D} = \begin{bmatrix} 2 & 1 & 0 & 0 & \dots & 1 \\ 1 & 2 & 1 & 0 & & 0 \\ 0 & 1 & 2 & 1 & & 0 \\ \vdots & & & & \ddots & \\ 1 & 0 & 0 & 0 & & 2 \end{bmatrix} \quad (15)$$

that can be easily diagonalized. From this result, we recover a linear lightcone, plotted in Fig. 1c, as originally predicted by Lieb and Robinson [8]. The generalized Lieb–Robinson bound in Eq. (14), however, is more powerful than the original result of Lieb and Robinson because it applies not only to regular lattice systems but also to quantum systems defined on arbitrary interaction graphs G . Moreover, the generalized bound contains detailed information about the graph structure, encoded in the matrices \mathcal{A}, \mathcal{D} .

Because the result in Eq. (14) bounds the operator norm $\|\cdot\|$, the bound characterizes operator growth at *infinite temperature* since $\|O\|^2 = \text{Tr} [\rho^\infty O^\dagger O]$, where ρ^∞ is the infinite-temperature ensemble. At finite temperature, operators necessarily grow more slowly; obtaining tighter bounds at finite temperature is still an open problem [17–20]. We generally expect the spreading of information to slow down at finite temperature since the system has a much smaller probability of exciting high-energy modes. Roughly speaking, another way to say this is that at finite temperature the effective Hilbert space is reduced to a subspace consisting of eigenvectors whose energies are comparable to or less than the temperature. Because of this reduced Hilbert space, there are fewer accessible states and therefore fewer ways for information to propagate.

2.3 Quasiparticle Approaches

The spreading of correlations through a system and its limitations in terms of Lieb–Robinson bounds is connected to the growth of entanglement entropies after quenches. This connection can be made by means of quasiparticle excitations in situations where a quadratic Hamiltonian can be brought to a diagonal form in second quantization. To illustrate the concept, let us take a long-range transverse Ising spin chain with interactions decaying as a power law. The Hamiltonian can be written as

$$H_{\text{LRTI}} = \sum_{i < j} \frac{\bar{J}}{|i - j|^\alpha} \sigma_i^x \sigma_j^x + B \sum_i \sigma_i^z. \quad (16)$$

Here, \bar{J} is the nearest-neighbor interaction strength, α is the power-law decay exponent, B is the transverse field strength, and $\sigma_i^{x,z}$ are the usual Pauli matrices. In one dimension, the Pauli matrices can be mapped to fermionic field operators c_i by a Jordan–Wigner transformation. Then, in the nearest-neighbor limit $\alpha \rightarrow \infty$ after a transformation to quasimomentum space, the fermionic model is quadratic and can be diagonalized with a Bogoliubov transformation [21] giving rise to a Hamiltonian of the form (up to constants)

$$H_{\text{LRTI}}^{\alpha \rightarrow \infty} = \sum_q \epsilon_q \gamma_q^\dagger \gamma_q. \quad (17)$$

Here, γ_q^\dagger are creation operators for fermionic quasiparticle excitations with quasimomentum q . They are superpositions of the fermionic field operators c_q with opposite quasimomenta $\gamma_q^\dagger = u c_q^\dagger - v c_{-q}$, where u and v are the Bogoliubov expansion coefficients, which depend on \bar{J} and B . The dispersion relation for the quasiparticles is given by $\epsilon_q = 2\sqrt{(\bar{J} - B)^2 + 4\bar{J}B \sin^2(q/2)}$. In a quench setup, the initial state is a highly excited state, which is not an eigenstate of the diagonal quasiparticle Hamiltonian. This gives rise to the following picture for entanglement build-up in the dynamics after the quench [22] (see illustration in Fig. 2a): The initially highly excited state serves as reservoir for producing quasiparticle excitations. Those quasiparticles are entangled superpositions of excitations with opposite momentum and spread through the system. The speed of their propagation is given by the group velocity $v_g = d\epsilon_q/dq$. For example, in the case of the nearest-neighbor transverse Ising model, their speed is limited by the maximum group velocity $\max |v_g| = 2J$. The propagating entangled pairs lead to a build-up of entanglement between blocks of the chain. A constant arrival rate of quasiparticles in the right half of the chain (R) that originated in the left half (L) therefore leads to a linear growth of entanglement entropies between L and R with time [22].

Importantly, the study of quasiparticle spectra can also be a useful approach for understanding entanglement growth in the presence of long-range interactions.

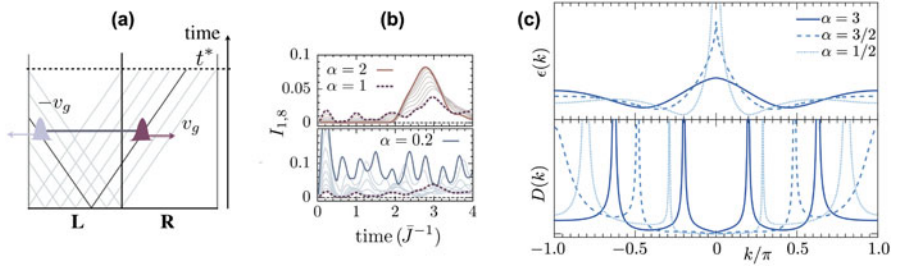


Fig. 2 (a) Illustration of entanglement distribution by propagation of entangled quasiparticles. Entangled quasiparticles spread through the system in opposite directions with group velocities $\pm v_g$. Finite size effects become important when the fastest quasiparticles reach the boundary, here at time t^* . This picture remains valid for relatively short-ranged interactions. (b) Quasiparticle propagation seen in the evolution of the mutual information I between distant spins $i = 1$ and $j = 8$ (here for a quench in a transverse Ising model with interactions decaying as a power law with distance $\sim \bar{J}/|i - j|^\alpha$). For relatively short-ranged interactions ($\alpha = 2$), the distant spins suddenly become entangled by a quasiparticle arrival at a time $t\bar{J} \sim 2$. For longer-ranged interactions $\alpha < 2$, this picture breaks down. (c) Entanglement growth can be analyzed by means of quasiparticle spectra. Here, quasiparticle dispersion relations $\epsilon(k)$ and the corresponding densities of states $D(k)$ are shown for an exactly solvable long-range fermionic hopping model (power-law exponent α , see [23]). Shorter-range interactions (large α) lead to smooth $\epsilon(k)$ and thus quasiparticles with well-defined group velocities. Long-range hoppings (small α) can lead to cusps and divergences in $\epsilon(k)$. ((a) and (b) reproduced from [24], (c) reproduced from [23])

While in general a Bogoliubov diagonalization is not possible for Hamiltonians such as (16), exceptions exist. For example in certain limits, linear spin-wave theories remain a valid approximation [23, 25, 26], or for related models with long-range fermionic hopping, also exact diagonalizations are sometimes possible [23, 27, 28].

We will exemplify the linear spin-wave approach for Hamiltonian (16), which is based on Holstein–Primakoff transformation. Traditionally defined for spin- S operators, this transformation reads

$$S_i^z = a_i^\dagger a_i - S \quad (18)$$

$$S_i^- = \sqrt{2S - a_i^\dagger a_i} a_i \quad (19)$$

$$S_i^+ = a_i^\dagger \sqrt{2S - a_i^\dagger a_i}. \quad (20)$$

Here, the spin operators for a spin at site i are expressed in terms of bosonic field operators a_i^\dagger . We assume a quench setup, where the initial state is given by the fully polarized state $|\psi(t=0)\rangle = \prod_i |\downarrow\rangle_i$ with $S_i^z |\downarrow\rangle_i = -S |\downarrow\rangle_i$. For short enough times where the state remains sufficiently close to $|\psi(t=0)\rangle$, one can linearize the Holstein–Primakoff transformation using the assumption of small occupation

number of the bosonic modes, $\langle a_i^\dagger a_i \rangle \ll 2S$. Then,

$$S_i^- \approx \sqrt{2S} a_i \quad (21)$$

$$S_i^+ \approx \sqrt{2S} a_i^\dagger. \quad (22)$$

Using $\sigma_i^z = 2a_i^\dagger a_i - 1$ and $\sigma_i^x \approx a_i + a_i^\dagger$ in this limit, Hamiltonian (16) becomes quadratic (constants are dropped):

$$H_{\text{LRTI}} \approx \sum_{i < j} \frac{\bar{J}}{|i-j|^\alpha} \left(a_i a_j + a_i^\dagger a_j + a_i a_j^\dagger + a_i^\dagger a_j^\dagger \right) + 2B \sum_i a_i^\dagger a_i. \quad (23)$$

A discrete Fourier transform into quasimomentum space for a spin chain with N spins, $b_q = \sum_j \exp(-iqj)/\sqrt{N}$ for N discrete momentum values $-\pi/2 < q \leq \pi/2$, leads to

$$H_{\text{HP}} \approx \sum_q \mathcal{J}(q) \left(b_{-q} b_q + b_q^\dagger b_{-q}^\dagger \right) + \sum_q \left(\mathcal{J}(q) + \frac{B}{2} \right) \left(b_q^\dagger b_q + b_{-q} b_{-q}^\dagger \right). \quad (24)$$

Here a crucial quantity is the Fourier transform of the power-law decaying function

$$\mathcal{J}(q) = \bar{J} \sum_d \frac{e^{-idq}}{|d|^\alpha} \xrightarrow{N \rightarrow \infty} 2\bar{J} \text{Re} \left(\text{Li}_\alpha(e^{iq}) \right), \quad (25)$$

where in the first term the distance d runs over all pairwise distances from $-N+1 < d < N-1$ and the last term is an analytical expression in terms of the polylogarithm $\text{Li}_n(z)$ of order n in the infinite system size limit $N \rightarrow \infty$.

Using a bosonic Bogoliubov transformation [23], the Hamiltonian can again be transformed into a diagonal form with new bosonic field operators that are a superposition of the Holstein–Primakoff bosons $b_{\pm q}$ of opposite momenta. Crucially, the dispersion relation of the new quasiparticle excitations can be computed to be

$$\epsilon(q) = 2B \sqrt{1 + \frac{\mathcal{J}(q)}{B}}. \quad (26)$$

It is important to re-emphasize that this quasiparticle dispersion result is only valid in the limit $\langle b_q^\dagger b_q \rangle \ll 1$, which is true for sufficiently short times, i.e., sufficiently few quasiparticle excitations. It is clear that the timescale of validity increases with B since for $B \rightarrow \infty$ the initial state $|\psi(t=0)\rangle$ becomes an eigenstate and remains constant in time. The constraint of the validity of the Holstein–Primakoff ansatz is also visible in Eq. (26), which requires $B > \mathcal{J}(q)$ for $\epsilon(q)$ to remain real.

In the limit of its validity, Eq.(26) allows to make statements about the quasiparticle nature of the entangling dynamics after the quench. For example, considering the limit of long-wavelength excitations $|q| \rightarrow 0$, one can derive that the limiting behavior of the dispersion relation for $\alpha < 0$ is given by

$$\epsilon(q) \propto q^{\frac{\alpha-1}{2}}. \quad (27)$$

The negative exponent implies that for $\alpha < 1$, there are quasiparticle excitations with infinite group velocities that ultimately have to lead to a breakdown of the picture of propagating entangled quasiparticles. Furthermore, from this analytical ansatz, one can deduce that for $1 < \alpha < 2$ a cusp at $q = 0$ appears in the dispersion relation $\epsilon(q)$. This means that the group velocity $v_g = d\epsilon(q)/dq$ is already starting to diverge for $\alpha \lesssim 2$ [25]. In contrast, in general for $\alpha \gtrsim 2$, the quasiparticle propagation picture remains to be valid, as e.g. demonstrated in Fig. 2b. There we show the propagation of correlations between spins at two distant sites $i = 1$ and $j = 8$ of a chain. Here this correlation is quantified by the mutual information $I_{i,j} = S_{\text{VN}}(\rho_i) + S_{\text{VN}}(\rho_j) - S_{\text{VN}}(\rho_{ij})$ with $S_{\text{VN}}(\rho_i)$ and $S_{\text{VN}}(\rho_{ij})$ the von Neumann entropies of reduced density matrices on single- and two-spin Hilbert spaces, respectively. For the case of a clear entangled quasiparticle propagation ($\alpha = 2$), the correlation between distant sites suddenly starts to establish at a ‘‘quasiparticle’’ arrival time of $t\bar{J} \sim 2$. In contrast, for $\alpha < 2$, the distant sites become entangled immediately.

Finally, we want to point out that in a quasiparticle analysis, it is important to not only consider quasiparticle dispersion relations, but also to analyze the density of states at the respective quasimomenta. In Fig. 2c, we show the dispersion relation $\epsilon(k)$ and the density of states $D(k)$ for Bogoliubov excitations with quasimomentum k for a long-range fermionic hopping model [23] that can be computed exactly. Interestingly, qualitatively, this model has very similar features as the long-range interacting transverse Ising model in the linear spin-wave limit. Importantly, one finds that while the group velocity diverges for $\alpha < 2$ and $k \rightarrow 0$, here one also finds that $D(k) \rightarrow 0$ is even more strongly suppressed, leading to an effective overall suppression of the correlation build-up.

2.4 Matrix Product States (MPS)

In one dimension, the study of entanglement growth in spin models can be assisted by very powerful numerical methods based on the so-called matrix product states (MPS). Let us consider the general time-evolved state of a chain with N spin- D particles and focus on pure Hamiltonian dynamics. The state at time t can be written

in the basis of the local spin Hilbert spaces:

$$|\psi(t)\rangle = \sum_{i_1, i_2, \dots, i_N} c_{i_1, i_2, \dots, i_N}(t) |i_1\rangle |i_2\rangle \dots |i_N\rangle. \quad (28)$$

Here, $i_n = 1, \dots, d$ are the local indices for an orthogonal basis of spin n , $|i_n\rangle$, with dimension $d = 2S + 1$. The difficulty of numerically simulating Hamiltonian dynamics of a spin chain on a classical computer stems from the exponential growth of the size of the complex states tensor c_{i_1, i_2, \dots, i_N} with system size N , $\dim(c_{i_1, i_2, \dots, i_N}) = d^N$. Importantly, the size of this state tensor can be drastically reduced by restricting the amount of entanglement. For example, let us consider the most extreme scenario and restrict the state tensor to product states only, which by definition excludes any entanglement. Then,

$$c_{i_1, i_2, \dots, i_N}^{\text{PS}}(t) \approx c_{i_1}^{[1]}(t) c_{i_2}^{[2]}(t), \dots, c_{i_N}^{[N]}(t), \quad (29)$$

and the state representation only requires Nd normalized complex amplitudes, $\sum_{i_n} |c_{i_n}^{[n]}(t)| = 1$. Choosing for example some sub-system block A with indices $\{i_1, \dots, i_c\}$, the reduced density matrix is

$$\rho_A^{\text{PS}}(t) = \sum_{\substack{i_1, \dots, i_c \\ j_1, \dots, j_c}} c_{j_1}^*(t) c_{i_1}(t) \dots c_{j_c}^*(t) c_{i_c}(t) |i_1\rangle \dots |i_c\rangle \langle j_1| \dots \langle j_c|. \quad (30)$$

This is a pure density matrix since $\text{tr} \left\{ [\rho_A^{\text{PS}}(t)]^2 \right\} = 1$, and therefore, the entanglement entropy (see Sect. 2.1) vanishes, $S_{\text{VN}}(\rho_A^{\text{PS}}(t)) = 0$, for all times. Therefore, by choosing the product state ansatz (29), the numerical memory requirement is drastically reduced from $\mathcal{O}(d^N)$ to $\mathcal{O}(dN)$, which however comes at the cost of neglecting entanglement entropies entirely.

A matrix product state (MPS) can be thought of as a generalization of the product state ansatz (29) to states with finite entanglement. An MPS is a decomposition of the state tensor of the form

$$c_{i_1, i_2, \dots, i_N}^{\text{MPS}} = \Gamma_{i_1}^{[1]} \Gamma_{i_2}^{[2]} \dots \Gamma_{i_N}^{[N]} = \sum_{\alpha_1}^{\chi_1} \sum_{\alpha_2}^{\chi_2} \dots \sum_{\alpha_{N+1}}^{\chi_{N+1}} \Gamma_{i_1}^{[1]; \alpha_1 \alpha_2} \Gamma_{i_2}^{[2]; \alpha_2 \alpha_3} \dots \Gamma_{i_N}^{[N]; \alpha_N \alpha_{N+1}}. \quad (31)$$

Here we introduced N three-dimensional tensors, $\Gamma_{i_n}^{[n]; \alpha_n \alpha_{n+1}}$, which can be thought of as $\chi_n \times \chi_{n+1}$ matrices where the matrix elements are local kets on site n , $\Gamma_{i_n}^{[n]}$. The state tensor is decomposed into a matrix multiplication of the $\Gamma_{i_n}^{[n]}$ matrices on different sites, hence the name matrix product state. A common diagrammatic depiction of an MPS is shown in Fig. 3a: There, each colored box denotes an MPS

tensor $\Gamma_{i_n}^{[n]}$. Each line represents an index, and each line connecting the colored boxes implies a summation over that index. A tensor at site n connects to the tensors at sites $n - 1$ and $n + 1$, and the connecting indices α_n are also known as “bond indices.” Note that at the edge we kept two “dummy indices” for which (assuming the case of box boundary conditions) we will choose $\chi_1 = \chi_{N+1} = 1$. Note that if we restrict all virtual “bond” indices to a dimension of $\chi_n = 1$, the MPS decomposition (31) becomes equivalent to the product state form (29) and again neglects entanglement. The core idea behind MPS simulations of quantum states is to increase the matrix size to a manageable magnitude, thereby allowing for enough entanglement in the dynamics to keep the simulation of the system exact. In a key approximation step, we therefore can limit the bond dimensions of all bipartitions in the chain to a numerically manageable value, $\chi_n \lesssim \chi$. One can then show [29] that in an MPS with maximum bond dimension χ we can at most capture an entanglement entropy of

$$S_{\text{VN}}(\rho_A^{\text{MPS},\chi}) \leq \log_2(\chi). \quad (32)$$

Generalizing the result for the product state ansatz, an MPS with maximum bond dimension χ reduces the memory requirement for storing a quantum state from $\mathcal{O}(d^N)$ to $\mathcal{O}(Nd\chi^2)$. This comes at the cost of limiting von Neumann entanglement entropy across any bipartition to $\log_2(\chi)$. Note again that the product state ansatz is equivalent to $\chi = 1$ for which $S_{\text{VN}}(\rho_A^{\text{MPS},\chi=1}) = 0$.

The MPS representation (31) has been an extremely useful tool for both analyzing ground states of quantum many-body systems, e.g., the famous density matrix renormalization algorithm (DMRG) [30] is based on MPS, and studying non-equilibrium dynamics. Focusing on quench dynamics, typically, the initial states of interest are either in a trivial product state form (e.g., the fully polarized state, $|\psi(t=0)\rangle = \prod_i |\downarrow\rangle_i$) or they are the ground state of a Hamiltonian that can be computed using DMRG. To then compute the time evolution of a many-body quantum state over a time step, Δt , one needs an algorithm to update the MPS tensors time dependently such that ($\hbar \equiv 1$)

$$|\psi(t + \Delta t)\rangle = e^{-i\hat{H}\Delta t} |\psi(t)\rangle. \quad (33)$$

Several algorithms exist (for sketches of the concepts, see Fig. 3b–d).

For example, algorithms can be devised on the concept of “gate applications.” In particular, since most spin Hamiltonians of interest are based on two-body terms, i.e., Hamiltonians are of the form $\hat{H} = \sum_{i>j} \hat{H}_{i,j}$, one can use a Trotter decomposition of the full matrix exponential $e^{-i\hat{H}\Delta t}$ into two-site gates $\hat{U}_{i,j} = e^{-i\hat{H}_{i,j}\Delta t}$ up to a controllable error depending on a small time-step size Δt [31]. For example, commonly a 2-nd- or 4-th-order decomposition is used with errors $\mathcal{O}(\Delta t^3)$ or $\mathcal{O}(\Delta t^5)$, respectively. Then time evolution can be simulated by applying the two-site gates $\hat{U}_{i,j}$ to an MPS. Note that this approach is equivalent to the concept of

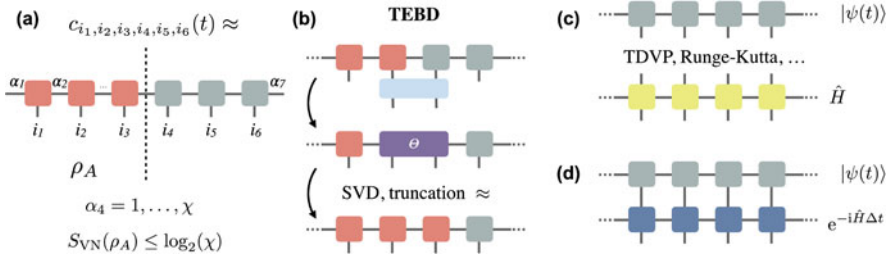


Fig. 3 (a) Sketch of an MPS decomposition of the state tensor in a system with $N = 6$ spins. Limiting the virtual indices α_n to a maximum bond dimension $\alpha_n \leq \chi$, the von Neumann entanglement entropy for a bipartite splitting across the bond n is limited to $\log_2(\chi)$. (b–d) Sketches of various algorithms for time-evolving an MPS. (b) The TEBD algorithm is a prescription for updating two tensors of the MPS after application of a gate. An approximation is made in the final step when after a singular value decomposition of the tensor Θ the new virtual index is truncated to $\alpha_n \leq \chi$. Using a Trotter decomposition of the time-evolution operator $e^{-i\hat{H}\Delta t}$ into two-site gates in combination with swap gates can be used to simulate time evolution under Hamiltonians with long-range interactions. (c) Another class of MPS time-evolution algorithms makes use of a matrix product operator (MPO) description of the Hamiltonian, using, e.g., the time-dependent variational principle (TDVP) or Runge–Kutta. They rely on variational algorithms to find an MPS approximation for the state $\hat{H} |\psi(t)\rangle$. (d) When the time-evolution operator can be constructed in MPO form, variational algorithms to find an MPS approximation for $e^{-i\hat{H}\Delta t} |\psi(t)\rangle$ can be used

digital quantum simulation [32], where the gates would be applied in a quantum circuit. An algorithm to apply two-site gates between neighboring spins is known as time-evolving block decimation algorithm (TEBD) [33] or time-dependent DMRG [34]. The scheme is sketched in Fig. 3b. It relies on straightforward tensor contraction, followed by a singular value decomposition. Crucially, the final step consists of a truncation of the bond dimension to χ , which introduces a gate error depending on the truncated weight, $\sum_{\alpha=\chi+1}^{d\chi} \lambda_{\alpha}^2$. One main disadvantage of the TEBD approach is that an error is made in each gate application. For treating systems with long-range couplings, it is also required to apply swap gates that interchange the physical indices between sites, which again result in an additional error for each swap operations.

To avoid such consecutive errors, it is also possible to construct the Hamiltonian in a matrix product form. In general, the matrix product operator (MPO) form is a full description of operators on a many-body Hilbert space analogous to MPS, but with two physical indices per site (see Fig. 3c, d for a sketch). There exist variational algorithms that, for an MPO (\hat{O}) and an MPS $|\psi\rangle$, find an optimal new MPS $|\phi\rangle$ with bond dimension χ such that $|\phi\rangle \approx \hat{O} |\psi\rangle$ with a known minimal error $\epsilon = |\langle \phi | \psi \rangle|^2 \ll 1$. Typically, such algorithms make use of sweeps, consecutively updating the tensors on single or neighboring sites [29]. For nearest-neighbor Hamiltonians, it is straightforward to construct \hat{H} in an exact MPO form. For systems with long-range interactions, this can usually be done approximately. In particular, systems with power-law interactions allow to approximate \hat{H} with

an MPO of moderate MPO bond dimension by utilizing an expansion of the power-law decay into a sum of exponentials (see, e.g., [35]). Having an algorithm that can apply a Hamiltonian MPO to a state (Fig. 3c) approximately, one can then rely on standard time-evolution algorithms making use of such Hamiltonian applications, such as Runge–Kutta. A popular algorithm making use of Hamiltonian applications is for example based on the time-dependent variational principle (TDVP), which in addition to the Hamiltonian application also relies on an application of a tangent space projection operator, see e.g., [36]. Lastly, an alternative way for simulating time evolution of an MPS is to directly compute an MPO expression of the time-evolution operator over a small time step $\hat{U} = e^{-i\hat{H}\Delta t}$ and to use an MPO application algorithm directly. Several ways have been proposed to construct a time-evolution MPO, e.g., based on Taylor expansions of the matrix exponential (e.g., notably the so-called $W^{1,II}$ representations [37] or methods based on “MPO doubling” [38]). In general, the computational complexity for evolving an MPS in time with one of the algorithms described above is bottle-necked by the tensor constructions and in general the computational timescales as $\sim \chi^3$. For a recent review summarizing MPS time-evolution algorithms, see e.g., [39].

Finally, let us emphasize again that MPSs provide an ideal tool to study entanglement growth after quenches. The eigenvalues of reduced density matrices of bipartitions, $\lambda_{\alpha_n}^2$, are readily available from an MPS, and entanglement entropies can be computed through Eqs. (3) and (4) (see Fig. 1 for an example MPS result of entanglement growth). MPS methods make it also possible to directly connect the entanglement entropy growth behavior after a quench to a numerical complexity for simulating the quench dynamics on a classical computer. For example, in the case of a linear entropy growth as shown in Fig. 1, we can conclude that since $S_{VN} \propto t$ and since for an MPS with bond dimension χ , $S_{VN} \leq \log_2(\chi)$ as a function of time χ needs to grow as $\chi \propto \exp(t)$, and therefore, this scenario is computationally hard to simulate with an MPS.

3 Power-Law Interacting Models

Here, we will focus on spin models with long-range interactions that decay as a function of the distance between spins with a power law, i.e., with interactions of the form

$$J_{ij} \propto \frac{1}{|\mathbf{r}_i - \mathbf{r}_j|^\alpha}. \quad (34)$$

Here, \mathbf{r}_i are the spin position vectors, and $\alpha \geq 0$ is the power-law exponent. The main motivation for considering such interactions is that they are realized in nature, e.g., in the case of electromagnetic interactions (Coulomb: $\alpha = 1$, dipole–dipole: $\alpha = 3$, van der Waals: $\alpha = 6$). Furthermore, they allow to arrive at mathematical conclusions depending on only a single parameter, α . The fact that

interactions always decay as a function of distance allows to also keep a notion of “dimensionality.” With respect to the dimensionality d , one can classify the range of interactions into “true” long-range interactions for $\alpha < d$, in which case interaction energy of the system diverges in the infinite system limit, and to scenarios where $\alpha > d$ and the interaction energy remains finite.

In a very general form, we can define our power-law interacting spin models of interest as

$$\hat{H} = \sum_{i>j} \left(J_{ij}^x S_i^x S_j^x + J_{ij}^y S_i^y S_j^y + J_{ij}^z S_i^z S_j^z \right) + \sum_i \mathbf{h}_i \cdot \mathbf{S}_i \quad \text{with} \quad J_{ij}^{x,y,z} = \frac{\bar{J}^{x,y,z}}{|\mathbf{r}_i - \mathbf{r}_j|^\alpha}. \quad (35)$$

Here, $\mathbf{S}_i = (S_i^x, S_i^y, S_i^z)$ is a vector of the three spin- S operators $S_i^{x,y,z}$. The long-range coupling constants are denoted as $J_{ij}^{x,y,z}$, and they quantify the interaction energy of two spins at distance $|\mathbf{r}_i - \mathbf{r}_j|$ when they are both aligned along the x, y, z direction, respectively. $\bar{J}_{ij}^{x,y,z}$ quantifies the energy at unit distance $|\mathbf{r}_i - \mathbf{r}_j| \equiv 1$. In the following, we will focus on models on a lattice, for which we define a lattice constant $a \equiv 1$, and thus $\bar{J}_{ij}^{x,y,z}$ reduces to the nearest-neighbor coupling strengths. In addition, we allow for local “magnetic” fields along the different dimensions given by the vector $\mathbf{h}_i = (h_i^x, h_i^y, h_i^z)$.

The general Hamiltonian (35) includes for example a long-range Heisenberg model, for which $J_{ij}^x = J_{ij}^y = J_{ij}^z$ or a long-range XY model with $J_{ij}^z = 0$. Both are special cases of an XXZ model with $J_{ij}^x = J_{ij}^y \neq J_{ij}^z$. XY couplings are, e.g., realized for systems interacting with dipole–dipole far-field interactions for which $\alpha = 3$. Such a model describes pairwise coherent energy exchange between the spins since $(S_i^x S_j^x + S_i^y S_j^y) \propto (S_i^+ S_j^- + S_i^- S_j^+)$. Note that true dipole–dipole couplings typically also feature an interaction anisotropy, i.e., an interaction term depending on the relative dipole orientation; however, we will here be mostly interested in 1D scenarios and aligned dipoles. In ultra-cold atom physics, dipole–dipole couplings appear for example in systems with polar molecules [40] or with magnetic atoms [41, 42]. In the case where in Eq. (35) only the spin couplings for a single particular dimension remain finite, e.g., $J_{ij}^y = J_{ij}^z = 0 \neq J_{ij}^x$, the model reduces to an Ising model. Since in this case all the interaction terms in the Hamiltonian commute with each other, the addition of a non-commuting transverse field typically leads to a richer quantum non-equilibrium entanglement dynamics and therefore long-range transverse Ising models of the form of (16), i.e., $J_{ij}^y = J_{ij}^z = 0 \neq J_{ij}^x$ and $h_i^x = h_i^y = 0 \neq h_i^z$ have been intensively studied [43, 44]. The Ising interaction is, e.g., relevant for van der Waals-type interactions for which $\alpha = 6$. In ultra-cold atom physics, such interactions appear, e.g., for interacting Rydberg atom setups [45, 46]. They also play a crucial role in effective spin model implementations with trapped ions, which feature a unique possibility for Ising models with widely tunable interaction range, $\alpha \lesssim 2$ [47, 48]. Additionally, coupling to cavity modes allows to also realize spin models of the

form of (35) with infinite range interactions ($\alpha = 0$). See Sect. 5 for more details on experimental realizations.

The potential for harnessing long-range interactions of the form (35) to rapidly generate many-body entanglement between distant degrees of freedom has inspired a large body of the literature establishing fundamental bounds on the propagation of information in systems with power-law interactions [11–13, 49–53]. Recent work has established a hierarchy of Lieb–Robinson bounds in systems with power-law interactions [12] as well as concrete protocols for exploiting the resulting long-distance entanglement for quantum state transfer [54, 55].

In the following, we will summarize results for the entanglement growth dynamics in a long-range interacting transverse Ising model, as defined in Sect. 2.3:

$$H_{\text{LRTI}} = \sum_{i < j} \frac{\bar{J}}{|i - j|^\alpha} \sigma_i^x \sigma_j^x + B \sum_i \sigma_i^z. \quad (36)$$

We will focus on the results in a 1D chain of M spins. Note that the entanglement evolution is usually most interesting in lower-dimensional systems. For example, in equilibrium statistical physics, it is well known that mean-field theories that are equivalent to the product state ansatz from (29) become a very good approximation, as quantum fluctuations are typically argued to become less important if the spins couple to an increasing amount of neighbors. This is to some extent equivalent to a limit of very long-ranged interactions $\alpha \rightarrow 0$. In such a limit, the system can also be imagined as being high-dimensional since every spin couples equally to a very large number of “neighbors.” Below we will indeed see that with an increasing range of interactions the bipartite entanglement entropies in quench dynamics become generally suppressed when increasing the range of the power-law interactions.

We introduce three different regimes of power-law interaction ranges, for which one finds that entanglement growth exhibits qualitatively very different behavior: (i) The short-range regime for power-law exponents $\alpha > 2$; (ii) the intermediate-range regime for power-law exponents $1 < \alpha < 2$; and (iii) the long-range regime for $\alpha < 1$.

3.1 Short-Range Regime, $\alpha > 2$

In the case of $S = 1/2$ and in the limit of nearest-neighbor interactions, $\alpha \rightarrow \infty$, Hamiltonians for Heisenberg, XY, XXZ or Ising models are generally integrable [56]. This means that they can be solved by Bethe ansatz solutions, which allows to understand the system dynamics in terms of elementary excitations. In some cases, easy analytical solutions for the dispersion relations and the shape of elementary excitations can be given, e.g., for the XY or transverse Ising model, where a Jordan–Wigner transformation can be used to map the chain to a quadratic fermionic Hamiltonian as shown above. As described in Sect. 2.3, in such a scenario,

the dynamics of the quasiparticles after a quench leads to a linear growth of entanglement as a function of time until a saturation value depending on the system size. In particular, taking the fully polarized state $|\psi(t=0)\rangle = \prod_i |\downarrow\rangle_i$ as input state for the transverse Ising Hamiltonian (36) with $\alpha = \infty$ (note that this corresponds to a quench of the field strength from $\infty \rightarrow B$ since $|\psi(t=0)\rangle$ is the ground state for $B \rightarrow \infty$), one finds that [22]

$$S_{\text{VN}}(\rho_A, t) = c_t t + M_A c_\infty \quad (37)$$

with constants c_t and c_∞ and M_A the number of spins in the sub-system state ρ_A . The two constants c_t and c_∞ are largest for the scenario where $B = \bar{J}$ [22]. This means the entanglement growth is fastest for parameters that correspond to the transition point from a paramagnetic to an anti-ferromagnetic phase in the ground state of the Hamiltonian.

Remarkably, the same linear entanglement growth behavior is also observed for finite range interactions $\infty > \alpha > 2$ in the long-range transverse Ising model (36). This is for example shown in Fig. 4a that plots the time-dependent growth of the von Neumann entanglement entropy, S_{VN} , for half the chain as sub-system (from [24]). To compute dynamics, we utilize numerically exact MPS simulations of a chain with $M = 50$ spins and also compare them to an exact diagonalization simulation (ED) in a smaller system with $M = 20$ spins. Focusing on the results with $\alpha > 2$, strikingly, while the entanglement growth rate is reduced with the range of interactions, the linear behavior persists. This hints to the conclusion that for $\alpha \geq 2$ the quasiparticle picture known for the nearest-neighbor case also survives for finite range interactions in the $\alpha > 2$ regime. This conclusion is furthermore strengthened by the observation that the $M = 50$ and $M = 20$ simulations perfectly agree with each other. As explained in Sect. 2.3 (see Fig. 2), in the quasiparticle picture, the entanglement entropy growth is independent of the system size until entangled quasiparticles reach the edges of the chain. On the timescale considered in Fig. 4a (\sim five inverse spin interaction energies), quasiparticles cannot reach the boundary for both system sizes. It is also worth pointing out that in [24] it was shown that the linear growth rate of entanglement (constant c_t in Eq. 37) remains to be largest at the point of the ground-state phase transition, which with decreasing values of α shifts to values of $B(J) < 1$.

To better analyze the quasiparticle picture, it is instructive to analyze the evolution of correlations between two distant spins (summarized, e.g., by the mutual information in Fig. 2b). In Fig. 4b, c, we analyze the time evolution of the spin–spin correlations $C_d(t) = |\langle \sigma_i^+ \sigma_{i+d}^- \rangle|$, averaged over several starting sites i , as a function of the distance between spins, d (exact results from an MPS simulation, from [23]). Panel (b) shows the simulations for $\alpha = 3$. The color-coded logarithmic scale shows that there is a clear linear lightcone effect, within which C_d evolves, whereas outside C_d is strongly suppressed.

Analytically, this lightcone behavior can be rationalized by the dispersion relation of the linearized Holstein–Primakoff quasiparticles from Eq. (26). As long as $\alpha > 2$, this dispersion remains a smooth function of the quasimomentum, and

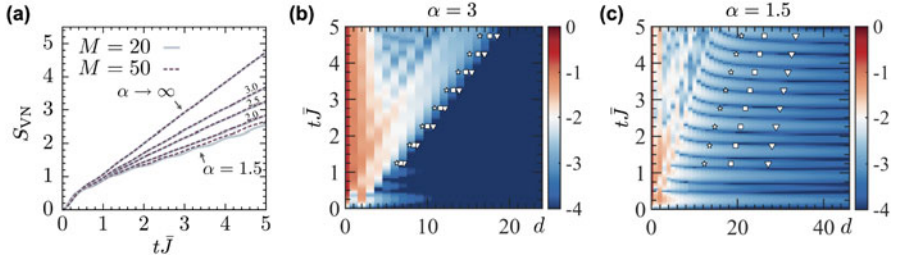


Fig. 4 (a) Time-dependent growth of the von Neumann entanglement entropy in a transverse Ising chain with M spins, for an initially fully polarized state, $|\psi(t=0)\rangle = \prod_i |\downarrow\rangle_i$ and $B = \bar{J}$. Shown are results for $M = 20$ (solid lines) and $M = 50$ (dashed lines), which are obtained from exact diagonalization and numerically exact MPS simulations, respectively. Various power-law exponents are compared ($\alpha = \infty, 3.0, 2.5, 2.0, 1.5$). (b, c) Corresponding time evolution of the spin-spin correlation $C_d(t) = |\langle \sigma_i^+ \sigma_{i+d}^- \rangle|$ as a function of distance d (the color scale corresponds to $\log_{10}[C_d(t)]$). The three white markers correspond to $\log_{10}[C_d(t)] = -4, -3.5, -3$ in (b) and to $\log_{10}[C_d(t)] = -3.25, -3, -2.75$ in (c) (triangle, square, star, respectively). Panel (b) is for the short-range regime ($\alpha = 3$), and panel (c) for the intermediate-range regime ($\alpha = 1.5$). ((a) reproduced from [24], (b) and (c) reproduced from [23])

therefore, elementary excitations with well-defined and maximum possible group velocities will be excited in the dynamics. It is however important to re-emphasize that the linearization of the Holstein–Primakoff transformation (22) only remains valid for states that fulfill $\langle a_i^\dagger a_i \rangle \ll 2S$ and thus for low-energy quenches or for short times. In the low-energy quench limit, the quasiparticle dynamics can be verified [25]. Surprisingly also for high-energy quenches, one finds that the qualitative spreading of correlations is still very well captured when comparing the Holstein–Primakoff ansatz to exact MPS simulations [23]. We also want to note again that the Holstein–Primakoff dispersion has the same features as the quasiparticle dispersion of a fermionic long-range hopping shown in Fig. 2c that remains exact for arbitrary high-energy quenches and times. In this model, exact calculations of correlation functions in very large systems can be performed, which furthermore allows for a clear characterization of the lightcone boundaries for $\alpha > 2$ [23]. Finally, it is worth remarking that while here we focused on results for a $S = 1/2$ model, the same conclusions of the Holstein–Primakoff solution also hold for larger spins. In fact, one may expect that the validity of the model is extended to higher energies and longer times, since $\langle a_i^\dagger a_i \rangle \ll 2S$ can be more easily fulfilled for larger S .

3.2 Intermediate Range Regime, $1 < \alpha < 2$

The dynamics of entanglement build-up starts to qualitatively change when the interactions become longer-ranged, i.e., for $\alpha < 2$. For example, while for a large system simulation with $M = 50$ and $\alpha = 1.5$ in Fig. 4a, the entanglement entropy

growth still looks linear with additional small oscillations, now strikingly the growth dynamics strongly depends on the system size. Large differences in comparison with the $M = 20$ simulation appear, already at short times. This implies that distant parts of the chain must already become entangled at very short times, and thus in a quasiparticle picture, there must be entangling quasiparticle excitations with very large group velocities.

Analytically, this is justified by the fact that the dispersion relation for Holstein–Primakoff excitations (26) [25], or for the related fermionic long-range hopping model (Fig. 2c), starts to feature a cusp for $\alpha < 2$, which implies the existence of elementary excitations with diverging group velocity. However, it is important to emphasize that whether such excitations can be created or not crucially depends on the initial state and on the density of states in the vicinity of the diverging group velocities in quasimomentum space (see Fig. 2c). There, one for example finds crucial differences in the correlation build-up between the long-range interacting transverse Ising model and the long-range fermionic hopping model [23]. For the Ising model, in Fig. 4c, we show the evolution of $C_d(t)$ for $\alpha = 1.5$. There, it is clearly visible that it becomes impossible to define a clear edge of the lightcone. Instead, the decay of the correlations as a function of the distance is significantly broadened and is not fully linear anymore.

To summarize, in the intermediate regime, entanglement and correlation build-up still exhibit certain features of a lightcone propagation leading to a linear long-time entanglement entropy growth, but on the other hand the existence of quasiparticles with diverging group velocity already leads to significant beyond lightcone features. It is important to note that those features have been experimentally measured in ion trap setups, both after single-spin flip quenches [47] and for fully polarized initial states [48].

3.3 Long-Range Regime, $\alpha < 1$

Another drastic qualitative change in the entanglement growth dynamics can be observed when the power-law interaction decays more slowly than $\alpha < 1$. Note that in this regime the overall interaction energy starts to diverge in the infinite system limit, and therefore, the bare interaction energy \bar{J} has to be re-scaled with M for meaningful statements in the $M \rightarrow \infty$ limit. Strikingly, the change in behavior at $\alpha = 1$ is displayed in the quasiparticle dispersion of the Holstein–Primakoff excitations (26) (or equivalently in the dispersion relation for the long-range fermionic hopping model in Fig. 2c). For $q \rightarrow 0$, one finds that the energy of the elementary excitations is diverging. Therefore, for initial states where the quench excites significant excitations near $q = 0$, the dynamics of such quasiparticles dominates the entanglement spreading. This is for example seen in the evolution of the spin–spin correlations, which lose any type or lightcone features [23]. For example, in Fig. 2b, we find that the mutual information between distant spins is

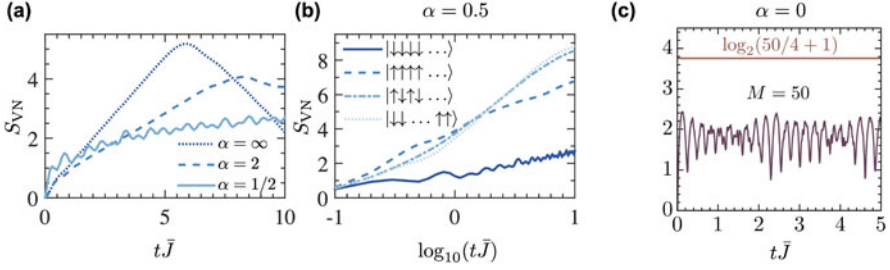


Fig. 5 (a) Time-dependent growth of the von Neumann entanglement entropy in a transverse Ising chain with M spins, for an initially fully polarized state, $|\psi(t = 0)\rangle = \prod_i |\downarrow\rangle_i$ and $B = \bar{J}$. Shown are results for $M = 20$. Various power-law exponents are compared ($\alpha = \infty, 3.0, 2.0, 1.5$). Rapid entropy at short times and sub-linear increase at later times are observed for $\alpha < 1$. (b) Same plot as in (a) for $\alpha = 0.5$ on a logarithmic timescale, and for various initial states. Initial states without full permutation symmetry lead to stronger entropy growth at later times. (c) Evolution for infinite-range interactions $\alpha = 0$ and the fully polarized symmetric state ($M = 50$). S_{VN} remains bounded by the constant $\log_2(M/4 + 1)$ due to the reduced dimension of the symmetric Hilbert subspace. ((a, b) reproduced from [23], (c) reproduced from [24])

building up immediately after the quench, and any feature indicating a quasiparticle arrival at later times vanishes for $\alpha < 1$.

Also the time-dependent growth of the von Neumann entanglement entropy changes characteristically at $\alpha < 1$. As shown in Fig. 5a, one finds in general (here $\alpha = 0.5$) a sub-linear oscillatory growth, which for the fully polarized initial state exhibits a logarithmic increase. However, it is important to point out that the growth behavior now also strongly depends on the initial state, as shown in Fig. 5b. In particular, states that do not have permutation symmetry feature a faster increase rate of the entanglement entropy for $t\bar{J} > 1$. On the one hand, this is again plausible since also excited quasiparticle states around $q \sim 0$ do possess permutation symmetry and thus can be more directly excited in the dynamics. Another intuitive explanation of this observation can be made in the infinite-range limit of $\alpha \rightarrow 0$.

For $\alpha = 0$, Hamiltonian (36) becomes

$$H_{\text{LRTI}}^{\alpha=0} = \bar{J} \sum_{i < j} \sigma_i^x \sigma_j^x + B \sum_i \sigma_i^z \tag{38}$$

$$= \frac{J}{2} (S^x)^2 + B S^z - \frac{\bar{J}}{2} M. \tag{39}$$

In the second line, we have defined the collective spin operators $S^{x,z} = \sum_i \sigma_i^{x,z}$. The collective model in Eq. (39) is also known as Lipkin–Meshkov–Glick (LMG) Hamiltonian, and its entanglement properties can be analytically studied [57]. Due to the permutation symmetry of the problem, a complete basis for Hamiltonian (39) can be constructed in terms of collective spin states, the $M + 1$ symmetric Dicke

states:

$$|S = \frac{M}{2}, m_S = n_\uparrow - \frac{M}{2}\rangle = \mathcal{S}|\{n_\uparrow\}\rangle. \quad (40)$$

These states are eigenstates of the collective operator spin- $S = M/2$ operator S^z with quantum number $m_S = -M/2, \dots, M/2$, and they can be written as the symmetrized superposition of all states with a certain number of spins, n_\uparrow , pointing “up.” Here, \mathcal{S} denotes a symmetrization operator, and $|\{n_\uparrow\}\rangle$ are all states with n_\uparrow spins in the state $|\uparrow\rangle$, and consequently $M - n_\uparrow$ spins in the state $|\downarrow\rangle$. The bipartite von Neumann entropy for a sub-system density matrix containing half of the spins can be straightforwardly computed from simple combinatorial factors [24, 58]:

$$S_{\text{VN}}^{\text{LMG}} = - \sum_l p_l(n_\uparrow) \log_2[p_l(n_\uparrow)] \quad \text{with} \quad p_l(n_\uparrow) = \frac{\binom{M/2}{l} \binom{M/2}{n_\uparrow - l}}{\binom{M/2}{n_\uparrow}} \quad (41)$$

with $0 \leq l \leq M/2$. Importantly, since the sum in (41) only features a maximum of $M/2 + 1$ terms, the entanglement entropies in symmetric Dicke states are fundamentally limited to a quantity only growing logarithmic in the system size $S_{\text{VN}}^{\text{LMG}} \leq \log_2(M/2 + 1)$. It is therefore also easy to see that in our quench evolution on the small symmetric Hilbert space, entanglement entropies will remain limited to this bound. Note that since the quadratic term in S^x in (39) only couples Dicke states with $m_S \leftrightarrow m_S \pm 2$, the bound can furthermore be tightened to $S_{\text{VN}}^{\text{LMG}}(t) \leq \log_2(M/4 + 1)$ [24]. In Fig. 5c, the evolution is demonstrated in an example simulation for $M = 50$. We again point out that for initial states that are outside of the symmetric Dicke manifold, a much larger Hilbert space can be accessed, which can lead to much larger von Neumann entanglement entropies, consistent with our observation of the initial-state dependence of the growth rate in Fig. 5c for $\alpha = 0.5$.

4 Fast Scrambling and Sparse Models

In previous section, we explored how naturally occurring long-range interactions could be leveraged to generate many-body entanglement in spin chains. We now consider pushing this process of entanglement growth to its extremes. In particular, is there a “speed limit” on how rapidly entanglement can build up in any given system? The fast scrambling conjecture places a fundamental upper bound on the rate of entanglement growth in arbitrary quantum systems. Below we present explicit spin chain models that saturate this bound and highlight the central role played by nonlocal interactions. Systems that saturate these bounds and generate maximal entanglement in the shortest possible time are known as *fast scramblers*. Such systems share key properties with the dynamics of black holes [59] and

show prospects for efficient entanglement generation in near-term experiments [60]. In studying these fast scrambling models, we will also find that the pattern of entanglement developed in these systems can determine the effective geometry of the underlying dynamics, which may differ substantially from the linear geometry of the original spin chain.

4.1 Sparse Nonlocal Interactions for Fast Scrambling

What kinds of physical systems are capable of generating such rapid entanglement growth? We can get a good handle on this question by first studying the Lieb–Robinson bounds derived in Sect. 2.2. Because these bounds are completely general, we can use them to characterize the growth of entanglement on any arbitrary coupling graph G . First, consider averaging Eq. (14) over all vertices i, j in the graph G ,

$$\sum_{i,j} \frac{1}{N^2} \frac{\|[O_j, O_i(t)]\|}{2\|O_j\|\|O_i\|} \leq \frac{1}{N} \exp\left[\frac{4ck_{\max}}{K}|t|\right], \quad (42)$$

where k_{\max} is the maximal degree in the graph. Whenever k_{\max}/K is finite, we see that operator growth is constrained to be exponentially fast. In particular, for chaotic systems that exhibit Lyapunov growth $\|[O_j, O_i(t)]\|^2 \sim \frac{1}{N} e^{\lambda_L t}$, the bound (42) establishes that the Lyapunov exponent λ_L can be no larger than

$$\lambda_L \leq \frac{4ck_{\max}}{K}, \quad (43)$$

thereby placing a bound on quantum many-body chaos at infinite temperature. Note that this bound on the Lyapunov exponent is distinct from the chaos bound of Maldacena et al, which places a bound on the Lyapunov exponent at *finite* temperature [61]. Moreover, since scrambling cannot occur until almost all OTOCs have grown to be order unity [6], the result (42) establishes that scrambling cannot occur before a time

$$t_* \geq \frac{K}{4ck_{\max}} \log N. \quad (44)$$

This therefore provides a proof of the fast scrambling conjecture on any graph for which k_{\max}/K is finite.

The generalized Lieb–Robinson bound also constrains which graphs G are capable of supporting fast scrambling. Further manipulations to (14) (see Appendix

B of Ref. [17]) lead to

$$\exp \left[\frac{2c|t|}{K} (\mathcal{D} + \mathcal{A}) \right]_{ij} < \exp \left[\frac{4eck_{\max}}{K} |t| - r_{ij} \right], \quad (45)$$

where $e \approx 2.718$ and the *graph distance* r_{ij} is the minimal path length between vertices i and j , i.e.,

$$r_{ij} = \min \{n \in \mathbb{N} \text{ s.t. } [\mathcal{A}^n]_{ij} = 1\}. \quad (46)$$

Equation (45) is the classic Lieb–Robinson bound [8]. From this expression, we see that the timescale required for an arbitrary operator to spread throughout the entire system is limited by the path length between the two most distant sites $r \equiv \max_{i,j} (r_{ij})$, or the *graph diameter*. We immediately conclude that only graphs with diameter $r \lesssim \log N$ can support fast scrambling [10, 17]. Fast scrambling is therefore impossible for all systems defined on a regular lattice in D dimensions, which have graph diameter $r = N^{1/D}$.

4.2 Sparse Nonlocal Fast Scramblers

We argued above that nonlocal interactions are crucial to engineering fast scrambling; in particular, square lattices in any dimension D have diameter $N^{1/D} \gg \log N$ and therefore are incapable of supporting fast scrambling dynamics even in principle. Here, we introduce sufficiently nonlocal spin models that feature a logarithmic graph diameter and are also sufficiently chaotic to generate strong scrambling dynamics. These models feature sparse couplings that can be implemented in near-term cold atom experiments employing trapped Rydberg atoms or neutral atoms coupled to an optical cavity, as we review in Sect. 5.

Here we consider sparse nonlocal Hamiltonians of the form

$$H = \frac{1}{2S} \sum_{i,j} J(i-j) S_i^+ S_j^-, \quad (47)$$

with translation-invariant couplings $J(i-j)$ defined on a sparse graph where sites i, j are coupled if and only if they are separated by a power of two,

$$J(i-j) = \begin{cases} J_s 2^{\ell s} & \text{when } |i-j| = 2^\ell, \ell = 0, 1, 2, 3 \dots \\ 0 & \text{otherwise,} \end{cases} \quad (48)$$

as illustrated in Fig. 6a. The couplings in Eq. (48) are normalized by setting $J_s = J_0$ when $s \leq 0$ and $J_s = J_0(N/2)^{-s}$ for $s > 0$, such that the largest coupling is always a constant J_0 . Here, by tuning the exponent s from $-\infty$ to $+\infty$, we interpolate

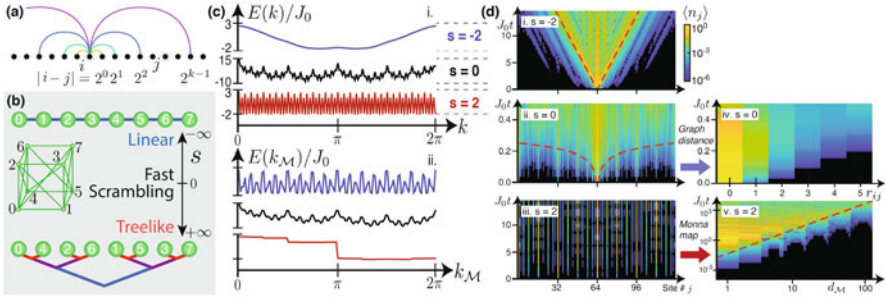


Fig. 6 Sparse nonlocal spin models with tunable geometry. (a) In the power-of-2 model, pairs of spins in a 1D chain are coupled if and only if they are separated by an integer power of 2. (b) By varying the envelope exponent s , we can tune the sparse model from a linear limit for $s \rightarrow -\infty$ to a treelike limit for $s \rightarrow +\infty$. Between these two limits $s = 0$, the sparse couplings form an “improved hypercube” graph that allows for fast scrambling. (c) The quasiparticle dispersion relation for $s = -2, 0, 2$ as a function of real-space momentum k (top) and as a function of Monna-mapped momentum k_M (bottom). (d) Quasiparticle density $\langle n_j \rangle$ in the power-of-2 model for $s = -2, 0, 2$ (i–iii). The clear lightcone present in the linear regime (i) breaks down in the fast scrambling and treelike regimes (ii, iii). A lightcone re-emerges when the system is organized either by graph distance (iv) or by 2-adic treelike distance (v). (Reproduced from [62])

between a *linear* limit ($s \rightarrow -\infty$) where the physics resembles a nearest-neighbor spin chain, and a *treelike* limit ($s \rightarrow +\infty$) in which the underlying geometry is radically reorganized as illustrated in Fig. 6b [62]. In between these two limits, with $s = 0$, all nonzero couplings are equal and the coupling graph is highly nonlocal. These nonlocal couplings permit information to spread exponentially quickly throughout the system because the number of pairwise interactions required for a particle to hop between any two sites i, j is never more than the Hamming distance $|i - j|_{\text{Hamming}} < \log_2 N$ when the site indices i, j are written in binary. The rapid spreading of information afforded by the nonlocal couplings at $s = 0$ allows this model to generate fast scrambling dynamics.

The primary features of the model can already be observed by considering quasiparticle dynamics described by a nonlocally coupled harmonic Hamiltonian similar to the discussion in Sect. 2.3. Because the couplings $J(i - j)$ are translation-invariant, we can easily diagonalize this harmonic model by performing a Fourier transform of the creation and annihilation operators a, a^\dagger . This yields a single-particle dispersion relation

$$\epsilon_k = \sum_d J(d) e^{ikd} = 2J_s \sum_{l=0}^{\log_2(N/2)} 2^{ls} \cos(2^l k). \quad (49)$$

We plot this dispersion relation as a function of momentum k in Fig. 6c for exponents $s = -2, 0, 2$ (blue, black, red). For $s < 0$, the dispersion relation is smooth and resembles the dispersion relation for a free particle in a chain with nearest-neighbor interactions. By contrast, for $s > 0$, the dispersion relation

becomes jagged and consists of features on the scale of the inverse lattice spacing $2\pi/N$. When $s = 0$, the dispersion relation appears to have a fractal structure.

Using the dispersion relation, we may immediately compute the particle density $\langle n_j \rangle(t)$, which we plot in Fig. 6d. For $s < 0$, the system exhibits a clear linear lightcone as the initially localized excitation spreads ballistically through the system. By contrast, for $s > 0$, the excitation jumps discontinuously between distant sites, and a lightcone is not immediately apparent. It is tempting to interpret the absence of an obvious lightcone at $s > 0$, along with the discontinuities in the dispersion relation ϵ_k , as indicating the absence of any notion of locality in this regime. Instead, we find that a new version of locality emerges in the limit $s \rightarrow \infty$ based on the treelike structure shown in Fig. 6b.

A dramatic reconception of geometry—where we significantly alter the definition of which spins are “close” to one another and which are “far apart”—allows us to recover a sense of locality from the apparently discontinuous hopping we observe for $s > 0$. Specifically, we may restore a sensible notion of spatial locality by defining distance in terms of the 2-adic norm $|x|_2 = 2^{-v(x)}$, where $2^{v(x)}$ is the largest power of 2 that divides x . The distance $|i - j|_2$ between sites i and j is called ultrametric because the distance of the sum of two steps is never greater than the larger of the two steps’ distance; by contrast, the usual distance $|i - j|$ is called Archimedean because many small steps can be combined into a large jump. We can understand the 2-adic norm as a treelike measure of distance because $|i - j|_2 = 2^{d_{\text{tree}}(i,j)/2}/N$, where $d_{\text{tree}}(i, j)$ is the number of edges between sites i and j along the regular tree in Fig. 6b. The leaves are numbered in order of increasing $\mathcal{M}(i)$, where the discrete Monna map \mathcal{M} reverses the bit order in the site number. For example, for $N = 8$ sites, $\mathcal{M}(1) = 4$ because in binary, $\mathcal{M}(001_2) = 100_2$. Noting that $Nk/2\pi$ is an integer, we may likewise define a Monna-mapped wavenumber $k_{\mathcal{M}}$ by

$$N \frac{k_{\mathcal{M}}}{2\pi} = \mathcal{M} \left(N \frac{k}{2\pi} \right). \quad (50)$$

For large positive s , we rearrange the spins according to the Monna map and find that a lightcone reappears (Fig. 6d(v)) and the dispersion relation is smoothed out (Fig. 6c, bottom), corroborating the transformation to the treelike geometry defined by the 2-adic norm.

At the crossover point $s = 0$ where all nonzero couplings are of equal strength, neither the linear nor the treelike geometries are suitable for describing the spread of quantum information. Instead, the sparse nonlocal couplings facilitate rapid spreading of information throughout the entire system on a logarithmic timescale $t_* \sim \log N$, as demonstrated already in the single-particle dynamics shown in Fig. 6d(ii). In this limit, the coupling graph is equivalent to the “improved hypercube” illustrated in Fig. 6b, consisting of edges from a regular hypercube plus a few extra diagonal couplings to ensure the system is translationally invariant. The improved hypercube has graph diameter $\lceil \frac{1}{2} \log_2 N \rceil$ and is therefore capable

of hosting fast scrambling dynamics by the graph-theoretic arguments presented in Sect. 4.1.

To examine the structure of entanglement naturally generated by the nonlocal power-of-2 couplings (48), we numerically simulate the evolution of the system using exact diagonalization for a system of $N = 16$ spins with $S = 1/2$ and compute the resulting entanglement entropy between a variety of sub-systems. We initialize the system in a polarized state along S_x , evolve the system for a time t , then partition the system into (not necessarily sequential) sub-systems $Q = A \cup B$, and compute the von Neumann entanglement entropy S_A of sub-system A .

Figure 7 shows the resulting entanglement entropy for bipartitions A, B as a function of the partition size $L = |A|$ and time. We partition spins into sub-systems A, B either according to their physical position in the linear chain (top) or their Monna-mapped ordering (bottom). When $|s|$ is large, we observe that there is a natural way to partition the system such that the entanglement entropy is low regardless of the length L of the partition. That is, for $s < 0$, we minimize the entanglement entropy by cutting the system between nearest neighbors in the linear chain, while for $s > 0$ we must cut the system between branches of the Bruhat–Tits tree. By contrast, if we use the “wrong” partitioning (e.g., Monna-mapped partition for $s < 0$), we find a very large entanglement entropy that depends sensitively on the region’s length L .

At the crossover point $s = 0$, however, we find that entanglement entropy is large no matter how we partition the system. As shown in Fig. 7b, both the linear ordering (blue dotted) and the Monna-mapped ordering (red dash-dotted) give bipartitions with large entanglement entropy at $s = 0$. Moreover, we can consider the entanglement entropy across bipartitions A, B without regard to any sort of locality. In Fig. 7b, we also consider *all* possible bipartitions of size $L = |A|$

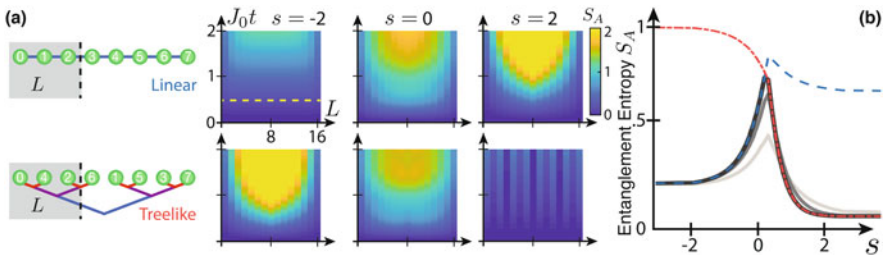


Fig. 7 Entanglement entropy as a probe of geometry. (a) Entanglement entropy for contiguous subregions of length L in the linear (top) or treelike (bottom) geometry. When $s = -2$, a linear partitioning of the system yields area-law entanglement at short times, whereas a treelike partitioning yields spurious volume-law entanglement; this suggests that a linear geometry is a suitable description for the dynamics. When $s = 2$, a treelike partitioning yields area-law entanglement, suggesting a treelike geometry. When $s = 0$, neither geometry produces area-law entanglement. In fact, at $s = 0$, every partition of the system has volume-law entanglement, as demonstrated in (b). This indicates that the $s = 0$ model is a fast scrambler. (Reproduced from [62])

and choose the bipartition with the smallest entanglement entropy at each value of s . Even so, we still find that the entanglement entropy is large at $s = 0$. In fact, at $s = 0$, we find that the entanglement entropy grows linearly with the partition size L , indicating a *volume law* in which entanglement extends into the bulk of the region A . These results indicate that there really is no notion of locality at the crossover point $s = 0$: all spins are equally “close” to one another, and there is entanglement between all pairs of spins.

5 Implementation in Experiments

Here, we briefly survey some of the state-of-the-art experimental platforms that can be used to explore entanglement growth in spin chains with structured long-range interactions using cold atoms and ions. This list is not exhaustive and represents only a small fraction of the experimental platforms available for controlled studies of entanglement growth.

5.1 Long-Range Interactions with Trapped Ions

Important motivation for studying information propagation with structured long-range interactions has come from experiments with trapped ions, in which the spin states are encoded on long-lived internal states of trapped ion chains in 1D Paul traps or 2D Penning traps [63]. In these experiments, controllable spin–spin interactions that decay algebraically with distance can be realized by using laser driving of spin transitions that couple also to the collective motional modes of the ions. Coupling off-resonantly to many motional modes produces effective Hamiltonians such as that in Eq. 16, with an algebraic decay exponent that can in principle vary from $\alpha = 0$ to $\alpha = 3$, and typically ranges in experiments from $0.5 \lesssim \alpha \lesssim 2.5$.

There have been extensive experiments on information spreading [47, 48] and recent experimental work exploring the growth of entanglement and scrambling in these systems [64]. Future combinations with gate operations typical of quantum computing setups open the possibility for flexible programmable quantum simulation, which could access a broad variety of spin models with structured long-range interactions in these experiments [63].

5.2 Long-Range Interactions with Rydberg Atoms

Hydrogen-like alkali atoms whose outermost electron has been excited to a Rydberg state $|r\rangle$ with very high principal quantum number n are extremely sensitive to external electric fields due to the Rydberg state’s large electric susceptibility. This

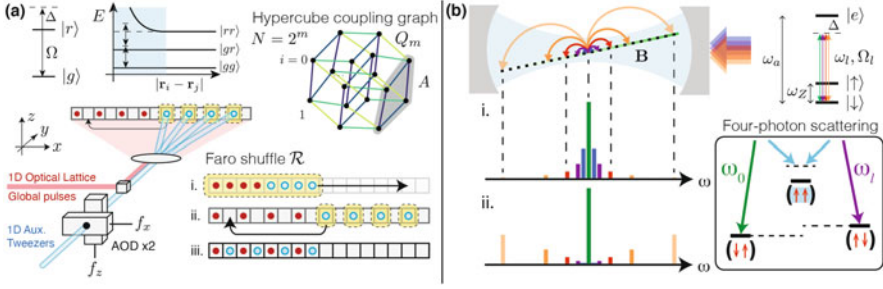


Fig. 8 Experimental platforms for studying entanglement growth in quantum spin chains with long-range interactions. **(a)** Rydberg atoms in 1D optical lattices interact via long-range Van der Waals forces that shift the doubly occupied Rydberg state $|rr\rangle_{ij}$ for nearby atoms, leading to a Rydberg blockade effect. Repeated tweezer-assisted shuffling can be used to engineer effective pairwise interactions on a nonlocal hypercube coupling graph amenable to fast scrambling. (Reproduced from [60]). **(b)** Atoms coupled to the optical mode of a high-finesse cavity interact pairwise via a four-photon scattering process. Applying a linear magnetic field gradient along the cavity axis and driving the cavity with a multi-frequency drive field, we may engineer sparse nonlocal spin-spin interactions whose strengths are individually tuned by the relative strengths of the drive sidebands. Using this flexible drive scheme, we may engineer sparse interactions that either decay (i) or grow (ii) with distance. (Reproduced from [62])

sensitivity leads to long-range van der Waals forces between pairs of Rydberg atoms that decay as a power law $1/|\mathbf{r}_i - \mathbf{r}_j|^6$; these interactions can be harnessed to process quantum information [65]. In modern experiments, an ensemble of atoms $i = 0, \dots, N - 1$ are typically prepared in a stable ground state $|g\rangle_i$ and trapped in a lattice of optical tweezers as shown in Fig. 8a [66–76]. To generate interactions, the atoms are then optically excited by an applied drive laser to the Rydberg state $|r\rangle_i$. The pairwise Van der Waals interactions strongly shift the doubly excited Rydberg state $|rr\rangle_{ij}$, prohibiting nearby pairs of atoms i, j from being simultaneously excited (Fig. 8a). This “Rydberg blockade” effect yields an effective Hamiltonian

$$H = \sum_{i < j} J_{ij} n_i n_j - \sum_i \Delta_i \sigma_i^z + \sum_i \frac{\Omega_i}{2} \sigma_i^x, \quad (51)$$

where Ω_i, Δ_i are the Rabi frequency and detuning of the drive laser from the Rydberg state $|r\rangle_i$, and where the couplings $J_{ij} = C/|\mathbf{r}_i - \mathbf{r}_j|^6$ are naturally long-ranged. Additional optical and magnetic fields can be used to engineer a variety of additional non-commuting terms in this Hamiltonian or to simulate non-equilibrium (time-dependent) dynamics, and Rydberg dressing schemes or other state and field choices can be used to generate alternative long-range interaction models.

While these Rydberg interactions are naturally long range, they are ultimately still constrained by the D -dimensional geometry of flat spacetime and are therefore incapable of executing fast scrambling dynamics by the arguments of Sect. 4.1. We can get around this problem by significantly altering the effective geometry

of the interactions using tweezer-assisted shuffling [60]. Stretching and interleaving tweezer operations [77–80] can be used to rapidly shuffle the atom positions, as shown in Fig. 8b, thereby generating effective nonlocal interactions. For example, repeated interleaving of the atoms rapidly generates an m -regular hypercube graph Q_m [81, 82], a highly nonlocal, sparsely connected coupling graph shown in Fig. 8b. Many-body entanglement can be rapidly and efficiently built up on this graph using far fewer Rydberg interaction layers than would be needed in strictly 1D systems without shuffling.

5.3 Long-Range Interactions in Cavity Quantum Electrodynamics

Cavity QED systems can be engineered to mediate highly nonlocal spin–spin interactions between pairs of atoms trapped in the optical mode of the cavity [3, 83–85]. This coupling allows the atoms to exchange excitations with the cavity mode with an effective Hamiltonian:

$$H = \omega_c c^\dagger c + \sum_i (\omega_Z |\uparrow\rangle \langle \uparrow|_i + \omega_a |e\rangle \langle e|_i) + \sum_i (g_i c |e\rangle \langle \uparrow|_i + g_i c |e\rangle \langle \downarrow|_i + \text{h.c.}), \quad (52)$$

where c is the annihilation operator for the cavity mode with resonance frequency ω_c and g_i is the atom–cavity coupling. Here, each atom i is a three-level system with ground states $|\uparrow\rangle_i, |\downarrow\rangle_i$ separated by a ground-state energy splitting ω_Z , and excited state $|e\rangle_i$ with energy ω_a as illustrated in Fig. 8b.

By optically driving the cavity at a large detuning $\Delta = \omega_c - \omega_a \gg g_i \langle c^\dagger c \rangle$ from atomic resonance, the cavity mode c and the atomic excited state $|e\rangle_i$ are unlikely to be populated and can be integrated out of the dynamics via standard perturbation theory [86]. In this case, the dominant processes are four-photon scattering transitions in which a pair of atoms i, j mutually flip their spins $|\downarrow\rangle_i |\uparrow\rangle_j \rightarrow |\uparrow\rangle_i |\downarrow\rangle_j$ by exchanging a cavity photon as illustrated in Fig. 8b. These four-photon scattering processes generate effective spin–spin interactions between the atoms with effective Hamiltonian:

$$H_{\text{eff}} \propto \sum_{ij} \xi_i \xi_j S_i^+ S_j^- + \text{h.c.}, \quad (53)$$

which describes all-to-all spin-exchange interactions between all pairs of atoms, where the coefficients ξ_i are determined by the local couplings g_i [3].

By applying a linear magnetic field gradient along the cavity axis and driving the cavity with multiple drive fields, as shown in Fig. 8b, it is possible to impose a further structure on the natural all-to-all couplings and realize sparse nonlocal interactions [62, 85, 87]. The linear magnetic field gradient along the length of

the chain splits the $|\downarrow\rangle_i, |\uparrow\rangle_i$ energies of the spins in a staircase pattern, where the ground-state energy splitting $\omega_{Z,i}$ is now a function of atomic position i and increases linearly with atomic position. As a result of this energy splitting, the four-photon process introduced above is off-resonant and the interactions are shut off. However, by driving the cavity with two or more frequencies simultaneously, we may selectively reintroduce interactions between pairs of atoms that are separated by a particular distance d . That is, driving the system at the resonant frequency $\Delta\nu_d = \omega_{i+d} - \omega_i$ generates pairwise spin flip processes $|\downarrow\rangle_i |\uparrow\rangle_{i+d} \rightarrow |\uparrow\rangle_i |\downarrow\rangle_{i+d}$ only between spins that are separated by exactly $d = j - i$ sites, and all other pairs are off-resonant to this drive. We can then build up additional interaction terms by adding more frequencies to our drive. As a result, we obtain a highly tunable set of distance-dependent interactions between atoms controlled by the spectrum of the drive light. With this flexible driving scheme in hand, we are able to implement a large class of nonlocal spin-exchange models including the translation-invariant sparse models (47) studied in Sect. 4.2. This drive scheme has recently been demonstrated in cavity experiments where it was used to engineer a variety of exotic coupling patterns that are not accessible in any other experimental system [85].

6 Outlook and Further Connections

In summary, experimental systems available in experiments with trapped ions, atoms in cavities, and tweezer arrays motivate an interesting new area where we can look at dynamics well beyond what we usually see in local interacting systems. In this chapter, we have only begun to introduce a wide range of possibilities to explore many-body physics in these systems, solely focusing on entanglement growth without disorder. There are large sub-fields discussing phenomena such as many-body localization [88, 89] in these systems, as well as topological effects. Long-range interactions occur in many systems in addition to those discussed here, including systems of polar molecules [40, 90], or harmonically trapped gases [91]. Dressed Rydberg excitations can also provide another way to generate controlled long-range interactions [65, 92].

The entanglement build-up discussed here can also be used as a building block for wider applications. Fast scrambling circuits like those described here can be leveraged to generate nearly random many-body matrices U , which are valuable resources in a variety of information processing contexts. For example, random matrices naturally generate random error-correcting codes, which can be used to protect quantum information from the effects of dissipation [93]. Random matrices can also be used to directly probe entanglement entropies in experiments without the need to introduce SWAP operators between multiple copies [64]. Finally, these fast scrambling circuits can be harnessed to teleport quantum information via Hayden–Preskill-type protocols, which rely on the fast scrambling dynamics to successfully teleport information [94–96].

References

1. A.K. Ekert, C.M. Alves, D.K.L. Oi, M. Horodecki, P. Horodecki, L.C. Kwak, Phys. Rev. Lett. **88**(21), 217901 (2002)
2. A.J. Daley, H. Pichler, J. Schachenmayer, P. Zoller, Physical Rev. Lett. **109**(2), 020505 (2012)
3. G.S. Bentsen, *Nonlocal Light-Mediated Interactions for Fast Scrambling* (Stanford University, 2019)
4. D.N. Page, Phys. Rev. Lett. **71**, 1291 (1993)
5. S.H. Shenker, D. Stanford, J. High Energy Phys. **2014**, 67 (2014)
6. P. Hosur, X.L. Qi, D.A. Roberts, B. Yoshida, J. High Energy Phys. **2016**(2), 1 (2016)
7. B. Swingle, G. Bentsen, M. Schleier-Smith, P. Hayden, Phys. Rev. A **94**(4), 040302 (2016)
8. E.H. Lieb, D.W. Robinson, Commun. Math. Phys. **28**(3), 251 (1972)
9. M.B. Hastings, T. Koma, Commun. Math. Phys. **265**(3), 781 (2006)
10. N. Lashkari, D. Stanford, M. Hastings, T. Osborne, P. Hayden, J. High Energy Phys. **2013**(4), 22 (2013)
11. M. Foss-Feig, Z.X. Gong, C.W. Clark, A.V. Gorshkov, Phys. Rev. Lett. **114**, 157201 (2015)
12. M.C. Tran, C.F. Chen, A. Ehrenberg, A.Y. Guo, A. Deshpande, Y. Hong, Z.X. Gong, A.V. Gorshkov, A. Lucas, Phys. Rev. X **10**, 031009 (2020)
13. M.C. Tran, A.Y. Guo, C.L. Baldwin, A. Ehrenberg, A.V. Gorshkov, A. Lucas, Phys. Rev. Lett. **127**, 160401 (2021)
14. F.R. Chung, F.C. Graham, *Spectral Graph Theory*, vol. 92 (American Mathematical Soc., 1997)
15. B. Bollobás, *Random Graphs* (Springer, Berlin, 1998)
16. A. Bondy, M.R. Murty, *Graph Theory*, vol. 244 (Springer-Verlag, London, 2008)
17. G. Bentsen, Y. Gu, A. Lucas, Proc. National Acad. Sci. **116**(14), 6689 (2019)
18. D.A. Roberts, B. Swingle, Phys. Rev. Lett. **117**, 091602 (2016)
19. Z. Huang, X.K. Guo, Phys. Rev. E **97**, 062131 (2018)
20. Y.D. Lensky, X.L. Qi, J. High Energy Phys. **2019**(6), 25 (2019)
21. P. Pfeuty, Ann. Phys. **57**(1), 79 (1970)
22. P. Calabrese, J. Cardy, J. Stat. Mech.: Theory Exp. **2005**(04), P04010 (2005)
23. A.S. Buyskikh, M. Fagotti, J. Schachenmayer, F. Essler, A.J. Daley, Phys. Rev. A **93**, 053620 (2016)
24. J. Schachenmayer, B.P. Lanyon, C.F. Roos, A.J. Daley, Phys. Rev. X **3**(3), 031015 (2013)
25. P. Hauke, L. Tagliacozzo, Phys. Rev. Lett. **111**(20), 207202 (2013)
26. I. Frérot, P. Naldesi, T. Roscilde, Phys. Rev. Lett. **120**(5), 050401 (2018)
27. D. Vodola, L. Lepori, E. Ercolessi, G. Pupillo, New J. Phys. **18**(1), 015001 (2015)
28. M. Van Regemortel, D. Sels, M. Wouters, Phys. Rev. A **93**(3), 032311 (2016)
29. U. Schollwöck, Ann. Phys. **326**(1), 96 (2011)
30. S.R. White, Phys. Rev. Lett. **69**(19), 2863 (1992)
31. A.T. Sornborger, E.D. Stewart, Phys. Rev. A **60**(3), 1956 (1999)
32. S. Lloyd, Science **273**(5278), 1073 (1996)
33. G. Vidal, Phys. Rev. Lett. **91**(14), 147902 (2003)
34. A.J. Daley, C. Kollath, U. Schollwöck, G. Vidal, J. Stat. Mech.: Theory Exp. **2004**(4), P04005 (2004)
35. B. Pirvu, V. Murg, J.I. Cirac, F. Verstraete, New J. Phys. **12**(2), 025012 (2010)
36. J. Haegeman, C. Lubich, I. Oseledets, B. Vandereycken, F. Verstraete, Phys. Rev. B **94**(16), 165116 (2016)
37. M.P. Zaletel, R.S.K. Mong, C. Karrasch, J.E. Moore, F. Pollmann, Phys. Rev. B **91**(16), 165112 (2015)
38. F. Fröwis, V. Nebendahl, W. Dür, Phys. Rev. A **81**(6), 062337 (2010)
39. S. Paeckel, T. Köhler, A. Swoboda, S.R. Manmana, U. Schollwöck, C. Hubig, Ann. Phys. **411**, 167998 (2019)
40. S.A. Moses, J.P. Covey, M.T. Mienikowski, D.S. Jin, J. Ye, Nat. Phys. **13**(1), 13 (2017)

41. A. Frisch, M. Mark, K. Aikawa, S. Baier, R. Grimm, A. Petrov, S. Kotochigova, G. Quéméner, M. Lepers, O. Dulieu, F. Ferlaino, *Phys. Rev. Lett.* **115**(20), 203201 (2015)
42. S. Lepoutre, J. Schachenmayer, L. Gabardos, B. Zhu, B. Naylor, E. Maréchal, O. Gorceix, A.M. Rey, L. Vernac, B. Laburthe-Tolra, *Nat. Commun.* **10**(1714), 1 (2019)
43. L. Amico, R. Fazio, A. Osterloh, V. Vedral, *Rev. Mod. Phys.* **80**(2), 517 (2008)
44. J. Eisert, M. Cramer, M.B. Plenio, *Rev. Mod. Phys.* **82**(1), 277 (2010)
45. A. Browaeys, T. Lahaye, *Nat. Phys.* **16**(2), 132 (2020)
46. M. Morgado, S. Whitlock, *AVS Quantum Sci.* **3**(2), 023501 (2021)
47. P. Jurcevic, B.P. Lanyon, P. Hauke, C. Hempel, P. Zoller, R. Blatt, C.F. Roos, *Nature* **511**(7508), 202 (2014)
48. P. Richerme, Z.X. Gong, A. Lee, C. Senko, J. Smith, M. Foss-Feig, S. Michalakis, A.V. Gorshkov, C. Monroe, *Nature* **511**(7508), 198 (2014)
49. J. Eisert, M. van den Worm, S.R. Manmana, M. Kastner, *Phys. Rev. Lett.* **111**, 260401 (2013)
50. D.M. Storch, M. van den Worm, M. Kastner, **17**(6), 063021 (2015)
51. L. Cevolani, J. Despres, G. Carleo, L. Tagliacozzo, L. Sanchez-Palencia, *Phys. Rev. B* **98**, 024302 (2018)
52. C.F. Chen, A. Lucas, *Phys. Rev. Lett.* **123**, 250605 (2019)
53. D.V. Else, F. Machado, C. Nayak, N.Y. Yao, *Phys. Rev. A* **101**, 022333 (2020)
54. Z. Eldredge, Z.X. Gong, J.T. Young, A.H. Moosavian, M. Foss-Feig, A.V. Gorshkov, *Phys. Rev. Lett.* **119**(17), 170503 (2017)
55. T. Kuwahara, K. Saito, *Phys. Rev. X* **10**, 031010 (2020)
56. F. Franchini, *An Introduction to Integrable Techniques for One-Dimensional Quantum Systems* (Springer, Berlin, 2017)
57. J. Vidal, G. Palacios, C. Aslangul, *Phys. Rev. A* **70**(6), 062304 (2004)
58. J.I. Latorre, R. Orús, E. Rico, J. Vidal, *Phys. Rev. A* **71**(6), 064101 (2005)
59. Y. Sekino, L. Susskind, *J. High Energy Phys.* **2008**(10) (2008)
60. T. Hashizume, G.S. Bentsen, S. Weber, A.J. Daley, *Phys. Rev. Lett.* **126**, 200603 (2021)
61. J. Maldacena, S.H. Shenker, D. Stanford, *J. High Energy Phys.* **2016**(8) (2016)
62. G. Bentsen, T. Hashizume, A.S. Buyskikh, E.J. Davis, A.J. Daley, S.S. Gubser, M. Schleier-Smith, *Phys. Rev. Lett.* **123**(13), 130601 (2019)
63. C. Monroe, W.C. Campbell, L.M. Duan, Z.X. Gong, A.V. Gorshkov, P.W. Hess, R. Islam, K. Kim, N.M. Linke, G. Pagano, P. Richerme, C. Senko, N.Y. Yao, *Rev. Mod. Phys.* **93**, 025001 (2021)
64. T. Brydges, A. Elben, P. Jurcevic, B. Vermersch, C. Maier, B.P. Lanyon, P. Zoller, R. Blatt, C.F. Roos, *Science* **364**(6437), 260 (2019)
65. M. Saffman, T.G. Walker, K. Mølmer, *Rev. Mod. Phys.* **82**, 2313 (2010)
66. J. Yang, X. He, R. Guo, P. Xu, K. Wang, C. Sheng, M. Liu, J. Wang, A. Derevianko, M. Zhan, *Phys. Rev. Lett.* **117**(12), 123201 (2016)
67. H. Kim, W. Lee, H.g. Lee, H. Jo, Y. Song, J. Ahn, *Nat. Commun.* **7**, 1 (2016)
68. C. Gross, I. Bloch, *Science* **357**, 995 (2017)
69. H. Bernien, S. Schwartz, A. Keesling, H. Levine, A. Omran, H. Pichler, S. Choi, A.S. Zibrov, M. Endres, M. Greiner, V. Vuletić, M.D. Lukin, *Nature* **551**, 579 (2017)
70. J. Zhang, G. Pagano, P. Hess, A. Kyprianidis, P. Becker, H. Kaplan, A. Gorshkov, Z.X. Gong, C. Monroe, *Nature* **551**, 601 (2017)
71. H. Levine, A. Keesling, A. Omran, H. Bernien, S. Schwartz, A.S. Zibrov, M. Endres, M. Greiner, V. Vuletić, M.D. Lukin, *Phys. Rev. Lett.* **121**, 123603 (2018)
72. H. Levine, A. Keesling, G. Semeghini, A. Omran, T.T. Wang, S. Ebadi, H. Bernien, M. Greiner, V. Vuletić, H. Pichler, M.D. Lukin, *Phys. Rev. Lett.* **123**, 170503 (2019)
73. M. Kim, Y. Song, J. Kim, J. Ahn, *PRX Quantum* **1**, 020323 (2020)
74. P. Scholl, M. Schuler, H.J. Williams, A.A. Eberharter, D. Barredo, K.N. Schymik, V. Lienhard, L.P. Henry, T.C. Lang, T. Lahaye, et al. (2020). arXiv preprint arXiv:2012.12268
75. S. Ebadi, T.T. Wang, H. Levine, A. Keesling, G. Semeghini, A. Omran, D. Bluvstein, R. Samajdar, H. Pichler, W.W. Ho, S. Choi, S. Sachdev, M. Greiner, V. Vuletić, M.D. Lukin (2020). arXiv:2012.12281

76. A.W. Young, W.J. Eckner, W.R. Milner, D. Kedar, M.A. Norcia, E. Oelker, N. Schine, J. Ye, A.M. Kaufman, *Nature* **588**, 408 (2020)
77. J. Beugnon, C. Tuchendler, H. Marion, A. Gaëtan, Y. Miroshnychenko, Y.R. Sortais, A.M. Lance, M.P. Jones, G. Messin, A. Browaeys, P. Grangier, *Nat. Phys.* **3**, 696 (2007)
78. M. Endres, H. Bernien, A. Keesling, H. Levine, E.R. Anschuetz, A. Krajenbrink, C. Senko, V. Vuletić, M. Greiner, M.D. Lukin, *Science* **354**, 1024 (2016)
79. D. Barredo, S. de Léséleuc, V. Lienhard, T. Lahaye, A. Browaeys, *Science* **354**, 1021 (2016)
80. D. Barredo, V. Lienhard, S. de Léséleuc, T. Lahaye, A. Browaeys, *Nature* **561**, 79 (2018)
81. D.B. West, et al., *Introduction to Graph Theory*, vol. 2 (Prentice Hall, Upper Saddle River, 2001)
82. B. Bollobás, *Modern Graph Theory*, vol. 184 (Springer, Berlin, 2013)
83. H. Walther, B.T.H. Varcoe, B.G. Englert, T. Becker, *Rep. Prog. Phys.* **69**(5), 1325 (2006)
84. I.D. Leroux, M.H. Schleier-Smith, V. Vuletić, *Phys. Rev. Lett.* **104**(7), 073602 (2010)
85. A. Periwal, E.S. Cooper, P. Kunkel, J.F. Wienand, E.J. Davis, M. Schleier-Smith (2021). arXiv preprint arXiv:2106.04070
86. F. Reiter, A.S. Sørensen, *Phys. Rev. A* **85**, 032111 (2012)
87. C.L. Hung, A. González-Tudela, J.I. Cirac, H.J. Kimble, *Proc. Nat. Acad. Sci.* **113**(34), E4946 (2016)
88. R. Nandkishore, D.A. Huse, *Ann. Rev. Condens. Matter Phys.* **6**(1), 15 (2015)
89. D.A. Abanin, E. Altman, I. Bloch, M. Serbyn, *Rev. Mod. Phys.* **91**, 021001 (2019)
90. B. Gadway, B. Yan, *Journal of Physics B: Atomic, Mol. Opt. Phys.* **49**(15), 152002 (2016)
91. A. Chu, J. Will, J. Arlt, C. Klempt, A.M. Rey, *Phys. Rev. Lett.* **125**, 240504 (2020)
92. J. Zeiher, R. Van Bijnen, P. Schauß, S. Hild, J.y. Choi, T. Pohl, I. Bloch, C. Gross, *Nat. Phys.* **12**(12), 1095 (2016)
93. M.J. Gullans, S. Krastanov, D.A. Huse, L. Jiang, S.T. Flammia, *Phys. Rev. X* **11**, 031066 (2021)
94. P. Hayden, J. Preskill, *J. High Energy Phys.* **2007**, 120 (2007)
95. B. Yoshida, N.Y. Yao, *Phys. Rev. X* **9**, 011006 (2019)
96. K. Landsman, C. Figgatt, T. Schuster, N. Linke, B. Yoshida, N. Yao, C. Monroe, *Nature* **567**, 61 (2019)

Quantum Map Approach to Entanglement Transfer and Generation in Spin Chains



Salvatore Lorenzo, Francesco Plastina, Mirko Consiglio,
and Tony J. G. Apollaro

Abstract Quantum information processing protocols are efficiently implemented on spin- $\frac{1}{2}$ networks. A quantum communication protocol generally involves a certain number of parties having local access to a subset of a larger system, whose intrinsic dynamics are exploited in order to perform a specific task. In this chapter, we address such a scenario with the quantum dynamical map formalism, where the intended protocol is cast into the form of a map acting on the local subset of spins. We reformulate widely investigated protocols, such as one-qubit quantum state transfer and two-qubit entanglement distribution, with the quantum map formalism and demonstrate its usefulness in exploring less investigated protocols such as multi-qubit entanglement generation.

1 Introduction

Due to their formal analogy to quantum registers, quantum spin- $\frac{1}{2}$ networks have become the ideal testbed for many quantum information processing (QIP) protocols, ranging from quantum key distribution to quantum computation [1]. The availability of accurate theoretical models governing their dynamics, being amenable to solutions through either analytical techniques (especially for one-dimensional systems [2]) or powerful numerical techniques, such as those based on tensor network algorithms [3], allows for the investigation of various and distinct protocols. These include, on the one hand, standard QIP protocols such as one-qubit

S. Lorenzo

Dipartimento di Fisica e Chimica, Università di Palermo, Palermo, Italy
e-mail: salvatore.lorenzo@unipa.it

F. Plastina (✉)

Dipartimento Fisica, Università della Calabria, Rende, Malta
e-mail: francesco.plastina@fis.unical.it

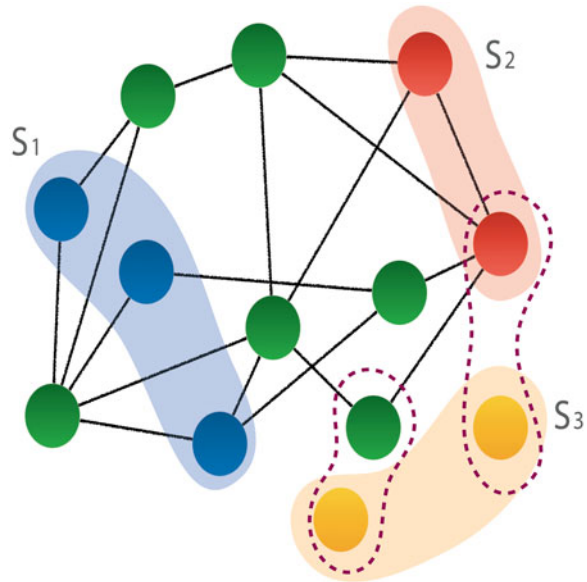
M. Consiglio · T. J. G. Apollaro

Department of Physics, University of Malta, Msida, Malta
e-mail: mirko.consiglio.16@um.edu.mt; tony.apollaro@um.edu.mt

quantum state transfer or bipartite Bell-type entanglement generation, taking place in a Hilbert space having dimensionality higher than that generally accessible via exact diagonalisation techniques. On the other hand, new QIP protocols are being introduced, aimed at exploring the complexity of the geometry of high-dimensional Hilbert spaces [4], such as in particular quantum state transfer [5]. At the same time, remarkable progress has been made in order to experimentally verify these QIP protocols and communication processes on a variety of experimental platforms, with which the simulation of some quantum spin networks has been successfully achieved, using: cold atoms [6–8], Rydberg atoms [9–11], integrated photonic chips [12], trapped ions [13–15], atom–cavity systems [16, 17], and superconducting circuits [18, 19], among others.

In the realm of the QIP tasks implementable with spin systems, a series of basic operations have been identified falling into the class of quantum communication protocols [20], which includes both the distribution and the generation of quantum resources at different space-time locations. A common communication scenario, depicted in Fig. 1, is represented by the circumstance in which a certain number of parties P_i , $i = 1, \dots, n$, each one having access to only a relatively small subset S_i of a larger physical system S (e.g., to a limited number of sites of a spin network), are required to receive/transfer quantum information from/to the others. Each party is then allowed to perform only *local quantum operations*; that is, P_i is able to act on S_i only, with the complementary system, $\bar{S}_i : S \setminus S_i$, being inaccessible to any quantum operation it can carry out. Additionally, one can also allow for classical communication, i.e., the exchange of classical information among the parties. This combination is referred to as LOCC (local operations and classical communication),

Fig. 1 Sketch of a generic quantum spin- $\frac{1}{2}$ network S , where each party P_i has access to the subset S_i ($i = 1, 2, 3$), on which local quantum operations are allowed. In addition, the parties can exchange classical communication among them. The shaded area encloses the subsets S_i , the dashed lines indicate quantum correlations between the spins entering the QIP protocol, and the black continuous lines are the interactions among the spins in the network



and the properties of LOCC operations determine to a large extent the fundamental limits for the performance of QIP protocols [21].

In this chapter, we will employ the quantum dynamical map formalism, typically used in the theory of open quantum systems [22], to illustrate QIP protocols for quantum state transfer, entanglement distribution, and generation on a homogeneous system, made up of a spin- $\frac{1}{2}$ network. We will assume that each party i has access to a subset of n_i spins of the network and has control over the interactions of the spins of this subset with the complementary system. Our aim is to derive the form of the dynamical map and, whenever possible, its analytical expression, in order to determine which LOCC operations maximise the efficiency of the investigated QIP protocols. We will focus, in particular, on the case of quantum dynamical maps obtained from spin Hamiltonians exhibiting $U(1)$ symmetry and, in order to obtain analytical results, investigate specific instances where the spin Hamiltonian is integrable.

The chapter is organised as follows: in Sect. 2, we review the quantum dynamical map formalism and apply it to $U(1)$ -symmetric Hamiltonians in Sect. 3. In Sect. 4, we illustrate the use of the formalism for case of single-qubit quantum state transfer and Bell-state distribution; in Sect. 5, we derive the two-qubit map for entanglement generation and distribution; in Sect. 7, we explore the use of a 4-qubit dynamical map for investigating multipartite entanglement; and, finally, in Sect. 8, we draw our conclusions and provide some outlooks.

2 Quantum Dynamical Maps

A quantum dynamical map between two systems associated to the Hilbert spaces \mathcal{H}_1 , \mathcal{H}_2 can be identified with a linear homomorphism $\Phi : \mathcal{D}(\mathcal{H}_1) \rightarrow \mathcal{D}(\mathcal{H}_2)$ mapping the space of density matrices acting on the *input* Hilbert space, into the space of density matrices acting on the *output* Hilbert space. Therefore, any Φ preserves the basic properties of the quantum states:

- Self-adjointness: $\Phi(\rho^\dagger)^\dagger = \Phi(\rho)$
- Complete positivity: $\Phi(\rho) > 0$
- Normalisation condition: $\text{Tr}(\rho) = 1$
- Linearity: $\Phi(a\rho_A + b\rho_B) = a\Phi(\rho_A) + b\Phi(\rho_B)$

For the purpose of our investigation, we consider, from now on, finite-dimensional Hilbert spaces. For such finite-dimensional case, the space of linear maps $\mathcal{L}(\mathbb{C}^n)$ can be identified with the algebra of $n \times n$ complex matrices, M_n . Any orthonormal basis $|i\rangle : i=1, \dots, n$ in \mathbb{C}^n allows to define the orthonormal basis of elementary matrices in M_n :

$$e_\alpha = e_{ij} = |i\rangle\langle j|, \quad (1)$$

and any map can be expressed as

$$\Phi(\rho) = \sum_{\alpha,\beta} A_{\alpha}^{\beta} \text{Tr}\{e_{\beta}\rho\}e_{\alpha}. \tag{2}$$

In this basis, the matrix A satisfies the following properties:

$$A_{\alpha}^{\beta} \equiv A_{ij}^{nm}, \quad \begin{cases} (A_{ij}^{nm})^* = A_{ji}^{mn}, \\ A_{ii}^{nm} = \delta_{mn}, \\ A_{ij}^{nm} \rho_{nm} > 0. \end{cases} \tag{3}$$

The map Φ is completely positive if there exists a family of N operators $K_i : i=1, \dots, N$ in M_n , which satisfy the condition $\sum_i K_i^{\dagger} K_i = \mathbb{1}$, and such that Φ can be decomposed as [23–25]

$$\Phi(\rho) = \sum_{k=1}^N E_k \rho E_k^{\dagger}. \tag{4}$$

By explicitly writing the matrix elements, we immediately find the relationship between map and Kraus operators:

$$(\Phi(\rho))_{ij} = \sum_{k=1}^N \sum_{nm} (E_k)_{in} (\rho)_{nm} (E_k^{\dagger})_{mj} = \sum_{nm} A_{ij}^{nm} (\rho)_{nm}. \tag{5}$$

Note that, from Eq. (4), it is evident that for $N = 1$ the map Φ represents a unitary map $\mathcal{U} = U\rho U^{\dagger}$.

In this chapter, we are interested in entanglement generation and transfer between two sub-parties that we dub sender and receiver, each of them taking care, controlling and possibly making measurements on a subset of the system’s spins. We denote the states of the subsystems pertaining to sender and receiver as ρ_S and ρ_R , respectively, and assume that these are the marginals obtained from the state of a larger system σ , whose time evolution is dictated by a Hamiltonian generating a unitary map, i.e., $\sigma(t) = \mathcal{U}(t)(\sigma(0))$. We assume that the initial state of this larger system, $\sigma(0)$, is a product state between ρ_S and a reference pure state $|\Psi\rangle_{\bar{S}}$. In other words, we are concerned with maps of the following form:

$$\rho_R = \Phi(\rho_S) = \text{Tr}_{\bar{R}}\{\mathcal{U}(\rho_S \otimes |\Psi\rangle_{\bar{S}}\langle\Psi|)\}, \tag{6}$$

where we indicate with $\text{Tr}_{\bar{R}}$ the partial trace over all but R degrees of freedom. Denoting with $|r\rangle_{\bar{R}}$ an orthonormal basis of $\mathcal{H}_{\bar{R}}$, we have

$$\rho_R = \Phi(\rho_S) = \sum_r \left({}_{\bar{R}}\langle r | U | \Psi \rangle_{\bar{S}} \right) \rho_S \left({}_{\bar{S}}\langle \Psi | U^{\dagger} | r \rangle_{\bar{R}} \right) = \sum_r E_r \rho_S E_r^{\dagger}. \tag{7}$$

It is important to remember that the Kraus operators E_r are time-dependent and that they depend on the choice of the basis in $\mathcal{H}_{\overline{R}}$ and, more generally, on the choice of sender and receiver subsets themselves. The matrix representation of the corresponding map can be found according to Eq. (5).

3 U(1)-Symmetric Hamiltonians

In this section, we will derive the general form of the quantum dynamical map in Eq. (5) when the unitary evolution operator entering Eq. (6) exhibits $U(1)$ symmetry. Without loss of generality, we focus on spin- $\frac{1}{2}$ Hamiltonians with isotropic Heisenberg-type interactions in the XY plane:

$$\hat{H} = \sum_{i,j} \left(J_{ij} \left(\hat{\sigma}_i^x \hat{\sigma}_j^x + \hat{\sigma}_i^y \hat{\sigma}_j^y \right) + \Delta_{ij} \hat{\sigma}_i^z \hat{\sigma}_j^z \right) + \sum_i h_i \hat{\sigma}_i^z, \tag{8}$$

where $\hat{\sigma}_i^\alpha$ ($\alpha = x, y, z$) are the usual Pauli matrices, i denotes the index of the site, J_{ij} and Δ_{ij} are, respectively, the two-qubit interaction terms in the XY plane and along the Z -axis, and h_i is the magnetic field along the Z -axis. In fact, the class of Hamiltonians exhibiting the $U(1)$ symmetry is larger than that described by Eq. (8) and encompasses Hamiltonians with Dzyaloshinskii–Moriya [26] and XY isotropic cluster interaction terms [27], among others.

In terms of spin operators, the $U(1)$ symmetry implies that the total magnetisation along the Z -axis, $\langle \hat{M} \rangle = \sum_{i=1}^N \langle \hat{\sigma}_i^z \rangle$, is a conserved quantity and the operator \hat{M} commutes with U . Hence, it is possible to divide the whole Hilbert space into invariant subspaces, labelled by the eigenvalues of \hat{M} , with each subspace having the dimension determined by the degeneracy of the eigenvalue, $\binom{N}{i}$, where i denotes the number of flipped spins. Indeed, by writing the spectral decomposition of \hat{M} as

$$\hat{M} = \sum_k \sum_d \lambda_k \left| \phi_k^d \right\rangle \left\langle \phi_k^d \right|, \tag{9}$$

we know that $U \left| \phi_k^d \right\rangle$ is an eigenstate of \hat{M} with eigenvalue λ_k , i.e.,

$$\left\langle \phi_{k'}^{d'} \right| U \left| \phi_k^d \right\rangle = \left\langle \phi_{k'}^{d'} \right| U \left| \phi_k^d \right\rangle \delta_{kk'} = (f_k)_d^{d'} \delta_{kk'}. \tag{10}$$

Thus, we can then write U as a direct sum of unitary operators acting in each subspace

$$U = U_0 \oplus U_1 \oplus U_2 \oplus \dots \tag{11}$$

If we now observe the elements of the Kraus operators entering in Eq. (7), they take the form

$$(E_r)_{in} = {}_R \langle i | E_r | n \rangle_S = {}_R \langle i | {}_{\bar{R}} \langle r | U | \Psi \rangle_{\bar{S}} | n \rangle_S . \tag{12}$$

This inherently places some constraints on the elements of the Kraus operators and consequently on the map elements. Indeed, if the state $|\Psi\rangle_{\bar{S}} |n\rangle_S$ belongs in a given subspace, then ${}_R \langle i | {}_{\bar{R}} \langle r |$ must belong to that subspace as well in order for the above equation to be non-zero. Without loss of generality, we take $|\Psi\rangle_{\bar{S}} |n\rangle_S$ as living in the n -th subspace, implying that $i+r = n$. In the following, we will assume $|\Psi\rangle_{\bar{S}} = |\mathbf{0}\rangle$, i.e., a fully polarised state.

4 One-Qubit Map

To begin our analysis, let us consider the simplest case: a map from qubit i (the sender) to qubit j (the receiver): $\hat{\rho}_j(t) = \Phi(t)\hat{\rho}_i(0)$, where i and j are (possibly identical) positions in a spin network. In this case, we have two possible values of $r = 0, 1$ and, consequently, two Kraus operators:

$$E_0 = \begin{pmatrix} 1 & 0 \\ 0 & f_i^j \end{pmatrix}, \quad E_1^k = \begin{pmatrix} 0 & 0 \\ f_i^k & 0 \end{pmatrix} \text{ with } k \neq j . \tag{13}$$

By using Eq. (5), we can write the map as

$$\begin{pmatrix} \rho_{00} \\ \rho_{01} \\ \rho_{10} \\ \rho_{11} \end{pmatrix}_j = \begin{pmatrix} 1 & 0 & 0 & 1 - |f_i^j|^2 \\ 0 & f_i^j & 0 & 0 \\ 0 & 0 & (f_i^j)^* & 0 \\ 0 & 0 & 0 & |f_i^j|^2 \end{pmatrix} \begin{pmatrix} \rho_{00} \\ \rho_{01} \\ \rho_{10} \\ \rho_{11} \end{pmatrix}_i , \tag{14}$$

where we use the completeness relation $\sum_n |f_i^n|^2 = 1$.

In this simple case, perfect state transfer, i.e., $\hat{\rho}_{nm}^j = \hat{\rho}_{nm}^i$, entails $f_i^j = (f_i^j)^* = 1$. A considerable amount of research has been performed in order to investigate the conditions that allow to maximise the transition amplitude [28].

In Bose’s original protocol [29], this is achieved by a local magnetic field acting on the spins. The map in Eq. (14) is also informative about remote state preparation protocols: the coherence (in the computational basis) of spin j cannot increase with respect to that of spin i under the action of this map as the off-diagonal elements of the output density matrix can only be suppressed, or, at most, maintain their initial amplitude.

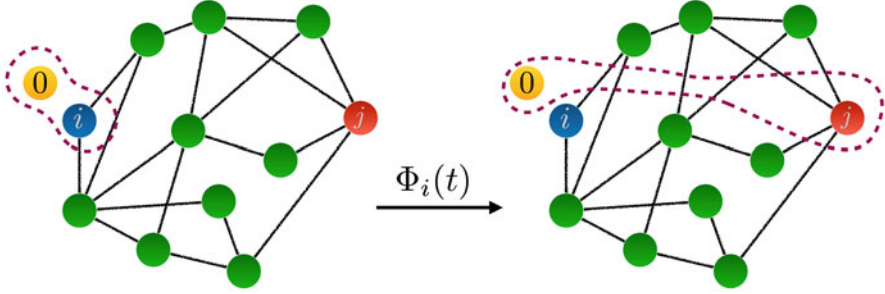


Fig. 2 A schematic picture of an entanglement distribution protocol. Initially, the external qubit 0 is entangled with qubit i , and the aim is to exploit the map in Eq. (16) to entangle the former with qubit j

Apart from quantum state transfer protocols, the map in Eq. (14) can be used to analyse entanglement distribution protocols, like the one reported in Refs. [29, 30] and sketched in Fig. 2. Explicitly, the map is given by

$$\hat{\rho}(t)_{0j} = (\mathbb{1}_0 \otimes \Phi_i(t)) \hat{\rho}(0)_{0i} , \tag{15}$$

where $\mathbb{1}_0$ is the 4-dimensional identity map acting on qubit 0 and $\Phi_i(t)$ is given by the map in Eq. (14) acting on qubit i . The map reads

$$\begin{pmatrix} \rho_{00} \\ \rho_{01} \\ \rho_{02} \\ \rho_{03} \\ \rho_{10} \\ \rho_{11} \\ \rho_{12} \\ \rho_{13} \\ \rho_{20} \\ \rho_{21} \\ \rho_{22} \\ \rho_{23} \\ \rho_{30} \\ \rho_{31} \\ \rho_{32} \\ \rho_{33} \end{pmatrix}_{0,j} = \begin{pmatrix} 1 & 0 & 0 & 0 & 0 & 1-|f|^2 & 0 & 0 & 0 & 0 & 0 & 0 & 0 & 0 & 0 & 0 \\ 0 & f & 0 & 0 & 0 & 0 & 0 & 0 & 0 & 0 & 0 & 0 & 0 & 0 & 0 & 0 \\ 0 & 0 & 1 & 0 & 0 & 0 & 0 & 1-|f|^2 & 0 & 0 & 0 & 0 & 0 & 0 & 0 & 0 \\ 0 & 0 & 0 & f & 0 & 0 & 0 & 0 & 0 & 0 & 0 & 0 & 0 & 0 & 0 & 0 \\ 0 & 0 & 0 & 0 & f^* & 0 & 0 & 0 & 0 & 0 & 0 & 0 & 0 & 0 & 0 & 0 \\ 0 & 0 & 0 & 0 & 0 & |f|^2 & 0 & 0 & 0 & 0 & 0 & 0 & 0 & 0 & 0 & 0 \\ 0 & 0 & 0 & 0 & 0 & 0 & f^* & 0 & 0 & 0 & 0 & 0 & 0 & 0 & 0 & 0 \\ 0 & 0 & 0 & 0 & 0 & 0 & 0 & |f|^2 & 0 & 0 & 0 & 0 & 0 & 0 & 0 & 0 \\ 0 & 0 & 0 & 0 & 0 & 0 & 0 & 0 & 1 & 0 & 0 & 0 & 1-|f|^2 & 0 & 0 & 0 \\ 0 & 0 & 0 & 0 & 0 & 0 & 0 & 0 & 0 & f & 0 & 0 & 0 & 0 & 0 & 0 \\ 0 & 0 & 0 & 0 & 0 & 0 & 0 & 0 & 0 & 0 & 1 & 0 & 0 & 0 & 0 & 1-|f|^2 \\ 0 & 0 & 0 & 0 & 0 & 0 & 0 & 0 & 0 & 0 & 0 & f & 0 & 0 & 0 & 0 \\ 0 & 0 & 0 & 0 & 0 & 0 & 0 & 0 & 0 & 0 & 0 & 0 & f^* & 0 & 0 & 0 \\ 0 & 0 & 0 & 0 & 0 & 0 & 0 & 0 & 0 & 0 & 0 & 0 & 0 & |f|^2 & 0 & 0 \\ 0 & 0 & 0 & 0 & 0 & 0 & 0 & 0 & 0 & 0 & 0 & 0 & 0 & 0 & f^* & 0 \\ 0 & 0 & 0 & 0 & 0 & 0 & 0 & 0 & 0 & 0 & 0 & 0 & 0 & 0 & 0 & |f|^2 \end{pmatrix} \begin{pmatrix} \rho_{00} \\ \rho_{01} \\ \rho_{02} \\ \rho_{03} \\ \rho_{10} \\ \rho_{11} \\ \rho_{12} \\ \rho_{13} \\ \rho_{20} \\ \rho_{21} \\ \rho_{22} \\ \rho_{23} \\ \rho_{30} \\ \rho_{31} \\ \rho_{32} \\ \rho_{33} \end{pmatrix}_{0,i} . \tag{16}$$

In the original entanglement distribution protocol given in Ref. [29], the entanglement encoded in a singlet state on sites 0 and i is distributed to sites 0 and j resulting in a concurrence $C = |f_i^j(t)|$. From the map in Eq. (16), it is evident that the same holds true for any Bell state. On the other hand, for X -type density matrices [31], the distributed entanglement does not increase linearly with the (modulus of the) transition amplitude f but instead reads

$$C = 2 \max [0, C_1, C_2] , \tag{17}$$

where

$$C_1 = |f| \left(|\rho_{12}| - \sqrt{\rho_{33} (\rho_{00} + \rho_{11} (1 - |f|^2))} \right) , \tag{18}$$

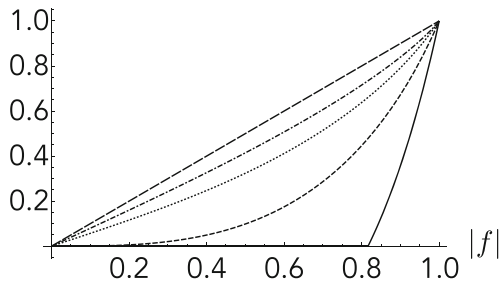
$$C_2 = |f| \left(|\rho_{03}| - \sqrt{\rho_{11} (\rho_{22} + \rho_{33} (1 - |f|^2))} \right) \tag{19}$$

denote the so-called anti-parallel and parallel concurrences, respectively [32]. Looking carefully at the map, one can see that the ratio of transferred entanglement over initial entanglement depends only on the transition amplitude and not on the fact that entanglement is of the parallel or anti-parallel type. The dependence on $|f|$ is not linear, as in the pure Bell-state scenario, and in Fig. 3, we show the ratio of the transferred concurrence vs. the initial concurrence ($C = \frac{3p-1}{2}$) for an initial Werner state

$$\hat{\rho}_W = p |\Psi_B\rangle \langle \Psi_B| + (1 - p) \frac{\mathbb{1}}{4} , \tag{20}$$

where $|\Psi_B\rangle$ is any Bell state.

Fig. 3 Ratio of transferred entanglement vs. $|f|$ for a Werner state for different values of p in Eq. (20). The curves, from bottom to top, are drawn for $p = 0.4, 0.5, 0.7, 0.9, 1$



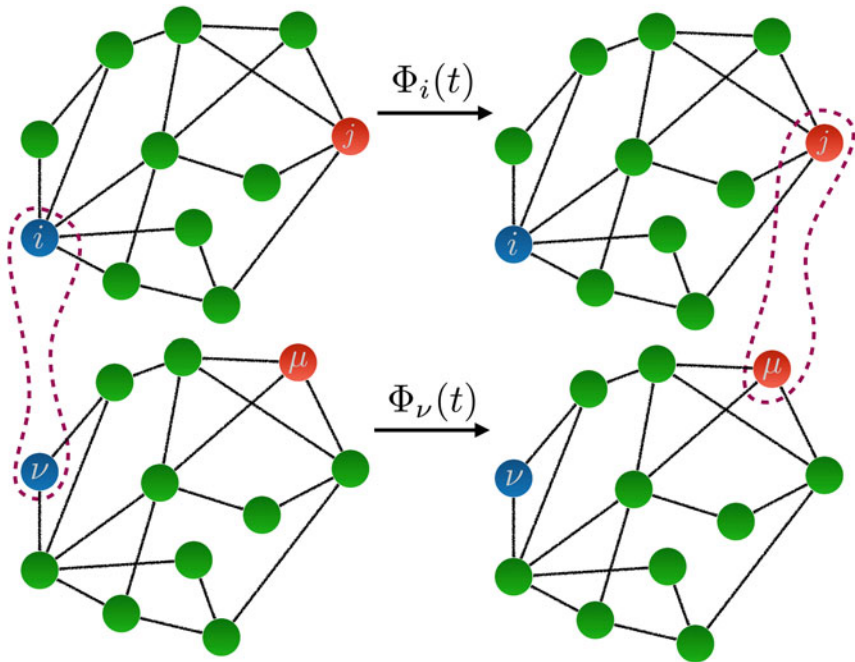


Fig. 4 A schematic picture of an entanglement distribution protocol. Initially, qubit i is entangled with qubit ν , and the aim is to exploit the map in Eq. (16) to entangle qubit j with qubit μ

Now we consider the case where the entanglement distribution protocol is designed in order to send to sites (n, μ) (the receiver sites), and the entanglement initially shared between sites (i, ν) (sending sites) using two independent spin networks. A particular instance of this setup is given in Fig. 4, and both there and in the setting of the problem above, Latin (Greek) letters are used to denote the sites on the first (second) chain. This protocol is reminiscent of the dual-rail encoding protocol for sending a single-qubit state [33].

The map is given by

$$\hat{\rho}(t)_{j\mu} = (\Phi_i(t) \otimes \Phi_\nu(t)) \hat{\rho}(0)_{i\nu} \tag{21}$$

and reads

$$\left(\begin{array}{cccccccccccccccc} 1 & 0 & 0 & 0 & 0 & 1-|g|^2 & 0 & 0 & 0 & 0 & 1-|f|^2 & 0 & 0 & 0 & 0 & (1-|f|^2)(1-|g|^2) \\ 0 & g & 0 & 0 & 0 & 0 & 0 & 0 & 0 & 0 & 0 & g(1-|f|^2) & 0 & 0 & 0 & 0 \\ 0 & 0 & f & 0 & 0 & 0 & 0 & f(1-|g|^2) & 0 & 0 & 0 & 0 & 0 & 0 & 0 & 0 \\ 0 & 0 & 0 & fg & 0 & 0 & 0 & 0 & 0 & 0 & 0 & 0 & 0 & 0 & 0 & 0 \\ 0 & 0 & 0 & 0 & g^* & 0 & 0 & 0 & 0 & 0 & 0 & 0 & 0 & 0 & (1-|f|^2)g^* & 0 \\ 0 & 0 & 0 & 0 & 0 & |g|^2 & 0 & 0 & 0 & 0 & 0 & 0 & 0 & 0 & 0 & (1-|f|^2)|g|^2 \\ 0 & 0 & 0 & 0 & 0 & 0 & fg^* & 0 & 0 & 0 & 0 & 0 & 0 & 0 & 0 & 0 \\ 0 & 0 & 0 & 0 & 0 & 0 & 0 & f|g|^2 & 0 & 0 & 0 & 0 & 0 & 0 & 0 & 0 \\ 0 & 0 & 0 & 0 & 0 & 0 & 0 & 0 & f^* & 0 & 0 & 0 & 0 & (1-|g|^2)f^* & 0 & 0 \\ 0 & 0 & 0 & 0 & 0 & 0 & 0 & 0 & 0 & gf^* & 0 & 0 & 0 & 0 & 0 & 0 \\ 0 & 0 & 0 & 0 & 0 & 0 & 0 & 0 & 0 & 0 & |f|^2 & 0 & 0 & 0 & 0 & |f|^2(1-|g|^2) \\ 0 & 0 & 0 & 0 & 0 & 0 & 0 & 0 & 0 & 0 & 0 & g|f|^2 & 0 & 0 & 0 & 0 \\ 0 & 0 & 0 & 0 & 0 & 0 & 0 & 0 & 0 & 0 & 0 & 0 & f^*g^* & 0 & 0 & 0 \\ 0 & 0 & 0 & 0 & 0 & 0 & 0 & 0 & 0 & 0 & 0 & 0 & 0 & |g|^2f^* & 0 & 0 \\ 0 & 0 & 0 & 0 & 0 & 0 & 0 & 0 & 0 & 0 & 0 & 0 & 0 & 0 & |f|^2g^* & 0 \\ 0 & 0 & 0 & 0 & 0 & 0 & 0 & 0 & 0 & 0 & 0 & 0 & 0 & 0 & 0 & |f|^2|g|^2 \end{array} \right) \quad (22)$$

where we have used the short-hand notation $f = f_i^j$ and $g = f_v^\mu$. If we assume that the two spin networks are identical and that the locations of the initially correlated sites and of the receiving ones are also the same on the two networks, the matrix above simplifies as $f = g$. Again, this is the same settings adopted in the dual-rail protocol [34] to attain perfect state transfer. In such a case, with $\hat{\rho}_{i\nu}$ being an X -type state, the anti-parallel and parallel concurrences reported in Eq. (17) are given by

$$C_1 = |f|^2 \left(|\rho_{12}| - \sqrt{\rho_{33} (\rho_{00} + (1 - |f|^2) (\rho_{11} + \rho_{22} + (1 - |f|^2) \rho_{33}))} \right) \quad (23)$$

$$C_2 = |f|^2 \left(|\rho_{03}| - \sqrt{(\rho_{11} + (1 - |f|^2) \rho_{33}) (\rho_{22} + (1 - |f|^2) \rho_{33})} \right). \quad (24)$$

Due to the use of two channels, as depicted in Fig. 4, the ratio of transferred over initial entanglement depends, this time, not only on the transition amplitude, but also on the type of entanglement (whether parallel or anti-parallel). This is also the case when investigating the effect of the spin environment on the entanglement, which has been carried out in Ref. [35], by analysing the properties of the map $\hat{\rho}(t)_{j\mu} = (\Phi_i(t) \otimes \Phi_v(t)) \hat{\rho}(0)_{j\mu}$.

As one can expect, the anti-parallel entanglement C_1 attains larger values with respect to C_2 at fixed transition amplitude $|f|$. Intuitively, this is due to the fact that in the former case, only one excitation is present in the system, whereas, in the

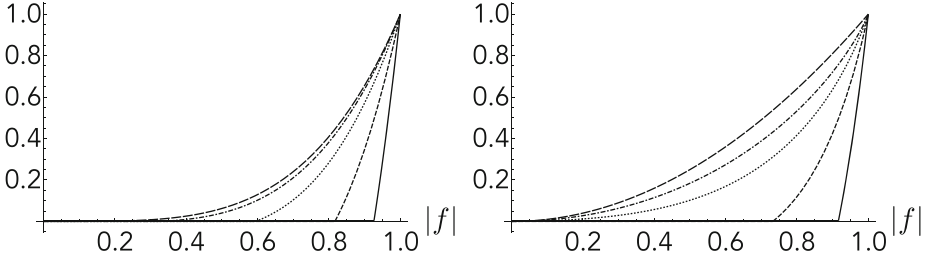


Fig. 5 Ratio of transferred over initial entanglement vs. $|f|$ for a Werner state for different values of p in Eq. (20). The curves, from bottom to top, are drawn for $p = 0.4, 0.5, 0.7, 0.9, 1$. The left plot corresponds to a Werner state with maximally entangled component given by $|\Psi_B\rangle = |\Phi^+\rangle$, whereas for the right plot we have chosen $|\Psi_B\rangle = |\Psi^+\rangle$

latter, two excitations enter the dynamics. This leads to an increase in the effects of decoherence due to the dispersion of the extra excitation all over the network. A figure of merit describing the amount of transferred entanglement is reported in Fig. 5, in the case of initial Werner states (Eq. 20).

5 Two-Qubit Map

In this section, we derive the expression of Φ for the case of two sender qubits located at arbitrary positions i and j in a spin network. For a generic two-qubit receiver at sites n, m , it is instructive to write the map in matrix form.

$$\begin{pmatrix} \rho_{00} \\ \rho_{01} \\ \rho_{02} \\ \rho_{03} \\ \rho_{10} \\ \rho_{11} \\ \rho_{12} \\ \rho_{13} \\ \rho_{20} \\ \rho_{21} \\ \rho_{22} \\ \rho_{23} \\ \rho_{30} \\ \rho_{31} \\ \rho_{32} \\ \rho_{33} \end{pmatrix}_{i,j} = \begin{pmatrix} A_{00}^{00} & 0 & 0 & 0 & 0 & 0 & A_{00}^{11} & A_{00}^{12} & 0 & 0 & A_{00}^{21} & A_{00}^{22} & 0 & 0 & 0 & 0 & 0 & 0 & A_{00}^{33} \\ 0 & A_{01}^{01} & A_{01}^{02} & 0 & 0 & 0 & 0 & 0 & A_{01}^{13} & 0 & 0 & 0 & A_{01}^{23} & 0 & 0 & 0 & 0 & 0 & 0 \\ 0 & A_{02}^{01} & A_{02}^{02} & 0 & 0 & 0 & 0 & 0 & A_{02}^{13} & 0 & 0 & 0 & A_{02}^{23} & 0 & 0 & 0 & 0 & 0 & 0 \\ 0 & 0 & 0 & A_{03}^{03} & 0 & 0 & 0 & 0 & 0 & 0 & 0 & 0 & 0 & 0 & 0 & 0 & 0 & 0 & 0 \\ 0 & 0 & 0 & 0 & A_{10}^{10} & 0 & 0 & 0 & 0 & A_{10}^{20} & 0 & 0 & 0 & 0 & 0 & A_{10}^{31} & A_{10}^{32} & 0 & 0 \\ 0 & 0 & 0 & 0 & 0 & A_{11}^{11} & A_{11}^{12} & 0 & 0 & A_{11}^{21} & A_{11}^{22} & 0 & 0 & 0 & 0 & 0 & 0 & 0 & A_{11}^{33} \\ 0 & 0 & 0 & 0 & 0 & A_{12}^{11} & A_{12}^{12} & 0 & 0 & A_{12}^{21} & A_{12}^{22} & 0 & 0 & 0 & 0 & 0 & 0 & 0 & A_{12}^{33} \\ 0 & 0 & 0 & 0 & 0 & 0 & 0 & 0 & A_{13}^{13} & 0 & 0 & 0 & A_{13}^{23} & 0 & 0 & 0 & 0 & 0 & 0 \\ 0 & 0 & 0 & 0 & A_{20}^{10} & 0 & 0 & 0 & 0 & A_{20}^{20} & 0 & 0 & 0 & 0 & 0 & A_{20}^{31} & A_{20}^{32} & 0 & 0 \\ 0 & 0 & 0 & 0 & 0 & A_{21}^{11} & A_{21}^{12} & 0 & 0 & A_{21}^{21} & A_{21}^{22} & 0 & 0 & 0 & 0 & 0 & 0 & 0 & A_{21}^{33} \\ 0 & 0 & 0 & 0 & 0 & A_{22}^{11} & A_{22}^{12} & 0 & 0 & A_{22}^{21} & A_{22}^{22} & 0 & 0 & 0 & 0 & 0 & 0 & 0 & A_{22}^{33} \\ 0 & 0 & 0 & 0 & 0 & 0 & 0 & 0 & 0 & A_{23}^{13} & 0 & 0 & 0 & A_{23}^{23} & 0 & 0 & 0 & 0 & 0 \\ 0 & 0 & 0 & 0 & 0 & 0 & 0 & 0 & 0 & 0 & 0 & 0 & 0 & 0 & 0 & A_{30}^{30} & 0 & 0 & 0 \\ 0 & 0 & 0 & 0 & 0 & 0 & 0 & 0 & 0 & 0 & 0 & 0 & 0 & 0 & 0 & A_{31}^{31} & A_{31}^{32} & 0 & 0 \\ 0 & 0 & 0 & 0 & 0 & 0 & 0 & 0 & 0 & 0 & 0 & 0 & 0 & 0 & 0 & A_{32}^{31} & A_{32}^{32} & 0 & 0 \\ 0 & 0 & 0 & 0 & 0 & 0 & 0 & 0 & 0 & 0 & 0 & 0 & 0 & 0 & 0 & 0 & 0 & 0 & A_{33}^{33} \end{pmatrix} \begin{pmatrix} \rho_{00} \\ \rho_{01} \\ \rho_{02} \\ \rho_{03} \\ \rho_{10} \\ \rho_{11} \\ \rho_{12} \\ \rho_{13} \\ \rho_{20} \\ \rho_{21} \\ \rho_{22} \\ \rho_{23} \\ \rho_{30} \\ \rho_{31} \\ \rho_{32} \\ \rho_{33} \end{pmatrix}_{n,m} \tag{25}$$

The map in Eq. (25) can be written in a more compact form defining the Kraus operators in all of magnetisation sectors, as illustrated in Sect. 3, where Eq. (12) has elements

$$A = E_0 \otimes E_0^* + E_1 \otimes E_1^* + E_2 \otimes E_2^*, \quad (26)$$

and

$$E_0 = \begin{pmatrix} 1 & 0 & 0 & 0 \\ 0 & f_j^m & f_i^m & 0 \\ 0 & f_j^n & f_i^n & 0 \\ 0 & 0 & 0 & f_{ij}^{nm} \end{pmatrix}, \quad E_1^{k \neq i, j} = \begin{pmatrix} 0 & f_j^k & f_i^k & 0 \\ 0 & 0 & 0 & f_{ij}^{km} \\ 0 & 0 & 0 & f_{ij}^{kn} \\ 0 & 0 & 0 & 0 \end{pmatrix}, \quad E_2^{k, l \neq i, j} = \begin{pmatrix} 0 & 0 & 0 & f_{ij}^{kl} \\ 0 & 0 & 0 & 0 \\ 0 & 0 & 0 & 0 \\ 0 & 0 & 0 & 0 \end{pmatrix}. \quad (27)$$

This explicit form of the map shows, for example, that $\rho_{03}(t) = A_{03}^{03} \rho_{03}(0)$. As a consequence (and analogously to the impossibility of amplifying coherence in the single-qubit case), the Bell states $|\Phi^\pm\rangle$ cannot be generated by this map, irrespective of the initial state of the qubits. On the other hand, the Bell states $|\Psi^\pm\rangle$ can be generated by LOCC as the coherences ρ_{12} can be build up starting from ρ_{11} , ρ_{22} , and/or ρ_{33} , i.e., by locally flipping the spins on the sender and/or receiver sites.

From Ref. [36], we can borrow the following two-qubit map's elements for the case in which the receiver coincides with the sender (so that, in fact, we are evaluating how good is information storage at sites i, j), $\hat{\rho}_{ij}(t) = \Phi_i \hat{\rho}_{ij}(0)$

$$\begin{aligned} A_{00}^{00} &= 1, \quad A_{00}^{11} = 1 - |f_i^i|^2 - |f_j^j|^2, \quad A_{00}^{22} = 1 - |f_j^i|^2 - |f_i^j|^2, \\ A_{00}^{33} &= 1 - |f_{ij}^{mi}|^2 - |f_{ij}^{mj}|^2 - |f_{ij}^{ij}|^2, \quad A_{00}^{12} = -f_i^i (f_j^j)^* - f_i^i (f_j^j)^*, \\ A_{00}^{21} &= -f_j^j (f_i^i)^* - f_j^j (f_i^i)^*, \\ A_{01}^{01} &= (f_i^j)^*, \quad A_{01}^{02} = (f_j^i)^*, \quad A_{01}^{13} = f_i^m (f_{ij}^{mj})^*, \quad A_{01}^{23} = f_j^m (f_{ij}^{mj})^*, \\ A_{02}^{01} &= (f_i^i)^*, \quad A_{02}^{02} = (f_j^j)^*, \quad A_{02}^{13} = f_i^m (f_{ij}^{mi})^*, \quad A_{02}^{23} = f_j^m (f_{ij}^{mi})^*, \\ A_{03}^{03} &= (f_{ij}^{ij})^*, \\ A_{11}^{11} &= |f_i^j|^2, \quad A_{11}^{12} = f_i^j (f_j^i)^*, \quad A_{11}^{21} = f_j^i (f_i^j)^*, \quad A_{11}^{22} = |f_j^i|^2, \quad A_{11}^{33} = |f_{ij}^{mj}|^2, \\ A_{12}^{11} &= f_i^j (f_i^i)^*, \quad A_{12}^{12} = f_i^j (f_j^i)^*, \quad A_{12}^{21} = f_j^i (f_i^i)^*, \quad A_{12}^{22} = f_j^i (f_j^j)^*, \quad A_{12}^{33} = f_{ij}^{mj} (f_{ij}^{mi})^*, \\ A_{13}^{13} &= f_i^j (f_{ij}^{ij})^*, \quad A_{13}^{23} = f_j^i (f_{ij}^{ij})^*, \end{aligned}$$

$$\begin{aligned}
A_{22}^{33} &= |f_{ij}^{mi}|^2, \quad A_{22}^{11} = |f_i^i|^2, \quad A_{22}^{22} = |f_j^j|^2, \quad A_{22}^{12} = f_i^i (f_j^j)^*, \quad A_{22}^{21} = f_j^j (f_i^i)^*, \\
A_{23}^{13} &= f_i^i (f_{ij}^{ij})^*, \quad A_{23}^{23} = f_j^j (f_{ij}^{ij})^*, \quad A_{33}^{33} = |f_{ij}^{ij}|^2,
\end{aligned} \tag{28}$$

where, whenever the index m appears, a summation over all $m \neq S, R$ is intended.

For the general case describing the transfer of a given two-qubit state from the sending pair i, j to the receiving pair n, m , $\hat{\rho}_{nm}(t) = \Phi_t \hat{\rho}_{ij}(0)$, the matrix elements read

$$\begin{aligned}
A_{00}^{00} &= 1, \quad A_{00}^{11} = f_j^k (f_j^k)^*, \quad A_{00}^{12} = f_j^k (f_i^k)^*, \\
A_{00}^{21} &= f_i^k (f_j^k)^*, \quad A_{00}^{22} = f_i^k (f_i^k)^*, \quad A_{00}^{33} = f_{ij}^{kl} (f_{ij}^{kl})^*, \\
A_{01}^{01} &= (f_j^m)^*, \quad A_{01}^{02} = (f_i^m)^*, \quad A_{01}^{13} = f_j^k (f_{ij}^{km})^*, \quad A_{01}^{23} = f_i^k (f_{ij}^{km})^*, \\
A_{02}^{01} &= (f_j^n)^* A_{02}^{02} = (f_i^n)^*, \quad A_{02}^{13} = f_j^k (f_{ij}^{nk})^*, \quad A_{02}^{23} = f_i^k (f_{ij}^{nk})^*, \\
A_{03}^{03} &= (f_{ij}^{nm})^*, \\
A_{10}^{10} &= f_j^m, \quad A_{10}^{20} = f_i^m, \quad A_{10}^{31} = f_{ij}^{km} (f_j^k)^*, \quad A_{10}^{32} = f_{ij}^{km} (f_i^k)^*, \\
A_{11}^{11} &= f_j^m (f_j^m)^*, \quad A_{11}^{12} = f_j^m (f_i^m)^*, \quad A_{11}^{21} = f_i^m (f_j^m)^*, \\
A_{11}^{22} &= f_i^m (f_i^m)^*, \quad A_{11}^{33} = f_{ij}^{km} (f_{ij}^{km})^*, \\
A_{12}^{11} &= f_j^m (f_j^n)^*, \quad A_{12}^{12} = f_j^m (f_i^n)^*, \quad A_{12}^{21} = f_i^m (f_j^n)^* A_{12}^{22} = f_i^m (f_i^n)^*, \\
A_{12}^{33} &= f_{ij}^{km} (f_{ij}^{nk})^*, \\
A_{13}^{13} &= f_j^m (f_{ij}^{nm})^*, \quad A_{13}^{23} = f_i^m (f_{ij}^{nm})^*, \\
A_{20}^{10} &= f_j^n, \quad A_{20}^{20} = f_i^n, \quad A_{20}^{31} = f_{ij}^{nk} (f_j^k)^*, \quad A_{20}^{32} = f_{ij}^{nk} (f_i^k)^*, \\
A_{21}^{11} &= f_j^n (f_j^m)^*, \quad A_{21}^{12} = f_j^n (f_i^m)^*, \quad A_{21}^{21} = f_i^n (f_j^m)^* A_{21}^{22} = f_i^n (f_i^m)^*, \\
A_{21}^{33} &= f_{ij}^{nk} (f_{ij}^{km})^*, \\
A_{22}^{11} &= f_j^n (f_j^n)^*, \quad A_{22}^{12} = f_j^n (f_i^n)^*, \quad A_{22}^{21} = f_i^n (f_j^n)^* A_{22}^{22} = f_i^n (f_i^n)^*, \\
A_{22}^{33} &= f_{ij}^{nk} (f_{ij}^{nk})^*, \\
A_{23}^{13} &= f_j^n (f_{ij}^{nm})^*, \quad A_{23}^{23} = f_i^n (f_{ij}^{nm})^*,
\end{aligned}$$

$$\begin{aligned}
A_{30}^{30} &= f_{ij}^{nm}, \\
A_{31}^{31} &= f_{ij}^{nm} (f_j^m)^*, \quad A_{31}^{32} = f_{ij}^{nm} (f_i^m)^*, \\
A_{32}^{31} &= f_{ij}^{nm} (f_j^n)^*, \quad A_{32}^{32} = f_{ij}^{nm} (f_i^n)^*, \\
A_{33}^{33} &= f_{ij}^{nm} (f_{ij}^{nm})^*.
\end{aligned} \tag{29}$$

6 Two-Qubit Entanglement Generation

In the simplest setting, Alice and Bob aim at generating entanglement between the qubits in their possession, respectively, A and B , located at some positions in the spin network, by performing local operations on their qubits and exchanging classical communication between them. By definition, LOCC by itself does not allow for neither the increase nor the generation of entanglement between qubits A and B ; but the presence of the spin network can give rise to an effective interaction between these qubits, resulting in the possible generation of quantum correlation. In Fig. 6, an instance of such an entanglement generation protocol is depicted, where Alice and Bob have access to one spin at each end of a 1D spin chain. In Ref. [37], it has been shown that, by weakly coupling the end qubits to the wire, their state evolves into a Bell state at half of the transfer time of the excitation between the edges. This result has been extended in Ref. [38] to the generation of a Bell state between two users coupled at arbitrary positions in a spin network, provided control over the local magnetic field is allowed on the sites chosen to be entangled. Results similar to the weak-coupling scheme can be obtained by strong local magnetic fields on neighbouring spins both for one- and two-qubit quantum state transfer [39, 40].

In Ref. [41], the authors showed that initialising the system in $|\Psi\rangle_{AB} = |+\rangle_A |+\rangle_B |\psi\rangle_W$, where $|+\rangle = \frac{1}{\sqrt{2}}(|0\rangle + |1\rangle)$ and $|\psi\rangle_W$ is an arbitrary state with fixed parity of the wire, and a maximally entangled state between qubits A and B can be achieved in a ballistic time, provided Alice and Bob can tune the strength of the couplings of their qubits to the wire to an optimal value [42].



Fig. 6 Alice and Bob have access, respectively, to qubits A and B , located at the two ends of a spin chain (wire). Entanglement between the two qubits can be generated by exploiting the dynamics of the quantum wire, whose Hamiltonian includes a nearest-neighbour interaction term

7 Four-Qubit Entanglement Generation

In Sect. 5, we have analysed the case where Alice and Bob each have access to one qubit in the spin network. Here, instead, we consider the case where they each have access to two qubits. An instance where each pair of qubits is located at an edge of a spin chain is depicted in Fig. 7. A general analysis of the entanglement generated in an arbitrary four-qubit state has not yet been performed, except for pure states [43, 44], due to the complexity of defining entanglement quantifiers for an arbitrary four-qubit mixed state (as a result of the mixed state being in the presence of infinitely many SLOCC classes [45]).

Restricting only to the $A|B$ partition, in Ref. [46], it is shown that starting from $|\Psi\rangle_{AB} = |1100\rangle$ and $|\Psi\rangle_{AB} = |1010\rangle$ (or their mirror-symmetric states $|\Psi\rangle_{AB} = |0011\rangle$ and $|\Psi\rangle_{AB} = |0101\rangle$), a product of two Bell states, i.e., $|\Psi\rangle_{AB} = |\Phi\rangle_{A_1B_2} \otimes |\Phi\rangle_{A_2B_1}$ or $|\Psi\rangle_{AB} = |\Phi\rangle_{A_1B_1} \otimes |\Phi\rangle_{A_2B_2}$, is attained at specific times during the evolution for $g \ll J$. On the other hand, the initial state $|1001\rangle$ (and its mirror-symmetric state $|0110\rangle$) does not generate any entanglement in the $A|B$ partition at any time.

Let us now characterise the type of entanglement these initial states achieve during the evolution of the dynamical map. Starting from the state $|\Psi\rangle_{AB} = |1100\rangle$ results in the evolution

$$\begin{aligned}
 |\Psi(t)\rangle_{AB} = \frac{1}{2} \left[\left(1 - \cos \frac{g^2 t}{J} \right) |0011\rangle + i \sin \frac{g^2 t}{J} |0101\rangle \right. \\
 \left. - i \sin \frac{g^2 t}{J} |1010\rangle + \left(1 + \cos \frac{g^2 t}{J} \right) |1100\rangle \right], \tag{30}
 \end{aligned}$$

which can be written in a biseparable form

$$\begin{aligned}
 |\Psi(t)\rangle_{AB} = \left| \sin \frac{g^2 t}{2J} \right| \left[\left(|01\rangle + -i \cot \frac{g^2 t}{2J} |10\rangle \right)_{A_1B_2} \right. \\
 \left. \otimes \left(|01\rangle + i \cot \frac{g^2 t}{2J} |10\rangle \right)_{A_2B_1} \right], \tag{31}
 \end{aligned}$$



Fig. 7 Alice and Bob have access to qubits A_1, A_2 and B_1, B_2 , respectively, located at the two ends of a spin chain (wire), which is capable of generating an entangled state by exploiting its intrinsic dynamics

implying that the concurrence in each two-qubit state is equal to $C_{A_1B_2} = C_{A_2B_1} = \left| \sin \frac{g^2 t}{J} \right|$. This means that a product of two Bell states is created after a time $t = \frac{\pi J}{2g^2}$. It is also noteworthy to consider the four-tangle [47], a measure of multipartite entanglement, which is defined for pure states as

$$\tau_4(|\psi\rangle) = \left| \langle \psi | \sigma_y \otimes \sigma_y \otimes \sigma_y \otimes \sigma_y | \psi^* \rangle \right|^2 . \tag{32}$$

In this case, the calculation can be carried out explicitly, and we get that $\tau_4(|\Psi(t)\rangle_{AB}) \equiv \tau_{A_1A_2B_1B_2} = \left| \sin \frac{g^2 t}{J} \right|^4$. This means that even though the state (31) is biseparable, the four-tangle is non-zero when the two-qubit concurrences are non-zero, implying that the four-tangle is not a measure of exclusive four-way entanglement per se. One can also consider the three-tangle [48] of the three-qubit partitions, which contrary to the four-tangle, is exclusively a measure of three-way entanglement. The caveat of this measure is that it is only defined for pure states, while the generalisation to mixed states is described via the convex roof extension. Thus, the three-tangle of a mixed state ρ is given as the average pure state three-tangle minimised over all possible pure state decompositions:

$$\tau_3(\rho) = \min_{\{p_i, |\psi_i\rangle\}} \sum_i p_i \tau_3(|\psi_i\rangle) , \tag{33}$$

which for a pure state

$$\tau_3(|\psi\rangle) = C_{A(BC)}^2 - C_{AB}^2 - C_{AC}^2 , \tag{34}$$

and $C_{A(BC)} = \sqrt{2(1 - \text{Tr}(\rho_A^2))}$. If we now consider taking the Eigendecompositions of the partial trace of state (31) with respect to every qubit, we find that the three-tangle of each decomposed pure state for each traced out qubit is equal to zero. This means that we have found a minimal pure state decomposition so that the three-tangle of state (31), with respect to any partition involving three qubits, is equal to zero, implying there is no three-way entanglement generation between the senders and receivers at any time t . This is a consequence of the fact that the initial state does not exhibit any coherence between states having support in the magnetisation sectors with zero and three excitations, and the dynamics are not able to generate any. Clearly, multipartite entanglement distribution protocols are feasible whenever the initial state contains some amount of entanglement, as shown in Ref. [49] for the case of the three-tangle when the sender’s state is GHZ-like.

Let us now move to analyse the evolution of the state generated from $|\Psi\rangle_{AB} = |1010\rangle$. We get that the evolution results in

$$|\Psi(t)\rangle_{AB} = \frac{1}{2} \left[\left(\cos 2Jt + \cos \frac{g^2 t}{J} \right) |1010\rangle + \left(\cos 2Jt - \cos \frac{g^2 t}{J} \right) |0101\rangle, \right. \\ \left. -i \sin 2Jt (|1001\rangle + |0110\rangle) - i \sin \frac{g^2 t}{J} (|1100\rangle - |0011\rangle) \right]. \quad (35)$$

To characterise the different types of entanglement in Eq. (35), we need to look towards a new entanglement measure further to the two-qubit concurrence and three- and four-tangles. We will specifically use the four-qubit concurrence given in Ref. [50], which is defined for a pure state as

$$C_{1234} = (C_{1(234)}C_{2(134)}C_{3(124)}C_{4(123)}C_{(12)(34)}C_{(13)(24)}C_{(14)(23)})^{\frac{1}{7}}, \quad (36)$$

where $C_{A(BCD)} = \sqrt{2(1 - \text{Tr}(\rho_A^2))}$ and $C_{(AB)(CD)} = \sqrt{\frac{4}{3}(1 - \text{Tr}(\rho_{AB}^2))}$. The n -partite concurrence is essentially the geometric mean of the concurrence over the set of all possible bipartitions, which is similar to the GME concurrence [51], although the latter is defined as the minimum value of the concurrence over all bipartitions. This inherently implies that the four-qubit concurrence is zero if and only if the four-qubit pure state is separable to some degree. Plotting the four-qubit concurrence $C_{A_1 A_2 B_1 B_2}$ along with the two-qubit concurrences $C_{A_1 B_2} (= C_{A_2 B_1})$ and $C_{A_1 A_2} (= C_{B_1 B_2})$, and the four-tangle $\tau_{A_1 A_2 B_1 B_2}$, for $\frac{J^2}{g^2} = 10^4$, we obtain Fig. 8.

The two-qubit concurrences $C_{A_1 B_1}$ and $C_{A_2 B_2}$ are equal to zero at all times t . We make a note that at time $t = \frac{\pi J}{2g^2}$ we acquire a product of two Bell states similar to when we use state (31). Once again, by taking the Eigendecompositions of the partial trace of state (35) with respect to every qubit, we find that the three-tangle is zero at all times t for every partition consisting of three qubits. Combining

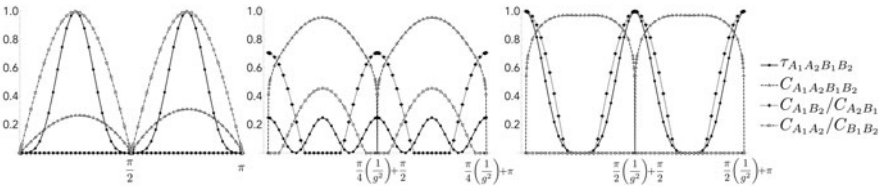


Fig. 8 Plot of the two- and the four-qubit concurrences and of the four-tangle for the state (35) with t in units of J/g^2 . The three panels are at $t = [0, \pi]$ (left), $t = \left[\frac{\pi}{4g^2}, \frac{\pi}{4g^2} + \pi \right]$ (centre), and $t = \left[\frac{\pi}{2g^2}, \frac{\pi}{2g^2} + \pi \right]$ (right), corresponding, respectively, to the beginning, a quarter and an half of the period of the longest time-scale dictated by g^{-2}

this with the fact that at certain times t , we have that the only non-zero two-qubit concurrences are $C_{A_1A_2}$ and $C_{B_1B_2}$ and that the four-qubit concurrence $C_{A_1A_2B_1B_2}$ is also non-zero, meaning that the state is fully inseparable, implies that there must be some non-zero value of exclusive four-way entanglement shared between the senders and the receivers.

8 Conclusion

In this chapter, we have adopted the general framework of quantum dynamical maps in order to investigate some instances of controlled quantum information dynamics on spin networks. Specifically, we considered those maps emerging from the dynamics of a subset of spin- $\frac{1}{2}$ particles embedded in a larger network that we divided into sender and receiver parts for convenience. Focusing on the case of a $U(1)$ -symmetric Hamiltonian governing the dynamics of the network, we have derived the explicit form of the dynamical map in terms of the excitation transfer amplitude and applied it to review both single-qubit quantum state transfer and two-qubit transfer and corresponding entanglement generation. Finally, we have considered a specific topology of the network where analytical solutions are available for the transfer amplitude and have shown that the quantum map formalism allows the analysis of more complex scenarios such as multi-qubit entanglement generation. It is interesting to note that Ref. [52] provides another means of investigating entanglement generation in quantum state transfer protocols that has not been investigated in this chapter.

The range of applicability of the illustrated approach goes well beyond the cases investigated in this chapter, as it can be easily extended to include classical communication feedback, constraints on the achievable quantum information protocols stemming from the symmetries of the Hamiltonian reflected in the quantum map, and spin networks exposed to external noise.

Acknowledgments TJGA acknowledges funding from the UM SEA-EU Research Seed Fund STATED. All Authors thank Karol Życzkowski for useful discussions.

References

1. M.A. Nielsen, I.L. Chuang, *Quantum Computation and Quantum Information* (Cambridge University Press, Cambridge, 2010)
2. F. Franchini, *An introduction to integrable techniques for one-dimensional quantum systems*. Lect. Notes Phys. (Springer, Berlin, 2017)
3. R. Orús, Tensor networks for complex quantum systems. *Nat. Rev. Phys.* **1**(9), 538–550 (2019)
4. I. Bengtsson, K. Życzkowski, *Geometry of Quantum States* (Cambridge University Press, Cambridge, 2017)

5. W. Qin, C. Wang, G.L. Long, High-dimensional quantum state transfer through a quantum spin chain. *Phys. Rev. A* **87**, 012339 (2013)
6. D. Jaksch, P. Zoller, The cold atom Hubbard toolbox. *Ann. Phys.* **315**(1), 52–79 (2005)
7. J. Simon, W.S. Bakr, Ruichao Ma, M Eric Tai, P.M. Preiss, M. Greiner, Quantum simulation of antiferromagnetic spin chains in an optical lattice. *Nature* **472**(7343), 307–312 (2011)
8. I. Bloch, J. Dalibard, S. Nascimbène, Quantum simulations with ultracold quantum gases. *Nat. Phys.* **8**(4), 267–276 (2012)
9. H. Labuhn, D. Barredo, S. Ravets, S. de Léséleuc, T. Macrì, T. Lahaye, A. Browaeys, Realizing quantum Ising models in tunable two-dimensional arrays of single Rydberg atoms. *Nature* **534**(7609), 667–670 (2015)
10. E. Guardado-Sanchez, P. T. Brown, D. Mitra, T. Devakul, D.A. Huse, P. Schauf, W.S. Bakr, Probing the quench dynamics of antiferromagnetic correlations in a 2d quantum Ising spin system. *Phys. Rev. X* **8**, 021069 (2018)
11. A. Browaeys, T. Lahaye, Many-body physics with individually controlled Rydberg atoms. *Nat. Phys.* **16**(2), 132–142 (2020)
12. I. Pitsios, L. Banchi, A.S. Rab, M. Bentivegna, D. Caprara, A. Crespi, N. Spagnolo, S. Bose, P. Mataloni, R. Osellame, F. Sciarrino, Photonic simulation of entanglement growth and engineering after a spin chain quench. *Nat. Commun.* **8**(1), 1569 (2017)
13. D. Porras, J.I. Cirac, Effective quantum spin systems with trapped ions. *Phys. Rev. Lett.* **92**(20), 1–4 (2004)
14. A. Friedenauer, H. Schmitz, J.T. Glueckert, D. Porras, T. Schaetz, Simulating a quantum magnet with trapped ions. *Nat. Phys.* **4**(10), 757–761 (2008)
15. C. Monroe, W.C. Campbell, L.M. Duan, Z.X. Gong, A.V. Gorshkov, P.W. Hess, R. Islam, K. Kim, N.M. Linke, G. Pagano, P. Richerme, C. Senko, N.Y. Yao, Programmable quantum simulations of spin systems with trapped ions. *Rev. Mod. Phys.* **93**(2), 25001 (2021)
16. A. Kay, D.G. Angelakis, Reproducing spin lattice models in strongly coupled atom-cavity systems. *EPL* **84**(2), 20001 (2008)
17. C. Noh, D.G. Angelakis, Quantum simulations and many-body physics with light. *Rep. Progr. Phys.* **80**(1), 016401 (2017)
18. U. Las Heras, A. Mezzacapo, L. Lamata, S. Filipp, A. Wallraff, E. Solano, Digital quantum simulation of spin systems in superconducting circuits. *Phys. Rev. Lett.* **112**(20), 1–5 (2014)
19. A. Vepsäläinen, G.S. Paraoanu, Simulating spin chains using a superconducting circuit: gauge invariance, superadiabatic transport, and broken time-reversal symmetry. *Adv. Quantum Technol.* **3**(4), 1–12 (2020)
20. N. Gisin, R. Thew, Quantum communication. *Nat. Photon.* **1**(3), 165–171 (2007)
21. S. Pirandola, R. Laurenza, C. Ottaviani, L. Banchi, Fundamental limits of repeaterless quantum communications. *Nat. Commun.* **8**, 1–5 (2017)
22. K. Kraus, A. Böhm, J.D. Dollard, W.H. Wootters, *States, Effects, and Operations Fundamental Notions of Quantum Theory*. LNP0190 (Springer, Berlin, 1983)
23. W. Forrest Stinespring, Positive functions on c^* -algebras. *Proc. Am. Math. Soc.* **6**(2), 211–216 (1955)
24. K. Kraus, General state changes in quantum theory. *Ann. Phys.* **64**(2), 311–335 (1971)
25. K. Życzkowski, I. Bengtsson, an O'Reilly Media Company Safari, *Geometry of Quantum States*, 2nd edn. (Cambridge University Press, Cambridge, 2017)
26. H. Verma, L. Chotorlishvili, J. Berakdar, S.K. Mishra, Qubit(s) transfer in helical spin chains. *EPL (Europhysics Letters)* **119**(3), 30001 (2017)
27. S. Campbell, L. Mazzola, G. De Chiara, T.J.G. Apollaro, F. Plastina, Th. Busch, M. Paternostro, Global quantum correlations in finite-size spin chains. *New J. Phys.* **15**(4), 043033 (2013)
28. X. Chen, R. Mereau, D.L. Feder, Asymptotically perfect efficient quantum state transfer across uniform chains with two impurities. *Phys. Rev. A* **93**(1), 12343 (2016)
29. S. Bose, Quantum communication through an unmodulated spin chain. *Phys. Rev. Lett.* **91**(20), 1–4 (2003)
30. A. Bayat, L. Banchi, S. Bose, P. Verrucchi, Initializing an unmodulated spin chain to operate as a high-quality quantum data bus. *Phys. Rev. A* **83**(6), 1–9 (2011)

31. L. Amico, A. Osterloh, F. Plastina, R. Fazio, G. Massimo Palma, Dynamics of entanglement in one-dimensional spin systems. *Phys. Rev. A* **69**(2), 022304 (2004)
32. A. Fubini, T. Roscilde, V. Tognetti, M. Tusa, P. Verrucchi, Reading entanglement in terms of spin configurations in quantum magnets. *Eur. Phys. J. D* **38**(3), 563–570 (2006)
33. S. Bose, Quantum communication through spin chain dynamics: an introductory overview. *Contemp. Phys.* **48**(1), 13–30 (2007)
34. D. Burgarth, S. Bose, Perfect quantum state transfer with randomly coupled quantum chains. *New J. Phys.* **7**, 135–135 (2005)
35. T.J.G. Apollaro, A. Cuccoli, C. Di Franco, M. Paternostro, F. Plastina, P. Verrucchi, Manipulating and protecting entanglement by means of spin environments. *New J. Phys.* **12**(8), 083046 (2010)
36. T.J.G. Apollaro, S. Lorenzo, A. Sindona, S. Paganelli, G.L. Giorgi, F. Plastina, Many-qubit quantum state transfer via spin chains. *Phys. Scr.* **T165**(T165), 014036 (2015)
37. A. Wójcik, T. Łuczak, P. Kurzyński, A. Grudka, T. Gdala, M. Bednarska, Unmodulated spin chains as universal quantum wires. *Phys. Rev. A* **72**(3), 034303 (2005)
38. A. Wójcik, T. Łuczak, P. Kurzyński, A. Grudka, T. Gdala, M. Bednarska, Multiuser quantum communication networks. *Phys. Rev. A* **75**(2), 022330 (2007)
39. S. Lorenzo, T.J.G. Apollaro, A. Sindona, F. Plastina, Quantum-state transfer via resonant tunneling through local-field-induced barriers. *Phys. Rev. A* **87**, 042313 (2013)
40. S. Lorenzo, T.J.G. Apollaro, S. Paganelli, G.M. Palma, F. Plastina, Transfer of arbitrary two-qubit states via a spin chain. *Phys. Rev. A* **91**, 042321 (2015)
41. L. Banchi, A. Bayat, P. Verrucchi, S. Bose, Nonperturbative Entangling Gates between Distant Qubits Using Uniform Cold Atom Chains. *Phys. Rev. Lett.* **106**(14), 140501 (2011)
42. L. Banchi, T.J.G. Apollaro, A. Cuccoli, Long quantum channels for high-quality entanglement transfer. *New J. Phys.* **13**, 123006 (2011)
43. F. Verstraete, J. Dehaene, B. De Moor, H. Verschelde, Four qubits can be entangled in nine different ways. *Phys. Rev. A - At. Mol. Opt. Phys.* **65**(5), 521121–521125 (2002)
44. M.G. Ghahi, S.J. Akhtarshenas, Entangled graphs: a classification of four-qubit entanglement. *Eur. Phys. J. D* **70**(3), 1–6 (2016)
45. C. Eltschka, J. Siewert, Quantifying entanglement resources. *J. Phys. A: Math. Theor.* **47**(42), 424005 (2014)
46. T.J.G. Apollaro, G.M.A. Almeida, S. Lorenzo, A. Ferraro, S. Paganelli, Spin chains for two-qubit teleportation. *Phys. Rev. A* **100**(5), 052308 (2019)
47. A. Wong, N. Christensen, Potential multiparticle entanglement measure. *Phys. Rev. A* **63**, 044301 (2001)
48. V. Coffman, J. Kundu, W.K. Wootters, Distributed entanglement. *Phys. Rev. A* **61**(5), 5 (2000)
49. T.J.G. Apollaro, C. Sanavio, W.J. Chetcuti, S. Lorenzo, Multipartite entanglement transfer in spin chains. *Phys. Lett. A* **384**(15), 126306 (2020)
50. P.J. Love, A.M. Van Den Brink, A. Yu Smirnov, M.H.S. Amin, M. Grajcar, E. Il'ichev, A. Izmailkov, A.M. Zagoskin, A characterization of global entanglement. *Quantum Inf. Process.* **6**(3), 187–195 (2007)
51. Z.H. Ma, Z.H. Chen, J.L. Chen, C. Spengler, A. Gabriel, M. Huber, Measure of genuine multipartite entanglement with computable lower bounds. *Phys. Rev. A* **83**(6), 1–5 (2011)
52. L. Anticoli, M.G. Ghahi, Modeling tripartite entanglement in quantum protocols using evolving entangled hypergraphs. *Int. J. Quantum Inform.* **16**(7), 1850055 (2018)

Weak Ergodicity Breaking Through the Lens of Quantum Entanglement



Zlatko Papić

Abstract Recent studies of interacting systems of quantum spins, ultracold atoms, and correlated fermions have shed a new light on how isolated many-body systems can avoid rapid equilibration to their thermal state. It has been shown that many such systems can “weakly” break ergodicity: they possess a small number of non-thermalising eigenstates and/or display slow relaxation from certain initial conditions, while the majority of other initial states equilibrate fast, like in conventional thermalising systems. In this chapter, we provide a pedagogical introduction to weak ergodicity breaking phenomena, including Hilbert space fragmentation and quantum many-body scars. Central to these developments have been the tools based on quantum entanglement, in particular matrix product states and tangent space techniques, which have allowed to analytically construct non-thermal eigenstates in various non-integrable quantum models, and to explore semiclassical quantisation of such systems in the absence of a large- N or mean-field limit. We also discuss recent experimental realisations of weak ergodicity breaking phenomena in systems of Rydberg atoms and tilted optical lattices.

1 Introduction

Experimental progress in cold atoms, trapped ions, and superconducting circuits [1, 2] has generated a flurry of interest into foundational questions of many-body quantum mechanics, such as how a statistical-mechanics description emerges in isolated quantum systems comprising many degrees of freedom. In experiments with quantum simulators, the process of thermalisation can be conveniently probed in real time by quenching the system: one prepares a non-equilibrium initial state $|\psi(0)\rangle$, typically a product state of atoms, and observes its fate after time t , see Fig. 1a.

Z. Papić (✉)

School of Physics and Astronomy, University of Leeds, Leeds, UK

e-mail: Z.Papic@leeds.ac.uk

© The Author(s), under exclusive license to Springer Nature Switzerland AG 2022

A. Bayat et al. (eds.), *Entanglement in Spin Chains*, Quantum Science and Technology, https://doi.org/10.1007/978-3-031-03998-0_13

341

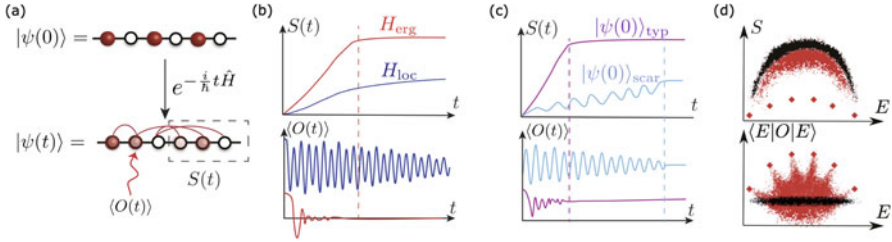


Fig. 1 Strong vs. weak breakdown of thermalisation. **(a)** Experiments probe thermalisation of isolated many-body systems using a quantum quench: the system is prepared in a simple initial state $|\psi(0)\rangle$, and the dynamics of some local observable O and entanglement entropy S are measured during unitary evolution. **(b)** Strong breakdown of ergodicity caused by (many-body) localisation leads to qualitatively different dynamical behaviours compared to an ergodic system. This difference persists for broad classes of initial states. **(c)** In contrast to **(b)**, *weak* ergodicity breaking results in strikingly different dynamical behaviour when *different* initial states evolve under the same thermalising Hamiltonian. Quantum scarred systems, discussed in Sect. 6, are an important class of systems where such behaviour has been experimentally observed. **(d)** Manifestations of weak ergodicity breaking in entanglement and expectation values of local observables in the system’s eigenstates. Red dots correspond to eigenstates of a weakly non-ergodic system, where enhanced fluctuations and outlier states (red diamonds) are visible, compared to typical eigenstates of conventional thermalising systems (black dots) whose properties vary smoothly with energy E . This chapter focuses on the mechanisms and physical realisations of the phenomenology summarised in **(c, d)**

Well-isolated systems can be assumed to evolve according to the Schrödinger equation for the system’s Hamiltonian H . Thermalisation can be characterised by the time evolution of local observables, $\langle O(t) \rangle$, or entanglement entropy, $S(t) = -\text{tr} \rho_A(t) \ln \rho_A(t)$. The latter is defined as the von Neumann entropy for the reduced density matrix, ρ_A , of the subsystem A . Here we assume that the entire system is bipartitioned into A and B subsystems, and $\rho_A(t) = \text{tr}_B |\psi(t)\rangle \langle \psi(t)|$ is obtained by tracing out the degrees of freedom belonging to B . Entanglement entropy quantifies the spreading of quantum correlations between spatial regions as the entire system remains in a pure state.

The results of measurements described above are schematically illustrated in Fig. 1b, which contrasts the behaviour of two large classes of physical systems: quantum-ergodic systems [3, 4] and many-body localised (MBL) systems [5–7]. In the first case, parts of the system act as heat reservoirs for other parts, and an initial non-equilibrium state relaxes to a thermal equilibrium, with some well-defined effective temperature. This behaviour is reminiscent of classical chaotic systems, which effectively “forget” their initial condition in the course of time evolution. In contrast, in MBL systems, local observables reach some stationary value that is non-thermal, retaining the memory of the initial state. As a result, systems with strong ergodicity breaking can sustain much longer quantum coherence. For example, the information stored in certain local observables would not decay in MBL systems, while it would rapidly decohere in an ergodic system (Fig. 1b, bottom panel). The behaviour of local observables is mirrored by that of quantum entanglement: in

thermalising systems, entanglement typically grows linearly with time, $S(t) \sim t$, corresponding to quasiparticles moving at a finite speed [8]. In MBL systems, quasiparticles are localised, with residual, exponentially decaying interactions that lead to slow, logarithmic increase of entanglement, $S(t) \propto \log t$ [9–11], see the top panel of Fig. 1b.

The generic behaviour of quantum-chaotic systems sketched in Fig. 1b is expected to hold irrespective of the chosen initial state. This is a consequence of the eigenstate thermalisation hypothesis (ETH) [3, 4], a powerful conjecture governing the behaviour of quantum-ergodic systems—see Box 1. In contrast, the present chapter focuses on recent theoretical works and experiments that pointed to the existence of a new class of behaviours, which can be loosely thought of as “intermediate” between thermalisation in fully chaotic systems and strong-ETH breakdown like in MBL systems. In such *weakly* non-ergodic systems, certain initial states show relaxation to thermal ensembles, yet other states exhibit non-stationary dynamics including persistent oscillations, illustrated in Fig. 1c. Moreover, such systems also weakly violate the ETH in their eigenstate properties: e.g., they exhibit a few “outlier” states with anomalously low-entropy and local observable matrix elements that do not vary smoothly with energy, see Fig. 1d.

This new regime of ergodicity breaking attracted broader attention after the experimental observation of dynamical revivals in large-scale Rydberg atom quantum simulators [12]. Weak ergodicity breaking observed in such systems was subsequently named *quantum many-body scarring* [13, 14], highlighting its analogy with chaotic stadium billiards, which had been known to host non-ergodic eigenfunctions bearing “scars” of classical periodic orbits [15]. The discovery of many-body quantum scars fuelled a broader quest to understand physical consequences of weak ergodicity breaking. Importantly, during this quest, it came to light that some examples of weak ergodicity breaking had previously been known. For example, non-integrable models, such as the Affleck–Kennedy–Lieb–Tasaki (AKLT) spin chain, had been rigorously proven to possess non-thermal eigenstates [16, 17], which are now understood to share a similar algebraic structure with the non-thermal eigenstates in Rydberg atom systems. Other, more general, mechanisms of weak ergodicity breaking, such as Hilbert space fragmentation [18, 19] and “embedding” constructions [20], have also come into light and are being experimentally probed [21].

This chapter provides a pedagogical introduction to weak ergodicity breaking phenomena, expanding upon a recent short overviewed in Ref. [22]. As will become clear from the many physical examples presented below, the phenomenology of weak ergodicity breaking is quite rich and still rapidly evolving as this chapter is being written. Instead of giving an exhaustive review of all these developments, the aim is to highlight common themes between currently known examples of non-thermal dynamics, in particular focusing on the insights obtained by studying quantum entanglement in such systems. In Sect. 2, we start by introducing the relevant methodology based on matrix product states that has successfully been used in recent works to analytically construct non-thermal eigenstates and to define the semiclassical limit of non-integrable many-body systems. In Sect. 3, we discuss

in detail three main mechanisms of weak ergodicity breaking and highlight their realisations in physical systems. Section 4 introduces the so-called PXP model that has played one of the key roles in understanding weak ergodicity breaking in Rydberg atom experiments. In Sect. 5, we relate the semiclassical quantisation of many-body systems with the time-dependent variational principle applied to manifolds spanned by tensor network states. In Sect. 6, we explain how these ideas allow to explore parallels between weak ergodicity breaking in many-body systems and quantum scars in few-body systems. Finally, in Sect. 7, we discuss two experimental platforms—Rydberg atoms and cold atoms in tilted optical lattices—that have recently observed signatures of weak ergodicity breaking. Conclusions and some open questions are presented in Sect. 8.

Box 3 : Eigenstate Thermalisation Hypothesis (ETH)

Eigenstate thermalisation hypothesis (ETH) [3, 4] governs the process of thermalisation in closed quantum systems in the absence of coupling to a thermal bath. For present purposes, the following three consequences of the ETH are most relevant (for more information, see one of the recent reviews [23–25]):

1. The expectation values of physical observables in individual, highly excited eigenstates of ergodic systems are “thermal”, i.e., they are identical to those evaluated using the microcanonical ensemble. Thus, highly excited states of ergodic systems can be intuitively viewed as random vectors in the Hilbert space, and expectation values of local observables in such eigenstates are a smooth function of energy, independent of other microscopic details.
2. By postulating the form of the off-diagonal matrix elements, the ETH makes predictions for the temporal fluctuations of local observables: independent of the initial state, an observable approaches its equilibrium value and then remains near that value most of the time, with fluctuations exponentially suppressed by the thermodynamic entropy.
3. For a large finite subsystem A of an infinite ETH system, the reduced density matrix ρ_A is equal to the thermodynamic density matrix at the effective temperature set by the energy of the corresponding eigenstate.

The equality between thermal and reduced density matrices (3) implies that the entanglement entropy scales as the *volume* of region A . For example, in one spatial dimension, volume law implies $S \propto L_A$. This reflects the fact that ergodic eigenstates are highly entangled, and agrees with the intuition that the ETH eigenstates are similar to random vectors. In some physical systems considered below, we will encounter global kinetic constraints, similar to those occurring in classical glasses [26]. In such systems, the Hilbert space is globally constrained, and a “random” vector is understood

(continued)

Box 3 (continued)

to be one compatible with the constraints. Consequently, the entropy of such constrained random vectors can differ [27] from the so-called Page value attained by random qubit states [28].

In systems that obey the so-called strong ETH [29], the above properties are expected to hold for *all* states [30]. On the other end, maximal violation of ETH is known to occur in integrable systems [31] and MBL systems [32], both of which have macroscopic numbers of conservation laws. Between these extremes lie the weak ergodicity breaking phenomena discussed in this chapter, where the majority of eigenstates follows the predictions of the ETH, while a smaller number of eigenstates (e.g., polynomially many in system size) violate these properties. Similarly, out-of-equilibrium dynamics from most initial conditions results in fast relaxation, consistent with ETH expectations, while special initial conditions can lead to non-stationary dynamics at relatively long times.

2 Matrix Product State Methods

The investigation of weak ergodicity breaking in non-integrable quantum systems has greatly benefited from matrix product states (MPS) [33], a formalism designed to compactly represent and perform algebraic manipulations on a class of quantum states that are weakly entangled. These methods are naturally suited to capture aspects of weak ergodicity breaking, as the main signatures of the latter are the suppression of entanglement or its growth rate compared to conventional thermalising systems. Recent works have demonstrated the utility of MPS methods in two new settings: (i) the MPS have allowed to *exactly* construct highly excited eigenstates (i.e., eigenstates at finite-energy density above the system's ground state) of a wide class of physical systems; (ii) the MPS have been used to effectively *define* the system's semiclassical dynamics by projecting the Schrödinger time evolution into the manifold of MPS states while conserving the total energy of the system. In this section, we provide a brief overview of this methodology that yielded much of the physical insights into weak ergodicity breaking phenomena presented in subsequent sections.

2.1 Towers of Quasiparticles

Consider a one-dimensional quantum chain with a d -dimensional Hilbert space on each of the L sites. The many-body basis of the system is formed by tensor products

of single-site Hilbert spaces, $|\sigma_1, \sigma_2, \dots, \sigma_L\rangle$. Any state can be decomposed in this basis as

$$|\psi\rangle = \sum_{\sigma_1, \sigma_2, \dots, \sigma_L} c_{\sigma_1 \sigma_2 \dots \sigma_L} |\sigma_1, \sigma_2, \dots, \sigma_L\rangle \quad (1)$$

by specifying its d^L coefficients $c_{\sigma_1 \sigma_2 \dots \sigma_L}$. This illustrates the “exponential barrier” to studying many-body systems: one must specify $\sim \exp(L)$ coefficients to fully describe a generic state of a system of size L .

The idea of MPS is that each of the coefficients in Eq. (1) can be viewed as resulting from a product of matrices $A_i^{[\sigma_i]}$ of dimensions $\chi \times \chi$,

$$c_{\sigma_1 \sigma_2 \dots \sigma_L} = b_l^T A_1^{[\sigma_1]} A_2^{[\sigma_2]} \dots A_L^{[\sigma_L]} b_r. \quad (2)$$

The matrices A are defined over the so-called auxiliary space with dimension χ , but they also depend on the physical degrees of freedom σ_i . Moreover, for open boundary conditions, the matrices also vary from site to site in general; hence, they carry a label i . The boundary χ -dimensional vectors, b_l and b_r , determine the boundary conditions for the wave function. Thus, we have re-expressed a d^L -dimensional tensor $c_{\sigma_1 \sigma_2 \dots \sigma_L}$ in terms of $d \times \chi \times \chi$ tensors A_i .

If the system is translation-invariant, the matrices are the same on every site (or between different unit cells, more generally), and the boundary vectors are replaced with a trace over the auxiliary space,

$$c_{\sigma_1 \sigma_2 \dots \sigma_L} = \text{Tr} \left(A_1^{[\sigma_1]} A_2^{[\sigma_2]} \dots A_L^{[\sigma_L]} \right). \quad (3)$$

Equations (2)–(3) furnish an MPS representation for the wave function in Eq. (1).

Intuitively, χ controls the degree of entanglement in the wave function. When $\chi=1$, we have a mean-field description where degrees of freedom on different sites are independent of each other; increasing χ builds in quantum correlations between different sites. For a general state, rewriting the coefficients $c_{\sigma_1 \sigma_2 \dots \sigma_L}$ in MPS form would require χ to be exponentially large in L . However, for states in one spatial dimension that obey the “area law” [34], i.e., whose entanglement entropy obeys $S \leq \text{const}$, χ is also bounded by a constant. This results in a major simplification when describing such states using the MPS. Moreover, the same language also offers a complete algebraic framework to manipulate the MPS, for example, we can efficiently add two MPS states or calculate expectation values of local observables sandwiched between MPS states. The latter is achieved by expressing local operators in a similar representation known as “matrix product operator” (MPO) [35].

Ground states of many important condensed-matter systems are known to possess elegant MPS representations. A notable example is the Affleck–Kennedy–Lieb–

Tasaki (AKLT) [36] quantum spin-1 model:

$$H = \sum_{j=1}^L \left(\frac{1}{3} + \frac{1}{2} \vec{S}_j \cdot \vec{S}_{j+1} + \frac{1}{6} (\vec{S}_j \cdot \vec{S}_{j+1})^2 \right), \quad (4)$$

where \vec{S} are the spin-1 operators, and we assume periodic boundary condition, i.e., $L+1 \equiv 1$. The ground state of this model has an *exact* MPS representation, Eq. (3), with

$$A^{[+]} = \sqrt{\frac{2}{3}} \sigma^+, \quad A^{[0]} = -\frac{1}{\sqrt{3}} \sigma^z, \quad A^{[-]} = -\sqrt{\frac{2}{3}} \sigma^-, \quad (5)$$

where the labels $+$, 0 , and $-$ denote the $S_z = +1$, 0 , and -1 spin-1 basis states, respectively, and σ^\pm , σ^z are the *spin-1/2* Pauli operators. Thus, for the AKLT state, the physical dimension $d=3$, and the bond dimension is only $\chi=2$. This state and the model in Eq. (4) played an important role in establishing the existence of the Haldane gap in integer-spin chains [37].

Beyond examples such as AKLT, where the MPS *exactly* describe certain states, it has been shown more generally that the ground-state wave functions of gapped local Hamiltonians can be *approximated* by an MPS with a small bond dimension χ [38]. This result can be intuitively understood from the fact that the ground states of gapped local Hamiltonians are necessarily weakly entangled [39] and hence well-represented by the MPS. However, this intuition does not immediately extend to highly excited states at a finite-energy density above the ground state. As previously discussed in Sect. 1, in a generic quantum many-body system, finite-energy-density states are expected to be governed by the ETH; hence, their entanglement is expected to be high (i.e., scaling with the volume of the subsystem), so their MPS representation would not be efficient (as mentioned above, it would require $\chi \propto \exp(L)$).

Recent work by Moudgalya et al. [17] on the AKLT model has shown that the MPS can nevertheless capture some ETH-violating eigenstates of a non-integrable model, *regardless* of how high in the energy spectrum such states occur. The technique used in these works is the construction of quasiparticle excitations above the ground state, originally introduced in works on tangent space methods [40–42]. Following Ref. [17], a single-site quasiparticle excitation with momentum k on top of a general MPS state, $|\psi_A\rangle$, is given by

$$|\psi_A(B, k)\rangle = \sum_{j=1}^L e^{ikj} \sum_{\{\sigma_j\}} \text{Tr} \left(\dots A^{[\sigma_{j-1}]} B^{[\sigma_j]} A^{[\sigma_{j+1}]} \dots \right) |\sigma_1 \sigma_2 \dots \sigma_L\rangle, \quad (6)$$

where $B^{[\sigma_j]}$ is a $\chi \times \chi$ matrix with physical dimension d and k denotes the momentum, see Fig. 2a. In the framework of the single-mode approximation [43], the quasiparticles are usually described in terms of a single-site “quasiparticle

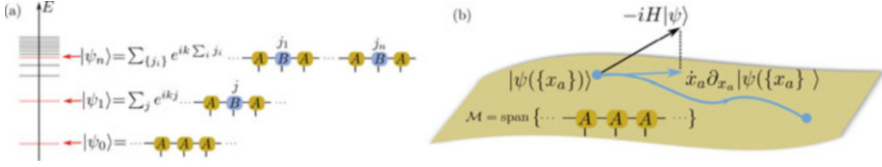


Fig. 2 MPS methods for weak ergodicity breaking. **(a)** Constructions of exact, highly excited eigenstates using MPO-MPS techniques from Ref. [17]. This method allows to construct a tower of quasiparticle states $|\psi_n\rangle$ by acting with a local operator on the MPS ground state $|\psi_0\rangle$, as in Eq. (6) and (10). **(b)** Time-dependent variational principle captures the optimal projection of quantum dynamics onto a given variational manifold \mathcal{M} , here parametrised by MPS. Limiting the bond dimension of the MPS to be low, this approach defines a semiclassical limit for quantum dynamics. The corresponding classical system is formed by equations of motions for the coefficients x_a , which parametrise the projection of the wave function into the MPS manifold. The equations of motions follow from minimising the leakage outside the manifold, i.e., the deviation of $-iH|\psi(t)\rangle$ from $\dot{x}_a \partial_{x_a} |\psi(\{x_a\})\rangle$, see Eq. (14)

creation operator” \widehat{O} , such that $B^{[\sigma]} = \sum_{\sigma,\sigma'} \widehat{O}_{\sigma,\sigma'} A^{[\sigma']}$, which we denote in shorthand as $|B\rangle = \widehat{O} |A\rangle$. Note that this is a special case, as for example \widehat{O} could act on several neighbouring sites—such states have been considered in Ref. [44].

To illustrate Eq. (6), some examples of low-lying excited eigenstates of the AKLT include the Arovas “A” and “B” states [45]:

$$|A\rangle = \sum_{j=1}^L (-1)^j \vec{S}_j \cdot \vec{S}_{j+1} |\psi_0\rangle, \tag{7}$$

$$|B\rangle = \sum_{j=1}^L (-1)^j \{\vec{S}_{j-1} \cdot \vec{S}_j, \vec{S}_j \cdot \vec{S}_{j+1}\} |\psi_0\rangle, \tag{8}$$

where $|\psi_0\rangle$ is the AKLT ground state, $\{\dots\}$ denotes the anticommutator, and we have omitted the normalisation factors. Another exact excited state, as shown by Moudgalya et al. [17], is the spin-2 magnon state with momentum π ,

$$|\psi_{2\text{-magnon}}\rangle = \sum_{j=1}^L (-1)^j (S_j^+)^2 |\psi_0\rangle. \tag{9}$$

All of these states can be written in the form of Eq. (6). For example, the state in Eq. (9) can be expressed in such a form using the ground-state matrices $A^{[\sigma]}$ in Eq. (5) and the $B^{[\sigma]}$ matrices given by $B^{[+]} = -\sqrt{\frac{2}{3}}\sigma^-$, $B^{[0]} = B^{[-]} = 0$. Note $B^{[+]}$ is the only non-trivial matrix, a direct consequence of the $(S^+)^2$ operator acting on spin-1.

In addition to single quasiparticles, multiple quasiparticle states can be described in the MPS formalism using multiple tensors. For example, a state with two

quasiparticles described by tensor B with momentum k is given by [17]

$$|\psi_A(B^2, k)\rangle \equiv \left(\sum_j e^{ikj} \widehat{O}_j \right)^2 |\psi_0\rangle. \quad (10)$$

Expanding the square, we see that we can have two cases: when B s act on the same site or different sites. Since in the AKLT chain we have $\widehat{O} = (S^+)^2$, we will have $\widehat{O}^2 |\psi_0\rangle = 0$ and the expression simplifies

$$\begin{aligned} |\psi_A(B^2, k)\rangle &= \sum_{j_1 \neq j_2} e^{ik(j_1+j_2)} \\ &\times \sum_{\{m_j\}} \text{Tr} \left(\dots A^{[\sigma_{j_1-1}]} B^{[\sigma_{j_1}]} A^{[\sigma_{j_1+1}]} \dots A^{[\sigma_{j_2-1}]} B^{[\sigma_{j_2}]} A^{[\sigma_{j_2+1}]} \dots \right) \\ &|\sigma_1 \sigma_2 \dots \sigma_L\rangle. \end{aligned} \quad (11)$$

Extending this formally to more quasiparticles appears straightforward. However, the difficulty that arises is that the successive applications of the quasiparticle operator increase the bond dimension of the resulting state. Thus, one needs to find a way to compress this state and compute its properties. These advances have been made in Ref. [17], allowing to evaluate the entanglement properties of highly excited states in the AKLT model, obtained by acting with \widehat{O} on the ground state an extensive number of times $n \sim L/2$. The physical consequences of this for weak ergodicity breaking will be discussed further in Sect. 3.1 below.

Finally, while the emphasis in this section has been on *analytical* constructions of exact eigenstates containing finite density of quasiparticle excitations, one could envision employing similar methods to *variationally* construct quasiparticle towers in other models that are less tractable than the AKLT. Indeed, such studies have been used to numerically characterise dynamical properties of quantum spin systems such as the XXZ model, including quasiparticle dispersion relations and dynamical structure factor, albeit at much lower energies than the phenomena discussed here [46].

2.2 Time-Dependent Variational Principle

In the previous subsection, we mentioned that some non-integrable quantum spin chains have highly excited energy eigenstates with a particularly simple structure, encoded in a local MPO acting on the ground state written as MPS. ‘‘Simple’’ structure means that such eigenstates have sub-volume-law entanglement, i.e., they are much less entangled than random vectors in the Hilbert space (cf. Box 1). Now we ask a complementary question: if the system undergoes anomalously slow

unitary dynamics, e.g., the spreading of correlations is inhibited compared to a thermalising system, could we compactly describe such dynamics using the MPS?

The natural framework to address the previous question is the time-dependent variational principle (TDVP), originally formulated by Dirac [47], which yields the optimal projection of quantum dynamics onto a given variational manifold, $\mathcal{M} = \text{span}\{|\psi(\mathbf{x})\rangle\}$, parametrised by some parameters $\mathbf{x} \equiv \{x_a\} \in \mathbb{R}^N$, Fig. 2b. TDVP equations of motion are obtained by extremising the action $\int dt \mathcal{L}$, with an effective Lagrangian [48]

$$\mathcal{L} = \frac{i}{2}(\langle\psi|\dot{\psi}\rangle - \langle\dot{\psi}|\psi\rangle) - \langle\psi|H|\psi\rangle. \quad (12)$$

In the present case, we assume that \mathcal{M} is spanned by the MPS of some given bond dimension, i.e., by matrices $A^\sigma(\mathbf{x})$ like in Eq. (3) with bond dimension χ , and the matrices depend on variational parameters, $\mathbf{x} \in \mathbb{R}^N$. These parameters can be given an interpretation in terms of pairs of coordinate and momenta (we assume N is even). In Box 2, we motivate this approach using a very simple example of a single spin.

Extremising the action in Eq. (12) results in Euler–Lagrange equations of motion for the \mathbf{x} variables [48, 49]:

$$\sum_a \dot{x}_a \text{Im}\langle\partial_{x_b}\psi|\partial_{x_a}\psi\rangle = -\frac{1}{2}\partial_{x_b}\langle\psi|H|\psi\rangle. \quad (13)$$

This set of equations constitutes an effective mapping of quantum dynamics onto a classical non-linear dynamical system.

While TDVP has been successfully applied to manifolds spanned by the MPS [49] and finite tensor tree states [50], in cases when it is possible to *analytically* calculate $\langle\psi|\dot{\psi}\rangle$ and $\langle\dot{\psi}|H|\psi\rangle$, further insights can be obtained from studying the non-linear system using the tools of classical dynamical systems [51] and few-body chaos [52]. In practice, such studies are naturally limited to sufficiently simple manifolds that have low bond dimensions. Nevertheless, this approach proved extremely valuable in establishing an analogy between non-thermal eigenstates in Rydberg atom chains and their counterparts in few-body systems, justifying the name “quantum many-body scars”—these developments will be the subject of Sects. 5 and 6.

We note that there are some caveats to mapping quantum dynamics onto low-dimensional manifolds \mathcal{M} . At late times, the error of the TDVP approximation necessarily grows because the exact quantum dynamics generally brings the system out of the variational manifold—see Fig. 2b. Intuitively, the TDVP error for a given initial state is linked to the rate of entanglement growth for that state, since the MPS with low bond dimension can only successfully capture weakly entangled states. When the entanglement grows significantly, the state starts to require an MPS description with a bond dimension that extends beyond the variational manifold. This discrepancy is the error of the TDVP approximation, also known as *quantum*

leakage [14, 49]:

$$\gamma^2(\{x_a\}) = \lim_{L \rightarrow \infty} \frac{1}{L} \|(iH + \dot{x}_b \partial_{x_b}) |\psi(\{x_a\})\rangle\|^2. \quad (14)$$

This is the instantaneous rate at which the exact quantum wave function leaves the variational manifold. Equations of motion can be obtained by minimising the discrepancy between exact quantum dynamics and its projection onto \mathcal{M} . Explicit computation of γ^2 is possible within the TDVP framework, but since it involves the square of the Hamiltonian operator, it contains information that goes beyond the TDVP equations of motion. Understanding γ^2 is key to understanding the relation between quantum dynamics and its classical counterpart. We postpone a more extensive discussion of the subtleties of the TDVP approach to many-body systems to Sect. 5.

Box 4 : TDVP for a Single Spin

To illustrate the TDVP way of thinking, consider the simplest example of a quantum spin prepared in a product state $|\psi(\theta, \phi)\rangle = \cos\theta |\uparrow\rangle + \sin\theta e^{i\phi} |\downarrow\rangle$, parametrised by angles θ and ϕ on the Bloch sphere. For concreteness, we can think of the spin Hamiltonian as $H = \epsilon \sigma^x$, corresponding to the magnetic field along the x -direction. Our aim is to find the equations of motion for the angles, $\theta(t)$ and $\phi(t)$, as the spin evolves under the influence of the magnetic field.

The expectation value of the Hamiltonian in the given state is $\langle H \rangle = \epsilon \sin(2\theta) \cos\phi$. Moreover, we have $\langle \psi | \dot{\psi} \rangle = -i\dot{\phi} \sin^2\theta$. Plugging this into Eq. (12), our Lagrangian takes the form $\mathcal{L} = \dot{\phi} \sin^2\theta - \langle H \rangle$. We see that we can identify the canonical “position” and “momentum” variables as $\phi \rightarrow q$ and $\sin^2\theta \rightarrow p$. Thus, we have mapped the quantum spin dynamics onto a classical dynamical system described by the equations of motion $\dot{\phi} = 2\epsilon \cot(2\theta) \cos\phi$ and $\dot{\theta} = -\epsilon \sin\phi$. Notice that the line $\phi = \pi/2$ is stationary—this corresponds to the simple precession dynamics, $\dot{\theta} = -\epsilon$, which in this case is easy to derive directly by solving the Schrödinger equation.

This example of a single spin can also be viewed as a particularly simple mean-field picture for the dynamics. This approach is generally insufficient to describe dynamics in more complex many-body systems, and, as discussed in Sect. 5, recent works have been exploring generalisations to variational manifolds beyond the mean field using MPS states.

3 Mechanisms of Weak Ergodicity Breaking

ETH-violating eigenstates have recently been theoretically identified in a variety of non-integrable quantum models, revealing a complex landscape of weak ergodicity breaking phenomena. The common feature of these models is the emergence of a decoupled subspace within the many-body Hilbert space, in general without any underlying symmetry. In this section, we focus on idealised models where such a subspace is perfectly decoupled from the rest of the spectrum, resulting in a decomposition of the Hamiltonian

$$H = H_{\text{non-ETH}} \oplus H_{\text{thermal}}, \quad (15)$$

where $H_{\text{non-ETH}}$ is the non-thermalising subspace, exactly decoupled from the thermalising bulk of the spectrum, H_{thermal} . The eigenstates that inhabit the subspace $H_{\text{non-ETH}}$ violate the ETH and have different properties compared to the majority of thermal eigenstates residing in H_{thermal} . Below we elucidate three commonly encountered mechanisms that produce such decoupled subspaces. We would like to point out that in much of the recent literature, the non-thermalising eigenstates that span $H_{\text{non-ETH}}$ are commonly referred to as “quantum many-body scars”. We will discuss the precise meaning of quantum many-body scarring in Sect. 6.

3.1 Spectrum Generating Algebra

Using the MPS techniques introduced in Sect. 2, Moudgalya et al. [17], building on the early work by Arovas [45], analytically constructed a tower of exact eigenstates in the AKLT model in Eq. (4), which were shown to have sub-volume entanglement entropy, thus providing the first rigorous demonstration of the strong-ETH violation. Later on, Schecter and Iadecola [53] introduced a tower of exact eigenstates in a family of non-integrable spin-1 XY models as well in a particular non-integrable spin-1/2 model that conserves the number of domain walls [54]. In these and many other similar examples that followed, the non-thermal eigenstates form a so-called spectrum generating algebra (SGA), first introduced in the context of high-energy physics [55] and subsequently applied to the Hubbard model [56, 57].

To define the SGA, we follow the presentation given by Mark, Lin and Motrunich [58]. Suppose we have a Hamiltonian H ; a linear subspace W ; a state $|\Psi_0\rangle \in W$, which is an eigenstate of H with energy E_0 ; and an operator Q^\dagger such that $Q^\dagger W \subset W$ and

$$\left([H, Q^\dagger] - \omega Q^\dagger \right) W = 0. \quad (16)$$

Then it can be easily proven that the family of states

$$|\mathcal{S}_n\rangle = (Q^\dagger)^n |\Psi_0\rangle, \quad (17)$$

as long as they are non-vanishing vectors, are eigenstates of H with eigenvalues $E_0 + n\omega$. The non-thermalising nature of these states becomes non-trivial when W is *not* the entire Hilbert space and Q^\dagger is not associated with a symmetry of the Hamiltonian. The latter crucially distinguishes these non-thermal states from somewhat similar “eta-pairing” states in the Hubbard model [56, 57], a point discussed further at the end of this subsection.

As an example, in the AKLT model, one of the possible SGA operators is a spin-2 magnon excitation that we have previously seen in Eq. (9), with

$$Q^\dagger = \sum_{j=1}^L (-1)^j (S_j^+)^2. \quad (18)$$

This generates the tower of states in Eq. (17) for $n = 0, \dots, L/2$, which extend from the ground state ($n=0$) up to the ferromagnetic state $|1, 1, \dots, 1\rangle$ ($n=L/2$), and the state in Eq. (9) is a member of this family. It is also worth noting that these states are not unique, as they have total spin $s = 2n$; hence, we can obtain equivalent spin-rotated versions of these states by applying the $SU(2)$ spin-lowering operator.

Generally, it is clear that states of the form in Eq. (17) can be non-thermal, provided $|\Psi_0\rangle$ is sufficiently “simple” (e.g., the ground state of H if the latter is gapped) and Q^\dagger is a local operator. The AKLT tower of states in Eqs. (17)–(18) is the first example of a rigorous construction of non-thermal states in a non-integrable model that are not protected by a global symmetry. Any Hamiltonian with the SGA property explicitly decomposes as in Eq. (15), where $H_{\text{non-ETH}}$ contains the tower of states obtained by the action of Q^\dagger . Note that this algebraic structure is not powerful enough to fully diagonalise H ; indeed, H could well be a non-integrable Hamiltonian with an energy spectrum obeying the Wigner–Dyson statistics.

Physically, Q^\dagger creates a wave packet corresponding to a “quasiparticle” excitation (e.g., a magnon), and repeated applications of Q^\dagger create a condensate of such quasiparticles. In a class of frustration-free models that include the AKLT [44], the quasiparticle condensates are non-thermal, e.g., their entanglement entropy scales logarithmically with the subsystem size:

$$S \propto \log L_A. \quad (19)$$

Another important clue when looking for non-thermalising SGA states is that they appear at energies that are integer multiples of ω . Thus, SGA eigenstates can be detected as regularly spaced entropy outliers, with entanglement much lower than the ETH volume law, as depicted in Fig. 1d. Perhaps more practically, the SGA states also have very low entanglement *rank*, i.e., many eigenvalues of ρ_A strictly vanish, which is how these states were originally identified numerically in Ref. [17].

We mentioned that the SGA traces back to the so-called eta-pairing states in the Hubbard model [56, 57]. For eta-pairing states, the subspace W is the entire Hilbert space, and Q^\dagger essentially corresponds to a symmetry of the Hamiltonian [59]. However, it is possible to perturb the Hubbard model [60, 61] in a way that destroys the aforementioned symmetry and makes these states similar to the SGA states in the AKLT model discussed above. Note that the high degree of symmetry in Hubbard-type models can also lead to disconnected subspaces that host free-particle eigenstates with ballistic dynamics [62]. This “fragmentation” of the Hilbert space is a much more general phenomenon beyond just the Hubbard model, as we discuss in the following section. Finally, we note that generalisations of the SGA construction can be found in a number of models in various dimensions [54, 58, 63–68] (see Box 3). It has also been pointed out that the SGA can arise in open quantum systems in the presence of dissipation or driving [69, 70].

Box 5 : Constructions of Non-Thermal Towers of Eigenstates

Towers of non-thermal eigenstates can be systematically constructed using the “tunnels-to-towers” approach in Ref. [68] based on generators of the Lie algebra of a symmetry group G . For simplicity, consider the case when G is $SU(2)$, and we have a model defined by an $SU(2)$ -symmetric Hamiltonian, H_{sym} . The generators of the symmetry $\{Q^+, Q^-, Q^z\}$ are associated with the corresponding $\mathfrak{su}(2)$ algebra. The spectrum of H_{sym} is organised into “tunnels” of degenerate eigenstates, with the same eigenvalue for the Casimir Q^2 but different eigenvalues for Q^z . One can “move” between states in a tunnel using Q^\pm (Fig. 3).

Now imagine perturbing the model by adding $H_{\text{SGA}} \propto Q^z$. This perturbation preserves the eigenstates but breaks the degeneracy of the tunnels. Instead, states in each tunnel get promoted to “towers” and acquire an evenly spaced harmonic spectrum because of the SGA, $[Q^z, Q^\pm] = \pm Q^\pm$. Finally, we can further add a symmetry-breaking term H_{SB} , such that it annihilates a specific tower of states but generically breaks all symmetries and mixes between the other states so as to make the rest of the spectrum thermal. In the full model, $H = H_{\text{sym}} + H_{\text{SGA}} + H_{\text{SB}}$, our chosen tower of states is a collection of non-thermalising eigenstates, evenly distributed throughout the spectrum but not protected by a global symmetry; hence, we arrive at a similar phenomenology to the AKLT model discussed in the main text. Various extensions of this construction to non-Abelian groups and their q -deformed versions are possible [68].

(continued)

Box 5 (continued)

To illustrate the tunnels-to-towers construction, consider the spin-1 XY-like model introduced in Ref. [53]:

$$H = \sum_i J(S_i^x S_{i+1}^x + S_i^y S_{i+1}^y) + J_3(S_i^x S_{i+3}^x + S_i^y S_{i+3}^y) + \sum_i h S_i^z + D(S_i^z)^2. \quad (20)$$

A tower of non-thermalising states is built by the action of the same Q^\dagger as in the AKLT model [58]:

$$|S_n^{XY}\rangle = (Q^+)^n |\Omega\rangle, \quad Q^+ = \sum_j (-1)^j (S_j^+)^2, \quad (21)$$

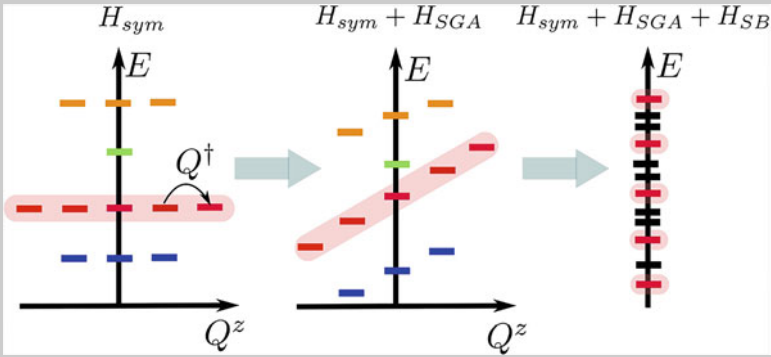


Fig. 3 Tunnels-to-towers scheme for constructing non-thermal eigenstates from Ref. [68]

where $|\Omega\rangle$ is the fully polarised down state $|\Omega\rangle = |-\dots-\rangle$. Note that Q^+ (and the corresponding Q^-), together with $Q^z = \frac{1}{2}[Q^+, Q^-]$, form an $su(2)$ algebra, but they are distinct from the spin- $su(2)$ operators. The first term $\propto J$ breaks Q - $SU(2)$ symmetry and annihilates the tower, the term hS^z acts as H_{SGA} and gives energy to the states in the tower, while the term $\propto D$ commutes with Q^z and Q^+ . The third neighbour term is added to break a non-local $SU(2)$ symmetry for which the states belonging to the tower are the only states in their symmetry sector.

3.2 Hilbert Space Fragmentation

Spectrum generating algebra relies on the tower operator Q^\dagger to construct the non-thermalising subspace. We now describe a related mechanism that produces

exactly embedded subspaces but does not require *a priori* knowledge of Q^\dagger . For a Hamiltonian H and some arbitrary vector in the Hilbert space, $|\psi_0\rangle$, the *Krylov subspace*, \mathcal{S} , is defined as the set of all vectors obtained by repeated action of H on $|\psi_0\rangle$,

$$\mathcal{S}(H, |\psi_0\rangle) \equiv \text{span}\{|\psi_0\rangle, H|\psi_0\rangle, H^2|\psi_0\rangle, \dots\}. \quad (22)$$

Readers familiar with numerical linear algebra will recall the same subspace \mathcal{S} is used in iterative methods for finding extremal eigenvalues of large matrices, such as the Arnoldi and Lanczos algorithms. By definition, \mathcal{S} is closed under the action of H . While $|\psi_0\rangle$ in Eq. (22) can in principle be an arbitrary state, in physics one is primarily interested in initial product states (also called the “root” states), which are more easily preparable in experiment. For a generic non-integrable Hamiltonian H without any symmetries, one expects that $\mathcal{S}(H, |\psi_0\rangle)$ for *any* initial product state $|\psi_0\rangle$ is the *full* Hilbert space of the system. If H has some symmetry (and assuming $|\psi_0\rangle$ an eigenstate of the symmetry), $\mathcal{S}(H, |\psi_0\rangle)$ is expected to span all states with the same symmetry quantum number as $|\psi_0\rangle$.

Surprisingly, it has been shown that in many cases the system can exhibit *fragmentation*, i.e., even after resolving the symmetries, $\mathcal{S}(H, |\psi_0\rangle)$ does *not* span all states with the same symmetry quantum numbers as $|\psi_0\rangle$ [18, 19, 71, 72]. Following the notations in Ref. [72], we can formally state this as

$$\mathcal{H} = \bigoplus_{\mathbf{s}} \mathcal{H}^{(\mathbf{s})}, \quad \mathcal{H}^{(\mathbf{s})} = \bigoplus_{i=1}^{\#(\mathbf{s})} \mathcal{S}(H, |\psi_i^{(\mathbf{s})}\rangle), \quad (23)$$

where \mathbf{s} labels the distinct symmetry quantum numbers, $\#(\mathbf{s})$ denotes the number of disjoint Krylov subspaces generated from product states with the same symmetry quantum numbers, and $|\psi_i^{(\mathbf{s})}\rangle$ are the root states generating the Krylov subspaces. Note that the root states in Eq. (23) are chosen such that they generate distinct disconnected Krylov subspaces (the same subspace can be generated by different root states). If one (or more) Krylov sector is non-thermalising, we recognise Eq. (23) is of the same form as our previous Eq. (15).

Fragmentation as in Eq. (23), where the total number of Krylov subspaces is exponentially large in the system size, was recently shown to *always* exist in Hamiltonians and random-circuit models with conservation of dipole moment (see Box 4). Before illustrating this for a particular model, we note that, generally, one can distinguish between “strong” and “weak” fragmentation, depending, respectively, on whether or not the ratio of the largest Krylov subspace to the Hilbert space within a given global symmetry sector vanishes in the thermodynamic limit. Strong (resp. weak) fragmentation is associated with the violation of weak (resp. strong) ETH with respect to the full Hilbert space. Moreover, different fragments can exhibit vastly different dynamical properties. For example, some fragments (even though exponentially large in system size) may be integrable, while others may be non-

integrable. Among the non-integrable ones, more subtle ETH-breaking phenomena are also possible [73].

To illustrate fragmentation, consider the following model of fermions hopping on an open 1D chain while preserving their centre of mass position [72]:

$$H = \sum_j \left(c_j^\dagger c_{j+3}^\dagger c_{j+2} c_{j+1} + \text{h.c.} \right), \quad (24)$$

where c_j^\dagger, c_j are the standard fermion creation/annihilation operators on site j . This model has a variety of physical realisations, which we discuss at the end of this section. We now demonstrate the dynamical fragmentation in this model, closely following the presentation in Ref. [72].

At filling factor $\nu = 1/2$, i.e., with half as many fermions as sites in the chain L , it is convenient to split the chain into 2-site cells assuming L is even. For each cell, define the new degrees of freedom:

$$|\uparrow\rangle \equiv |01\rangle, \quad |\downarrow\rangle \equiv |10\rangle, \quad |+\rangle \equiv |11\rangle, \quad |-\rangle \equiv |00\rangle. \quad (25)$$

It is fruitful to name these composite degrees of freedom: $|+\rangle, |-\rangle$ are called “fractons”, $|+-\rangle, |-+\rangle$ are “dipoles”, and $|\uparrow\rangle, |\downarrow\rangle$ are “spins”. By inspecting the possible action of the Hamiltonian in Eq. (24) on these states, we find several types of allowed processes. For example, the following processes can be interpreted as free propagation of dipoles when separated by spins:

$$|\downarrow + -\rangle \leftrightarrow |+- \downarrow\rangle, \quad (26)$$

$$|-\uparrow \uparrow\rangle \leftrightarrow |\uparrow -+\rangle. \quad (27)$$

Similarly, the following processes imply that a fracton can only move through the emission or absorption of a dipole:

$$|\downarrow + \uparrow\rangle \leftrightarrow |+ - +\rangle, \quad (28)$$

$$|\uparrow - \downarrow\rangle \leftrightarrow |- + -\rangle. \quad (29)$$

Here, Eqs. (26)–(29) resemble the rules restricting the mobility of fracton phases of matter [74]. However, in contrast to the usual fracton phenomenology, here the movement of fractons is also sensitive to the background spin configuration. For example, the fracton in the configuration $|\cdots \downarrow + \uparrow \cdots\rangle$ can move by emitting a dipole (see Eq. (28)), while that in the configuration $|\cdots \uparrow + \downarrow \cdots\rangle$ cannot.

The model in Eq. (24) has several symmetries; most notably the total charge (the number of fermions) and the total dipole moment are conserved,

$$\widehat{Q} = \sum_j \widehat{Q}_j, \quad \widehat{D} \equiv \sum_j j \widehat{Q}_j, \quad (30)$$

with $\hat{Q}_j \equiv \hat{n}_{2j-1} + \hat{n}_{2j} - 1$, where j is the unit cell index and $2j - 1, 2j$ are the site indices of the original configuration.

Exponentially many of Krylov subspaces in the model in Eq. (24) are one-dimensional frozen configurations. For instance, the Hamiltonian vanishes on any product state that does not contain the patterns “...0110...” or “...1001...” since those are the only configurations on which terms of H act non-trivially. The state

$$|1111000011110000 \dots 1111000011110000\rangle$$

is one example of a static configuration that is an eigenstate. In terms of the composite degrees of freedom, we can equivalently consider configurations with only $+$, $-$, and no spins, such as

$$|\dots ++ -- ++ -- \dots\rangle,$$

with a pattern that alternates between $+$ and $-$ with “domain walls” that are at least 2 sites apart. Once again, it is easy to see that all terms of the Hamiltonian vanish on these configurations: since there are *exponentially* many such patterns, there are equally many one-dimensional Krylov subspaces.

In Ref. [72], it was found that large fragments (with dimension exponential in system size L) can be integrable (mappable to spin-1/2 XX spin model) as well as non-integrable. See Fig. 4 for an illustration of some of the disconnected sectors of the Hilbert space. The dynamics initialised in any of the states, e.g., in Fig. 4a cannot reach any of the states in plots (b) and (c).

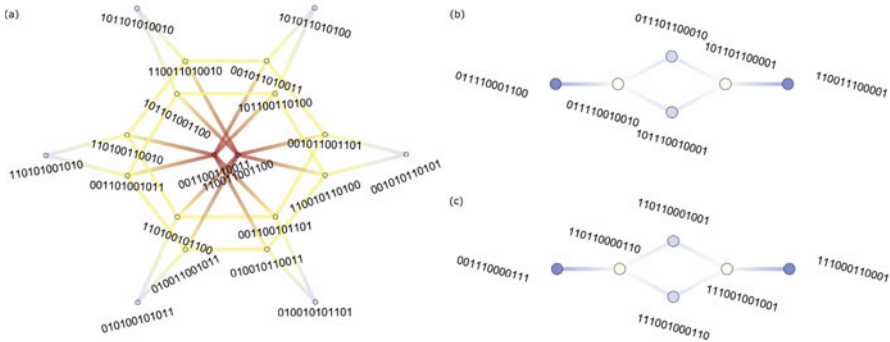


Fig. 4 Hilbert space fragmentation in the pair-hopping model in Eq. (24) studied in Ref. [72]. Plots (a), (b), and (c) show graphs of three disconnected sectors of the Hilbert space for a small chain with $N=6$ electrons at filling factor $\nu=1/2$. Each vertex represents a Fock basis state, and vertices are connected by an edge if the Hamiltonian matrix element is non-zero between those basis states. This type of graph is known as the adjacency graph of the Hamiltonian. In this case, because all the matrix elements of the Hamiltonian are equal in magnitude, the adjacency graph is unweighted. The graph has been coloured according to the vertex degree (with red colour indicating high connectivity)

We previously announced that the pair-hopping model in Eq. (24) arises in a number of different physical contexts: (i) it arises as the dominant hopping process for electrons in the regime of the fractional quantum Hall effect in a quasi-1D limit [73]; (ii) it arises in the Wannier–Stark problem, i.e., spinless fermions hopping on a one-dimensional lattice, subject to a large electric field [75]; (iii) it can be mapped to the following spin-1 fractonic model studied in Ref. [19]: $H_4 = -\sum_n (S_n^+ S_{n+1}^- S_{n+2}^- S_{n+3}^+ + \text{h.c.})$; (iv) at filling factor $\nu=1/3$, one of the Krylov sectors can be mapped to the so-called PXP model, introduced in Eq. (35) below, which describes a chain of strongly interacting Rydberg atoms. Note that in realisations (i), (ii), there are usually additional diagonal terms in the Hamiltonian that are of the same order as the hopping. While this does not affect the fragmentation, it may significantly impact other dynamical properties within the fragments. The realisation (ii) has recently been investigated as a platform for many-body localisation without disorder [76, 77].

Signatures of fragmentation have been observed in other models including, e.g., the Fermi–Hubbard model and its cousins [59, 62], various constrained models [78–80], and bosons in optical lattices [81, 82]. In the latter case, the Krylov subspaces are only *approximately* exact in the sense that there exist non-zero matrix elements that connect different Krylov subspaces, but their magnitude is much smaller than the matrix elements within a given Krylov subspace. Finally, we mention that Krylov fragmentation may also arise as a consequence of measurements performed on a system, e.g., in Ref. [83], it was shown that the analogue of Eq. (22) occurs when a quantum walk is interrupted by repeated projective measurements.

Box 6 : Fragmentation in Quantum Circuits

Beyond Hamiltonian systems, fragmentation generally arises in models of 1D random unitary circuit dynamics, constrained to conserve both $U(1)$ charge and its dipole moment [18, 71]. Consider a model from Ref. [71] with a chain of $S=1$ quantum spins, with the local z -basis $|+\rangle, |-\rangle, |0\rangle$, and unitary gates that locally conserve charge $\hat{Q} = \sum_j S_j^z$ and dipole moment $\hat{D} = \sum_j j S_j^z$. These intertwined conservation laws greatly restrict the allowed movement of charges, e.g., a single $+$ or $-$ charge on site x has dipole moment $D = \pm x$. Such a charge cannot hop to the left or right because this would change the net dipole moment by one unit. On the other hand, bound states of charges or “dipoles” of the form $(-+)$ have net charge zero and net dipole moment $D = \pm 1$ independent of position, and these can move freely. Additionally, dipoles can enable the movement of charges because a charge can move if it simultaneously emits a dipole to keep D unchanged: $|0+0\rangle \rightarrow |+-+\rangle$.

The above phenomenology is very similar to the pair-hopping model discussed in the main text, but following Ref. [18], we realise it using Floquet circuits composed of ℓ -site unitary gates, which locally conserve Q and

(continued)

Box 6 (continued)

D. These ℓ -site gates are therefore block-diagonal, and they are applied periodically in time. Assuming for simplicity $\ell=3$, we tile the chain by 3-site unitaries, staggered across three layers, i.e., $U^F = U^1 U^2 U^3$, with $U^1 \equiv U_{1,2,3}^1 U_{4,5,6}^1 \cdots$ illustrated in blue colour in Fig. 5 below (and similarly for U^2 , U^3 in red and green colours, respectively). The complete circuit consists of repeatedly applying U^F some number of times. Note that U^1 , U^2 , and U^3 can be chosen at random for a given realisation but then remain fixed throughout the circuit (Fig. 5).

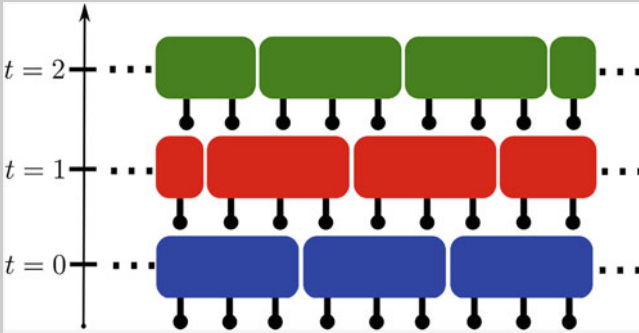


Fig. 5 Illustration of the Floquet operator $U^F = U^1 U^2 U^3$, staggered across three layers, from Ref. [18]

Reference [18] showed that local fractonic circuits of this type must have exponentially many Krylov sectors. To see this, note that *any* pattern that alternates between locally “all plus” and locally “all minus”, with domain walls in between at least ℓ sites apart, must be inert. These are states of the form $|++++-----++++\cdots\rangle$. The argument is similar to the one given in the main text for the Hamiltonian system. One can then lower bound the size of the disconnected subspace by dividing the system up into blocks of length ℓ and allowing each block to be either “all plus” or “all minus”. This yields an inert subspace of dimension at least $2^{L/\ell} = c^L$, where $c = 2^{1/\ell}$. This bound is not tight [18], but it proves the existence of an exponentially large, localised subspace for any finite gate size. We emphasise that the exponentially large number of sectors goes beyond simple symmetry considerations, which would only predict $\propto L^3$ sectors, since the allowed values of quantum numbers are $-L \leq Q \leq L$ and $-L(L-1)/2 \leq D \leq L(L-1)/2$, where L is the length of the chain.

3.3 Projector Embedding

At the highest level of abstraction, we can ask if one could embed an arbitrary subspace into the spectrum of a thermalising system? For concreteness, assume we are given an arbitrary set of states $|\psi_i\rangle$ that span our target non-thermalising subspace $H_{\text{non-ETH}} = \text{span}\{|\psi_i\rangle\}$, which we wish to embed into a thermalising Hamiltonian H as in Eq. (15). This can be achieved via the “projector embedding” construction first introduced by Shiraishi and Mori [20].

Our target states $|\psi_i\rangle$ are assumed to be non-thermal; hence, we furthermore assume there exists a set of local projectors, P_i , which annihilate these states, $P_i|\psi_j\rangle = 0$, for any i ranging over lattice sites $1, 2, \dots, L$. Next, consider a lattice Hamiltonian of the form

$$H = \sum_{i=1}^L P_i h_i P_i + H', \quad (31)$$

where h_i are arbitrary operators that have support on a finite number of sites around i , and $[H', P_i] = 0$ for all i . It follows

$$P_i H |\psi_j\rangle = P_i H' |\psi_j\rangle = H' P_i |\psi_j\rangle = 0, \quad (32)$$

and thus $[H, \sum_i P_i] = 0$. Therefore, H takes the desired block-diagonal form in Eq. (15). The target eigenstates can in principle be embedded at arbitrarily high energies for a suitably chosen H' , which also ensures that the model is overall non-integrable [20]. However, there is no guarantee that the embedded states must be equidistant in energy, and they may even be degenerate, such that this scheme could clearly result in a model without an SGA property discussed in Sect. 3.1.

Physical applications of projector embedding include various topologically ordered systems [84, 85] and models with lattice supersymmetry [86], which are themselves defined in terms of local projectors (see Box 5). While the projector construction allows to embed general classes of states into a thermalising spectrum, in practice one is often more interested in the reverse question: given a Hamiltonian H belonging to some known physical system, can one identify non-thermal embedded states $|\psi_i\rangle$? Although this task is obviously much harder, for some physical models such as the PXP model, introduced in Sect. 4 below, this question has been answered affirmatively for a single target state at zero energy in the middle of the spectrum, which has been identified with the AKLT ground state in Eq. (5) [87]. However, for the AKLT non-thermal eigenstates constructed via the SGA in Sect. 3.1, in particular for the tower of states in Eqs. (17)–(18), at present, it is not known whether it is possible to find a set of local projectors and cast the entire tower of AKLT states in the Shiraishi–Mori form. This suggests there may be broader classes of models with non-thermal eigenstates that extend beyond the form in Eq. (31). Indeed, in a very recent work [88], a scheme based on a double copy of the system has been proposed for embedding eigenstates with high entanglement.

Box 7 : Physical Realisations of Projector Embedding

To illustrate constructions of non-thermal eigenstates via projector embedding, we consider a class of topological lattice models defined in terms of local projectors, following Ref. [84]. A typical Hamiltonian of such models has the form

$$H(\beta) = \sum_p \alpha_p Q_p(\beta), \quad (33)$$

where p labels, e.g., elementary plaquettes of a lattice, such as in toric code [89]. The operators $Q_p(\beta)$ are Hermitian, positive-semidefinite, and local. They contain only sums of products of operators defined within the bounded region labelled by p , e.g., at the Rokhsar–Kivelson point of the quantum dimer model on the square lattice [90], $Q_p(\beta)$ are projectors that encode both the potential and kinetic (plaquette flip) terms. The dimensionless parameter β is used to deform solvable models and break integrability.

The operators $Q_p(\beta)$ are built so as to share a common null state $|\Psi(\beta)\rangle$, i.e., for every p , we have $Q_p(\beta) |\Psi(\beta)\rangle = 0$. If all the couplings α_p are positive, the state $|\Psi(\beta)\rangle$ is the ground state of $H(\beta)$. If, instead, α_p takes both positive and negative values, then it is not guaranteed that $|\Psi(\beta)\rangle$ is a ground state. Nevertheless, $|\Psi(\beta)\rangle$ is still an eigenstate with energy $E=0$. When this state is a high-energy eigenstate of $H(\beta)$, it is an atypical state in that it displays area-law entanglement entropy since it is also a ground state of a *different* local Hamiltonian:

$$H'(\beta) = \sum_p |\alpha_p| Q_p(\beta). \quad (34)$$

Hence, $|\Psi(\beta)\rangle$ is a non-thermal state, if $H(\beta)$ is non-integrable. By deforming exactly solvable models—the toric code, for instance—one can break integrability while retaining the $E=0$ state [84]. The construction outlined here can be shown to be equivalent to the embedding construction in Eq. (31) by diagonalising the operators $Q_p(\beta)$ and separating the terms belonging to zero eigenvalues (which must exist by construction) from other eigenvalues.

4 PXP Model

In the previous section, we introduced several mechanisms of weak ergodicity breaking, realised by diverse physical systems. While these mechanisms are mutually independent and different systems may only exhibit some of them, we next show how these mechanisms “co-exist” within a paradigmatic model of weak

ergodicity breaking known as the PXP model. This model arises as the effective description of Rydberg atoms in the regime of a strong Rydberg blockade, and its experimental realisation will be the topic of Sect. 7. As we explain below, the PXP model realises much of the weak ergodicity breaking phenomenology discussed previously; in particular, its Hilbert space is fragmented, and it contains non-thermal eigenstates that form an approximate SGA.

4.1 The Model

The PXP model describes a chain of coupled two-level systems, where each system can be in one of the two possible states, $|\circ\rangle$ and $|\bullet\rangle$. In the Rydberg atom realisation, these states correspond to an atom being in its ground state or in the excited Rydberg state, respectively. However, for present purposes, we can view these two states as \downarrow, \uparrow projections of a spin-1/2 degree on the given site. We consider a 1D chain of such two-level systems coupled according to the ‘‘PXP’’ Hamiltonian [91],

$$H_{\text{PXP}} = \sum_i P_{i-1} \sigma_i^x P_{i+1}, \quad (35)$$

where $\sigma_i^x \equiv |\circ_i\rangle \langle \bullet_i| + |\bullet_i\rangle \langle \circ_i|$ is the standard Pauli x -matrix on site i and $P_i = |\circ_i\rangle \langle \circ_i|$ is the projector on the ground state at site i . Equivalently, the projectors can be defined as $P_i = \frac{1}{2}(1 - \sigma_i^z)$, with $\sigma_i^z \equiv |\circ_i\rangle \langle \circ_i| - |\bullet_i\rangle \langle \bullet_i|$.

Without projectors, the Hamiltonian in Eq. (35) is that of a free paramagnet: each spin would independently precess with the Rabi frequency set to 1. P introduces a kinetic constraint: it allows a spin to flip only if both of its nearest neighbours are in \circ state. For example, the process $\dots \circ \circ \circ \dots \leftrightarrow \dots \circ \bullet \circ \dots$ is allowed, while $\dots \bullet \circ \circ \dots \leftrightarrow \dots \bullet \bullet \circ \dots$ is forbidden. This makes the model intrinsically interacting, as it is no longer possible to describe the state of each spin independently of other spins. Numerical simulations based on exact diagonalisation of the PXP model with up to $L=32$ spins have demonstrated that the statistics of its energy-level spacings approaches the prediction of random matrix theory [13] as the system size is increased. Hence, despite its very simple form, we expect the PXP model cannot be fully ‘‘solved’’ using the known integrability techniques [31].

Another consequence of projectors is the fragmentation of the PXP Hamiltonian: H_{PXP} splits into sectors corresponding to different numbers of adjacent spin excitations. The largest connected component of the Hilbert space is one that excludes any configurations with adjacent excitations, $\dots \bullet \bullet \dots$. The number of classical configurations that satisfy such a constraint is still exponentially large—more precisely, it scales asymptotically

$$\mathcal{D}_L \propto \varphi^L, \quad \varphi = \frac{1 + \sqrt{5}}{2}, \quad (36)$$

where φ is the golden ratio. This unusual scaling is a manifestation of the global constraint. Similar type of constraints can arise due to emergent gauge fields and have been used to model interactions between anyon excitations in topological phases of matter [92]. Apart from this largest sector, there are further sectors that contain some number of nearest-neighbour spin flips; however, in the remainder of this section, we will focus on the *largest* connected component of the Hilbert space, which already displays non-trivial weak ergodicity breaking phenomenology.

4.2 Ergodicity Breaking in the PXP Model

While the PXP model is quantum-chaotic, numerical simulations of its quench dynamics [13, 93–95] have revealed surprising non-ergodic behaviour. For example, the return probability in global quenches with the PXP Hamiltonian is shown in Fig. 6a [13, 95]. “Global quench” means that the system is prepared in a highly non-equilibrium initial state, $|\psi_0\rangle$, at time $t=0$, and the system is subsequently evolved with the many-body Hamiltonian, H_{PXP} in Eq. (35). Since the PXP Hamiltonian is purely off-diagonal in the standard z -basis, any classical product state has an average energy equal to zero and extensive energy variance, thus effectively playing the role of an “infinite temperature” ensemble. In Fig. 6a, three choices of density wave states were considered for $|\psi_0\rangle$: $|\mathbb{Z}_2\rangle \equiv |\cdots \bullet \bullet \bullet \cdots\rangle$, $|\mathbb{Z}_3\rangle \equiv |\cdots \bullet \bullet \bullet \bullet \bullet \cdots\rangle$ and $|\mathbb{Z}_4\rangle \equiv |\cdots \bullet \bullet \bullet \bullet \bullet \bullet \cdots\rangle$. We note that these states can be prepared in Rydberg atom experiments by modulating the so-called detuning term introduced below in Eq. (45).

As the system evolves following the quench, one can characterise its behaviour by the return probability, also known as many-body fidelity, which quantifies the probability of observing the initial state after unitary dynamics,

$$F(t) = |\langle \psi_0 | \psi(t) \rangle|^2 = |\langle \psi_0 | e^{-iHt} | \psi_0 \rangle|^2. \quad (37)$$

Intuitively, thermalising dynamics leads to a quick spreading of the many-body wave function over the full Hilbert space. According to Fig. 1b, fidelity is expected to rapidly decrease to an exponentially small value, $F \propto 1/\mathcal{D}_L$, and remain near that value at late times. The numerical result in Fig. 6a defies this expectation for *certain* initial states. In particular, the \mathbb{Z}_2 and \mathbb{Z}_3 density wave states show pronounced revivals at certain times, $F(nT) \sim O(1)$. In contrast, quench dynamics from \mathbb{Z}_4 (and many other initial product states not shown) displays fast relaxation without revivals. We note that the dynamics of local observables, such as the density of domain walls nucleated in \mathbb{Z}_2 , i.e., the number of $\cdots \bullet \bullet \cdots$ patterns, is very similar to the fidelity dynamics. In particular, the frequency of revivals in local observables is the same as that of fidelity for the initial state $|\mathbb{Z}_2\rangle$. Below we focus on understanding the dynamics for this initial state.

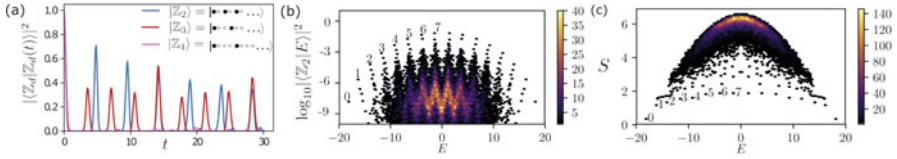


Fig. 6 (a) Numerical simulation of quantum fidelity in a large PXP model with $L=30$ atoms reveals strong atypicality with respect to the initial state [95]. For period-2 and -3 density waves, the fidelity features robust revivals, while period-4 density wave shows no revivals. (b,c): Non-thermal eigenstates violate the ETH by their anomalously large projection on $|Z_2\rangle$ state, and by their low entanglement entropy, S [95]. Each point represents a single eigenstate with energy E in a large PXP chain with $L=30$ atoms. Scarred eigenstates have been numbered by $0, 1, \dots, 7$. Colour scale represents the density of data points. Panels reproduced with permission from Ref. [95] APS, under a Creative Commons licence CC BY 4.0

In order to understand the origin of the atypical dynamical behaviour in the PXP model, we write the return amplitude as

$$\langle Z_2 | e^{-itH} | Z_2 \rangle = \sum_n e^{-itE_n} |\langle E_n | Z_2 \rangle|^2, \tag{38}$$

where $E_n, |E_n\rangle$ denote the eigenenergies and eigenvectors of H_{PXP} , respectively. Thus, quantum evolution is fully determined by the eigenenergies, $\{E_n\}$, and overlaps of energy eigenstates with the initial state, $\{|\langle E_n | Z_2 \rangle|^2\}$. Any special features in the dynamics translate into atypical properties of these overlaps. Indeed, Fig. 6b reveals a set of eigenstates that have strongly enhanced overlaps with Z_2 state, $|\langle E | Z_2 \rangle|^2$. These eigenstates violate the ETH [3, 4, 30] since we expect that individual eigenstates of thermalising systems should behave like thermal ensembles. By contrast, Fig. 6b demonstrates that special eigenstates have strongly enhanced overlaps with a particular product state, and thus they are anomalously concentrated in the Hilbert space and do not resemble random vectors.

Note that violations of the ETH are traditionally probed by studying the matrix elements of local observables [96]. The overlaps with $|Z_2\rangle$ state indeed probe the matrix elements of the alternating magnetic field operator, $\sum_j (-1)^j \sigma_j^z$, for which $|Z_2\rangle$ is the highest weight state. The higher the overlap with $|Z_2\rangle$, the stronger the violation of the ETH—thus, the special eigenstates are the “most” ETH-violating states in the spectrum of the PXP model. Intriguingly, the highest overlaps with $|Z_2\rangle$ are achieved in the *middle* of the spectrum, i.e., at the highest effective temperature in this system.

The total number of special states in Fig. 6b scales with the number of spins as $L+1$ [95]. Moreover, the special states are equidistant in energy, especially near the middle of the spectrum. Along with their large overlap with $|Z_2\rangle$ state, this explains the existence of fidelity revivals. However, as seen from the coloured density of data points in Fig. 6b, while the majority of other states in the spectrum has vanishingly small overlap with $|Z_2\rangle$, there is still a considerable number of

states forming “towers” that cluster around the energy of the special eigenstates. Towers of scarred eigenstates are also found in the PXP model in the presence of periodically driven detuning [97], and in a two-dimensional PXP model [98], where the overlap is computed with a charge-density wave state having a checkerboard pattern [99, 100].

Furthermore, the same $L+1$ special eigenstates show anomalously low entanglement entropy as seen in Fig. 6c. For a thermalising eigenstate, the bipartite entanglement entropy of a subsystem of length L_A is expected to scale extensively with the volume of the subsystem, $S \propto L_A$. In contrast, the entanglement entropy of special eigenstates is found to scale approximately with the logarithm of the subsystem size, as in Eq. (19) [95]. This is another evidence of ETH violation as it shows that special eigenstates are not uniformly spread over the Hilbert space.

Recall that the logarithmic scaling of entanglement entropy is commonly found in other models with SGA, Eq. (19). Indeed, approximations to special eigenstates can be constructed starting from an approximate ground state of the PXP model and creating spin wave excitations on top of it [101]. Although the accuracy of this scheme deteriorates for special eigenstates near the middle of the spectrum, the scheme provides an intuitive picture of special eigenstates as condensates of weakly interacting magnons, similar to models with an SGA. An alternative approach in Ref. [102] focused on the middle of the energy spectrum of the PXP model, where a few exact eigenstates can be constructed, thus rigorously demonstrating the ETH violation (see Box 6). While exact MPS constructions similar to Ref. [102] can be generalised to other models, e.g., a transverse Ising ladder [103] and the Floquet versions of the PXP model [104, 105], they remain limited to a small number of states in the middle of the spectrum, and in particular, they do not capture the top states in the towers, which are not simple MPS due to having larger-than-area-law entanglement.

Finally, we note that the model in Eq. (35) with the addition of a few diagonal terms can be made integrable [92, 106, 107], and it has a very rich phase diagram in its the ground state. However, these terms that render the PXP model integrable have magnitude $O(1)$, i.e., they are strong perturbations and are not expected to be relevant for explaining the physics presented in this section. Furthermore, several studies explored the effect of (generally, weaker) perturbations on the PXP model [95, 108, 109]. While non-thermal eigenstates are generally not robust to perturbations, some aspects of atypical dynamical behaviour are found to persist, including in the presence of disorder [110]. Finally, we mention that similar phenomenology of weak ergodicity breaking has also been found in the two-dimensional PXP model [99, 100], and in related models of transverse Ising ladders [103] and the periodically driven PXP model [97, 104, 105].

Box 8 : Ergodicity Breaking in Null Spaces

Among the special properties of the PXP model is the existence of an exponentially large number of states that are exactly annihilated by the PXP Hamiltonian in Eq. (35). This null space contains states with energy $E=0$ that reside in the middle of the spectrum [13, 95, 111]. This exponential zero-energy degeneracy is a consequence of the combined action of particle-hole transformation $C = \prod_i \sigma_i^z$, which *anticommutes* with the PXP Hamiltonian, and spatial inversion that maps site j to $L-j+1$ [112, 113].

Among the exponentially many $E=0$ eigenstates in the PXP model, there are also a few weakly entangled states that have been analytically constructed by Lin and Motrunich [102]. Such states are compactly written as MPS in Eq. (3) with $\chi=2$:

$$A^{\circ\circ} = \begin{pmatrix} 0 & -1 \\ 1 & 0 \end{pmatrix}, \quad A^{\circ\bullet} = \begin{pmatrix} \sqrt{2} & 0 \\ 0 & 0 \end{pmatrix}, \quad A^{\bullet\circ} = \begin{pmatrix} 0 & 0 \\ 0 & -\sqrt{2} \end{pmatrix}. \quad (39)$$

The local Hilbert space on which these matrices are defined is a 2-site block of the chain; due to the constraint, this block can be in three states, $(\circ\circ)$, $(\bullet\circ)$, and $(\bullet\circ)$. The constraint automatically prevents configurations with $(\circ\bullet)(\bullet\circ)$ on consecutive blocks since $A^{\circ\bullet}A^{\bullet\circ} = 0$. Using the block representation, it can be proven [102] that such an MPS state is exactly annihilated by the PXP Hamiltonian in Eq. (35).

In fact, from the state defined in Eq. (39), we can construct its partner translated by one site, also at $E=0$. These two states thus display translational symmetry breaking with a period-2 bond-centred pattern, despite being in 1D and at an infinite temperature. They also manifestly violate the ETH via their entanglement entropy, which must obey the area law due to their explicit MPS form. We note that Ref. [114] has recently shown that MPS states such as the one in Eq. (39) can arise more generally in random quantum networks due to connectivity bottlenecks.

In Ref. [115], the null spaces were investigated more generally in models of Abelian lattice gauge theories. In Ref. [116], a systematic exploration of null spaces was performed by applying a “subspace disentangling” algorithm in order to construct the least entangled state belonging to $E=0$ subspace. It was numerically demonstrated on several examples that this least entangled null state obeys area-law entanglement scaling, and as such, violates strong ETH. Thus, although protected by symmetry, null spaces provide another non-trivial mechanism for realising non-thermal states.

4.3 The Origin of Non-thermal Eigenstates and Quantum Revivals

In quantum physics, the simplest system that exhibits non-trivial dynamics and revivals is an elementary spin: a spin pointing along the z -direction precesses when the magnetic field is turned on in the x -direction, causing the spin to periodically return to its initial orientation as time passes. The revivals in the PXP model can also be understood as precession of a spin with magnitude $s=L/2$. The latter spin, however, is a collective degree of freedom representing L atoms [117]. More precisely, the $L+1$ scarred eigenstates identified in Fig. 6 form an approximate representation of an $\text{su}(2)$ algebra for spin- $L/2$. This perspective brings the PXP model in line with other models discussed in Sect. 3.1, with the main difference being that the SGA in the PXP model is only *approximate*.

Specifically, the spin picture follows from the mapping of the PXP model to a tight-binding chain—see Box 7. For the initial $|\mathbb{Z}_2\rangle$ state, the “big spin”-raising operator

$$H^+ = \sum_{i \in \text{even}} \tilde{\sigma}_i^+ + \sum_{i \in \text{odd}} \tilde{\sigma}_i^- \quad (40)$$

excites an atom anywhere on the even sublattice and deexcites an atom on the odd sublattice, where $\tilde{\sigma}_i^\pm = P_{i-1}\sigma_i^\pm P_{i+1}$ are the on-site raising and lowering operators that respect the constraint [13]. Similarly, the spin-lowering operator H^- performs the same process with the sublattices exchanged.

The reason for this choice of H^\pm is that their commutator defines the z projection of spin, $H^z \equiv \frac{1}{2}[H^+, H^-]$, for which $|\mathbb{Z}_2\rangle$ plays the role of the extremal weight state. Now the analogy with spin precession is almost complete because the PXP Hamiltonian in Eq. (35) is given by the sum $H_{\text{PXP}} = H^+ + H^-$, i.e., it plays the role of an x -component of spin. Thus, preparing the atoms in $|\mathbb{Z}_2\rangle$ state is equivalent to initialising the spin along the z -axis, and the state revives because the PXP Hamiltonian acts like a transverse magnetic field.

If the above spin picture were exact, the revivals in the PXP model would be perfect, with fidelity in Eq. (37) reaching 1 at certain late times. This is not seen, either in experiments discussed below or in the numerical simulations of the PXP model—recall Fig. 6a. The reason is that the mentioned $\text{su}(2)$ spin algebra is only approximate, $[H^z, H^\pm] \approx \pm H^\pm$ [117, 118], where “ \approx ” means there are additional operators on the right-hand side with smaller numerical prefactors from the leading H^\pm .

It has been realised that the structure of the $\text{su}(2)$ algebra and the robustness of the revivals can be significantly improved by small deformations of the PXP model [117, 119]. The inclusion of deformations completely arrests the entanglement growth, resulting in the band of scarred eigenstates nearly fully separated from the rest of the spectrum. We note that a similar procedure can be used to enhance revivals from other initial states, such as $|\mathbb{Z}_3\rangle$ and $|\mathbb{Z}_4\rangle$, for suitably redefined H^\pm

operators [118]. Thus, the PXP model could be deformed to stabilise different embedded $su(2)$ algebras. The deformations of the PXP model that enhance the $su(2)$ algebra and improve the $|\mathbb{Z}_2\rangle$ revival fidelity suggest the existence of an idealised parent model that hosts “perfect” many-body scars. Unfortunately, the parent model is defined by a long-ranged Hamiltonian with exponentially decaying tails [117], and it remains unknown whether it can be expressed in a more compact (short-range) form.

Box 9 : Forward Scattering Approximation

A free paramagnet is an example of a perfectly reviving system: any product state of spins pointing along the z -axis exhibits periodic dynamics under the magnetic field along the x -direction. Alternatively, the free paramagnet can be viewed as a hypercube graph of dimension L , where each of the 2^L spin product states represents a vertex, while the edges connect vertices that can be reached by flipping one spin. This picture helps to understand the PXP model, which is a *partial cube*, i.e., a hypercube where all the vertices violating the constraint have been removed—see Fig. 7. The resulting PXP graph contains two smaller hypercubes of dimension $L/2$, with $|\mathbb{Z}_2\rangle$ and $|\mathbb{Z}'_2\rangle$ states as extremal vertices, and the polarised state $|\circ\circ\dots\rangle$ at the intersection point of the two hypercubes. Additionally, there are also “bridges” that connect the two hypercubes, e.g., in Fig. 7, one such configuration is $\circ\bullet\circ\bullet\circ\bullet$.

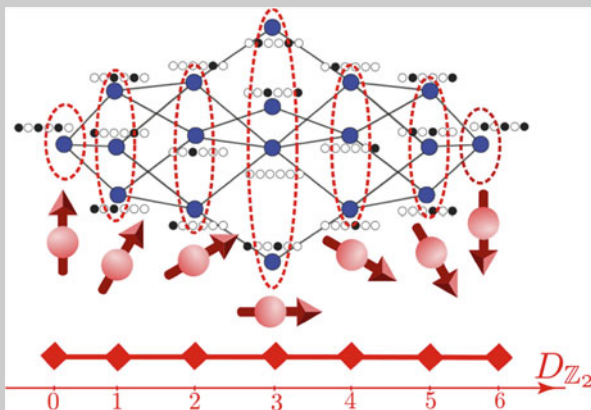


Fig. 7 Graph representation of the PXP Hamiltonian for $L=6$ spins. Vertices represent all states compatible with the constraint, while lines connect states related by a single spin flip. The FSA models the non-thermal eigenstates and revivals from $|\mathbb{Z}_2\rangle$ state by compressing the graph to a one-dimensional ladder of states, which are identified with basis states of a large spin of magnitude $s = \frac{L}{2}$ (red arrows). The states are labelled by their z projection of spin or, equivalently, by their Hamming distance $D_{\mathbb{Z}_2}$ from the leftmost vertex

(continued)

Box 9 (continued)

Quantum walk on the PXP graph starting in the $|\mathbb{Z}_2\rangle$ vertex can be accurately modelled by assuming the wave function spreads only in the forward direction, a scheme known as the forward scattering approximation (FSA) [13]. The FSA compresses the partial cube down to a one-dimensional chain, where each site $|n\rangle$ is a superposition of states with the same number of excitations relative to $|\mathbb{Z}_2\rangle$ vertex. Thus, for L atoms, the chain contains $L+1$ sites. The FSA interprets each site $|n\rangle$ as an eigenstate of a big spin with magnitude $s=L/2$ and pointing at an angle $\pi n/L$ with respect to the z -axis. As mentioned in the text, the spin-raising and -lowering operators directly follow from a decomposition of the PXP Hamiltonian [13]. The FSA not only allows to construct remarkably accurate approximations to the exact eigenstates of the PXP and several other models [13, 73, 95, 120], but it also provides the foundation for the elegant interpretation of the revivals as precession of an emergent spin.

5 Semiclassical Dynamics

Quantum-classical correspondence has been at the heart of quantum mechanics since the early 20th century. Parallels between the behaviour of a quantum system and its classical counterpart have been extensively studied in the context of few-body systems, such as the free propagating particle in a bounded domain (stadium billiard being a particular example), coupled harmonic oscillators, and a rotor subject to periodic driving [52]. In all these cases, the semiclassical limit can be taken by sending $\hbar \rightarrow 0$, and the behaviour of the quantum system is often found to closely parallel its classical counterpart. For instance, quantum counterparts of classically chaotic systems can be typically described by random matrix theory [121].

Intrinsically many-body systems, such as the PXP chain in Eq. (35), present challenges for the semiclassical description based on the conventional large- N limit or the mean-field approximation. The latter, for example, ignores any correlations between different spatial degrees of freedom and thus violates the constraint in the PXP model in Eq. (35). The constraint introduces non-local correlations: if a given spin is in $|\bullet\rangle$ state, its neighbours must be in $|\circ\rangle$ state. Such correlations build in quantum entanglement, which cannot be ignored unless one relaxes the constraint.

The MPS methods discussed in Sect. 2 allow to incorporate entanglement in a systematic way that goes beyond mean field [49]. For the PXP model, it has been first shown by Ho et al. [14] that this approach can be tailored to capture dynamics from the initial $|\mathbb{Z}_2\rangle$ state. This state is a period-2 density wave, which can be described using a 2-atom unit cell. Hence, the variational MPS state is parametrised

by two sets of angles, $\mathbf{x}_i = (\theta_i, \phi_i)$, $i=1, 2$, that describe the state of spins on odd and even sites in the lattice. The MPS matrices can be taken to be [98]

$$A^\bullet(\theta_i, \phi_i) = \begin{pmatrix} 0 & i e^{-i\phi_i} \\ 0 & 0 \end{pmatrix}, \quad A^\circ(\theta_i, \phi_i) = \begin{pmatrix} \cos \theta_i & 0 \\ \sin \theta_i & 0 \end{pmatrix}, \quad (41)$$

where we notice that $A^\bullet \alpha \sigma^+$ satisfies the condition $A^\bullet(\theta, \phi) A^\bullet(\theta', \phi') = 0$, which effectively imposes the constraint that no two adjacent spins are in $|\bullet\rangle$ state. The special points $(\theta_1, \theta_2) = (0, \pi/2)$ and $(\theta_1, \theta_2) = (\pi/2, 0)$ correspond to $|\mathbb{Z}_2\rangle = |\bullet\circ\bullet\circ\dots\rangle$ product state and its partner shifted by one lattice site, $|\mathbb{Z}'_2\rangle = |\circ\bullet\circ\bullet\dots\rangle$.

By projecting quantum dynamics onto the MPS manifold spanned by Eq. (41) using TDVP, as outlined in Sect. 2.2, one obtains a classical non-linear system for $\theta_i(t)$, $\phi_i(t)$. The derivation is cumbersome, and the final equations are also rather complicated (many useful technical details can be found in the Supplementary Material of Ref. [14]). To give an idea, we quote the final equations of motion from Ref. [98]

$$\dot{\theta}_1 = \tan \theta_2 \sin \theta_1 \cos^2 \theta_1 \cos \phi_1 + \cos \theta_2 \cos \phi_2, \quad (42a)$$

$$\dot{\phi}_1 = -\mu_z + 2 \tan \theta_1 \cos \theta_2 \sin \phi_2 - \frac{1}{2} \tan \theta_2 \cos \theta_1 \left(2 \sin^{-2} \theta_2 + \cos 2\theta_1 - 5 \right) \sin \phi_1, \quad (42b)$$

which were derived for the PXP model in the presence of a chemical potential, $\mu_z \sum_j n_j$, where $n_j \equiv \frac{1}{2}(1 + \sigma_j^z)$. The equations for θ_2, ϕ_2 can be obtained by substitution $1 \leftrightarrow 2$.

Before discussing the solutions of the equations of motion (42), we note that the expectation value of the Hamiltonian is a conserved quantity, provided the equations of motion are satisfied. This conservation law effectively reduces the dimensionality of the phase space from four down to three dimensions, as it restricts the dynamics to constant energy surfaces. However, when $\mu_z=0$ the system in Eqs. (42) actually has a class of solutions with *two* angles being stationary, $\phi_{1,2}=0$ [14]. This class of solutions corresponds to a flow-invariant subspace, here arising due to particle-hole symmetry and time-reversal invariance of the PXP Hamiltonian in Eq. (35) [98].

Restricting to the flow-invariant subspace $\phi_i=0$ (with $\mu_z=0$), we plot the flow diagram in θ_1 - θ_2 plane in Fig. 8a. Shown in red colour is the periodic trajectory first identified in Ref. [14]. This trajectory is intimately linked with quantum revivals for the initial Néel state $|\mathbb{Z}_2\rangle$ in Fig. 6a, since this state is represented by the point $(\theta_1, \theta_2)=(\pi/2, 0)$ on the trajectory. We note that the variational description in Fig. 8a is not accurate at long times: the fidelity in the full quantum evolution in Fig. 6a shows a visible decay, which is in contrast with the variational description that implies perfect oscillations. As we mentioned in Sect. 2.2, this discrepancy between the exact quantum evolution and its projection onto the variational manifold can be quantified via quantum leakage in Eq. (14). The leakage measures the instantaneous disagreement between exact dynamics and its projection onto the

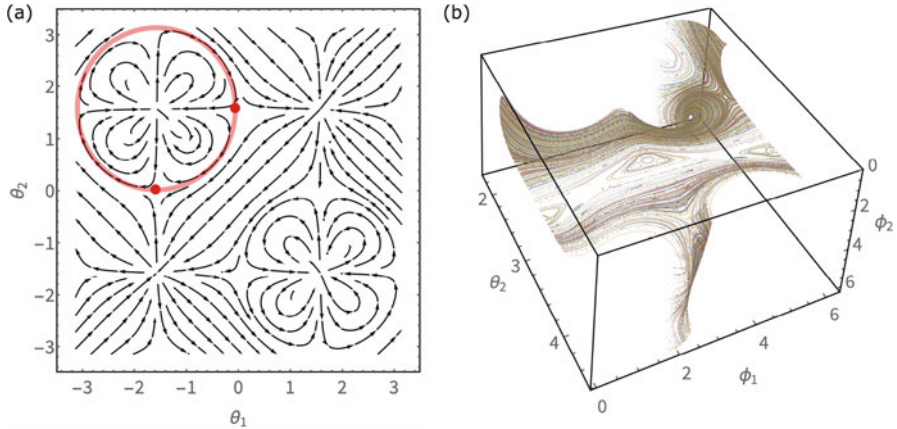


Fig. 8 (a) Flow diagram obtained from the variational ansatz with two degrees of freedom reveals an unstable periodic trajectory (red line), which is responsible for the fidelity revivals from the period-2 density wave state in the quantum case [14]. The periodic trajectory passes through the Néel states, $|\mathbb{Z}_2\rangle$ and $|\mathbb{Z}'\rangle$, shown by red dots and avoids the polarised state, $|0\rangle \equiv |\circ\circ\circ\dots\rangle$, located at $(0, 0)$. As shown in Ref. [14], quantum leakage outside the variational manifold is minimised in the vicinity of the periodic orbit, thus explaining the relevance of this trajectory in the fully quantum dynamics. (b) In the presence of the chemical potential $\mu_z \neq 0$, the dynamical system develops mixed phase space containing large regular regions, as shown in Ref. [98]. The plot shows the associated Poincaré section for $\mu_z = 0.325$ at fixed $(\theta_1^* = 1.25\pi, \dot{\theta}_1 < 0)$

variational manifold. Remarkably, the periodic trajectory is located entirely in the low leakage region [14], thus providing *a posteriori* justification for the coherent quantum dynamics when the system is prepared in $|\mathbb{Z}_2\rangle$ state.

Two-dimensional phase space, however, is special as it precludes chaos. Dynamical systems with phase spaces higher than two-dimensional are known to display both classical chaos as well as regions of stable motion—the so-called Kolmogorov–Arnold–Moser (KAM) tori [122]. These features are prominent in Fig. 8b that shows the Poincaré section of the dynamical system in Eq. (42) when the chemical potential is present ($\mu_z = 0.325$) and the variables ϕ_i cannot be fixed to zero. To obtain such a graph, we follow the standard recipe: we choose some value for θ_1 and follow the successive intersections of the flow with the chosen section. This produces a discrete mapping known as the Poincaré map—this maps a given point $(\theta_1^*, \phi_1, \theta_2, \phi_2)$ on the chosen hyperplane to a position $(\theta_1^*, \phi_1', \theta_2', \phi_2')$, where the trajectory intersects this plane again. Periodic trajectories correspond to stationary points of the Poincaré map, while a chaotic system returns to the same plane at a location that is generally far away from the previous encounter. This procedure for evaluating the Poincaré sections can be conveniently implemented, e.g., in Mathematica using the built-in `NDSolve` routine.

Figure 8b illustrates a typical example of *mixed phase space* [52]: there exist (in general, multiple) KAM tori with stable periodic orbits in their centres, surrounded by the chaotic sea. Energy conservation results in complicated surfaces in the space $(\phi_1, \theta_2, \phi_2)$ that cannot be globally projected. Therefore, the figure shows a small

part of the Poincaré section in the vicinity of the stationary point, $(\phi_1, \theta_2) \approx (2.92, 2.98)$, corresponding to a stable periodic trajectory [98]. This periodic trajectory is surrounded by circle-shaped contours that are the intersections of KAM tori by our section plane. Unlike the pure PXP model ($\mu_z=0$) where the periodic orbit passes through a product state ($|\mathbb{Z}_2\rangle$), in this case, the states on the trajectory are entangled in general (though entanglement is necessarily small, since the orbit passes through MPS states of low bond dimension).

5.1 Discussion: Benefits and Pitfalls of TDVP

To summarise, the TDVP discussed above allows to obtain classical equations of motion and analyse parallels between the dynamics of a quantum system and its projection onto the variational manifold. The presence of (stable or unstable) classical periodic trajectories with small quantum leakage leads to slow relaxation in the full many-body dynamics.

There are several useful insights we glean from TDVP. (i) The KAM tori inform us about special features of quantum dynamics in the underlying model. For example, when dynamics is initialised precisely on the periodic orbit, there is slower relaxation of local observables and slower entanglement growth in quench dynamics [98]. Furthermore, initialising the dynamics in the centre of a big KAM torus results in slower entanglement growth. This highlights the role of quantum leakage in determining which of the trajectories give rise to slow thermalisation in exact quantum dynamics. (ii) Revivals in the PXP model are robust to various deformations of the Hamiltonian, provided that in the course of the deformation one follows the periodic trajectory that is influenced by the deformation [98]. (iii) The TDVP approach has also been fruitful in obtaining a more complete understanding of the PXP dynamics in manifolds with more degrees of freedom. In particular, this approach can describe the dynamics from the period-3 density wave state, $|\mathbb{Z}_3\rangle$, which also shows revivals of fidelity, as seen in Fig. 6a. The corresponding variational ansatz for this state includes three angles θ_i , $i=1, 2, 3$, which parametrise the state of three atoms within a unit cell (the corresponding ϕ_i once again can be fixed to zero in the flow-invariant subspace). While the equations of motion are considerably more complicated than ones in Eq. (42), their numerical solution also generally gives rise to mixed phase space, similar to Fig. 8b.

At the same time, one must beware some caveats to the TDVP approach. First, the variational manifold is not unique—one can always enlarge the MPS ansatz by including additional parameters that build in longer-range entanglement. This leads to potential ambiguities in the definition of the trajectory. While some TDVP ansätze may find unstable periodic trajectories, more generic embeddings may result in mixed phase space. Second, at present, there is no understanding under which conditions the quantum leakage is small. Hence, even if one recovers a large number of periodic trajectories, they may all have strong leakage and not lead to any revivals in quantum dynamics, e.g., as in the chaotic Ising model in Ref. [98].

Finally, many questions remain about quantum-classical correspondence in TDVP as a function of bond dimension χ . Complementing the study of weak-ergodicity breaking at small χ , TDVP has been used to study thermalisation at larger χ . In particular, Ref. [123] demonstrated that physical properties saturate in the case of the transverse field Ising model for bond dimensions $\chi > 2$. In addition, Ref. [124] studied the spectrum of Lyapunov exponents in the case of a high bond dimension TDVP. The work in Ref. [98] shows that in the case of low bond dimensions one may encounter non-chaotic behaviour in the TDVP dynamics, limiting the utility of the Lyapunov exponent. On the one hand, one may expect that mixed phase space does not persist for large bond dimensions, as increasing χ increases the dimension of the phase space where the TDVP dynamics occurs, making it more susceptible to chaos. On the other hand, for local Hamiltonians, the Lieb–Robinson bound [125] suggests that a small bond dimension is sufficient to capture quantum dynamics at early times. Thus, it is important to understand how the mixed phase space evolves upon including additional MPS parameters that describe longer-range entanglement.

6 Quantum Many-Body Scars

In Sect. 3, we discussed different mechanisms that lead to the emergence of non-thermal eigenstates in highly excited energy spectra of non-integrable systems. In the past few years, the name *quantum many-body scars* has been widely adopted as an umbrella term for such non-thermal eigenstates, regardless of the underlying mechanism of ergodicity breaking. In this section, we explain in more detail the reasons why this name was adopted by Turner et al. [13]. The inspiration was the PXP model and its many parallels with a single particle confined to a stadium-shaped billiard. In the latter case, the particle’s eigenfunctions can concentrate around certain periodic orbits in the limit $\hbar \rightarrow 0$, a phenomenon Heller [15] called quantum scarring in the early 1980s. In the remainder of this section, we discuss the semiclassical aspects of the PXP physics that make it the many-body analogue of quantum scarring.

6.1 Scars in Few-Body Systems

What can we learn about the behaviour of a quantum system by looking at its classical counterpart? The Bohr–Sommerfeld quantisation demonstrates that classical integrable systems, such as the harmonic oscillator or hydrogen atom, have rather special quantum spectra and eigenstates. For classically chaotic systems, e.g., the Bunimovich stadium, the traditional quantisation methods do not work. Typically, quantum counterparts of classically chaotic systems display level repulsion in their spectrum and their eigenstates look random. However, short unstable periodic orbits may leave a strong imprint on the system’s quantum dynamics

and eigenstate properties—this influence of classical periodic orbits is known as “quantum scarring” [15]:

Definition (From Ref. [126]) A quantum eigenstate of a classically chaotic system has a “scar” of a periodic orbit if its density on the classical invariant manifolds near the periodic orbit is enhanced over the statistically expected density.

Utilising this definition, one can detect scars by visualising the wave function probability density, which can be seen to concentrate around certain periodic classical orbits, e.g., the diamond-shaped “bow tie” orbit in the Bunimovich stadium [126]. Moreover, scars leave an imprint on the dynamics: when a wave packet is launched in the vicinity of an unstable periodic orbit, it will tend to cluster around the orbit at later times, displaying a larger return probability than a wave packet launched elsewhere in the phase space. Furthermore, such a wave packet can be expanded over a small number of eigenstates that have approximately similar energy spacing, in contrast to an arbitrary wave packet. Much of this phenomenology was originally acquired through numerical solutions of quantum billiard problems since the latter are non-integrable and do not admit analytical solution.

Nevertheless, rigorous proofs [127–129] have established that individual eigenstates of the billiard are “almost always” ergodic since the phase space area affected by scarring vanishes in the semiclassical limit $\hbar \rightarrow 0$, shrinking around the periodic orbit. These proofs of scarring have been based on constructions of *approximate* eigenstates or “quasimodes”, i.e., special states designed to be strongly localised around a classical periodic orbit. For example, in the Bunimovich stadium, some of the quasimodes have the form $\psi(x, y) = \phi(x) \sin(n\pi y)$, i.e., they represent a standing wave in one direction with a suitably chosen envelope function in the other direction. By carefully controlling the density of states, it was possible to show that there exist eigenstates with an anomalously high overlap with a small number of quasimodes, hence “inheriting” their scarring properties [126].

Although the above suggests that scars are “rare” anomalies, they do have physical significance. For example, scars provide an important counterexample to the intuitive expectation that every eigenstate of a classically chaotic system should locally look like a random superposition of plane waves [130]. Furthermore, also counterintuitively, a scarred quantum system appears more “regular” than its classical counterpart since in the latter case there is no enhancement of density along the periodic orbit in the long-time limit. Finally, scars play a role in many experiments, including microwave cavities [131], semiconductor quantum wells [132], and the hydrogen atom in a magnetic field [133].

6.2 Quasimodes in the PXP Model

In few-body systems, the understanding of quantum scars rests on two pillars: the existence of unstable classical periodic orbits and the quasimodes that leave a scar

upon some of the eigenfunctions. The main difficulty in passing to the many-body case is how to give precise meaning to this terminology: the physics now takes place in the many-particle Hilbert space, precluding “easy” visualisation of the classical trajectory. In Sects. 2.2 and 5, we introduced one way of defining the classical trajectory via TDVP, wherein many-body dynamics is projected onto a restricted space of MPS states. This approach systematically builds in entanglement, controlled by the MPS bond dimension; thus it forms a natural framework to define the semiclassical limit of the PXP model that does have an obvious $\hbar \rightarrow 0$ limit.

The application of the TDVP method to the PXP model successfully captures the revivals following quenches from specific product states; hence, it is natural to suggest that this approach defines an effective “semiclassical” description of the quantum dynamics and holds the same relation with the exact PXP model as expected from the Bohr correspondence principle. However, in order to complete the analogy with single-particle scars, it is necessary to show that this limit also gives rise to quasimodes that, in turn, accurately approximate the quantum eigenstates of the PXP model.

In Ref. [134], this correspondence was achieved by constructing a subspace \mathcal{K} , which is fully symmetric over permutations within each of the two sublattices, comprising even and odd sites in the PXP chain—see Box 8. This forms a mean-field approximation for the PXP model wherein one describes the dynamics in terms of numbers of excitations on even or odd sites while discarding any detailed local information (such as the precise positions of excitations within a sublattice). This approximation reduces the exponential complexity of the many-body problem down to polynomial in system size, and the quasimodes are obtained by simply diagonalising the Hamiltonian projected into the symmetric subspace, $\mathcal{K}H_{\text{PXP}}\mathcal{K}$. As can be seen in Fig. 9a, these quasimodes are excellent approximations to the exact eigenstates of the PXP model; in particular, they capture the $L+1$ non-thermal eigenstates with the largest projection on $|\mathbb{Z}_2\rangle$ state in Fig. 6a.

It turns out that the symmetric subspace \mathcal{K} has an intimate relationship with the subspace \mathcal{M} of MPS states discussed in Sect. 5, which can be viewed as a Gutzwiller projection of spin coherent states with a unit cell of two sites [14]. The states in \mathcal{M} are parametrised by two angles that represent probabilities for a site of each sublattice to hold an excitation, while \mathcal{K} consists of states with definite occupation numbers for each sublattice. In this sense, there is a direct relationship between the two subspaces, reminiscent of the relationship between canonical and grand canonical ensembles in statistical mechanics. More formally, it can be proven that the linear span of \mathcal{M} is equal to the symmetric subspace \mathcal{K} , for every fixed system size L [134]. This implies that the dynamics within \mathcal{K} necessarily includes all quantum fluctuations on top of the equations of motion in Eq. (42).

The correspondence between the classical system \mathcal{M} and the quantum system in its linear span (\mathcal{K}) finally allows us to view the quasimodes $|\psi\rangle \in \mathcal{K}$ as wave functions $\psi(\theta, \phi)$:

$$\psi(\theta, \phi) = \langle \Psi(\theta, \phi) | S_\mu^{-1/2} | \psi \rangle. \quad (43)$$

Here $\Psi(\theta, \phi) \in \mathcal{M}$ is the MPS state parametrised by Eq. (41), and S_μ is the frame operator [134]. This operator is needed because we need to equip the classical state space with an integration measure μ in order to have a well-defined quantisation. In the more familiar manifolds of quantum states, such as spin coherent states [135] or unconstrained MPS [136], the measure μ is simply given by the Haar measure for a transitive group action. However, for the subspace \mathcal{K} with angles θ_i, ϕ_i having 2-site periodicity, the measure is non-trivial, and one must use the frame operator.

Using the above correspondence Eq. (43), the real part of the quasimode wave functions is plotted in Fig. 9b,c. For one of the top-band quasimodes near the middle of the spectrum (denoted by a cross in Fig. 9a), we observe enhanced concentration around the $|\mathbb{Z}_2\rangle$ classical trajectory (shown by the black line in Fig. 9b). This behaviour is strikingly reminiscent of wave function scarring in quantum billiards. In particular, following the classical trajectory, the phase of the wave function winds, and integrality of this winding number leads to the quasimodes' approximately equal spacing in energy. We recognise this behaviour from quantisation of regular trajectories [52]: in the old quantum theory, this underpins Sommerfeld–Wilson quantisation and leads to the de Broglie standing-wave condition for the Bohr

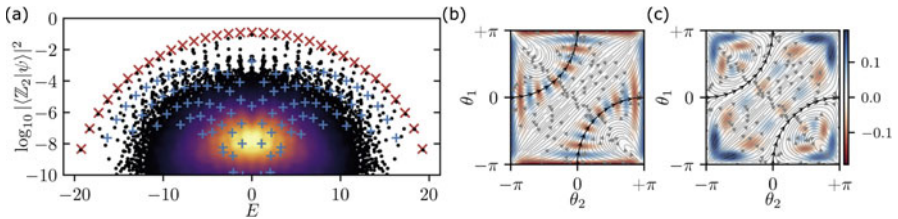


Fig. 9 (a) Scatter plot showing energies of all eigenstates of the PXP model vs. their overlap with $|\mathbb{Z}_2\rangle$ state. Red crosses denote top-band quasimodes, and blue pluses are the remaining quasimodes. Both of types of quasimodes are obtained by projecting the PXP model into the symmetric subspace \mathcal{K} defined in the text. Colour indicates the density of data points. (b,c) Viewing a selected top-band (b) and non-top-band (c) quasimode as wave functions over θ_1 and θ_2 for $L=128$. Colour scale represents the real part of the wave function. Top-band quasimodes concentrate around the classical periodic orbit (black line), displaying quantum scarring. The other quasimodes avoid this periodic trajectory and concentrate around the corners of the square. Note that the $|\mathbb{Z}_2\rangle$ and its translated partner correspond to $(\theta_1, \theta_2) = (\pi, 0)$ and $(0, \pi)$ in the notation of this figure. Due to the MPS parametrisation, the wave function in (b) visibly spreads out towards the boundary and becomes completely delocalised at the edges, $\theta_i = \pm\pi$, where the points are indistinguishable in the transverse direction. Panels reproduced from Ref. [134] under a Creative Commons licence CC BY 4.0

model. These features are inherited by the exact scarred eigenstates given their strong overlap with the quasimodes. In contrast, Fig. 9c shows one of quasimodes deeper in the bulk of the spectrum. Such quasimodes are typically found around the orbits connecting corners of the manifold, where quantum leakage is large (see Sect. 5). It is expected that these quasimodes would not survive the “injection” into the full Hilbert space, i.e., while the top-band quasimodes accurately approximate the true eigenstates of the full PXP model, this is not the case for the other quasimodes.

Box 10 : Mean-Field Approximation for the PXP Model

The essence of mean-field theory is the erasure of unnecessary local information. For example, to describe a free paramagnet, which is obtained by dropping the projectors in the PXP Hamiltonian in Eq. (35), we only need to know the *total number* of excitations relative to some reference state, not their precise positions in the lattice. This idea has been generalised to describe the reviving dynamics in the PXP model where the important information is the number of excitations on each of the two *sublattices*, comprising even and odd sites in the chain [134]. Such an approach is reminiscent of the symmetric subspaces in studies of fully connected models [137, 138]. However, the key difference is that in the PXP model the permutation symmetry is broken to the sublattice level, and many of the permutation shuffles violate the constraint and therefore have to be excluded, which makes the analysis more involved.

To illustrate the approach, the symmetric subspace \mathcal{K} is defined by forming a set of equivalence classes (n_1, n_2) , where integers n_1, n_2 label the number of excitations on the two sublattices, encompassing the odd and even sites, respectively. Elements in these classes are equivalent under the action of the product of two symmetric groups $S_{L/2}$ that “shuffle” the sites in each sublattice. For example, states $|\bullet\bullet\bullet\bullet\bullet\bullet\bullet\bullet\rangle$ and $|\bullet\bullet\bullet\bullet\bullet\bullet\bullet\bullet\rangle$ belong to the same class as they both have two excitations in the first sublattice and one in the second. An example of the construction of \mathcal{K} for the PXP model of size $L=8$ is presented in Fig. 10. The orthonormal basis for \mathcal{K} is built from symmetric combinations of members of each class, $|(n_1, n_2)\rangle \propto \sum_{x \in (n_1, n_2)} |x\rangle$, where the sum runs over all product states $|x\rangle$ that are members of the class (n_1, n_2) . Class sizes and matrix elements of the PXP Hamiltonian projected to \mathcal{K} can be calculated using combinatorics [134], allowing for a highly efficient description of the PXP model and its dynamical properties.

(continued)

Box 10 (continued)

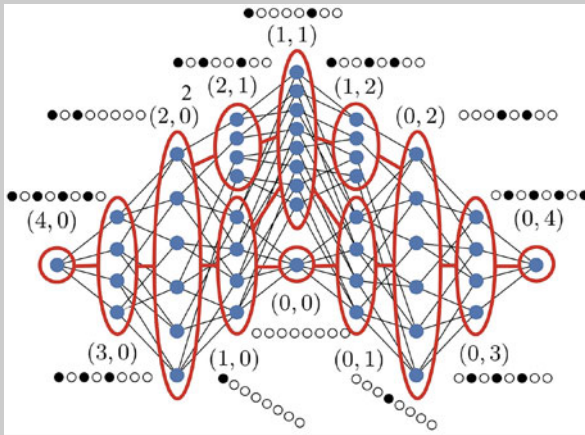


Fig. 10 Construction of the symmetric subspace \mathcal{K} in the PXP model for $L=8$ spins. Each blue dot represents an allowed product state compatible with the constraint. The states are grouped into equivalence classes, denoted by ellipses. Each class is labelled by a representative state, e.g., the class (0,3) contains the representative state $\circ\circ\circ\bullet\circ\circ\circ$ and all other obtained by permuting sites in each of the two sublattices. Reproduced from Ref. [134] under a Creative Commons licence CC BY 4.0

6.3 Discussion: Scars or Not?

The results presented in this section and Sect. 5 provide justification for referring to the non-thermal eigenstates in the PXP model as a many-body analogue of single-particle scars. One of the crucial ingredients that allows to make such a connection is the quantum-classical correspondence. At the same time, in Sect. 3, we introduced a number of other models that also feature non-thermal eigenstates, quite reminiscent of those in the PXP model. Here we briefly discuss the main similarities and differences of these models.

The PXP model, with its generalisations to higher spins [14] and clock models [120], is broadly similar to models whose non-thermal eigenstates form an SGA. The main difference is that the SGA in the PXP model is only *approximate*, and the subspace has weak residual couplings to the thermal bulk. In addition, the PXP model also realises an *approximate* Krylov subspace built upon $|\mathbb{Z}_2\rangle$ root state. The Krylov subspace becomes exact when generated by H^+ in Eq. (40). Finally, a single PXP eigenstate at zero energy in the middle of the spectrum can be viewed as projector-embedded AKLT ground state [87]. While similar connections between

scarring mechanisms may be anticipated in other models mentioned in Sect. 3, their demonstration remains an open problem.

In particular, the existence of classical periodic trajectories underlying quantum revivals in the PXP model calls for exploration of semiclassical dynamics in other scarred models discussed in Sect. 3. For example, in the spin-1 XY model [53] in Eq. (20), the initial state with perfect revivals was identified to be

$$|\psi_0\rangle = \bigotimes_j \frac{1}{\sqrt{2}} \left(|1\rangle_j - (-1)^j |-1\rangle_j \right). \quad (44)$$

This state is a superposition of the scar tower states $|\mathcal{S}_n^{XY}\rangle$ in Eq. (21), and it can be prepared as the ground state of the Hamiltonian $H = Q^\dagger + Q \propto J^x$. Since these states are equally spaced in energy with spacing $2h$ [see Eq. (20)], time evolving $|\psi_0\rangle$ gives perfect revivals with frequency $2h$. For the AKLT tower of scars, such “rotations” in the space of scar states do not seem to produce a very simple initial state. However, as shown in Ref. [58], the AKLT scar tower can be compressed into a state with finite MPS bond dimension (e.g., bond dimension equal to 8 in a system with periodic boundary conditions).

We expect that similar constructions of reviving initial states can be performed for other models with an SGA using the properties of Q^\dagger . By contrast, for non-thermal eigenstates produced via the projector-based embedding scheme, we generally do not expect underlying periodic trajectories. Similarly, models with Krylov fragmentation (Sect. 3.2) are not guaranteed to have revivals, even if the root state $|\psi_0\rangle$ is experimentally preparable. This is because general tridiagonal matrices do not support revivals, unless their matrix elements are tuned to special values [139]. Thus, the study of classical periodic trajectories in a broader family of models could be helpful as a finer classification scheme for models displaying weak ETH violation in their eigenstate properties, in particular as a way of distinguishing many-body scarring from more generic embeddings of non-thermal eigenstates.

7 Weak Ergodicity Breaking in Experiment

The experiments that opened the door to the investigation of weak ergodicity breaking discussed above were performed using quantum simulators based on Rydberg atom arrays [12, 140]. Here, we provide a brief overview of these experiments, focusing on the work by Bernien et al. [12] that reported the first experimental observation of quantum many-body scarring. Following this, we discuss more recent experiments realising the tilted Fermi–Hubbard in optical lattices, where signatures of non-ergodicity due to Hilbert space fragmentation have been detected [21].

7.1 Rydberg Atoms

An individual Rydberg atom may be viewed as an effective two-level system, where the two states $|\circ\rangle$, $|\bullet\rangle$ correspond, respectively, to an atom in the ground state and an atom in the so-called Rydberg state, i.e., with a highly excited electron in the outer shell, see Fig. 11a. The state of an individual Rydberg atom may be manipulated via coupling to circularly polarised radiation that causes Rabi oscillations with frequency Ω . The relative detuning Δ of the Rydberg state off-resonance can also be controlled, leading to an effective single-atom Rydberg Hamiltonian $H = (\Omega/2)\sigma^x + \Delta\hat{n}$, where the operator $\sigma^x = |\circ\rangle\langle\bullet| + |\bullet\rangle\langle\circ|$ is the Pauli matrix that describes Rabi oscillations, and $\hat{n} = |\bullet\rangle\langle\bullet|$ measures the population of the Rydberg state.

Atoms in Rydberg states interact via dipole–dipole interactions; thus the many-body Hamiltonian describing this system is given by

$$H = \frac{\Omega}{2} \sum_i \sigma_i^x - \Delta \sum_i \hat{n}_i + \sum_{i<j} V_{ij} \hat{n}_i \hat{n}_j, \quad (45)$$

where $V_{i,j} = 1/r_{ij}^6$ and r_{ij} is the distance between the atoms. By tuning r_{ij} , one can achieve the regime of the Rydberg blockade, as illustrated in Fig. 11a. In this regime, the shift of an energy level with two excited Rydberg atoms is so strong that the state $|\bullet\bullet\rangle$ is off-resonant and cannot be reached from the ground state. Rydberg blockades with varying radii were demonstrated experimentally [140, 141] via the frequency renormalisation of the Rabi oscillations. Coherent dynamics was observed in small arrays of Rydberg atoms in both 1D and 2D when the blockade radius exceeded the linear size of the chain.

More recent experiments [12] have studied Rydberg arrays in a qualitatively different regime with a relatively *short* radius of the Rydberg blockade. In particular, long Rydberg chains, containing up to 51 atoms with the nearest-neighbour blockade, were quenched from a period-2 density wave initial state, $|\mathbb{Z}_2\rangle \equiv |\bullet\circ\bullet\circ\dots\rangle$, corresponding to the state with the maximal possible number of Rydberg excitations allowed by the blockade. The dynamics of the domain-wall density, where domain walls are defined as adjacent $|\circ\circ\rangle$ or $|\bullet\bullet\rangle$ configurations (the latter is excluded in the regime of perfect blockade), revealed long-time oscillations, similar to Fig. 6a.

The density revivals observed in Ref. [12] were challenging to explain theoretically, for the following reasons. First, the density wave state $|\mathbb{Z}_2\rangle$ forms an infinite-temperature ensemble for the atoms in the Rydberg blockade; thus it should display fast equilibration. Indeed, for other initial states at infinite temperature, such as $|0\rangle \equiv |\circ\circ\circ\dots\rangle$, the domain-wall density was found to relax quickly to the steady-state value. Second, the persistence of crystalline order far from equilibrium was surprising because the Rydberg atom system was not known to have any conserved quantities other than the total energy. Finally, the frequency of domain-wall density oscillations did not coincide with $\sqrt{2}\Omega$, which would be naïvely expected for collective oscillations of two atoms in the Rydberg blockade regime, signalling

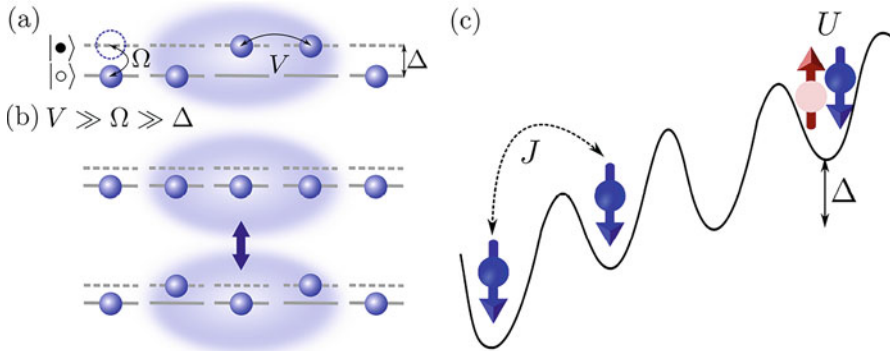


Fig. 11 (a) Rydberg atom as a two-level system, where the empty circle corresponds to the ground state and the filled circle denotes the excited Rydberg state. The Rabi frequency is denoted as Ω , and the detuning of the $|\bullet\rangle$ state from resonance is Δ . The Rydberg blockade (shaded) leads to a shift of the energy level where both atoms are in the $|\bullet\rangle$ state, bringing it strongly off-resonance. (b) When the Rydberg blockade is strong ($V \gg \Omega \gg \Delta$), excitations of neighbouring atoms are energetically suppressed. In this limit, the effective model describing the Rydberg atom chain is the PXP model in Eq. (35). (c) Fermi–Hubbard model realised in an optical lattice [21], with nearest-neighbour hopping J and on-site interaction U . Tilt of the lattice is controlled by the parameter Δ (with a different meaning from the detuning Δ in (a,b) and Eq. (45)!)

that many-body effects played an important role. As we have already seen, these puzzles are now understood based on the studies of the PXP model summarised in Sect. 4. The PXP model arises as the effective model for the Hamiltonian in Eq. (45) when $V_{i,i}$ is infinite and interactions beyond nearest neighbour are set to zero [91]. An important step towards the explanation of the observed oscillations was made by identifying the non-thermalising eigenstates in the spectrum of the PXP model in Fig. 6b. The core phenomenology of the PXP model—the small number of ETH-violating eigenstates within the thermalising spectrum and the presence of many-body revivals and slow relaxation in quenches from specific initial states—led to the identification of the phenomenon in Ref. [12] with a many-body analogue of quantum scarring [15].

We note that since the experiment in Ref. [12], there have been further advances in similar Rydberg platforms. In Ref. [142], it was shown that coherent revivals associated with quantum many-body scars can be enhanced via periodic driving, which generates a robust subharmonic response akin to discrete-time-crystalline order [143]. The driving is realised by modulation of the detuning term, $\Delta(t) = \Delta_0 + \Delta_m \cos(\omega_m t)$, and the enhancement is found in the non-perturbative regime of $\Delta_m, \Delta_0, \omega_m \sim \Omega$. It was found that such time-dependent detuning can lead to a five-fold increase of scar lifetime compared to the fixed-detuning case [142]. Notably, parametric driving not only delays thermalisation, but also alters the actual trajectory being stabilised, which can be used to effectively “steer” complex dynamics in many-body systems [144]. This opens the door to robust creation and control of complex entangled states in the exponentially large Hilbert spaces of many-body

systems, with intriguing potential applications in areas such as quantum metrology. Other fundamental phenomena recently realised in the same Rydberg platform include dynamical phase transitions and Kibble–Zurek scaling [145] and topological spin liquids [146] (see also Ref. [147] for a realisation in superconducting qubits).

7.2 Tilted Optical Lattices

Another platform for probing weak ergodicity breaking are ultracold atoms in tilted optical lattices, which realise the 1D Fermi–Hubbard model [21]:

$$H = -J \sum_{j, \sigma=\uparrow, \downarrow} \hat{c}_{j, \sigma}^\dagger \hat{c}_{j+1, \sigma} + \text{h.c.} + \Delta \sum_{j, \sigma} j \hat{n}_{j, \sigma} + U \sum_j \hat{n}_j \uparrow \hat{n}_j \downarrow, \quad (46)$$

where $\hat{c}_{j, \sigma}^\dagger$ denotes the usual electron creation operator on site j with spin projection σ , $\hat{n}_{j, \sigma} \equiv \hat{c}_{j, \sigma}^\dagger \hat{c}_{j, \sigma}$, and J and U are the hopping and on-site interaction terms, respectively. Compared to the standard Hubbard model, Eq. (46) includes the tilt potential Δ , which has the form of a dipole term, $\sim j \hat{n}_j$.

The experimental setup in Ref. [21] consists of a degenerate Fermi gas of ^{40}K atoms that is prepared in an equal mixture of two spin components. The atoms are loaded into a 3D optical lattice from which 1D chains are isolated along x direction with the length of about 290 lattice sites. The on-site interaction strength U is controlled by a Feshbach resonance, and a magnetic field gradient is used to create the tilt Δ (approximately independent of spin). We note, however, that linear potentials similar to the tilt one in Eq. (46) can also be realised in other platforms such as trapped ions [148] and superconducting qubits [149], where signatures of strong ergodicity breaking have been recently observed and attributed to “Stark many-body localisation” [76, 77].

The model in Eq. (46) is a natural setting for exploring Hilbert space fragmentation. Ignoring the spin degree of freedom, in the limit of large tilt, $\Delta \gg U, J$, the leading-order off-diagonal term [72] is precisely the pair-hopping Hamiltonian in Eq. (24). With spin included, the effective Hamiltonian in the limit of large tilt (at third order) comprises an off-diagonal term [21]

$$\hat{T}_3 = \sum_{i, \sigma} \hat{c}_{i, \sigma} \hat{c}_{i+1, \sigma}^\dagger \hat{c}_{i+1, \bar{\sigma}}^\dagger \hat{c}_{i+2, \bar{\sigma}} + \text{h.c.}, \quad (47)$$

whose strength is proportional to $J^{(3)} = J^2 U / \Delta^2$ ($\bar{\sigma}$ denotes the opposite spin of σ). At the same order, the effective Hamiltonian also contains another off-diagonal term, $\propto 2J^{(3)} \hat{T}_{XY}$, where $\hat{T}_{XY} = \sum_{i, \sigma} \hat{c}_{i, \bar{\sigma}}^\dagger \hat{c}_{i+1, \bar{\sigma}} \hat{c}_{i+1, \sigma}^\dagger \hat{c}_{i, \sigma}$, as well as two diagonal terms, $U \left(1 - \frac{4J^2}{\Delta^2}\right) \sum_i \hat{n}_{i, \uparrow} \hat{n}_{i, \downarrow}$ and $2J^{(3)} \sum_{i, \sigma} \hat{n}_{i, \sigma} \hat{n}_{i+1, \bar{\sigma}}$.

The effective model in Eq. (47) conserves the dipole moment, $\sum_{i,\sigma} i\hat{n}_{i,\sigma}$. The fact that the hopping rate $J^{(3)}$ is proportional to the interaction strength highlights that interactions are necessary to generate dipole-conserving processes [21]. For initial states that are products of singlons, the connected dynamical sector \mathcal{S} only represents a vanishing fraction of the whole (effective) symmetry sector, thus severely restricting the dynamics of the system. The dipole-conserving processes in general involve the generation of doublons. This is, however, penalised by the Fermi–Hubbard on-site interaction, and therefore, we expect a slowing down of the dipole-conserving dynamics. The additional spin exchange \hat{T}_{XY} increases the connectivity but cannot fully connect the whole dipole symmetry sector, and the system remains fragmented.

In experiment, ergodicity breaking was probed by quenching the system from an initial state chosen to be a charge-density wave of singlons on even sites (filling factor $\nu=1/2$), which is prepared using a bichromatic optical superlattice. The initial state can be described as an incoherent mixture of site-localised particles with random spin configuration. The subsequent evolution is monitored by extracting the spin-resolved imbalance $I^\sigma = (N_e^\sigma - N_o^\sigma)/N^\sigma$, where $N_{e(o)}^\sigma$ denotes the total number of spin- σ atoms on even (odd) sites and $N^\sigma = N_e^\sigma + N_o^\sigma$. A non-zero steady-state imbalance signals a memory of the initial state, where $I^\sigma(t=0) = 1$. In the regime $\Delta \gg J, |U|$, the effective Hamiltonian is dipole-conserving up to third order in J/Δ , which was argued [21] to be responsible for the non-ergodic behaviour of imbalance I , which did not decay to its thermal value at moderate times. At much later times, higher-order processes, beyond the ones in Eq. (47), are expected to reconnect the different Krylov sectors.

Tilted Fermi–Hubbard model is a promising platform to investigate a range of ergodicity breaking beyond fragmentation. Although experimentally challenging due to finite evolution times, it would be interesting to reconcile the phenomenon of Stark MBL and Hilbert space fragmentation, by studying the impact of weak disorder or residual harmonic confinement on the long-time dynamics. Moreover, it would be interesting to explore the connection between lattice gauge theories and Hilbert space fragmentation, which could be addressed experimentally in a similar system [150]. Finally, recent work [151] has proposed that quantum many-body scars could also be realised in the same model, albeit at a different filling factor compared to Ref. [21]—see Box 9.

Box 11 : Proposal for Scars in the Fermi–Hubbard Model

In the regime $\Delta \approx U \gg J$, the tilted Fermi–Hubbard model in Eq. (46) was argued to host many-body scars at filling factor $\nu=1$ [151]. In this case, the sum of the dipole moment and the number of doublons are effectively

(continued)

Box 11 (continued)

conserved, giving rise to the effective Hamiltonian

$$H_{\text{eff}} = -J \sum_{j,\sigma} \hat{c}_{j,\sigma}^\dagger \hat{c}_{j+1,\sigma} \hat{n}_{j,\bar{\sigma}} (1 - \hat{n}_{j+1,\bar{\sigma}}) + \text{h.c.}, \quad (48)$$

where hopping to the left (which decreases the total dipole moment by 1) is only allowed if it increases the number of doublons by the same amount ($\bar{\sigma}$ is opposite spin from σ).

The action of the Hamiltonian in Eq. (48) within the $\nu=1$ sector fragments the Hilbert space beyond the simple conservation of $U+\Delta$. The largest connected component of the Hilbert space is the one containing the state with alternating \uparrow and \downarrow fermions. In such large sectors, after resolving all the symmetries, the model can be shown to be non-integrable [151].

The proposal for many-body scars in the effective Hamiltonian in Eq. (48) is based on the existence of a regular subgraph that has the form of the hypergrid—a Cartesian product of line graphs (in our case, of length 3), i.e., the hypergrid is isomorphic to an adjacency graph of a free spin-1 paramagnet, as illustrated below (Fig. 12).

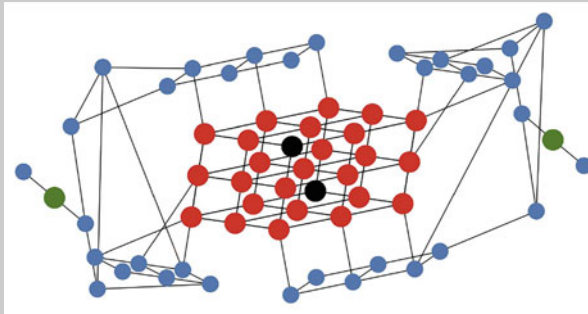


Fig. 12 Adjacency graph of the model in Eq. (48) for $L=6$. Red vertices denote the states belonging to the hypergrid, with the black vertices corresponding to $|-\rangle$, $|+\rangle$ states defined in the text. Green vertices are the isolated states $|\downarrow 2 \uparrow\rangle$, $|\uparrow 2 \downarrow\rangle$ that live on the tails of the graph

The mapping to the hypergrid follows from analysing pairs of sites, which can be in states “ $-$ ” $\equiv (\downarrow\uparrow)$, “ 2 ” $\equiv (\downarrow 0)$ or “ $+$ ” $\equiv (\uparrow\downarrow)$, leading to a three-level system. Note that the configuration $(0\downarrow)$ is omitted, as doublons can only be formed by hopping to the left. Inside the hypergrid, there are two states for which the cell alternates between $-$ and $+$. These are the state $|-\rangle \equiv |-\rangle \equiv |-\rangle \equiv |-\rangle \equiv |-\rangle \equiv |-\rangle$ and its spin-inverted partner,

(continued)

Box 11 (continued)

$|+-\rangle = |+-+--\dots\rangle \equiv |\uparrow\downarrow\downarrow\uparrow\uparrow\downarrow\downarrow\uparrow\dots\rangle$. The states $|+-\rangle$ and $|+--\rangle$ are shown in black colour in Fig. 12. These two states are the only corners of the hypergrid (state with only + and - cells) with no edges going out of it. When the system is initialised in either of these states, it was numerically shown to exhibit persistent oscillations in the quench dynamics and other scarring phenomenology similar to the PXP model discussed in Sect. 4.

8 Conclusions

The goal of this chapter was to present a pedagogical introduction to the new kind of dynamical behaviour in many-body systems—weak ergodicity breaking. While we refrained from giving a formal definition, weak ergodicity breaking was intuitively introduced as a strong dependence of relaxation dynamics on the system’s initial configuration. We contrasted this behaviour against conventional ergodic systems, by showing that certain many-body states can be long-lived and they exhibit parametrically slow relaxation, unlike other initial configurations that quickly reach thermal equilibrium. Many recent studies discussed above, theoretical as well as experimental, have revealed that a number of familiar physical systems do not conform to the expectations of the ETH in its strong form, in that such systems can host non-thermal eigenstates and exhibit long-time coherent dynamics. The common pattern that arises in these diverse physical systems is an emergent non-thermalising subspace, which is dynamically decoupled from the rest of the many-body Hilbert space. Quantum entanglement, in particular, has been the vital tool for identifying such non-thermal subspaces in different models.

At this stage, a complete classification of non-thermal subspaces and their underlying mechanisms is still lacking. In particular, more work is needed to understand the connection between many-body scarring and two broad classes of weak ergodicity breaking phenomena: theories with confinement [152–156] and lattice gauge theories [157–159]. The latter, in particular, the one-dimensional quantum link model—which has recently been realised in a Bose–Hubbard quantum simulator [150]—have intriguing connections with the PXP model [160]. It would be interesting to explore possible connections with PXP in higher dimensions [161], as well as to understand the relation with kinetic constraints, which can generally lead to slow glassy-like dynamics [79, 162–165].

On the theory side, many questions remain about the quantum-classical correspondence in the physical systems discussed above. The TDVP variational approach complements recent efforts in understanding parallels between classical chaos measures, on the one hand, and thermalising quantum dynamics and its underlying transport coefficients on the other hand [123, 124]. While many-body scarred

models are quantum-chaotic, their properties deviate from other chaotic models such as the Sachdev–Ye–Kitaev (SYK) model [166, 167], which has attracted much attention as the fastest scrambler of quantum information [168]. Such deviations could be identified and studied more systematically using the variational approach and its resulting mixed phase portraits, which appear to be a generic feature of local Hamiltonians. One of the outstanding challenges is to bring together this approach to real-time dynamics with approaches that target the many-body eigenstates, possibly using quantum entanglement and other quantum information techniques as a way of linking quantum revivals and eigenstate properties [169].

Finally, there is strong experimental and practical interest in weak ergodicity breaking. For example, many-body scarred revivals provide a mechanism for maintaining coherence, despite the presence of interactions that normally scramble local quantum information. In particular, scars in Rydberg chains have already been utilised for the preparation of specific entangled states [170]. This application made use of quantum control based on the variational TDVP approach and its identification of entangled periodic trajectories that simultaneously have small quantum leakage. Thus, scars may have a wider range of applications, for example in protected state transfer on quantum networks or in quantum sensing [171]. Such applications require deeper theoretical understanding of the effects that protect the coherence of scars, as well as the development of general experimental techniques for creating them on demand, e.g., using periodic driving in Rydberg arrays [142], pumping protocols in dipolar Bose gases [172], or by tilting the Fermi–Hubbard model [21].

Acknowledgments I would like to thank my collaborators Kieran Bull, Soonwon Choi, Jean-Yves Desautels, Wen Wei Ho, Ana Hudomal, Mikhail Lukin, Ivar Martin, Hannes Pichler, Nicolas Regnault, Ivana Vasić, and in particular Dmitry Abanin, Alexios Michailidis, Maksym Serbyn and Christopher Turner. Moreover, I am grateful to Maksym Serbyn for designing Fig. 1 and to Alexios Michailidis for help with replotting Fig. 8b. I would also like to acknowledge useful discussions with B. Andrei Bernevig, Paul Fendley, Thomas Iadecola, and Lesik Motrunich. This work has been supported by the Leverhulme Trust Research Leadership Award RL-2019-015.

References

1. I. Bloch, J. Dalibard, S. Nascimbène, Quantum simulations with ultracold quantum gases. *Nature Physics* **8**, 267–276 (2012)
2. I.M. Georgescu, S. Ashhab, F. Nori, Quantum simulation. *Rev. Mod. Phys.* **86**, 153–185 (2014)
3. J.M. Deutsch, Quantum statistical mechanics in a closed system. *Phys. Rev. A* **43**, 2046–2049 (1991)
4. M. Srednicki, Chaos and quantum thermalization. *Phys. Rev. E* **50**, 888–901 (1994)
5. I.V. Gornyi, A.D. Mirlin, D.G. Polyakov, Interacting electrons in disordered wires: Anderson localization and low- t transport. *Phys. Rev. Lett.* **95**, 206603 (2005)
6. D.M. Basko, I.L. Aleiner, B.L. Altshuler, Metal–insulator transition in a weakly interacting many-electron system with localized single-particle states. *Ann. Phys.* **321**, 1126–1205 (2006)

7. A. Pal, D.A. Huse, Many-body localization phase transition. *Phys. Rev. B* **82**, 174411 (2010)
8. P. Calabrese, J. Cardy, Time dependence of correlation functions following a quantum quench. *Phys. Rev. Lett.* **96**, 136801 (2006)
9. M. Žnidarič, T. Prosen, P. Prelovšek, Many-body localization in the Heisenberg XXZ magnet in a random field. *Phys. Rev. B* **77**, 064426 (2008)
10. J.H. Bardarson, F. Pollmann, J.E. Moore, Unbounded growth of entanglement in models of many-body localization. *Phys. Rev. Lett.* **109**, 017202 (2012)
11. M. Serbyn, Z. Papić, D.A. Abanin, Universal slow growth of entanglement in interacting strongly disordered systems. *Phys. Rev. Lett.* **110**, 260601 (2013)
12. H. Bernien, S. Schwartz, A. Keesling, H. Levine, A. Omran, H. Pichler, S. Choi, A.S. Zibrov, M. Endres, M. Greiner, V. Vuletić, M.D. Lukin, Probing many-body dynamics on a 51-atom quantum simulator. *Nature* **551**, 579–584 (2017)
13. C.J. Turner, A.A. Michailidis, D.A. Abanin, M. Serbyn, Z. Papić, Weak ergodicity breaking from quantum many-body scars. *Nature Physics* **14**, 745–749 (2018a)
14. W. W. Ho, S. Choi, H. Pichler, M.D. Lukin, Periodic orbits, entanglement, and quantum many-body scars in constrained models: Matrix product state approach. *Phys. Rev. Lett.* **122**, 040603 (2019)
15. E.J. Heller, Bound-state eigenfunctions of classically chaotic Hamiltonian systems: Scars of periodic orbits. *Phys. Rev. Lett.* **53**, 1515–1518 (1984)
16. S. Moudgalya, S. Rachel, B.A. Bernevig, N. Regnault, Exact excited states of nonintegrable models. *Phys. Rev. B* **98**, 235155 (2018a)
17. S. Moudgalya, N. Regnault, B.A. Bernevig, Entanglement of exact excited states of Affleck-Kennedy-Lieb-Tasaki models: Exact results, many-body scars, and violation of the strong eigenstate thermalization hypothesis. *Phys. Rev. B* **98**, 235156 (2018b)
18. V. Khemani, M. Hermele, R. Nandkishore, Localization from Hilbert space shattering: From theory to physical realizations. *Phys. Rev. B* **101**, 174204 (2020)
19. P. Sala, T. Rakovszky, R. Verresen, M. Knap, F. Pollmann, Ergodicity breaking arising from Hilbert space fragmentation in dipole-conserving Hamiltonians. *Phys. Rev. X* **10**, 011047 (2020)
20. N. Shiraishi, T. Mori, Systematic construction of counterexamples to the eigenstate thermalization hypothesis. *Phys. Rev. Lett.* **119**, 030601 (2017)
21. S. Scherg, T. Kohlert, P. Sala, F. Pollmann, B. Hebbe Madhusudhana, I. Bloch, M. Aidelsburger, Observing non-ergodicity due to kinetic constraints in tilted Fermi-Hubbard chains. *Nature Communications* **12**, 4490 (2021)
22. M. Serbyn, D.A. Abanin, Z. Papić, Quantum many-body scars and weak breaking of ergodicity. *Nature Physics* **17**, 675–685 (2021)
23. R. Nandkishore, D.A. Huse, Many-body localization and thermalization in quantum statistical mechanics. *Annual Review of Condensed Matter Physics* **6**, 15–38 (2015)
24. C. Gogolin, J. Eisert, Equilibration, thermalisation, and the emergence of statistical mechanics in closed quantum systems. *Rep. Prog. Phys.* **79**, 056001 (2016)
25. T. Mori, T.N. Ikeda, E. Kaminishi, M. Ueda, Thermalization and prethermalization in isolated quantum systems: a theoretical overview. *J. Phys. B Atomic Mol. Optic. Phys.* **51**, 112001 (2018)
26. J.P. Garrahan, P. Sollich, C. Toninelli, Kinetically constrained models. *Dynamical Heterogeneities in Glasses, Colloids, and Granular Media*, vol. 150, (Oxford University Press, 2011), pp. 111–137
27. S.C. Morampudi, A. Chandran, C.R. Laumann, Universal entanglement of typical states in constrained systems. *Phys. Rev. Lett.* **124**, 050602 (2020)
28. D.N. Page, Average entropy of a subsystem. *Phys. Rev. Lett.* **71**, 1291–1294 (1993)
29. M. Ueda, Quantum equilibration, thermalization and prethermalization in ultracold atoms. *Nat. Rev. Phys.* **2**, 669–681 (2020)
30. M. Rigol, V. Dunjko, M. Olshanii, Thermalization and its mechanism for generic isolated quantum systems. *Nature* **452**, 854–858 (2008)

31. B. Sutherland, *Beautiful Models: 70 Years of Exactly Solved Quantum Many-body Problems* (World Scientific, 2004)
32. D.A. Abanin, E. Altman, I. Bloch, M. Serbyn, Colloquium: Many-body localization, thermalization, and entanglement. *Rev. Mod. Phys.* **91**, 021001 (2019)
33. D. Pérez-García, F. Verstraete, M.M. Wolf, J.I. Cirac, Matrix product state representations. *Quantum Inf. Comput.* **7**, 401–430 (2007)
34. J. Eisert, M. Cramer, M.B. Plenio, Colloquium: Area laws for the entanglement entropy. *Rev. Mod. Phys.* **82**, 277–306 (2010)
35. F. Verstraete, V. Murg, J.I. Cirac, Matrix product states, projected entangled pair states, and variational renormalization group methods for quantum spin systems. *Adv. Phys.* **57**, 143–224 (2008)
36. I. Affleck, T. Kennedy, E.H. Lieb, H. Tasaki, Rigorous results on valence-bond ground states in antiferromagnets. *Phys. Rev. Lett.* **59**, 799–802 (1987)
37. I. Affleck, T. Kennedy, E.H. Lieb, H. Tasaki, Valence bond ground states in isotropic quantum antiferromagnets. *Commun. Math. Phys.* **115**, 477–528 (1988)
38. F. Verstraete, J.I. Cirac, Matrix product states represent ground states faithfully. *Phys. Rev. B* **73**, 094423 (2006)
39. M.B. Hastings, An area law for one-dimensional quantum systems. *J. Stat. Mech. Theory Exp.* **2007**, P08024 (2007)
40. J. Haegeman, T.J. Osborne, F. Verstraete, Post-matrix product state methods: To tangent space and beyond. *Phys. Rev. B* **88**, 075133 (2013)
41. L. Vanderstraeten, M. Mariën, F. Verstraete, J. Haegeman, Excitations and the tangent space of projected entangled-pair states. *Phys. Rev. B* **92**, 201111 (2015)
42. L. Vanderstraeten, J. Haegeman, F. Verstraete, Tangent-space methods for uniform matrix product states. *SciPost Phys. Lect. Notes*, **7** (2019)
43. D.P. Arovas, A. Auerbach, F.D.M. Haldane, Extended Heisenberg models of antiferromagnetism: Analogies to the fractional quantum Hall effect. *Phys. Rev. Lett.* **60**, 531–534 (1988)
44. S. Moudgalya, E. O’Brien, B.A. Bernevig, P. Fendley, N. Regnault, Large classes of quantum scarred Hamiltonians from matrix product states. *Phys. Rev. B* **102**, 085120 (2020a)
45. D.P. Arovas, Two exact excited states for the $s = 1$ AKLT chain. *Phys. Lett. A* **137**, 431–433 (1989)
46. L. Vanderstraeten, *Tensor Network States and Effective Particles for Low-Dimensional Quantum Spin Systems*, Springer Theses (Springer International Publishing, 2017)
47. P.A.M. Dirac, Note on exchange phenomena in the Thomas atom. *Math. Proc. Camb. Phil. Soc.* **26**, 376–385 (1930)
48. P. Kramer, M. Saraceno, *Geometry of the Time-Dependent Variational Principle in Quantum Mechanics*, Lecture Notes in Physics (Springer Berlin Heidelberg, 1981)
49. J. Haegeman, J.I. Cirac, T.J. Osborne, I. Pižorn, H. Verschelde, F. Verstraete, Time-dependent variational principle for quantum lattices. *Phys. Rev. Lett.* **107**, 070601 (2011)
50. D. Bauernfeind, M. Aichhorn, Time dependent variational principle for tree tensor networks. *SciPost Phys.* **8**, 24 (2020)
51. S.H. Strogatz, *Nonlinear Dynamics and Chaos: With Applications to Physics, Biology, Chemistry, and Engineering*, Studies in Nonlinearity (Avalon Publishing, 2014)
52. M.C. Gutzwiller, *Chaos in classical and quantum mechanics*, Vol. 1 (Springer Science & Business Media, 2013)
53. M. Schecter, T. Iadecola, Weak ergodicity breaking and quantum many-body scars in spin-1 XY magnets. *Phys. Rev. Lett.* **123**, 147201 (2019)
54. T. Iadecola, M. Schecter, Quantum many-body scar states with emergent kinetic constraints and finite-entanglement revivals. *Phys. Rev. B* **101**, 024306 (2020)
55. B. Arno, A.O. Barut, et al., *Dynamical groups and spectrum generating algebras*, Vol. 1 (World Scientific, 1988)

56. C.N. Yang, η pairing and off-diagonal long-range order in a Hubbard model. *Phys. Rev. Lett.* **63**, 2144–2147 (1989)
57. S. Zhang, Pseudospin symmetry and new collective modes of the Hubbard model. *Phys. Rev. Lett.* **65**, 120–122 (1990)
58. D.K. Mark, C.-Ju. Lin, O.I. Motrunich, Unified structure for exact towers of scar states in the Affleck-Kennedy-Lieb-Tasaki and other models. *Phys. Rev. B* **101**, 195131 (2020)
59. O. Vafek, N. Regnault, B.A. Bernevig, Entanglement of Exact Excited Eigenstates of the Hubbard Model in Arbitrary Dimension. *SciPost Phys.* **3**, 043 (2017)
60. D.K. Mark, O.I. Motrunich, η -pairing states as true scars in an extended Hubbard model. *Phys. Rev. B* **102**, 075132 (2020)
61. S. Moudgalya, N. Regnault, B.A. Bernevig, η -pairing in Hubbard models: From spectrum generating algebras to quantum many-body scars. *Phys. Rev. B* **102**, 085140 (2020b)
62. T. Iadecola, M. Žnidarič, Exact localized and ballistic eigenstates in disordered chaotic spin ladders and the Fermi-Hubbard model. *Phys. Rev. Lett.* **123**, 036403 (2019)
63. N. Shibata, N. Yoshioka, H. Katsura, Onsager’s scars in disordered spin chains. *Phys. Rev. Lett.* **124**, 180604 (2020)
64. S. Chattopadhyay, H. Pichler, M.D. Lukin, W.W. Ho, Quantum many-body scars from virtual entangled pairs. *Phys. Rev. B* **101**, 174308 (2020)
65. K. Lee, R. Melendrez, A. Pal, H.J. Changlani, Exact three-colored quantum scars from geometric frustration. *Phys. Rev. B* **101**, 241111 (2020)
66. K. Pakrouski, P.N. Pallegar, F.K. Popov, I.R. Klebanov, Many-body scars as a group invariant sector of Hilbert space. *Phys. Rev. Lett.* **125**, 230602 (2020)
67. J. Ren, C. Liang, C. Fang, Quasi-symmetry groups and many-body scar dynamics. Preprint (2020). arXiv:2007.10380
68. N. O’Dea, F. Burnell, A. Chandran, V. Khemani, From tunnels to towers: Quantum scars from Lie algebras and q -deformed Lie algebras. *Phys. Rev. Res.* **2**, 043305 (2020)
69. B. Buča, J. Tindall, D. Jaksch, Non-stationary coherent quantum many-body dynamics through dissipation. *Nature Communications* **10**, 1730 (2019)
70. J. Tindall, B. Buča, J.R. Coulthard, D. Jaksch, Heating-induced long-range η pairing in the Hubbard model. *Phys. Rev. Lett.* **123**, 030603 (2019)
71. S. Pai, M. Pretko, R.M. Nandkishore, Localization in fractonic random circuits. *Phys. Rev. X* **9**, 021003 (2019)
72. S. Moudgalya, A. Prem, R. Nandkishore, N. Regnault, B.A. Bernevig, Thermalization and its absence within Krylov subspaces of a constrained Hamiltonian. e-prints (2019), arXiv:1910.14048 [cond-mat.str-el]
73. S. Moudgalya, B.A. Bernevig, N. Regnault, Quantum many-body scars in a Landau level on a thin torus. *Phys. Rev. B* **102**, 195150 (2020c)
74. M. Pretko, X. Chen, Y. You, Fracton phases of matter. *Int. J. Modern Phys. A* **35**, 2030003 (2020)
75. G.H. Wannier, Dynamics of band electrons in electric and magnetic fields. *Rev. Mod. Phys.* **34**, 645–655 (1962)
76. M. Schulz, C.A. Hooley, R. Moessner, F. Pollmann, Stark many-body localization. *Phys. Rev. Lett.* **122**, 040606 (2019)
77. E. van Nieuwenburg, Y. Baum, G. Refael, From Bloch oscillations to many-body localization in clean interacting systems. *Proc. Natl. Acad. Sci.* **116**, 9269–9274 (2019)
78. O. Sikora, N. Shannon, F. Pollmann, K. Penc, P. Fulde, Extended quantum $U(1)$ -liquid phase in a three-dimensional quantum dimer model. *Phys. Rev. B* **84**, 115129 (2011)
79. Z. Lan, M. van Horssen, S. Powell, J.P. Garrahan, Quantum slow relaxation and metastability due to dynamical constraints. *Phys. Rev. Lett.* **121**, 040603 (2018)
80. S. Gopalakrishnan, B. Zakirov, Facilitated quantum cellular automata as simple models with non-thermal eigenstates and dynamics. *Quantum Sci. Tech.* **3**, 044004 (2018)
81. A. Hudomal, I. Vasić, N. Regnault, Z. Papić, Quantum scars of bosons with correlated hopping. *Communications Physics* **3**, 99 (2020)

82. H. Zhao, J. Vovrosh, F. Mintert, J. Knolle, Quantum many-body scars in optical lattices. *Phys. Rev. Lett.* **124**, 160604 (2020)
83. F. Thiel, I. Muallem, D. Kessler, E. Barkai, Uncertainty relation between detection probability and energy fluctuations. *Entropy* **23** (2021), 10.3390/e23050595
84. S. Ok, K. Choo, C. Mudry, C. Castelnuovo, C. Chamon, T. Neupert, Topological many-body scar states in dimensions one, two, and three. *Phys. Rev. Res.* **1**, 033144 (2019)
85. J. Wildeboer, A. Seidel, N.S. Srivatsa, A.E.B. Nielsen, O. Erten, Topological quantum many-body scars in quantum dimer models on the Kagome lattice. *Phys. Rev. B* **104**, 121103 (2021). <https://doi.org/10.1103/PhysRevB.104.L121103>
86. F.M. Surace, G. Giudici, M. Dalmonte, Weak-ergodicity-breaking via lattice supersymmetry. *Quantum* **4**, 339 (2020a)
87. N. Shiraishi, Connection between quantum-many-body scars and the Affleck–Kennedy–Lieb–Tasaki model from the viewpoint of embedded Hamiltonians. *J. Stat. Mech. Theory Exp.* **2019**, 083103 (2019)
88. C.M. Langlett, Z.-C. Yang, J. Wildeboer, A.V. Gorshkov, T. Iadecola, S. Xu, Rainbow scars: From area to volume law. *Phys. Rev. B* **105**, L060301 (2022). <https://doi.org/10.1103/PhysRevB.105.L060301>
89. A.Yu. Kitaev, Fault-tolerant quantum computation by anyons. *Ann. Phys.* **303**, 2–30 (2003)
90. D.S. Rokhsar S.A. Kivelson, Superconductivity and the quantum hard-core dimer gas. *Phys. Rev. Lett.* **61**, 2376–2379 (1988)
91. I. Lesanovsky, H. Katsura, Interacting Fibonacci anyons in a Rydberg gas. *Phys. Rev. A* **86**, 041601 (2012)
92. A. Feiguin, S. Trebst, A.W.W. Ludwig, M. Troyer, A. Kitaev, Z. Wang, M.H. Freedman, Interacting anyons in topological quantum liquids: The golden chain. *Phys. Rev. Lett.* **98**, 160409 (2007)
93. B. Sun, F. Robicheaux, Numerical study of two-body correlation in a 1d lattice with perfect blockade. *New J. Phys.* **10**, 045032 (2008)
94. B. Olmos, R. González-Férez, I. Lesanovsky, Collective Rydberg excitations of an atomic gas confined in a ring lattice. *Phys. Rev. A* **79**, 043419 (2009)
95. C.J. Turner, A.A. Michailidis, D.A. Abanin, M. Serbyn, Z. Papić, Quantum scarred eigenstates in a Rydberg atom chain: Entanglement, breakdown of thermalization, and stability to perturbations. *Phys. Rev. B* **98**, 155134 (2018b)
96. M. Rigol, V. Dunjko, V. Yurovsky, M. Olshanii, Relaxation in a completely integrable many-body quantum system: An *Ab Initio* study of the dynamics of the highly excited states of 1d lattice hard-core bosons. *Phys. Rev. Lett.* **98**, 050405 (2007)
97. B. Mukherjee, S. Nandy, A. Sen, D. Sen, K. Sengupta, Collapse and revival of quantum many-body scars via Floquet engineering. *Phys. Rev. B* **101**, 245107 (2020)
98. A.A. Michailidis, C.J. Turner, Z. Papić, D.A. Abanin, M. Serbyn, Slow quantum thermalization and many-body revivals from mixed phase space. *Phys. Rev. X* **10**, 011055 (2020a)
99. A.A. Michailidis, C.J. Turner, Z. Papić, D.A. Abanin, M. Serbyn, Stabilizing two-dimensional quantum scars by deformation and synchronization. *Phys. Rev. Res.* **2**, 022065 (2020b)
100. C.-Ju. Lin, V. Calvera, T.H. Hsieh, Quantum many-body scar states in two-dimensional Rydberg atom arrays. *Phys. Rev. B* **101**, 220304 (2020a)
101. T. Iadecola, M. Schecter, S. Xu, Quantum many-body scars from magnon condensation. *Phys. Rev. B* **100**, 184312 (2019)
102. C.-Ju. Lin, O. I. Motrunich, Exact quantum many-body scar states in the Rydberg-blockaded atom chain. *Phys. Rev. Lett.* **122**, 173401 (2019)
103. B. van Voorden, J. Minář, K. Schoutens, Quantum many-body scars in transverse field Ising ladders and beyond. *Phys. Rev. B* **101**, 220305 (2020)
104. S. Sugiura, T. Kuwahara, K. Saito, Many-body scar state intrinsic to periodically driven system. *Phys. Rev. Res.* **3**, L012010 (2021)

105. K. Mizuta, K. Takasan, N. Kawakami, Exact Floquet quantum many-body scars under Rydberg blockade. *Phys. Rev. Res.* **2**, 033284 (2020)
106. P. Fendley, K. Sengupta, S. Sachdev, Competing density-wave orders in a one-dimensional hard-boson model. *Phys. Rev. B* **69**, 075106 (2004)
107. I. Lesanovsky, Liquid ground state, gap, and excited states of a strongly correlated spin chain. *Phys. Rev. Lett.* **108**, 105301 (2012)
108. C.-Ju. Lin, A. Chandran, O.I. Motrunich, Slow thermalization of exact quantum many-body scar states under perturbations. *Phys. Rev. Res.* **2**, 033044 (2020b)
109. F.M. Surace, M. Votto, E.G. Lazo, A. Silva, M. Dalmonte, G. Giudici, Exact many-body scars and their stability in constrained quantum chains. *Phys. Rev. B* **103**, 104302 (2021a)
110. I. Mondragon-Shem, M.G. Vavilov, I. Martin, The fate of quantum many-body scars in the presence of disorder. *PRX Quantum* **2**, 030349 (2021). <https://doi.org/10.1103/PRXQuantum.2.030349>
111. M. Schecter, T. Iadecola, Many-body spectral reflection symmetry and protected infinite-temperature degeneracy. *Phys. Rev. B* **98**, 035139 (2018)
112. B. Sutherland, Localization of electronic wave functions due to local topology. *Phys. Rev. B* **34**, 5208 (1986)
113. M. Inui, S.A. Trugman, E. Abrahams, Unusual properties of midband states in systems with off-diagonal disorder. *Phys. Rev. B* **49**, 3190 (1994)
114. F.M. Surace, M. Dalmonte, A. Silva, Quantum local random networks and the statistical robustness of quantum scars. (2021b), [arXiv:2107.00884 \[cond-mat.stat-mech\]](https://arxiv.org/abs/2107.00884)
115. D. Banerjee, A. Sen, Quantum scars from zero modes in an abelian lattice gauge theory on ladders. *Phys. Rev. Lett.* **126**, 220601 (2021)
116. V. Karle, M. Serbyn, A.A. Michailidis, Area-law entangled eigenstates from nullspaces of local Hamiltonians. *Phys. Rev. Lett.* **127**, 060602 (2021). <https://doi.org/10.1103/PhysRevLett.127.060602>
117. S. Choi, C.J. Turner, H. Pichler, W. W. Ho, A.A. Michailidis, Z. Papić, M. Serbyn, M. D. Lukin, D.A. Abanin, Emergent SU(2) dynamics and perfect quantum many-body scars. *Phys. Rev. Lett.* **122**, 220603 (2019)
118. K. Bull, J.-Y. Desaulles, Z. Papić, Quantum scars as embeddings of weakly broken Lie algebra representations. *Phys. Rev. B* **101**, 165139 (2020)
119. V. Khemani, C.R. Laumann, A. Chandran, Signatures of integrability in the dynamics of Rydberg-blockaded chains. *Phys. Rev. B* **99**, 161101 (2019)
120. K. Bull, I. Martin, Z. Papić, Systematic construction of scarred many-body dynamics in 1d lattice models. *Phys. Rev. Lett.* **123**, 030601 (2019)
121. M.L. Mehta, *Random Matrices*, Vol. 142 (Elsevier, 2004)
122. V.I. Arnol'd, *Mathematical methods of classical mechanics*, Vol. 60 (Springer Science & Business Media, 2013)
123. E. Leviatan, F. Pollmann, J.H. Bardarson, D.A. Huse, E. Altman, Quantum thermalization dynamics with matrix-product states. (2017), [arXiv:1702.08894 \[cond-mat.stat-mech\]](https://arxiv.org/abs/1702.08894)
124. A. Hallam, J.G. Morley, A.G. Green, The Lyapunov spectra of quantum thermalisation. *Nature Communications* **10**, 2708 (2019)
125. E.H. Lieb, D. Robinson, The finite group velocity of quantum spin systems. *Commun. Math. Phys.* **28**, 251–257 (1972). https://doi.org/10.1007/978-3-662-10018-9_25
126. E.J. Heller, Wavepacket dynamics and quantum chaology, in *Chaos and Quantum Physics*, Vol. 52 (North-Holland, Amsterdam, 1991)
127. A.I. Schnirelman, Ergodic properties of eigenfunctions. *Uspekhi Mat. Nauk* **29**, 181 (1974)
128. Y.C. De Verdiere, Ergodicité et fonctions propres du laplacien. *Commun. Math. Phys.* **102**, 497–502 (1985). <https://doi.org/10.1007/BF01209296>
129. S. Zelditch et al., Uniform distribution of eigenfunctions on compact hyperbolic surfaces. *Duke Math. J.* **55**, 919–941 (1987). <https://doi.org/10.1215/S0012-7094-87-05546-3>
130. M.V. Berry, in *Chaotic Behaviour of Deterministic Systems*, Vol. 36, ed. by A. Chenciner, A. Patera, D.D. Joseph, R.M. May, S.E. Newhouse, J.A. Libchaber, J.-P. Eckmann, J.P. Gollub, M. Hénon, M. Misiurewicz, et al. (North-Holland, 1983)

131. S. Sridhar, Experimental observation of scarred eigenfunctions of chaotic microwave cavities. *Phys. Rev. Lett.* **67**, 785–788 (1991)
132. P.B. Wilkinson, T.M. Fromhold, L. Eaves, F.W. Sheard, N. Miura, T. Takamasu, Observation of 'scarred' wavefunctions in a quantum well with chaotic electron dynamics. *Nature* **380**, 608–610 (1996)
133. D. Wintgen A. Hönig, Irregular wave functions of a hydrogen atom in a uniform magnetic field. *Phys. Rev. Lett.* **63**, 1467–1470 (1989)
134. C.J. Turner, J.-Y. Desautels, K. Bull, Z. Papić, Correspondence Principle for Many-Body Scars in Ultracold Rydberg Atoms. *Phys. Rev. X* **11**, 021021 (2021). <https://doi.org/10.1103/PhysRevX.11.021021>
135. J.-P. Gazeau, *Coherent States in Quantum Physics* (Wiley-VCH, 2009)
136. A.G. Green, C.A. Hooley, J. Keeling, S.H. Simon, Feynman path integrals over entangled states. (2016), [arXiv:1607.01778](https://arxiv.org/abs/1607.01778) [cond-mat.str-el]
137. B. Sciolla, G. Biroli, Dynamical transitions and quantum quenches in mean-field models. *J. Stat. Mech. Theory Exp.* **2011**, P11003 (2011)
138. T. Mori, Classical ergodicity and quantum eigenstate thermalization: Analysis in fully connected Ising ferromagnets. *Phys. Rev. E* **96**, 012134 (2017)
139. M. Christandl, N. Datta, A. Ekert, A.J. Landahl, Perfect state transfer in quantum spin networks. *Phys. Rev. Lett.* **92**, 187902 (2004)
140. H. Labuhn, D. Barredo, S. Ravets, S. de Léséleuc, T. Macrì, T. Lahaye, A. Browaeys, Tunable two-dimensional arrays of single Rydberg atoms for realizing quantum Ising models. *Nature* **534**, 667–670 (2016)
141. A. Browaeys, T. Lahaye, Many-body physics with individually controlled Rydberg atoms. *Nature Physics* **16**, 132–142 (2020)
142. D. Bluvstein, A. Omran, H. Levine, A. Keesling, G. Semeghini, S. Ebadi, T.T. Wang, A.A. Michailidis, N. Maskara, W.W. Ho, S. Choi, M. Serbyn, M. Greiner, V. Vuletić, M. D. Lukin, Controlling quantum many-body dynamics in driven Rydberg atom arrays. *Science* **371**, 1355–1359 (2021)
143. D.V. Else, C. Monroe, C. Nayak, N.Y. Yao, Discrete time crystals. *Annu. Rev. Condens. Matter Phys.* **11**, 467–499 (2020)
144. N. Maskara, A.A. Michailidis, W.W. Ho, D. Bluvstein, S. Choi, M.D. Lukin, M. Serbyn, Discrete time-crystalline order enabled by quantum many-body scars: entanglement steering via periodic driving. *Phys. Rev. Lett.* **127**, 090602 (2021). <https://doi.org/10.1103/PhysRevLett.127.090602>
145. A. Keesling, A. Omran, H. Levine, H. Bernien, H. Pichler, S. Choi, R. Samajdar, S. Schwartz, P. Silvi, S. Sachdev, P. Zoller, M. Endres, M. Greiner, V. Vuletić, M.D. Lukin, Quantum Kibble-Zurek mechanism and critical dynamics on a programmable Rydberg simulator. *Nature* **568**, 207–211 (2019)
146. G. Semeghini, H. Levine, A. Keesling, S. Ebadi, T.T. Wang, D. Bluvstein, R. Verresen, H. Pichler, M. Kalinowski, R. Samajdar, A. Omran, S. Sachdev, A. Vishwanath, M. Greiner, V. Vuletić, M.D. Lukin, Probing topological spin liquids on a programmable quantum simulator. (2021), [arXiv:2104.04119](https://arxiv.org/abs/2104.04119) [quant-ph]
147. K.J. Satzinger, Y. Liu, A. Smith, C. Knapp, M. Newman, C. Jones, Z. Chen, C. Quintana, X. Mi, A. Dunsworth, C. Gidney, I. Aleiner, F. Arute, K. Arya, J. Atalaya, R. Babbush, J.C. Bardin, R. Barends, J. Basso, A. Bengtsson, A. Bilmes, M. Broughton, B.B. Buckley, D.A. Buell, B. Burkett, N. Bushnell, B. Chiaro, R. Collins, W. Courtney, S. Demura, A. R. Derk, D. Eppens, C. Erickson, E. Farhi, L. Foaro, A.G. Fowler, B. Foxen, M. Giustina, A. Greene, J. A. Gross, M.P. Harrigan, S.D. Harrington, J. Hilton, S. Hong, T. Huang, W.J. Huggins, L. B. Ioffe, S.V. Isakov, E. Jeffrey, Z. Jiang, D. Kafri, K. Kechedzhi, T. Khattar, S. Kim, P.V. Klimov, A.N. Korotkov, F. Kostritsa, D. Landhuis, P. Laptev, A. Locharla, E. Lucero, O. Martin, J.R. McClean, M. McEwen, K.C. Miao, M. Mohseni, S. Montazeri, W. Mruczkiewicz, J. Mutus, O. Naaman, M. Neeley, C. Neill, M.Y. Niu, T.E. O'Brien, A. Opremcak, B. Pató, A. Petukhov, N.C. Rubin, D. Sank, V. Shvarts, D. Strain, M. Szalay, B. Villalonga,

- T.C. White, Z. Yao, P. Yeh, J. Yoo, A. Zalcman, H. Neven, S. Boixo, A. Megrant, Y. Chen, J. Kelly, V. Smelyanskiy, A. Kitaev, M. Knap, F. Pollmann, P. Roushan, Realizing topologically ordered states on a quantum processor. *Science* **374**, 1237–1241 (2021). <https://doi.org/10.1126/science.abi8378>
148. W. Morong, F. Liu, P. Becker, K.S. Collins, L. Feng, A. Kyprianidis, G. Pagano, T. You, A.V. Gorshkov, C. Monroe, Observation of Stark many-body localization without disorder. *Nature* **599**, 393 (2021). <https://www.nature.com/articles/s41586-021-03988-0>
 149. Q. Guo, C. Cheng, H. Li, S. Xu, P. Zhang, Z. Wang, C. Song, W. Liu, W. Ren, H. Dong, R. Mondaini, H. Wang, Stark many-body localization on a superconducting quantum processor. *Phys. Rev. Lett.* **127**, 240502 (2021). <https://doi.org/10.1103/PhysRevLett.127.240502>
 150. B. Yang, H. Sun, R. Ott, H.-Y. Wang, T.V. Zache, J.C. Halimeh, Z.-S. Yuan, P. Hauke, and J.-W. Pan, Observation of gauge invariance in a 71-site Bose–Hubbard quantum simulator. *Nature* **587**, 392–396 (2020a)
 151. J.-Y. Desaulès, A. Hudomal, C.J. Turner, Z. Papić, Proposal for realizing quantum scars in the tilted 1d Fermi-Hubbard model. *Phys. Rev. Lett.* **126**, 210601 (2021)
 152. R.M. Nandkishore S.L. Sondhi, Many-body localization with long-range interactions. *Phys. Rev. X* **7**, 041021 (2017)
 153. M. Kormos, M. Collura, G. Takács, P. Calabrese, Real-time confinement following a quantum quench to a non-integrable model. *Nature Physics* **13**, 246–249 (2017)
 154. N.J. Robinson, A.J.A. James, R.M. Konik, Signatures of rare states and thermalization in a theory with confinement. *Phys. Rev. B* **99**, 195108 (2019)
 155. Z.-C. Yang, F. Liu, A.V. Gorshkov, T. Iadecola, Hilbert-space fragmentation from strict confinement. *Phys. Rev. Lett.* **124**, 207602 (2020b)
 156. O.A. Castro-Alvaredo, M. Lencsés, I.M. Szécsényi, J. Viti, Entanglement oscillations near a quantum critical point. *Phys. Rev. Lett.* **124**, 230601 (2020)
 157. G. Magnifico, M. Dalmonte, P. Facchi, S. Pascazio, F.V. Pepe, E. Ercolessi, Real time dynamics and confinement in the \mathbb{Z}_n Schwinger-Weyl lattice model for 1+1 QED. *Quantum* **4**, 281 (2020)
 158. T. Chanda, J. Zakrzewski, M. Lewenstein, L. Tagliacozzo, Confinement and lack of thermalization after quenches in the bosonic Schwinger model. *Phys. Rev. Lett.* **124**, 180602 (2020)
 159. U. Borla, R. Verresen, F. Grusdt, S. Moroz, Confined phases of one-dimensional spinless fermions coupled to \mathbb{Z}_2 gauge theory. *Phys. Rev. Lett.* **124**, 120503 (2020)
 160. F.M. Surace, P.P. Mazza, G. Giudici, A. Lerose, A. Gambassi, M. Dalmonte, Lattice gauge theories and string dynamics in Rydberg atom quantum simulators. *Phys. Rev. X* **10**, 021041 (2020b)
 161. A. Celi, B. Vermersch, O. Viyuela, H. Pichler, M.D. Lukin, P. Zoller, Emerging two-dimensional gauge theories in Rydberg configurable arrays. *Phys. Rev. X* **10**, 021057 (2020)
 162. N. Pancotti, G. Giudice, J.I. Cirac, J.P. Garrahan, M.C. Bañuls, Quantum East model: Localization, nonthermal eigenstates, and slow dynamics. *Phys. Rev. X* **10**, 021051 (2020)
 163. S. Roy, A. Lazarides, Strong ergodicity breaking due to local constraints in a quantum system. *Phys. Rev. Res.* **2**, 023159 (2020)
 164. J. Feldmeier, F. Pollmann, M. Knap, Emergent glassy dynamics in a quantum dimer model. *Phys. Rev. Lett.* **123**, 040601 (2019)
 165. O. Hart, G. De Tomasi, C. Castelnuovo, From compact localized states to many-body scars in the random quantum comb. *Phys. Rev. Res.* **2**, 043267 (2020)
 166. S. Sachdev, J. Ye, Gapless spin-fluid ground state in a random quantum Heisenberg magnet. *Phys. Rev. Lett.* **70**, 3339–3342 (1993)
 167. A. Kitaev, A simple model of quantum holography, talk at KITP. Univ. Calif. Santa Barbara USA **7** (2015)
 168. J. Maldacena, S.H. Shenker, D. Stanford, A bound on chaos. *J. High Energy Phys.* **2016**, 106 (2016)
 169. Á.M. Alhambra, A. Anshu, H. Wilming, Revivals imply quantum many-body scars. *Phys. Rev. B* **101**, 205107 (2020)

170. A. Omran, H. Levine, A. Keesling, G. Semeghini, T.T. Wang, S. Ebadi, H. Bernien, A.S. Zibrov, H. Pichler, S. Choi, J. Cui, M. Rossignolo, P. Rembold, S. Montangero, T. Calarco, M. Endres, M. Greiner, V. Vuletić, M.D. Lukin, Generation and manipulation of Schrödinger cat states in Rydberg atom arrays. [Science 365, 570–574 \(2019\)](#)
171. S. Dooley, Robust quantum sensing in strongly interacting systems with many-body scars. [PRX Quantum 2, 020330 \(2021\)](#)
172. W. Kao, K.-Y. Li, K.-Y. Lin, S. Gopalakrishnan, B.L. Lev, Topological pumping of a 1d dipolar gas into strongly correlated prethermal states. [Science 371, 296–300 \(2021\)](#)

Quench Dynamics of Rényi Negativities and the Quasiparticle Picture



Sara Murciano, Vincenzo Alba, and Pasquale Calabrese

Abstract The study of the moments of the partially transposed density matrix provides a new and effective way of detecting bipartite entanglement in a many-body mixed state. This is valuable for cold-atom and ion-trap experiments, as well as in the general context of quantum simulation of many-body systems. In this work we study the time evolution after a quantum quench of the moments of the partial transpose, and several related quantities, such as the Rényi negativities. By combining Conformal Field Theory (CFT) results with integrability, we show that, in the space-time scaling limit of long times and large subsystems, a quasiparticle description allows for a complete understanding of the Rényi negativities. We test our analytical predictions against exact numerical results for free-fermion and free-boson lattice models, even though our framework applies to generic interacting integrable systems.

1 Introduction

During the last decades, the study of entanglement became a powerful tool to explore the out-of-equilibrium dynamics of quantum systems. The simplest and most broadly studied protocol is the quantum quench [1, 2]: a system is prepared

S. Murciano
SISSA and INFN Sezione di Trieste, Trieste, Italy
e-mail: smurcian@sissa.it

V. Alba (✉)
Institute for Theoretical Physics, Universiteit van Amsterdam, Amsterdam, The Netherlands
Dipartimento di Ingegneria Industriale, Università degli Studi di Salerno, Fisciano, Salerno, Italy
Dipartimento di Fisica, Università di Pisa, INFN Sezione di Pisa, Largo Bruno, Pisa, Italy
e-mail: vincenzo.alba@unipi.it

P. Calabrese
SISSA and INFN Sezione di Trieste, Trieste, Italy
International Centre for Theoretical Physics (ICTP), Trieste, Italy
e-mail: calabrese@sissa.it

in the ground state of a translationally invariant Hamiltonian, and at a given time a sudden change modifies the Hamiltonian. In integrable systems, the entanglement dynamics after a quench is captured by a well-known quasiparticle picture [3–6]. The key tenet of the quasiparticle picture is that the entanglement dynamics is described by the ballistic propagation of pairs of entangled excitations, which are produced after the quench (see Fig. 1). An intense theoretical activity was accompanied by a remarkable experimental progress, e.g., to measure the many-body entanglement of non-equilibrium states [7–10]. For closed bipartite systems, the von Neumann and the Rényi entropies of reduced density matrices can be used as *bona fide* measures of the entanglement shared between the two complementary parts. On the other hand, neither the entropies nor the associated mutual information can be used to quantify the entanglement between two noncomplementary subsystems (see Fig. 1 for the situation with two disjoint sets in a one-dimensional system). The reason is that the state of the two subsystems is in general a mixed one. In this situation, the entanglement can be understood via the *partial transpose* of the reduced density matrix (RDM) which is defined as follows. Given the RDM ρ_A of a subsystem $A = A_1 \cup A_2$ (see Fig. 1), obtained after tracing out the rest of the system B as $\rho_A \equiv \text{Tr}_B \rho$, the partial transpose $\rho_A^{T_1}$ is obtained by taking the matrix transposition with respect to the degrees of freedom of one of the two subsystems (say A_1). The key point now is that the presence of negative eigenvalues in the spectrum of $\rho_A^{T_1}$ is a sufficient condition for A_1 and A_2 to be entangled [11, 12]. These negative eigenvalues are witnessed by the (logarithmic) negativity $\mathcal{E} \equiv \ln \text{Tr} |\rho_A^{T_1}|$ [13] which turns out also to be an entanglement monotone [14].

Unfortunately, computing the negativity or measuring it experimentally in quantum many-body systems is a daunting task. This fact sparked a lot of activity aiming at finding alternative entanglement witnesses for mixed states always starting from the partially transposed RDM. To this aim, several protocols to measure the moments $\text{Tr}(\rho_A^{T_1})^n$ of the partial transpose have been proposed [15–18] culminating with the actual experimental measure in an ion-trap setting using shadow tomography [15, 16]. However, these moments are not direct indicators of the sign of the eigenvalues of $\rho_A^{T_1}$ and hence of entanglement. Nevertheless, some linear combinations of them are sufficient conditions (known as p_n -PPT conditions, see below) for the presence of negative eigenvalues in the spectrum [15, 16] and

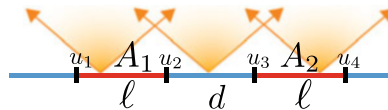


Fig. 1 Quasiparticle picture for the time evolution after a quench of the entanglement between two disjoint intervals ($A_1 = [u_1, u_2]$ and $A_2 = [u_3, u_4]$) embedded in the infinite line. Pairs of entangled quasiparticles are emitted from every point in space at $t = 0$. At a given time t the entanglement between A and the remainder is proportional to the number of pairs shared between A and its complement. Similarly, the entanglement between A_1 and A_2 is proportional to the pairs that are shared between them, and not between A_1 (or A_2) with the rest separately

so are witnesses of entanglement in mixed states. However, in contrast with the logarithmic negativity, for which a quasiparticle picture was derived in Ref. [19], results for the dynamics of the moments of the partial transpose are available only for Conformal Field Theories (CFTs) [20–22].

Here, by combining CFT and integrability, we derive the quasiparticle picture describing the dynamics of the moments of the partial transpose, and several related quantities, after a quantum quench in integrable systems. Specifically, we consider the Rényi negativities \mathcal{E}_n defined as

$$\mathcal{E}_n = \ln\left(\text{Tr}(\rho_A^{T_1})^n\right). \tag{1}$$

Note that \mathcal{E}_n are not proper entanglement measures, although the limit $\lim_{n_e \rightarrow 1} \mathcal{E}_{n_e}$, with n_e an even integer, defines the logarithmic negativity. We also consider the ratios R_n as

$$R_n = \frac{\text{Tr}(\rho_A^{T_1})^n}{\text{Tr}\rho_A^n}. \tag{2}$$

The ratios R_n are studied in CFT [23–27], due to their universality. Recently, they were studied at finite-temperature critical points [28], and to probe thermalization [29, 30] (note that the authors of Ref. [29] refer to the ratios R_n as Rényi negativities, unlike here). Here we derive the quasiparticle picture for both \mathcal{E}_n and R_n , focusing on the situation in which the subsystem A is made of two equal-length intervals at distance d . The formulas that we derive hold in the space-time scaling limit of $t, \ell, d \rightarrow \infty$, with the ratios $t/\ell, d/\ell$ fixed. Furthermore, these results allow us to obtain predictions for all the p_n -PPT conditions introduced in Refs. [15, 16]. Interestingly, we argue that the ratios R_n in the space-time scaling limit become proportional to the Rényi mutual information. Finally, we provide numerical benchmarks of our results for both free-fermion and free-boson models, although they are expected to hold for generic integrable systems.

The paper is organized as follows. In Sect. 2 we review the definitions of some entanglement measures, i.e., Rényi entropy, mutual information, Rényi negativity. In particular, in Sect. 2.1 we introduce the moments of the partial transpose and the negativities. In Sect. 2.2 we introduce the p_n -PPT conditions. In Sect. 3 we review the CFT predictions for the out-of-equilibrium behavior of the Rényi negativities. Specifically, in Sect. 3.1 we review the representation of the Rényi negativities in terms of twist fields. In Sect. 3.2 we derive the out-of-equilibrium behavior of the Rényi negativities and the ratios R_n in CFTs. In Sect. 4 we introduce the quasiparticle picture (in Sect. 4.1) for the spreading of entanglement and negativity, generalizing it to the moments of the partial transpose in Sect. 4.2. In Sect. 5 we present numerical benchmarks for free bosonic (in Sect. 5.1) and fermionic theories (in Sect. 5.2). In Sect. 5.3 we discuss the quasiparticle predictions for the p_n -PPT

conditions. Finally, in Sect. 6 we draw our conclusions and we discuss some possible extensions of our work.

2 Entanglement Measures for Mixed States

The Rényi entanglement entropies are the most successful way to characterize the bipartite entanglement of a subsystem A of a many-body quantum system prepared in a pure state (see, e.g., the reviews [31–34]), also from the experimental perspective [7–10, 35, 36]. Given the reduced density matrix (RDM) ρ_A of a subsystem A , the Rényi entropies are defined as

$$S_A^{(n)} = \frac{1}{1-n} \ln \text{Tr} \rho_A^n. \quad (3)$$

From these, the von Neumann entropy is obtained as the limit $n \rightarrow 1$ of Eq. (3) and also the entire spectrum of ρ_A can be reconstructed [37]. The Rényi entropies in Eq. (3) can be very conveniently computed in field theory because for integer n , in the path-integral formalism, $\text{Tr} \rho_A^n$ is the partition function on an n -sheeted Riemann surface \mathcal{R}_n obtained by joining cyclically the n sheets along the region A [38–40].

For a mixed state, the entanglement entropies are no longer good measures of entanglement because they mix classical and quantum correlations (e.g., in a high temperature state, $S_A^{(n)}$ gives the extensive result for the thermal entropy that has nothing to do with entanglement). In this respect, a useful quantity to consider is the Rényi mutual information

$$I_{A_1:A_2}^{(n)} \equiv S_{A_1}^{(n)} + S_{A_2}^{(n)} - S_{A_1 \cup A_2}^{(n)}, \quad (4)$$

which is not a measure of the entanglement between A_1 and A_2 , but for $n \rightarrow 1$ it quantifies the amount of global correlations between the two subsystems (we mention that for $n \neq 1$, $I_{A_1:A_2}^{(n)}$ can be also negative [41] and a more complicated definition of mutual information must be employed [42]).

As anticipated, we are interested here in the entanglement between two different regions, and the goal of the following section is to define the tools to compute it.

2.1 Entanglement in Mixed States and Logarithmic Negativity

A very useful starting point to quantify mixed state entanglement is the Peres criterion [11, 12], also known as PPT condition. It states that given a system described by the density matrix ρ_A , a sufficient condition for the presence of entanglement between two subsystems A_1 and A_2 (with $A = A_1 \cup A_2$) is that the

partial transpose $\rho_A^{T_1}$ with respect to the degrees of freedom in A_1 (or equivalently A_2) has at least one negative eigenvalue. Let us introduce the partial transpose operation as follows. We can write down the density matrix as

$$\rho_A = \sum_{ijkl} \langle e_i^1, e_j^2 | \rho_A | e_k^1, e_l^2 \rangle | e_i^1, e_j^2 \rangle \langle e_k^1, e_l^2 |, \quad (5)$$

where $|e_j^1\rangle$ and $|e_k^2\rangle$ are orthonormal bases in the Hilbert spaces \mathcal{H}_1 and \mathcal{H}_2 corresponding to the A_1 and A_2 regions, respectively. The partial transpose of a density matrix for the subsystem A_1 is defined by exchanging the matrix elements in the subsystem A_1 , i.e.,

$$\rho_A^{T_1} = \sum_{ijkl} \langle e_k^1, e_j^2 | \rho_A | e_i^1, e_l^2 \rangle | e_i^1, e_j^2 \rangle \langle e_k^1, e_l^2 |, \quad (6)$$

In terms of its eigenvalues λ_i , the trace norm of $\rho_A^{T_1}$ can be written as

$$\text{Tr}|\rho_A^{T_1}| = \sum_i |\lambda_i| = \sum_{\lambda_i > 0} |\lambda_i| + \sum_{\lambda_i < 0} |\lambda_i| = 1 + 2 \sum_{\lambda_i < 0} |\lambda_i|, \quad (7)$$

where in the last equality we used the normalization $\sum_i \lambda_i = 1$. Here $\text{Tr}|O| \equiv \text{Tr}\sqrt{O^\dagger O}$ denotes the trace norm of the operator O . This expression makes evident that the negativity measures “how much” the eigenvalues of the partial transpose of the density matrix are negative, a property which is the reason for the name negativity. Therefore, starting from the Peres criterion, a measure of the bipartite entanglement for a general mixed state can be naturally defined as [13]

$$\mathcal{E} \equiv \ln \text{Tr}|\rho_A^{T_1}|, \quad (8)$$

which is known as *logarithmic negativity*. By considering the moments of the partial transpose RDM, one can define the Rényi negativities \mathcal{E}_n as

$$\mathcal{E}_n \equiv \ln \text{Tr} \left(\rho_A^{T_1} \right)^n. \quad (9)$$

The logarithmic negativity \mathcal{E} is given by the following replica limit [23, 24]

$$\mathcal{E} = \lim_{n_e \rightarrow 1} \mathcal{E}_{n_e}, \quad (10)$$

where n_e denotes an even number $n_e = 2m$ with m integer. For future convenience, we also introduce the ratios

$$R_n \equiv \frac{\text{Tr} \left(\rho_A^{T_1} \right)^n}{\text{Tr} \rho_A^n}. \quad (11)$$

The Rényi negativities \mathcal{E}_n with integer $n \geq 2$ can also be measured in experiments [15, 17, 18], but they are not entanglement monotones. The entanglement negativity and Rényi negativities have been used to characterize mixed states in various quantum systems such as in harmonic oscillator chains [43–51], quantum spin models [25, 26, 52–63], (1 + 1)d conformal and integrable field theories [18, 23–27, 64–75], out-of-equilibrium settings [15, 19–21, 29, 30, 49, 76–80].

Crucially, while for free-boson models the Rényi negativities for arbitrary real n can be efficiently computed from the two-point correlation function [43], this is not the case for free-fermion systems. The main problem is that the partial transpose in Eq. (8) is not a gaussian operator, although it can be written as the sum of two gaussian (non-commuting) operators O_{\pm} as [81]

$$\rho_A^{T_1} = \frac{1-i}{2} O_+ + \frac{1+i}{2} O_- . \quad (12)$$

From this observation a procedure to extract the Rényi negativities of integer order was proposed [81] and was also used in many subsequent studies [82–88]. Still, proceeding in this way, it is not possible to perform the replica limit $n_e \rightarrow 1$, implying that the negativity, i.e., the only genuine measure of entanglement, is not accessible. To overcome this problem, an alternative estimator of mixed state entanglement for fermionic systems has been introduced based on the time-reversal partial transpose (a.k.a *partial time reversal*) [22, 89–95]. The new estimator has been dubbed *fermionic negativity*. It has been shown that the fermionic negativity is an entanglement monotone [91] and it is also an upper bound for the standard negativity. In the following, we denote $\mathcal{E}_n^{(b)}$ the standard negativity in Eq. (9) (that is an entanglement monotone for both bosonic and fermionic systems) and $\mathcal{E}_n^{(f)}$ the fermionic one (that exists only for fermionic models). The (fermionic) Rényi negativities can be defined as [92]

$$\mathcal{E}_n^{(f)} = \begin{cases} \ln[\text{Tr}(O_+ O_- \dots O_+ O_-)], & n \text{ even,} \\ \ln[\text{Tr}(O_+ O_- \dots O_+)], & n \text{ odd,} \end{cases} \quad (13)$$

from which $\mathcal{E}^{(f)} = \lim_{n_e \rightarrow 1} \mathcal{E}_{n_e}^{(f)}$. Specifically, $\mathcal{E}^{(f)}$ reads as

$$\mathcal{E}^{(f)} = \ln \text{Tr} \sqrt{O_+ O_-} , \quad (14)$$

with O_{\pm} as defined implicitly in Eq. (12). The products involving O_+ and O_- are still gaussian fermionic operators, so all the above quantities can be efficiently computed, including the negativity (14).

2.2 Entanglement Detection Through Partial Transpose Moments

Despite several sufficient conditions for entanglement in mixed states have been developed in the literature, many of them cannot be straightforwardly implemented experimentally since they require the knowledge of the full density matrix [31]. This is, for instance, the case of the PPT condition. To overcome this difficulty, it was shown in [15] that the first few moments of the partial transpose can be used to define some simple yet powerful tests for bipartite entanglement. Given $\rho_A^{T_1}$ (cf. Eq. (6)), we denote its k -th order moment as

$$p_k \equiv \text{Tr} \left(\rho_A^{T_1} \right)^k, \tag{15}$$

with $p_1 = \text{Tr}(\rho_A^{T_1}) = 1$ and p_2 equal to the purity $p_2 = \text{Tr}\rho_A^2$. The p_3 -PPT condition states that any positive semi-definite partial transpose satisfies [15]

$$p_3 p_1 > p_2^2, \tag{16}$$

or, in other words, if $p_3 < p_2^2$, then ρ_A violates the PPT condition and must, therefore, be entangled. The condition in Eq. (16) belongs to a more general set of conditions, dubbed Stieltjes $_n$, involving inequalities among the moments p_k of order up to n . They were introduced in [16] together with a set of experimentally accessible conditions for detecting entanglement in mixed states. The condition Stieltjes $_3$ is equivalent to p_3 -PPT, and so we rename here the Stieltjes $_n$ -conditions as p_n -PPT. As examples, p_5 -PPT and p_7 -PTT read, respectively [16]

$$D_5 \equiv \det \begin{pmatrix} p_1 & p_2 & p_3 \\ p_2 & p_3 & p_4 \\ p_3 & p_4 & p_5 \end{pmatrix} \geq 0, \quad D_7 \equiv \det \begin{pmatrix} p_1 & p_2 & p_3 & p_4 \\ p_2 & p_3 & p_4 & p_5 \\ p_3 & p_4 & p_5 & p_6 \\ p_4 & p_5 & p_6 & p_7 \end{pmatrix} \geq 0, \tag{17}$$

from which one deduces easily the rationale for higher order condition.

3 Quench Dynamics of Rényi Negativities in Conformal Field Theory

In this section we review the CFT calculation of the temporal evolution of the Rényi negativities between two intervals after a global quench in CFT as derived in Ref. [20]. We consider $A = A_1 \cup A_2$, where the intervals A_1 and A_2 can be either adjacent or disjoint (see Fig. 1).

3.1 Rényi Negativities from Twist Field Correlation Functions

A powerful method to calculate the Rényi negativities is based on a particular type of twist fields in quantum field theory that are related to branch points in the Riemann surface \mathcal{R}_n [40, 96]. We denote twist and anti-twist fields by \mathcal{T}_n and $\tilde{\mathcal{T}}_n$, respectively. One can show that the moments of the reduced density matrix $\text{Tr}(\rho_A)^n$ can be written as correlators of twist fields [40]. For example, when $A = [u_1, u_2] \cup [u_3, u_4]$ (see Fig. 1), one has that

$$\text{Tr}\rho_A^n = \langle \mathcal{T}_n(u_1)\tilde{\mathcal{T}}_n(u_2)\mathcal{T}_n(u_3)\tilde{\mathcal{T}}_n(u_4) \rangle. \quad (18)$$

Notice that the twist and anti-twist fields are inserted at the endpoints of A . The expectation value in Eq. (18) is taken with respect to the action living on a plane. As shown in [24], if we take the partial transpose $\rho_A^{T_1}$ with respect to the degrees of freedom living on the interval $A_1 = [u_1, v_1]$, $\text{Tr}(\rho_A^{T_1})^n$ can be written as a twist field correlator as in Eq. (18), the only difference being that the twist fields \mathcal{T}_n and $\tilde{\mathcal{T}}_n$ at the endpoints of A_1 are exchanged while the remaining ones stay untouched, i.e., [23, 24]

$$\text{Tr}(\rho_A^{T_1})^n = \langle \tilde{\mathcal{T}}_n(u_1)\mathcal{T}_n(u_2)\mathcal{T}_n(u_3)\tilde{\mathcal{T}}_n(u_4) \rangle. \quad (19)$$

This procedure can be generalized straightforwardly to the case where A is the union of more than two intervals, and the partial transposition involves more than two intervals.

The situation in which the two intervals are adjacent can be obtained from Eq. (19) by taking the limit $u_3 \rightarrow u_2$ in Eq. (19), giving $\text{Tr}(\rho_A^{T_1})^n = \langle \tilde{\mathcal{T}}_n(u_1)\mathcal{T}_n^2(u_2)\tilde{\mathcal{T}}_n(u_4) \rangle$. In a generic CFT characterized by a central charge c , the expectation values (18) and (19) are evaluated straightforwardly by knowing the scaling dimensions of \mathcal{T}_n , $\tilde{\mathcal{T}}_n$, \mathcal{T}_n^2 , and $\tilde{\mathcal{T}}_n^2$. The scaling dimensions of \mathcal{T}_n^2 and $\tilde{\mathcal{T}}_n^2$ are equal and depend on the parity of n as [23]

$$\Delta_n^{(2)} \equiv \begin{cases} \Delta_n & \text{odd } n \\ 2\Delta_{n/2} & \text{even } n \end{cases}, \quad \Delta_n = \frac{c}{12} \left(n - \frac{1}{n} \right), \quad (20)$$

where Δ_n are the scaling dimensions of \mathcal{T}_n , $\tilde{\mathcal{T}}_n$.

3.2 Out-of-Equilibrium Dynamics of the Rényi Negativities

Before discussing the out-of-equilibrium dynamics after a quantum quench of the Rényi negativities in CFTs, it is useful to recall the imaginary time formalism for the description of quantum quenches [1–3]. The family of initial states that are easy

to work with in CFT have the form $e^{-\tau_0 H} |\psi_0\rangle$, with $|\psi_0\rangle$ being a boundary state. The expectation value of a local operator O is then

$$\langle O(t, x) \rangle = Z^{-1} \langle \psi_0 | e^{iHt - \tau_0 H} O(x) e^{-iHt - \tau_0 H} | \psi_0 \rangle, \tag{21}$$

where the damping factors $e^{-\tau_0 H}$ have been introduced to make the path integral absolutely convergent (see below), and $Z = \langle \psi_0 | e^{-2\tau_0 H} | \psi_0 \rangle$ is the normalization factor. The correlator in Eq. (21) may be represented by a path integral in imaginary time τ as [2]

$$\langle O(t, x) \rangle = Z^{-1} \int [d\phi(x, \tau)] O(x, \tau = \tau_0 + it) e^{-\int_{\tau_1}^{\tau_2} L d\tau} \langle \psi_0 | \phi(x, \tau_2) \rangle \langle \phi(x, \tau_1) | \psi_0 \rangle, \tag{22}$$

where L is the (Euclidean) Lagrangian corresponding to the dynamics induced by H , τ_1 can be identified with 0 and τ_2 with $2\tau_0$. As shown in [1, 3], the computation of the path integral in Eq. (22) can be done considering τ real and only at the end analytically continuing it to the complex value $\tau = \tau_0 + it$.

In this way, the problem of the dynamics is mapped to the thermodynamics of a field theory in a strip geometry of width $2\tau_0$ and boundary condition $|\psi_0\rangle$ at the two edges of the strip in the imaginary time direction. At this point we have all the ingredients to derive the dynamics of the Rényi negativities after a global quench in CFT. To calculate the time-dependent $\text{Tr}(\rho_A^{T_1})^n$ one has to compute the correlator

$$\text{Tr}(\rho_A^{T_1})^n = \langle \tilde{\mathcal{T}}_n(\omega_1) \mathcal{T}_n(\omega_2) \mathcal{T}_n(\omega_3) \tilde{\mathcal{T}}_n(\omega_4) \rangle, \tag{23}$$

where the expectation value has to be calculated in the field theory confined in a strip, and where we denoted by $\omega_i = u_i + i\tau$ the complex coordinate on the strip ($u_i \in \mathbb{R}$ and $0 < \tau < 2\tau_0$). It is convenient to employ the conformal transformation $z = e^{\pi\omega/(2\tau_0)}$, which maps the strip onto the half plane, where the four point correlation functions of the twist fields can be computed by knowing that they behave as primary fields with scaling dimensions Δ_n (cf. (20)). After the analytic continuation to real time, in the space-time scaling limit $t, |u_i - u_j| \gg \tau_0$, from Eq. (23), the Rényi negativities \mathcal{E}_n (cf. Eq. (9)) read [20]

$$\begin{aligned} \mathcal{E}_n = & -\frac{\pi}{\tau_0} \left[2\Delta_n t + \Delta_n \left(\frac{\ell_1 + \ell_2}{2} - \max(t, \ell_1/2) - \max(t, \ell_2/2) \right) + (\Delta_n^{(2)}/2 - \Delta_n) \right. \\ & \left. \times (\max(t, (\ell_1 + \ell_2 + d)/2) + \max(t, d/2)) - \max(t, (\ell_1 + d)/2) - \max(t, (\ell_2 + d)/2) \right], \end{aligned} \tag{24}$$

where $\Delta_n^{(2)}$ is in Eq. (20), and we defined $\ell_1 = |u_1 - u_2|$, $\ell_2 = |u_3 - u_4|$, and $d = |u_3 - u_2|$ (see Fig. 1). In deriving Eq. (24) we neglected an additive time-independent constant that originates from the correlation function of the twist fields and that depends on the details of the CFT under consideration. This is justified

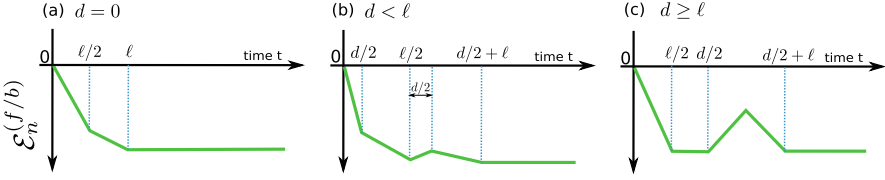


Fig. 2 Time dependence of the Rényi negativities for quasiparticles with linear dispersion. We consider two disjoint subsystems with equal length ℓ at distance $d = 0$ (a), $d < \ell$ (b), $d \geq \ell$ (c). The piecewise linear behavior is described by Eq. (24)

because Eq. (24) holds in the scaling limit $\ell_1, \ell_2, d, t \rightarrow \infty$ with their ratios fixed, and it describes only the leading behavior of the Rényi negativities \mathcal{E}_n in that limit. Crucially, Eq. (24) depends on both Δ_n and $\Delta_n^{(2)}$. Notice that even for finite d , \mathcal{E}_n exhibits a linear behavior at short times, due to the first term in Eq. (24). This signals that \mathcal{E}_n are not good measures of the entanglement or the correlation between A_1 and A_2 . The reason is that for $t \ll d$ no correlation can be shared between A_1 and A_2 because the maximum velocity in the system is finite (see Fig. 2). We stress that Eq. (24) is not directly applicable to microscopic integrable models: Eq. (24) is only valid for CFT, in which there is a perfect linear dispersion, i.e., only one velocity. This is not the case in integrable lattice models, where the excitations have a nonlinear dispersion. In the next sections, we will show how to adapt Eq. (24) to describe the dynamics of the Rényi negativities after a quantum quench in microscopic integrable systems.

Finally, the dynamics of the ratio R_n in Eq. (11) can be derived combining Eq. (24) with the results for $\text{Tr}\rho_A^n$ in [3]. The final result reads [20]

$$\ln R_n = \frac{\pi \Delta_n^{(2)}}{\tau_0} \times (-\max(t, (\ell_1 + \ell_2 + d)/2) - \max(t, d/2)) + \max(t, (\ell_1 + d)/2) + \max(t, (\ell_2 + d)/2). \quad (25)$$

In contrast with Eq. (24), Eq. (25) does not depend explicitly on Δ_n , but only on $\Delta_n^{(2)}$.

Before concluding, it is useful to discuss the qualitative behavior of $\mathcal{E}_n^{(f/b)}$ and $-\ln(R_n^{(f/b)})$. The typical behavior of the Rényi negativities, as obtained from Eq. (24), is reported in Fig. 2 for three typical values of the distance d between the two intervals of equal length ℓ . \mathcal{E}_n is always a piecewise linear function and it is negative at any time. For $d = 0$ one has a two-slope linear behavior followed by a saturation to a volume-law scaling at long times. At intermediate distance $0 < d < \ell$ the behavior is more complicated with a change in the sign of the slope. For $d > \ell$, $\mathcal{E}_n^{(f/b)}$ exhibits an initial linear decrease followed by a saturation, and a dip-like feature at $d/2 \leq t \leq d/2 + \ell$.

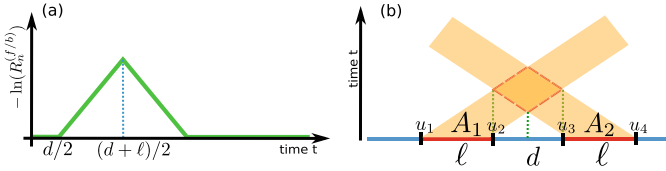


Fig. 3 Illustration of the dynamics of $-\ln R_n^{(f/b)}$ for two disjoint subsystems with equal length ℓ at distance d . On the left we report the shape of $-\ln R_n^{(f/b)}$ with a single velocity of quasiparticles. On the right, there is a graphical representation for the quasiparticle spreading of entanglement (for the case with all quasiparticles having the same velocity $v = 1$ as in a CFT). Horizontal slices of the dark orange region count the quasiparticles shared between the two disjoint sets at a given time

The dynamics of $-\ln(R_n^{(f/b)})$ (cf. Eq. (25)) is shown in Fig. 3 for two equal-length intervals. For $t < d/2$, it vanishes; for $d/2 \leq t \leq (d + \ell)/2$ it linearly increases, then it linearly decreases with the same (in absolute value) slope until $t \leq (d + 2\ell)/2$, when it vanishes and stays zero for all larger times. Therefore, at a given time t , it is proportional to the width of the intersection between the two shaded areas starting from $A_1 \cup A_2$ and showed in Fig. 3b. In other words, it is proportional to the total number of entangled pairs shared between A_1 and A_2 . This property suggests that in the scaling limit, R_n becomes an indicator of the mutual entanglement between the intervals, although in general it is not an entanglement monotone.

Let us remark that Eq. (25) is identical to the evolution of the Rényi mutual information in Eq. (4) apart from the prefactor. We will come back to the connection between these two quantities in the following sections.

4 Quasiparticle Picture for the Rényi Negativities in Integrable Systems

The goal of this section is to adapt Eq. (24) and Eq. (25) to describe the dynamics of the Rényi negativities and the ratios R_n after a quantum quench in integrable systems. The main observation is that Eq. (24) and Eq. (25) admit an interpretation in terms of a simple hydrodynamic picture, a.k.a. the quasiparticle picture.

4.1 Quasiparticle Picture

The quasiparticle picture for the entanglement dynamics after a global quantum quench has been proposed in Ref. [3]. The underlying idea is that the pre-quench initial state has very high energy with respect to the ground state of the Hamiltonian

governing the dynamics; hence it can be seen as a source of quasiparticle excitations at $t = 0$. We assume that quasiparticles are uniformly created in uncorrelated pairs with quasimomenta $(k, -k)$ and traveling with opposite velocities $v(k) = -v(-k)$ (for free models the uncorrelated pair assumption can be released, see [97–100]; for interacting integrable models it has been argued that the pair structure is what makes the quench integrable [101]). Quasiparticles produced at the same point in space are entangled, whereas quasiparticles created far apart are incoherent. The quasiparticles travel through the system as free-like excitations. At a generic time t , the von Neumann entropy and the Rényi entropies between a subsystem A and the rest are proportional to the total number of quasiparticles that were created at the same point at $t = 0$ and are shared between A and its complement at time t (see Fig. 2a). Let us focus on the quasiparticle picture for the Rényi entropies in free models (the quasiparticle picture has been derived rigorously for free-fermion models in Ref. [102]). In formulas it reads as

$$S_A^{(n)}(t) = \int \frac{dk}{2\pi} s_{GGE}^{(n)}(k) \min(2|v(k)|t, \ell). \quad (26)$$

Here ℓ is the length of subsystem A , and $v(k)$ is the group velocity of the fermionic excitations. Importantly, in Eq. (26) $s_{GGE}^{(n)}(k)$ is the density (in momentum space) of the Rényi entropies of the GGE thermodynamic state [103–105] that describes the steady state after the quench. Eq. (26) predicts a linear growth for $t \leq \ell/(2v_{\max})$, with $v_{\max} \equiv \max_k(v(k))$ the maximum velocity in the system, and then saturates to an extensive value at $t \rightarrow \infty$.

For $n = 1$, i.e., for the von Neumann entropy the validity of Eq. (26) for a generic interacting integrable model has been conjectured in Ref. [4, 5]. Eq. (26) remains essentially the same. Precisely, the contribution of the quasiparticles to the von Neumann entropy $s_{GGE}^{(1)}$ is the density of GGE thermodynamic entropy. The group velocities of the quasiparticles are obtained as particle-hole excitations over the GGE thermodynamic macrostate [5, 106]. This conjecture has been explicitly worked out in several cases [4, 5, 107, 108] and tested against numerics in several interacting integrable models [4, 5, 109, 110]. Eq. (26) has been generalized to describe the steady-state value of the Rényi entropies [111–113]. On the other hand, the full-time dynamics of the Rényi entropies is still an open problem, with the exception of one model [114, 115]. Eq. (26) can be straightforwardly generalized to describe the dynamics of the mutual information between two intervals. This allows to reveal how quantum information is scrambled in integrable systems [116, 117]. Remarkably, the quasiparticle picture for the logarithmic negativity has been derived in Ref. [66]. By combining the quasiparticle picture with the framework of the Generalized Hydrodynamics [118, 119] it is possible to describe the entanglement dynamics after quenches from inhomogeneous initial states [120–125]. The quasiparticle picture for the entanglement dynamics has been also tested in the rule 54 chain, which is believed to be a representative “toy model” for generic interacting integrable systems [114, 115]. Very recently, the quasiparticle picture has been generalized to take into account dissipative effects, at least in

free-fermion and free-boson models [126–129], to describe the evolution of the symmetry-resolved entanglement entropies [130, 131], and for the characterization of the prethermalization dynamics [132].

To proceed it is useful to compare Eq. (26) with the CFT prediction for the dynamics of the Rényi entropies [3]

$$S_A^{(n)} = -\frac{1}{1-n} \frac{\pi \Delta_n}{2\tau_0} \min(2t, \ell). \tag{27}$$

A crucial observation is that Eq. (26) can be formally obtained from the CFT result in Eq. (27) by replacing $t \rightarrow |v(k)|t$, integrating over the quasiparticles with quasimomentum k , and replacing $-\pi \Delta_n/(2\tau_0) \rightarrow s_{GGE}^{(n)}$.

4.2 The Quasiparticle Description for Rényi Negativities

The quasiparticle picture described above can be adapted to describe the Rényi negativities $\mathcal{E}_n^{(f/b)}$ and the ratios $\ln(R_n^{(f/b)})$, in integrable systems after a global quench.

Indeed, similarly to the Rényi entropies, from Eqs. (24) and (25), by using Eq. (20), after replacing $-\pi \Delta_n/(2\tau_0) \rightarrow s_{GGE}^{(n)}$, and by integrating over k , one obtains that

$$\begin{aligned} \mathcal{E}_n^{(f/b)} = \int \frac{dk}{2\pi} & \left[4\varepsilon_n |v|t + 2\varepsilon_n \left(\frac{\ell_1 + \ell_2}{2} - \max(|v|t, \ell_1/2) - \max(|v|t, \ell_2/2) \right) \right. \\ & - (2\varepsilon_n - \varepsilon_n^{(2)}) (\max(|v|t, (\ell_1 + \ell_2 + d)/2) + \max(|v|t, d/2) \\ & \left. - \max(|v|t, (\ell_1 + d)/2) - \max(|v|t, (d + \ell_2)/2)) \right], \tag{28} \end{aligned}$$

while the ratios $R_n^{(f/b)}$ read

$$\begin{aligned} \ln(R_n^{(f/b)}) = \int \frac{dk}{2\pi} & \varepsilon_n^{(2)} (\max(|v|t, d/2) - \max(|v|t, (\ell_1 + d)/2) \\ & - \max(|v|t, (\ell_2 + d)/2) + \max(|v|t, (\ell_1 + \ell_2 + d)/2)). \tag{29} \end{aligned}$$

We defined

$$\varepsilon_n^{(2)}(k) \equiv \begin{cases} \varepsilon_n(k) & \text{odd } n \\ 2\varepsilon_{n/2}(k) & \text{even } n \end{cases}, \quad \varepsilon_n(k) = s_{GGE}^{(n)}(k). \tag{30}$$

Clearly, Eq. (30) mirrors the structure of Eq. (20). Here $s_{GGE}(k)$ is the density of GGE thermodynamic entropy.

It is interesting to remark that by comparing Eq. (29) with the quasiparticle picture for the Rényi mutual information [5] $I_{A_1:A_2}^{(n)}$, one obtains

$$\ln(R_n^{(f/b)}) = \begin{cases} (1 - n/2)I_{A_1:A_2}^{(n/2)} & n \text{ even} \\ (1 - n)\frac{I_{A_1:A_2}^{(n)}}{2}, & n \text{ odd.} \end{cases} \quad (31)$$

Moreover, by taking the replica limit $n_e \rightarrow 1$ in $\mathcal{E}_{n_e}^{(f/b)}$, we recover the quasiparticle prediction for the negativity [19]

$$\mathcal{E}^{(f/b)} = \int \frac{dk}{2\pi} \varepsilon_{1/2}(k) (\max(2|v|t, d) - \max(2|v|t, \ell_1 + d) - \max(2|v|t, \ell_2 + d) + \max(2|v|t, \ell_1 + \ell_2 + d)). \quad (32)$$

It was pointed out in [19] that Eq. (32) is the same as for the Rényi mutual information (of any index) by replacing $\varepsilon_{1/2}$ with the density of Rényi entropy. We stress that the same prediction is valid for both standard (bosonic) partial transpose and for the fermionic one.

Finally, it is useful to observe that Eq. (31) can be derived by using that if $A_1 \cup A_2$ is in a pure state, then $\text{Tr}((\rho_A^{T_1})^n)$ can be expressed in terms of $\text{Tr}(\rho_{A_1}^n)$. More precisely, one can prove that [24]

$$\text{Tr}(\rho_A^{T_1})^n = \begin{cases} \text{Tr}\rho_{A_1}^n & n \text{ odd} \\ (\text{Tr}\rho_{A_1}^{n/2})^2 & n \text{ even} \end{cases}, \quad (33)$$

where $\rho_{A_1} = \text{Tr}_{A_2}\rho_A$. Now, one can recover Eq. (31) by using Eq. (33), and the definition in Eq. (4), and that if $A_1 \cup A_2$ is in a pure state, $S_{A_1}^{(n)} = S_{A_2}^{(n)}$. The fact that the result of the quasiparticle picture (24) is not sensitive to $A_1 \cup A_2$ not being in a pure state reflects that the initial state has low entanglement and that during the dynamics the entanglement is transported ballistically.

Finally, for Eq. (28) and Eq. (29) to be predictive one has to fix the function $s_{GGE}(k)$ (cf. Eq. (30)). Here we focus on out-of-equilibrium protocols for free-fermion and free-boson models. In this situation, $s_{GGE}(k)$ is determined from the population of the modes $\rho(k)$ of the post-quench Hamiltonian in the stationary state (see Refs. [6, 133] for a pedagogical review). Actually, since $\rho(k)$ are conserved they can be equivalently computed in the initial state, without solving the dynamics. Specifically, one has that

$$s_{GGE}^{(n, f/b)}(k) = \pm \ln(\pm \rho(k)^n + (1 \mp \rho(k))^n), \quad (34)$$

where the upper and lower signs are for fermionic and bosonic systems, respectively (and not to fermionic and bosonic negativity). We remark that, although the quasiparticle prediction in Eqs.(28) and (29) is expected to be valid also for interacting integrable models, the full quasiparticle picture for the Rényi entropies is not known.

5 Time Evolution of Rényi Negativities in Free Models: Numerical Results

In this section we provide numerical benchmarks for the results of Sect.4.2. As an example of free-bosonic system, we consider the harmonic chain. Our results for free-fermion systems are tested against exact numerical data for a fermionic chain.

5.1 Mass Quench in the Harmonic Chain

Let us start discussing the dynamics of the Rényi negativities after a mass quench in the harmonic chain. The harmonic chain is described by the Hamiltonian

$$H = \frac{1}{2} \sum_{n=0}^{L-1} p_n^2 + m^2 q_n^2 + (q_{n+1} - q_n)^2, \quad q_0 = q_L, \quad p_0 = p_L, \quad (35)$$

where L is the number of lattice sites, q_n and p_n are canonically conjugated variables, with $[q_n, p_m] = i\delta_{nm}$, and m is a mass parameter. The harmonic chain can be diagonalized in Fourier space and is equivalent to a system of free bosons. The dispersion relation of the bosons is given by [6]

$$e(k) = [m^2 + 2(1 - \cos(k))]^{1/2}. \quad (36)$$

The group velocities are obtained from the single-particle energies $e(k)$ as

$$v(k) = \frac{de(k)}{dk} = \sin(k)[m^2 + 2(1 - \cos(k))]^{-1/2}, \quad (37)$$

and the maximum one is $v_{\max} = \max_k v(k)$. In the mass quench protocol, the system is prepared in the ground state $|\psi_0\rangle$ of the Hamiltonian (35) with $m = m_0$. At $t = 0$ the mass parameter is quenched from m_0 to a different value m and the system unitarily evolves under the new Hamiltonian $H(m)$, namely $|\psi(t)\rangle = e^{-iH(m)t} |\psi_0\rangle$. The density $\rho(k)$ (cf. Eq. (34)) of the bosons is written in terms of the pre- and post-

quench dispersions $e_0(k)$ and $e(k)$ as [2, 3, 6]

$$\rho(k) = \frac{1}{4} \left(\frac{e(k)}{e_0(k)} + \frac{e_0(k)}{e(k)} \right) - \frac{1}{2}. \quad (38)$$

For free-bosonic systems the Rényi negativities can be constructed from the two-point correlation functions $\langle q_i q_j \rangle$, $\langle p_i p_j \rangle$, and $\langle q_i p_j \rangle$. Indeed, given a subsystem A containing $\tilde{\ell}$ sites, which could be either all in one interval or in disjoint intervals, the reduced density matrix for A can be studied [20, 134] by constructing the $\tilde{\ell} \times \tilde{\ell}$ matrices $Q_{ij}^A = \langle q_i q_j \rangle$, $P_{ij}^A = \langle p_i p_j \rangle$ and $R_{ij}^A = \text{Re} \langle q_i p_j \rangle$, where the superscript A means that the indices i, j are restricted to subsystem A . Crucially, a similar strategy can be used to construct the Rényi negativities (for the details we refer to Ref. [20]). The main idea is that the net effect of the partial transposition with respect to a subinterval A_1 is the inversion of the signs of the momenta corresponding to the sites belonging to A_1 .

For the following, we restrict ourselves to the physical situation with A made of two disjoint parts, i.e., $A = A_1 \cup A_2$, with A_1, A_2 two equal-length intervals of length ℓ . We denote as d the distance between A_1 and A_2 (see Fig. 1). We only discuss the ratios $-\ln(R_n^{(b)})$ (cf. Eq. (11)). The results are shown in Fig. 4. Panels (a) and (b) show the quantities $-\ln(R_n^{(b)})/\ell$ for adjacent intervals, i.e., $d = 0$. The data are for several values of the intervals' length ℓ up to $\ell = 80$. Since we are interested in the scaling limit, we plot $-\ln(R_n^{(b)})/\ell$ versus the rescaled time t/ℓ . For two adjacent intervals, the ratio exhibits a linear growth for $t/\ell \sim 1.25$, which reflects the maximum velocity being $v_{\text{max}} \sim 0.4$. For larger times we observe a slow decrease toward zero for $t/\ell \rightarrow \infty$. This slow decay is due to the slower quasiparticles with $v < v_{\text{max}}$. The solid line is the theoretical prediction in Eq. (29). At finite ℓ and t the data exhibit some small corrections from Eq. (29), which is recovered in the scaling limit $t, \ell \rightarrow \infty$ with their ratio fixed.

It is also useful to investigate directly the validity of Eq. (31), which establishes a relationship between $R_n^{(f/b)}$ and the mutual information. To this aim, we introduce the difference $d_n^{(f/b)}$ as

$$d_n^{(f/b)} = \begin{cases} \ln(R_n^{(f/b)}) - (1-n)I_{A_1:A_2}^{(n/2)} & n \text{ even} \\ \ln(R_n^{(f/b)}) - (1-n)\frac{I_{A_1:A_2}^{(n)}}{2}, & n \text{ odd.} \end{cases} \quad (39)$$

As it is clear from the insets in Fig. 4, $d_n^{(b)}$ is very small in the region of linear growth, i.e., for $2v_{\text{max}}t/\ell \leq 1$ (an obvious fact, since in the scaling limit it is just $0 - 0$). At fixed ℓ , in the nontrivial region, i.e., for larger values of the scaling variable $2v_{\text{max}}t/\ell$, $d_n^{(b)}$ is larger. However, at fixed t/ℓ , the deviations $d_n^{(b)}$ decrease with increasing ℓ , and in the scaling limit $\ell \rightarrow \infty$ one recovers Eq. (31). Precisely, the data suggest a behavior $d_n^{(b)} \propto 1/\ell$.

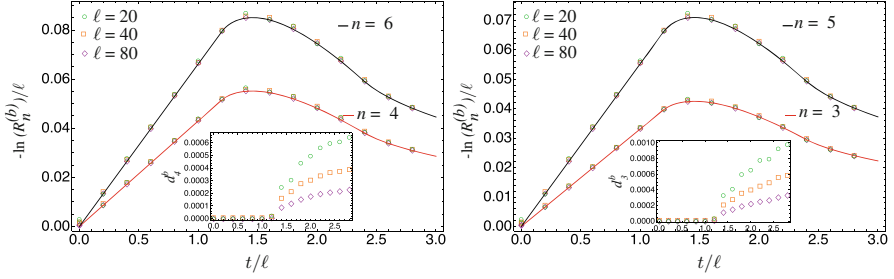


Fig. 4 Logarithms of the moments of the (bosonic) partial transpose after the mass quench from $m_0 = 1$ to $m = 2$ in the harmonic chain. The quantity $-\ln(R_n^{(b)})/\ell$ is plotted versus rescaled time t/ℓ , with ℓ the intervals' length. The analytical predictions represented by continuous lines correspond to Eq. (29). The insets represent Eq. (39) and they prove the validity of Eq. (31), i.e., the connection between the ratio R_n and the Rényi mutual information

5.2 Quench in a Free-Fermion Chain

We now discuss numerical results for free-fermion systems described by the Hamiltonian

$$H = \sum_{j=1}^L \left(\frac{1}{2} [c_j^\dagger c_{j+1}^\dagger + c_{j+1} c_j + c_j^\dagger c_{j+1} + c_{j+1}^\dagger c_j] - h c_j^\dagger c_j \right), \quad (40)$$

where $\{c_i, c_j^\dagger\} = \delta_{ij}$ are anti-commuting fermionic operators, h is a coupling parameter, e.g., a magnetic field, and we neglect boundary terms (we are interested in the thermodynamic limit $L \rightarrow \infty$). A Jordan–Wigner transformation maps the Hamiltonian to the well-known transverse field Ising chain. However, the spin RDM is not simply mapped to the fermion RDM for two disjoint intervals [135, 136]. Instead, for the case of adjacent intervals they are mapped into each other and so the following results for fermions apply also to the spin variables.

In terms of the momentum space Bogoliubov fermions the Hamiltonian is diagonal and the single-particle energies are

$$e(k) = [h^2 - 2h\cos(k) + 1]^{1/2}. \quad (41)$$

We consider the non-equilibrium unitary dynamics that follows from a quench of the field h at $t = 0$ from h_0 to $h \neq h_0$. In order to parametrize the quench it is useful to introduce the angle $\Delta(k)$ as [2]

$$\cos(\Delta(k)) = \frac{1 + hh_0 - (h + h_0)\cos(k)}{e(k)e_0(k)}. \quad (42)$$

As for free bosons, the central object to obtain the quasiparticle prediction is the density $\rho(k)$ of the Bogoliubov fermions. This is given by [137, 138]

$$\rho(k) = \frac{1}{2}(1 - \cos(\Delta(k))). \tag{43}$$

The reduced density matrix can be completely characterized [134] by the two-point correlation functions restricted to the subsystem A . From the covariance matrix associated with ρ_A , one can build the covariance matrix corresponding to the partial time reversal $\rho_A^{R_1}$ (see Ref. [89–94]). The fermionic Rényi negativities $\mathcal{E}_n^{(f)}$ introduced in Eq. (13) can be efficiently computed in terms of the eigenvalues of the covariance matrix.

We discuss the numerical results for both $\mathcal{E}_n^{(f)}$ and $R_n^{(f)}$ for two adjacent intervals in Fig. 5, for the quench with $h_0 = 10$ and $h = 2$. We first discuss the Rényi negativities $\mathcal{E}_n^{(f)}$ in Fig. 4(top) plotting $\mathcal{E}_n^{(f)}/\ell$ versus t/ℓ . We consider only the geometry with two adjacent intervals. The numerical data exhibit the expected behavior as in Fig. 2a. One has $\mathcal{E}_n^{(f)} \leq 0$ at all times. The negatives exhibit a two-slope decrease at short times, which is followed by a saturation at long times.

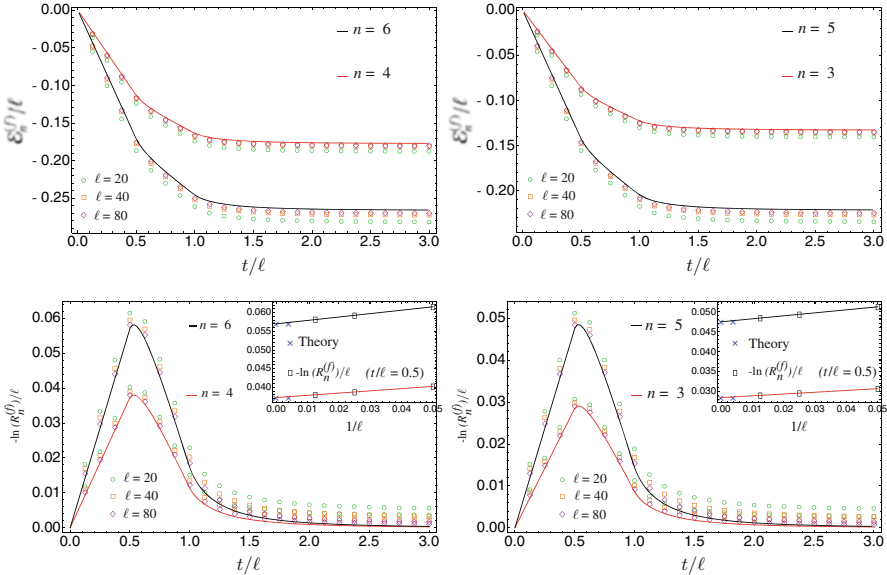


Fig. 5 Logarithms of the moments of the (fermionic) partial transpose after a quench in the fermionic chain (with $h_0 = 10$ and $h = 2$) for two adjacent intervals. Both $-\ln(R_n^{(f)})/\ell$ and $\mathcal{E}_n^{(f)}/\ell$ are plotted versus rescaled time t/ℓ , with ℓ the intervals’ length. The analytical predictions represented by continuous lines correspond to Eq. (28) (top panels) and (29) (bottom panels). The insets investigate the finite-size scaling corrections: the symbols are for the fermionic negativity at fixed $t/\ell = 0.5$; the crosses are the theoretical results in the thermodynamic limit; the solid lines are linear fits

In contrast with the CFT case, the saturation is not abrupt due to the fact that the quasiparticles have a nontrivial dispersion. The different symbols in the figure denote different subsystem size ℓ . In the thermodynamic limit $\ell \rightarrow \infty$ the numerical data approach the prediction of the quasiparticle picture (continuous line in the figure). We discuss the behavior of the ratios $-\ln(R_n^{(f)})$ in Fig. 4(bottom). Again, we consider only the case of adjacent intervals. The data for $-\ln(R_n^{(f)})$ exhibit a linear behavior up to $t/\ell \sim 0.5$, reflecting that $v_{\max} \sim 1$. Similar to the bosonic case, finite-size corrections are present, although the analytical prediction in Eq. (25) is recovered in the scaling limit. In the inset, we also investigate these scaling corrections. The symbols are the data at fixed $t/\ell = 0.5$ while the x -axis shows $1/\ell$. The crosses are the theoretical results in the scaling limit. The solid lines are fits to the behavior $1/\ell$ and are clearly consistent with the data.

We now remind that for free-fermion systems (see Sect. 2) it is not straightforward to compute the standard negativity defined from the partial transpose $\rho_A^{T_1}$. On the other hand, the Rényi negativities can be computed effectively. The reason is that the powers of $\rho_A^{T_1}$ can be written as sum of products of gaussian operators (cf. Eq. (12)). Since each term of the sum is a gaussian operator, its trace can be effectively computed [81, 136]. For instance, for the Rényi negativity $\mathcal{E}_3^{(b)}$, we have to compute

$$\text{Tr}(\rho_A^{T_1})^3 = -\frac{1}{2}\text{Tr}(O_+^3) + \frac{3}{2}\text{Tr}(O_+^2 O_-). \quad (44)$$

By using Eq. (44) the ratio $-\ln(R_3^{(b)})$ can be calculated and, for the quench with $h_0 = 0.1 \rightarrow h = 2$, is reported in Fig. 6. The symbols in the figure are numerical results for $-\ln(R_3^{(b)})$ for two adjacent intervals of length ℓ . The line is the quasiparticle prediction in Eq. (25). The good agreement between the data and the analytic curve confirms that $-\ln(R_n^{(b)})$ and $-\ln(R_n^{(f)})$ are the same in the space-time scaling limit. Interestingly, we observe that the fermionic Rényi negativity $\mathcal{E}_3^{(f)}$ corresponds to the term $\text{Tr}(O_+^2 O_-)$ in Eq. (44), as can be read in Eq. (13). The fact that the quasiparticle description correctly describes both $\text{Tr}(O_+^2 O_-)$ and the weighted sum in Eq. (44) suggests that the terms in Eq. (44) become the same in the space-time scaling limit.

Finally, let us shortly discuss the connection between the reduced density matrices of fermionic and spin models that are connected by the Jordan–Wigner transformation. Due to the non-locality of this transformation, the reduced density matrices corresponding to $A_1 \cup A_2$ in a spin chain model and its fermionic counterpart are usually not equivalent unless A_1 and A_2 are adjacent intervals [81, 88]. The same holds also for the (standard) transposed density matrices, for which the identity in Eq. (12) should be slightly modified to take into account the Jordan–Wigner string along the interval of length d connecting the two blocks in spin models.

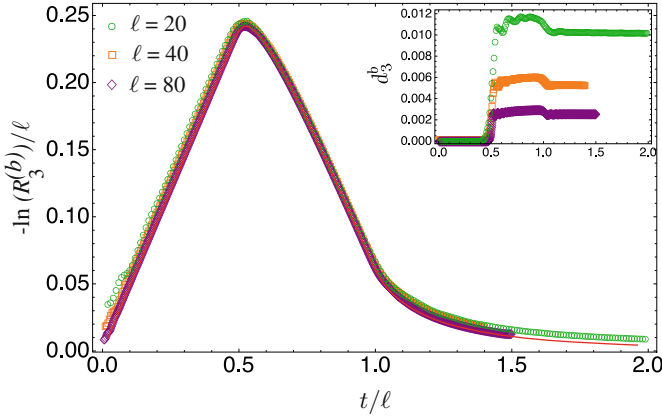


Fig. 6 Standard Rényi negativity for $n = 3$ after a quench in the free-fermion chain (with $h_0 = 0.1$ and $h = 2$). The numerical data (symbols) have been obtained by expanding the third power of $\rho_A^{T_1}$ as in Eq. (44) while the solid red line corresponds to Eq. (29). The inset represents Eq. (39) and it proves the validity of Eq. (31) in the space-time scaling limit

5.3 Quasiparticle Prediction for the p_n -PPT Conditions

Using the quasiparticle predictions obtained in the previous sections for the Rényi negativity, one can write down the quasiparticle formulas for the p_n -PPT conditions introduced in Sect. 2.1, see Eq. (17). For instance, the p_3 -PPT condition quantifies the violation of Eq. (16). Specifically, the condition $D_3 \equiv p_3 - p_2^2 < 0$ signals the presence of quantum entanglement. As explained in Sect. 2.1, other conditions $D_n \geq 0$ can be obtained by considering higher moments of the partial transpose.

We numerically investigate the p_n -PPT conditions in Fig. 7 for $n = 3, 5, 7$, and for quenches in both the fermionic and harmonic chains. We focus on the situation with two adjacent intervals and we are interested in understanding how the p_n -PPT conditions are violated as a function of time. The results in Fig. 7 are obtained by using the quasiparticle picture prediction. As it is clear from the figure, all p_n -PPT conditions are violated at short times in both models. At infinite times all the p_n -PPT conditions give zero. These results are consistent with the behavior of the logarithmic negativity [19].

Also the fine structure of these p_n -PPT conditions is very interesting. In the short-time region with a lot of entanglement (compare with the previous figures for R_n) all the conditions are violated. As the time increases and the entanglement becomes much less, the first condition to be satisfied is p_3 (i.e., $D_3 > 0$) and only after the other one (the panel on the left is particularly clear in this respect). This implies that higher and higher p_n -PPT conditions are necessary to detect the very little amount of entanglement present at large time. This fact is not surprising, but it is remarkable that it is captured so neatly by the quasiparticle picture.

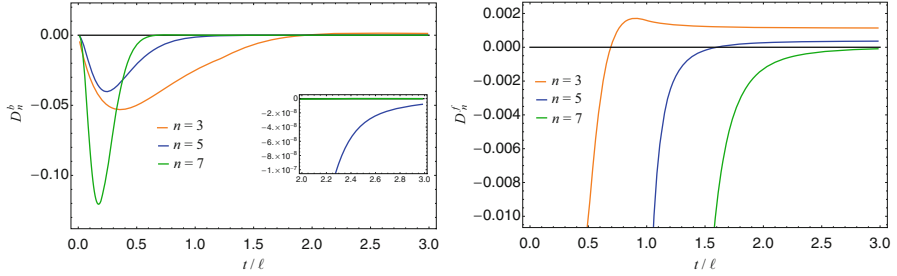


Fig. 7 The p_n -PPT conditions for $n = 3, 5, 7$ for the quasiparticle predictions of the moments of the partial transpose introduced in Eq. (15). The quench parameters are $h_0 = 10, h = 2$ for the fermionic chain and $m = 2, m_0 = 0.1$ for the harmonic chain. We plot the quantity D_n in Eq. (17). The p_n -PPT condition is $D_n \geq 0$. To compare data for different n we multiply the D_5 by 10 and D_7 by 10^6 for bosons ($\ell = 30$). For fermions the D_5 is multiplied by 10^7 and D_7 by 10^{19} ($\ell = 50$). The violation of these conditions for at least one value of n reveals the presence of entanglement between A_1 and A_2

6 Conclusions

In this paper, we derived the quasiparticle picture for the dynamics of the moments of the partially transposed reduced density matrix after a quantum quench in integrable systems, and several related quantities such as the Rényi negativities \mathcal{E}_n (cf. Eq. (9)) and the ratios R_n (cf. Eq. (11)). An interesting result is that the ratio R_n is proportional to the Rényi mutual information. Furthermore, this ratio is qualitatively similar to the negativity and so it is then an indicator of the entanglement barrier for the quench dynamics at intermediate time [19, 139–141]. Moreover, our results allow us to derive the behavior of the p_n -PPT conditions, which in contrast with standard entanglement measures for mixed states, such as the logarithmic negativity, are easily computable and experimentally measurable for quantum many-body systems [15, 16]. We tested our predictions against exact numerical results for both free-fermion and free-boson systems.

We now discuss future research directions. The first natural follow-up of the results presented here is to test numerically the equality between Rényi mutual information and the ratios R_n for interacting integrable models. A possible extension to this work would be to study the dynamics of negativity and the moments of the partial transpose in the presence of a globally conserved charge. While it is known that the negativity of two subsystems may be decomposed into contributions associated with their charge imbalance [18, 75], it would be interesting to understand whether a quasiparticle prediction similar to the one presented for the entropy in Ref.[130] could be worked out. Another important research direction is to investigate the Rényi negativities and the ratios R_n in the presence of dissipation [128].

Acknowledgments P.C. and S.M. acknowledge support from ERC under Consolidator grant number 771536 (NEMO). V.A. acknowledges support from the European Research Council under ERC Advanced grant No. 743032 DYNAMINT.

References

1. P. Calabrese, J. Cardy, Time dependence of correlation functions following a quantum quench. *Phys. Rev. Lett.* **96**, 136801 (2006). <https://doi.org/10.1103/PhysRevLett.96.136801>
2. P. Calabrese, J. Cardy, Quantum quenches in extended systems. *J. Stat. Mech.* P06008 (2007). <https://doi.org/10.1088/1742-5468/2005/04/P04010>
3. P. Calabrese, J. Cardy, Evolution of entanglement entropy in one-dimensional systems. *J. Stat. Mech.* P04010 (2005). <https://doi.org/10.1088/1742-5468/2005/04/P04010>
4. V. Alba, P. Calabrese, Entanglement and thermodynamics after a quantum quench in integrable systems. *PNAS* **114**, 7947 (2017). <https://doi.org/10.1073/pnas.1703516114>
5. V. Alba, P. Calabrese, Entanglement dynamics after quantum quenches in generic integrable systems. *SciPost Phys.* **4**, 017 (2018). <https://doi.org/10.21468/SciPostPhys.4.3.017>
6. P. Calabrese, *Entanglement Spreading in Non-equilibrium Integrable Systems*. Lectures for Les Houches Summer School on “Integrability in Atomic and Condensed Matter Physics”. *SciPost Physics Lecture Notes*, vol. 20 (2020). <https://doi.org/10.21468/SciPostPhysLectNotes.20>
7. A.M. Kaufman, M.E. Tai, A. Lukin, M. Rispoli, R. Schittko, P.M. Preiss, M. Greiner, Quantum thermalisation through entanglement in an isolated many-body system. *Science* **353**, 794 (2016). <https://doi.org/10.1126/science.aaf6725>
8. A. Elben, B. Vermersch, M. Dalmonte, J.I. Cirac, P. Zoller, Rényi entropies from random quenches in atomic Hubbard and spin models. *Phys. Rev. Lett.* **120**, 050406 (2018). <https://doi.org/10.1103/PhysRevLett.120.050406>
9. T. Brydges, A. Elben, P. Jurcevic, B. Vermersch, C. Maier, B.P. Lanyon, P. Zoller, R. Blatt, C.F. Roos, Probing entanglement entropy via randomized measurements. *Science* **364**, 260 (2019). <https://doi.org/10.1126/science.aau4963>
10. A. Lukin, M. Rispoli, R. Schittko, M.E. Tai, A.M. Kaufman, S. Choi, V. Khemani, J. Leonard, M.Z. Greiner, Probing entanglement in a many-body localized system. *Science* **364**, 256 (2019). <https://doi.org/10.1126/science.aau0818>
11. A. Peres, Separability criterion for density matrices. *Phys. Rev. Lett.* **77**, 1413 (1996). <https://doi.org/10.1103/PhysRevLett.77.1413>
12. R. Simon, Peres-Horodecki separability criterion for continuous variable systems. *Phys. Rev. Lett.* **84**, 2726 (2000). <https://doi.org/10.1103/PhysRevLett.84.2726>
13. G. Vidal, R.F. Werner, A computable measure of entanglement. *Phys. Rev. A* **65**, 032314 (2002). <https://doi.org/10.1103/PhysRevA.65.032314>
14. M.B. Plenio, Logarithmic negativity: a full entanglement monotone that is not convex. *Phys. Rev. Lett.* **95**, 090503 (2005); J. Eisert, Entanglement in quantum information theory. <https://doi.org/10.1103/PhysRevLett.95.090503>. <https://arxiv.org/abs/quant-ph/0610253>
15. A. Elben, R. Kueng, H.-Y. Huang, R. van Bijnen, C. Kokail, M. Dalmonte, P. Calabrese, B. Kraus, J. Preskill, P. Zoller, B. Vermersch, Mixed-state entanglement from local randomized measurements. *Phys. Rev. Lett.* **125**, 200501 (2020). <https://doi.org/10.1103/PhysRevLett.125.200501>
16. A. Neven, J. Carrasco, V. Vitale, C. Kokail, A. Elben, M. Dalmonte, P. Calabrese, P. Zoller, B. Vermersch, R. Kueng, B. Kraus, Symmetry-resolved entanglement detection using partial transpose moments. *NPJ Quantum Inf.* **7**, 152 (2021). <https://doi.org/10.1038/s41534-021-00487-y>
17. J. Gray, L. Banchi, A. Bayat, S. Bose, Machine learning assisted many-body entanglement measurement. *Phys. Rev. Lett.* **121**, 150503 (2018). <https://doi.org/10.1103/PhysRevLett.121.150503>

18. E. Cornfeld, E. Sela, M. Goldstein, Measuring fermionic entanglement: entropy, negativity, and spin structure. *Phys. Rev. A* **99**, 062309 (2019). <https://doi.org/10.1103/PhysRevA.99.062309>
19. V. Alba, P. Calabrese, Quantum information dynamics in multipartite integrable systems. *EPL* **126**, 60001 (2019). <https://doi.org/10.1209/0295-5075/126/60001>
20. A. Coser, E. Tonni, P. Calabrese, Entanglement negativity after a global quantum quench. *J. Stat. Mech.* P12017 (2014). <https://doi.org/10.1088/1742-5468/2014/12/p12017>
21. X. Wen, P.-Y. Chang, S. Ryu, Entanglement negativity after a local quantum quench in conformal field theories. *Phys. Rev. B* **92**, 075109 (2015). <https://doi.org/10.1103/PhysRevB.92.075109>
22. J. Kudler-Flam, H. Shapourian, S. Ryu, The negativity contour: a quasi-local measure of entanglement for mixed states. *SciPost Phys.* **8**, 063 (2020). <https://doi.org/10.21468/SciPostPhys.8.4.063>
23. P. Calabrese, J. Cardy, E. Tonni, Entanglement negativity in quantum field theory. *Phys. Rev. Lett.* **109**, 130502 (2012). <https://doi.org/10.1103/PhysRevLett.109.130502>
24. P. Calabrese, J. Cardy, E. Tonni, Entanglement negativity in extended systems: a field theoretical approach. *J. Stat. Mech.* P02008 (2013). <https://doi.org/10.1088/1742-5468/2013/02/P02008>
25. V. Alba, Entanglement negativity and conformal field theory: a Monte Carlo study. *J. Stat. Mech.* P05013 (2013). <https://doi.org/10.1088/1742-5468/2013/05/P05013>
26. C.-M. Chung, V. Alba, L. Bonnes, P. Chen, A.M. Lauchli, Entanglement negativity via replica trick: a Quantum Monte Carlo approach. *Phys. Rev. B* **90**, 064401 (2014). <https://doi.org/10.1103/PhysRevB.90.064401>
27. P. Calabrese, L. Tagliacozzo, E. Tonni, Entanglement negativity in the critical Ising chain. *J. Stat. Mech.* P05002 (2013). <https://doi.org/10.1088/1742-5468/2013/05/P05002>
28. K.-H. Wu, T.-C. Lu, C.-M. Chung, Y.-J. Kao, T. Grover, Entanglement Rényi negativity across a finite temperature transition: a Monte Carlo study. *Phys. Rev. Lett.* **125**, 140603 (2020). <https://doi.org/10.1103/PhysRevLett.125.140603>
29. T.-C. Lu, T. Grover, Entanglement transitions as a probe of quasiparticles and quantum thermalization. *Phys. Rev. B* **102**, 235110 (2020). <https://doi.org/10.1103/PhysRevB.102.235110>
30. E. Wybo, M. Knap, F. Pollmann, Entanglement dynamics of a many-body localized system coupled to a bath. *Phys. Rev. B* **102**, 064304 (2020). <https://doi.org/10.1103/PhysRevB.102.064304>
31. L. Amico, R. Fazio, A. Osterloh, V. Vedral, Entanglement in many-body systems. *Rev. Mod. Phys.* **80**, 517 (2008). <https://doi.org/10.1103/RevModPhys.80.517>
32. P. Calabrese, J. Cardy, B. Doyon, Entanglement entropy in extended quantum systems. *J. Phys. A* **42**, 500301 (2009). <https://doi.org/10.1088/1751-8121/42/50/500301>
33. J. Eisert, M. Cramer, M.B. Plenio, Area laws for the entanglement entropy. *Rev. Mod. Phys.* **82**, 277 (2010). <https://doi.org/10.1103/RevModPhys.82.277>
34. N. Laflorencie, Quantum entanglement in condensed matter systems. *Phys. Rep.* **643**, 1 (2016). <https://doi.org/10.1016/j.physrep.2016.06.008>
35. R. Islam, R. Ma, P.M. Preiss, M.E. Tai, A. Lukin, M. Rispoli, M. Greiner, Measuring entanglement entropy in a quantum many-body system. *Nature* **528**, 77 (2015). <https://doi.org/10.1038/nature15750>
36. V. Vitale, A. Elben, R. Kueng, A. Neven, J. Carrasco, B. Kraus, P. Zoller, P. Calabrese, B. Vermersch, M. Dalmonte, Symmetry-resolved dynamical purification in synthetic quantum matter. <https://arxiv.org/abs/2101.07814>
37. P. Calabrese, A. Lefevre, Entanglement spectrum in one-dimensional systems. *Phys. Rev. A* **78**, 032329(R) (2008). <https://doi.org/10.1103/PhysRevA.78.032329>
38. C.G. Callan, F. Wilczek, On geometric entropy. *Phys. Lett. B* **333**, 55 (1994). [https://doi.org/10.1016/0370-2693\(94\)91007-3](https://doi.org/10.1016/0370-2693(94)91007-3)
39. P. Calabrese, J. Cardy, Entanglement entropy and quantum field theory. *J. Stat. Mech.* P06002 (2004). <https://doi.org/10.1088/1742-5468/2004/06/P06002>

40. P. Calabrese, J. Cardy, Entanglement entropy and conformal field theory. *J. Phys. A* **42**, 504005 (2009). <https://doi.org/10.1088/1751-8113/42/50/504005>
41. M. Kormos, Z. Zimboras, Temperature driven quenches in the Ising model: appearance of negative Rényi mutual information. *J. Phys. A* **50**, 264005 (2017). <https://doi.org/10.1088/1751-8121/aa70f6>
42. S.O. Scalet, A.M. Alhambra, G. Styliaris, J.I. Cirac, Computable Rényi mutual information: area laws and correlations. *Quantum* **5**, 541 (2021). <https://doi.org/10.22331/q-2021-09-14-541>
43. K. Audenaert, J. Eisert, M.B. Plenio, R.F.Werner, Entanglement properties of the harmonic chain. *Phys. Rev. A* **66**, 042327 (2002). <https://doi.org/10.1103/PhysRevA.66.042327>
44. A. Ferraro, D. Cavalcanti, A. García Saez, A. Acín, Thermal bound entanglement in macroscopic systems and area law. *Phys. Rev. Lett.* **100**, 080502 (2008). <https://doi.org/10.1103/PhysRevLett.100.080502>
45. D. Cavalcanti, A. Ferraro, A. García Saez, A. Acín, Distillable entanglement and area laws in spin and harmonic-oscillator systems. *Phys. Rev. A* **78**, 012335 (2008). <https://doi.org/10.1103/PhysRevA.78.012335>
46. J. Anders, W. Andreas, Entanglement and separability of quantum harmonic oscillator systems at finite temperature. *Quantum Inf. Comput.* **8**, 0245 (2008). <https://arxiv.org/abs/0705.3026>
47. J. Anders, Thermal state entanglement in harmonic lattices. *Phys. Rev. A* **77**, 062102 (2008). <https://doi.org/10.1103/PhysRevA.77.062102>
48. S. Marcovitch, A. Retzker, M.B. Plenio, B. Reznik, Critical and noncritical long-range entanglement in Klein-Gordon fields. *Phys. Rev. A* **80**, 012325 (2009). <https://doi.org/10.1103/PhysRevA.80.012325>
49. V. Eisler, Z. Zimborás, Entanglement negativity in the harmonic chain out of equilibrium. *New J. Phys.* **16**, 123020 (2014). <https://doi.org/10.1088/1367-2630/16/12/123020>
50. N.E. Sherman, T. Devakul, M.B. Hastings, R.R.P. Singh, Nonzero-temperature entanglement negativity of quantum spin models: area law, linked cluster expansions, and sudden death. *Phys. Rev. E* **93**, 022128 (2016). <https://doi.org/10.1103/PhysRevE.93.022128>
51. C.D. Nobili, A. Coser, E. Tonni, Entanglement negativity in a two dimensional harmonic lattice: area law and corner contributions. *J. Stat. Mech.* 083102 (2016). <https://doi.org/10.1088/1742-5468/2016/08/083102>
52. H. Wichterich, J. Molina-Vilaplana, S. Bose, Scaling of entanglement between separated blocks in spin chains at criticality. *Phys. Rev. A* **80**, 010304 (2009). <https://doi.org/10.1103/PhysRevA.80.010304>
53. A. Bayat, S. Bose, P. Sodano, Entanglement routers using macroscopic singlets. *Phys. Rev. Lett.* **105**, 187204 (2010). <https://doi.org/10.1103/PhysRevLett.105.187204>
54. A. Bayat, S. Bose, P. Sodano, H. Johannesson, Entanglement probe of two-impurity Kondo physics in a spin chain. *Phys. Rev. Lett.* **109**, 066403 (2012). <https://doi.org/10.1103/PhysRevLett.109.066403>
55. H. Wichterich, J. Vidal, S. Bose, Universality of the negativity in the Lipkin-Meshkov-Glick model. *Phys. Rev. A* **81**, 032311 (2010). <https://doi.org/10.1103/PhysRevA.81.032311>
56. R.A. Santos, V. Korepin, S. Bose, Negativity for two blocks in the one-dimensional spin-1 Affleck-Kennedy-Lieb-Tasaki model. *Phys. Rev. A* **84**, 062307 (2011). <https://doi.org/10.1103/PhysRevA.84.062307>
57. A. Bayat, P. Sodano, S. Bose, Negativity as the entanglement measure to probe the Kondo regime in the spin-chain Kondo model. *Phys. Rev. B* **81**, 064429 (2010). <https://doi.org/10.1103/PhysRevB.81.064429>
58. T.C. Lu, T. Grover, Singularity in entanglement negativity across finite temperature phase transitions. *Phys. Rev. B* **99**, 075157 (2019). <https://doi.org/10.1103/PhysRevB.99.075157>
59. P. Ruggiero, V. Alba, P. Calabrese, Entanglement negativity in random spin chains. *Phys. Rev. B* **94**, 035152 (2016). <https://doi.org/10.1103/PhysRevB.94.035152>
60. X. Turkeshi, P. Ruggiero, P. Calabrese, Negativity spectrum in the random singlet phase. *Phys. Rev. B* **101**, 064207 (2020). <https://doi.org/10.1103/PhysRevB.101.064207>

61. G.B. Mbeng, V. Alba, P. Calabrese, Negativity spectrum in 1D gapped phases of matter. *J. Phys. A* **50**, 194001 (2017). <https://doi.org/10.1088/1751-8121/aa6734>
62. S. Wald, R. Arias, V. Alba, Entanglement and classical fluctuations at finite-temperature critical points. *J. Stat. Mech.* 033105 (2020). <https://doi.org/10.1088/1742-5468/ab6b19>
63. H. Shapourian, S. Liu, J. Kudler-Flam, A. Vishwanath, Entanglement negativity spectrum of random mixed states: a diagrammatic approach. *PRX Quant.* **2**, 030347 (2021). <https://doi.org/10.1103/PRXQuantum.2.030347>
64. P. Calabrese, J. Cardy, E. Tonni, Finite temperature entanglement negativity in conformal field theory. *J. Phys. A* **48**, 015006 (2015). <https://doi.org/10.1088/1751-8113/48/1/015006>
65. P. Ruggiero, V. Alba, P. Calabrese, Negativity spectrum of one-dimensional conformal field theories. *Phys. Rev. B* **94**, 195121 (2016). <https://doi.org/10.1103/PhysRevB.94.195121>
66. V. Alba, P. Calabrese, E. Tonni, Entanglement spectrum degeneracy and the Cardy formula in 1+1 dimensional conformal field theories. *J. Phys. A* **51**, 024001 (2018). <https://doi.org/10.1088/1751-8121/aa9365>
67. M. Kulaxizi, A. Parnachev, G. Policastro, Conformal blocks and negativity at large central charge. *JHEP* **09**, 010 (2014). [https://doi.org/10.1007/JHEP09\(2014\)010](https://doi.org/10.1007/JHEP09(2014)010)
68. C. De Nobili, A. Coser, E. Tonni, Entanglement entropy and negativity of disjoint intervals in CFT: some numerical extrapolations. *J. Stat. Mech.* P06021 (2015). <https://doi.org/10.1088/1742-5468/2015/06/P06021>
69. D. Bianchini, O.A. Castro-Alvaredo, Branch point twist field correlators in the massive free Bessel theory. *Nucl. Phys. B* **913**, 879 (2016). <https://doi.org/10.1016/j.nuclphysb.2016.10.016>
70. O. Blondeau-Fournier, O.A. Castro-Alvaredo, B. Doyon, Universal scaling of the logarithmic negativity in massive quantum field theory. *J. Phys. A* **49**, 125401 (2016). <https://doi.org/10.1088/1751-8113/49/12/125401>
71. O.A. Castro-Alvaredo, C. De Fazio, B. Doyon, I.M. Szecsenyi, Entanglement content of quantum particle excitations II. Disconnected regions and logarithmic negativity. *JHEP* **11**, 58 (2019). [https://doi.org/10.1007/JHEP11\(2019\)058](https://doi.org/10.1007/JHEP11(2019)058)
72. O.A. Castro-Alvaredo, C. De Fazio, B. Doyon, I.M. Szecsenyi, Entanglement content of quantum particle excitations III. Graph partition functions. *J. Math. Phys.* **60**, 082301 (2019). <https://doi.org/10.1063/1.5098892>
73. J. Kudler-Flam, S. Ryu, Entanglement negativity and minimal entanglement wedge cross sections in holographic theories. *Phys. Rev. D* **99**, 106014 (2019). <https://doi.org/10.1103/PhysRevD.99.106014>
74. F. Ares, R. Santachiara, J. Viti, Crossing-symmetric twist field correlators and entanglement negativity in minimal CFTs. *JHEP* **10**, 175 (2021). [https://doi.org/10.1007/JHEP10\(2021\)175](https://doi.org/10.1007/JHEP10(2021)175)
75. S. Murciano, R. Bonsignori, P. Calabrese, Symmetry decomposition of negativity of massless free fermions. *SciPost Phys.* **10**, 111 (2021). <https://doi.org/10.21468/SciPostPhys.10.5.111>
76. M. Hoogeveen, B. Doyon, Entanglement negativity and entropy in non-equilibrium conformal field theory. *Nucl. Phys. B* **898**, 78 (2015). <https://doi.org/10.1016/j.nuclphysb.2015.06.021>
77. M.J. Gullans, D.A. Huse, Entanglement structure of current-driven diffusive fermion systems. *Phys. Rev. X* **9**, 021007 (2019). <https://doi.org/10.1103/PhysRevX.9.021007>
78. J. Kudler-Flam, Y. Kusuki, S. Ryu, Correlation measures and the entanglement wedge cross-section after quantum quenches in two-dimensional conformal field theories. *JHEP* **04**, 074 (2020). [https://doi.org/10.1007/JHEP04\(2020\)074](https://doi.org/10.1007/JHEP04(2020)074)
79. J. Kudler-Flam, Y. Kusuki, S. Ryu, The quasi-particle picture and its breakdown after local quenches: mutual information, negativity, and reflected entropy. *JHEP* **03**, 146 (2021). [https://doi.org/10.1007/JHEP03\(2021\)146](https://doi.org/10.1007/JHEP03(2021)146)
80. B. Shi, X. Dai, Y.-M. Lu, Entanglement negativity at the critical point of measurement-driven transition. <https://arxiv.org/abs/2012.00040>
81. V. Eisler, Z. Zimborás, On the partial transpose of fermionic Gaussian states. *New J. Phys.* **17**, 053048 (2015). <https://doi.org/10.1088/1367-2630/17/5/053048>
82. A. Coser, E. Tonni, P. Calabrese, Towards the entanglement negativity of two disjoint intervals for a one dimensional free fermion. *J. Stat. Mech.* 033116 (2016). <https://doi.org/10.1088/1742-5468/2016/03/033116>

83. A. Coser, E. Tonni, P. Calabrese, Spin structures and entanglement of two disjoint intervals in conformal field theories. *J. Stat. Mech.* 053109 (2016). <https://doi.org/10.1088/1742-5468/2016/05/053109>
84. V. Eisler, Z. Zimborás, Entanglement negativity in two-dimensional free lattice models. *Phys. Rev. B* **93**, 115148 (2016). <https://doi.org/10.1103/PhysRevB.93.115148>
85. P.-Y. Chang, X. Wen, Entanglement negativity in free-fermion systems: an overlap matrix approach. *Phys. Rev. B* **93**, 195140 (2016). <https://doi.org/10.1103/PhysRevB.93.195140>
86. C.P. Herzog, Y. Wang, Estimation for entanglement negativity of free fermions. *YITP-SB-15-17* (2016). <https://doi.org/10.1088/1742-5468/2016/07/073102>
87. J. Eisert, V. Eisler, Z. Zimborás, Entanglement negativity bounds for fermionic Gaussian states. *Phys. Rev. B* **97**, 165123 (2018). <https://doi.org/10.1103/PhysRevB.97.165123>
88. A. Coser, E. Tonni, P. Calabrese, Partial transpose of two disjoint blocks in XY spin chains. *J. Stat. Mech.* P08005 (2015). <https://doi.org/10.1088/1742-5468/2015/08/P08005>
89. H. Shapourian, K. Shiozaki, S. Ryu, Many-body topological invariants for fermionic symmetry-protected topological phases. *Phys. Rev. Lett.* **118**, 216402 (2017). <https://doi.org/10.1103/PhysRevLett.118.216402>
90. K. Shiozaki, H. Shapourian, K. Gomi, S. Ryu, Many-body topological invariants for fermionic short-range entangled topological phases protected by antiunitary symmetries. *Phys. Rev. B* **98**, 035151 (2018). <https://doi.org/10.1103/PhysRevB.98.035151>
91. H. Shapourian, S. Ryu, Entanglement negativity of fermions: monotonicity, separability criterion, and classification of few-mode states. *Phys. Rev. A* **99**, 022310 (2019). <https://doi.org/10.1103/PhysRevA.99.022310>
92. H. Shapourian, K. Shiozaki, S. Ryu, Partial time-reversal transformation and entanglement negativity in fermionic systems. *Phys. Rev. B* **95**, 165101 (2017). <https://doi.org/10.1103/PhysRevB.95.165101>
93. H. Shapourian, S. Ryu, Finite-temperature entanglement negativity of free fermions. *J. Stat. Mech.* 043106 (2019). <https://doi.org/10.1088/1742-5468/ab11e0>
94. H. Shapourian, P. Ruggiero, S. Ryu, P. Calabrese, Twisted and untwisted negativity spectrum of free fermions. *SciPost Phys.* **7**, 037 (2019). <https://doi.org/10.21468/SciPostPhys.7.3.037>
95. H. Shapourian, R.S.K. Mong, S. Ryu, Anyonic partial transpose I: quantum information aspects. <https://arxiv.org/abs/2012.02222>
96. J.L. Cardy, O.A. Castro-Alvaredo, B. Doyon, Form factors of branch-point twist fields in quantum integrable models and entanglement entropy. *J. Stat. Phys.* **130**, 129 (2008). <https://doi.org/10.1007/s10955-007-9422-x>
97. B. Bertini, E. Tartaglia, P. Calabrese, Quantum quench in the infinitely repulsive Hubbard model: the stationary state. *J. Stat. Mech.* 103107 (2017). <https://doi.org/10.1088/1742-5468/aa8c2c>
98. B. Bertini, E. Tartaglia, P. Calabrese, Entanglement and diagonal entropies after a quench with no pair structure. *J. Stat. Mech.* 063104 (2018). <https://doi.org/10.1088/1742-5468/aac73f>
99. A. Bastianello, P. Calabrese, Spreading of entanglement and correlations after a quench with intertwined quasiparticles. *SciPost Phys.* **5**, 033 (2018). <https://doi.org/10.21468/SciPostPhys.5.4.033>
100. A. Bastianello, M. Collura, Entanglement spreading and quasiparticle picture beyond the pair structure. *SciPost Phys.* **8**, 045 (2020). <https://doi.org/10.21468/SciPostPhys.8.3.045>
101. L. Piroli, B. Pozsgay, E. Vernier, What is an integrable quench? *Nucl. Phys. B* **925**, 362 (2017). <https://doi.org/10.1016/j.nuclphysb.2017.10.012>
102. M. Fagotti, P. Calabrese, Evolution of entanglement entropy following a quantum quench: analytic results for the XY chain in a transverse magnetic field. *Phys. Rev. A* **78**, 010306 (2008). <https://doi.org/10.1103/PhysRevA.78.010306>
103. P. Calabrese, F.H.L. Essler, G. Mussardo, Introduction to “Quantum integrability in out of equilibrium systems”. *J. Stat. Mech.* 064001 (2016). <https://doi.org/10.1088/1742-5468/2016/06/064001>
104. L. Vidmar, M. Rigol, Generalized Gibbs ensemble in integrable lattice models. *J. Stat. Mech.* 064007 (2016). <https://doi.org/10.1088/1742-5468/2016/06/064007>

105. F.H.L. Essler, M. Fagotti, Generalized Gibbs ensemble in integrable lattice models. *J. Stat. Mech.* 064002 (2016). <https://doi.org/10.1088/1742-5468/2016/06/064002>
106. L. Bonnes, F.H.L. Essler, A.M. Läuchli, Light-cone dynamics after quantum quenches in spin chains. *Phys. Rev. Lett.* **113**, 187203 (2014). <https://doi.org/10.1103/PhysRevLett.113.187203>
107. M. Mestyán, B. Bertini, L. Piroli, P. Calabrese, Exact solution for the quench dynamics of a nested integrable system. *J. Stat. Mech.* 083103 (2017). <https://doi.org/10.1088/1742-5468/aa7df0>
108. L. Piroli, E. Vernier, P. Calabrese, B. Pozsgay, Integrable quenches in nested spin chains I: the exact steady states. *J. Stat. Mech.* 063103 (2019). <https://doi.org/10.1088/1742-5468/ab1c51>
109. L. Piroli, E. Vernier, P. Calabrese, M. Rigol, Correlations and diagonal entropy after quantum quenches in XXZ chains. *Phys. Rev. B* **95**, 054308 (2017). <https://doi.org/10.1103/PhysRevB.95.054308>
110. R. Modak, L. Piroli, P. Calabrese, Correlations and entanglement spreading in nested spin chains. *J. Stat. Mech.* 093106 (2019). <https://doi.org/10.1088/1742-5468/ab39d5>
111. V. Alba, P. Calabrese, Quench action and Rényi entropies in integrable systems. *Phys. Rev. B* **96**, 115421 (2017). <https://doi.org/10.1103/PhysRevB.96.115421>
112. V. Alba, P. Calabrese, Rényi entropies after releasing the Néel state in the XXZ spin-chain. *J. Stat. Mech.* 113105 (2017). <https://doi.org/10.1088/1742-5468/aa934c>
113. M. Mestyán, V. Alba, P. Calabrese, Rényi entropies of generic thermodynamic macrostates in integrable systems. *J. Stat. Mech.* 083104 (2018). <https://doi.org/10.1088/1742-5468/aad6b9>
114. K. Klobas, B. Bertini, L. Piroli, Exact thermalization dynamics in the “Rule 54” Quantum Cellular Automaton. *Phys. Rev. Lett.* **126**, 160602 (2021). <https://doi.org/10.1103/PhysRevLett.126.160602>
115. K. Klobas, B. Bertini, Entanglement dynamics in Rule 54: exact results and quasiparticle picture. <https://arxiv.org/abs/2104.04513>
116. V. Alba, P. Calabrese, Quantum information scrambling after a quantum quench. *Phys. Rev. B* **100**, 115150 (2019). <https://doi.org/10.1103/PhysRevB.100.115150>
117. R. Modak, V. Alba, P. Calabrese, Entanglement revivals as a probe of scrambling in finite quantum systems. *J. Stat. Mech.* 083110 (2020). <https://doi.org/10.1088/1742-5468/aba9d9>
118. O.A. Castro-Alvaredo, B. Doyon, T. Yoshimura, Emergent hydrodynamics in integrable quantum systems out of equilibrium. *Phys. Rev. X* **6**, 041065 (2016). <https://link.aps.org/doi/10.1103/PhysRevX.6.041065>
119. B. Bertini, M. Collura, J. De Nardis, M. Fagotti, Transport in out-of-equilibrium XXZ chains: exact profiles of charges and currents. *Phys. Rev. Lett.* **117**, 207201 (2016). <https://doi.org/10.1103/PhysRevLett.117.207201>
120. V. Alba, Towards a generalized hydrodynamics description of Rényi entropies in integrable systems. *Phys. Rev. B* **99**, 045150 (2019). <https://doi.org/10.1103/PhysRevB.99.045150>
121. V. Alba, Entanglement and quantum transport in integrable systems. *Phys. Rev. B* **97**, 245135 (2018). <https://doi.org/10.1103/PhysRevB.97.245135>
122. V. Alba, B. Bertini, M. Fagotti, Entanglement evolution and generalised hydrodynamics: interacting integrable systems. *SciPost Phys.* **7**, 005 (2019). <https://doi.org/10.21468/SciPostPhys.7.1.005>
123. B. Bertini, M. Fagotti, L. Piroli, P. Calabrese, Entanglement evolution and generalised hydrodynamics: noninteracting systems. *J. Phys. A* **51**, 39LT01 (2018). <https://doi.org/10.1088/1751-8121/aad82e>
124. M. Mestyán, V. Alba, Molecular dynamics simulation of entanglement spreading in generalised hydrodynamics. *SciPost Phys.* **8**, 055 (2020). <https://doi.org/10.21468/SciPostPhys.8.4.055>
125. V. Alba, B. Bertini, M. Fagotti, L. Piroli, P. Ruggiero, Generalized-hydrodynamic approach to inhomogeneous quenches: correlations, entanglement and quantum effects. <https://arxiv.org/abs/2104.00656>
126. V. Alba, Unbounded entanglement production via a dissipative impurity. <https://arxiv.org/abs/2104.10921>

127. V. Alba, F. Carollo, Spreading of correlations in Markovian open quantum systems. *Phys. Rev. B* **103**, 020302 (2021). <https://doi.org/10.1103/PhysRevB.103.L020302>
128. F. Carollo, V. Alba, Emergent dissipative quasi-particle picture in noninteracting Markovian open quantum systems. <https://arxiv.org/abs/2106.11997>
129. V. Alba, F. Carollo, Hydrodynamics of quantum entropies in Ising chains with linear dissipation. <https://arxiv.org/abs/2109.01836>
130. G. Perez, R. Bonsignori, P. Calabrese, Quasiparticle dynamics of symmetry-resolved entanglement after a quench: examples of conformal field theories and free fermions. *Phys. Rev. B* **103**, L041104 (2020). <https://doi.org/10.1103/PhysRevB.103.L041104>
131. G. Perez, R. Bonsignori, P. Calabrese, Exact quench dynamics of symmetry resolved entanglement in a free fermion chain. *J. Stat. Mech.* 093102 (2021). <https://doi.org/10.1088/1742-5468/ac21d7>
132. B. Bertini, P. Calabrese, Prethermalisation and thermalisation in the entanglement dynamics. *Phys. Rev. B* **102**, 094303 (2020). <https://doi.org/10.1103/PhysRevB.102.094303>
133. P. Calabrese, Entanglement and thermodynamics in non-equilibrium isolated quantum systems. *Physica A* **504**, 31 (2018). <https://doi.org/10.1016/j.physa.2017.10.011>
134. V. Eisler, I. Peschel, Reduced density matrices and entanglement entropy in free lattice models. *J. Phys. A* **42**, 504003 (2009). <https://doi.org/10.1088/1751-8113/42/50/504003>
135. F. Igloi, I. Peschel, On reduced density matrices for disjoint subsystems. *EPL* **89**, 40001 (2010). <https://doi.org/10.1209/0295-5075/89/40001>
136. M. Fagotti, P. Calabrese, Entanglement entropy of two disjoint blocks in XY chains. *J. Stat. Mech.* P04016 (2010). <https://doi.org/10.1088/1742-5468/2010/04/P04016>
137. P. Calabrese, F.H.L. Essler, M. Fagotti, Quantum quench in the transverse-field Ising chain. *Phys. Rev. Lett.* **106**, 227203 (2011). <https://doi.org/10.1103/PhysRevLett.106.227203>
138. P. Calabrese, F.H.L. Essler, M. Fagotti, Quantum quench in the transverse field Ising chain I: time evolution of order parameter correlators. *J. Stat. Mech.* P07016 (2012). <https://doi.org/10.1088/1742-5468/2012/07/P07016>
139. J. Dubail, Entanglement scaling of operators: a conformal field theory approach, with a glimpse of simulability of long-time dynamics in 1+1d. *J. Phys. A* **50**, 234001 (2017). <https://doi.org/10.1088/1751-8121/aa6f38>
140. E. Leviatan, F. Pollmann, J.H. Bardarson, D.A. Huse, E. Altman, Quantum thermalization dynamics with Matrix-Product States. <https://arxiv.org/abs/1702.08894>
141. C. Jonay, D.A. Huse, A. Nahum, Coarse-grained dynamics of operator and state entanglement. <https://arxiv.org/abs/1803.00089>

Phases and Dynamics of Ultracold Bosons in a Tilted Optical Lattice



Krishnendu Sengupta

Abstract We present a brief overview of the phases and dynamics of ultracold bosons in an optical lattice in the presence of a tilt. We begin with a brief summary of the possible experimental setup for generating the tilt. This is followed by a discussion of the effective low-energy model for these systems and its equilibrium phases. We also chart the relation of this model to the recently studied system of ultracold Rydberg atoms. Next, we discuss the non-equilibrium dynamics of this model for quench, ramp, and periodic protocols with emphasis on the periodic drive which can be understood in terms of an analytic, albeit perturbative, Floquet Hamiltonian derived using Floquet perturbation theory (FPT). Finally, taking cue from the Floquet Hamiltonian of the periodically driven tilted boson chain, we discuss a spin model which exhibits Hilbert space fragmentation and exact dynamical freezing for wide range of initial states.

1 Introduction

The physics of ultracold bosonic atoms in an optical lattice has attracted tremendous attention in recent years [1–5]. This enthusiasm stemmed from the fact that such a boson system acts as one of the simplest emulator of the Bose-Hubbard model [6]. Thus the study of the low-energy physics of these bosons allows one to access the superfluid-insulator quantum phase transition for ultracold bosons which is well-known to be present in the phase diagram of a clean Bose-Hubbard model [7–12].

The Mott phase of the bosons in this system, at integer filling, constitutes a localized state with no broken symmetry. It was long realized that additional broken translational or other discrete symmetries may lead to interesting strongly interacting phases of matter within the Mott phase. To this end, several theoretical suggestions have been put forth. These include study of bosons with nearest-

K. Sengupta (✉)

School of Physical Sciences, Indian Association for the Cultivation of Science, Jadavpur, India
e-mail: tpks@iacs.res.in

neighbor repulsive interaction leading to the possibility of different competing density-wave ground states at half-filling due to broken translational symmetry. The precise nature of these states depends on the geometry of the underlying lattice leading to a projective symmetry group (PSG) based classification of the possible Mott phases [13–15]. In addition, systems with multiple species and/or spinor bosons have also been studied; the low-energy physics of their Mott phases are mostly controlled by effective models arising out of an order-by-disorder mechanism. The effective Hamiltonians obtained for such bosons may be described in terms of interacting spins which may represent either real spin or species degrees of freedom. These Hamiltonians lead to several spin (or species) ordered bosonic ground states [16–21]. However, experimental realization of such strongly correlated states of bosonic systems has not been yet achieved.

Instead, such a symmetry broken Mott phase was experimentally realized through a slightly unexpected route. The key idea was to generate an “electric field” for these neutral bosons [1, 3, 4]. As shall be detailed later, such a field may be generated experimentally by shifting the center of the trap which confines the bosons leading to a linear potential term in their Hamiltonian. Alternatively, it can also be realized by application of a linearly spatially varying Zeeman magnetic field to spinor bosons. The presence of such a field leads to the realization of bosonic Mott ground states with broken Z_2 symmetry [3, 22]. In addition, it has recently been realized that the model used [22] to describe such systems can also describe the physics of Rydberg chains [23–26]. The study of non-equilibrium dynamics of these Rydberg atoms has shown that they may host several anomalous features [27–35] including scar-induced dynamics [27–32, 36–39] and possibility of drive induced tuning of ergodicity properties [33–35]. The main aim of this chapter is to provide a summary of some of the theoretical and experimental aspects of this rapidly developing field.

The rest of this chapter is organized as follows. In Sect. 2, we provide a brief discussion of the experimental platforms that lead to the realization of such tilted bosons. This is followed by Sect. 3 where we describe a low-energy model which describes the ground states phases of these system and discuss its relation with models describing a chain of ultracold Rydberg atoms. This is followed by Sect. 4 where we discuss non-equilibrium dynamics of the model. Next in Sect. 5 we discuss possible related models with interesting properties which may be realized using such boson platforms. Finally, we conclude in Sect. 6.

2 Experimental Platforms

In this section, we shall describe the essential ingredients of three experimental setups. The first two involves generating a tilt for ultracold bosons in an optical lattice while the third involves Rydberg atoms in one-dimensional (1D) lattice.

The first experiment on tilted bosons in an optical lattice was carried out in Ref. [1]. In this experiment, spinor ^{87}Rb atoms in their angular momenta $F = 2$ and

$m_F = 2$ state (where F is the total and m_F is the azimuthal angular momenta) were cooled in a trap. The trap was chosen to be a cigar shaped magnetic trap with radial and axial frequencies $\nu_{\text{radial}} = 240$ Hz and $\nu_{\text{axial}} = 24$ Hz. The trap included 2×10^5 bosonic atoms. After the condensate was formed, the radial trapping frequency was relaxed to 240 Hz over a time period of 500ms. This led to a spherically symmetric condensate.

To generate an optical lattice, six orthogonal lasers with wavelength $\lambda = 852$ nm were applied. This resulted in a potential of

$$V(x, y, z) = V_0(\sin^2 kx + \sin^2 ky + \sin^2 kz), \quad (1)$$

where $k = 2\pi/\lambda$ and λ is the wavelength of light used for the lasers. For such optical lattices, all energies are typically measured in terms of the recoil energy given by $E_r = \hbar^2 k^2 / (2m)$; this is the basic energy scale in the problem which can be created out of the wavelength λ of the laser and mass m of the atoms. It can be shown that in such a lattice, the atoms see an approximately harmonic potential with strength $V' \simeq \sqrt{V_0 E_r}$ leading to a trapping frequency $\nu_r \simeq V'/h \simeq 30$ kHz. In the experimental setup of Ref. [1], the strength of the trapping potential could be up to $V' = 22E_r$. These values of parameters were sufficient to obtain a Mott insulating state of bosons with one boson per site of the optical lattice.

In addition, to apply the tilt, the center of the trap confining the bosons was shifted. This led to a shifted harmonic potential. The bosons thus see a linear gradient since $V_{\text{shifted}} = K_0(x - x_0)^2/2 \simeq V_{x_0=0} - cx$, where $c = K_0 x_0$, x_0 is the shift of the trap center, and we have ignored an irrelevant constant term. Thus the shift is analogous to having an electric field for the neutral bosons with $eE = K_0 x_0$; the magnitude of the field can be controlled by controlling the shift. It was found in Ref. [1] that in the Mott phase, the presence of such a shift leads to resonant energy absorption at special values of electric field eE (or shift x_0) which satisfies $eE = nU$ where U is the on-site interaction between the bosons and n is an integer.

The measurement which confirmed this resonant absorption in the experiments of Ref. [1] involved several steps. First, the condensate was subjected to optical lattice potential whose amplitude was slowly ramped up (over a period of 80ms) to the final value. This value is chosen ($V' = 22E_r$) such that the system would be in its Mott state with one boson per site. Second, the system is allowed to equilibrate in this potential for a period of 20ms. During this time, the tilt of a fixed magnitude is applied to the system. Third the optical lattice potential is reduced to $V' = 9E_r$ (for which the bosons are in a superfluid state) within a short time interval of 3ms. Finally, the trap and lattice are turned off, and the real space imaging of the flying out bosons are carried out. It is to be noted that after turning off the trap and the lattice, the bosons undergo a free flight. Thus their position distribution during the flight provides information about their momentum distribution (or initial velocity distribution) inside the trap just before it was turned off. Consequently, in the superfluid phase, the position distribution of the bosons would have a large central peak signifying the presence of a large number of bosons in the state $\vec{k} = 0$ inside the trap. The experiment in Ref. [1] further noted that if the system absorbed

energy when the tilt is applied, it is not going to equilibrate to the superfluid ground state when the lattice potential is reduced. Instead, it will be in an excited state where the boson wavefunction has larger weight in the $\vec{k} \neq 0$ states in the trap. This will broaden their position distribution leading to a broader central peak during imaging. A large width of the central peak of the image, therefore, is a signature of large energy absorption due to the perturbation; such a large width is observed around $eE = nU$.

The measurement technique of Ref. [1] did not allow for a direct measurement of the number distribution of the bosons within the lattice in the Mott phase. This is clearly desirable if one wanted to distinguish between several competing ground states in the Mott regime. The later experiments, performed in Ref. [3, 4], made significant progress in this direction. In these experiments, which also used ^{87}Rb atoms, lasers with wavelength of $\lambda = 680\text{nm}$ were used to generate the optical lattice. The trap used to confine the bosons was also optical. The maximum allowed lattice depth achieved in these experiments were $V' = 45E_r$ which brought the bosons close to their Mott state in the atomic limit. The lattice obtained was a 2D lattice; however, the experiment had separate control over the lattice depth in the x (along the chain) and the y (between the chains) direction. The inter-chain lattice depth could be ramped to very high to achieve an effectively 1D optical lattice (almost disconnected chains).

The tilt generated in these experiments were carried out via application of Zeeman magnetic field which varied linearly in space. Such a Zeeman field leads to a potential term $H_1 = -g\mu_B B_0 \sum_j j \hat{n}_j$ where μ_B is the Bohr magneton, g is the gyromagnetic ratio, B_0 is the amplitude of the field on the first site ($j = 1$) and \hat{n}_j is the number operator for the bosons. Such a field, therefore, creates an effective electric field for the bosons with $eE = g\mu_B B_0$. Note that the intensity of this field can be controlled by tuning the magnetic field which is experimentally much more convenient than shifting the trap center.

To measure the density distribution of the bosons inside a trap, the experiments in Ref. [3, 4] used an ingenious fluorescence imaging technique. In this technique, the depth of the lattice potential is suddenly increased just before the measurement so that the bosons within the lattice freeze for a long time scale. Then fluorescent light is applied to the bosons; the frequency of this light is chosen in such a way that any boson pair on a lattice site can scatter via light assisted collision and move out of the trap. Thus such a fluorescent light leaves behind an empty lattice site if there were, initially, an even number of bosons on that site; in contrast, if there are odd number of bosons, at least one boson remains on the site. Thus an imaging of the bosons after the fluorescent light is applied provides information about their parity of occupation in the Mott state. If a boson remains on a lattice site, it may scatter several photons leading to bright spots. Thus it provides a direct distinction between Mott states with even and odd occupations (for example, between $0 - 2 - 0 - 2 \dots$ and $1 - 1 - 1 - 1 \dots$ occupations) of bosons; the sites with even occupations lead to dark spots while that with odd occupation appear bright. This proves to be very useful while measuring boson occupation in the presence of a tilt.

Finally we briefly discuss some experiments on ultracold bosonic Rydberg atoms in a 1D optical lattice [23–26]. The atoms used for such experiments are again ^{87}Rb . These atoms are confined in a 1D optical lattice as discussed earlier. In these experiments, the atoms are subjected to a Raman laser which induces a transition between the ground ($|g\rangle = |5S_{1/2}; F = 2; m_F = -2\rangle$) and the Rydberg excited ($|r\rangle = |70S_{1/2}; F = 1/2; m_F = -1/2\rangle$) state of the atoms via an intermediate state ($|p\rangle = |6P_{3/2}; F = 3, m_F = 3\rangle$). The experiment used two lasers with wavelength 420 nm and 1024 nm (corresponding to single photon Rabi frequencies of $\Omega_B = 2\pi \times 36$ and $\Omega_R = 2\pi \times 60$ MHz, respectively) so that there is a detuning δ between the $|g\rangle$ and the $|p\rangle$ levels: $\hbar\Omega_B = \delta + (E_p - E_g)$. Similarly the detuning Δ between the $|r\rangle$ and the $|g\rangle$ levels are given by $\Delta = \hbar(\Omega_B + \Omega_R) - (E_r - E_g)$. For $\Delta = 0$ the atoms would be in an equal linear superposition of $|g\rangle$ and $|r\rangle$ states. Δ can be tuned in experiments to have either positive or negative values. The effective coupling between the atoms in the ground and Rydberg state is given by $\Omega = \hbar^2\Omega_B\Omega_R/(2\delta)$. Further experimental details regarding the setup can be found in Ref. [23].

The atoms experience a strong repulsive dipolar interactions ($V(r) \sim 1/|r|^6$) when excited in the Rydberg state. This interaction can be tuned by controlling the relative position of the atoms in the lattice; in particular, a regime can be reached which precludes two Rydberg excited atoms within a certain length R . This phenomenon is called the dipole blockade and R is termed as the blockade radius. In experiments, it is possible to control the dipolar interaction strength between the atoms leading to an effective tuning of the blockade radius. Such a tuning of the blockade radius may lead to translational symmetry broken phases as follows. In experiments the blockade radius can be tuned to next neighbor; moreover, the parameters are so adjusted that it is energetically favorable for each individual atom to be in its Rydberg excited state. A competition between these two phenomenon leads to a state where atoms in every alternate site can be in the state $|r\rangle$ leading to a symmetry broken state. Similarly states with blockade radius of two lattice sites can be achieved; these states, for large negative Δ , shall have a Rydberg excited in every three sites. In the next section, we shall find that the physics of such a system can be understood in terms of a model which has several common features with the tilted Bose-Hubbard model.

3 Model and Phases

The low-energy effective model for the bosons in a tilted 1D optical lattice has been derived in Ref. [22]. An extension of this model has been studied in Ref. [40]. In the first part of this section, we briefly sketch the method of derivation of this model from the microscopic. In the next part, we shall discuss the similarity of the model with a spin model appropriate for describing the Rydberg atoms discussed in the previous section. The extension of this model to higher dimension [41–43], its application to tilted dipolar bosons [44, 45], tilted spin chains [46], and other models

with modified constraint [47] has also been worked out; however, in the rest of this work, we shall restrict ourselves to the initial 1D model proposed in Ref. [22].

In the presence of a tilt, the Hamiltonian of ultracold bosons in a 1D optical lattice is given by

$$H_b = -w \sum_{\langle jj' \rangle} (b_j^\dagger b_{j'} + \text{h.c.}) - \mu \sum_j \hat{n}_j + \frac{U}{2} \sum_j \hat{n}_j (\hat{n}_j - 1) - \mathcal{E} \sum_j j \hat{n}_j, \quad (2)$$

where b_j denotes the boson annihilation operator at site j , $\hat{n}_j = b_j^\dagger b_j$ is the boson number operator, w is their nearest-neighbor hopping amplitude, U is the amplitude of the on-site interaction between the bosons, and μ denotes their chemical potential. In Eq. 2, $\langle jj' \rangle$ indicates that j and j' are nearest neighbors, and \mathcal{E} denotes amplitude of the applied electric field in units of energy. In absence of the field, the bosons are in the in Mott state so that $\mu, U \gg w$; moreover in what follows, we shall address the physics of the system for $U, \mathcal{E} \gg w, |U - \mathcal{E}|$.

Before embarking on the description of the ground state of this model, it is useful to think about the limit $U = 0$. In this case the model represents Wannier-Stark ladder for the bosons. The single-particle Schrodinger equation for such non-interacting bosons is given by (with energies $\epsilon = E + \mu$)

$$\epsilon \psi_j = -\mathcal{E} j \psi_j - w [\psi_{j-1} + \psi(j+1)]. \quad (3)$$

The solution to this problem is well-known [48]. The energy of the bosons are given by $\epsilon_m = \mathcal{E} m$ where m denotes integers ranging from $-\infty$ to ∞ . Note that the energy is not bounded from below and this arises from the fact that the potential is also not bounded on an infinite lattice. The eigenfunctions of the bosons are given by

$$\psi_m(j, t) = J_{j-m}(2w/\mathcal{E}) \exp[-i\mathcal{E}mt/\hbar], \quad (4)$$

where $J_n(x)$ denotes the Bessel function. Note that the wavefunction returns to its original value at regular time intervals $t_0 = 2\pi\hbar/\mathcal{E}$ which indicates Bloch oscillations. The bosons are strongly localized to their respective site for $w \ll \mathcal{E}$. This behavior can also be understood from the fact that $J_{j-m}(x)$ has appreciable weight at $j = m$ for $x \ll 1$ leading to more than exponentially localized wavefunctions [22]. This behavior is in contrast to the classical expectation where an electric field shall accelerate the bosons to the end of the chain causing an electric breakdown. This feature shall be a key component in constructing the effective theory in the limit $\mathcal{E} \gg w$. Such a breakdown can happen in realistic quantum systems due to electric field assisted tunneling to higher single-particle bands; however, for ultracold bosons, such bands are well separated in energy from the lowest bands. This leads to a tunneling time which is larger than the typical system lifetime and allows us to ignore such electric breakdown. In the absence of such breakdown, the system remains in the metastable parent state $|\psi(t=0)\rangle$. Thus the strategy adapted in Ref. [22] for finding out the equilibrium phase of the

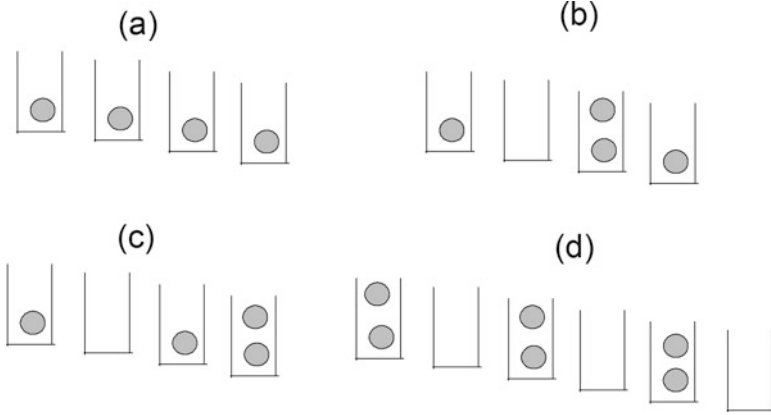


Fig. 1 (a) Schematic representation of the parent Mott state with $n_0 = 1$. (b) The state with a single dipole. (c) A state with two neighboring dipoles which is equivalent to a single dipole of length two and is not a part of the low-energy subspace. (d) A state with maximal number of dipoles which is also a part of the low-energy subspace

tilted bosons was to start from the metastable parent Mott state and find out the manifold of states whose energies are close to the parent Mott state in the regime $\mathcal{E}, U \gg w, |\mathcal{E} - U|$.

To understand the nature of the effective theory of the interacting bosons, we, therefore, start from the parent Mott state (the Mott ground state in the absence of the electric field) with n_0 bosons on every lattice site (see Fig. 1a) and ask how the electric field may destabilize such a bosonic system. A possibility is that this can be achieved by addition of an extra particle or hole in over the parent Mott state. The energy cost of adding a particle to the Mott state is $E_p = U(n_0 + 1) - \mu$ while that for a hole is $E_h = \mu - Un_0$. Note that $E_p, E_h > 0$ as long as the system is in the Mott ground state. However, once added, the particle[hole] sees the electric field and is thus described by an effective Hamiltonian which is identical to Eq. 3 with $\mu = 0$ and $w \rightarrow w(n_0 + 1)[wn_0]$. They are, therefore, localized and cannot reduce their energy via hopping (which would have been the case if \mathcal{E} was absent). Thus such excitations are not effective in destabilizing the Mott states. This situation is, therefore, different from that of bosons without the tilt, where such additional particles or holes destabilize the Mott state to bring about the superfluid-insulator transition [10, 11].

The excited states which are part of the low-energy manifold around the parent Mott state correspond to dipole excitations where a particle hops from a lattice site to the next (Fig. 1b) [22]. Such an excitation creates an additional particle on the site $j + 1$ and a hole at site j and thus have an energy cost

$$E_{\text{dipole}} = E(n_0 + 1) + E(n_0 - 1) - 2E(n_0) - \mathcal{E} = U - \mathcal{E}. \quad (5)$$

A state with one or multiple dipoles thus become a part of the low energy manifold for $U \simeq \mathcal{E}$. These states are schematically represented in Fig. 1d. These dipoles live

on the link ℓ between two adjacent lattice site j and $j+1$. Identifying the parent Mott state as the dipole vacuum, the operators describing the creation of such dipoles can be written in terms of the boson operators as

$$d_\ell^\dagger |\text{vac}\rangle = \frac{1}{\sqrt{n_0(n_0+1)}} b_j b_{j+1}^\dagger |\text{Mott}\rangle \quad (6)$$

We note the following properties of the dipoles. First, there can be at most one dipole on any given link. This is seen by noting that creating another dipole on the same link cost an energy $E_2 = 4U - 2\mathcal{E}$ (for $n_0 > 1$). Thus a state with two dipoles on the same link is not a part of the low-energy manifold. Second, two dipoles on adjacent links cost an energy $U - 2\mathcal{E}$ (Fig. 1c) (this is equivalent to a length two dipoles where a boson hops two sites as shown in Fig. 1c) and thus such states are also not a part of this manifold. In fact it can be shown that all longer length dipoles do not play a role [22]. This leads to an effective dipole Hamiltonian supplemented by the constraints

$$H_d = -w' \sum_\ell (d_\ell + d_\ell^\dagger) + \lambda \sum_\ell \hat{n}_\ell, \quad \hat{n}_\ell \leq 1, \quad \hat{n}_\ell \hat{n}_{\ell+1} = 0, \quad (7)$$

where $\hat{n}_\ell = d_\ell^\dagger d_\ell$, $\lambda = U - \mathcal{E}$, and $w' = w\sqrt{n_0(n_0+1)}$. We note that the model does not conserve dipole numbers since spontaneous hopping of bosons leads to formation/annihilation of dipoles. Moreover, the model is non-integrable due to the presence of the second constraint. The number of states in the Hilbert space of this Hamiltonian does not scale as 2^L (as that of hardcore bosons or spins); it can be shown that they scale as φ^L for large L where $\varphi = (1 + \sqrt{5})/2$ is the golden ratio. It was shown that it is possible to write down a recursion relation for the Hilbert space dimension, \mathcal{N}_L , of the constrained dipole system with periodic boundary condition: $\mathcal{N}_L = \mathcal{N}_{L-1} + \mathcal{N}_{L-2}$. This relates \mathcal{N}_L to Fibonacci numbers F_L for integer L : $\mathcal{N}_L = F_L$ [33].

It is easy to see that H_d admits a representation in terms of spin-half Pauli matrices due to the constraint $\hat{n}_\ell \leq 1$. Indeed the mapping

$$\sigma_\ell^z = 2\hat{n}_\ell - 1, \quad \sigma_\ell^x = (d_\ell + d_\ell^\dagger), \quad \sigma_\ell^y = i(d_\ell - d_\ell^\dagger) \quad (8)$$

leads to the spin Hamiltonian [29, 49] (up to an irrelevant constant)

$$H_s = \sum_\ell (-w' \tilde{\sigma}_\ell^x + \lambda \sigma_\ell^z / 2), \quad \tilde{\sigma}_\ell^a = P_{\ell-1} \sigma_\ell^a P_{\ell+1}, \quad P_\ell = (1 - \sigma_\ell^z) / 2. \quad (9)$$

Here we have implemented the constraint $\hat{n}_\ell \hat{n}_{\ell+1} = 0$ by using a local projection operator P_ℓ and it is understood that H_{spin} operates in the constrained Hilbert space where one cannot have two up-spins on the neighboring link. The projection operator P_ℓ ensures that this constraint is obeyed by H_s . We note here that the model, at $\lambda = 0$, has been dubbed as the PXP model [27–32].

Next, we note that addition of longer-range density–density interaction to H_d leads to the Hamiltonian [40]

$$H'_d = H_d + V \sum_{\ell} \hat{n}_{\ell} \hat{n}_{\ell+2}. \tag{10}$$

We shall not discuss the details of the phases or the dynamics of this model here but refer the readers to Refs. [40, 50–52] for details. The model displays a rich phase diagram and supports non-Ising quantum phase transition. Moreover, this also serves the low-energy effective model for the Rydberg atoms discussed in the last section in certain limit; we shall detail this point towards the end of this section.

The ground phase diagram of H_d can be understood in a straightforward manner. For $\lambda \gg w'(U \gg \mathcal{E} + w')$, the dipole excitations are energetically costly and the ground state is the dipole vacuum $|\text{vac}\rangle$ (the parent Mott state $|\text{Mott}\rangle$). In contrast, for $|\lambda| \gg 0$ with $\lambda < 0$ ($\mathcal{E} \gg U + w'$), the ground state is clearly a state with maximal number of dipoles. However, due to the constraint, there are two such maximal dipole states. The first consists of dipoles that are formed on the even links of the 1D lattice while the second where they are formed on the odd links. These states, for a chain of length $2L$ whose links are labeled from 0 to $2L - 1$, are (see Fig. 1d)

$$|\mathbb{Z}_2\rangle = d_0^\dagger d_2^\dagger \dots d_{2L-2}^\dagger |\text{vac}\rangle, \quad |\bar{\mathbb{Z}}_2\rangle = d_1^\dagger d_3^\dagger \dots d_{2L-1}^\dagger |\text{vac}\rangle. \tag{11}$$

The ground state chooses one of the two states and hence breaks Z_2 symmetry. This implies that it must be separated from the dipole vacuum ground state by a transition; this quantum phase transition belongs to the Ising universality class and occurs at [22]

$$\mathcal{E}_c = U + 1.31\sqrt{n_0(n_0 + 1)}w. \tag{12}$$

Such a transition can be understood to be the result of competition between the dipole number fluctuation arising from the first term in Eq. 7 and the effect of the electric field in the second term which makes such fluctuation energetically costly. A rough estimate of \mathcal{E}_c can also be obtained from a variational wavefunction approach. The ordered state which breaks the Z_2 symmetry is characterized by an Ising order parameter. In the dipole language this order parameter can be written as

$$O = \frac{1}{2L} \sum_{\ell=0}^{2L-1} (-1)^\ell \hat{n}_\ell \tag{13}$$

which is the dipole density at $k = \pi$ signifying the broken translational symmetry of the ground state.

The presence of such a translational symmetry broken state was directly verified in the experiment carried out in Ref. [3] using the fluorescence imaging technique

discussed earlier. The experiment started with a Mott state having $n_0 = 1$ bosons per lattice site and generated a tilt using a linearly varying Zeeman field. Thus the parent Mott state corresponds to an odd number of bosons per site and provided bright patterns in an imaging measurement. In contrast, the maximal dipole state, which constitutes an even number of states per site, would provide a dark image. It was found that an increase of the strength of the magnetic field providing the tilt indeed led to a dark pattern; moreover, one could coherently interpolate between such bright and dark imaging patterns by tuning the strength of the magnetic field. This constituted the realization of the symmetry broken Mott state for ultracold bosons in an optical lattice.

Before ending this section, we briefly comment on the Rydberg atom experiments and the relation of the Hamiltonian of such Rydberg atoms with the model developed here. The low-energy effective Hamiltonian of these atoms describes the physics of the system for times which is smaller compared to typical decay scales of Rydberg excited atoms. The Hamiltonian involves two states $|g\rangle$ and $|r\rangle$. Defining τ_α ($\alpha = x, y, z$) to be standard Pauli matrices in the space of these two states, one can write

$$H_{\text{Ryd}} = - \sum_j (\Omega \tau_j^x + \Delta \tau_j^z) + \sum_{jj'} V_{jj'} \hat{n}'_j \hat{n}'_{j'}, \quad (14)$$

where Δ and Ω has been defined in Sect. 2, $V_{jj'}$ is the dipolar interaction between two Rydberg excited atoms. Here $\hat{n}'_j = (1 + \tau_j^z)/2$ denotes the number operator for Rydberg excitations. We note that for $V_{j,j+1} \gg \Omega, |\Delta|$ and $V_{j,j+n} \ll \Omega, |\Delta|$ for $n > 2$, Eq. 14 reduces to Eq. 10 with $\Omega \rightarrow -w\sqrt{n_0(n_0+1)}$, $\Delta \rightarrow \lambda$ and $V_{j,j+2} \rightarrow V$. Moreover if $V \ll \Omega, |\Delta|$, Eq. 14 reduces to Eq. 7 (and hence to Eq. 9). It is, therefore, expected that the ground state phase diagram of Rydberg atoms would also reflect translational symmetry broken states for $\Delta < 0$ and $|\Delta| \gg \Omega$.

In experiments carried out in Ref. [23], Δ could be tuned to large negative values to achieve the translational symmetry broken states. Such states had a period 2 when $V_{j,j+1} \gg \Omega, |\Delta|$ and $V_{j,j+n} \ll \Omega, |\Delta|$ for $n > 1$, in accordance with the prediction of the dipole model. In addition, it was possible to tune the strength of the Rydberg interaction such that $V_{j,j+1}, V_{j,j+2} \gg \Omega, |\Delta|$ and $V_{j,j+n} \ll \Omega, |\Delta|$ for $n > 2$. In this case, the ground state broke Z_3 symmetry and led to a period 3 density-wave in accordance with that found in Ref. [40] by analyzing the Hamiltonian given in Eq. 10.

4 Non-equilibrium Dynamics

In this section, we shall discuss the non-equilibrium dynamics of the tilted bosons in the presence of an optical lattice. The quench and the ramp dynamics of the bosons shall be discussed in Sect. 4.1 while the periodic dynamics will be addressed in Sect. 4.2.

4.1 Quench and Ramp Protocols

It is well-known that ultracold atoms provide a perfect platform for studying non-equilibrium dynamics of closed quantum systems [5, 53–57]. One of the simplest protocol for such dynamics is the quench, where a parameter in the Hamiltonian of the system is changed suddenly. Consequently, the state of the system does not have time to react. The old ground state of the system (or any initial state the system might be in when the quench is performed) evolves according to the new Hamiltonian. Since the old state is no longer an eigenstate of the new Hamiltonian, it displays non-trivial dynamics. For non-integrable systems, such dynamics is expected to be led to a thermal steady state at long times. This follows from the eigenstate thermalization hypothesis (ETH) [58–61] which predicts eventual thermalization of a typical many-body state under unitary dynamics. At short times, the system is expected to display transient oscillations.

For the tilted boson system, such oscillations were studied in Ref. [62]. The bosons were initially assumed to a state of dipole vacuum $|0\rangle$. At $t = 0$, the electric field \mathcal{E} is changed from its initial value $\mathcal{E}_i < U$ to its final value \mathcal{E}_f . The state of the system at time t can then be described by

$$|\psi(t)\rangle = \sum_n c_n e^{-iE_n t/\hbar} |n\rangle, \quad H(\mathcal{E}_f)|n\rangle = E_n|n\rangle, \quad c_n = \langle n|0\rangle. \quad (15)$$

Under such evolution, the dipole order parameter given by Eq. 13 oscillates as

$$O(t) = \sum_{m,n} c_m c_n O_{mn} \cos \omega_{mn} t, \quad O_{mn} = \langle m|O|n\rangle, \quad \omega_{mn} = (E_m - E_n)/\hbar, \quad (16)$$

where we have used the fact that c_m could be chosen to be real. A numerical evaluation of $O(t)$, carried out in Ref. [62] (left panel of Fig. 2), showed that the

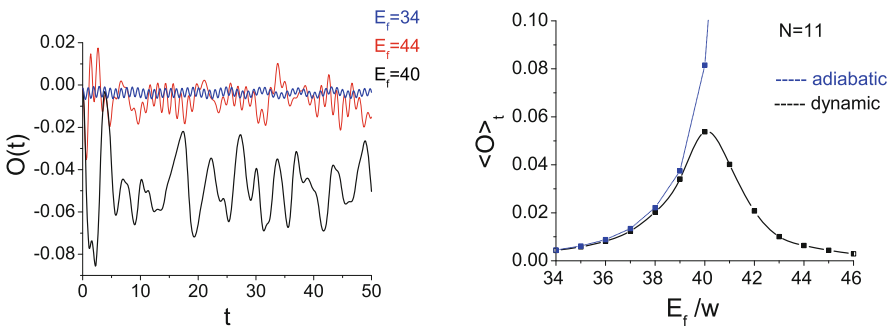


Fig. 2 Left panel: Plot of $O(t)$ as a function of time for several representative values of \mathcal{E}_f/w . For all plots $U/w = 40$ and initial state is the dipole vacuum ground state $|0\rangle$. Right panel: Plot of $\bar{O} \equiv \langle O \rangle_t$ as a function of \mathcal{E}_f/w showing a peak near the critical point. In the figs N represents the chain length in units of lattice spacing. This figure is adapted from Ref. [62]

transient oscillations have maximal amplitude when $\mathcal{E}_f = U$ near the critical point; they are tiny deep inside both the maximal dipole and dipole vacuum phases as shown in the left panel of Fig. 2. Thus transition can act as a qualitative marker for change in state of the system.

To understand why the amplitude peaks around $U = \mathcal{E}_f$, we focus on the time averaged value of these oscillations

$$\bar{O} = \lim_{T \rightarrow \infty} \frac{1}{T} \int_0^T O(t) = \sum_m c_m^2 O_{mm}. \quad (17)$$

The amplitude of these oscillations is maximal when the product of overlap c_m and order parameter expectation O_{mm} is large. When \mathcal{E}_f is deep inside the dipole vacuum, $c_m \sim 1$ when m correspond to the old ground state. However, $O_{mm} \rightarrow 0$ for this state leading to a small \bar{O} . In contrast, when \mathcal{E}_f corresponds to deep inside the maximal dipole ground state, O_{mm} is large for the new ground state; however, $c_m \sim 0$ for this ground state leading, once again, to a small \bar{O} . In between, near the critical point, \bar{O} could be large since both c_m and O_{mm} can be non-zero for several m . This leads to a peak of \bar{O} near the critical point as shown in the right panel of Fig. 2.

More recently, the quench dynamics of Rydberg atoms has been studied experimentally starting from the $|\mathbb{Z}_2\rangle$ state [23]. It was found that the evolution of such a state, following a quench of the parameter $\Delta \rightarrow 0$, displays long-lived coherent oscillations. Since the system is non-integrable, ETH predicts that such dynamics will lead to an eventual thermal steady state; however, such a steady state was not observed in experiments for dynamics starting from $|\mathbb{Z}_2\rangle$. In contrast, dynamics starting from the all spin-down state ($|0\rangle$ or the dipole vacuum state) showed expected, ETH predicted, thermalization. This phenomenon, therefore, constituted a weak (initial-state dependent) violation of ETH in such finite-sized chains.

The theoretical explanation of this phenomenon followed soon [27–32]. The details of this has been summarized in Ref. [27] and the references therein. It was found at $\Delta = 0$, or in the PXP limit, the eigenspectrum of H_s (or equivalently H_{Ryd} for large $V_{i,i+1}$) supports a special class of eigenstates called quantum scars [27–32, 36–39]. These states have finite energy density but anomalously low half-chain entanglement entropy [27]. Being anomalous, they have very little overlap with the thermal band of mid-spectrum eigenstates. Consequently, they form an almost closed subspace. It was also found that they have a strong overlap with the $|\mathbb{Z}_2\rangle$ state; thus dynamics starting from the $|\mathbb{Z}_2\rangle$ state is almost confined within the closed subspace formed by the scars leading to coherent long-lived oscillations. This does not happen for dynamics starting from the $|0\rangle$ state since it has very little overlap with the scar states. Further details of this phenomenon and properties of quantum scars are summarized in Ref. [27].

Next, we discuss the ramp dynamics of such a system addressed in Ref. [49]. In this case, one ramps the electric field via a linear protocol from its initial value \mathcal{E}_i at $t = 0$ to a final value \mathcal{E}_f at $t = \tau$ with a rate τ^{-1} : $\mathcal{E}(t) = \mathcal{E}_i + (\mathcal{E}_f - \mathcal{E}_i)t/\tau$. The values of \mathcal{E}_f and \mathcal{E}_i are so chosen so that the system starts from the dipole vacuum

state (ground state for $\mathcal{E} = \mathcal{E}_i < U$) and reaches the critical point at $\mathcal{E} = \mathcal{E}_f = \mathcal{E}_c$. It is well-known that such a passage to the critical point leads to excitation production; the density of these excitations, for slow ramp rates, scales with τ according to the Kibble-Zurek (KZ) scaling law $n_{\text{ex}} \sim \tau^{-\nu d/(z\nu+1)}$, where ν and z are the correlation length and dynamical critical exponents and d is the spatial dimension of the system [53–57, 63–69]. However, such scaling laws are strictly appropriate when the system size is large. For finite-sized systems such as the Rydberg chain, the system size L provides a length scale which restrict the applicability of the scaling laws.

To understand why the presence of a finite-system size changes things, let us consider that the length scale L leads to an energy scale $\epsilon_0(L)$. When the ramp rate $\tau^{-1} \leq \epsilon_0(L)/\hbar$, the system does not see the critical point; instead the dynamics is similar to a two-level system (the two states correspond to the instantaneous ground and first excited states near the transition where excitations are formed) with avoided level crossing, where the minimum gap is $O(\epsilon_0(L))$. In this case, the excitation density scales as $n_{\text{ex}} \sim \tau^{-2}$ and is independent of the critical exponents; this is known as Landau-Zener (LZ) scaling [70]. Also, when τ^{-1} is large, i.e., for fast drives, n_{ex} saturates and KZ scaling is not obeyed. In between, there is a finite window of drive rates for which one finds KZ scaling law. This behavior can be summed up by noting that for finite-sized system, the scaling of excitation density is described by

$$n_{\text{ex}} = N^d \tau^{-\nu d/(z\nu+1)} f(N^{1/\nu+z} \tau^{-1}), \quad (18)$$

where $N = L/a$, a is the lattice spacing, and the scaling function $f(x)$ satisfies $f(x) = x^{2-\nu d/(z\nu+1)}$ for $x \ll 1$ and $f(x) = 1$ for $x \gg 1$. Note that n_{ex} crosses over from LZ to KZ scaling regime with decreasing τ around $x \simeq 1$ $\tau \sim N^{2-\nu d/(z\nu+1)}$.

The dynamics of dipole chain for such ramps have been numerically studied using exact diagonalization (ED) and time-dependent matrix product states (tmPS) methods. For ED, the analysis involves finding the instantaneous eigenvalues and eigenvectors of the driven chain at $t = t_f = \tau$; $H[t = \tau]|n\rangle = \epsilon_n|n\rangle$. One can then expand the time-dependent state $|\psi(t)\rangle = \sum_n c_n(t)|n\rangle$, where $c_n(t) = \langle n|\psi(t)\rangle$. The Schrodinger equation for the driven system can thus be written as coupled differential equations for the coefficients $c_n(t)$ given by

$$i \frac{dc_n(t)}{dt} = \epsilon_n c_n(t) + \sum_m \lambda_{mn}(t) c_m(t), \quad c_n(0) = \langle n|\psi(0)\rangle, \quad \lambda_{mn}(t) = (E_f - E_i)(t/\tau - 1) \langle m|\sum_j \hat{n}_j|n\rangle. \quad (19)$$

These equations need to be solved numerically to obtain $|\psi(t)\rangle$. Having obtained $|\psi(t)\rangle$, one may compute several quantities such as residual energy Q , log fidelity F (which is same as the excitation density), the dipole density n_d and the defect density D given by

$$Q = \langle \psi(\tau)|H(\tau)|\psi(\tau)\rangle - \epsilon_0, \quad F = \ln |\langle \psi(\tau)|0\rangle|, \quad C_{\ell\ell'} = \langle \psi(\tau)|S_\ell^z S_{\ell'}^z|\psi(\tau)\rangle$$

$$n_d = \langle \psi(\tau)|\sum_\ell \hat{n}_\ell|\psi(\tau)\rangle, \quad D = n_d - \langle 0|\sum_\ell \hat{n}_\ell|0\rangle, \quad (20)$$

where $|0\rangle$ and ϵ_0 denote the wavefunction and energy of the final ground state at $t = \tau$ and $S_\ell^z = 2\hat{n}_\ell - 1$.

A plot of these quantities is shown in Figs. 3 and 4 for several representative values of L . It was found that they exhibit KZ scaling (with exponent $\nu d / (z\nu + 1) = 1/2$ for $d = z = \nu = 1$) within a finite window of ramp rate which depends on L . As L increases the KZ regime holds for slower ramp rates; the crossover between the LZ and the KZ regime is shown by the sharp drops in the figures. Thus these ramped boson chains can provide experimental platform for testing KZ scaling.

Before ending this section, we would like to note that the ramp dynamics for H'_d (Eq. 10) has also been studied in details [51, 52]. Ref. [52] found KZ scaling consistent with the presence of a 3-state Potts transition in these chains. However,

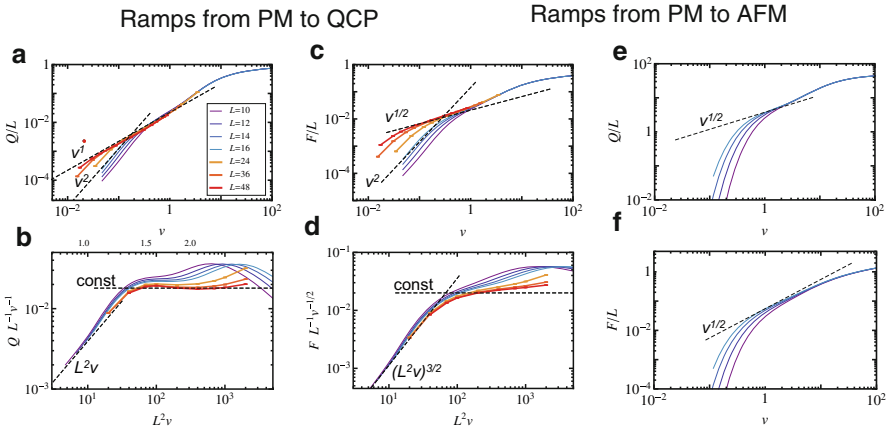


Fig. 3 Plots showing behavior of (a) residual energy Q as a function of $v = \tau^{-1}$ (b) $Q/(Lv)$ as a function of v (c) overlap F as a function of L^2v and (d) $F/(L\sqrt{v})$ as a function of L^2v for quench from the dipole vacuum or paramagnetic ground state(PM) to the quantum critical point (QCP). In the plot, all quantities are dimensionless, $U/w = 40$, and the lattice spacing a has been set to unity. For ramp from the PM to the maximal dipole or antiferromagnetic (AFM) state, the behavior of Q and F are shown as a function of v in panels (e) and (f), respectively. This figure is adapted from Ref. [49]

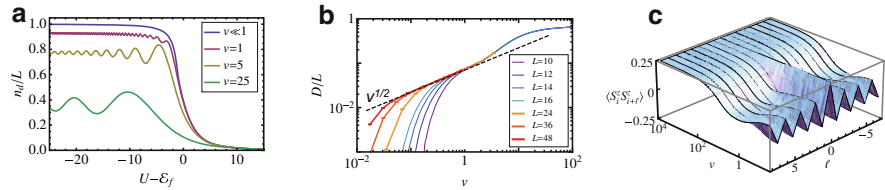


Fig. 4 Plots of (a) dipole density n_d as a function of the ramp amplitude $U - \mathcal{E}_f$ for several $v = \tau^{-1}$, (b) excitation density D as a function of v when $\mathcal{E}_f = \mathcal{E}_c$, and (c) C_{ii+l} as a function of ℓ and v . For all plots $U/w = 40$ and the lattice spacing a has been set to unity. This figure is adapted from Ref. [49]

work of Ref. [51], which accessed larger chain lengths, has predicted the existence of non-Ising like critical points with $z \neq 1$ (where z is the dynamical critical exponent) in such chains. Since H'_d with large V is easily reproduced in Rydberg chains, these chains can also act as platform for hosting such non-Ising quantum critical points. We shall not discuss this issue further in this article but refer the interested reader to Refs. [40, 51, 52]. Furthermore, the dynamics of tilted bosons in the presence of a two-rate protocol [71] has also been discussed; it was found that such protocols may aid suppression of excitation formation in these systems [72].

4.2 Periodic Protocols

In this section, we shall discuss the periodically driven tilted boson chains [33–35]. For the rest of this article, we shall explicitly use the spin representation and work with H_s (Eq. 9). The connection of the spins with the original dipoles is given by Eq. 8. The methods used shall be briefly discussed in Sect. 4.2.1 while the main results shall be presented in Sect. 4.2.2.

4.2.1 Methods

The properties of a periodically driven system are best described in terms of its Floquet Hamiltonian H_F which is related to the unitary time evolution operator U by $U(T, 0) = \exp[-iH_F T/\hbar]$, where $T = 2\pi/\omega_D$ is the time period of the drive, ω_D is the drive frequency, and the wavefunction of the driven system at any time t is related to the initial wavefunction by $|\psi(t)\rangle = U(t, 0)|\psi(0)\rangle$. Thus the stroboscopic dynamics of the system at $t = nT$, where n is an integer, is completely controlled by its Floquet Hamiltonian [73–75].

The Floquet Hamiltonian of any periodically can be computed by comparing two equivalent expressions for $U(T, 0)$

$$U(T, 0) = T_t \left\{ \exp \left[-i \int_0^T dt H(t)/\hbar \right] \right\} = \exp[-iH_F T/\hbar]. \quad (21)$$

For an interacting many-body system, it is usually not possible to obtain H_F exactly. This has led to several approximation schemes for such computations [75]. In what follows, we shall mostly use one of these schemes, namely the Floquet perturbation theory (FPT) [75–78], to obtain the Floquet Hamiltonian for the driven dipole chain. This method involves a perturbation in drive amplitude; the term in $H(t)$ with the largest amplitude is treated exactly, while the other terms are treated using standard time-dependent perturbation theory [75]. In contrast to the Magnus expansion technique, the drive period T need not be a small parameter here; thus, the method allows us to access the intermediate drive-frequency regime which cannot be accessed using Magnus expansion.

To study the properties of the periodically driven chain, we choose to vary the electric field according to the square pulse protocol such that

$$\lambda(t) = -(+) \lambda_0/2 \quad \text{for } t \leq (>) T/2, \quad (22)$$

where λ_0 denotes the amplitude of the drive. In what follows, we shall address the regime where $\lambda_0 \gg w$. In this regime, the drive term is the one which has the largest amplitude. Thus we write

$$H_s(t) = H_{s0}(t) + H_{s1}, \quad H_{s0}(t) = \lambda(t) \sum_j \sigma_j^z, \quad H_{s1} = -w \sum_j \tilde{\sigma}_j^x \quad (23)$$

and treat $H_{s0}(t)$ exactly. Noting that H_{s0} is diagonal in the spin basis, we consider a complete set of states in the constrained Hilbert space which has m up-spins and denotes these states as $|m\rangle$. Note that the positions of these spins (as long as they are not nearest neighbors) do not change their instantaneous energy under action of H_{s0} ; thus each $|m\rangle$ represents a degenerate manifold of states. Using these states as basis states one finds

$$\begin{aligned} U_0(t, 0) &= e^{i\lambda_0 t \sum_j \sigma_j^z / (2\hbar)} \quad \text{for } t \leq T/2 \\ &= e^{i\lambda_0 (T-t) \sum_j \sigma_j^z / (2\hbar)} \quad \text{for } t \geq T/2 \end{aligned} \quad (24)$$

so that $\langle m|U_0|n\rangle \sim \delta_{mn}$. We also note that for $t = T$, $U_0(T, 0) = I$ (where I is the identity matrix); thus $H_F^{(0)} = 0$ for this protocol. This is a consequence of the symmetric nature of the drive (Eq. 22) which leads to a vanishing average of $\lambda(t)$ over a drive cycle.

The first order perturbative correction to the evolution operator U can be obtained using standard time-dependent perturbation theory. This is given by

$$U_1(T, 0) = \frac{-i}{\hbar} \int_0^T dt U_0^\dagger(t, 0) H_{s1} U_0(t, 0). \quad (25)$$

We note that $\tilde{\sigma}_j^x$ flips a spin on the j^{th} site, $\langle m|H_{s1}|n\rangle \sim \delta_{m, n \pm 1}$. Denoting a state $|m + (-) \uparrow_j\rangle$ to be the one with one additional (less) spin-up residing at the j^{th} site, we can, therefore, write [33–35]

$$U_1(T, 0) = \sum_m \sum_j \sum_{s_j = \pm 1} c_{s_j}^{(1)} |m\rangle \langle m + s_j|, \quad c_s^{(1)} = \frac{4iw}{\lambda_0} e^{i\lambda_0 T s / (4\hbar)} \sin \lambda_0 T / (4\hbar), \quad (26)$$

where $s = \pm 1$. Noting that $\tilde{\sigma}^\pm |m\rangle = |m \pm 1\rangle$, and using Eq. 21 we get, to first order in w/λ_0

$$H_F^{(1)} = -w \frac{\sin \gamma}{\gamma} \sum_j \left(\cos \gamma \tilde{\sigma}_j^x + \sin \gamma \tilde{\sigma}_j^y \right), \quad \gamma = \lambda_0 T / (4\hbar). \quad (27)$$

We note that for $T \rightarrow 0$, $\gamma \rightarrow 0$, and in this limit $H_F^{(1)} = -w \sum_j \tilde{\sigma}_j^x = H_{\text{PXP}}$. This is also consistent with the Magnus result for H_F which demands that H_F shall be average Hamiltonian given by

$$H_F^{\text{magnus}} = \frac{1}{T} \int_0^T H(t) dt = H_{\text{PXP}}. \quad (28)$$

Also, at this order, $H_F^{(1)}$ represents a PXP like Hamiltonian up to a rotation and an overall renormalization by a factor $\sin\gamma/\gamma$; it was noted in Ref. [33] that this result constitutes a resummation of a class of terms in the Magnus expansion.

The higher order terms in the Floquet Hamiltonian can also be computed. This has been carried out systematically in Ref. [35] and leads to $H_F^{(2)} = 0$ at second order. This null result for H_F to second order owes its existence to the fact that there exists an operator $C = \prod_j \sigma_j^z$ which satisfies $CU(T, 0)C = U^{-1}(T, 0)$ leading to $\{H_F, C\} = 0$. As shown in Refs. [27, 33], such anti-commutation only allows for odd orders in the Floquet Hamiltonian. At third order, a straightforward but tedious calculation [35]

$$H_F^{(3)} = -\alpha_0 \sum_j \left[\left(\tilde{\sigma}_{j+1}^+ \sigma_{j-1}^+ + \tilde{\sigma}_{j-1}^+ \tilde{\sigma}_{j+1}^+ \right) \tilde{\sigma}_j^- - 6\tilde{\sigma}_j^+ \right] + \text{h.c.},$$

$$\alpha_0 = \left[e^{3i\lambda_0 T/(2\hbar)} + 3e^{i\lambda_0 T/(2\hbar)} (1 + i\lambda_0 T/\hbar) + 2(1 - 3e^{i\lambda_0 T/\hbar}) \right] \frac{\hbar w^3 e^{-i\lambda_0 T/\hbar}}{3i\lambda_0^3 T}. \quad (29)$$

The first term in $H_F^{(3)}$ involves three spin on neighboring sites. We note that the form of this term, i.e., the order in which the $\tilde{\sigma}^\pm$ operators appear, is dictated by the presence of the constraint; the order of appearance ensures that two neighboring sites can never have two up-spins. The second term of the Floquet Hamiltonian provides a shift to $H_F^{(1)}$ and renormalizes its coefficients. In what follows, we shall use this perturbative Floquet Hamiltonian to understand the numerical results.

The numerical approach to this problem, carried out in Ref. [33, 35], used exact diagonalization(ED). The first step in this direction involves numerical diagonalization of $H[\pm\lambda_0]$. We denote the corresponding energy eigenvalues and eigenvectors by

$$H[\pm\lambda_0]|p_\pm\rangle = \epsilon_p^\pm |p_\pm\rangle. \quad (30)$$

In terms of this, the evolution operator can be written as

$$U(T, 0) = e^{-iH[\lambda_0]T/(2\hbar)} e^{-iH[-\lambda_0]T/(2\hbar)} = \sum_{p,q} c_{pq}^{-+} e^{-i(\epsilon_p^- + \epsilon_q^+)T/(2\hbar)} |p^-\rangle \langle q^+|,$$

$$c_{pq}^{-+} = \langle p^- | q^+ \rangle. \quad (31)$$

Thus one has a finite-dimensional matrix (for finite-sized L) which can then be diagonalized. Since U is an unitary operator, its eigenvalues are unimodular. Thus one can express it in term of its eigenspectra as

$$U(T, 0) = \sum_{\alpha} e^{-i\epsilon_{\alpha}^F T/\hbar} |\alpha\rangle\langle\alpha|, \quad H_F |\alpha\rangle = \epsilon_{\alpha}^F |\alpha\rangle, \quad (32)$$

where $|\alpha\rangle$ are the eigenfunctions of $U(T, 0)$, ϵ_{α}^F are the eigenvalues of the corresponding Floquet Hamiltonian, and the last equation follows from Eq. 21. This procedure thus allows access to the exact Floquet quasienergies and eigenfunctions for finite-sized systems. The stroboscopic evolution, at $t = nT$ (where n is an integer), for any operator \mathcal{O} , can thus be computed as [33]

$$\mathcal{O}_n = \langle\psi(0)|(U^{\dagger}(T, 0))^n \mathcal{O} U^n(T, 0)|\psi(0)\rangle = \sum_{\alpha, \beta} c_{\beta}^* c_{\alpha} e^{-i(\epsilon_{\alpha}^F - \epsilon_{\beta}^F)T/\hbar} \langle\beta|\mathcal{O}|\alpha\rangle, \quad (33)$$

where $|\psi(0)\rangle$ is the initial state and $c_{\alpha} = \langle\psi(0)|\alpha\rangle$.

In what follows, we shall also be computing the half-chain entanglement entropy of the Floquet eigenstates. The procedure for this is as follows. First, corresponding to any eigenstate $|\psi_n\rangle$, we construct a density matrix $\rho_n = |\psi_n\rangle\langle\psi_n|$ which is defined on the full chain with periodic boundary condition. Next we divide the chain into two equal halves, A and B , with open boundary condition and trace out the contribution of states residing in B . Thus each matrix element of the reduced density matrix ρ_n^A after tracing out B can be written as [33]

$$\langle\rho_n^A\rangle_{\alpha\beta} = \sum_{\mu \in B=1}^{\mathcal{N}_B} \langle\alpha; \mu|\rho_n|\beta; \mu\rangle, \quad (34)$$

where \mathcal{N}_B denotes the Hilbert space dimension corresponding to states residing in B with open boundary condition and the states $|\alpha\rangle$ and $|\beta\rangle$ have weights in region A [33]. While carrying out this procedure, one has to be careful in excluding states where the right end of A and the left end of B both have spin-up (or dipoles) since these states were not part of the Hilbert space of the full chain owing to the constraint. The half-chain entanglement $S_{L/2}^{(n)}$ can then be obtained numerically using

$$S_{L/2}^{(n)} = - \sum_{j=1}^{\mathcal{N}_A} q_j \ln q_j, \quad (35)$$

where q_j denotes the eigenvalues of ρ_n^A obtained via numerical diagonalization. We shall use $S_{L/2}^{(n)}$ to distinguish between states with volume- and area-law entanglement entropies in the rest of this article.

4.2.2 Results

To study the physics of the driven dipole chain, we concentrate on half-chain entanglement $S_{L/2}$ (Eq. 35) of the Floquet eigenstates and the density–density correlator $\langle O_{j2} \rangle = \langle \psi(nT) | \hat{n}_j \hat{n}_{j+2} | \psi(nT) \rangle$, where $\hat{n}_j = (1 + \sigma_j^z)/2$. In what follows, we shall discuss the property of the stroboscopic evolution of $\langle O_{22} \rangle$ (i.e., choosing $j = 2$) starting from either the $|\mathbb{Z}_2\rangle$ (antiferromagnetic state with up-spins on even sites) or the $|0\rangle$ (ferromagnetic all spin-down state) state. The evolution of $\langle O_{jj+2} \rangle$ for other values of j is identical as long as j is chosen to be even [33–35].

We first consider the dynamics starting from the $|\mathbb{Z}_2\rangle$ initial state. For this state, for $\lambda_0/(\hbar\omega_D) \ll 1$, the dynamics is similar to that of quench studied in Ref. [27]. In this regime, we expect scar-induced coherent oscillations with a frequency which is determined by the energy separation between the quantum scar eigenstates. In the opposite limit, $w/(\hbar\omega_D) \gg 1$ (where FPT and Magnus expansion both fail) it is expected that the system shall heat up due to the drive and reach the thermal steady state as predicted by ETH. This expectation is verified from the behavior of $\langle O_{22} \rangle$ shown for high and low frequencies in the plots shown at the top of the left panel in Fig. 5. The bottom plots of the left panel of Fig. 5 show the half-chain entanglement entropies of the Floquet eigenstates at these drive frequencies; the high frequency eigenstates clearly show the presence of athermal scars separated from the thermal band of states. No such athermal states are seen at low drive frequency; in this regime, all the states fall within the thermal band. The red dots indicate eigenstates with large overlap with the initial $|\mathbb{Z}_2\rangle$ state. These are the states which primarily

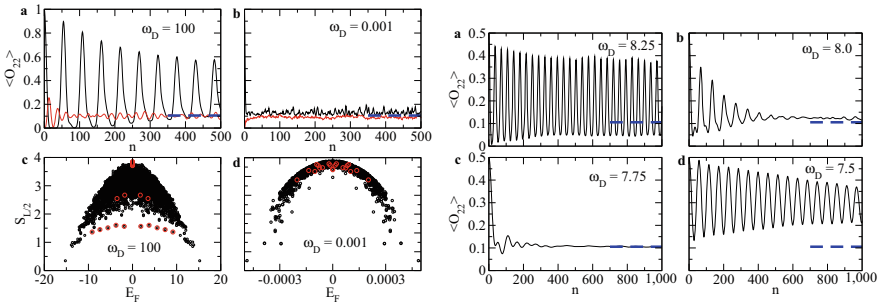


Fig. 5 Left Panel: Plot of $\langle O_{22} \rangle$ as a function of number of drive cycles n for (a) $\hbar\omega_D = 100$ and (b) $\hbar\omega_D = 0.01$. The red lines indicate dynamics starting from the state $|0\rangle$ while the black lines indicate $|\mathbb{Z}_2\rangle$. The ETH predicted thermal steady state value of $\langle O_{22} \rangle$ is ~ 0.11 as shown in blue dotted line. Plots (c) and (d) show the corresponding half-chain entanglement $S_{L/2}$. Note the presence of athermal scar states below the thermal band for $\hbar\omega_D = 100$. Such states are absent for $\hbar\omega_D = 0.01$. The red circles correspond to states which has high overlap with the initial $|\mathbb{Z}_2\rangle$ state. For all plots $\lambda = 15$, $w = \sqrt{2}$, \hbar is set to unity, and $L = 18$. Right Panel: Plot of $\langle O_{22} \rangle$ as a function of n for (a) $\hbar\omega_D = 8.25$, (b) $\hbar\omega_D = 8$, (c) $\hbar\omega_D = 7.75$, and (d) $\hbar\omega_D = 7.5$. The plots for (a) and (d) show coherent oscillation while those for (b) and (c) exhibit rapid approach to ETH predicted thermalization. All other parameters are same that in the left panel. This figure is adapted from Ref. [33]

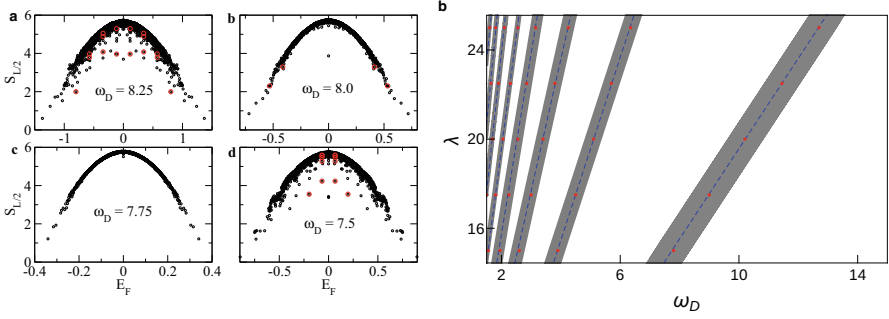


Fig. 6 Left Panel: Plots of half-chain entanglement entropy $S_{L/2}$ for (a) $\hbar\omega_D = 8.25$ (b) $\hbar\omega_D = 8$, (c) $\hbar\omega_D = 7.75$, and (d) $\hbar\omega_D = 7.5$. The plots show athermal scar states below the thermal band with low $S_{L/2}$ at $\hbar\omega_D = 8.25$ and $\hbar\omega_D = 7.5$ while no such states are found for $\hbar\omega_D = 8$ and 7.75 . The red circles exhibit states which has high overlap with the initial $|\mathbb{Z}_2\rangle$. For all plots, $\lambda = 15$, $w = \sqrt{2}$, and $L = 18$ and we have set $\hbar = 1$. Right Panel: Phase diagram in the $\lambda - \omega_D$ plane showing ergodic (shaded) and coherent (white) regions with reentrant crossover between them. All other parameters are same as those in the left panel. This figure is adapted from Ref. [33]

drive the dynamics. At high frequency, these states are athermal and lie well outside the thermal band. Thus the dynamics exhibit coherent oscillations since it involves a small, $O(L)$, subspace of the full Hilbert space. In contrast, at low frequency, the eigenstates having large overlap with $|\mathbb{Z}_2\rangle$ are part of the thermal band leading to thermalization.

Naively, one would expect a crossover between these two regimes at some intermediate drive frequency. In contrast, as shown, in the right panel Fig. 5, the system exhibits non-monotonic reentrant behavior at multiple intermediate frequencies. This is most easily noted by comparing the four plots in the right panel of Fig. 5. Clearly, ETH predicted thermalization is restored around $\hbar\omega_D \simeq 7.75w$; however, scar-induced oscillations take over at a *lower* drive frequency $\hbar\omega_D \simeq 7.5w$. The corresponding half-chain entanglement entropies, shown in the left panels of Fig. 6, indicate the presence of scars at $\hbar\omega_D = 7.5w$ and their absence at $\hbar\omega_D = 7.75w$. Further studies, carried out in Ref. [33], demonstrate multiple crossovers between ETH predicted ergodic and scar-induced coherent oscillatory behaviors at intermediate frequencies leading to the phase diagram shown in the right panel of Fig. 6. The density of the ergodic regimes increases with lower frequency and they completely cover the phase diagram at low drive frequencies leading to ergodic behavior in this regime. However, at intermediate frequencies, as shown in Ref. [33], it is possible to tune into and out of such ergodic regimes by tuning the drive frequency. This leads to the possibility of drive-frequency induced tuning of ergodicity in a driven non-integrable system.

This tunability of ergodicity can be qualitatively understood from the analytical Floquet Hamiltonian (Eqs. 27 and 29) as follows. For $\hbar\omega_D \gg \lambda_0$, $\sin\gamma \sim \gamma$ and $H_F^{(1)} \simeq H_{\text{PXP}}$. Moreover since $w/\lambda_0 \ll 1$, $H_F^{(3)}$ is negligible compared to $H_F^{(1)}$ in

this limit. Thus the Floquet Hamiltonian is of the PXP form and supports quantum scars. For an initial state $|\mathbb{Z}_2\rangle$, the dynamics gets maximal contribution from the scar subspace leading to coherent oscillation [27]. In contrast around $\gamma \simeq m\pi$ (where m is a non-zero integer), $H_F^{(1)} \rightarrow 0$ and $H_F^{(3)}$ dominates. The Floquet Hamiltonian is then not of the PXP form anymore and does not support scar states with large overlap with $|\mathbb{Z}_2\rangle$. Consequently, the dynamics becomes ergodic around $\omega_D = \omega_D^c = \gamma_0/(2m\hbar)$; the width of the ergodic regime depends on the relative magnitudes of $H_F^{(1)}$ and $H_F^{(3)}$ as we move away ω_D^c . Of course, this estimate of ω_D^c does not take into account the renormalization of $H_F^{(1)}$ from the higher order terms (such as the one from $H_F^{(3)}$) and is thus not exact. However, since these terms are typically small in the intermediate frequency regime by a factor of at least $w^3/\lambda_0^3 \ll 1$, this estimate turns out to be qualitatively correct.

Next, we consider the stroboscopic dynamics of $\langle O_{22} \rangle$ starting from the $|0\rangle$ state. We note that for $\hbar\omega_D/\lambda_0 \gg 1$, the dynamics exhibits thermalization consistent with the ETH prediction as can be seen from the left panel of Fig. 5. Thus in the quench limit, scars do not play a role in the dynamics since they have negligible overlap with the $|0\rangle$ state. As the drive frequency is lowered, however, the situation changes as can be seen from left panel of Fig. 7. Around $\hbar\omega_D = 8.5w$, we find the presence of long-time coherent oscillations while at $\hbar\omega_D = 7.88w$, $\langle O_{22} \rangle$ remains completely frozen to its initial value. The latter behavior constitutes dynamic freezing in an otherwise ergodic non-integrable system. Finally, for $\hbar\omega_D = 7.26w$, we find that $\langle O_{22} \rangle$ reaches a steady state value which is lower than the ETH predicted value (shown by the blue dotted line). This constitutes a qualitatively different violation of ETH since coherent scar-induced oscillatory dynamics (such as the one seen for $\hbar\omega_D = 8.5w$) usually leads to superthermal steady state values in contrast to the subthermal value found in the present case. The steady state behavior of $\langle O_{22} \rangle$ starting from $|0\rangle$ initial state is shown in the right panel of Fig. 7. We find that the steady state reaches its thermal value, shown by the dotted line, at large ω_D . As the

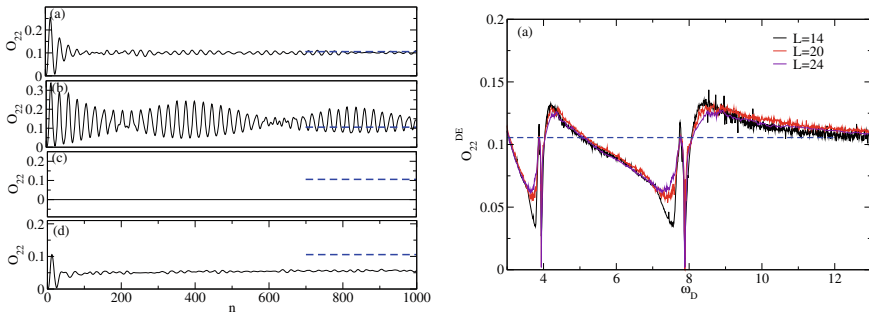


Fig. 7 Left panel: plot of $\langle O_{22} \rangle \sim O_{22}$ as a function of n for (a) $\hbar\omega_D = 100$ (b) $\hbar\omega_D = 8.5$, (c) $\hbar\omega_D = 7.88$, and (d) $\hbar\omega_D = 7.25$. For all plots, $\lambda = 15$, $w = \sqrt{2}$ and $L = 26$ and we have set $\hbar = 1$. Right panel: the steady state value of $\langle O_{22} \rangle \equiv O_{22}^{\text{DE}}$ as a function of ω_D for several L . For all plots $\lambda = 15$, $w = \sqrt{2}$ and \hbar is set to unity. This figure is adapted from Ref. [35]

frequency is lowered, it reaches superthermal steady state value. Here the dynamics indicates coherent long-time stroboscopic oscillation. Just below $\hbar\omega_D < 8w$, the steady state value of $\langle O_{22} \rangle$ drops and reaches zero at $\hbar\omega_D \simeq 7.88w$. This constitutes an example of dynamical freezing [79, 80]. This is followed by a wide range of frequency at which the steady state value remains subthermal. We also note the presence of a second freezing point at around $\hbar\omega_D \simeq 3.95w$. These steady state values of O_{22} seem to be independent of system size within the range of L accessible within ED.

The oscillatory behavior of O_{22} starting from $|0\rangle$ can be understood by observing the nature of the Floquet eigenstates as shown in the leftmost panel of Fig. 8. The plot shows the presence of a different set of athermal states (indicated by red circles) which has large overlap with the $|0\rangle$. These states are different from the scars which has large overlap with $|\mathbb{Z}_2\rangle$ shown by green circles. Thus the Floquet Hamiltonian at these frequencies supports at least two separate set of scar states; this phenomenon has no analog in scars of the PXP model. Indeed, as the frequency is increased, the set of scar states which has large overlap with $|0\rangle$ merge into the continuum of thermal states leaving behind only athermal $|\mathbb{Z}_2\rangle$ scars. This brings out the central role of higher order terms in the Floquet Hamiltonian for generation of such scars. The presence of such scars leads to coherent oscillatory dynamics of O_{22} . Its steady state value turns out to be superthermal which can be seen from the left-center panel of Fig. 8. This is due to the fact that for most scar eigenstates that have large overlap with $|0\rangle$ (shown as red circles in the left-center panel of Fig. 8), $\langle O_{22} \rangle$ is larger than the ETH predicted thermal value.

Similar scar states with large overlap with $|0\rangle$ are shown by red circles in the right-center panel of Fig. 8 for $\hbar\omega_D = 7.26w$. Here in contrast to the case $\hbar\omega_D = 8.5$, the initial state $|0\rangle$ turns out to have relatively large overlap (>0.01) with a few scars states as shown in the figure and small overlap with a large number of thermal states. The presence of these thermal states do not allow for long-time coherent oscillations. However, the steady state value of $\langle O_{22} \rangle$ is controlled by the athermal scar states since they have relatively large overlap with $|0\rangle$. It turns out that these athermal scar states have a subthermal value of $\langle O_{22} \rangle$ (as can be seen from

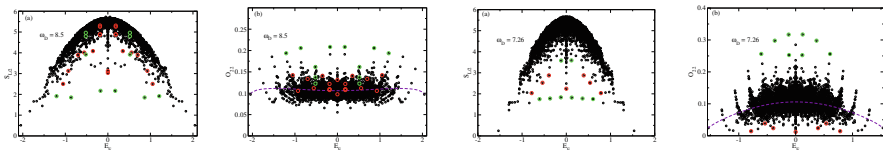


Fig. 8 Leftmost panel: plot of $S_{L/2}$ as a function of E_F for $\hbar\omega_D = 8.5$. The green circles indicate states having large overlap with $|\mathbb{Z}_2\rangle$ while the red circles indicate those having large overlap with $|0\rangle$. For all plots, $\lambda = 15$, $w = \sqrt{2}$, and $L = 26$. Left-center panel: plot of $\langle O_{22} \rangle \equiv O_{22}$ for all Floquet eigenstates. The red and the green circles indicate contribution from states with large overlap with $|0\rangle$ and $|\mathbb{Z}_2\rangle$, respectively. The violet dotted line indicates the ETH prediction for O_{22} . Right-center and rightmost panels: same as the leftmost and the left-center panels, respectively, but for $\hbar\omega_D = 7.26$. This figure is adapted from Ref. [35]

the rightmost panel of Fig. 8). Thus $\langle O_{22} \rangle$ quickly decays to a subthermal steady state value leading to violation of ETH. We note that such a violation does not involve oscillatory dynamics and thus constitutes a separate route of scar-induced ETH violation in finite boson chains which has no analogue in chains subjected to quench. [35].

Finally, we discuss the phenomena of dynamic freezing at $\hbar\omega_D \simeq 7.88$ for $w = \sqrt{2}$ and $\lambda = 15$. Qualitatively, the existence of such freezing is easy to understand by noting that the state $|0\rangle$ is annihilated by all non-PXP higher order terms of the Floquet Hamiltonian. This follows from the fact that such terms necessarily involve $\tilde{\sigma}_j^-$ operator which annihilates the state $|0\rangle$. Thus for drive period, where the coefficient of $H_F^{(1)}$ vanishes, $U(T, 0) \rightarrow I$ and one encounters freezing. This argument, in conjunction with the first order perturbative Floquet Hamiltonian, suggests that the freezing would occur at frequencies for which $w_r = 0$: $\hbar\omega_D = \lambda/(2n)$. This predicts a freezing frequency of $\hbar\omega_D = 7.5$ which differs quite a bit with the exact result.

This discrepancy can be understood by noting that the first order Floquet Hamiltonian neglects the normalization of w_r due to contribution of higher order term such as the one from $H_F^{(3)}$ (Eq. 29). To see this, we consider an exact analytical calculation of H_F for $L = 3$. Here the exact analytic calculation is feasible since the Hilbert space consists of just two states in the zero momentum sector; this reduces the problem to a driven two-state problem [35]. These two states are $|0\rangle = |\downarrow, \downarrow, \downarrow\rangle$ and $|1\rangle = (|\downarrow, \uparrow, \downarrow\rangle + |\uparrow, \downarrow, \downarrow\rangle + |\downarrow, \downarrow, \uparrow\rangle)/\sqrt{3}$. The Hamiltonian, the space of these two states, reads

$$H_2(t) = \begin{pmatrix} 0 & -\sqrt{3}w \\ -\sqrt{3}w & \lambda(t) \end{pmatrix}. \quad (36)$$

For the square pulse protocol given by Eq. 22 the Floquet Hamiltonian H'_F corresponding to $H_2(t)$ can be exactly computed [35]. A straightforward calculation shows that

$$\langle 0|H'_F T|1\rangle = \cos^{-1} \left[1 - \frac{12w^2}{\Delta_0^2} \{1 - \cos(\Delta_0 T/2)\} \right], \quad \Delta_0 = \sqrt{\lambda_0^2 + 12w^2}. \quad (37)$$

This matrix element, which needs to be finite for the driven system to evolve, vanishes for $\Delta_0 T = 4m\pi$ (where m is an integer). For $\lambda = 15$ and $w = \sqrt{2}$, $\hbar\omega_D \simeq 7.86$ for $m = 1$, and this provides a near exact match to the observed freezing frequency. Moreover, it also predicts the second freezing point at $\hbar\omega_D \simeq 3.93$ which correspond to $m = 2$. We note that for $\lambda \gg w$, this frequency will reduce to that predicted by first order Floquet theory ($\hbar\omega_D = \lambda/2m$) as expected. The reason for the accuracy of the result obtained with this simplistic calculation is that the higher order multiple spin terms in H_F do not contribute to the freezing phenomenon as discussed earlier. We note that at the freezing point the state $|0\rangle$ is disconnected from all other states in the Hilbert space of the system; this constitutes an example of (weak) fragmentation of the Hilbert space of H_F .

Before ending this section, we note that the periodic dynamics of Rydberg atoms has been studied experimentally in Ref. [26]. The experiment used a continuous drive protocol using a damped cosine drive and starting from $|Z_2\rangle$; it was found that the system exhibits a robust subharmonic response to the drive. It was noted that this response depended on the initial state and its relation to quantum scars in the system was discussed. However, the dynamics of the system starting from $|0\rangle$ state or that in the presence of a square pulse protocol has not been studied in this work.

5 Hilbert Space Fragmentation: A Minimal Model

It has been recently pointed out that the presence of dynamical constraints in a many-body system may lead to fragmentation of its Hilbert space into several disconnected sectors. This phenomenon, termed as Hilbert space fragmentation (HSF), provides yet another route to violation of ETH in non-integrable quantum systems [81–90]. This phenomenon naturally arises in constrained systems where the presence of additional conservation laws provide the constraint [81–89]. The resulting physics has close similarity with those of fractons [91, 92]. The realization of such constrained systems using circuit models whose Hilbert space is identical to that of a $S = 1$ spin chain of length L provides a neat example in this context [83]. In this case, it was shown that the presence of two simultaneous $U(1)$ conserved quantities, namely $Q = \sum_j S_j^z$ (which is analogous to total charge in a fractonic model) and $P = \sum_j j S_j^z$ (dipole moment of a fractonic model), provides the necessary constraints for fragmentation. Typically, in most of the models studied, such conservation comes from the commutation $[Q, H] = [P, H] = 0$ and remains valid for all states in the Hilbert space; moreover, they lead to an exponentially large number of inert zero-energy states in the Hilbert space. We note here such fragmentation may even separate states with same symmetry into different, disconnected, segments within the Hilbert space. Such fragmentation is dubbed as “strong” if the Hilbert space is fragmented in exponentially many separate sectors; in this case, the number of states that leads to violation of ETH increases exponentially with system size [81, 84]. If this condition is not satisfied, the fragmentation is termed as weak; in this sense, scars constitute an example of weak fragmentation of Hilbert space. A recent experiment involving Fermi-Hubbard model has observed non-ergodic behavior in a tilted Fermi-Hubbard system which can possibly be attributed to such fragmentation [93]. In the rest of this section, we shall discuss such fragmentation in a model which was inspired by the Floquet Hamiltonian of the tilted Bose-Hubbard model; the details of HSF and its realization in other model can be found in Ref. [81].

5.1 Model and Fragmentation

The tilted Bose-Hubbard model constitutes an example of a spin-half system in a constrained Hilbert space. However, the model does not show HSF. The reason for this becomes clear when one analyzes the connectivity of the states of the model in the number basis in the PXP limit. It turns out, as noted in Ref. [90], that most states in the Hilbert space are connected under the action of H_{PXP} via the state $|0\rangle$. Thus a Hamiltonian which would annihilate the state $|0\rangle$ may lead to HSF. Taking cue from the structure of the Floquet Hamiltonian for the periodic driven tilted Bose-Hubbard model, Ref. [90] pointed out that one such possible model involving spin-half Pauli matrices on a 1D chain is given by

$$H_{\text{fr}} = w \sum_{j=1}^L (\tilde{\sigma}_{j-1}^+ \tilde{\sigma}_{j+1}^+ \tilde{\sigma}_j^- + \text{h.c.}), \quad (38)$$

where w is an arbitrary energy scale which shall be set to unity for the rest of this section and it is understood that H_{fr} acts on the constrained Hilbert where two up-spins cannot be neighbors. We note that H_{fr} is identical to the three-spin term in the third order Floquet Hamiltonian (Eq. 29) but with its coefficient set to unity. Such a term becomes the largest term in H_F around the point where renormalized $H_F^{(1)}$ (Eq. 27) vanishes. We note that H_{fr} do not have any simultaneous conserved quantities and thus differ from a class of earlier studied models [81].

The simplest class of states that demonstrates such fragmentation corresponds to blocks of length $\ell = 3$ with one or two up-spins in a background of down-spins [90]. These states can be written as

$$|X_{1,j}\rangle = |\dots 1_{j-1} 0_j, 1_{j-1} \dots\rangle, \quad |X_{2,j}\rangle = |\dots 0_{j-1} 1_j, 0_{j-1} \dots\rangle, \quad (39)$$

where we have denoted up- and down-spins by 1 and 0, respectively, and ellipsis indicates down-spins on all other sites. It is easy to see that under action of H_{fr} , these blocks transform to each other: $H_{\text{fr}}|X_{1,j}\rangle = |X_{2,j}\rangle$ and $H_{\text{fr}}|X_{2,j}\rangle = |X_{1,j}\rangle$. They are connected to any other states in the Hilbert state and thus constitute a fragment. Their linear combination

$$|X_{\pm,j}\rangle = \frac{1}{\sqrt{2}}(|X_{1,j}\rangle \pm |X_{2,j}\rangle) \quad (40)$$

yields eigenstates of H_{fr} with eigenvalues ± 1 (we have set $w = 1$). Moreover, if two such blocks are spaced with at least two down-spins separating them, they act as non-interacting entities and the total energy of the system becomes a sum of the energy of the individual blocks. This leads to a class of eigenstates with zero and integer (in units of w) energies: $E = (n_+ - n_-)$, where n_{\pm} are the number of isolated $|X_{\pm}\rangle$ blocks in the state. We note that these blocks are localized and are dubbed as ‘‘bubbles’’ in Ref. [90].

These bubbles develop dispersion when two individual bubbles are allowed to interact by placing them next to one another. The simplest of these states can be understood analytically, and they form a closed Hilbert space fragment spanned by the states [90]

$$\begin{aligned}
 |\psi_{1,k}\rangle &= \sum_j e^{ikj} T_j |\dots X_{2,j} X_{2,j+3} \dots\rangle \equiv \sum_j e^{ikj} T_j |\dots 0_{j-1} 1_j 0_{j+1} 0_{j+2} 1_{j+3} 0_{j+4} \dots\rangle \\
 |\psi_{2,k}\rangle &= \sum_j e^{ikj} T_j |\dots X_{1,j} X_{2,j+3} \dots\rangle \equiv \sum_j e^{ikj} T_j |\dots 1_{j-1} 0_j 1_{j+1} 0_{j+2} 1_{j+3} 0_{j+4} \dots\rangle \quad (41)
 \end{aligned}$$

where T_j denotes the translation operator, the lattice spacing has been set to unity, and the ellipsis denotes all down-spins. It was shown in Ref. [90] that $|\psi_{1(2),k}\rangle$ form a closed subspace with

$$H_{\text{fr}} \begin{pmatrix} |\psi_{1,k}\rangle \\ |\psi_{2,k}\rangle \end{pmatrix} = \begin{pmatrix} 0 & (1 + e^{ik}) \\ (1 + e^{-ik}) & 0 \end{pmatrix} \begin{pmatrix} |\psi_{1,k}\rangle \\ |\psi_{2,k}\rangle \end{pmatrix}. \quad (42)$$

This leads to a pair of eigenstates in the momentum space given by

$$E_k = \pm 2 \cos k/2. \quad (43)$$

It was noted in Ref. [90] that Eq. referenmom provide an analytical explanation for the presence another class of eigenstates with $E = \pm 2$ (for $k = 0$), $E = \pm 1$ (for $k = 2\pi/3$), and $E = 0$ (for $k = \pi$). Further for $L \geq 8$ such that $L = 4n$ ($n \in \mathbb{Z}$), $k = \pi/2$ leads to $E = \pm\sqrt{2}$; this provides a natural explanation of such eigenstates with simple irrational eigenvalues that was found in the spectrum of H_{fr} .

Apart from such simple fragments, more complicated fragments with much longer bubbles leading to flat bands were discussed in Ref. [90]. We shall not discuss them in detail here. However, we would like to point out that the model exhibits a phenomenon, dubbed as secondary fragmentation in Ref. [90], which was not found in earlier works. Such secondary fragmentation happens when basis states within a primary fragments form a further closed subspace under action of H_{fr} ; these states are constructed out of specific linear combination of a fixed number of basis states and they turn out to be orthogonal to other states within the same primary fragment. The eigenvalues corresponding to such eigenstates, for the model discussed in Ref. [90], are integers, and their number increases with increasing L ; importantly, their existence can not be straightforwardly tied local classical conservation conditions.

5.2 Adding a Staggered Field

In this section, we shall focus on the structure of the zero-energy eigenstates of the model in the ‘‘bubble’’ sector. To this end, as pointed out in Ref. [90], it is useful to

add a staggered magnetic field to the model leading to

$$H = H_{\text{fr}} + H_{\Delta}, \quad H_{\Delta} = \frac{\Delta}{2} \sum_j (-1)^j \sigma_j^z. \quad (44)$$

We note that there exists two operators

$$Q = \prod_j \sigma_j^z, \quad C = \prod_j (\sigma_{2j}^z + \sigma_{2j+1}^z). \quad (45)$$

We note that $[H, Q] = 0$ so that the spectrum of H is symmetric around E . Moreover, we note that H_{Δ} anticommutes with C . This allows for presence of zero-energy modes of H . The details of these zero modes have been worked out in Ref. [90].

Since H_{Δ} is diagonal in the number basis, it makes sense to work in the diagonal basis in $|X_{1(2)}\rangle$ states. In the space of these states, it is possible to represent H in terms of pseudospin operators τ_j^{α} ($\alpha = x, y, z$) such that $\tau_j^x |X_{1,j}\rangle = |X_{2,j}\rangle$. In terms of these pseudospin operators, one can write H as [90]

$$H = \epsilon_0 \sum_j \sum_{\alpha=x,y,z} \eta^{\alpha} \tilde{\tau}_j^{\alpha} + \frac{\Delta}{2} (n_{\text{odd}} - n_{\text{even}}), \quad \epsilon_0 = \sqrt{1 + 9\Delta^2/4}, \quad \eta = (\eta^x, \eta^y, \eta^z) = (1, 0, 3\Delta/2)/\epsilon_0 \quad (46)$$

where $n_{\text{odd/even}}$ are the number of bubbles centered on odd or even sites. Here we have defined $\tilde{\tau}_j^{y,z} = (-1)^j \tau_j^{y,z}$ and $\tilde{\tau}_j^x = \tau_j^x$ for all j , where j denotes the center of the bubbles and the sum over j indicates sum over number of such bubbles. Thus we find H reduces to a collection of non-interacting pseudospins (with $s = 1/2$) on every site. This indicates that the sector will contribute states to the Hilbert space of H which has area-law entanglement. Moreover, these states indicate a novel feature when it comes to out-of-equilibrium dynamics of initial states belonging to the bubble sector.

To see this, let us consider a square pulse protocol for which $\Delta(t) = -(+)\Delta_0$ for $t \leq (>)T/2$, where $T = 2\pi/\omega_D$ is the driving frequency. We shall assume that we start the dynamics from a state which belongs to the bubble sector; HSF then ensures that the dynamics will be controlled by states within the sector. Since H constitutes non-interacting pseudospins on every center site of a bubble, $U(T, 0)$ corresponding to a square pulse drive protocol can be found exactly. The reason for this stems from the fact that here one deals with a $s = 1/2$ pseudospin on every such site; this is similar to an analogous problem for Ising or other integrable model where an analogous structure can be seen in momentum space [56]. A straightforward analysis yields for $n_{\text{odd}} = n_{\text{even}}$ [90]

$$U(T, 0) = \prod_{j=1..L} \begin{pmatrix} p_j & q_j \\ -q_j^* & p_j \end{pmatrix}, \quad p_j = \frac{(3\Delta_0/2)^2 + \cos(\epsilon_0 T)}{\epsilon_0^2},$$

$$q_j = \frac{(-1)^j (3\Delta/2) [1 - \cos(\epsilon_0 T)] - i\epsilon_0 \sin(\epsilon_0 T)}{\epsilon_0^2}. \quad (47)$$

This shows that $U(T, 0) = I$ when $\omega_D = \omega_f = \epsilon_0/n$. At these frequencies, the stroboscopic dynamics of the system, starting from any of the states in the bubble sector, exhibits dynamical freezing [35, 72, 79, 80]. Such freezing clearly stems from fragmentation and is a non-perturbative exact phenomenon. Moreover, its existence shows up in the dynamics of simple initial states in the Fock space (such as $|X_{1,j}\rangle$) making it experimentally accessible.

5.3 Connection to Lattice Gauge Theories

Finally, we point out the connection of these systems to lattice gauge theories. The possibility of simulating lattice gauge theories using optical lattice systems has been a subject of recent interest [94–99]. The reason for this is partly the possibility of realization of an experimental platform for study of confinement. It is well-known from the seminal work of Ref. [100] that in 1D quantum electrodynamics, charges (charge $\pm e$ for particles and anti-particles) display the phenomenon of confinement in the presence of a background of electric field E_b . This confinement stems from the fact that the energy of these charges increases linearly with the distance between them. This is characterized by a parameter θ which is proportional to the background electric field E_b : $\theta = 2\pi E_b/e$. It was shown for all $\theta \neq \pi$, a pair of charges remains confined since their energy grows linearly with distance when they are attempted to be separated. It was also pointed out in Ref. [100] that this form of confinement holds in $d = 1$; for higher dimensions, the presence of transverse photons changes the scenario and leads to deconfinement.

A variant of this phenomenon is expected to be found in possible realization of $U(1)$ lattice gauge theories, generically termed as quantum link models [94–99], using optical lattice platforms. Indeed, a recent work on the PXP model in the presence of an additional staggered magnetic field of strength Δ showed that such a model can be mapped to a $U(1)$ lattice gauge theory with $\Delta = J(\theta/\pi - 1)$ [99], where J is a microscopic energy scale. Thus the absence of Δ that corresponds to $\theta = \pi$ in the gauge theory language corresponds to the PXP model that shows deconfined behavior. In contrast, the presence of a large Δ leads to confining behavior whose signature can be picked up in quench dynamics of such system [99]. We note here that an active field of research in this area involves understanding the role of gauge invariance in the dynamical evolution of these systems both experimentally [101] and theoretically [102, 103].

To understand the mapping of H_{fr} to lattice gauge theory, we begin by writing the spin variables in the language of Kogut-Susskind fermions [104]. This provides a simple dictionary which relates the Rydberg spins σ_j^α to the fermionic matter (denoted by fields ψ) and gauge fields (denoted by field \hat{E}) which are the degrees of freedom in the gauge theory. The gauge (electric) field and the Rydberg spins live on the link ℓ of the dual 1D lattice (i.e., sites of the original lattice) while the fermionic matter fields live on the sites j of the dual lattice. The electric fields take

value $\pm 1/2$ and are related to the Rydberg spins via the relation [90]

$$E_\ell = S_\ell^z = \eta_j \sigma_\ell^z / 2, \quad (48)$$

where $\eta_j = \pm 1$ refers to the site j at the left of the link ℓ and is $1(-1)$ if that site is odd(even). The fermionic matter field ψ_j is related to the electric field by the Gauss's law $G_j = 0$ where [94]

$$G_j = E_\ell - E_{\ell+1} - \hat{n}_j - [1 + (-1)^j] / 2, \quad \hat{n}_j = \psi_j^\dagger \psi_j. \quad (49)$$

It turns out that the constraint of having no two up-spins as neighbors is exactly implemented by this law; moreover, the number of gauge-invariant states for a chain of length L exactly equals the number of states within the constrained Hilbert space of the PXP model. In this language, the PXP model, supplemented by the staggered magnetic field term, can be written as [99]

$$H_{\text{spin}} = - \sum_j \tilde{\sigma}_j^x + \frac{\Delta}{2} \sum_j (-1)^j \sigma_j^z \equiv - \sum_i (\psi_i^\dagger U_\ell \psi_{i+1} + \text{h.c.}) + m \sum_i \psi_i^\dagger \psi_i, \quad (50)$$

where $U_\ell = S_\ell^+$ leading to $[E_\ell, U_\ell] = U_\ell$ and ℓ joins the dual lattice sites i and $i + 1$. Thus the staggered spin term acts as the mass of the fermion fields.

It turns out that H_{fr} can also be written in the gauge theory language leading to a Hamiltonian [90]

$$H_{\text{fr}} = \sum_{i=1}^L \psi_i^\dagger U_\ell U_{\ell+1} U_{\ell+2} \psi_{i+3} \Gamma_{i+1} \Gamma_{i+2} + \text{h.c.}, \quad (51)$$

where ℓ is the link between the sites i and $i + 1$ on the dual lattice and $\Gamma_i = \hat{n}_i$ for odd and $(1 - \hat{n}_i)$ for even i , respectively. It was shown in Ref. [90] that $[H_{\text{fr}}, G_j] = 0$ which ensures that H_{fr} obeys Gauss's law. The key point about the gauge theory representations of H_{fr} (Eq. 51) is that it only conserves local charge. There is no dipole moment conservation associated with this model unlike most models of Hilbert space fragmentation (see Refs. [82–85]) studied earlier.

Instead, such fractonic behavior may appear as emergent phenomenon in certain sectors of theory [90]. This was demonstrated in Ref. [90] in the bubble sector. To see this let us consider a single bubble state. All the down spin outside this bubble are annihilated by H_{fr} . In the gauge theory language, this means that within this sector, all the fermionic charges outside the bubble are immobile. It was shown that the dynamics involve only the bubble which, here, constitutes dipoles involving three lattice sites (length three dipoles). Only these dipoles have significant dynamics under action of H_{fr} and this leads to emergent fractonic physics. We note that this emergence occurs in a fragment of the Hilbert space which is not necessarily a low-energy sector. Other fragmented sectors may show similar emergence, and this is discussed in detail in Ref. [90].

6 Discussion

In this review, we have touched upon several aspects of the tilted boson chain which can be realized in 1D optical lattices hosting trapped ultracold bosons. It turns out that the physics of this system has close parallel to that of Rydberg atoms in the sense that both systems are described by similar effective Hamiltonians in their low-energy sector.

The ground state phase diagram of such bosonic system provides a route to realizing translational symmetry broken Mott states. In addition, they also host a quantum phase transition between Mott states with broken and unbroken translational symmetries. For the tilted boson chain, this transition belongs to the Ising universality class and can be understood in terms of a dipole model of the bosons. A modification of this dipole model may lead to realization of non-Ising critical points, as has been seen in Rydberg atom arrays.

The quench dynamics of these systems provided the key clue to unraveling the presence of quantum scars in their Hilbert space. Such states lead to a weak violation of the eigenstate thermalization hypothesis in finite chain as has been seen in recent experiments involving these systems. The ramp dynamics of these systems near their critical point may provide a platform to test Kibble-Zurek scaling law; this is particularly interesting for the Rydberg arrays where the transition is non-Ising like.

The study of periodic dynamics of such systems shows the possibility of tuning their ergodicity properties using the drive frequency. It was found that these systems shows unconventional phenomenon such as the presence of subthermal steady states, long term coherent oscillations, and dynamical freezing in the presence of a periodic drive. These effects can be analyzed using the Floquet Hamiltonian of these driven system; moreover, they occur, in contrast to their quench counterparts, for both $|0\rangle$ and $|\mathbb{Z}_2\rangle$ initial states and constitute different routes to violation of ETH in finite-sized chains.

The Floquet Hamiltonian of this periodically driven system provides a class of terms which can act as a minimal model for $s = 1/2$ spins exhibiting HSF. This model, unlike some earlier models displaying HSF, does not have simple conserved quantities which causes the fragmentation; instead, such conservation emerges in specific sector of the model. Also, the model provides an example of secondary fragmentation which does not follow from classical conservation laws. As a consequence of HSF, the model exhibits exact dynamical freezing for an infinite number of drive frequencies and for an exponentially large number initial classical Fock states.

Several aspects of this tilted boson chains and/or Rydberg ladders remain to be studied. These include the effect of staggered detuning term on the driven system, the physics of multiple interacting Rydberg chains and manifestation of the physics of these driven system in higher dimensions. These studies are expected to add to the already large class of the physical phenomenon seen in these systems.

Acknowledgments KS thanks D. Banerjee, B. K. Clark, U. Divakaran, P. Fendley, S. M. Girvin, R. Ghosh, S. Kar, M. Kolodrubetz, B. Mukherjee, S. Nandy, D. Pekker, S. Powell, S. Sachdev, A. Sen, and D. Sen for collaborations on several related projects. KS thanks DST, India for support through SERB project JCB/2021/000030.

References

1. M. Greiner, O. Mandel, T. Esslinger, T.W. Hansch, I. Bloch, *Nature (London)* **415**, 39 (2002)
2. C. Orzel, A.K. Tuchman, M.L. Fenselau, M. Yasuda, M.A. Kasevich, *Science* **291**, 2386 (2001)
3. W. Bakr, J. Gillen, A. Peng, S. Foelling, M. Greiner, *Nature* **462**, 74 (2009)
4. W. Bakr, A. Peng, E. Tai, R. Ma, J. Simon, J. Gillen, S. Foelling, L. Pollet, M. Greiner, *Science* **329**, 547 (2010)
5. I. Bloch, J. Dalibard, W. Zwerger, *Rev. Mod. Phys.* **80**, 885 (2008)
6. D. Jaksch, C. Bruder, J.I. Cirac, C.W. Gardiner, P. Zoller, *Phys. Rev. Lett.* **81**, 3108 (1998)
7. M.P.A. Fisher, P.B. Weichman, G. Grinstein, D.S. Fisher, *Phys. Rev. B* **40**, 546 (1989)
8. W. Krauth, N. Trivedi, D. Ceperley, *Phys. Rev. Lett.* **67**, 2307 (1991); J.K. Freericks, H.R. Krishnamurthy, Y. Kato, N. Kawashima, N. Trivedi, *Phys. Rev. B* **79**, 053631 (2009); A. Kuklov, N. Prokofiev, B. Svistunov, *Phys. Rev. Lett.* **93**, 230402 (2004)
9. K. Sheshadri, H.R. Krishnamurthy, R. Pandit, T.V. Ramakrishnan, *Europhys. Lett.* **22**, 257 (1993)
10. J. Freericks, P. Monien, *ibid.* **26**, 545 (1995)
11. K. Sengupta, N. Dupuis, *Phys. Rev. A* **71**, 033629 (2005); J.K. Freericks, H.R. Krishnamurthy, Y. Kato, N. Kawashima, N. Trivedi, *Phys. Rev. A* **79**, 053631 (2009)
12. C. Trefzger, K. Sengupta, *Phys. Rev. Lett* **106**, 095702 (2011)
13. L. Balents, L. Bartosch, A. Burkov, S. Sachdev, K. Sengupta, *Phys. Rev. B* **71**, 144508 (2005); *ibid.*, *Phys. Rev. B* **71**, 144509 (2005)
14. R.G. Melko, A. Paramekanti, A.A. Burkov, A. Vishwanath, D.N. Sheng, L. Balents, *Phys. Rev. Lett.* **95**, 127207 (2005)
15. S.V. Isakov, S. Wessel, R.G. Melko, K. Sengupta, Y.B. Kim, *Phys. Rev. Lett.* **97**, 147202 (2006); K. Sengupta, S.V. Isakov, Y.B. Kim, *Phys. Rev. B* **73**, 245103 (2006)
16. A. Isacsson, M.-C. Cha, K. Sengupta, S.M. Girvin, *Phys. Rev. B* **72**, 184507 (2005)
17. E. Altman, W. Hofstetter, E. Demler, M.D. Lukin, *New J. Phys.* **5**, 113 (2003)
18. T. Grass, K. Saha, K. Sengupta, M. Lewenstein, *Phys. Rev. A* **84**, 053632 (2011)
19. S. Mandal, K. Saha, K. Sengupta, *Phys. Rev. B* **86**, 155101 (2012)
20. W.S. Cole, S. Zhang, A. Paramekanti, N. Trivedi, *Phys. Rev. Lett.* **109**, 085302 (2012)
21. J. Radic, T. Sedrakyan, I. Spielman, V. Galitski, *Phys. Rev. A* **84**, 063604 (2011)
22. S. Sachdev, K. Sengupta, S.M. Girvin, *Phys. Rev. B* **66**, 075128 (2002)
23. H. Bernien, S. Schwartz, A. Keesling, H. Levine, A. Omran, H. Pichler, S. Choi, A.S. Zibrov, M. Endres, M. Greiner, V. Vuletic, M.D. Lukin, *Nature (London)* **551**, 579 (2017)
24. H. Levine, A. Keesling, A. Omran, H. Bernien, S. Schwartz, A.S. Zibrov, M. Endres, M. Greiner, V. Vuletic, M.D. Lukin, *Phys. Rev. Lett.* **121**, 123603 (2018)
25. S. Ebadi, T.T. Wang, H. Levine, A. Keesling, G. Semeghini, A. Omran, D. Bluvstein, R. Samajdar, H. Pichler, W.W. Ho, S. Choi, S. Sachdev, M. Greiner, V. Vuletic, M.D. Lukin, *Nature* **595**, 227 (2021)
26. D. Bluvstein, A. Omran, H. Levine, A. Keesling, G. Semeghini, S. Ebadi, T.T. Wang, A.A. Michailidis, N. Maskara, W.W. Ho, S. Choi, M. Serbyn, M. Greiner, V. Vuletic, M.D. Lukin, *Science* **371**, 1355 (2021)
27. For a recent review on quantum scars, see arXiv:2108.03460

28. S. Choi, C.J. Turner, H. Pichler, W.W. Ho, A.A. Michailidis, Z. Papic, M. Serbyn, M.D. Lukin, D.A. Abanin, Phys. Rev. Lett. **122**, 220603 (2019); W.W. Ho, S. Choi, H. Pichler, M.D. Lukin, Phys. Rev. Lett. **122**, 040603 (2019)
29. C.J. Turner, A.A. Michailidis, D.A. Abanin, M. Serbyn, Z. Papic, Nat. Phys. **14**, 745 (2018); C.J. Turner, A.A. Michailidis, D.A. Abanin, M. Serbyn, Z. Papic, Phys. Rev. B **98**, 155134 (2018); K. Bull, I. Martin, Z. Papic, Phys. Rev. Lett. **123**, 030601 (2019)
30. S. Moudgalya, N. Regnault, B.A. Bernevig, Phys. Rev. B **98**, 235156 (2018)
31. V. Khemani, C.R. Laumann, A. Chandran, Phys. Rev. B **99**, 161101(R) (2019); N. Shiraishi, J. Stat. Mech. (2019) 083103
32. T. Iadecola, M. Schechter, S. Xu, Phys. Rev. B **100**, 184312 (2019); M. Schechter, T. Iadecola, Phys. Rev. Lett. **123**, 147201 (2019)
33. B. Mukherjee, S. Nandy, A. Sen, D. Sen, K. Sengupta, Phys. Rev. B **101**, 245107 (2020)
34. B. Mukherjee, A. Sen, D. Sen, K. Sengupta, Phys. Rev. B **102**, 014301 (2020)
35. B. Mukherjee, A. Sen, D. Sen, K. Sengupta, Phys. Rev. B **102**, 075123 (2020)
36. D. Banerjee, A. Sen, Phys. Rev. Lett. **126**, 220601 (2021); K. Lee, R. Melendrez, A. Pal, H. J. Changlani, Phys. Rev. B **101**, 241111(R) (2020); P.A. McClarty, M. Haque, A. Sen, J. Richter, Phys. Rev. B **102**, 224303 (2020)
37. S. Moudgalya, B.A. Bernevig, N. Regnault, Phys. Rev. B **102**, 195150 (2020); B. Nachtergaele, S. Warzel, A. Young, arXiv:2006.00300
38. S. Sugiura, T. Kuwahara, K. Saito, arXiv:1911.06092; S. Pai, M. Pretko, Phys. Rev. Lett. **123**, 136401 (2019)
39. H. Zhao, J. Vovrosh, F. Mintert, J. Knolle, Phys. Rev. Lett. **124**, 160604 (2020); K. Mizuta, K. Takasan, N. Kawakami, Phys. Rev. Res. **2**, 033284 (2020)
40. P. Fendley, K. Sengupta, S. Sachdev, Phys. Rev. B **69**, 075106 (2004)
41. S. Pielawa, T. Kitagawa, E. Berg, S. Sachdev, Phys. Rev. B **83**, 205135 (2011); S. Pielawa, E. Berg, S. Sachdev, Phys. Rev. B **86**, 184435 (2012); R. Samajdar, W.W. Ho, H. Pichler, M.D. Lukin, S. Sachdev Phys. Rev. Lett. **124**, 103601 (2020)
42. A.R. Kolovsky, Phys. Rev. A **93**, 033626 (2016); *ibid*, Phys. Rev. A **98**, 013603 (2018); R. Yao, J. Zakrzewski, Phys. Rev. B **102**, 104203 (2020)
43. M. Yue, Z. Wang, B. Mukherjee, Z. Cai, Phys. Rev. B **103**, 201113 (2021)
44. C. Zhang, A. Safavi-Naini, A.M. Rey, B. Capogrosso-Sansone, New. J. Phys. **17**, 123014 (2017); S. Bandyopadhyay, R. Bai, S. Pal, K. Suthar, R. Nath, D. Angom, Phys. Rev. A **100**, 053623 (2019); C. Zhang, J. Zhang, J. Yang, B. Capogrosso-Sansone, Phys. Rev. A **103**, 043333 (2021)
45. C.P. Rubbo, S.R. Manmana, B.M. Peden, M.J. Holland, A.M. Rey, Phys. Rev. A **84**, 033638 (2011); A.V. Gorshkov, S.R. Manmana, G. Chen, J. Ye, E. Demler, M.D. Lukin, A.M. Rey, Phys. Rev. Lett. **107**, 115301 (2011)
46. R. Yao, T. Chanda, J. Zakrzewski, Phys. Rev. B. **104**, 014201 (2021); *ibid*, arXiv:2101.11061
47. B. Mukherjee, Z. Cai, W. Vincent Liu, Phys. Rev. Res. **3**, 033201 (2021)
48. J.H. Davies, J.W. Wilkins, Phys. Rev. B **38**, 1667 (1998)
49. M. Kolodrubetz, D. Pekker, B.K. Clark, K. Sengupta, Phys. Rev. B **85** 100505(R) (2012)
50. S. Whitsitt, R. Samajdar, S. Sachdev, Phys. Rev. B **98**, 205118 (2018)
51. R. Samajdar, S. Choi, H. Pichler, M.D. Lukin, S. Sachdev, Phys. Rev. A **98**, 023614 (2018)
52. R. Ghosh, A. Sen, K. Sengupta, Phys. Rev. B **97**, 014309 (2018)
53. A. Polkovnikov, K. Sengupta, A. Silva, M. Vengalattore, Rev. Mod. Phys. **83**, 863 (2011)
54. J. Dziarmaga, Adv. Phys. **59**, 1063 (2010)
55. A. Dutta, U. Divakaran, D. Sen, B.K. Chakrabarti, T.F. Rosenbaum, G. Aeppli, *Quantum Phase Transitions in Transverse Field Spin Models: From Statistical Physics to Quantum Information* (Cambridge University Press, Cambridge, 2015)
56. S. Mondal, D. Sen, K. Sengupta, in *Quantum Quenching, Annealing and Computation*, ed. by A. Das, A. Chandra, B.K. Chakrabarti, Lecture Notes in Physics, vol. 802 (Springer, Heidelberg, 2010), p. 21

57. C. De Grandi, A. Polkovnikov, in *Quantum Quenching, Annealing and Computation*, ed. by A. Das, A. Chandra, B.K. Chakrabati, Lecture Notes in Physics, vol. 802 (Springer, Heidelberg, 2010); C. De Grandi, V. Gritsev, A. Polkovnikov, Phys. Rev. B **81**, 012303 (2010)
58. J.M. Deutsch, Phys. Rev. A **43**, 2046 (1991)
59. M. Srednicki, Phys. Rev. E **50**, 888 (1994); *ibid.*, J. Phys. A **32**, 1163 (1999)
60. M. Rigol, V. Dunjko, M. Olshanii, Nature (London) **452**, 854 (2008)
61. L. D'Alessio, Y. Kafri, A. Polkovnikov, M. Rigol, Adv. Phys. **65**, 239 (2016)
62. K. Sengupta, S. Powell, S. Sachdev, Phys. Rev. A **69**, 053616 (2004)
63. T.W.B. Kibble, J. Phys. A **9**, 1387 (1976)
64. W.H. Zurek, Nature (London) **317**, 505 (1985)
65. A. Polkovnikov, Phys. Rev. B **72**, 161201(R) (2005)
66. K. Sengupta, D. Sen, S. Mondal, Phys. Rev. Lett. **100**, 077204 (2008)
67. D. Sen, K. Sengupta, S. Mondal, Phys. Rev. Lett. **101**, 016806 (2008)
68. A. Polkovnikov, Phys. Rev. Lett. **101**, 220402 (2008)
69. A. Chandran, A. Erez, S.S. Gubser, S.L. Sondhi, Phys. Rev. B **86**, 064304 (2012)
70. A. Polkovnikov, V. Gritsev, Nat. Phys. **4**, 477 (2008)
71. J.D. Sau, K. Sengupta, Phys. Rev. B **90**, 104306 (2014)
72. U. Divakaran, K. Sengupta, Phys. Rev. B **90**, 184303 (2014); S. Kar, B. Mukherjee, K. Sengupta, Phys. Rev. B **94**, 075130 (2016)
73. M. Bukov, L. D'Alessio, A. Polkovnikov, Adv. Phys. **64**, 139 (2015)
74. R. Moessner, S.L. Sondhi, Nat. Phys. **13**, 424 (2017)
75. A. Sen, D. Sen, K. Sengupta, J. Phys. Cond. Mat. **33** 443003 (2021)
76. A. Soori, D. Sen, Phys. Rev. B **82**, 115432 (2010); A. Haldar, D. Sen, R. Moessner, A. Das, Phys. Rev. X, **11**, 021008 (2021)
77. T. Bilitewski, N.R. Cooper, Phys. Rev. A **91**, 063611 (2015)
78. R. Ghosh, B. Mukherjee, K. Sengupta, Phys. Rev. B **102**, 235114 (2020)
79. A. Das, Phys. Rev. B **82**, 172402 (2010); S. Bhattacharyya, A. Das, S. Dasgupta, Phys. Rev. B **86**, 054410 (2012); S.S. Hegde, H. Katiyar, T.S. Mahesh, A. Das, Phys. Rev. B **90**, 174407 (2014)
80. S. Mondal, D. Pekker, K. Sengupta, Europhys. Lett. **100**, 60007 (2012); S. Lubini, L. Chirondojan, G.-L. Oppo, A. Politi, P. Politi, Phys. Rev. Lett. **122**, 084102 (2019)
81. For a review see, S. Moudgalya, B. Andrei Bernevig, N. Regnault, arXiv:2109.00548
82. S. Pai, M. Pretko, R.M. Nandkishore, Phys. Rev. X **9**, 021003 (2019)
83. V. Khemani, R. Nandkishore, arXiv:1904.04815; V. Khemani, M. Hermele, R. Nandkishore, Phys. Rev. B **101**, 174204 (2020)
84. P. Sala, T. Rakovszky, R. Verresen, M. Knap, F. Pollmann, Phys. Rev. X **10**, 011047 (2020)
85. S. Moudgalya, A. Prem, R. Nandkishore, N. Regnault, B.A. Bernevig, arXiv:1910.14048; S. Moudgalya, O. I. Motrunich, arXiv:2108.10324
86. Z.-C. Yang, F. Liu, A.V. Gorshkov, T. Iadecola, Phys. Rev. Lett. **124**, 207602 (2020)
87. G. De Tomasi, D. Hetterich, P. Sala, F. Pollmann, Phys. Rev. B **100**, 214313 (2019); C.M. Langlett, S. Xu, arXiv:2102.06111
88. S. Moudgalya, O.I. Motrunich, arXiv:2108.10324
89. D. Hahn, P.A. McClarty, D.J. Luitz, arXiv: 2104.00692; K. Lee, A. Pal, H.J. Changlani, arXiv: 2011.01936
90. B. Mukherjee, D. Banerjee, K. Sengupta, A. Sen, arXiv:2106.14897
91. R.M. Nandkishore, M. Hermele, Ann. Rev. Cond. Mat **10**, 295 (2019)
92. M. Pretko, X. Chen, Y. You, Int. Jour. Mod. Phys. A **35**, 2030003 (2020)
93. S. Scherg, T. Kohlert, P. Sala, F. Pollmann, H.M. Bharath, I. Bloch, M. Aidelsburger, arXiv:2010.12965
94. S. Chandrasekharan, U.-J. Wiese, Nucl. Phys. B **492**, 455 (1997); R. Brower, S. Chandrasekharan, U.-J. Wiese, Phys. Rev. D **60**, 094502 (1999); R. Brower, S. Chandrasekharan, S. Riederer, U.-J. Wiese, Nucl. Phys. B **693**, 149 (2004)
95. U.J. Wiese, Ann. Phys. **525**, 777 (2013); E. Zohar, J. Cirac, B. Reznik, Rep. Prog. Phys. **79**, 014401 (2015); M. Dalmonte, S. Montangero, Contemp. Phys. **57**, 388 (2016)

96. D. Banerjee, M. Dalmonte, M. Muller, E. Rico, P. Stebler, U.-J. Wiese, P. Zoller, *Phys. Rev. Lett.* **109**, 175302 (2012); D. Banerjee, M. Bogli, M. Dalmonte, E. Rico, P. Stebler, U.-J. Wiese, P. Zoller, *Phys. Rev. Lett.* **110**, 125303 (2013)
97. E. Zohar, J. Cirac, B. Reznik, *Phys. Rev. Lett.* **109**, 125302 (2012); E. Zohar, B. Reznik, *Phys. Rev. Lett.* **107**, 275301 (2011); L. Tagliacozzo, A. Celi, A. Zamora, M. Lewenstein, *Ann. Phys.* **330**, 160 (2012)
98. I.-C. Chen, T. Iadecola, *Phys. Rev. B* **103**, 214304 (2021)
99. F.M. Surace, P.P. Mazza, G. Giudici, A. Lerose, A. Gambassi, M. Dalmonte, *Phys. Rev. X* **10**, 021041 (2020)
100. S. Coleman, R. Jackiw, L. Susskind, *Ann. Phys.* **93**, 267 (1975); S. Coleman, *ibid.* **101**, 239 (1976)
101. B. Yang, H. Sun, R. Ott, H.-Y. Wang, T.V. Zache, J.C. Halimeh, Z.-S. Yuan, P. Hauke, J.-W. Pan, *Nature* **587**, 392 (2020)
102. Z.-Y. Zhou, G.-X. Su, J.C. Halimeh, R. Ott, H. Sun, P. Hauke, B. Yang, Z.-S. Yuan, J. Berges, J.-W. Pan, [arXiv:2107.13563](https://arxiv.org/abs/2107.13563)
103. J.C. Halimeh, H. Lang, J. Mildenerberger, Z. Jiang, P. Hauke, [arXiv:2007.00668](https://arxiv.org/abs/2007.00668)
104. J. Kogut, *Rev. Mod. Phys.* **55**, 775 (1983)

NMR Experimental Study of Out-of-Equilibrium Spin Models



Paola Cappellaro, Pai Peng, and Chandrasekhar Ramanathan

Abstract Characterizing many-body quantum systems requires experimental systems with a large number of (spin-)qubits and with long coherent evolution times. As the focus in recent years has shifted to out-of-equilibrium dynamics, nuclear spins at the solid state emerge as an ideal experimental platform. Their potential to address fundamental questions in many-body physics has indeed a long-history, harking back to the early days of nuclear magnetic resonance. Building on early investigation of quantum thermodynamics and on a powerful suite of control techniques, recent experiments have introduced Hamiltonian engineering tools and metrics of correlation and entanglement. These experimental techniques allow bypassing challenges associated with the high temperature of nuclear spin systems as well as the lack of individual spin addressability and instead exploit these features to investigate regimes and observables not accessible in other experimental platforms. We thus focus on an in-depth description of such methods that could be successfully adopted in other experimental systems, before reviewing paradigmatic examples of integrable and non-integrable dynamics in large nuclear spin systems.

1 Nuclear Magnetic Resonance

1.1 Nuclear Magnetic Resonance in Condensed Matter

The coherent control of nuclear spins has a long and successful history driven in large part by the development of nuclear magnetic resonance (NMR) techniques in biology, chemistry, physics, and medicine [1, 2]. In addition to practical applica-

P. Cappellaro (✉) · P. Peng (✉)
Massachusetts Institute of Technology, Cambridge, MA, USA
e-mail: pcappell@mit.edu; paipeng@mit.edu

C. Ramanathan
Dartmouth College, Hanover, NH, USA
e-mail: chandrasekhar.ramanathan@dartmouth.edu

tions, (solid-state) NMR has also been a fertile platform for exploring fundamental condensed matter, quantum thermodynamics, and quantum information questions. For example, early NMR experiments in LiF [3] produced a state displaying negative magnetic susceptibility, by a rapid inversion of the magnetic field. This state was interpreted [4] as having negative temperature, triggering interesting discussions about thermodynamics. Similarly, early spin echo experiments [5] were initially suspected to violate the second law of thermodynamics for their apparent ability to reverse the natural growth of entropy [6, 7]. Initially spin echoes were believed to only apply to “incoherent” dynamics, due to ensemble averaging over system inhomogeneities, while the many-body—but closed and thus unitary—dynamics due to spin-spin interaction was seen as able to drive the system to thermodynamics equilibrium, as later formalized by the ETH. However, control sequences able to cancel or even reverse the spin-spin dipolar coupling soon emerged [8]. The ability to reverse seemingly irreversible processes, such as the diffusion of spin polarization [9] and even of spin correlations [10], led to a close inspection of potentially non-ergodic behavior in isolated NMR systems, both via small numerical simulations [11–13] and with experiments [14–16]. The statistical mechanics phenomenon of time reversal of a microscopic ensemble was typically described as arising from the actions of a “Loschmidt demon,” able to invert the local velocities of each molecule in a gas—or the Hamiltonian sign of each spin in NMR. Loschmidt echoes [17] were thus introduced to experimentally study this behavior, giving rise, as we will see, to fruitful investigation of many-body dynamics.

This rich history of theoretical and experimental contributions of NMR to the understanding of many-body out-of-equilibrium dynamics is based on a few key advantages. First, the nuclear spin themselves are an ideal testbed, as they provide well-defined spin qubits (or qudits) with exceptionally long relaxation times. Focusing, as we do in this review, on solid-state systems, the crystalline structures provide a regular geometry that sets the spin-spin couplings, while their macroscopic size allows to immediately access a large number of spins (thermodynamic limit). Taking advantage of these natural properties is a powerful suite of control tools, that have been refined over the years for spectroscopic applications, but can be adapted not only for quantum simulations and quantum control with NMR systems, but extended also to other quantum platforms.

1.1.1 NMR Hamiltonian

In a typical NMR experiment a small (mm-sized) sample is placed in a large, uniform magnetic field. A few-tesla field (3-7T) is typical in these experiments, leading to Larmor frequencies (the Zeeman energy of the spin coupling to the magnetic field) of a few hundred of MHz's. The field is generated by superconducting coils kept at liquid-helium temperatures. A wide bore at room temperature at the center of the magnet houses the sample.

The Hamiltonian of a homonuclear solid-state spin system in an external magnetic field is given by $\mathcal{H} = \mathcal{H}_Z + \mathcal{H}_D$, where $\mathcal{H}_Z = (\hbar\omega_0/2) \sum_i \sigma_z^i$ is the Zeeman interaction with the external magnetic field and \mathcal{H}_D the inter-nuclear dipolar interaction. In high magnetic fields ($\omega_0/2\pi \sim 100$ s MHz), the Zeeman interaction is much stronger than the nuclear dipolar interaction ($d_{ij}/2\pi \sim 10$ s of kHz) and most other interactions, such as chemical shifts, quadrupolar interactions, or indirect dipole-dipole (J-)coupling. The dipolar Hamiltonian is then truncated to its *secular* (energy-conserving) part [18]

$$\mathcal{H}_D = \sum_{i < j} d_{ij} \left(3\sigma_z^i \sigma_z^j - \vec{\sigma}^i \cdot \vec{\sigma}^j \right), \quad \text{where} \quad d_{ij} = \frac{\gamma^2 \hbar^2}{8r_{ij}^3} (1 - 3 \cos^2 \theta_{ij}) \quad (1)$$

with γ the gyromagnetic ratio, r_{jl} the distance between nucleus j and l , and θ_{jl} the angle between \mathbf{r}_{jl} and the external magnetic field. Couplings to heteronuclear spins are further simplified, since the “flip-flop” terms, $\propto \sigma_+ \sigma_-$, are no longer secular (energy-conserving) and can be neglected,

$$H'_D = \sum_{k, \kappa} J_{k, \kappa} \sigma_z^k \sigma_z^\kappa, \quad (2)$$

where the indexes k and κ label spins of different species (that is, energy).

While the Zeeman energy determines the thermal equilibrium states that yield the typical initial states prior to any manipulation, the dynamics of the system can be observed in the *rotating frame* set by the Larmor frequency, and it is thus dominated by the spin-spin couplings and the radio-frequency fields that are applied to control them.

1.1.2 Equilibrium States

At magnetic fields of a few Tesla, as $\hbar\omega_0 \ll k_B T$ above a few millikelvin, the thermal equilibrium density operator is highly mixed and the spins are typically infinitesimally polarized [19]:

$$\rho = \frac{\exp(-\beta \mathcal{H}_Z)}{\mathcal{Z}} \approx \frac{1}{D} \left(\mathbb{1} - \frac{\beta \hbar \omega_0}{2} \sum_i \sigma_z^i \right) = \frac{\mathbb{1}}{D} - \epsilon \delta \rho, \quad \text{with} \quad \mathcal{Z} = \text{Tr} \left(e^{-\beta \mathcal{H}_Z} \right), \quad (3)$$

where $\beta = 1/k_B T$ and given that the Zeeman Hamiltonian dominates all spin-spin interactions. This small ϵ (typically smaller than 10^{-5}) is the reason for the relative insensitivity of NMR experiments, which thus need to perform ensemble averaged measurements over more than 10^{11} – 10^{13} spins to achieve a detectable signal (the induction measurement is also a relatively insensitive readout method). Solid-state samples typically contain on the order of 10^{18} spins. The low polarization of the spins also results in the spins evolving in a very large configuration space in most

experiments (close to infinite temperature). As we will see below, this state can be advantageous to measure metrics relevant to quantum dynamics. Conversely, the high temperature is an obstacle to the observation of phenomena, e.g., ground state phase transition, that require pure states.

In solids with hyperfine-coupled electron and nuclear spins, microwave irradiation can enhance the nuclear spin polarization by polarization transfer from the electron spins, achieving nuclear spin polarizations greater than 90% at 7 T and about 1 K [20]. Polarizing the spins dramatically reduces the configurational broadening, potentially constraining the many-body dynamics observed.

1.1.3 Dynamics

While the Zeeman energy dominates the equilibrium state, the spin-interaction Hamiltonian drives a coherent many-body dynamic. Consider, for example, the NMR free induction decay (FID) where we observe a rapidly decaying signal following the application of a 90-degree RF pulse. After the pulse, the system evolves under the action of the internal interaction, as dictated by the Liouville equation,

$$\frac{d\rho}{dt} = i[H, \rho]. \quad (4)$$

The density operator at a short time t following the RF pulse is given by a short-time expansion of the Liouville equation, giving the nested commutators,

$$\begin{aligned} \rho(t) \propto & \frac{1}{2} \sum_j (\sigma_+^j + \sigma_-^j) + \frac{3it}{2} \sum_{jk} d_{jk} (\sigma_z^j \sigma_+^k - \sigma_z^j \sigma_-^k) \\ & - \frac{3t^2}{4} \sum_{jkl} d_{lk} d_{jk} (\sigma_z^j \sigma_z^l \sigma_+^k + \sigma_z^j \sigma_z^l \sigma_-^k) + \dots, \end{aligned} \quad (5)$$

where $\sigma_{\pm} = \sigma_x \pm i\sigma_y$. Only the first term contributes to the NMR signal, giving rise to the observed decay, as the initial polarization is transformed into correlated states. This simple analysis confirms that the observed decay in local observables is due not to decoherence, but to the growth of unobserved multi-spin correlations.

Still, the presence of multi-spin correlations can be observed, e.g., using Multiple Quantum Coherence (MQC) techniques [21], as we will review in Sect. 5.2.

1.1.4 Control by Radio-Frequency Fields

The nuclear spins are controlled by radio-frequency (rf) driving. A field on resonance with the spin Larmor frequency and transverse to the main magnetic field can drive the spins out of equilibrium, even if its strength is a few order of magnitude

smaller than the Zeeman energy. As the field is, however, typically stronger than spin-spin couplings, it is often enough to apply a *delta-pulse* approximation, where short burst of rf fields are assumed to apply a finite-angle rotation instantaneously. The rf is driven through a coil, which is also used to pick up the signal from the precessing spin magnetization. Due to the coil and sample size, the rf fields drive *all* resonant spins, and thus only collective spin rotation is achievable, precluding single-spin addressability.

The Hamiltonian describing the interaction of the spins with the rf field can be written as:

$$H_{rf} = e^{-i\phi(t) \sum_k \sigma_z^k} \left(\frac{1}{2} \omega_{rf}(t) \sum_k \sigma_x^k \right) e^{i\phi(t) \sum_k \sigma_z^k}, \quad (6)$$

where σ_a^k are the usual Pauli matrices and the sum is over all spins. Here $\phi(t) = \omega_0 t + \varphi(t)$ is a time-dependent phase, with ω_0 close to the spin resonance frequency, and $\omega_{rf}(t)$ is a time-dependent amplitude. The phase and amplitude can be controlled with high precision and bandwidth, allowing many controlled schemes. To improve control precision, NMR experimentalists, also inspired by quantum information ideas and needs, have developed several advanced techniques, such as shaped pulses, composite pulses [22], or numerically optimized pulse shapes [23–25]. As we will show below, multiple-pulse sequences have also been developed to achieve complex tasks with improved robustness.

1.2 Nuclear Spin Systems

While NMR is maybe best known for its spectroscopic analysis of molecules in liquid solvents, experiments to explore many-body dynamics are typically conducted in solid-state (crystalline) samples. Indeed, in such samples the strong, position dependent dipolar interaction are not canceled out by the random molecular tumbling that occur in solution. Still, a choice of the material and crystal properties can give rise to a few dynamic models of interest that we now review.

1.2.1 3D Spin Systems

One of the main advantages of NMR techniques is their ready to access large numbers of spins that allow probing the thermodynamic limit. This is exemplified when using bulk 3D crystals, where the geometry of couplings yields fast creation of spin-spin correlations, with coherences developing over hundreds of spins [26, 27]. Among the systems that have been routinely used are calcium fluoride and adamantane.

The 100% abundant spin-1/2 ^{19}F nuclei of a single crystal sample of calcium fluoride (CaF_2) form a simple cubic lattice (Fig. 1). The only isotope of calcium

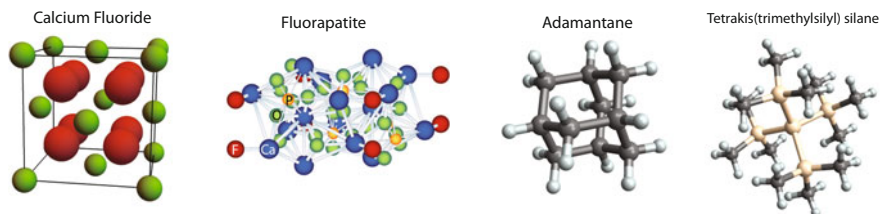


Fig. 1 Crystal structure of a few spin systems discussed in the text, used to probe quantum many-body dynamics

with spin is ^{43}Ca that has a natural abundance of 0.135% and a spin of $7/2$ and can be neglected in most situations. The fluorine spins have been used as a testbed for decoupling sequences, to measure spin [28] and energy [29] diffusion, multiple quantum coherences [30], and the onset of irreversible dynamics [10, 31]. The strong couplings among spins also represent a drawback, since it makes experiments (such as control calibration) more challenging.

A more forgiving system is adamantane ($\text{C}_{10}\text{H}_{16}$), a plastic crystal that permits the generation of extremely large coherence orders at room temperature while providing slightly weaker couplings. Albeit at the solid state (in crystalline or powder form), the adamantane molecules still tumble rapidly. The isotropic motion averages to zero the intramolecular dipolar couplings but retains some intermolecular interactions. In practice, the motion reduces each adamantane molecule to an effective point dipole source located at each point of a face-centered-cubic lattice. The source contains 16 protons (and 10 Carbons). The 16 protons do not interact with each-other but only with protons in other molecules, thus giving rise to a complex network of spins, but with somehow weaker couplings due to the longer distances involved.

The ^{13}C spins in adamantane ($\text{C}_{10}\text{H}_{16}$) can be used to both introduce disorder, as well as to act as local probes of the many-body dynamics. A similar role can be played by the ^{43}Ca in the ^{19}F lattice of CaF_2 , although its natural abundance is even lower.

Many other crystalline samples have been used over the years, from Silicon [32] (even with variable isotopic content of Si-29), to Ytria (Y_2O_7) [33], to ammonium dihydrogen phosphate (ADP) [34], and to Buckminsterfullerene (C_{60}) crystals.

1.2.2 Quasi-1D Spin Systems

While 3D systems allow for a fast growth of spin correlations, their complex dynamics makes the analysis more difficult and limits the comparison with known models or numerical simulations.

Nuclear spin systems in apatite crystals have emerged as a testbed to probe quasi-one-dimensional (1D) dynamics, including transport and decoherence [35–

41]. The crystal structure of fluorapatite [$\text{Ca}_5(\text{PO}_4)_3\text{F}$, FAp] and hydroxylapatite [$\text{Ca}_5(\text{PO}_4)_3(\text{OH})$, HAp] presents a favorable geometry where ^{19}F or ^1H nuclear spins are aligned in chains along the crystal c-axis with inter-spin spacing much shorter than the distance to other parallel chains (Fig. 1). In addition, each ^{19}F (^1H) spin is surrounded by three ^{31}P spin-1/2 nuclei.

The apatite geometry gives a ratio of intra-chain to inter-chain couplings of about 40, allowing the evolution to approximate well the expected 1D dynamics over sufficiently short-time scales [36].

The heteronuclear dipolar interaction between F and P spins, $\sum_{j,k} h_{j,k} \sigma_z^{Fj} s_z^{Pk}$, provides additional routes to control the system.

Finally, the coupling to the thermal bath of phonon is extremely low. Relaxation, mostly mediated by the paramagnetic impurities, is thus slow, ranging from 1s-600s, much longer than the ms time scale of the evolution.

Crystals of FAp can be obtained easily as they occur naturally. Synthetic single crystals of FAp can also be grown by the flux method [42–44] that offer much longer thermal relaxation times and thus a better isolation from the thermal bath. Fluorine atoms can be introduced as substitutional defects in HAp by ion exchange under hydrothermal conditions [45–47] to provide access to local probes of the dynamics.

1.2.3 Finite-Size Systems

In addition to large crystalline systems, even smaller systems, e.g., based on molecules or liquid crystals, can serve as powerful platforms to explore many-spin dynamics. Smaller molecules in liquid solution have been used since the start of quantum information processing as testbeds to demonstrate basic principles of quantum algorithms and quantum control. Such systems allow the individual control of spin qubits and thus can act as small quantum processors [48]. However, their size is limited to the number of resolvable chemical shifts and the couplings among spins are typically weak. If single-spin addressing is not needed, as it is often the case to explore quantum dynamics, larger molecules can provide useful properties, for example, in “star” systems, where a central spin is used to probe the dynamics of an “environment” of coupled spins. This type of geometry has been explored both in molecules in liquid solution (analyzing systems of increasing sizes, such as acetonitrile, trimethyl phosphite, and tetrakis(trimethylsilyl) silane, that containing 4, 10, and 37 spins respectively [49]) and in polycrystalline solid such as Triphenylphosphine molecules [50], where the couplings among spins can be stronger, as they are dipolar in nature.

2 Control Techniques for Hamiltonian Engineering

Nuclear Magnetic Resonance (NMR) has a long tradition of control sequences able to modify the naturally occurring Hamiltonians into desired operators. The most prominent application is in the refocusing of unwanted interactions, which further evolved into the theory of dynamical decoupling (DD) in quantum information processing. While most of DD is concerned with single qubit operation, NMR also routinely deals with many-body Hamiltonians. Pioneering work extended the ideas of “spin echo” [5] to the refocusing of two-body interactions via “solid echoes” [51], obtained with more complex periodic pulse sequences [52, 53]. These early discoveries led to a robust theoretical framework (Average Hamiltonian Theory [54]) that enabled the discoveries of powerful pulse sequences with increasing performance. Similar ideas are a current area of active exploration in the context of digital quantum simulation and programmable quantum emulators [55].

2.1 Average Hamiltonian Design

Early NMR sequences were designed by analyzing the dynamics of piece-wise constant Hamiltonians and considering the lowest order approximation. While higher-order corrections were already taken into account using Average Hamiltonian Theory (AHT [53]), here we first provide an intuitive introduction to this Hamiltonian engineering approach.

As it is now common in digital quantum simulation, a desired Hamiltonian can be built by evolving the system under a sequence of experimentally accessible Hamiltonians,

$$\mathcal{H}_{\text{des}}T = \sum_k \tau_k \mathcal{H}_k, \quad (7)$$

by considering the first-order approximation of the Trotter expansion,

$$\prod_k e^{-i\tau_k \mathcal{H}_k} \approx e^{-i\mathcal{H}_{\text{des}}T}, \quad \sum_k \tau_k = T. \quad (8)$$

The naturally occurring Hamiltonian and the achievable control in NMR further constrain the set of accessible $\{H_k\}$. Indeed, naively the only accessible Hamiltonians would be either the dipolar Hamiltonian, $H_{k=0} = \mathcal{H}_D$, or the dipolar Hamiltonian with an added collective rf Hamiltonian, $H_k = (\mathcal{H}_D) + H_{rf}$, see Eq. (6) and (1). Here the parenthesis indicates that one can usually neglect the effects of the spin interaction during driving. However, not only this description makes it hard to design protocol for desired (many-body) Hamiltonians, but it also provides an inaccurate approximation of the real evolution since typically

Table 1 Spherical tensors for two spin-1/2 (a and b) [56]. σ_α are the usual Pauli operators

$T_{10}^a = \sigma_z^a/2$	$T_{10}^b = \sigma_z^b/2$	$T_{00} = (\sigma_x^a \sigma_x^b + \sigma_y^a \sigma_y^b + \sigma_z^a \sigma_z^b)/\sqrt{3}$
$T_{11}^a = \sigma_+^a/\sqrt{2}$	$T_{11}^b = \sigma_+^b/\sqrt{2}$	$T_{11} = (\sigma_+^a \sigma_z^b - \sigma_z^a \sigma_+^b)/2$
$T_{1-1}^a = \sigma_-^a/\sqrt{2}$	$T_{1-1}^b = \sigma_-^b/\sqrt{2}$	$T_{1-1} = (\sigma_-^a \sigma_z^b - \sigma_z^a \sigma_-^b)/2$
$T_{21} = (\sigma_+^a \sigma_z^b + \sigma_z^a \sigma_+^b)/2$	$T_{2-1} = (\sigma_-^a \sigma_z^b + \sigma_z^a \sigma_-^b)/2$	$T_{10} = (\sigma_+^a \sigma_-^b - \sigma_-^a \sigma_+^b)/2$
$T_{22} = \sigma_+^a \sigma_+^b/2$	$T_{2-2} = \sigma_-^a \sigma_-^b/2$	$T_{20} = (2\sigma_z^a \sigma_z^b - \sigma_x^a \sigma_x^b - \sigma_y^a \sigma_y^b)/\sqrt{6}$

the driving strength breaks the Trotter approximation. A better strategy is then to describe the evolution in the *toggleing* frame defined by the rf control. Then, this gives rise to an (infinite) set of accessible Hamiltonians, $H_k = R_k \mathcal{H}_D R_k^\dagger$, where $R_k = \exp[-i\tau_k(\Omega_k^x \sum_j \sigma_x^j + \Omega_k^y \sum_j \sigma_y^j)]$ are collective rotations around an axis in the x/y plane. As explained below, rotations around the z axis can also be obtained by either working off-resonance or by phase shifts of the rf drive.

Given that the available transformations are described by (collective) rotations, it is natural to rewrite the natural Hamiltonian in terms of spherical tensors, in order to more easily determine the achievable H_k . Consider, for example, spherical tensors for two spin-1/2 (see Table 1). The coupling between the two spins can be written in the spherical tensor basis, $\mathcal{H}_{nat} = \sum_{l,m} (-1)^m A_{l,-m}^{nat} T_{l,m}$. In particular, the usual secular dipolar Hamiltonian is $\mathcal{H}_D \propto T_{20}$. Since collective rotations conserve the rank l , there are restrictions on what Hamiltonians can be achieved to lowest order. Using the spherical tensors, Eq. (8) can be rewritten as a set of equations

$$\sum_{k,m} (-1)^m A_{l,-m}^{nat} D_{m,n}^l(R_k) = (-1)^n A_{l,-n}^{des}, \quad (9)$$

where $D_{m,n}^l(R_k)$ is the Wigner matrix associated with the rotation R_k . Group theory methods can be used to help solving Eq. (9) by reducing the number of conditions using symmetries.

While these simple construction rules are efficient for finding control protocols, they do not take into account higher-order terms nor experimental imperfections. A more refined approach is to analyze the dynamics based on the Magnus expansion and Floquet theory. This allows, as we see in the next sections, to systematically analyze the dynamics and devise strategies to improve the control.

2.2 Magnus Expansion and Average Hamiltonian Theory

The dynamics of NMR systems under periodic (rf) driving has been historically described using the Magnus Expansion (ME) in the *toggleing* frame. Rules that apply to the typical control sequences and Hamiltonian considered, as well as many insights into how to treat control imperfections, have been codified into the so-called Average Hamiltonian Theory [54].

As explained in the previous section, the system Hamiltonian is divided into the natural (typically the secular dipolar) Hamiltonian and an external Hamiltonian due to the rf driving pulses, $H = H_{\text{nat}} + H_{\text{ext}}$. The dynamics is analyzed in the interaction frame defined by $H' = U_{\text{rf}}^\dagger H_{\text{nat}} U_{\text{rf}}$, where $U_{\text{rf}}(t) = \mathcal{T} \exp \left[-i \int_0^t H_{\text{ext}}(t') dt' \right]$ and \mathcal{T} is the time ordering operator. The internal Hamiltonian H_{nat} then becomes time-dependent in this *toggling* frame, but it can be accurately approximated using a ME to the lowest few orders. Similar to the Trotter approximation considered above, the ME (compared to other approximation such as the Dyson expansion) is convenient, since it defines a time-independent effective Hamiltonian, \overline{H} . Average Hamiltonian Theory then aims at making such effective Hamiltonian equivalent to the desired interaction.

The effective Hamiltonian \overline{H} can be expanded in successive orders of approximations in the evolution time, $\overline{H} = H^{(0)} + H^{(1)} + \dots$, where according to the ME the first few terms are given by

$$H^{(0)} = \frac{1}{T} \int_0^T H'(t) dt, \quad H^{(1)} = \frac{-i}{2T} \int_0^T dt_2 \int_0^{t_2} dt_1 [H'(t_2), H'(t_1)]. \quad (10)$$

While the ME is generic, its power in AHT is due to the special construction of the pulse sequences. Indeed, typically the rf driving is periodic, based on a unit cycle of period t_c repeated n times, $T = nt_c$. In addition, sequences are typically built so that $U_{\text{rf}}(t_c) = \mathbb{1}$, so that the toggling and rotating frame coincide stroboscopically at every cycle. Then, the ME can be calculated over one cycle, since H' inherits the periodicity of H_{rf} , keeping the approximation good as $\|H_{\text{nat}}\| t_c \ll 1$, and the evolution over longer times is stroboscopically given by $U(nt_c) \approx e^{-i\overline{H}nt_c}$ and the evolution is only probed at stroboscopic times.

We note, however, that the periodicity of the Hamiltonian is not explicitly accounted for in this derivation, beyond defining the stroboscopic effective Hamiltonian. A slightly different approach is then to use Floquet theory and, in particular, define a Floquet-Magnus expansion for the problem.

Still, Average Hamiltonian Theory has led to the development of many successful sequences, in particular, thanks to its ability to systematically take into account experimental imperfection as well as higher-order terms. The simplest step for improving the control sequences is to exploit symmetries, in the same way as the symmetrized Trotter expansion cancel errors to second order. Symmetrized versions of the simplest sequence are routinely used in NMR experiments [57], as, for example, they are able to cancel all odd-terms in the ME.

2.3 Floquet-Magnus Expansion

Floquet theory has proven to be a powerful description for quantum systems with time-periodic Hamiltonians. Here we review some of the basic theory in the context

of its use as a Hamiltonian engineering tool (that is, as a way to obtain a desired effective Hamiltonian).

Given a time-periodic Hamiltonian of period $t_c = 2\pi/\omega$, it can be expanded in a Fourier series, $H(t) = \sum_{k=-\infty}^{\infty} H_k e^{ik\omega t}$. The system dynamics is described by a unitary propagator $U(t)$ which is the solution to a Schrödinger equation, $dU(t)/dt = -iH(t)U(t)$, $U(0) = \mathbb{1}$. Exploiting the periodicity of the Hamiltonian, a formal solution for $U(t)$ can be written as

$$U(t) = \left(\sum_k U_k e^{ik\omega t} \right) e^{i\Lambda t}, \tag{11}$$

where Λ is diagonal, while the rest of the operator displays the same periodicity of the Hamiltonian. To find these operators, it is convenient to work in the *Floquet* (Fourier) space, defined by a basis $|k\rangle$ of states linked to the k th frequency. In analogy to harmonic oscillator systems, we introduce the ladder operators $\langle k+h|F_h|k\rangle = 1$ and the number operator $\langle k|N|h\rangle = \delta_{kh}$. The system is then represented in the tensor product of the Hilbert and Fourier space, $|\psi, k\rangle$ and the Hamiltonian can be written as a time-independent operator

$$H(t) = \sum_{k=-\infty}^{\infty} H_k e^{ik\omega t} \quad \rightarrow \quad H_F = \sum_{k=-\infty}^{\infty} H_k \otimes F_k + \omega(\mathbb{1} \otimes N). \tag{12}$$

We can then in principle solve for the Floquet propagator, $U_F = e^{iH_F t}$, and project back to the Hilbert space

$$U(t) = \sum_k \langle k|U_F|0\rangle e^{ik\omega t}. \tag{13}$$

The solution can be cast in the form of Eq. (11) by first diagonalizing $H_F = D_F \Lambda_F D_F^{-1}$, where Λ_F is diagonal in the Hilbert-Fourier space, $\Lambda_F = \Lambda F_0 + \omega N$, and $U_k = \langle k|D_F|0\rangle$. We thus obtain an explicit form for the propagator,

$$U(t) = \sum_k \langle k|D_F e^{i\Lambda_F t} D_F^{-1}|0\rangle e^{ik\omega t} = \sum_k \langle k|D_F e^{i\Lambda_F t} \sum_h |h\rangle \langle h|D_F^{-1}|0\rangle e^{ik\omega t}. \tag{14}$$

While this provides an elegant solution, the Floquet matrix H_F is an infinite operator and thus one typically needs to truncate it to numerically obtain a practical solution. In order to use Floquet theory for Hamiltonian engineering, it is, however, more convenient to instead directly apply an approximation to the Floquet Hamiltonian and then project it back to Hilbert space. This approach provides an effective Hamiltonian that can be used for quantum simulation. The key idea is to perform a(n approximate) block-diagonalization of the Floquet Hamiltonian, typically following the Van-Vleck transformation [58].

The goal is to find, perturbatively, the unitary operator $D_F = e^S$. We define $H_F^0 = H_0 F_0 + \omega N$ (we drop the explicit tensor product for conciseness) and write $H_F = H_F^0 + H_F^1$. The diagonalization proceeds as

$$\Lambda_F = e^{-S} H_F e^S = H_F + [H_F, S] + \frac{1}{2} [[H_F, S], S] + \dots \tag{15}$$

By setting

$$S = \sum_{k \neq 0} \frac{H_k}{k\omega} F_k, \quad \rightarrow \quad [\omega N, S] = - \sum_{k \neq 0} H_k F_k \tag{16}$$

we have that $\Lambda = H_F^0 + \frac{1}{2} [[H_F, S], S] + \dots$, that is, the lowest order off-diagonal term is canceled. Keeping only diagonal terms, we obtain the effective (time-independent) Hamiltonian to first order,¹

$$\Lambda \approx H^0 - \frac{1}{2} \sum_{k \neq 0} \frac{[H_{-k}, H_k]}{k\omega}. \tag{17}$$

Given $U = \sum \langle k | e^S | 0 \rangle e^{ik\omega t} e^{i\Lambda t}$, we find that the evolution at stroboscopic times $2\pi n/\omega$ is given by the effective Hamiltonian

$$\tilde{H} \approx H_0 - \frac{1}{2} \sum_{k \neq 0} \frac{[H_{-k}, H_k]}{k\omega} + \sum_{k \neq 0} \frac{[H_0, H_k]}{k\omega}. \tag{18}$$

We can compare this result to the predictions from AHT. The first order is indeed equivalent to what found before,

$$\bar{H}^0 = \frac{1}{t_c} \int_0^{t_c} H(t) dt = \frac{1}{t_c} \int_0^{t_c} \sum_k H_k e^{i\omega t} = H_0. \tag{19}$$

Higher-order terms of the stroboscopic Hamiltonians show small differences when derived from the Magnus vs. the so-called *Floquet-Magnus expansion*, for example,

$$\bar{H}^1 = -\frac{i}{2t_c} \int_0^{t_c} \int_0^{t_2} [H(t_1), H(t_2)] dt_1 dt_2 \tag{20}$$

$$= -\frac{i}{2t_c} \sum_{k,h} [H_k, H_h] \int_0^{t_c} \int_0^{t_2} e^{i\omega(k t_1 + h t_2)} dt_1 dt_2 \tag{21}$$

$$= -\frac{1}{2} \sum_{k \neq 0} \frac{[H_{-k}, H_k]}{k\omega} + \sum_{k \neq 0} \frac{[H_0, H_k]}{k\omega}.$$

¹ See, e.g., [59] for the higher-order terms, as well as for multi-mode Floquet Hamiltonians.

While the Floquet approach is in principle more powerful, since it can also tackle the dynamics beyond the stroboscopic time-points, AHT might be more convenient when tackling piecewise-constant evolutions.

2.3.1 Convergence of the Expansions

The convergence of the Magnus (and Floquet-Magnus) expansion has been analyzed extensively [60], with improving convergence radii over the years. Criteria have been found for the ME convergence for both bound and infinite-dimensional Hilbert spaces. For the time-evolution equation $\frac{dU}{dt} = iHU$, the ME convergence is established for times $t \leq T$ such that $\int_0^T \|H(t)\| dt < \pi$. A similar bound (with a smaller convergence radius) also holds for the Floquet-Magnus expansion *over one period* [61]. A related question links the rate of the Floquet periodic driving with the absorbed heat and ensuing thermalization of the system [62]. While a generic interacting Floquet system absorbs energy from the drive and is expected to heat up to infinite temperature, exceptions to this rule have been extensively studied for their practical importance in quantum simulation, as we will discuss more in detail in Sect. 7.2

2.3.2 Examples of Sequences

Hamiltonian engineering have a long tradition in nuclear magnetic resonance (NMR) and have more recently extensively adopted in quantum information applications, especially to tackle the problem of decoupling spins from noise (dynamical decoupling).

A first class of pulse sequences is for dynamical decoupling for single-body interactions, e.g., dephasing noise, “*heteronuclear*” coupling between qubits (nuclear spins) with very distinct energies. In principle, a single π pulse (spin echo) would be sufficient for decoupling in the case of an ideal scenario, as this pulse refocuses a single-body Hamiltonian (e.g., $\omega\sigma_z$ is refocused by a $\sigma_{x,y}$ π pulse). However, time dependence or inhomogeneities in ω and imperfections in the control itself make the decoupling incomplete. Many sequences have been developed to deal with this [63], including CPMG [64, 65], XY [66, 67], Uhrig [68], and KDD [69].

A second class of pulse sequences aims at decoupling interactions among the qubits themselves. In particular, in the context of NMR, this class (*homonuclear decoupling*) has focused on decoupling the secular dipolar Hamiltonian—that is, the part of the magnetic dipole-dipole interaction that commutes with a uniform Zeeman energy. That decoupling was possible even for spin-spin interaction, even when it was not possible to separately control each spin, it was first realized with the introduction of solid echoes [70]. Improved sequences were introduced considering symmetry properties as well as strategies to reduce control imperfections, from the celebrated WHH [52] to MREV8, MREV16, BLEW-12, and BR24. We note that

these sequences should be more properly considered “Hamiltonian engineering” and not decoupling sequences, as they aim at engineering a pure chemical shift Hamiltonian (while indeed suppressing interactions). True dynamical decoupling sequences have also been considered (see, e.g., Cory48 [71] and more recently a WHH-CPMG combination [32]). We remark that more recent advances in NMR decoupling have been achieved by combining rotations in spin space (rf control) with rotations in the physical space, via *magic angle* spinning [72, 73]. These are typically combined with continuous-wave (CW) decoupling schemes (CRAMPS), inspired by early schemes such as the Lee-Goldburg sequence [74] and extended to numerically optimized schemes (DUMBO [75]).

At the same time, the desire to tailor the spin dynamics in order to extract further spectroscopic information has also led the NMR community to design pulse sequences aimed at engineering particular Hamiltonian. A specific example is the case of multiple quantum coherence (MQC) sequences [76], with pulse sequences designed to create single quantum [77, 78], double quantum (DQ) [79], and even higher coherences [80].

More recently, variations of the MQC sequences have been used as decoupling sequences [81], and even to achieve a broader range of interactions to study different spin models [82, 83], including non-interacting, interactions, longitudinal and transverse fields and disorders (see Sect. 7.1). The key idea was to move away from constant (and constrained) pulse delays that are constant and freely vary the delay lengths of standard DQ sequence [39, 79] (see Fig. 2).

In the context of Hamiltonian engineering it is also useful to introduce uniform “fields,” that is, operators that implement collective rotations around a desired axis. While it is always possible to, e.g., apply the rf driving off-resonance to introduce an effective z-field, this might reduce the pulse quality. An alternative, more robust strategy, is to modify the pulse phases of an existing multiple-pulse sequence. Indeed, by rotating the n -th cycle of the pulse sequence by $(n - 1)\phi$

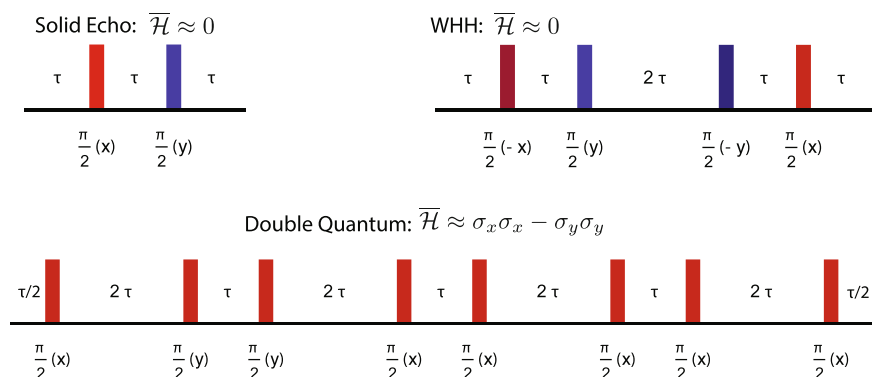


Fig. 2 Examples of NMR sequences used for decoupling (top row) and Hamiltonian engineering (bottom). If the last sequences is implemented with all pulses phase shifted by 90° , it would implement the opposite DQ Hamiltonian, $-(\sigma_x \sigma_x - \sigma_y \sigma_y)$

around the $Z = \sum \sigma_z$ operator, which can be accomplished by phase shifting all the pulse axes in the n -th cycle by $(n - 1)\phi$, the evolution operator is given by $U(nt_c) = e^{-in\frac{\phi}{2}Z} e^{-iHnt_c}$, with $H_t = H - \frac{\phi}{2t_c}Z$.

We note that Hamiltonian engineering can also be used to implement the opposite of a Hamiltonian, $-H$, thus effectively inverting the arrow of time. For certain sequences, this can be obtained in a robust way by simply appropriately changing the *phase* of the $(\pi/2)$ pulses applied (see Fig. 2). This allows to achieve time reversal with a fixed amount of experimental errors.

In addition of relying on the well-tested average Hamiltonian theory design, a recent direction in Hamiltonian engineering is to look for optimal solutions either numerically [84], in particular, exploiting machine learning [85], or with new analytical insights [86].

3 State and Observable Preparation

While in typical NMR experiments the initial state and observable are fixed, various control tools have been developed to broaden the set of achievable operators. Consider, for example, the observable. In the NMR spectrometer, the spin magnetization is measured inductively by a pick-up coil. The signal is the ensemble average of the transverse polarization over the whole sample. Indeed, only the portion of the spin state that is dipolar and oriented along the coil axis will couple and be detected, although other parts of the density operator might evolve into detectable states during the measurement evolution time. As the measurement is weak, both transverse components (x/y) can be effectively measured at the same time.

A simple $\pi/2$ pulse just before acquisition can rotate the transverse polarization observable, e.g., $X = \sum_k \sigma_x^k$ into an effective longitudinal observable, $Z = \sum_k \sigma_z^k$. It is thus easy to detect the magnetization along any axis. More complex evolutions U before signal acquisition can similarly provide a strategy to detect more complex operators, $O = U^\dagger X U$. Further combining unitary, incoherent, and decoherent evolutions can reveal a broader class of initial states and observables.

In the following, we review some of the tools that have been used to access such operators. We will treat the measurement of Multiple Quantum Coherences to Sect. 5.1.

3.1 Phase Cycling

Phase cycling is routinely used in magnetic resonance (and other experimental techniques) to remove background signals and suppress unwanted noise. In the simplest implementation, by alternating phases of the excitation pulses, followed by either addition or subtraction of the measured signals, one can amplify the signal of

interest while canceling noisy background. More advanced phase cycles have also been used to select particular components of the NMR signal that display special coherent properties under collective rotations. It is thus possible to select particular *coherence pathways* that the spins must follow in order to give rise to a non-zero signal [87].

Similar ideas can be used to prepare desired initial states by combining signals arising from two (or more) initialization. Expanding on this method, one can also devise a strategy to, e.g., create effective pure states (pseudo-pure states) using a *temporal average* of many initial, mixed states [88].

3.2 Dipolar Order State

Using the thermalization or adiabatic transfer, it is possible to map the Hamiltonian to the states. As an example, the dipolar order state $\delta\rho \propto \mathcal{H}_D$ can be created using Jeener-Broekaert pulse pair [89] or adiabatic demagnetization [90, 91].

3.2.1 Jeener-Broekaert Pulse Pair

For simplicity, assume there is only one spin species, so that natural Hamiltonian contains only the homonuclear dipolar interaction \mathcal{H}_D . The central idea is that any state will be locally indistinguishable from a Gibbs state $\rho_{eq} \propto e^{-\tilde{\beta}\mathcal{H}_D}$ after evolving under \mathcal{H}_D for long time, a phenomenon known as eigenstate thermalization hypothesis [92, 93] (notice that, however, this method was developed well before the ETH was formulated.) $\tilde{\beta}$ is determined by the initial state energy density with respect to \mathcal{H}_D and can be different to the actual inverse temperature. As any state in solid-state NMR is always close to totally mixed state \mathbb{I} , $\tilde{\beta}$ is close to zero, then $\rho_{eq} \propto \mathbb{I} - \tilde{\beta}\mathcal{H}_D$. The state deviating from the identity is then $\delta\rho \propto \mathcal{H}_D$ as long as $\tilde{\beta} \neq 0$.

The detailed sequence is shown in Fig. 3a, where the left part shows the creation sequence and the right part shows the detection sequence. The first $\pi/2$ pulse brings the polarization to the x direction, then the free evolution for time t_e and $\pi/4$ pulse create a state that has non-zero energy density with respect to \mathcal{H}_D . The following

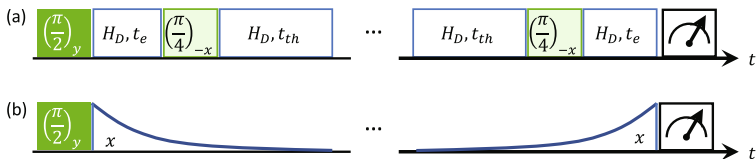


Fig. 3 Jeener-Broekaert pulse pair (a) and ADRF (b) for creation and detection of dipolar order states

thermalization $|\mathcal{H}_D|t_{th} \gg 1$ leads to the dipolar order state. The reverse sequence can be used to engineer an observable $O \propto \mathcal{H}_D$. The only difference is that we can directly measure magnetization along x , so the initial $\pi/2$ pulse is not needed.

State preparation via thermalization is very robust, as any error term not conserved by the Hamiltonian will thermalize into highly nonlocal terms that cannot be detected in local measurements. One possible contamination is the Zeeman state $\sum_i \sigma_z^i$, because Z is also conserved by \mathcal{H}_D . If the state before thermalization contains a finite Zeeman component, it can survive thermalization and contaminate the final dipolar order state. Zeeman contamination can be avoided by fine tuning t_e such that the state before thermalization does not contain a Zeeman component, or phase cycling out the Zeeman component after the thermalization.

3.2.2 Adiabatic Demagnetization in the Rotating Frame

The mechanism for adiabatic demagnetization in the rotating frame (ADRF) is that when slowly tuning the Hamiltonian from \mathcal{H}_{start} to \mathcal{H}_{end} , the eigenstates of \mathcal{H}_{start} will evolve into the eigenstates of \mathcal{H}_{end} . Specifically, ADRF evolves the Zeeman state into the dipolar order state by tuning $\mathcal{H} = \mathcal{H}_D + \Omega(t) \sum_i \sigma_x^i$, where the x -field arises from resonant RF field whose strength $\Omega(t)$ can be continuously swept in time. The sequence is shown in Fig. 3b. In the beginning, the state is brought to the transverse state $\delta\rho = \sum_i \sigma_x^i$ by a $\pi/2$ pulse. Immediately after that, a large RF field ($\Omega(0) \gg |\mathcal{H}_D|$) is turned on, so that the state is a high-temperature Gibbs state of the instantaneous Hamiltonian (spin-locked state). Then the amplitude Ω is slowly decreased to zero. At the end of the sweep, the Hamiltonian only contains \mathcal{H}_D , thus the final state should be a high-temperature Gibbs state of this Hamiltonian, $\delta\rho \propto \mathcal{H}_D$, as long as the sweep is adiabatic. The dipolar observable can be engineered using the reverse sequence, again without the $\pi/2$ pulse, where the ramping up of the rf fields maps the dipolar state onto the observable transverse magnetization. (this is called adiabatic remagnetization in the rotating frame, ARRF.)

The advantage of ADRF over the Jeener-Broekaert pulse pair is the resulting magnitude of the dipolar order state. In the ideal case, there is no polarization loss during ADRF; however, the thermalization part in Jeener-Broekaert pulse pair is a locally nonunitary process (some part of the initial state evolves into highly nonlocal state that is not measurable) that leads to a reduced polarization in the end. On the other hand, Jeener-Broekaert pulse pair does not require continuous modification of RF power, thus is easier to implement.

3.2.3 Verification and Extension

The correct preparation of the dipolar order state can be verified via MQC experiments [30] (see also Sect. 5.1). Under encoding along both x and z axes, any state can be decomposed into a Fourier series $\rho = \sum_{q_x, q_z=-L}^L \rho_{q_x, q_z}$ with

$e^{-i\phi Z} \rho_{q_x, q_z} e^{i\phi Z} = e^{-iq_z\phi} \rho_{q_x, q_z}$ and $e^{-i\theta X} \rho_{q_x, q_z} e^{i\theta X} = e^{-iq_x\phi} \rho_{q_x, q_z}$. The 2D MQC intensities are $I_{q_x, q_y} = \langle \rho_{q_x, q_z}^2 \rangle$ and the dipolar state should have $I_{-2,0} = I_{2,0} = 1.5I_{0,0}$ with all other $I_{q_x, q_y} = 0$, where the first (second) subscript is the coherence number for x (z) encoding. The Zeeman state would have $I_{-1,0} = I_{1,0}$ with all other $I_{q_x, q_y} = 0$.

Combing the dipolar order state creation and phase cycling technique, we can prepare states and observables $\delta\rho = O = H$ as long as we can engineering H from Floquet engineering (e.g. H shown in Eq. (76)). For example, a double quantum state $\delta\rho_{DQ} \propto \sum_{j,k} J_{jk} (\sigma_x^j \sigma_x^k - \sigma_y^j \sigma_y^k)$ can be created by subtracting dipolar state along x and dipolar state along y, $\delta\rho_{DQ} \propto \sum_{j,k} J_{jk} (2\sigma_x^j \sigma_x^k - \sigma_y^j \sigma_y^k - \sigma_z^j \sigma_z^k) - \sum_{j,k} J_{jk} (2\sigma_y^j \sigma_y^k - \sigma_x^j \sigma_x^k - \sigma_z^j \sigma_z^k)$.

3.3 Local Observables

In many scenarios it would be interesting to evaluate local correlations, (OTOCs or two-point correlators), instead of their collective counterparts. That would require the ability to prepare—and detect—single-spin operators. Unfortunately, collective control of all the pulses in the system, as given by on-resonance RF pulses, seems to preclude the preparation and detection of such states. However, exploiting defects and disorder in the spin system, and combining coherent and incoherent control of the natural evolution, cannot only prepare [35] but even detect these types of states [39] with good approximation.

In particular, spin chains in fluorapatite are typically interrupted by defects (e.g., substitutional OH terms). Then, even in the absence of frequency addressability, the dynamics of the end-chain spins under the internal dipolar Hamiltonian is sufficiently different from the bulk spins, as the end-spins have only one nearest neighbor, to allow for an approximate state preparation.

Indeed, the transverse polarization σ_x^k of the first and bulk spins evolves at different rates under the internal dipolar Hamiltonian. The end-spin evolution rate is slower by a factor $\approx 1/\sqrt{2}$ as compared to the rest of the chain, due to fewer numbers of couplings with neighboring spins. Thus, there exists a time t_1 when the state of the end-spins is still mainly σ_x , whereas the rest of the spins have evolved to many-body correlations. A second $\pi/2$ pulse brings the end-spin magnetization back to the longitudinal axis, while an appropriate phase cycling scheme cancels out other terms, thus obtaining the state

$$\delta\rho_{end} \approx \delta\rho_z^1 + \delta\rho_z^N. \quad (22)$$

As the phase cycling does not cancel zero-quantum coherences, they will be the main source of errors in the initialization scheme [35, 36].

A similar control strategy can be as well used to read out the spins at the end of the chain. The initialization technique described above was first introduced in [35]

(see also [36, 94]); Kaur [39] later demonstrated both the initialization and readout techniques. The effectiveness of the initialization and readout methods was verified by probing the transport dynamics, as driven by the DQ Hamiltonian, comparing the end-polarized states and observables with the thermal equilibrium state (see Sect. 6.2). We note that these transport experiments evolve the system under a non-interacting Hamiltonian and thus do not evolve the zero-coherence error terms into observable signal. For more general experiments, these error terms might be more important and different strategies to access local correlations need to be developed.

4 Time-Ordered Correlations

4.1 Echoes and Fidelity Decay

Spin echoes [5] have long been used, first in NMR and then in other realms, to study the dynamics of quantum systems while isolating them from external noise. Well before the emergence of thermodynamic equilibrium from reversible (unitary) dynamics was codified in the ETH, the NMR community realized that “*isolated systems of many particles often appear to behave irreversibly, though they are in principle dynamically reversible*” [7]. While the original Hahn echo [5] was a single-spin phenomena, which can be explained from the effects of classical inhomogeneities (and thus the action of an external, classical noise), the NMR community soon after developed other pulses control sequence that could reveal how the irreversible dynamics can be due to intrinsic interactions among the many-body system spins. When the external control affects such dynamics, the reversible character of an isolated quantum system is revealed again. Realizing that the “*reversibility can be made evident in ‘echo’ phenomena, in which the system is literally restored to a dynamical state which existed in the past*” [7], led to the development of one of the first metrics for quantum dynamics, the *Loschmidt Echo*.

In the context of quantum information, the fidelity of the time evolution was adopted as a metric of the quality of any experimental implementation in quantum information devices. The suspicion that practical implementation performance might be spoiled by the presence of chaotic properties of the evolution led to a unified picture of Loschmidt echo and fidelity as good indicators of the properties of the quantum dynamics [95].

Given an evolution under an unperturbed Hamiltonian, H_0 , the overlap (fidelity) of the evolved state, $|\psi_0(t)\rangle = e^{-iH_0t} |\psi(0)\rangle$ with a state evolving under a perturbed Hamiltonian, H , $|\psi(t)\rangle = e^{-iHt} |\psi(0)\rangle$ gives the fidelity or Loschmidt echo,

$$\mathcal{L}(t) = |\langle \psi(t) | \psi_0(t) \rangle|^2 = |\langle \psi(0) | e^{iHt} e^{-iH_0t} |\psi(0)\rangle|^2. \quad (23)$$

This expression describes an “echo” since it can be interpreted as the attempt to revert the arrow of time after an evolution under H_0 for time t . A divergence from $\mathcal{L} = 1$ indicates that the time reversal is imperfect.

While the Loschmidt echo is defined with respect to a pure state, related metrics can be defined based on the evolution of mixed states, e.g.,

$$\mathcal{L} = \text{Tr}[\rho(t)\rho_0(t)] = \text{Tr}\left[e^{-iHt}\rho(0)e^{iHt}e^{-iH_0t}\rho(0)e^{iH_0t}\right]. \quad (24)$$

As a common requirement for many of the metrics used to characterize quantum dynamics, the measurement of the Loschmidt echo requires, as it is evident from its expression, to achieve time reversal of the Hamiltonian.

4.2 Two-Point Correlators

The fidelity can be considered as the expectation value of an *echo operator*, $L = e^{iHt}e^{-iH_0t}$. In the high-fidelity regime, we can relate the fidelity to a two-point correlator. Assume that the perturbed Hamiltonian can be written as $H = H_0 + \epsilon V$ and work in the interaction picture defined by H_0 . Then, the fidelity becomes

$$\tilde{\mathcal{L}}(t) = |\langle \psi(0) | \mathcal{T} \left[e^{-i\epsilon \int_0^t \tilde{V}(t') dt'} \right] | \psi(0) \rangle|^2, \quad (25)$$

where $\tilde{V}(t) = e^{-iH_0t} V e^{iH_0t}$. Using a Dyson expansion to second order (which is sufficient for $\epsilon \ll 1$ or equivalently high fidelity) we find that

$$\langle \mathcal{T} \left[e^{-i\epsilon \int_0^t \tilde{V}(t') dt'} \right] \rangle \approx 1 - i\epsilon \int_0^t \langle \tilde{V}(t') \rangle dt' - \frac{\epsilon^2}{2} \int_0^t \int_0^t \langle \mathcal{T} [\tilde{V}(t') \tilde{V}(t'')] \rangle dt' dt''. \quad (26)$$

Keeping only terms up to ϵ^2 , we find the approximated fidelity

$$\mathcal{L}(t) \approx 1 - \epsilon^2 \int_0^t \int_0^t \left[\langle \tilde{V}(t') \tilde{V}(t'') \rangle - \langle \tilde{V}(t') \rangle \langle \tilde{V}(t'') \rangle \right]. \quad (27)$$

We thus find that the fidelity is approximately related to the 2-point time-correlation function of the perturbation, $C(t, t') = \langle \tilde{V}(t) \tilde{V}(t') \rangle - \langle \tilde{V}(t) \rangle \langle \tilde{V}(t') \rangle$, in the interaction picture. We can further define the average perturbation,

$$\bar{V} = \int_0^t \tilde{V}(t') dt' \quad (28)$$

and rewrite

$$\mathcal{L}(t) \approx 1 - \epsilon^2 \left[\langle \bar{V}(t)^2 \rangle - \langle \bar{V}(t) \rangle^2 \right]. \quad (29)$$

We note that in order to measure the Loschmidt echo it is imperative to be able to invert the arrow of time, in order to implement a time reversal under H . The various control sequences and echoes schemes described in Sect. 1 provide a strategy to achieve this goal. The task can be, however, simplified if we restrict to measuring $C(0, t)$ for a highly mixed state, as it is often the case in NMR experiments.

As introduced in Sect. 1.1.2, the spin systems probed in NMR are typically initialized in a high temperature, thermal equilibrium state, $\rho = e^{-\beta H} / \text{Tr}[e^{-\beta H}] \approx \mathbb{1}/N - \beta H/N$. In a large magnetic field, the Hamiltonian can be accurately approximated by the Zeeman energy only, $\propto Z = \sum_k \sigma_z^k$, the total magnetization in the z-direction. As the NMR observable (the total transverse magnetization, $X = \sum_k \sigma_x^k$) is traceless, the identity can be neglected and the signal is given by

$$S(t) = \text{Tr} \left[U(t) Z U(t)^\dagger X \right]. \quad (30)$$

It is easy to rotate the initial state to the x direction (or to effectively rotate the observable to z by applying a $\pi/2$ pulse to the state before the measurement). Then, calling V the total magnetization in any direction, the signal can be written as a two-point correlator at infinite temperature,

$$S(t) = \text{Tr}[V(t)V(0)] \equiv C_{\beta=0}(0, t) = \langle V(0)V(t) \rangle_{\beta=0}. \quad (31)$$

Given the similarity between this expression and the (high-fidelity) Loschmidt echo, this simpler quantity can be taken as a proxy for the fidelity or Loschmidt echo when analyzing the quantum many-spin dynamics at high temperature.

5 Out-of-Time-Ordered Correlations

The out-of-time-order (OTO) correlation function for two operators A, B evolving under a Hamiltonian H is

$$OTO(t) = \langle \psi | B(t)^\dagger A(0)^\dagger B(t) A(0) | \psi \rangle. \quad (32)$$

We can interpret this expression as the fidelity of the two states $B(t)A(0)|\psi\rangle$ and $A(0)B(t)|\psi\rangle$, where the order of applying A and B is inverted. (thus creating an “out-of-time” order where A at $t = 0$ is applied after B at time t .)

In contrast, the two-point correlator defined above can be considered as a time-ordered correlation [96]. Consider the commutator norm between the two operators

A and $B(t)$, $C(t) = \langle [B(t), A][B(t), A]^\dagger \rangle$. This can be expanded as

$$\begin{aligned} C &= \langle (B(t)A - AB(t))(A^\dagger B(t)^\dagger - B(t)^\dagger A^\dagger) \rangle \\ &= \langle B(t)AA^\dagger B(t)^\dagger + AB(t)B(t)^\dagger A^\dagger - \langle B(t)AB(t)^\dagger A^\dagger + AB(t)A^\dagger B(t)^\dagger \rangle, \end{aligned} \quad (33)$$

where the first two terms correspond to two-point, time-ordered correlators, while the second two terms are equivalent to the OTO correlator. These relationships can be made more evident in special cases. For example, consider the average at infinite temperature for Hermitian operators A , B . Then we have

$$C = 2[\langle A^2 B(t)^2 \rangle - OTO(t)], \quad (34)$$

and, in particular, for $A = B$ we have that the time-ordered part is equivalent to the two-point correlator. Furthermore, when A and B are both unitary and Hermitian, such as Pauli operators or tensor products of Pauli operators, the time-ordered part $\langle A^2 B(t)^2 \rangle = 1$, so that only the OTO correlator contributes non-trivially to the commutator.

We note that the OTO four-point correlator can be evaluated approximatively in NMR (with a scheme similar to the two-point correlator) in a scheme that has been called *polarization echo* [9, 97]. We combine the description of NMR experiments in Eqs. (30)–(31) with the (Loschmidt) echo evolution, Eq. (23). The NMR signal for the polarization echo is

$$PE(t) = \text{Tr} \left[Z e^{iHt} e^{-iH_0 t} Z e^{iH_0 t} e^{-iHt} \right] = \text{Tr} [Z_0(t) Z(t)], \quad (35)$$

where $Z_{(0)}(t) = e^{-iH_{(0)} t} Z e^{iH_{(0)} t}$. As done for the two-point correlator, we can work in the interaction picture defined by H_0 and analyze the effects of the perturbation to second order. We can first write the polarization echo signal using the echo evolution $\mathcal{E} = e^{iHt} e^{-iH_0 t}$ as

$$PE(t) = \text{Tr} \left[Z \mathcal{E} Z \mathcal{E}^\dagger \right] \quad (36)$$

and expand \mathcal{E} using the average perturbation,

$$\mathcal{E} \approx \mathbb{1} - \epsilon \bar{V}(t) - \frac{\epsilon^2}{2} \bar{V}(t)^2. \quad (37)$$

Keeping only terms to second order in the trace, we thus obtain

$$PE(t) \approx 1 - \epsilon^2 \left(\text{Tr} \left[\bar{V}(t)^2 Z^2 \right] - \text{Tr} \left[\bar{V}(t) Z \bar{V}(t) Z \right] \right) = 1 - \epsilon^2 \text{Tr} \left([\bar{V}(t), Z]^2 \right). \quad (38)$$

Quite interestingly, we find that the polarization echo give thus access to a 4-point correlator (or the expectation value of the commutator square), that is, to OTO correlations. While this expression is only valid in the limit of weak perturbation, in the following we present a strategy (based on another NMR technique) that allows measurement of the out-of-time ordered commutator.

5.1 Multiple Quantum Coherences and Spin Counting

Out-of-time ordered correlators have been proposed to measure the spread of quantum information and correlations (entanglement) in an interacting many-body system. A similar task had been developed in NMR for the purpose of spectrographic reconstruction of complex molecules and crystal structure. In that context, the complex dynamics of many-spin correlations has been traditionally explored in NMR with the so-called *spin counting* experiments [98–100] that measure Multiple Quantum Coherence (MQC) intensities (see Fig. 4). A quantum coherence of order k describes the contribution of terms $|m_{\mathbf{n}}\rangle\langle m'_{\mathbf{n}}|$ in a density matrix such that $m_{\mathbf{n}} - m'_{\mathbf{n}} = k$, with $m_{\mathbf{n}}$ the collective $\sigma_{\mathbf{n}}$ eigenvalue (\mathbf{n} here denote direction). Then, a state of coherence order q , when rotated around the axis \mathbf{n} by an angle φ , will pick up a phase equal to $q\varphi$. This property is used in NMR experiments to select a particular coherence order, by the so-called *phase cycling* [87], that amounts to averaging measurements done with phase-shifted pulse sequences.

This concept might be broadened to quantum coherences with respect to any operator P satisfying $e^{-2im\pi P} = \mathbb{1}$, where m is an integer. (we assume here P to be traceless for convenience.) A typical example, easy to implement, is $P = \sum_j S_j \cdot \mathbf{n}$, the generator of global spin rotations around the \mathbf{n} -axis.

We can define q -coherence operators \mathcal{P}_q with respect to the operator P that satisfy the following two equivalent relations:

$$e^{-i\theta P}\mathcal{P}_qe^{i\theta P} = e^{-iq\theta}\mathcal{P}_q, \quad [P, \mathcal{P}_q] = q\mathcal{P}_q. \quad (39)$$

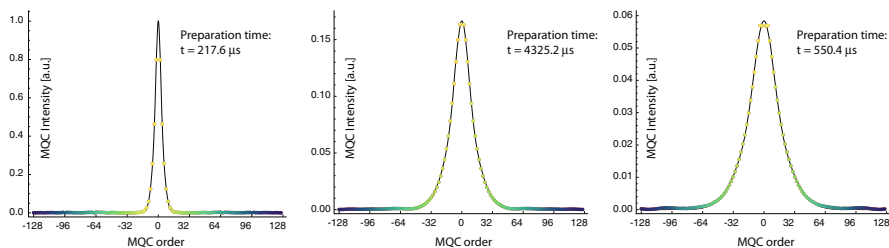


Fig. 4 Multiple Quantum Coherence intensities measured in adamantane. Here the preparation step was performed using a Double Quantum Hamiltonian engineered with an 8-pulse sequence. As the preparation time increases (from left to right) the number of coherences that are excited also increase. The variance of the MQC intensity distribution can reveal the number of correlated spins, here from ~ 30 to more than 500 spins

From the first relation it is evident that $\mathcal{P}_{-q} = \mathcal{P}_q^\dagger$. In addition, it can also be shown that different \mathcal{P}_q are orthogonal, and they can be normalized such that $\text{Tr}[\mathcal{P}_q \mathcal{P}_{q'}^\dagger] = \text{Tr}[\mathcal{P}_q \mathcal{P}_{-q'}] = \delta_{q(q')}$. Then, although the coherence operators do not form a basis, they can still be used to decompose any traceless Hermitian operator O as

$$O = \sum_{q=1}^L p_q \mathcal{P}_q, \tag{40}$$

where L is the number of unique eigenvalues of P . (for example, L is the number of spins if $P \equiv Z$.) This decomposition follows from the properties in Eq. (39) and can be thought as a Fourier decomposition with respect to P ,

$$\mathcal{P}_q = \frac{1}{2p_q\pi} \int_0^{2\pi} d\theta e^{iq\theta} e^{-i\theta P} O e^{i\theta P}. \tag{41}$$

Since we are considering discrete operators, we can replace Eq. (41) with a discrete Fourier transformation:

$$\mathcal{P}_q = \frac{1}{2p_q L} \sum_{m=0}^{2L-1} e^{i\frac{qm\pi}{L}} e^{-i\frac{m\pi P}{L}} O e^{i\frac{m\pi P}{L}}. \tag{42}$$

We can use this relationship to define multiple quantum coherence intensities, $I_q = p_q p_{-q} = |p_q|^2$, which characterize the contribution of each coherence to a given operator :

$$\frac{1}{2L} \sum_{m=0}^{2L-1} e^{i\frac{qm\pi}{L}} \text{Tr}\left[O e^{-i\frac{m\pi P}{L}} O e^{i\frac{m\pi P}{L}}\right] = p_q \text{Tr}[O \mathcal{P}_q] = I_q. \tag{43}$$

We can thus extract the quantum coherence intensities of any operator O by measuring its autocorrelation with the same operator rotated by P .

A typical experimental protocol then comprises four steps. First, a system is let to evolve under an (engineered) Hamiltonian to be studied. A $\phi_m = \pi m/L$ rotation around P is then applied to *tag* the quantum coherences. The evolution is then reverted back in time (by engineering the same Hamiltonian with opposite sign). The signal intensity S_m is then measured and the experiment is repeated L times while sweeping m from 0 to $2L - 1$. A Fourier transform of S_m yields the quantum coherence intensities. Taking advantage of the high-temperature approximation already discussed, where $\rho(0) - 1/D \propto Z$, this protocols yields the signals

$$\begin{aligned} S_m(t) &= \text{Tr}\left[U(-t)e^{i\pi m P/L} U(t) Z U(t)^\dagger e^{-i\pi m P/L} U(-t)^\dagger Z\right] \\ &\equiv \text{Tr}\left[Z(t)e^{i\pi m P/L} Z(t)e^{-i\pi m P/L}\right] \end{aligned} \tag{44}$$

and the MQC intensities are

$$I_q = \frac{1}{2L} \sum_{m=0}^{2L-1} e^{i \frac{qm\pi}{L}} S_m. \tag{45}$$

We note that in experiments it might not be possible to probe all coherences, since L might be too large. The phase step (and L) is thus usually truncated to capture most of the coherences while keeping the experimental time reasonable.

In traditional NMR experiments, P has been taken as the collective Z operator (or sometimes as the collective magnetization along a different axis [57]). The experiment typically involves creating MQC by using, e.g., the so-called double quantum Hamiltonian, $H_{DQ} \propto \sigma^x \sigma^x - \sigma^y \sigma^y$ (preparation) before letting the system evolve under the internal Hamiltonian. The preparation Hamiltonian is then applied back in time to refocus the MQC, after having applied the encoding ϕ_m rotation. The free evolution time then might transport (or scramble) the quantum coherences, in a manner that reflects the spin-spin interactions and hence the structure of a molecule [76, 98]. The distribution of I_q has then been traditionally used to approximate the average number of correlated spins created by the preparation Hamiltonian, under the assumptions that all correlation are created equally [100]. Indeed, the collective magnetization (the Z -operator) has degenerate eigenvalues; for L spins, an eigenvalue corresponding to m magnetization has a degeneracy $\binom{2L}{L-m}$. Correspondingly, if all MQC were to be populated, they would follow a binomial distribution with variance L .

5.2 OTO Commutator and Multiple Quantum Coherences

While the assumptions that all MQC are equally populated according to their (degeneracy) weight will fail when disorder or perturbations are introduced, and in 1D or integrable systems, the variance of the MQC distribution can still provide useful information as it is related to the OTOC.

Consider the signal in Eq. (44) with $\phi_m = \pi m/L$. We can expand the signal in power of ϕ_m as

$$\begin{aligned} S_\phi &= \text{Tr} \left[Z(t) e^{i\phi P} Z(t) e^{-i\phi P} \right] \approx \text{Tr} [Z(t) Z(t)] \\ &+ i\phi \text{Tr} [Z(t) P Z(t) - Z(t) Z(t) P] \\ &+ \frac{\phi^2}{2} \text{Tr} \left[2Z(t) P Z(t) P - Z(t) P^2 Z(t) - Z(t) Z(t) P^2 \right] + \dots \end{aligned} \tag{46}$$

Note that the first term is just the LE (or a constant, if the time inversion were perfect) and equal to $\sum_q S_q(t)$, while the second term, linear in ϕ , is zero due to the

symmetry of coherences. The third order term can be rewritten as

$$C_{ZP} \equiv \frac{\phi^2}{2} \text{Tr}[[Z(t), P]^2],$$

which is indeed the desired OTO commutator. Similarly, we can expand the signal decomposition in MQC intensities to second order, finding

$$S_\phi = \sum_q e^{-i\phi q} I_q(t) \approx \sum_q I_q(t) - i\phi \sum_q q I_q(t) - \frac{\phi^2}{2} \sum_q q^2 I_q(t) + \dots \quad (47)$$

We thus find that the OTO commutator at infinite temperature ($\rho \propto \mathbb{1}$) is given by the second moment of the MQC, $C_{ZP}(t) = \sum_q q^2 S_q(t)$.² Equation (47) was first derived in a different context in Ref. [101] for NMR systems. When applied to pure states, it relates the second moment of the MQC distribution to the quantum Fisher information [102].

Multiple quantum coherences have also been detected indirectly using a (heteronuclear) central spin coupled to a homonuclear spin system [103]. The central spin is used to probe how the initially local information (encoded in the polarization of the central spin) spreads into a coupled 15-spin “environment.” The spread is monitored by measuring the MQC with respect to the x -quantization basis [50, 57], C_n^x . Terms in the coupled spin state with a given coherence are tagged by a collective rotation of the “environment” around the x -axis. By inverting the time-evolution operator driving the central spin to environment interaction the information is mapped to the central spin that is then read out. The variance of the MQC distribution in the environment is related to the number of correlated spins, which increases linearly in time in the absence of spin-spin interactions (canceled by a decoupling sequence). When interactions are turned on, the information is scrambled in the environment and cannot be recovered anymore.

5.3 Entanglement Measures

Multiple quantum coherences provide a powerful window to the complex correlated states produced by many-body dynamics. It is natural to search for a relationship between these quantities and entanglement. Indeed, for pure states, it is possible to exactly link the second moment of the MQC distribution to the quantum Fisher information [102], which is itself an entanglement witness. Local control is typically needed to experimentally estimate entanglement measures [104–106].

² Notice that exchanging the roles of Z and P will result in a different MQC distribution I_q ; however, its second moment remains the same.

Various strategies to overcome NMR limitations in this regard have been taken, ranging from selecting fully controllable—but small—systems to introducing partial local control and a combination of several MQCs to devise new entanglement-like measures in special systems.

5.3.1 OTOC with Full Control to Detect the Rényi Entropy

Universal control provides an alternative method, not relying on MQC, to measure OTOCs and even gives access to the Rényi entropy. The method has been implemented in a small, liquid-state molecule [107]. In that NMR quantum simulator, full control of individual spins allows the direct measurement of the OTO correlation, Eq. (32). Similarly to what described for MQC and echoes, the experiment simulates a system at infinite temperature, while the initial state at high (but not infinite) temperature acts as the observable A . The second observable B is chosen to be a unitary operator implemented as a selective rotation of a single spin. By choosing the rotation angle to be π , the unitary operator is simply proportional to an (Hermitian) Pauli matrix, thus effectively simulating a second observable. The evolution of the system then consists of a period of Hamiltonian evolution (here the Ising Hamiltonian with a field, H_I), the selective rotation implementing B and another period of evolution under $-H_I$. The evolved state is then

$$\rho(t) = e^{iH_I t} B e^{-iH_I t} \rho_0 e^{-iH_I t} B^\dagger e^{iH_I t} \quad (48)$$

and the signal $S(t) = \text{Tr}[\rho(t)A]$ with from the initial state $\rho(0) = \mathbb{1}/2^L + \epsilon A$ yields the desired OTO correlator

$$S(t) = \text{Tr}\left[B(t)AB^\dagger(-t)A\right] = \langle B(t)^\dagger A(0)^\dagger B(t)A(0) \rangle_{\beta=0}. \quad (49)$$

Even more interesting, preparing the initial state and observable to be $A = \sigma_\alpha^1$, $\alpha = \{x, y, z\}$ enables reconstructing the Rényi entropy for qubit 1. Indeed, summing over a whole basis \mathcal{B} for that subsystem, we have [108]

$$\sum_{k \in \mathcal{B}} \langle B(t)^\dagger A_k(0)^\dagger B(t)A_k(0) \rangle_{\beta=0} = \exp\left(-S_1^{(2)}\right). \quad (50)$$

Unfortunately, scaling up this method to larger system can quickly become prohibitive.

5.3.2 Correlation Rényi Entropies

While the method used for small system to reconstruct the Rényi entropy is not applicable to large systems where the number of experiments would scale

exponentially, the idea of combining several OTOCs (or MQCs) experiments is a fruitful one, especially when combined with systems where the dynamics is constrained by their properties, such as a central spin system or a 1D geometry, and the high-temperature approximation further simplifies the analysis of the density operator. The Rényi entropy of order α for a reduced density operator $\rho_A = \text{Tr}_B[\rho_{AB}]$ is given as

$$S_\alpha(\rho_A) = \frac{1}{1-\alpha} \log(\text{Tr}[\rho_A^\alpha]) \equiv S_\alpha(\rho_B). \quad (51)$$

Measuring the Rényi entropy thus typically entails performing state tomography of a reduced system. By expanding the state in terms of the Hamiltonian eigenstates, $|\Psi\rangle = \sum_n C_n |n\rangle$, we can also write [50, 109].

$$S_\alpha = -\log\left(\sum_n |C_n|^{2\alpha}\right). \quad (52)$$

As already mentioned, the MQC coherences do not provide information about the occupation of the system eigenstates—or in other words, the number of correlated spins—but only a proxy to this quantity. Still, for a central spin system coupled to an “environment” via $\sigma_z^C \sum_i \sigma_z^i$ coupling, it is possible to replace the projection of the environment state on its σ_z eigenstates, $C_z^{\{1011\dots\}} = |\langle 1011\dots | \Psi(t) \rangle|^2$ with the MQC coherences C_x measured via the central spin (see Sect. 5.2) in the formula for the Rényi entropies. The resulting metrics, dubbed “correlation Rényi entropies,” reliably capture the buildup of multi-spin correlations and the loss of information from the central spin.

5.4 Approximate Rényi Entropy and Average Correlation Length

A different strategy to approximatively estimate the Rényi entropy takes advantage of properties of the evolution of 1D (quasi-)integrable system [82].

Consider a generic high-temperature density matrix at time t . It can be decomposed using the *product* operators \mathcal{B}_k^s composed of tensor products of k Pauli matrices and $L - k$ identity operators

$$\rho(t) = \frac{\mathbb{1}}{2^L} - \epsilon \delta\rho = \frac{\mathbb{1}}{2^L} - \epsilon \frac{\sqrt{L}}{2^L} \sum_{k=1}^L \sum_{s=1}^{\zeta_k} b_k^s(t) \mathcal{B}_k^s, \quad (53)$$

where ζ_k is the number of configurations with exactly k non-identity Pauli operators.

Taking the partial trace of the state expressed in terms of the traceless operators \mathcal{B}_k^s , we obtain the Rényi entropy, $S_L^{(2)} = -\log[\text{Tr}(\rho_L^2)]$ for the left half of the spin chain:

$$S_L^{(2)} = -\log\left[\frac{1}{2^{L/2}} + \epsilon^2 \text{Tr}(\delta\rho_L^2(t))\right] \approx \frac{L}{2} \log(2) - \frac{\epsilon^2}{2^{L/2}} \sum_{k=1}^{L/2} \sum_s \zeta_k^L (b_k^s)^2,$$

where ζ_k^L counts only the configurations in the left half of the chain. We note that most generally, for $k > 1$, we have $\zeta_k^L = \frac{L/2-k+1}{L-k+1} \zeta_k$, where ζ_k are all the k -spin configurations in the whole chain. We can define $f_k = \sum_{s=1}^{\zeta_k} (b_k^s)^2$ as the contribution of all possible spin correlations with Hamming weight k (with $\sum_{k=1}^L f_k = 1$) to the density operator. For a translationally invariant system, the coefficients b_k^s do not depend on the spin position, and thus we have $\sum_s \zeta_k^L (b_k^s)^2 = (\zeta_k^L / \zeta_k) f_k$. While this is not exactly true for finite systems with open boundaries (and generally in the presence of disorder), we can still extract an approximated Rényi entropy:

$$S_L^{(2)} \approx \frac{L}{2} \log(2) - \frac{\epsilon^2}{2^{L/2}} \left(\sum_{k=1}^{L/2} \frac{L/2 - k + 1}{L - k + 1} f_k \right). \quad (54)$$

A related quantity that has been used to quantify localization [82] is the **average correlation length**

$$L_c = \sum_{k=1}^L k f_k, \quad (55)$$

describing the average length over which spins have become correlated.

For some density operators—in particular, as emerging from (quasi-)integrable dynamics—it is possible to extract the coefficients f_k from MQC along different axis. This allows to evaluate the average correlation length and the approximated Rényi entropy experimentally.

In particular, starting from an initial state at high temperature, $\rho_{\text{eq}} \approx e^{-\beta\omega_0 Z} \approx \frac{1}{2^L} (\mathbb{1} - \epsilon Z)$, with $\epsilon = \beta\omega_0$, the time-dependent component of the density matrix $\delta\rho(t) \propto U \rho_{\text{eq}} U^\dagger - 1/2^L$ evolves as

$$\begin{aligned} \frac{\delta\rho}{\sqrt{L}} &= \sum_j 2\mu_{jj} S_z^j + 2 \prod_{j < l < k} S_z^l \\ &\times \sum_{j,k > j} 2^{k-j} \left[(\eta - \mu)_{jk} S_y^j S_y^k - (\eta + \mu)_{jk} S_x^j S_x^k + (\nu + \chi)_{jk} S_y^j S_x^k + (\nu - \chi)_{jk} S_x^j S_y^k \right], \end{aligned} \quad (56)$$

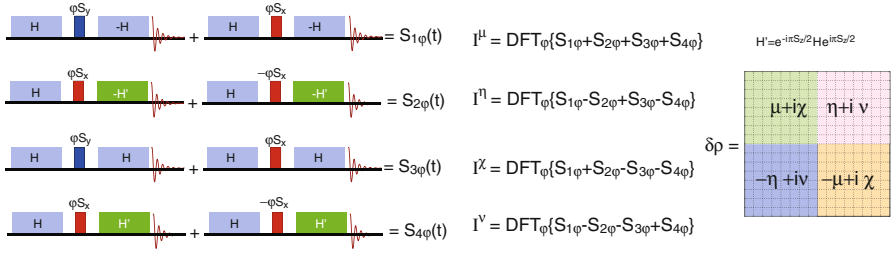


Fig. 5 Experimental scheme for extracting the correlation length from measurements of the MQC. For one measurement of L_c , we perform four MQC experiments according to the above to obtain $S_{1\phi}$, $S_{2\phi}$, $S_{3\phi}$, and $S_{4\phi}$. The MQC intensities for each sector of the density matrix are obtained by first taking the appropriate linear combinations of $S_{j\phi}$ and Fourier transforming with respect to ϕ

where μ is real and symmetric, whereas χ , η , ν are real and antisymmetric; they correspond to the four possible ways to correlate spins in a non-interacting system. We can express the coefficients f_k by using these matrices, finding the relations

$$f_1 = \bar{\mu}_0, \quad f_{k>1} = 2(\bar{\mu}_{k-1} + \bar{\chi}_{k-1} + \bar{\eta}_{k-1} + \bar{\nu}_{k-1}), \quad (57)$$

where $\bar{\mu}_k = \sum_j \mu_{jj+k}^2$, and similar expressions hold for χ , η , and ν . Because of the different symmetry properties of the operators connected with each of the μ , χ , ... matrices, we can extract their values by using MQC, following the scheme in Fig. 5.

First, note that the real part of the density operator, $\text{Re}[\rho]$, only contains correlations with an even number of S_y and S_x operators, i.e., operators such as $\mathcal{B}^{(\text{re})} \propto S_x^i \prod_{k=i+1}^{j-1} S_z^k S_x^j \pm S_y^i \prod_{k=i+1}^{j-1} S_z^k S_y^j$. The imaginary part, instead, $\text{Im}[\rho]$, is composed of $\mathcal{B}^{(\text{im})}$ operators with S_x , S_y operators (and vice versa) as end-spins. This thus distinguishes between η , μ and χ , ν . Since $\rho(-t) = \rho^*(t)$, we can obtain the real and imaginary parts of ρ from $\rho(t) \pm \rho(-t)$, using time reversal to engineer $\rho(-t)$.

Next we note that terms $\propto (S_y S_y + S_x S_x)$ are zero-quantum coherences, while terms $\propto (S_y S_y - S_x S_x)$ are double quantum coherences. Then, the first terms are invariant under rotations around z whereas the second terms acquire a minus sign when rotated by $\pi/2$. As similar properties are valid for the other terms in $\delta\rho$, we can use phase cycling to single out only the desired terms and extract only contributions from the four sectors corresponding to μ , η , χ , ν .

Finally, we measure the MQC intensities encoded in the x axis for each of these four sectors which are given by

$$\begin{aligned} I_q^\mu &= \frac{\delta_{1|q|}}{2} \bar{\mu}_0 + \sum_{k=1} \left[\frac{1}{2^{k+1}} \binom{k+1}{\frac{k+1-q}{2}} + \frac{1}{2^{k-1}} \binom{k-1}{\frac{k-1-q}{2}} \right] \bar{\mu}_k & I_q^\chi &= \sum_{k=1} \frac{1}{2^{k-1}} \binom{k}{\frac{k-q}{2}} \bar{\chi}_k \\ I_q^\eta &= \sum_{k=1} \left[\frac{1}{2^{k+1}} \binom{k+1}{\frac{k+1-q}{2}} + \frac{1}{2^{k-1}} \binom{k-1}{\frac{k-1-q}{2}} \right] \bar{\eta}_k & I_q^\nu &= \sum_{k=1} \frac{1}{2^{k-1}} \binom{k}{\frac{k-q}{2}} \bar{\nu}_k. \end{aligned} \quad (58)$$

I_q^μ and I_q^η are defined for $k - q \in \text{odd}$, whereas I_q^χ and I_q^ν are defined for $k - q \in \text{even}$. By inverting these relations we can write f_k as a linear combination of the MQC intensities, $f_k = \sum_{jq} M_{kq}^{(j)} I_q^j$, and thus calculate the experimentally measured average correlation length and the approximate entropy [82]. This powerful metrics has been used (see Sect. 7.1) to investigate localization in spin chains [82].

6 Integrable Models

6.1 Kicked Evolution

The behavior of systems evolving under a Hamiltonian that is (periodically) perturbed by strong kicks is of intrinsic interest as it might lead to appearance of chaos. Conversely, it is also interesting to study the dynamics of integrable kicked models, such as the XY model kicked by a uniform transverse field. While the XY model is not directly accessible in dipolarly coupled spins, Hamiltonian engineering can simulate an analogous system.

In the 1D tight-binding limit the DQ Hamiltonian can be diagonalized by via a Jordan-Wigner transformation and has been shown to be unitarily equivalent to the isotropic XY spin chain [35, 110, 111]. The DQ spin chain remains integrable in the presence of a uniform magnetic field along the z direction

$$\mathcal{H} = \frac{J}{2} \sum_{j=1}^{N-1} \left(\sigma_j^x \sigma_{j+1}^x - \sigma_j^y \sigma_{j+1}^y \right) + \Delta \sum_{j=1}^N \sigma_j^z. \quad (59)$$

The eigenenergies of the system are given by

$$\Lambda_k = 2\sqrt{J^2 \cos^2 k + \Delta^2}. \quad (60)$$

Starting from a thermal initial state $\rho_0 = \mathbb{1} - \epsilon \sum_{j=1}^N \sigma_j^z$, only zero and DQ z -basis coherences are predicted by the analytical model—as was previously shown for the case $\Delta = 0$ [35, 110]. The ZQ intensity is given by

$$\mathcal{J}_0 = \left(\sin^2 2\theta_k \cos 2\phi_k + \cos^2 2\theta_k \right)^2 \quad (61)$$

while the DQ intensity is given by

$$\mathcal{J}_{\pm 2} = (\sin 2\theta_k \cos 2\theta_k (1 - \cos 2\phi_k))^2 + \sin^2 2\theta_k \sin^2 2\phi_k, \quad (62)$$

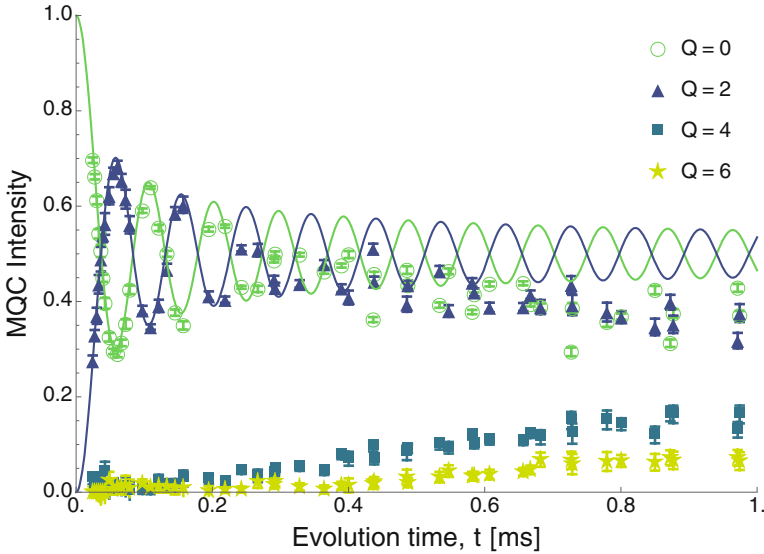


Fig. 6 Evolution of z-basis multiple quantum coherences from the thermal Zeeman initial state under the double quantum Hamiltonian in fluorapatite. Loss of signal at long evolution times is compensated by normalizing the data by total signal at each time point. The lines are the ideal zero- and double quantum intensities (see Eqs. (61)–(62))

where $\phi_k = \Lambda_k t$ and

$$\tan 2\theta_k = \frac{J \cos k}{\Delta}. \tag{63}$$

Figure 6 shows the experimental measurement of z-basis MQCs on a fluorapatite sample with $\Delta = 0$. The slow growth of higher-order coherences is due to long-range couplings in the experimental system that leads to a breakdown of integrability.

We can experimentally simulate the DQ Hamiltonian in a longitudinal field using a Trotterized approximation, where we interleave periods of evolution under the engineered DQ Hamiltonian with evolution under the z-field. The z-field evolution is performed by selectively shifting the phases of the RF pulses used in the experiment.

If the collective z magnetization ($Z = \sum_i \sigma_i^z$) is used as the observable, the average signal measured during evolution under this Hamiltonian (starting from the same thermal initial state) is

$$S(t) = \sum_k \frac{1}{\Lambda_k^2} \left(J^2 \cos^2 k \cos \left(4t \sqrt{\Delta^2 + J^2 \cos^2 k} \right) + \Delta^2 \right). \tag{64}$$

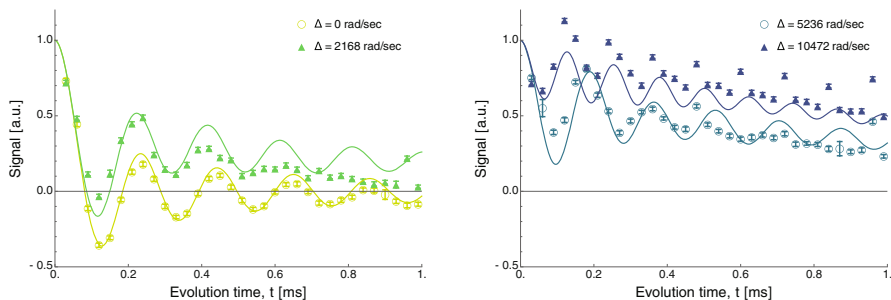


Fig. 7 Evolution of collective z -magnetization from the thermal Zeeman initial state under the double quantum Hamiltonian with an external z field in fluorapatite of variable magnitude. The simulations (lines) use a value of $J = 7.6 \times 10^3$ rad/s rather than the ideal value of 8.17×10^3 rad/s to give a better fit to the data—indicating a slight mis-alignment of the crystal in the external static magnetic field

Figure 7 shows a comparison between the experimental results on fluorapatite and the theoretical model.

6.2 Quantum State Transfer

While the dynamics of spin systems is of intrinsic interest, its direct applications to quantum information processing beyond quantum simulation are also possible. Among various tasks, the transfer of a quantum state between (not too) distant qubits mediated by a chain of spin qubit has been the focus of NMR implementations [41, 112]. The underlying strategy was first proposed by Bose [113] and quickly refined to achieve perfect fidelity [114, 115]. Proof-of-principle experiments were carried out exploiting NMR techniques [35, 39, 112, 116], by taking advantage of an interesting correspondence between transport of a single excitation (in the pure state 1-excitation manifold) with state transfer of mixed states.

State transfer can be driven by a ballistic transport induced by an integrable Hamiltonian such as the XY model,

$$H_{XY} = \sum_i b(\sigma_x^i \sigma_x^{i+1} + \sigma_y^i \sigma_y^{i+1}). \quad (65)$$

The goal of state transfer is to map the state $\alpha|0\rangle + \beta|1\rangle$ from spin 1 to spin L of an L -spin chain initially in the ground state $|00\dots\rangle$ using only free evolution under H . Since the ground state itself does not evolve, the focus is on the dynamics of the state $|\psi(0)\rangle = |100\dots\rangle$ and its overlap with $|00\dots 1\rangle$ at time t , $F(t) = |\langle\psi(t)|00\dots 1\rangle|^2$, where $|\psi(t)\rangle = e^{-iHt}|\psi(0)\rangle$. The state evolves thanks to energy-conserving flip-flops that drive the excitation along the chain.

More generally, we can consider the transfer from spin i to j and define the corresponding fidelity, $F_{ij}(t) = |\langle i | e^{-iHt} | j \rangle|^2$, where $|j\rangle$ describes a spin chain in the ground state with a single excitation on spin j .

Since states are highly mixed in NMR, we can only hope to simulate the pure-state behavior. We then consider the *quantum operator transfer* from the operator

$$\delta\rho_z^i = \mathbb{1}_{i-1} \otimes \sigma_z^i \otimes \mathbb{1}_{L-i} \quad (66)$$

to the operator $\delta\rho_z^j$. The normalized operator overlap,

$$C_{ij}(t) = \text{tr} \left[\delta\rho_z^i(t) \delta\rho_z^j \right] / \text{tr} \left[\delta\rho_z^i(0)^2 \right] \quad (67)$$

can be obtained by evolving an initial state $\rho_i(0) = (\mathbb{1} + \epsilon \delta\rho_z^i) / 2^L$, since the identity does not contribute to the signal and does not evolve for any unitary dynamics. This state represents a completely mixed-state chain with a single-spin partially polarized along the z axis. Notice that the operator in Eq. (66) does not reside in the lowest excitation manifold, in which quantum state transfer is usually calculated, and instead involves the dynamics of the transport Hamiltonian in all the manifolds. However, since transport Hamiltonians, such as the XY Hamiltonian Eq. (65), should conserve the spin excitation number (or an equivalent excitation number) in order to enable transport, it is always possible to diagonalize them in separate excitation subspaces. Then, the eigenfunctions of higher excitation manifolds can be exactly expressed in terms of Slater determinants of the one-excitation manifold eigenstates, $|E_i\rangle$ and the eigenenergies are the corresponding linear combinations of 1-excitation eigenvalues.

Consider, for example, 2-excitation states such as $|hk\rangle$ and $|ij\rangle = |0..1_i 0..1_j..0\rangle$, with excitations at the spins hk and ij , respectively. Their overlap after an evolution for a time t can be written by expanding in terms of the 2-excitation eigenstates, $|E_{nm}\rangle$ with energy $E_{nm} = E_n + E_m$,

$$\langle hk | U(t) | ij \rangle = \sum_{nm} \langle hk | E_{nm} \rangle \langle E_{nm} | ij \rangle e^{i\omega_n t} e^{i\omega_m t} = \frac{1}{2} (A_{ih} A_{jk} - A_{ik} A_{jh}),$$

where we defined the one-excitation transfer amplitudes, $A_{ij} = \langle j | U(t) | i \rangle$. Note that the last expression can be written as the determinant of the 2×2 matrix of transfer amplitudes. Similarly, we can calculate the propagator matrix element between any two states in the n th excitation manifold, e.g., $|\mathbf{j}\rangle = |0, \dots, 1_{j_1}, 0, \dots, 1_{j_2}, \dots\rangle$, $\langle \mathbf{j} | U(t) | \mathbf{i} \rangle$ from the $n \times n$ matrix of corresponding single-excitation amplitudes.

$$\langle \mathbf{j} | U(t) | \mathbf{i} \rangle = \begin{vmatrix} A_{i_1 j_1}(t) & A_{i_1 j_2}(t) & \dots \\ A_{i_2 j_1}(t) & A_{i_2 j_2}(t) & \dots \\ \dots & \dots & \dots \end{vmatrix} \equiv \mathcal{A}_{\mathbf{i}, \mathbf{j}}(t). \quad (68)$$

We can then evaluate the transfer of any initial mixed state $\rho_a = \sum_{\mathbf{i}, \mathbf{j}} a_{\mathbf{i}\mathbf{j}} |\mathbf{i}\rangle \langle \mathbf{j}|$ to another mixed state ρ_b by calculating the relevant correlation between the evolved state and the final desired state,

$$\text{Tr}(\rho_a(t)\rho_b) = \sum_{\mathbf{h}, \mathbf{k}, \mathbf{i}, \mathbf{j}} b_{\mathbf{h}\mathbf{k}} a_{\mathbf{i}\mathbf{j}} \mathcal{A}_{\mathbf{i}\mathbf{h}}(t) \mathcal{A}_{\mathbf{j}\mathbf{k}}^*(t). \quad (69)$$

Note that for the states of interest ($\delta\rho_z^i$), this can be simplified and we find

$$C_{ij}(t) = |A_{ij}|^2 \equiv F_{ij}. \quad (70)$$

It is this equivalence that allows for a simple simulation of the pure-state dynamics with mixed state.

Note that as discussed in Sect. 2.1, there are often limitations to what Hamiltonians can be engineered, and indeed the XY Hamiltonian is often not accessible. Still, state transfer can be simulated using mixed states and the so-called Double Quantum (DQ) Hamiltonian,

$$H_{DQ} = \sum_i b(\sigma_x^i \sigma_x^{i+1} - \sigma_y^i \sigma_y^{i+1}). \quad (71)$$

Note that this Hamiltonian does not conserve the usual excitations linked to the total magnetization. However, it does conserve analogous excitation for the staggered magnetization, $\sum_j (-1)^j \sigma_z^j$, and thus we can follow a derivation similar to what outlined above to find the system evolution, as long as we transform the relevant states $|\mathbf{j}\rangle$ with the transformation $\prod_{j \in \text{odd}} \sigma_x^j$. Note that, in particular, the mixed state of interest only acquires at most a minus sign under this transformation, and thus, with the mapping

$$C_{ij}^{DQ} = (-1)^{j-i} |A_{ij}|^2 \equiv (-1)^{j-i} F_{ij} \quad (72)$$

we can still simulate the XY state transfer with the DQ Hamiltonian and mixed states.

These ideas have been applied to simulate quantum state transfer in NMR systems (see Fig. 8) and extended to the transport of other states [39] and to analyze the transport velocity [38].

7 Non-Integrable Models

7.1 Many-Body Localization

The large size and long relaxation times of NMR systems naturally lend itself to explore questions related to thermalization, and the lack thereof. In particular, a central issue is the role of disorder and interaction in preventing or driving thermalization. Many-body localization then describes the regime where disorder is large enough to make the system an effective insulator, but where interactions can still drive a (logarithmically slow) growth of entanglement. While probing this entanglement growth is challenging, insight can come from different metrics, such as OTOCs and correlation lengths described in Sect. 5, that can witness the same dynamics even at higher temperatures.

An NMR quantum simulator was used to engineer and characterize localization in a solid-state nuclear spin system. The system used in the experiment was a single crystal of fluorapatite (see Sect. 1.2) for its quasi-1D geometry that enabled the experimental measurement of the average localization length.

The total Hamiltonian of the system is given by the Zeeman interactions of the F(S) and P(s) spins, $H_Z = \omega_F \sum_k S_z^k + \omega_P \sum_\kappa s_z^\kappa$ and their magnetic dipolar interactions

$$H_{tot} = H_Z + H_{FF} + H_{PP} + H_{FP}. \quad (73)$$

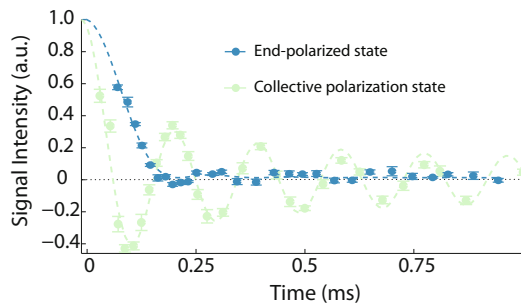


Fig. 8 Ballistic dynamics and transport under the DQ Hamiltonian, first reported in [39]. The two experiments highlight the different signals arising from the initial state and observables. The end-polarized state and observable displays a simple decay of the initial state, since because of the average length chain, the arrival at the other end is not recorded. The collective magnetization state instead shows characteristic oscillations, since the transport Hamiltonian does not conserve the uniform magnetization but creates spin-coherences. Data points are the experimental data (Blue: collective magnetization; Red end of chain magnetization), with error bars obtained from the FID. The measurement was done using a single scan (collective polarization) and 4 scans (end-polarized state). The lines are the fits using the analytical model

Since the Zeeman energies, $\omega_F = \gamma_F B = (2\pi)282.37$ MHz and $\omega_P = \gamma_P B = (2\pi)121.51$ MHz, where $\gamma_{F/P}$ are the gyromagnetic ratios, are much larger than the dipole-dipole interaction among the spins, we can truncate the dipolar Hamiltonian to its energy-conserving part (secular Hamiltonian). We then obtain the homonuclear Hamiltonians

$$H_{FF} = \frac{1}{2} \sum_{j < k} J_{jk}^F (2S_z^j S_z^k - S_x^j S_x^k - S_y^j S_y^k) \quad H_{PP} = \frac{1}{2} \sum_{\lambda < \kappa} J_{\lambda\kappa}^P (2s_z^\lambda s_z^\kappa - s_x^\lambda s_x^\kappa - s_y^\lambda s_y^\kappa) \quad (74)$$

and the heteronuclear interaction between the F and P spins,

$$H_{FP} = \sum_{k,\kappa} J_{k,\kappa}^{FP} S_z^k s_z^\kappa. \quad (75)$$

The maximum values of the couplings (for the closest spins) are given, respectively, by $J^F = -32.76$ krad s⁻¹, $J^P = 1.21$ krad s⁻¹ and $J^{FP} = 6.13$ krad s⁻¹.

Due to the strong dependence of the dipolar coupling on distance, the couplings between one chain of fluorine spins to the surrounding ones can be neglected, as they are 40-times weaker. Similarly, to first approximation, just the nearest-neighbor couplings can be retained, as they are 8-times stronger than other couplings. Finally, as the phosphorus spins are never driven, and their dynamics is slower, they can be considered to always be in a thermal, static state. Thanks to all these approximations the system can be effectively modeled by a 1D spin chain in the presence of a static magnetic noise. Indeed, at room temperature the P spins are in an equal mixture of their $m_z = \pm 1/2$ states. The heteronuclear interactions can then be approximated by $\sum_j h_j S_z^j$, where h_j is now a classical random variable representing the disordered field seen locally by each ¹⁹F. The resulting effective Hamiltonian can be then written as $H_{\text{nat}}^{\text{eff}} = \frac{J}{2} \sum_j (2S_z^j S_z^{j+1} - S_x^j S_x^{j+1} - S_y^j S_y^{j+1}) + \sum_j h_j S_z^j$.

The approximation breaks down at longer time, with a convergence of various effects: long-range in-chain and cross chain couplings, as well as pulse errors in the sequences used for Hamiltonian engineering. In addition, the system also undergoes spin relaxation, although on a much longer time-scale ($T_1 = 0.8$ s for our sample).

Using the tools described in Sect. 2, a broad range of Hamiltonians can be engineered to explore different behaviors of the spin chains, ranging from integrable, to single particle and many-body localized. These Hamiltonians can be engineering by a pulse sequence based on a basic building block consisting of a 4-pulse sequence [79] originally developed to study MQC. We show the sequence in Fig. 9, where 8-pulses are used for improved performance [81]. A further extension to 16 pulses, with the 8-pulses repeated but with a 180° shift, yields an increase robustness and was used to engineer a tunable Hamiltonian [82, 83, 117]. Contrary to canonical pulse sequences in NMR, the delays are tunable and given by

$$\begin{aligned} \tau_1 &= \tau(1 + 3g - v + w), & \tau_2 &= \tau(1 - u + v), \\ \tau_3 &= \tau(1 + u - w), & \tau_4 &= \tau(1 - 3g - v + w), \end{aligned}$$

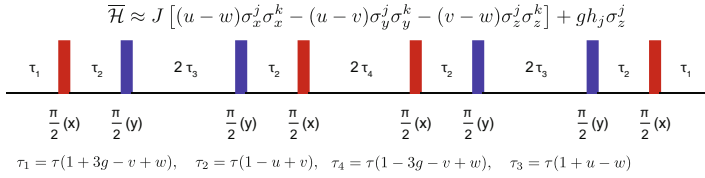


Fig. 9 Pulse sequence to engineer a tunable Hamiltonian, Eq. (76)

where τ is typically 4 μs . The total time of the sequence, that is, the cycle time t_c , is then $t_c = 24\tau$. The range of the adjustable dimensionless parameters u , v , w , and g is restricted by the requirement that none of the inter-pulse spacings becomes negative.

The average Hamiltonian H_0 to second order approximation, accounting for finite pulse width, is given by

$$H_0(u, v, w) = \frac{1}{2} \sum_{j < k} J_{jk} [(u-w)\sigma_x^j \sigma_x^k - (u-v)\sigma_y^j \sigma_y^k - (v-w)\sigma_z^j \sigma_z^k] + g \sum_j h_j \sigma_z^j, \tag{76}$$

including non-interacting, interactions, longitudinal and transverse fields and disorders. (Here the first order $H_1 = 0$, thanks to a proper symmetrization of the sequence.) By properly modifying the timing and the phases of the pulses, it is also possible to engineering $-H_0$, that is, to invert the arrow of time.

Note that this Hamiltonian includes most element needed to study localization both in non-interacting systems (Anderson localization) or when interactions are present (many-body localization).

First, by setting $v = 0$, the system is non-interacting (and the staggered magnetization is conserved). The non-interacting Hamiltonian still gives rise to a growth in the localization length L_c (since local magnetization would transport ballistically). Increasing the disorder strength (by varying g) results in the saturation of L_c at increasingly earlier times and lower levels, consistent with Anderson (single-body) localization. Figure 10a shows the experimental results (symbols) and numerical simulations (lines).

The many-body localization regime can be explored by turning on the interactions (setting $v > 0$) while keeping the disorder. The experimental results—shown in Fig. 10b—reveal that the average correlation length keeps growing (although slowly) when the interactions are added, even when for $v = 0$ there is already saturation.

Due to experimental imperfections it is difficult to explore the transition from MBL to ergodic behavior. Indeed, when interactions dominate disorder, the correlation length is expected to growth fast, but it is more heavily affected by the saturation of its value due to the approximation made in extracting L_c from the MQC, as well

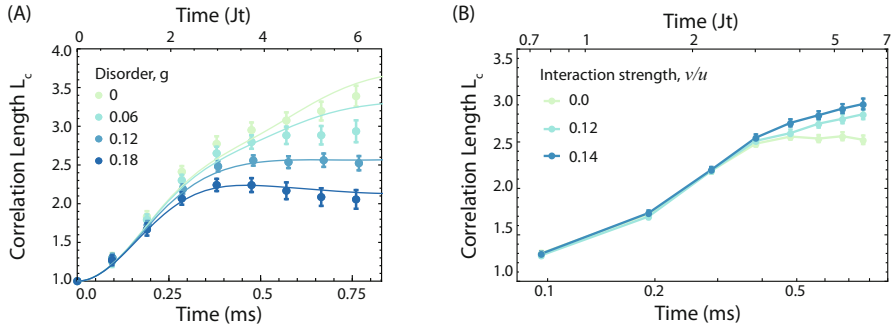


Fig. 10 Experimentally measured average correlation length from Ref. [82]. (a) Correlation length L_c in a non-interacting system for various strength $\propto g$ of disordered transverse fields, with $u = 0.24$ and $v = 0$ (Eq. 76). Error bars are determined from the noise in the free induction decay. The lines are numerical simulations using 6 spins, averaged over 126 disorder realizations. (b) Growth of L_c for interacting spin chains in a log-linear scale for varying interaction strengths v , in the presence of disorder. Data are for $u = 0.24$ and $g = 0.12$. After an initial growth of correlations, L_c saturates for the non-interacting systems, while it shows a slow growth in the presence of interactions, indicating MBL

as the challenges to collect higher multiple quantum coherences that would reveal larger spin correlations.

7.2 Prethermal Regime

Prethermalization refers to a special thermalization process wherein the system stays in an intermediate state for long time before reaching the final thermal state. Two commonly studied cases are (i) weakly interacting systems with the intermediate state being a thermal state of the non-interacting part of the Hamiltonian and (ii) periodically driven (Floquet) systems with the intermediate state being a thermal state of an effective time-independent Hamiltonian. The first case can be understood using perturbation theory; while the origin of the second case is more complicated and is the focus of this section.

As mentioned in Sect. 2.3.1, the Magnus expansion does not converge in generic many-body systems. The convergence radius is $\int_0^T \|H(t)\| dt < \pi$, but the norm of a many-body Hamiltonian is extensive $\|H(t)\| \propto L$, thus a priori forbidding a convergent expansion. From a physics point of view, a generic many-body system has a dense and extensive energy spectrum so that it always possesses a pair of eigenlevels that are $\hbar\omega = 2\pi\hbar/T$ apart and can thus absorb energy from the drive with period T . Given that the Magnus expansion diverges, and the system will eventually heat up, why and how accurately does low-order average Hamiltonian describe the system dynamics? This question is important to not only for the fundamental understanding of driven systems but also for the validity of quantum simulations.

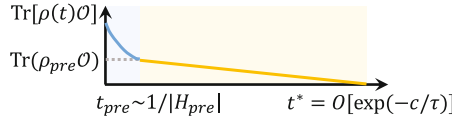


Fig. 11 Typical thermalization process of a Floquet system with large driving frequency. For short time, the dynamics is governed by a static Hamiltonian H_{pre} . An out-of-equilibrium state would first thermalize to a prethermal state $\rho_{pre} = e^{-\tilde{\beta}H_{pre}}/\mathcal{Z}$, with inverse temperature $\tilde{\beta}$ and partition function $\mathcal{Z} = \text{Tr}(e^{-\tilde{\beta}H_{pre}})$. The characteristic time to reach prethermal state is $t_{pre} = 1/|H_{pre}|$. For long time, the small time-dependent part of the Hamiltonian thermalizes the system to infinite temperature with characteristic time $t^* = O(\exp(-c/\tau))$

A series of theory works [118–121] establish that, although the Magnus expansion diverges, a truncation of the series still captures the dynamics of the system up to a small correction. Specifically, the stroboscopic dynamics is governed by an effective Hamiltonian $H_{eff}(t) = H_F^{(n^*)} + \delta H(t)$. The time-independent part $H_F^{(n^*)}$, also known as prethermal Hamiltonian H_{pre} , is given by the Magnus series (see Eq. (10)) truncated at optimal order $n^* = O(1/T)$. The residual time-dependent part is exponentially small in driving frequency $\|\delta H(t)\| = O(e^{-c/T})$ for some constant c . As a result, for time $t < 1/\|\delta H(t)\|$, the dynamics of a Floquet system is almost identical to a time-independent system Fig. 11. An out-of-equilibrium state first thermalizes according to the time-independent Hamiltonian H_{pre} and reaches an intermediate prethermal state ρ_{pre} . At late time t^* , the small residual $\delta H(t)$ thermalizes the system to infinite temperature. An intuitive understanding is that, when the energy quantum $2\pi\hbar/T$ is much larger than the single-spin energy, absorption of one energy quantum would require changing the state of a large number of spins, which is a high-order process that takes a very long time. The prethermalization mechanism states that quantum simulation is accurate up to an exponentially small correction, and dynamic phases of matter realized by Floquet engineering can survive thermalization for exponentially long time [122].

Although Floquet Hamiltonian engineering has been used for a long time, the direct experimental observation of the exponentially slow heating is achieved at a much later time. The main challenge is to resolve the Floquet heating from trivial effects, such as decoherence or control errors, as both lead to a signal decay. In solid-state NMR systems, two groups observed Floquet prethermalization using different methods—Peng et al. separate the Floquet heating from trivial effects using the Hamiltonian engineering technique [83]; Beatz et al. directly reduce the trivial effects by working with a dilute spin ensemble [123].

Reference [83] observed Floquet prethermalization in fluorapatite, where the ^{19}F spins form quasi-1D structure. The pulse sequence is shown in Fig. 12a. In the first part of the sequence, the 16-pulse sequence was adopted to engineer dipolar interaction along the y axis with tunable interaction strength J . In the second part, a collective rotation along the z axis is implemented as phase shifts between consecutive sequences. The rotation angle can also be tuned continuously. The

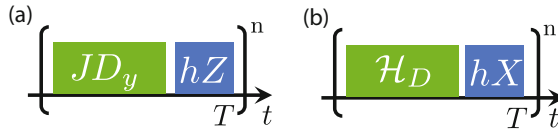


Fig. 12 Floquet sequence studied in Ref. [83] (a) and Ref. [123] (b)

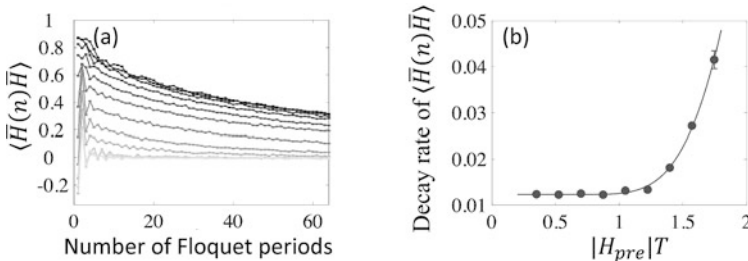


Fig. 13 (a) Autocorrelation of average Hamiltonian \bar{H} as a function of Floquet periods n for driving period $|H_{pre}|T$ from 0.35 (light) to 2.27 (dark) in steps of 0.175. (b) Autocorrelation decay rate as a function of $|H_{pre}|T$ (dots). The solid lines show a fitting of the experiment data to $ae^{-c/(|H_{pre}|T)} + b$. The driving sequence is shown in Fig. 12a

leading order average Hamiltonian is $\bar{H} = JD_y + hZ$, with $D_y = \frac{1}{2} \sum_{j < k} (S_y^j S_y^k - \frac{1}{2} S_x^j S_x^k - \frac{1}{2} S_z^j S_z^k) / (k - j)^3$ (Fig. 13a). To probe the slow heating to infinite temperature, the authors measure the autocorrelation of the average Hamiltonian $\text{Tr}[\bar{H}(t)\bar{H}] = h^2 \text{Tr}[Z(t)Z] + Jh \text{Tr}[Z(t)D_y] + Jh \text{Tr}[D_y(t)Z] + J^2 \text{Tr}[D_y(t)D_y]$. Each of the four correlators can be measured directly (see Sect. 3.2 for creating dipolar states and observables). The authors investigate the Floquet system with different normalized driving period $|H_{pre}|T$ by varying J and h proportionally while keeping T fixed. The advantage is that, when comparing signal after given Floquet sequences, the experiment time and number of pulses are the same for different $|H_{pre}|T$. Therefore, trivial effects, such as decoherence and pulse errors, stay constant when varying the Floquet period $|H_{pre}|T$. As shown in Fig. 13b, the decay rate is well captured by a constant trivial decay and an exponentially slow heating.

Reference [123] observed the exponentially slow heating by directly reducing the trivial effects. The authors worked with ^{13}C spins in diamond that form dilute spin ensembles, i.e., ^{13}C only occupies a small portion of lattice sites, while the majority is ^{12}C . The dilute ensembles lead to smaller interaction strength, allowing for a smaller decoherence and more accurate control (longer pulses). To enhance the signal from the dilute ensemble, the authors use nitrogen vacancy centers in the sample to hyperpolarize the ^{13}C spins. The Floquet sequence is shown in Fig. 12b, where the first part is free evolution under natural Hamiltonian \mathcal{H}_D , and the second part is a pulse along x with angle close to $\pi/2$. The average Hamiltonian is dipolar interaction along x axis (this can be most easily seen in the toggling frame),

which conserves the magnetization along x , $[\bar{H}, \sum_j \sigma_x^j] = 0$. The thermalization to infinite temperature is characterized by the decay of $\text{Tr}(\sum_i \sigma_x^i(t) \sum_j \sigma_x^j)$. By tuning T over one order of magnitude, the authors confirmed the heating rate is exponentially small over a large parameter range.

Acknowledgments SR acknowledges Natania Antler, Christopher Zeitler, and Laurel Anderson for assistance in collecting some of the data. PC acknowledge partial support from NSF grant PHY1915218.

References

1. R. Ernst, G. Bodenhausen, A. Wokaun, *Principles of Nuclear Magnetic Resonance in One and Two Dimensions* (Clarendon Press Oxford, 1987)
2. M.H. Levitt, *Spin Dynamics*, 2nd edn. (Wiley, Chichester [u.a.], 2008)
3. E.M. Purcell, R.V. Pound, *Phys. Rev.* **81**, 279 (1951). <https://doi.org/10.1103/PhysRev.81.279>
4. A. Abragam, W.G. Proctor, *Phys. Rev.* **106**, 160 (1957). <https://doi.org/10.1103/PhysRev.106.160>
5. E.L. Hahn, *Phys. Rev.* **80**(4), 580 (1950). <https://doi.org/10.1103/PhysRev.80.580>
6. A. Pines, D. Budker, *Biogr. Mems Fell. R. Soc.* **68**, 219–230 (2020). <https://doi.org/10.1098/rsbm.2019.0038>
7. J.S. Waugh, W.K. Rhim, A. Pines, *Pure Appl. Chem.* **32**(1–4), 317 (1972). <https://doi.org/10.1351/pac197232010317>
8. W.K. Rhim, A. Pines, J.S. Waugh, *Phys. Rev. B* **3**, 684 (1971). <https://doi.org/10.1103/PhysRevB.3.684>
9. S. Zhang, B.H. Meier, R.R. Ernst, *Phys. Rev. Lett.* **69**, 2149 (1992). <https://doi.org/10.1103/PhysRevLett.69.2149>
10. V.A. Skrebnev, V.A. Safin, *J. Phys. C Solid State Phys.* **19**(21), 4105 (1986). <https://doi.org/10.1088/0022-3719/19/21/014>
11. R. Brueschweiler, R. Ernst, *Chem. Phys. Lett.* **264**(3–4), 393 (1997). [https://doi.org/10.1016/S0009-2614\(96\)01310-3](https://doi.org/10.1016/S0009-2614(96)01310-3). <https://www.sciencedirect.com/science/article/pii/S0009261496013103>
12. J.b. Waugh, *Molecular Physics* **95**(5), 731 (1998). <https://www.scopus.com/inward/record.url?eid=2-s2.0-0008364325&partnerID=40&md5=7393e4b77d026f0d699195694e42b812>
13. E.B. Fel'dman, R. Bruschweiler, R. Ernst, *Chem. Phys. Lett.* **294**, 297 (1998). [https://doi.org/10.1016/S0009-2614\(98\)00887-2](https://doi.org/10.1016/S0009-2614(98)00887-2)
14. D. Sakellariou, P. Hodgkinson, L. Emsley, *Chem. Phys. Lett.* **293**(1–2), 110 (1998). [https://doi.org/10.1016/S0009-2614\(98\)00725-8](https://doi.org/10.1016/S0009-2614(98)00725-8)
15. D. Sakellariou, P. Hodgkinson, S. Hediger, L. Emsley, *Chem. Phys. Lett.* **308**(5–6), 381 (1999). [https://doi.org/10.1016/S0009-2614\(99\)00648-X](https://doi.org/10.1016/S0009-2614(99)00648-X)
16. A.K. Khitrin, B.M. Fung, *J. Chem. Phys.* **111**, 7480 (1999). <https://doi.org/10.1063/1.480072>
17. H. Pastawski, P. Levstein, G. Usaj, J. Raya, J. Hirschinger, *Physica A* **283**(1–2), 166 (2000). <https://www.sciencedirect.com/science/article/pii/S0378437100001461>
18. M. Munowitz, A. Pines, *Principles and Application of Multiple-Quantum NMR*, *Adv. Chem. Phys.*, vol. 66 (Wiley, 1987)
19. C.P. Slichter, *Principles of Magnetic Resonance*, 3rd edn. (Springer, 1996)
20. A. Abragam, M. Goldman, *Nuclear Magnetism : Order and Disorder* (Clarendon Press, Oxford, 1982)

21. H.J. Cho, T.D. Ladd, J. Baugh, D.G. Cory, C. Ramanathan, *Phys. Rev. B* **72**(5), 054427 (2005). <https://doi.org/10.1103/PhysRevB.72.054427>
22. M.H. Levitt, *Prog. Nucl. Mag. Res. Spect.* **18**(2), 61 (1986). [https://doi.org/10.1016/0079-6565\(86\)80005-X](https://doi.org/10.1016/0079-6565(86)80005-X)
23. E.M. Fortunato, M.A. Pravia, N. Boulant, G. Teklemariam, T.F. Havel, D.G. Cory, *J. Chem. Phys.* **116**, 7599 (2002). <https://doi.org/10.1063/1.1465412>
24. M.A. Pravia, N. Boulant, J. Emerson, A. Farid, E.M. Fortunato, T.F. Havel, R. Martinez, D.G. Cory, *J. Chem. Phys.* **119**, 9993 (2003). <https://doi.org/10.1063/1.1619132>
25. N. Khaneja, T. Reiss, C. Kehlet, T. Schulte-Herbuggen, S. Glaser, *J. Mag. Res.* **172**, 296 (2005). <https://doi.org/10.1016/j.jmr.2004.11.004>
26. H.G. Krojanski, D. Suter, *Phys. Rev. Lett.* **93**(9), 090501 (2004). <https://doi.org/10.1103/PhysRevLett.93.090501>
27. H. Cho, P. Cappellaro, C. Ramanathan, D.G. Cory, in *47 Experimental Nuclear Magnetic Resonance Conference* (2006)
28. W. Zhang, D.G. Cory, *Phys. Rev. Lett.* **80**, 1324 (1998). <https://doi.org/10.1103/PhysRevLett.80.1324>
29. G.S. Boutis, D. Greenbaum, H. Cho, D.G. Cory, C. Ramanathan, *Phys. Rev. Lett.* **92**(13), 137201 (2004). <https://doi.org/10.1103/PhysRevLett.92.137201>
30. H. Cho, D.G. Cory, C. Ramanathan, *J. Chem. Phys.* **118**(8), 3686 (2003). <https://doi.org/10.1063/1.1538244>
31. V.A. Skrebnev, R.N. Zaripov, *Appl. Magn. Reson.* **16**(1), 1 (1999). <https://doi.org/10.1007/BF03161910>
32. T.D. Ladd, D. Maryenko, Y. Yamamoto, E. Abe, K.M. Itoh, *Phys. Rev. B* **71**, 014401 (2005). <https://doi.org/10.1103/PhysRevB.71.014401>
33. D. Li, A.E. Dementyev, Y. Dong, R.G. Ramos, S.E. Barrett, *Phys. Rev. Lett.* **98**, 190401 (2007). <https://doi.org/10.1103/PhysRevLett.98.190401>
34. J. Rovny, R.L. Blum, S.E. Barrett, *Phys. Rev. Lett.* **120**, 180603 (2018). <https://doi.org/10.1103/PhysRevLett.120.180603>
35. P. Cappellaro, C. Ramanathan, D.G. Cory, *Phys. Rev. A* **76**(3), 032317 (2007). <https://doi.org/10.1103/PhysRevA.76.032317>
36. W. Zhang, P. Cappellaro, N. Antler, B. Pepper, D.G. Cory, V.V. Dobrovitski, C. Ramanathan, L. Viola, *Phys. Rev. A* **80**(5), 052323 (2009). <https://doi.org/10.1103/PhysRevA.80.052323>
37. E. Ruffeil-Fiori, C.M. Sánchez, F.Y. Oliva, H.M. Pastawski, P.R. Levstein, *Phys. Rev. A* **79**(3), 032324 (2009). <https://doi.org/10.1103/PhysRevA.79.032324>
38. C. Ramanathan, P. Cappellaro, L. Viola, D.G. Cory, *New J. Phys.* **13**(10), 103015 (2011). <https://doi.org/10.1088/1367-2630/13/10/103015>
39. G. Kaur, P. Cappellaro, *New J. Phys.* **14**(8), 083005 (2012). <https://doi.org/10.1088/1367-2630/14/8/083005>
40. G. Kaur, A. Ajoy, P. Cappellaro, *New J. Phys.* **15**, 093035 (2013). <https://doi.org/10.1088/1367-2630/15/9/093035>
41. P. Cappellaro, in *Quantum State Transfer and Network Engineering*, ed. by G.M. Nikolopoulos, I. Jex, Quantum Science and Technology (Springer, Berlin, Heidelberg, 2014), pp. 183–222. https://doi.org/10.1007/978-3-642-39937-4_6
42. S. Oishi, T. Kamiya, *Nippon Kagaku Kaishi* **9**, 800 (1994)
43. K. Teshima, S. Lee, K. Yubuta, Y. Kamenno, T. Suzuki, T. Shishido, M. Endo, S. Oishi, *Cryst. Growth Des.* **9**(9), 3832 (2009). <https://doi.org/10.1021/cg900418w>
44. K. Teshima, S. Lee, T. Ishizaki, S. Mori, C. Mori, K. Yubuta, T. Ichiki, T. Shishido, S. Oishi, *Cryst. Eng. Comm.* **13**(6), 1749 (2011). <https://doi.org/10.1039/C0CE00405G>
45. J. Yanagisawa, K. Rendon-Angeles, N. Ishizawa, S. Oishi, *American Mineralogist* **84**(11-12), 1861 (1999). <https://www.scopus.com/inward/record.url?eid=2-s2.0-0033398106&partnerID=40&md5=2f7556d3107c08456acb5898741903c5>
46. J.C. Rendon-Angeles, K. Yanagisawa, N. Ishizawa, S. Oishi, *J. Solid State Chem.* **151**(1), 65 (2000). <https://doi.org/10.1006/jssc.1999.8623>

47. J.C. Rendon-Angeles, K. Yanagisawa, N. Ishizawa, S. Oishi, *Chem. Mater.* **12**(8), 2143 (2000). <https://doi.org/10.1021/cm990797x>
48. C. Negrevergne, T.S. Mahesh, C.A. Ryan, M. Ditty, F. Cyr-Racine, W. Power, N. Boulant, T. Havel, D.G. Cory, R. Laflamme, *Phys. Rev. Lett.* **96**(17), 170501 (2006). <https://doi.org/10.1103/PhysRevLett.96.170501>
49. S. Pal, N. Nishad, T.S. Mahesh, G.J. Sreejith, *Phys. Rev. Lett.* **120**, 180602 (2018). <https://doi.org/10.1103/PhysRevLett.120.180602>
50. M. Niknam, L.F. Santos, D.G. Cory, *Phys. Rev. Lett.* **127**, 080401 (2021). <https://doi.org/10.1103/PhysRevLett.127.080401>
51. P. Mansfield, D. Ware, *Phys. Rev.* **168**, 318 (1968). <https://doi.org/10.1103/PhysRev.168.318>
52. J. Waugh, L. Huber, U. Haeberlen, *Phys. Rev. Lett.* **20**, 180 (1968). <https://doi.org/10.1103/PhysRevLett.20.180>
53. U. Haeberlen, J. Waugh, *Phys. Rev.* **175**(2), 453 (1968). <https://doi.org/10.1103/PhysRev.175.453>
54. U. Haeberlen, *High Resolution NMR in Solids: Selective Averaging* (Academic Press, New York, 1976)
55. S. Ebadi, T.T. Wang, H. Levine, A. Keesling, G. Semeghini, A. Omran, D. Bluvstein, R. Samajdar, H. Pichler, W.W. Ho, S. Choi, S. Sachdev, M. Greiner, V. Vuletić, M.D. Lukin, *Nature* **595**(7866), 227 (2021). <https://doi.org/10.1038/s41586-021-03582-4>
56. M.E. Rose, *Elementary Theory of Angular Momentum* (Wiley, New York, 1957)
57. C. Ramanathan, H. Cho, P. Cappellaro, G.S. Boutis, D.G. Cory, *Chem. Phys. Lett.* **369**, 311 (2003). [https://doi.org/10.1016/S0009-2614\(02\)02020-1](https://doi.org/10.1016/S0009-2614(02)02020-1)
58. J.H. Van Vleck, *Phys. Rev.* **33**, 467 (1929). <https://doi.org/10.1103/PhysRev.33.467>
59. M. Leskes, P.K. Madhu, S. Vega, *Prog. Nucl. Magn. Reson. Spectrosc.* **57**(4), 345 (2010). <https://doi.org/10.1016/j.pnmrs.2010.06.002>
60. S. Blanes, F. Casas, J. Oteo, J. Ros, *Physics Reports* **470**(5–6), 151 (2009). <https://doi.org/10.1016/j.physrep.2008.11.001>
61. F. Casas, J.A. Oteo, J. Ros, *J. Phys. A Math. Gen.* **34**(16), 3379 (2001). <https://doi.org/10.1088/0305-4470/34/16/305>
62. A. Lazarides, A. Das, R. Moessner, *Phys. Rev. E* **90**, 012110 (2014). <https://doi.org/10.1103/PhysRevE.90.012110>
63. D. Suter, G.A. Álvarez, *Rev. Mod. Phys.* **88**, 041001 (2016). <https://doi.org/10.1103/RevModPhys.88.041001>
64. H.Y. Carr, E.M. Purcell, *Phys. Rev.* **94**(3), 630 (1954). <https://doi.org/10.1103/PhysRev.94.630>
65. S. Meiboom, D. Gill, *Rev. Sc. Instr.* **29**(8), 688 (1958). <https://doi.org/10.1063/1.1716296>
66. A.A. Maudsley, *J. Magn. Reson.* (1969) **69**(3), 488 (1986). [https://doi.org/10.1016/0022-2364\(86\)90160-5](https://doi.org/10.1016/0022-2364(86)90160-5)
67. T. Gullion, D.B. Baker, M.S. Conradi, *J. Mag. Res.* **89**(3), 479 (1990). [https://doi.org/10.1016/0022-2364\(90\)90331-3](https://doi.org/10.1016/0022-2364(90)90331-3)
68. G.S. Uhrig, *Phys. Rev. Lett.* **98**(10), 100504 (2007). <https://doi.org/10.1103/PhysRevLett.98.100504>
69. A.M. Souza, G.A. Álvarez, D. Suter, *Phys. Rev. Lett.* **106**, 240501 (2011). <https://doi.org/10.1103/PhysRevLett.106.240501>
70. J.G. Powles, P. Mansfield, *Physics Letters* **2**, 58 (1962). [https://doi.org/10.1016/0031-9163\(62\)90147-6](https://doi.org/10.1016/0031-9163(62)90147-6)
71. D.G. Cory, J.B. Miller, A.N. Garroway, *J. Mag. Res.* **90**, 205 (1990). [https://doi.org/10.1016/0022-2364\(90\)90380-R](https://doi.org/10.1016/0022-2364(90)90380-R)
72. E.R. Andrew, A. Bradbury, R.G. Eades, *Nature* **182**(4650), 1659 (1958). <https://doi.org/10.1038/1821659a0>
73. I.J. Lowe, *Phys. Rev. Lett.* **2**, 285 (1959). <https://doi.org/10.1103/PhysRevLett.2.285>
74. M. Lee, W.I. Goldburg, *Phys. Rev.* **140**, A1261 (1965). <https://doi.org/10.1103/PhysRev.140.A1261>

75. A. Lesage, D. Sakellariou, S. Hediger, B. Eleena, P. Charmont, S. Steuernagel, L. Emsleya, J. Magn. Reson. **163**, 105 (2003)
76. M. Munowitz, A. Pines, *Principle and Applications of Multiple-Quantum NMR, Advances in Chemical Physics* (Wiley, 1975). <https://onlinelibrary.wiley.com/doi/10.1002/9780470142929.ch1/summary>
77. D. Suter, S. Liu, J. Baum, A. Pines, Chem. Phys. **114**(1), 103 (1987). [https://doi.org/10.1016/0301-0104\(87\)80023-X](https://doi.org/10.1016/0301-0104(87)80023-X)
78. R. Tycko, J. Mag. Res. **139**(2), 302 (1999). <https://doi.org/10.1006/jmre.1999.1776>
79. Y.S. Yen, A. Pines, J. Chem. Phys. **78**(6), 3579 (1983). <https://doi.org/10.1063/1.445185>
80. W.S. Warren, S. Sinton, D.P. Weitekamp, A. Pines, Phys. Rev. Lett. **43**, 1791 (1979). <https://doi.org/10.1103/PhysRevLett.43.1791>
81. C.M. Sánchez, A.K. Chattah, K.X. Wei, L. Buljubasich, P. Cappellaro, H.M. Pastawski, Phys. Rev. Lett. **124**, 030601 (2020). <https://doi.org/10.1103/PhysRevLett.124.030601>
82. K.X. Wei, C. Ramanathan, P. Cappellaro, Phys. Rev. Lett. **120**, 070501 (2018). <https://doi.org/10.1103/PhysRevLett.120.070501>
83. P. Peng, C. Yin, X. Huang, C. Ramanathan, P. Cappellaro, Nat. Phys., s41567 (2021). <https://doi.org/10.1038/s41567-020-01120-z>
84. M.F. O’Keeffe, L. Horesh, J.F. Barry, D.A. Braje, I.L. Chuang, New J. Phys. **21**(2), 023015 (2019). <https://doi.org/10.1088/1367-2630/ab00be>
85. P. Peng, X. Huang, C. Yin, L. Joseph, C. Ramanathan, P. Cappellaro, arXiv:2102.13161 (2021). <https://arxiv.org/abs/2102.13161>
86. J. Choi, H. Zhou, H.S. Knowles, R. Landig, S. Choi, M.D. Lukin, Phys. Rev. X **10**, 031002 (2020). <https://doi.org/10.1103/PhysRevX.10.031002>
87. G. Bodenhausen, H. Kogler, R. Ernst, J. Mag. Res. **58**(3), 370 (1984). [https://doi.org/10.1016/0022-2364\(84\)90142-2](https://doi.org/10.1016/0022-2364(84)90142-2)
88. E. Knill, I. Chuang, R. Laflamme, Phys. Rev. A **57**(5), 3348 (1998). <https://doi.org/10.1103/PhysRevA.57.3348>
89. J. Jeener, P. Broekaert, Phys. Rev. **157**, 232 (1967). <https://doi.org/10.1103/PhysRev.157.232>
90. A.G. Anderson, S.R. Hartmann, Phys. Rev. **128**, 2023 (1962). <https://doi.org/10.1103/PhysRev.128.2023>
91. F.M. Lurie, C.P. Slichter, Phys. Rev. **133**, A1108 (1964). <https://doi.org/10.1103/PhysRev.133.A1108>
92. J.M. Deutsch, Phys. Rev. A **43**, 2046 (1991). <https://doi.org/10.1103/PhysRevA.43.2046>
93. M. Rigol, V. Dunjko, M. Olshanii, Nature **452**(7189), 854 (2008). <https://doi.org/10.1038/nature06838>
94. P. Cappellaro, Quantum information processing in multi-spin systems. PhD dissertation, Massachusetts Institute of Technology, Department of Nuclear Science and Engineering (2006). <https://hdl.handle.net/1721.1/41282>
95. T. Gorin, T. Prosen, T.H. Seligman, M. Žnidarič, Physics Reports **435**(2), 33 (2006). <https://doi.org/10.1016/j.physrep.2006.09.003>
96. B. Swingle, G. Bentsen, M. Schleier-Smith, P. Hayden, Phys. Rev. A **94**, 040302 (2016). <https://doi.org/10.1103/PhysRevA.94.040302>
97. P.R. Levstein, G. Usaj, H.M. Pastawski, J. Chem. Phys. **108**(7), 2718 (1998). <https://doi.org/10.1063/1.475664>
98. J. Baum, A. Pines, J. Am. Chem. Soc. **108**, 7447 (1986)
99. M. Munowitz, A. Pines, M. Mehring, J. Chem. Phys. **86**(6), 3172 (1987). <https://doi.org/10.1063/1.452028>
100. G.A. Álvarez, D. Suter, R. Kaiser, Science **349**(6250), 846 (2015). <https://doi.org/10.1126/science.1261160>
101. A.K. Khitrin, Chem. Phys. Lett. **274**, 217 (1997)
102. M. Garttner, J.G. Bohnet, A. Safavi-Naini, M.L. Wall, J.J. Bollinger, A.M. Rey, Nat. Phys. **13**(8), 781 (2017). <https://doi.org/10.1038/nphys4119>
103. M. Niknam, L.F. Santos, D.G. Cory, Phys. Rev. Res. **2**, 013200 (2020). <https://doi.org/10.1103/PhysRevResearch.2.013200>

104. R. Islam, R. Ma, P.M. Preiss, M. Eric Tai, A. Lukin, M. Rispoli, M. Greiner, *Nature* **528**(7580), 77 (2015). <https://doi.org/10.1038/nature15750>
105. A.M. Kaufman, M.E. Tai, A. Lukin, M. Rispoli, R. Schittko, P.M. Preiss, M. Greiner, *Science* **353**, 794 (2016). <https://doi.org/10.1126/science.aaf6725>
106. B. Tiff, E. Andreas, J. Petar, V. Benoît, M. Christine, P. Lanyon Ben, Z. Peter, B. Rainer, F. Roos Christian, *Science* **364**(6437), 260 (2019). <https://doi.org/10.1126/science.aau4963>
107. J. Li, R. Fan, H. Wang, B. Ye, B. Zeng, H. Zhai, X. Peng, J. Du, *Phys. Rev. X* **7**(3), 031011 (2017). <https://doi.org/10.1103/PhysRevX.7.031011>
108. R. Fan, P. Zhang, H. Shen, H. Zhai, *Science Bulletin* **62**(10), 707 (2017). <https://doi.org/10.1016/j.scib.2017.04.011>
109. L.F. Santos, F. Borgonovi, F.M. Izrailev, *Phys. Rev. E* **85**, 036209 (2012). <https://doi.org/10.1103/PhysRevE.85.036209>
110. E.B. Fel'dman, S. Lacelle, *J. Chem. Phys.* **107**(18), 7067 (1997). <https://doi.org/10.1063/1.474949>
111. S. Doronin, I. Maksimov, E. Fel'dman, *JETP* **91**, 597 (2000). <https://doi.org/10.1134/1.1320096>
112. P. Cappellaro, C. Ramanathan, D.G. Cory, *Phys. Rev. Lett.* **99**(25), 250506 (2007). <https://doi.org/10.1103/PhysRevLett.99.250506>
113. S. Bose, *Phys. Rev. Lett.* **91**(20), 207901 (2003). <https://doi.org/10.1103/PhysRevLett.91.207901>
114. M. Christandl, N. Datta, A. Ekert, A.J. Landahl, *Phys. Rev. Lett.* **92**, 187902 (2004). <https://doi.org/10.1103/PhysRevLett.92.187902>
115. M. Christandl, N. Datta, T.C. Dorlas, A. Ekert, A. Kay, A.J. Landahl, *Phys. Rev. A* **71**(3), 032312 (2005). <https://doi.org/10.1103/PhysRevA.71.032312>
116. J. Zhang, X. Peng, D. Suter, *Phys. Rev. A* **73**, 062325 (2006). <https://doi.org/10.1103/PhysRevA.73.062325>
117. K.X. Wei, P. Peng, O. Shtanko, I. Marvian, S. Lloyd, C. Ramanathan, P. Cappellaro, *Phys. Rev. Lett.* **123**(9), 090605 (2019). <https://doi.org/10.1103/PhysRevLett.123.090605>
118. D.A. Abanin, W. De Roeck, W.W. Ho, F. Huveneers, *Phys. Rev. B* **95**, 014112 (2017). <https://doi.org/10.1103/PhysRevB.95.014112>
119. D.A. Abanin, W. De Roeck, F. Huveneers, *Phys. Rev. Lett.* **115**, 256803 (2015). <https://doi.org/10.1103/PhysRevLett.115.256803>
120. T. Kuwahara, T. Mori, K. Saito, *Ann. Phys.* **367**, 96 (2016). <https://doi.org/10.1016/j.aop.2016.01.012>
121. D. Abanin, W. De Roeck, W.W. Ho, F. Huveneers, *Commun. Math. Phys.* **354**, 809 (2017). <https://doi.org/10.1007/s00220-017-2930-x>
122. A. Kyprianidis, F. Machado, W. Morong, P. Becker, S. Collins K., V. Else D., L. Feng, W. Hess P., C. Nayak, G. Pagano, Y. Yao N., C. Monroe, *Science* **372**(6547), 1192 (2021). <https://doi.org/10.1126/science.abg8102>
123. W. Beatrez, O. Janes, A. Akkiraju, A. Pillai, A. Oddo, P. Reshetikhin, E. Druga, M. McAllister, M. Elo, B. Gilbert, D. Suter, A. Ajoy, *Phys. Rev. Lett.* **127**, 170603 (2021). <https://doi.org/10.1103/PhysRevLett.127.170603>

Quantum-Dot Spin Chains



John M. Nichol

Abstract Semiconductor quantum dots are a promising platform for quantum simulation and computing. This chapter will review the fundamentals of semiconductor quantum dots and the Heisenberg exchange coupling that occurs between neighboring quantum dots. Despite directly coupling only nearest-neighbor quantum dots, exchange coupling underlies a great many approaches for quantum information processing, quantum state transfer, and the simulation of spin chain dynamics. This chapter will review recent progress and future work along these directions.

1 Introduction

Semiconductor quantum dots are three-dimensional confining potentials for electrons. They enable trapping, manipulating, and measuring the charge and spin states of single electrons in semiconductors. As a result of these capabilities, semiconductor quantum dots are a leading platform for quantum computing and simulation. A unique feature of electrons in semiconductor quantum dots is Heisenberg exchange coupling between neighboring electrons, which results from the interplay of the Pauli exclusion principle, the electrostatic confinement potential, the Coulomb interaction between electrons, and the external magnetic field. The possibility of

This work was sponsored by the Defense Advanced Research Projects Agency under grant D18AC00025; the Army Research Office under grants W911NF-17-1-0260 and W911NF-19-1-0167; the National Science Foundation under grants DMR-1809343, DMR 2003287, and OMA 1936250; and the Office of Naval Research under grant N00014-20-1-2424. The views and conclusions contained in this document are those of the authors and should not be interpreted as representing the official policies, either expressed or implied, of the Army Research Office or the U.S. Government. The U.S. Government is authorized to reproduce and distribute reprints for government purposes notwithstanding any copyright notation herein.

J. M. Nichol (✉)

Department of Physics and Astronomy, University of Rochester, Rochester, NY, USA
e-mail: john.nichol@rochester.edu

exchange coupling between electrons together with the capabilities of single-charge and single-spin control and readout means that semiconductor quantum dots offer a natural environment in which to explore both tunnel-coupled and exchange-coupled spin chains. Indeed, significant progress has been made in recent years in simulating and exploring different aspects of the Hubbard and Heisenberg models in quantum-dot spin chains, finally bringing to fruition several decades of previous theoretical work.

This chapter will describe recent progress in this field. We begin with an overview of gate-defined semiconductor quantum dots and how they work. We then describe the origins of exchange coupling in quantum-dot spin chains and some of the many uses of exchange coupling in quantum computing with semiconductor spin qubits. Then, we discuss recent advances in the experimental realization and exploration of quantum-dot spin chains, including simulation of the Hubbard model and the Heisenberg model. A recurring theme in this chapter is that technological advances driven primarily by potential applications in quantum computing have also created new opportunities in quantum simulation. In turn, advances in quantum simulation have also enabled new capabilities for quantum computing. A notable example is that the studies of Hubbard and Heisenberg physics in quantum-dot spin chains have enabled advances in methods for quantum state transfer in spin chains, which are beneficial for quantum computing.

The experimental and theoretical development of quantum-dot spin chains has remained an active area of research for several decades at institutions around the world. The interested reader is encouraged to consult the references herein for further information. Portions of this chapter are reprinted from Kandel et al., *App. Phys. Lett.*, 119, 030501 (2021) with the permission of AIP Publishing.

2 Gate-Defined Quantum Dots

Although different experimental platforms exist that feature exchange coupling [2, 3], and although different types of quantum dots exist, this chapter focuses on gate-defined quantum dots in semiconductors [4–8], one of the most promising systems for the creation and exploration of spin chains. In this section, we will discuss the basic operation of quantum dots, how tunneling and exchange coupling can occur in quantum dots, and experimental demonstrations of exchange.

2.1 *Quantum-Dot Fabrication*

Gate-defined quantum dots are usually created using a layered semiconductor heterostructure, such as GaAs/AlGaAs, Si/SiGe, Si/SiO₂, or Ge/SiGe [4–10]. Such heterostructures are often grown by advanced material growth techniques, like molecular beam epitaxy or chemical vapor deposition. A common feature of all

of these material platforms is that they enable the creation and control of two-dimensional electron or hole systems, called two-dimensional electron (or hole) gasses. In GaAs/AlGaAs and Si/SiO₂ systems, electrons are confined to the interface between two materials, while in Si/SiGe or Ge/SiGe quantum wells, the electrons or holes are confined within a thin semiconductor layer, called a “quantum well.” In all cases, the confinement is enabled by the band gap mismatch between the various materials involved, and the two-dimensional electron or hole system typically resides within tens of nanometers of the semiconductor surface. Lithographically defined metal wires, or “gates,” are typically fabricated on top of the heterostructure. Voltages applied to these gates generate electrostatic potentials that fully confine the electrons. The magnitude and sign of the voltages depend on the details of the heterostructure and device design. For example, GaAs/AlGaAs heterostructures usually feature a layer of Si dopants in the heterostructure to create a nonzero density of electrons in the two-dimensional electron gas without any applied voltages to the gates. Therefore, to create electrostatic confinement, negative voltages are applied to the gates to “deplete” various regions of the two-dimensional electron gas. Heterostructures based on Si are typically undoped, and positive voltages must generally be applied to the gates to “accumulate” electrons. In addition to the dots themselves, the gates can also define electronic reservoirs, from which the dots are loaded or unloaded, and tunnel barriers between dots or between dots and reservoirs. Figure 1 illustrates typical quantum-dot designs.

The growth, characterization, and optimization of two-dimensional electron or hole systems are the focus of significant research worldwide. The development of high-quality Si/SiO₂ transistors underlies the modern microelectronics industry. Si/SiGe and Ge/SiGe quantum wells are also the focus of significant development for transistor applications, and GaAs/AlGaAs heterostructures find significant use in optical and solar applications. The development of quantum-dot spin qubits and related systems has thus benefited tremendously from advances in the fabrication of semiconductor devices.

Early gate-defined quantum dots were fabricated in GaAs/AlGaAs heterostructures [4–8]. This material features extremely high electron mobilities and correspondingly long mean free paths. (Gate-defined quantum dots cannot usually be formed in materials with low mobilities, because the associated strong disorder typically means that electrons will localize around defect sites instead of the desired electrostatic potential.) However, all nuclear isotopes of Ga and As have nuclear spin $I = 3/2$. These nuclear spins generate an effective magnetic field experienced by electrons in the quantum dots through the hyperfine interaction [11]. On the one hand, hyperfine fields generally increase dephasing rates and decrease coherence times of electrons [11]. On the other hand, nuclear spins can create a convenient source of magnetic disorder [12], which is potentially useful for quantum simulation, as discussed further below.

Si/SiGe and Ge/SiGe quantum wells and Si/SiO₂ systems partly solve the challenge of hyperfine fields because both Si and Ge can be isotopically purified to select isotopes with zero nuclear spin [9]. However, Si two-dimensional electron systems generally feature larger conduction band effective masses than carriers in

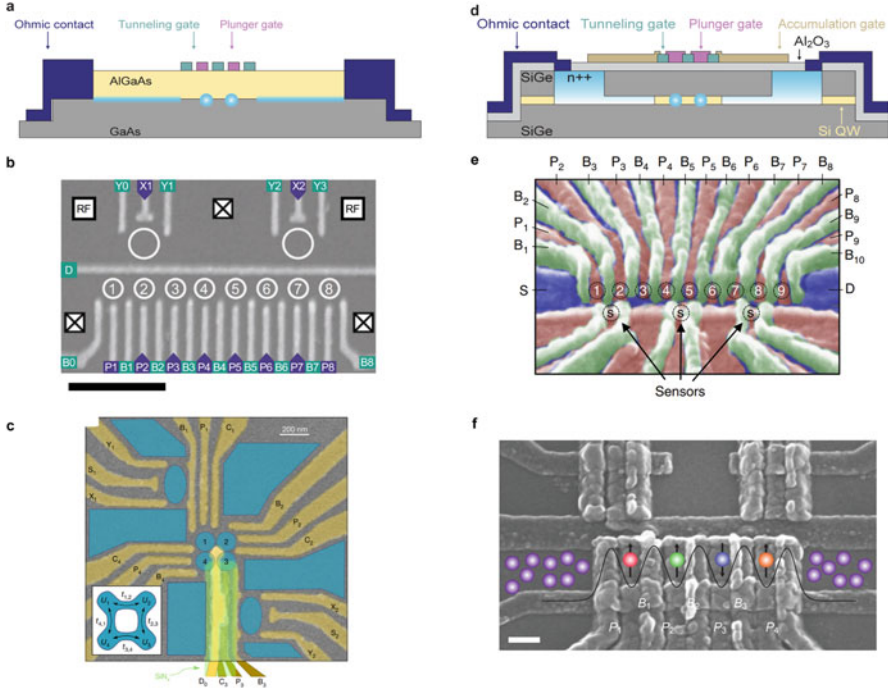


Fig. 1 Quantum-dot spin chains. (a) Schematic of a typical depletion-mode quantum-dot device in GaAs. Electrons from metal Ohmic contacts populate the two-dimensional electron gas (light blue) and are confined with tunneling and plunger gates. (b) Eight-quantum-dot linear array in GaAs, Volk et al., Nat. Comm., 5, 29 (2019). Copyright the Authors, licensed under a Creative Commons Attribution (CC BY) license. (c) Four-quantum-dot square array in GaAs/AlGaAs. Reprinted with permission from Deholain et al., Nature, 579, 528–533 (2020). Copyright Springer Nature (2020). (d) Schematic of a typical overlapping-gate device in Si/SiGe. Here, positive voltages applied to accumulation gates define the electronic reservoirs. (e) Nine-dot linear array in Si/SiGe. Mills et al., Nat. Comm., 10, 1063 (2019). Copyright the Authors, licensed under a Creative Commons Attribution (CC BY) license. (f) Four-dot linear array with the overlapping gate architecture in GaAs/AlGaAs. Reprinted from Kandel et al., App. Phys. Lett., 119, 030501 (2021) with the permission of AIP Publishing. In all panels, circles denote the locations of the electrons

GaAs/AlGaAs. Because orbital energy splittings generally scale inversely with the effective mass of the carriers, typical quantum dots in Si must be smaller than GaAs dots to compensate for the increased effective mass. An additional complication results from the fact that Si is an indirect gap semiconductor, and there are multiple equivalent valleys in the conduction band near the edges of the Brillouin zone [9]. Thus, electrons in Si quantum dots have an additional valley degree of freedom that must typically be accounted for. Germanium quantum wells, which support two-dimensional hole systems can potentially overcome these two obstacles, with relatively small effective masses and a valence band maximum at the center of the Brillouin zone, eliminating the valley degeneracy of Si systems [10]. In the

following, we will primarily discuss quantum-dot spin chains in the context of electrons in GaAs- and Si-based systems, because most of the advances have occurred in these material platforms. The exploration of spin chains in Ge/SiGe systems is an exciting prospect for future work.

2.2 *Quantum-Dot Operation*

Individual quantum dots are typically operated at cryogenic temperatures, where the thermal energy of the environment is much less than the charging energy (the energy to overcome the Coulomb repulsion and add another electron to the dot) and the orbital energy spacings of the quantum dots. In such a regime, quantum dots are frequently connected via tunnel barriers to source and drain reservoirs, which are held at fixed potential via galvanic contacts to external voltage sources. The physics of electrons in quantum dots is reviewed in Refs. [4–8], and the interested reader is encouraged to consult these references.

When the electrochemical potential of a quantum-dot state lies between the electrochemical potential of the source and drain reservoirs, current can flow through the quantum dot, as a result of tunneling from the source, through the dot, and into the drain. When the electrochemical potential of the dot is not between those of the source and drain reservoirs, the current flow is blocked, and the dot is the Coulomb blockade regime. By tuning the gate voltages to be less positive or more negative, the number of electrons in the dot reduces, until all electrons are gone, resulting in no further current peaks. Thus, the Coulomb blockade allows one to concretely identify the number of electrons in a quantum dot. The detection of quantum-dot charge states most often relies on a proximal charge sensor, such as a quantum point contact or quantum dot, whose electrical conductance depends sensitively on local electric fields, including those from nearby charged quantum dots [16–19]. Quantum dots may be tunnel coupled, usually in series, between reservoirs [6]. A prototypical example is a double quantum dot, with two dots coupled in series between two reservoirs.

Many studies of individual and few quantum-dot systems have occurred over the last several decades, leading to significant advances in quantum information processing with semiconductor quantum dots [20]. As spin-based quantum information processors scale up, a primary challenge in creating many-qubit systems is the difficulty in “tuning up” devices with many quantum dots. Typically, an experimenter must spend time tuning the gate voltages to achieve the right potential landscape. A major difficulty in achieving the proper potential for many dots simultaneously is the effect of defects in the semiconductor. Indeed, a major effort in the development of quantum dots in recent decades has been to improve the tunability of the potential landscape to overcome this challenge. For example, the first quantum dots used a vertical architecture, in which the parameters of the confinement potential were set by the growth of the heterostructure [21, 22]. To promote better in-situ tunability, early lateral quantum dots featured a “stadium-style” architecture [23], in which

electric fields from nearby metal gates create the confinement potential (Fig. 1a–c). Such an architecture features significantly improved tunability over earlier vertical architectures. Recently, a new generation of quantum dots with an “overlapping-gate” architecture has emerged [24–26] (Fig. 1d–f). In contrast to the stadium-style architecture, the overlapping-gate architecture involves voltages applied to gates directly above the quantum-dot location. These devices feature strong electrostatic confinement and tight control over nearly all of the relevant parameters of the quantum-dot confinement. Additional advances that have enabled the creation of extended spin chains are various procedures for computer automated tuning and independent control of the quantum-dot potential parameters [27–35].

2.3 Exchange Coupling in Quantum Dots

Electrons are fermions. Thus, according to the Pauli exclusion principle, no two electrons can have the same quantum numbers. In nanoscale quantum systems, a direct manifestation of the Pauli exclusion principle is the Heisenberg exchange coupling between two electrons $H = JS_1 \cdot S_2 - 1/4$, where S_1 and S_2 are spin-1/2 operators associated with the spins of the two electrons [36–38].

Although a detailed calculation of the exchange coupling J presents a substantial challenge, the following heuristic picture illuminates the mechanism behind exchange coupling in semiconductor quantum dots. Consider two electrons in a single quantum dot. The overall wavefunction of the two electrons must be antisymmetric under particle exchange. If the two electrons occupy the spin singlet state $|S\rangle = \frac{1}{\sqrt{2}}(|\uparrow\downarrow\rangle - |\downarrow\uparrow\rangle)$, the spin component of the wavefunction is antisymmetric under exchange. Therefore, the orbital part of the wavefunction must be symmetric in order to guarantee that the overall wavefunction is antisymmetric under exchange. In particular, both electrons can occupy the ground state orbital of the quantum dot. Similarly, if the two electrons have any of the triplet states $\{|T_0\rangle = \frac{1}{\sqrt{2}}(|\uparrow\downarrow\rangle + |\downarrow\uparrow\rangle), |T_-\rangle = |\downarrow\downarrow\rangle, |T_+\rangle = |\uparrow\uparrow\rangle\}$, the electrons must have an antisymmetric orbital wavefunction to guarantee the overall antisymmetry of the total wavefunction. In particular, both electrons cannot occupy the ground state orbital of the quantum dot, and the triplet states will have a higher energy than the singlet. The energy splitting between the singlet and triplet states is the exchange coupling energy.

The phrase “Pauli spin blockade” is also used to describe a related phenomenon. Similar to the Coulomb blockade, where the presence of an electron in a quantum dot prevents the addition of further electrons until the Coulomb repulsion is overcome, the Pauli spin blockade describes a scenario in which the presence of a spin in a quantum dot prevents the addition of another spin in a symmetric spin configuration until the exchange energy can be overcome.

It is straightforward to show that the singlets and triplets are eigenstates of the Heisenberg Hamiltonian discussed above, and when $J > 0$, the singlet has a lower energy than the triplets. To understand some of the important physical mechanisms

underlying exchange coupling, let us consider the following Hubbard model for electrons in N quantum dots:

$$H_{Hub} = \sum_{i=1}^N \left[\frac{\tilde{U}}{2} n_i (n_i - 1) + V_i n_i \right] + \sum_{\langle i,j \rangle} U_C n_i n_j + \sum_{\langle i,j \rangle} t \sum_{\sigma=\uparrow\downarrow} (c_{i,\sigma}^\dagger c_{j,\sigma} + \text{h.c.}). \quad (1)$$

Here, $c_{i,\sigma}^\dagger$ is a fermionic operator that creates an electron in dot i with spin σ , and $n_i = \sum_{\sigma} c_{i,\sigma} c_{i,\sigma}^\dagger$ is the number operator for dot i . V_i is the gate-controlled energy of dot i , \tilde{U} is the on-site Coulomb energy, U_C is the nearest-neighbor Coulomb energy, $\langle i, j \rangle$ indicates a sum over nearest neighbors, and t is the hopping energy between dots. It can be shown that when the number of electrons in the system is the same as the number of quantum dots, this Hamiltonian can be transformed to the Heisenberg Hamiltonian in certain parameter regimes [39].

To see how exchange coupling can occur in the Hubbard model, we consider two electrons in a double quantum dot, and we consider the matrix elements of this Hamiltonian in the following basis:

$$|T_0(1, 1)\rangle = \frac{1}{\sqrt{2}}(c_{1,\uparrow}^\dagger c_{2,\downarrow}^\dagger + c_{1,\downarrow}^\dagger c_{2,\uparrow}^\dagger) |0\rangle \quad (2)$$

$$|S(1, 1)\rangle = \frac{1}{\sqrt{2}}(c_{1,\uparrow}^\dagger c_{2,\downarrow}^\dagger - c_{1,\downarrow}^\dagger c_{2,\uparrow}^\dagger) |0\rangle \quad (3)$$

$$|S(2, 0)\rangle = c_{1,\uparrow}^\dagger c_{1,\downarrow}^\dagger |0\rangle \quad (4)$$

$$|S(0, 2)\rangle = c_{2,\uparrow}^\dagger c_{2,\downarrow}^\dagger |0\rangle, \quad (5)$$

where $|0\rangle$ indicates the state with no electrons, and the numbers in parentheses give the numbers of the electrons in both quantum dots. In this basis, the Hubbard Hamiltonian has the following form:

$$H_{Hub} = \begin{pmatrix} 0 & 0 & 0 & 0 \\ 0 & 0 & \sqrt{2}t & \sqrt{2}t \\ 0 & \sqrt{2}t & U + \epsilon' & 0 \\ 0 & \sqrt{2}t & 0 & U - \epsilon' \end{pmatrix}, \quad (6)$$

up to an overall energy shift, and where $U = \bar{U} - U_C$, and $\epsilon' = V_1 - V_2$. Below, we refer to ϵ' as the detuning of the double quantum dot. We set $\epsilon = U + \epsilon'$ [i.e., we set the zero of the detuning to the (1,1)-(2,0) charge transition], and then we diagonalize the subspace spanned by $|S(1, 1)\rangle$ and $|S(2, 0)\rangle$ to give new effective singlet states $|S_-\rangle$ and $|S_+\rangle$. We isolate the subspace spanned by $\{|T_0(1, 1)\rangle, |S_-\rangle,$

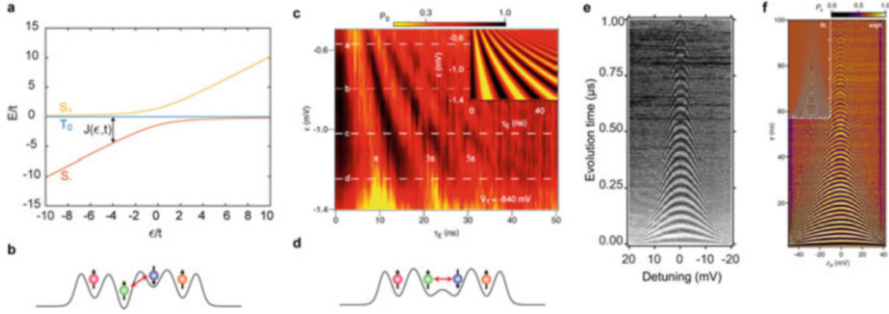


Fig. 2 Exchange coupling in double quantum dots. **(a)** Energies of the effective single-triplet Hamiltonian Eq. (7). The different states and the exchange coupling are labelled. **(b)** Schematic of detuning-controlled exchange oscillations. **(c)** Detuning-controlled exchange oscillations in a GaAs quantum dot. Reprinted from Petta et al., *Physica E*, 35, 2, 251–256 (2006) with the permission of Elsevier. **(d)** Schematic of barrier-controlled exchange oscillations. **(e)** Barrier-controlled exchange oscillations in a Si/SiGe quantum dot. Reed et al., *Phys. Rev. Lett.*, 116, 110402 (2016). Copyright the Authors, licensed under a Creative Commons Attribution (CC BY) license. **(f)** Barrier-controlled exchange oscillations in a GaAs quantum dot. Reprinted with permission from Martins et al., *Phys. Rev. Lett.*, 116, 116801 (2016). Copyright (2016) by the American Physical Society

and $|S_+\rangle$. In this basis, and in the absence of magnetic fields, the effective singlet-triplet Hamiltonian is

$$H_{ST} = \begin{pmatrix} 0 & 0 & 0 \\ 0 & \frac{1}{2} \left(\epsilon - \sqrt{\epsilon^2 + 8t^2} \right) & 0 \\ 0 & 0 & \frac{1}{2} \left(\epsilon + \sqrt{\epsilon^2 + 8t^2} \right) \end{pmatrix}. \quad (7)$$

One can see that $|S_-\rangle$ has a lower energy than the $|T_0\rangle$ state. This difference in energy is the exchange coupling $J(\epsilon, t) = \frac{1}{2} \left(\epsilon - \sqrt{\epsilon^2 + 8t^2} \right)$. The energies of this Hamiltonian are shown in Fig. 2a. More detailed methods of calculating exchange couplings in quantum-dot systems involve using the actual eigenfunctions of the quantum-dot confinement potentials through the Heitler–London and Hund–Mulliken approaches [40] and various configuration interaction techniques [41, 42]. These approaches generally rely on a detailed knowledge of the quantum-dot confinement potential.

The previous discussion shows that the two main tools an experimenter has at their disposal to control exchange couplings include the detuning ϵ and the interdot tunnel coupling t (Fig. 2). Historically, exchange couplings in semiconductor quantum dots were manipulated through detuning control [43] (Fig. 2b,c), in part because experimental manipulation of electron states in quantum dots typically requires rapid control of electrochemical potentials, and detuning-controlled exchange oscillations require no extra experimental overhead. A downside to detuning-controlled

exchange coupling is that this method increases the exposure of the spin system to charge noise, and the quality factor of exchange oscillations induced in this way tends to be on the order of 10 [46].

An alternate method to create exchange coupling, which has gained traction in recent years, is to rapidly modify the tunnel barrier between two quantum dots by pulsing the voltage applied to a barrier gate [44, 45] (Fig. 2d–f). This method, called “barrier-controlled,” or “symmetric” exchange involves fully separating the electrons into the (1,1) charge configuration and then applying a rapid, positive voltage pulse to the barrier gate. This voltage pulse both lowers the potential barrier between the dots and causes the electron wavefunctions to move closer toward each other [42, 47]. Both effects increase the exchange coupling between electrons. Perhaps most importantly, barrier-controlled exchange coupling is first-order insensitive to charge noise associated with the electrochemical potentials of the dots, leading to significantly improved exchange-oscillation quality factors, at least compared with detuning-controlled exchange.

In principle, both barrier- and detuning-controlled exchange are possible to implement in extended systems of quantum dots. A significant challenge in this regard, however, is that the action of voltages applied to barrier gates modifies not only the tunnel barriers and locations of the dots but also their electrochemical potentials. Likewise, the action of a plunger gate will change not only the electrochemical potential of its associated dot but also all of the other parameters of the confinement potential. The development of “virtual gates” has allowed experimenters to overcome this problem and adjust parameters of quantum-dot spin chains independently [13, 15, 28, 32, 48]. This concept involves measuring how voltages applied to all gates affect all the electrochemical potentials in a system of quantum dots. Assuming that the electrochemical potentials vary linearly with the gate voltages, the exact gate voltages required to create an arbitrary change to the electrochemical potentials may be computed. Recent advances exploiting this concept have demonstrated controlled multiple nonzero exchange couplings in extended arrays of quantum dots [47, 49], as well as charge displacement through multiple quantum dots in series [15]. In addition to the notion of virtual gates, various computer-automated and machine learning tuning approaches have undergone rapid progress in recent years and will no doubt provide a key enabling technology for the exploration of quantum-dot spin chains [27, 32, 34].

3 Quantum Information Processing with Exchange-Coupled Quantum-Dot Spins

Spin qubits based on gate-defined quantum dots are an excellent platform for quantum information processing [20]. Individual electrons can possess extremely long coherence times [50, 51], and semiconductor quantum dots are compatible with advanced semiconductor manufacturing techniques [52, 53]. Exchange coupling

underlies a host of different mechanisms for quantum information processing with semiconductor quantum-dot spin qubits. In this section, we review the different ways in which exchange coupling can facilitate quantum information processing with spins in semiconductor quantum dots.

3.1 *Single-Spin Qubits*

Conceptually, the simplest spin qubit consists of a single electron, which can either point up or down with respect to an external magnetic field [59] (Fig. 3a). Single-qubit rotations can be driven by applying a real or effective alternating magnetic field perpendicular to the quantizing field. Individual single-spin qubits can have extremely high gate fidelities, far exceeding 99% [50, 60].

A challenge for single-spin qubits, however, is the implementation of a robust multi-qubit operation. The magnetic dipole–dipole coupling between electrons is weak and not usually strong enough to implement high-fidelity two-qubit operations. However, the exchange coupling between two electrons provides a natural route for a two-qubit gate. Specifically, when two spins i and $i + 1$ evolve under exchange J_i for a time $T = \frac{1}{2J_i}$, the exchange coupling generates a SWAP gate (Fig. 4a). Evolution for $\frac{T}{2}$ produces a $\sqrt{\text{SWAP}}$ gate, which can entangle the two electrons. Together with single-qubit gates, a $\sqrt{\text{SWAP}}$ gate is sufficient for universal quantum computing [59, 61, 62]. These facts illustrate on a basic level the potential of exchange coupling for quantum computing and information transfer and motivated initial proposals for quantum computing architectures based on semiconductor quantum dots [55, 59, 63].

In the presence of magnetic gradients between electrons, exchange coupling can enable other two-qubit gates for single spins, such as controlled-phase (CPHASE) (Fig. 4c) or controlled-not (CNOT) (Fig. 4b) gates [64, 65], both of which are also sufficient for universal quantum computing. In spin chains, magnetic gradients are routinely employed to provide single-spin addressability, making the realization of these gates a natural goal [66–69]. The principles of two-qubit gates based on exchange have been experimentally developed in the past decades [43, 50, 61], culminating recently in the demonstration of a CPHASE gate with fidelity exceeding 99%. Such an achievement is a significant milestone for quantum-dot-based quantum information processing [70] because it corroborates the feasibility of operating spin qubits with gate fidelities above the threshold for quantum error correction [71].

Beyond two-qubit gates, exchange coupling can also enable three-qubit operations, such as a Toffoli gate [72] and entangling operations [47].

3.2 Two-Spin Qubits

Although the basic spin qubit consists of an individual electron spin, the ability to manipulate exchange opens up the possibility to form new qubits out of multiple-spin states, as shown in Fig. 3. The potential advantage of such a qubit is the possibility of electrical spin-state control [55] and the potential to operate qubits in decoherence-free subspaces [73], which feature long-lived coherence even in the presence of environmental noise.

Perhaps the simplest exchange-enabled multi-spin qubit is the singlet–triplet (ST) qubit [43, 54], formed from two electrons in a double quantum dot (Fig. 3b). The ST qubit Hamiltonian is $H_{ST} = J(\epsilon, t)S_z + \Delta B_z S_x$, in the $\{|S\rangle, |T_0\rangle\}$ subspace, where $J(\epsilon, t)$ is the exchange coupling between the two dots, and ΔB_z is the difference

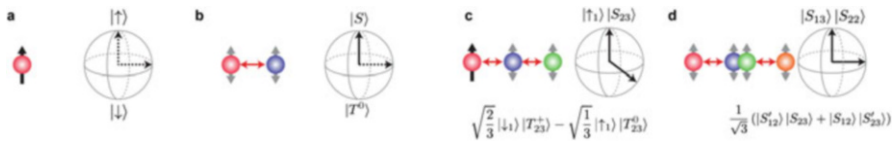


Fig. 3 Comparison between different types of spin qubits. In each panel, the number of spins involved in each qubit is shown. Relevant exchange couplings are highlighted in red, and entangled states are shown with gray arrows. Solid lines on the Bloch sphere indicate exchange-based qubit control axes, and dashed arrows indicate magnetic control axes. (a) Single-spin qubit, requiring two magnetic control axes. (b) Singlet–triplet qubit, requiring one magnetic control axis [43, 54]. (c) Exchange-only qubit with two exchange-based control axes [55]. (d) Exchange-only qubit with four (or more electrons) with two orthogonal exchange-based control axes [56–58]. Primed states involve excited levels, such as orbitals or valley states. Reprinted from Kandel et al., *App. Phys. Lett.*, 119,030501 (2021) with the permission of AIP Publishing

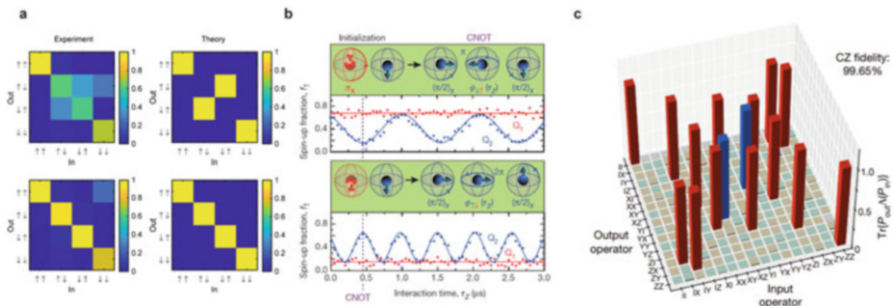


Fig. 4 Exchange coupling in single-spin qubits. (a) Top: truth table of a SWAP gate between single spins in GaAs quantum dots driven by exchange. Bottom: truth table of a 2π exchange rotation, from Ref. [61]. (b) Evidence for a CNOT gate between single spins in Si/SiO₂ quantum dots driven by exchange. Reprinted with permission from Veldhorst et al., *Nature*, 526, 410–414 (2015). Copyright Springer Nature (2015). (c) Gate-set tomography of a CPHASE gate between single spins in a Si/SiGe quantum well driven by exchange. Xue et al., *Nature* 601, 343–347 (2022). Copyright the Authors, licensed under a Creative Commons Attribution (CC BY) license

in longitudinal magnetic field between the dots (Fig. 5a). This system occupies a decoherence-free subspace with respect to global magnetic fields that couple to the spin of the electron, because the energies of the $|S\rangle$ and $|T_0\rangle$ states do not depend on the external magnetic field, in contrast to the energies of single-spin states. In addition, the S_z term in H_{ST} depends on electric fields (both ϵ and t depend on electrostatic potentials), which are often easier to generate than pulsed magnetic fields in cryogenic environments. A final benefit of exchange coupling for ST qubits is the possibility of spin-to-charge conversion via the Pauli spin blockade, which enables fast, high-fidelity electrical measurement of spin states [19]. Singlet–triplet qubits, and variations thereof, have been the subject of significant theoretical and experimental research [43, 74, 75, 77–88].

Exchange coupling also enables significant enhancements in the coherence time in ST qubits through dynamical decoupling. Early experiments demonstrated inhomogeneously broadened coherence times of ΔB_z rotations of around 10 ns, due to the fluctuating hyperfine field in GaAs quantum dots [43]. By using dynamical decoupling sequences, with periodic exchange pulses interspersed during the qubit evolution, the coherence time of an ST qubit can be extended to nearly 1 ms [51, 75] (Fig. 5b,c), 4 orders of magnitude larger than the inhomogeneously broadened coherence time.

Exchange coupling also enables two-qubit gates between ST qubits [89–92]. This operation can be intuitively understood in the following picture. Although the ST qubit eigenstates are commonly expressed as the set $\{|S\rangle, |T^0\rangle\}$, an alternative

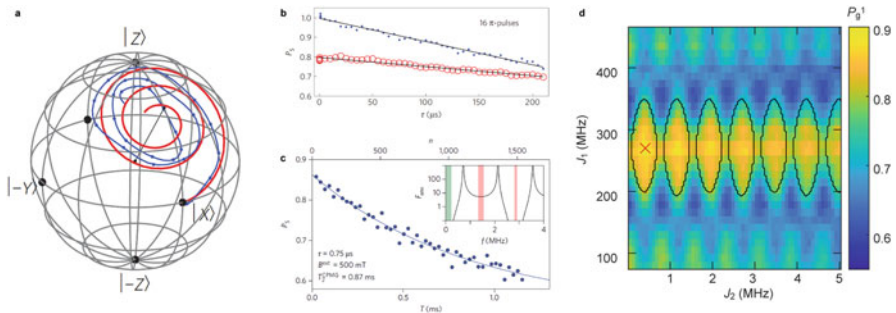


Fig. 5 Exchange coupling in singlet–triplet qubits. **(a)** Exchange coupling, together with controlled magnetic gradients, enables universal quantum control of ST qubits. Reprinted with permission from Foletti et al., *Nature Physics*, 5, 903–908 (2009). Copyright Springer Nature (2009). **(b)** Exchange coupling also enables decoupling ST qubits from hyperfine noise, extending the coherence time to several hundred μ s. Reprinted with permission from Bluhm et al., *Nature Physics*, 7, 109–113 (2011). Copyright Springer Nature (2011). **(c)** Carefully optimized decoupling pulses can further reduce magnetic fluctuations resulting from the Larmor precession of the individual Ga and As nuclei, resulting in coherence times approaching the millisecond range. Reprinted with permission from Malinowski et al., *Nature Nanotechnology*, 12, 16–20 (2017). Copyright Springer Nature (2017). **(d)** Evidence of the effective Ising coupling predicted to emerge between exchange-coupled ST qubits. Qiao et al., *Nat. Comm.*, 12, 2142 (2021). Copyright the Authors, licensed under a Creative Commons Attribution (CC BY) license

basis consists of the set $\{|\uparrow\downarrow\rangle, |\downarrow\uparrow\rangle\}$. Considering a chain of four electrons (two ST qubits) with a nonzero exchange coupling between the second and third electrons, one can see that the state $|\uparrow\downarrow\rangle \otimes |\uparrow\downarrow\rangle$ will have a lower energy than the state $|\uparrow\downarrow\rangle \otimes |\downarrow\uparrow\rangle$, which leads to an effective Ising coupling between ST qubits, though care must be taken to prevent leakage. Recently, evidence of this effective Ising coupling has been observed [76] (Fig. 5d).

3.3 Three-Spin Qubits

Three electrons in a triple quantum dot create an “exchange-only” qubit [55, 93, 95–99] (Figs. 3d, 6). In contrast to ST qubits, which feature one electrical control axis and one magnetic control axis (single-spin qubits require two magnetic control axes), exchange-only qubits enable complete electrical control, and the two control axes correspond to exchange coupling between the two nearest-neighbor pairs of electrons in the triple dot. The eigenstates of a three-electron exchange-only qubit usually consist of spin states with fixed total spin and triplet- or singlet-like states on one of the outer pairs of spins [55, 93, 96]. In addition to conventional exchange-only qubits, resonant exchange qubits [94, 100] (Fig. 6b) and hybrid qubits [101, 102] leverage exchange couplings to enable control of systems with three electrons [39]. Extending this approach, qubits can also be formed with more than three electrons in three or more quantum dots, and exchange couplings provide complete control over the qubit dynamics [56–58] (Fig. 3d). Such “singlet-only” qubits are predicted to be robust against magnetic field noise. Exchange coupling between triple dots in various configurations can also lead to multi-qubit operations, including CNOT gates [55, 103–105] and CPHASE gates [106].

Since the initial demonstrations by Medford et al. [93, 94] in GaAs quantum dots (Fig. 6a,b), the development of exchange-only qubits has steadily continued,

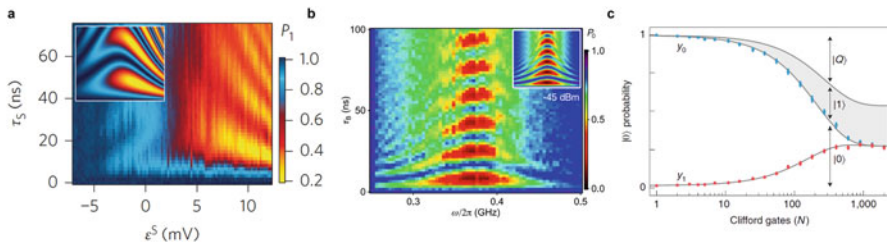


Fig. 6 Exchange coupling in three-electron spin qubits. **(a)** Coherent oscillations in a three-electron exchange only qubit. Reprinted with permission from Medford et al., *Nature Nanotechnology*, 8, 654–659 (2013). Copyright Springer Nature (2013). **(b)** Rabi oscillations of a resonant-exchange qubit. Reprinted with permission from Medford et al., *Phys. Rev. Lett.*, 111, 050501 (2013). Copyright (2013) by the American Physical Society. **(c)** Randomized benchmarking of an exchange-only qubit. Reprinted with permission from Andrews et al., *Nature Nanotechnology*, 14, 747–750 (2019). Copyright Springer Nature (2019)

with a recent demonstration of high-fidelity single-qubit gates through randomized benchmarking [95] (Fig. 6c) and advanced device architectures compatible with scaling up systems of exchange-only qubits [53].

4 Quantum Simulation with Quantum-Dot Spin Chains

In addition to uses for quantum information processing, chains of semiconductor quantum dots have great potential for quantum simulation, which is the experimental realization of Hamiltonians that are difficult or impossible to simulate on classical computers, using quantum systems. For example, the Hubbard model, which we discussed above in Sect. 2.3, is a fundamental model of condensed matter physics, and it is thought to underlie phenomena as important as high-temperature superconductivity [107]. In different experimental platforms, especially cold-atom systems [108], simulating the Hubbard phase diagram remains the focus of intense research. While other platforms, like cold-atom systems have made significant progress in understanding different features of the Hubbard model, semiconductor quantum dots also provide an attractive platform in which to study the Hubbard model [109], because they can access parameter regimes not easily accessible to cold-atom systems, including the ultra-low temperature regime. Quantum-dot systems also provide a natural way to study Hubbard physics in solid-state environments. Since the Hubbard model is predicted to underlie important solid-state phenomena, such as high-temperature superconductivity, the study of such models in condensed matter environments seems especially worthwhile.

In another example, the Heisenberg spin chain is predicted to exhibit a host of interesting phenomena, ranging from quantum magnetism [107] and spin chain dynamics [110] to non-equilibrium physics like many-body localization [111]. Semiconductor quantum dots also provide a natural platform in which to explore this model, given the ease of implementing exchange coupling between neighboring spins, together with the capabilities of single-spin control and readout.

In this section, we review recent efforts to explore different aspects of the Hubbard and Heisenberg models. These exciting results show that this is a promising avenue of research, with more exciting results yet to come in the future.

4.1 Charge Physics in the Hubbard Model

Single and double quantum dots are mainstays of semiconductor spin-qubit technology. The tune-up of double quantum-dot systems into the single-charge regime is a routine occurrence in research laboratories throughout the world and the starting point for many quantum-information processing experiments. In some sense, double-quantum-dot systems serve as small-scale simulations of the Hubbard model. For example, the Hubbard model can be used to provide a phenomenological quantum-mechanical description of charge-stability diagrams [113].

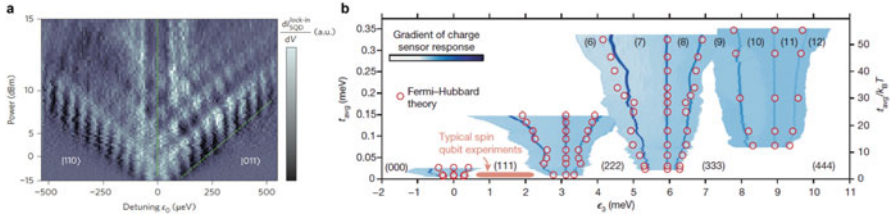


Fig. 7 Quantum simulation of charge physics in the Hubbard model. **(a)** Landau–Zener–Stückelberg interferometry of a single charge tunneling back and forth between distant dots. Reprinted with permission from Braakman et al., *Nature Nanotechnology*, 8, 432–437 (2013). Copyright Springer Nature (2013). **(b)** Transition from collective to conventional Coulomb blockade in a linear array of three dots. Reprinted with permission from Hensgens et al., *Nature*, 528, 70–73 (2017). Copyright Springer Nature (2017)

Going beyond double-dot systems, semiconductor quantum dots provide an appealing platform for the simulation of Hubbard physics involved in systems of more than two sites. Early work in this direction was reported by Singha et al. in Ref. [114]. In a GaAs/AlGaAs heterostructure, the authors created an artificial honeycomb lattice by etching the surface of the heterostructure [115]. The resulting pattern created an attractive, periodic potential for electrons, with about 8 electrons per site in an area of about $10^4 \mu\text{m}^2$. A characteristic prediction of the Hubbard model for this system is that the on-site energy \bar{U} should scale inversely with the square root of the in-plane magnetic field strength [114]. Inelastic light-scattering experiments revealed both the expected conventional cyclotron mode (with a frequency that scales linearly with the magnetic field), in addition to a mode with the predicted sublinear behavior. This low-frequency mode was taken to represent evidence that Hubbard physics in this artificial honeycomb lattice can be engineered and behaves as expected.

Although such large-scale arrays of quantum dots seem attractive for quantum simulation of many-particle systems [109], recent research has focused on building up such systems one site at a time. In 2013, Braakman et al. presented evidence for the coherent tunneling of an electron between the outer dots of a three-dot linear array [112] (Fig. 7a). Such long-distance coupling between quantum dots can be understood as a second-order tunneling effect within the context of the Hubbard model. The coherence of this tunneling effect was verified through Landau–Zener–Stückelberg interferometry of the charge states near the tunneling transition between the outer dots.

Further exploration of charge physics in the Hubbard model was presented by Hensgens et al. in Ref. [28] (Fig. 7b). The authors studied the transition between individual and collective charge transitions in a series of three quantum dots, as the chemical potentials and tunnel barriers between dots varied. In the limit of high barrier potentials between dots, the three dots acquire charges separately, analogous to a Mott insulating solid. However, when the tunnel barriers are lowered, the three separate dots effectively merge to form a large dot, and the large dot acquires charges one at a time [28].

Although such three-site Hubbard experiments can still be simulated on classical computers without much difficulty, the transition from simulating the Hubbard physics of more than two electrons required significant experimental advances that have set the stage for further developments in this direction. Specifically, an important driver of these results was the ability to tune the chemical potentials and barriers in the linear array simultaneously and independently [13, 15, 28, 32, 48]. This involved establishing a set of virtual plunger and barrier gates, together with computer automated tuning of the device [27, 32, 34]. Such an advance marked an important shift in thinking toward the use of computer automated tuning procedures to aid in the operation of large-scale quantum-dot devices. These advances also paved the way for the exploration of spin effects in the Hubbard and Heisenberg models, as we discuss in the next sections.

4.2 Spin Physics in the Hubbard Model

In addition to charge physics, semiconductor quantum-dot arrays also enable exploring different spin effects in the Hubbard model. The advances described in the previous section focusing on tuning large quantum-dot systems have also translated to advances in the simulation of spin physics in the Hubbard model.

Building on the advances presented by Braakman et al. in Ref. [112], which demonstrated coherent coupling between charge states in distant dots, Baart et al. demonstrated coherent spin interactions between distant dots in Ref. [48]. As discussed above, in the presence of tunnel coupling between two quantum dots (in this case, between the outer dots of a linear three-dot array), one generally expects exchange coupling between spins in those dots to occur. Baart et al. observed evidence for this effect, by initializing and measuring a pair of spins in an outer quantum dot using Pauli spin blockade (Fig. 8a). After allowing the electrons to

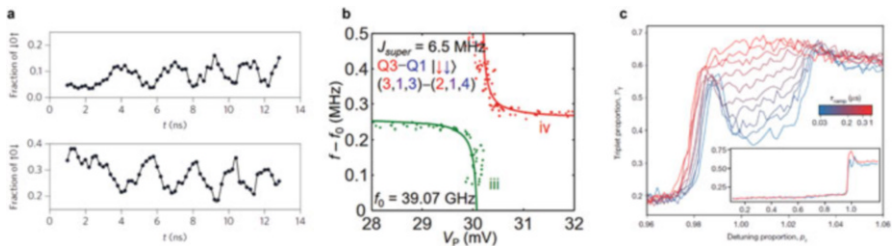


Fig. 8 Quantum simulation of spin physics in the Hubbard model. (a) Superexchange between distant electron spins, mediated by an empty quantum dot. Reprinted with permission from Baart et al., *Nature Nanotechnology*, 12, 26–30 (2017). Copyright Springer Nature (2017). (b) Interactions between distant electrons measured in a Si triple dot. Reprinted with permission from Chan et al., *Nano Letters*, 21, 3, 1517–1522 (2021). Copyright (2021) by the American Chemical Society. (c) Signatures of Nagaoka ferromagnetism in a square array of four dots. Reprinted with permission from Deholain et al., *Nature* 579, 528–533 (2020). Copyright Springer Nature (2020)

evolve when separated, the electrons were recombined and measured via Pauli spin blockade in the same dot. Such an experiment is analogous to experiments demonstrating singlet–triplet exchange oscillations in double quantum dots [43], except that in this case, the electrons were in distant dots.

Similar effects have also been observed in Si triple quantum dots [116] (Fig. 8b), where an effective coupling between electrons in the outer dots of a three-dot array mediated by an occupied quantum dot was observed. By observing how the resonance frequencies of the electron spins in the outer dots changed with detuning, Chan et al. observed an effective nonzero coupling between electrons in the outer two quantum dots.

Collectively, such effects, which create an effective exchange coupling between distant spins, are usually known as superexchange. While many different types of superexchange exist, nearly all rely on virtual excitation of an intermediate entity, such as an empty, singly occupied, or multiply occupied quantum dot. Below, we will discuss superexchange in a spin chain, where an effective coupling between electrons separated by more than one site can be achieved.

A step forward for quantum simulation of spin physics in the Hubbard model in quantum dots occurred with a recent demonstration of Nagaoka ferromagnetism [14]. Working with a 2×2 quantum-dot array [29], Dehollain et al. presented evidence for this phenomenon in Ref. [14]. The theory of Nagaoka [117] provides a prediction for itinerant ferromagnetism in metals for the case of a nearly half-filled band. In the 2×2 quantum-dot array, Dehollain et al. created a nearly half-filled band by filling the array with only three electrons. As in Nagaoka’s original theory, the absence of an electron at one of the locations stabilizes the ground state where all of the spins have the same orientation. Experimentally, the system of three electrons was initialized and readout using the Pauli spin blockade associated with a pair of electrons in one dot and an electron with a random spin in another dot. After separating the two electrons in the singlet state via tunneling, the gate voltages were pulsed to different configurations. After allowing the system of three electrons to evolve for a period of time, the researchers measured the system by projecting two of the electrons onto the singlet/triplet basis with a Pauli spin-blockade measurement. The researchers observed an enhanced triplet return probability in the range of gate voltages predicted to demonstrate the ferromagnetic ground state (Fig. 8c).

4.3 *Spin Physics in the Heisenberg Model*

A special case of the Hubbard model occurs when each site or quantum dot contains only one electron. When the occupancy of each dot remains fixed, the effective Hamiltonian for the spin degrees of freedom can be expressed as the Heisenberg Hamiltonian:

$$H_H = \sum_{i=1}^N J_i \mathbf{S}_i \cdot \mathbf{S}_{i+1} + \mathbf{B}_i \cdot \mathbf{S}_i, \quad (8)$$

where \mathbf{S}_i is an operator that corresponds to electron i , and \mathbf{B}_i is the magnetic field experienced by that electron.

In contrast to the Hubbard model, which contains parameters that describe the tunnel couplings and on-site energies, the Heisenberg Hamiltonian involves only the exchange couplings and magnetic fields. While advances in the independent control of chemical potentials have enabled progress in simulating Hubbard physics, the independent control of exchange couplings, which is required to simulate the Heisenberg model, has remained challenging, though recent advances have taken steps toward overcoming this obstacle.

The primary challenge is that exchange couplings depend on both the electrochemical potentials and tunnel couplings. Moreover, tunnel couplings generally depend in a highly nonlinear and nonlocal way on gate voltages [47]. Heuristically, exchange coupling depends on the degree of overlap between electronic wavefunctions, and such overlaps depend sensitively on the barrier potentials and positions of the wavefunctions. A final complication is that when multiple exchange couplings are present, one cannot simply extract the exchange couplings from the measured oscillation frequencies, because the energy gaps in the spectrum of a spin chain do not usually correspond to the bare exchange couplings themselves. These challenges make it difficult to use trial-and-error or interpolation approaches [28–33], which have been used to control tunnel couplings in quantum dots, to modulate exchange couplings.

Qiao et al. overcame this problem and demonstrated coherent exchange coupling between multiple spins in a linear four-dot array. Through a combination of

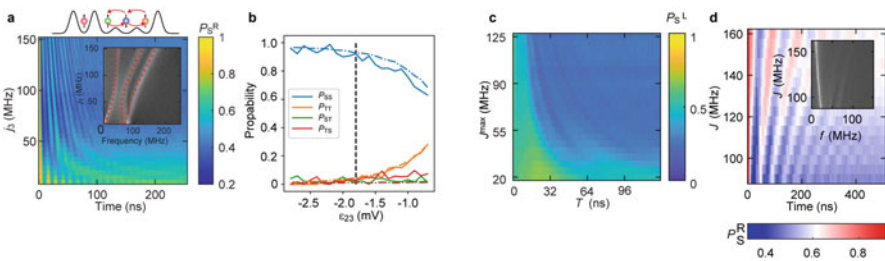


Fig. 9 Quantum simulation of Heisenberg spin chains. (a) Coherent multi-spin exchange coupling. Qiao et al., Phys. Rev. X, 10, 031006 (2021). Copyright the Authors, licensed under a Creative Commons Attribution (CC BY) license. (b) Preparation of the Heisenberg antiferromagnet. Van Diepen et al., Phys. Rev. X, 11, 041025 (2021). Copyright the Authors, licensed under a Creative Commons Attribution (CC BY) license. (c) Adiabatic quantum state transfer. Kandel et al., Nat. Comm. 12, 2156 (2021). Copyright the Authors, licensed under a Creative Commons Attribution (CC BY) license. (d) Superexchange between distant electron spins. Reprinted with permission from Qiao et al., Phys. Rev. Lett, 126, 017701 (2021). Copyright (2021) by the American Physical Society

theoretical calculations and electrostatic modeling, they showed that a primary cause of this difficulty is the electronic wavefunction shifts that occur during exchange pulses [42, 47]. For example, during a typical barrier-gate pulse, the electrons on either side of the barrier move closer to or farther away from each other, depending on the sign of the voltage pulse. This motion of the electronic wavefunctions has a significant impact on the magnitude of the exchange coupling. Electrostatic modeling of the potential during a barrier-gate pulse confirmed this picture [47]. Qiao et al. also showed that two models based on the Heitler–London formalism [40, 120] could be used to predict the barrier-gate voltages given a set of desired exchange couplings (Fig. 9a). The model parameters, which describe how much the electrons move in response to voltage pulses, were found by measuring how each of the exchange couplings depended on all of the barrier gate voltages. These models were sufficient to enable the generation of coherent three- and four-spin exchange oscillations within a reasonably wide range of exchange-coupling values [47]. This approach is also extensible to longer arrays of quantum-dot spin qubits.

Van Diepen et al. have also reported the creation of multiple nonzero exchange couplings by adjusting the detunings, instead of the barrier heights, in a linear array of four quantum dots [49]. In addition to demonstrating coherent exchange coupling between all four spins in the array, van Diepen et al. also demonstrated the creation of the ground state of the Heisenberg Hamiltonian, by adiabatically manipulating the exchange couplings beginning from a state composed to two separated singlets (Fig. 9b).

Building on the possibility of precise control of exchange couplings in a quantum-dot array, Kandel et al. demonstrated adiabatic quantum state transfer (AQT) in a chain of four quantum dots [118]. Adiabatic quantum state transfer (AQT), sometimes referred to as adiabatic quantum teleportation [121], is a process that is reminiscent of stimulated Raman adiabatic passage, a time-honored technique from the optical physics community [122]. The basic process of AQT involves a chain of three spins. By starting from a configuration with a strong exchange coupling between two spins, say 2 and 3, and by adiabatically modulating the exchange couplings to a final configuration with a strong coupling between dots 1 and 2, the initial state of dot 1 can be transferred to dot 3, and the joint state of spins 2 and 3 is transferred to dots 1 and 2. Although it has been studied in great detail theoretically over the past decades [121, 123–132], it has only recently been achieved experimentally, despite its great potential for use in quantum information processing experiments.

Kandel et al. implemented AQT in a GaAs/AlGaAs quadruple quantum-dot array [118] (Fig. 9c). To transfer a spin eigenstate from dot 3 to dot 1, a singlet was prepared in dots 1 and 2, by electron exchange with the reservoirs in the presence of large exchange coupling J_1 . Then, J_1 was decreased to zero, while J_2 was simultaneously increased. During this process, the spin state of dot 3 was transferred to dot 1, and the singlet state of dots 1 and 2 was transferred to dots 2 and 3. For spin eigenstates, the simulated fidelity of this process in GaAs quantum dots is about 0.95. The simulated fidelity for the transfer of arbitrary quantum states

in GaAs quantum dots is lower, because of the nuclear hyperfine noise. Crucially, the precise fidelity of this operation does not depend on the details of the pulses. This process could also be cascaded to enable long-distance transfer of both single-spin states and spin singlet states.

Another possibility enabled by the ability to independently control exchange couplings in spin chains is long-distance superexchange. As mentioned above, superexchange is an effective coupling between distant spins [110, 133–138], unlike conventional exchange, which only couples nearest-neighbor spins. Generally, superexchange involves an intermediate set of quantum dots that may be empty [139], singly [116], or multiply [140] occupied. One of the most frequently studied systems predicted to exhibit superexchange is a spin chain, consisting of two qubits weakly coupled to the ends of a strongly coupled spin chain [134, 135, 137].

To explore superexchange mediated by a spin chain, Qiao et al. implemented the following Hamiltonian in a system of four quantum dots [119]: $H = j\mathbf{S}_1 \cdot \mathbf{S}_2 + J\mathbf{S}_2 \cdot \mathbf{S}_3 + j\mathbf{S}_3 \cdot \mathbf{S}_4$. When $j \ll J$, superexchange between spins 1 and 4 can occur when spins 2 and 3 have the singlet state, via virtual excitation to the polarized triplet configurations, and at an oscillation frequency of $J' = \frac{j^2}{2J} \left(1 + \frac{3j}{2J}\right)$, up to third order in j (Fig. 9d). If spins 2 and 3 have any of the triplet states, which are nominally degenerate, those spins will evolve in time at a frequency scale of j , and superexchange between the end spins cannot occur with a reasonable fidelity. To realize this scenario, where the chain is prepared as a singlet, Qiao et al. harnessed the AQT process described above to transfer a spin singlet, originally prepared in one of the outer dots, to the interior of the array. After implementing the exchange couplings discussed above, the AQT process was reversed to transfer the end spins to one of the outer pairs of dots, which could be read out with Pauli spin blockade. End-spin oscillations were observed with the expected dependence on the J and j (Fig. 9d).

In addition to pure Heisenberg spin chains, disordered Heisenberg spin chains, [e.g. those with random \mathbf{B}_i in Eq. (8)] are also systems of great interest. Because of the naturally occurring nuclear hyperfine fluctuations, quantum-dot spin qubits enable a straightforward realization of this model. One interesting feature of disordered Heisenberg spin chains is the possibility of many-body localization [111], a phase of matter that seems to violate conventional assumptions about statistical mechanics. In a many-body localized system, despite the presence of interactions, disorder in the system prevents a subset of the system from fully entangling or thermalizing with the rest. The prototypical system thought to exhibit many-body localization is the disordered Heisenberg spin chain. Although many experiments in other platforms have presented evidence for many-body localization [141–145], few have been able to reproduce this seminal model and instead involve longer-range interactions. Because quantum dots enable an exact realization of the disordered Heisenberg spin chain model, semiconductor quantum dots present an attractive platform in which to realize this phenomenon and related effects [12].

The time crystal is another phase of matter that can occur in disordered spin chains [146–150]. In a time crystal, a parent non-thermalizing phase, such as a

many-body localized phase, can stabilize a subharmonic response of the system to a periodic drive indefinitely. The prototypical model for a time crystal is a disordered Ising spin chain. As in the case of many-body localization, the exact realization of this model has evaded implementation, though evidence of phases related to time crystals has been observed in different systems [151–154]. Although disordered Heisenberg spin chains do not enable creating a time crystal [150], it is possible to convert the Heisenberg interaction to an Ising form, through various mechanisms, including magnetic gradients [64, 155] and control pulses [150]. Recent experimental work has suggested that exchange-coupled singlet–triplet qubits can also realize a form of discrete time-crystalline behavior [76, 91]. Although the practical applications of the many-body localized and time-crystal phases are not yet entirely clear, they may be useful in quantum information processing applications as ways to stabilize many-body quantum states [12, 156].

5 Quantum State Transfer in Spin Chains

Some of the features of Heisenberg spin chains we have discussed above, especially superexchange and AQT, have potential applications in quantum computing for the transfer of quantum states between qubits. Transferring quantum information between qubits is essential for quantum error correction [160], and quantum processors with high connectivity can perform more efficiently than those with lower connectivity [161]. Recent years have seen significant progress in this direction. Building on the advances discussed above relating to quantum-dot architectures and fabrication, as well as the independent control of chemical potentials, single electrons can now be shuttled through extended arrays of quantum dots. Mills et al. demonstrated the ability to pump a single charge through an array of nine quantum dots in Si [15]. Depending on the number of charges involved and the repetition rate, this charge pump generated a measurable current that agreed with predictions (Fig. 10a). These experiments demonstrated the high degree of control over charge states afforded by modern quantum-dot architectures.

When electrons move to different dots during tunneling, the spin state of the electron can also be preserved. Initially demonstrated through the preservation of the coherence of a spin singlet during tunneling [43], the preservation of spin coherence has also been demonstrated during tunneling between distant quantum dots [48, 162, 163], in square arrays of quantum dots [157] (Fig. 10b), and in Si quantum dots [164].

One potential drawback to the transfer of spin states through tunneling is that empty quantum dots between the starting and ending locations are required. A route to overcoming this obstacle is to exploit the exchange coupling between neighboring quantum dots. An especially simple way to transfer quantum states with exchange coupling involves pulsed SWAP gates [158]. Although straightforward in concept, this idea had evaded implementation in a system of more than two dots until recently. Kandel et al. demonstrated this approach in a GaAs/AlGaAs quadruple

dot device with overlapping gates, transferring both single-spin eigenstates and entangled states back and forth across the array of four quantum dots through different sequences of SWAP operations [158] (Fig. 10c). Before and after each step, the two pairs of electrons were read out using spin-to-charge conversion techniques associated with Pauli spin blockade [43, 74]. A limiting factor in the previous experiment was the hyperfine interaction between the electron and nuclear spins in the GaAs/AlGaAs heterostructure. As discussed above, the hyperfine-induced dephasing can be minimized by working in Si quantum dots. Sigillito et al. demonstrated the transfer of quantum spin states using “resonant” SWAP gates in the presence of a large magnetic gradient [30] in Si quantum dots. Such gates are generated by an oscillating exchange coupling [80, 83].

An exciting illustration of how exchange coupling can enable long-distance state transfer involves quantum teleportation [165]. Teleportation involves distributing two members of an entangled pair to two experimenters, Alice and Bob. To teleport an unknown qubit state to Bob, Alice should measure the unknown state together

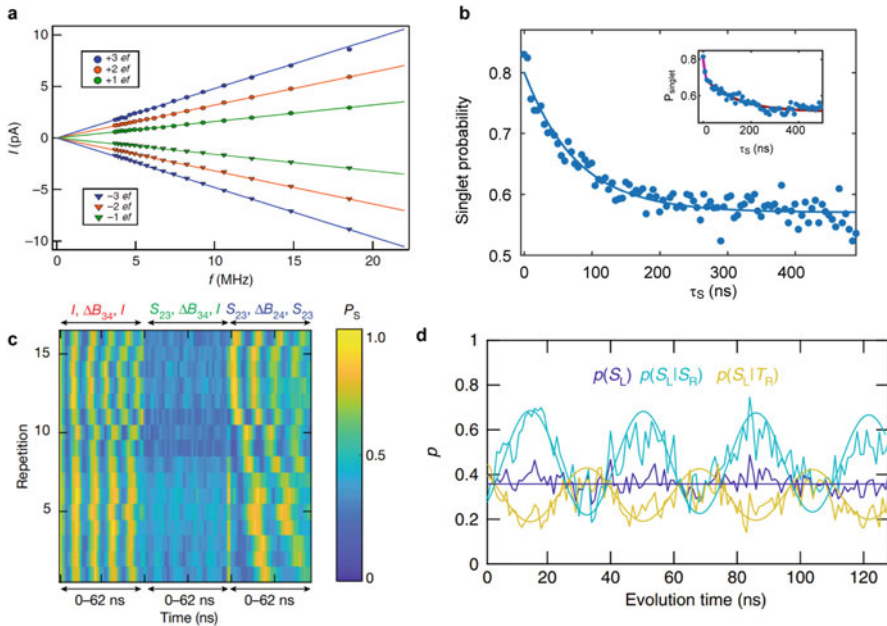


Fig. 10 State transfer in quantum-dot spin chains. (a) Current generated by shuttling single electrons through a nine-dot array. Mills et al., Nat. Comm., 10, 1063 (2019). Copyright the Authors, licensed under a Creative Commons Attribution (CC BY) license. (b) Motional narrowing of a pair of electron spins shuttled through a square array. Flentje et al., Nat. Comm., 8, 501 (2017). Copyright the Authors, licensed under a Creative Commons Attribution (CC BY) license. (c) Entangled state transfer via SWAP operations. Reprinted with permission from Kandel et al., Nature, 573, 553–557 (2019). Copyright Springer Nature (2019). (d) Quantum teleportation of entangled states. Qiao et al., Nat. Comm. 11, 3022, (2020). Copyright the Authors, licensed under a Creative Commons Attribution (CC BY) license

with her member of the entangled pair in the Bell-state basis. This measurement projects Bob's member of the entangled pair onto the unknown state, up to a single-qubit rotation that depends on Alice's measurement. Creating the long-distance entangled pair had presented the most challenging obstacle to teleportation in quantum dots [88, 166] and has been the focus of intense research [157, 162, 163]. However, spin-state transfer via Heisenberg exchange [158] solved this challenge. In Ref. [159], Qiao et al. leveraged this advance to perform teleportation in quantum dots (Fig. 10d). To implement teleportation in quantum dots, Qiao et al. created an entangled pair of electrons via Pauli spin blockade in dots 3 and 4 of a four-dot array. The entangled pair was distributed through the array via exchange-based SWAP gates such that it occupied dots 2 and 4. To teleport a state from dot 1 to dot 4, a joint measurement was performed on dots 1 and 2 together via Pauli spin blockade. When this measurement yielded a singlet, which is a maximally entangled Bell state, the state of spin 1 was teleported to spin 4. This procedure was conditional because teleportation occurs only when the measurement of qubits 1–2 yielded a singlet. (A triplet result from this measurement could be any one of the three other Bell states and thus does not provide enough information for complete teleportation.) The experiments of Ref. [159] demonstrated the essence of this procedure by teleporting a classical spin state and entangled states (Fig. 10d).

6 Future Directions and Outlook

In this chapter, we have described the exciting advances and great potential associated with quantum-dot spin chains. In addition to enabling different promising qubits for quantum computing, quantum-dot spin chains also facilitate studying different aspects of the Hubbard and Heisenberg models. In large part, advances along these directions have been driven by parallel developments in the technology of gate-defined semiconductor quantum-dot spin qubits. Today, extended chains of quantum dots can be fabricated and operated with controlled occupancy, and these capabilities directly enable exploring the different features of spin chains that we have described in this chapter.

Despite the significant advances in controlling and exploiting quantum-dot spin chains in recent years, much exciting work remains to be done. On a fundamental level, continuing to understand, model, and predict parameters like tunnel couplings and exchange couplings will continue to drive forward progress in this field. In particular, understanding how to control multiple exchange couplings independently and simultaneously in larger spin chains for many-body quantum simulation or multi-qubit algorithms will create important and exciting opportunities and capabilities for both quantum computing and simulation. It is likely that computer-automated and machine learning approaches [27, 32, 34] for extended quantum-dot systems will become increasingly important.

On the device level, most of the results we have discussed have involved one-dimensional chains. The creation and operation of two-dimensional quantum-dot

arrays [29, 157, 167] is an exciting and active area of research. In addition, the use of materials like Si-based quantum dots [9], which feature lower electron-spin-induced dephasing rates compared with GaAs/AlGaAs quantum dots, may offer new routes to exploring coherent spin phenomena. Further work to understand and minimize effects like charge noise [46, 168, 169] will also become increasingly important.

These expected advances in device design and operation will directly benefit single- and multi-qubit gates driven by exchange. In addition to the theoretical and model-based approaches mentioned above, methods to design and implement noise-resistant exchange pulses [170–172] will likely become increasingly important as gate fidelities and device architectures mature. The possibility of two-dimensional arrays opens up the possibility of efficient error correction schemes [71], as well as dense arrays of qubits with high connectivity [161].

Different multi-spin qubit types also have yet to be experimentally investigated. In general, increasing the number of electrons in multi-spin qubits opens up pathways for reduced sensitivity to noise, at the expense of more complex device designs or control. Whether or not these multi-spin qubits can offer an improvement for quantum computing applications remains to be seen, but they deserve to be explored. In fact, the great variety of potential qubits that can be formed from electrons in quantum dots is one of the unique features of the platform.

As quantum dots continue to mature, new avenues in quantum simulation become available. In particular, it may become possible to explore the Hubbard model in the ultra-low temperature regime [109], where electron–electron interactions are expected to dominate, and which is hypothesized to underlie phenomena like high-temperature superconductivity [109]. Improvements in single-qubit initialization, control, and readout, which will occur through developments in quantum computing, will also benefit simulation efforts.

Besides benefiting from the same technological advances, quantum simulation in spin chains and quantum information processing overlap in the area of long-distance coupling between qubits. We have discussed multiple routes for quantum state transfer, including spin-state transfer via Heisenberg exchange, teleportation, adiabatic state transfer, and superexchange, which exploit some of the unique features of spin chains, mostly in GaAs/AlGaAs quantum dots. The implementation and exploration of these techniques in Si quantum dots, which have longer electron spin coherence times, will be necessary to precisely quantify and benchmark the performance of these techniques and to explore how they might be useful for quantum computing experiments. Although the use of spin chain physics in quantum computing is still in early stages, methods to transfer quantum states between qubits are generally helpful for error correction [160], and it may be that these techniques can enable progress in this direction. In the coming years, it is likely that this exploration will continue and that connections to quantum information science will become stronger and more apparent.

References

1. Y.P. Kandel, H. Qiao, J.M. Nichol, Perspective on exchange-coupled quantum-dot spin chains. *Appl. Phys. Lett.* **119**, 030501 (2021). <https://doi.org/10.1063/5.0055908>
2. M. Anderlini, P.J. Lee, B.L. Brown, J. Sebby-Strabley, W.D. Phillips, J.V. Porto, Controlled exchange interaction between pairs of neutral atoms in an optical lattice. *Nature* **448**, 452 (2007). <https://doi.org/10.1038/nature06011>
3. Y. He, S.K. Gorman, D. Keith, L. Kranz, J.G. Keizer, M.Y. Simmons, A two-qubit gate between phosphorus donor electrons in silicon. *Nature* **571**, 371 (2019). <https://doi.org/10.1038/s41586-019-1381-2>
4. L. Kouwenhoven, C. Marcus, Quantum dots. *Physics World* **11**(6), 35 (1998). <https://doi.org/10.1088/2058-7058/11/6/26>
5. L. Kouwenhoven, D.G. Austing, S. Tarucha, Few-electron quantum dots. *Rep. Prog. Phys.* **64**, 701 (2001). <https://stacks.iop.org/0034-4885/64/i=6/a=201>
6. W.G. van der Wiel, S. De Franceschi, J.M. Elzerman, T. Fujisawa, S. Tarucha, L.P. Kouwenhoven, Electron transport through double quantum dots. *Rev. Mod. Phys.* **75**, 1 (2002). <https://doi.org/10.1103/RevModPhys.75.1>
7. W.G. van der Wiel, M. Stopa, T. Kodera, T. Hatano, S. Tarucha, Semiconductor quantum dots for electron spin qubits. *New J. Phys.* **8**(2), 28 (2006). <https://doi.org/10.1088/1367-2630/8/2/028>
8. R. Hanson, L.P. Kouwenhoven, J.R. Petta, S. Tarucha, L.M.K. Vandersypen, Spins in few-electron quantum dots, *Rev. Mod. Phys.* **79**, 1217 (2007). <https://doi.org/10.1103/RevModPhys.79.1217>
9. F.A. Zwanenburg, A.S. Dzurak, A. Morello, M.Y. Simmons, L.C.L. Hollenberg, G. Klimeck, S. Rogge, S.N. Coppersmith, M.A. Eriksson, Silicon quantum electronics. *Rev. Mod. Phys.* **85**, 961 (2013). <https://doi.org/10.1103/RevModPhys.85.961>
10. G. Scappucci, C. Kloeffel, F.A. Zwanenburg, D. Loss, M. Myronov, J.J. Zhang, S. De Franceschi, G. Katsaros, M. Veldhorst, The germanium quantum information route. *Nature Rev. Mater.*, 1–18 (2020)
11. J.M. Taylor, J.R. Petta, A.C. Johnson, A. Yacoby, C.M. Marcus, M.D. Lukin, Relaxation, dephasing, and quantum control of electron spins in double quantum dots. *Phys. Rev. B* **76**(3), 035315 (2007). <https://doi.org/10.1103/PhysRevB.76.035315>
12. E. Barnes, D.L. Deng, R.E. Throckmorton, Y.L. Wu, S. Das Sarma, Noise-induced collective quantum state preservation in spin qubit arrays. *Phys. Rev. B* **93**, 085420 (2016). <https://doi.org/10.1103/PhysRevB.93.085420>
13. C. Volk, A.M.J. Zwerver, U. Mukhopadhyay, P.T. Eendebak, C.J. van Diepen, J.P. Dehollain, T. Hensgens, T. Fujita, C. Reichl, W. Wegscheider, L.M.K. Vandersypen, Loading a quantum-dot based “qubyte” register. *npj Quantum Inf.* **5**, 29 (2019). <https://doi.org/10.1038/s41534-019-0146-y>
14. J.P. Dehollain, U. Mukhopadhyay, V.P. Michal, Y. Wang, B. Wunsch, C. Reichl, W. Wegscheider, M.S. Rudner, E. Demler, L.M. Vandersypen, Nagaoka ferromagnetism observed in a quantum dot plaquette. *Nature* **579**, 528 (2020). <https://doi.org/10.1038/s41586-020-2051-0>
15. A.R. Mills, D.M. Zajac, M.J. Gullans, F.J. Schupp, T.M. Hazard, J.R. Petta, Shuttling a single charge across a one-dimensional array of silicon quantum dots. *Nature Communications* **10**(1), 1063 (2019). <https://doi.org/10.1038/s41467-019-08970-z>
16. M. Field, C.G. Smith, M. Pepper, D.A. Ritchie, J.E.F. Frost, G.A.C. Jones, D.G. Hasko, Measurements of coulomb blockade with a noninvasive voltage probe. *Phys. Rev. Lett.* **70**, 1311 (1993). <https://doi.org/10.1103/PhysRevLett.70.1311>
17. L. DiCarlo, H.J. Lynch, A.C. Johnson, L.I. Childress, K. Crockett, C.M. Marcus, M.P. Hanson, A.C. Gossard, Differential charge sensing and charge delocalization in a tunable double quantum dot. *Phys. Rev. Lett.* **92**, 226801 (2004). <https://doi.org/10.1103/PhysRevLett.92.226801>

18. D.J. Reilly, C.M. Marcus, M.P. Hanson, A.C. Gossard, Fast single-charge sensing with a rf quantum point contact. *Appl. Phys. Lett.* **91**(16), 162101 (2007). <https://doi.org/10.1063/1.2794995>
19. C. Barthel, D.J. Reilly, C.M. Marcus, M.P. Hanson, A.C. Gossard, Rapid single-shot measurement of a singlet-triplet qubit. *Phys. Rev. Lett.* **103**, 160503 (2009). <https://doi.org/10.1103/PhysRevLett.103.160503>. <https://link.aps.org/doi/10.1103/PhysRevLett.103.160503>
20. L.M.K. Vandersypen, M.A. Eriksson, Quantum computing with semiconductor spins. *Physics Today* **72**(8), 38 (2019). <https://doi.org/10.1063/PT.3.4270>
21. S. Tarucha, D.G. Austing, T. Honda, R.J. van der Hage, L.P. Kouwenhoven, Shell filling and spin effects in a few electron quantum dot. *Phys. Rev. Lett.* **77**(17), 3613 (1996). <https://doi.org/10.1103/PhysRevLett.77.3613>. <https://link.aps.org/doi/10.1103/PhysRevLett.77.3613>
22. L.P. Kouwenhoven, T.H. Oosterkamp, M.W.S. Danoesastro, M. Eto, D.G. Austing, T. Honda, S. Tarucha, Excitation spectra of circular, few-electron quantum dots. *Science* **278**, 1788 (1997). <https://doi.org/10.1126/science.278.5344.1788>. <https://www.sciencemag.org/content/278/5344/1788.abstract>
23. M. Ciorga, A.S. Sachrajda, P. Hawrylak, C. Gould, P. Zawadzki, S. Jullian, Y. Feng, Z. Wasilewski, Addition spectrum of a lateral dot from coulomb and spin-blockade spectroscopy. *Phys. Rev. B* **61**, R16315 (2000). <https://doi.org/10.1103/PhysRevB.61.R16315>. <https://link.aps.org/doi/10.1103/PhysRevB.61.R16315>
24. S.J. Angus, A.J. Ferguson, A.S. Dzurak, R.G. Clark, Gate-defined quantum dots in intrinsic silicon. *Nano Lett.* **7**, 2051 (2007). <https://doi.org/10.1021/nl070949k>
25. M.G. Borselli, K. Eng, R.S. Ross, T.M. Hazard, K.S. Holabird, B. Huang, A.A. Kiselev, P.W. Deelman, L.D. Warren, I. Milosavljevic, A.E. Schmitz, M. Sokolich, M.F. Gyure, A.T. Hunter, Undoped accumulation-mode Si/SiGe quantum dots. *Nanotechnol.* **26**, 375202 (2015). <https://doi.org/10.1088/0957-4484/26/37/375202>
26. D.M. Zajac, T.M. Hazard, X. Mi, E. Nielsen, J.R. Petta, Scalable gate architecture for a one-dimensional array of semiconductor spin qubits. *Phys. Rev. Appl.* **6**, 054013 (2016). <https://doi.org/10.1103/PhysRevApplied.6.054013>
27. T.A. Baart, P.T. Eendebak, C. Reichl, W. Wegscheider, L.M.K. Vandersypen, Computer-automated tuning of semiconductor double quantum dots into the single-electron regime. *Appl. Phys. Lett.* **108**(21), 213104 (2016). <https://doi.org/10.1063/1.4952624>
28. T. Hensgens, T. Fujita, L. Janssen, X. Li, C.J. Van Diepen, C. Reichl, W. Wegscheider, S. Das Sarma, L.M.K. Vandersypen, Quantum simulation of a Fermi-Hubbard model using a semiconductor quantum dot array. *Nature* **548**, 70 EP (2017). <https://doi.org/10.1038/nature23022>
29. U. Mukhopadhyay, J.P. Dehollain, C. Reichl, W. Wegscheider, L.M.K. Vandersypen, A 2 x 2 quantum dot array with controllable inter-dot tunnel couplings. *Appl. Phys. Lett.* **112**(18), 183505 (2018). <https://doi.org/10.1063/1.5025928>
30. A.J. Sigillito, M.J. Gullans, L.F. Edge, M. Borselli, J.R. Petta, Coherent transfer of quantum information in a silicon double quantum dot using resonant swap gates. *npj Quantum Inf.* **5**(1), 110 (2019). <https://doi.org/10.1038/s41534-019-0225-0>
31. C.J. van Diepen, P.T. Eendebak, B.T. Buijtenorp, U. Mukhopadhyay, T. Fujita, C. Reichl, W. Wegscheider, L.M.K. Vandersypen, Automated tuning of inter-dot tunnel coupling in double quantum dots. *Appl. Phys. Lett.* **113**(3), 033101 (2018). <https://doi.org/10.1063/1.5031034>
32. A.R. Mills, M.M. Feldman, C. Monical, P.J. Lewis, K.W. Larson, A.M. Mounce, J.R. Petta, Computer-automated tuning procedures for semiconductor quantum dot arrays. *Appl. Phys. Lett.* **115**(11), 113501 (2019). <https://doi.org/10.1063/1.5121444>
33. T.K. Hsiao, C. van Diepen, U. Mukhopadhyay, C. Reichl, W. Wegscheider, L. Vandersypen, Efficient orthogonal control of tunnel couplings in a quantum dot array. *Phys. Rev. Appl.* **13**, 054018 (2020). <https://doi.org/10.1103/PhysRevApplied.13.054018>
34. J.P. Zwolak, T. McJunkin, S.S. Kalantre, J. Dodson, E. MacQuarrie, D. Savage, M. Lagally, S. Coppersmith, M.A. Eriksson, J.M. Taylor, Autotuning of double-dot devices in situ with machine learning. *Phys. Rev. Appl.* **13**, 034075 (2020). <https://doi.org/10.1103/PhysRevApplied.13.034075>

35. S.S. Kalantre, J.P. Zwolak, S. Ragole, X. Wu, N.M. Zimmerman, M.D. Stewart, J.M. Taylor, Machine learning techniques for state recognition and auto-tuning in quantum dots. *npj Quantum Inf.* **5**(1), 6 (2019). <https://doi.org/10.1038/s41534-018-0118-7>
36. P.A.M. Dirac, R.H. Fowler, On the theory of quantum mechanics. *Proc. R. Soc. Lond. A Contain. Papers Math. Phys. Character* **112**(762), 661 (1926). <https://doi.org/10.1098/rspa.1926.0133>
37. W. Heisenberg, Mehrkörperproblem und resonanz in der quantenmechanik. *Zeitschrift für Physik* **38**(6), 411 (1926). <https://doi.org/10.1007/BF01397160>
38. N.W. Ashcroft, N.D. Mermin, *Solid State Physics* (Saunders College Publishing, 1976)
39. M. Russ, G. Burkard, Three-electron spin qubits. *J. Phys. Condens. Matter* **29**(39), 393001 (2017). <https://doi.org/10.1088/1361-648x/aa761f>
40. G. Burkard, D. Loss, D.P. DiVincenzo, Coupled quantum dots as quantum gates. *Phys. Rev. B* **59**, 2070 (1999). <https://doi.org/10.1103/PhysRevB.59.2070>. <https://link.aps.org/doi/10.1103/PhysRevB.59.2070>
41. E. Nielsen, R.P. Muller, A configuration interaction analysis of exchange in double quantum dots. arXiv:1006.2735 (2010). <https://arxiv.org/abs/1006.2735>
42. A. Pan, T.E. Keating, M.F. Gyure, E.J. Pritchett, S. Quinn, R.S. Ross, T.D. Ladd, J. Kerckhoff, Resonant exchange operation in triple-quantum-dot qubits for spin–photon transduction. *Quantum Sci. Technol.* **5**(3), 034005 (2020). <https://doi.org/10.1088/2058-9565/ab86c9>. <https://iopscience.iop.org/article/10.1088/2058-9565/ab86c9>
43. J.R. Petta, A.C. Johnson, J.M. Taylor, E. Laird, A. Yacoby, M.D. Lukin, C.M. Marcus, M.P. Hanson, A.C. Gossard, Coherent manipulation of coupled electron spins in semiconductor quantum dots. *Science* **309**(5744), 2180 (2005). <https://doi.org/10.1126/science.1116955>
44. M.D. Reed, B.M. Maune, R.W. Andrews, M.G. Borselli, K. Eng, M.P. Jura, A.A. Kiselev, T.D. Ladd, S.T. Merkel, I. Milosavljevic, E.J. Pritchett, M.T. Rakher, R.S. Ross, A.E. Schmitz, A. Smith, J.A. Wright, M.F. Gyure, A.T. Hunter, Reduced sensitivity to charge noise in semiconductor spin qubits via symmetric operation. *Phys. Rev. Lett.* **116**, 110402 (2016). <https://doi.org/10.1103/PhysRevLett.116.110402>
45. F. Martins, F.K. Malinowski, P.D. Nissen, E. Barnes, S. Fallahi, G.C. Gardner, M.J. Manfra, C.M. Marcus, F. Kueemmeth, Noise suppression using symmetric exchange gates in spin qubits. *Phys. Rev. Lett.* **116**, 116801 (2016). <https://doi.org/10.1103/PhysRevLett.116.116801>
46. O.E. Dial, M.D. Shulman, S.P. Harvey, H. Bluhm, V. Umansky, A. Yacoby, Charge noise spectroscopy using coherent exchange oscillations in a singlet-triplet qubit. *Phys. Rev. Lett.* **110**, 146804 (2013). <https://doi.org/10.1103/PhysRevLett.110.146804>. <https://link.aps.org/doi/10.1103/PhysRevLett.110.146804>
47. H. Qiao, Y.P. Kandel, K. Deng, S. Fallahi, G.C. Gardner, M.J. Manfra, E. Barnes, J.M. Nichol, Coherent multispin exchange coupling in a quantum-dot spin chain. *Phys. Rev. X* **10**, 031006 (2020). <https://doi.org/10.1103/PhysRevX.10.031006>
48. T.A. Baart, M. Shafiei, T. Fujita, C. Reichl, W. Wegscheider, L.M.K. Vandersypen, Single-spin CCD. *Nature Nanotechnology* **11**, 330 (2016). <https://doi.org/10.1038/nnano.2015.291>
49. C.J. van Diepen, T.K. Hsiao, U. Mukhopadhyay, C. Reichl, W. Wegscheider, L.M.K. Vandersypen, Quantum simulation of antiferromagnetic Heisenberg chain with gate-defined quantum dots. *Phys. Rev. X* **11**, 041025 (2021). <https://doi.org/10.1103/PhysRevX.11.041025>
50. M. Veldhorst, J.C.C. Hwang, C.H. Yang, A.W. Leenstra, B. de Ronde, J.P. Dehollain, J.T. Muhonen, F.E. Hudson, K.M. Itoh, A. Morello, A.S. Dzurak, An addressable quantum dot qubit with fault-tolerant control-fidelity. *Nature Nanotechnology* **9**, 981 (2014). <https://doi.org/10.1038/nnano.2014.216>
51. F.K. Malinowski, F. Martins, P.D. Nissen, E. Barnes, M.S. Rudner, S. Fallahi, G.C. Gardner, M.J. Manfra, C.M. Marcus, F. Kueemmeth, Notch filtering the nuclear environment of a spin qubit. *Nature Nanotechnology* **12**, 16–20 (2016). <https://doi.org/10.1038/nnano.2016.170>
52. A.M.J. Zwerver, T. Krähenmann, T.F. Watson, L. Lampert, H.C. George, R. Pillarisetty, S.A. Bojarski, P. Amin, S.V. Amitonov, J.M. Boter, R. Caudillo, D. Corras-Serrano, J.P. Dehollain, G. Droulers, E.M. Henry, R. Kotlyar, M. Lodari, F. Luthi, D.J. Michalak, B.K. Mueller, S. Neyens, J. Roberts, N. Samkharadze, G. Zheng, O.K. Zietz, G. Scappucci, M. Veldhorst, L.M.K. Vandersypen, J.S. Clarke, Qubits made by advanced semiconductor manufacturing. arXiv:2101.12650 [cond-mat, physics:quant-ph] (2021). <https://arxiv.org/abs/2101.12650>

53. W. Ha, S.D. Ha, M.D. Choi, Y. Tang, A.E. Schmitz, M.P. Levendorf, K. Lee, T.s. Chappell, J. M. ad Adams, D.R. Hulbert, E. Acuna, R.S. Noah, J.W. Matten, M.P. Jura, J.A. Wright, M.T. Rakher, M.G. Borselli, A flexible design platform for Si/SiGe exchange-only qubits with low disorder. *Nano Letters* **22**(3), 1443 (2022). <https://doi.org/10.1021/acs.nanolett.1c03026>
54. J. Levy, Universal quantum computation with spin-1/2 pairs and Heisenberg exchange. *Phys. Rev. Lett.* **89**(14), 147902 (2002). <https://doi.org/10.1103/PhysRevLett.89.147902>
55. D.P. DiVincenzo, D. Bacon, J. Kempe, G. Burkard, K.B. Whaley, Universal quantum computation with the exchange interaction. *Nature* **408**(6810), 339 (2000). <https://doi.org/10.1038/35042541>
56. A. Sala, J. Danon, Exchange-only singlet-only spin qubit. *Phys. Rev. B* **95**, 241303 (2017). <https://doi.org/10.1103/PhysRevB.95.241303>
57. A. Sala, J.H. Qvist, J. Danon, Highly tunable exchange-only singlet-only qubit in a GaAs triple quantum dot. *Phys. Rev. Res.* **2**, 012062 (2020). <https://doi.org/10.1103/PhysRevResearch.2.012062>
58. M. Russ, J.R. Petta, G. Burkard, Quadrupolar exchange-only spin qubit. *Phys. Rev. Lett.* **121**, 177701 (2018). <https://doi.org/10.1103/PhysRevLett.121.177701>
59. D. Loss, D.P. DiVincenzo, Quantum computation with quantum dots. *Phys. Rev. A* **57**(1), 120 (1998). <https://doi.org/10.1103/PhysRevA.57.120>
60. J. Yoneda, K. Takeda, T. Otsuka, T. Nakajima, M.R. Delbecq, G. Allison, T. Honda, T. Kodera, S. Oda, Y. Hoshi, N. Usami, K.M. Itoh, S. Tarucha, A quantum-dot spin qubit with coherence limited by charge noise and fidelity higher than 99.9%. *Nature Nanotechnology* **13**(2), 102 (2018). <https://doi.org/10.1038/s41565-017-0014-x>
61. K.C. Nowack, M. Shafiei, M. Laforest, G.E.D.K. Prawiroatmodjo, L.R. Schreiber, C. Reichl, W. Wegscheider, L.M.K. Vandersypen, Single-shot correlations and two-qubit gate of solid-state spins. *Science* **333**(6047), 1269 (2011). <https://doi.org/10.1126/science.1209524>
62. R. Brunner, Y.S. Shin, T. Obata, M. Pioro-Ladrière, T. Kubo, K. Yoshida, T. Taniyama, Y. Tokura, S. Tarucha, Two-qubit gate of combined single-spin rotation and interdot spin exchange in a double quantum dot. *Phys. Rev. Lett.* **107**, 146801 (2011). <https://doi.org/10.1103/PhysRevLett.107.146801>
63. B.E. Kane, A silicon-based nuclear spin quantum computer. *Nature* **393**, 133 (1998). <https://doi.org/10.1038/30156>
64. T. Meunier, V.E. Calado, L.M.K. Vandersypen, Efficient controlled-phase gate for single-spin qubits in quantum dots. *Phys. Rev. B* **83**, 121403 (2011). <https://doi.org/10.1103/PhysRevB.83.121403>
65. M. Russ, D.M. Zajac, A.J. Sigillito, F. Borjans, J.M. Taylor, J.R. Petta, G. Burkard, High-fidelity quantum gates in Si/SiGe double quantum dots. *Phys. Rev. B* **97**, 085421 (2018). <https://doi.org/10.1103/PhysRevB.97.085421>
66. M. Veldhorst, C.H. Yang, J.C.C. Hwang, W. Huang, J.P. Dehollain, J.T. Muhonen, S. Simmons, A. Laucht, F.E. Hudson, K.M. Itoh, A. Morello, A.S. Dzurak, A two-qubit logic gate in silicon. *Nature* **526**(7573), 410 (2015). <https://doi.org/10.1038/nature15263>
67. D.M. Zajac, A.J. Sigillito, M. Russ, F. Borjans, J.M. Taylor, G. Burkard, J.R. Petta, Resonantly driven CNOT gate for electron spins. *Science* **359**, 439 (2018). <https://doi.org/10.1126/science.aao5965>
68. T.F. Watson, S.G.J. Philips, E. Kawakami, D.R. Ward, P. Scarlino, M. Veldhorst, D.E. Savage, M.G. Lagally, M. Friesen, S.N. Coppersmith, M.A. Eriksson, L.M.K. Vandersypen, A programmable two-qubit quantum processor in silicon. *Nature* **555**, 633 (2018). <https://doi.org/10.1038/nature25766>
69. W. Huang, C.H. Yang, K.W. Chan, T. Tanttu, B. Hensen, R.C.C. Leon, M.A. Fogarty, J.C.C. Hwang, F.E. Hudson, K.M. Itoh, A. Morello, A. Laucht, A.S. Dzurak, Fidelity benchmarks for two-qubit gates in silicon. *Nature* **569**(7757), 532 (2019). <https://doi.org/10.1038/s41586-019-1197-0>
70. X. Xue, M. Russ, N. Samkharadze, B. Undseth, A. Sammak, G. Scappucci, L.M.K. Vandersypen, Computing with spin qubits at the surface code error threshold. *Nature* **601**, 343 (2022). <https://doi.org/10.1038/s41586-021-04273-w>

71. A.G. Fowler, M. Mariantoni, J.M. Martinis, A.N. Cleland, Surface codes: Towards practical large-scale quantum computation. *Phys. Rev. A* **86**, 032324 (2012). <https://doi.org/10.1103/PhysRevA.86.032324>. <https://link.aps.org/doi/10.1103/PhysRevA.86.032324>
72. M.J. Gullans, J.R. Petta, Protocol for a resonantly driven three-qubit Toffoli gate with silicon spin qubits. *Phys. Rev. B* **100**, 085419 (2019). <https://doi.org/10.1103/PhysRevB.100.085419>
73. D. Bacon, J. Kempe, D.A. Lidar, K.B. Whaley, Universal fault-tolerant quantum computation on decoherence-free subspaces. *Phys. Rev. Lett.* **85**, 1758 (2000). <https://doi.org/10.1103/PhysRevLett.85.1758>. <https://link.aps.org/doi/10.1103/PhysRevLett.85.1758>
74. S. Foletti, H. Bluhm, D. Mahalu, V. Umansky, A. Yacoby, Universal quantum control of two-electron spin quantum bits using dynamic nuclear polarization. *Nature Physics* **5**(12), 903 (2009). <https://doi.org/10.1038/nphys1424>
75. H. Bluhm, S. Foletti, I. Neder, M.S. Rudner, D. Mahalu, V. Umansky, A. Yacoby, Dephasing time of GaAs electron-spin qubits coupled to a nuclear bath exceeding 200 μ s. *Nature Physics* **7**(2), 109 (2010). <https://doi.org/10.1038/nphys1856>
76. H. Qiao, Y.P. Kandel, J.S.V. Dyke, S. Fallahi, G.C. Gardner, M.J. Manfra, E. Barnes, J.M. Nichol, Floquet-enhanced spin swaps. *Nature Communications* **12**(1), 2142 (2021). <https://doi.org/10.1038/s41467-021-22415-6>
77. H. Bluhm, S. Foletti, D. Mahalu, V. Umansky, A. Yacoby, Enhancing the coherence of a spin qubit by operating it as a feedback loop that controls its nuclear spin bath. *Phys. Rev. Lett.* **105**(21), 216803 (2010). <https://doi.org/10.1103/PhysRevLett.105.216803>
78. M.D. Shulman, O.E. Dial, S.P. Harvey, H. Bluhm, V. Umansky, A. Yacoby, Demonstration of entanglement of electrostatically coupled singlet-triplet qubits. *Science* **336**(6078), 202 (2012). <https://doi.org/10.1126/science.1217692>
79. B.M. Maune, M.G. Borselli, B. Huang, T.D. Ladd, P.W. Deelman, K.S. Holabird, A.A. Kiselev, I. Alvarado-Rodriguez, R.S. Ross, A.E. Schmitz, M. Sokolich, C.A. Watson, M.F. Gyure, A.T. Hunter, Coherent singlet-triplet oscillations in a silicon-based double quantum dot. *Nature* **481**(7381), 344 (2012). <https://doi.org/10.1038/nature10707>
80. M.D. Shulman, S.P. Harvey, J.M. Nichol, S.D. Bartlett, A.C. Doherty, V. Umansky, A. Yacoby, Suppressing qubit dephasing using real-time Hamiltonian estimation. *Nature Communications* **5**(May), 5156 (2014). <https://doi.org/10.1038/ncomms6156>
81. X. Wu, D.R. Ward, J.R. Prance, D. Kim, J.K. Gamble, R.T. Mohr, Z. Shi, D.E. Savage, M.G. Lagally, M. Friesen, S.N. Coppersmith, M.A. Eriksson, Two-axis control of a singlet—triplet qubit with an integrated micromagnet. *Proc. Natl. Acad. Sci.* **111**(33), 11938 (2014). <https://doi.org/10.1073/pnas.1412230111>
82. J.M. Nichol, S.P. Harvey, M.D. Shulman, A. Pal, V. Umansky, E.I. Rashba, B.I. Halperin, A. Yacoby, Quenching of dynamic nuclear polarization by spin-orbit coupling in GaAs quantum dots. *Nature Communications* **6**, 7682 (2015). <https://doi.org/10.1038/ncomms8682>
83. J.M. Nichol, L.A. Orona, S.P. Harvey, S. Fallahi, G.C. Gardner, M.J. Manfra, A. Yacoby, High-fidelity entangling gate for double-quantum-dot spin qubits. *npj Quantum Inf.* **3**(1), 3 (2017). <https://doi.org/10.1038/s41534-016-0003-1>
84. A. Noiri, T. Nakajima, J. Yoneda, M.R. Delbecq, P. Stano, T. Otsuka, K. Takeda, S. Amaha, G. Allison, K. Kawasaki, Y. Kojima, A. Ludwig, A.D. Wieck, D. Loss, S. Tarucha, A fast quantum interface between different spin qubit encodings. *Nature Communications* **9**(1), 5066 (2018). <https://doi.org/10.1038/s41467-018-07522-1>
85. P. Harvey-Collard, N.T. Jacobson, C. Bureau-Oxton, R.M. Jock, V. Srinivasa, A.M. Mounce, D.R. Ward, J.M. Anderson, R.P. Manginell, J.R. Wendt, T. Pluym, M.P. Lilly, D.R. Luhman, M. Pioro-Ladrière, M.S. Carroll, Spin-orbit interactions for singlet-triplet qubits in silicon. *Phys. Rev. Lett.* **122**, 217702 (2019). <https://doi.org/10.1103/PhysRevLett.122.217702>
86. M.A. Fogarty, K.W. Chan, B. Hensen, W. Huang, T. Tanttu, C.H. Yang, A. Laucht, M. Veldhorst, F.E. Hudson, K.M. Itoh, D. Culcer, T.D. Ladd, A. Morello, A.S. Dzurak, Integrated silicon qubit platform with single-spin addressability, exchange control and single-shot singlet-triplet readout. *Nature Communications* **9**(1), 4370 (2018). <https://doi.org/10.1038/s41467-018-06039-x>

87. P. Cerfontaine, T. Botzem, J. Ritzmann, S.S. Humpohl, A. Ludwig, D. Schuh, D. Bougeard, A.D. Wieck, H. Bluhm, Closed-loop control of a GaAs-based singlet-triplet spin qubit with 99.5% gate fidelity and low leakage. *Nature Communications* **11**(1), 1 (2020). <https://doi.org/10.1038/s41467-020-17865-3>
P. Cerfontaine, T. Botzem, J. Ritzmann, S.S. Humpohl, A. Ludwig, D. Schuh, D. Bougeard, A.D. Wieck, H. Bluhm, Closed-loop control of a GaAs-based singlet-triplet spin qubit with 99.5% gate fidelity and low leakage. *Nature Communications* **11**(1), 1 (2020)
88. K. Takeda, A. Noiri, J. Yoneda, T. Nakajima, S. Tarucha, Resonantly driven singlet-triplet spin qubit in silicon. *Phys. Rev. Lett.* **124**, 117701 (2020). <https://doi.org/10.1103/PhysRevLett.124.117701>
89. J. Klinovaja, D. Stepanenko, B.I. Halperin, D. Loss, Exchange-based CNOT gates for singlet-triplet qubits with spin-orbit interaction. *Phys. Rev. B* **86**, 085423 (2012). <https://link.aps.org/doi/10.1103/PhysRevB.86.085423>
90. R. Li, X. Hu, J.Q. You, Controllable exchange coupling between two singlet-triplet qubits. *Phys. Rev. B* **86**, 205306 (2012). <https://doi.org/10.1103/PhysRevB.86.205306>
91. M.P. Wardrop, A.C. Doherty, Exchange-based two-qubit gate for singlet-triplet qubits. *Phys. Rev. B* **90**, 045418 (2014). <https://doi.org/10.1103/PhysRevB.90.045418>
92. P. Cerfontaine, R. Otten, M.A. Wolfe, P. Bethke, H. Bluhm, High-fidelity gate set for exchange-coupled singlet-triplet qubits. *Phys. Rev. B* **101**, 155311 (2020). <https://doi.org/10.1103/PhysRevB.101.155311>. <https://link.aps.org/doi/10.1103/PhysRevB.101.155311>
93. J. Medford, J. Beil, J.M. Taylor, S.D. Bartlett, A.C. Doherty, E.I. Rashba, D.P. DiVincenzo, H. Lu, A.C. Gossard, C.M. Marcus, Self-consistent measurement and state tomography of an exchange-only spin qubit. *Nature Nanotechnology* **8**, 654 (2013). <https://doi.org/10.1038/nnano.2013.168>
94. J. Medford, J. Beil, J.M. Taylor, E.I. Rashba, H. Lu, A.C. Gossard, C.M. Marcus, Quantum-dot-based resonant exchange qubit. *Phys. Rev. Lett.* **111**, 050501 (2013). <https://doi.org/10.1103/PhysRevLett.111.050501>
95. R.W. Andrews, C. Jones, M.D. Reed, A.M. Jones, S.D. Ha, M.P. Jura, J. Kerckhoff, M. Levendorf, S. Meenehan, S.T. Merkel, A. Smith, B. Sun, A.J. Weinstein, M.T. Rakher, T.D. Ladd, M.G. Borselli, Quantifying error and leakage in an encoded Si/SiGe triple-dot qubit. *Nature Nanotechnology* **14**(8), 747 (2019). <https://doi.org/10.1038/s41565-019-0500-4>
96. E.A. Laird, J.M. Taylor, D.P. DiVincenzo, C.M. Marcus, M.P. Hanson, A.C. Gossard, Coherent spin manipulation in an exchange-only qubit. *Phys. Rev. B* **82**, 075403 (2010). <https://doi.org/10.1103/PhysRevB.82.075403>
97. L. Gaudreau, G. Granger, A. Kam, G.C. Aers, S.A. Studenikin, P. Zawadzki, M. Pioro-Ladriere, Z.R. Wasilewski, A.S. Sachrajda, Coherent control of three-spin states in a triple quantum dot. *Nature Physics* **8**, 54 (2012). <https://doi.org/10.1038/nphys2149>
98. K. Eng, T.D. Ladd, A. Smith, M.G. Borselli, A.A. Kiselev, B.H. Fong, K.S. Holabird, T.M. Hazard, B. Huang, P.W. Deelman, I. Milosavljevic, A.E. Schmitz, R.S. Ross, M.F. Gyure, A.T. Hunter, Isotopically enhanced triple-quantum-dot qubit. *Sci. Adv.* **1**, 1500214 (2015). <https://doi.org/10.1126/sciadv.1500214>. <https://advances.sciencemag.org/content/1/4/e1500214>
99. Y.P. Shim, C. Tahan, Charge-noise-insensitive gate operations for always-on, exchange-only qubits. *Phys. Rev. B* **93**, 121410 (2016). <https://doi.org/10.1103/PhysRevB.93.121410>
100. F.K. Malinowski, F. Martins, P.D. Nissen, S. Fallahi, G.C. Gardner, M.J. Manfra, C.M. Marcus, F. Kuemmeth, Symmetric operation of the resonant exchange qubit. *Phys. Rev. B* **96**, 045443 (2017). <https://doi.org/10.1103/PhysRevB.96.045443>
101. Z. Shi, C.B. Simmons, J.R. Prance, J.K. Gamble, T.S. Koh, Y.P. Shim, X. Hu, D.E. Savage, M.G. Lagally, M.A. Eriksson, M. Friesen, S.N. Coppersmith, Fast hybrid silicon double-quantum-dot qubit. *Phys. Rev. Lett.* **108**, 140503 (2012). <https://doi.org/10.1103/PhysRevLett.108.140503>
102. D. Kim, Z. Shi, C.B. Simmons, D.R. Ward, J.R. Prance, T.S. Koh, J.K. Gamble, D.E. Savage, M.G. Lagally, M. Friesen, S.N. Coppersmith, M.A. Eriksson, Quantum control and process tomography of a semiconductor quantum dot hybrid qubit. *Nature* **511**(7507), 70 (2014). <https://doi.org/10.1038/nature13407>

103. B.H. Fong, S.M. Wandzura, Universal quantum computation and leakage reduction in the 3-qubit decoherence free subsystem. *Quantum Inf. Comput.* **11**(11-12) 1003–1018 (2011)
104. F. Setiawan, H.Y. Hui, J.P. Kestner, X. Wang, S.D. Sarma, Robust two-qubit gates for exchange-coupled qubits. *Phys. Rev. B* **89**, 085314 (2014). <https://doi.org/10.1103/PhysRevB.89.085314>. <https://link.aps.org/doi/10.1103/PhysRevB.89.085314>
105. M.P. Wardrop, A.C. Doherty, Characterization of an exchange-based two-qubit gate for resonant exchange qubits. *Phys. Rev. B* **93**, 075436 (2016). <https://doi.org/10.1103/PhysRevB.93.075436>. <https://link.aps.org/doi/10.1103/PhysRevB.93.075436>
106. D. Zeuch, R. Cipri, N.E. Bonesteel, Analytic pulse-sequence construction for exchange-only quantum computation. *Phys. Rev. B* **90**, 045306 (2014). <https://doi.org/10.1103/PhysRevB.90.045306>. <https://link.aps.org/doi/10.1103/PhysRevB.90.045306>
107. A. Auerbach, *Interacting electrons and quantum magnetism* (Springer Science & Business Media, 2012)
108. L. Tarruell, L. Sanchez-Palencia, Quantum simulation of the Hubbard model with ultracold fermions in optical lattices. *Comptes Rendus Physique* **19**(6), 365 (2018). <https://doi.org/10.1016/j.crhpy.2018.10.013>
109. P. Barthelemy, L.M.K. Vandersypen, Quantum dot systems: a versatile platform for quantum simulations. *Annalen der Physik* **525**(10-11), 808 (2013). <https://doi.org/10.1002/andp.201300124>
110. S. Bose, Quantum communication through spin chain dynamics: an introductory overview. *Contemporary Physics* **48**(1), 13 (2007). <https://doi.org/10.1080/00107510701342313>
111. A. Pal, D.A. Huse, Many-body localization phase transition. *Phys. Rev. B* **82**, 174411 (2010). <https://doi.org/10.1103/PhysRevB.82.174411>
112. F.R. Braakman, P. Barthelemy, C. Reichl, W. Wegscheider, L.M.K. Vandersypen, Long-distance coherent coupling in a quantum dot array. *Nature Nanotechnology* **8**, 432 (2013). <https://doi.org/10.1038/nnano.2013.67>
113. X. Wang, S. Yang, S. Das Sarma, Quantum theory of the charge-stability diagram of semiconductor double-quantum-dot systems. *Phys. Rev. B* **84**, 115301 (2011). <https://doi.org/10.1103/PhysRevB.84.115301>. <https://link.aps.org/doi/10.1103/PhysRevB.84.115301>
114. A. Singha, M. Gibertini, B. Karmakar, S. Yuan, M. Polini, G. Vignale, M. Katsnelson, A. Pinczuk, L. Pfeiffer, K. West, et al., Two-dimensional Mott-Hubbard electrons in an artificial honeycomb lattice. *Science* **332**(6034), 1176 (2011). <https://doi.org/10.1126/science.1204333>
115. M. Gibertini, A. Singha, V. Pellegrini, M. Polini, G. Vignale, A. Pinczuk, L.N. Pfeiffer, K.W. West, Engineering artificial graphene in a two-dimensional electron gas. *Phys. Rev. B* **79**, 241406 (2009). <https://doi.org/10.1103/PhysRevB.79.241406>. <https://link.aps.org/doi/10.1103/PhysRevB.79.241406>
116. K.W. Chan, H. Sahasrabudhe, W. Huang, Y. Wang, H.C. Yang, M. Veldhorst, J.C.C. Hwang, F.A. Mohiyaddin, F.E. Hudson, K.M. Itoh, A. Saraiva, A. Morello, A. Laucht, R. Rahman, A.S. Dzurak, Exchange coupling in a linear chain of three quantum-dot spin qubits in silicon. *Nano Letters* **21**(3), 1517–1522 (2020). <https://doi.org/10.1021/acs.nanolett.0c04771>
117. Y. Nagaoka, Ferromagnetism in a narrow, almost half-filled *s* band. *Phys. Rev.* **147**, 392 (1966). <https://doi.org/10.1103/PhysRev.147.392>. <https://link.aps.org/doi/10.1103/PhysRev.147.392>
118. Y.P. Kandel, H. Qiao, S. Fallahi, G.C. Gardner, M.J. Manfra, J.M. Nichol, Adiabatic quantum state transfer in a semiconductor quantum-dot spin chain. *Nature Communications* **12**(1), 2156 (2021). <https://doi.org/10.1038/s41467-021-22416-5>
119. H. Qiao, Y.P. Kandel, S. Fallahi, G.C. Gardner, M.J. Manfra, X. Hu, J.M. Nichol, Long-distance superexchange between semiconductor quantum-dot electron spins. *Phys. Rev. Lett.* **126**, 017701 (2021). <https://doi.org/10.1103/PhysRevLett.126.017701>
120. R. de Sousa, X. Hu, S. Das Sarma, Effect of an inhomogeneous external magnetic field on a quantum-dot quantum computer. *Phys. Rev. A* **64**, 042307 (2001). <https://doi.org/10.1103/PhysRevA.64.042307>
121. D. Bacon, S.T. Flammia, Adiabatic gate teleportation. *Phys. Rev. Lett.* **103**, 120504 (2009). <https://doi.org/10.1103/PhysRevLett.103.120504>

122. N.V. Vitanov, A.A. Rangelov, B.W. Shore, K. Bergmann, Stimulated Raman adiabatic passage in physics, chemistry, and beyond. *Rev. Mod. Phys.* **89**, 015006 (2017). <https://doi.org/10.1103/RevModPhys.89.015006>
123. E. Farhi, J. Goldstone, S. Gutmann, M. Sipser, Quantum computation by adiabatic evolution, arXiv:quant-ph/0001106 (2000). <https://doi.org/10.48550/arXiv.quant-ph/0001106>
124. A.D. Greentree, J.H. Cole, A.R. Hamilton, L.C.L. Hollenberg, Coherent electronic transfer in quantum dot systems using adiabatic passage. *Phys. Rev. B* **70**, 235317 (2004). <https://doi.org/10.1103/PhysRevB.70.235317>
125. V. Srinivasa, J. Levy, C.S. Hellberg, Flying spin qubits: A method for encoding and transporting qubits within a dimerized Heisenberg spin- $\frac{1}{2}$ chain. *Phys. Rev. B* **76**, 094411 (2007). <https://doi.org/10.1103/PhysRevB.76.094411>
126. D. Petrosyan, G.M. Nikolopoulos, P. Lambropoulos, State transfer in static and dynamic spin chains with disorder. *Phys. Rev. A* **81**, 042307 (2010). <https://doi.org/10.1103/PhysRevA.81.042307>
127. N. Chancellor, S. Haas, Using the J_1 - J_2 quantum spin chain as an adiabatic quantum data bus. *New J. Phys.* **14**(9), 095025 (2012). <https://doi.org/10.1088/1367-2630/14/9/095025>
128. S. Oh, Y.P. Shim, J. Fei, M. Friesen, X. Hu, Resonant adiabatic passage with three qubits. *Phys. Rev. A* **87**, 022332 (2013). <https://doi.org/10.1103/PhysRevA.87.022332>
129. U. Farooq, A. Bayat, S. Mancini, S. Bose, Adiabatic many-body state preparation and information transfer in quantum dot arrays. *Phys. Rev. B* **91**, 134303 (2015). <https://doi.org/10.1103/PhysRevB.91.134303>
130. R. Menchon-Enrich, A. Benseny, V. Ahufinger, A.D. Greentree, T. Busch, J. Mompart, Reports on progress in physics spatial adiabatic passage: A review of recent progress related content. *Rep. Prog. Phys.* **79**, 074401 (2016). <https://doi.org/10.1088/0034-4885/79/7/074401>
131. Y. Ban, X. Chen, S. Kohler, G. Platero, Spin entangled state transfer in quantum dot arrays: Coherent adiabatic and speed-up protocols. *Adv. Quantum Tech.* **2**(10) (2019). <https://doi.org/10.1002/qute.201900048>
132. M.J. Gullans, J.R. Petta, Coherent transport of spin by adiabatic passage in quantum dot arrays. *Phys. Rev. B* **102**, 155404 (2020). <https://doi.org/10.1103/PhysRevB.102.155404>
133. S. Bose, Quantum communication through an unmodulated spin chain. *Phys. Rev. Lett.* **91**, 207901 (2003). <https://doi.org/10.1103/PhysRevLett.91.207901>
134. A. Wójcik, T. Łuczak, P. Kurzyński, A. Grudka, T. Gdala, M. Bednarska, Unmodulated spin chains as universal quantum wires. *Phys. Rev. A* **72**, 034303 (2005). <https://doi.org/10.1103/PhysRevA.72.034303>
135. L. Campos Venuti, C. Degli Esposti Boschi, M. Roncaglia, Long-distance entanglement in spin systems. *Phys. Rev. Lett.* **96**, 247206 (2006). <https://doi.org/10.1103/PhysRevLett.96.247206>
136. M. Friesen, A. Biswas, X. Hu, D. Lidar, Efficient multiqubit entanglement via a spin bus. *Phys. Rev. Lett.* **98**, 230503 (2007). <https://doi.org/10.1103/PhysRevLett.98.230503>
137. S. Oh, M. Friesen, X. Hu, Even-odd effects of heisenberg chains on long-range interaction and entanglement. *Phys. Rev. B* **82**, 140403 (2010). <https://doi.org/10.1103/PhysRevB.82.140403>
138. S. Oh, L.A. Wu, Y.P. Shim, J. Fei, M. Friesen, X. Hu, Heisenberg spin bus as a robust transmission line for quantum-state transfer. *Phys. Rev. A* **84**, 022330 (2011). <https://doi.org/10.1103/PhysRevA.84.022330>
139. T.A. Baart, T. Fujita, C. Reichl, W. Wegscheider, L.M.K. Vandersypen, Coherent spin-exchange via a quantum mediator. *Nature Nanotechnology* **12**, 26 (2016). <https://doi.org/10.1038/nnano.2016.188>
140. F.K. Malinowski, F. Martins, T.B. Smith, S.D. Bartlett, A.C. Doherty, P.D. Nissen, S. Fallahi, G.C. Gardner, M.J. Manfra, C.M. Marcus, F. Kuemmeth, Fast spin exchange across a multielectron mediator. *Nature Communications* **10**(1), 1196 (2019). <https://doi.org/10.1038/s41467-019-09194-x>

141. M. Schreiber, S.S. Hodgman, P. Bordia, H.P. Lüschen, M.H. Fischer, R. Vosk, E. Altman, U. Schneider, I. Bloch, Observation of many-body localization of interacting fermions in a quasirandom optical lattice. *Science* **349**(6250), 842 (2015). <https://doi.org/10.1126/science.aaa7432>
142. J.y. Choi, S. Hild, J. Zeiher, P. Schauß, A. Rubio-Abadal, T. Yefsah, V. Khemani, D.A. Huse, I. Bloch, C. Gross, Exploring the many-body localization transition in two dimensions. *Science* **352**(6293), 1547 (2016). <https://doi.org/10.1126/science.aaf8834>
143. S.S. Kondov, W.R. McGehee, W. Xu, B. DeMarco, Disorder-induced localization in a strongly correlated atomic Hubbard gas. *Phys. Rev. Lett.* **114**, 083002 (2015). <https://doi.org/10.1103/PhysRevLett.114.083002>
144. J. Smith, A. Lee, P. Richerme, B. Neyenhuus, P.W. Hess, P. Hauke, M. Heyl, D.A. Huse, C. Monroe, Many-body localization in a quantum simulator with programmable random disorder. *Nature Physics* **12**(10), 907 (2016). <https://doi.org/10.1038/nphys3783>
145. K.X. Wei, C. Ramanathan, P. Cappellaro, Exploring localization in nuclear spin chains. *Phys. Rev. Lett.* **120**, 070501 (2018). <https://doi.org/10.1103/PhysRevLett.120.070501>
146. V. Khemani, A. Lazarides, R. Moessner, S.L. Sondhi, Phase structure of driven quantum systems. *Phys. Rev. Lett.* **116**, 250401 (2016). <https://doi.org/10.1103/PhysRevLett.116.250401>
147. D.V. Else, B. Bauer, C. Nayak, Floquet time crystals. *Phys. Rev. Lett.* **117**, 090402 (2016). <https://doi.org/10.1103/PhysRevLett.117.090402>
148. C.W. von Keyserlingk, S.L. Sondhi, Phase structure of one-dimensional interacting Floquet systems. II. symmetry-broken phases. *Phys. Rev. B* **93**, 245146 (2016). <https://doi.org/10.1103/PhysRevB.93.245146>
149. N.Y. Yao, A.C. Potter, I.D. Potirniche, A. Vishwanath, Discrete time crystals: Rigidity, criticality, and realizations. *Phys. Rev. Lett.* **118**, 030401 (2017). <https://doi.org/10.1103/PhysRevLett.118.030401>
150. E. Barnes, J.M. Nichol, S.E. Economou, Stabilization and manipulation of multispin states in quantum-dot time crystals with heisenberg interactions. *Phys. Rev. B* **99**, 035311 (2019). <https://doi.org/10.1103/PhysRevB.99.035311>
151. J. Zhang, P.W. Hess, A. Kyprianidis, P. Becker, A. Lee, J. Smith, G. Pagano, I.D. Potirniche, A.C. Potter, A. Vishwanath, N.Y. Yao, C. Monroe, Observation of a discrete time crystal. *Nature* **543**(7644), 217 (2017). <https://doi.org/10.1038/nature21413>
152. S. Choi, J. Choi, R. Landig, G. Kucsko, H. Zhou, J. Isoya, F. Jelezko, S. Onoda, H. Sumiya, V. Khemani, C. von Keyserlingk, N.Y. Yao, E. Demler, M.D. Lukin, Observation of discrete time-crystalline order in a disordered dipolar many-body system. *Nature* **543**(7644), 221 (2017). <https://doi.org/10.1038/nature21426>
153. J. Rovny, R.L. Blum, S.E. Barrett, Observation of discrete-time-crystal signatures in an ordered dipolar many-body system. *Phys. Rev. Lett.* **120**, 180603 (2018). <https://doi.org/10.1103/PhysRevLett.120.180603>
154. S. Pal, N. Nishad, T.S. Mahesh, G.J. Sreejith, Temporal order in periodically driven spins in star-shaped clusters. *Phys. Rev. Lett.* **120**, 180602 (2018). <https://doi.org/10.1103/PhysRevLett.120.180602>
155. B. Li, J.S. Van Dyke, A. Warren, S.E. Economou, E. Barnes, Discrete time crystal in the gradient-field heisenberg model. *Phys. Rev. B* **101**, 115303 (2020). <https://doi.org/10.1103/PhysRevB.101.115303>
156. J.S. Van Dyke, Y.P. Kandel, H. Qiao, J.M. Nichol, S.E. Economou, E. Barnes, Protecting quantum information in quantum dot spin chains by driving exchange interactions periodically. *Phys. Rev. B* **103**, 245303 (2021). <https://doi.org/10.1103/PhysRevB.103.245303>
157. H. Flentje, P.A. Mortemousque, R. Thalineau, A. Ludwig, A.D. Wieck, C. Bäuerle, T. Meunier, Coherent long-distance displacement of individual electron spins. *Nature Communications* **8**(1), 501 (2017)
158. Y.P. Kandel, H. Qiao, S. Fallahi, G.C. Gardner, M.J. Manfra, J.M. Nichol, Coherent spin-state transfer via heisenberg exchange. *Nature* **573**(7775), 553 (2019). <https://doi.org/10.1038/s41586-019-1566-8>

159. H. Qiao, Y.P. Kandel, S.K. Manikandan, A.N. Jordan, S. Fallahi, G.C. Gardner, M.J. Manfra, J.M. Nichol, Conditional teleportation of quantum-dot spin states. *Nature Communications* **11**(1), 3022 (2020). <https://doi.org/10.1038/s41467-020-16745-0>
160. A.G. Fowler, C.D. Hill, L.C.L. Hollenberg, Quantum-error correction on linear-nearest-neighbor qubit arrays. *Phys. Rev. A* **69**, 042314 (2004). <https://doi.org/10.1103/PhysRevA.69.042314>
161. N.M. Linke, D. Maslov, M. Roetteler, S. Debnath, C. Figgatt, K.A. Landsman, K. Wright, C. Monroe, Experimental comparison of two quantum computing architectures. *Proc. Natl. Acad. Sci.* **114**(13), 3305 (2017). <https://doi.org/10.1073/pnas.1618020114>
162. T. Fujita, T.A. Baart, C. Reichl, W. Wegscheider, L.M.K. Vandersypen, Coherent shuttle of electron-spin states. *npj Quantum Inf.* **3**(1), 22 (2017). <https://doi.org/10.1038/s41534-017-0024-4>
163. T. Nakajima, M.R. Delbecq, T. Otsuka, S. Amaha, J. Yoneda, A. Noiri, K. Takeda, G. Allison, A. Ludwig, A.D. Wieck, X. Hu, F. Nori, S. Tarucha, Coherent transfer of electron spin correlations assisted by dephasing noise. *Nature Communications* **9**(1), 2133 (2018). <https://doi.org/10.1038/s41467-018-04544-7>
164. J. Yoneda, W. Huang, M. Feng, C.H. Yang, K.W. Chan, T. Tanttu, W. Gilbert, R. Leon, F. Hudson, K. Itoh, et al., Coherent spin qubit transport in silicon. *Nature Communications* **12**(1), 1 (2021). <https://doi.org/10.1038/s41467-021-24371-7>
165. C.H. Bennett, G. Brassard, C. Crépeau, R. Jozsa, A. Peres, W.K. Wootters, Teleporting an unknown quantum state via dual classical and Einstein-Podolsky-Rosen channels. *Phys. Rev. Lett.* **70**, 1895 (1993). <https://doi.org/10.1103/PhysRevLett.70.1895>
166. R.L. de Visser, M. Blaauboer, Deterministic teleportation of electrons in a quantum dot nanostructure. *Phys. Rev. Lett.* **96**, 246801 (2006). <https://doi.org/10.1103/PhysRevLett.96.246801>
167. P.A. Mortemousque, E. Chanrion, B. Jadot, H. Flentje, A. Ludwig, A.D. Wieck, M. Urdampilleta, C. Bäuerle, T. Meunier, Coherent control of individual electron spins in a two-dimensional quantum dot array. *Nature Nanotechnology* **16**(3), 296 (2021). <https://doi.org/10.1038/s41565-020-00816-w>
168. E.J. Connors, J. Nelson, H. Qiao, L.F. Edge, J.M. Nichol, Low-frequency charge noise in Si/SiGe quantum dots. *Phys. Rev. B* **100**, 165305 (2019). <https://doi.org/10.1103/PhysRevB.100.165305>
169. E.J. Connors, J. Nelson, J.M. Nichol, Charge-noise spectroscopy of Si/SiGe quantum dots via dynamically-decoupled exchange oscillations, *Nature Communications* **13**, 940 (2022). <https://doi.org/10.1038/s41467-022-28519-x>
170. X. Wang, L.S. Bishop, J.P. Kestner, E. Barnes, K. Sun, S. Das Sarma, Composite pulses for robust universal control of singlet-triplet qubits. *Nature Communications* **3**, 997 (2012). <https://doi.org/10.1038/ncomms2003>
171. J.P. Kestner, X. Wang, L.S. Bishop, E. Barnes, S. Das Sarma, Noise-resistant control for a spin qubit array. *Phys. Rev. Lett.* **110**, 140502 (2013). <https://doi.org/10.1103/PhysRevLett.110.140502>. <https://link.aps.org/doi/10.1103/PhysRevLett.110.140502>
172. G.T. Hickman, X. Wang, J.P. Kestner, S. Das Sarma, Dynamically corrected gates for an exchange-only qubit. *Phys. Rev. B* **88**, 161303 (2013). <https://doi.org/10.1103/PhysRevB.88.161303>. <https://link.aps.org/doi/10.1103/PhysRevB.88.161303>

Index

- A**
Affleck–Kennedy–Lieb–Tasaki (AKLT)
 model, vii, 4, 9, 89–122, 343, 346–349,
 352–355, 361, 379, 380
Anderson localization, 61, 64–72, 83, 406
- C**
Cluster-Ising, 155–158
Conformal field theory (CFT), vi, viii, 6,
 41–56, 58, 77, 212, 214, 216, 234, 235,
 245, 255, 261, 399, 402–407, 409, 415
Critical
 exponents, 216, 223, 235, 237, 259,
 261–263, 437, 439
 point, vi, 15–20, 23, 24, 28, 29, 31, 32, 41,
 42, 64, 78, 81, 145, 162, 175, 177, 179,
 204, 242, 259, 261, 262, 264, 266, 278,
 399, 435–439, 454
- D**
Defects, vi, 41–58, 91, 437, 465, 476, 507, 509
Density matrix renormalization group
 (DMRG), 23, 34, 42, 43, 45, 46, 48,
 113, 116, 155, 163, 298, 299
Disorder, vi, 20, 61–84, 91, 101, 111, 121, 174,
 178, 204, 234, 254, 277, 316, 359, 366,
 384, 464, 472, 476, 483, 487, 494–497,
 507, 524, 525
Dynamical maps, 323–325, 335, 338
- E**
Echo, 17, 18, 37, 460, 466, 471, 477–481, 485
Eigenstate thermalisation, 252, 277, 343, 344,
 435, 454, 474
Entanglement, 1, 14, 41, 61, 107, 127, 151,
 197, 211, 252, 285, 321, 341, 397, 436,
 481
 distribution, vii, 81–83, 154, 181–183, 294,
 323, 327–329, 336
 entropy, vi, 1, 3, 6, 9, 21, 23, 28, 35, 41–58,
 61–84, 152, 171, 172, 215, 222, 223,
 225, 226, 228, 234, 235, 238, 242,
 254–257, 260–265, 267, 268, 274,
 286–289, 293, 297–300, 302–307, 312,
 313, 316, 342, 344, 346, 352, 353, 362,
 365–367, 400, 409, 436, 442–444
 negativity, vii, 17, 75, 127–132, 137–139,
 141–145, 147, 298, 399–402, 408, 410,
 411, 414–416, 417
 spectra, 1–9
 von Neuman entropy, 73
Entanglement spectrum, vi, 1, 3, 4, 6–9, 23,
 56, 156–162, 165
Exchange coupling, viii, 505, 506, 510–518,
 520–527
- H**
Haldane phase, 2, 4–6, 9, 102, 105, 156, 158,
 159
Haldane–Shastry (HS) model, 7, 9
Hamiltonian engineering, viii, 466–473, 482,
 489, 495, 498
Heisenberg model (or Heisenberg chain),
 v, 2, 6–8, 63–64, 80, 81, 83, 90,
 113, 272, 273, 275, 301, 506, 5018,
 520–525

Hilbert space fragmentation, vii, 343, 355–360, 363, 380, 383, 384, 448–453
 Hubbard model, 17, 18, 21–23, 29, 30, 288, 352–354, 359, 382–386, 425, 429, 448, 506, 511, 518–522, 528
 Hydrodynamics, 212, 218, 219, 252, 271, 273, 274, 278, 279, 407, 408

I

Integrability, v, 14, 362, 363, 377, 399
 Ising chain, v, 45, 46, 49, 51–53, 55, 63–65, 72–80, 83, 145, 155, 166–174, 203, 293, 304, 306, 413, 525

L

Lambda (λ)– D model, 155–162
 Lieb–Robinson bounds, 285, 286, 288–293, 302, 308, 309, 374
 Local convertibility, vii, 151–184
 Local operations and classical communications (LOCCs), vii, 152, 154, 322, 323, 332, 334
 Logarithmic negativity, 128–132, 137–139, 141–147, 398–402, 408, 416, 417
 Long-range interactions, vii, 285–316
 Loschmidt echo, 17, 18, 37, 460, 477–480

M

Machine learning, vii, 127–147, 473, 513, 527
 Many-body entanglement, 68–72, 83, 181–183, 225, 302, 307, 312, 398
 Many-body localization (MBL), vi, 63–65, 70, 80–84, 214, 223, 252, 254, 277, 279, 316, 342, 343, 345, 359, 383, 384, 494–497, 518, 524, 525
 Many-body quantum chaos, 212, 308
 Many-body systems, v, 1, 9, 15, 37, 43, 127–147, 252–254, 268, 271, 278, 298, 342–344, 346, 347, 351, 370, 382–383, 386, 398, 417, 439, 448, 497
 Matrix product states (MPS), vii, 3, 5, 6, 91–95, 97–102, 105, 117, 118, 146, 163, 164, 173, 192, 197, 214, 253, 279, 296–300, 303, 304, 343, 345–352, 366, 367, 370, 371, 373, 374, 376, 377, 380, 437
 Mixed states, v, 5, 25, 26, 52, 53, 128, 129, 133, 134, 140, 146, 147, 154, 177, 213, 224, 225, 227, 228, 242, 244, 255, 256, 258, 287, 335, 336, 398–403, 417, 474, 478, 479, 491–493

N

Non-equilibrium dynamics, 140, 212, 298, 314, 426, 434–448
 Nuclear magnetic resonance (NMR), vi, vii, 18, 459–500

O

Open quantum systems, 191, 206, 212, 213, 253, 267, 323, 354
 Out-of-time-order correlators (OTOCs), 37, 218, 289–292, 308, 476, 479–489, 494

P

Partial trace, 2, 140, 177, 197, 230, 234, 324, 336, 337, 487
 Partial transpose, 129, 130, 135, 398, 399, 401–404, 410, 413–417
 Parent Hamiltonian, vii, 95, 96, 118–120, 189–206
 Phase transitions, 13, 117, 143, 153, 212, 253, 303, 425, 462
 PXP model, 344, 359, 361–371, 373–380, 382, 386, 432, 446, 452, 453

Q

Quantum
 chaos, 212, 218, 252
 circuits, vii, 103, 153, 206, 211–246, 252, 255–268, 270, 278, 279, 299, 359–360
 control, 252, 387, 460, 465, 516
 correlations, 14, 19, 25–26, 29, 33, 36, 37, 154, 176–180, 199, 252, 253, 322, 334, 342, 346, 400
 dot, viii, 14, 147, 239, 505–528
 entanglement, v, vii, 1, 3, 14–20, 23, 25, 26, 29, 61, 128, 227, 253, 254, 341–387, 416
 ergodicity, 341–387
 estimation, vii, 144
 information, vi–viii, 3, 14–20, 22, 33, 37, 128, 138, 212, 213, 224, 226, 227, 245, 252, 257, 268, 279, 289, 290, 311, 314, 316, 322, 338, 387, 408, 460, 463, 465, 466, 471, 477, 481, 491, 509, 513–518, 523, 525, 528
 many-body chaos, 308
 many-body physics, 3, 26, 211, 271–278, 316
 measurements, 127–147, 255

- phase transition, v, vi, 13–37, 143–144, 153, 155, 159, 164, 167, 173, 425, 433, 454
 quantum state transfer, vii, viii, 302, 322, 323, 327, 334, 338, 491–493, 506, 522, 523, 525–528
 quenches, 37, 140, 144, 145, 342, 397, 399, 404, 406, 407, 417
 scars, 342–344, 374, 375, 377, 382, 436, 443, 445, 448, 454
 simulation, vii, 251–279, 288, 299, 464, 466, 469, 471, 491, 497, 498, 506, 507, 518–525, 528
 simulators, vi, vii, 18, 37, 212, 285, 341, 343, 380, 386, 485, 494
 spin chains, 2, 13–37, 41–58, 80, 314, 321–338
 Quasiparticle picture, 303, 305, 397–417
- R**
 Randomness, 61–63, 65, 67, 72–80, 83, 84, 110, 223, 268, 273
 Random quantum states, vii, 147, 276, 279
 Random singlet, 63, 72–75, 77, 83
 Random unitary circuits, 212–220, 260
 Reduced density matrix (RDM), 2, 4, 6, 19, 21, 24, 33–37, 56, 80, 140, 152, 157, 158, 160, 162, 164, 170–172, 175–177, 180, 197, 198, 214, 222, 254, 259, 260, 274, 286, 287, 289, 296, 297, 300, 342, 344, 398, 400, 401, 404, 412–415, 417, 442
 Rényi entropy, 152, 172, 173, 220, 230, 233, 259–261, 267, 287, 399, 410, 485–489
- S**
 Schmidt
 decomposition, 2, 3, 169
 rank, 152, 164, 216
 Scrambling, 212, 213, 221, 222, 225, 227, 229, 243, 257, 286, 288, 289, 307–314, 316, 387, 408, 483, 484
 Semiclassical dynamics, 345, 370–374, 380
 Semiconductor, viii, 505–510, 512–514, 518–520, 524, 527
 Spin chain, 1, 13, 41, 77, 91, 143, 279, 285, 321, 343, 415, 429, 476, 505
 Spin ladders, 3, 6, 22
 Spin qubit, 239, 271, 460, 465, 491, 506, 507, 513–518, 523, 524, 527, 528
- T**
 Tensor network, vii, 89–122, 142, 212–214, 216, 224, 229, 231, 246, 268, 321, 344
 Toric code, 155, 161–166, 241, 362
- U**
 Ultracold bosons, viii, 425–454
 Universality of detector, 18
- X**
 XXZ model (or XXZ chain), 18, 20, 27, 31, 32, 43, 48, 54, 55, 62, 63, 72, 301, 349
 XY model (or XY chain), 17, 19, 20, 301, 352, 380, 489, 491